The Dissertation Committee for John Noel Hooker certifies that this is the approved version of the following dissertation:

Fracture Scaling and Diagenesis

Committee:

Stephen E. Laubach, Supervisor

Randall Marrett, Co-Supervisor

Peter Eichhubl

Sergey Fomel

Brian K. Horton

Richard A. Ketcham

Jon E. Olson

John M. Sharp, Jr.

Fracture Scaling and Diagenesis

by

John Noel Hooker, B.A., M.S. Geo. Sci.

Dissertation

Presented to the Faculty of the Graduate School of
The University of Texas at Austin
in Partial Fulfillment
of the Requirements
for the Degree of

Doctor of Philosophy

The University of Texas at Austin
December 2012

For Jill and Augie

You're all I see

Acknowledgments

I began collecting microfracture data as part of my work as a graduate research assistant in support of my master's research. Specifically, I collected fracture scaling data from the Cozzette Formation (SHCT well) starting in 2004 with the help of the co-authors of Hooker et al. (2009), in which most of those data were originally published. The scaling data from the Eriboll Formation, samples 1 and 3-6 (see Appendix A), were collected by Kira Diaz-Tushman and Edgar Pinzon, and published in Hooker et al. (2011). Some data from Figure 4-17 and 4-18, also from the Eriboll Formation, were collected with the help of Frank Morgan and reported in Morgan (2011). Sample 42 was collected with the help of Meghan Playton (née Ward) and Leonel Gomez.

Fracture size data from carbonate rocks (Chapter 4) not included in Marrett et al. (1999) were collected by me, Leonel Gomez, and Julia Gale, with various field assistants. These data were assembled and published in Hooker et al. (2012). The fracture growth simulation introduced in Chapter 5 is a generalized version of that described in Hooker et al. (2012). Most SEM-CL imaging was performed at the Scanning Electron Microscopy Lab at the Bureau of Economic Geology (BEG); the rest was done at the SEM lab in the Jackson School of Geosciences building at the University of Texas at Austin. Fluid inclusion analyses were performed at the Fracture Research and Application Consortium (FRAC) Fluid Inclusion Lab at the BEG. The stable isotope analysis (Chapter 6) was supervised by Toti Larson at the Jackson School of Geosciences High Temperature Stable Isotope Lab. Jaime Barnes and Dan Breecker provided guidance and discussion. András Fall provided a helpful review for that chapter. An early version of Chapter 7, based on less data and without the comparison to Narr's (1996) method, was published in Hooker and

Laubach (2010). Contributions to the petrographic data in Chapter 8 were made by Tarek Elshayeb, Astrid Makowitz, Orlando Ortega, and Aysen Ozkan.

Most of the core samples were provided by FRAC industrial associates. This research was funded in part by FRAC, the GDL Foundation, and a Jackson School of Geosciences Seed Grant (Sandstone Provenance, 2006). This research was supported by grant DE-FG02-03ER15430 from Chemical Sciences, Geosciences and Biosciences Division, Office of Basic Energy Sciences, Office of Science, U.S. Department of Energy.

Thanks to Steve Laubach, who for years has shown me how to do good science, from looking at rock to telling a peer about it. Thanks to Randy Marrett, whose skill at observing and interpreting the Earth is unparalleled. My deepest gratitude to Peter Eichhubl, Jon Olson, Rich Ketcham, Brian Horton, Jack Sharp, and Sergey Fomel for greatly improving this work.

Julia Gale has provided invaluable direction for me. More than once she has taken a manuscript or presentation of mine from embarrassing to acceptable, including much of what is in this dissertation.

I have lots of reasons to thank András Fall, Esti Ukar, Tobias Weisenberger, and Maria Nikolinakou, but their reliable presence—with insight, advice, and coffee—especially through the final birthing throes of this work, tops them. Thank you, thank you, thank you.

I am especially grateful to have worked with many talented master's students associated with FRAC over the years, including Kira Diaz-Tushman, Juan Iñigo, Pete Hargrove, Maggie Ellis, Autumn Eakin (née Kaylor), Meghan Playton, Cecilia Xu, Alex Urquhart, Brandon Barber, Tim Gibbons, Natalia Kalitynska, Luke Fidler, Laura Pommer, and Edgar Pinzon. The pleasure, and probably most of the learning, was all mine.

Likewise I must thank Leonel Gomez, Orlando Ortega, Faustino Monroy, Gareth Cross, Arash Dahi, and Peggy Rijken for showing me how to navigate the treacherous waters of Ph.D. research in fracture science.

Rob Reed trained me to use the SEM and has proven time and again to be a veritable wizard in producing quality images of tiny fractures. Thanks to Hyein Ahn and Karen Black for imaging help.

I am grateful for years of support, guidance, and encouragement from Scott Tinker and Eric Potter. My work at the BEG was facilitated in countless ways by many staff members, including Sammy Jacobo, Lana Dieterich, Claudia Gerardo, Kenneth Edwards, Josh Lambert, George Bush, Chuck Garza, Ron Russell, James Donnelly, Gwen Hebert, Melissa Garcia, and Jenny Turner.

Valuable discussion was provided by Kitty Milliken, Larry Lake, Steve Becker, Jon Holder, Alison Mote, Jack Holt, David Freire, Aysen Ozkan, Martin Jackson, Bill Ambrose, Iona Williams, Gail Christeson, Farrokh Sheibani, Li Ji, Volker Braun, Steve Davis, Massimo Bonora, Scott Wilkins, Wayne Narr, Lucre Jorgensen, and Frank Morgan.

What could have been incredibly complicated vicissitudes within the Jackson School were made mercifully easy by Philip Guerrero.

In ways directly or tangentially related to my research, life for the past several years was made easy and fun by Ted Playton, Adam Krawiec, Liz Roller, Ned Frost and family, Ann Laubach and family, Uschi Hammes and family, Virginio Neumann and family, Joe Schaefer and family, Nathan Ivicic, John Shaw, Kyle Womack, Rebecca Comeaux, Mike Ramirez, Ben Andrews, Megan Franks, Peter Polito, Ephraim Taylor, Jay Banner, Isaac Smith, and Chris Bell.

Thanks to my family, and so many dear friends outside the geology community, who are the real reason the rocks are holding us up, after all.

Last, and most: thank you, Jill and Augie. Without you, what for?

Fracture Scaling and Diagenesis

John Noel Hooker, Ph.D.
The University of Texas at Austin, 2012

Supervisor: Stephen E. Laubach
Co-Supervisor: Randall Marrett

Abstract: Sets of natural opening-mode fractures in sedimentary rocks may show a variety of types of aperture-size distributions. A frequently documented size distribution type, in the literature and in data presented here, is the power law. The emergence of power-law distributions of fracture aperture and length sizes has been simulated using various quasi-mechanical fracture-growth routines but models based on linear-elastic fracture mechanics rarely produce such patterns. I collected a fracture-size dataset of unprecedented size and resolution using core and field methods and scanning electron microscope-based cathodoluminescence (SEM-CL) images. This dataset confirms the prevalence of power laws with a narrow range of power-law exponents among fractures that contain synkinematic cement. Organized microfractures are ubiquitous in sandstones. A fracture-growth simulation I devised reproduces observed size-scaling patterns by distributing fracture-opening increments among actively growing fractures. The simulated opening increments have a uniform size, which can be specified; uniform opening size is consistent with observations of narrow ranges of micron-scale widths of opening increments within crack-seal texture in natural fractures. Thus power-law size scaling of natural fractures can be explained using non-power-law (uniform-sized) opening increments, arranged using rules designed to simulate the effects of cement precipitation during fracture opening. A fundamental shortcoming of previous models of fracture-set evolution is the absence of a test because only natural fracture end states, not growth histories, could be measured. Using a technique to constrain fracture timing based on fluid inclusion microthermometry and thermal history modeling, I tested growth models by reconstructing the opening history of a set of natural fractures in the Triassic El Alamar Formation in northeast Mexico. The natural-fracture data show that, consistent with simulations, new microscopic fractures are continually introduced during natural fracture pattern evolution. As well, larger fractures represent sites of concentrated reactivation, although smaller fractures may be reactivated after long periods of quiescence. The pattern likely arises through feedback between fracture growth and the mechanically adhesive effects of contemporaneous fracture cement deposition. The narrow range in power-law exponents documented among fractures can help improve estimates of meter-scale large-fracture spacing where limited fracture samples are available.

Table of Contents

List of Tables

List of Figures

INTRODUCTION

Chapter 1: Progress in understanding natural-fracture size distributions in sedimentary rocks

Brittle fracture is one of the most common deformation mechanisms in the upper crust (Pollard and Aydin, 1988) but distribution of deformation within a growing fracture set remains mysterious. Many unknowns impede our understanding of fracture network evolution. For example, the timing of fracture formation is rarely well constrained and many loading paths can in principle account for fracture growth (Engelder, 1985). The rate of fracture growth for most fracture arrays is unknown; only recently have combined fluid inclusion and burial history models revealed the widening rates of some fractures (Becker et al., 2010). Discovering how fractures form and grow in natural fracture arrays is a central issue in understanding brittle fracture in the Earth. Numerical models of fracture growth and observations of fracture arrays in many different rock types and settings are compatible with many ways in which the architecture of a fracture set (i.e., the orientation, displacement, and spatial arrangement of the fractures) can accommodate strain in rock.

Predictive models combine first-principles of physics with hypothetical crustal deformation processes to simulate fracture sets. These sets vary in their statistical attributes, depending on how various factors, including rock properties, fluid pressure and migration, layer thickness, neighboring and pre-existing fractures, and magnitude of local and regional tectonic strain combine to control fracture growth (Hobbs, 1967; Olson, 1993; Cladouhos and Marrett, 1996; Aydin, 2000; Bai et al., 2000; Bergbauer and Pollard, 2004; Brenner and Gudmundsson, 2004; Olson, 2007; Poblet and Bulnes, 2007; Davy et al., 2010; Mróz and Mróz, 2010).

The sophistication and realism of such models have been guided by empirical research. For example, Gross and Engelder (1995) demonstrated how fracture size distribution, spatial distribution, and kinematic offset mode (opening versus shear) vary by rock type (dolostone versus mudstone) within the Miocene Monterey Formation. Gillespie et al. (2001) explained variations in fracture size distribution by the degree to which mechanical layering influenced fracture propagation in the Mississippian Burren limestones. Such empirical studies provide quantitative descriptions of natural fracture sets and establish possible host-rock controls on fracture formation and propagation. The accuracy and usefulness of any fracture model can be judged by how well it reproduces fracture patterns found in nature.

The most recent comprehensive review of fracture attributes does not describe size distributions or identify power-law size attributes (Pollard and Aydin, 1988). Inspection of outcrop joint sets (barren opening mode fractures) shows these fractures typically do not possess a wide range of sizes. Yet convincing power-law size distributions of some fractures have been documented (Gudmundsson, 1987; Wong et al., 1989; Sanderson et al., 1994; Bohnenstiehl and Kleinrock, 1999; Marrett et al., 1999; Bonnet et al., 2001; Ortega et al., 2006; Guerriero et al., 2010). Although fracture size is of critical importance to fluid storage, fluid flow, and rock strength (Marrett, 1996; Odling et al., 1999; Laubach et al., 2004b; Philip et al., 2005), the link between the *observation* that fractures sometimes follow power laws and our *understanding* of the mechanics that produce the power-law fracture-size distribution remains tenuous. In fact, geomechanical models that account for many aspects of brittle elastic fracture mechanics do not typically produce power-law fracture-size distributions (Olson et al., 2009).

Power-law size distributions arise in some numerical routines that postulate rules for fracture interaction during growth (Cowie et al., 1993; Clark et al., 1995; Cladouhos and Marrett, 1996). A common theme among such models is that large fractures emerge from dynamic interaction (e.g., linkage) among nearby smaller fractures. Indeed a common general observation of natural systems is that power laws result from *self-organized* interaction of components within dynamic systems (Bak et al., 1987; Barabási and Albert, 1999; Amaral et al., 2000; Albert and Barabási, 2002; Murray, 2007).

However, a mechanical understanding of the emergence of power-law size distributions among fractures, particularly opening-mode fractures, still does not exist. Attempts to model how fracture-size distributions arise have followed two paths. Models either employ rigorous treatments of fracture mechanics (Olson, 2007) or postulate growth and interaction rules that capture the effects of fracture mechanics or other processes, as described above. These two strategies have different advantages.

Adherence to fracture mechanics has the advantage of using non-arbitrary, realistic rules to produce quantifiable, scaled results. Two disadvantages to this approach are the limited capability of computers to reproduce the complexity of natural geologic settings, and the possibility that natural processes affect fracture growth that are not accounted for in the model. For example, models based on linear-elastic fracture mechanics might not accurately reproduce fracture patterns in settings affected by inelastic processes like pressure solution.

Conversely, abstract rule-based models have the advantage that they can potentially simulate a wide range of observed geologic phenomena when physically rigorous models will not, either because of conceptual incompleteness or limited computing capacity. The disadvantage to such *ad hoc* approaches is that their outcomes have limited physical justification—such models may be right for the wrong reason(s).

To deduce the key processes of brittle fracture empirical studies describe end states of fracture arrays. These studies have focused on the size, shape and arrangement of the fractures and their relationship to host rocks (Gross and Engelder, 1995; Odling, 1997; Gillespie et al., 2001). The descriptive focus of these studies is therefore on what would normally be considered the end products of mechanical processes. The field observations are comparable to the final output of mechanical and rule-based models. One obvious value of such studies is to test whether models replicate nature. Another is to discover phenomena currently not accounted for in either kind of model.

Unexplained discrepancies in fracture size predictions between various models, between models and field observations, and between field observations in different settings suggest that current modeling approaches do not adequately account for the development of fracture-size populations. New field data presented in this study highlight this inadequacy.

Although many geologic fracture arrays contain cement deposits, previous empirical studies and models neglect chemical or diagenetic aspects of fracture growth. Both modeling approaches make the implicit assumption that the key interactive processes that lead to size scaling are mechanical. What if they are not? Evidence from metamorphic rocks, in which mineral precipitation is not as easily overlooked, point to a mechanical importance of fracture fill. For example, Fagereng (2011) posits that strong vein material in fractures within the Otago Schist may have favored the creation of new fractures over the re-fracturing of extant ones, thus affecting the veins’ thickness distribution. This hypothesis is close to the concept that I have been exploring for sedimentary rocks (Hooker et al., 2012).

Cement precipitation during fracture growth could be a critical ingredient affecting the size distribution of the evolving fracture set. Cement is commonly found in fracture arrays that exhibit power-law opening displacement distributions (Marrett et al., 1999; Ortega et al., 2006; Hooker et al., 2009; Hooker et al., 2011) and is lacking (by definition) in joint sets that typically have narrow size ranges (Peacock, 2004). Under moderate to deep subsurface conditions (>80°C) cement is commonly deposited in fractures while they grow (Laubach et al., 2004a). Although we lack a full incorporation of the effects of cement precipitation within linear-elastic fracture mechanics models (Olson et al., 2009), the resistance to further opening by partial or complete filling of fracture cement could radically alter the resulting aperture-size distribution.

Here I test the hypothesis that the interaction between fracture opening and sealing produces power-law size distributions. I show that the mineral cements and fluid inclusions trapped during fracture growth provide an independent approach to exploring how fracture size scaling arises by showing direct evidence for the first time of how natural fracture arrays grow.

In Chapter 2 I describe the method I employed for collecting fracture size data and some important pitfalls in objectively characterizing the size distribution of natural fractures. This study is based on 1D line-of-observation (scanline) data of the opening displacements or widths of fractures, called kinematic apertures by Marrett et al. (1999). This measurement represents the cumulative opening displacement of fractures, regardless of fill. The parts of the fracture which are open versus cement-filled are measured separately. Kinematic aperture measurements, like all fracture-size surveys, are afflicted by certain sampling biases, both previously documented in the literature and newly identified in this study. In the same chapter I argue that irregular fracture-scaling data trends derive from a variety of sources, both artificial and natural.

In Chapter 3 I support my central claim by introducing a kinematic-aperture scanline dataset of unprecedented size and resolution. I collected the data from large scanlines (up to meter-scale lengths) mapped using scanning electron microscope-based cathodoluminescence (SEM-CL), as well as from field data measured using a hand lens. This dataset comprises 59 scanlines, containing over 4,200 fractures, from eight formations on three continents (Table 1-1; Appendix A). The data show that natural fracture sets in sandstones follow various types of size distributions, and that power-law size distributions have two important characteristics in common. Namely, power-law size distributions feature exponents (see Chapter 2, Equation 1) of a characteristic value, with a narrow range. Also, in many cases power-law-distributed fractures grew by characteristic-sized opening increments, preserved in bridges of cement that precipitated while the fractures were opening.

	Sub-topic	Title	Hypothesis	Approach
Chapter 2	**Empirical approach to fracture scaling**	1: Interpreting size distribution curves	Scaling data curves are affected by familiar and undocumented sampling biases, and natural complexities	Simulate effects of pixelation on fracture-size measurement
				Examine fractures using SEM-CL at different magnifications
				Literature review of known biases
Chapter 3		2: A new high-resolution scaling dataset	Opening-mode fractures in sandstone show broadly consistent size distributions over a wide range of geologic settings	Collect aperture-size data from sandstones, in the field and using SEM-CL
				Fracture scaling dataset: 59 scanlines, 8 formations, **4286** fractures
Chapter 4		3: Controls on scaling exponent	The characteristic fracture scaling exponent is a natural attractor	Demonstrate correlation of scaling exponent with host-rock type, degree of fracture clustering
				Explore the relationship between scaling exponent and structural position
Chapter 5	**Understanding fracture-set evolution**	1: Simulations	Simulations of the distribution of opening increments among fractures in a set are consistent with observed size distributions and cement textures	Develop rule-based model for growing sets of fractures
				Incorporate the effect of competing fracture opening rate, fracture cementation rate
Chapter 6		2: Tracking fracture opening using fluid inclusion microthermometry	Consistent with simulation history, fractures open over protracted histories and simultaneously with other fractures	Constrain fracture timing using fluid inclusion microthermometry and independently-established burial history
				Trace fluid-rock evolution using oxygen isotopes from synkinematic fracture cements
Chapter 7	**Fracture scaling applied**	Subsurface fracture frequency estimation using core samples	The characteristic scaling exponent can be used to improve subsurface fracture frequency estimation	Extrapolate fracture frequency using core-width scanlines and compare to observed large-fracture frequency from slant cores
				Derive error estimation assuming Poissonian fracture intersection probability
Chapter 8	**Intragranular microfractures**	An inventory of microfractures in sandstones observed using SEM-CL	Natural sandstones have myriad microfractures of various origin and applicability to scaling studies	Describe and map fractures within SEM-CL mosaics from sandstone thin sections
				Microfracture morphology/density dataset: 18 formations, **27,270** microfractures

Table 1-1. Summary of chapters within this dissertation.

In Chapter 4 I investigate the small amount of variation that is present in the scaling exponent. I document some systematic variation of the exponent with rock type (between thoroughly indurated quartzarenites and other sandstones), and the degree to which fractures are clustered versus evenly spaced. The scaling exponent appears to be unrelated to host-rock grain size. Tests of exponent versus structural position produced mixed results.

In Chapter 5 I illustrate how cement precipitation might affect fracture growth using a rule-based numerical model. The model generates fractures iteratively, by adding increments of fracture growth to new and pre-existing fractures. Depending on the setup parameters, including increment width, fracture-growth selection probability, and flaw size distribution, resulting size distributions may be best fit by power-law, exponential, or log-normal equations. As well, the simulated fracture sets may be stable, with growth shared among the fractures, or unstable, with a small subset of fractures growing at the expense of others. Specific parameter setups are consistent with the statistics of opening-increment widths as well scaling exponents, both of which I describe in Chapter 3. I use the model to test the effects of changing temperature (cementation rate), which can influence the resulting size distribution.

In Chapter 6 I test the model introduced in Chapter 5 using a novel approach to constraining the timing of fracture opening based on fluid inclusion microthermometry (Becker et al., 2010). This study tests the model by attempting to demonstrate when fractures of various sizes formed and over what time intervals each fracture grew. This study provides for the first time a way to link fracture growth models, which show how fracture patterns change, with empirical studies, which hitherto could only show the end result and no development history. The fracture set under investigation is within outcrops of the Triassic El Alamar Formation in NE Mexico. Though broadly consistent with the predictions from the model introduced in Chapter 5, the fluid inclusion data suggest that the fracture opening occurred amid migrating fluids, the presence of which complicates the reconstruction. I use evidence from oxygen isotopes to argue that fluids that had interacted with overlying evaporites infiltrated the opening fractures.

Chapter 7 explores some of the practical implications of my work. I show how the narrow range in scaling exponent, which I established in Chapter 3 and investigated in Chapter 4, can improve estimations of fracture spacing at the meter-scale in natural gas reservoirs from which only vertical cores are recovered, and no other fracture-pattern information is known.

The work detailed in Chapters 2 through 7 is based on demonstrably *in situ* fractures arranged in parallel or sub-parallel sets. Such fractures actually represent a small minority of the typical grain-scale fracture populations revealed using SEM-CL. In Chapter 8 I review a dataset which comprises microfracture size and abundance data collected from unfiltered 2D sampling of SEM-CL mosaics. This dataset contains over 27,000 fractures from 61 samples of 18 formations (Table 1-1; Chapter 8).

All of these results imply that a wide range of fracture sizes should be typical of fractures formed in the subsurface. My conclusions are based on a fairly large and representative sampling of rocks and tectonic settings. The conclusions are sufficiently general to characterize a wide range of possible size distribution nuances while still explaining broad trends in detail. Chapter 9 summarizes my findings and identifies directions for future work.

EMPIRICAL APPROACH TO FRACTURE SCALING

Chapter 2: Interpreting size distribution curves

This chapter is a guide for interpreting fracture-size frequency data measured along 1D scanlines. This chapter also describes methods for collecting fracture size data and some important pitfalls in objectively characterizing the size distribution of natural fractures. One-dimensional line-of-observation (scanline) data (Figure 2-1) of opening displacements of fractures, or *kinematic apertures* (Marrett et al., 1999) are portrayed on cumulative frequency-size plots so that the size distribution of the set of fractures measured can be quantified. Kinematic aperture measurements are afflicted by certain sampling biases, both previously documented in the literature and newly identified in this study. Irregular fracture-scaling data trends derive from a variety of sources, both artificial and natural, as described below.

Ascertaining the relationships between fracture frequency and size is an area of much scientific focus. Scaling equations enable the observer to estimate several aggregate properties of fracture populations, including fracture strain and fracture spacing, in unsampled parts of the subsurface (Marrett and Allmendinger, 1992). Fracture systems that scale have implications for strain localization and can influence fluid flow at a range of geologic scales (Eichhubl et

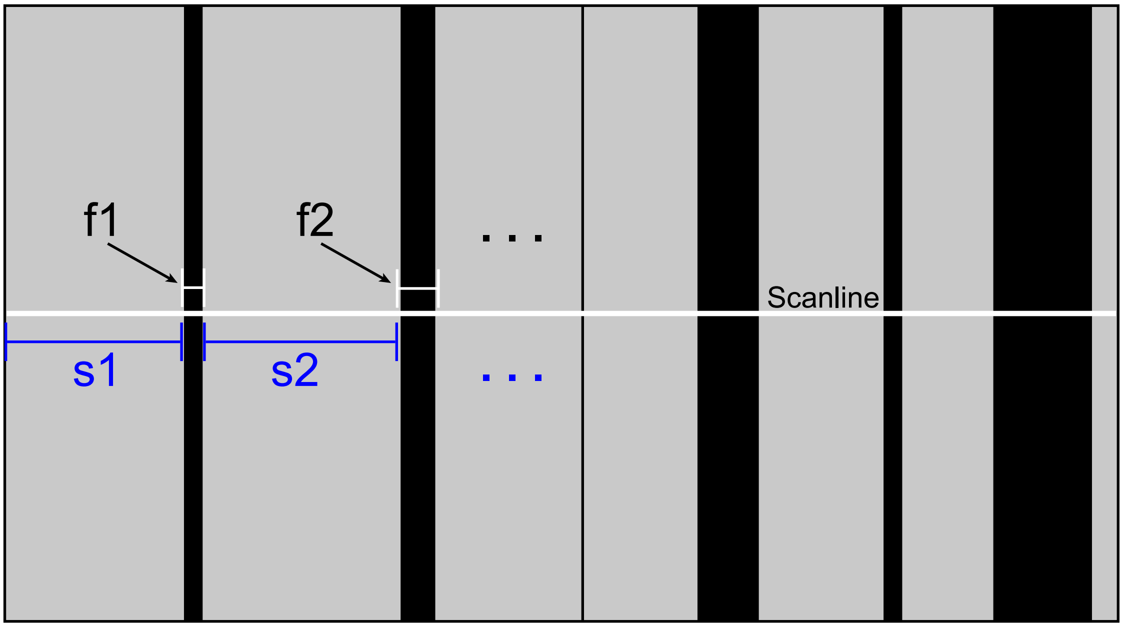

Figure 2-1. Diagram of a scanline, from Hooker et al. (2009). Fracture apertures (f1, f2) are measured along the 1D line of observation. Spacings (s1, s2) are the regions in between fractures. If the scanline is not perpendicular to fracture trace, fracture apertures and spacings are trigonometrically corrected (Gomez and Laubach, 2006).

al., 2004). However, understanding the scaling properties of natural fracture networks is fraught with difficulties that begin with initial observation.

Observer biases are understood to produce downward deflections to fracture-size frequency curves because of various sources of undersampling, as discussed below. A result of this understanding of sampling bias has been for geologists to interpret straight-line size-frequency trends (in log-log space) as power laws, and curved trends as power laws tainted with observer or sampling biases. To the end of establishing objective standards for size-frequency curve interpretation, and therefore to establish some confidence in claims of fractal properties of fracture networks and other phenomena, previous studies note the importance of collecting statistically adequate (large; $n > 200$) datasets (Bonnet et al., 2001) and testing other hypothetical governing scaling equation types (Clauset et al., 2009).

In this chapter I review how various observer biases and imperfections in sampling method can affect fracture intensity (scaling) curves. In some cases such errors in the sampling process can account for local deviations from a *simple* real size distribution, i.e. one that is well described by a simple equation. In other cases these artificial explanations are not appropriate and the curves are real (inherent to the actual fracture population). Whether real or artificial, *complexity* in size-frequency data here refers to any deviation from a simple governing equation.

SCANLINE METHODS

Methods for collecting 1D fracture scanline data are described by LaPointe and Hudson (1985) and for 1D kinematic aperture data by Ortega et al. (2006). For a set of parallel, opening-mode fractures, draw a 1D scanline perpendicular to the fracture strike (Figure 2-1). Using a scale or comparator (Ortega et al., 2006) measure each fracture's kinematic aperture, or entire opening displacement irrespective of porous or cemented fracture fill, where the fracture intersects the scanline. The spacings are the distances in between fractures along the scanline, so that a completed scanline consists of a series of fracture widths and inter-fracture spacings, which collectively add up to the entire scanline length. In cases where fractures are not perpendicular to the scanline, both the fracture aperture and spacing may be trigonometrically corrected. Fracture scaling studies can be based on fracture length, which can in turn be related to fracture offset/aperture (see Olson, 2003) but for many fracture arrays fracture length measurements are impractical.

For example, horizontal cores rarely preserve a continuous length of rock sufficient for fracture length measurement. Outcrop studies are not as limited, but even in large exposures the length of a fracture can be difficult to measure objectively. If once-separate fractures grew by linking (Figure 2-2a) or if fractures branch as they grow (Figure 2-2b), the measurer must decide where one fracture begins and the other ends. A fracture exposed on a planar surface may allow for

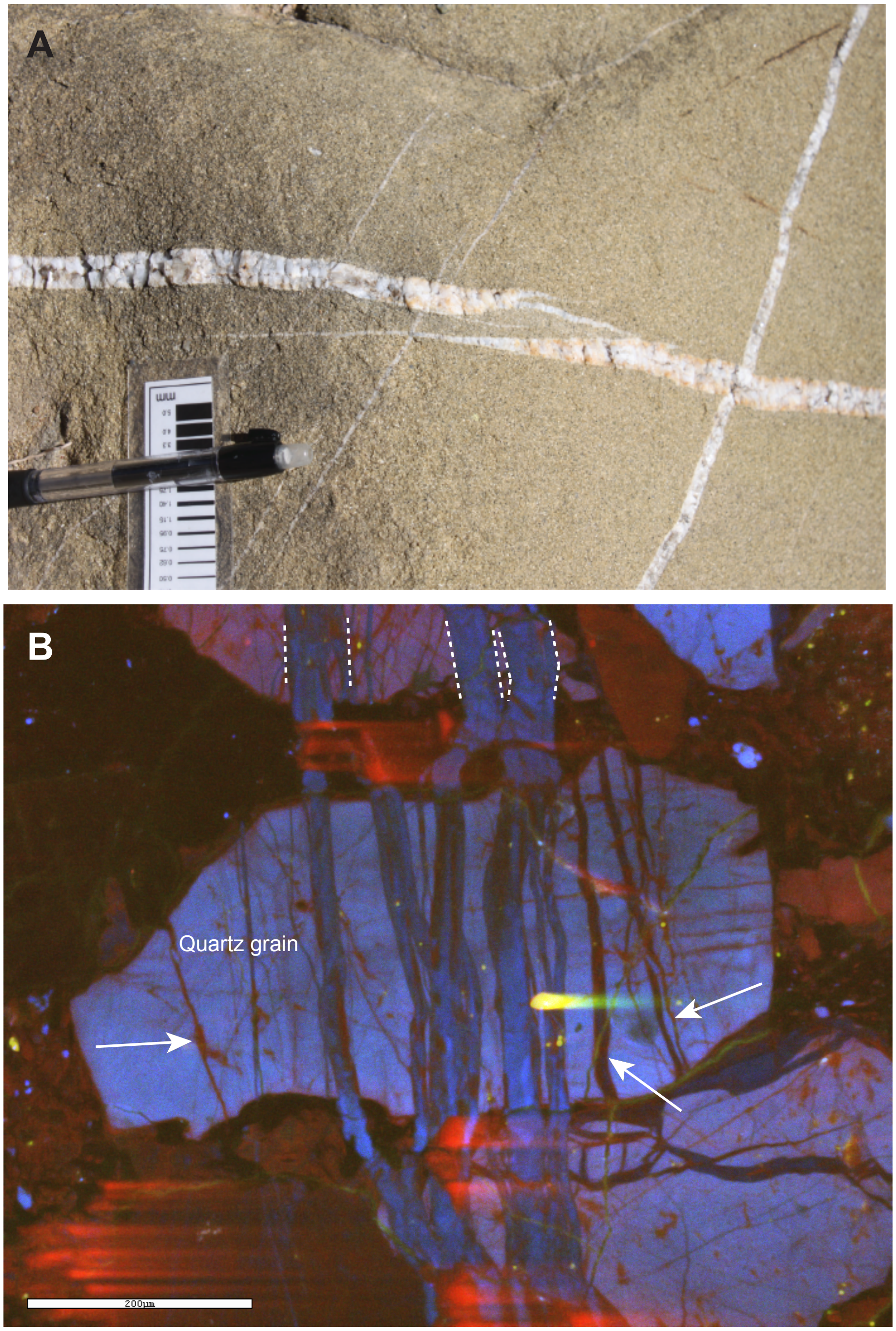

Figure 2-2. (A) Field picture of linking macrofractures, El Alamar Formation. Photo by Steve Laubach. (B) SEM-CL image of branching microfracture, El Alamar Formation. Dashed lines indicate fracture walls away from quartz grain, in which the fracture branches into numerous segments. Note CL-dark microfractures (denoted by arrows) of obscure origin within quartz grain. These fractures are parallel to transgranular microfracture segments but they have different luminescence and do not appear to extend beyond grain boundaries.

a unique length measurement but this measurement requires assumptions about the 3D shape of the fracture, and what cut the outcrop or core surface makes through the fracture. This problem is present in aperture measurements as well, but measurements of kinematic aperture along a 1D scanline are relatively objective and should not be plagued by censoring biases (Pickering et al., 1995) as are fracture length measurements in maps. This study therefore focuses on fracture aperture.

Analogous to the difficulty in measuring the lengths of linked fractures is the difficulty in measuring the aperture of a fracture that has grown episodically, by repeated cracking and sealing (Ramsay, 1980; Hilgers and Urai, 2002; Laubach et al., 2004a,c). In cases where host rock slivers are present within the crack-seal texture of a fracture (Figure 2-2) the distinction between separate fractures and separate opening increments within a single fracture can be subjective. In this study such occurrences are usually few enough as to be insignificant, but exceptions are addressed in Chapter 3.

For data presentation, to the largest fracture intersected by the scanline assign a cumulative number of 1; the second-largest, 2; and the *n*th-largest, *n*. Cumulative number can therefore be understood as the number of fractures encountered along a scanline of a given size or larger. So that fracture size data collected at different scales of observation can be compared, and so that average fracture spacing can be computed, divide cumulative number by scanline length, normalizing cumulative number to cumulative frequency (fractures per unit length).

CRITERIA FOR GOODNESS OF FIT

How many fractures should be sampled before an observer can say with confidence what type of size distribution is present? As summarized by Bonnet et al. (2001), this depends on the size-distribution-equation parameters of the set in question; however, from a synthetic fracture population that follows an ideal distribution equation, sampling 200 fractures generally produces representative statistics.

Of course, there is no reason to presuppose that natural fracture sets follow ideal, simple size distribution equations. An alternative approach to studying fracture-size distributions is to use the goodness of fit between the natural data and commonly recognized size distribution equations as a descriptive tool. In doing so, one may accept the natural size distribution as complex and non-ideal while still approximating fracture frequency with simple equations. A further challenge is to account for artifacts, defined here as any difference between the true frequency and the observed frequency that arises because of imperfect or statistically inadequate fracture- and or spacing-size measurement. Upon accounting for artifacts, the natural size distribution, replete with any natural complexities, can be interpreted.

SIZE DISTRIBUTION EQUATIONS

Commonly observed size-frequency governing equations include power-law relationships:

$$F = aX^{-b} \qquad (2\text{-}1)$$

where F is cumulative frequency, X is fracture size, and a and b are empirical parameters. Power-law size distributions can be thought of as scale-invariant because Equation 2-1 implies that as the length, area, or volume of rock under observation is increased, so too will the number of larger fractures, in proportion. Moreover, any positive X value used in Equation 2-1 will yield a positive F value, implying that a fracture of any conceivable size will be present at some frequency in a power-law size distribution. Theoretical and geological considerations provide limits to actual fracture size, but because of the unique potential for scaling in Equation 2-1, any other size distribution type will be referred to as having a characteristic size. In contrast to a power-law or scale-invariant size distribution, characteristic size distributions imply that fractures are common within a limited size range and rare outside this range.

Characteristic size distributions that have been used to describe the size distributions of natural fractures include exponential relationships (Nur, 1982; Deschamps et al., 2007):

$$F = c\exp(-dX) \qquad (2\text{-}2)$$

where the variables are equivalent to those in Equation 2-1.

The gamma distribution is a power law with an exponential tail (Bonnet et al., 2001):

$$F = aX^{-b} \exp(-dX) \qquad (2\text{-}3)$$

giving an upper limit to a power-law size distribution. The gamma distribution has been used to describe earthquake magnitudes (Kagan, 1997; Sornette and Sornette, 1999) near the high-magnitude end of the distribution where data are not well fit by power laws and data are, by definition, scarce (Pisarenko and Sornette, 2004).

Classical types of characteristic size distributions include normal size distributions (e.g., Abramowitz and Stegun, 1965):

$$F = \frac{1}{2}\left[1 + \operatorname{erf}\left(\frac{x-\mu}{\sigma\sqrt{2}}\right)\right] \qquad (2\text{-}4)$$

where μ is the average fracture size, σ is the standard deviation, and *erf* is the error function (Abramowitz and Stegun, 1965). For a normal distribution, a characteristic, average size is present and frequency decays away from that average size for both larger and smaller fractures. Log-normal distributions are similar to normal distributions except that the variation about the mean size is logarithmically graduated (Abramowitz and Stegun, 1965):

$$F = \frac{1}{2}\left[1 + \operatorname{erf}\left(\frac{\ln x - M}{S\sqrt{2}}\right)\right] \qquad (2\text{-}5)$$

where M and S are the average and standard deviation, respectively, of the natural logarithm of fracture size.

The relative quality of fit among various equations best-fit to a given dataset can be objectively determined by comparing chi^2 error calculations for each equation type:

$$chi^2 = \Sigma\,[(F_{obs} – F_{calc})^2 / |F_{calc}|] \qquad (2\text{-}6).$$

Comparing the relative quality of fit of these equation types can be performed on fracture populations with as few as three fractures. In such cases, sampling statistics are poor even at the observed size range, so reliable extrapolations of fracture frequency to unobserved size ranges are difficult. (In Chapter 7 a method is described to estimate far-field fracture frequency based on small samples; this method entails many further assumptions.) However, the relative quality-of-fit exercise represents one attribute in a comprehensive description of a fracture population of any number of fractures. In Chapter 3 this exercise is performed on 67 fracture populations having a wide range of numbers of fractures (< 10 to > 400). In doing so the debate is set aside about whether natural fractures follow any particular simple size distribution equation in favor of a quantitative description of natural fracture size distributions in general.

CONCEPTUAL LIMIT OF FRACTURE-SIZE FREQUENCY CURVES

Let V_r represent a volume of rock containing fractures, within which V_f is the volume of rock representing fractures (including fracture cement and pore space) and V_h the volume represented by the unfractured host rock, so that V_r equals V_f plus V_h. V_f cannot therefore be greater than V_r. This tautology describes a conceptual limit to fracture-size frequency space (Figure 2-3). The area above line A represents a forbidden region implying V_f greater than V_r. Line A represents the equation

$$F(X_D) = 1/X_D \qquad (2\text{-}7);$$

where X_D is fracture size measured in the same dimension as the sampling space (Dershowitz and Herda, 1992). That is, X_D is aperture if fractures are measured along scanlines; fracture area if fractures are measured upon 2D maps; fracture volume if fractures are measured within 3D volumes. In Equation 2-7, fractures of size X_D occur once per every X (length, area, or volume) of rock. This is a theoretical maximum frequency. For example, point Q indicates a frequency of 2000 fractures *per meter* of scanline for fractures 1 mm wide or larger. Such a frequency of fractures is impossible because would take a minimum of 2 m to fit 2000 fractures of 1 mm aperture within the scanline.

Previous studies, for example Hatton et al. (1994), Marrett et al. (1999), Bonnet et al. (2001), and Hooker et al. (2009), have established that characteristic-scale bounds of fracture sizes exist in the Earth. These bounds may include the size of atoms or of the Earth’s crust, if not much more mesoscopic-scale features. It is likely that these practical scaling limits circumscribe a narrower region over which scaling laws persist, but the conceptual limit illustrated in Figure 2-3 describes limits to frequency equations observed at a given size range. For example, a power-law fracture-size

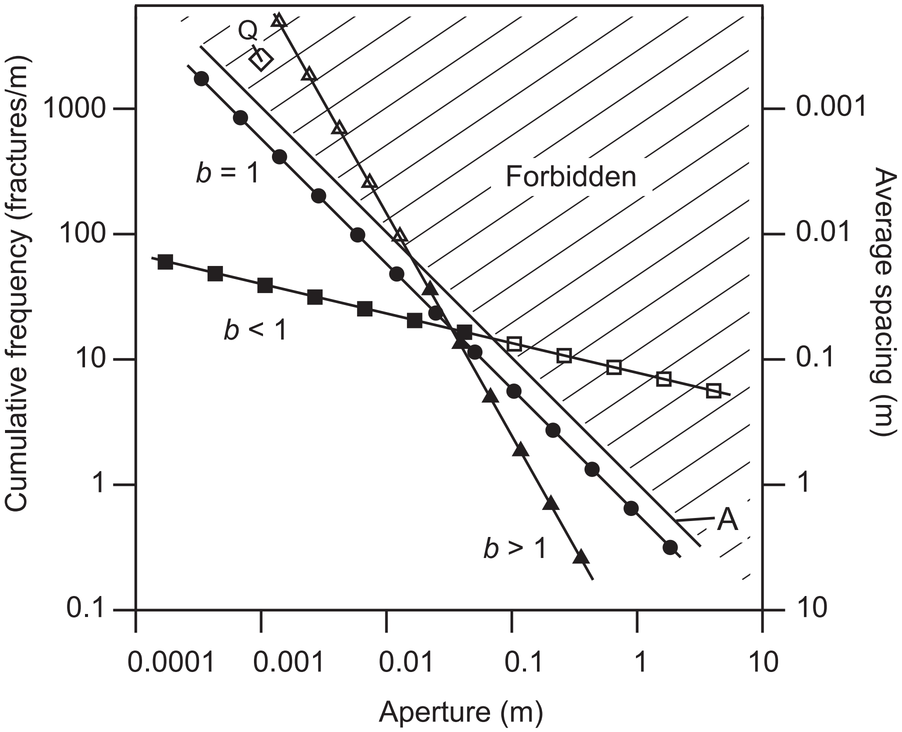

Figure 2-3. Geometrical limit to fracture-size data in cumulative-frequency space, because the frequency of fractures of a given size cannot be greater than the space available in the host rock. Therefore if an observed fracture size distribution is best fit by a power-law equation with b≠1, that equation is necessarily limited at either the upper (b<1) or lower (b>1) size-end of the distribution. White symbols are geometrically impossible. Line A represents the equation F=1/X. After Hooker et al., 2011.

distribution whose *b* value does not equal 1 is bound by this conceptual limit. The conceptual limit bounds such populations at the large-size end of the scaling law for exponents less than 1 and at the small-size end for *b* values greater than 1. (Power laws of *b* value equal to 1 can theoretically persist at all size scales; such equations are only bound by geological limits.) Therefore, though power-law size distributions can be thought of as scale-free in some sense, it is important to bear in mind that such equations do not predict reasonable frequencies for all sizes.

The probability that a fracture within a rock volume will intersect a scanline decreases with decreasing fracture length (Marrett, 1996). Thus if length and aperture are systematically related (Vermilye and Scholz, 1995; Johnston and McCaffrey, 1996; Moros, 1999; Olson, 2003), narrower fractures can be systematically undersampled along 1D scanlines, relative to thorough sampling in a 2D or 3D analysis (Heffer and Bevan, 1990; Glazner and Mills, 2012). Consider a fracture population that follows a power-law size distribution with a *b* value of *B*, and the fractures are penny shaped and homogeneously distributed in an isometric rock volume. Barring other sampling problems, data plotted from a 3D analysis would indicate the true *b* value, *B*. The same data analyzed in 2D would indicate a *b* value of *B*-(1/*N*) and 1D analysis would show a *b* value of *B*-(2/*N*), where *N* is the scaling exponent between fracture aperture and length (Marrett, 1996). These effects would be muted if the assumptions of penny-shape and/or homogeneous distribution are relaxed (Borgos et al., 2000).

Consider a geologically common case wherein the majority of fractures extend from the top to the bottom of a fracture-prone sedimentary layer amidst a fracture resistant sequence (Figure 2-4). Fractures sampled upon 2D maps and 1D scanlines will not underrepresent the total population to the same extent as they would in Marrett's (1996) idealized case, and the resulting *b* values will be lower than *B* by some amount less than 1.

If N is small, indicating sub-linear aperture to length scaling (Olson, 2003), the effects of 1D and 2D sampling on *B* would be exaggerated—*b* would decrease by more than 1 for 2D sampling and more than 2 for 1D sampling.

COMPLEXITY AMONG SMALL APERTURE SIZES

Bias in measuring the smallest fractures observable within a population can arise in two ways. The first way is well established and is truncation of the fracture population caused by limited resolution; the second way is by limited precision of the measuring technique.

Resolution-limited truncation bias

In many cases the resolution of the measuring technique provides the lower limit to fracture detection and measurement. For example there may be low contrast between host-rock and fracture-fill color, or fractures may be measured from microscope images which were made at the resolution limit. In such cases, fractures may be of a size sufficient for measurement but may be missed entirely because of poor resolution. Baecher and Lanney (1978) recognized that fracture-

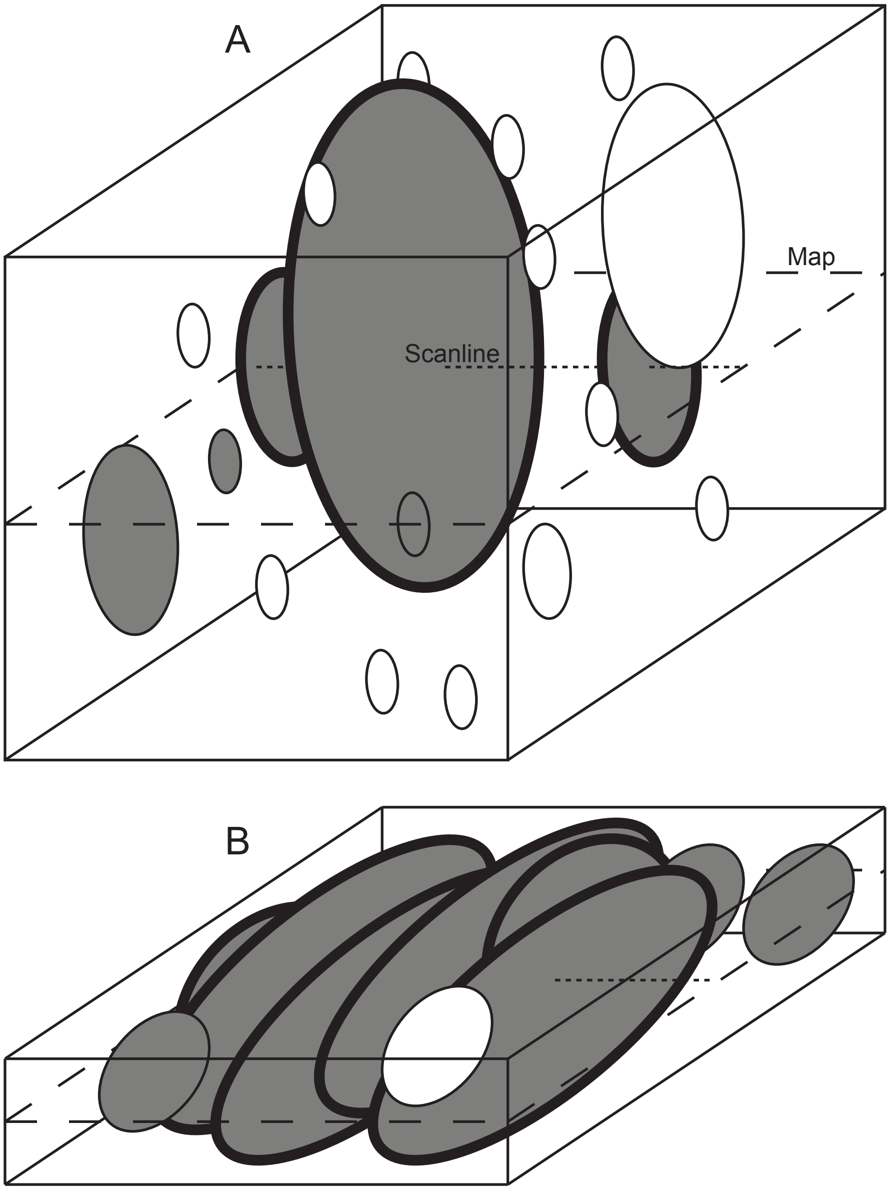

Figure 2-4. The number of spatial dimensions to the sample space can affect the resulting *b* value by the systematic omission of small fractures (Heffer and Bevan, 1990; Marrett, 1996; Glazner and Mills, 2012). (A) This effect is greatest for disc-shaped fractures dispersed throughout an equidimensional 3D volume. 3D sampling would record all fractures; 2D (map) sampling would record only gray fractures; 1D (scanline) sampling would record only bold-outline fractures. (B) The same effect is present to a lesser degree for cases in which most fractures span the height of a fracture-prone layer (Ortega, 2002). 2D sampling captures almost all fractures of sizes shown; smaller, non-layer-bound fractures would be undersampled as in (A).

size cumulative frequency data typically underrepresent the true fracture population at the smallest sizes measured because the smallest fractures are incompletely detected. This phenomenon is manifest in cumulative frequency curves by a downward deviation from true fracture sizes (Figure 2-5).

Precision-limited truncation bias

In addition to that *truncation* artifact, an artifact may be introduced among the smallest measured aperture sizes as a result of the precision limits inherent in the measuring technique. For example, if measuring microscopic fractures (*microfractures*) on digital images, the smallest fractures present may be pixelated, such that easily *resolvable* fractures may nonetheless have *imprecise* boundaries and as such, imprecise size measurements (Figure 2-6). If the smallest measured fractures in an ideal power-law population are near or below the size range of the measurement precision limits, then the resulting errors in fracture aperture sizes measured will form an artificial concave-downwards curve to an aperture size distribution that would otherwise form a straight line. This artifact is simulated in Figure 2-6. The true fracture-size distribution is assumed to follow a simple equation (here, power law). The measured aperture sizes are assigned a value of:

$$X_m = X_t + p \qquad (2\text{-}8)$$

where p is a random number between zero and the precision limit (e.g., pixel width, if measuring fracture sizes on digital images). Overestimations of fracture

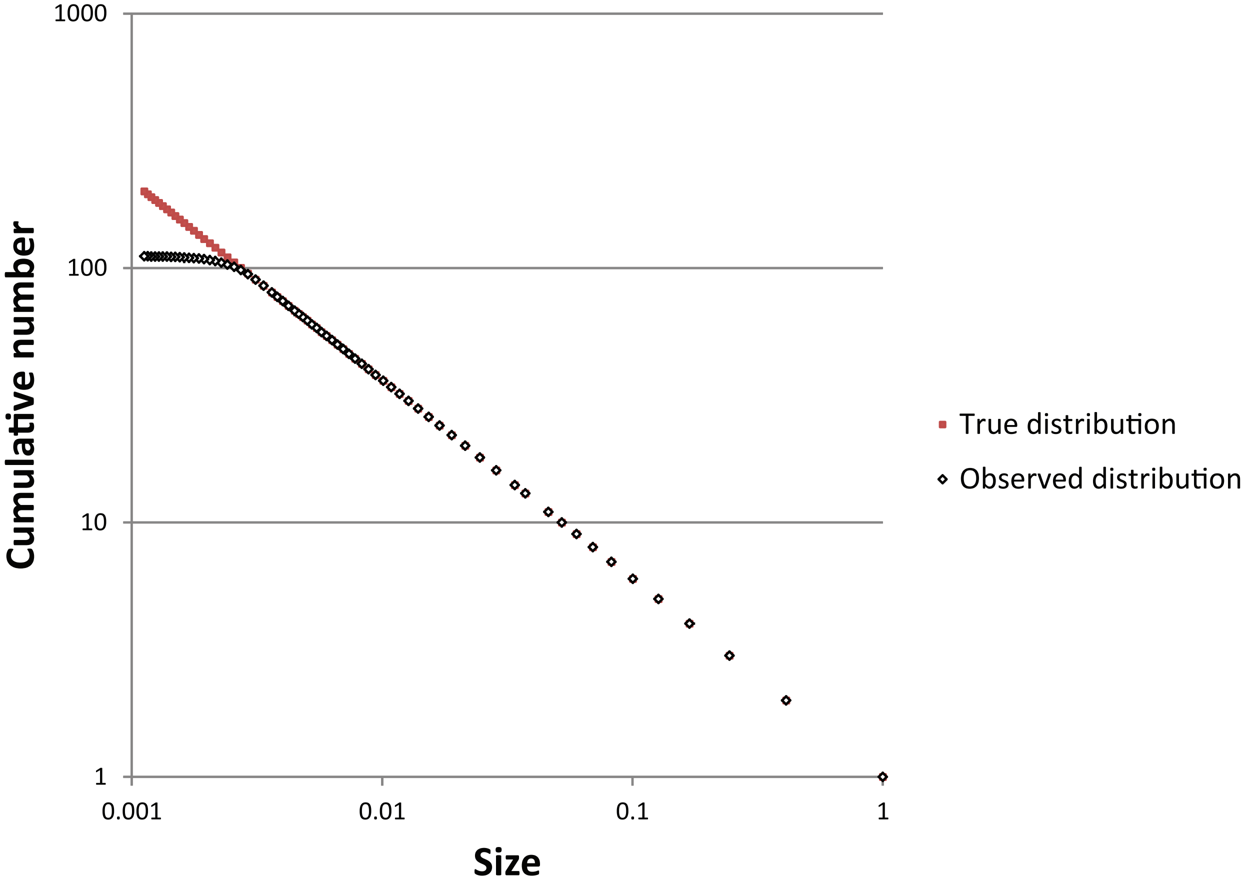

Figure 2-5. Truncation bias from limited resolution. The smallest fractures present are incompletely sampled, resulting in an observed cumulative number that is lower than the true cumulative number at the small-fracture end of the distribution. The example shown above is for an ideal power-law size distribution.

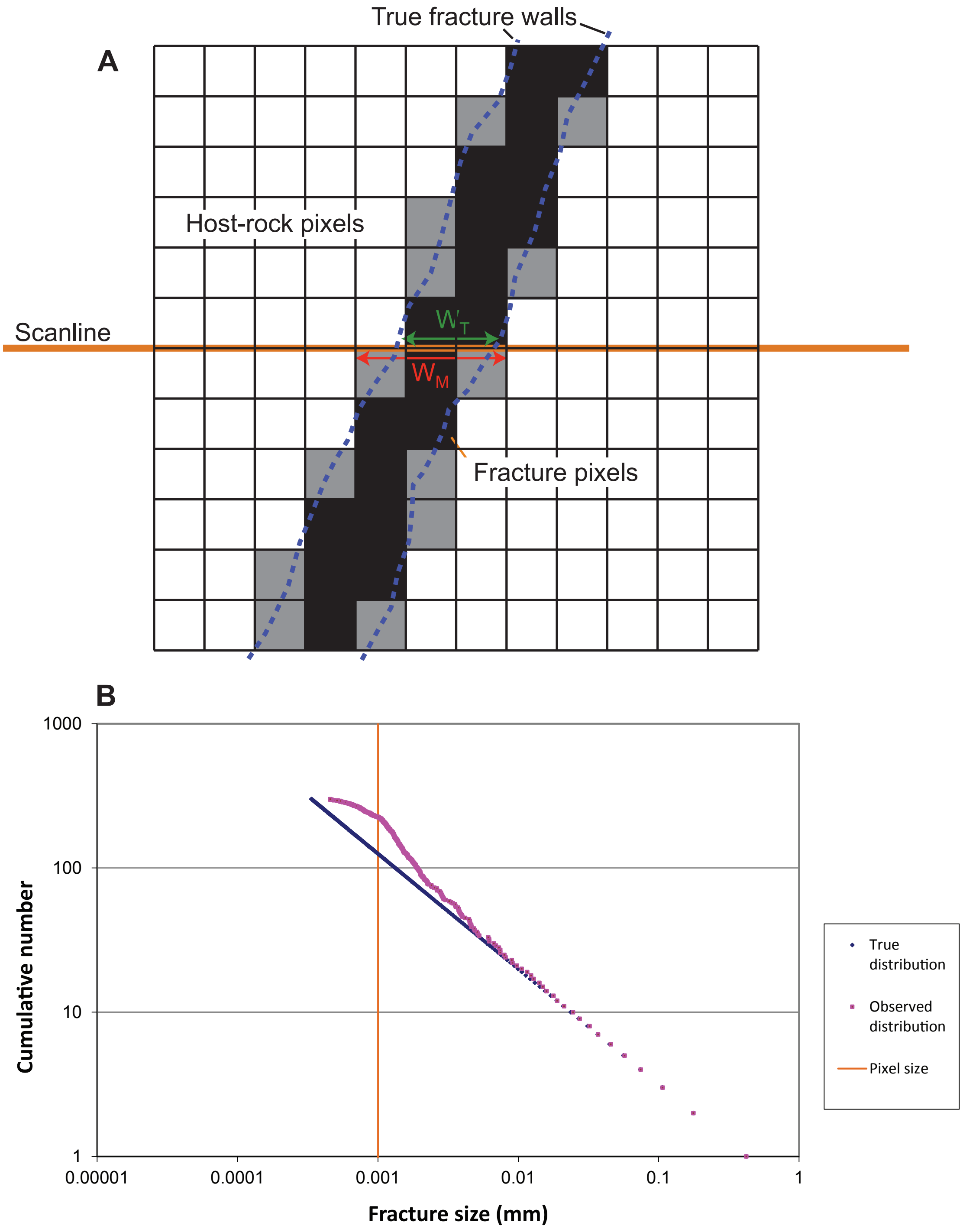

Figure 2-6.Precision-limited truncation bias. (A) Drawing of a pixellated image of a fracture. In this case the fracture is easily resolved but the pixellation makes the intersection between the scanline and the fracture walls imprecise. If all non-gray pixels are counted as fracture pixels, the true width (W_T) can be overestimated by up to a pixel width, corresponding to a larger measured width (W_M). (B) To the true size of each fracture, in an ideal power-law size distribution, a random number between zero and the pixel width is added.

size resulting from precision-limited truncation cause an upwards-deflected artifact as fracture sizes approach the precision limit.

Precision can be limited by factors besides pixel size. In SEM-CL images, fracture traces may locally cut pore-filling cements having low contrast with respect to fracture cements. Moreover, deviations from ideal aperture size-distribution equations resembling that shown in Figure 2-6 need not be solely the result of imprecise measurement. Similar deviations can also be expected from two sources. The first source is fracture size distortion by natural causes including erosive widening—although this would not be expected to artificially narrow any fractures, it could explain a concave-downwards curve to the size distribution data at the scale at which the erosive widening occurs. A second potential source of precision-limit-type truncation curves in aperture size distributions are real changes in the scaling properties of the fracture sizes. Size-scaling variations could arise from characteristic-scale rugosity of fracture surfaces, mechanical effects at the scale of host-rock grains, or other unknown causes.

Resolution-limited truncation may work in concert with precision-limited truncation. The prevalence of precision-limited truncation bias can be assessed by the overestimation of fracture size, though of course without explicitly testing the data with a more precise sampling method, the presence of bias cannot be definitively assessed.

COMPLEXITY AMONG LARGE APERTURE SIZES

It is well established that artifacts plague fracture-size frequency data at the large-size end of the curve as well as the small-size end. A common artifact of fracture scaling studies is an under-representation of the size of the largest fracture sizes recorded, called a *censoring* bias (Baecher, 1980; Pickering et al., 1995). This artifact of scaling curves is common among studies of fracture trace length in 2D (on fracture maps). Fractures whose tips extend beyond the boundaries of the map must either be omitted from the dataset or assigned a minimum estimate of true fracture length. Because the lengths of the longest fractures in a sample are most likely to be underestimated, a concave-down rolloff is commonly observed on the large-fracture end of the scaling curve. Pickering et al. (1995) and Bonnet et al. (2001) also describe a finite-range effect that produces a similar rolloff. This artifact is encountered when the range of fracture sizes observed and the size of the sampling region are not ideally matched. In 2D analyses this may preferentially cause a downward rolloff in the cumulative frequency curve because it is easier to expand the number of fractures measured than to expand the size range of fractures observed.

Maximum-size frequency undersampling

A similar artifact to the finite-range effect affects 1D analyses. The cumulative frequency assigned to the largest fracture measured along a scanline is by definition statistically inadequate, as only one fracture of this size or greater was measured. Guerriero et al. (2010) explain that the error associated with the measured frequency of a given fracture size increases towards the large-size end of cumulative frequency plots because of low cumulative sampling at those sizes. This is true in general for 1D fracture-size frequency data. The widest fracture to intersect a scanline of length L is assigned a frequency of 1/L, but the actual abundance of fractures of this size or larger, throughout the rock and away from the small observed region, cannot be accurately judged directly by measuring the cumulative frequency of one fracture. This can be illustrated by a simulation of randomly sampling fractures from an ideal power-law size distribution population consisting of 500 fractures (Figure 2-7). For 50 random fractures sampled 100 times, the average size for each cumulative number and the 5th and 95th largest fracture sampled for each cumulative number are plotted. The uncertainty in fracture frequency for a given size decays as the size becomes smaller. This decay is a consequence of the scanline length becoming long compared to the average spacing of the fracture size observed. Error in frequency measurements, and subsequent effects on frequency extrapolations, are further explored in Chapter 7.

COMPARISON TO REAL FRACTURE DATA

The three preceding sections describe ways in which deviations from otherwise scale-free size-frequency patterns may be expected, resulting from

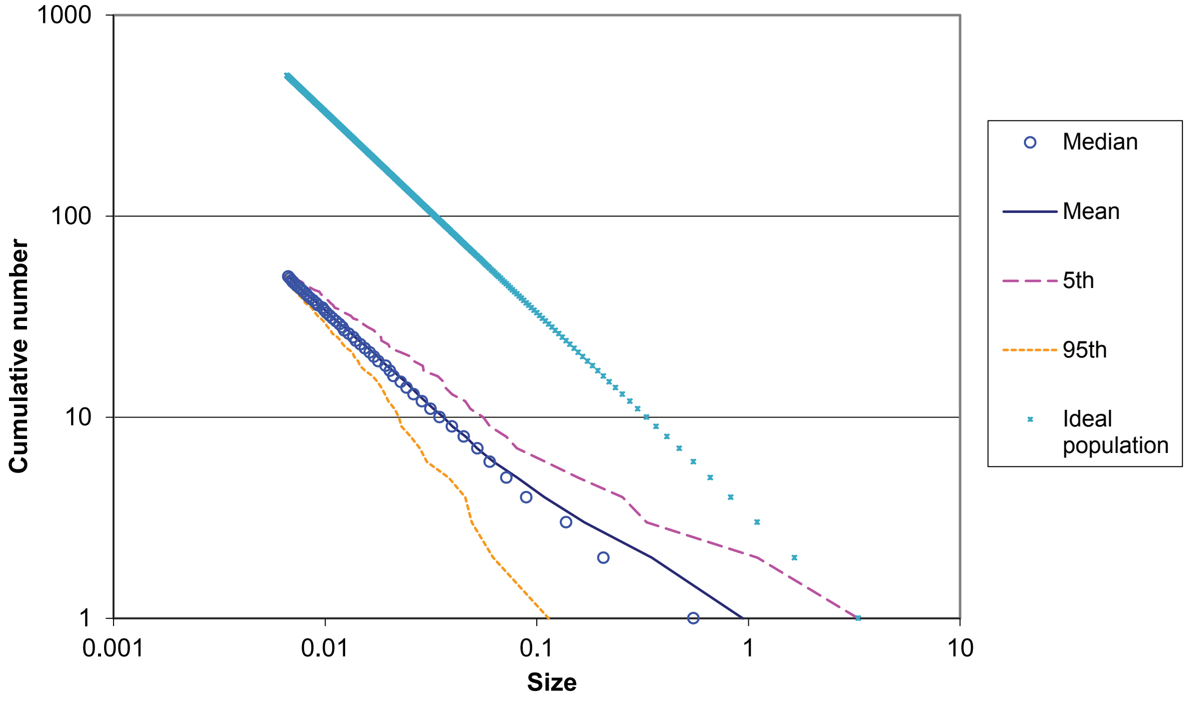

Figure 2-7. Poor cumulative statistics of largest fractures sampled. Beginning with an ideal population of 500 fractures that follow a power-law size distribution, 50 fractures were sampled at random and re-plotted; this sub-sampling was done 100 times. Note wider dispersion in cumulative frequency space among larger fracture sizes, owing to limited (cumulative) sampling at this scale. At smaller scales, sampling is more statistically robust and the variation in sampled frequency regresses towards the expected value. Quantification of error in observed cumulative frequency is addressed in Chapter 7.

both real and artificial factors. This section describes deviations in real datasets and attributes the variations to factors discussed above.

Small-size frequency complexity

The aperture size-frequency curve from fractures measured in the Eriboll Group sandstone (Cambrian) of northwest Scotland (see Appendix A) is irregular (Figure 2-8). Macrofractures were measured from a field exposure using a hand lens and comparator (Ortega et al., 2006). Microfractures were measured using SEM-CL at 150X. (See Chapter 3 for a thorough review of sampling method.) Microfractures and the large (greater than 1 mm wide) macrofractures are well fit by a power-law equation; small macrofracture sizes show a deviation from this equation. Macrofractures were measured in a stream bed wherein slimy coatings and rushing water obscured the fracture walls and typically led to overestimation of fracture aperture. Thus, the macrofracture measurements are plagued by an observer bias related to the quality of the outcrop. Microfracture sizes, though smaller, were measured using a higher-resolution technique and on a smooth thin section surface devoid of rushing water and vegetation. In this example a strong case may be made for simple, power-law scaling of fracture apertures, despite artificial corruption of the data over a limited size range.

A similar concave-down curve among the smallest aperture sizes observed along a scanline is present in Figure 2-9. The data were collected from an SEM-CL image mosaic of a sample from the Mesón Group (Cambrian) of NW

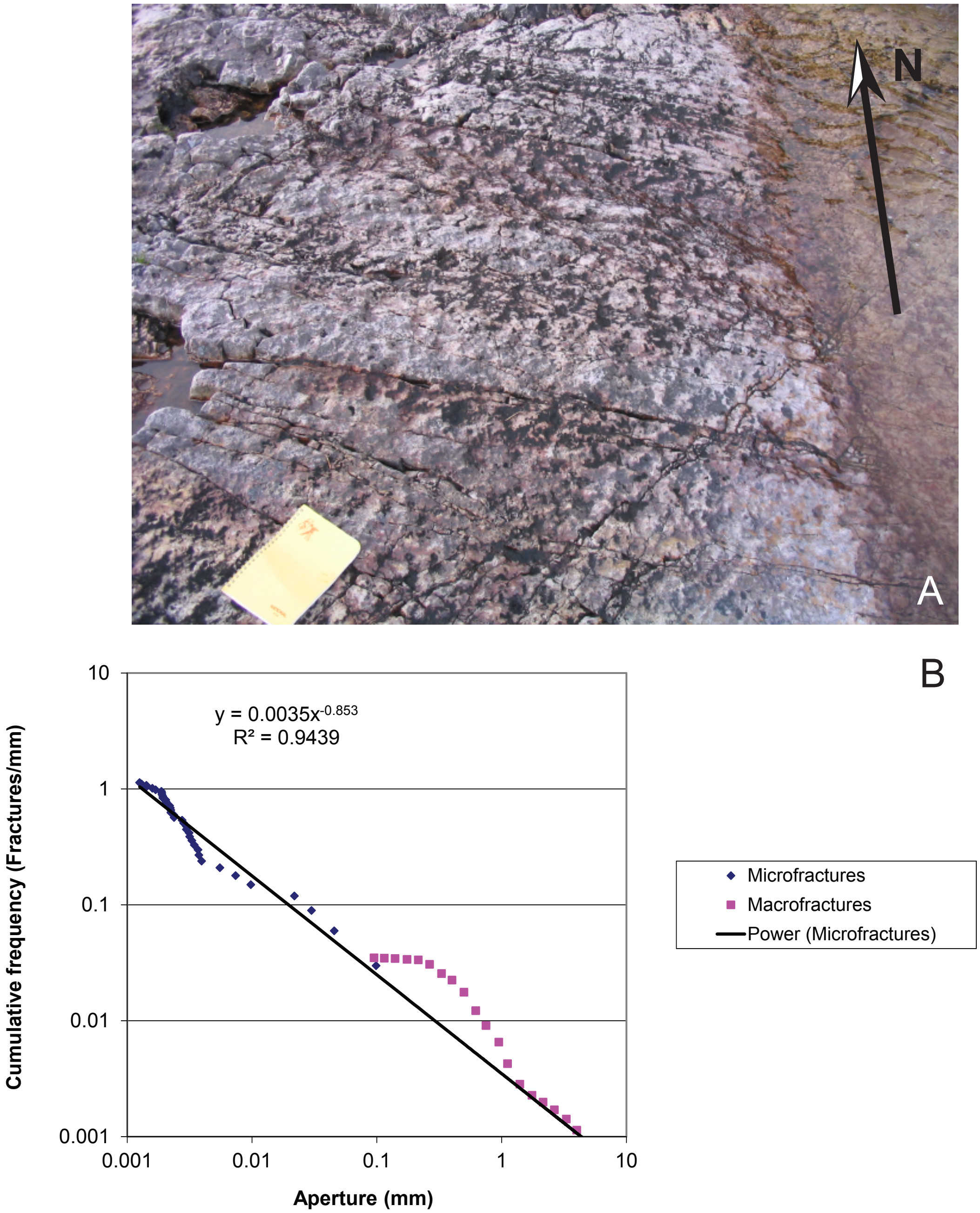

Figure 2-8. (A) Outcrop exposure, Eriboll Formation. Fractures in scanline strike ~110°. Field notebook is 12 x 18 cm. (B) Size distributions of macrofractures and parallel microfractures, measured using SEM-CL. Irregular size distribution curve for macrofractures in (B) is likely the result of submillimetric over-estimations of fracture width. Widths were over-estimated because of erosive widening and organic coatings on the outcrop exposure. Overall size distribution is well fit by a power law of *b* = 0.853.

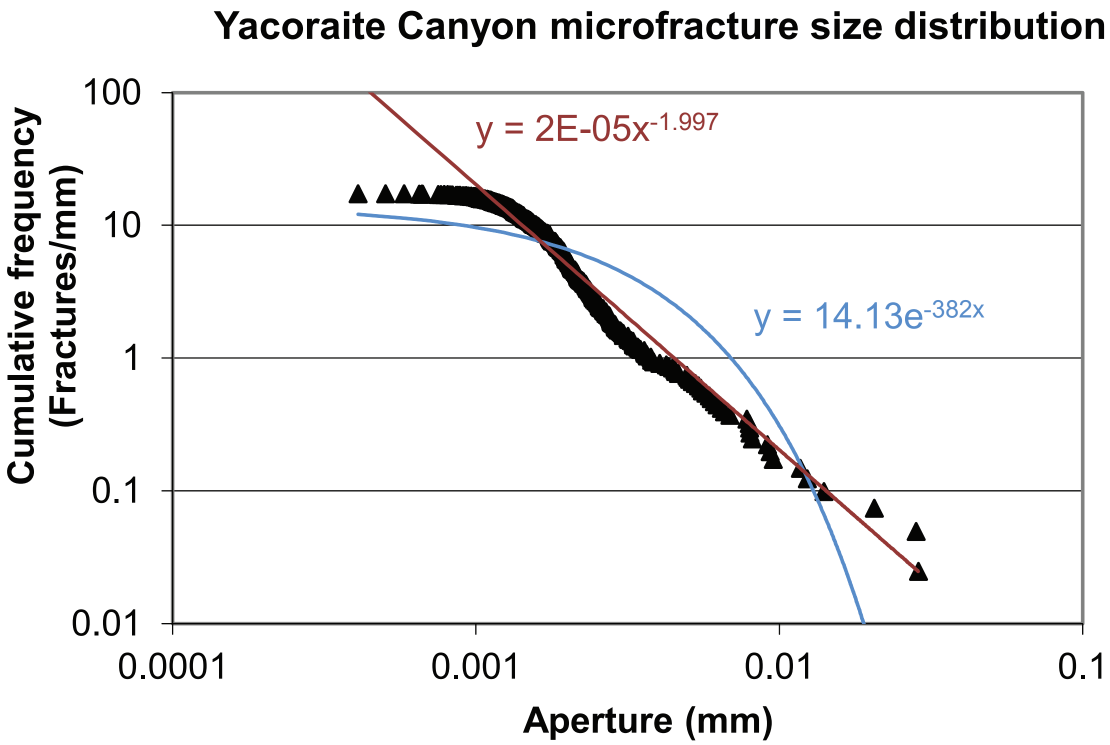

Figure 2-9. Size distribution of microfractures measured from 150X SEM-CL images. Note irregular curve and poor fit by power-law and exponential equations (for chi^2 comparison, see Appendix A).

Argentina. This sample was collected at an outcrop in Yacoraite Canyon (see Chapter 3) at which limited exposure precluded macrofracture observation. Although the data trend qualitatively resembles that among macrofractures in Figure 2-8, the same interpretation is unsupportable. That is, the complexity within the Yacoraite Canyon size distribution is not likely artificial.

The Yacoraite Canyon fractures were originally imaged at a resolution of 0.77 μm/pixel. To test whether the curving of the cumulative frequency trend towards horizontal (indicating a minimum fracture size near 0.5 μm) is real or simply an effect of limited precision, the same fracture set was imaged at a resolution of 0.15 μm/pixel (Figure 2-10) resulting in a smallest fracture size near 0.3 μm (Figure 2-11). Fractures and other features from the images were measured at both magnifications in order to quantify magnification errors. Sizes of features measured at the original magnification (150X) are equal to roughly 105% of the measured size of the same fractures at higher resolution. A 5% error correction to the smallest fracture size observed at 750X makes that size roughly 0.32 μm. It is unclear which magnification level is more precise. Conversely, an error correction of -5% could be applied to sizes measured at 150X. Either way, at 750X all observed fractures are wider than the pixel size.

If the curve to the small-size portion of the data were caused by precision limits, the curve should persist over a smaller size range when the fractures are observed under increased magnification. Because the shape of the distribution is

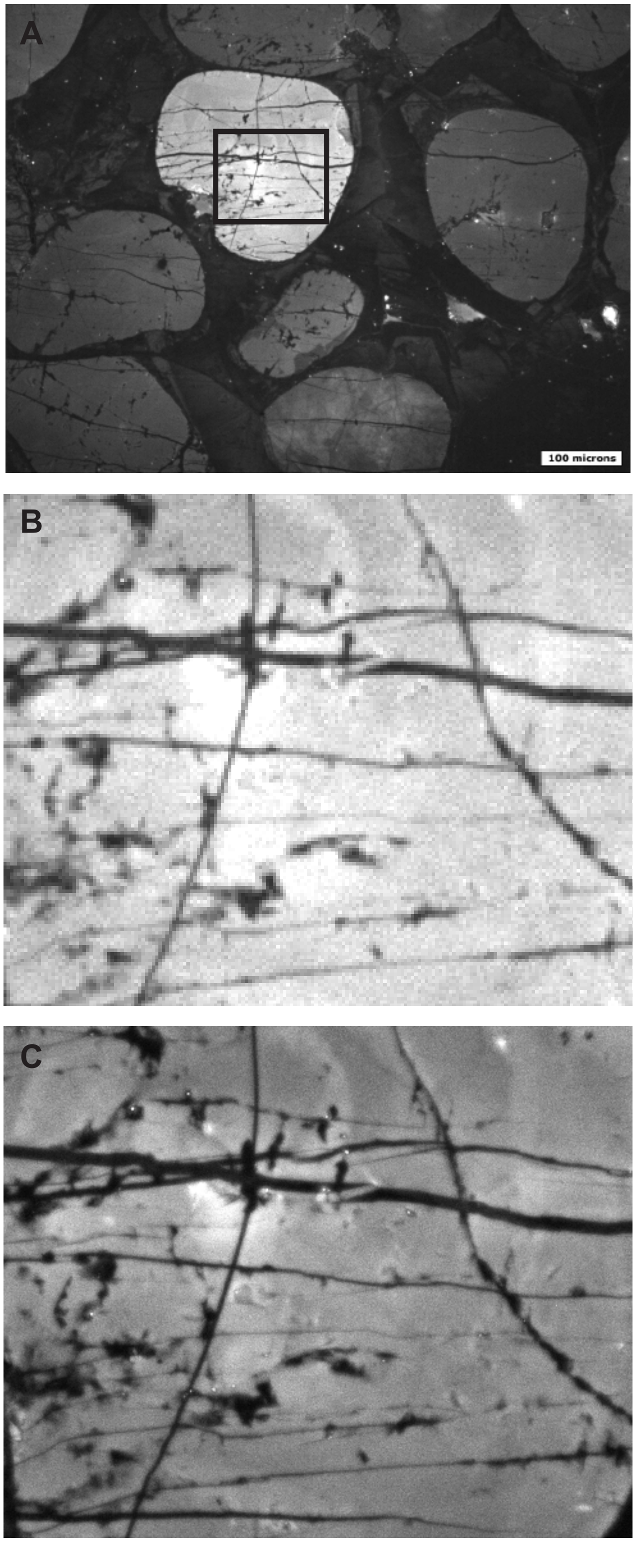

Figure 2-10. SEM-CL images of Meson Group microfractures from Yacoraite Canyon. (A) Original resolution, 150X. (B) Same resolution, boxed area in (A). (C) Same area as (B), imaged at 750X. Note higher resolution/smaller pixel size.

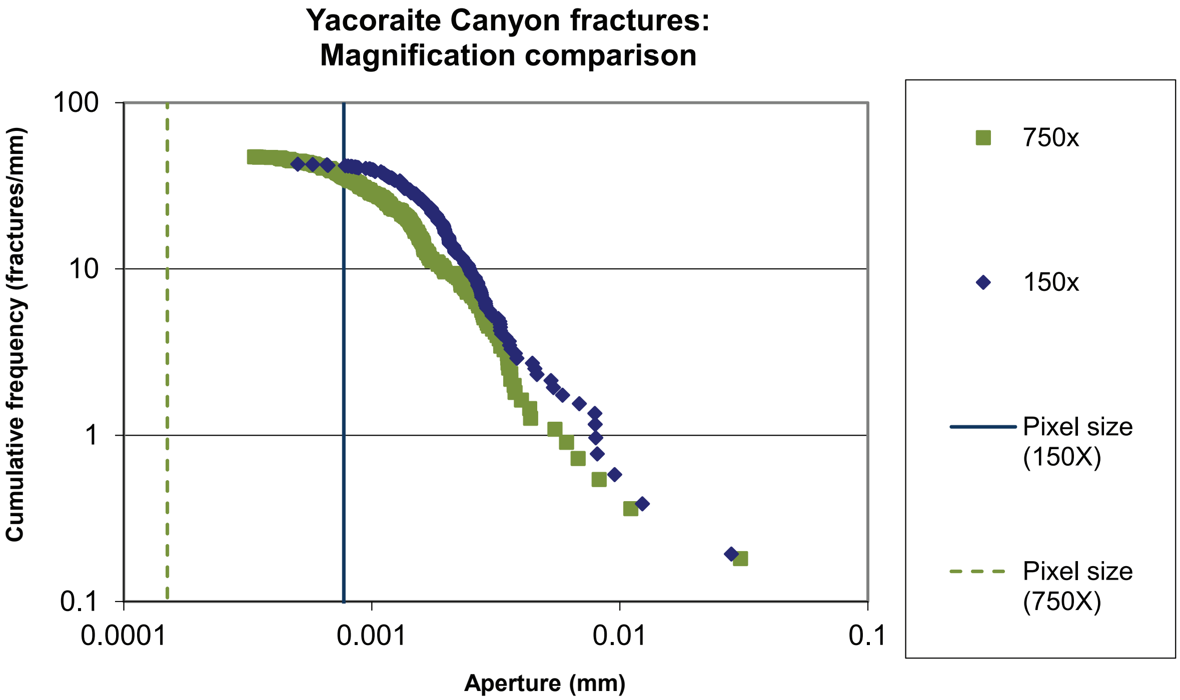

Figure 2-11. Size distribution of a subset of the microfractures in Figure 2-9. The subset was measured from the same images (150X) and at higher magnification (750X).

the same under higher magnification, and because higher magnification permitted the detection of smaller fractures, suggesting the resolution limit was not reached, the complexity of the size distribution is better interpreted as real.

This fracture population follows a complex size distribution that is not well-described by any single, simple equation. For fractures < 40 μm in aperture, fracture cumulative frequency is best-fit by a log-normal distribution (compared with normal, exponential, and power-law—see Table 2-1). Larger fractures are best-fit by a power law of b = 1.73. The concave-downwards curve among small aperture sizes represents a *real* departure from possible power-law scaling at larger size scales, not sampling bias.

The rolloff towards horizontal among the smallest fracture sizes present may result from resolution-limited truncation bias, but such bias does not account for the upwards deviation of small-fracture frequencies, relative to the apparent power-law among larger fractures.

Large-size frequency complexity

A different natural-fracture data set from the Mesón Group illustrates the effect of a finite largest fracture size present within a fracture population. This population is from Perchel Canyon, where multiple sets are exposed around an Andean fold (see Chapter 4 and Appendix A for location and structural setting). For this example fractures of all observed orientations are included. Macro- and microfractures were measured using the same methods as given above for the

		chi^2 error			
Size range	No. fractures	Power law	Exponential	Normal	Log-normal
All data	499	**330.6**	345.7	5.88×10^{10}	785.5
< 40 μm	465	174.1	44.7	118.0	**31.7**
> 40 μm	34	**0.1**	1.1	1.4	1.5

Table 2-1. Best-fit equation comparison for Yacoraite Canyon microfractures, Meson Group. Best-fit chi^2 value in bold.

Eriboll Formation fractures. Scanlines intersected 67 macrofractures and 342 microfractures (Figure 2-12). Extrapolation of the microfracture power-law size distribution (Figure 2-13) predicts an average spacing of 5 mm-wide fractures to be approximately 313 mm. The macroscopic scanline, 3595 mm long, intersects a largest fracture size of 2.65 mm. Thus the power-law size distribution observed among microfractures appears to be inapplicable at the cm-scale. The resulting size distribution resembles the gamma law (Equation 2-3).

The exponent for the power-law size distribution fit to the microfractures is < 1. This low exponent suggests the power law must necessarily break down at some large size scale (Figure 2-3). For the power-law equation best fit to the data in Figure 2-13, the geometrical upper limit to the aperture size is approximately 10^4 km. Therefore in this case the power law breaks down at a much smaller size scale than the conceptual limit shown in Figure 2-3.

This data set illustrates the need for discretion when predicting the frequencies of large fractures based on the intensity of small fractures (see Chapter 7).

In summary, the size distributions of natural fractures can feature complexities and thus not be precisely characterized by simple equations. The causes of such complexities will be investigated in Chapter 3 and Chapter 5. However, before the real size distribution of a natural fracture set can be studied, a variety of artifacts must be accounted for. These artifacts are related to the

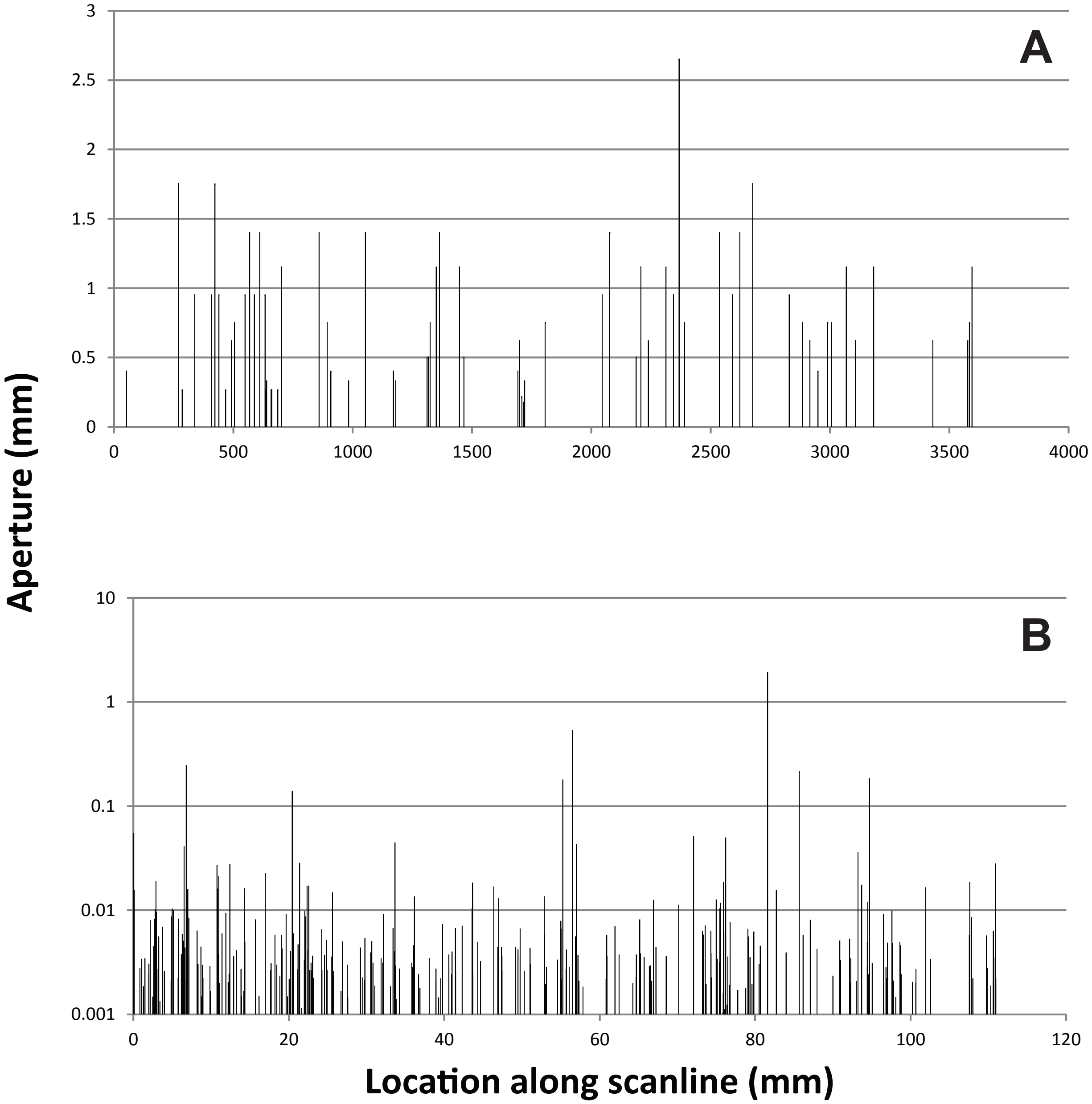

Figure 2-12. Kinematic aperture sizes of fractures measured along scanlines, Meson Group at Perchel Canyon. (A) Macrofractures, measured using a hand lens and comparator. (B) Microfractures, measured using SEM-CL. Data are unfiltered by orientation.

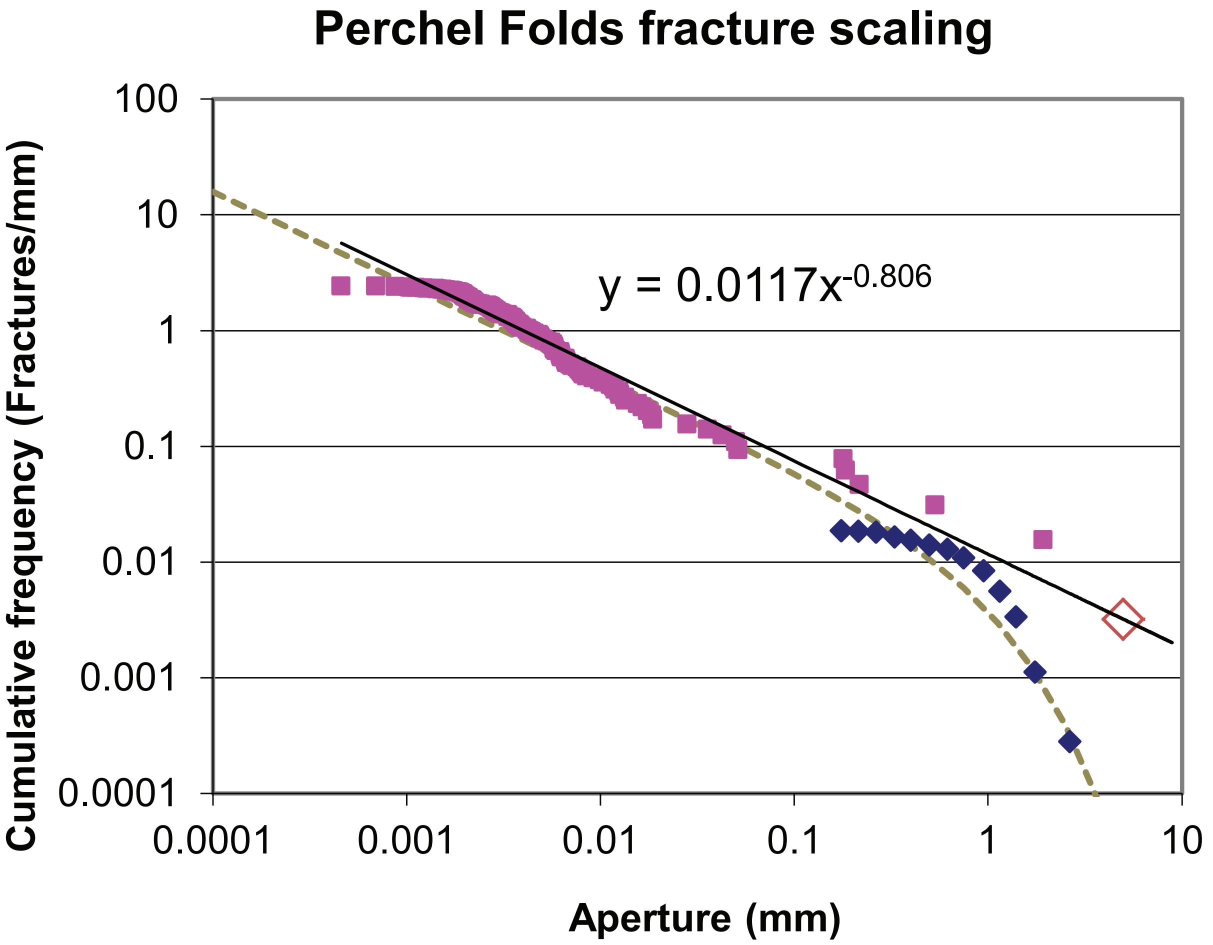

Figure 2-13. Extrapolation of a power-law equation best fit to microfracture data predicts an average frequency for 5 mm-wide fractures of 0.0032 per mm; the reciprocal average spacing is 313 mm per fracture. The macrofracture scanline is more than ten times this length (Figure 2-12) and the largest fracture it intersects is 2.65 mm wide. Dashed line is a gamma law (Bonnet et al., 2001), which better fits the size distribution at larger size scales.

observer’s imperfect ability to detect and measure small fractures, and the inherently poor statistical sampling of the largest fractures present (for cumulative frequency calculation).

Considering the presence of natural complexities within fracture scaling data, it is clear that natural fracture datasets do not perfectly conform to simple size-distribution equations. Indeed, many ideal equations have geometrical limits to the range of fracture size abundances that they can approximate. Moreover, the deviations from such simple equations potentially reveal information about how fractures grow. Therefore, rather than arguing explicitly that a given fracture-size distribution *follows* a particular simple equation, and collecting at least 200 fracture sizes to support such a claim as being statistically rigorous, the approach pursued here will be to examine natural fracture-size distributions, of any number of fractures, in aggregate, so that patterns present among natural fracture networks can be identified and interpreted. A relevant *description* of each fracture set includes which common, simple equation best fits the data, relative to the other simple equations, and judged via the chi^2 method (Equation 2-4). However, such equations should not be construed as the *underlying* or *real* distribution without accounting for natural complexities that are not encompassed by the simple equation or even reducible to general, non-site-specific growth histories.

Chapter 3: A new high-resolution dataset

How do natural fractures scale? Are natural fracture patterns scale-invariant, or do fractures have a characteristic size? To address these questions, this chapter describes a kinematic aperture scanline dataset of unprecedented size and resolution as well as attributes of microtextures of the fractures in these datasets. The data are from large (up to meter-scale in length) sandstone samples mapped using scanning electron microscope-based cathodoluminescence (SEM-CL), as well as from field data measured using a hand lens. This dataset comprises 59 scanlines, containing over 4,200 fractures, from eight formations on three continents (Table 1-1; Appendix A). The data show that natural fracture sets in sandstones are well-fit by various types of size distributions, and that those best-fit by power-law size distributions have two important characteristics in common. First, power-law size distributions feature exponents (Equation 2-1) of a characteristic value, with a narrow range. Second, in many cases power-law-distributed fractures are composed of characteristic-sized opening increments, preserved in bridges of cement that precipitated while the fractures were opening.

SYSTEMATICS OF FRACTURE APERTURE-SIZE SCALING

In the previous chapter I reviewed and added to the list of known biases that can affect quantification of fracture aperture-size scaling. Although many opening-mode fracture arrays, commonly including barren joints, are apparently scale-restricted (Odling et al., 1999), many other fracture arrays clearly possess a range of sizes spanning multiple orders of magnitude.

Opening-mode fractures commonly show size distributions that can be statistically well-fit by power-law equations (Gudmundsson, 1987; Barton and Zoback, 1992; Clark et al., 1995; Gross and Engelder, 1995; Loriga, 1999; Marrett et al., 1999; Ortega and Marrett, 2000; Gillespie et al., 2001; Laubach and Ward, 2006; Ortega et al., 2006; Guerriero et al., 2010; Davy et al, 2010; Hooker et al., 2011). Other fracture-size distributions may possess a more limited size range constituting mostly very small fractures (microfractures) or mostly large fractures (many joint arrays) and are best described as possessing *characteristic* size distributions. This category comprises fracture sets which are best fit by exponential, normal, and log-normal size distributions, or any other equations that do not feature the scale-free properties of a power law (Bonnet et al., 2001).

The reason or reasons why fracture-size distributions might follow power laws versus characteristic size distributions are unknown, although possible models have been explored (Chapter 1). To address the problem of fracture-size distributions I measured fractures from six sample localities (Table 3-1). The dataset in aggregate represents a new opportunity for studying size distribution systematics because of its combined breadth and consistent methods. As mentioned above, the dataset is large, comprising fracture populations from a

Sample numbers	Formation/Group	Folk classification	Structural setting	Major fracture-cement phases	Average microfracture strain
7-12	Travis Peak Fm.	Quartzarenite	Unstructured*	1. Quartz	$1.4x10^{-3}$
13-41	Mesaverde Gp.	Sub-litharenite, litharenite	Unstructured*	1. Quartz 2. Carbonate	$4.7x10^{-3}$
45-52	Nikanassin Fm.	Sub-litharenite	Foreland basin, fold-thrust belt	1. Quartz 2. Carbonate	$1.4x10^{-2}$
42-44	Huizachal Gp.	Feldspathic litharenite, litharenite	Sub-decollement	1. Quartz 2. Carbonate	$1.6x10^{-2}$
1-6	Eriboll Fm.	Quartzarenite	Sub-thrust belt	1. Quartz	$2.6x10^{-2}$
53-59	Meson Gp.	Quartzarenite	Fold-thrust belt	1. Quartz	$4.8x10^{-2}$

Table 3-1. Overview of fracture scaling dataset. Sample numbers correspond to those listed in Appendix A and Table 3-3. *Fractures from the Travis Peak Formation and Mesaverde Group are not related to obvious folds or faults; see text.

wide range of tectonic settings—including high-strain settings within fold and thrust belts, as well as relatively undeformed intramontane basins. Despite this variety, the data collection method was consistently deployed: all fracture size measurements are measurements of kinematic aperture along 1D scanlines, using SEM-CL to examine fractures down to the micron scale. All data derive from sandstones, which partially controls for systematic differences in fracture patterns by rock type; these data will be compared to fractures in carbonate rocks in Chapter 4.

SEM-CL images show textures within fracture cements that provide insight into the differences in fracture growth processes between scaling fractures and fractures having a characteristic size. Such textures are described in this chapter and used to guide modeling of fracture growth (Chapter 5).

Best-fitting equations to scaling data

One way to characterize the type of fracture size distribution present within rock is to best-fit equations to fracture size distribution curves (i.e., to cumulative-frequency—fracture-size data; see Chapter 2). Such a best-fit equation relates fracture size and abundance and represents the scaling behavior of the fracture population; however, as stated in Chapter 2, natural fracture sets should not be assumed to follow a simple size distribution equation perfectly. For this study, the best-fit equation, judged by the minimum chi^2 error associated with normal, log-normal, exponential, and power-law size distributions, is regarded as part of a description of the scaling behavior of a fracture set. This description is improved after accounting for artifacts to the intensity curves, associated with undersampling at the small- and large-size ends of the distribution (Chapter 2).

It is likely that gamma-law equations would in many cases better fit observed size distributions than would power-law equations. For example, if fractures are sampled at the real large-size-limit of the power-law size distribution (Figure 2-13), the observed size distribution would likely approximate a gamma law. However, as discussed in Chapter 2, the large-size end of observed scaling data commonly features such real complexity as well as artificial complexity, as for example from inherent poor sampling. Therefore the best-fit parameters of gamma laws could mean different things, depending on the reason for the large-size rolloff. Moreover, if the interpretation of a gamma law is a power law with an upper size limit (Bonnet et al., 2001), then the gamma-size distribution begs the same interpretation that the power-law size distribution does. Thus gamma-law equations were not best fit to each dataset.

Similarly, scaling complexity at the small-size end of the distribution might be statistically well described by a von Karman distribution (e.g., Mai and Beroza, 2002). But because improved statistical description relative to the simple equations used (which derives from a greater number of model parameters within the von Karman and Gamma Law distributions) would not help interpret the source of the complexity, I did not fit these more complex equations to the fracture-frequency data.

With the aim of minimizing one sampling artifact, data collection in this study adheres to the fracture selection criteria used in Hooker et al. (2009) with respect to intra- or transgranularity of fractures. By omitting fractures that do not crosscut grain boundaries and/or intergranular cement, this procedure leaves out any fractures that may have already been present within host sand grains at deposition. Inspection using SEM-CL shows that many such fractures exist in sandstones (Chapter 8), and some of these can be identified by textural or color criteria (Laubach, 1997; Hooker and Laubach, 2007), but these criteria cannot unambiguously identify all such fractures. Therefore all intragranular fractures are removed for this analysis. It is likely that filtering out all intragranular fractures also omits some post-depositional fractures. Because such fractures are sub-granular in scale their omission is equivalent to a truncation bias, whereby the smallest fractures observed are systematically under recorded (Chapter 2). Other than this potential source, the data presented here are not strongly affected by truncation bias, because few recorded fracture apertures are smaller than 1 μm (Appendix B), and the pixel size of the SEM-CL images is ~0.77 μm wide at the magnification used (150X).

The poor statistics inherently associated with the largest fractures in cumulative frequency data (Chapter 2) can result in irregular, spurious large-size tails to facture intensity curves. However, because such spurious data are not expected to *systematically* under- or over-record fracture frequency, the method does not call for the omission of large-fracture frequencies for equation best-fitting.

For the purposes of accurately extracting statistical information from a fracture set, such as fractal dimension, data which appear to be biased may be removed before equations are best-fit, in the interest of deriving an equation that most closely approximates the underlying distribution (Pickering et al., 1995; Bonnet et al., 2001). A disadvantage to such an approach is that it can be difficult to distinguish real and artificial complexities within fracture intensity curves (Chapter 2). In this chapter individual size distribution curves are described in order to identify consistent patterns among natural fracture-size distributions, including possible real complexities. Thus it is important not to assume any bias at the outset, beyond the two types described above (i.e., small-size truncation from omission of intragranular fractures and large-size poor sampling). Size distribution equations are here fit to the all the data without accounting for further artifacts, and thus no datapoints are removed before best-fitting. Interpretation of complex scaling behavior can then follow, with the best-fit equations serving as a guide to the interpretation.

The relative quality of best-fits of the four common scaling equations to these data can be quantitatively assessed using the chi^2 method described in

Chapter 2. It is worth noting two consequences of this method for arguments concerning the persistence of power-law scaling among natural fractures. First, chi^2 testing only tests the relative quality of fit among the size distribution equations tried; it is therefore not to be inferred that any of these fits represents a *true* equation which the fracture sizes follow, only that some equations fit the data better than others. Second, the method is likely biased towards identification of natural data as characteristic and not power law. This is because truncation bias tends to result in concave-downwards curves to scaling data. Similarly, downwards rolloffs are expected at the large-size end if the fractures are sampled at their maximum size range (Pickering et al., 1995; Amaral et al., 2000). Thus data collected from a natural fracture set which strongly follows a power law or gamma law could nonetheless be better fit statistically by a characteristic distribution. Therefore, the effects of biases could overestimate the occurrence of characteristic-sized fracture sets in this study.

SCANLINE PROCEDURE

Scanlines in bedded rock

In the simplest case, extensional strain is manifest in a single set of parallel opening-mode fractures. Many such fracture arrays exist perpendicular to sedimentary bedding in flat-lying or gently dipping beds (Pollard and Aydin, 1988). Macrofractures in such a case could be measured along layer-parallel, fracture-perpendicular scanlines, without the need for trigonometric corrections.

In this study, in general, for microfractures, thin sections were cut parallel to bedding such that a fracture-perpendicular scanline, parallel to the macrofracture scanline, could be digitally drawn across SEM-CL images. Samples were processed such that no rock was lost between serial thin sections for long multi-thin section analyses (Gomez and Laubach, 2006). Combined macroscopic and microscopic scanline measurements allow data from different scales of observation from the same body of rock to be compared on the same graph. Because the microscopic scanlines are shorter than those for large fractures such a comparison requires normalizing the cumulative number of fractures to the scanline length. This is done by dividing cumulative number by scanline length, the result being the cumulative frequency. Such data represent the number of fractures encountered per unit length of rock rather than per scanline. Thus not only does the technique facilitate observation of fractures at different scales, but the technique also controls for scanlines of different length collected at a single scale of observation.

Fractures observed in this study that lack cement entirely are assumed to have either formed near the Earth's surface or be artificial, because fractures that propagated in the subsurface, in the presence of diagenetically reactive fluids, can be expected to contain some cement. Barren fractures in outcrop likely formed near the surface and so are not representative of fracture growth in the subsurface. Barren fractures in core likely formed during retrieval or handling.

Barren fractures in thin section may result from damage during sawing and polishing. Such barren fractures are omitted from the data collected for this study.

Scanlines in core

In all core samples, microfracture scanlines were constructed from the longest layer-parallel (fracture-perpendicular) scanline possible; core from deviated wells commonly allows for longer multi-thin-section scanlines than does vertical core, whose diameter limits scanline length to 2.5-4 inches in typical cases (Figure 3-1). Several vertical core samples are included in this dataset (Table 3-2). In cases where bedding dips steeply and fractures dip gently, long fracture-perpendicular scanlines can be constructed from vertical-core samples (Ortega, 2002).

DATASET SUMMARY

The geologic settings of all field sites are described in Appendix A. Strain recorded among microfractures (thus over the same fracture-size range) varies over more than an order of magnitude. At the low end, strain near 10^{-3} is achieved among fracture sets in unstructured settings; at the high end, strain near 5×10^{-2} is achieved among fracture sets in fold- and thrust-belts (Table 3-1). The Piceance Basin and East Texas Basin settings are listed as *unstructured* in the sense that samples were collected distant (> 0.5 km in most cases) from mapped faults or folds on broad (tens to hundreds of km) gentle arches within

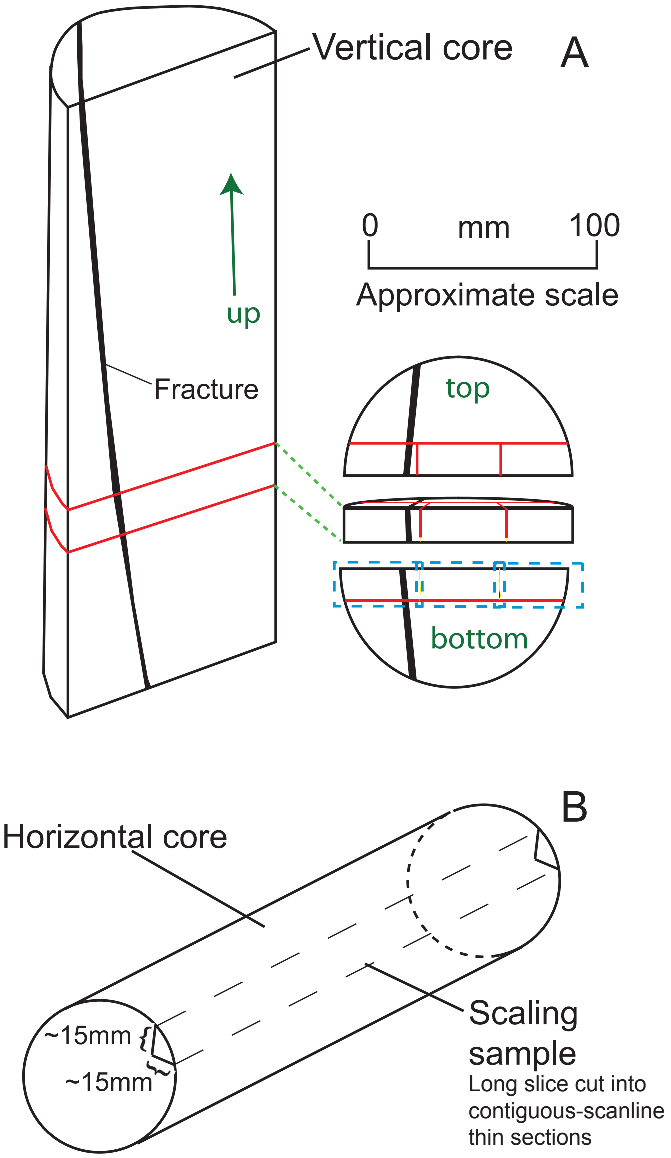

Figure 3-1. Diagrams of sample collection technique for scanline measurements from vertical (A) and horizontal (B) core.

Sample number	Formation	Sample type
1	Eriboll	Outcrop
2	Eriboll	Outcrop
3	Eriboll	Outcrop
4	Eriboll	Outcrop
5	Eriboll	Outcrop
6	Eriboll	Outcrop
7	Travis Peak	Vertical core
8	Travis Peak	Vertical core
9	Travis Peak	Vertical core
10	Travis Peak	Vertical core
11	Travis Peak	Vertical core
12	Travis Peak	Vertical core
13	Williams Fork	Vertical core
14	Williams Fork	Vertical core
15	Williams Fork	Vertical core
16	Williams Fork	Vertical core
17	Williams Fork	Vertical core
18	Williams Fork	Vertical core
19	Williams Fork	Vertical core
20	Williams Fork	Vertical core
21	Williams Fork	Vertical core
22	Williams Fork	Vertical core
23	Williams Fork	Vertical core
24	Williams Fork	Vertical core
25	Williams Fork	Vertical core
26	Williams Fork	Vertical core
27	Williams Fork	Vertical core
28	Williams Fork	Vertical core
29	Williams Fork	Vertical core
30	Williams Fork	Vertical core
31	Williams Fork	Vertical core
32	Williams Fork	Vertical core
33	Williams Fork	Vertical core
34	Williams Fork	Vertical core
35	Williams Fork	Vertical core
36	Williams Fork	Vertical core
37	Williams Fork	Deviated core
38	Williams Fork	Deviated core
39	Williams Fork	Vertical core
40	Cozzette	Deviated core
41	Cozzette	Deviated core
42	El Alamar	Outcrop
43	La Boca	Outcrop
44	El Alamar	Outcrop
45	Nikinassin	Vertical core
46	Nikinassin	Vertical core
47	Nikinassin	Vertical core
48	Nikinassin	Vertical core
49	Nikinassin	Vertical core
50	Nikinassin	Vertical core
51	Nikinassin	Vertical core
52	Nikinassin	Vertical core
53	Meson	Outcrop
54	Meson	Outcrop
55	Meson	Outcrop
56	Meson	Outcrop
57	Meson	Outcrop
58	Meson	Outcrop
59	Meson	Outcrop

Table 3-2. Type of sample (outcrop, vertical core, or deviated core) from which each dataset was collected.

sedimentary basins. These are “regional fractures” (Nelson, 1985) in that curvature associated with these arches are unlikely to affect fracture development (see Becker et al., 2010; Fall et al., 2012; and English, 2012 for discussion of fracture origins). As is typical for sandstones, quartz is the primary framework grain type, primary-pore-filling cement, and fracture cement. Carbonate cement is also common within fractures and primary pores.

The fracture sizes within the dataset range between 0.0005 and 14 mm (Figure 3-2). The small-size end of this range is near the pixel resolution for SEM-CL images, and close to the width of fractures which are ubiquitous in natural quartz grains (Hooker and Laubach, 2007; Chapter 8). Thus the fracture sizes observed are likely bounded at the small end by image resolution and the indeterminate genesis of intragranular fractures (Laubach, 1997; Hooker and Laubach, 2007). However, it is not necessarily true that the fracture sets observed contain narrower, unmeasureable fractures. I address whether the dataset might include the smallest extant fracture sizes in this chapter. The large-size end of this range is not close to the theoretical fracture intensity limit (Equation 2-5) for the measured fracture spacings. In other words, much larger fractures could be present, but the sets studied feature a cm-scale maximum observed fracture aperture size. Where the upper size limit is well sampled (e.g., Figure 2-13), the upper size limit likely reflects finite strain within bedded rocks deformed under diagenetic (~50 to < 250°C) conditions.

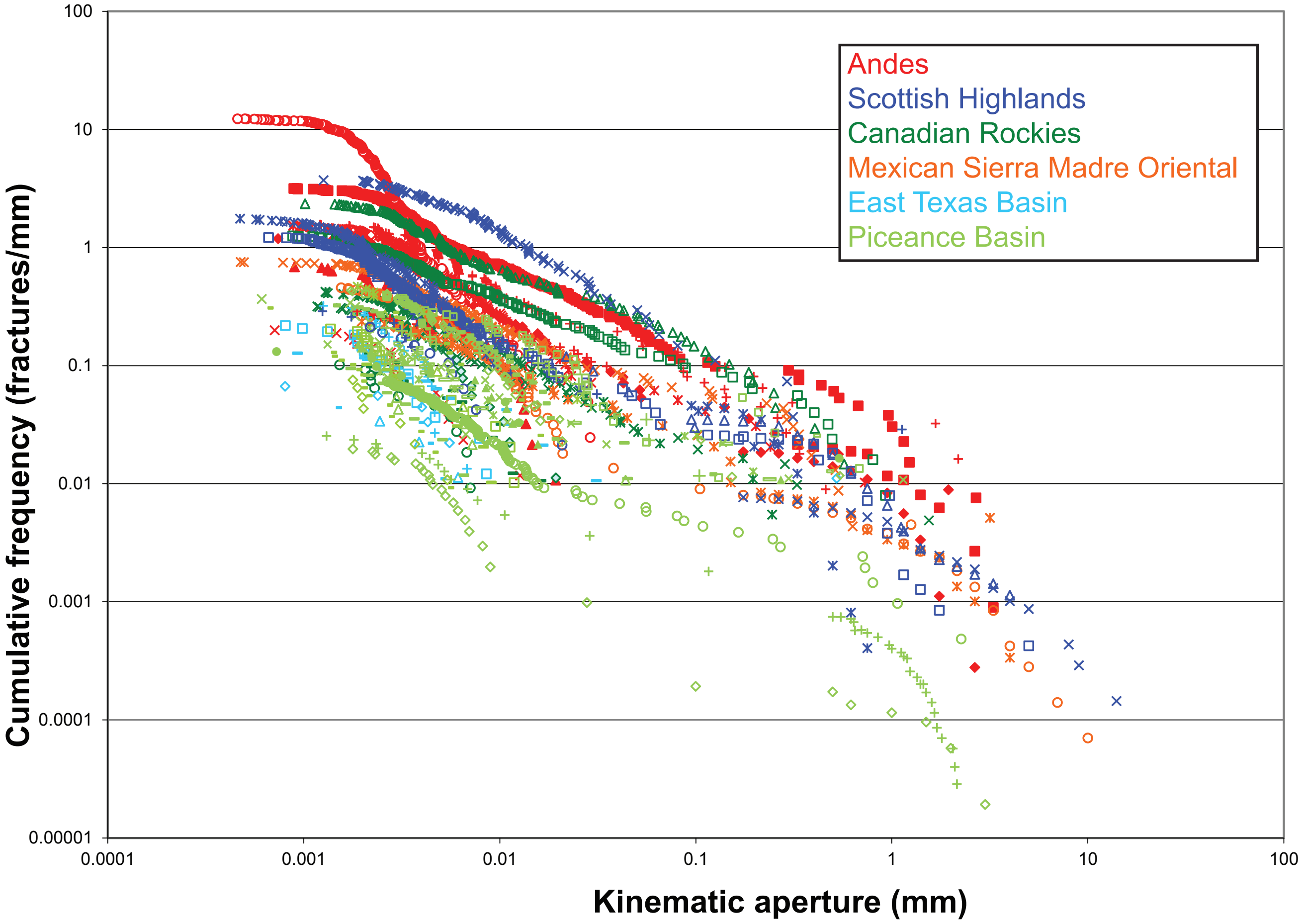

Figure 3-2. Cumulative frequency versus kinematic aperture for all samples listed in Table 3-3.

Best-fit equation statistics

The aperture-size distributions from each scanline can be fitted with a variety of curves (Figure 3-2). The equation type that best fits each sampled size distribution—among power law, exponential, normal, and log-normal—can be judged by the chi^2 value for each equation type (Table 3-3). The dataset comprises 59 microfracture scanlines. Of these, eight intersect fractures arranged in multiple sets. For these eight scanlines, intensity curves were calculated for strike-filtered subsets as well as for all fractures together. Therefore the dataset comprises 67 microfracture populations and sub-populations. Of these, 12 datasets derive from outcrop samples or slant cores and have corresponding macrofracture data.

Of 67 fracture size datasets, 44 are best fit by power-law equations (Table 3-3). Twenty-one are best fit by either exponential or log-normal size distributions. There are two scanlines that intersect zero fractures; both were made from bed-parallel (horizontal) scanlines across vertical cores taken from the Piceance Basin. No fracture set is best characterized by a normal size distribution.

Power-law size distribution parameters

In this section I focus on those scanline data within the entire dataset which are best fit by power-law equations. In order to assess general characteristics of such distributions, with the ultimate goal of inferring the

Table 3-3. Summary of scanline results. Chi^2 values for each of the four best-fit equation types are listed; the lowest value (best fit) is given in bold. Rows in green are strike-filtered subsets. b and a refer to power-law parameters (Equation 2-1). *Excel returned Division-by-zero error, signifying poor fit. **Zero fractures observed.

	Microfractures		Macrofractures		chi2 values					
Sample Number	**No. fractures**	**Scanline length (mm)**	**No. fractures**	**Scanline length (mm)**	**Power law**	**Exponential**	**Normal**	**Log-normal**	***b***	***a***
1	153	125.3	61	2308.1	**1.144**	65.553	*	23.843	0.830	4.2E-03
2	38	29.8	123	3091.3	**0.833**	33.417	17.41934347	17.419	0.781	5.5E-03
3	101	27.1	52	6523.1	**23.192**	301.205	1016465.468	57.170	1.152	5.1E-03
4	104	47.9	47	7198.0	**3.519**	35.424	28.1169189	21.732	0.926	2.9E-03
5	11	37.1			**0.024**	0.071	0.639509	0.151	1.102	3.0E-04
6	11	16.3			**0.046**	0.326	2.161231583	0.703	0.354	2.3E-02
7	24	74.8			0.340	**0.086**	0.230873955	0.092	1.890	2.0E-06
8	4	90.9			0.009	**0.007**	0.013783275	0.019	0.848	2.0E-04
9	12	94.4			0.036	0.027	0.243545344	**0.023**	0.738	1.1E-03
10	6	89.7			**0.010**	0.030	0.096239871	0.062	0.274	8.5E-03
11	18	82.7			0.152	**0.042**	0.34760285	0.059	1.213	6.0E-05
12	3	88.8			0.001	**0.000**	0.010495749	0.009	1.195	3.0E-05
13	7	79.0			**0.005**	0.024	0.091525478	0.040	0.406	7.4E-03
14	8	61.1			**0.017**	0.100	0.359589804	0.137	0.335	1.1E-02
15	18	86.0			0.062	0.068	0.751135858	**0.041**	0.696	4.2E-03
16	27	83.5			**0.239**	0.890	741.8968778	0.317	0.823	2.1E-03
17	10	91.7			**0.015**	0.063	0.180786197	0.083	0.461	6.5E-03
18	37	85.6			**0.242**	2.787	102226.3073	18.222	0.769	3.5E-03
19	10	74.5			**0.022**	0.041	0.248782049	0.048	0.318	1.9E-02
20	5	93.7			**0.004**	0.011	0.048457395	0.029	0.561	1.7E-03
21	14	92.9			**0.039**	0.287	3.181684041	0.508	0.455	7.9E-03
22	12	78.4			**0.042**	0.142	0.317100103	0.190	0.399	1.2E-02
23	3	90.4			0.004	**0.004**	0.016324941	0.017	0.607	2.3E-03
24	0	87.3			**	**	**	**	**	**
25	12	88.0			**0.036**	0.148	1.236744158	0.123	0.644	3.1E-03
26	36	89.2			0.332	0.609	780.8925971	**0.109**	0.817	3.7E-03
27	14	92.6			**0.029**	0.266	3.123432534	0.422	0.579	3.6E-03
28	3	90.6			0.002	**0.000**	0.009712431	0.011	0.290	9.5E-03
29	14	108.1			0.058	**0.018**	0.113630672	0.058	1.764	1.0E-06
30	10	97.6			0.014	**0.003**	0.038447633	0.021	1.429	2.0E-05
31	7	92.7			**0.005**	0.007	0.043684484	0.028	1.588	3.0E-06
32	20	98.1			**0.042**	0.100	0.329448568	0.174	1.242	7.0E-05
33	6	22.4			0.005	**0.001**	0.115726286	0.082	1.991	2.0E-06
34	14	38.3			0.471	**0.159**	0.742599873	0.161	1.252	8.0E-05
35	0	20.1			**	**	**	**	**	**
36	18	38.8			**0.047**	0.625	21.88516147	0.242	0.745	4.8E-03
37	174	2067.3			**0.172**	2.847	18.64398342	3.507	0.738	8.0E-04
38	32	111.8			**0.130**	0.287	1.046115698	0.135	0.454	1.9E-02
39	12	43.2			0.290	**0.032**	0.178071364	0.057	0.782	2.1E-03
40	16	554.0	26	33053.5	**0.018**	0.139	0.228183499	0.206	0.743	3.0E-04
41	20	1016.7	10	52151.3	**0.012**	0.204	0.099397593	0.071	0.873	8.0E-05
42	173	229.5			**1.441**	16.723	83662.30091	4.576	0.647	1.1E-02
42a	131	229.5			**0.638**	8.428	949.5758745	2.818	0.597	1.2E-02
43ew	14	194.7	25	2972.2	**0.018**	0.407	0.428016624	0.268	0.524	3.1E-03
43ne	26	194.7			**0.013**	0.219	3.209752776	0.122	0.888	8.0E-04
43	46	194.7	25	2972.2	**0.080**	4.214	2.758382854	1.497	0.733	3.3E-03
44	101	222.0	114	14235.3	**0.654**	23.121	217533.3623	9.279	0.874	2.0E-03
45	157	121.6			**0.555**	28.096	446211337.3	5.341	0.635	2.0E-02
46	160	67.5			**1.805**	45.646	8.22235E+11	10.335	0.728	2.4E-02
47	65	204.6			**0.067**	3.804	6315956208	1.789	0.643	5.0E-03
48	77	182.8			**0.190**	3.563	9381.749456	0.715	0.776	3.2E-03
49	11	108.7			0.027	**0.016**	0.038559546	0.042	1.216	5.0E-05
50	12	94.2			0.070423	**0.012**	0.128974935	0.029	1.142	1.0E-04
51	8	81.6			0.026	**0.007**	0.024862578	0.023	1.053	2.0E-04
52	19	89.6			0.215	**0.058**	1.2788972	0.077	1.592	3.0E-05
53a	134	112.1	42	3594.3	**1.079**	37.310	54.22450117	13.746	0.846	5.5E-03
53	342	112.1	67	3594.3	**16.213**	268.136	2492.191532	86.850	0.974	5.5E-03
54a	150	97.1			**4.595**	45.040	*	115.185	0.895	5.0E-03
54	395	97.1			**40.088**	337.007	*	28863.286	1.120	3.4E-03
55a	97	61.4			**1.284**	29.228	12921861017	26.333	0.664	2.4E-02
55	131	61.4			**2.089**	56.545	*	90.209	0.737	2.2E-02
56	416	131.1	24	1120.5	**10.037**	294.359	*	56.142	0.824	1.6E-02
57	499	40.5			**330.612**	345.662	58779320049	785.524	1.746	9.0E-05
58	64	93.7			1.746	**0.057**	1.21717298	0.116	1.172	4.0E-04
58a	38	93.7			0.587	**0.032**	0.566381016	0.056	1.229	2.0E-04
59	17	85.3			0.224	0.061	1.148255777	**0.055**	1.127	1.0E-04
59a	4	85.3			**0.005**	0.007	0.030890913	0.028	0.703	5.0E-04

geologic controls on size distributions, for the moment I limit my attention to power-law datasets with more than ten fractures (Figure 3-2).

For size distributions best fit by a power-law relationship, the curve can be described with the coefficient *a* and the exponent *b.* The *a* (coefficient) parameter of the power-law equation represents the y-intercept of the line in log-log space (with the y-axis at log(x) = 0); the *b* (exponent) parameter represents the line's slope. It can be qualitatively appreciated from Figure 3-3 and Table 3-3 that variation in *a* among individual datasets is greater than variation in *b*. In fact, there is a systematic increase in *a* with increasing microfracture strain among power-law distributed fracture sets (Figure 3-4). The value of *b* remains roughly constant with increasing strain. In general, less variation in *b* exists among populations containing more fractures (Figure 3-5), suggesting that some variation of *b* can be attributed to statistically inadequate sampling.

The greatest value of *b* from the data subset (the large datasets that are best-fit by power laws) is 1.75, observed among microfractures in the Mesón Group at Yacoraite Canyon (Sample 57). As noted in Chapter 2, the size distribution of these fractures is not well characterized by any simple equation. Likely because of its steep slope, the Yacoraite Canyon size data are nearly equally as well fit by an exponential equation as by a power law. The quality of fit of an exponential equation, relative to that of a power law, is better among these fractures than any other large power-law distributed dataset (Figure 3-6).

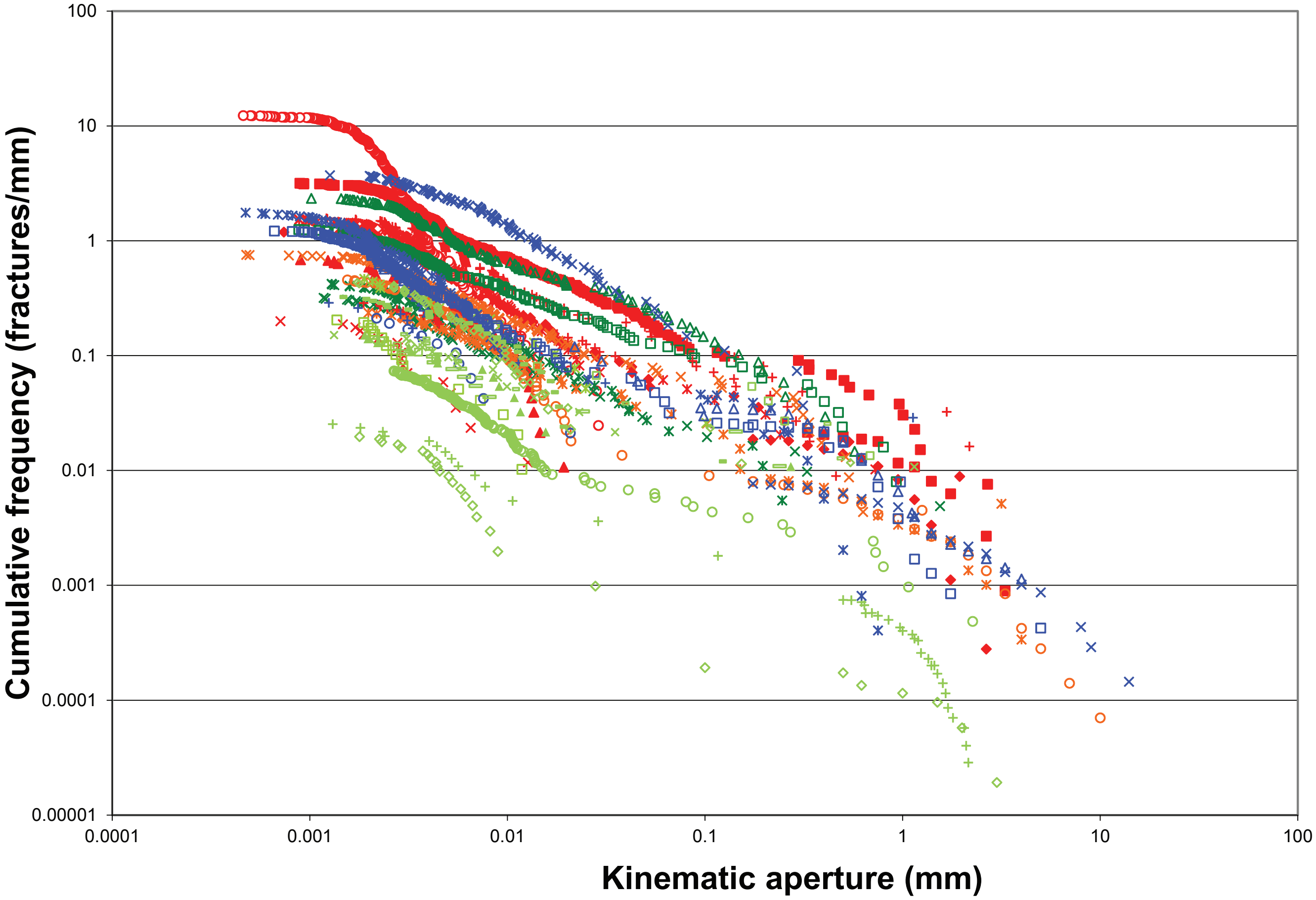

Figure 3-3. Data from Figure 3-2 filtered to include only data sets that 1) are best-fit by a power-law equation, and 2) contain ten or more fractures.

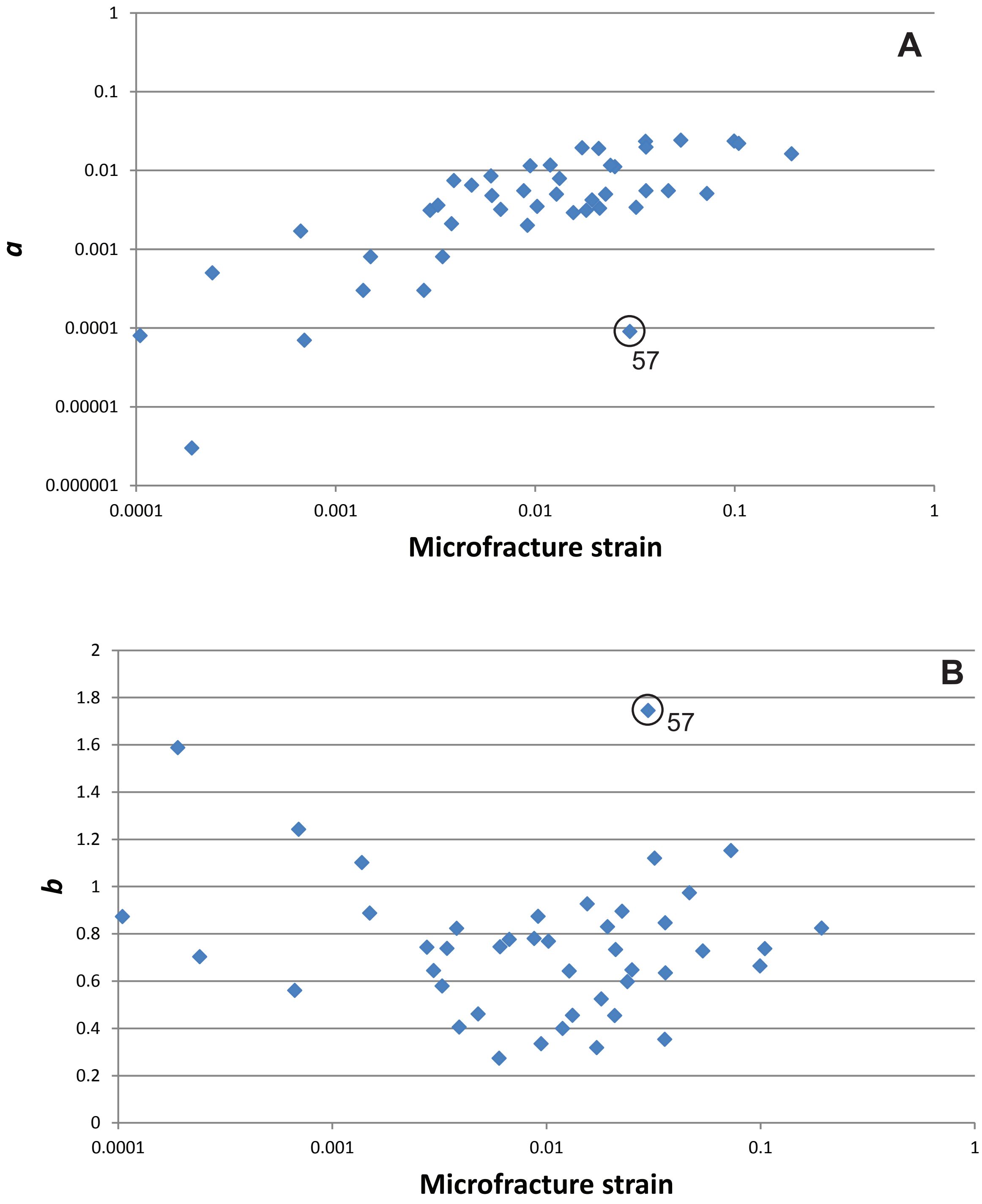

Figure 3-4. (A) Power-law coefficient versus microfracture strain, for samples best fit by a power-law equation. (B) Power-law exponent for same data. Sample 57 (Meson Group) is an outlier in both plots; see text for discussion.

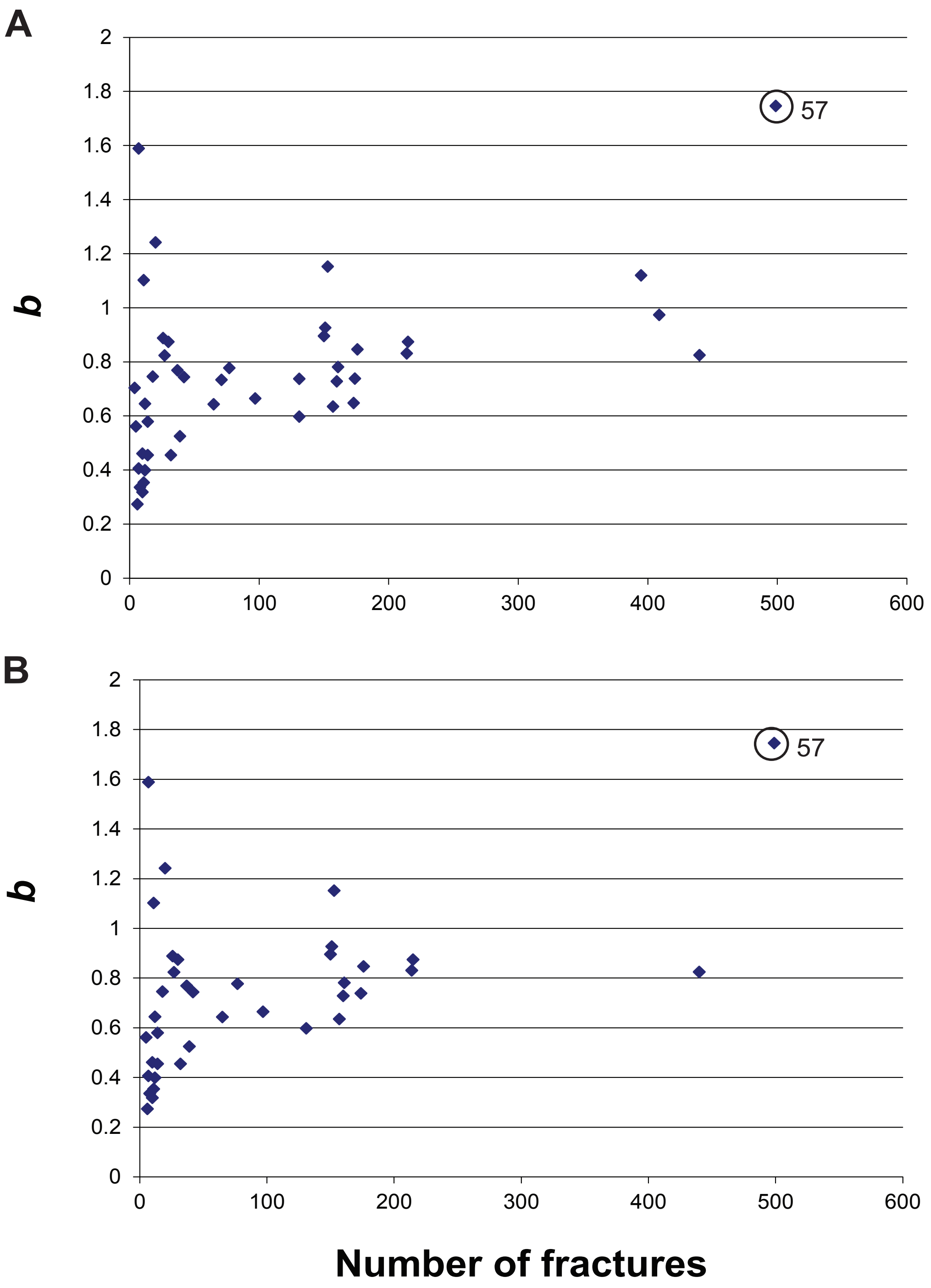

Figure 3-5. (A) Power-law exponent versus number of fractures intersected by scanline. (B) Same data, omitting datasets that include multiple distinct orientations of fractures (shaded rows, Table 3-3). In general, *b* value converges with higher number of fractures sampled. Sample 57 (Meson Group) is a notable exception.

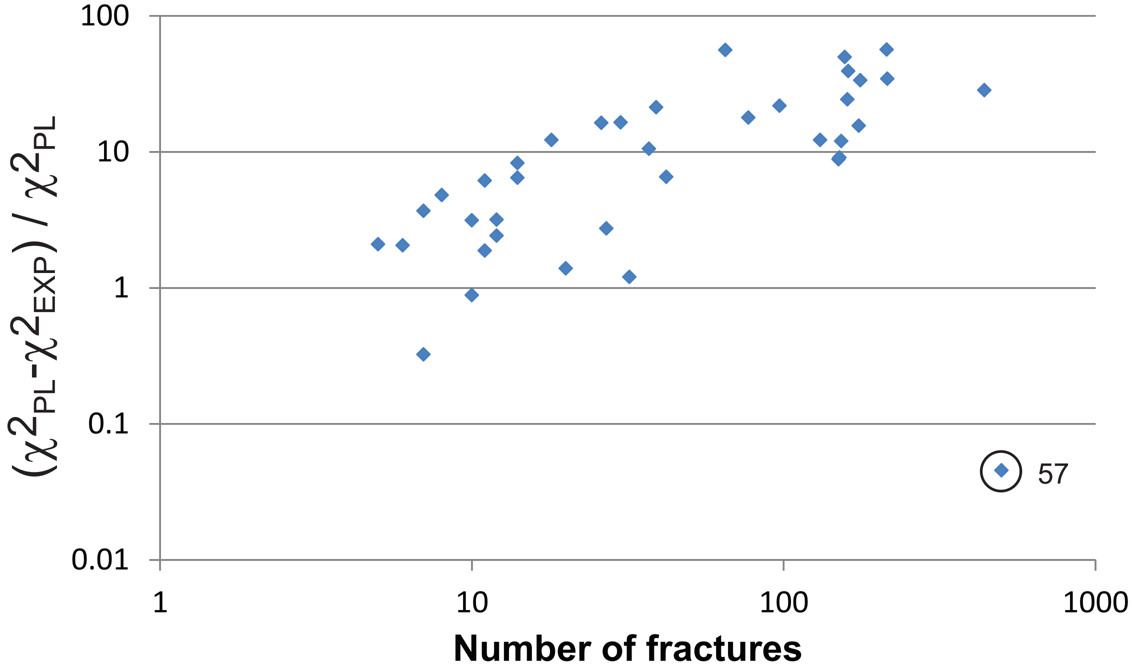

Figure 3-6. The y-axis is a relative measure of the quality of the power-law equation fit to the exponential equation fit. It is the difference between the chi^2 error from the two fits, divided by the chi^2 error from the power-law fit. This is plotted versus number of fractures within strike-filtered datasets that are best-fit by power-law size distributions. All values are negative because all data are better fit by power-law equations than by exponential distributions--the absolute values are plotted. But as more fractures are sampled, generally the relative fit of the power-law equation becomes progressively better; sample 57 is here again anomalous. Though best fit by a power-law size distribution equation, this dataset is nearly as well fit by an exponential equation; other large datasets are easier to distinguish.

Therefore, despite the large number of fractures present in the fracture set measured from Yacoraite Canyon (499), it is less clear that this fracture set follows a power-law size distribution equation, compared to fractures within smaller datasets. Setting aside for the moment the anomalous power-law equation parameters for Sample 57, it appears that power-law distributed fracture sets tend to display a characteristic *b* value, as measured in 1D. The remaining *b* values range from 0.35 to 1.24, with an average of 0.75 and a standard deviation of 0.21. The *b* value list, including the anomalous Sample 57, averages 0.78 and is well fit by normal and log-normal distributions (Figure 3-7). This suggests that *b* has a characteristic value that is common among natural fractures in sandstones. I explore this observation further in Chapter 4.

Characteristic size distributions

Of the 67 fracture populations studied, 21 are better fit by either exponential or log-normal size distribution equations than by power laws. Of these 21, three derive from outcrop samples and 18 from vertical core samples.

The outcrop samples were taken from the Mesón Group, where it is exposed at Huasamayo Canyon. In outcrop, the fracture set consists of bedding-perpendicular, opening-mode fractures with regular spacing and a low range of aperture sizes (no observed fractures are as wide as 1 mm). Almost all macrofractures preserved some porosity in the subsurface, as evidenced by euhedral quartz crystals covering fracture walls and the tendency for the rock to

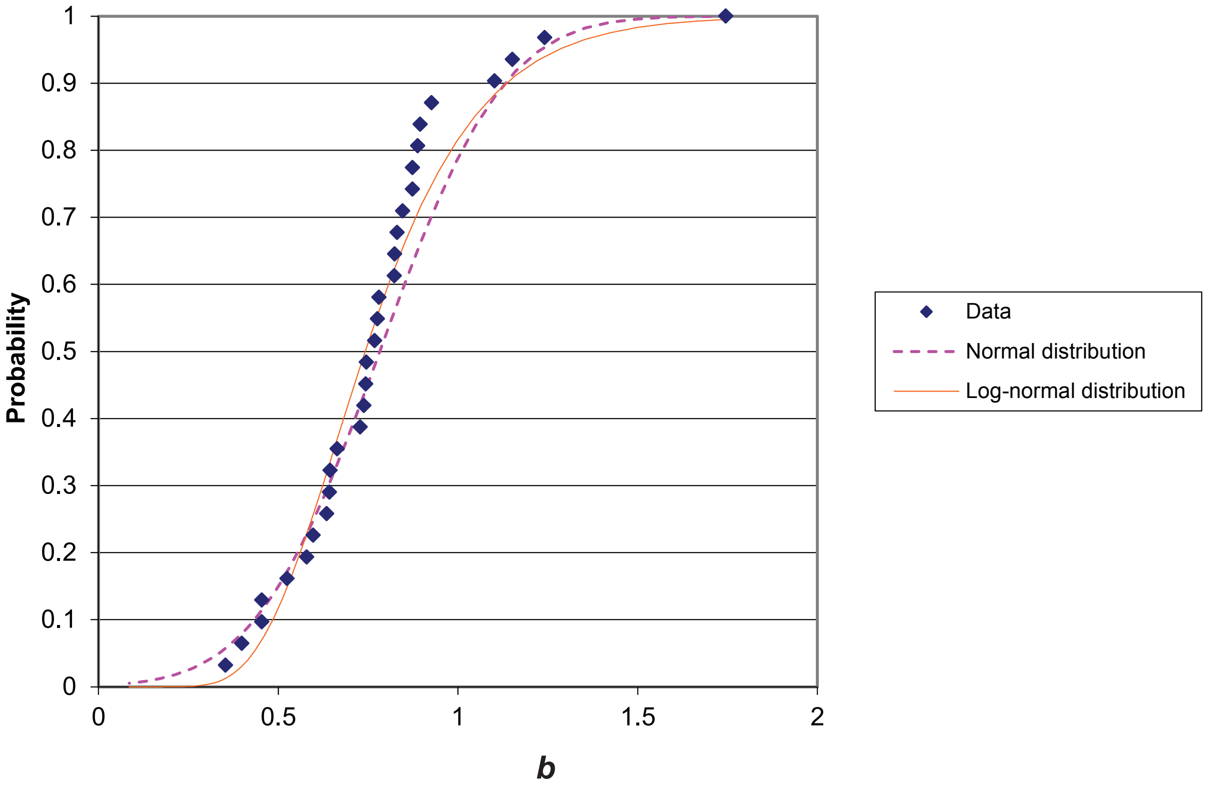

Figure 3-7. Cumulative distribution of *b* values for datasets best-fit by power-law size distributions.

break along these fractures at the outcrop. Macrofractures typically terminate at bedding planes. Microfractures, observed using SEM-CL, cut across grains and intergranular quartz cement. These microfractures are mostly sealed with quartz cement but locally are open, particularly where the fractures cut non-quartz grains (Figure 3-8). This porosity preservation likely stems from quartz precipitation being slower on non-quartz substrates (Lander and Walderhaug, 1999).

The remaining characteristic-size fracture sets all derive from scanlines drawn across vertical cores. Such fracture populations typically feature small numbers of fractures (average 12.6, maximum 36). As well, partially owing to the paucity of large fractures in such sets, these populations feature very low strain: the average strain manifest among microfractures, for the entire dataset, is 0.016; in contrast, the average strain for core-width scanline fractures best fit by characteristic size distribution equations is 0.0015.

FRACTURE CEMENT TEXTURES

Although this study is limited to fractures that contain cement, the type of cement played no role in the scanline selection process. Only upon observation in thin section was it confirmed that the first cement phase deposited within all fractures in each sample was quartz. Typically, this phase was deposited during fracture opening. In three of six field sites, later, overlapping carbonate cements are common, but in all three cases later carbonate cements are heterogeneously

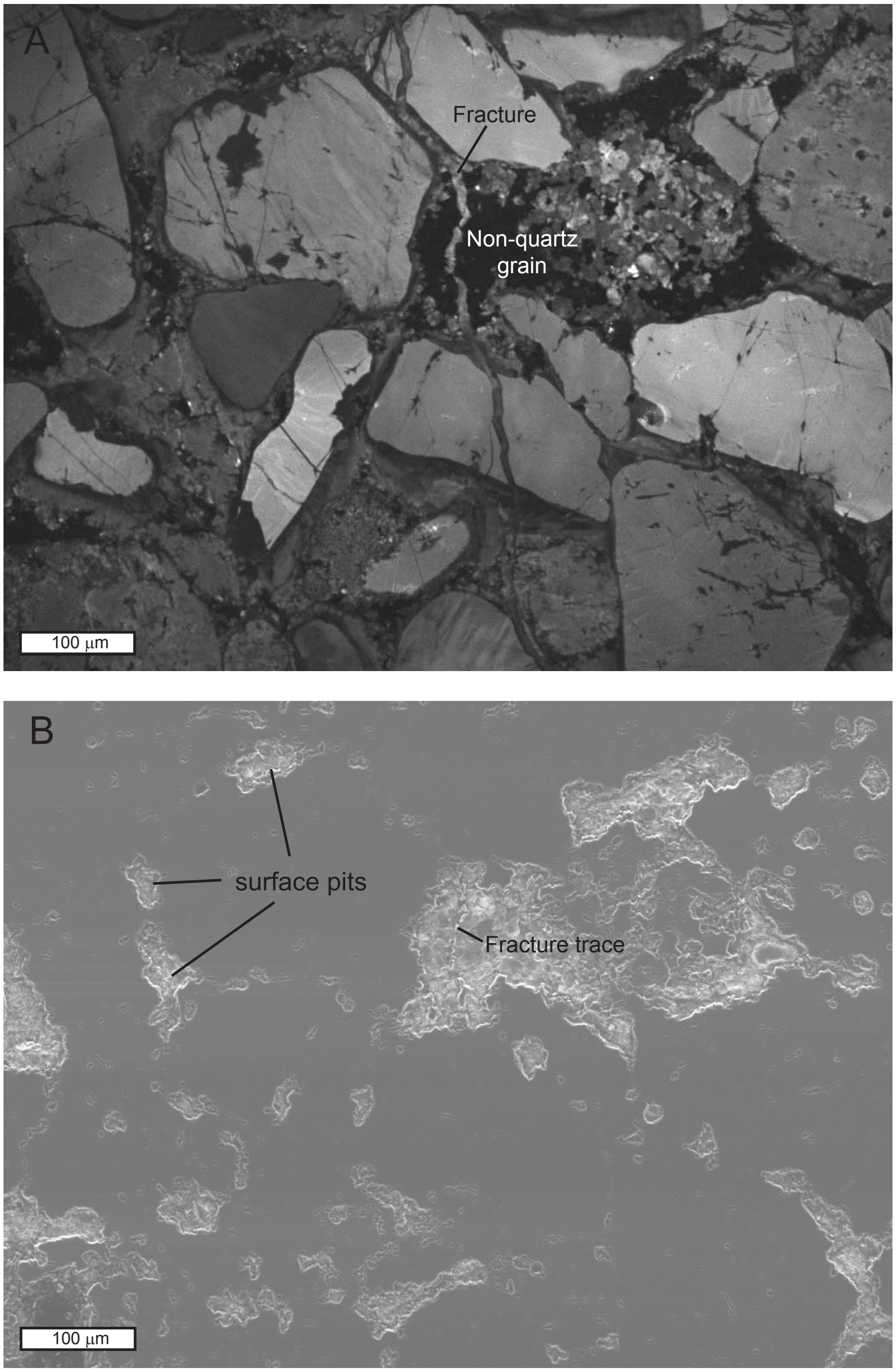

Figure 3-8. (A) Cathodoluminescence and (B) secondary electron images of microfracture from the Meson Group (Huasamayo Canyon exposure, Sample 58). Most of the fracture is entirely occluded with quartz cement (luminescing medium gray). Where the fracture cuts a non-quartz grain, visible in CL by irregular and dark luminescence, and in SE by pitted surface, the fracture is porous (bright CL and pitted trace in SE).

distributed. Such heterogeneous distributions of late-stage carbonate cement are common in fractured tight-gas sandstones (Laubach, 2003), but the causes of heterogeneity are obscure.

It is evident from SEM-CL images that crack-seal texture is common among fractures in the scanline datasets. Crack-seal texture consists of bands of cement that run parallel to the fracture walls, suggesting repeated cracking of the fracture along fracture-wall-parallel surfaces within the cement or at the cement-wall interface (Urai et al., 1991). These bands form as cement is deposited during fracture growth. During growth the fracture undergoes an increment of opening and cement fills in across the gap (Figure 3-9). These cement bands are broken during subsequent opening increments, and the crosscutting relations are evident in SEM-CL images (Becker et al., 2010). As this process repeats, crack-seal texture forms within the growing fracture.

Whether crack-seal develops within an opening fracture therefore depends on the relative rates of fracture opening and cement deposition. If fracture opening outpaces cement deposition, the local sealing step is not achieved, and crack-seal texture does not form. Because the rate of cement deposition is much faster on freshly broken surfaces than on euhedral crystal faces (Lander et al., 2008), crack-seal cementation commonly forms isolated bridge deposits upon host-rock grains whose fast-growth crystallographic axis is oriented at high angle to the fracture. This process potentially leaves porosity in

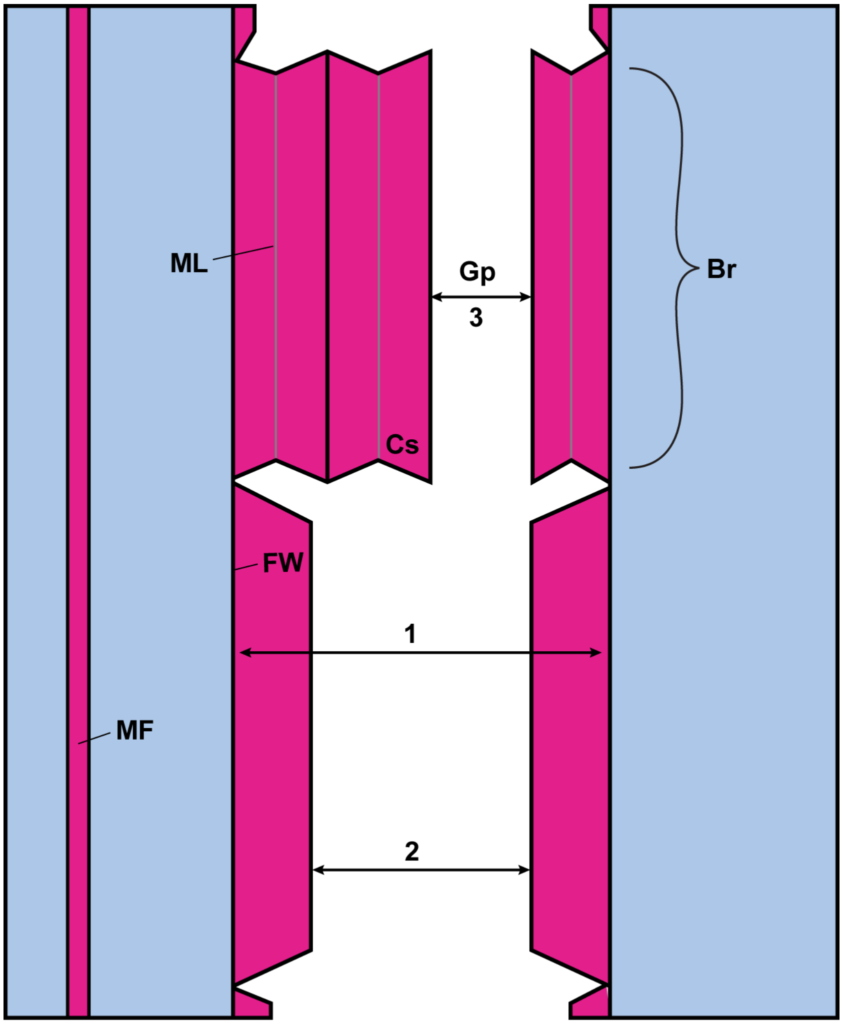

Figure 3-9. Diagram of synkinematic fracture cement, from Hooker et al. (2012). Host rock in blue; fracture cement in magenta, pore space in white. 1, Kinematic aperture (Marrett et al. 1999), distance fracture walls have moved apart, the opening displacement or fracture width. In this diagram, kinematic aperture is constant along fracture. 2, Aperture, the open dimension of the fracture perpendicular to fracture walls. In this diagram, aperture is variable. 3, Gap size, Gp (Laubach et al. 2004a), the opening displacement size recorded in cement textures within crack-seal bridge, marking incremental widening of the fracture. FW, fracture wall. ML, medial line, where cement deposits from opposite walls meet. Br, bridge. Cs, synkinematic cement. MF, microfracture.

between cement bridges (Laubach, 1988; Laubach et al., 2004c; Becker et al., 2010; Gale et al., 2010).

Gap-width size and overall-fracture aperture-size

The wide variation in fracture sizes inherent in power-law distributed fracture sets with b<1 appears to be achieved by the fractures having a wide range of *numbers* of opening increments, as opposed to a wide variation of opening increment *sizes*. For example, fractures within Sample 45, from the Jurassic Nikanassin Formation, are best fit by power-law size distributions. Within these fractures, overall-fracture kinematic aperture correlates better with the number of crack-seal increments than with the width of crack-seal increments (Figure 3-10). In other words, the larger fractures among power-law datasets feature more crack-seal increments than do smaller fractures. The relationship between crack-seal increment width and overall fracture width is not consistent. The gap widths are well fit by a log-normal size distribution, indicating a characteristic size to the opening increments. Similar distributions of gap widths within crack-seal textures were documented by Laubach et al. (2004a), Renard et al. (2005), and Hooker et al. (2012).

Most fracture sets within the collective dataset feature some crack-seal texture, but such texture is mostly absent from fractures that follow characteristic size distributions (Figure 3-8). Characteristic-size fractures are thin (<10 μm in aperture), dark-luminescing, and textureless. No characteristic size distributed

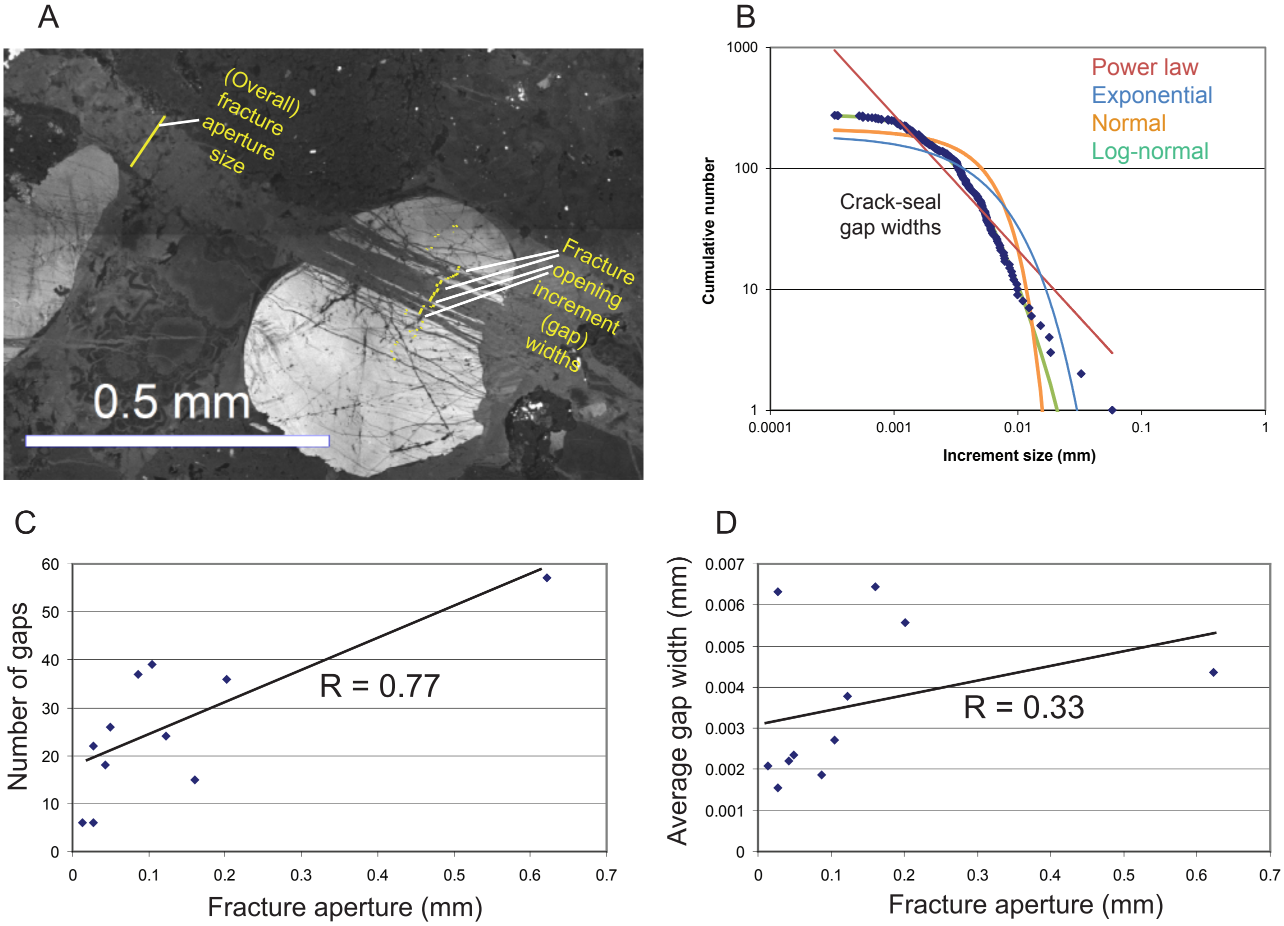

Figure 3-10. (A) SEM-CL image of fracture from the Nikanassin Formation (Sample 45) that grew by repeated, incremental opening (crack-seal). (B) Cumulative plot of the widths of 11 such fractures' opening increments, within the same sample. The fractures are well-fit by a log-normal equation. There appears to be little variation in the magnitude of opening among the increments; rather, larger fractures are larger because they have undergone more opening increments of roughly the same size as those undergone by smaller fractures. The stronger correlation between number of opening increments and fracture size (C) than between average increment width and fracture size (D) is consistent with this hypothesis (Pearson coefficients shown).

fracture sets feature fractures more than two to three increments wide, as preserved within crack-seal texture. Because of the limited resolution of the SEM-CL imaging technique these observations do not preclude the possibility of sub-micron-scale crack-seal bands within these fractures. However, such hypothetical, sub-micron-scale crack-seal bands do not appear to be organized within fractures so as to achieve wide variations in fracture size, as is the case for power-law distributed fracture sets.

INTERPRETATION OF CURVES WITHIN SIZE DISTRIBUTIONS

Curves among small-fracture sizes

For the majority of fracture sets observed, aperture-frequency data are well approximated by power-law equations over an aperture size range between approximately 0.001 and 1 mm (Figure 3-2, Table 3-3). Such sets of size-frequency data form generally straight lines on plots of log (frequency) versus log (size), yet nonetheless feature curves, in log-log space, over limited size ranges. If these curves are the result of inadequate sampling of ideal power-law populations, then best-fitting equations to the curves could potentially lead to spurious size-distribution interpretations (Odling, 1997).

Alternatively, curves in size distributions may signify natural complexity in scaling behavior. Take for example the size distribution of Sample 44, the E-W striking fractures in the El Alamar Formation (Figure 3-11). The overall population (combined micro- and macrofractures) is best fit by a power-law equation. The

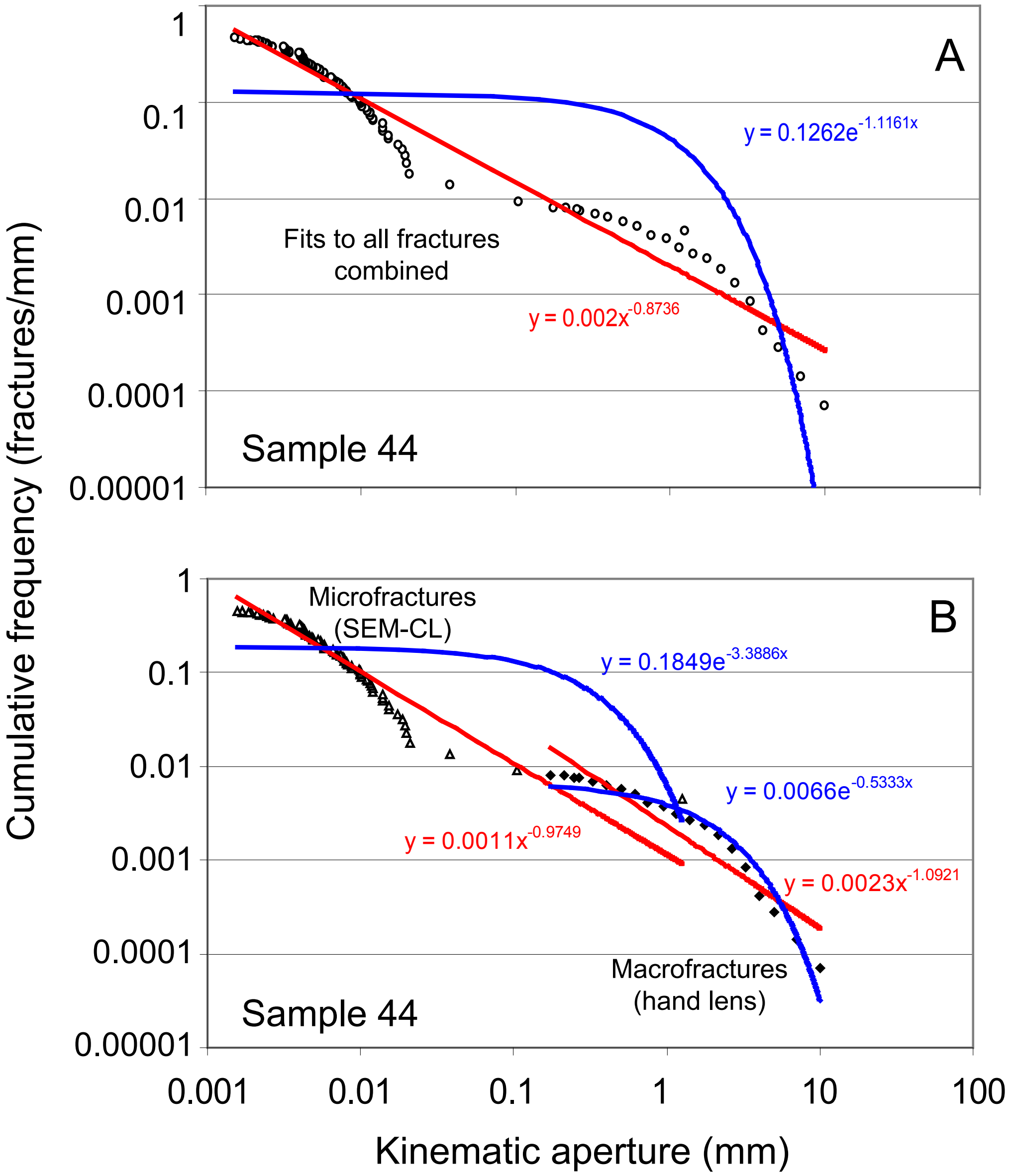

Figure 3-11. Size distribution of E-W striking fractures within the El Alamar Formation. Fractures included were measured at two scales: in the field, using a hand lens and comparator, and using SEM-CL. (A) All fractures, with size-distribution equations best-fit to entire population. (B) Micro- and macro-fracture populations with equations best-fit separately. Entire population is well-fit by a power-law size distribution equaiton; macrofractures alone are better fit by an exponential equation.

separate microfracture and macrofracture populations, however, do not follow a line in log-log space. Rather, the data form two concave-downwards curves, corresponding to the scale of observation (SEM-CL and outcrop). Consequently, if fractures observed using a hands lens on the outcrop and fractures observed using SEM-CL are viewed separately (Figure 3-11), these data are better fit by characteristic size distributions than by power-law size distributions. In this section I address the curves present in the size distributions in Figure 3-3, with the goals of 1) distinguishing sampling biases from real departures from power-law scaling, and 2) exploring the feasibility of predicting large-fracture spacing using only small-fracture size data, given these scaling irregularities.

The following are three interpretations of concave-downwards scaling curves among the smallest aperture sizes measured. Representative examples of such curves (Appendix B) are present for fractures < 0.03 mm wide among E-W striking fractures in the El Alamar Formation and for fractures < 0.02 mm wide among fractures from Sample 37, a slant core from the Cretaceous Williams Fork Formation. The first two interpretations invoke imperfect sampling of an ideal power-law size distribution; the third suggests a real departure from power law scaling. None of the three excludes any other.

Interpretation 1: truncation bias

As discussed in Chapter 2, the small-fracture end of the size distribution can be expected to show truncation bias, in the form of a concave downwards curve. Such bias can arise when fractures are measured near the resolution of the imaged fractures. For classically defined (resolution-limited) truncation bias (Baecher and Lanney, 1978), this bias assumes correct measurement of fracture size but incomplete fracture detection, and thus should represent only under-estimations of fracture frequency (Figure 2-5). As such, this form of bias poorly explains the shapes of the observed size distribution curves, which feature concave-*upward* segments above the smallest fracture sizes measured (> 0.01 mm for both Sample 37 and Sample 44). The observed curves could potentially be explained by precision-limited truncation bias, which involves imprecise measurement of fracture sizes near the (characteristic) pixel size. In log-log space, the error in size associated with this uncertainty should diminish towards larger size ranges; if the fractures present follow an ideal power-law size distribution, larger fractures should plot along a straight line. Moving towards smaller fractures, the curved part of the scaling data should deviate initially upwards from the power-law line, then deviate towards horizontal, crossing the ideal power-law line (Figure 2-6). This precision-limited truncation bias likely does not apply because the curves to the observed fracture-size distributions are well above the pixel width (<0.001 mm). Thus neither form of truncation bias well explains the observed curves.

Interpretation 2: inclusion of inappropriate measurements within the dataset

Upward deviation from ideal power-law size distributions may result from inclusion in the dataset of features which are not actually microscopic fractures related to the large-fracture population. For example, image artifacts may be misinterpreted as natural fractures. Such artifacts are linear features that resemble fractures, such as scratches or other imperfections of the thin section surface.

Another example of features that may be inappropriately included in the dataset is natural fractures that are not genetically related, for example inherited and grain-deformation fractures unrelated to a throughgoing fracture set. The protocol used to interpret which microfractures are genetically related to the macrofractures is described above and by Laubach (1997) and Hooker et al. (2009). To briefly reiterate: microfractures are assumed to be related to macrofractures if microfractures and macrofractures are parallel and occupy the same part of the diagenetic sequence (are filled with the same cement), and if microfractures are transgranular.

Despite careful adherence to this protocol, SEM-CL signal can still be ambiguous, especially for small features. For example, intragranular fractures may be aligned by chance in adjacent grains with little intervening cement, or cement with low contrast to the CL response of the fractures, giving the illusion of a single transgranular fracture (Figure 3-12).

Interpretation 3: a characteristic minimum fracture size

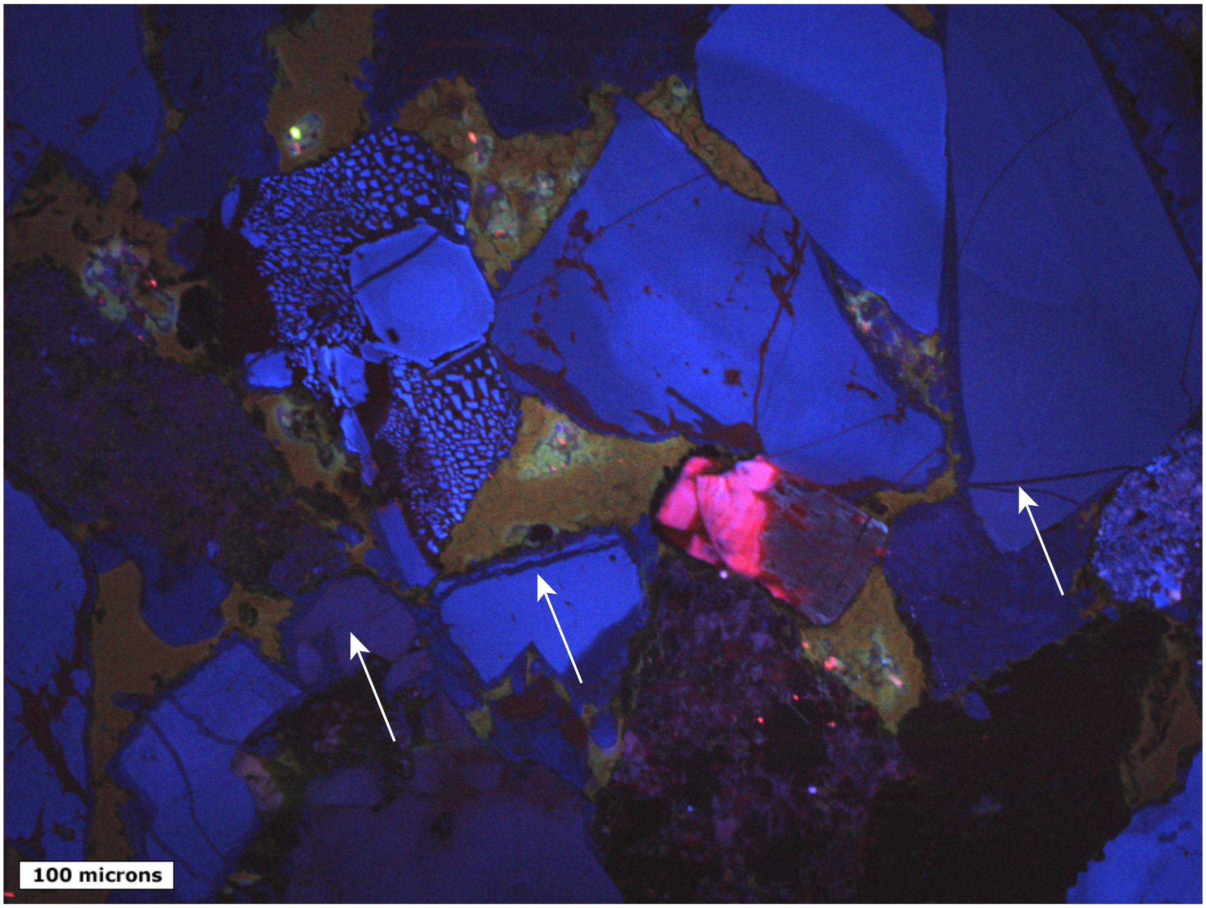

Figure 3-12. SEM-CL image of quartz grains in sandstone with microfractures of ambiguous timing. Epoxy (porosity) luminesces green. Arrows indicate intragranular microfractures that are aligned and so may be misinterpreted as a single through-going fracture. This ambiguity of fracture origin can be exacerbated by low CL-contrast between fracture cement and primary pore-filling cement, and the tendency for fractures to deflect at grain boundaries.

The concave-downwards curve may be real and represent a characteristic minimum opening distance achieved when fractures propagate. Two observations suggest this might be the case. One is the aforementioned characteristic size of crack-seal increment widths—fractures from the Nikanassin Formation, for example, appear to be composed of multiple characteristic-size opening increments. The other observation is apparent imperfect reactivation of fractures within the El Alamar Formation (Figure 2-2) and other samples. SEM-CL images reveal that neighboring opening increments may be generally connected and thought of as parts of a single fracture, but are locally dispersed, with host rock in between. Therefore the measured size distribution may change depending on the location at which the scanline intersects fractures that locally branch.

If power-law size distributions indeed arise from the grouping of micron-scale-width opening increments into larger fractures, perhaps size-distribution complexity would be introduced if this grouping mechanism is imperfect. The microfractures imaged in Figures 2-2 and 3-10 illustrate grain-scale cement precipitation effects on fracture opening. Where fractures cut quartz grains on which quartz cement precipitation was rapid enough to bridge the opening gaps as the fracture grew, the bridges had to re-crack with every widening increment. In regions of the same fracture where cement precipitation was slower, the fracture remained open and so there was no cohesive material to break as the fracture widened. Consequently, what appears to be a single fracture with unambiguous walls where cement precipitation was slow, elsewhere appears as a cluster of individual opening increments *with local intervening host rock slivers* where cement precipitation was fast. This local branching of the fracture trace is a consequence of inconsistency in the locations of re-cracking surfaces within the cement bridges. If a single fracture can be locally discrete where cement precipitated slowly and locally diffuse where cement precipitated quickly, then it is conceivable that an entire fracture, or at least most of a fracture, might be diffuse if cement precipitation was fast, relative to fracture opening, throughout. Microfractures within the El Alamar Formation superficially resemble fractures described by Caputo and Hancock (1999), which the authors interpret to branch because the host-rock material is weaker than the fracture fill.

Consider the hypothesis that the concave-downwards curve among the microfracture size distribution in Sample 44 represents natural complexity related to diffuse fracturing. If the cement precipitation rate had been slower, relative to the fracture opening rate, the fractures in this sample would have been less thoroughly sealed with cement during growth and would have formed as discrete larger fractures. Instead, the cementation rate was sufficiently fast to cause later opening increments to imperfectly localize along earlier ones, the same way in which the opening increments are locally diffuse in Figure 3-10. With slower cement precipitation, the characteristic-size opening increments would combine to make larger fractures, and thus there would be fewer fractures intersecting the scanline. As observed, the diffuse fracturing is manifest in the scanline data as a greater number of small (characteristic-sized, <0.01 mm-wide) fractures. Lacking a direct test of this hypothesis, the effect of diffuse fracturing on size distributions can still be done via a geometric experiment. Apply a threshold spacing value (for fractures in Sample 44, 0.15 mm) and treat as a *single fracture* any fracture increments separated by less than this threshold value. That is, sum the widths of individual fracture increments separated by less than the threshold value, and treat any summed widths as a single fracture. In doing so, the assumption is made that fractures separated by less than this threshold value would have formed together, as a larger fracture with no separation in between, if the cement precipitation rate had been slower. Figure 3-13 shows the original microfracture size distribution and that resulting from the summation of nearby fracture increments. The latter resulting size distribution is better fit by a power-law equation; as well, the power-law equation best fit to the resulting size distribution has a *b* value closer to the average of all large power-law datasets (0.8).

Curves among large-fracture sizes

Fracture size data also typically deviate from best-fit power-law equations at the large-size end of the data distribution, and systematically in a concave-downward sense. The reasons for this deviation are discussed in Chapter 2, and I summarize them as follows:

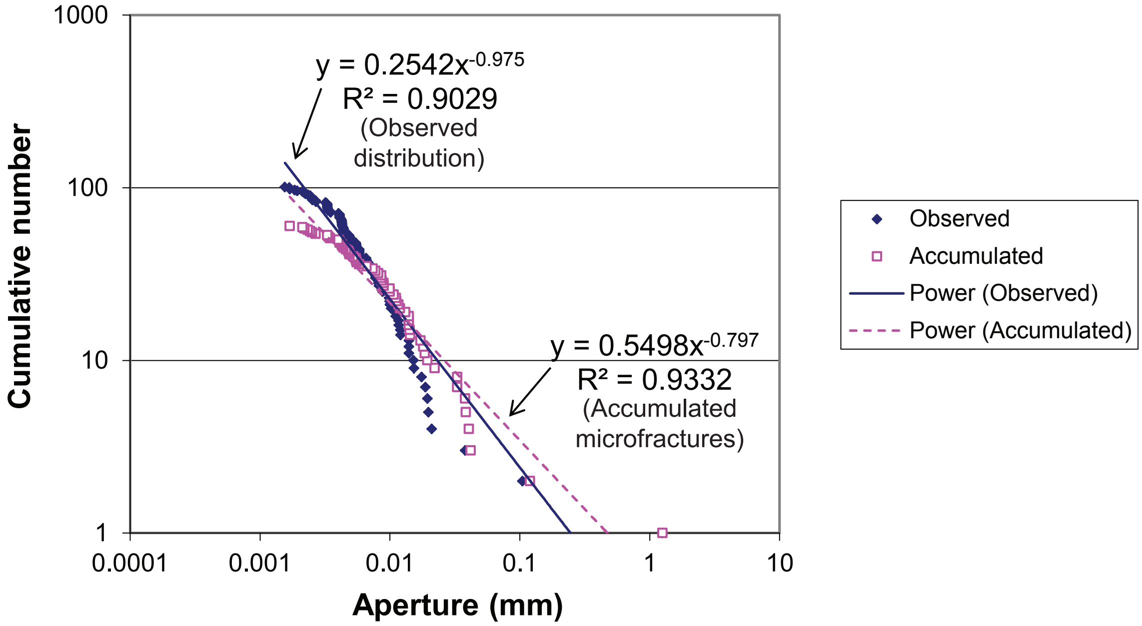

Figure 3-13. Fracture size distribution numerical experiment for E-W striking microfractures within the El Alamar Formation. Observed data are the same as presented in Figure 3-11. One likely reason for the irregularity of this size distribution is diffuse fracturing, especially where the growing fractures cut quartz substrates (Figure 2-2). As a way to test what the size distribution would be had these fracture increments formed together, all increments were accumulated into a single fracture if the spacing between the nearest neighbors was less than 0.15 mm. The resulting size distribution is better fit by a power-law equation with a *b* value closer to the typical *b* value observed in sandstones (Figure 3-3).

The largest fracture sizes sampled in a scanline are necessarily statistically inadequate.

As explained by Guerriero et al. (2010), progressively smaller cumulative sample sizes increase the statistical error of the cumulative frequency calculation towards the right side of the scaling plot. Thus greater deviation from any underlying ideal size distribution can be expected to increase among the largest fracture sizes encountered in a single dataset. This deviation may be upwards or downwards from the best-fit distribution among smaller fractures.

Finite strain and theoretical considerations necessitate an upper limit to the power law.

The large-size end of the distribution may systematically curve downwards from a power-law equation because the rocks have only undergone so much strain. Finite strain necessitates some upper limit to fracture size. As is likely the case for fractures measured at Perchel Canyon (Figure 2-13), fractures may be sampled near their upper-size limit, and the downwards curve to the size distribution is real.

Moreover, for fracture populations that follow a power-law aperture size distributions with *b* less than 1, the frequency of large fractures must necessarily fall below the best-fit size distribution equations because such equations eventually predict a greater frequency of large fractures than can fit within the rock observed (Hooker et al., 2011; Chapter 2).

The cumulative frequency (F) of fractures (in number of fractures per unit length of scanline) is the cumulative number of fractures (N in Equation 2-1) divided by the scanline length. Fracture size *X* cannot exceed *1/F* (i.e. the average spacing of 1 mm-wide fractures cannot be less than 1 mm). Setting *X* equal to *1/F* and rearranging Equation 2-1 gives a theoretical maximum fracture aperture size for given values of *a* and *b*:

$$X_{\max} = \frac{1}{a}^{\frac{1}{1-b}} \qquad (3\text{-}1)$$

That the 1D data observed here show best-fit *b* values averaging 0.8 suggests that a 3D survey of the same fractures might produce power-law exponents averaging as great as 2.8, because 1D observation systematically under-records small fractures (Marrett, 1996; Borgos et al., 2000; Bonnet et al., 2001). Power laws with *b* > 1 are likewise limited at the *small*-aperture-size end of the distribution, so the observed fracture sets may show scale invariance at larger and larger size scales. However, establishing the frequency of larger fractures would require measurement in 2D or 3D. Results of 2D fracture measurement are reported in Chapter 4.

The theoretical largest fracture sizes that may be present for a given fracture size distribution are shown in Figure 2-3. Using *b* = 0.8 and the greatest *a* value observed (0.024), the greatest possible fracture size is 1.3x10^8 mm (130 km) in width. Fracture size distributions with lower *a* values would have larger maximum theoretical fracture sizes. Therefore the fracture populations examined are more likely limited by finite strain rather than theoretical geometric considerations. Such geometric limitations do not explain the curves to the large-size ends of the distributions.

IMPLICATIONS FOR FRACTURE GROWTH AND THE EVOLUTION OF FRACTURE SETS

The consistency of the natural *b* value is an phenomenon that could provide evidence of an underlying consistent process. The set of *b* values recorded among fractures in sandstones is well fit by normal and log-normal equations, suggesting that 0.8 is a characteristic value whose development is favored by natural deformation conditions. What limited variation in *b* there is within the data might be systematically related to some geological condition or conditions. In Chapter 4 I test the fracture data for correlations between *b* value and various geologic variables. In Chapter 5 rule-based fracture models are explored as a way of testing the potential for creating such a pattern of *b* values by gradual accumulation of fracture strain in the presence of cement precipitation.

The relatively good fit of power-law versus characteristic size distribution equations suggest that as a general tendency, but not a strict rule, natural fractures that formed in the subsurface follow power-law size distributions. Previous simulations of fracture growth (Cowie et al., 1993; Cladouhos and

Marrett, 1996) show that power-law fracture-size distributions may arise by interaction among growing fractures, particularly when such interaction provides positive feedback mechanisms that promote the further growth of already-large fractures. In contrast, populations of characteristic-sized fractures might signify external controls on fracture size, such as sedimentary layer thickness (Gillespie et al., 2001).

In Chapter 5 a model is presented that reproduces the size distributions observed here, with the aim of providing hypotheses for how such size distributions develop. The narrow range in *b* among natural power-law distributed fractures suggests that the size distribution of these fracture sets develops a power law, of low coefficient, early in the fracture strain history. As fracture strain accumulates, the power law maintains its slope while its coefficient increases. This hypothesis is supported by the positive correlation between *a* and fracture strain, along with the poor correlation between *b* and strain (Figure 3-4). For fracture strain to increase, fractures must become larger or more numerous, or both. A power-law size distribution of consistent slope and increasing coefficient requires that fractures of all sizes present become more numerous. This may be achieved either by 1) the addition of new fractures having a variety of sizes, or by 2) the addition of microfractures and gradual widening of existing fractures. Either case suggests that new microfractures develop throughout the accumulation of fracture strain.

Chapter 4: Controls on the scaling exponent

In Chapter 3 analysis of scanlines from six sandstones within different geologic settings found a characteristic *b* value (slope) in power-law fracture-size distributions. The goal of this chapter is to correlate the variation in observed *b* values with other factors and so explore possible controls on the fracture scaling exponent.

The 31 *b* values from fracture sets best-fit by power-law size distributions and containing more than ten fractures (Figure 3-3) range from 0.35 to 1.75; the average is 0.78 and the standard deviation, 0.27. Similar values (between 0.6 and 1.0) have been documented in other 1D surveys of opening-mode fractures (Wong et al., 1989; McCaffrey and Johnston, 1996; McCaffrey and Petford, 1997; Marrett el al., 1999; Ortega et al., 2006; Hooker et al., 2011), suggesting that ~0.8 is a characteristic value whose development is favored under a range of natural fracture growth conditions. The dataset presented in Chapter 3 shows that *b* near 0.8 is present among fracture sets having wide ranges of strain, in a variety of structural settings. Accordingly, that *b* value may be thought of as a natural example of an *attractor* (Milnor, 1985). Attractors are persistent states of dynamic systems, i.e., systems involving time-dependent interactions of multiple variables. An evolving natural fracture-size distribution is a dynamic system which likely has many important factors: differential stress, strain rate, temperature, fluid pressure, fluid chemistry, etc. However, variation among these factors produces little variation in *b*. Perhaps *b* then is an inherently stable outcome of the dynamic process of fracture opening and variation from its characteristic value (0.8) represents only noise, as from poor sampling (Figure 3-5). Alternatively, *b* may vary with rock properties, structural setting, or with other fracture-pattern parameters.

It should also be noted that the *b* values reported in Chapter 3 were derived from best-fitting power-law equations to likely biased data. The method employed then was intended primarily to judge the relative quality-of-fit of different equations to size-frequency data. To best estimate *b*, it may be preferable to directly account for biases.

POTENTIAL VARIATION IN *b* BY SAMPLING METHOD

The consistent sampling method (scanlines) employed in the data collection for this dissertation should preclude any variation in *b* based on varying sampling method. However, it is important to review how *b* can vary by sampling method in order to establish the extent to which *b* values measured here are comparable to published *b* values.

1D versus 2D sampling

A given *b* value recorded by 1D sampling would likely be greater using 2D or 3D sampling (Chapter 2). This sampling dimension effect can have important consequences for the overall architecture of the fracture network because the *b* value implies bounds to size distribution. Size distributions with *b*>1 are limited at the lower-size end of the distribution by the amount of space within the host rock in which the fractures may be contained; the upper-size limit is constrained for size distributions with *b*<1 (Hooker et al., 2011; Chapter 2).

The extent to which 1D sampling results in lower observed *b* values, as compared to 2D sampling, can be assessed by comparing 1D and 2D analyses (e.g., Ortega, 2002). SEM-CL fracture maps enabled such a comparison for two datasets. To measure fractures in 2D, fracture traces were digitally represented using four-point polygons (Figure 4-1). Two points represent the fracture tips; the other two are drawn on opposite fracture walls where the fracture is widest. From Cartesian coordinates of these four points can be derived fracture azimuth (relative to the fracture map), fracture length, and maximum fracture aperture. Fracture maps were constructed from SEM-CL imaged areas from thin sections from the Mesón Group, Sample 53 (Figure 4-2, Figure 4-3) and the Nikanassin Formation, Sample 45 (Figure 4-4, Figure 4-5). In each case fractures are present in crisscrossing arrays and so *b* values can be compared for both the entire observed populations and the azimuth-filtered sub-populations.

Within the Mesón Group, *b* for all microfracture orientations is 0.930 (1D) and 1.507 (2D). Filtering fractures by strike results in *b* values of 0.773 (1D) and 1.017 (2D). The greater steepening of the unfiltered fracture intensity curve likely stems from greater strike-dispersion among small fractures than large (Figure 4-2). One interpretation of this outcome is that multiple genetically distinct, parallel

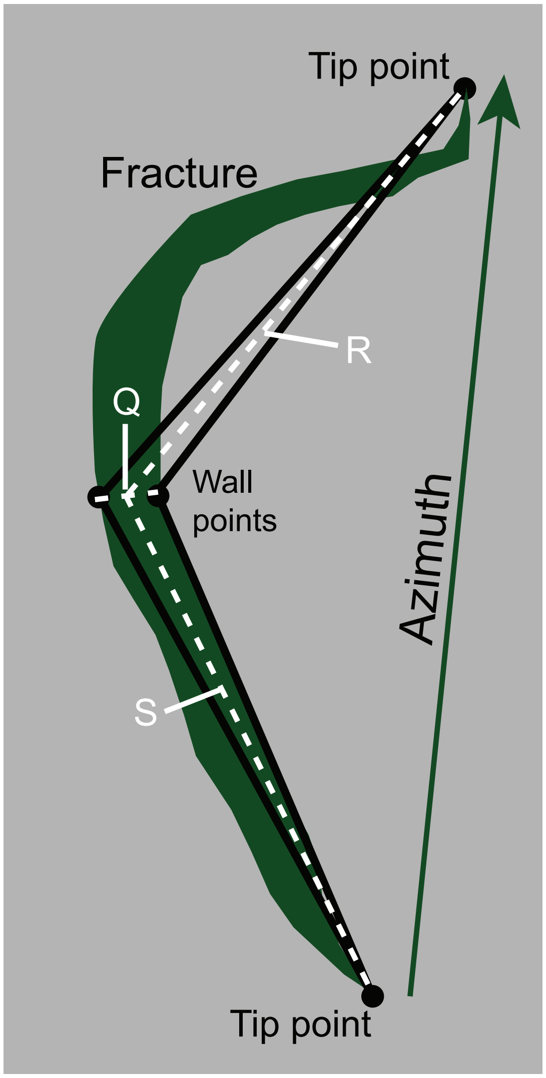

Figure 4-1. Four-point polygon fracture representation for 2D analysis. Polygon points are drawn at each fracture tip and at opposite points along each host rock wall (irrespective of cement or porosity between), where the fracture is widest. The points are given Cartesian coordinates, and the lengths of lines Q, R, and S are calculated. Fracture aperture is line Q; length is the sum of lines R and S. Azimuth can also be measured for oriented samples. Method after Ortega (2002).

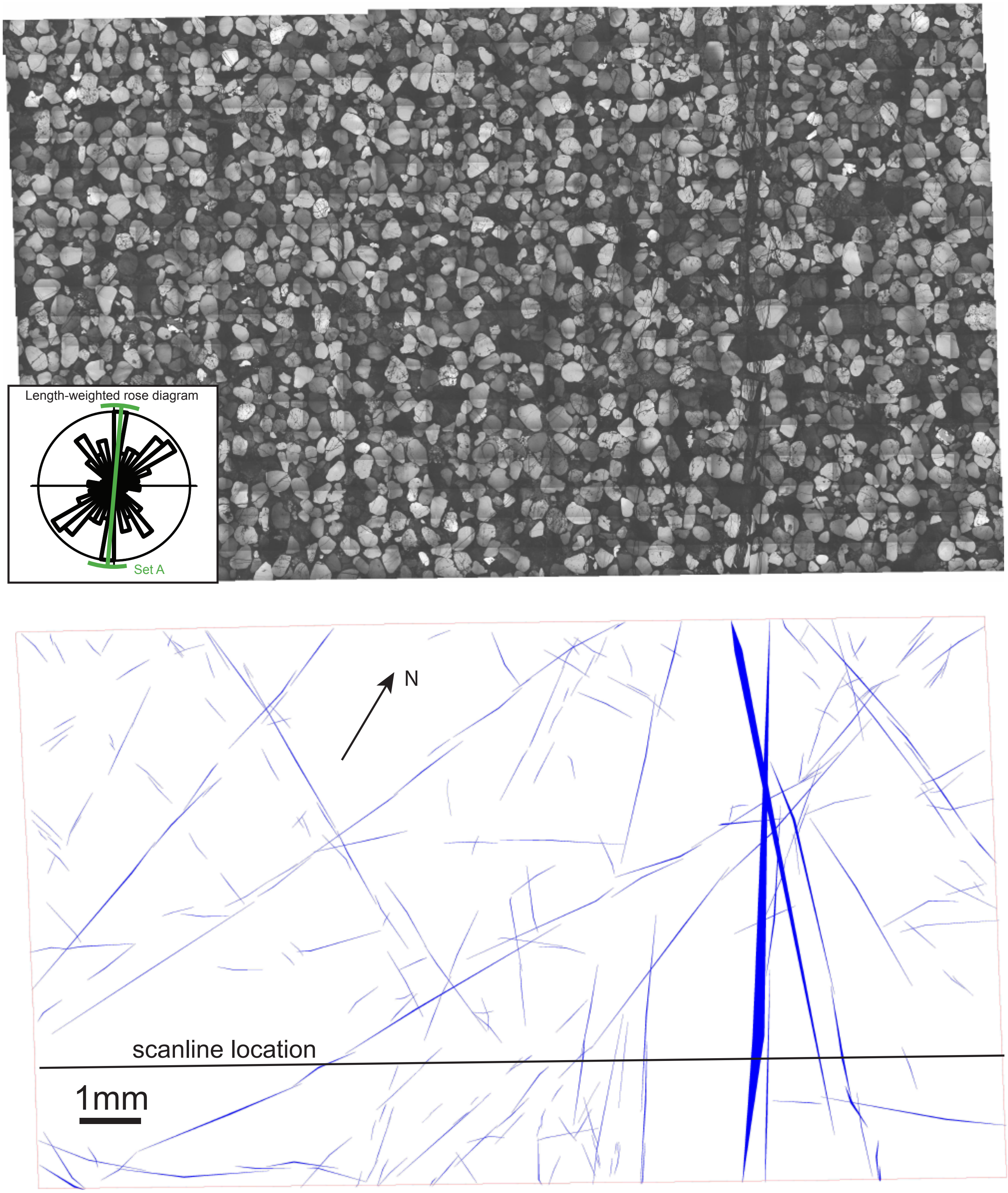

Figure 4-2. 2D map of microfractures identified in Sample 53 (Meson Group, Perchel Canyon). Thin section cut parallel to bedding. Fracture cement has low luminescence; grains have variable luminescence.

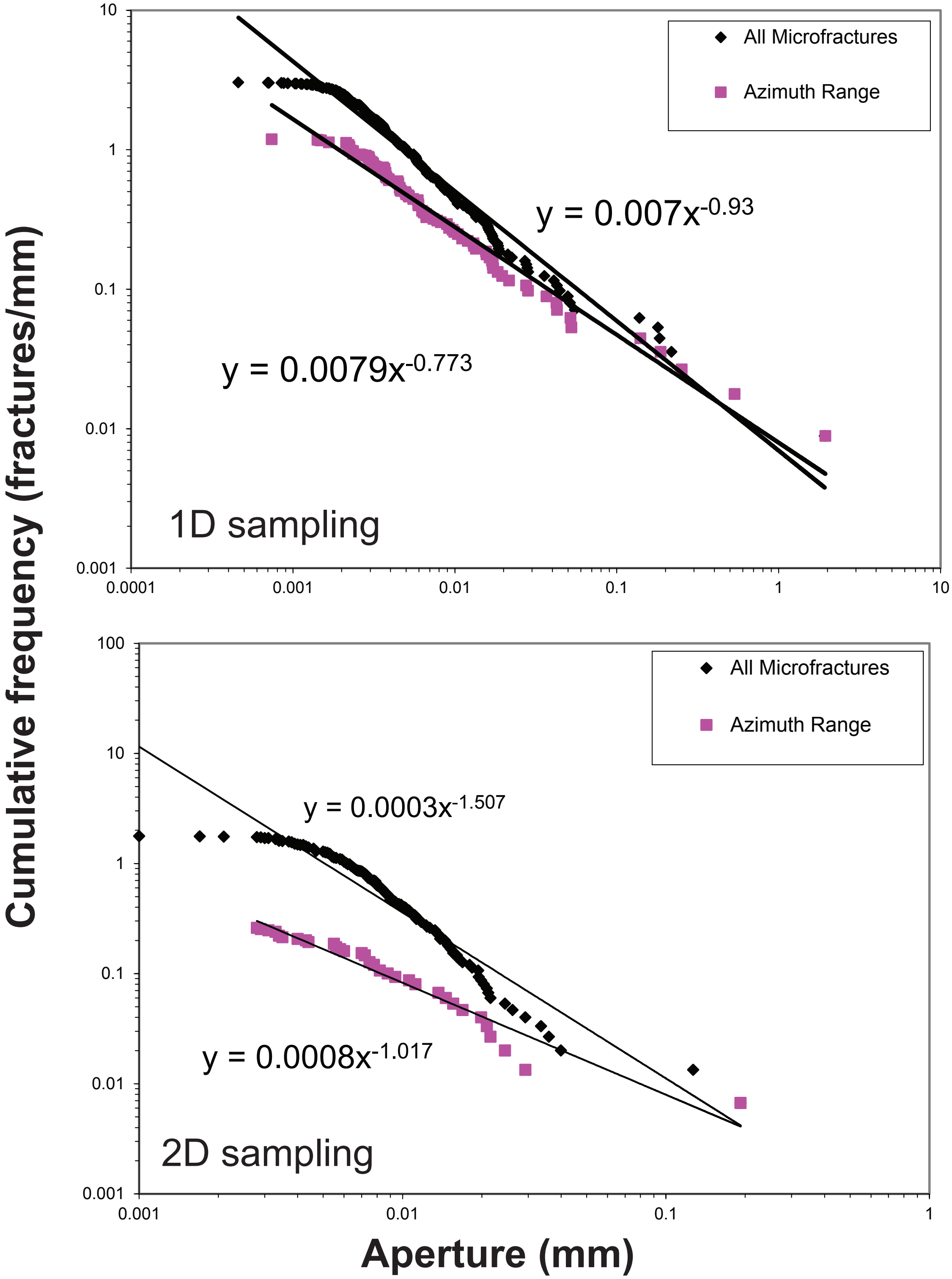

Figure 4-3. Fracture frequency curves from microfractures in Figure 4-2, sampled in 1D and 2D, and filtered by azimuth. Azimuth range subset represents fracture sizes for fractures that strike within 30 degrees of parallel to the primary fracture set (Set A).

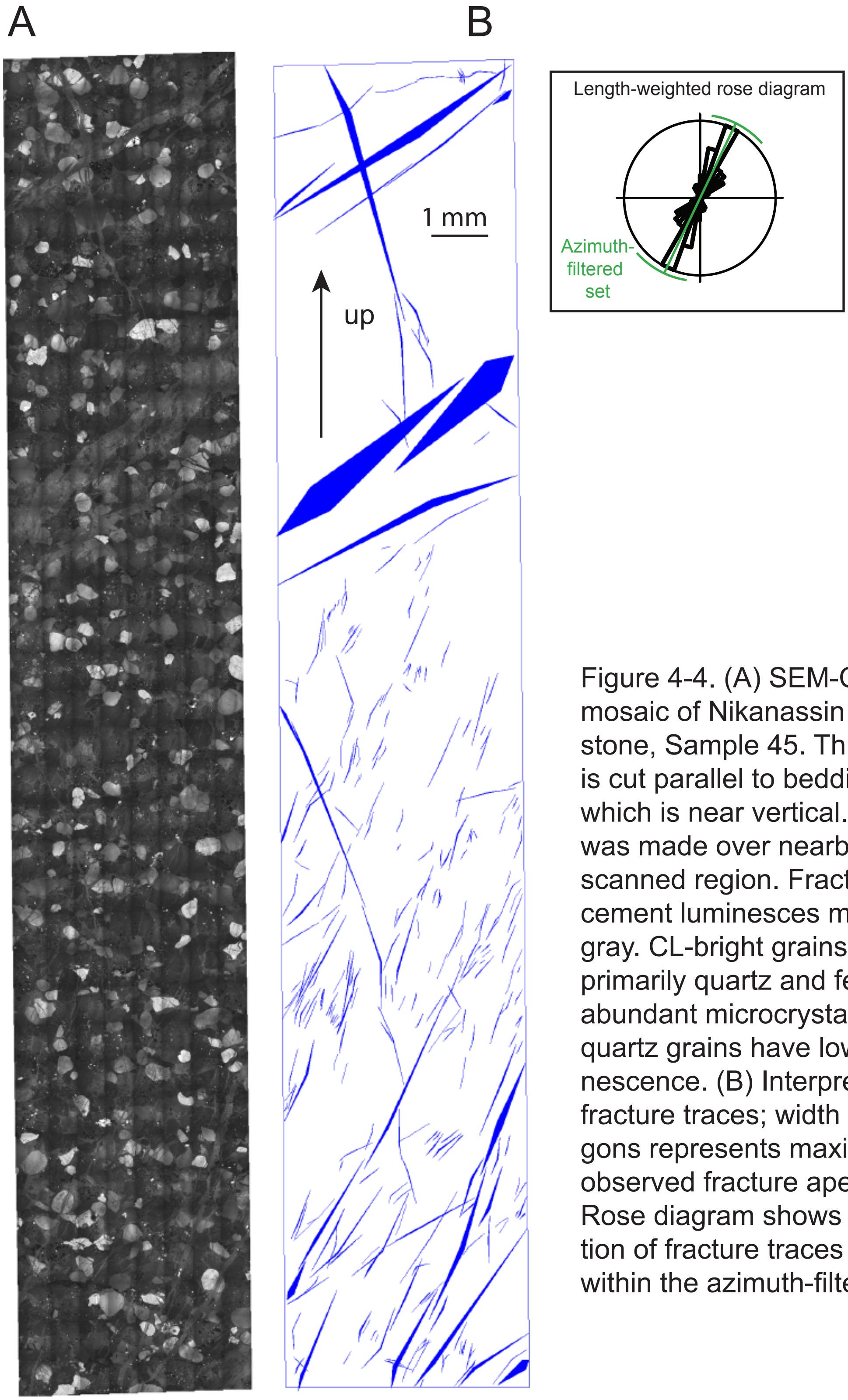

Figure 4-4. (A) SEM-CL mosaic of Nikanassin Sandstone, Sample 45. Thin section is cut parallel to bedding, which is near vertical. Scanline was made over nearby scanned region. Fracture cement luminesces medium gray. CL-bright grains are primarily quartz and feldspar; abundant microcrystalline quartz grains have low luminescence. (B) Interpreted fracture traces; width of polygons represents maximum observed fracture aperture. Rose diagram shows orientation of fracture traces included within the azimuth-filtered set.

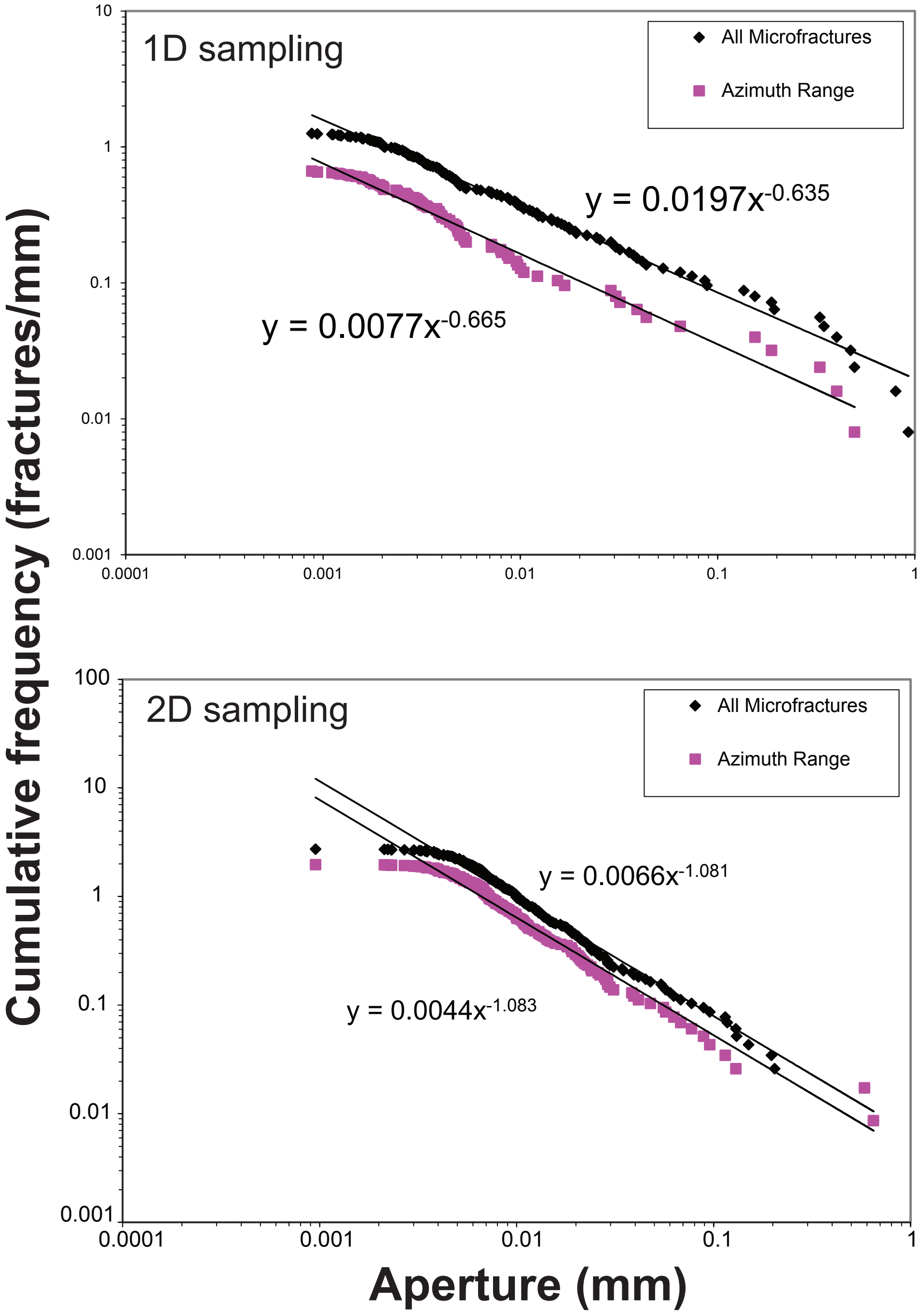

Figure 4-5. Fracture frequency curves from Nikanassin Sandstone (Sample 45) aperture data, sampled in 1D and 2D and filtered by azimuth (Figure 4-4).

fracture sets are present, some of which achieve small strains and so consist only of small fractures; by combining the sizes into one 2D dataset, a greater proportion of smaller fractures is present than would naturally develop within a single set. This fracture set is further examined below.

Within the Nikanassin Formation, *b* for all fracture orientations is 0.635 (1D) and 1.081 (2D). Azimuth filtering makes little difference in this case, yielding *b* values of 0.665 (1D) and 1.083 (2D). The similarity of these two results reflects the numerical dominance of a narrow strike-range within this fracture population.

In both sandstones the steepening of the fracture intensity curve is significant (relative to the standard deviation in 1D *b* values reported above) but by an amount less than theoretically possible (1, assuming linear aperture-length scaling—Marrett, 1996).

Box counting versus cumulative frequency scaling

Other methods of testing patterns for fractal characteristics have inherent limitations on exponent value. For example, box counts (Fuller and Sharp, 1992; Gillespie et al., 1993; Berkowitz and Hadad, 1997) are measures of patterns (pixel arrangements) wherein the number of overlain boxes of a given size contain no pixels of a given quality (e.g., no fracture-pixels) (Figure 4-6). Box counts of 2D patterns feature exponents between 1 (the box-count result for any line of pixels) and 2 (the box-count result for any plane of pixels).

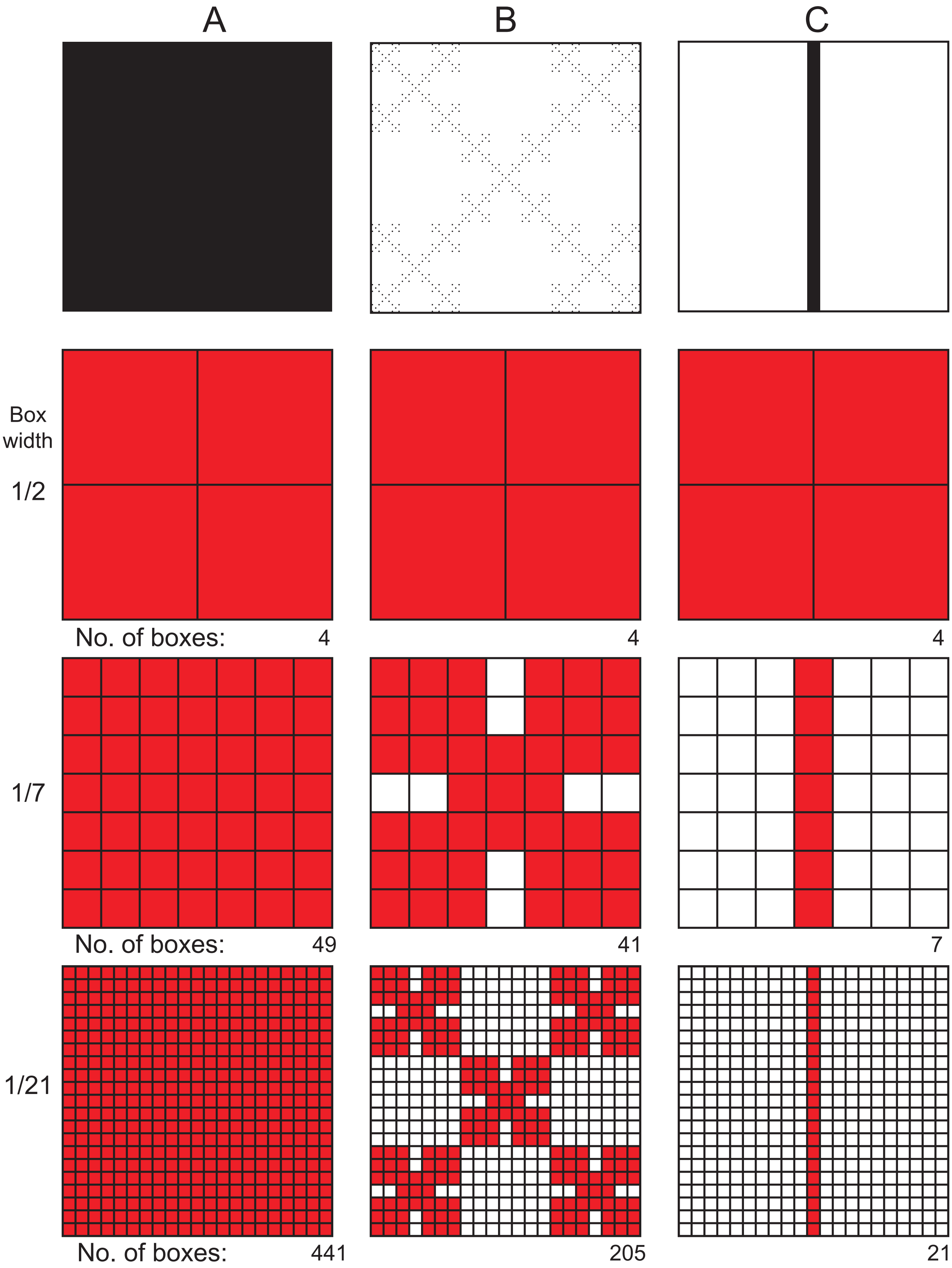
A
B
C
Box
width
1/2
No. of boxes:
4
4
4
1/7
No. of boxes:
49
41
7
1/21
No. of boxes:
441
205
21

Figure 4-6.

Figure 4-6 continued. Fractal dimension as measured by box counting (the exponent of a box-count versus box-size data curve) is inherently limited by pattern geometry. For example, a pattern made of pixels in a repeating quincunx array (B) will necessarily have a fractal dimension between 2 (the dimension of a plane of pixels, A) and 1 (the dimension of a line of pixels, C). No such limits apply for fracture scanline data.

The ruler-method of Mandelbrot (1982) to establish fractal properties of curves, relating the observed length of a line to the size of the measuring stick, faces the same type of exponent constraints as the box counting method. Such a method can be applied to the shapes of fractures (Aviles et al., 1987).

In contrast, there is no *a priori* reason why scanline data cannot show a *b* value greater than 1. To illustrate this, imagine a scanline with a single fracture of width 1; follow with ten fractures of width 1/2; one hundred fractures of width 1/4; one thousand fractures of width 1/8; ten thousand fractures of width 1/16; and so on—this produces a fracture-size distribution with a *b* value of approximately 3.3. Such an arrangement is not likely geologically realistic, only conceptually possible.

TESTS OF GEOLOGICAL CONTROLS

Tests of whether the *b* value measured from natural fractures varies systematically with some geologic control can be accomplished by subdividing the *b* values by a variety of factors in order to test for consistent correlations. These factors include host-rock mineralogy, grain size, extent of clustering, and structural position.

Host rock mineralogy: quartzarenites versus litharenites and arkoses

Taking fracture populations that are best-fit by power-law equations, and excluding the single Travis Peak example, which may be regarded as anomalous because of its low number of fractures sampled, the populations from quartzarenite samples (Eriboll Formation and Mesón Group) tend to have greater *b* values than populations from litharenitic and arkosic rocks (Figure 4-7). The overlap in error bars in Figure 4-7 suggests the greater b among quartzarenites is not statistically significant.

The Eriboll Formation unconformably overlies the Torridonian Supergroup sandstones, a fluvial-alluvial succession containing primarily arkosic red sandstones, but including conglomerates, mudstones, and limestones, deposited between ~1200 and 950 Ma (Turnbull et al., 1996; Trewin and Rollin, 2002; Darabi and Piper, 2004). The Torridonian Supergroup consists of the Stoer Group, the Sleat Group, and the Torridon Group (Young, 1999; Stewart, 2002; Kinnaird et al., 2007). The unconformity between the Torridonian Supergroup and the underlying Lewisian Gneiss juxtaposes each group within the supergroup against the underlying gneiss.

Despite the considerably older age of the Torridonian Supergroup, the Eriboll Formation is more pervasively fractured (Ellis et al., 2012). Greater fracture frequency within the younger Eriboll Formation is likely the result of that rock's higher Young's modulus or other mechanical-property contrasts (Ellis et al., 2012). Such contrasting mechanical properties, in turn, likely stem from the rocks' distinct depositional environments and mineralogies. The ideal test of the effects of host-rock mineralogy on the growth of a natural fracture set would be to observe a set of fractures which cuts the contact between two distinct beds, so

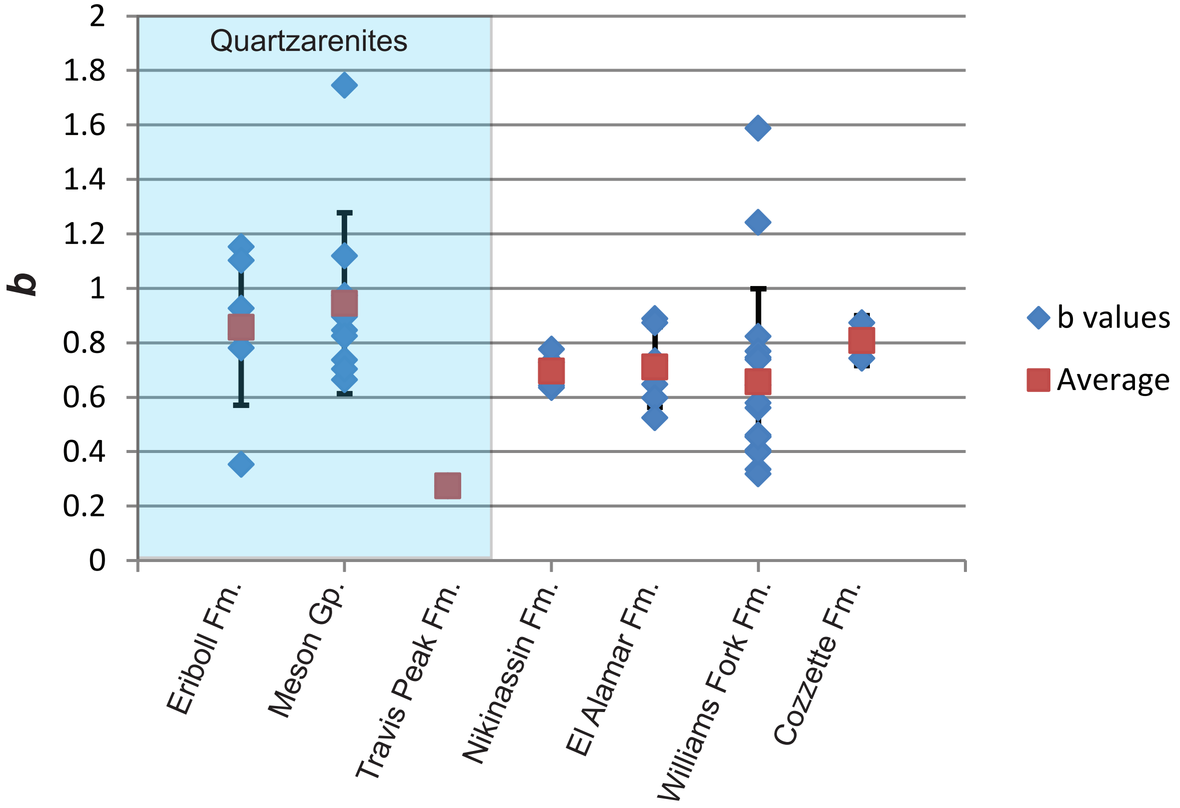

Figure 4-7. Comparison of *b* observed in quartzarenite samples to those from other sandstones. Black bars illustrate one standard deviation of values. Only datasets best-fit by power-law equations included. Travis Peak Fm. dataset (Sample 10) includes 6 fractures.

that differences in size distribution, of the fractures could be attributed to differences in the host rock. I was unable to find such a fracture set (i.e., one that cuts across the unconformity between the Torridonian Supergroup and the Eriboll Formation). Nevertheless, scaling attributes can be compared between fractures which may have developed within the same structural setting, but in rocks of vastly different mechanical fracture proneness, by comparing fractures within these two rocks.

Macro- and microfractures within the Torridonian Supergroup were sampled at two field locations. The first sample site is within the Stoer Group, where exposed at Rua Reidh (Figure A-6, Appendix A). Fracture scaling data were collected from fractures within a 5 cm-thick sandstone bed (Figure 4-8). Fractures are mostly confined to this layer, and dip 40 to 60° with respect to bedding. Fractures are kinematically consistent with layer-parallel lineations indicating slip along bedding planes, with the top to the east.

Four hundred and fifty-one macrofractures within this layer in outcrop have kinematic apertures ranging from 0.175 to 20 mm. Their size distribution (Figure 4-9) is well fit by a power-law equation over this size range. SEM-CL-based microfracture analysis was performed on two samples from this layer. Imaging and fracture measurement of these samples was performed according to the methods detailed in Chapter 3. From the two samples a microfracture scanline was constructed with a cumulative length of 163.8 mm. This scanline intersects

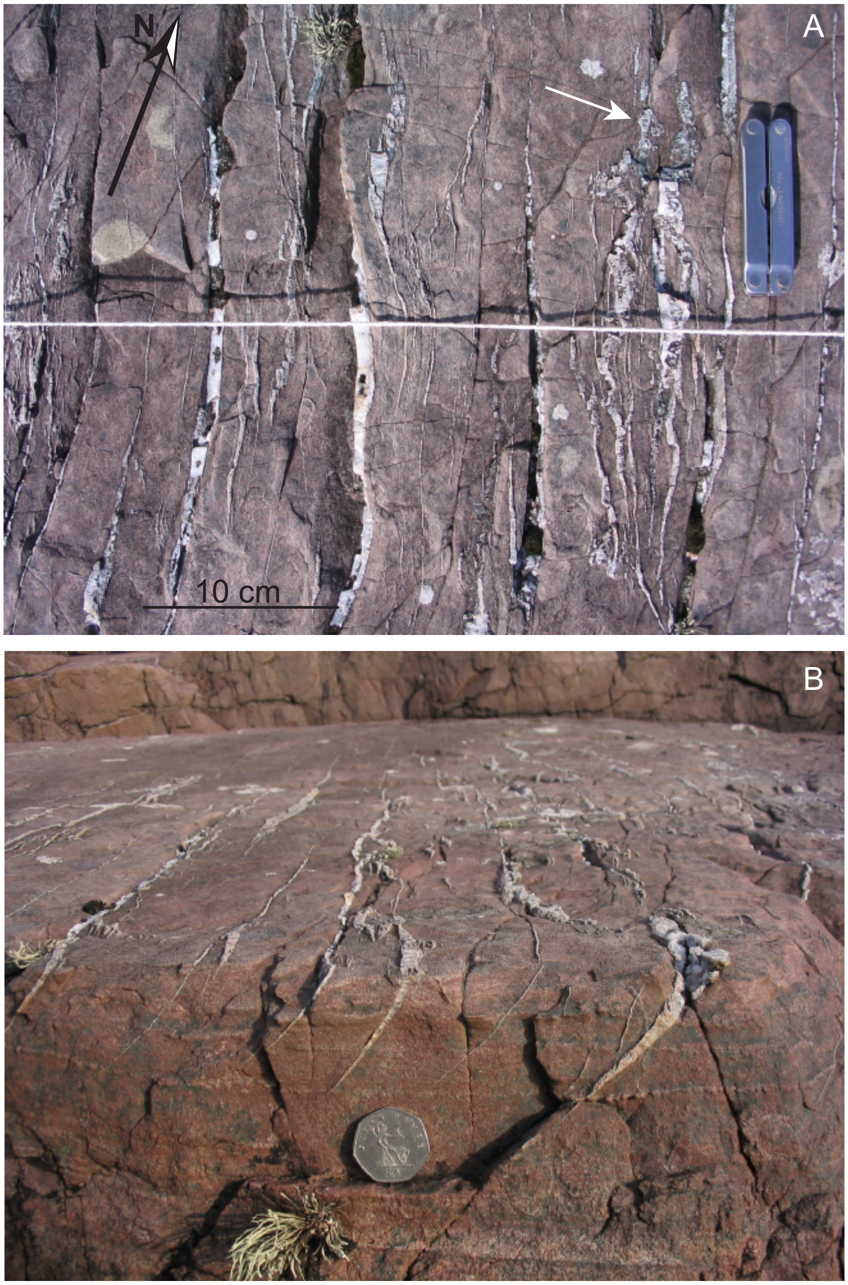

Figure 4-8. Fractures in the Torridonian Supergroup (Stoer Group) at Rua Reidh exposure, in plan view (A) and south-facing cross-section (B). Note shallow dip and with respect to bedding; fractures are opening-mode and appear to have accommodated layer-parallel shear. White arrow in (A) points to layer-parallel slip lineations.

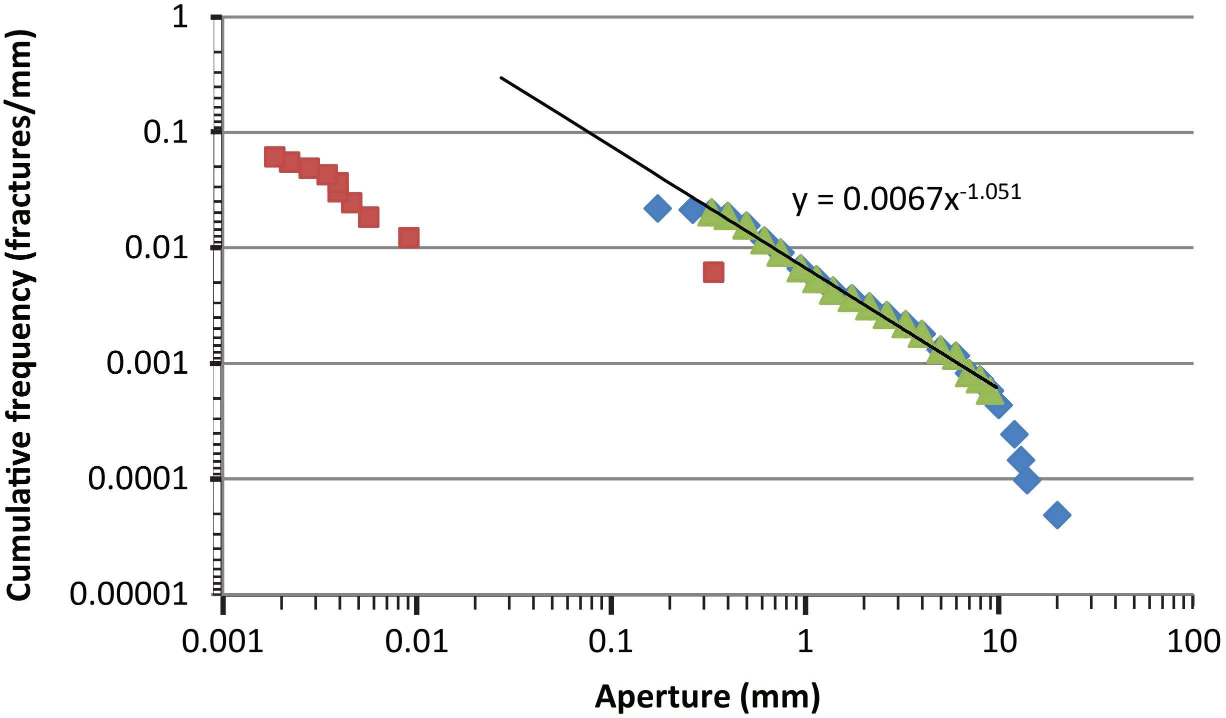

Figure 4-9. Macrofractures measured at Rua Reidh (aperture range 0.4 to 10 mm) are well fit by a power-law equation of *b* ~ 1, accounting for common sampling biases (Chapter 2). However, extrapolation of this power law to smaller size scales significantly over-predicts microfracture abundance.

39 total microfractures, the majority of which strike at high angle (60 to 70 degrees) to the macrofracture set (Figure 4-10). Ten of these microfractures strike within 25 degrees of the macrofracture strike. Compared to the fracture abundance that would be expected for microfractures (<0.1 mm aperture) by extrapolation of the macrofracture power law, this dataset has very few microfractures.

The second Torridonian Supergroup fracture sampling site is between the Dundonnell River and An Teallach (Figure 4-11). The fractures sampled are within the Applecross Formation of the Torridon Group, here less than 5 m from the overlying angular unconformity which separates the Torridonian Supergroup from the Eriboll Formation. The field scanline comprises 48 opening-mode, quartz-filled macrofractures. These fractures strike approximately 036 and dip approximately 70 degrees to the SE. From this scanline location a single sample was taken for SEM analysis. The resulting microfracture scanline intersects 22 parallel microfractures over 90.1 mm (Figure 4-12). The microfractures record a strain of 0.008; only one Eriboll Formation microfracture dataset has lower strain (Sample 5; N=11—Appendix A). The minimum fracture aperture is 0.0023 mm, larger than the smallest fracture size of any Eriboll Formation microfracture scanline (Appendix A). Thus although this Applecross Formation sample has abundant microfractures compared to the Stoer Group sample, both Torridonian

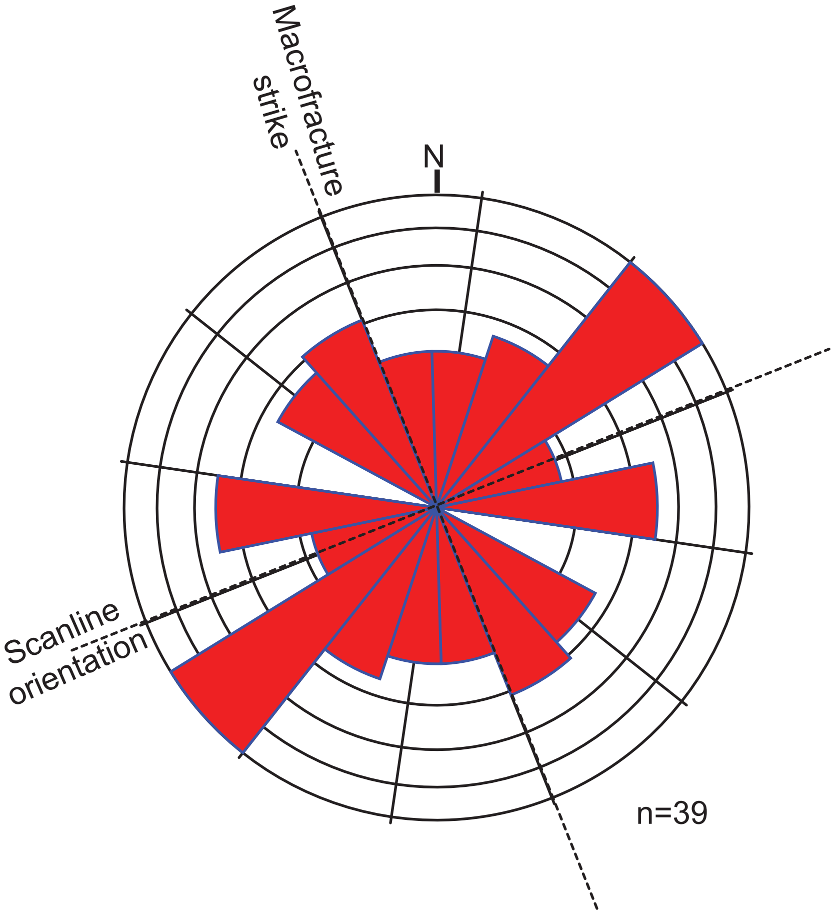

Figure 4-10. Rose diagram showing strike of microfractures observed in Stoer Group sample, Rua Reidh exposure. 4*n orientations are plotted, corresponding to four segments per digitally interpreted fracture polygon (Figure 4-1).

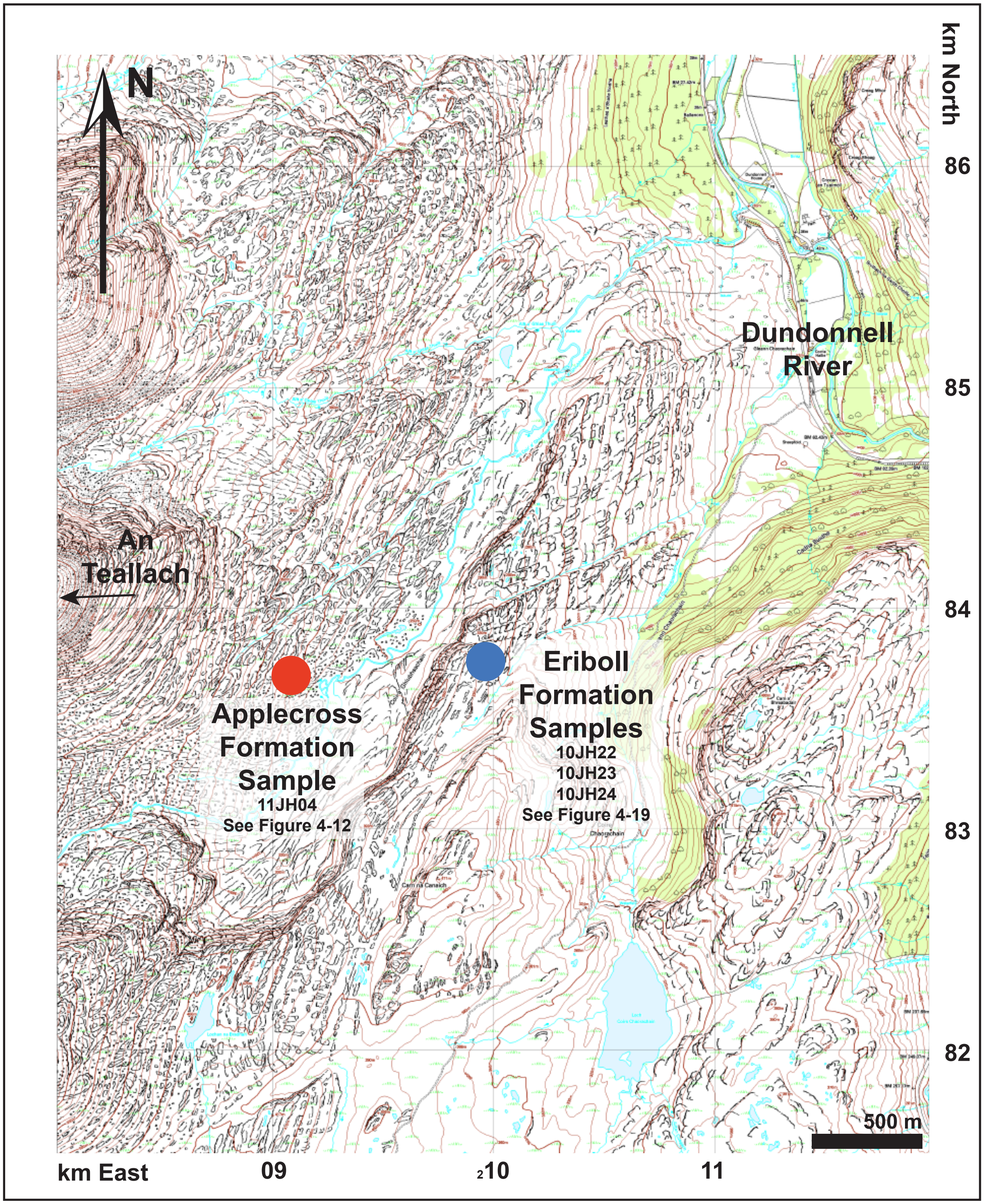

Figure 4-11. Locations of Applecross Formation and Eriboll Formation samples. Map by British Ordnance Survey, National Grid Reference NH.

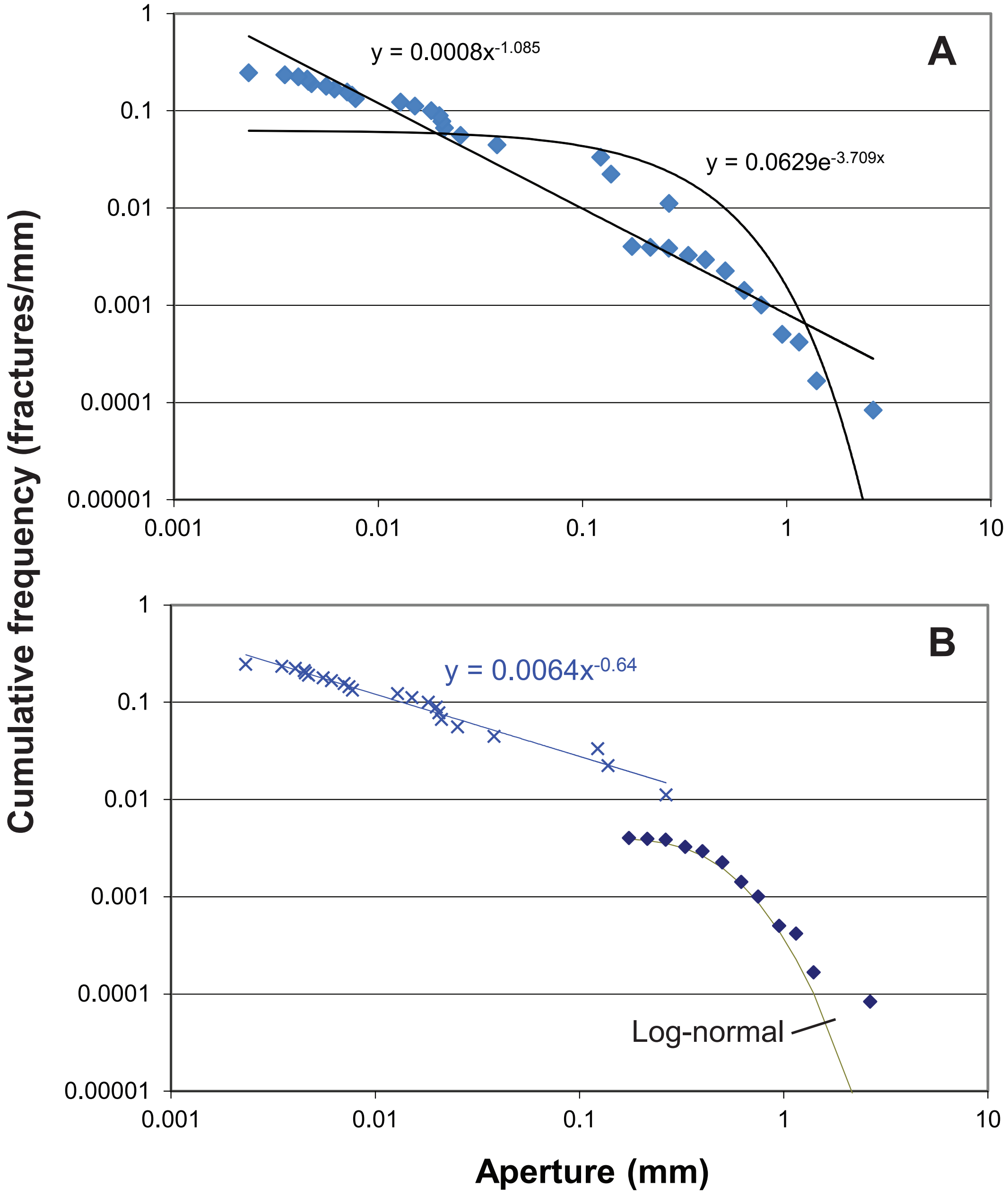

Figure 4-12. Fracture cumulative frequency versus aperture, measured in the Torridon Group (Applecross Formation) exposure between the Dundonnell River and An Teallach. (A) All fractures. (B) Microfractures, measured using SEM-CL, and macrofractures, measured using a hand lens, fit separately. A log-normal equation best fits the macrofractures.

Supergroup datasets contain sparse microfractures compared to the Eriboll Formation datasets.

Host rock mineralogy: sandstones versus carbonates

A further test of the effects of host-rock mineralogy can be made by comparing *b* values measured in carbonate rocks to the sandstone data presented in Chapter 3. Fracture populations were compared to data from the Pennsylvanian Marble Falls Limestone (Marrett et al., 1999) and from the Ordovician Ellenburger Dolostone, the Cretaceous Cupido Dolostone, and the Cretaceous Austin Chalk (Hooker et al., 2012). Each dataset is well-fit by power-law equations using the same chi^2 criterion applied to sandstone fracture populations in Chapter 3. Summaries of the geologic settings of these datasets are included in Appendix A. Like the sandstone data, the carbonate data represent a wide range of host-rock mineralogies and structural settings.

The average *b* value among the carbonate-rock fracture datasets (Table 4-1) is 0.81, which is close to the 0.8 average value among sandstone fractures. Moreover, the population means are statistically indistinguishable via a *t* Test (Jensen et al., 2000). Using the standard deviations of sets of *b* values from the five carbonate datasets (0.21) and from the sandstones (0.27), the *t* Test permits the hypothesis that the population means are the same even within low (~20%) confidence intervals. Thus no statistically significant difference is present

Formation	Age	No. fractures	Min fracture size (mm)	Max fracture size (mm)	Observation method	*b*	Reference
Ellenburger Dolostone	Ord.	61	0.0011	0.18	CL	0.815	Hooker et al., 2012
Marble Falls Limestone	Penn.	756	0.005	18	O, LM	1.042	Marrett et al., 1999
Cupido Dolostone	Cret.	1161	0.025	48	O	0.978	Hooker et al., 2012
Cupido Dolostone	Cret.	52	0.0036	3.8	CL	0.648	Hooker et al., 2012
Austin Chalk	Cret.	136	0.05	100	O	0.559	Hooker et al., 2012

Table 4-1. Summary of fracture-size data from carbonate rocks. Observation methods: CL = conventional CL; O = outcrop; LM = light microscope.

between the carbonate and sandstone *b*-value sets. Nevertheless a larger *b* population from carbonate samples would permit a more robust comparison.

To summarize, no evidence is present within the data to suggest that mineralogy affects *b*.

Grain size

From each sample in Chapter 3 whose fractures are best fit by a power-law size distribution, b can be plotted versus grain size in order to test for any systematic variation. Grain size is quantified as an average of 100 measurements of the maximum distance across an individual grain. No systematic variation is present between *b* and grain size or standard deviation of grain size, a measure of grain sorting (Figure 4-13).

Fracture clustering

The regularity of fracture spacing can be quantified by the coefficient of variation, $Cv = \sigma/\mu$, where σ is the standard deviation of the population of spacings and μ is the arithmetic mean (e.g., Kagan and Jackson, 1991; Gillespie et al., 1999; Supak et al., 2006). Therefore, the greater the value of Cv, the more irregular the fracture spacing. A Cv value of 1 is expected for a Poissonian distribution of spacings and therefore signifies a fracture spacing close to random (Gillespie et al., 1999). Accordingly, fracture sets having more clustering than expected for randomly arranged fractures will have $Cv > 1$; sets having less

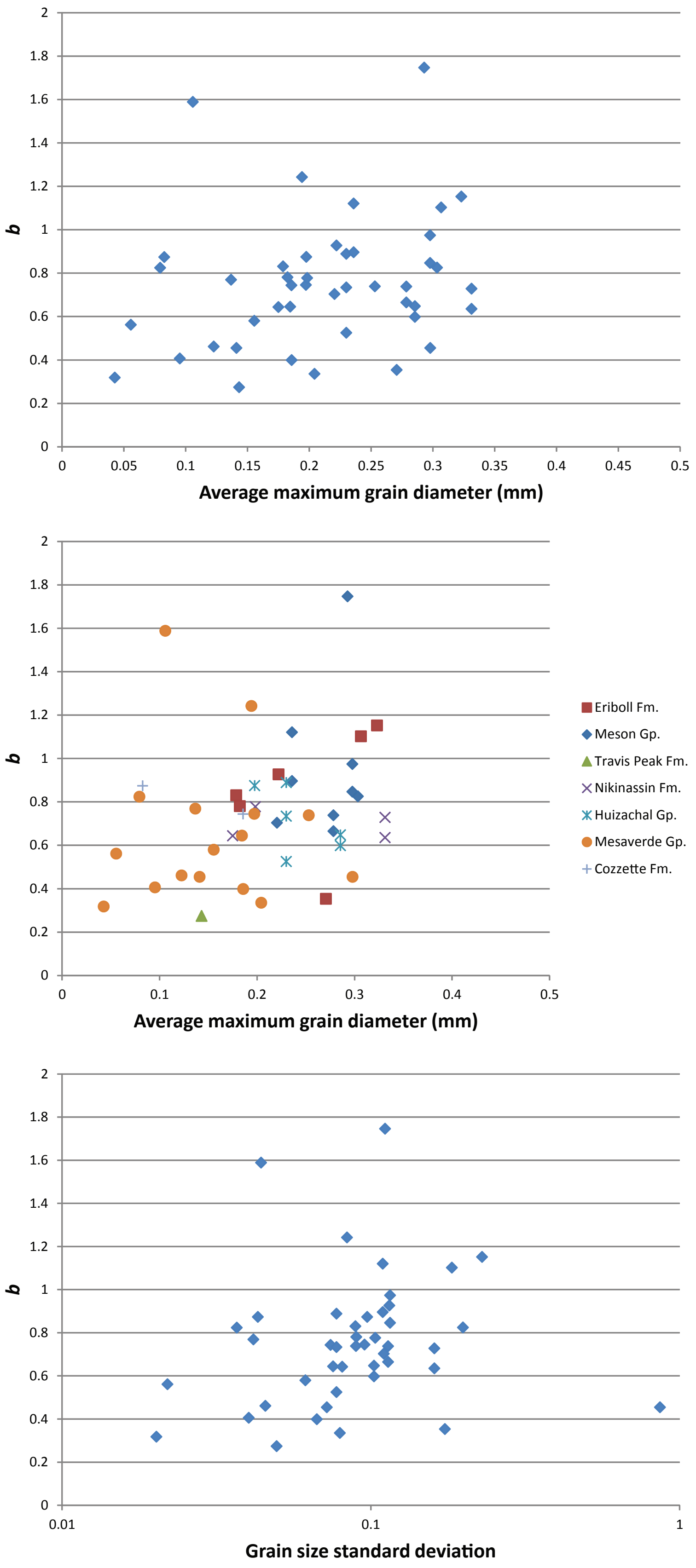

Figure 4-13. (A) *b* versus average grain size. (B) Same data as (B) but separated by formation. (C) *b* versus grain size standard deviation (a proxy for sorting).

clustering than random (closer to regular spacing) will have Cv < 1 (Gillespie et al., 1999). A perfectly regular fracture spacing would have Cv = 0.

However, the coefficient of variation for fracture spacings as a measure of fracture spatial arrangement does not account for fracture size. A method devised by Kuiper (1960) can quantify fracture spatial heterogeneity while accounting for fracture size. In this method, cumulative aperture (a running sum of apertures encountered from the beginning to the end of the scanline) is plotted versus scanline position. A line on this plot connecting the origin and the final cumulative aperture at the end of the scanline represents homogeneous strain. The more heterogeneous the fracture strain distribution, whether by fracture clustering, fracture size variation, or both, the greater the difference between the data and the homogeneous strain line. To quantify this variation the absolute values of the maximum and minimum deviations in cumulative aperture from the homogeneous strain line are summed; that sum is then divided by the total cumulative aperture. The result is a number, V', between 0 (perfect strain homogeneity) and 1 (maximum strain heterogeneity, which is possible if all strain is manifest in a single fracture).

The variation in *b* is uncorrelated with Cv but systematically decreases with V' (Figure 4-14). This result is consistent with low-*b* datasets having a higher proportion of strain among larger fractures. More large fractures intersected by the scanline would tend to lower *b* and increase V'.

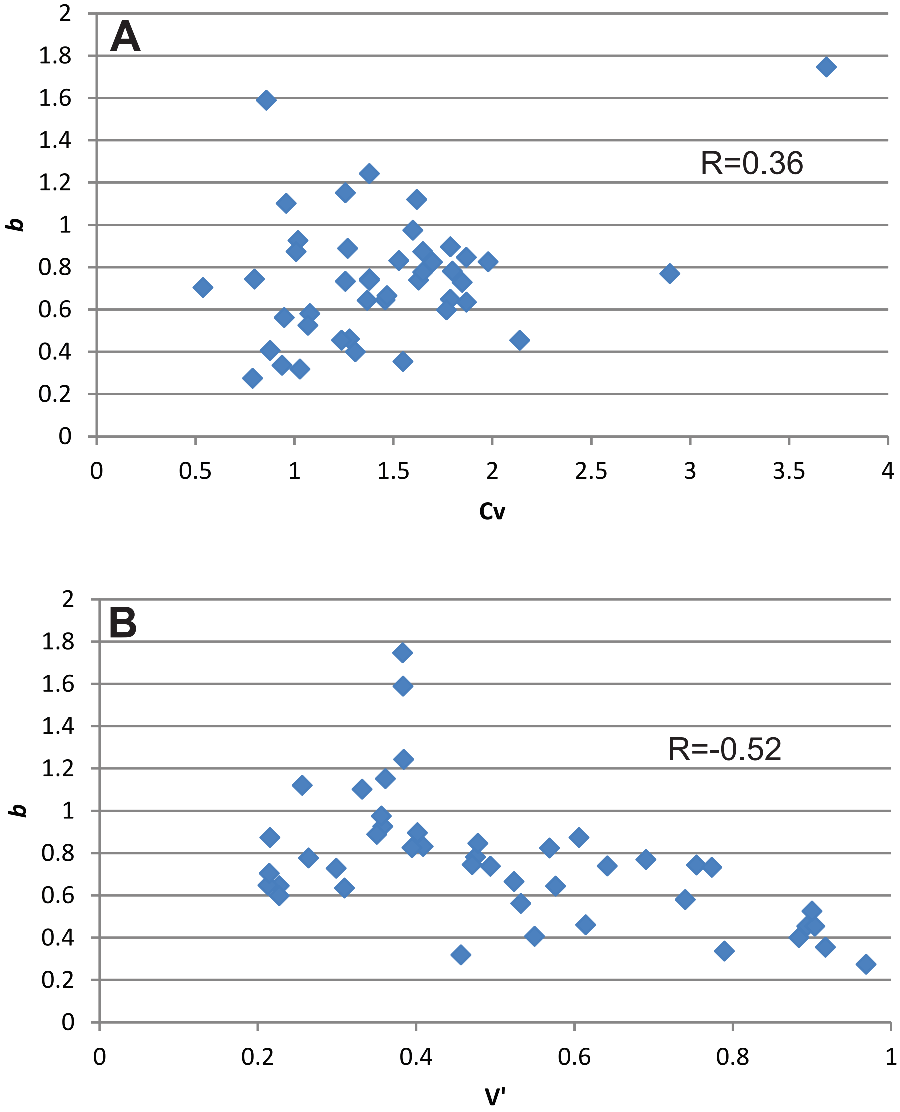

Figure 4-14. *b* plotted against (A) Cv, the coefficient of variation of spacing sizes (standard deviation divided by average size), and against (B) V’, a measure of fracture strain heterogeneity devised by Kuiper (1960). See text for details. Pearson coefficients listed suggest better (negative) correlation with V’ than Cv.

Structural position

From two formations data derive from various locations with respect to outcrop-scale folds and faults. Thus, these data may be used to test how fracture intensity varies with structural position. For instance, fracture frequency (size and abundance) may increase with proximity to faults (Anders and Wiltschko, 1994). Likewise, fractures may be genetically related to folds and thus systematically distributed with respect to folds (Bergbauer and Pollard, 2004; Iñigo et al., 2012). Alternatively, fractures may pre- or post-date folds and therefore scale independently of structural position.

Fractures and structural position, example 1: Mesón Group

The Cambrian Mesón Group is folded into map-scale Andean anticlines (having km-scale wavelengths) at Perchel Canyon (Figure A-3). The field location presently addressed is within the forelimb (western limb) of one such anticline. Here a smaller anticline-and-syncline pair is present (crest-trough length ~20 m) whose fold axis is roughly parallel to the map-scale fold axial trace. Therefore this anticline may be divided into three domains (Figure 4-15), from west to east: a regional limb, in which beds dip moderately to the west, a hinge zone (of the small fold), and a counter-regional limb, wherein beds dip moderately to the east.

Macrofractures

Macrofracture abundance, based on qualitative outcrop observation, increases within the fold hinge (Figure 4-15) and within a strike-slip fault zone on

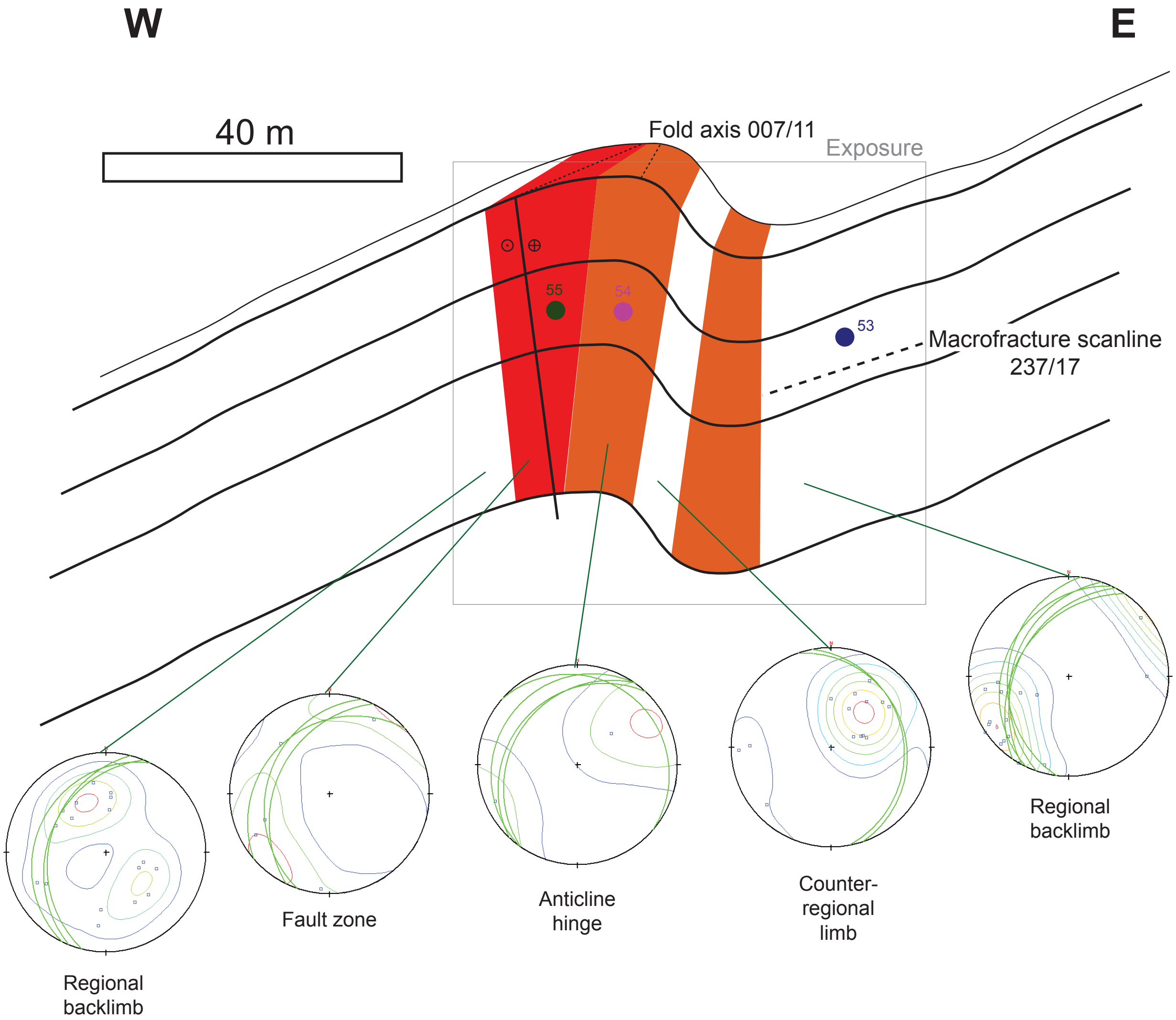

Figure 4-15. Schematic block diagram of small fold within western fold limb of regional-scale Andean fold, exposed at Perchel Canyon (see map, Figure A-3). Sample numbers and locations shown. Orange and red areas correspond to medium and high (respective) fracture intensity as observed in outcrop. Stereograms illustrate bedding (planes) and macrofracture (poles to planes, contoured) measurements made in the field.

the backlimb-side of the small fold, relative to frequency away from the small fold. Macrofractures are present in various orientations, but the majority strike northwest and dip at a high angle to bedding. The motion of the fault is likely left-lateral, judging by minor bedding offset and the orientation of the dominant opening-mode fracture set.

Microfractures

Locations of oriented samples taken for SEM-CL-based microfracture scanlines are shown in Figure 4-15. Thin sections were cut parallel to bedding. In each sample, multiple orientations of microfractures were encountered (Figure 4-2). Size distributions from each microfracture scanline, including for all fractures present and for fractures filtered by strike to only include the dominant NNW-striking fractures, are shown in Figure 4-16. Microfracture frequency for fracture apertures > 0.01 mm is highest within Sample 55, closest to the fault (Figure 4-15). Microfracture frequency is not elevated within the small-fold hinge zone, compared to the regional-fold limbs. For these microfracture scanlines, *a* and *b* appear to be inversely related, suggesting that higher fracture intensity is manifest in both an increase in *a* and a decrease in *b*.

Fractures and structural position, example 2: Eriboll Formation

Two outcrop-scale structures within the Eriboll Formation contain opening mode fractures that were measured in the field and using SEM-CL. The first structure is exposed on a pavement immediately to the west of Loch an Nid

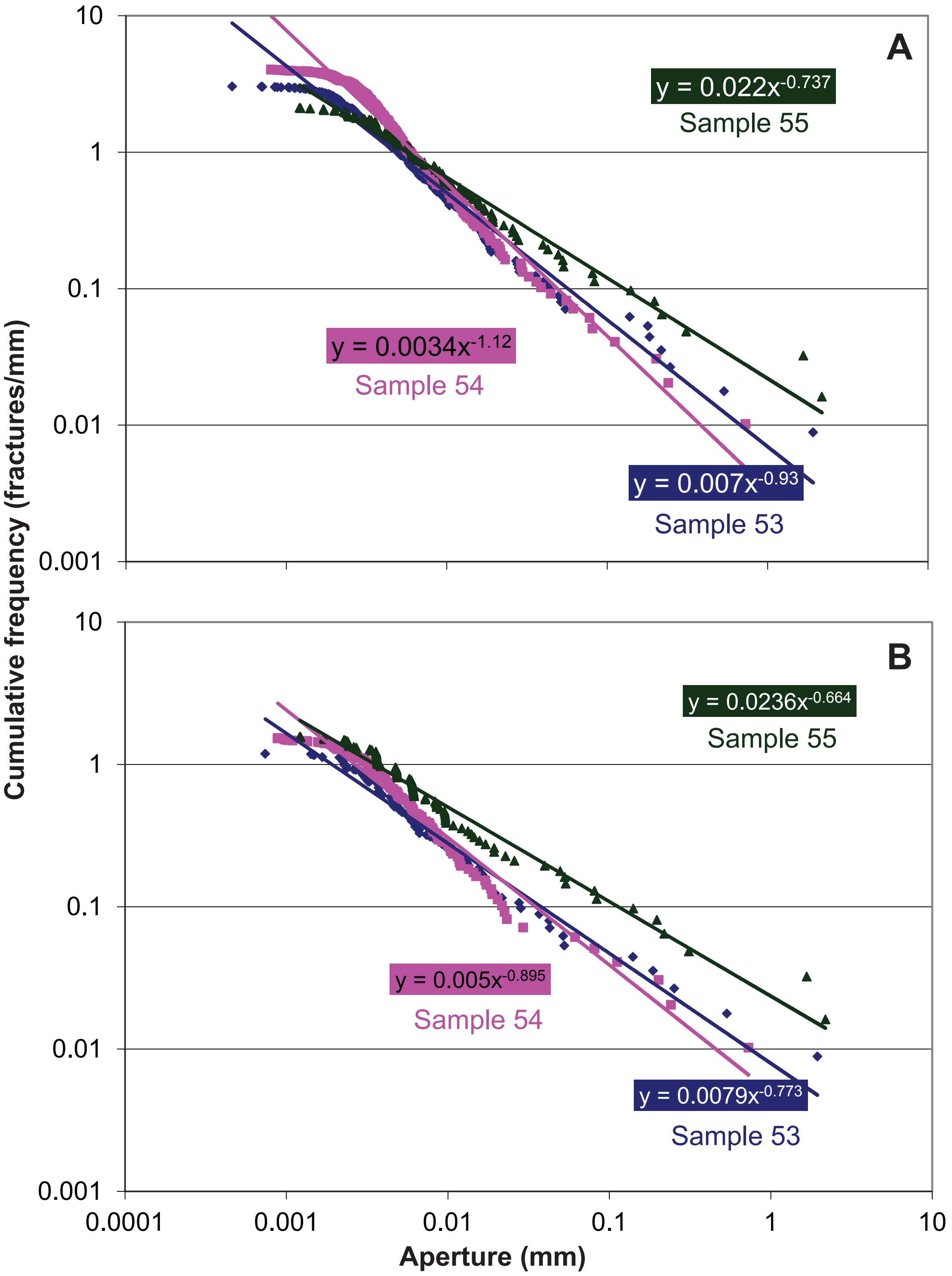

Figure 4-16. Cumulative frequency versus aperture size for sample locations in Figure 4-15. (A) All microfractures. (B) Set A (scanline-perpendicular) set only.

(Figure 4-17). A flexure is present, based on an interlimb angle of approximately 175 degrees, measured between E-dipping beds to the east and west of the N-trending hinge zone. N-S striking macrofractures appear clustered near the hinge in outcrop. Figure 4-17 includes the locations of twelve oriented samples taken for SEM-CL microfracture scanlines. These scanline data were analyzed to study spatial variation of fracture strain by Morgan (2011). Data from these samples consist of scanlines trending E-W to intersect N-S striking microfractures; strain and frequency are variable (Figure 4-18). For these samples, there is an inverse relationship between *b* and fracture strain, in contrast to the absence of systematic variation among the entire sandstone dataset (Chapter 3).

The second structure is a fracture swarm exposed between the Dundonnell River and An Teallach (Figure 4-11, Figure 4-19). The macrofracture cluster exposed at Dundonnell contains mutually abutting fractures in two dominant orientations (each steeply dipping, one set striking ~010 and the other striking ~060). In this case, three samples were collected for SEM-CL microfracture analysis: one sample from within the macrofracture cluster, one sample at the margin, and one sample at a distance of ~3m from the cluster. Microfracture scanlines trend N-S to intersect 060-striking microfractures. Scaling data (Figure 4-20) indicate that fracture intensity does not systematically increase with proximity to this incipient fault. Consistent with the fracture-size distributions

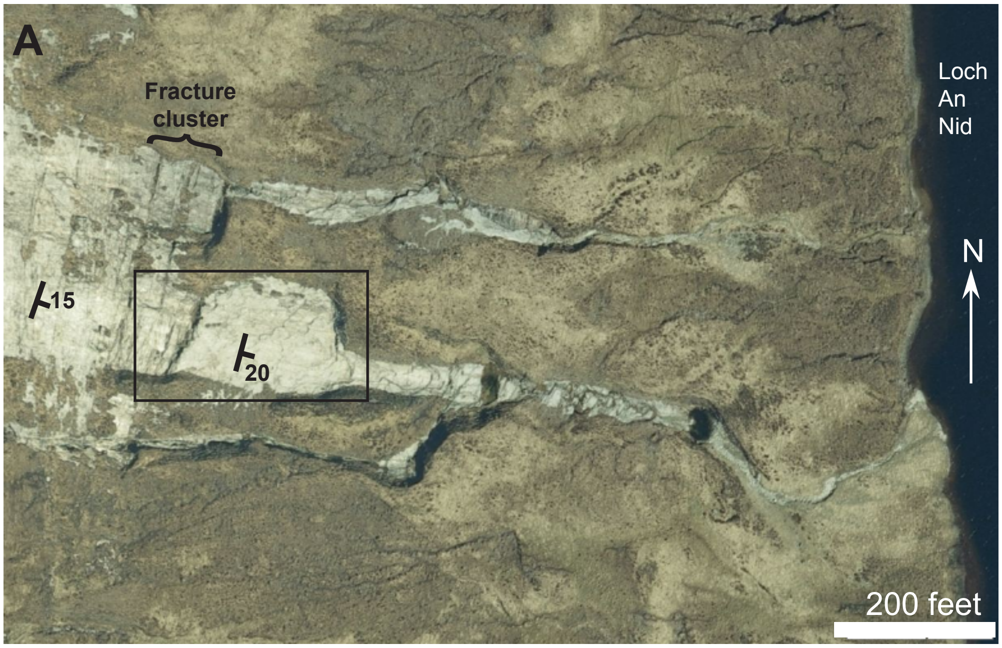

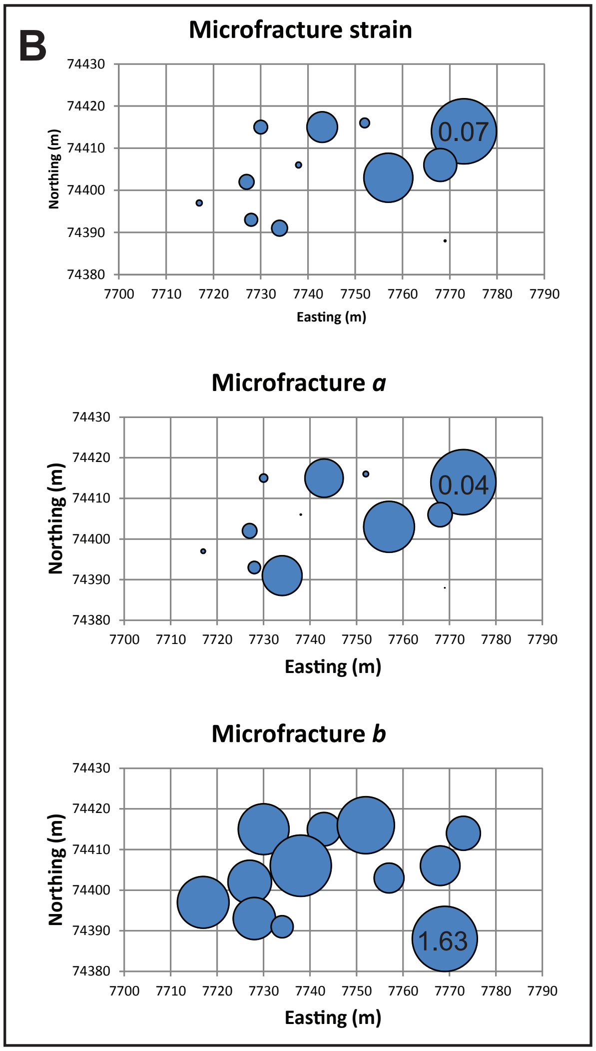

Figure 4-17. (A) Aerial photograph (from Bing.com) of Eriboll Formation outcrop exposure west of Loch An Nid (see large-scale map, Figure A-6). The fracture cluster is located at the hinge of a subtle fold. Strike-and-dip symbols refer to bedding. Box around pavement represents area delineated in graphs in (B). (B) Maps of strain, *a*, and *b* of data from SEM-CL microfracture scanlines. Number shown is maximum value, for scale. Most data originally reported in Morgan (2011). UK National Grid Reference NH.

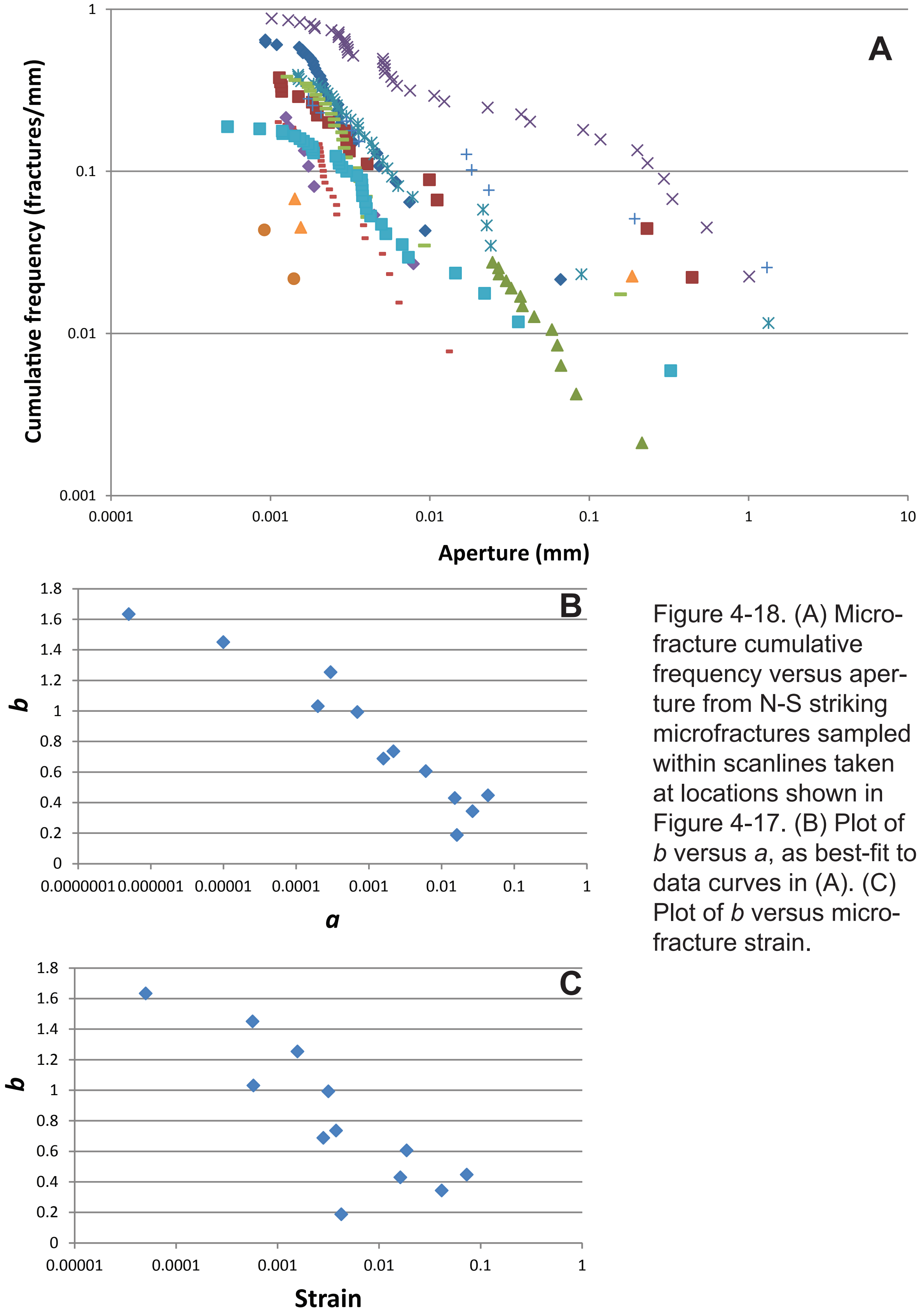

Figure 4-18. (A) Microfracture cumulative frequency versus aperture from N-S striking microfractures sampled within scanlines taken at locations shown in Figure 4-17. (B) Plot of *b* versus *a*, as best-fit to data curves in (A). (C) Plot of *b* versus microfracture strain.

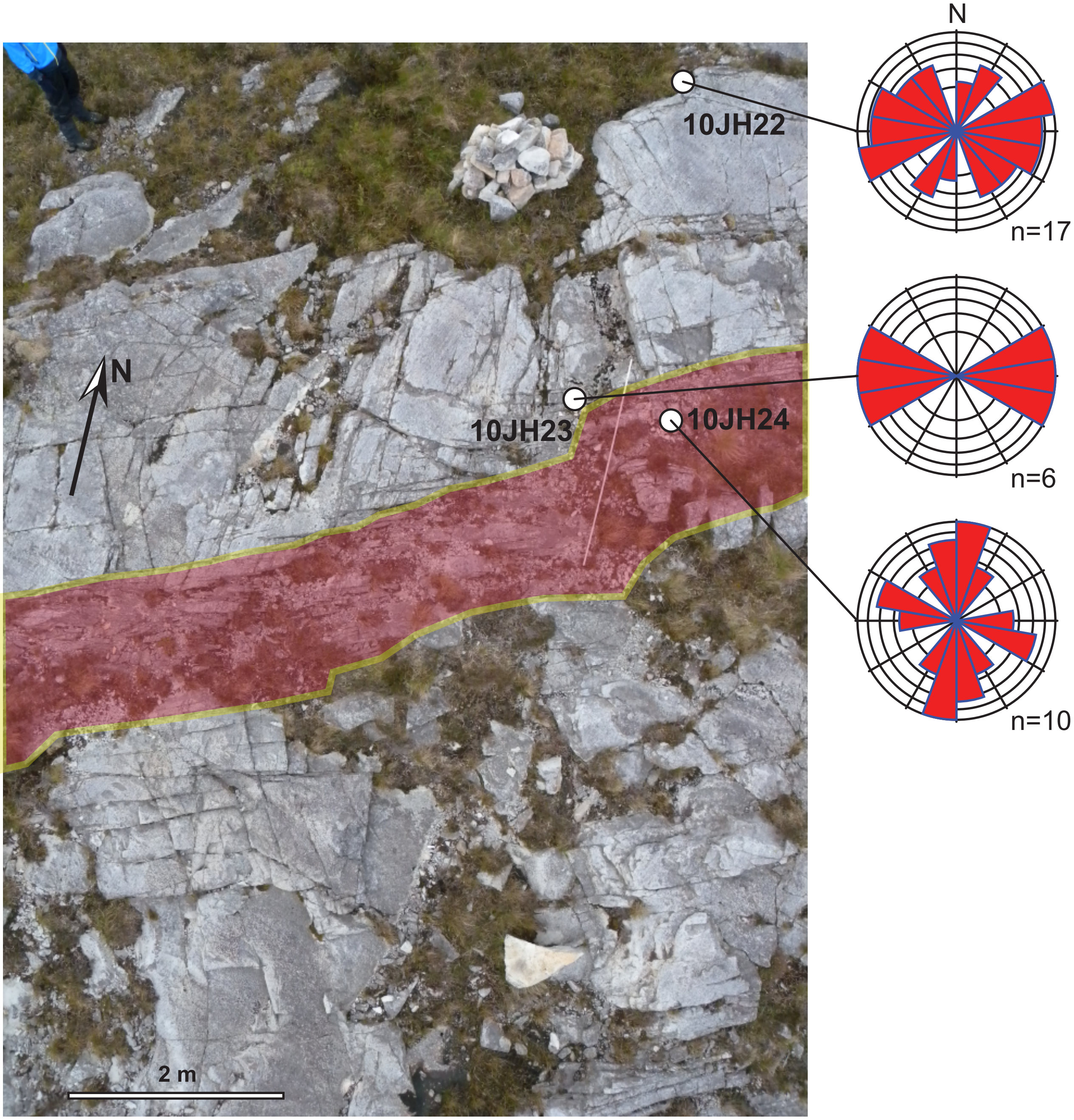

Figure 4-19. Locations of microfracture scaling samples collected from within (10JH24), at the margin of (10JH23), and ~3 m away from (10JH22) a macrofracture swarm (red-shaded zone). Rose diagrams show microfracture strike. UK national grid reference NH 09998 83757.

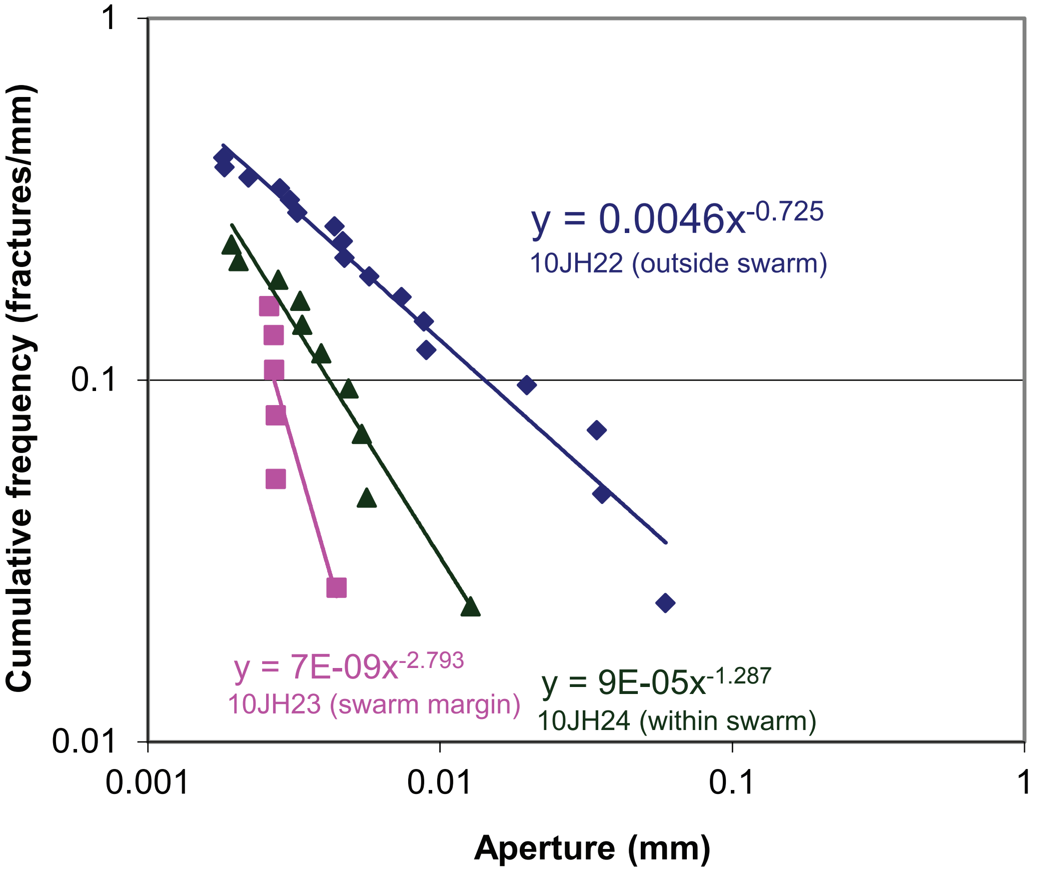

Figure 4-20. Microfracture cumulative frequency versus aperture from samples shown in Figure 4-19. Note the sample farthest from the macrofracture swarm has the highest microfracture frequency, suggesting microfracture frequency does not correlate spatially with macrofracture frequency.

measured within the folds at Perchel Canyon, higher fracture intensity is manifest in both an increase in *a* and a decrease in *b*.

INTERPRETATION OF VARIATION IN *b*

Some of the variation in observed *b* value derives from poor sampling. As explained in Chapter 3, *b* value converges to its average value with greater numbers of sampled fractures. Thus for a given fracture intensity, a wider range of *b* values may be expected from shorter scanlines. A direct test of this claim can be made by best-fitting power-law equations to subsets of power-law distributed scanline data. The best-fit *b* values to subsets of the Sample 56 microfracture data (Figure 4-21) confirm that as the scanline length is shortened and fewer fractures are sampled, variation in *b* is greater. This relationship between scanline length and observed *b* value has important consequences for attempts to constrain large-fracture spacing in the subsurface using core samples. These consequences will be further explored in Chapter 7.

Sampling of fractures in 2D records proportionally more small fractures, as evidenced by the change in *b* between scanlines and fracture maps from the Mesón Group and the Nikanassin Formation. Although the difference in *b* value is less than 1, which would be the difference in Marrett's (1996) ideal case, assuming linear aperture-length scaling, the difference present here does suggest that the 3D fracture populations have true *b* values of greater than 1.

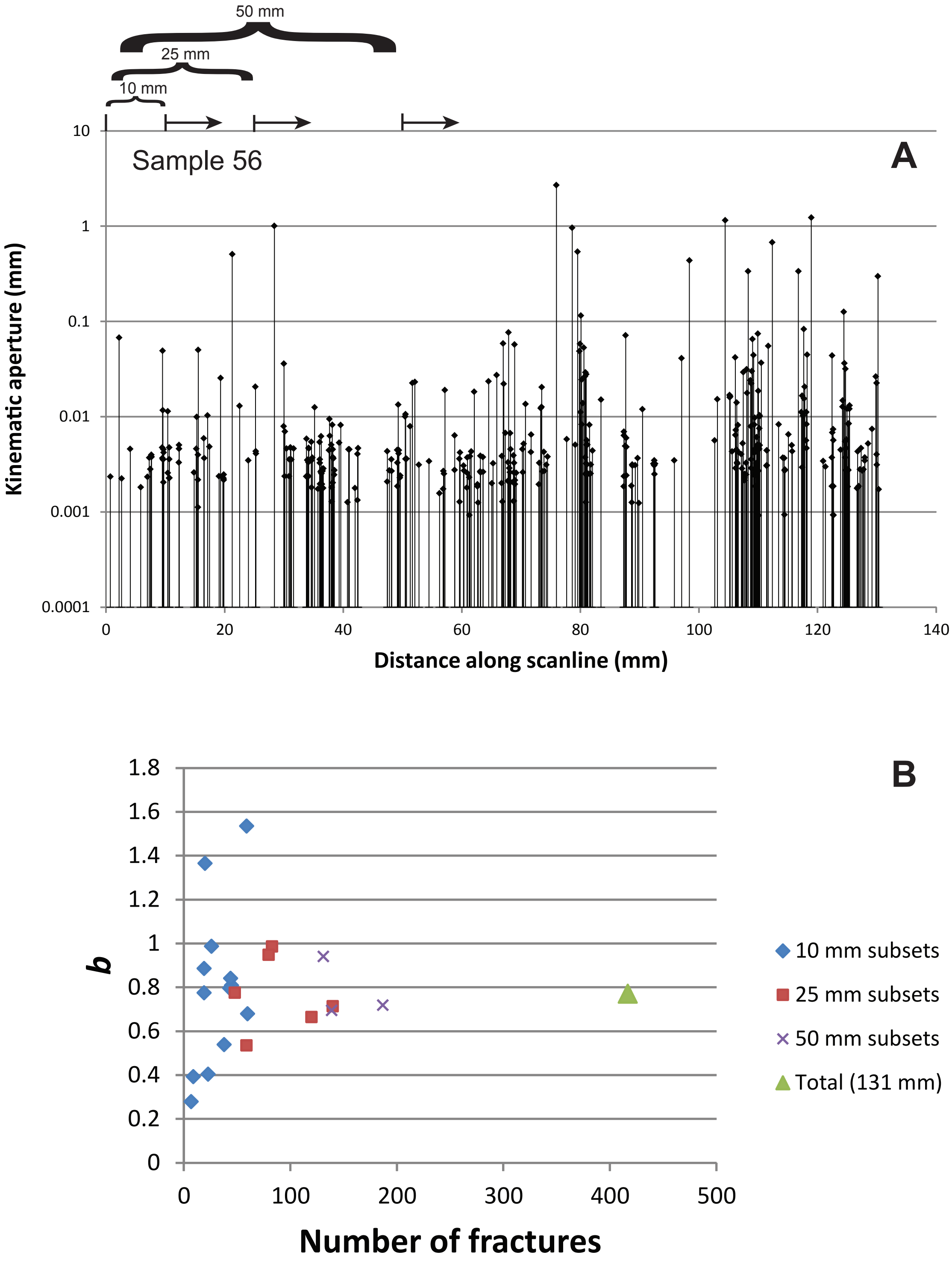

Figure 4-21. Effect of shortening the scanline length on *b*. (A) Scanline data from Sample 56 (Meson Group). (B) Best-fit *b* values from subsets of data in (A), from 10, 20, and 50 mm-long subsets, compared to the *b* value best-fit to all data. Note greater variation among smaller subsets.

Consequently the power-law distributed natural fracture populations are likely bound at the lower-size range by the space problem described in Chapter 2.

There appears to be no consistent relationship between *b* and grain size or degree of grain sorting. The greater *b* values among quartzarenites may reflect a more brittle nature of that rock type, which may more readily form microfractures (Ellis et al., 2012). I.e., a more brittle rock may fracture under a smaller applied displacement than a less brittle rock. This hypothetical mechanical effect is consistent with the paucity of microfractures in the Stoer Group fracture set (Figure 4-9), and with the absence of microtexture (crack-seal) within quartz fracture-cement (Figure 4-22).

The paucity of microfractures observed in association with macrofractures within the Stoer Group (Figure 4-9) also is consistent with the observation made in Chapter 3 that power-law distributed fracture sets are composed of characteristic-sized increments, and so can be expected to show a minimum *overall* fracture size near that characteristic *increment* size. The lack of crack-seal texture within the Rua Reidh fractures (Figure 4-22) suggests that in this case, the minimum characteristic size is large enough to be visible to the naked eye and therefore the smallest fractures qualify as macrofractures.

Moreover, the rate of cement infilling of fractures may influence scaling behavior. In most cases there is little direct evidence of the rate of cement infilling, but the degree to which fractures are filled with synkinematic cement

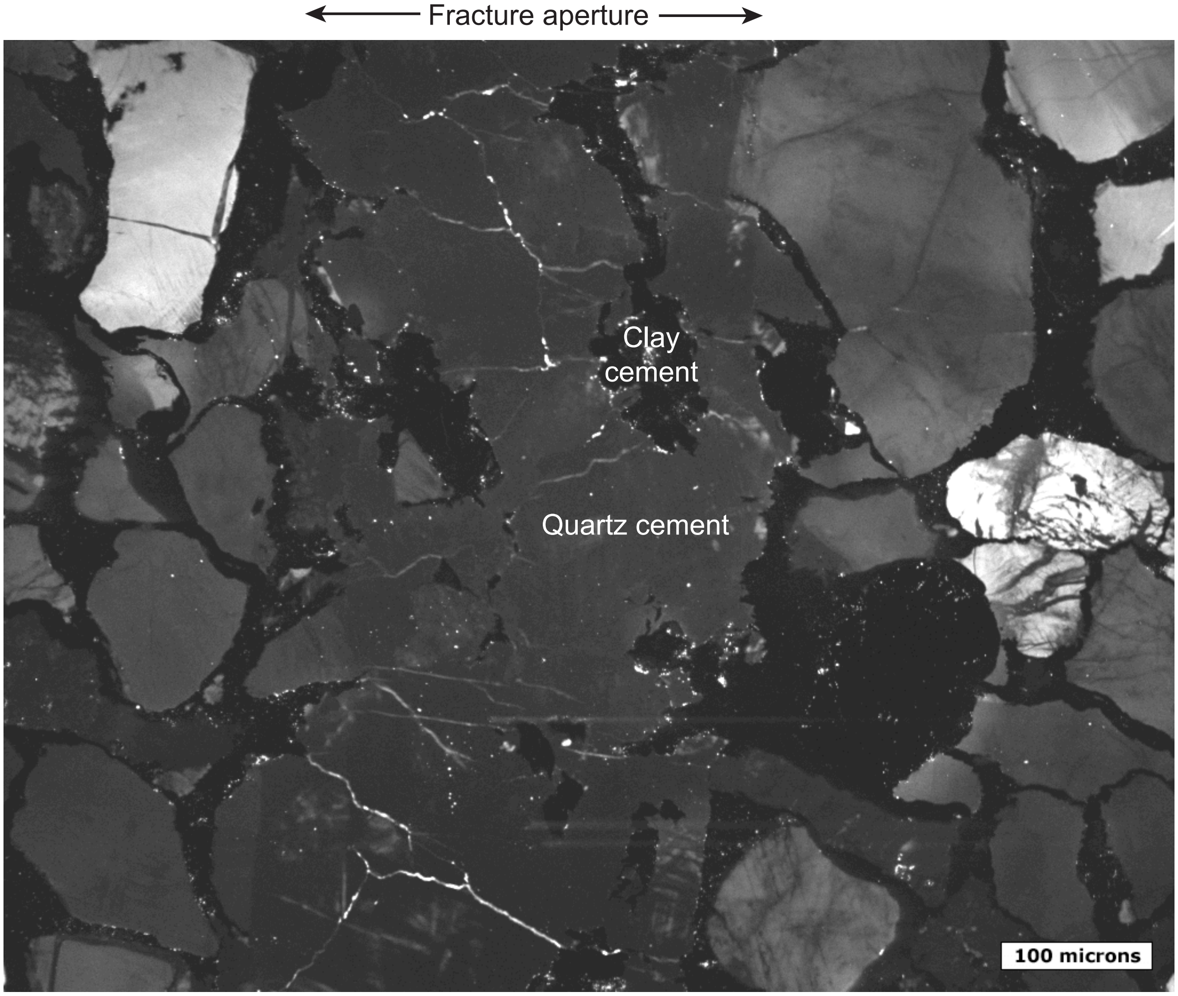

Figure 4-22. SEM-CL image of a small macrofracture from scanline measured at Rua Reidh. The fracture cement features little internal texture; CL-dark clay cement is entrained among blocky gray quartz crystals.

probably varies in part by host-rock mineralogy. The primary synkinematic cement in fracture sets observed is quartz. Quartz cement likely more thoroughly fills in growing fractures within quartzarenites than arkoses and litharenites owing to the greater relative abundance of quartz substrates within quartzarenites. This effect is consistent with locally thicker quartz cement deposits where fractures cut quartz grains (Figure 3-10). More thorough sealing might increase the likelihood of a new microfracture forming versus further opening of an existing fracture. Enhanced generation of new microfractures at the expense of opening in larger fractures would steepen the slope of size-distribution curves. Thus, higher *b* values might reflect more thorough fracture cementation within quartzarenites.. This idea will be further explored in Chapter 5.

At comparable burial depths, carbonate rocks should have faster cement precipitation rates than sandstones, because of relatively high diagenetic reactivity at low temperature and pressure (Morad et al., 2000; Morse et al., 2007). Thus it might be expected that whatever the effects of quartzarenitic host rock on fracture formation, those effects would be more acute in carbonate rocks. However, carbonate *b* values are statistically indistinguishable from sandstone *b* values. It may be that elasticity, subcritical crack index (Olson, 1993) or other mechanical properties related to mineralogy exert a more important control over *b* than does cement precipitation rate, but more data are needed to better test the idea.

There is a negative correlation between *b* and fracture clustering when fracture size is accounted for (i.e., for clustering measured by V’). This correlation may signify a dependence of *b* on how, spatially, fracture strain is arranged throughout the host rock. Specifically, increased clustering is associated with shallower power-law slopes, and therefore with a greater representation of larger fractures within the distribution. The characteristic size distribution of crack-seal gap widths (Chapter 3) suggests that, in general, geologic fracture strain accumulates in characteristic-sized increments. The specific case of a power-law size distribution is one wherein some of the increments form side-by-side, resulting a wide range of fracture sizes. The shallower the slope (lower the *b* value), the greater the proportion of the overall fracture strain within larger fractures, and by inference, the greater the tendency for fracture increments to localize and form larger fractures. Thus it may be that fracture clustering and shallow power-law slopes are both the result of an increased tendency for fractures to attract one another during fracture-set evolution.

The variation of fracture intensity with respect to structural position is inconsistent, but each structural-position case studied shows a consistent, inverse relationship between *a* and *b*. Graphically, this is represented by a *fanning* of the size distribution curves (Figure 4-18), as opposed to a parallel increase in distribution curve, with increasing strain (Figures 3-3, 3-4). Thus the entire dataset shows no consistent correlation between *b* and strain, but within samples from individual field sites, *b* and strain are negatively correlated.

This negative correlation can be explained by the relative rates of fracture opening and sealing by cement. Assuming that within a single structural setting fractures of the same orientation formed over the same time period, factors such as temperature, fluid chemistry, cement precipitation rate, and rock mechanical properties should be constant. Fracture opening rate may have been higher in high-fracture-intensity structural positions and thus explain lower *b* in higher-intensity positions. Such a relationship between fracture opening rate and *b* is consistent with the above speculation about the thoroughness of cement infilling, only now applied to the relative rates of fracture opening and cement precipitation. Within the Mesón Group fold, if the cement precipitation rate is constant throughout but fracture opening rate is locally variable by structural position, then fractures in positions of fast opening rate may be less susceptible to sealing. In these structural positions fracture reactivation might be favored over the formation of new microfractures, resulting in fewer, larger fractures and a shallower fracture intensity curve.

In the Eriboll Formation, microfracture intensity was measured with respect to two macrofracture clusters (one at the hinge of a subtle fold), and in neither case did microfracture intensity systematically increase towards the macrofracture cluster. Moreover, microfracture strike is not systematically parallel to macrofracture strike in the vicinity of the exposed fracture cluster (Figure 4-19). It has been documented that the Eriboll Formation is fracture prone and preserves a long (~500 m.y.) history of brittle deformation (Laubach and Diaz-Tushman, 2009); from this study it appears that barren or poorly-cemented fractures visible in outcrop are mostly unrelated to quartz-sealed microfractures. Nonetheless, that fractures are heterogeneously distributed implies local strain rate variability, and the same speculation applied above holds for these Eriboll Formation datasets. Namely, areas with faster fracture opening, related or unrelated to megascopic structures, may have had a lower tendency for fractures to seal and thus a lower *b* value.

As explained by Marrett (1996) and Hooker et al. (2011), for power-law distributed fractures with $b < 1$, longer scanlines will intersect proportionally more large fractures and record higher strain. When comparing data from short scanlines with fewer than 100 fractures (e.g., Figure 4-20), chance intersection of large fractures will result in high strain and low *b* values. Thus some of the correlation between *b* and strain may result from small datasets sampled from the same fracture population. Nevertheless, statistically robust fracture datasets (N ranging from 97 to 395) from the Mesón Group folds (Figure 4-16) suggest a greater proportional increase in large fractures relative to small ones within high-strain samples, thus a real variation in *b* that is not attributable to sampling variability.

SUMMARY OF GEOLOGICAL CONTROLS ON *b*

No correlation is present within the data between *b* and grain size. Weak correlation is present between *b* and host-rock mineralogy as well as the extent of clustering. Variation of fracture intensity with structural position is non-systematic, but across multiple samples collected within individual field sites, *a* and *b* are negatively correlated. Thus *b* is not unambiguously linked to any factors readily observed in the field or in thin section. Possible important controls include host-rock mechanical properties and the relative rates of cement precipitation and fracture opening.

UNDERSTANDING FRACTURE-SET EVOLUTION

Chapter 5: Simulations

In Chapter 1 a review of the literature showed that power-law aperture-size scaling is typically not replicated in fracture growth models based on linear-elastic fracture mechanics, leading to the inference that some key phenomenon of fracture growth is missing from these models. Yet a mechanical understanding of how power-law fracture scaling emerges undoubtedly needs to account for linear-elastic fracture mechanics. The literature review also showed that the mechanical effects of cement deposits in fractures, although likely to exist based on observations of fracture strength, are now ignored by all mechanics-based fracture growth simulation. Chapter 2 reviews various sampling and measurement problems that are commonly encountered in fracture surveys, and outlines how to interpret scaling data given these problems. In Chapter 3 textural observations from fracture fill show that fracture sets that are well-fit by power-law aperture size distributions include individual fractures that widened by the superposition of characteristic-size growth increments into larger fractures. In other words, the textural evidence from some fractures shows that fracture final fracture aperture arises from the accumulation of small (commonly micron scale) increments, and that the increment size range is narrow. Chapter 3 also showed that for many sandstones the power-law *b* (exponent) value has a narrow range around 0.8. In Chapter 4 data from individual field sites showed that *a* (the power-law coefficient) and strain are both negatively correlated with *b*, suggesting that within a geologic setting, locally variable fracture opening rates might influence *b*.

Although the size-scaling data reported in previous chapters is extensive, all of these observations are of end states of fracture array-evolution through time. The fracture-size scaling observations alone provide only indirect evidence for how these patterns arose. That is, the scaling patterns suggest feedback is at play during fracture-set evolution linking *current* fracture size and *future* fracture growth, but the scaling patterns do not identify the process(es) creating the feedback. In chapters 5 and 6, I use two independent approaches to investigate how the patterns develop. Both chapters also address the potential role of cement in the process. In Chapter 5 I describe a new rule-based model and illustrate how simulated cement precipitation affects fracture growth using the rule-based model.

The model assumes that cement plays a role in fracture strength or cohesion and therefore in the propensity for fractures to be reactivated (to continue growing). The model generates fractures iteratively, by progressively adding increments of fracture growth (aperture) to new and pre-existing fractures. Depending on the starting conditions and rules, resulting cumulative kinematic aperture size distributions may be best fit by power-law, exponential, or log-normal equations. Rules and starting conditions can include increment width, fracture-growth selection probability, and flaw-size distribution.

For a given strain rate, assuming that cement accumulation is temperature dependent and that cement accumulation controls fracture cohesion, the model can be used to test the effects of changing temperature (cementation rate) on the resulting size distribution.

The simulation allows tracking of the growth histories of individual fractures, and can therefore provide hypotheses of growth histories that can be compared to independent observations of actual fracture pattern growth histories (Chapter 6).

PREVIOUS MODELS OF FRACTURE POPULATION GROWTH

Fracture growth models have been developed that incorporate physical principles using statistical methods. Cowie et al. (1993) used such an approach to demonstrate how power-law size distributions may emerge as faults form and localize by dynamic interaction in response to tectonic displacement, without needing a pre-existing fabric. Cladouhos and Marrett (1996) simulated the development of a power-law distribution of fault lengths by size-dependent linkage of growing faults.

Davy et al. (2010) demonstrated that fracture length distributions can develop power-law size distributions over a wide range of geologic conditions, simply by virtue of the tendency for fractures to arrest when they intersect other fractures. This ad-hoc explanation of power-law size scaling is consistent with power-law length distributions modeled using linear-elastic fracture mechanics simulations of populations of fractures having varying strikes (Olson, 2007) and thus intersecting and terminating against one another.

A numerical model presented by Clark et al. (1995) simulates the widening of a population of fractures and results in a power-law aperture-size distribution. This model is run iteratively. At each iteration, a single extant fracture is selected at random (probability not based on size) from the population; this selected fracture grows (widens) by a given proportion of its current width; i.e.,

$$W' = W * p \qquad (5\text{-}1)$$

where W is the current (original) width, W' is the new width, and p is a growth factor. So if p = 1.1, then the selected fracture would become ten percent wider. In the model by Clark et al., this widening is achieved by adding a sufficient number of fixed-size growth increments until the fracture becomes [ten] percent wider.

Additionally, every X iterations, a new fracture is generated at some size W_o. This model is qualitatively consistent with the size distributions observed in Chapter 3 in that the model produces fracture populations that follow power-law aperture size distributions. However, the model assumes that fractures likely undergo growth increment sizes proportional to current fracture size, in the absence of a mechanism for the selected fracture to be repeatedly selected until it has grown to its proportional new size. This assumption is inconsistent with the observation that crack-seal increment sizes are mostly independent of overall fracture size (Figure 3-10) and that late gap widths are commonly narrower than earlier ones (Figure 5-1). The model assumes that *later* growth increments are systematically *larger*, which is consistent with complex shear-related vein-fill textures which Clark et al. (1995) described within the Kodiak Accretionary Complex.

A NEW FRACTURE POPULATION GROWTH SIMULATION

A new fracture growth model is described below. This model incorporates the new observations of natural fractures and fracture sets in Chapter 3. In particular, the incremental fracture opening recorded in synkinematic cements is replicated using simple rules to distribute progressive opening among a set of fractures (Figure 5-2). The objective of these rules is to capture the effects of mechanical and diagenetic processes, as discussed below. Natural fracture-fill textures (Chapter 3) show that fractures grow incrementally and amid cement precipitation. Synkinematic cement could provide feedback between current fracture size and future fracture growth if the cohesion provided by cement strengthens small, thoroughly cemented fractures more than large, less cemented fractures. To simulate this effect, fractures are grown iteratively, and each iteration involves the following steps:

1. Begin iteration

Figure 5-1. SEM-CL mosaic of fracture from the La Boca Formation, NE Mexico. Quartz cement bridge is composed of older, thick euhedral deposits crosscut by crack-seal increments having tens-of-microns-scale widths. This imples that an early, relatively wide opening increment is crosscut by later, narrower opening increments, although the absence of preserved increments does not definitively negate incremental opening (see text). Image by Rob Reed.

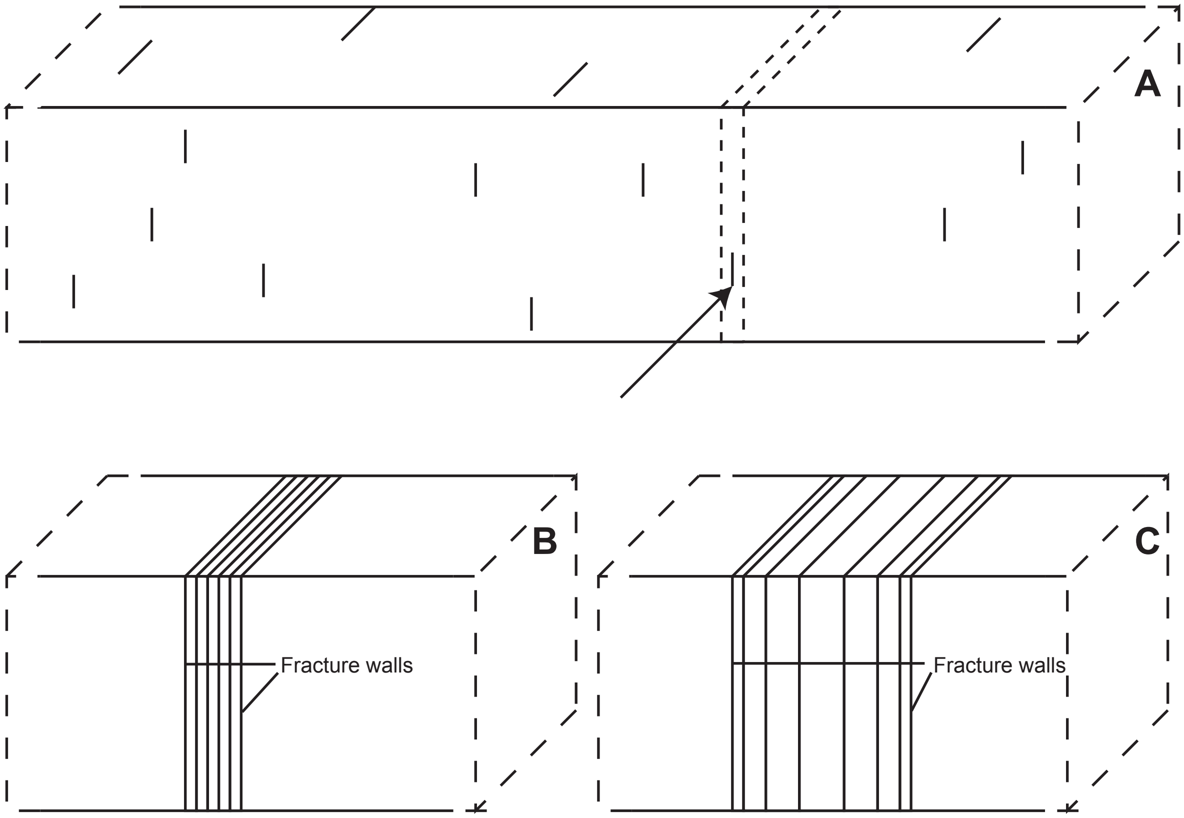

Figure 5-2. Fracture growth simulation used in this study. Dashed lines at end of simulated rock bodies emphasize that fracture location is not accounted for in the simulation. The simulation is run iteratively. Fractures may either grow from a pre-existing, static flaw population (A) or be introduced at regular time intervals. Each iteration, an extant flaw or fracture is selected for growth using a random number generator; selection probability can be equal among fractures or proportional to current size. In (A), the flaw indicated by an arrow is selected; dashed lines represent fracture walls after growth increment. Growth increments can either be additive and constant in magnitude (B) or proportional to current fracture size (C). Additionally, flaw size and/or additive opening-increment size, if applicable, can be uniform or log-normally distributed.

2. Select, among extant fracture population, a single fracture to be enlarged

3. Enlarge selected fracture

4. (Some permutations) create new fracture

5. End iteration (go to 1 for next iteration)

The simulation has a variety of *permutations* that are created by modifying four parameters. Below the resulting size distributions and growth histories of 24 such permutations are tested against observations from natural fractures. The modifiable parameters are:

Growth rule (G)

In each simulation, fractures grow incrementally. The magnitude of the new increment of growth can either be fixed (constant increment size) or proportional to the growing fracture's size at the beginning of the iteration (multiplicative increment size). For the following simulation output descriptions, including size distribution plots, I use a default opening increment width of 1 mm, which is large compared to the μm-scale opening increment widths observed in Chapter 3. However, the simulation is intended to be scalable to any appropriate natural opening increment size.

Probability for the selection of fracture to grow (P-GROWTH)

Each iteration of each simulation involves the selection of an extant fracture to grow. The selection rule may weight all extant fractures equally, or the probability of selection may be proportional to the current size of the fracture, at the beginning of the iteration. In the latter case, probability may be linearly proportional to the size or proportional to the logarithm of the fracture size.

Number of starter flaws (N-FLAWS)

In accordance with Griffith's (1920) theory explaining the weakness of natural materials, it may be realistic to assume that a pre-existing population of flaws exists, and that these flaws are then enlarged with progressive fracture strain. In reality there should be myriad flaws present in a host rock, which would prove computationally cumbersome. The simulations below involve at most 500 flaws. Some simulations reach a point at which each flaw has been selected and grown into a fracture, at which point the potential is severe that the simulation is unrealistic by virtue of too few flaws having been modeled. Potential artifacts of insufficient flaw density are addressed in the discussion. In other simulations not all flaws are selected even after a great number of iterations compared to N-FLAWS. In still other simulations, starter flaws are not explicitly modeled, but rather the number of fractures grows at a constant rate, by introducing a new fracture every so-many iterations. This was the approach used in the simulation of Clark et al. (1995).

Increment size distribution (D-INC-SIZE)

The size distribution of both the starter flaws and constant increment sizes, where applicable, may affect the resulting size distribution. One hypothesis is that small initial variation in size may be magnified by a size-proportional selection rule, P-GROWTH, potentially resulting in a power-law size distribution. To investigate this hypothesis, the simulations below include permutations with starter flaws and growth increments that are equally sized and, for comparison, log-normally distributed.

In this section the progression of the size distribution from each model permutation is described. Table 5-1 includes a summary of the resulting size distribution from each simulation permutation.

1. N-FLAWS fixed

1a. G fixed, D-INC-SIZE equal, P-GROWTH random

This permutation results in a characteristic (normal) size distribution (based on chi^2 test; Chapter 2) for all studied parameters (Figure 5-3). The permutation features no tendency for large fractures to outpace the growth of smaller fractures, in amount of size added or in selection probability.

1b. G fixed, D-INC-SIZE equal, P-GROWTH proportional (linear)

This permutation generally results in exponential size distributions (Figure 5-4), as for example using 100 starter flaws and increasing the fracture size by 1 at each selection. The permutation can be made *unstable*, i.e., may result in runaway growth by a small subset of large fractures, by using a growth size that is large compared to the number of starter flaws. For example, keeping N-

N-FLAWS	G	D-INC-SIZE	P-GROWTH		Power-law?*	Stable?	Permutation number
Fixed	Fixed	Equal	Random		N	Y	1a
			Proportional	Linear	L	L	1b
				Logarithmic	N	Y	1b-2
		Log-normal	Random		N	Y	1c
			Proportional	Linear	L	L	1d
				Logarithmic	N	Y	1d-2
	Proportional	Equal	Random		N	Y	1e
			Proportional	Linear	L	N	1f
				Logarithmic	Y	L	1f-2
		Log-normal	Random		N	Y	1g
			Proportional	Linear	L	N	1h
				Logarithmic	Y	L	1h-2
Increasing	Fixed	Equal	Random		N	Y	2a
			Proportional	Linear	Y	Y	2b
				Logarithmic	N	Y	2b-2
		Log-normal	Random		N	Y	2c
			Proportional	Linear	Y	Y	2d
				Logarithmic	N	Y	2d-2
	Proportional	Equal	Random		Y	Y	2e
			Proportional	Linear	L	L	2f
				Logarithmic	L	L	2f-2
		Log-normal	Random		Y	Y	2g
			Proportional	Linear	L	L	2h
				Logarithmic	L	L	2h-2

Table 5-1. Summary of results of each simulation permutation. *Whether the data fit a power law was judged by the relative quality of fit (chi^2 method, Chapter 2) between power-law and characteristic equations. Y=yes; L=limited; N=no. Limited power law means some parameters led to best-fits to power laws and other parameters result in characteristic size distributions. Limited stability means that some parameters led to stable growth shared among all or most simulated fractures; some parameters led to unstable runaway growth of a small subset of fractures, leaving most fractures with exceedingly low growth probability.

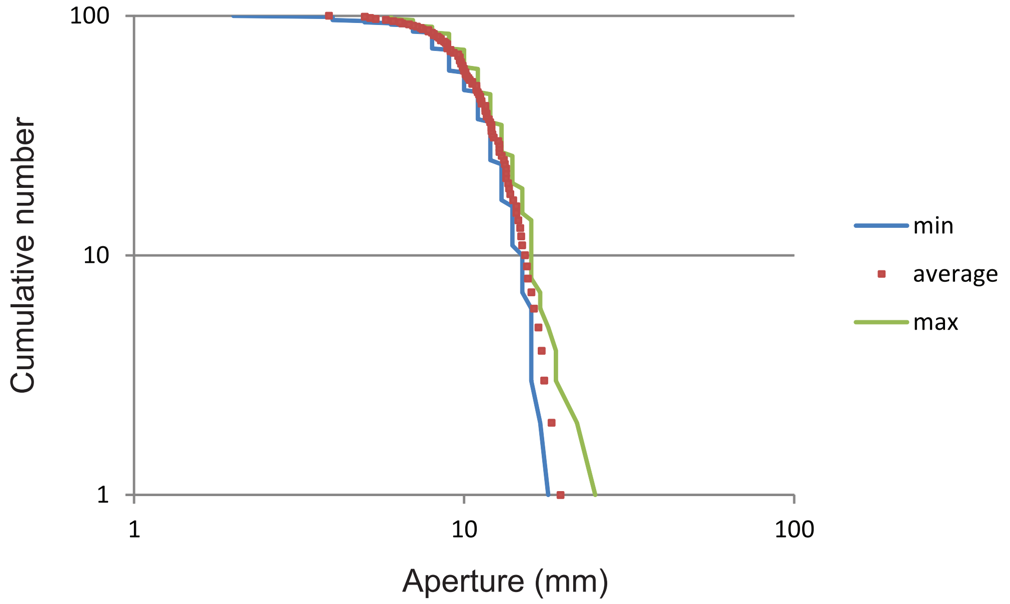

Figure 5-3. Size distribution resulting from permutation 1a--average, maximum, and minimum sizes after ten simulations; 1000 iterations, 100 flaws, initial flaw size = 1mm, growth increment size = 1mm.

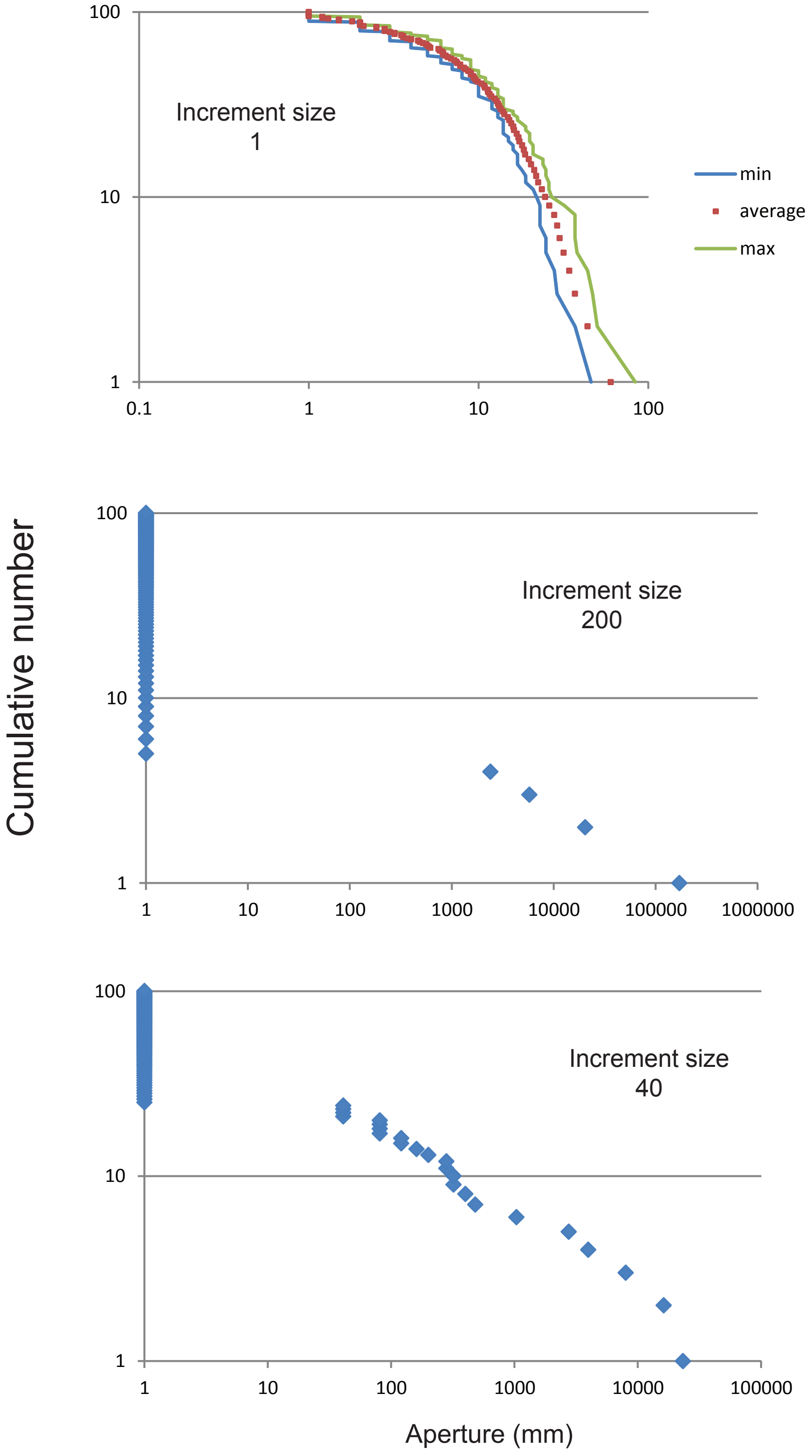

Figure 5-4. (A) Size distribution resulting from permutation 1b--average, maximum, and minimum fracture sizes after ten simulations; 1000 iterations, 100 flaws, initial flaw size = 1mm, growth increment size = 1mm. (B) Same permutation, growth size = 200mm. (C) Same permutation, growth size = 40mm.

FLAWS at 100 and making the growth amount 200, only a few (<10) fractures typically grow in the first 1000 iterations.

At intermediate additive growth amounts (~40) the resulting size distribution is well-fit by a power law, although most flaws do not grow.

1b-2. G fixed, D-INC-SIZE equal, P-GROWTH proportional (logarithmic)

Taking the same rules as in permutation 1b but making the probability for selection proportional to the logarithm of fracture size rather than linearly proportional increases the stability. For constant incremental fracture growth size of even 2000 (Figure 5-5), and a flaw size of 1, the selected fractures still do not dwarf the flaws in terms of selection probability even after 1000 iterations and a maximum fracture size of over 17000. However, the grown-fracture population does not approach a power law under any combination of parameters attempted; in general the grown fractures form a characteristic size distribution, with no large fracture out-pacing the rest in five simulations of up to 1000 iterations.

1c. G fixed, D-INC-SIZE lognormal, P-GROWTH random

This permutation introduces variation in flaw sizes and in growth increment size; it is otherwise identical to permutation 1a. The resulting size distribution is best fit by a log-normal equation after 1000 iterations (Figure 5-6). The change from normal final size distribution (1a) to log-normal is likely the result of the log-normal distribution of flaw size and/or growth increment size.

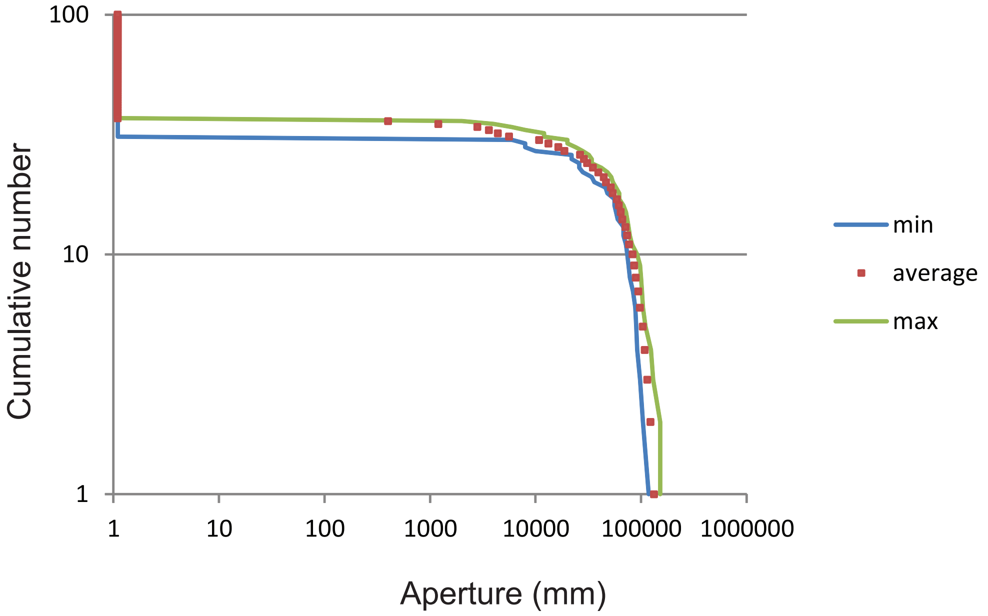

Figure 5-5. Size distribution resulting from permutation 1b-2--average, maximum, and minimum fracture sizes after five simulations; 1000 iterations, 100 flaws, initial flaw size = 1mm, growth increment size = 2000mm.

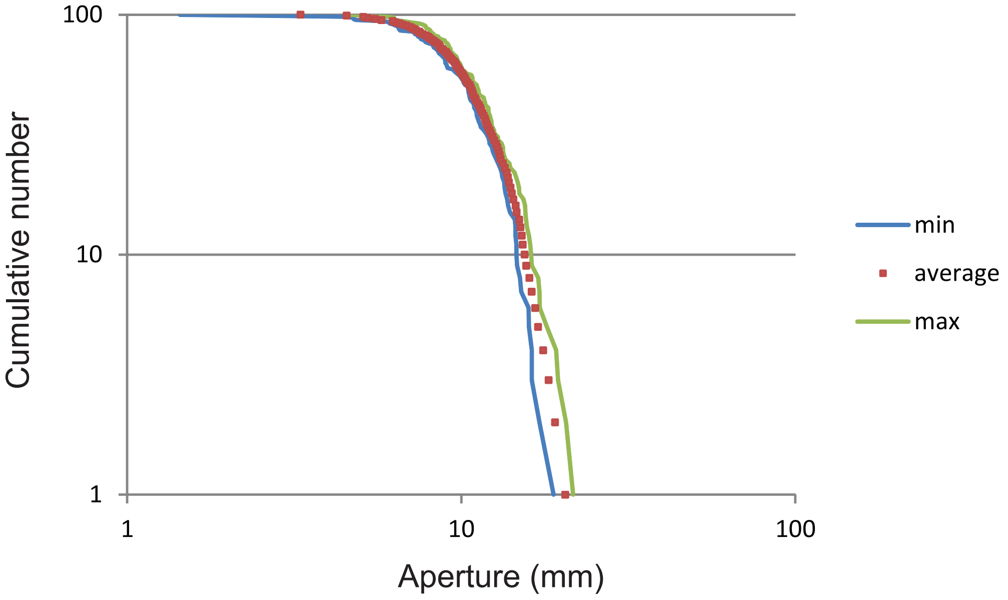

Figure 5-6. Size distribution resulting from permutation 1c--average, maximum, and minimum sizes after ten simulations; 1000 iterations, 100 flaws, average (initial flaw size and growth increment size) = 1mm, standard deviation (initial flaw size and growth increment size) = 1.35.

Like permutation 1a, 1c lacks any feedback between current size and susceptibility for future enlargement, so no power-law size distribution emerges.

1d. G fixed, D-INC-SIZE lognormal, P-GROWTH proportional (linear)

Permutation 1d is qualitatively the same as 1b in spite of a different flaw-size distribution. Introducing variation to the initial flaw size distribution and growth increment size distribution increases the variation in expanded-fracture sizes, but the general pattern is the same: with increasing (average) growth increment size, the final size distribution goes from exponential to a limited power law to an unstable arrangement wherein only a few fractures grow (Figure 5-7). Using an average growth size of 20.1 and standard deviation 1.3, the resulting size distribution (after 1000 iterations) is best-fit by a power law and features two concave-downwards curves, which qualitatively resembles natural size distributions (Figure 5-8) measured in the Piceance basin (Sample 37) and the El Alamar Formation (Sample 44). The bump at the smaller-size end represents the sizes of flaws that did not grow during the simulation; these correspond to the vertical-line segment of the output of permutation 1b (Figure 5-4). Increasing the standard deviation of growth increment sizes to 2.2, the grown fractures more quickly dwarf the selection probability of the remaining flaws, but the grown-fracture population no more resembles a power-law size distribution than does the lower-standard-deviation counterpart.

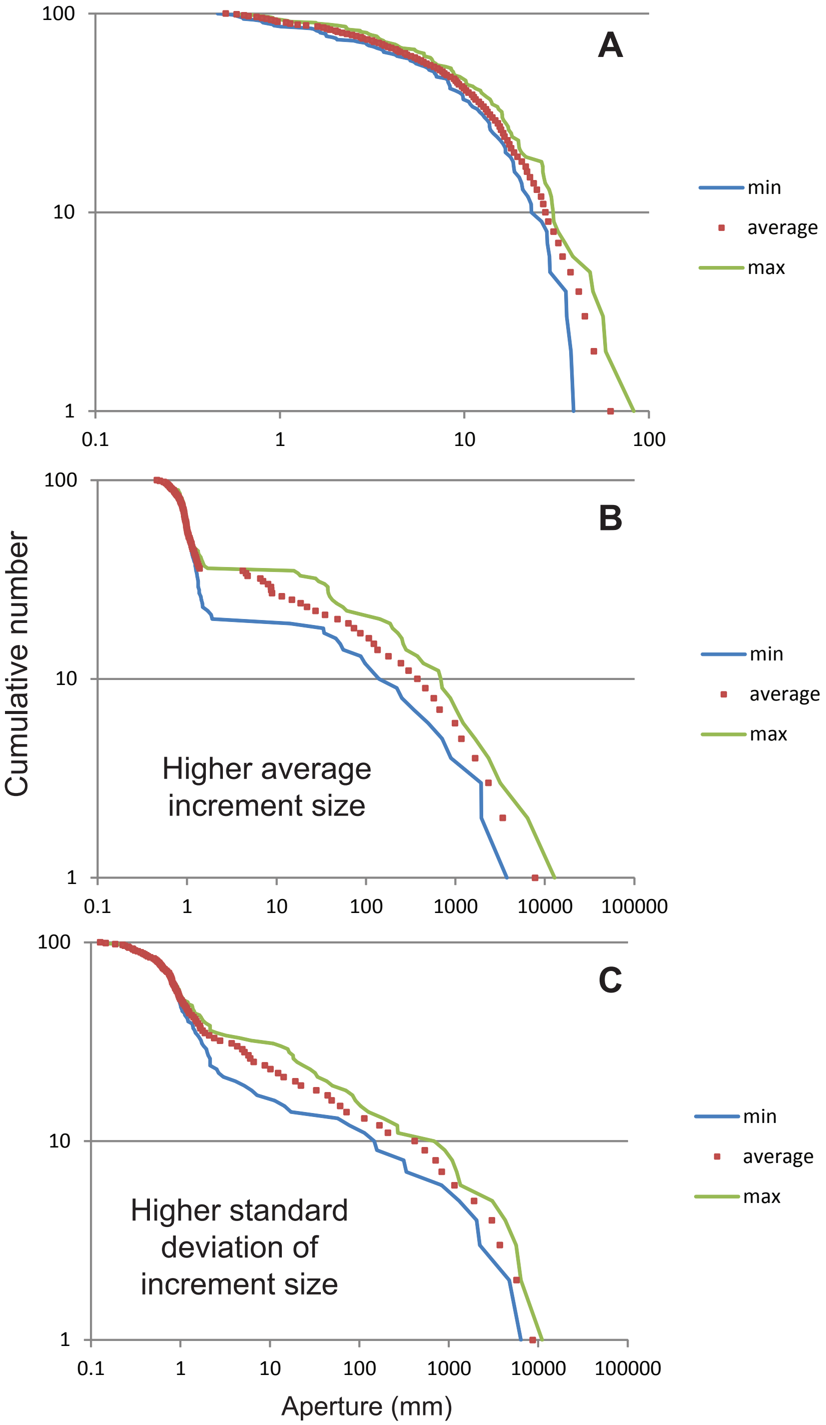

Figure 5-7. (A) Size distribution resulting from permutation 1d--average, maximum, and minimum fracture sizes after ten simulations; 1000 iterations, 100 flaws, average (initial flaw size and growth increment size) = 1mm, standard deviation = 1.3mm. (B) Same permutation, five simulations; average (initial flaw size and growth increment size) = 20.1mm. (C) Same permutation, five simulations; standard deviation = 2.2mm.

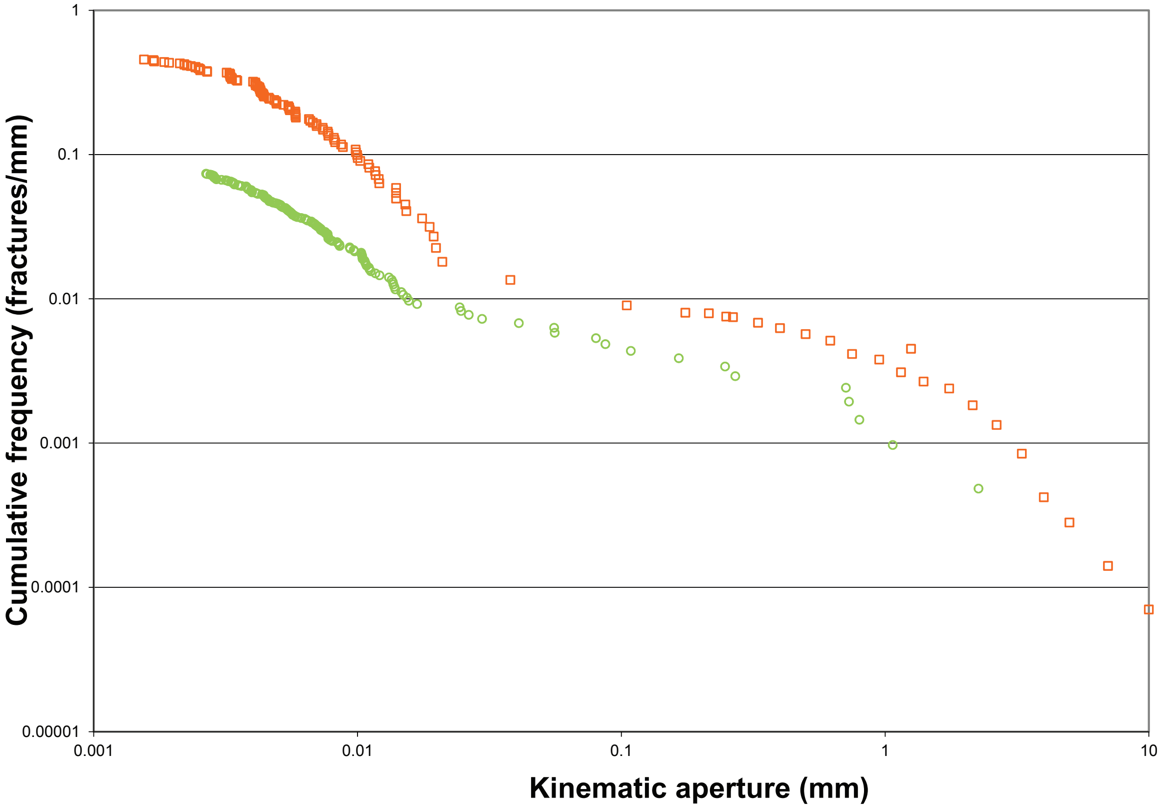

Figure 5-8. Fracture size-frequency data from NE Mexico (squares) and the Piceance Basin (circles). Mexico data include fractures measured in outcrop with a hand lens and from SEM-CL images; all Piceance Basin data were measured from SEM-CL images. Both size distributions comprise distinct large-scale and small-scale concave-downwards curves. Note similarity to results of simulation 1d, Figure 5-7b and 5-7c. Such curves suggest an abundance of fractures near a small, characteristic size, possibly analogous to the flaw size in simulations, and a distinct population of larger fractures, which may have grown by interaction among smaller fracture sizes.

The curves to the simulated (Figure 5-7b,c) and natural (Figure 5-8) size distribution likely represent two distinct growth processes to the factures. The small-size curve represents the characteristic flaw or opening-increment size, which is likely a function of the host rock mechanical and geological properties. The large-size curve to the size distributions represents the growth of accumulated fractures, which involves the spatial grouping of the individual opening increments.

1d-2 G fixed, D-INC-SIZE lognormal, P-GROWTH proportional (logarithmic)

This permutation is qualitatively equivalent to 1b-2; a log-normal distribution of starter-flaw sizes only varies the breadth of the resulting distributions, not their best-fit equation.

1e. G proportional, D-INC-SIZE equal, P-GROWTH random

This permutation results in a log-normal distribution (Figure 5-9). This result is the same for G multipliers between 1.1 and 2.

1f. G proportional, D-INC-SIZE equal, P-GROWTH proportional (linear)

This permutation likely has only limited stability with any combination of parameters. Runs to 1000 iterations produced runaway growth of the largest fracture at G multipliers of about 1.1 and above (using 100 starter flaws—Figure 5-10a). Within the stable region at lower G multipliers, the resulting size distributions are best-fit by power-law equations with steep *b* values (1.4 to 1.8). However, even at lower G multipliers the permutation is likely eventually

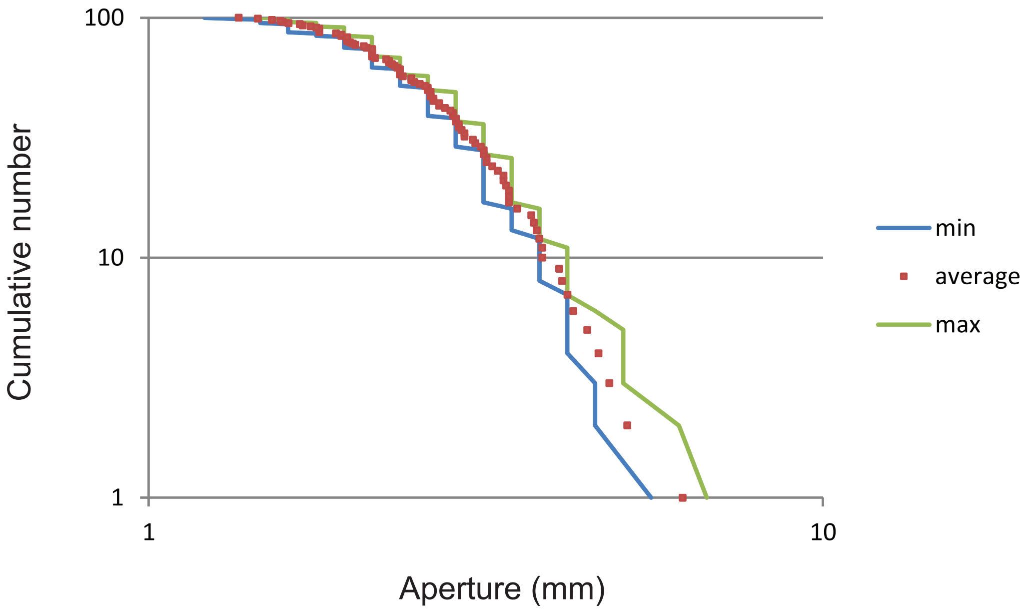

Figure 5-9. Size distribution resulting from permutation 1e--average, maximum, and minimum sizes after ten simulations; 1000 iterations, 100 flaws, initial flaw size = 1mm, growth multiplier = 1.1.

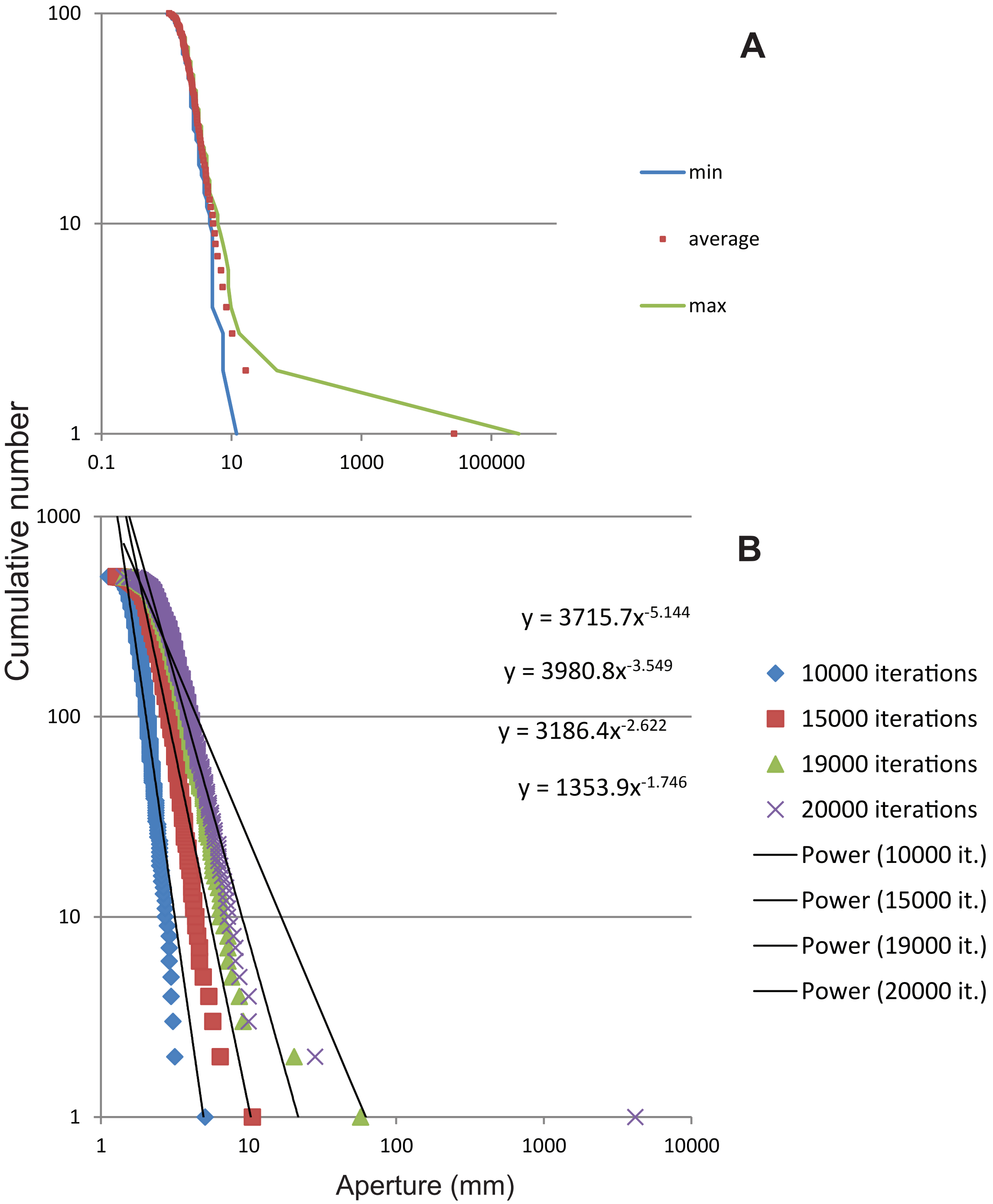

Figure 5-10. (A) Size distribution resulting from permutation 1f--average, maximum, and minimum sizes after ten simulations; 1000 iterations, 100 flaws, initial flaw size = 1mm, growth multiplier = 1.1. (B) Resulting size distribution with growth multiplier = 1.03, 500 flaws, after 10K, 15K, 19K, and 20K iterations. Both changes in initial parameters were intended to increase stability but the simulation still results in runaway growth of the largest fracture before a shallow power law develops.

unstable, after some number of iterations. After increasing the number of flaws to 500 and decreasing the G multiplier to 1.03, both changes intended to increase stability, the largest fracture still dwarfed the selection probability of the rest after approximately 20,000 iterations (Figure 5-10b). Therefore this permutation, which includes positive growth feedback loops both in its proportional growth rule and its proportional selection rule, appears to be universally unstable, and does not result in power laws with the natural *b* value (<1).

1f-2. G proportional, D-INC-SIZE equal, P-GROWTH proportional (logarithmic)

This permutation is stable at low G multipliers (1 to ~1.1) and starter-flaw size 1. The permutation with these parameters produces a power-law size distribution (Figure 5-11). At higher G multipliers the resulting size distribution is concave upwards on a log-log plot, and at G multipliers above about 2 very few fractures grow. With larger flaw sizes the stability increases: starter-flaw size of 5 is generally stable with a G multiplier of 2. Thus by modifying permutation 1f so that the probability of selection is proportional to the logarithm of current fracture size and not linearly proportional, the simulation creates stable power laws with shallow slopes (Figure 5-11).

1g. G proportional, D-INC-SIZE lognormal, P-GROWTH random

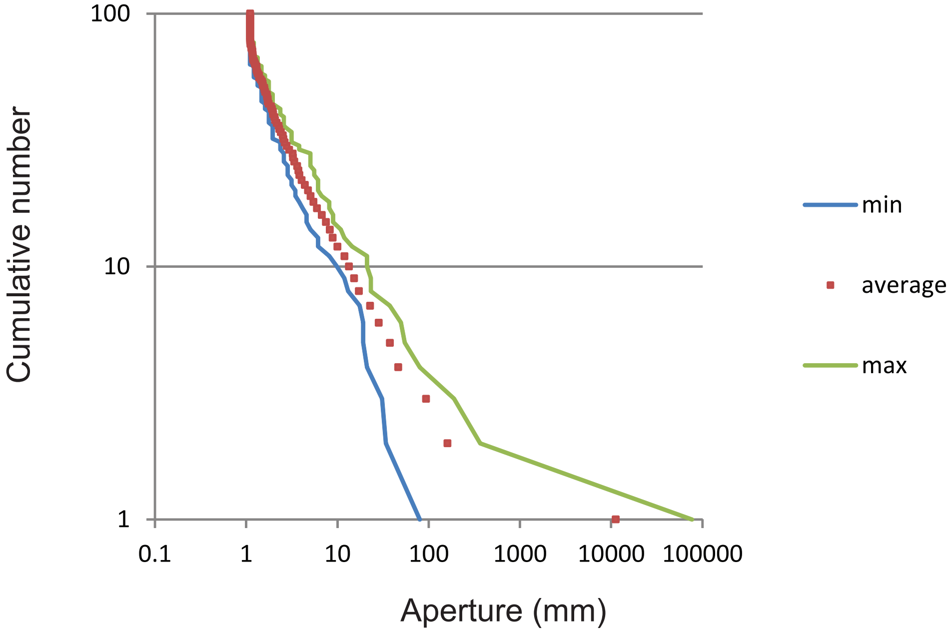

Figure 5-11. Size distribution resulting from permutation 1f-2--average, maximum, and minimum sizes after ten simulations; 1000 iterations, 100 flaws, initial flaw size = 1.1mm, growth multiplier = 1.1.

This permutation is qualitatively equivalent to permutation 1e. Adding variation to the starter-flaw size distribution does not change the resulting size distribution type (log-normal).

1h. G proportional, D-INC-SIZE lognormal, P-GROWTH proportional (linear)

This permutation is qualitatively the same as permutation 1f. The increase in variation of starter-flaw size tends to increase instability, but both permutations are likely universally unstable regardless.

1h-2. G proportional, D-INC-SIZE lognormal, P-GROWTH proportional (logarithmic)

This permutation is qualitatively equivalent to permutation 1f-2. Adding variation in starter-flaw size does not appear to have important effects on either stability or final size distribution.

2. N-FLAWS increasing

2a. G fixed, D-INC-SIZE equal, P-GROWTH random

This permutation is stable and results in an exponential size distribution using all attempted parameters (Figure 5-12).

2b. G fixed, D-INC-SIZE equal, P-GROWTH proportional (linear)

This permutation is generally stable and produces power-law size distributions with *b* varying systematically with the rate of introduction of new fractures (Figure 5-13). The permutation can be made unstable if the newly created fractures are of a size much smaller than the growth increment size.

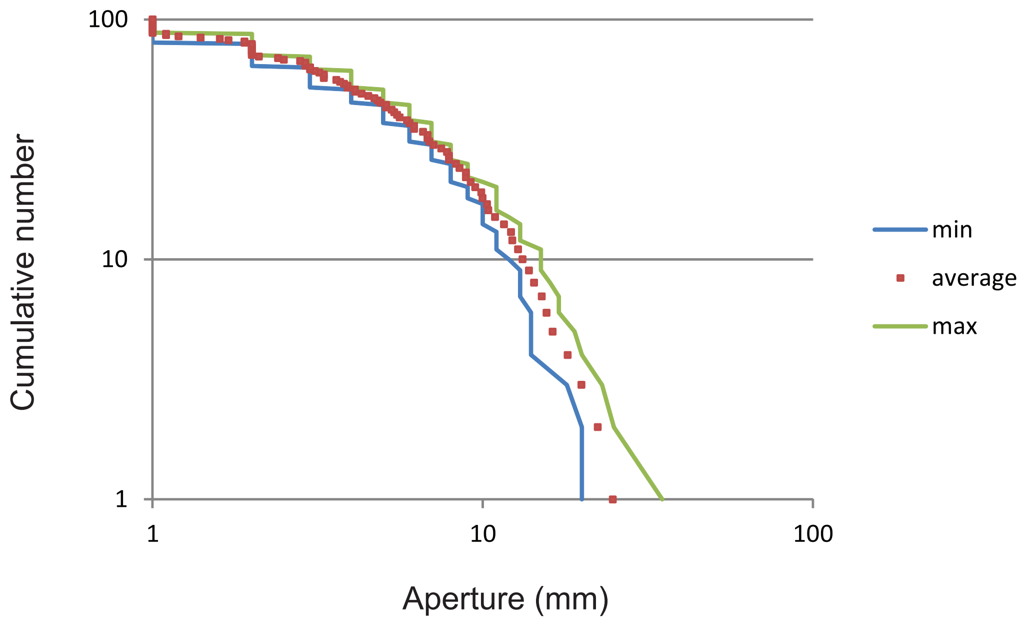

Figure 5-12. Size distribution resulting from permutation 2a--average, maximum, and minimum sizes after ten simulations; 100 fractures generated, 5 iterations per new fracture, growth size = 1mm.

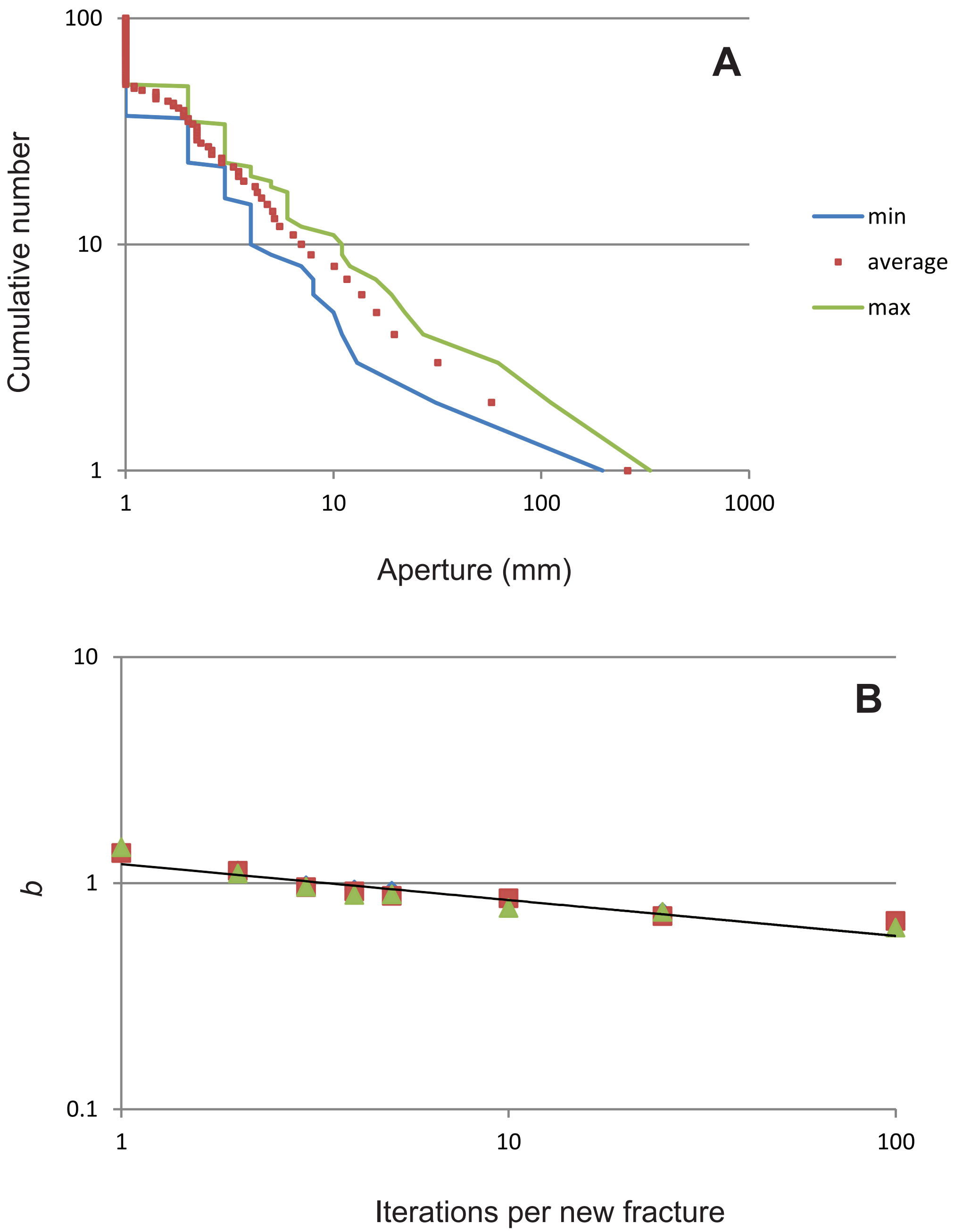

Figure 5-13. (A) Size distribution resulting from permutation 2b--average, maximum, and minimum sizes after ten simulations; 100 fractures generated, 5 iterations per new fracture, growth size = 1mm. (B) Resulting *b* values versus number of iterations per new fracture. Data are well-fit by a power-law equation but the residuals follow a concave-upwards curve on a log-log plot, suggesting a slower decline of *b* with increasing number-of-iterations than predicted by the plotted power-law equation.

2b-2. G fixed, D-INC-SIZE equal, P-GROWTH proportional (logarithmic)

Taking the previous permutation but making the selection probability proportional to the logarithm of fracture size results in a characteristic (log-normal) size distribution separating in log-log space from the newly-formed-fracture sizes (Figure 5-14).

2c. G fixed, D-INC-SIZE lognormal, P-GROWTH random

Modifying permutation 2a such that starting sizes and growth increment sizes are log-normally distributed does not change the resulting size distribution (exponential—Figure 5-15).

2d. G fixed, D-INC-SIZE lognormal, P-GROWTH proportional (linear)

This permutation gives the same general results as permutation 2b. However, using a large average starting size (ln[size]=4 or size~54.6) and a large standard deviation (ln[σ]=1) gives a resulting size distribution that is best-fit by a log-normal equation, but is also well fit by a power-law equation (Figure 5-16). Using the same average starting size but a lower standard deviation results in a better power-law fit. Thus by increasing variation in the starter sizes, this permutation results in better log-normal, and worse power-law, size distribution fits, using the chi^2 method criterion (Chapter 2).

2d-2. G fixed, D-INC-SIZE lognormal, P-GROWTH proportional (logarithmic)

Like permutation 2b-2, 2d-2 results in log-normal size distributions (Figure 5-17). The initial parameters used were a large flaw size (ln[size]=4, σ=1). To

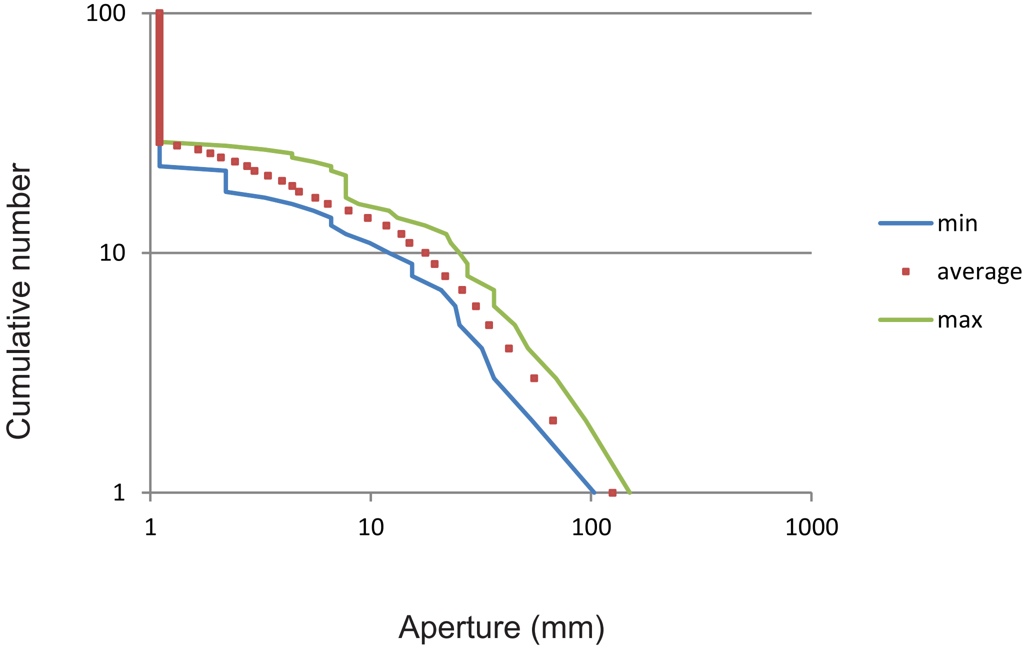

Figure 5-14. (A) Size distribution resulting from permutation 2b-2--average, maximum, and minimum sizes after ten simulations; 100 fractures generated, 5 iterations per new fracture, growth size = 1mm.

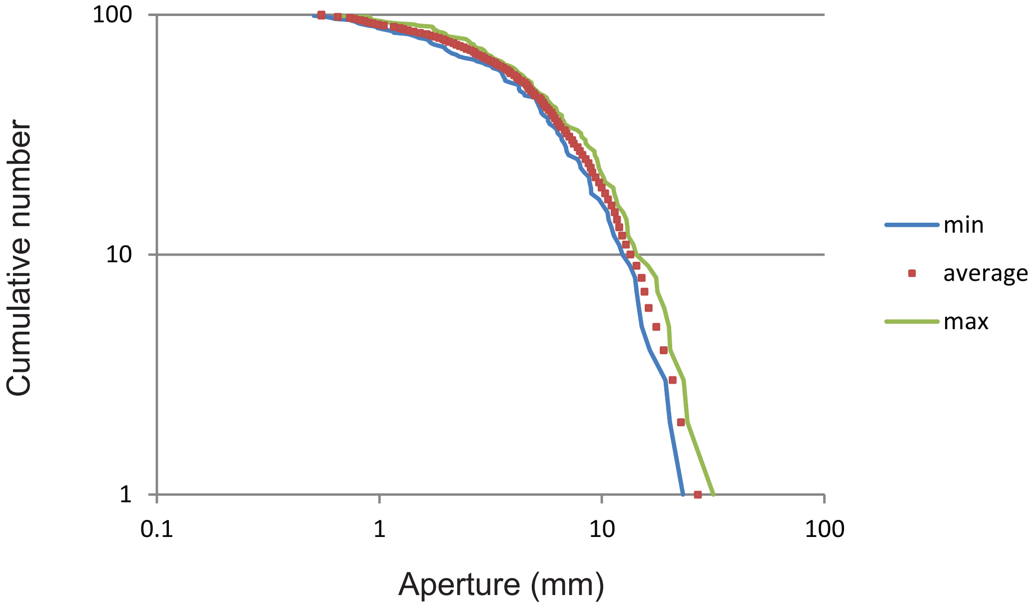

Figure 5-15. (A) Size distribution resulting from permutation 2c--average, maximum, and minimum sizes after ten simulations; 100 fractures generated, 5 iterations per new fracture, average growth size = 1mm, standard deviation = 1.35.

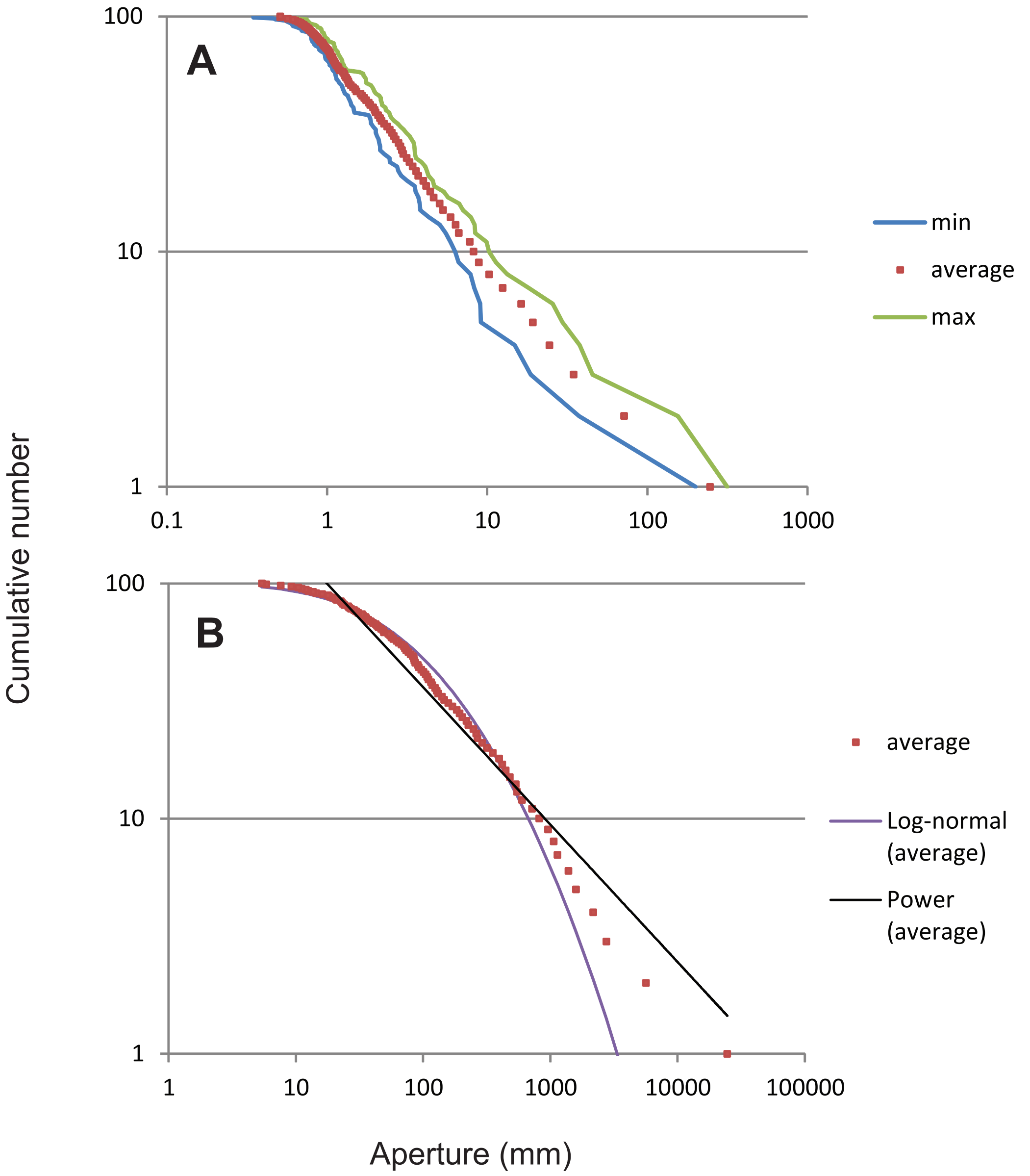

Figure 5-16. (A) Size distribution resulting from permutation 2d--average, maximum, and minimum sizes after ten simulations; 100 fractures generated, 5 iterations per new fracture, growth size = 1mm, standard deviation =1.35. (B) Resulting size distribution from the same permutation, average of 5 simulations, using average growth size = 54.6mm and standard deviation = 2.7.

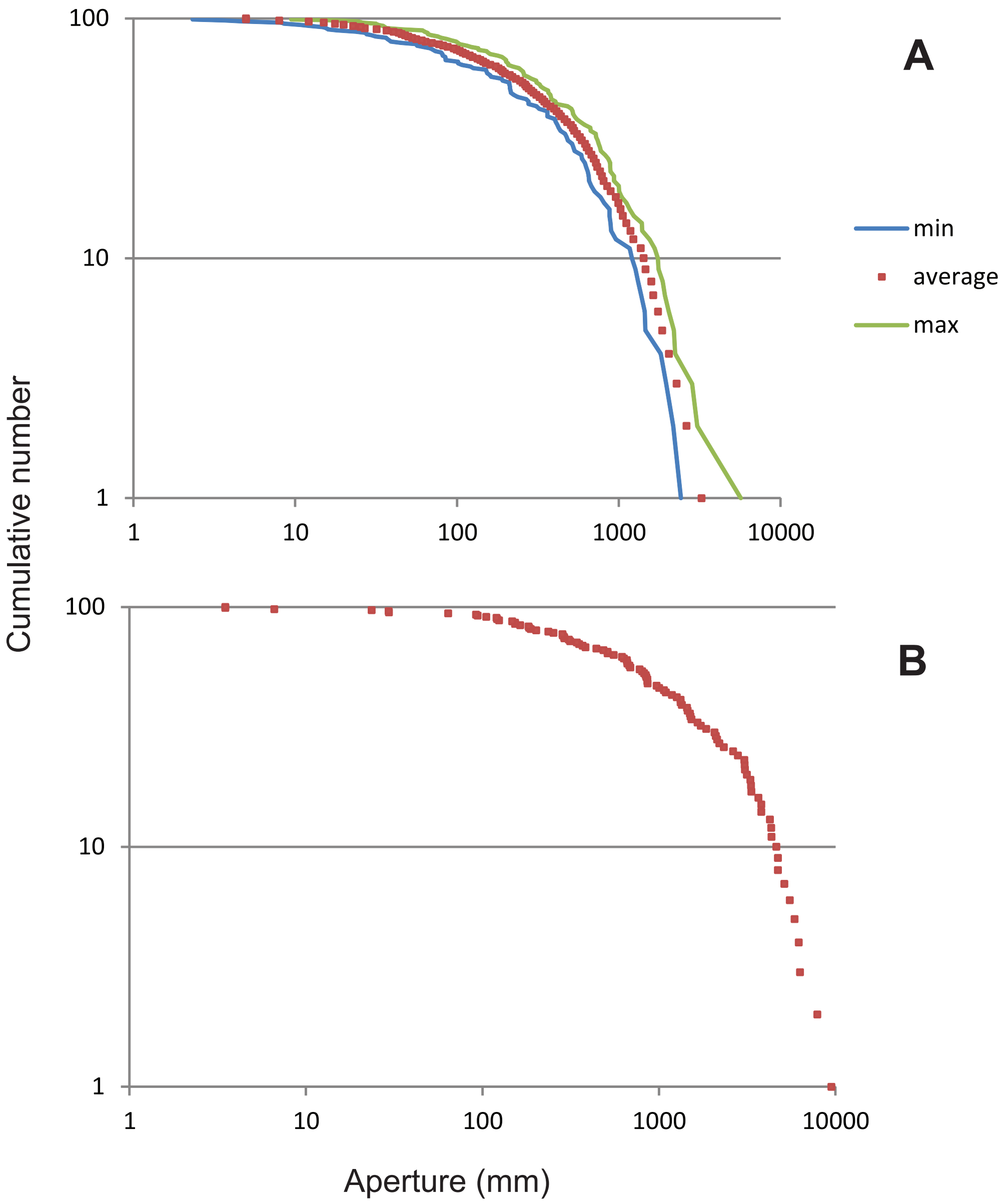

Figure 5-17. (A) Size distribution resulting from permutation 2d-2--average, maximum, and minimum sizes after ten simulations; 100 fractures generated, 5 iterations per new fracture, average growth size = 54.6mm, standard deviation =2.7. (B) Same permutation, average growth size = 20.1, standard deviation 2.7, 50 iterations per new fracture.

further test the idea that wider variation in initial fracture size could result in a power-law size distribution, two parameters were modified: first, the average starting size was lowered (ln[size]=3; size ~20.1) and the standard deviation kept the same (ln[σ]=1), thereby increasing the variation relative to the average. Second, increasing the number of iterations per new fracture to 50 allows more time for early fractures to grow to large sizes before more fractures are introduced. After 5000 iterations this modified permutation still produces a characteristic size distribution.

2e. G proportional, D-INC-SIZE equal, P-GROWTH random

This permutation is equivalent to the simulation introduced by Clark et al. (1995). The resulting size distribution is best-fit by a power-law equation (Figure 5-18a). The *b* value systematically increases with decreasing fracture-size multiplier and increasing number of iterations per new fracture (Figure 5-18b). With progressive iteration of this permutation, b is stable (Figure 5-19).

2f. G proportional, D-INC-SIZE equal, P-GROWTH proportional (linear)

The results of this permutation are similar to those of permutation 1f. The incorporation of both proportional/geometric growth and size-proportional selection probability generally results in unstable, runaway growth of a single largest fracture (Figure 5-20). The automatic introduction of new fractures tends to lend permutation 2f some stability over its fixed-N-FLAWS counterpart. However, given a G multiplier sufficiently low for stability (e.g., 1.01, at 5

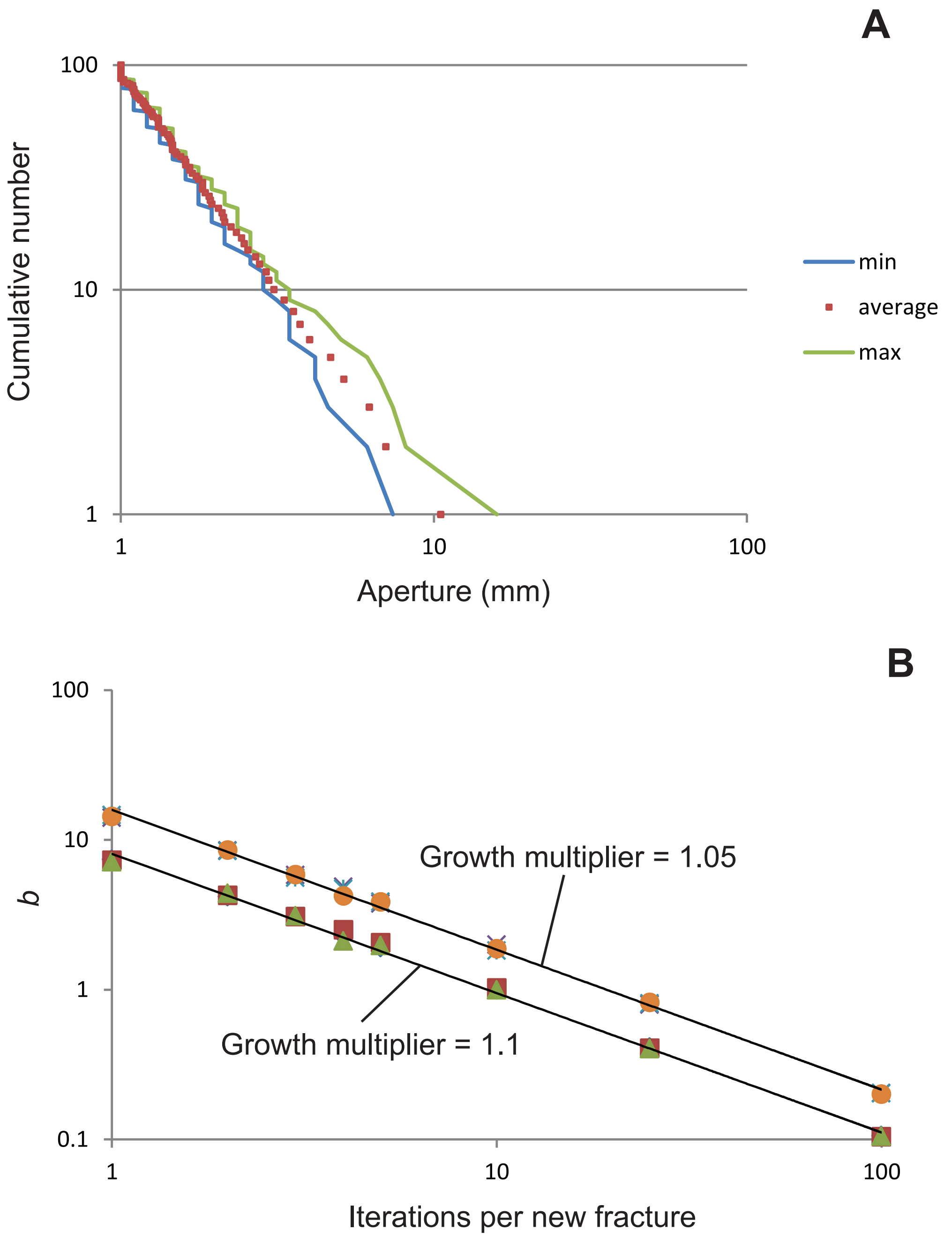

Figure 5-18. (A) Size distribution resulting from permutation 2e--average, maximum, and minimum sizes after ten simulations; 100 fractures generated, 5 iterations per new fracture, growth multiplier = 1.1. (B) Resulting best-fit *b* values with varying number of iterations per new fracture. Different symbols correspond to repeated simulation runs using identical parameters.

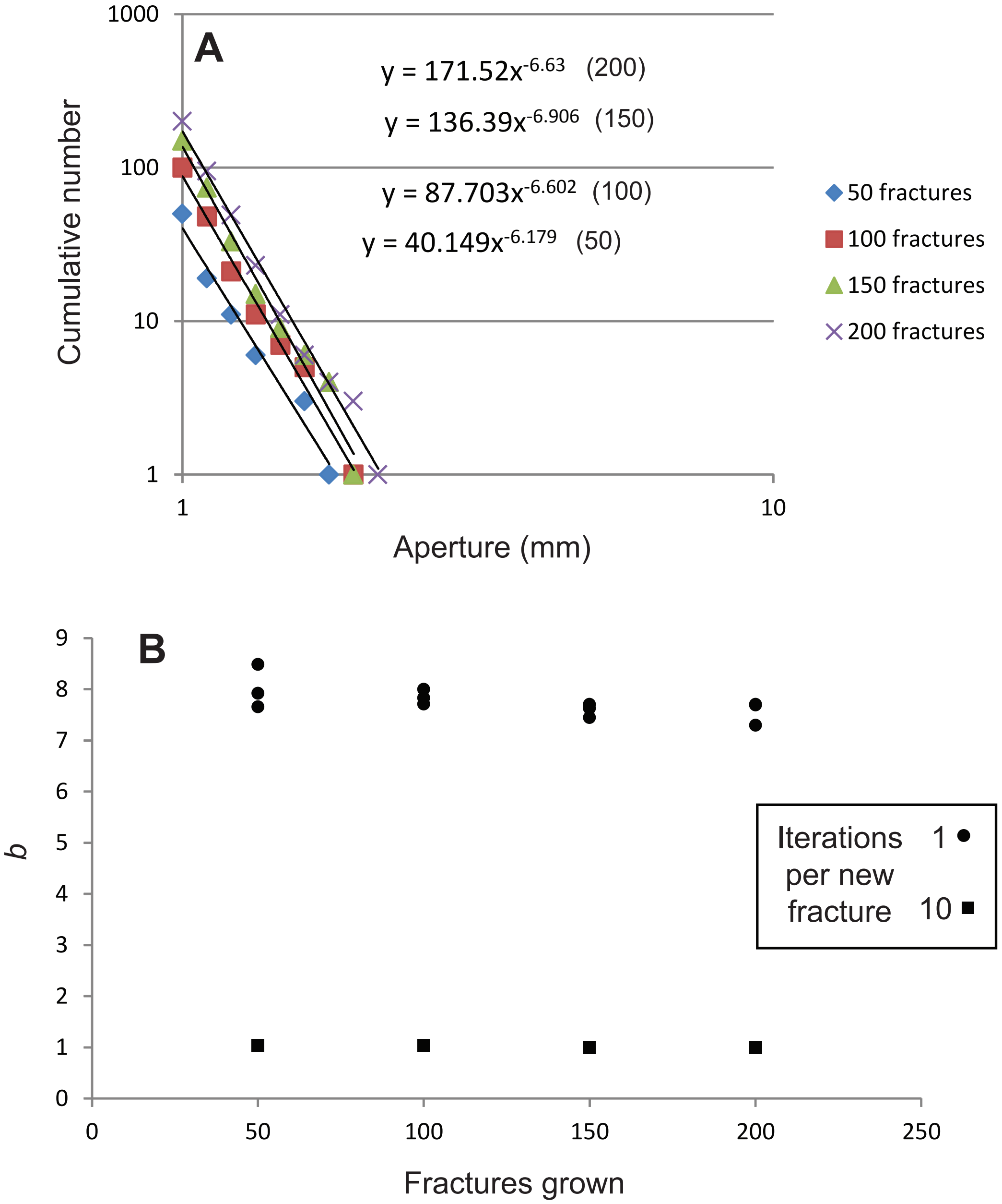

Figure 5-19. Evolution of *b* with iteration of permutation 2e. (A) Resulting size distribution after the generation of the 50th, 100th, 150th, and 200th fracture, using 1 iteration per new fracture and growth multiplier = 1.1. (B) Values of *b* plotted versus number of fractures developed, same parameter set up as in (A); also shown are the *b* values of the same permutation using 10 iterations per new fracture. Note for each of these simulations these data three simulations are plotted; the appearance of only one data point per x-value reflects the consistent *b* values resulting from this permutation with 10 iterations per new fracture.

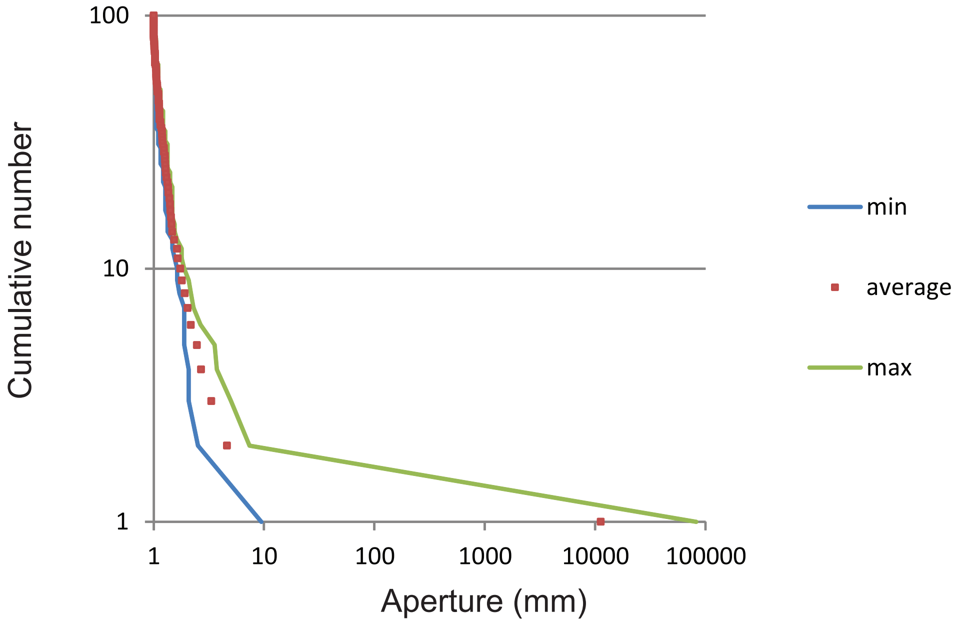

Figure 5-20. Size distribution resulting from permutation 2f--average, maximum, and minimum sizes after ten simulations; 100 fractures generated, 5 iterations per new fracture, growth multiplier = 1.05.

iterations per new fracture) yields power-law size distributions of exceedingly high *b* value (13.8 to 16.6 in five attempts to 500 iterations). Such *b* values are high compared to those from natural datasets. This permutation produces power laws of unrealistic *b* value and only over a limited stability range.

2f-2. G proportional, D-INC-SIZE equal, P-GROWTH proportional (logarithmic)

Permutation 2f-2 is more stable than permutation 2f; it produces concave-upwards or even L-shaped curves in log-log space with a growth multiplier of 1.01 and 5 iterations per new fracture (Figure 5-21). The concavity of the curve can be reduced, even to near zero and as such a power-law size distribution, by increasing the starting fracture size or by reducing the number of iterations per new fracture. Runaway growth in this permutation is resisted by the continual introduction of new fractures; the larger and more frequently introduced these new fractures, the more effectively runaway growth is suppressed and the closer the power-law fit to the resulting size distribution.

2g. G proportional, D-INC-SIZE lognormal, P-GROWTH random

Adding variation to the initial sizes of fractures in permutation 2e has either no important effect (for small amounts of variation, average starting size=54.6, σ=2.7) or it can change the resulting size distribution to a characteristic one (for a large variation relative to average initial size; average initial size=1, σ=1.35). These results are plotted in Figure 5-22.

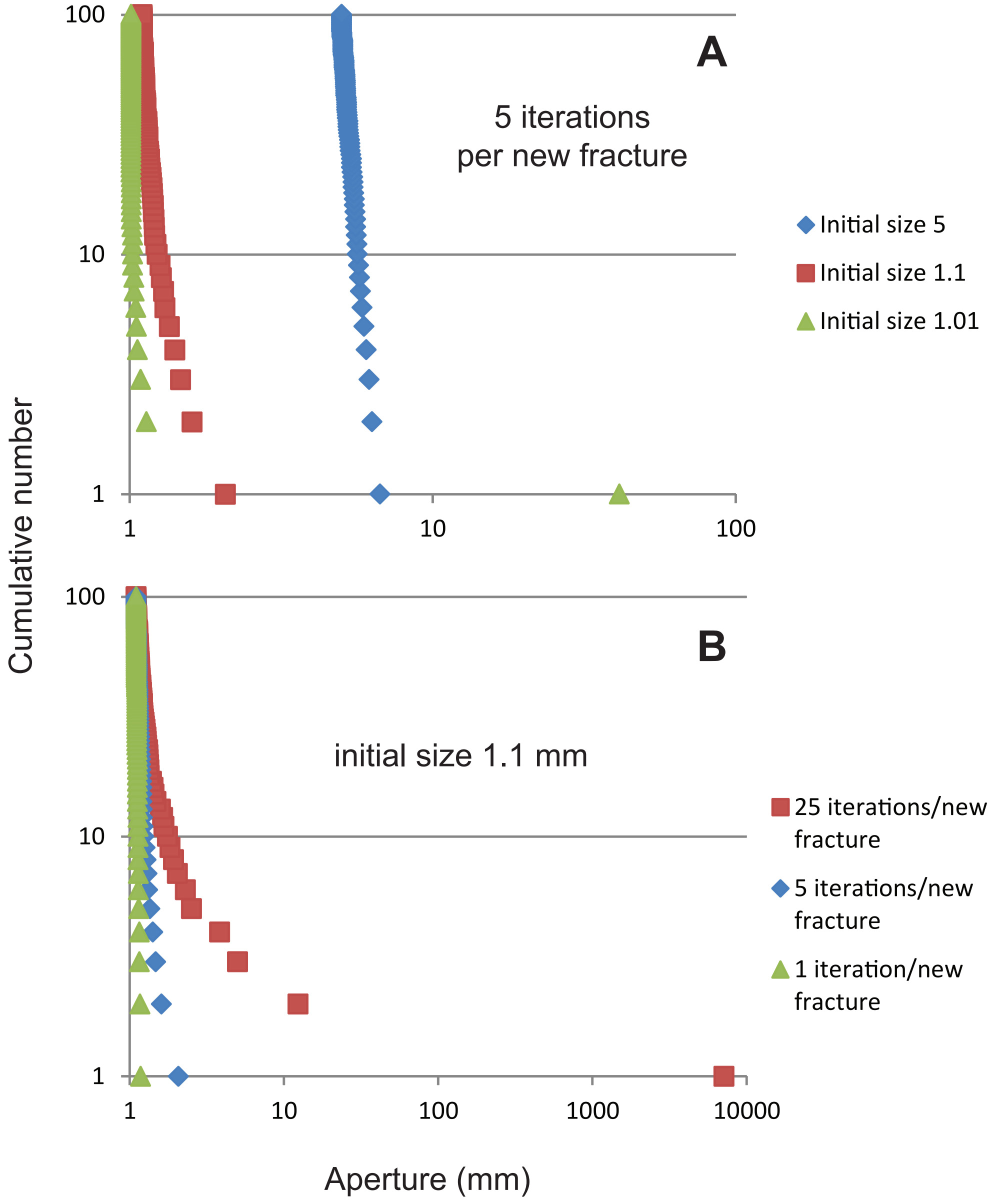

Figure 5-21. Size distribution resulting from permutation 2f-2; 100 fractures generated, growth multiplier 1.01. (A) Effect of initial size on resulting size distribution. Note increased stability with larger initial fracture size. (B) Effect of number of iterations per new fracture on resulting size distribution.

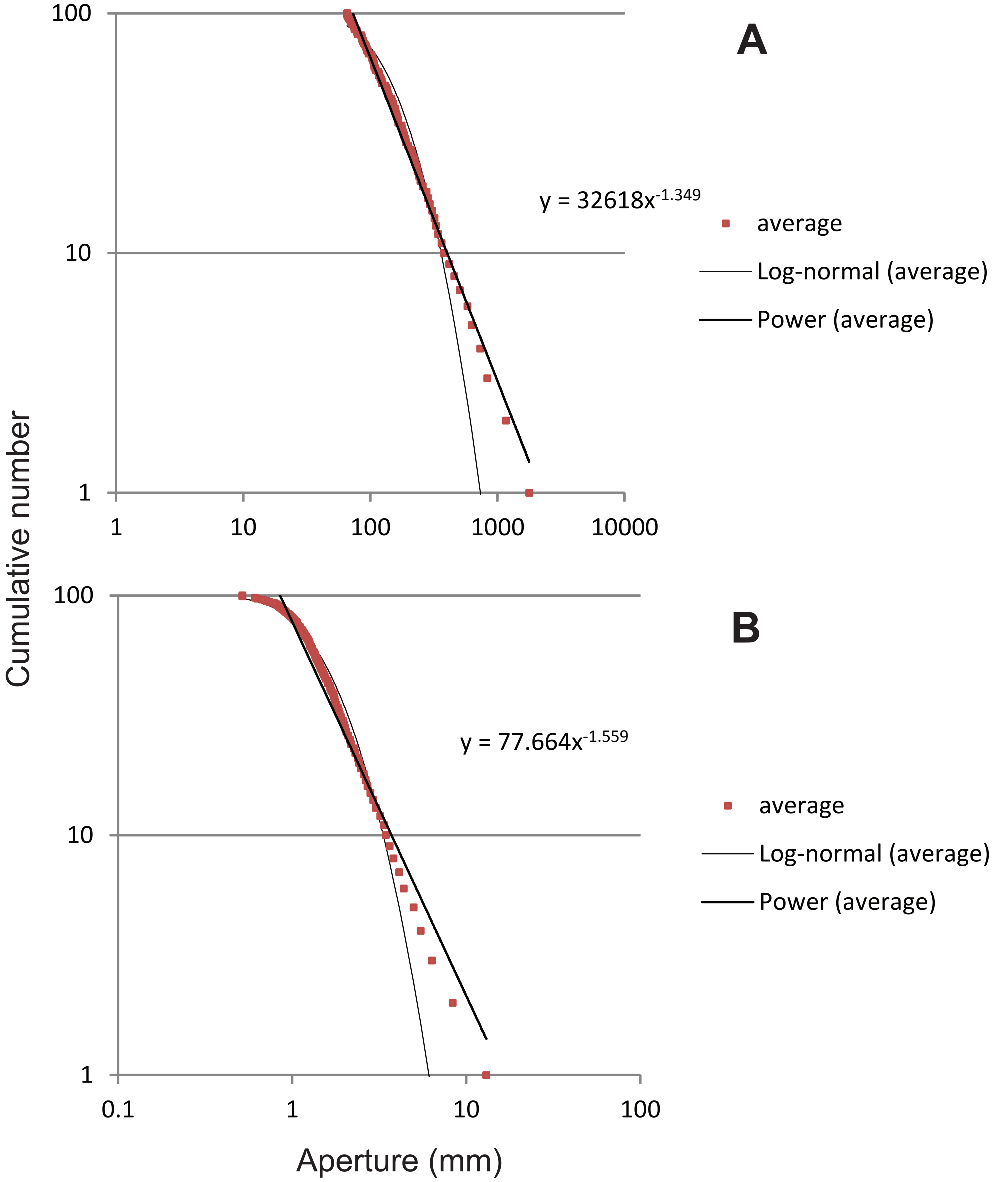

Figure 5-22. (A) Size distribution resulting from permutation 2g--average fracture sizes after ten simulations; 100 fractures generated, 5 iterations per new fracture, growth multiplier = 1.1, average initial size = 54.6, stdev = 2.7. (B) Average fracture sizes from same permutation, average starting size 1, standard deviation 1.35. The greater variation in initial sizes, relative to average starting size, in (B) results in a size distribution that is statistically better fit by a log-normal equation than by a power-law equation.

2h. G proportional, D-INC-SIZE lognormal, P-GROWTH proportional (linear)

As with permutation 2f, this permutation, within a stable range for the growth multiplier (<1.1 at 5 iterations per new fracture), yields power-law size distributions with steep slopes. Increasing the variation in fracture size may dwarf the tiny variation in sizes brought about by growing fractures by such small fractions, resulting in characteristic size distributions (Figure 5-23). Near the stability boundary (G multiplier 1.05, σ 1.35) this permutation can produce power-law size distributions with *b* values as high as 2.

2h-2. G proportional, D-INC-SIZE lognormal, P-GROWTH proportional (logarithmic)

This permutation results in similar size distributions compared to those from permutation 2f-2. The addition of variation in starter flaw size tends to increase stability and the resulting size distribution is better fit by characteristic equations when the variation of the initial fracture sizes dwarfs that brought about by the growth rule.

SUMMARY

In summary, the fracture population growth simulation described above produces a variety of size distributions by growing fractures iteratively. As summarized in Table 5-1, power-law size distributions typically emerge when *either* fracture growth is proportional (not constant) *or* when fracture growth-selection probability is proportional to size. When neither size-growth feedback

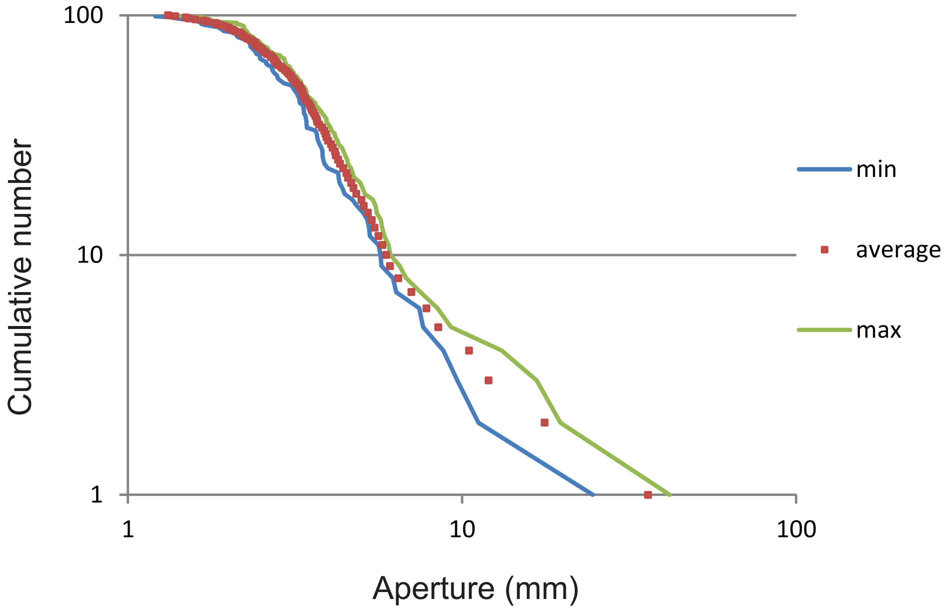

Figure 5-23. Size distribution resulting from permutation 2h--average, minimum and maximum fracture sizes after five simulations; 100 fractures generated, 5 iterations per new fracture, growth multiplier = 1.01, average initial size = 2.7, stdev = 1.35.

mechanism is present, a characteristic size distribution emerges; when both are present, the simulation produces unstable, runaway growth of the largest fractures. Varying the flaw-size distribution has little effect on the final size distribution type.

COMPARING SIMULATIONS TO NATURAL FRACTURE GROWTH

The simulation described above is based on stochastic realizations that might describe how increments of fracture opening, cementation, and re-cracking are grouped together, as discussed below. Thus they are intended to describe how natural fracture opening proceeds amid cementation.

Mechanical effects of synkinematic cement

In general, cements that bridge across growing fractures likely provide cohesion to both fracture opening and closure. The ability of fractures to close was suggested as a possible mechanism for decreasing crack-tip stress intensity during fracture propagation (Olson, 2003), and thus for stable natural fracture growth. Therefore filling a growing fracture with cement could prevent the relaxation of crack-tip stress intensity and promote propagation.

However, because bridges form by repeated cracking of cements that bridge across fractures, it follows that synkinematic cementation provides some degree of *resistance* to progressive fracture opening. For the cement bridge to fracture, effective tensile stress within the bridge must be sufficient to break a cement crystal. The idea that cements resist fracture opening is supported by strength tests in which siliceous mudrock samples failed where quartz-filled fractures were absent (Gale and Holder, 2008). For large, sparsely cemented fractures the resistance to opening might be negligible compared to the stress concentration at the fracture tips; for thoroughly cemented fractures the resistance to opening could exceed that of unfractured host rock.

Records of fracture opening

Synkinematic cement preserves a record of fracture opening in places where cement precipitation was fast enough to keep up with fracture opening. If fracture bridges are composed of crack-seal increments, we know that the fracture grew incrementally. But if the fracture is not filled with cement showing crack-seal increments we do not know whether the fracture opened incrementally, or what the sizes of any opening increments were, or whether the fracture opened all at once, or whether it opened continuously.

The size of opening increments that fractures can record depends on the cross-fracture accumulation rate of cement, the time between the opening increments, and the size of the opening increments. In other words, the size of the opening increment *that can be recorded* is finite. Many fractures in sandstone lack bridges; they may be quartz lined and otherwise open. The opening increment size of such fractures is unconstrained. Such fractures might arise by characteristic size increments, but such increments could feature a non-trivial variation in size. For example, if abrupt widening occurs when fractures link, the growth event may be of too high a magnitude to be recorded in the synkinematic cement record. Moreover the widened fracture may return to incremental growth but now be too wide for bridges to form.

Constant versus size-proportional growth

Does fracture widening accelerate as fractures grow? Evidence from opening increment sizes within quartz bridges suggests that opening increments may remain constant or decrease as the fracture grows (Figure 5-1). Such an opening history is consistent with observations of fractures within the Ordovician Ellenburger Group fractures by Hooker et al. (2012); later fracture opening increments are narrower than earlier ones.

Alternatively, the widths of synkinematic opening increments may systematically increase with time (Figure 5-24, Figure 5-25), consistent with progressively wider opening and shear zones within veins observed by Clark et al. (1995). The synkinematic cement textures in Figure 5-24 and Figure 5-25 suggest that the fracture opening rate increased with respect to the cementation rate; thus the opening rate may have increased and/or the cementation rate may have decreased. If fracture opening rate sufficiently exceeds the cementation rate, then incremental fracture opening might not be recorded in textures within cement bridges. Thus a sealed crack within a cement bridge is positive evidence of an increment of growth, but the absence of sealed cracks is evidence of

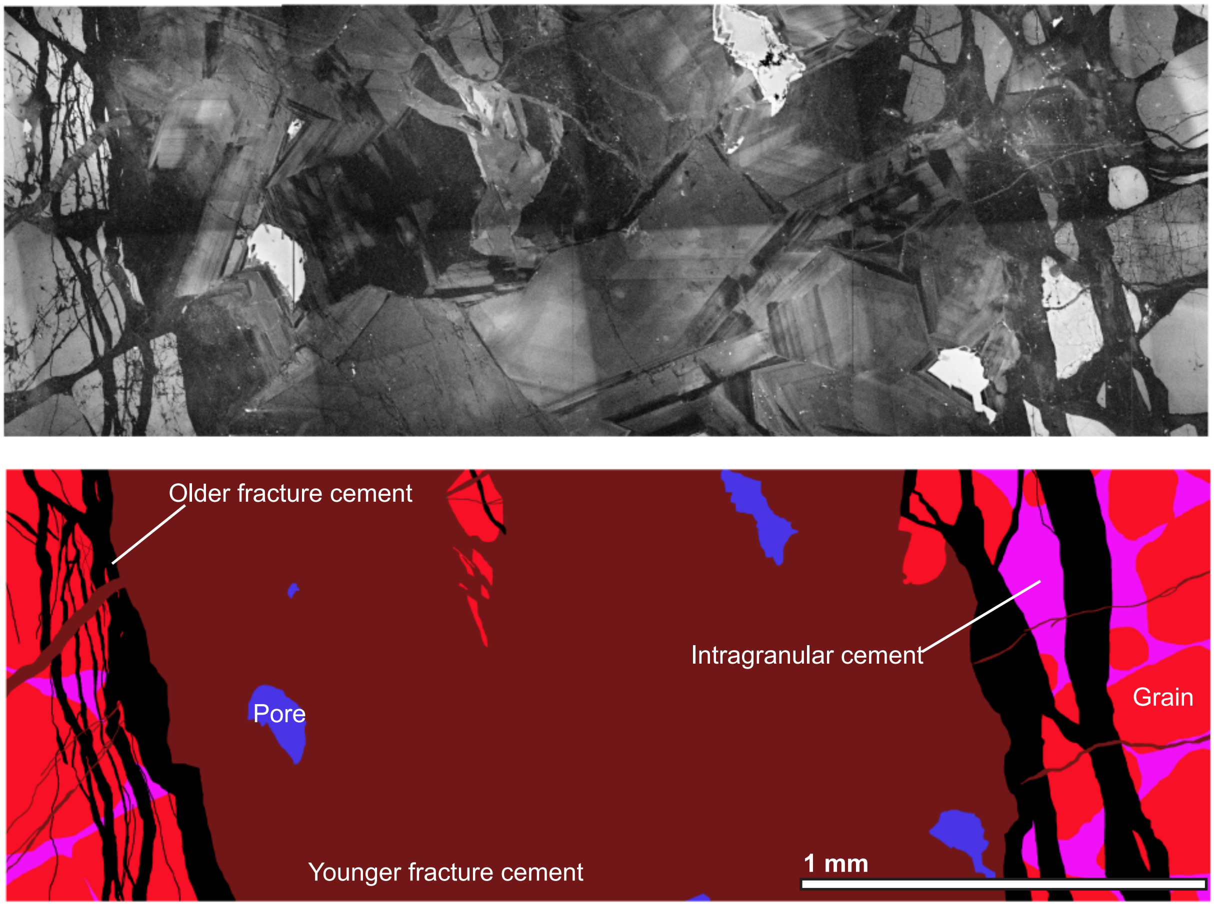

Figure 5-24. SEM-CL image and interpretation of a quartz-cement-filled fracture from the Meson Group (Sample 55). Thin crack-seal increments, filled with CL-dark cement ("Older fracture cement"), are present at the margins of the fracture. The cement filling the mid-region of the fracture is lighter in CL signal; this same generation of cement also fills microfractures which crosscut the CL-dark crack-seal increments (thus it is labeled "Younger fracture cement"). This younger cement generation has local crack-seal features near the center of the fracture but is mostly massive and euhedral. I therefore interpret that this fracture grew in two phases: an earlier phase of repeated cracking and sealing during which the fracture opened in small, characteristic-width increments; and a later phase, possibly in conjunction with a new, oblique set of microfractures, during which sealing mostly did not keep up with opening, unlike the first phase. This may be because of decreased cementation rate or increased opening rate or both, but in any case it is unclear whether the fracture continued opening incrementally, or whether these increments were of the same width range as the earlier opening increments.

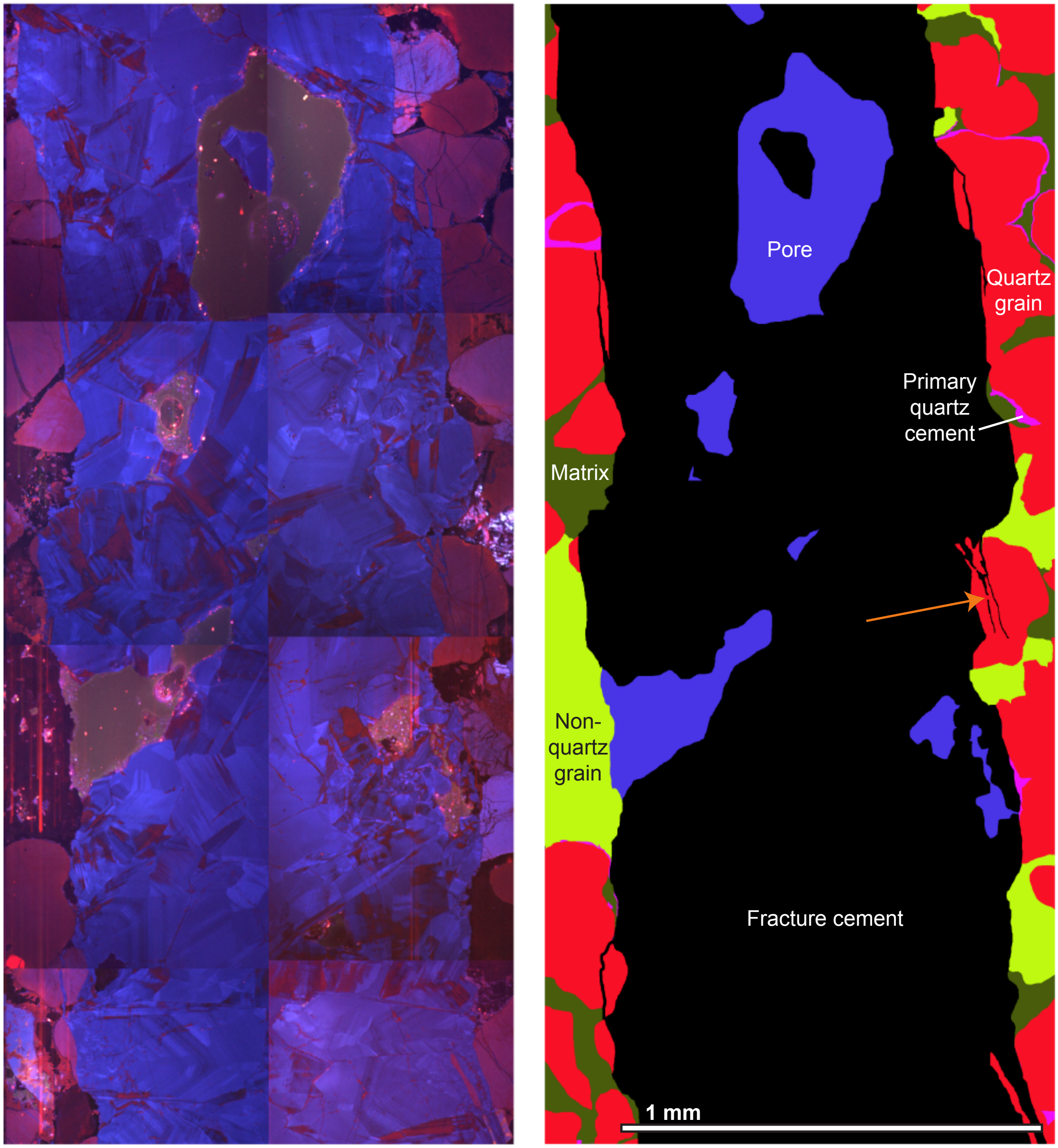

Figure 5-25. Quartz-cemented fracture from the Torridonian Sandstone. The fracture has thin crack-seal increments near its walls (e.g. those indicated by arrow); the mid-region of the fracture is mostly filled with massive, euhedral quartz cement. Thus the fracture appears to have initially grown by incremental cracking and sealing, possibly when the region imaged was at or near the fracture tip. Later the fracture opening was not matched by cement sealing/bridging. The fracture may still have grown incrementally, or it may have grown in one single large increment, in which case growth could be thought of as continuous.

neither a single, large growth increment nor continuous (non-incremental) growth.

A fracture may grow by constant or progressively increasing increment sizes provided that strain rate, temperature, etc., remain constant. But if these factors change (e.g., if strain rate decreases or if cement precipitation rate increases relative to strain rate), then the fracture might undergo smaller growth increments. Also, fracture opening need not be uniform, in extent or rate, everywhere throughout the fracture. For example, natural fractures typically broadly taper in aperture toward their tips (Vermilye and Scholz, 1995; Moros, 1999; Kaylor, 2011). This tapering may result from accumulation of the same number of narrower size increments or from a smaller number of equal-sized increments. To date there are few documented reconstructions of fracture widening histories (e. g. Becker et al., 2010). There are even fewer studies that address fracture height growth or length growth (Kaylor et al., 2011), beyond establishing episodic lengthening by documentation of arrest marks (e.g., Bahat et al., 2008). The paucity of reconstructions of actual fracture growth, in contrast to ample theoretical work, limits our understanding of how fractures grow and how fracture sets evolve.

Fixed versus increasing flaw population

For permutations with a fixed number of flaws, either all flaws eventually are selected and grow, or the probability for some flaws to grow becomes vanishingly small and these flaws never grow. In either case some assumptions and/or extrapolations need to be made in order to address how these simulations might illustrate natural fracture-growth processes. Natural rock, particularly sandstone, likely has a sub-millimetric-scale density of flaws from which a fracture might propagate. So a simulation using 200 flaws either limits the realism of the experiment to a very small amount of rock, or needs the assumption that the simulated flaws are the 200 largest/weakest/most-optimally-oriented flaws within a larger volume of the rock being modeled. If this assumption is made, then once all flaws have grown into fractures it must be considered whether smaller flaws might then become activated. In cases in which some flaws never grow and the rest of the accumulating fracture strain is localized to the existing fractures, it may be that too few flaws were modeled in order to simulate the development of a realistic fracture pattern.

Introduction of new fractures at a constant rate (permutations with N-FLAWS increasing) might better simulate a rock with sub-millimetric-scale flaws. In other words, if the flaw density is sufficiently high that it is impossible to explicitly model each flaw, it may be better to assume that at some given frequency one of the myriad flaws present propagates. Permutations with N-FLAWS increasing tend to be more stable, in that no matter how large the largest fracture or what its share of the growth-selection probability, new fractures will always by rule be introduced.

(In)stability

The simulated fracture aperture populations (sets) may be stable, with growth shared among the fractures, or unstable, with a small subset of fractures growing disproportionately at the expense of others. Characteristic size distributions emerge in the stablest permutations of the model; for example, permutation 1a has no mechanism to engender instability; if 100 fractures are grown with equal probability, the long-run average size will be proportional to the growth-size-per-iteration divided by 100, and any variation will only arise from random selection. Without any feedback between current fracture-size and fracture growth-selection probability, there is no mechanism by which large fractures will consistently outpace the growth of small fractures.

At the other end of the stability spectrum, some permutations result in growth of only a single fracture, whose selection probability dwarfs that of all other fractures. In reality, at a sufficiently large scale any natural fracture growth process is stable, lest the Earth be cleaved in twain. This is not to say that the instability displayed by some permutations has no natural equivalent. For example, any strain applied, under low confining stress, to an indurated quartzarenite with a single uncemented fracture in it, is likely to be localized within that barren fracture. Such a fracture is analogous to the single largest fracture which undergoes runaway growth at the expense of all other fractures in some permutations (e.g., permutation 1f).

Similarly, in diagenetically active, compressive environments, en echelon fractures may link to form through-going faults, which may accommodate orders of magnitude more strain, in shear, than isolated opening-mode fractures parallel to the original en echelon fractures. A plot of cumulative frequency versus displacement of fractures, including faults, within such a structure would resemble those of the simulations having runaway growth of the largest fracture(s).

Power-law size distributions emerge from permutations at intermediate positions on the stability spectrum. For a wide range of fracture sizes to emerge, like those in natural power-law datasets, some fractures must grow significantly faster or more often than others. Feedback loops between current fracture size and future fracture growth are applied in this model by size-dependent selection probability or size-dependent growth magnitude. If these feedback loops are too strong, the permutation is unstable (e.g., permutation 1f); if too weak or not present, a characteristic fracture-size distribution emerges (e.g., permutation 1a). Power laws seem to emerge when feedback loops are finely tuned, which contributes to the power law’s strangeness. Why is a phenomenon so widespread, that appears to require such narrowly defined starting conditions? I address this question in Chapter 9.

Equal versus size-proportional selection probability

To the extent that synkinematic cement impedes fracture opening, it can be anticipated that less completely filled fractures are more susceptible to further opening. The degree of synkinematic cement fill in natural fractures has been observed to depend on fracture size, with large fractures less thoroughly filled with cement (Laubach, 2003; Hooker et al., 2009; Laubach and Diaz-Tushman, 2009). Thus synkinematic cement could potentially make larger, less cement-filled fractures more probable to open than smaller, more cement-filled fractures. Experimental results show that small fractures fill with cement more quickly than large fractures (Brantley et al., 1990), so a realistic fracture system simulation might include a progressively vanishing growth probability for small fractures.

Qualitative observations of natural core breakage (see Chapter 7) suggest that suture planes of fracture-bridging cements may retain weakness that localizes later fracture increments (Figure 5-26). Also, the boundary between the host-rock and fracture cement may be weaker than the cement itself (Ramsay, 1980; Gale and Holder, 2008; Gale and Holder, 2010; Holland and Urai, 2010). For these reasons a selection probability proportional to the logarithm of fracture size might be appropriate in cases in which the growth rule is size-proportional. A fracture that has been selected for growth four times, and has doubled in size each time, now has a size 16 times its original size. Linear scaling of selection probability would result in the selection probability of this fracture being nearly an order of magnitude higher than that of its neighbor, which has only doubled in

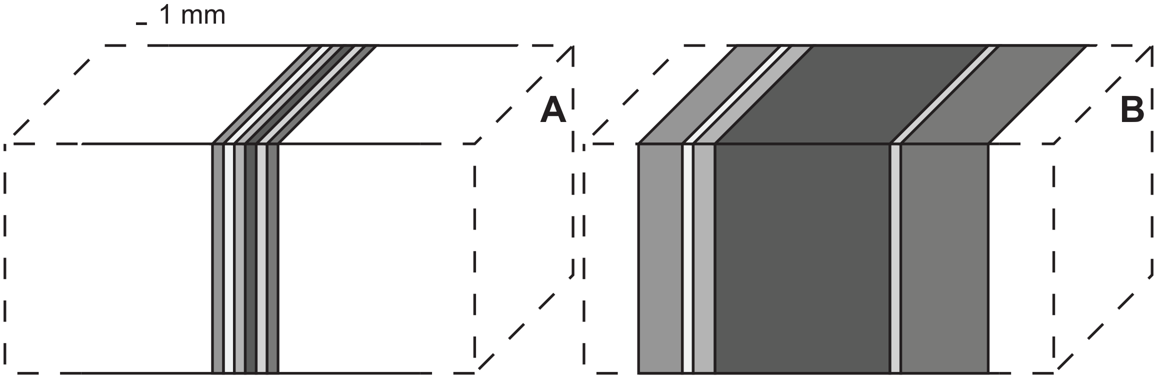

Figure 5-26. Two simulated cases of progressive fracture-increment accumulation; darker increments formed later. Dashed lines emphasize that fracture location is not accounted for in simulation. (A) Constant, additive growth size. (B) Multiplicative growth size, with growth multiplier = 2 (i.e., with each growth increment, this fracture doubles in aperture). The cumulative aperture of fracture (A) is 6 mm; (B) is 32 mm. If probability of selection is linearly proportional to current size, fracture (B) is more than 5 times as likely to be selected in subsequent iteration. An alternative simulation would be to treat each growth increment interface as equally likely to host the next growth increment, in which case the fractures would be equally likely to grow. This method can be approximated in simulations in which fractures grow proportionally to their current size by making the selection probability proportional to the logarithm of current fracture size.

size once. But if later fracturing increments necessarily occur along pre-existing fracture walls or cement-sealing planes, then the larger fracture would only be four times as likely to open as the smaller one, in which case selection probability should scale with the logarithm of fracture size.

Alternatively, it may be appropriate that selection probability scales with the square of current fracture size. For example, new fracture increments may appear at random locations upon the 3D surface areas of extant fractures. Assuming a linear relationship between aperture and length, and a penny shape to each fracture, a fracture twice as wide would have four times the surface area. By modifying permutation 1b to make the selection probability proportional to the square of the current aperture size, a power-law size distribution results (Figure 5-27) with an ever-decreasing *b* value with increasing iterations. In cases in which size-linear growth probability results in instability, size-squared growth probability would exacerbate this instability.

Equal flaw size versus log-normally distributed flaw size

Simulations tested the hypothesis that log-normally graduated variations in flaw size might systematically develop into a power-law size distribution through the application of selection and growth rules. This hypothesis is so far unsupportable; in no case did a permutation which initially produced a characteristic size distribution change to a power-law size distribution after adding variation to the flaw sizes. Indeed, the tendency was in the opposite

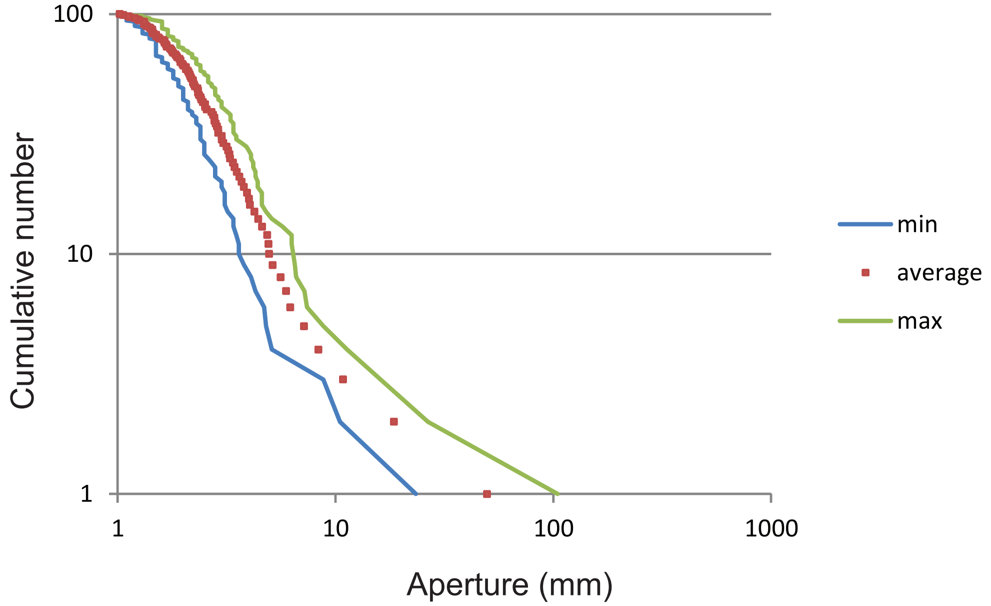

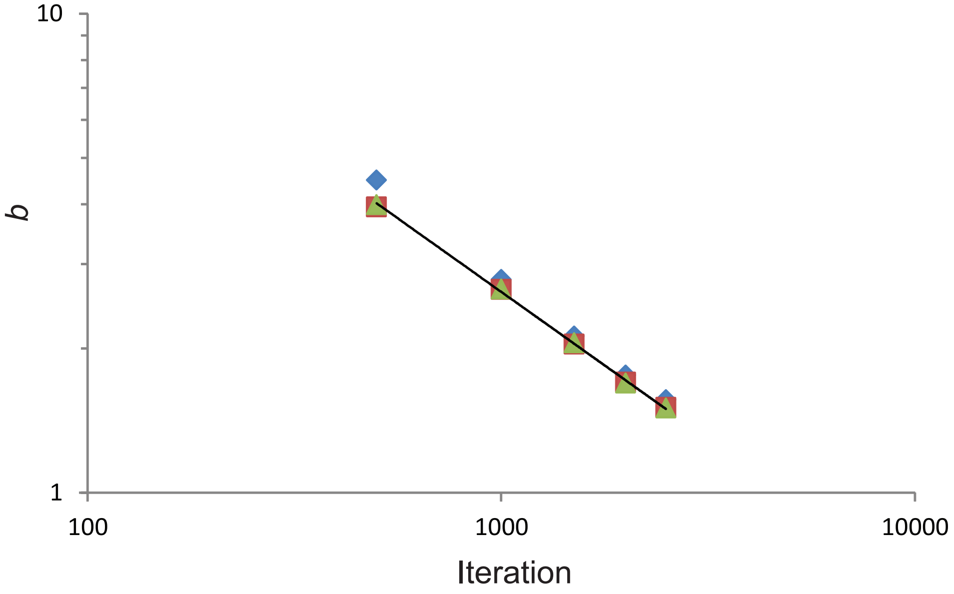

Figure 5-27. (A) Size distribution resulting from permutation 1b, with selection probability now proportional to the square of fracture size; growth increment size 0.1mm, starting size 1mm. The size distribution is best-fit by a power-law size distribution, with *b* decreasing with progressive iteration (B). Different symbols correspond to repeated simulation runs using identical parameters.

direction. Some permutations that produce power laws over limited parameter ranges (e.g. permutation 2f-2) actually produced characteristic size distributions after adding variation to the flaw size distribution (permutation 2h-2). This appears to be because a wide (high standard deviation) flaw size distribution dwarfs the variation in sizes achieved by the original, equal-flaw-size version (the steep power law, Figure 5-21).

Resulting *b* values

Are simulated *b* values close to those observed in nature? The *b* value for natural fractures remains loosely constrained: measured in 1D (Chapter 3), natural fracture sets have *b* values near 0.8. Theoretical extrapolation into 3D suggests *b* could be as high as 2.8, assuming linear aperture-length scaling (Marrett, 1996; Borgos et al., 2000). Measurement in 2D (Chapter 4) results in *b* values for parallel fractures near 1.0, suggesting that 2.8 is too high. For bedding-bound fracture sets in which 2D mapping of fractures likely provides samples that are close to representative (Ortega, 2002), the 3D *b* value is likely not much higher than the 2D value, ~1.0.

Six permutations produced stable power-law size distributions over a wide range of parameters: 1f-2, 1h-2, 2b, 2d, 2e, and 2g. These are really three pairs of permutations, each pair fundamentally the same but with a version that uses equal-sized flaws and a version that uses log-normally distributed flaw sizes. As explained above, using log-normally distributed flaw sizes does not appear to have important consequences for any permutation, so discussion of resulting *b* values will be limited to the three fundamentally different permutations, 1f-2, 2b, and 2e; and not their counterparts with log-normally distributed flaw sizes.

1f-2: G proportional, D-INC-SIZE equal, P-GROWTH proportional (logarithmic). The progression of the *b* value for the size distribution resulting from permutation 1f-2 was examined using an initial size of 1.1 and a G multiplier of 1.1. The *b* value decays as a power law between 100 and 2000 iterations (Figure 5-28). Over this iteration range the population begins with a vertical (infinite) slope and achieves a *b* value near 0.3. Using a G multiplier of 1.05, *b* increases by more than a factor of two at each iteration compared, but decays similarly.

2b: G fixed, D-INC-SIZE equal, P-GROWTH proportional (linear). As mentioned above, the *b* value for the size distribution resulting from permutation 2b is sensitive to the number of iterations per new fracture. Up to 100 fractures grown, the *b* value is greater than 1 at iterations-per-fracture near 1 and shallows to ~0.65 at 100 iterations per fracture. The *b* value gradually increases over time (in iterations), using a growth size of 1 and 1, 5, and 20 iterations per fracture (Figure 5-29). Thus permutation 2b returns *b* values near those of natural datasets over a wide range of stable parameters.

The single largest fracture from permutation 2b tends to be slightly larger than the power-law equation fit to the rest of the fractures would predict. This

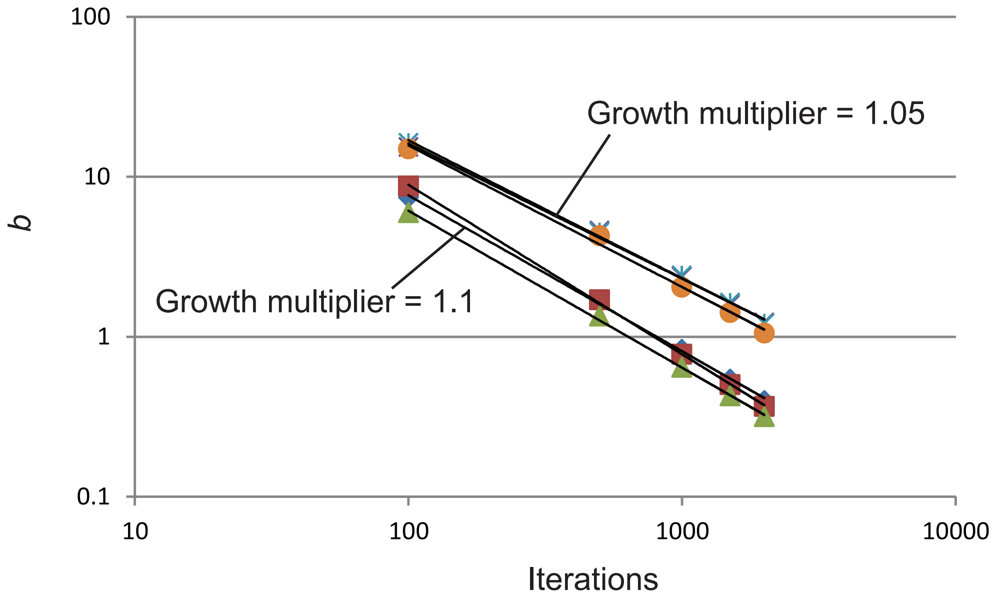

Figure 5-28. Permutation 1f-2, resulting *b* values best-fit to size distributions with progressive iteration. Note that the simulation produces a power law but the *b* value does not systematically favor any particular value, in contrast to the naural-fracture data. Different symbols correspond to repeated simulation runs using identical parameters.

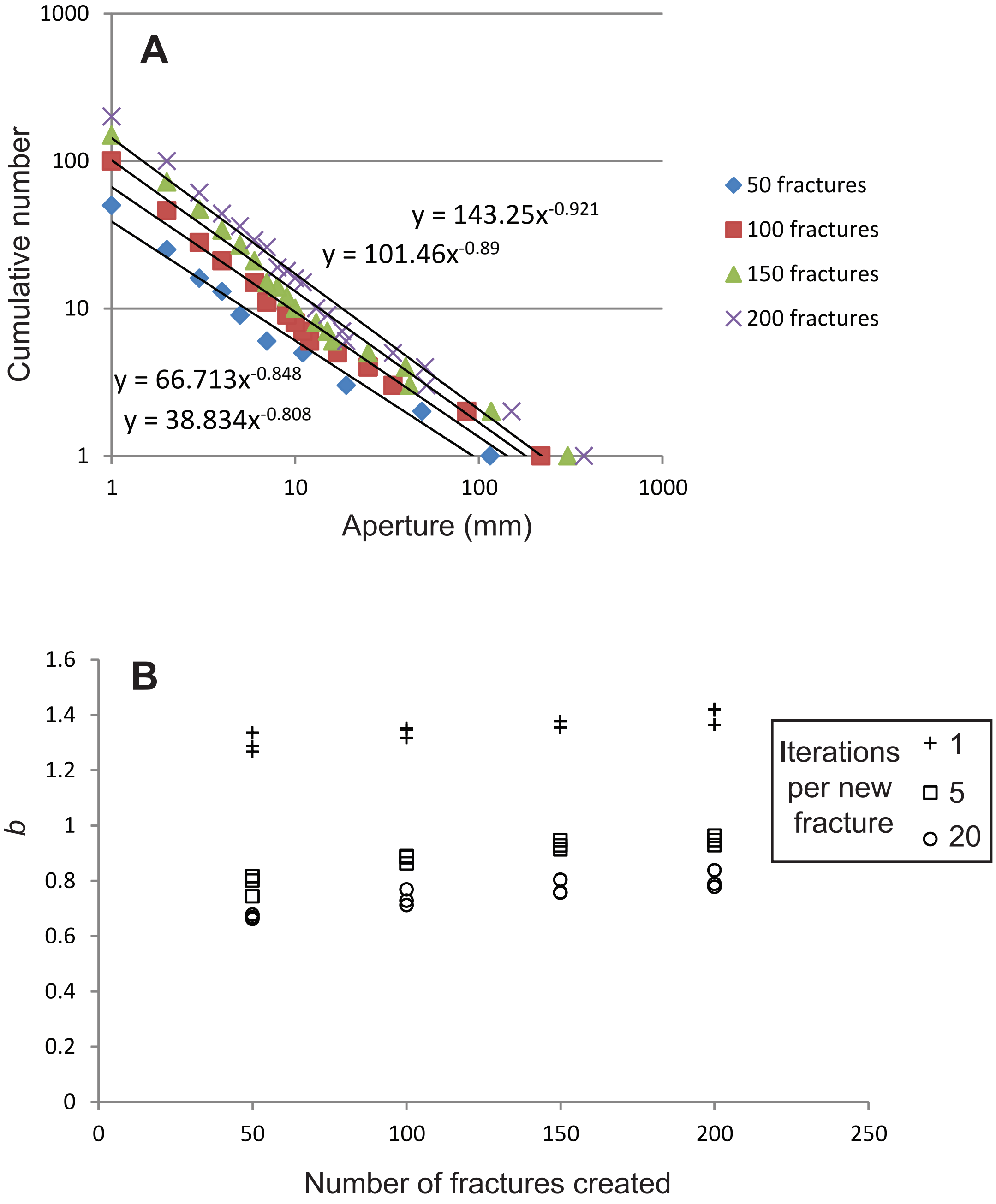

Figure 5-29. Evolution of *b* value for permutation 2b. (A) Size distribution resulting from permutation 2b after the 50th, 100th, 150th, and 200th fractures were generated; 5 iterations per new fracture, growth increment size 1 mm. (B) Values of *b* shown in (A), plus those of same permutation for 1 iteration per new fracture and 20 iterations per new fracture.

unexpectedly rapid growth comes about because the first-born fracture is automatically selected for growth at every iteration until the second fracture is introduced, thereby growing to a size that affords the first fracture a greater share of the selection probability. This effect is not akin to the instability apparent in many N-FLAWS-fixed permutations, because the largest fracture never dominates the selection probability to the point that other fractures never grow (this is due in part to the rule that introduces new fractures at regular intervals).

This result implies that a single largest fracture is present in each power-law fracture population; the other factures develop as accessory structures to this largest, first fracture. This effect may be a realistic description of strain dominated by a single largest fracture, with smaller fractures growing in its vicinity as accessory structures. In most datasets such a fracture arrangement is not typically observed. The permutation still produces qualitatively similar size distributions after beginning the simulation with ten equal-sized flaws rather than a single fracture (Figure 5-30). The output of this modified permutation (2b*) has a more even distribution of fractures at the large-size end. This version of the permutation may be a more realistic simulation of strain accumulation initiating within a rock having a spatially distributed flaw population.

2e: G proportional, D-INC-SIZE equal, P-GROWTH random. Permutation 2e results in a wider range of *b* values than does permutation 2b, given similar parameter inputs. For a G multiplier of 1.1, *b* varies from more than 7 at 1

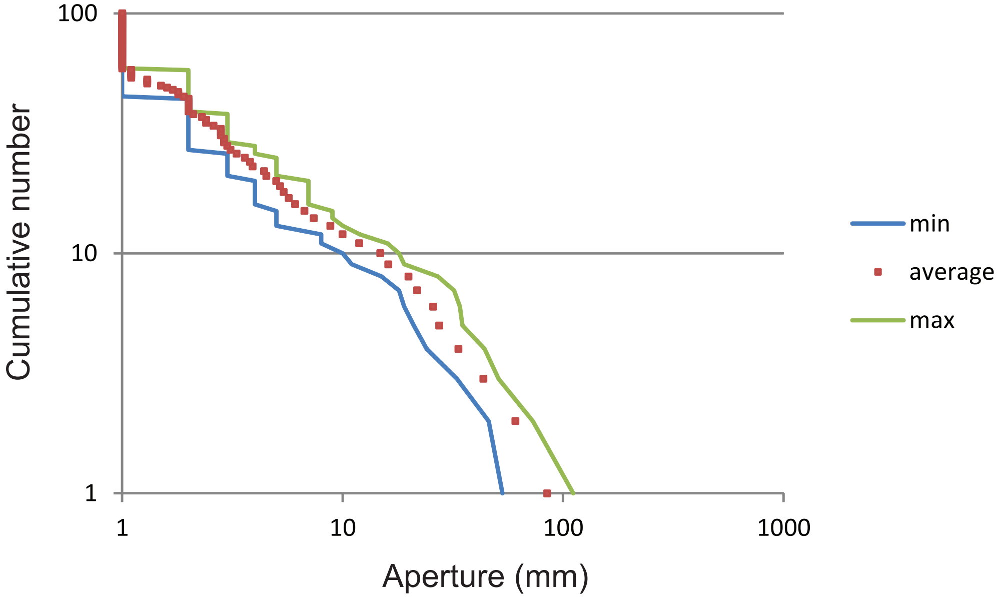

Figure 5-30. Size distribution resulting from permutation 2b*--average, maximum and minimum fracture sizes over ten simulations. Resulting size distribution is best-fit by a power-law equation. Compare to Figure 5-13; note that the largest fracture is not larger than expected from extrapolation of a power law from smaller fractures. This version of the permutation (2b*) begins with ten pre-existing flaws, thereby spreading the probability of fracture growth more evenly among a group of initial fractures.

iteration per fracture to ~0.1 for 100 iterations per new fracture. For a G multiplier of 1.05, *b* doubles (Figure 5-18). With progressive iteration of permutation 2e, *b* does not systematically change (Figure 5-19).

Consequences for prograde and retrograde diagenesis

Consider a spectrum of possibilities for the rate of synkinematic cement precipitation with respect to opening rate. If cement precipitation rate far exceeds fracture opening rate, synkinematic cements might entirely fill opening fractures as they develop. To the extent that synkinematic cement suppresses fracture opening, such entirely sealed fractures would lack any propensity to localize later opening increments, and thus would not grow over time. The resulting size distribution would be equivalent to that of the individual opening increments, except for fractures enlarged by chance.

At the other extreme, there may be no cement precipitation. Such may be the case with near-surface fracture patterns, where temperature and/or ion concentration would be insufficient for an appreciable cement precipitation rate. In these cases, depending on boundary conditions, stress shadows in the vicinities of growing fractures would tend to suppress fracture growth in the vicinity of extant fracture walls. Here again the result would be an overall fracture aperture-size distribution marked by the lack of a mechanism for sufficient selective widening to result in a power-law size distribution, and thus controlled by the characteristic opening size of individual fracture increments.

At intermediate cement-precipitation rates (rates comparable in magnitude to fracture opening rates) the interplay between fracture opening and cementation might favor the development of power-law fracture-size distributions. A fast cementation rate, relative to the opening rate, might fill 95% of extant fractures, leaving only the largest 5% with residual porosity, and thus making a fracture's susceptibility to future growth highly size-dependent. A slow cementation rate might fill only 5% of fractures, thus leaving future growth probability less dependent on current size.

Applying this reasoning to the fracture opening simulation permutation 2b*, the size-dependence of the selection probability can be modified to simulate the effect of the cement precipitation rate relative to the fracture opening rate. To calculate selection probability in permutation 2b* a new term, *C*, is added such that

$$P(S)_i = \frac{{x_i}^C}{\sum x^C} \qquad (5\text{-}2)$$

where *P(S)* is selection probability, *x* is current fracture aperture (at the start of the iteration), and Σ represents summation of all fracture sizes in the simulation.

A value of *C* less than 1 represents a low cementation rate and a suppression of the dependence of selection probability on size; a *C* value greater than 1 represents a fast cementation rate and an enhanced dependence of selection probability on size.

Using the added *C* term the cementation rate is modified throughout the simulation in order to mimic the effects of changes in temperature (cement precipitation rate) on a hypothetical fracture population undergoing burial or exhumation. Figure 5-31 shows the resulting size distributions from permutation 2b* with the added effects of monotonic heating and cooling, as from progressive burial and progressive exhumation.

The results suggest that the early history of each simulation has a strong effect on the long-term size distribution. Simulations that begin with high *C* values (runs 1 and 2, Figure 5-31) retain a tendency to concentrate fracture growth among the largest few fractures. Simulations that begin with low *C* values (runs 5 and 6) retain a broadly shared growth pattern, even after the cementation rate has increased. Put another way, pre-existing fracture patterns likely exert significant control over later pattern evolution.

PREDICTED GROWTH HISTORY OF FRACTURES IN A NATURAL SET

The simulation described above is interesting in that it can replicate observed fracture-size distributions. A test of the degree to which the simulation reflects natural fracture growth can be performed by tracking each simulated fracture's growth history and comparing those histories to histories of natural fractures.

The record of each fracture's opening history, over a run of permutation 2b* to 200 fractures (Figure 5-32) indicates that the earliest fractures dominate

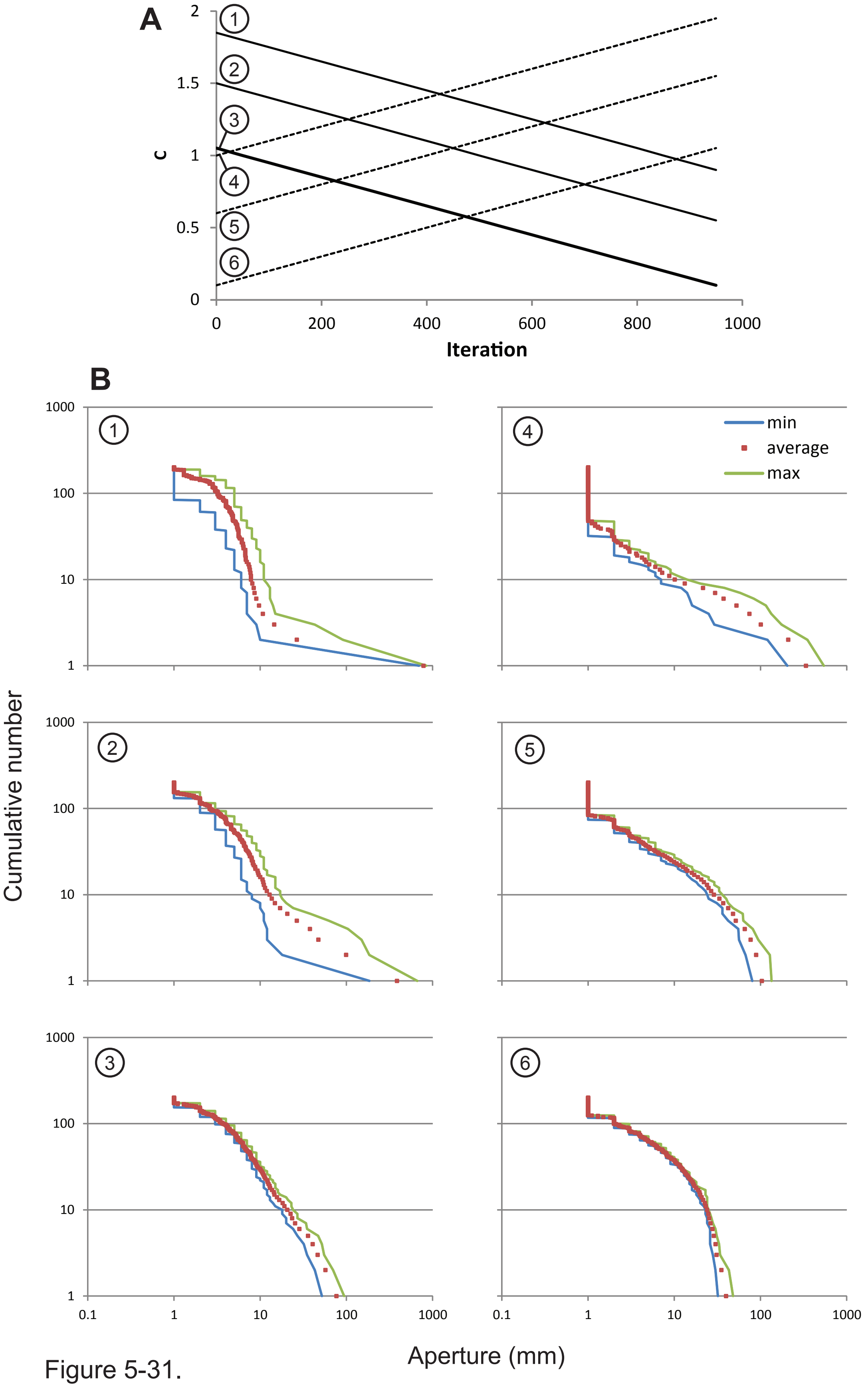
A
2
1.5
1
0.5
0
c
①
②
③
④
⑤
⑥
0
200
400
600
800
1000
Iteration
B
Cumulative number
1000
100
10
1
①
②
③
④
⑤
⑥
min
average
max
0.1
1
10
100
1000
Aperture (mm)

Figure 5-31.

Figure 5-31 continued. Results of permutation 2b*, incorporating the effects of varying cementation rate. (A) Cementation exponent, C, versus iteration, for six simulation runs. (B) Resulting size distributions. Runs 1 to 3 simulate monotonic cooling, as from fractures formed during uplift; runs 4 to 6 simulate monotonic heating as from fractures formed during burial.

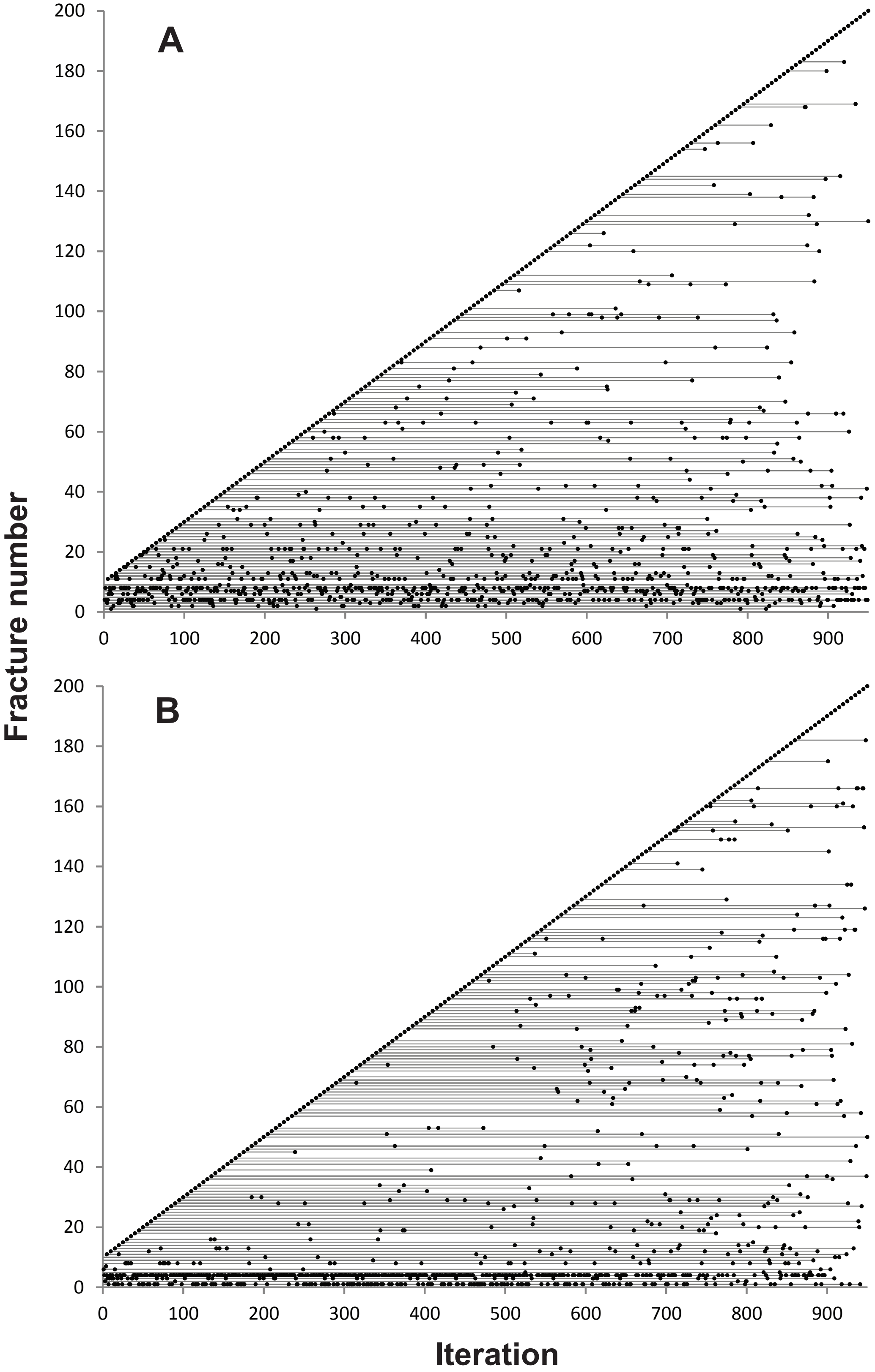
A
B
Fracture number
Iteration
0
20
40
60
80
100
120
140
160
180
200
0
100
200
300
400
500
600
700
800
900

Figure 5-32.

Figure 5-32 continued. Record of the sequence of opening-increment accumulation throughout simulations of permutation 2b*. Each dot represents an increment of fracture opening, including initial formation. X-axis is iteration, or model-time, progressing to the right. Each simulated fracture (n=200) plotted on the y-axis. (A) 5 iterations per new fracture, growth size = 1. (B) Same permutation, C (cementation exponent) monotonically decreasing from 1.5 to 0.55. Higher initial C value in (B) allows early fractures to grow to large sizes and dominate the fracture growth throughout the simulation.

the strain accumulation throughout the simulation. Fractures that form later receive progressively fewer growth increments. The largest fractures should have the oldest increments but also have been reactivated throughout the strain history. However, even very early fractures may have opened only once. Large fractures are not expected to have begun opening late in the evolution of the fracture set (Figure 5-33).

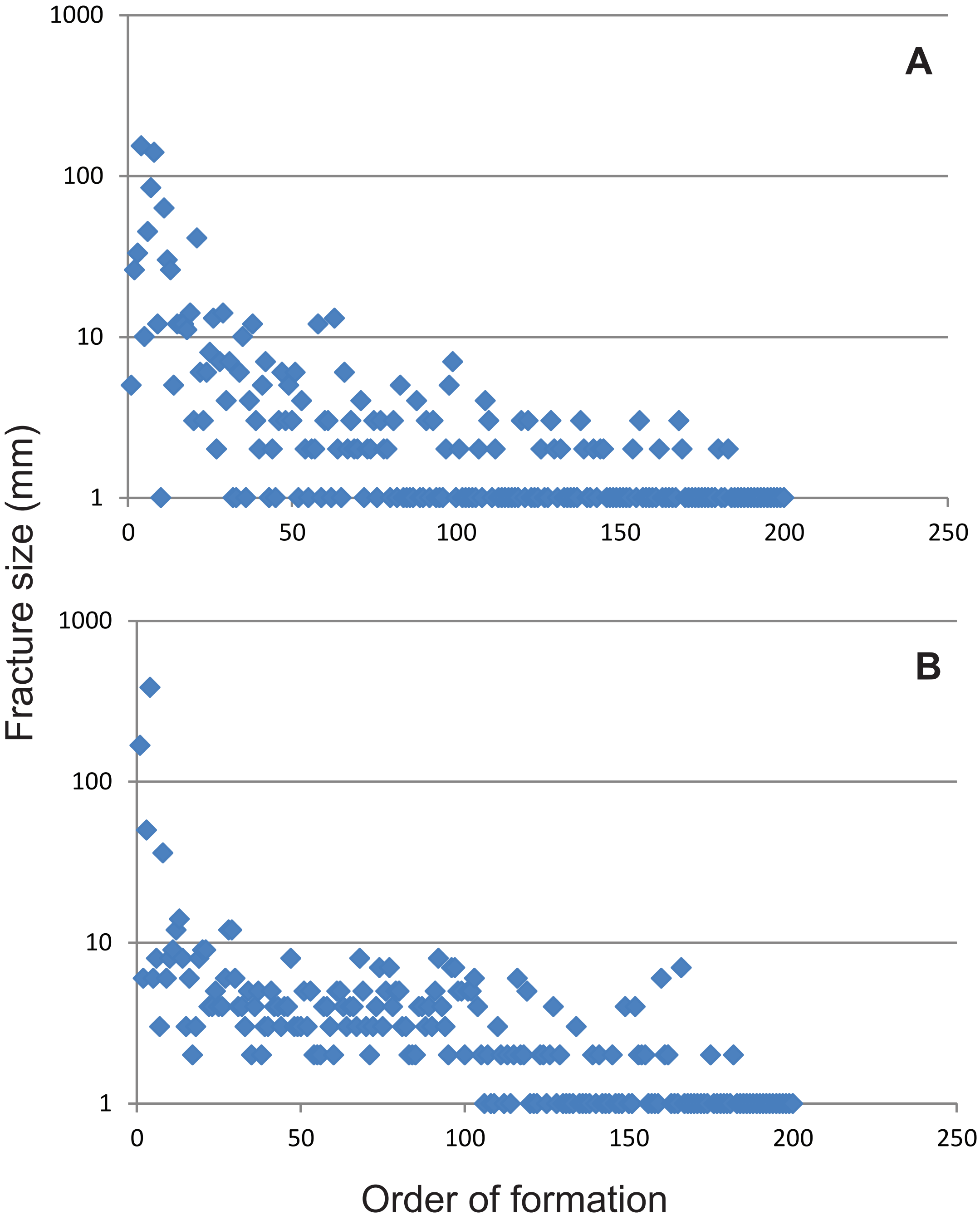

Figure 5-33. Fracture size versus order in which fractures formed (1 formed first, 2 second, and so on). (A) Permutation 2b*, corresponding to Figure 5-32a. (B) Permutation 2b* with cementation exponent monotonically decreasing from 1.5 to 0.55, corresponding to 5-32b. Note that no fractures grow to large sizes which formed late in the simulation.

Chapter 6: Tracking fracture opening using fluid inclusion microthermometry

In Chapter 5 I illustrated a simulation of fracture growth that is consistent with the size distributions and crack-seal texture documented in Chapter 3. Specifically, some model parameters of the simulation produce power-law size distributions of opening mode fractures that grew incrementally, in steps of a characteristic opening width. In this chapter I test the simulation against natural fracture growth by reconstructing the opening history of a natural fracture set. The simulation predicts that natural-fracture set growth includes the presence of multiple, concurrently active fractures, as opposed to short-lived factures that grow quickly to their final size and then stop. These contrasting hypotheses imply contrasting mechanisms for how fracture networks grow and achieve their fractal properties. Does the power-law size distribution emerge from interaction among growing fractures, or is a given fracture’s size independent of the nearby fracture population?

The duration and real timing of natural-fracture opening can be reconstructed if the opening history of a real fracture set can be measured. One technique to measure fracture timing is to correlate fluid inclusion temperatures measured within synkinematic fracture quartz cements and an independently derived burial history for the fractured host rock (Eichhubl and Boles, 1998;

Becker et al., 2010). However, if the rock thermal history involves any cooling while the fractures are filled, then a temperature of fracture opening alone does not uniquely resolve the time of fracture opening. That is, if the rock achieved any given temperature more than once in its burial history, the timing of fracture opening cannot be determined from fluid inclusions alone. To avoid this problem, Becker et al. (2010) additionally used SEM-CL mapping of crack-seal increments within cement bridges to determine the relative sequence of opening increments within a single fracture in sandstone of the Travis Peak Formation. Using the sequence of opening increments and their associated fluid inclusion temperatures, it was determined whether each increment formed during progressive burial or exhumation.

Here I use fracture opening temperatures of two large fractures and numerous microfractures determined from fluid inclusions within synkinematic quartz cement to document the absolute timing of opening of E-W striking fractures within the El Alamar Formation (Chapter 3, Sample 44). These fractures are well-fit by a power-law aperture size distribution of $b \approx 0.87$ (Figure 6-1). The small-size curve to this size distribution likely reflects the characteristic size of fracture opening increments (Chapter 3). Thus this analysis potentially allows the reconstruction of a power-law fracture set. By applying this method to establish absolute fracture timing, I tested the following hypotheses that define the fracture growth simulation:

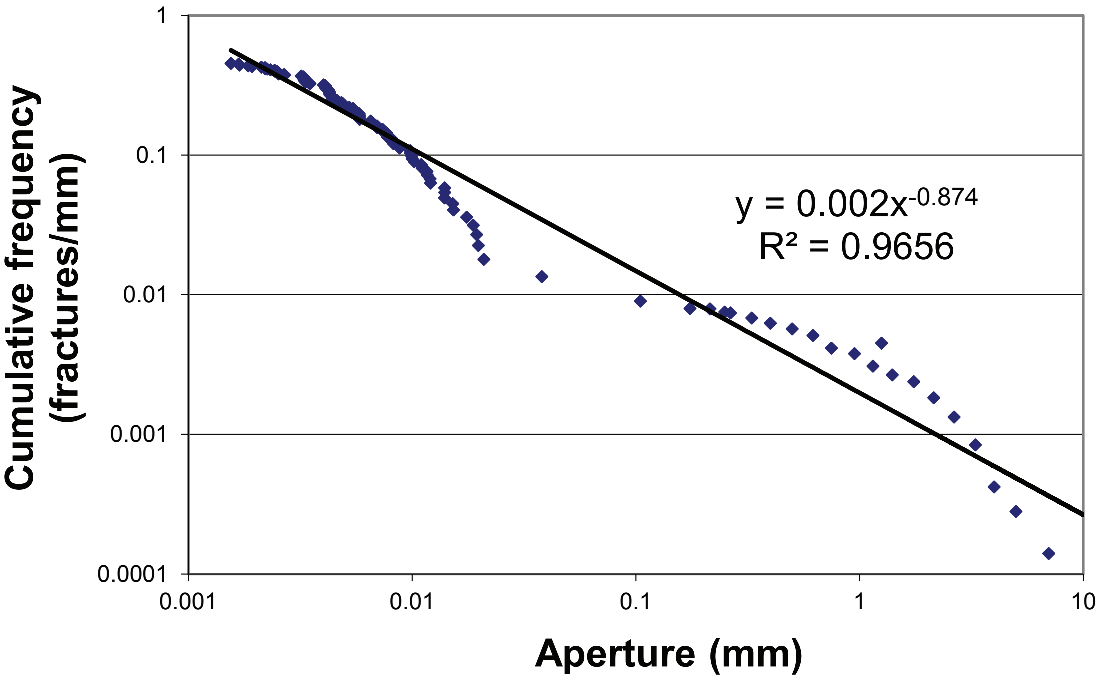

Figure 6-1. Size distribution of Set C fractures, El Alamar Formation (Sample 44). Combined microfractures and macrofractures.

Fractures have protracted opening histories that overlap with the opening of neighboring fractures. The simulation illustrates a dynamic system in which multiple fractures grow penecontemporaneously, and growth of a given fracture comes at the expense of other fractures that might have grown instead. If this hypothesis is true, then individual fractures in a set should show non-trivial opening duration compared to the total time span over which the fracture set grew. In other words, a ten thousand year opening history for an individual fracture, though long by some time scales, could be thought of as short if the overall fracture set opened over 20 million years—if most fractures grew so quickly, the hypothesis would be contradicted. Moreover, the hypothesis predicts that the opening durations of multiple natural fractures within the same set will overlap one another.

New microfractures develop continuously throughout deformation. Some permutations of the simulation show relative constancy of the power-law exponent, and the increase in power-law coefficient, with progressive fracture strain (Chapter 5). Moreover, I interpreted constant exponent and increasing coefficient with progressive strain on the basis of natural scaling data (Chapter 3). For such an evolution of size distribution to arise, new microfractures must form continuously, or else the power-law slope would become shallower as large fractures become still larger and/or more numerous without accompanying microfracture development. It is possible that all fractures initiated early within the evolution of the system but that only a progressively smaller subset of fractures remained active and grew to progressively larger sizes. If this is the case, the smaller fractures should be systematically older than the larger ones. By reconstructing the timing of opening of fractures having a range of sizes, I can test whether large and small fractures form together, or alternatively, whether there is a systematic relationship between fracture size and fracture timing.

The earliest opening is preserved within macrofractures. In the simulation, it is the earliest few fractures which grow to macroscopic sizes (for a 5 μm opening-increment size, ~20 growth increments); the growth probabilities of late-formed microfractures amid a population of growing macrofractures are exceedingly low relative to macrofractures. Thus microfractures that form once a macrofracture pattern has developed will likely not become macrofractures unless considerably more strain accumulates, with associated widening of earlier macrofractures.

Beyond what is predicted by the fracture growth simulation, this test of natural fractures enabled examination of the development of fracture clusters by comparing timing of fracture opening with fracture position along a scanline. It is possible that fractures that are close in space also formed close to one another in time.

To further constrain the history of fracture opening and associated fluid-rock interaction of the study area, oxygen isotope ratios of fracture cements were measured. Oxygen isotope ratios, combined with fluid inclusion temperatures, enable the determination of the isotopic ratios of the fluids from which the cements precipitated. Thus the oxygen isotope ratios provide an independent test of the fluid migration that is suggested by the fluid inclusion analysis.

METHODS USED FOR FRACTURE CEMENT ANALYSIS

Fluid inclusion microthermometry

Microthermometric analyses of fluid inclusions were performed using a FLUID, INC.-adapted, USGS-type, gas-flow, heating/freezing stage. The stage was calibrated using the CO_2-ice melting temperature at -56.6°C of H_2O–CO_2 synthetic fluid inclusions, the ice-melting temperature at 0°C, and the critical homogenization temperature at 374.1°C of pure H_2O synthetic fluid inclusion standards (Sterner and Bodnar, 1984).

Fluid inclusion microthermometry allows constraint of the ambient temperature at which the fractures opened. Incremental fracture opening and sealing traps fluid inclusions within synkinematic quartz cement bridges. By heating thin sections and observing the temperature at which the fluid within an inclusion homogenizes to the liquid phase (T_h), a minimum estimate of the trapping temperature (T_t) can be made (Goldstein and Reynolds, 1994). In order to estimate T_t a pressure correction must be added to T_h (Roedder, 1984). With increasing temperature the homogenized inclusion will travel along an isochore, which is a line of constant density (volume) in P-T space (Figure 6-2). Estimates of T_t can be obtained by assuming a hydrostatic fluid pressure gradient; that is, assuming the inclusion was trapped under hydrostatic pore pressure conditions. Estimated T_t is the temperature at which the hydrostatic gradient intersects the isochore determined by the measured T_h. Actual pore pressure conditions may have been higher than hydrostatic, and so this estimate of T_t is generally a minimum estimate of true T_t. Salinity, estimated from final ice-melting temperatures of the trapped aqueous fluid (see below) must also be taken into account in the hydrostatic pressure calculation.

Using an average salinity of 22.9 weight-percent NaCl equivalent, based on observed final ice melting temperatures (see below), and assuming a 30°C/km temperature gradient (Gray et al., 2001), T_t was computed using the equations in Steele-MacInnis et al. (2012). This pressure correction accounts for the difference in temperature between the trapping of the fluid at depth within the fracture-bridging quartz crystal and T_h, where the isochore intersects the liquid-vapor curve (Figure 6-2).

Hydrostatic pressure may be an underestimation of the true fluid pressure. Possible overpressure of the pore fluid could affect results: the pressure correction will increase linearly in proportion to overburden stress, resulting in

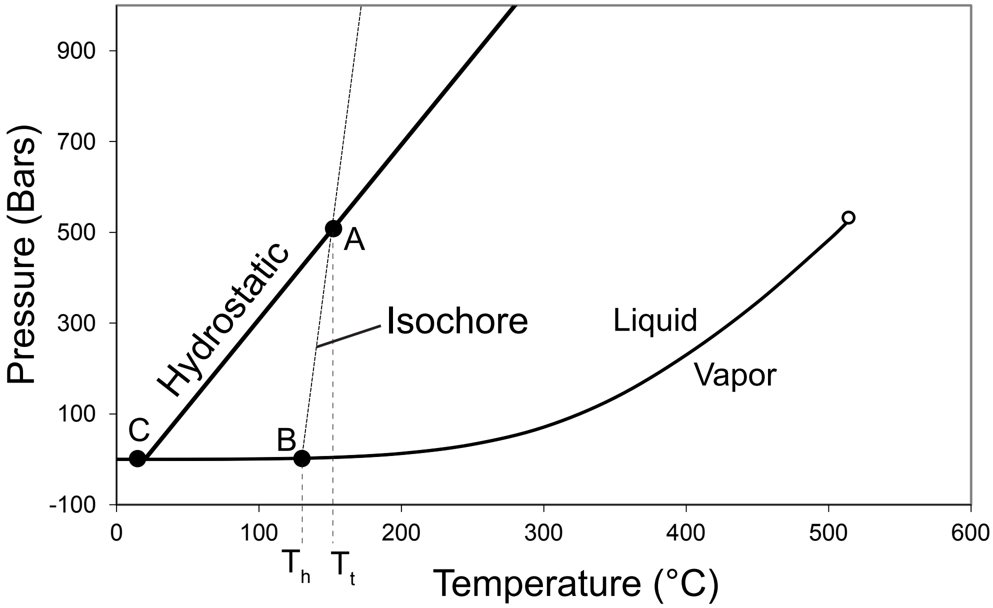

Figure 6-2. Pressure-temperature phase diagram for aqueous fluid inclusions with NaCl equivalent wt% salinity of 22.9 (see text), after Goldstein and Reynolds (1994). Liquid-vapor curve and isochore calculated according to Steele-MacInnis et al. (2012). Hydrostatic gradient assumes 30°C/km geothermal gradient (Gray et al., 2001). Measured homogenization temperature (T_h) is a minimum estimate of the trapping temperature (T_t) of fluid inclusions. A fluid inclusion forms at depth (point A) and, assuming no change in volume or fluid composition, moves along the isochore to the liquid-vapor curve, at which point a bubble nucleates (point B). This is the homogenization temperature and pressure. Further cooling enlarges the bubble and moves the inclusion along the liquid-vapor curve towards the left (point C). Point A can be estimated by assuming hydrostatic fluid pressure and extrapolating this gradient to where it intersects the isochore.

underestimations up to approximately 30°C for the temperature range observed. Consequences of this potential error source are addressed below.

In order to measure T_h, two-phase inclusions are heated until the vapor bubble disappears. Cooling of the sample allows spontaneous re-nucleation of the bubbles, usually at a lower temperature than T_h. Typically vapor bubbles in the studied samples did not spontaneously re-nucleate after cooling to room temperature. This presented a practical difficulty in establishing T_h, because the nucleation of the bubble allows for repeated observation of T_h of a given inclusion. Moreover, inclusions within the sample outside the viewing area may homogenize during heating. If those bubbles do not re-nucleate upon cooling to room temperature, T_h cannot be observed without further cooling the inclusion before re-heating. Repeated heating and cooling of samples risks damaging some inclusions, particularly large or irregularly shaped inclusions, or inclusions close to the thin section surface. To minimize this risk, before heating each sample an inventory of all two-phase inclusion bearing FIAs was made. Then each sample was heated in five-degree increments, starting near 75°C and ending near 135°C. Each two-phase fluid inclusion within the sample was observed after each five-degree heating step, and the heating step at which each inclusion homogenized was noted. For the rare case in which bubbles did spontaneously re-form T_h was measured individually, after recording T_h for the rest of the fluid inclusions. For inclusions with spontaneously re-nucleating bubbles T_h was measured with higher precision than the ±5°C for metastable inclusions. By cycling the temperature near T_h (Goldstein and Reynolds, 1994) and observing whether the bubble slowly grows with cooling (and thus has not homogenized) or re-nucleates quickly after several degrees of cooling (and thus has homogenized), T_h was measured to ±0.2°C.

SEM-CL imaging and mapping

Samples were imaged using the methods outlined in Chapter 2. To minimize persistent luminescence from post-kinematic calcite cement, which is most apparent in red wavelengths, (Figure 6-3), SEM-CL mapping was mostly performed on blue-pass-filtered images (350-500 nm wavelength—Reed and Milliken, 2003). This technique is particularly helpful for imaging fractures wider than ~0.5 mm, which commonly contain calcite cement surrounding quartz cement.

A key to determining the relative timing of opening increments was cement bridges, which comprise crack-seal increments towards the core of the bridge and lateral euhedral cement deposits along the bridge margins (Figure 6-3). The CL response from individual crack-seal bands within synkinematic quartz cements enables the distinction between cement that seals opening increments within the bridges and the euhedral cement that accumulates on the bridge margins as the fractures grow (Becker et al., 2010). Because lateral euhedral cement accumulates throughout fracture growth, the relative timing of crack-seal

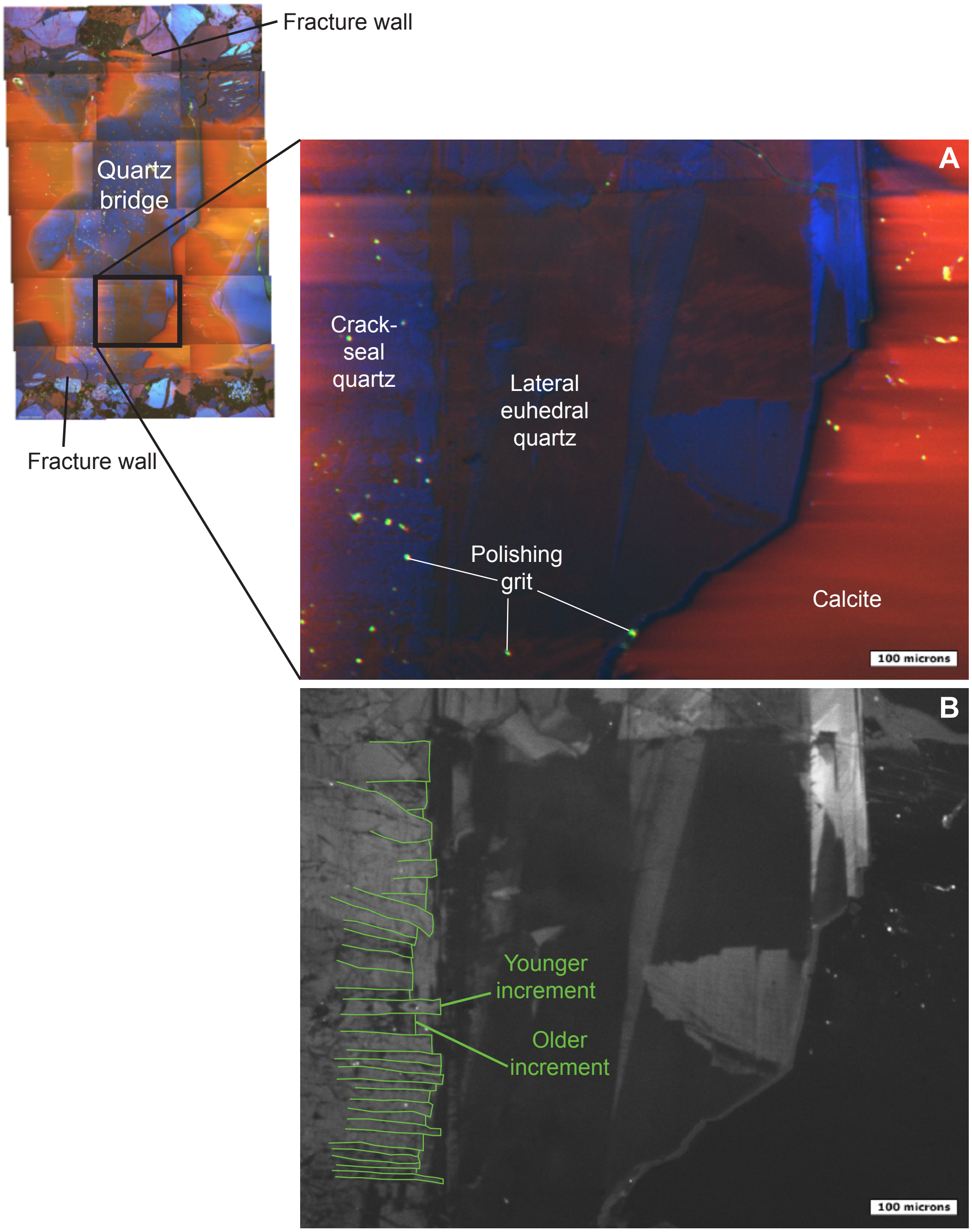

Figure 6-3. (A) RGB SEM-CL image showing detail of macrofracture bridge, El Alamar Formation. (B) Same image, blue-light pass filter only. The relative timing of crack-seal increments is determined by how far the increments cut into lateral euhedral cement, which accumulated along the margins of the bridge while the fracture grew. The blue filter eliminates persistent red-spectrum luminescence from calcite cement, which obscures crack-seal texture in quartz. Also embedded polishing grit is less luminescent under blue filter.

increments within the same bridge can be discerned by the extent to which the increment cuts into the lateral cement (Figure 6-3).

This CL mapping technique cannot typically be implemented on microfractures, which often comprise fewer than ten opening increments and thus do not feature bridges with lateral euhedral cement. Thus the key for establishing microfracture timing is to demonstrate, if possible, a steady temperature trend during fracture opening using macrofracture bridges. If the ambient temperature during the opening of a fracture set consistently increased or decreased, and if the calculated T_t within fracture cements reflects that ambient temperature trend, then temperature can serve as a proxy for time for any fracture in the set—any increment of fracture opening can be placed within the sequence of fracture-set growth using its temperature alone.

In order to minimize any possible damage to fluid inclusions from the SEM electron beam (Becker et al., 2010; Xu, 2012), I made narrow SEM-scanline image-swaths close to the edge of each thin section, then performed fluid inclusion analyses, and only afterwards made SEM-CL fracture maps (Appendix D).

Oxygen isotope analysis

Stable oxygen isotopes were analyzed from Set B and Set C fractures, using the laser fluorination technique of Sharp (1990). This entails reacting samples with BrF_5 and heating with a 25W Merchantek CO_2 laser. Liberated O_2

gas is then purified with liquid nitrogen traps and a heated NaCl trap to remove excess BrF_5 and other fluoride and bromide products. Purified O_2 gas is quantitatively collected on a 13x mol sieve. $\delta^{18}O$ values are measured on purified O_2 gas using a ThermoElectron MAT 253 light isotope mass spectrometer. The garnet standard UWG-2 ($\delta^{18}O$ =5.8‰; Valley et al., 1995) and the in-house quartz standards Gee Whiz ($\delta^{18}O$ =12.5‰) and Lausanne-1 ($\delta^{18}O$ =18.2‰) relative to NBS-28 = 9.6‰ are analyzed for calibration. This technique permitted a precision of ±0.17‰ for replicates of Lausanne-1. The measured calibrated $\delta^{18}O$ value for Gee Whiz was 12.5 ‰.

GEOLOGIC SETTING OF THE FLUID INCLUSION SAMPLES

At the exposure studied, within the Monterrey Salient, the El Alamar Formation contains multiple crosscutting fracture arrays (Appendix A, Figure A-5). The outcrop is a natural stream canyon floor exposure of feldspathic litharenite beds (Laubach and Ward, 2006) within the El Alamar Formation (Barboza-Gudiño et al., 2010). The exposed beds are part of the southwest limb of a doubly plunging anticline (Davis, 2005; Laubach and Ward, 2006; Cross, 2012) and bedding dips gently (~10°) to the southwest.

Laubach and Ward (2006) identified four pervasive fracture sets within the outcrop, which they named Sets A, B, C, and D, in order of formation identified by crosscutting relationships. All four fracture sets dip steeply and roughly perpendicular to bedding. My study focuses on their Set B, which strikes NW, and Set C, which strikes E-W. Both sets of fractures feature abundant quartz and carbonate cement. The quartz cement typically forms bridges that locally span between the fracture walls. Where present, carbonate cement overlaps quartz and typically fills any remnant fracture porosity.

The geology of the outcrops is described further in Appendix A.

Burial history of the El Alamar Formation

Having constrained T_t for a fracture-cement gap deposit, possible absolute ages of fracture opening can be determined by reference to independently derived burial history reconstructions (Becker et al., 2010). Possible absolute ages of fracture opening correspond to any point during the burial history of the formation studied at which the ambient temperature was equal to measured T_t.

Constraining fracture timing by fluid-inclusion microthermometry requires a geologic setting with an independently constrained burial history so that a reliable thermal history can be inferred. Regional-scale thermal data were synthesized by Gray et al. (2001) and used to construct a burial history curve in the vicinity of Ciudad Mante, ~220 km south of Linares (Figure A-5). That study constrained progressive burial by K-Ar dating of illite, which indicates the smectite-illite transition (near 80°C). Fluid inclusions from diagenetic calcite indicate a maximum burial of the Lower Cretaceous El Abra Formation to a temperature of 160°C (Gray et al., 2001). The El Abra Formation is the stratigraphic equivalent to the Upper Tamaulipas Formation in the Monterrey Salient (Goldhammer and

Johnson, 2001). Temperatures were hotter (near 200°C) towards the Monterrey Salient. This temperature anomaly was suggested to be a broad heating episode that spanned the Monterrey Salient and not the product of local heating or fluid migration effects, because of the broad concurrence of maximum temperatures near 200°C (Gray et al., 2001).

Timing of exhumation was constrained using apatite fission track lengths, which are annealed near 100°C and can thus be used to infer lower temperatures (Green et al., 1986). Between 80 and 40°C radiogenic He ages further constrain exhumation. Consistent results were obtained by Ferket et al. (2011) for Late Cretaceous strata in the Veracruz Basin to the south, where fluid inclusions from later diagenetic phases suggest that exhumation initiated during the Eocene. The timing of maximum burial for the regional study (Gray et al., 2001) is bracketed only between illite burial ages (~50 Ma) and helium exhumation ages (~25 Ma), or late Eocene-Oligocene.

Kaylor (2011) extrapolated a burial history for the study area based on the regional history of Gray et al. (2001) based on an inferred maximum stratigraphic thickness of ~ 2.6 km between the El Abra Formation and the Huizachal Group (Goldhammer et al., 1991; Gray et al., 2001). Based upon stratigraphic thickness, the maximum burial depth for the El Alamar Formation within the Monterrey Salient was roughly 8.4 km. To account for the thermal anomaly identified by Gray et al. (2001) a further 25°C was added to the maximum burial temperature of ~250°C. In the absence of a definitive cause of the thermal anomaly it may be attributed to ~0.8 km of structural thickening. The burial history from Kaylor (2011) is the best estimate of the true ambient temperature of the Huizachal Group sandstones at the study area (Figure 6-4). However, contributing to the uncertainties associated with this estimate are the paucity of temperature data from nearby samples, the unknown extent of structural thickening, the uncertain pre-Cretaceous burial history owing to lack of preserved section, and possible local thermal anomalies.

For example, igneous activity is preserved by dikes in the overlying strata of the La Boca Formation (Barboza-Gudiño et al., 2008). That study used major- and trace-element data as well as stratigraphic correlation to associate the dikes with volcanic rocks near Aramberri, about 50 km to the SE, whose timing was constrained to the Lower Jurassic by U-Pb dating. The fractures could have formed as accessory structures, recording elevated temperatures from contact heating by igneous material. If this is the case, the salinity and oxygen isotopic composition of the precipitating fluids should be near that of surface waters, reflecting shallow burial. I show evidence contradicting this hypothesis. Moreover, Ward (2006) found no evidence of local alteration near the dikes and sills. The same study presented crosscutting relations providing evidence that the fractures all postdate the igneous activity.

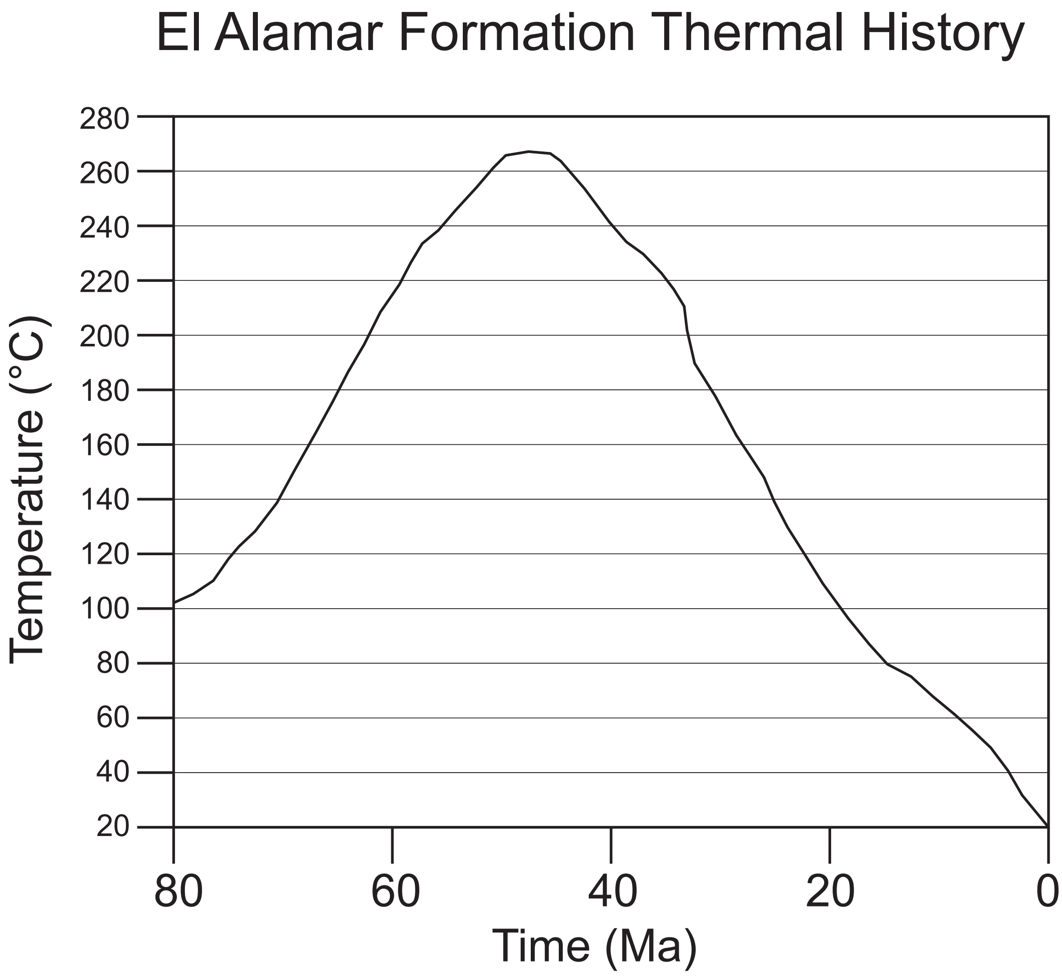

Figure 6-4. Burial history curve for the Triassic El Alamar Formation at the studied location. From Kaylor, 2011, which synthesized data from Gray et al. (2001) and Ferket et al. (2011). Burial history before ~80 Ma is largely unconstrained because no overlying section is preserved.

Uncertainties in the burial history curve could dramatically affect calculations of the absolute timing of fractures. However, despite these uncertainties, I show below that the fracture-set opening is still reconstructible. Set C fractures crosscut Set B, which formed during peak burial, and the exhumation history is continuous. By reconstructing opening histories preserved in cement bridges within macrofractures, and measuring the coincident trapping temperatures, it may be confirmed that temperatures generally declined during Set C fracture opening. Thus, upon accounting for uncertainty in the correlation between T_t and time of up to 20°C (see below), temperature can be used as a proxy for time for Set C fractures. The temporal sequence of Set C fracture opening is reflected in the temperature of fracture opening. Therefore, the relative timing of microfractures can be constrained.

Scanline data were collected at the outcrop scale using a hand lens and at the microscopic scale using SEM-CL (see Chapter 2 for a detailed description of these methods). The macrofractures are exposed along a plan-view exposure on a canyon floor (Figure 6-5). Fluid inclusions were collected from two macrofractures (Macrofracture 1 and Macrofracture 2—Figure 6-5) and from 31 microfractures which were detected in a series of contiguous thin sections (Figure 6-6). These thin sections also provide the microfracture scanline.

TEMPERATURE OF FRACTURE OPENING

Fluid inclusion description

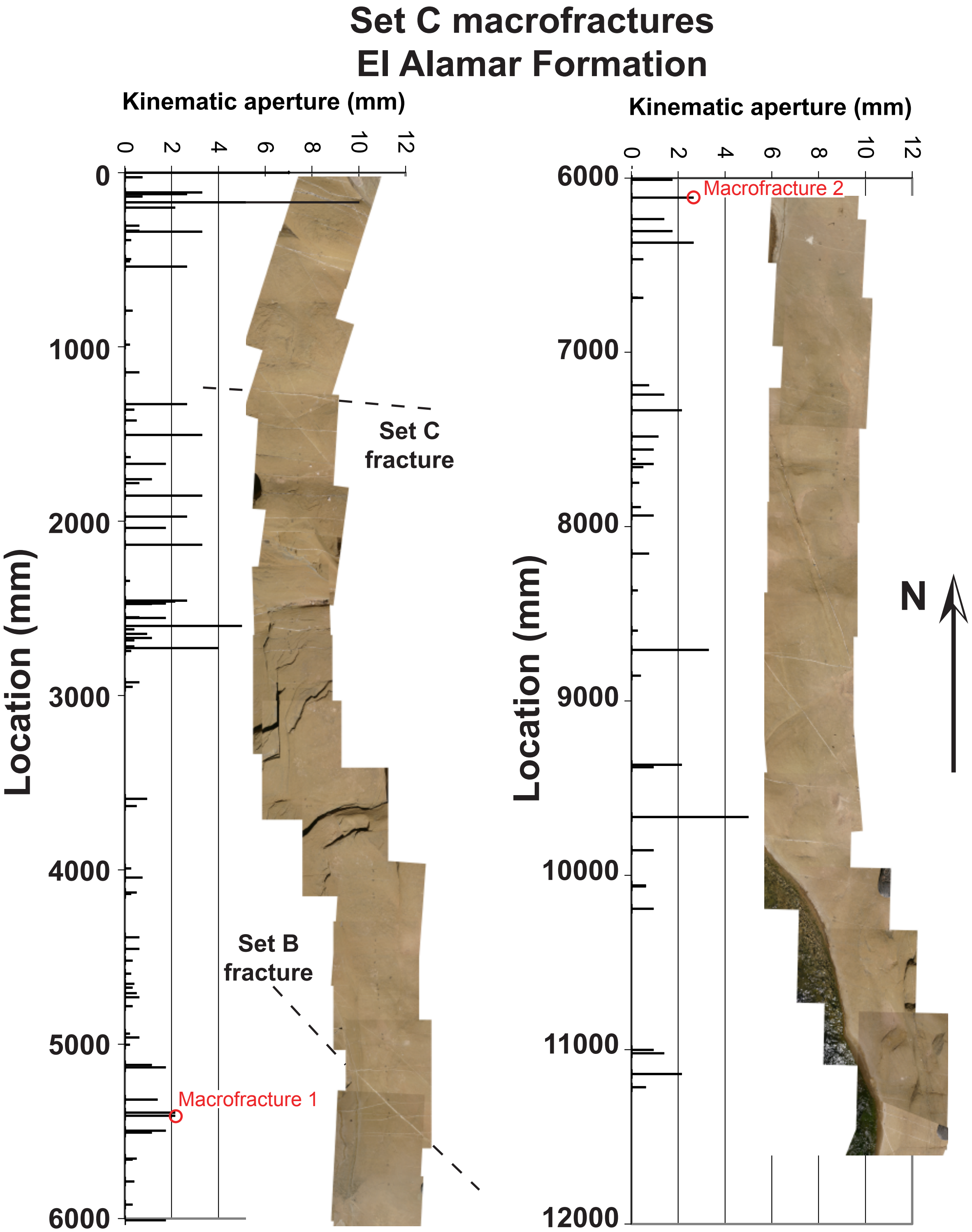

Figure 6-5. Set C macrofracture scanline. Kinematic aperture versus position along scanline. Crosscut NW-striking (Set B) microfractures not plotted. Earliest Set A and latest Set D (Laubach and Ward, 2006) also present but rare within this scanline and also not plotted.

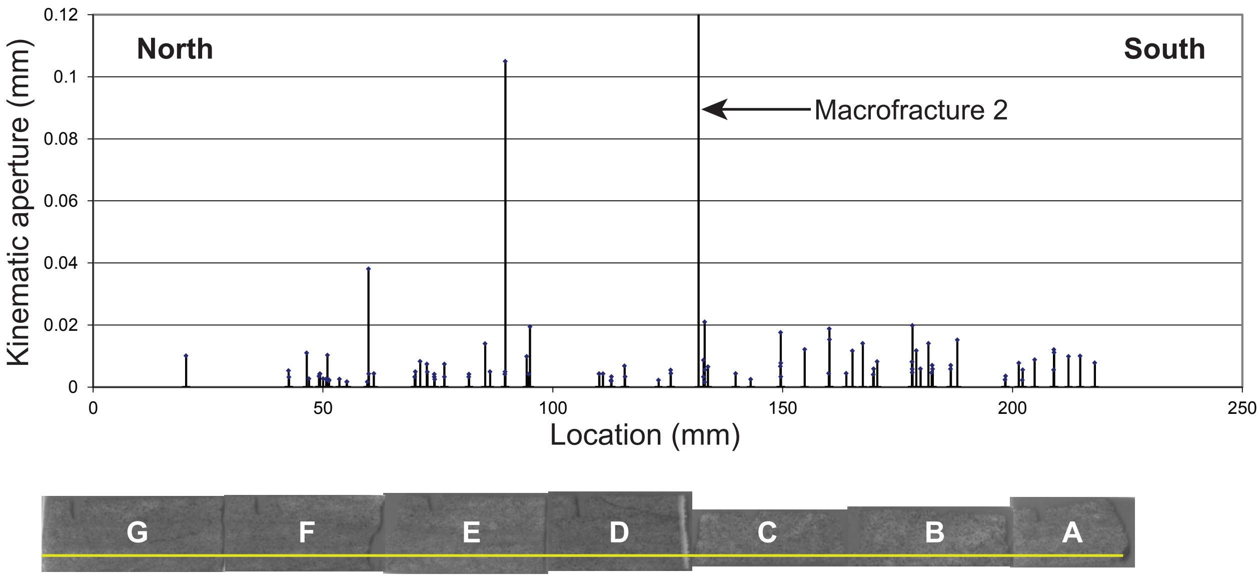
Set C microfractures, El Alamar Formation

Figure 6-6. Set C microfracture scanline. Kinematic aperture versus position along scanline for Set C microfractures, measured using SEM-CL. Line across thin sections represents approximate scanline location. Macrofracture 2 is visible in thin section near the D-C boundary. See Appendix C for locations of fluid inclusions sampled within microfractures in thin section.

Observed FIAs include single- and two-phase inclusions (Figure 6-7). T_h was measured from two-phase (aqueous + vapor) inclusions. Such inclusions typically have the same apparent liquid to vapor volume ratios, estimated visually. The average long-dimension of fluid inclusions, measured from a sub-population within Macrofracture 1, is 4.4 μm (standard deviation 2.4 μm). This average is likely larger than the overall inclusion-size average, because smaller inclusions are more often single-phase-aqueous (Figure 6-7) and not counted. This relationship between inclusion size and presence of a vapor phase is likely an effect of the kinetic energy required for vapor-bubble nucleation, which is more abundant in larger inclusions. Thus the single-phase fluids in small inclusions are likely metastable (Goldstein and Reynolds, 1994).

Trapping temperatures derived from fluid inclusions within synkinematic quartz cements in Set C range from 57 to 175°C (Figure 6-8). This range is cooler than that found within the older, crosscut, Set B set (129 to 280°C—Kaylor, 2011). Individual FIAs from Macrofracture 1 have an average range in T_h of 19.6°C (Figure 6-9); FIAs from the micro-scanline fractures (Macrofracture 2 and nearby microfractures) have an average range of 23.2°C (Figure 6-10). Possible causes of this variation and consequences for data interpretation are discussed in the interpretation.

Macrofracture 1

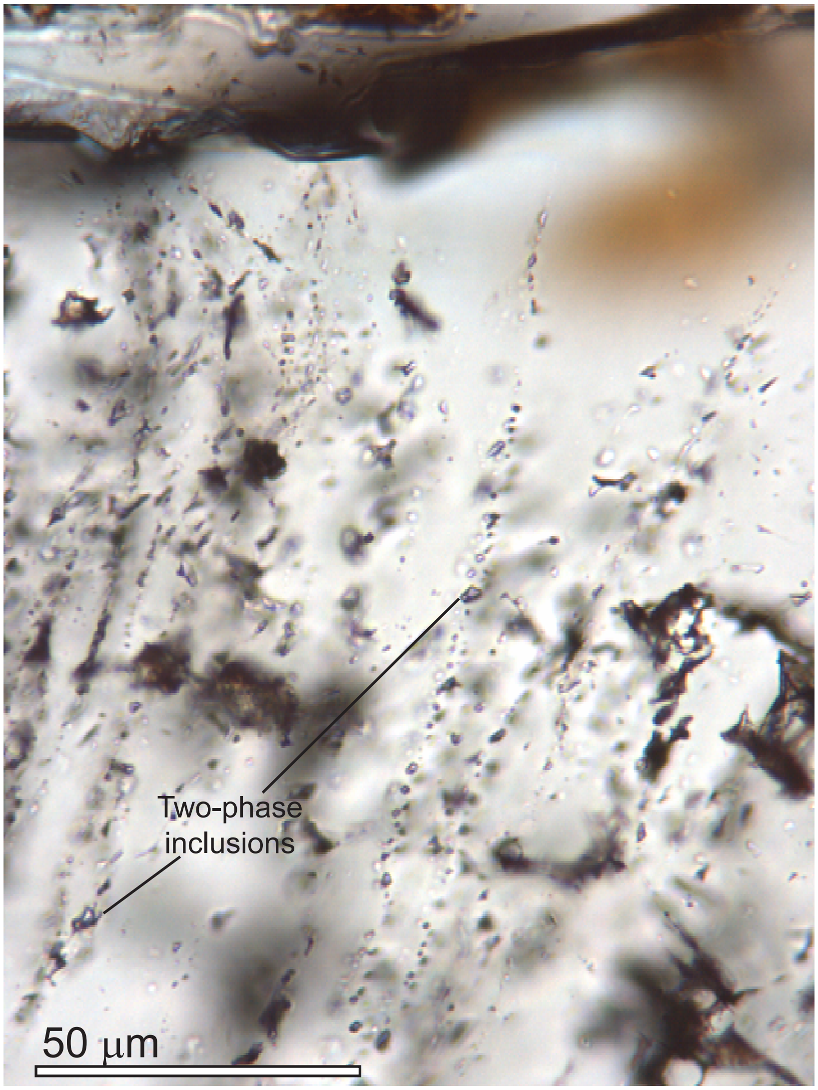

Figure 6-7. Fluid inclusion assemblages from synkinematic quartz cement within Macrofracture 1. Note presence of single- and two-phase fluid inclusions within individual FIAs, with two-phase inclusions typically larger.

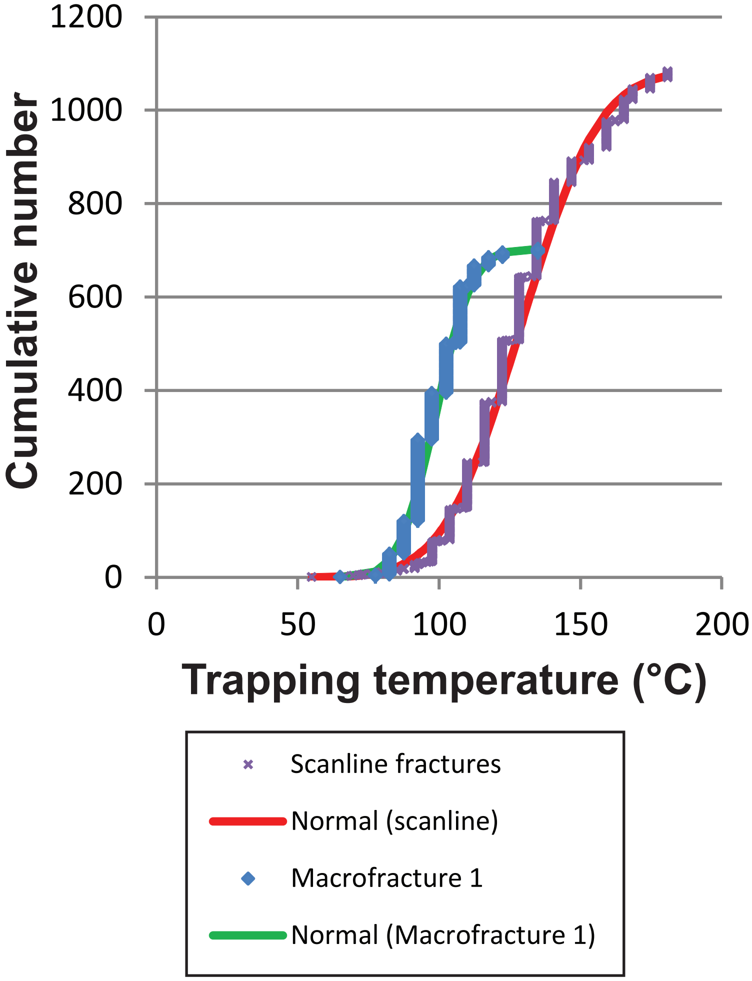

Figure 6-8. Cumulative distributions of Tt measured from scanline fractures (including Macrofracture 2) and Macrofracture 1. Curves are normal distributions.

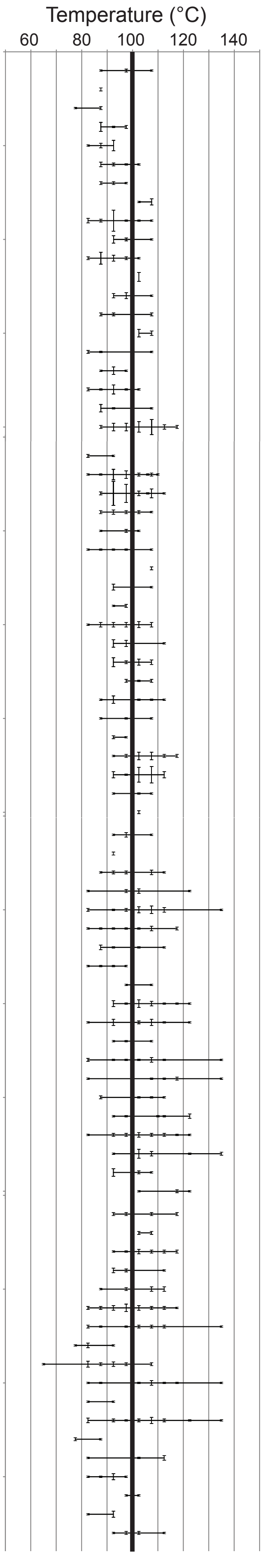

Figure 6-9. Homogenization temperatures from fluid inclusions within synkinematic quartz cement, Macrofracture 1. Horizontal bars represent data from individual fluid inclusion assemblages. Height of vertical lines is proportional to number of temperatures measured. To accurately represent trapping conditions, temperatures within a fluid inclusion assemblage should record the same temperature; the average range in temperatures from these FIAs is 19.6°C. Potential causes of this variation are discussed in the text.

I Scale: 5 inclusions

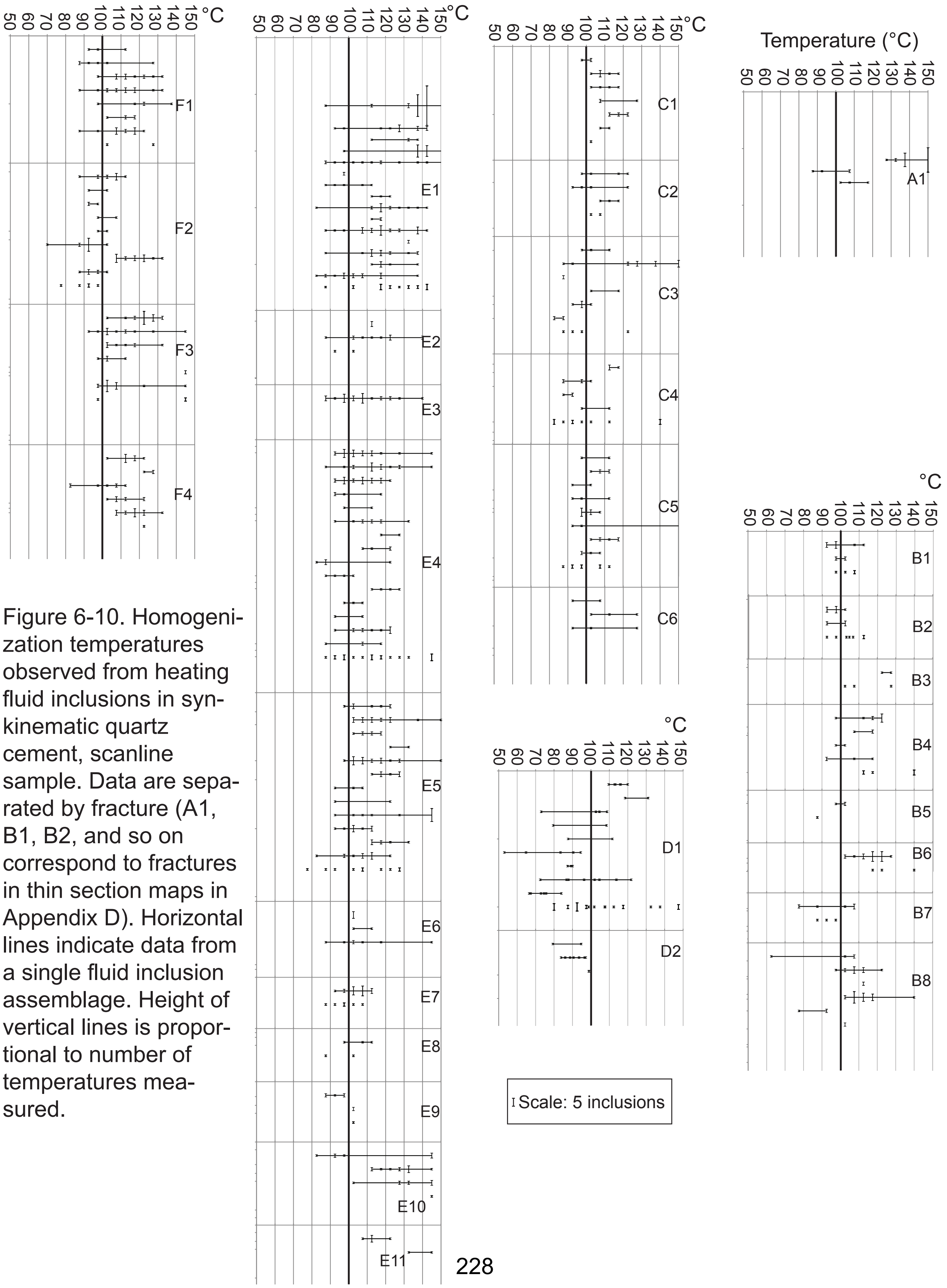

Figure 6-10. Homogenization temperatures observed from heating fluid inclusions in synkinematic quartz cement, scanline sample. Data are separated by fracture (A1, B1, B2, and so on correspond to fractures in thin section maps in Appendix D). Horizontal lines indicate data from a single fluid inclusion assemblage. Height of vertical lines is proportional to number of temperatures measured.

From SEM-CL image mapping of Macrofracture 1 six regions of quartz cement are apparent, each distinguished by the extent to which its gap deposits cut into the bridge-lateral euhedral cement (Figure 6-11). Figure 6-11 is a plot of average T_h within each FIA observed, separated into the six relative timing regions (Region I is earliest; Region VI is latest). I was not in general able to discern the relative timing of individual gap deposits within each region. Taking the average T_h of each FIA average T_h, the cooling trend is apparent. This cooling trend line in Figure 6-12 is an average of each FIA average recorded in each of the six timing regions within the macrofracture bridge. The range of FIA averages within each region is as great as 25°C. Possible causes of this variation are discussed below.

Macrofracture 2

The same approach was applied to a cement bridge within Macrofracture 2 as was performed on the bridge within Macrofracture 1. In this case, six regions of synkinematic quartz cement are apparent whose relative timing was discernible using SEM-CL mapping. However, the internal structure of Macrofracture 2 cement bridge is more complex than that of Macrofracture 1 (Figure 6-13). In four of the six regions (I, II, III, and VI), the margins of gap deposits are roughly parallel to the overall fracture strike; these regions record a cooling trend similar to that which I found in Macrofracture 1. The gap deposits in the remaining two regions (IV and V) are difficult to delineate and appear to be

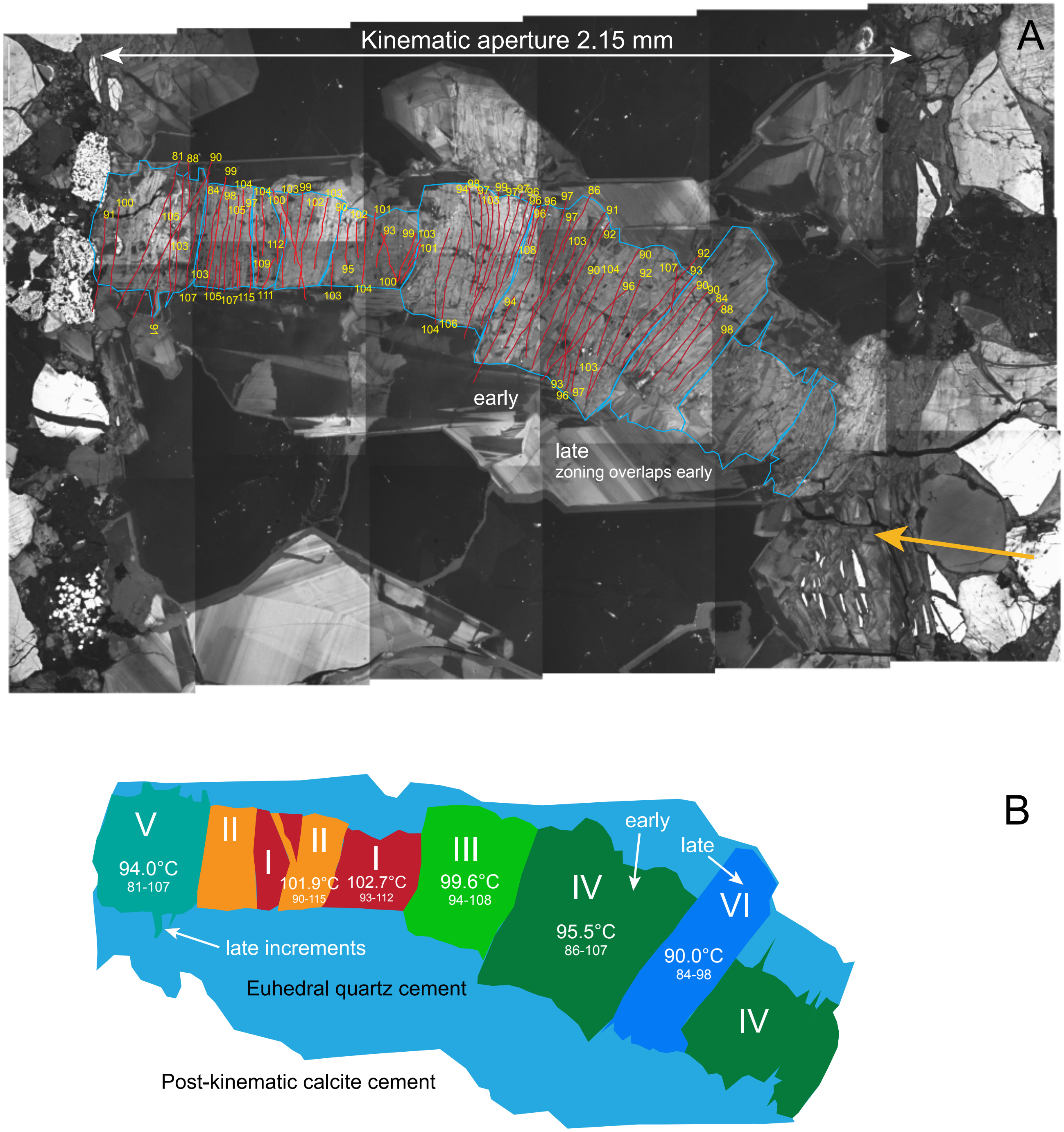
Kinematic aperture 2.15 mm
A
early
late
zoning overlaps early
B
V
94.0°C
81-107
II
I
II
I
101.9°C
90-115
102.7°C
93-112
III
99.6°C
94-108
IV
95.5°C
86-107
early
late
VI
90.0°C
84-98
IV
late increments
Euhedral quartz cement
Post-kinematic calcite cement

Figure 6-11.

Figure 6-11 continued. (A) SEM-CL mosaic of quartz cement bridging across Macrofracture 1. Note host-rock grains on both walls. Interpreted fluid inclusion assemblage traces and average T_h mapped. (B) Regions over which the relative timing of opening can be inferred, by overlap with layers of euhedral cement at the sides of the bridge (Becker et al., 2010). Average and range of T_h in (A) given for each timing region. The increments to the right of the bridge (orange arrow) likely formed earlier, when the fracture was smaller and quartz precipitation bridged a larger portion of the fracture. However, all observed inclusions within this region are single-phase.

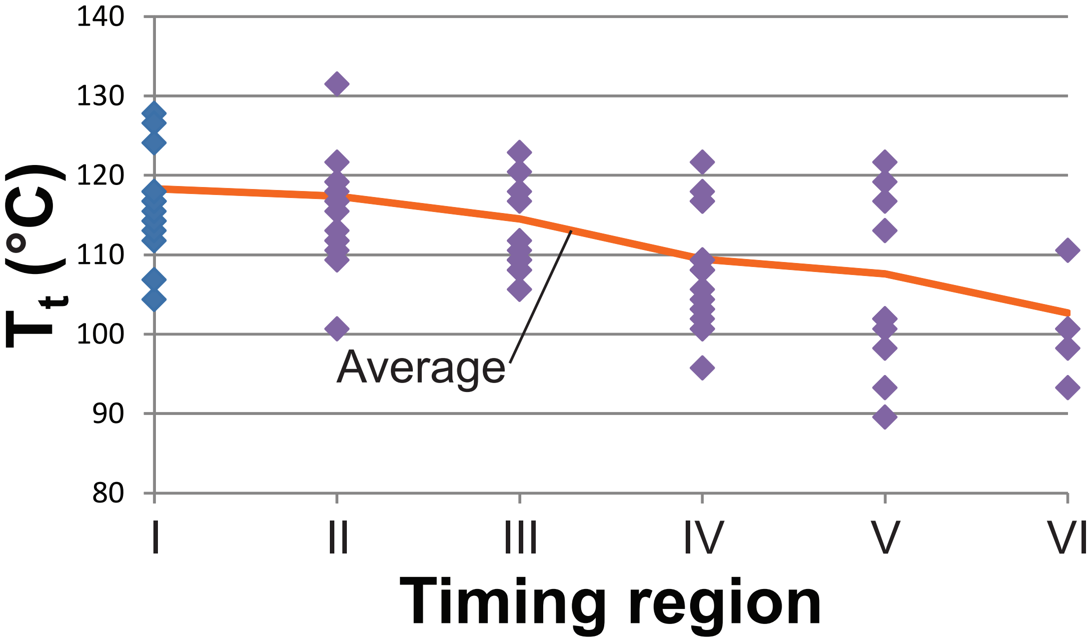

Figure 6-12. Homogenization temperatures from Figure 6-11, converted to trapping temperatures. Note consistent decrease in average temperature with time.

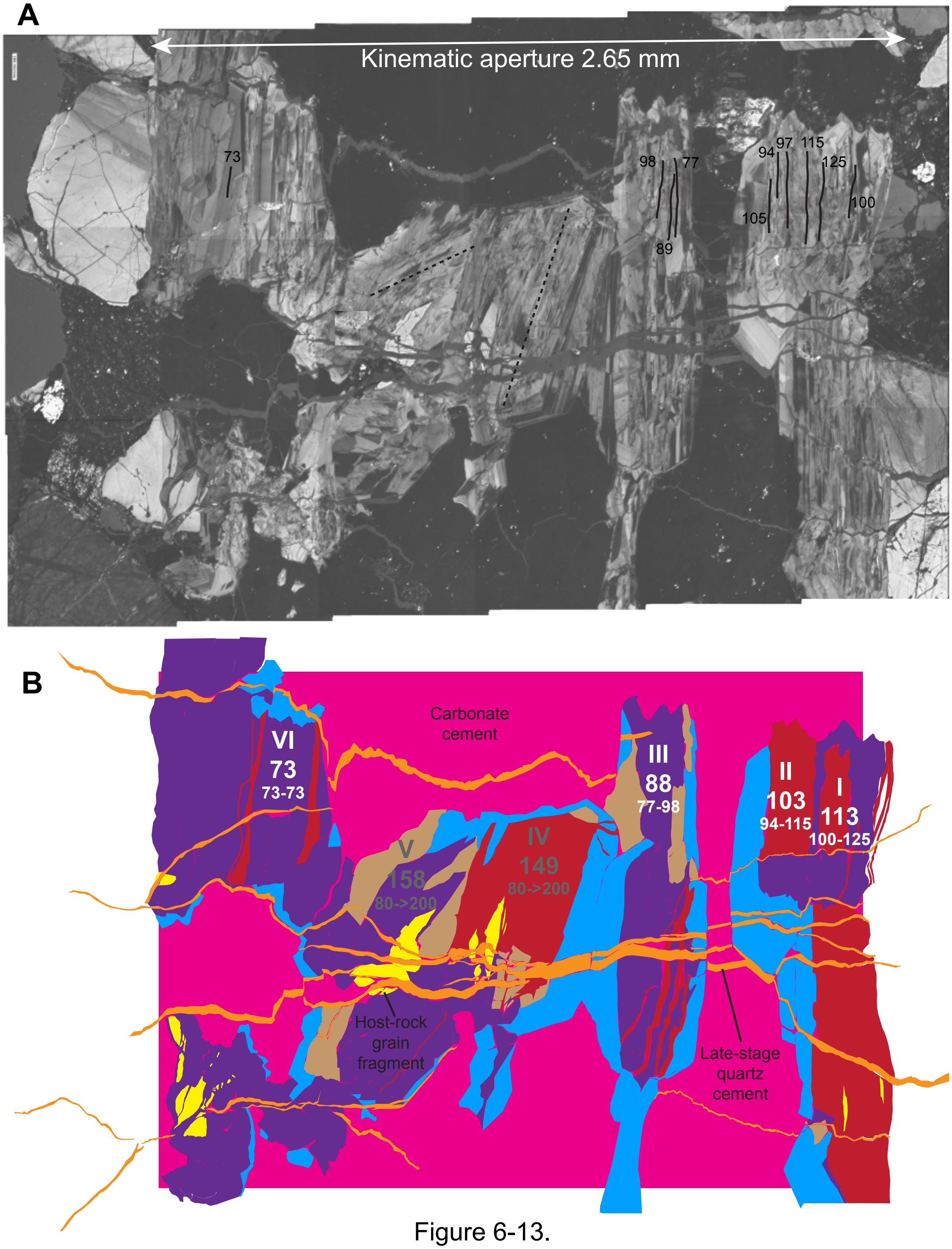
A
Kinematic aperture 2.65 mm
73
98
77
89
94
97
115
125
105
100
B
Carbonate cement
VI
73
73-73
V
158
80->200
IV
149
80->200
III
88
77-98
II
103
94-115
I
113
100-125
Host-rock grain fragment
Late-stage quartz cement

Figure 6-13.

Figure 6-13 continued. (A) SEM-CL mosaic of Macrofracture 2 quartz bridge. Quartz luminesces gray; carbonate is dark. Note host-rock grains at margins. Lines delineate FIA locations, numbers are average T_h for each FIA. (B) Interpretation of the relative timing regions, I through VI, with average T_h mapped. Regions IV and V appear rotated out of place with respect to the rest of the crack-seal increments; also they include anomalously high (>200°C) T_h for individual inclusions.

oriented at an angle of roughly 18 degrees (Region IV) and 65 degrees (Region V) to the overall fracture strike. Moreover, the T_h values I measured within these two regions are, on average, much hotter than those from Regions I, II, III, and VI (Figure 6-14). In the Discussion I interpret the cause of the anomalous orientations and T_h (and T_t) values within Regions IV and V.

Microfractures

Homogenization temperatures of fluid inclusions within microfractures overlap with those from macrofractures (Figure 6-10). Unlike macrofractures, in most cases it is not possible to constrain the relative timing between individual microfracture opening increments, because lateral bridge deposits are absent.

FLUID CHEMISTRY

Final-ice-melting temperatures

After heating, the Macrofracture 1 sample was cooled using liquid nitrogen in order to observe the final ice-melting temperature from inclusions. This allows constraint of the salinity of the fluid within the inclusions, in concentrations equivalent to dissolved NaCl (Figure 6-15). The relationship between NaCl-equivalent salinity and final-ice-melting temperature was best-fit to an equation derived by Bodnar (1993). As was the case with T_t, variation in NaCl-equivalent salinity is present within individual FIAs. As I discuss below, this consistent variation helps explain the source of the variation in T_h.

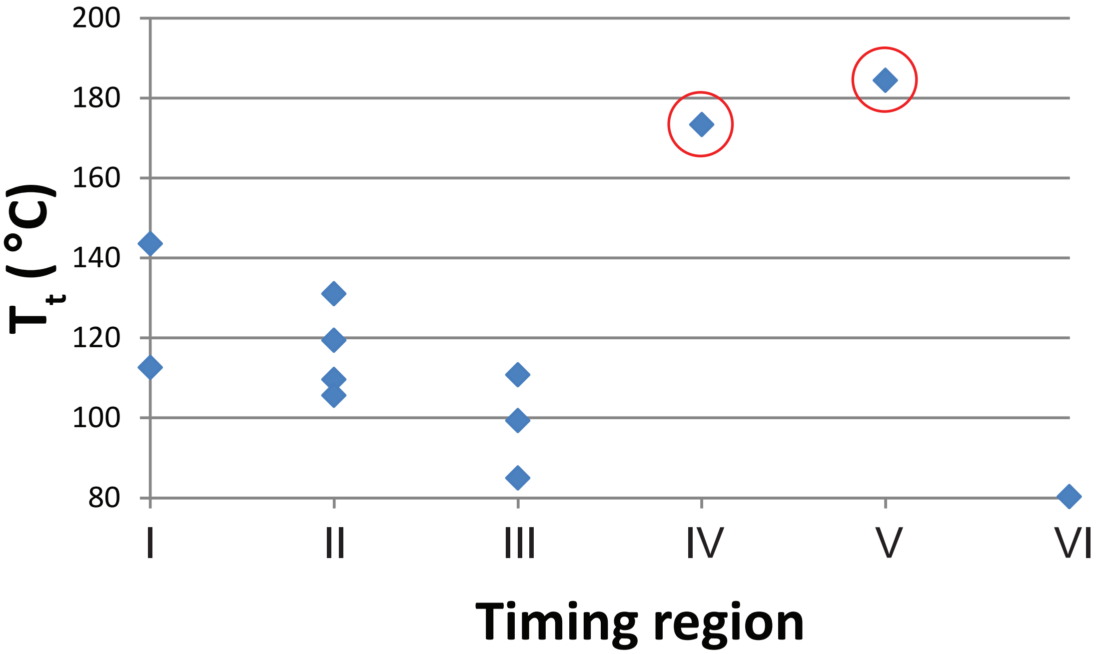

Figure 6-14. Homogenization temperatures from Figure 6-13, converted to trapping temperatures and plotted versus timing region. A decrease in temperature is apparent except in the two anomalous regions, IV and V. See text for discussion.

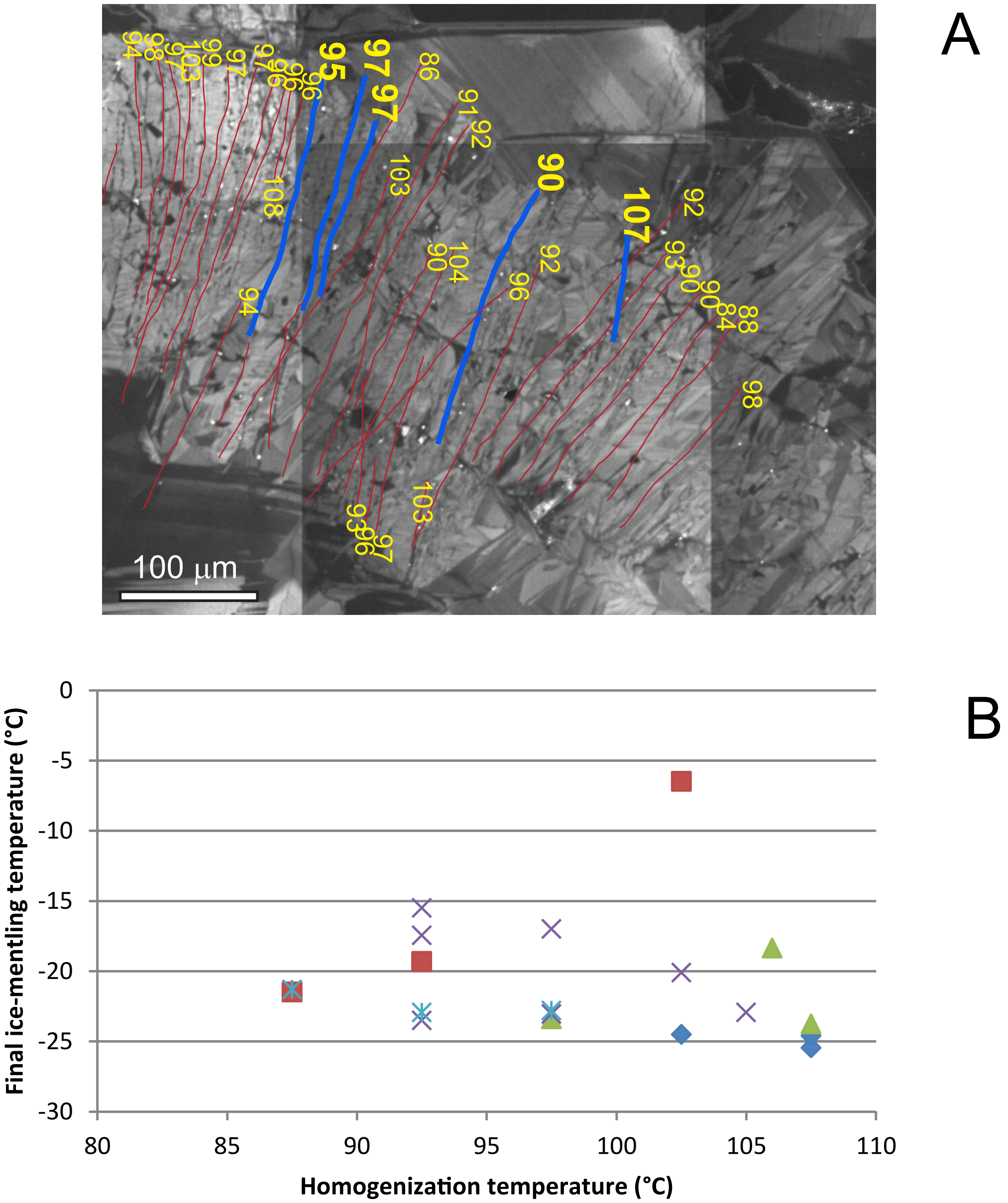

Figure 6-15. (A) Detail SEM-CL mosaic from Figure 6-10. FIA traces in blue represent where ice-melting data were taken. (B) Graph of final ice-melting temperatures versus homogenization temperature. Each symbol corresponds to a separate FIA in (A). Wide dispersion in homogenization temperature is matched by wide dispersion in final ice-melting temperature, and thus salinity.

The average final ice melting temperature measured within Set C cements is -20.7°C, which corresponds to an NaCl wt% equivalent salinity of 22.9%. Kaylor (2011) reported an equivalent salinity of 15% for Set B.

Quartz-fluid oxygen isotope fractionation

Measured $\delta^{18}O$ values are listed in Table 6-1. All data are reported in standard $\delta^{18}O$ notation relative to NBS-28 = 9.6‰. Samples analyzed include authigenic quartz from Set B and Set C; data were also collected from the host rock. Upon disaggregating fracture-filling quartz cement crystals it became apparent that some crystals were clear with euhedral facets and others were white with rough edges. These distinct colors and shapes likely reflect the presence of inclusions. The samples were separated by color (Table 6-1) in order to test whether $\delta^{18}O$ varies systematically with color. No consistent variation is present.

Average $\delta^{18}O$ values for Set B (18.71±0.1‰) and Set C (20.24±0.17‰) are 1.5‰ different from each other and are both heavier than the average $\delta^{18}O$ value of host rock quartz (15.52±0.18‰). These $\delta^{18}O$ values are based on average T_t calculated using all fracture-cement fluid inclusions analyzed. Average T_t is 176±21.6°C for Set B and 129±21.8°C for Set C. Fluid salinity increased from 15 wt% during Set B trapping to 22 wt% during Set C trapping.

The $\delta^{18}O$ value of quartz precipitated in quartz veins is dependent on the oxygen isotopic composition of the fluids it precipitated from and the temperature

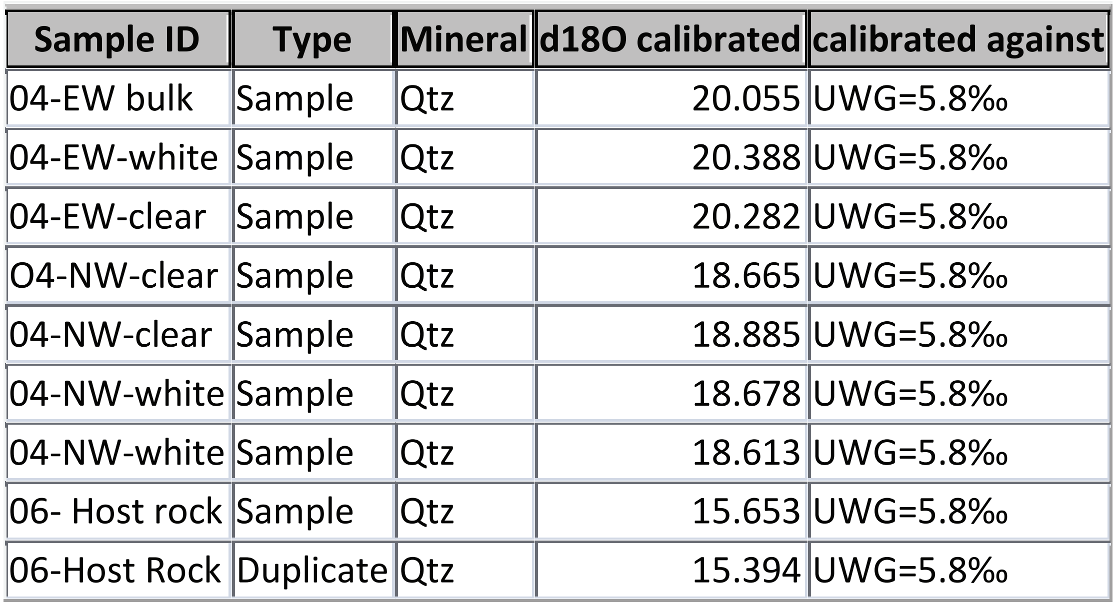

Sample ID	Type	Mineral	d18O calibrated	calibrated against
04-EW bulk	Sample	Qtz	20.055	UWG=5.8‰
04-EW-white	Sample	Qtz	20.388	UWG=5.8‰
04-EW-clear	Sample	Qtz	20.282	UWG=5.8‰
O4-NW-clear	Sample	Qtz	18.665	UWG=5.8‰
04-NW-clear	Sample	Qtz	18.885	UWG=5.8‰
04-NW-white	Sample	Qtz	18.678	UWG=5.8‰
04-NW-white	Sample	Qtz	18.613	UWG=5.8‰
06- Host rock	Sample	Qtz	15.653	UWG=5.8‰
06-Host Rock	Duplicate	Qtz	15.394	UWG=5.8‰

Table 6-1. Samples analyzed for oxygen isotopes. NW and EW refer to the strike of Set B (NW) and Set C (EW) fractures, respectively. Cement fragments appear white to clear, possibly from an abundance of fluid inclusions in the former, and were tested separately.

of precipitation. The temperature dependent equilibrium oxygen isotope fractionation between quartz and water has been experimentally determined (Clayton et al., 1972; Matthews and Beckinsale, 1979) and theoretically calculated (Kawabe, 1978). Quartz-water oxygen isotope fractionations (1000lnα = (1000+$\delta^{18}O_{Qtz}$)/ (1000+$\delta^{18}O_{Wat}$)), which are approximate ($\Delta^{18}O_{qtz\text{-}wat}$ = $\delta^{18}O_{Qtz}$-$\delta^{18}O_{wat}$) are illustrated in Figure 6-16 with respect to temperature.

Using the average T_t values from each fracture set with the quartz-water fractionation curve of Matthews and Beckinsale (1979) an estimate can be obtained of the $\delta^{18}O$ value of water in equilibrium with the precipitated quartz cement. These calculations yield $\delta^{18}O$ values of 5.68‰ (Set B) and 3.47‰ (Set C) for the water in equilibrium with the quartz cement.

VARIATION OF HOMOGENIZATION TEMPERATURE WITHIN FLUID INCLUSION ASSEMBLAGES

In most FIAs observed the requirement of a narrow range of T_h measured from multiple inclusions (Goldstein and Reynolds, 1994) is poorly met (Figure 6-9, Figure 6-10). Two possible interpretations of the wide variation in T_h among fluid inclusions within assemblages are 1) damaged or stretched inclusions, and 2) variation in the pressure, temperature, and or composition (P-T-X) of the fluids present during fracture opening.

T_h range interpretation 1: Secondary modification of inclusions after trapping

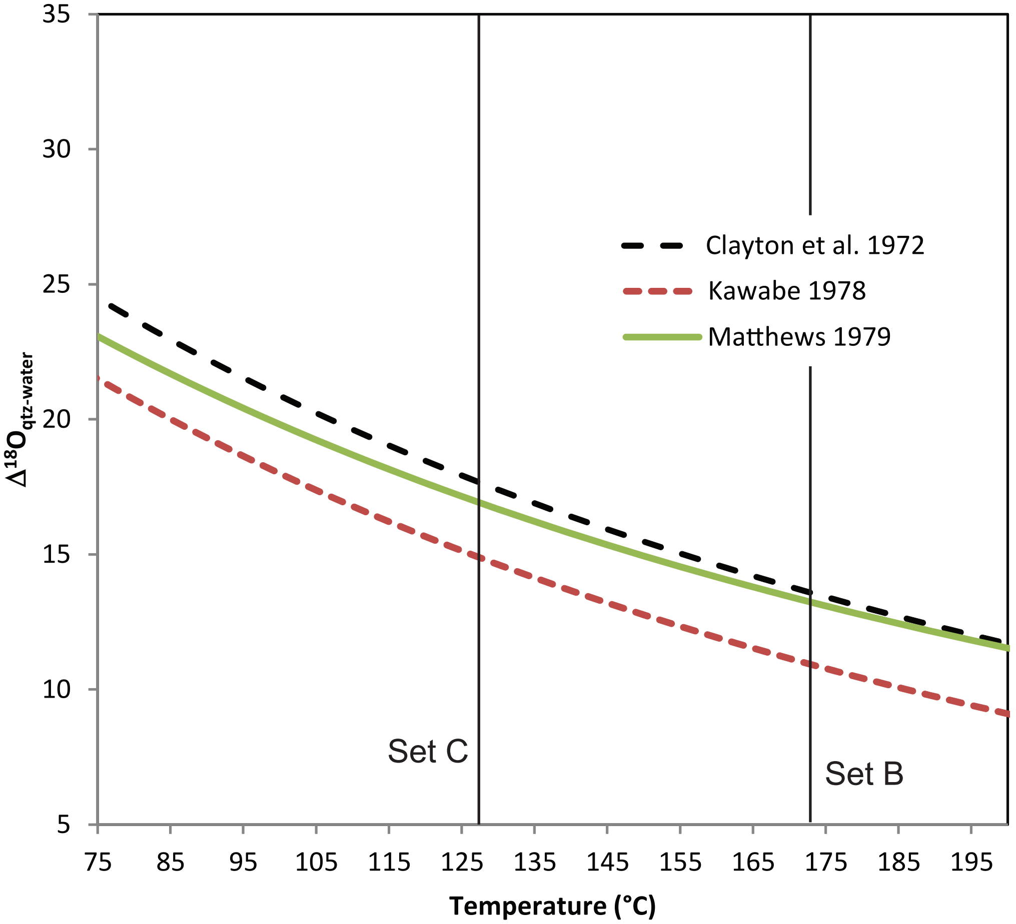

Figure 6-16. The difference in δ18O between water and precipitated quartz versus precipitation temperature, due to natural O-isotope fractionation. Having the temperature of fracture opening constrained and the δ18O of synkinematic quartz cement measured allows the calculation of δ18O of the precipitating water.

Fluid inclusion thermometry assumes the fluid composition and volume of the inclusions has not changed since trapping. Thus if fluid inclusions are damaged by shearing, stretching, excessive heating, or other processes, the resulting homogenization temperatures would not reflect the trapping conditions. In general the resulting T_h values would over-estimate the T_h that falls on the true isochore because damage would likely increase the volume of the inclusion. Thus minimum T_h values from assemblages of damaged inclusions may represent accurate temperatures or be closest to the true T_h. However, if this is the case a cluster of T_h values would be expected near the minimum observed value and a tail of higher values from increasingly stretched/damaged inclusions. Figures 6-9 and 6-10 do not show such a pattern in general. As well, although there is evidence of minor shear displacement along fractures (Figure 6-11, Figure 6-13), there is scant evidence for shearing or stretching of individual inclusions.

Similarly, if inclusions neck (i.e., divide into separate inclusions) after a vapor bubble nucleates, neither of the new inclusions will record the T_h of the original inclusion (Goldstein and Reynolds, 1994). The new inclusion that contains the bubble will have a higher T_h and that without will have a lower T_h. This problem can be diagnosed by different liquid to vapor volume ratios within fluid inclusions of the same assemblage. Such varying ratios are not typical among two-phase inclusions in this study. As explained above, the absence of bubbles within single-phase inclusions likely signifies a kinetic energy of bubble nucleation effect, and not stretching or necking of fluid inclusions. Moreover, significant necking is not likely within these samples because the vapor bubbles nucleate at low temperatures (<50°C—Figure 6-2), at which quartz dissolution/precipitation is minimal.

Fluid inclusion damage does not explain variation in salinity among inclusions within FIAs (Figure 6-15). Another symptom of FIA damage is a relationship between T_h and inclusion size. Larger inclusions may be more susceptible to stretching than smaller inclusions. No consistent variation is present between the long dimension of inclusions from Macrofracture 2 and the associated T_h values (Figure 6-17).

T_h range interpretation 2: High-frequency P-T-X variation during fracture opening

The expectation that all fluid inclusions within an assemblage have the same T_h is based on the idea that the assemblage was once a single, large inclusion that necked down into a series of smaller inclusions before forming a vapor bubble (Figure 6-18a). This ideal case might not hold for these samples. If the fracture surface is irregular and/or the sealing process uneven (Figure 6-18b), fluid inclusions that form along a single plane may not be the result of necking down of a parent inclusion but may have formed at different times. If the

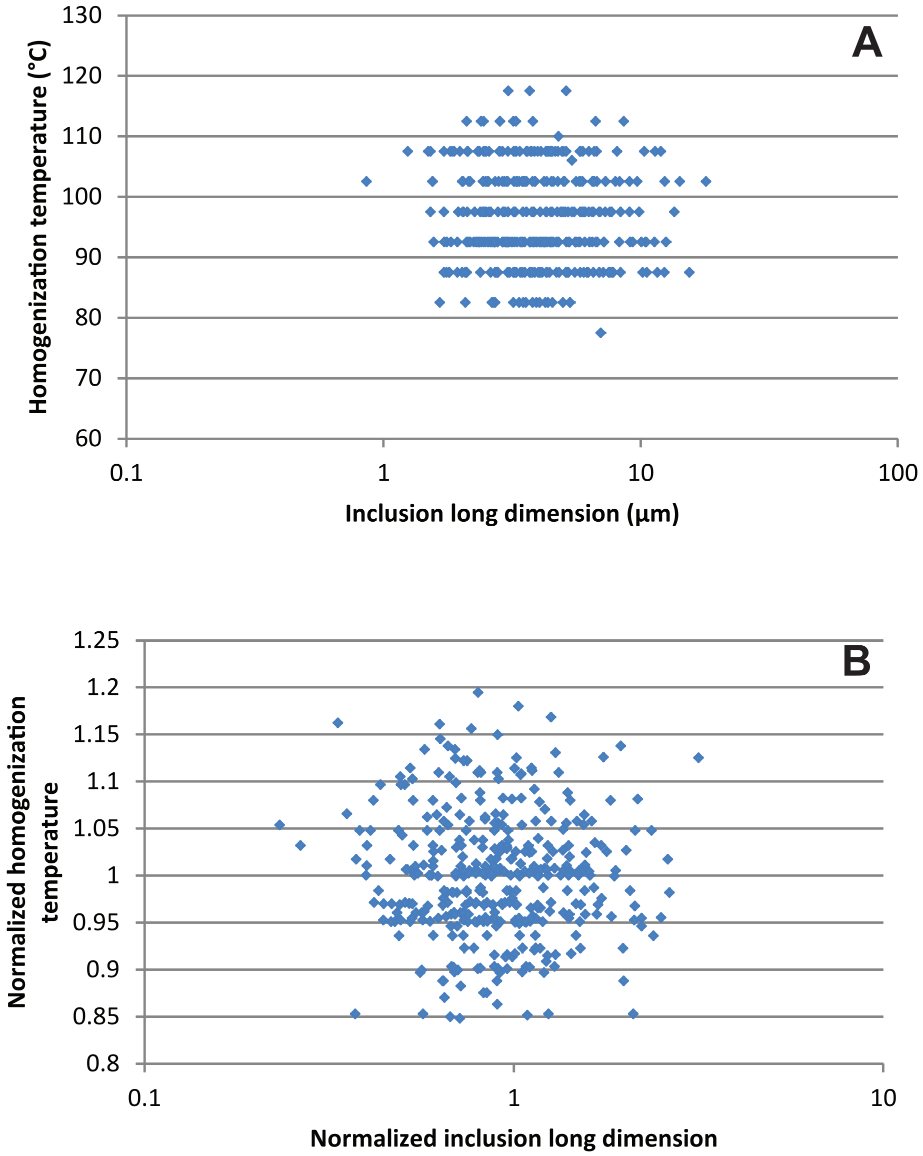

Figure 6-17. T_h versus fluid inclusion size. A correlation between fluid inclusion size and T_h may indicate damaged inclusions. (A) T_h versus longest dimension across fluid inclusion. No systematic correlation is present. In order to test whether some variation is present within fluid inclusion assemblages, normalized T_h (T_h divided by average assemblage T_h) is plotted (B) versus normalized long dimension (inclusion size divided by assemblage-average inclusion size). Again no systematic trend is evident.

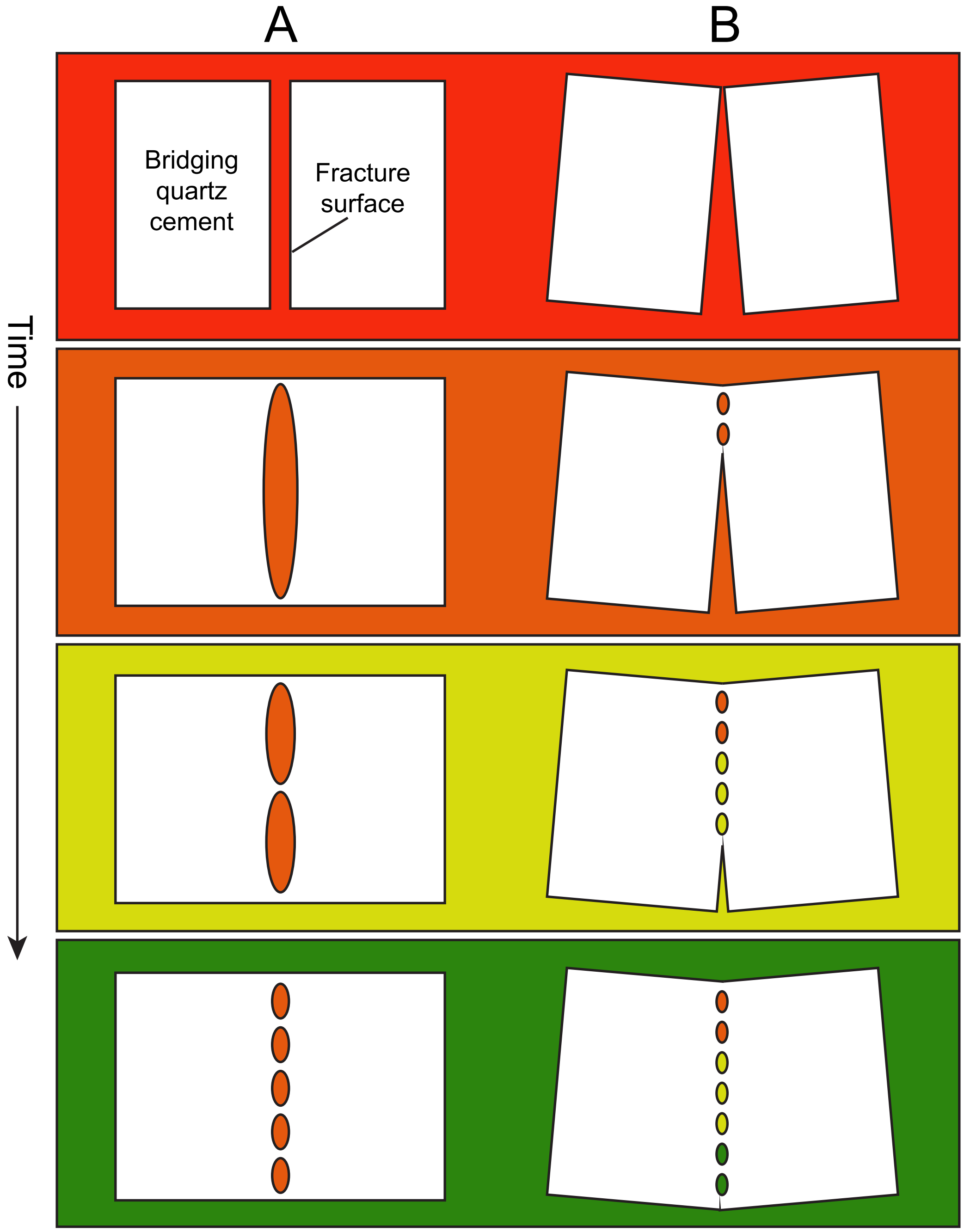

Figure 6-18. Real variation in fluid P-T-X conditions might be manifest in fluid inclusion assemblages by a sweeping or scissoring-style of bridging cement sealing. Background color varies with fluid P-T-X. (A) Ideally, a large, single, parent inclusion traps fluid and later necking creates multiple fluid inclusions with the same composition. (B) If assemblages do not come from the same single parent inclusion, as for example by an uneven sealing plane, variation in fluid P-T-X during sealing could result in variation in T_h within the assemblage.

fluid P-T-X conditions oscillated over time scales comparable in duration to that of fluid inclusion sealing, such P-T-X oscillations might be recorded within fluid inclusion assemblages. If such variation is present in temperature, it is present on a finer scale than that described by the burial history curve.

Similar variations of T_t within microfracture FIAs were attributed to partial reopening without a preserved cement precipitation record by Xu (2012). Such a reopening process may apply to these fractures as well, and be difficult to diagnose within preserved cements. The study by Xu (2012) was of fractures within the Cambrian Eriboll Formation, which has experienced a more complicated burial history (Laubach and Diaz-Tushman, 2009), and thus more fracturing episodes, than has the El Alamar Formation.

Thus P-T-X variation better explains the variation in T_h (and T_t) for the samples in this study. As such, an uncertainty of timing for a given observed temperature must be recognized. The magnitude of this uncertainty is equivalent to approximately ±10°C in temperature uncertainty (based on the range in T_h observed within FIAs). Consequences of this uncertainty on the test of the fracture simulation (Chapter 5) are discussed below.

The anomalously high T_h measured within timing regions IV and V of Macrofracture 2 require an alternate interpretation. These regions feature a cryptic CL texture (Figure 6-13) whose crack-seal bands appear rotated with respect to the other crack-seal bands in the fracture and the fracture walls. As well, variation of over 100°C is present among fluid inclusions within these regions (Appendix D). Individual FIAs are typically not discernible. It may be that minor shearing along Macrofracture 2 was focused near this mid-region of the bridge and thereby locally damaged the inclusions. Alternatively, these cements could have been deposited amid a local heat anomaly not recorded by any other fractures. In either case the temperatures present in this part of the bridge are not representative of fracture-opening temperatures for Set C, and thus are omitted from further analysis.

FRACTURE OPENING HISTORY

The observed range in T_t for Set C is narrow compared to the overall range of temperatures likely experienced by the rock based on the overall burial history and likely geothermal gradients (Figure 6-4). If the observed trapping-temperature range represents the true ambient fluid temperatures during fracture growth, then T_t can be used to constrain the timing of fracture opening using the burial history curve.

The ambient burial temperature experienced by the El Alamar Formation matches the observed T_t range during two intervals of geologic history (Figure 6-19). One period is during progressive burial of the El Abra Formation; the other is during exhumation. For two reasons it is likely that Set C formed during exhumation. First, Set C cuts Set B. Laubach and Ward (2006) interpreted set B to be related to regional tectonics and folding based on kinematic considerations.

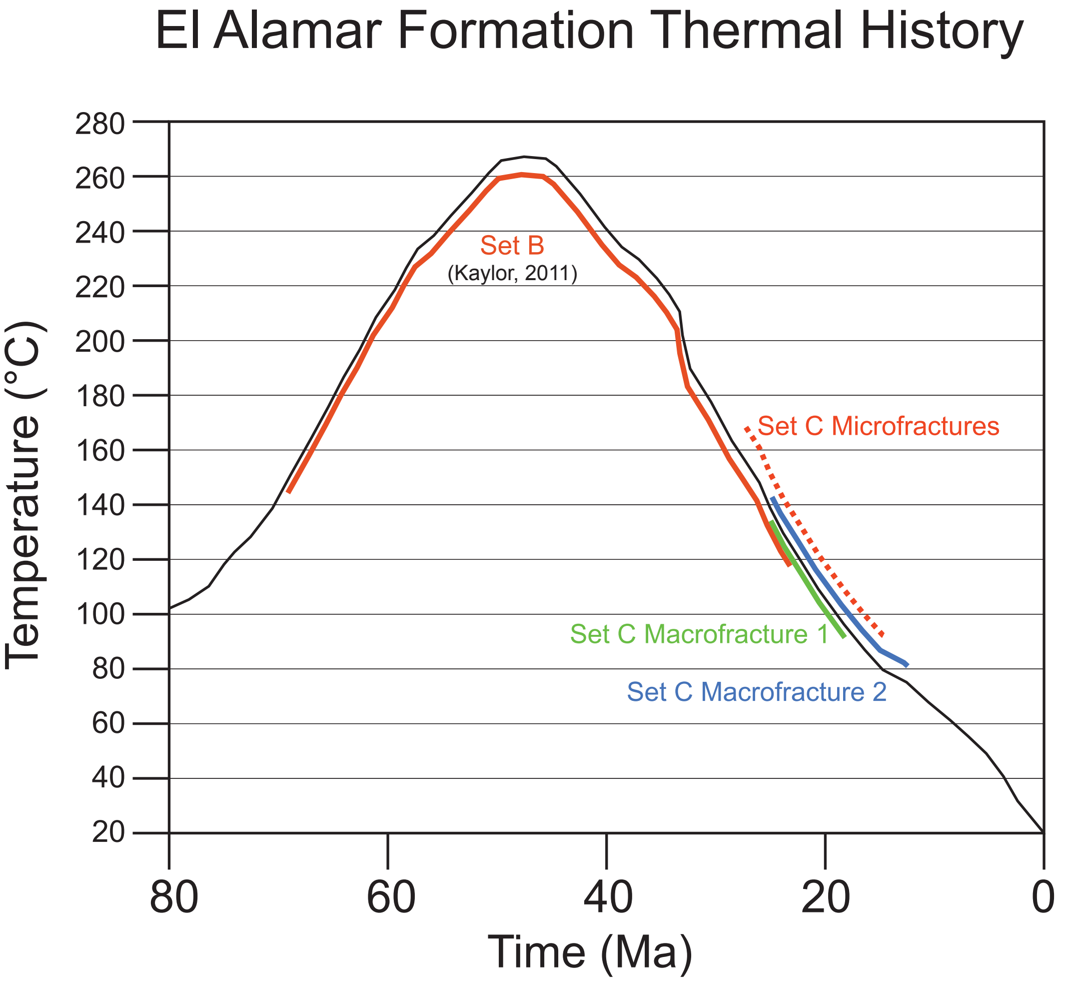

Figure 6-19. Burial history curve from Figure 6-4 with interpreted ages of fracture opening, based on T_t. Fracture opening ages assume the average T_t for an FIA indicates its position on the curve and that high-frequency changes in P-T-X, not visible at the resolution of this diagram, are responsible for variation in T_t within FIAs.

Fluid inclusions in sets B and C show that Set B formed amid hotter temperatures than Set C (Laubach and Ward, 2006; Kaylor, 2011), as would be the case if set B formed near maximum burial. Second, the results from the technique combining macrofracture cement bridge mapping and fluid inclusion analysis shows a cooling trend over time (Figure 6-12, Figure 6-14).

Average T_t within an FIA can provide an estimate of fracture timing via placing the corresponding opening increment on the burial history curve (Figure 6-19). If evidence were present of fluid inclusion damage or post-bubble-nucleation necking, then *minimum* T_t would provide a better timing estimate. Lacking such evidence of damage or necking, and given the consistency between average T_t for FIAs within Microfracture 1 and the progressive exhumation following the opening of Set B (Figure 6-19), average T_t provides the best estimate for timing of fracture opening.

Cement precipitation kinetics

A possible objection to the interpreted timing ranges shown in Figure 6-19 is that although Macrofractures 1 and 2 record a cooling trend, this trend might correspond to a short-term cooling event not accounted for within the burial history curve. However, the thickness of cement present on the margin of the Macrofracture 1 bridge is consistent with tens of millions of years of accumulation. Assuming cement precipitation is limited by kinetics (Walderhaug, 1994), then quartz precipitation rates can be calculated using the Arrhenius equation (Lander et al., 2008):

$$k = A_{\circ}\, e^{\frac{-E_a}{RT}} \qquad (6\text{-}1)$$

where *k* is the quartz precipitation rate, in mol/cm^{2}s; A_o is a constant (here 9x10^{-12} mol/cm^{2}s), E_a is the activation energy for quartz precipitation (here 60 kJ/mol); *R* is the universal gas law constant (8.31 J/mol K); and *T* is temperature (K). Using Equation 6-1 to calculate the precipitation rate parallel to the c-axis, on a 1 mm^2 non-euhedral surface, at a maximum T_t of 175°C, the result is approximately 46 μm/m.y. Thus at this maximum quartz precipitation rate, the ~300 μm-thick euhedral cement deposit along the Macrofracture 1 bridge would have taken ~6.5 m.y. to accumulate. Experimental work by Lander et al. (2008) suggests that the precipitation rate parallel to the a-axis is roughly 17% of that parallel to the c-axis, and that accumulation rates on euhedral surfaces are up to 20 times slower than those on non-euhedral surfaces. Both of these effects combined result in a required deposition time of ~767 m.y. for the euhedral cement deposit along the Macrofracture 1 bridge to accumulate. This time span is longer than the history of the rock, suggesting either that the measured thickness of the margin is not parallel to the a-axis, or the euhedral-rate effect is not as dramatic in this case. Nonetheless, this approach to cement precipitation modeling suggests a very protracted fracture opening history.

Uncertainty in fracture timing from fluid migration

The consistently lower FIA-average T_t present among later opening increments within the two macrofractures analyzed indicate an overall decrease in temperature as the fracture set grew. However, because of variation in T_h it is likely that a specific opening temperature does not uniquely constrain the timing of fracture opening. Indeed, limited precision of the time-temperature history and incomplete recording of fracture opening will result in multiple opening histories that will satisfy the data. This non-uniqueness of process reconstructions is inherent in any inverse model with imperfect data and or imperfect matching between data and model (Ketcham, 2005; Woodward, 2012).

A primary uncertainty within the data collected here comes from the high spread of T_h within individual FIAs. Though such a spread can result from stretching of inclusions, in this case the spread is better explained by fluid migration during fracture opening, because of varying freezing temperatures, and thus salinity, among inclusions in the same FIA (Figure 6-15). The small-scale variation in T_h (i.e., the noise in the cooling signal apparent in Figures 6-12 and 6-14) can be explained by oscillation in fluid P-T-X brought about by fluid migration during fracture opening. Such oscillation occurred at a time scale finer than that established by the burial history curve (Figure 6-4). Fracture opening may actually facilitate fluid migration (Eichhubl and Boles, 2000; Fall et al., 2012).

The general fluid-migration pattern can be investigated using the oxygen isotope results. Setting aside short-term noise and using average T_t, Set B opened early at a temperature near 176°C; Set C opened later at a temperature near 129°C. In principle such temperatures could have locally been reached during Lower-Jurassic-age igneous intrusion of the sandstone; however, the timing interpretation shown in Figure 6-19, based on the regional burial history curve, is more likely, for two reasons. First, no igneous intrusions are present in the observed layers (the El Alamar Formation); quartz-lined fractures crosscut igneous intrusions upsection in the La Boca Formation (Laubach and Ward, 2006). Temperature effects from igneous activity would likely be restricted to the immediate vicinity (meter-scale) of the intrusions, even in relatively permeable rocks (Parmentier and Schedl, 1981; Dutrow et al., 2001). Second, the isotopically heavy (positive $\delta^{18}O$) water from which the quartz cement precipitated also suggests a deep brine with long residence reacting with host rock rather than early meteoric or oceanic water, which should range from 0 to -15‰ (Longstaffe and Ayalon, 1991). Therefore the fractures likely formed during (Set B) and after (Set C) the peak of Laramide-age deformation of the study area.

Between the opening of Set B and Set C the pore fluids achieved a higher salinity and a lower $\delta^{18}O$. The decrease in $\delta^{18}O$ is consistent with the effects of uplift within (Longstaffe and Ayalon, 1991). The proposed mechanism was the downward infiltration of isotopically light meteoric and or oceanic water during uplift. If this was the case in the SMO, the light water would still have had to infiltrate through the overlying gypsum and anhydrite of the Zuloaga Group (Barboza-Gudiño et al., 2010), potentially explaining the increased salinity. This interpretation is also consistent with very high salinities (up to 34 wt% NaCl equivalent) in vein-cement fluid inclusions from siliciclastic units overlying the Zuloaga Group (La Casita Formation) in the northern Sierra Madre Oriental (Fischer et al., 2009). Thus in the El Alamar Formation, Set B opened near maximum burial, during which the pore waters had relatively little communication with overlying evaporites. Set C opened afterwards, during uplift and increased input from high salinity, isotopically light pore water. The uplift and or percolation of lighter water into the system was likely unsteady, resulting in the small-scale variation in P-T-X and thus the observed T_h of synkinematic fluid inclusions.

Fischer et al. (2009) used fluid inclusion temperatures and salinities to demonstrate that the Cretaceous beds exposed in the Nucios Fold Complex, about 150 km to the northwest, featured a highly stratified paleohydrology. Permeability barriers at three major formation boundaries are believed to have been more important hydrodynamic barriers than tectonic structures. Relative to the variations in salinity presented by Fischer et al. (2009), which range from nearly freshwater at the top of the section to very high salinities (34 wt% NaCl equivalent) at the bottom of the section, the difference between Set B and Set C in the El Alamar Formation is subtle. Nonetheless, uplift appears to have accompanied an increase in hydrologic communication between the El Alamar

Formation and overlying strata. The relative importance of stratigraphic permeability barriers this low in the stratigraphy and or at this geographic location is unclear. However, the data are consistent with significant hydrologic stratification which was affected by uplift.

IMPLICATIONS FOR THE FRACTURE GROWTH SIMULATION

Consistent with the model presented in Chapter 5, it is apparent that the E-W striking fractures grew over extended periods of time and their growth histories overlap. Plotting the T_t ranges of the two macrofractures on the exhumation segment of the burial history curve (Figure 6-19) suggests that the Macrofracture 1 opened between 25 and 18 Ma; Macrofracture 2 opened between 25 and 13 Ma. Thus the accumulation of fracture strain was a distributed and gradual phenomenon, allowing ample time for fracture interaction during growth (Olson, 1993; Cladouhos and Marrett, 1996; Renshaw and Park, 1997; Davy et al., 2010).

The opening history preserved in synkinematic fracture cements presents several implications for how Set C evolved. Ignoring for the moment the small-scale variation in pore-fluid P-T-X during fracture opening, the fractures opened during exhumation and cooling of the host rock. Thus a reasonable simplification is that cooler T_h values correspond to later opening/sealing events. Assuming that temperature linearly decreased over time, a time-series can be made using the average T_t of individual FIAs to illustrate the sequence of fracture opening

(Figure 6-20). This representation is analogous to Figure 5-32, showing the opening of simulated fracture increments over time.

Importantly, for most fractures studied the entire range of T_t is not constrained. Part of the reason for incomplete opening reconstruction is that not all crack-seal increments feature two-phase fluid inclusions. In particular, the regions near the fracture walls of Macrofracture 1 (Figure 6-11) are not interpretable using my methods. CL relations indicate that these parts of the fracture opened early, before sufficient intra-bridge pore space developed and allowed marginal euhedral cement to accumulate. Later these bridges were abandoned as the fracture opening became too fast for cementation to keep up, except within the main bridge segment. Blue lines in Figure 6-20 represent regions wherein significant fracture opening is present but no data are available.

Simulated and natural growth processes

By comparing Figure 6-20 and Figure 5-32, some qualitative similarities can be inferred between the simulation and the natural fracture data.

Attraction of growth increments to large fractures

In the simulation, fractures grow to large (macroscopic) sizes by being selected with anomalous frequency, compared with typical fractures. This is consistent with the opening history preserved within Macrofracture 1, compared to that of most observed microfractures. Throughout the time span over which

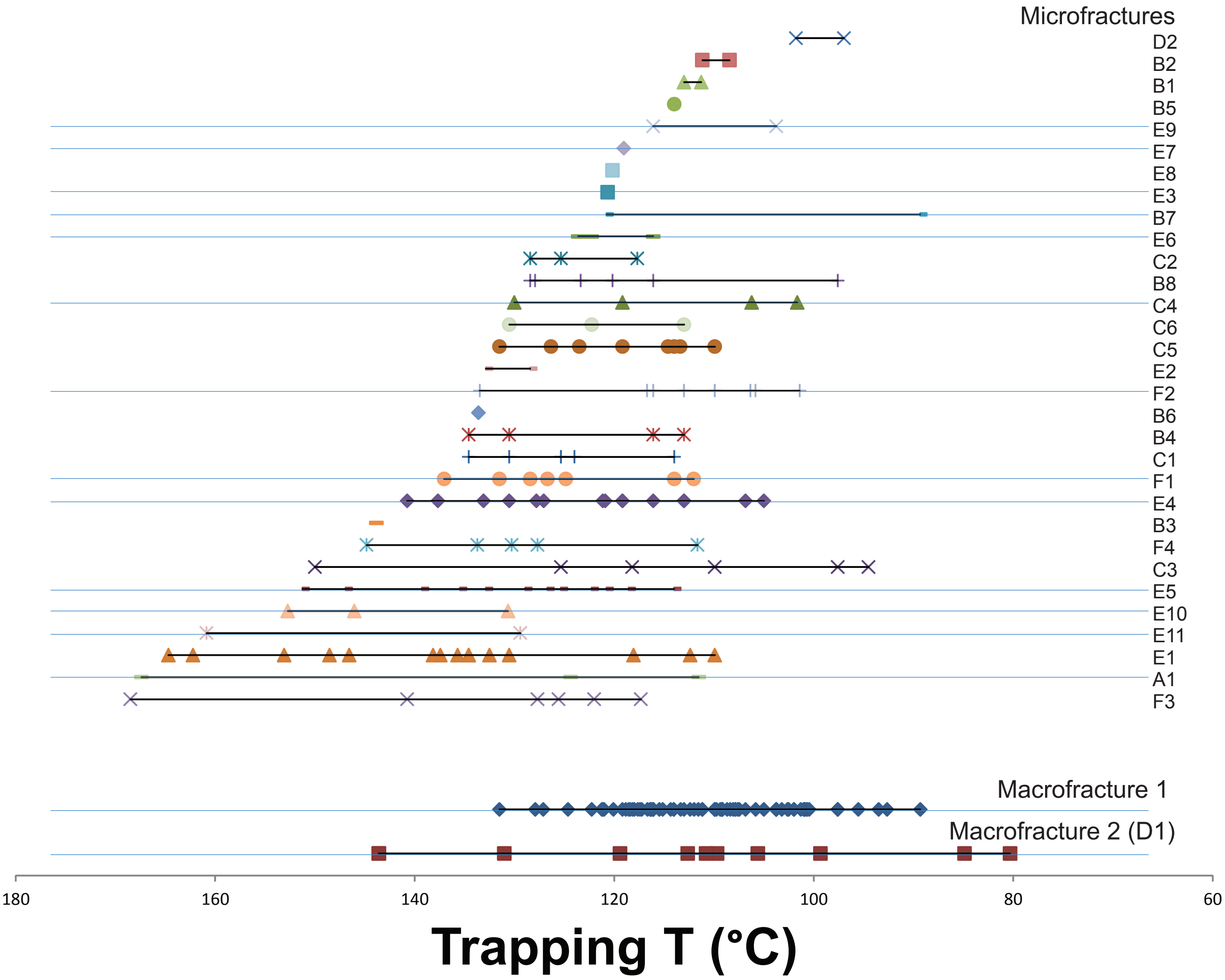

Figure 6-20. Ranges of T_t (average of FIA) observed from each Set C microfracture and macrofracture. Because Set C formed during exhumation, and assuming average FIA temperature reflects the fracture increment's position on the burial history curve, T_t is a proxy for time, with more recent fracturing events plotting towards the right. Blue lines indicate fractures haveing significant opening that is not recorded by two-phase inclusions, and therefore not plotted. Microfracture ranges are sorted by maximum T_t, or earliest observed opening increment. Thus the figure is analogous to Figure 5-32.

Macrofracture 1 opened 78 times, no other observed fracture's history comprises more than 11 increments.

In contrast, Microfracture B3 formed early in the fracture-set evolution. Where fluid inclusions were analyzed, this fracture contains two opening increments (Figure 6-21). One of the two featured two-phase inclusions, from which an average T_h of 125°C was recorded; the other increment preserves no two-phase inclusions. Regardless, half of the opening of this fracture is constrained to a time early in the evolution of Set C. Though the other half of the opening has unknown timing, it is clear that microfractures may form early on in the set evolution and grow very little or not at all afterwards. Most microfractures, however, are apparently long-lived (for example, Microfracture F3) with long gaps in between reactivations. It is important to reiterate that the fluid inclusion record preserved within fractures is never complete; observed fractures may have been growing in different locations than that sampled. Therefore the lack of *observed* growth does not definitively suggest fracture quiescence.

Continual introduction of microfractures

The hottest (earliest) opening increments of microfractures span the T_t range of the Set C fractures, suggesting that new microfractures form continually throughout deformation, assuming the thermal history is simple and representative; i.e. that no anomalous fracture-opening events occurred that went unobserved in this analysis. Also in agreement with the simulation, there is

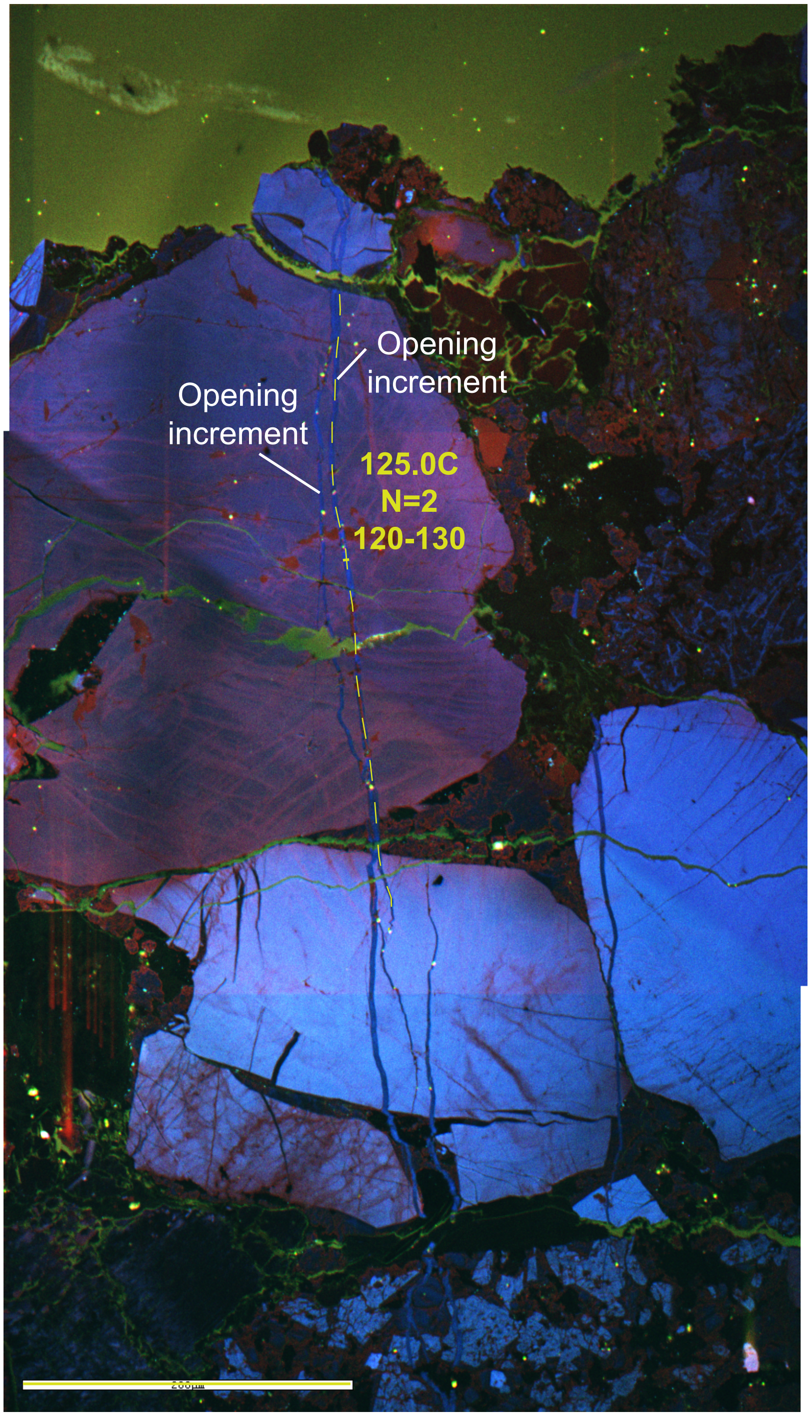

Figure 6-21. SEM-CL image of Microfracture B3, including average T_h, number of inclusions, and T_h range. Both inclusions are preserved within the opening increment on the right (dashed line).

a low probability that new microfractures, formed amid a population of actively growing macrofractures, will grow to macrofracture size, unless considerable fracture strain accumulates after nucleation. In this respect Figure 6-20 can be misleading in that the data suggest that Macrofracture 1 formed later than many of the microfractures, but again, no record was preserved for much of the early opening of Macrofracture 1.

Effects of temperature-time uncertainty on simulation test

The above comparisons, being based on Figure 6-20, do not take into account the ±10°C in temperature uncertainty associated with fine-scale P-T-X variation. This uncertainty may mask various short-term patterns of fracture opening. Normally such uncertainty could be represented by error bars, but error bars are difficult to represent on Figure 6-20. (Moreover, if the ±10°C variation reflects true temperature variations, the variation would not be an error but rather would reflect higher-frequency temperature variation than is shown on the burial history curve.) Another way to address the effects of this uncertainty on the claims made above (that macrofractures attract opening increments with anomalous frequency, and that microfractures form throughout) is to re-plot Figure 6-20 repeatedly, with random variation simulated by adding a random number to each T_t between -10 and 10. These new T_t figures can then be replotted in the same way as in Figure 6-20, after re-sorting the data fractures by the (new) hottest opening temperature (Figure 6-22).

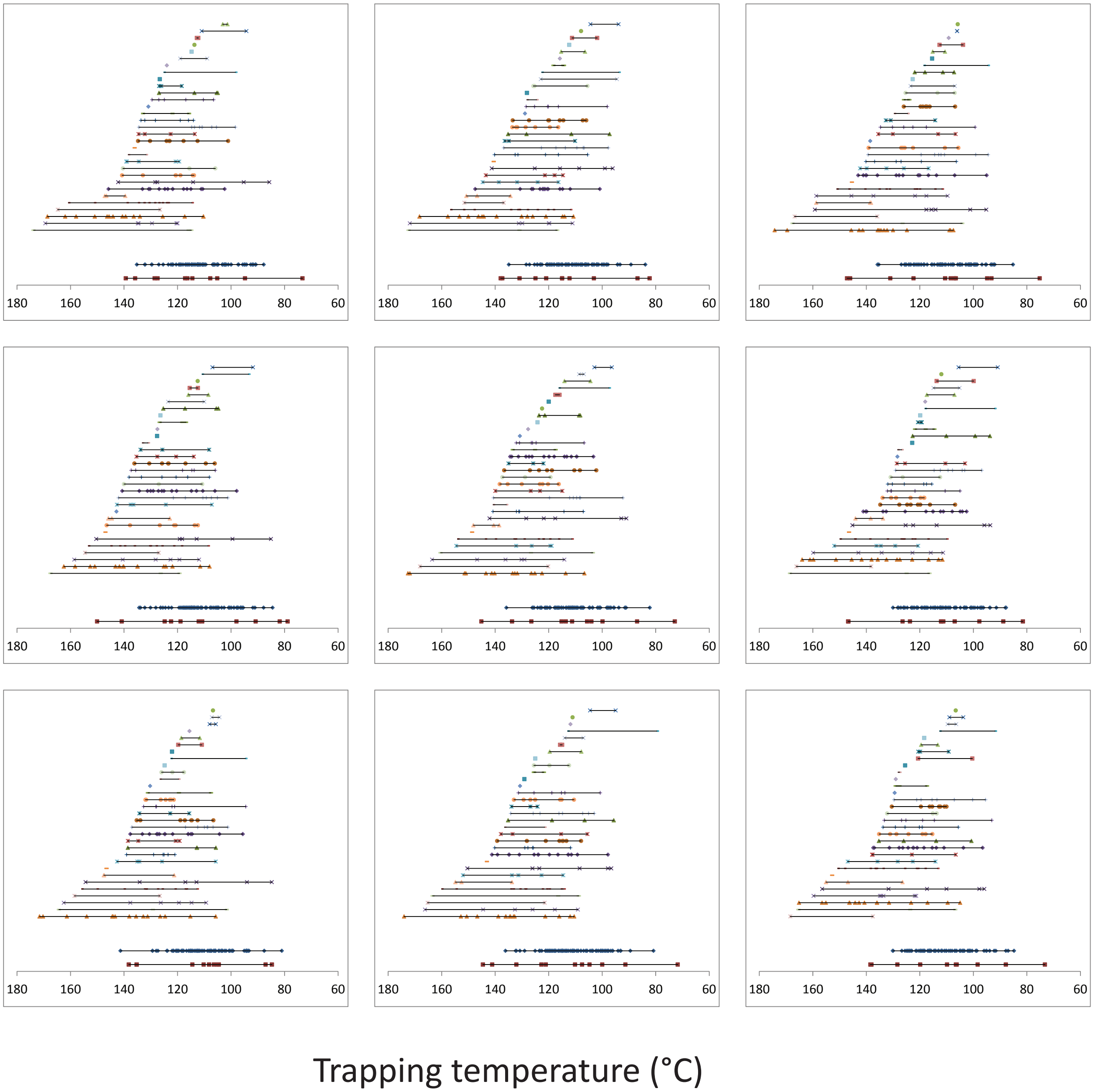

Figure 6-22. Data from Figure 6-20, replotted after accounting for ±10°C uncertainty. To each datum is added a random number between -10 and 10. The microfractures are then re-sorted by hottest (earliest) opening increment. See text for discussion.

Each randomization of the data shows early-forming, short-lived microfractures as well as microfractures reactivated after long periods of quiescence (Figure 6-22). The added uncertainty does not significantly change the T_t range over which the macrofractures opened; thus the data still support high-frequency opening of large fractures amid low-frequency opening of small fractures. One interesting consistent feature is the apparent non-steady introduction of microfractures (with the caveat that not all microfracture opening increments are included). As plotted on most randomizations, the data suggest a faster rate of microfracture introduction once the fluid temperature cooled to ~150°C. This range also coincides with most of the recorded growth within Macrofracture 1. Thus it is possible that the strain rate was not constant over time. This observation is not definitive, because alternatively, this temperature range may simply be better represented by two-phase fluid inclusions and not mark more extensive opening. This idea could be further tested on a fracture set with a more complete fluid inclusion record.

Fracture growth and spatial arrangement

The statistical simulation does not model the spatial arrangement of fractures, but there is possibly some systematic variation in temperature versus scanline position (Figure 6-23). Consistent with the observation that individual fractures appear to undergo periods of heightened activity, *clusters* of fractures in space may also form contemporaneously. Fractures within thin sections A, E,

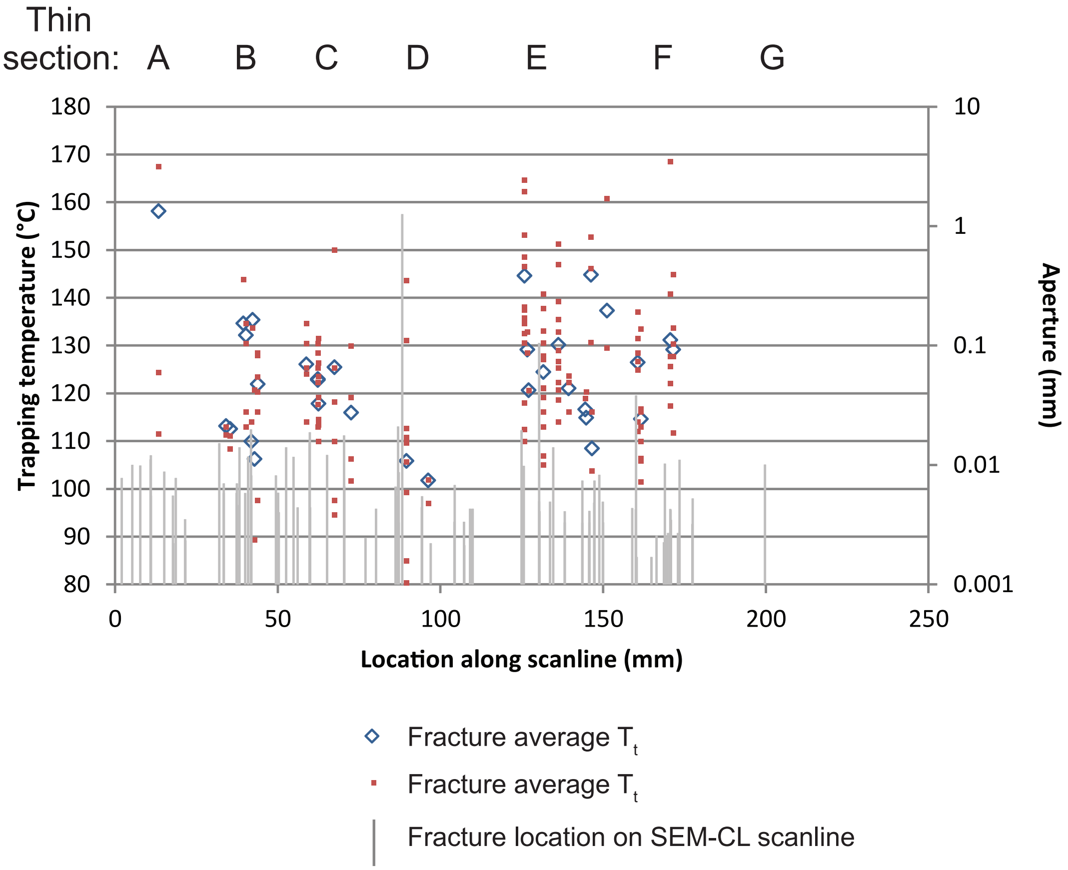

Figure 6-23. T_t for each FIA versus position along scanline, Set C microfractures.

and F appear to have formed under overall hotter temperatures, and therefore likely earlier. The apparent cluster of fractures within thin sections B, C, and D may represent a period of localized strain. This idea is consistent with the idea that newer, less-cemented fractures serve as attractors for later fracture opening increments. While a fracture is open (and relatively young) it may attract other fractures to form near it, or in connection to it; as the fracture fills with cement its propensity to attract other fractures is decreased.

Temperature and opening-increment width

Fracture opening increment sizes are characteristic, and do not systematically increase with decreasing temperature and age (Figure 6-24). Moreover, the widths of individual opening increments appear to be independent of overall fracture width. Holding rock type constant, other aspects such as temperature might influence the width of an opening increment, and in the present case of progressive cooling, it is conceivable that opening-increment width would decrease; likewise, the hypothetical effects of overall fracture size and temperature may compete against one another. Therefore an ideal test of the claim that fracture opening-increment widths do not increase as fractures grow would be better tested using the same fluid inclusion and CL analysis but on a fracture set that formed during progressive burial. Nonetheless, the fracture growth pattern documented here would be best simulated using characteristic, non-increasing fracture-opening increment sizes.

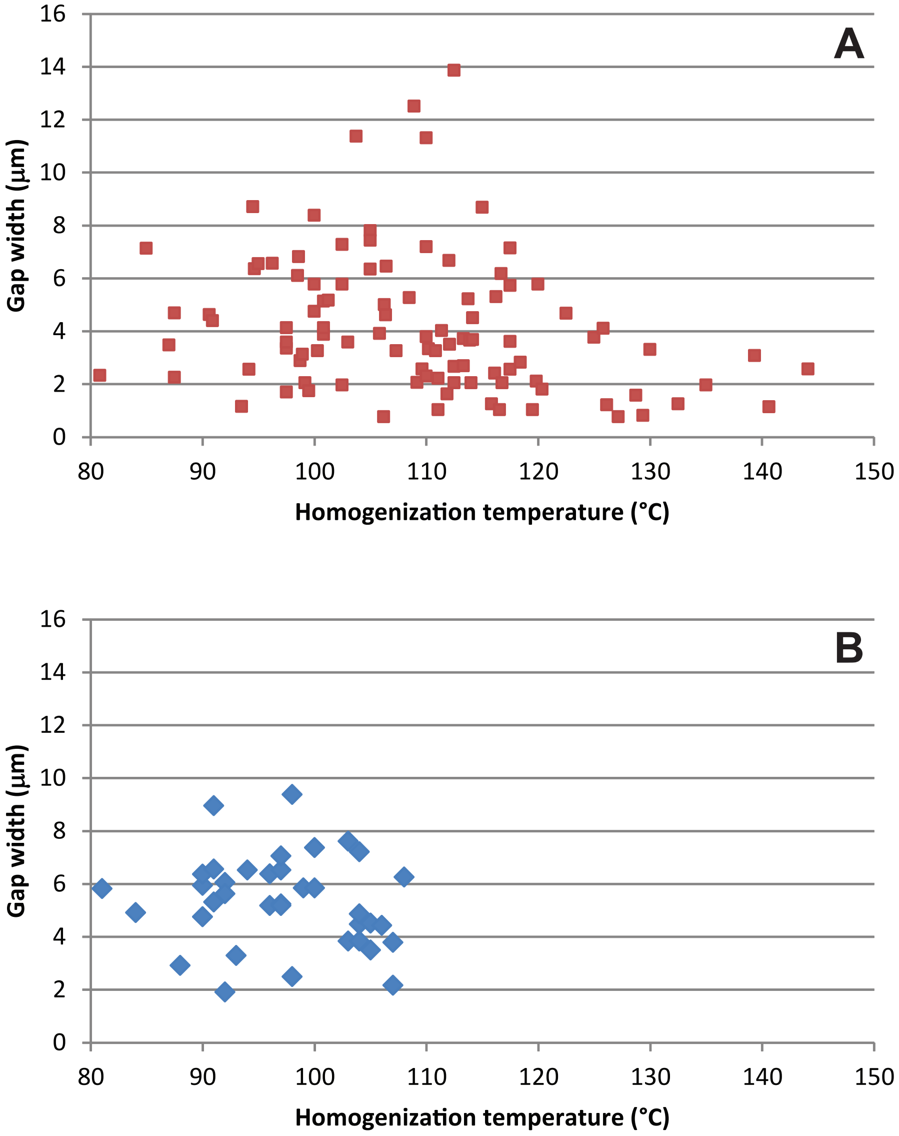

Figure 6-24. Fracture opening-increment width versus T_h, for scanline fractures (A) and Macrofracture 1 (B). Widths for opening increments with unclear or variable boundaries are omitted.

Effects of decreasing cementation rate

Because the Set C fractures formed during exhumation, their growth might best be simulated assuming a decreasing cementation rate. The statistical simulation thusly modified can be compared to the observed natural fracture-size distribution (Figure 6-25). This execution of the simulation consists of 200 total fractures at five iterations per new fracture, and starting with ten extant flaws (Chapter 5). Beginning the simulation with the cementation exponent, C, equal to 1.5 and decreasing by 0.05 every 50 iterations so as to end at C=0.5, the first half of the simulation features an exaggerated tendency for large fractures to grow. Midway through the simulation the cementation rule is unmodified from the original simulation permutation (i.e., selection probability is linearly related to current fracture size). By the end of the simulation, with C<1, the selection process is relatively egalitarian. Thus early on in the simulation a small subset of fractures grow and outpace the rest. Later, under slower cement precipitation rates, a wave of microfractures forms, resulting in a steep part of the curve near the middle of the size distribution. This version of the simulation results in curves to the final size distribution that are qualitatively similar to those of the natural fractures (Figure 6-25). Thus such curves can potentially be explained by a characteristic opening-increment size and a cement precipitation rate that varies according to temperature.

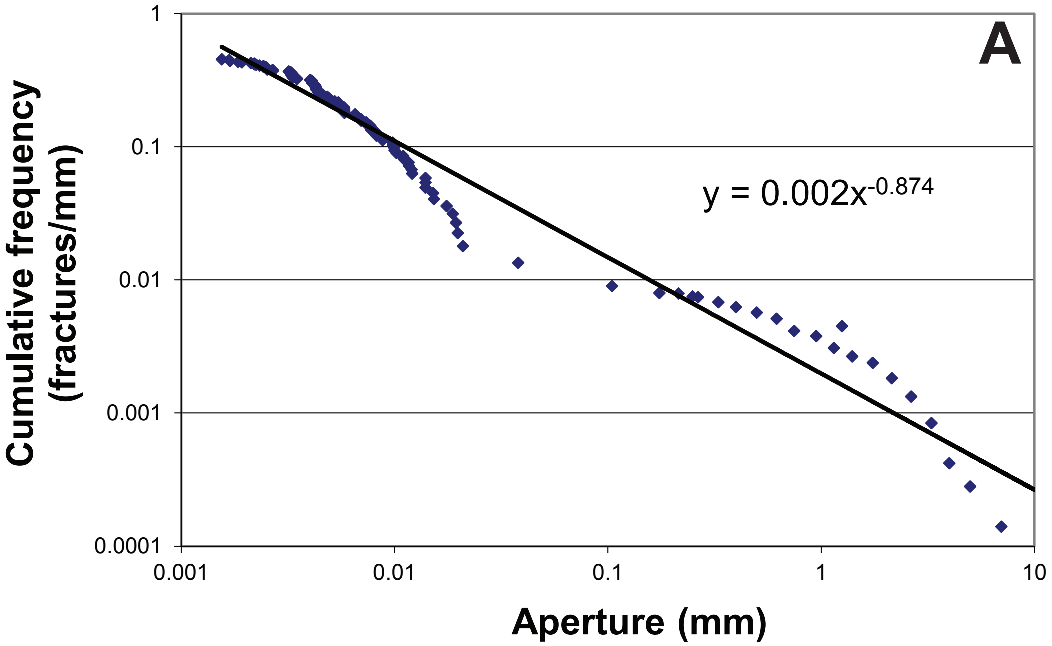

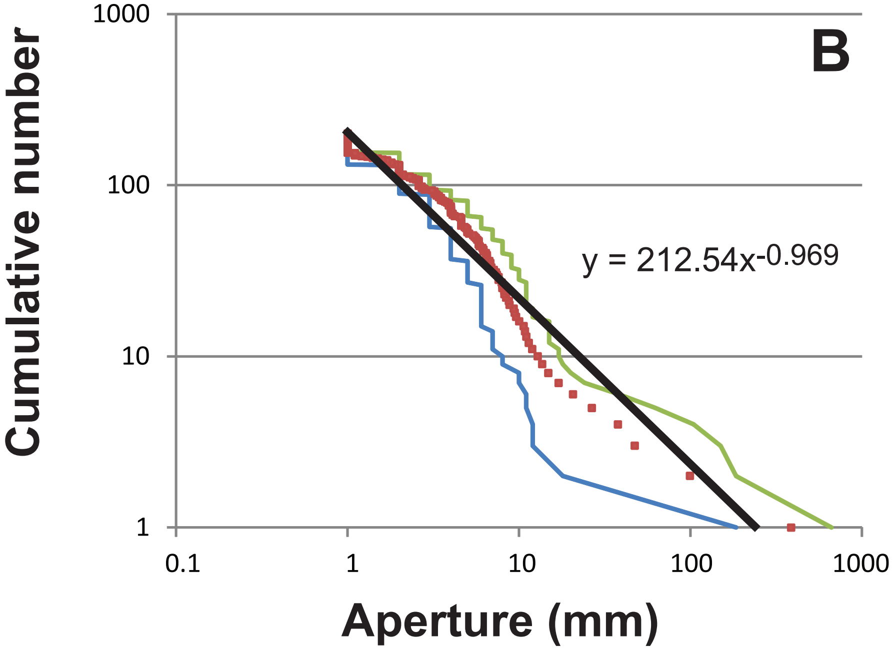

Figure 6-25. (A) Observed size distribution, Set C fractures. (B) Simulated size distribution assuming monotonically cooling temperatures.

FRACTURE SCALING APPLIED

Chapter 7: Subsurface fracture frequency estimation using core samples

Previous chapters documented fracture aperture-size scaling data and reported a rule-based model and a fluid-inclusion study aiming at explaining how scaling patterns arise. The empirical data shows that fracture-size scaling is widespread, and the modeling and structural diagenetic results suggest that the processes that lead to size scaling should be ubiquitous in moderate- to deep-seated (>80°C) sedimentary rocks. What practical applications follow from these conclusions?

Subsurface natural-fracture patterns are difficult to quantify. Fractures that are large enough to be important for fluid storage and permeability may still be difficult to detect seismically because they dip steeply and may not juxtapose reflecting horizons (Marrett et al., 2007; Burnett and Fomel, 2011). The subsurface is usually only directly sampled using vertical wellbores. In typical cases macrofracture spacing is considerably wider than wellbore diameter (Ladeira and Price, 1981). Fracture frequency (i.e., the number of fractures per unit length of rock), in the inter-wellbore space, can potentially be constrained using microfracture scaling (Marrett et al., 1999; Gomez and Laubach, 2006; Ortega et al., 2006; Guerriero et al., 2010; Hooker et al., 2009; Iñigo et al., 2012).

Using the size scaling technique, fractures are detected within a small rock sample; if enough fractures can be measured to establish a fracture intensity equation, the frequency of larger and more widely spaced fractures can be predicted. Although the scaling technique does not directly account for fracture spatial arrangement (Gomez, 2007), the reciprocal of fracture frequency is average fracture spacing, so establishing the intensity equation quantifies a statistical average fracture spacing. Thus fracture scaling potentially allows the characterization of subsurface fracture frequency by sampling vertical cores and collecting microfracture frequency data using SEM-CL.

Subsurface cores are typically a maximum of 10 cm wide. Sidewall cores are rarely longer than 5 cm. Therefore only short scanlines can be made within the subsurface except in the special case of horizontal core (Hooker et al., 2009). The primary difficulty associated with using the size scaling technique is that, empirically, in small volumes of rock few microfractures are typically observed which can be reliably associated with larger fractures. For example, within Travis Peak Formation samples the number of fractures (of any size) per thin section, identified by associated fluid inclusion planes, is as high as 10-15 but typically fewer than five (Laubach, 1989).

The paucity of microfractures is a consequence of the shallow (<1) observed *b* value fit to natural-fracture frequency curves, as explained below. In this chapter a method is described to maximize the utility of sampled microfractures from vertical core samples, and thereby minimize the problem of shallow intensity curves. The low observed *variation* in *b* can be used to increase the precision of microfracture frequency extrapolations based on short (core-width) scanlines. Assuming a Poissonian distribution of locations along the scanline allows estimation of the error associated with spacing predictions.

PREVIOUS MEASURES OF FRACTURE ABUNDANCE

The simplest measure of fracture abundance is the number of fractures observed within a given observation space—for example, the fracture abundance of a layer within a core can be quantified by counting the number of fractures present at a given depth (Haynes, 1984; Wilson and Paulsen, 1998). But for macrofracture spacing wider than a 10 cm core diameter, cores at many depths will likely lack any fractures even if they are present in the layer. A method of calculating fracture spacing in the vicinity of the wellbore using the limited sampling typically encountered with vertical wellbores and steeply dipping fractures was devised by Narr (1996). In this method the volume of rock represented by preserved core or image logs is assumed to statistically represent the reservoir rock, and the average fracture spacing is derived by dividing the cumulative rock volume by the cumulative fracture volume. Extensive subsurface observations and calibration with outcrops or other methods are helpful.

The advantages of the Narr method are its simplicity and its ease of application to any sampled subsurface interval. However, the errors associated with this method will potentially be great if the reservoir A) is poorly sampled, and or B) displays significantly heterogeneous fracture stratigraphy, and the preserved core or wellbore volume is insufficient to statistically represent each individual facies.

In sedimentary rocks, microfractures that are the small-size fraction of fracture populations containing larger fractures offer a way to circumvent this sampling problem. The advent of microfracture detection using SEM-CL greatly increased the statistical capability of sampling microfractures at a given depth (Laubach et al., 1995a). But to use this method a large population of microfractures that are demonstrably related to macrofractures is needed in the still relatively small rock volumes that can be obtained from the subsurface. For many sedimentary rocks in low-fracture-strain settings, SEM-CL data collection and analysis is far more challenging (Hooker et al., 2009; Chapter 2, Chapter 3).

In this Chapter I show how, despite low microfracture frequency in many basins in which fractures are nonetheless deemed important for subsurface fluid storage and flow, microfracture frequency measured using SEM-CL can be used to predict macrofracture frequency. I focus on the samples from Chapter 3 that were collected from the Piceance Basin, a tight-gas sandstone reservoir (Nuccio and Roberts, 2003) with low fracture frequency relative to highly deformed settings (Chapter 3). By focusing on rocks of low fracture-frequency I attempt to predict macrofracture spacing in a relatively challenging setting; macrofracture frequency extrapolation will be easier in rocks of higher fracture-frequency.

1D DATA COLLECTION FROM VERTICAL CORE

Macro- and microfracture size distributions are measured using the methods detailed in Chapter 3. Microfractures were imaged at a magnification of 150X, resulting in images with a pixel width equal to 0.76 μm. Size distribution equations are best-fit to scaling data using the chi^2 method (Chapter 2).

Typically in quartzose sandstones fractures filled with quartz can be reliably detected and measured down to apertures as small as ~1 μm. Although the pixel width is slightly smaller, the smallest transgranular (and therefore reliably post-depositional) microfractures are typically 1 μm or wider. Intragranular, post-depositional fractures could conceivably be much smaller, but a minimum size near 1 μm is consistent with that observed for opening increment sizes (gap sizes) in sandstones (Chapter 3).

To maximize the number of microfractures sampled at a given depth within subsurface core samples, an entire cross-section of core could be mapped using SEM-CL. For this study, however, fracture apertures were measured along 1D transects, as opposed to 2D maps, for four reasons. 1) The additional time and computing power required to assemble a fracture map using SEM-CL increases with the square of scanline length. 2) Aperture is both conceptually and practically easier to measure than length—fracture linkage makes grouping or splitting of linked fractures, and therefore length measurements, subjective. Aperture surveys within 2D maps are likewise subjective: if it is unclear where one fracture ends and another begins, the number of aperture measurements to make is also unclear. 3) Fractures measured from maps are susceptible to censoring bias (Pickering et al., 1995). 4) If fractures are present in parallel sets, then scanlines provide the same aperture-size information that fracture maps do, with the exception that using maps gives the option of measuring the aperture of each fracture where it is widest (on the map). These reasons notwithstanding, more microfractures might be sampled if core cross-sections are mapped in 2D; thus 2D map scaling might be preferable when data are scarce, and could be the subject of future study.

OPEN-FRACTURE SPACING FROM FRACTURE INTENSITY

Open-fracture spacing in the subsurface can be estimated by combining a power-law fracture frequency equation and an emergent threshold, or fracture aperture above which some porosity is preserved (Laubach, 2003). Open-fracture spacing is calculated by solving the frequency equation for the emergent threshold size. The reciprocal of this frequency is the average spacing of fractures.

Natural fracture sets that grew in diagenetically reactive environments commonly follow power-law aperture-size distributions with *b* values near 0.8, measured in 1D (Chapter 3). The prevalence of this *b* value has two important ramifications for estimating open-fracture spacing in the subsurface.

First, the characteristic *b* value means that for every macrofracture there aren't myriad microfractures present, especially considering the ambiguity of origin of fractures smaller than the grain scale (Hooker and Laubach, 2007; Chapter 8). In a hypothetical case of a power-law size distribution of $b = 0.8$ and coefficient (in fractures per mm) of 0.0016, the average spacing of 0.1 mm-wide fractures would be 100 mm; thus one could expect to encounter roughly one visible fracture within a core layer. Because of this shallow slope, approximately 40 fractures greater than 1 μm wide would be present, a sum well below the 200 called for by Bonnet et al. (2001) to independently establish a size-distribution equation. In contrast, if the typical scaling exponent were 2.5, there would be 1000 microfractures present, and statistically robust populations could be sampled within a single core-width.

On the other hand, the constancy of the observed exponent carries an implicit benefit: because the exponent is roughly constant, we can assume the characteristic exponent holds, and vary only the coefficient of the scaling equation to best-fit the data. Below macrofracture-frequency estimates are compared using best-fitting power-law equations by varying both the coefficient and the exponent versus holding the exponent constant at the characteristic value derived in Chapter 3 (0.8). Each type of estimate is tested against true macrofracture frequency, as measured from horizontal or slant cores using a hand lens.

CORE FRACTURES

Microfracture-derived scaling extrapolations were tested by sub-sampling scanlines made from horizontal and slant cores within the Piceance Basin (cores MF31-19G; SHCT-1; and GR1-3 SH—Figure A-1). These correspond to Samples 37, 40, and 41, respectively, from Chapter 3 and Appendix A.

Macrofractures preserved in core are typically planar and steeply dipping; fracture strike is E-W to WNW (Figure 7-1). Natural fractures are distinguished from those induced during or after core recovery by the presence of mineral linings on the fracture wall. Mineral linings can be expected to have precipitated on open fracture walls in quartz-rich rocks in the deep subsurface (Walderhaug, 1994). In all observed cases this lining is either quartz or calcite. Calcite linings are particularly thick in macrofractures from Sample 37 (Figure 7-2a) and may seal the fractures entirely, whereas most macrofractures in the other two cores contain only thin veneers of quartz (Figure 7-2b).

Where present, fracture-filling calcite overlaps quartz, and therefore post-dates quartz precipitation. Where the fractures are preserved as two broken core pieces with crystalline walls, a minimum fracture aperture is estimated by measuring the thickness of the layer of fracture-lining crystals.

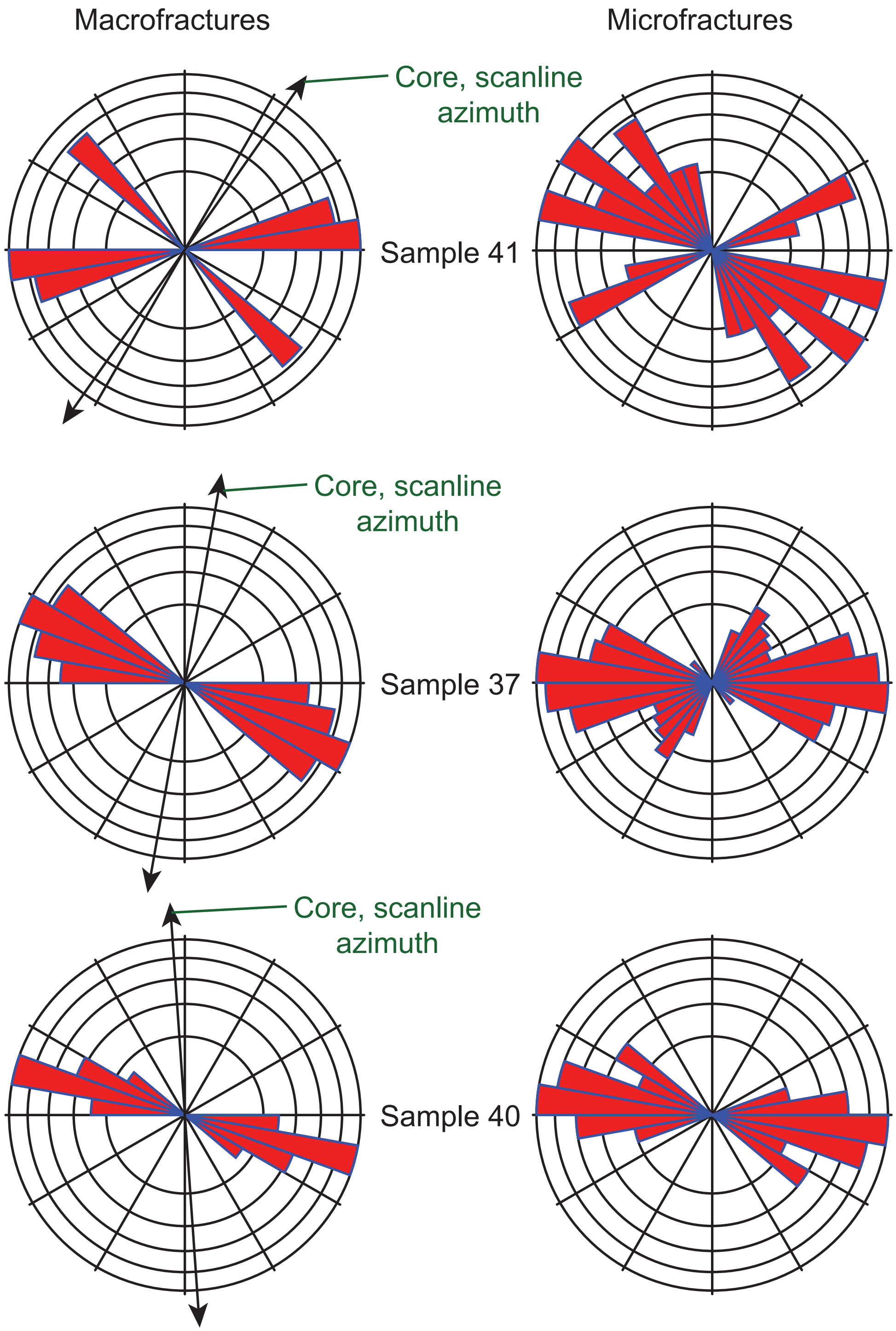

Figure 7-1. Rose diagrams of macro- and microfracture strike, with scanline azimuth. Note that rose diagrams taken from 1D scanline data naturally undersample fractures oriented at a low angle to the scanline, so full 2D rose diagrams may show more dispersion in fracture strike.

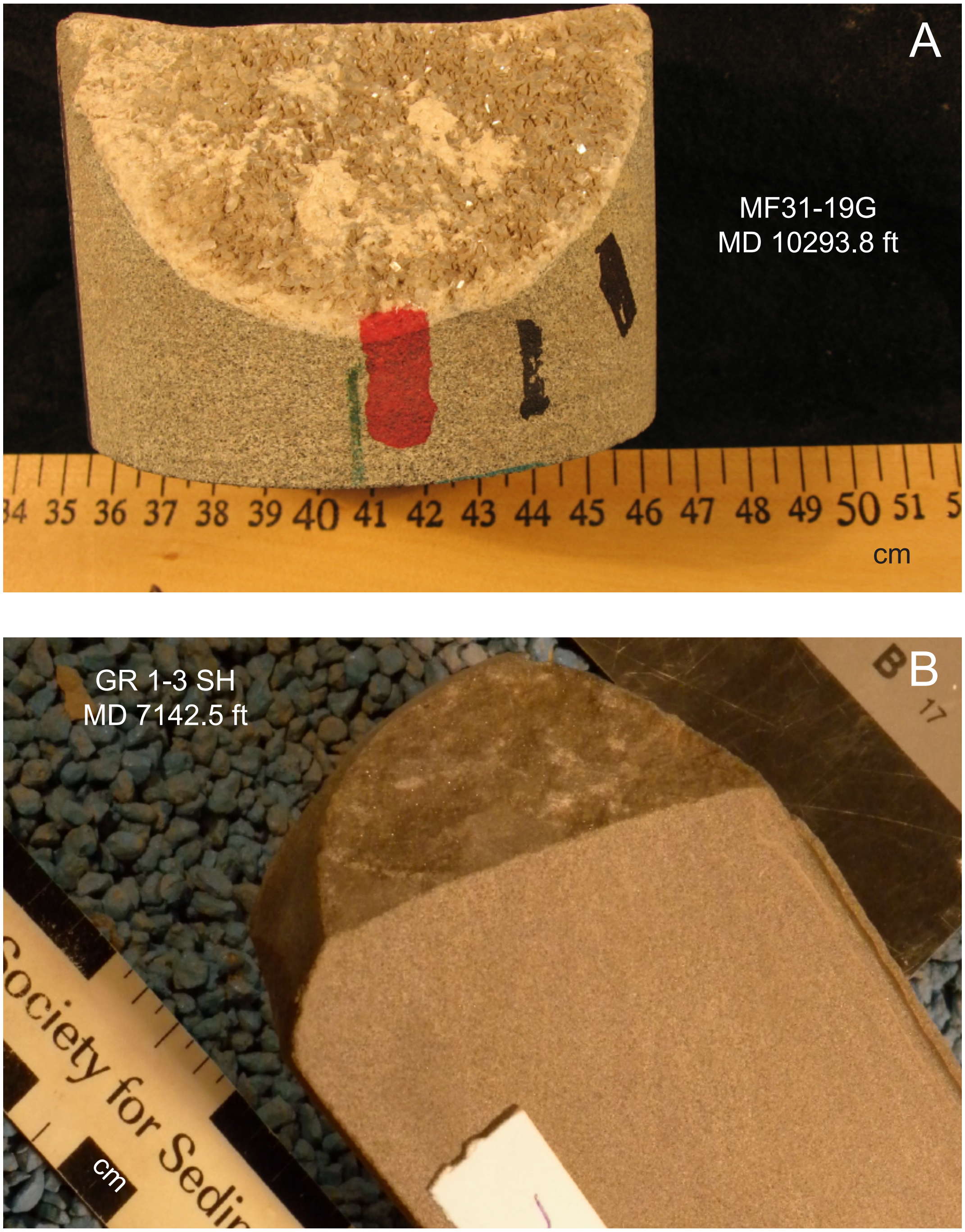

Figure 7-2. Natural macrofractures preserved in deviated cores, Piceance Basin. (A) From Sample 37, fracture features macroscopic euhedral calcite crystals overlapping a quartz lining visible in thin section. (B) From Sample 41, fracture is lined with thin veneer of quartz cement.

In each core, microfractures strike roughly parallel to macrofractures (Figure 7-1). There is generally greater dispersion in microfracture orientation relative to macrofractures, which likely reflects the tendency for microfractures to circumnavigate grains during propagation (Figure 7-3). No strike-azimuth filtering was performed for frequency calculations at either the macro- or microscopic scales. Statistics from these fracture sets are summarized in Appendices A, B, and C. Fracture cumulative frequency data are presented in Figure 7-4.

The macrofracture-size distribution measured from each sample forms a concave-down curve on a log-log plot, likely indicating 1) the large-size termination of a power-law size distribution that persists at the microfracture scale (Chapter 3); and 2) a resolution-limited truncation bias among the smallest macrofractures observed, which represents a disconnect on the size-frequency plots between micro- and macrofracture data. To test the quality of fit of a microfracture-based extrapolation to the observed macrofracture frequency, a chi^2 value was calculated for each derived frequency equation. The results are listed in Table 7-1 and displayed graphically in Figure 7-5.

Estimating open-fracture spacing

The size-frequency data were best-fit by power-law equations. First this was done using Excel's automated best-fitting routine, which varies *a* and *b*. As an alternative method this was done by holding *b* fixed at 0.8 and varying *a*.

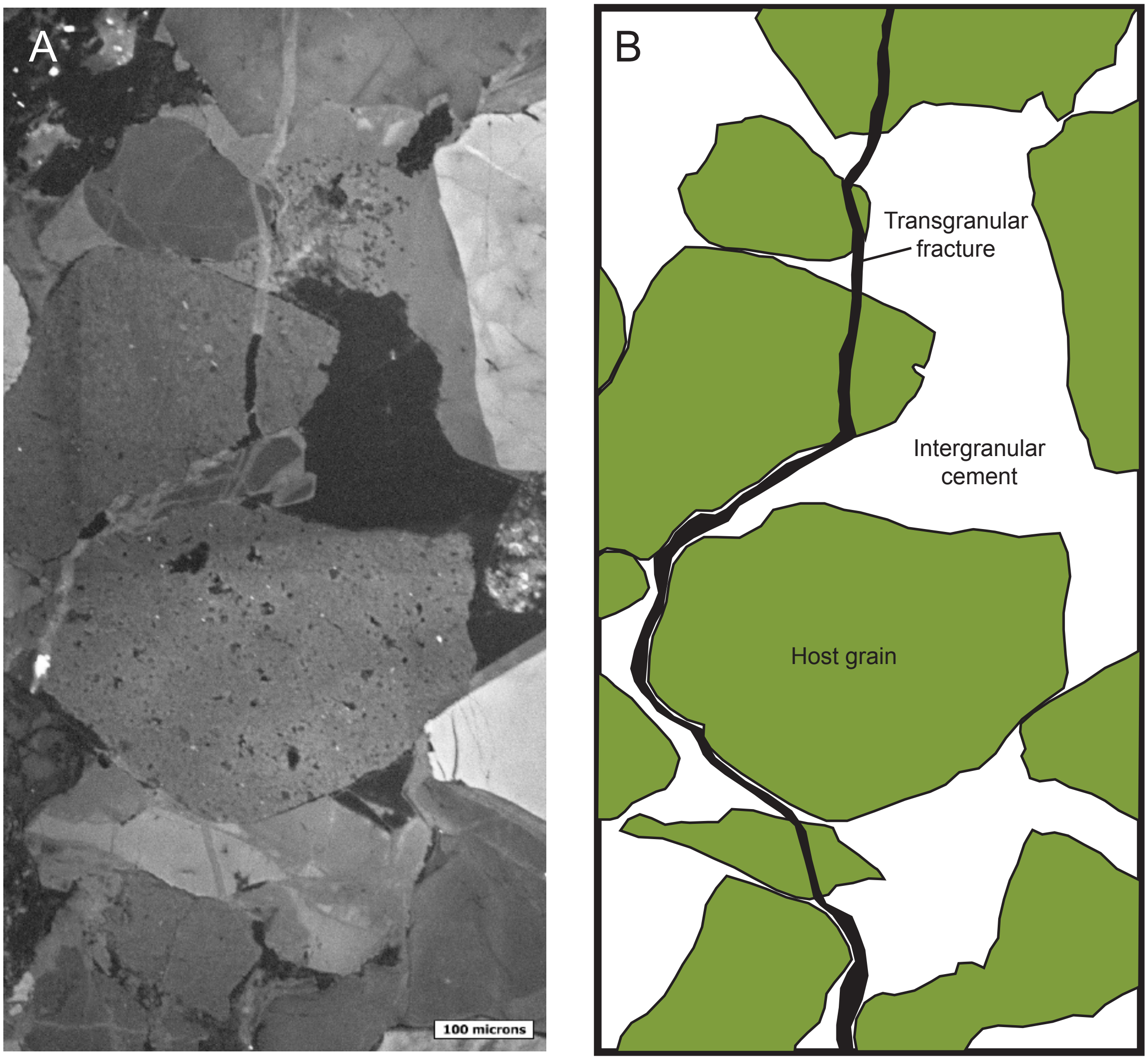

Figure 7-3. (A) SEM-CL image of a transgranular microfracture, Sample 37, measured depth ~ 10,302 ft., from Hooker and Laubach, 2010. (B) interpretation of region imaged in (A). The microfracture cuts through some grains and circumnavigates others. This tendency may partially explain the greater dispersion of strike present among microfractures than among macrofractures (Figure 7-1).

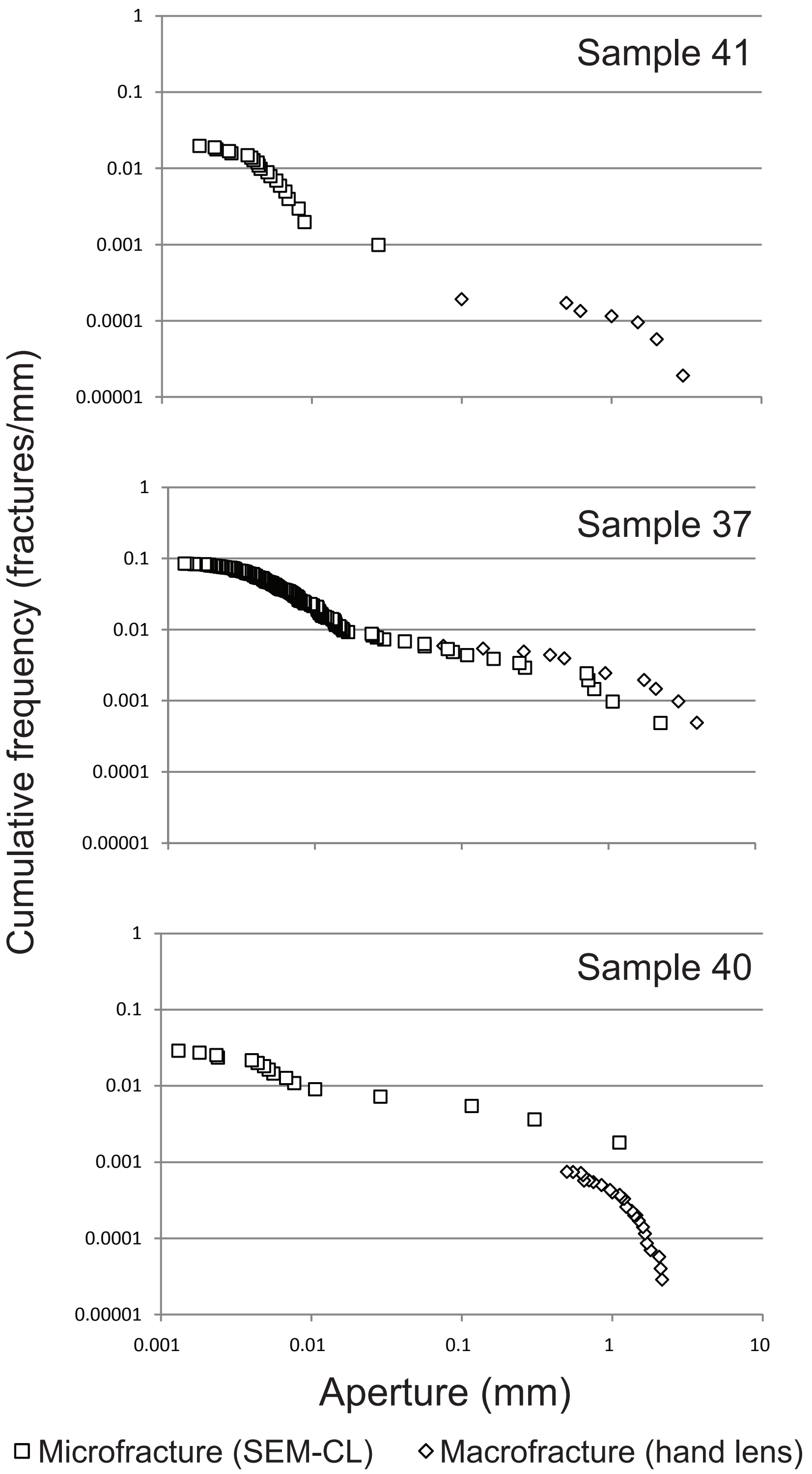

Figure 7-4. Size distributions of microfractures and macrofractures from Piceance Basin deviated cores. Best-fit equaiton parameters are listed in Appendix A.

		Best-fit method					Constant *b*-value method				
Sample	**Data subset**	***a***	***b***	***chi*^{2}**	**Avg. *chi*^{2}**		***a***	***b***	***chi*^{2}**	**Avg. *chi*^{2}**	
37	All	8.0E-04	0.75	0.02	**507**		6.6E-04	0.8	0.04	**0.05**	
37	100 mm (a)	1.0E-08	2.60	6705		**532**	3.0E-04	0.8	0.13		**0.05**
37	100 mm (b)	1.2E-02	0.23	0.08			1.2E-03	0.8	0.01		
37	100 mm (c)	8.8E-03	0.24	0.05			1.2E-03	0.8	0.01		
37	100 mm (d)	8.6E-03	0.41	0.06			1.6E-03	0.8	0.01		
37	100 mm (e)	8.0E-05	1.03	0.54			3.0E-04	0.8	0.13		
37	100 mm (f)	2.0E-04	0.96	0.19			5.0E-04	0.8	0.06		
37	100 mm (g)	*	*				*	0.8			
37	100 mm (h)	1.0E-05	1.41	4.31			3.0E-04	0.8	0.13		
37	100 mm (i)	2.0E-08	2.82	3932			5.0E-04	0.8	0.06		
37	100 mm (j)	3.0E-04	1.03	0.11			9.0E-04	0.8	0.02		
37	100 mm (k)	2.0E-04	1.18	0.17			1.5E-03	0.8	0.01		
37	100 mm (l)	9.0E-05	1.18	0.45			8.0E-04	0.8	0.02		
37	100 mm (m)	2.0E-04	0.90	0.20			4.0E-04	0.8	0.09		
37	100 mm (n)	6.0E-05	1.18	0.70			6.0E-04	0.8	0.04		
37	100 mm (o)	7.0E-04	0.80	0.03			8.0E-04	0.8	0.02		
37	100 mm (p)	2.0E-04	0.96	0.19			6.0E-04	0.8	0.04		
37	100 mm (q)	2.0E-04	0.91	0.20			3.0E-04	0.8	0.13		
37	100 mm (r)	1.0E-04	1.14	0.40			9.0E-04	0.8	0.02		
37	100 mm (s)	2.0E-05	1.30	2.16			4.0E-04	0.8	0.09		
37	100 mm (t)	1.4E-02	0.41	0.13			3.3E-03	0.8	0.03		
37	100 mm (u)	1.1E-02	0.48	0.10			2.9E-03	0.8	0.02		
40	All	1.9E-03	0.40	0.00	**0.17**		3.5E-04	0.8	0.10	**0.03**	
40	100 mm (a)	1.1E-03	0.63	0.01		**0.20**	5.3E-04	0.8	0.00		**0.01**
40	100 mm (b)	9.0E-06	1.54	0.30			3.8E-04	0.8	0.00		
40	100 mm (c)	*	*				1.8E-03	0.8	0.03		
40	100 mm (d)	7.0E-06	1.36	0.41			2.2E-04	0.8	0.00		
40	100 mm (e)	5.0E-04	0.57	0.00			1.3E-04	0.8	0.01		
40	100 mm (f)	1.2E-02	0.19	0.29			2.1E-03	0.8	0.04		
41	All	8.0E-06	1.29	5.50	**1.05**		1.2E-04	0.8	0.41	**0.04**	
41	100 mm (a)	4.0E-08	2.49	1.82		**0.31**	3.6E-04	0.8	0.00		**0.00**
41	100 mm (b)	*	*				1.3E-04	0.8	0.00		
41	100 mm (c)	*	*				2.4E-04	0.8	0.00		
41	100 mm (d)	2.0E-05	1.31	0.00			2.6E-04	0.8	0.00		
41	100 mm (e)	2.0E-06	1.61	0.03			2.6E-04	0.8	0.00		
41	100 mm (f)	2.0E-04	0.85	0.00			2.6E-04	0.8	0.00		
41	100 mm (g)	2.8E-03	0.36	0.02			4.1E-04	0.8	0.00		
41	100 mm (h)	*	*				7.0E-05	0.8	0.00		
41	100 mm (i)	1.3E-03	0.43	0.01			1.9E-04	0.8	0.00		

Table 7-1. Quality of fit of extrapolation of microfracture scaling data to macrofracture frequency. In each of the three wells studied, the constant-exponent method is a better predictor (lower chi^2 values) of macrofracture frequency than the best-fit power-law method.

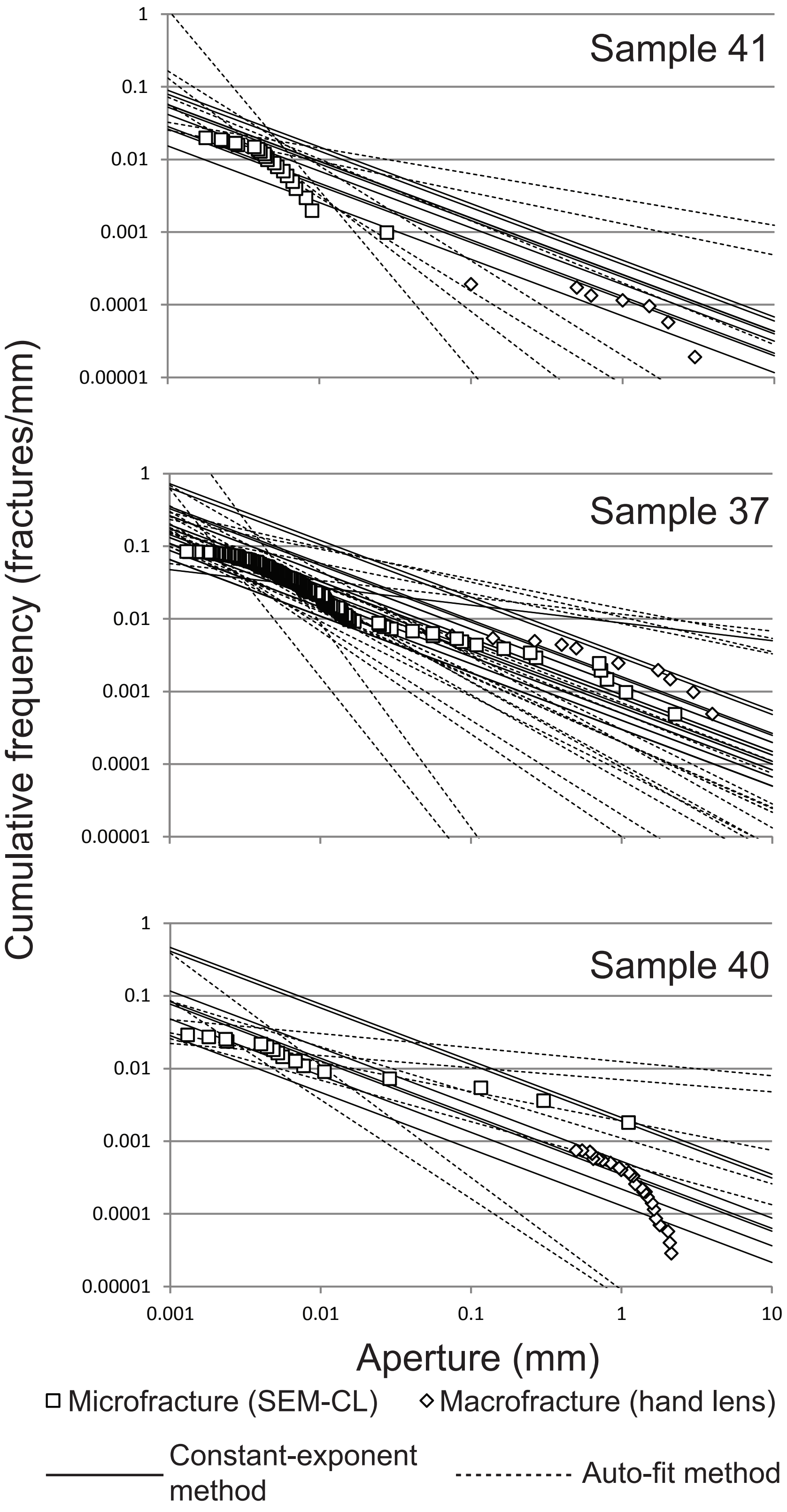
Sample 41
Sample 37
Sample 40
1
0.1
0.01
0.001
0.0001
0.00001
0.001
0.01
0.1
1
10
Cumulative frequency (fractures/mm)
Aperture (mm)
□ Microfracture (SEM-CL)
◇ Macrofracture (hand lens)
Constant-exponent method
Auto-fit method

Figure 7-5.

Figure 7-5 continued. Estimations of large-fracture frequency made by best-fitting power-law equations (straight lines) to microfracture size-frequency data (squares). Lines are based on sub-populations of microfractures located within 100 mm-long subdivisions of the overall scanline. Dashed lines are made by varying both the coefficient (*a*) and exponent (*b*) in Excel; solid lines assume a fixed *b* (0.8) and vary only *a*. The relative quality of fit of the two methods can be judged by how closely the lines match the observed frequency of macrofractures (diamonds). See text for method of measuring relative quality and Table 7-1 for results.

Varying *a* manually, and computing a chi^2 error for each a value tried, produces a local chi^2 minimum corresponding to the *a* value which most closely fits the data.

Once both fracture intensity equations are established, open-fracture spacing can be estimated by solving the power-law equations for a size equal to the empirically-observed emergent threshold. This number is the cumulative frequency (number per unit length of scanline) of fractures present with an aperture size equal to or larger than the emergent threshold. Thus, it is the frequency of open fractures. Average spacing (unit length of scanline per fracture) is the reciprocal of fracture frequency. From any scanline a spacing of fractures of any given size or larger can be estimated using this method. In the case of a scanline with zero fractures, the estimation is infinite spacing.

In all three Piceance Basin core samples analyzed, the quality of fit to macrofracture frequency of the microfracture-frequency equation was systematically better using the constant-*b* assumption, rather than varying both *a* and *b* (Figure 7-5, Table 7-1).

Error estimation: method 1

Given a single estimate of fracture frequency at the emergent threshold size, it is important to quantify the associated error. However the error is calculated, it will decrease with the number of fractures intersected by the scanline. Here I describe the first of two possible methods to quantify the error associated with macrofracture-frequency estimates based on microfractures.

Guerriero et al. (2010) applied error bars to fracture cumulative frequency data by assuming a Poissonian distribution of fracture occurrences within the scanline observed. That is, from scanline data the largest observed fracture has an *expected* frequency of once per scanline-length, the second-largest, twice, and so on. Assuming a random spatial distribution of fractures of all sizes, the probability of encountering a fracture of a given size Y times follows a Poissonian distribution:

$$P(Y) = \frac{e^{-\lambda}\lambda^{Y}}{Y!} \qquad (7\text{-}1)$$

where λ is the expected number of intersections (the cumulative number).

A 95% confidence interval for each cumulative number (Figure 7-6) can be established using the cumulative Poisson distribution in Excel:

$$P(Y \leq y) = \sum_{i=0}^{Y} \frac{e^{-\lambda}\lambda^{Y}}{Y!} \qquad (7\text{-}2)$$

Confidence interval bounds λ_L and λ_U were derived by solving this equation for a λ_L sufficiently low such that the observed frequency is at the top of its 95% confidence interval; and for a λ_U sufficiently high that the observed frequency is at the lower bound of its 95% confidence interval (Figure 7-7). Then a fracture intensity equation was derived at either end of the 95% confidence interval by best-fitting a power-law equation to the interval bounds, again using *b*=0.8 (Figure 7-6).

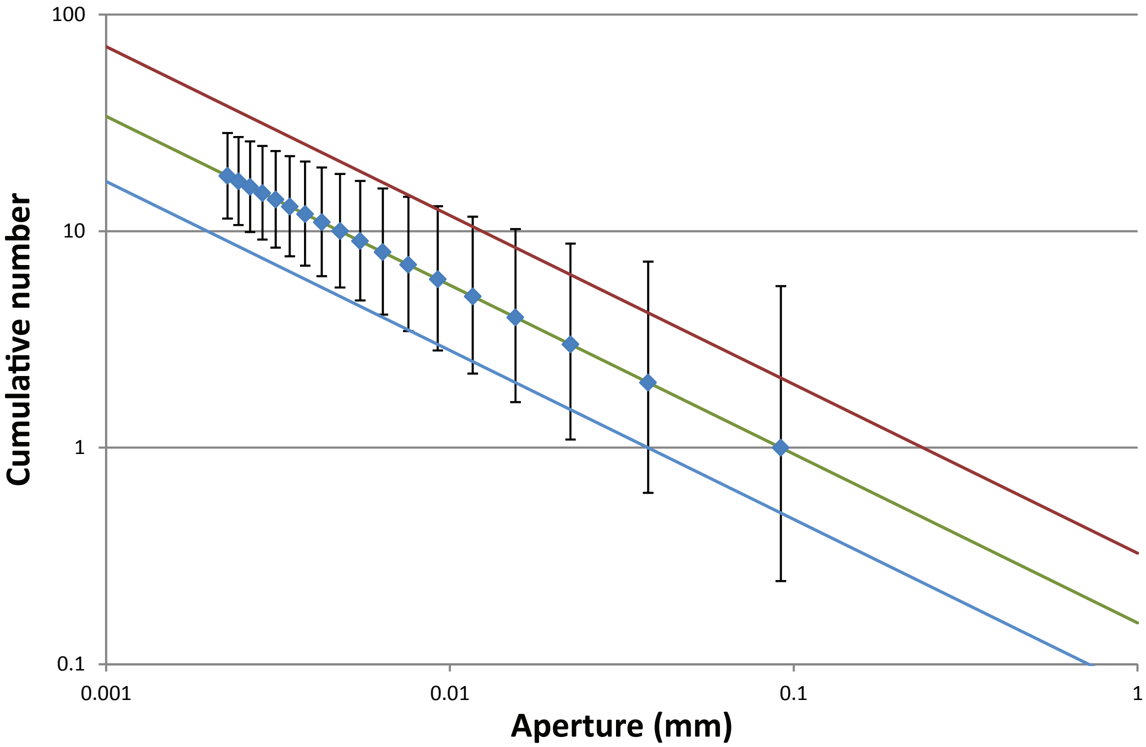

Figure 7-6. Cumulative frequency error-bars fit to ideal power-law size distribution (green line) data. Blue line is a power-law, with b=0.78, best fit to λ_L points (see Figure 7-7); red line is best-fit to λ_U points.

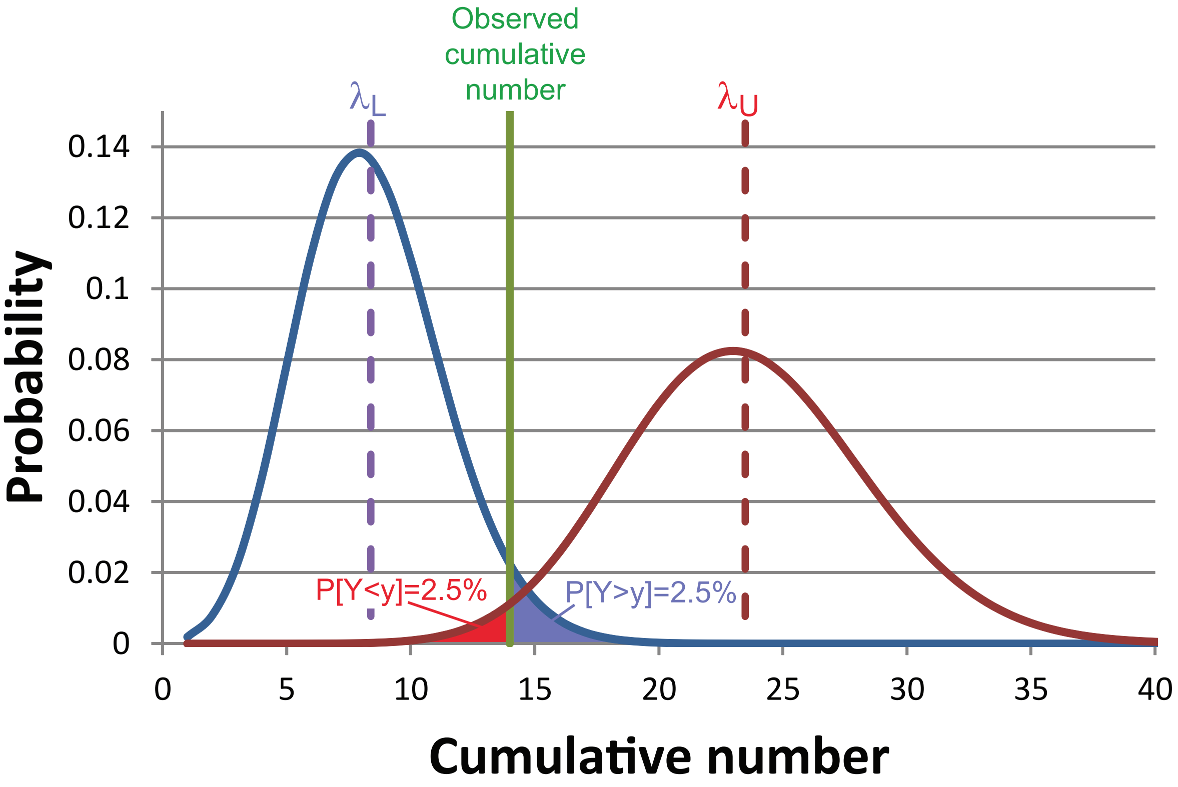

Figure 7-7. Estimation of 95% confidence interval for a given fracture cumulative number. The above example is for cumulative number = 14 (green line). The dashed lines represent λ_U (red) and λ_L (blue). λ_U is the long-term frequency of fractures for which there would be a 2.5% chance that fewer than 14 fractures would be observed within the scanline, assuming a Poissonian distribution of fractures. λ_L is the long-term frequency of fractures for which there would be a 2.5% chance that more than 14 would be observed within the scanline.

For an ideal power-law size distribution with *b*=0.8, like that shown in Figure 7-6, the power-law equations best-fit to the 95% confidence envelopes would not have exponents of 0.8, because of the decay in error towards greater measured cumulative frequencies. A less conservative approach to error estimation would be to vary *a* to best-fit a power law, with *b*=0.8, to the smallest fracture size recorded, which has the smallest frequency-error-bar. However, because the smallest fracture sizes observed are commonly afflicted by natural and artificial factors which make those data fall away from a power-law present among larger sizes (Chapter 2), such a technique may lead to spurious results.

Error estimation: method 2

An alternative way to derive the error associated with measured fracture frequency at a given size is to solve Equation 2-1 for *a*:

$$a = \frac{N}{X^{-b}} \qquad (7\text{-}3).$$

For each data point, given a measured *X* and *N* and an assumed b (0.8), *a* can be calculated. Using this method, each data point is used as an independent estimate of *a*, and the standard deviation of these estimates can represent the confidence interval, assuming the estimates are normally distributed. For this study, I only performed error estimation method 1.

Effects of clustering

An assumption of the Poissonian-distribution error estimation method is random fracture locations. Gomez (2007) documented that natural fractures are not typically randomly arranged in rock but rather are systematically clustered. Clustering beyond what is expected for random fracture locations is common in the scanline data (Appendix C). If a fracture population is more clustered than random, then the observed intensity from core-width sub-samples will show more variation than do the results of the random-location experiment described above. Importantly, clustering of fractures can be either *externally* or *internally* controlled.

If fracture clusters are externally controlled, as from changes in layer thickness, proximity to folds or faults, or preferential fracturing of heterogeneously distributed cements, then an adequate description of the far-field fracture frequency must take into account the external control(s). It may be the case that frequency systematically varies within different spatial domains of the fracture population.

Internally controlled fracture clustering may arise from the dynamic nature of fracture-set evolution. Fracture clusters are predicted by linear-elastic fracture mechanics under some conditions, including host rocks having extreme subcritical crack index values (Olson et al., 2009). Such fractures may open from increased effective tension near the tips of *other growing fractures*, resulting in clusters that formed by feedback inherent to the growing fracture population. Internally imposed clusters present a unique challenge to subsurface fracture pattern characterization, which is a topic for future work.

COMPARISON TO THE NARR (1996) METHOD

The method described by Narr (1996) was applied, in that study, to fractures within the Multiwell Experiment Site (MWX) cores, which are vertical cores drilled at the same site as the SHCT-1 core (Sample 40). Thus, the fracture spacings measured from the SHCT-1 core were used as a test of Narr’s method. Unlike the scaling method presented in this study, the Narr method is not specific to a single stratigraphic interval, but rather core-fracture geometries are collected from as many intervals as are believed to be represented within the core. Narr’s method was first applied to the sandstone layers within the MWX core and not to intervening fractureless mudstones.

Open-fracture spacing estimations using the scaling method described above, with associated error bars, are comparable to those made by Narr (1996). However, scaling estimations are based on an emergent threshold of 0.1 mm wide fractures; Narr’s estimated fracture size is 0.5 mm, equivalent to the minimum visible fracture size recorded in core, using a hand lens. Therefore a better comparison of the two methods is to use 0.5 mm as the fracture size for the spacing estimation, even though there are smaller porous fractures present. Estimations based on both sizes overlap with those made using Narr’s (1996) method (Figure 7-8).

Spacing estimates were also calculated for this study based on microfracture frequencies observed from four depths within the Williams Fork

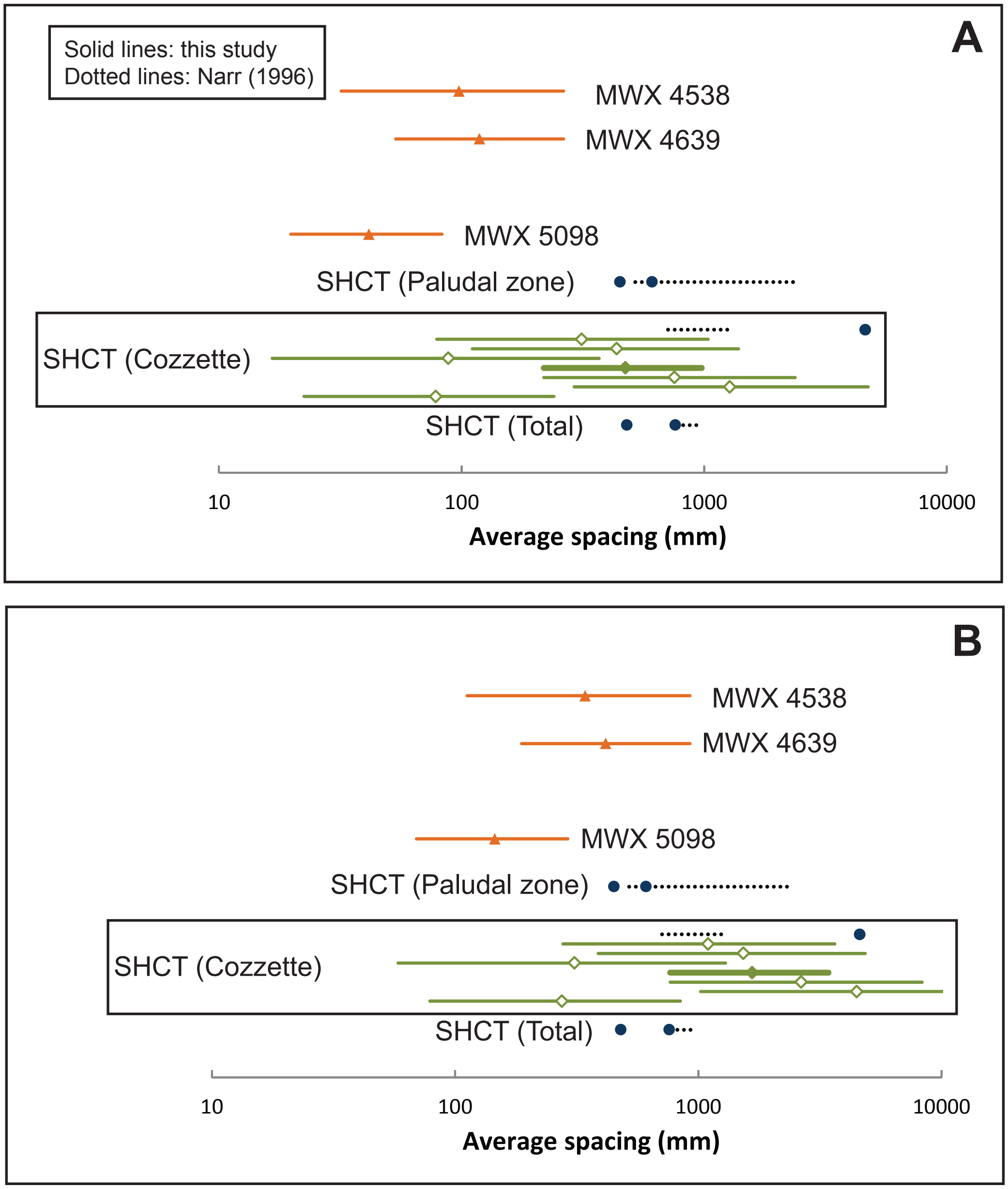

Figure 7-8. Comparison of this study's spacing estimations to those of Narr (1996). (A) Spacing estimation of aperture size 0.1 mm or greater; i.e., the spacing of open fractures given an emergent threshold of 0.1 mm (Hooker et al., 2009). (B) Spacing estimation of aperture size 0.5 mm or greater, corresponding to Narr's (1996) general estimated fracture aperture. Narr (1996) data are the same in (A) and (B). Dotted line represents Narr's (1996) macrofracture spacing measurement from two intervals of the SHCT core. The large dots are Narr's (1996) spacing estimations. This study's spacing estimations include error bars calculated from 95% confidence envelope; filled diamond is based on all SHCT microfractures, empty diamonds are based on 100 mm-long sub-scanlines.

interval of the MWX well (Samples 33-36, Appendix A). MWX microfracture scanlines span single thin sections only. From one scanline (depth 4931 ft) no fractures are present, and so infinite spacing is predicted using the scaling method. Estimations from the other three scanlines indicate closer fracture spacing within the Williams Fork interval compared to the paludal zone and the Cozzette sandstone. This result is consistent with higher fracture intensity in the Williams Fork Formation as measured in Sample 37 (Figure 7-4, Table 7-1), although that sample derives from another part of the basin (Figure A-1).

In summary, the typically shallow slopes to the best-fit power-law slopes that characterize the size-frequency data presented in Chapter 3 have important consequences for the application of fracture size scaling to subsurface fracture spacing estimations. Because the typical *b* value is less than 1, microfractures are not excessively abundant in natural fracture sets. This inhibits scaling exercises. However, because there is little variation in *b*, assuming a fixed *b* of 0.8 can substantially increase the precision of subsurface fracture spacing estimations. Such a method represents a viable complement or alternative to existing methods, and may be preferable when only small amounts of core are retrieved or otherwise available.

A BROADER VIEW OF SANDSTONE MICROFRACTURES

Chapter 8: An inventory of microfractures in sandstones observed using SEM-CL

In the course of this study a dataset of over 27,000 microfracture measurements was collected from 61 samples of 18 sandstone units worldwide (Table 8-1). As noted, not all of the microfractures are suitable for scaling analysis, and many unsuitable fractures have been systematically filtered from the results shown in previous chapters. The criteria used therein to filter fractures (Hooker et al., 2009) removes the vast majority of microfractures. This is primarily accomplished by the filter requirement that fractures cut across grain boundaries.

Fractures whose tips are within the same grain may be inherited; i.e., they may have formed within the rock out of which the grain was eroded before deposition into the sandstone; or the fractures may have formed as a result of local grain-to-grain interactions and so are not necessarily genetically related to transgranular fractures, including macrofractures (Laubach, 1997). The fracture sizes within separate genetic populations might scale differently. Such fractures cannot be included within a scaling survey without the risk of corrupting the frequency curve with non-scaling fractures. However, some intragranular fractures could constitute useful data if methods were available to distinguish the

Table 8-1. Sample information for intragranular fracture dataset.

Sample no.	Thin section	No. of micro-fractures	Formation	Formation Number	Age	Area imaged (sq. mm)	Micro-fracture density (no./sq. mm)	Depth (m)	Well
i1	7068	524	Dakota	5	U. Cretaceous	10.06	52.06	2154.3	1
i2	A2H11115C	173	Almond	1	U. Cretaceous	2.19	78.82	?	2
i3	AD6568	490	Thorold	17	Silurian			2001.9	3
i4	AD6590	490	Grimsby	8	Silurian	4.64	105.56	2008.6	3
i5	AD6612C	245	Grimsby	8	Silurian	3.19	76.89	2014.9	3
i6	AD6680C	221	Lower Whirlpool	10	Silurian	1.12	198.02	2036.0	3
i7	AL6338C	205	Thorold	17	Silurian	2.97	69.08	1931.8	4
i8	AL6368.2C	353	Grimsby	8	Silurian	3.86	91.56	1941.0	4
i9	AL6462C	286	Upper Whirlpool	10	Silurian	0.96	296.72	1969.6	4
i10	AL6467C	206	Lower Whirlpool	10	Silurian	3.15	65.50	1971.1	4
i11	AS7450.0	34	Travis Peak	18	L. Cretaceous	0.76	44.82	2270.8	5
i12	AS7454.9	139	Travis Peak	18	L. Cretaceous	1.00	139.12	2270.8	5
i13	bam36	289	Pottsville	12	Pennsylvanian	8.26	35.00	1109.2	6
i14	bbd	534	Tensleep	16	Penn-Permian	3.12	171.42	0.0	outcrop
i15	BCZ 7111.4	896	Cozzette	4	U. Cretaceous	9.92	90.31	2055.3	7
i16	CB-12165	321	Frontier	7	U. Cretaceous	5.22	61.50	3707.9	8
i17	CC6402.5	283	Ozona Canyon	11	L. Permian			1935.7	9
i18	CS6350.8	69	Sonora Canyon	14	L. Permian	1.73	39.97	1935.7	10
i19	cz9034	762	Cozzette	4	U. Cretaceous	11.66	65.35	2753.6	11
i20	cz9035	633	Cozzette	4	U. Cretaceous	10.20	62.08	2753.9	11
i21	cz9061.8 h	692	Cozzette	4	U. Cretaceous	18.69	37.02	2762.0	11
i22	cz9067	291	Cozzette	4	U. Cretaceous	28.40	10.25	2763.6	11
i23	da7561	583	Canyon	3	L. Permian	4.99	116.91	2304.6	12
i24	da7608	446	Canyon	3	L. Permian	5.87	75.98	2318.9	12
i25	dpr6567	381	Canyon	3	L. Permian	7.95	47.90	2001.6	13
i26	dpr7649	439	Canyon	3	L. Permian	13.84	31.72	2331.4	13
i27	ec26	448	Mesaverde	4	U. Cretaceous	9.60	46.67	2323.8	14
i28	fc40c	503	Mesaverde	4	U. Cretaceous	5.55	90.69	3860.3	15
i29	FR12384.8C	169	Fall River	6	L. Cretaceous	4.38	38.58	3774.9	16
i30	HH-6119.0C	92	Travis Peak	18	L. Cretaceous	0.68	135.82	1865.1	17
i31	L15-5618C	749	Weber	20	Penn-Permian	3.27	228.97	1712.4	18
i32	mg785	176	Misoa	22	Eocene	4.83	36.44	1990.4	19
i33	mg801-9811	176	Misoa	22	Eocene	4.73	37.18	2990.4	20
i34	mg9363	257	Misoa	22	Eocene	5.36	47.95	2853.8	20
i35	mwx-1-5736	1012	Mesaverde	4	U. Cretaceous	25.45	39.77	1748.3	21
i36	OBK4455C	1393	Ozona Canyon	11	L. Permian	6.55	212.63	1357.9	22
i37	ofp4868.5	2212	Frontier	7	U. Cretaceous	8.65	255.78	1483.9	23
i38	orc26-1	1449	Middle San Juan	9	Cretaceous	13.74	105.43	4366.9	24
i39	orc26-2	1486	Lower San Juan	9	Cretaceous	23.47	63.31	4434.2	24
i40	PM9214.6C	35	Travis Peak	18	L. Cretaceous	0.63	55.52	2808.6	25
i41	PPO7664.9Cx	45	Spraberry	15	L. Permian			2160.7	26
i42	PPO7664.9Cx	46	Spraberry	15	L. Permian			2808.6	26
i43	PPO7682.9Cx	38	Spraberry	15	L. Permian			2160.7	26
i44	PPO7682.9Cx	62	Spraberry	15	L. Permian	1.13	54.98	2160.7	26
i45	PPO7684.9Cx	158	Spraberry	15	L. Permian			2160.7	26
i46	SFE2 9834.4	149	Travis Peak	18	L. Cretaceous	3.34	44.62	2997.5	27
i47	SFE2 9914.3	70	Travis Peak	18	L. Cretaceous	1.09	64.49	3021.9	27
i48	SP-03497	72	Bone Spring	2	L. Permian	3.82	18.86	5321.4	28
i49	ST16027C	120	Frontier	7	U. Cretaceous	1.39	86.57	4885.0	29
i50	ST16042.5	106	Frontier	7	U. Cretaceous	0.70	152.47	4889.4	29
i51	TP2-9871.4vh	1003	Travis Peak	18	L. Cretaceous	8.14	123.20	3008.8	30
i52	tpc13975	933	San Juan	13	U. Cretaceous	11.98	77.91	4259.6	31
i53	tpc14007	751	San Juan	13	U. Cretaceous	3.25	231.14	4269.3	31
i54	tr17531	1073	Tensleep	16	Pennsylvanian	4.09	262.41	5343.4	32
i55	w-026-97	846	Weber	20	Pennsylvanian	4.55	185.81	0.0	outcrop
i56	W-036-97	181	Weber	20	Penn-Permian			0.0	outcrop
i57	w-043-97	970	Weber	20	Pennsylvanian	6.30	153.91	0.0	outcrop
i58	W-1-98	198	Weber	20	Penn-Permian	4.08	48.57	0.0	outcrop
i59	WM7828.9C	164	Wolfcamp	21	L. Permian	2.89	56.81	2386.2	33
i60	WU8256.8c	82	Wolfcamp	21	L. Permian	1.00	81.74	2516.4	34
i61	WU8305.45	61	Wolfcamp	21	L. Permian	2.19	27.90	2531.5	34

signal (the small-size portion of tectonic-fracture sets) from the noise (inherited fractures and those caused by grain-scale crushing during compaction).

Another limitation of the 1D aperture scaling data examined in previous chapters is that transgranular microfractures are typically long relative to the width of SEM-CL photomosaics, and having been measured in 1D, necessarily are devoid of any meaningful length data, and lack other potentially useful morphological characteristics.

The frequency of microfractures, unfiltered for transgranularity and collected from 2D maps, show that sandstones with typical microfracture abundances contain *hundreds of thousands* of microfractures within the cross-sectional area of one wellbore (Table 8-1). Most microfractures are sealed with quartz cement in crystallographic continuity with host grains, rendering SEM-CL indispensable to intragranular-microfracture detection and measurement.

In this chapter I summarize the characteristics of the intragranular fracture inventory, including fracture abundance and physical characteristics when observed using SEM-CL. I seek to identify the genesis of such fractures using their physical characteristics and abundance as evidence. In doing so I will establish the utility of such fractures in scaling studies, and investigate other possible uses of intragranular-fracture data.

MICROFRACTURE IMAGING

Previous work detecting and interpreting microfractures using CL

Cathodoluminescence has been recognized for years as an effective way to detect microscopic fractures in quartz (Sprunt and Nur, 1979; Milliken, 1994; Seyedolali et al., 1997; Watt et al., 2000; Rusk and Reed, 2002; Makowitz and Milliken, 2003; Bignall et al., 2004; Bernet and Bassett, 2005; Hooker and Laubach, 2007). Fracture-filling quartz commonly luminesces more weakly than host grain quartz. CL intensity is believed to increase with increasing lattice defects and trace element incorporation (see Götze et al. (2001) for a review). The lower temperature and rate of crystal growth of diagenetic quartz cement results in less trace element incorporation and fewer lattice defects than commonly found in igneous or metamorphic quartz (Zinkernagel, 1978; Ramseyer and Mullis, 1990; Müller et al., 2003; van den Kerkhof et al., 2004a; Müller et al., 2010). Thus one way to help distinguish inherited versus *in situ* fractures is the generally higher CL response in the former.

However, fractures are nearly ubiquitous in quartz. Networks of poorly aligned, CL-dark fractures with associated web-like textures are common in plutonic quartz that has no evidence of throughgoing fractures (Sprunt and Nur, 1979; Bernet and Bassett, 2005). Thus microcracking is thought to be an intrinsic part of the process of quartz crystallization from magma, and can result in features with a range of CL intensities and wavelengths. Microfractures have also been shown to form during metamorphism (Watt et al., 2000; van den Kerkhof et al., 2004b). In light of the propensity of microcracks to form in quartz under a variety of geological conditions, most microfractures in typical sandstones have nothing to do with *in situ* fracture populations (Hooker et al., 2009).

Imaging methods

SEM-CL images were acquired using an Oxford Instruments MonoCL2 system with a Philips XL30 SEM operating at 15kV. Samples were imaged using a secondary electron detector and a CL detector at each imaging site (Figure 8-1). Secondary electron images allow for the discernment between quartz and other multi-phase minerals such as feldspars (Figure 8-1). As well, secondary electron images highlight porosity in low-relief (Figure 8-1). Porosity delineation is useful for identifying natural porosity as well as for distinguishing natural cement-filled fractures from fractures that developed during thin section grinding or polishing.

The CL detector detects cathodoluminescence in the ultraviolet through near-infrared range and converts it to a grayscale value. Color CL images are created by placing blue, green, and red filters in front of the CL detector and taking a grayscale image with each in place. The three grayscale images are assembled into an RGB image in Photoshop.

Fractures were interpreted and measured on 2D maps using the polygon method (Figure 4-1) created by Orlando Ortega and refined by Gomez and Laubach (2006). These fractures were not measured along scanlines; rather, each fracture imaged within the map was measured. In each method, SEM-CL

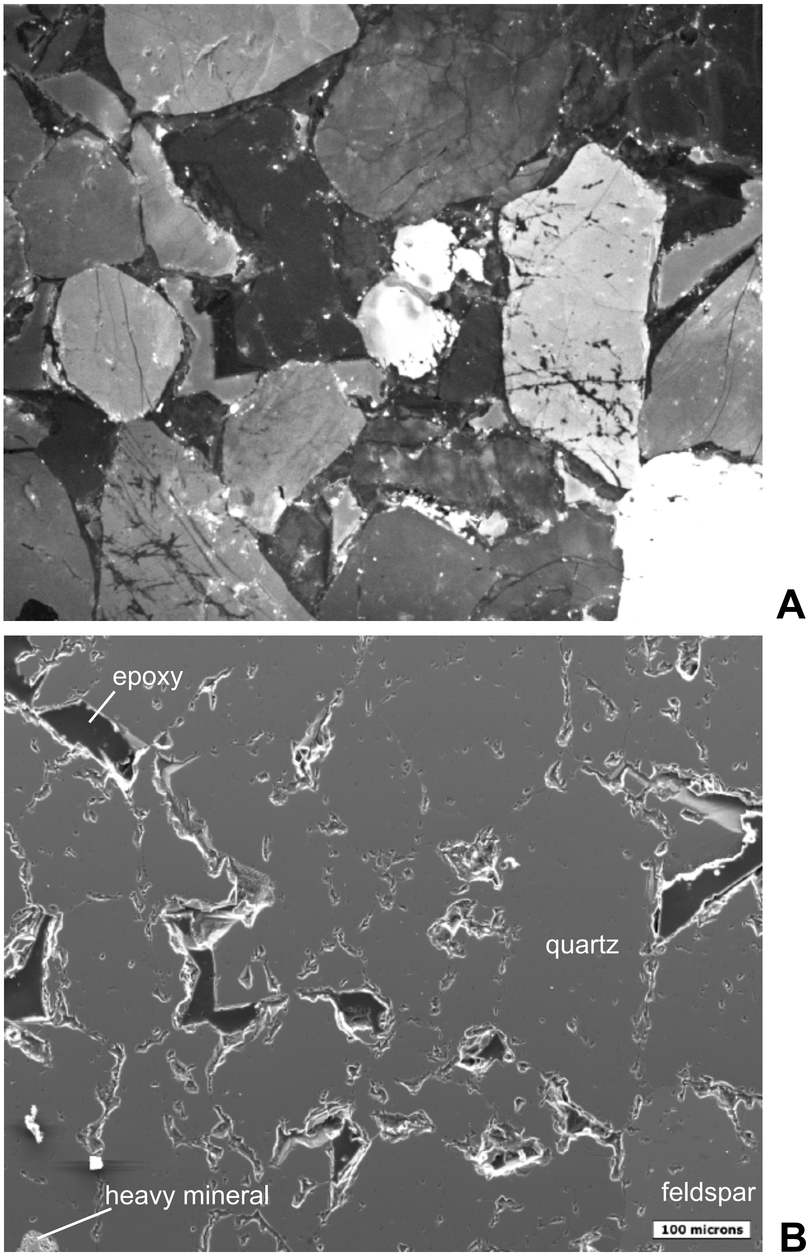

Figure 8-1. SEM-CL (A) and secondary electron (B) images of the same part of sample i52. Dark recessed areas in (B) represent porosity; grain in lower right corner is identified as a feldspar because it luminesces much more brightly than quartz in (A) and its two mineral phases are apparent from shade changes in (B).

images are exported (from software) in the Tagged Image File (.TIF) format; their brightness and contrast are adjusted for clarity in Photoshop. An individual image only represents approximately 0.46 mm^2 at 150X, so areally-adjacent images from a single thin section are assembled into a mosaic in Photoshop.

The mosaic is imported into a vector-based image program (Canvas for the Ortega method, Didger for the Gomez and Laubach method), in which the observer draws four-point polygons (Figure 4-1), each delineating a fracture. Two points represent each fracture tip; the remaining two points are placed on either fracture wall, across from one another, where aperture is measured; this is generally where the fracture is widest. The points are given Cartesian coordinates so that their length, aperture, and orientation may be calculated using customly developed software (Gomez and Laubach, 2006). The aperture measured is the *kinematic* aperture: the distance between the two separated host-rock walls, irrespective of cement. The fracture *aspect ratio* calculated in this study is fracture length divided by fracture aperture.

MICROFRACTURE CL CHARACTERISTICS

Features interpreted as microfractures are usually linear and may offset host rock features, such as grain boundaries, euhedral zones within cement, or earlier microfractures. Because grain boundaries are zones of weakness, especially in poorly cemented sandstones, fractures with aperture sizes near or below sand grain size are often deflected at grain boundaries (Figure 8-2). Most

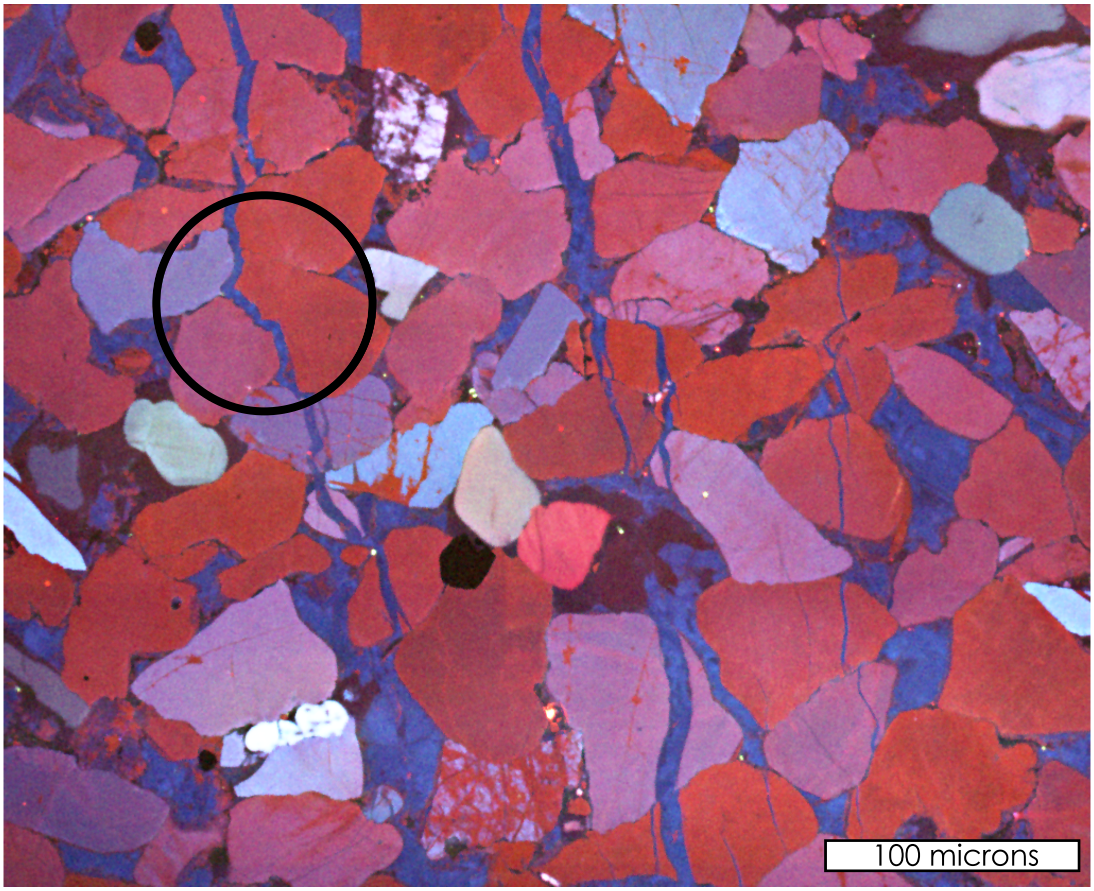

Figure 8-2. Transgranular fracture deflected at grain boundaries. Tensleep Formation, Sample i54. Note within circle that the fracture (with blue luminescence) follows grain boundaries.

transgranular microfractures are filled with weakly luminescent quartz cement, typical of low-temperature, diagenetic quartz precipitation (Zinkernagel, 1978; Seyedolali et al., 1997; Rusk and Reed, 2002).

Intragranular fractures range in color from black to red and blue (Figure 8-3). In rare cases fracture fill is more luminescent than host grain quartz (Figure 8-4). Intragranular fractures may be straight and strike parallel to nearby fractures, or display complicated crisscrossing networks, or in other cases the fractures may be curved (Figure 8-4). Intragranular fractures may be sharp or have gradational or blotchy (Figure 8-4) boundaries. These textures have been associated with plutonic quartz (D'Lemos et al., 1997), dissolution/reprecipitation in hydrothermal vein quartz (Rusk and Reed, 2002; Rusk et al., 2006), and granulite facies metamorphosis (van den Kerkhof et al., 2004b). Blotchy texture is rare but present in some transgranular fractures (Figure 8-5). Intragranular fractures can be wedge-shaped and in intersecting arrays that cut grains and displace grain fragments such that they may be visually restored (Figure 8-6).

MICROFRACTURE DENSITY

One way to quantify microfracture abundance is to measure microfracture *density*, the number of fractures measured per unit area (here, mm^2). A potential drawback to this method is that it disregards size, orientation, and other potentially important factors for fracture studies. An advantage is that it is a simple measure of the abundance of microfractures at a given depth.

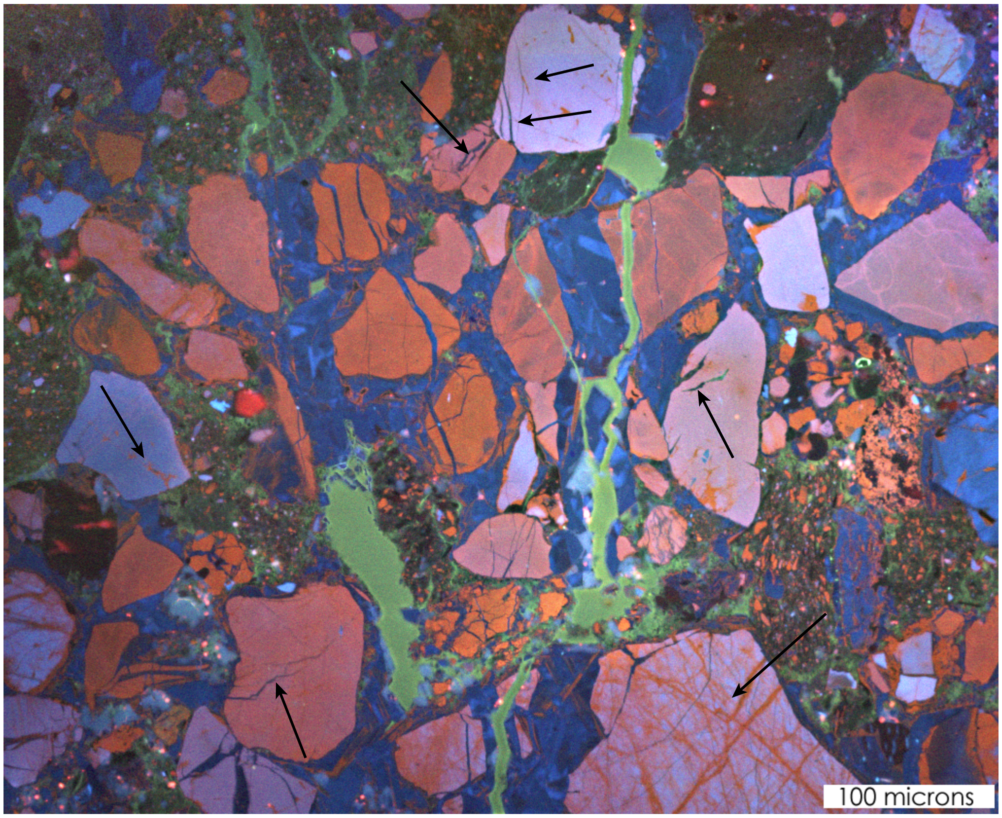

Figure 8-3. SEM-CL image from sample i26. Intra-granular fractures display a variety of colors; mostly red to blue and black (non-luminescent). Transgranular fractures, in contrast, are typically dark blue to non-luminescent; similar to the intragranular cement shown here.

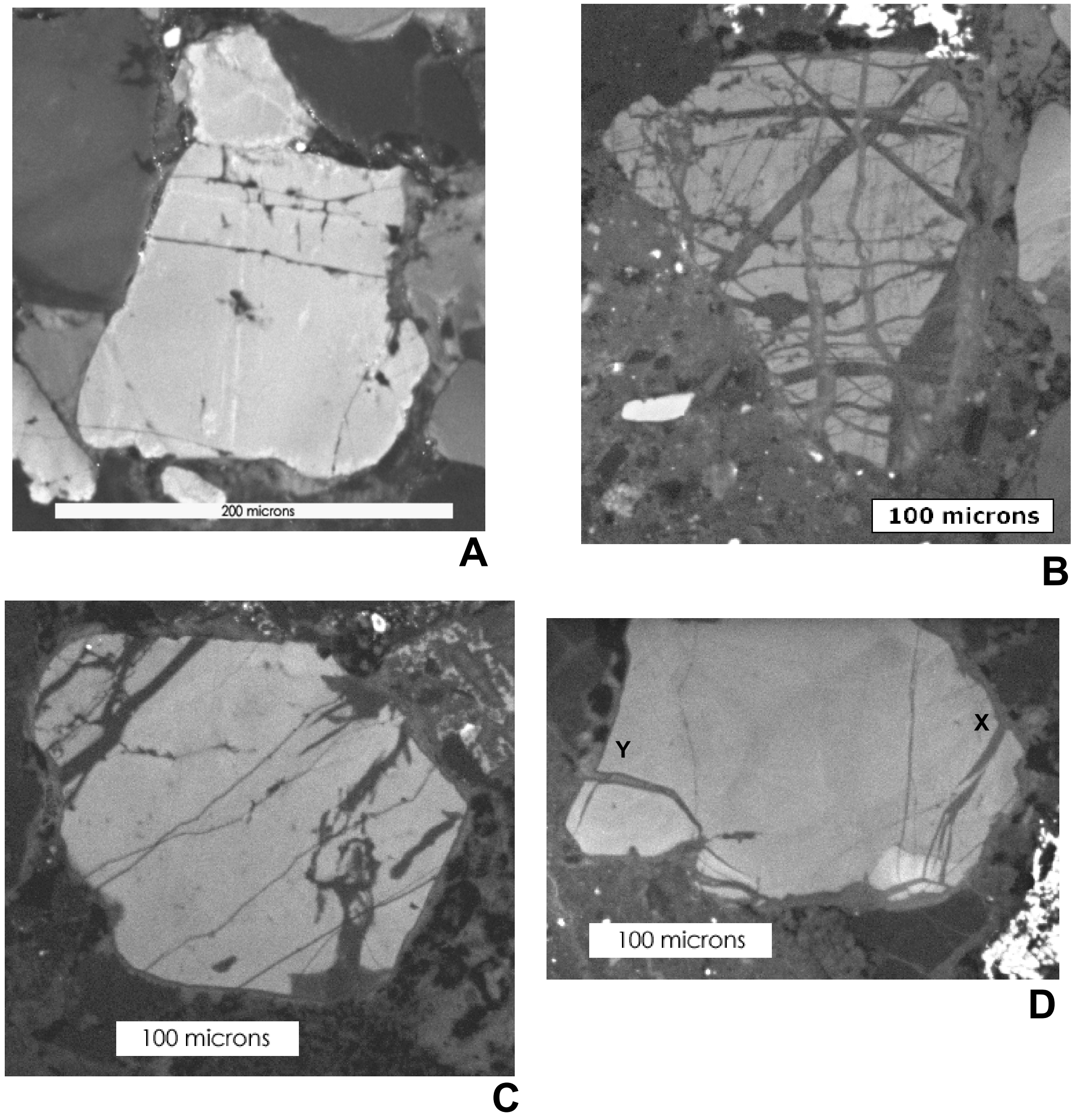

Figure 8-4. Intragranular fractures display various CL characteristics. (A) Fractures are typically darker than host grains, with some exceptions (<5%). (B) Fractures are present in crisscrossing arrays, often revealing a complex inherited microstructural history via crosscutting relationships. (C) Some intragranular fractures are straight and occur in parallel sets. (D) Some intragranular fractures are curved; note the fracture filling cement is locally synchronous with grain-coating cement (X) and elsewhere post-dates post-dates grain-coating cement (Y).

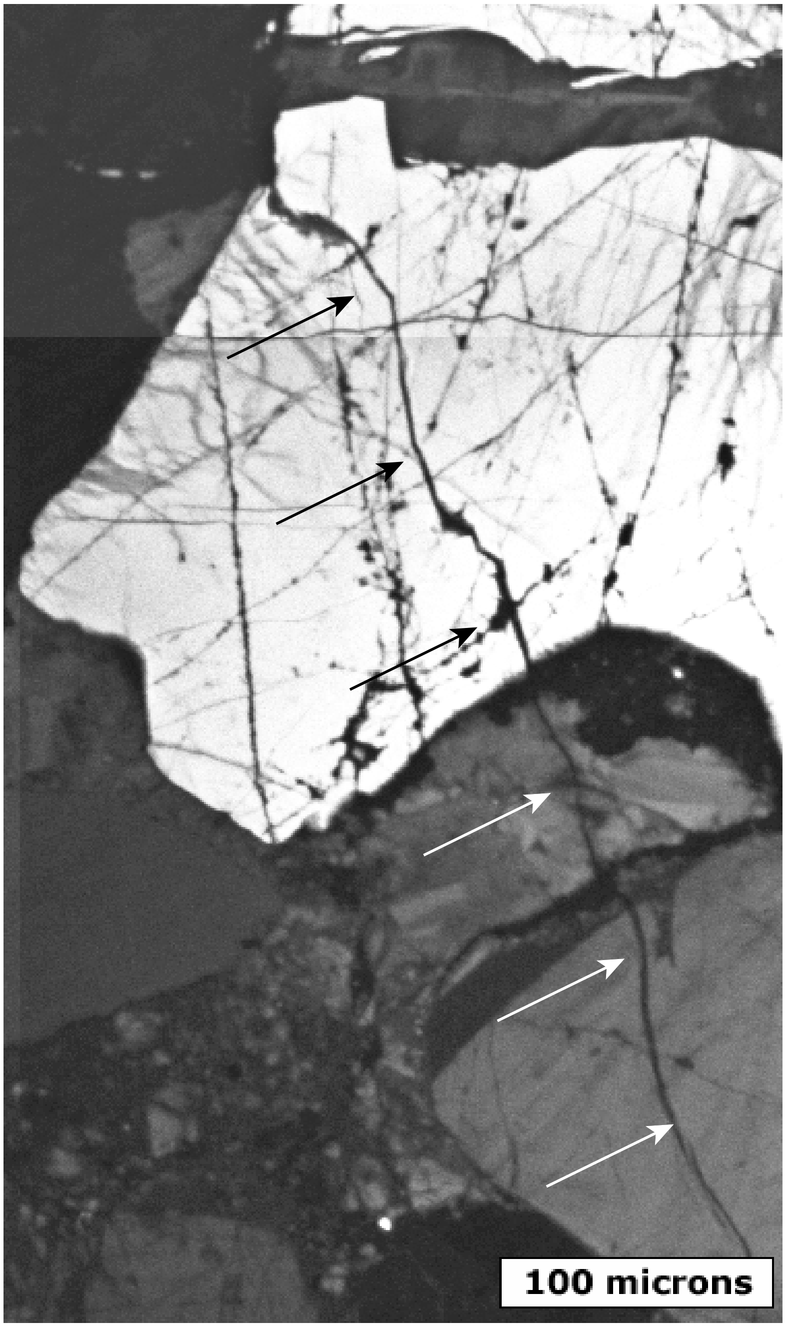

Figure 8-5. SEM-CL image of transgranular fracture (arrowed), El Alamar Formation. Blotchy texture is rare but present in transgranular microfractures, indicating it is not solely the product of primary quartz crystallization processes.

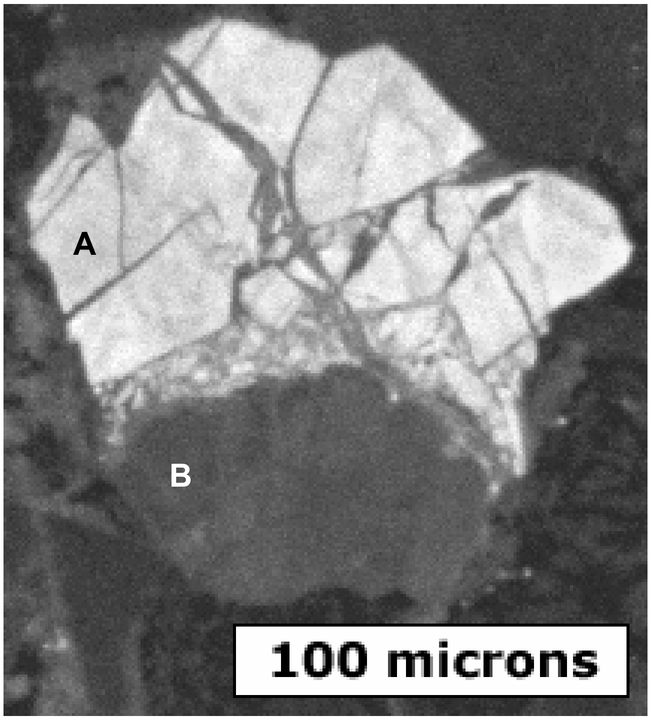

Figure 8-6. Some microfractures appear to be the result of grain-scale crushing or brecciation. A less resistant grain (A) was intensely fractured as it pressed against a stronger grain (B). Many of the fracture-bound fragments of grain (A) may be visibly restored. These microfractures developed *in situ*, but are not believed to reveal much information about associated macrofractures. Rather the fractures result from local grain-scale deformation.

Fracture density with depth

Depth *at the time of fracturing* may be a controlling factor of fracture formation: differential stress, and thus the tendency to achieve brittle failure for a given mean stress, is understood to increase with depth in the Earth's crust (Sibson, 1977). Some fracture arrays can be associated with exhumation and/or cooling (Vollbrecht et al., 1991; Gillespie et al., 2001; Persaud and Pfiffner, 2004; Chapter 6). The compiled dataset includes present-day depth, which of course may be misleading for rocks that have undergone complex burial and exhumation histories. The 2000-3000 m present-day depth range appears to feature relatively low microfracture density (Figure 8-7). This low fracture-density depth range will be addressed in the discussion. This range notwithstanding, it is more likely that each fracture population reflects the specific strain history undergone by its respective host basin than by depth in general.

To further test for correlation between fracture density and present-day depth, data from multiple samples of the same well can be compared, thus controlling for variation among separate basins. Data from multiple depths within the same core are available for 12 wells (3, 4, 5, 11, 12, 13, 20, 24, 27, 29, 31, 34). There is no systematic variation of microfracture density with present-day depth among samples from the same core (Figure 8-8). The variation in microfracture density within the overall dataset appears to dwarf that present in individual wells.

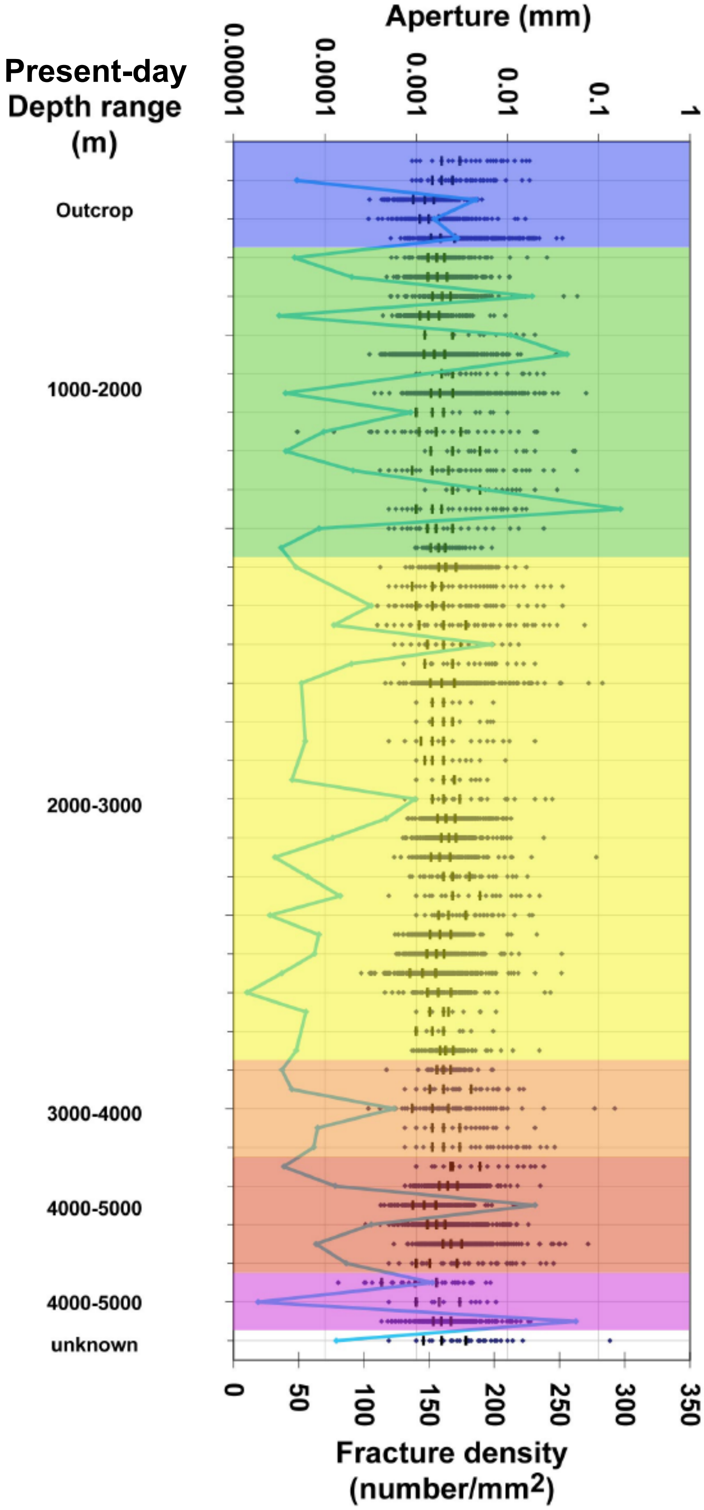

Figure 8-7. Microfracture aperture and density versus depth range, for the 2D microfracture dataset including intragranular microfractures. Each sample's microfracture size population is plotted in a row. Aperture sizes include median size as well as 25th and 75th percentile (black dots). Blue line-series represents fracture density.

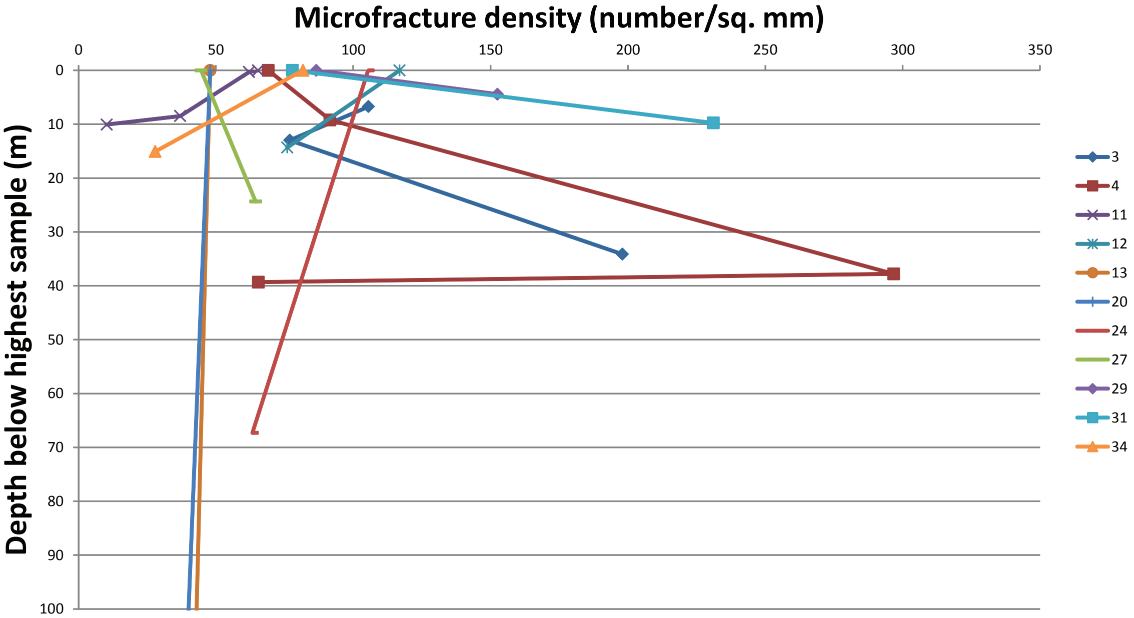

Figure 8-8. Microfracture density versus depth. Data are separated by well in order to control for variation in fracture density by geologic setting. Microfracture density varies extensively within individual wells and does not systematically vary with depth. Max depth difference sampled for Well 13 is 329.8 feet; for Well 20, 136.6 feet.

Fracture density with formation and formation age

The 61 samples that comprise the 2D dataset derive from 18 different geological formations or units. A characteristic fracture size or density for a given formation would imply fracture formation properties specific to rock units, including sedimentary source or provenance (Bernet and Bassett, 2005; Hooker and Laubach, 2007), rate of deposition, or loading history. A comparison of fracture density with formation age is shown in Figure 8-9. Formations are sorted by age. There is some positive correlation between microfracture density and age but high-density samples from the late Cretaceous suggest other factors are more important. Many individual formations display a wide range in fracture density.

SIZE AND ASPECT RATIO

The method used in this study to image fractures includes the calculation of the length and aperture of detected microfractures. To derive accurate statistics of microfracture size and shape, the dataset was filtered by omitting those microfractures in the dataset whose traces extend beyond the boundary of the SEM-CL image. A data subset of such fully-imaged fractures was compiled, which numbers 9,277 total fractures. This subset was used to examine fracture size and aspect ratio. The length and aperture of these non-truncated microfractures show a broad positive correlation (Figure 8-10).

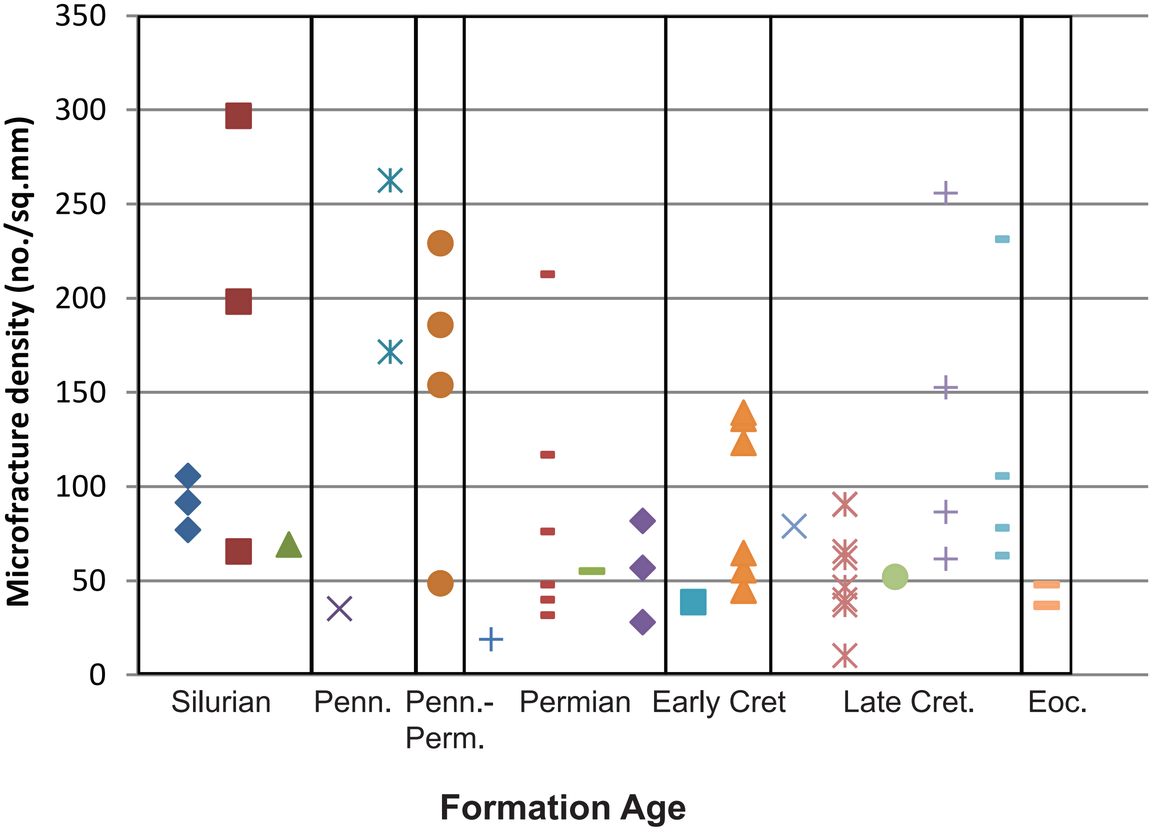

Figure 8-9. Microfracture density versus formation age. Data are subdivided by individual formation.

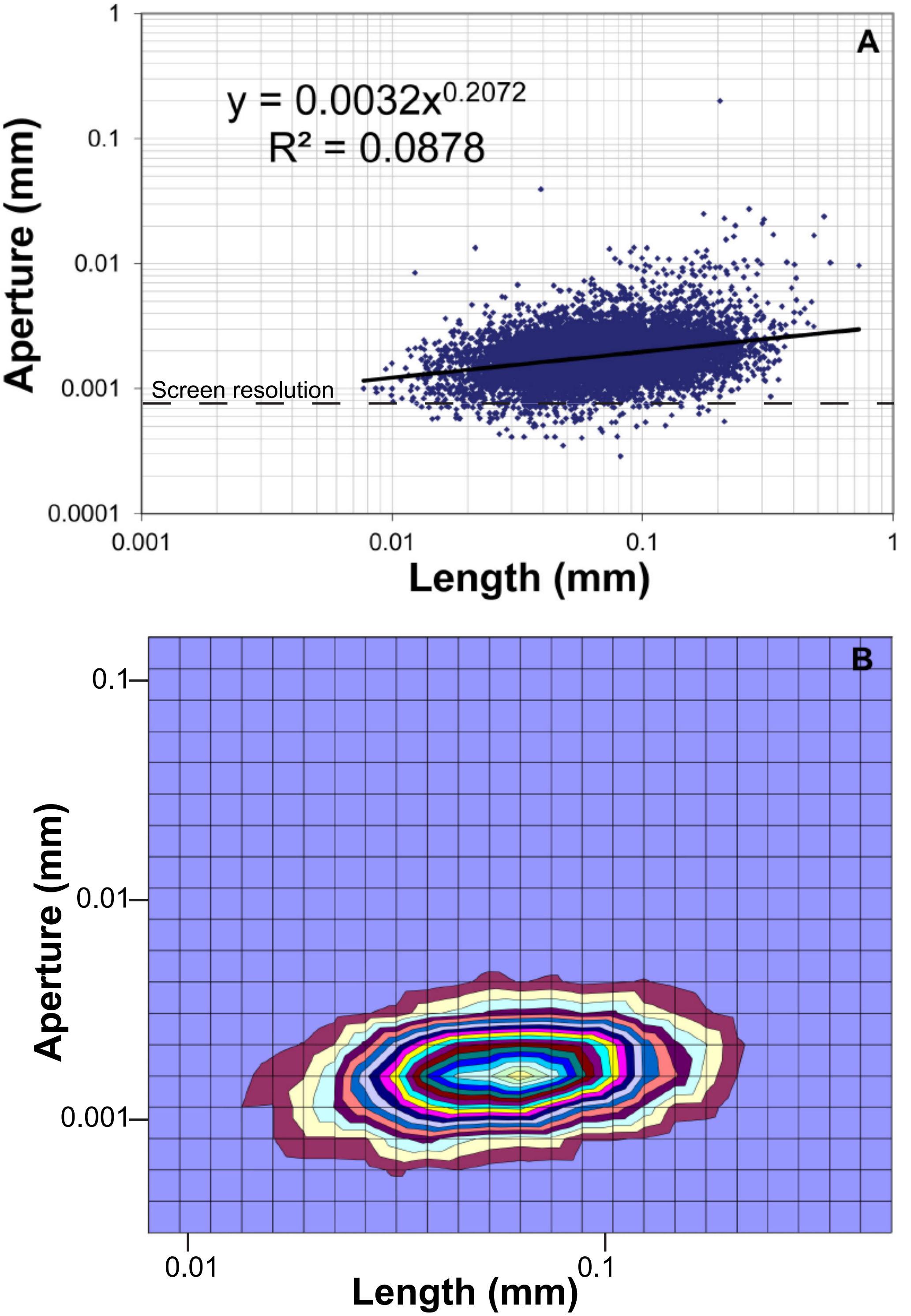

Figure 8-10. (A) Scatter plot of aperture versus length for 9,277 non-truncated microfractures within dataset. (B) Contour plot showing internal structure of scatter in (A). Contour interval = 20 fractures.

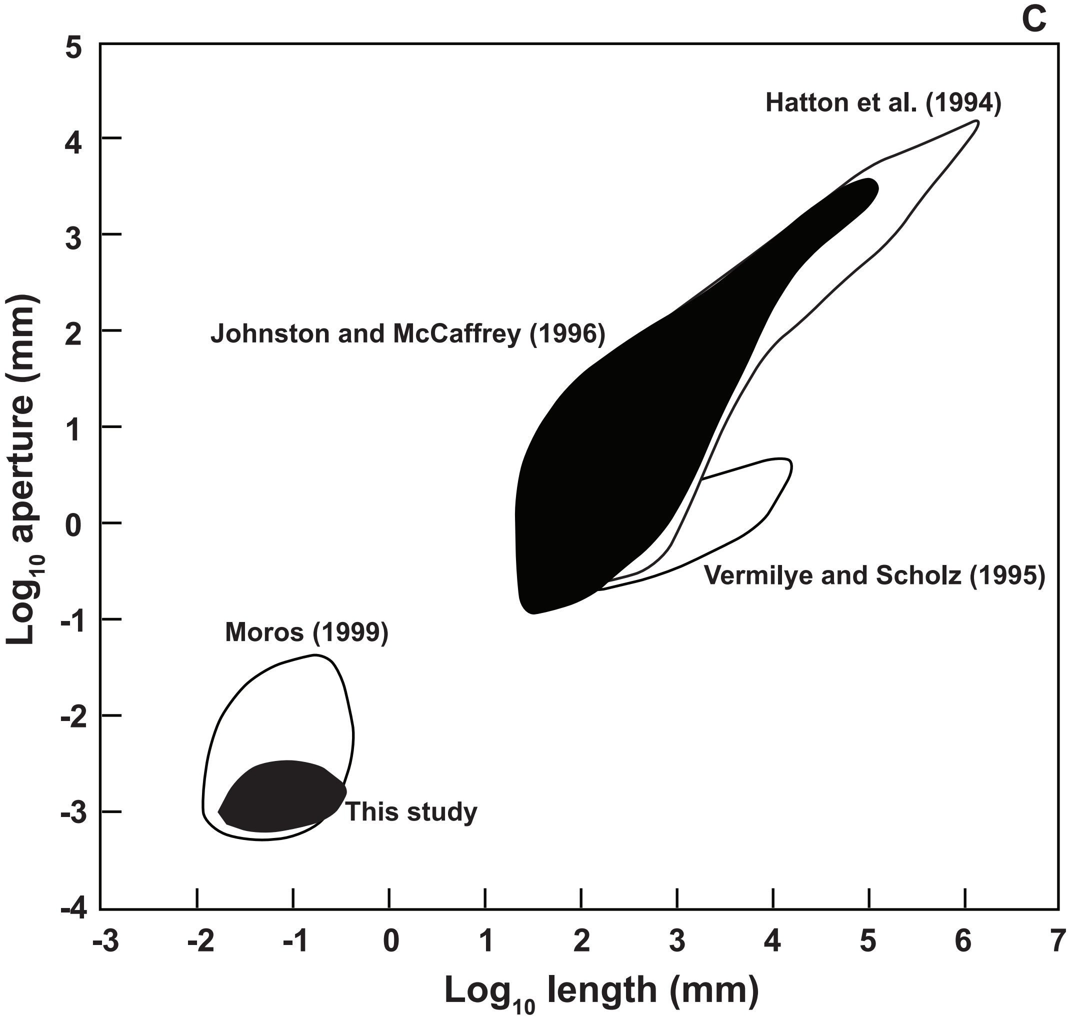

Figure 8-10, continued. (C) Aperture versus length data from this study compared to previous studies. Data presented here mostly overlap with those reported by Moros (1999). The sublinear scaling equation from (A) does not extrapolate to match previously published data from larger fractures.

The resolution of the TIF images created from SEM-CL microscopy is approximately 0.76µm/pixel width at 150X, 0.58µm/pixel width at 200X, and 0.37µm/pixel width at 300X. Many measured apertures fall below the resolution of the SEM-CL images (Figure 8-10); this is possible because the vector-based fracture picking software used calculates lengths between picked points based on screen resolution, and fractures were measured at a zoom at which pixelation is apparent (Chapter 2).

Fracture size with depth

Fracture aperture was studied over depths ranging from outcrop to near 5,000 m (Figure 8-8). Thus even the deepest samples studied are upper-crustal (Sibson, 1977) where opening-mode fractures can be expected to form and in some cases dominate extensional strain. Many fractures observed could have formed at deeper depths than those at which they were sampled; however, it is unlikely that the fractures formed below the upper crust because of the absence of metamorphic textures within the sandstones. Any fractures observed, except quartz cemented fractures in outcrop samples, could have formed at their current sample depths. However, very little constraint exists of fracture timing with respect to burial, so the fractures studied do not necessarily reflect brittle deformation styles specific to any depth. Figure 8-11 shows average fracture length, aperture, and aspect ratio distributions by depth.

Fracture size with grain size

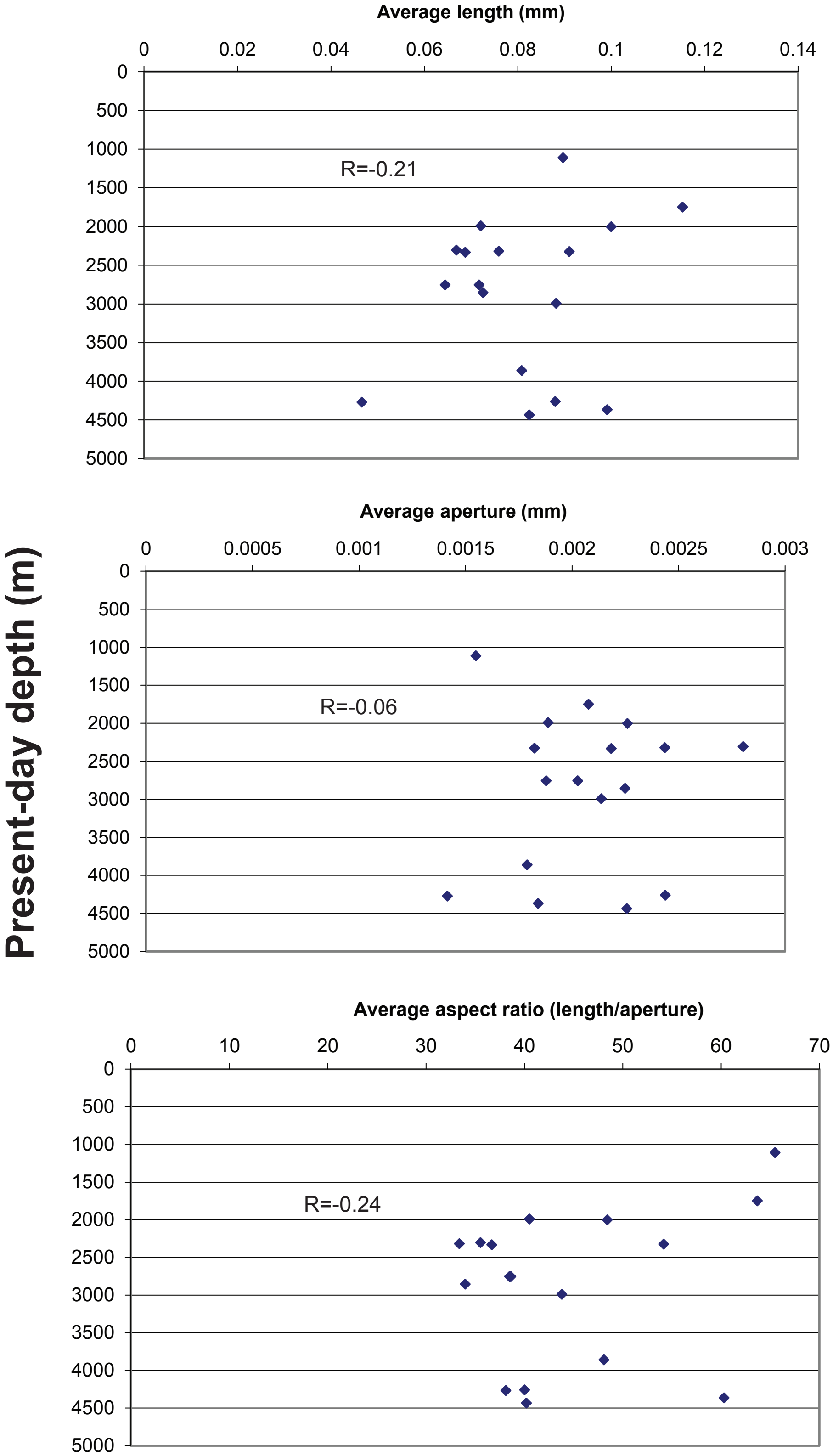

Figure 8-11. Fracture length, aperture, and aspect ratio, averaged from all fractures measured per sample, versus depth, truncated microfracture subset. Note all three size/shape measures poorly correlate with depth.

Lastly, grain sizes were measured among a subset of the dataset. There is some positive correlation between both fracture length and aperture with increasing grain size (Figure 8-12).

INTERPRETATION OF MICROFRACTURE POPULATIONS

Fracture scaling

Scaling extrapolations using only transgranular microfractures (Hooker et al., 2009; Chapter 7) yield data approximating power-law size distributions with *b* close to 0.8; however, omitting all intragranular fractures likely removes some genetically related fractures from the throughgoing fracture population, thus biasing the calculated frequency. One alternative to omitting all intragranular fractures is to count all fractures and look for signal among the noise in orientation or size distribution. To date such a task has not revealed such a signal (Hooker et al., 2009) and the absence of systematic trends of intragranular-microfracture frequency present in this dataset are consistent with the signal being very low. That is, the majority of intragranular microfractures are likely unrelated to larger fractures.

There remains the possibility of further filtering the microfractures based on color or texture in order to improve fracture frequency estimations. The irregular textures commonly associated with microfractures, aptly described as *splatter* and *cobweb*-like by Rusk and Reed (2002), resemble textures that have been identified with quartz-forming processes such as crystallization from melt

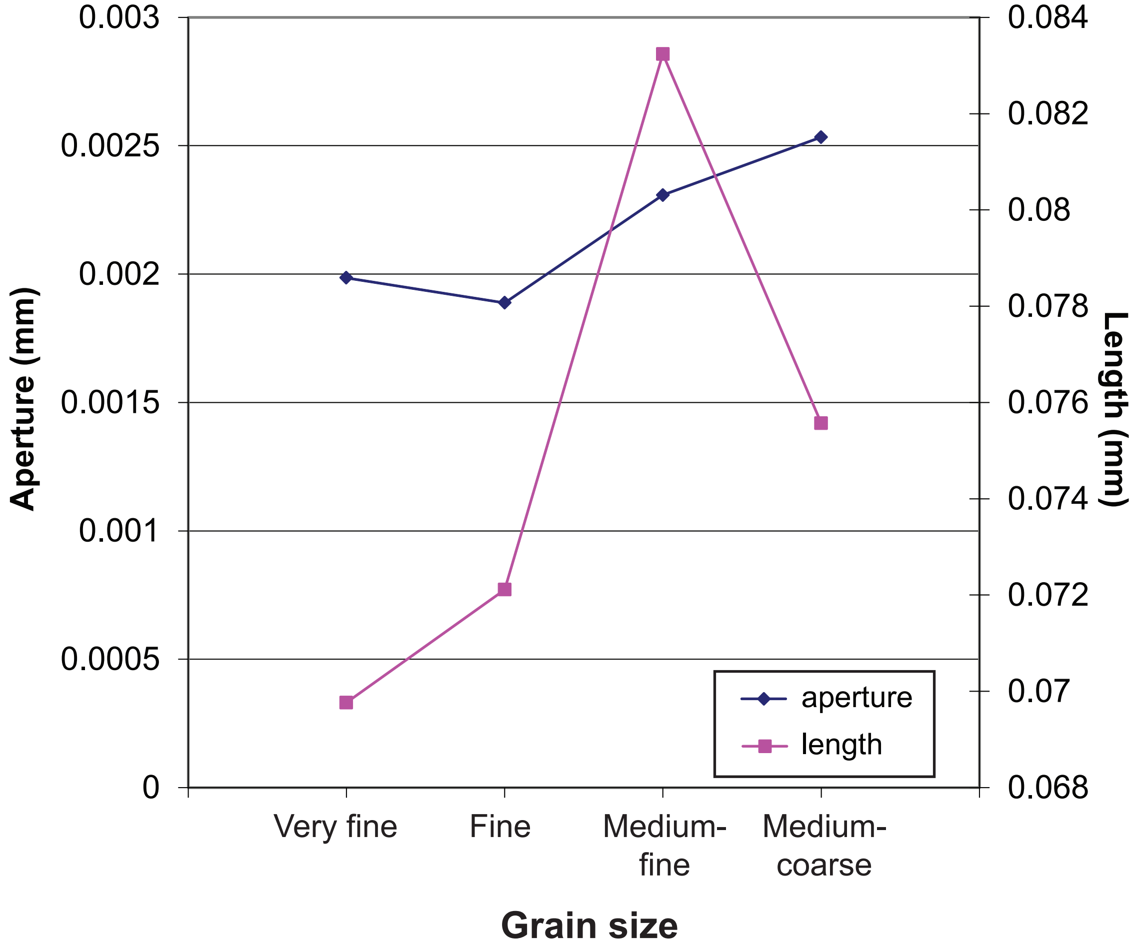

Figure 8-12. Average microfracture length and aperture versus grain size.

and hydrothermal precipitation. These textures appear to be more common in intragranular fractures. It is therefore likely that fractures featuring these textures are inherited. However, some of these textures are associated with transgranular fractures (Figure 8-5), so such textures can develop during sandstone diagenesis.

Microfracture density

The apparent reduction in microfracture density over intermediate (2000-4000 ft) depths (Figure 8-7) could be explained by an increase in fracture development at great depth, under greater differential stress, and further fracture development during exhumation. Each depth range shown features high fracture density variability, however, so depth is likely not a major control on intragranular-fracture density. The correlation between in fracture size and grain size (Figure 8-12), and the absence a progressive relationship between size or density and depth (Figures 8-7, 8-8, 8-11), suggest that fracture size and density are more likely related to the host-rock grain framework itself, whether by inheritance from source rocks or by grain-scale fracturing mechanisms.

In summary, the intragranular fractures are ubiquitous in sandstones. Their size and abundance appear to be controlled by formation and grain size more than depth or other characteristics which may otherwise influence rock fracture-proneness. Most of these fractures are either inherited or, if *in situ*, dominated by grain scale stress field heterogeneities. Such fractures therefore display little information about possible associated macrofractures in the rocks from which they are sampled.

CONCLUSION

Chapter 9: New progress in understanding natural fracture-size distributions in sedimentary rocks

This study illustrates, using examples mostly from sandstones, the variety of aperture-size distributions that natural fractures in bedded rocks can display. Many natural fracture sets are not well fit by a single, simple size distribution equation, even after attributing some scaling irregularities to sampling artifacts. However, the majority of natural fracture sets observed are reasonably well-fit by power-law equations with exponents near 0.8. Other fracture sets are better fit by characteristic (log-normal or exponential) size distributions. Although the reason or reasons for the difference between the two types of fracture-size scaling are unknown, simulations of the mechanical effects of cement precipitation during fracture opening can explain the difference.

The surveys of microfractures presented in this study, both of transgranular microfractures (Chapter 3, Chapter 4) and combined transgranular and intragranular microfractures (Chapter 8), test the hypothesis that sedimentary rocks subjected to tectonic strains host pervasive sets of microscopic fractures (Laubach, 1989). The power-law scaling patterns, apparent in the majority of fracture sets observed, extend to the micron-size range for fracture apertures. Thus in general, tectonic-fracture strain in brittle rocks is partially manifest among closely spaced microscopic fractures.

Fracture strain accumulates in characteristic-sized increments. Some fractures are bridged by opening increment gap-widths of consistent size. In contrast, other fractures show narrow ranges in gap-width near the fracture margins with wide, blocky euhedral cement towards the fracture center. Such variation in cement texture could result either from progressively quickening opening or slowing cementation as the fracture grows; moreover, the variation does not preclude that opening was still episodic while euhedral cement precipitated. In any case, the wide range of fracture sizes which defines power-law scaling does not require strain increments of wide-ranging magnitude, but can be explained by the internal organization, among active fractures, of characteristic-size strain increments.

Fractures in the same geologic setting can show a variety of scaling properties. For example, the Cambrian Eriboll Formation is commonly riddled with microfractures; the underlying Torridonian Supergroup locally has few microfractures amidst a high-strain macrofracture population. The Cambrian Mesón Group contains some fractures that follow characteristic size distributions lacking synkinematic, cement as well as power-law distributed fractures with abundant crack-seal texture, consistent with the idea that the relative rates of fracture opening and sealing exert a fundamental control on how the fractures scale. Comparing fracture intensity with structural position indicates some systematic variation between power-law exponent and local strain. Such a relationship suggests that, holding temperature, water chemistry, and rock type constant, local variation in the rate of fracture opening may impart variation in the relative abundances of large and small fractures.

Natural fracture sets that are well fit by power-law aperture-size equations typically have scaling exponents, measured in 1D, near 0.8. Two fracture sets measured in 2D (Chapter 4) test whether the 2D scaling exponent is greater because of topological effects. The exponent in these cases (Samples 45 and 53) is slightly greater than 1, suggesting the 0.8 figure is to some degree the result of a scanline’s natural tendency to under-represent small fractures that would be better represented if maps or volumes were interrogated. Nonetheless, a characteristic 3D scaling exponent likely exists, because it is implausible that the topological effect of 1D sampling works upon a wide range of 3D exponents to produce a characteristic 1D exponent. A direct test of this claim could be the subject of future study. At the present, the 0.8 value has two important implications. First, it may be used to improve estimates of large-fracture frequency, given small rock samples (Chapter 7). Second, it informs the selection of appropriate and realistic simulation parameters (Chapter 5).

Among the 24 permutations of this simulation tested, permutation 2b best satisfies the observed size distribution statistics and fracture-cement textures.

Permutation 2b grows fractures in equal-sized (i.e., characteristic-sized) increments, with each fracture's growth-selection probability proportional to its current size. New microfractures are created at a constant rate. Consistent with observation, permutation 2b produces fractures that are 1) composed of characteristic-sized opening increments, and 2) arranged in power-law size distributions featuring exponents near 1 over a wide range of input parameters (Figure 5-13). Results of the simulation also suggest that some of the observed irregular scaling patterns can be explained by variable cement-precipitation and or fracture-opening rates.

Increased fracture cohesion imparted by synkinematic cementation can explain power-law aperture-size scaling. By providing resistance to fracture opening, synkinematic cement allows larger, less completely filled fractures to grow faster than smaller, more completely filled fractures. This effect is simulated in Chapter 5 in the forms of size-proportional growth magnitude and size-proportional growth-selection probability.

Evidence from fluid inclusions and SEM-CL mapping of synkinematic quartz cements within the Triassic El Alamar Formation allow partial reconstruction of the evolution of a natural fracture set, providing a test of the simulation in Chapter 5. Fractures open gradually, over millions of years. Consistent with results from Becker et al. (2010) and Fall et al. (2012) for individual fractures, this study shows that large fractures have slow opening rates. A new result from this study is that fractures within a set have overlapping growth histories. Microfractures form and open throughout the evolution of a fracture set. This observation is consistent with overlapping fracture opening histories reconstructed from rocks within the Piceance Basin by Fall et al. (2012). Fractures within the El Alamar Formation may open early and never reactivate or reactivate after long periods of quiescence. New microfractures may form amid dense arrays of pre-existing, actively growing fractures.

The fracture growth simulation (Chapter 5) postulates that the important controls on the emergence of power-law scaling of fractures are the relative rates of opening and cement precipitation. It is unclear whether these two variables are entirely independent. Both are potentially sensitive to fluid transport and pressure, and it is unclear whether cement precipitation is generally limited by fluid transport or kinetics (Worden and Morad, 2000). The crack-seal textures within fractures in this study are best explained by kinetics-limited quartz precipitation (Walderhaug, 1994; Lander et al., 2008). But not all fracture systems are the same; for example, Rusk and Reed (2002) used evidence from CL to demonstrate that fracturing in a hydrothermal system involved feedback between fracturing, fluid pressure, and quartz precipitation and dissolution.

The evidence from fluid inclusions, fracture cement mapping, and oxygen isotopes in synkinematic cements from fractures in the El Alamar Formation suggest that the cement precipitation rate was fast enough to keep up with fracture opening despite fluctuations in pressure, temperature, and or fluid composition. The final aperture-size distribution of Set C is typical of natural fractures (i.e., it is well fit by a power-law equation with an exponent near 0.8), despite a greater tendency than normal for microfracture segments to form in dispersed clusters at the micron scale, rather than as connected single-fracture increments. Thus the evolution of the El Alamar Formation fractures is consistent with the notion that fractures that open and are filled at comparable rates form power-law size distributions with the characteristic exponent value, as illustrated by the fracture simulation of Chapter 5. This is a common, but not universal, phenomenon. It remains to be explored why two seemingly independent variables (fracture opening rate and cementation rate) should so commonly be similar in natural settings.

On the other hand, compared to the radius of the Earth, the range of depths at which the fractures studied herein formed is quite narrow. No rocks studied here have experienced significant metamorphism, and so burial below ~20 km is unlikely. Perhaps rates of fracture opening and cement precipitation are independent but coincidentally matched within the upper crust. Near the Earth's surface, extreme tectonic strain rates have been measured from $10^{-10}yr^{-1}$ at intraplate sites (Eichhubl et al., 2009) to $10^{-6}yr^{-1}$ at plate boundaries (Kreemer et al., 2003). If this strain were accommodated by fracture opening, then these strain rates could be translated into average fracture opening rates using an average fracture spacing. Using the following definition of strain rate

$$\dot{\epsilon} = \frac{L_f - L_0}{L_0} \times \frac{1}{t} \qquad (9\text{-}1)$$

where L_f is the length of an average-sized fracture-spacing pair (i.e., the scanline length divided by the number of fractures), L_0 is the initial length (i.e., L_f minus the average fracture size), and *t* is time elapsed. It is clear from the wide range of fracture apertures and the fractures' overlapping opening histories that individual fractures undergo a wide range of opening rates, but for a first-order approximation I can neglect fracture size variation. Fracture opening rate is then:

$$R = \frac{L_f - L_0}{t} = L_0\dot{\epsilon} \qquad (9\text{-}2).$$

Within datasets collected for this study, average microfracture spacing is 7.6 mm, ranging from 0.1 to 50.8 mm (Appendix A). Using the strain rates cited above, a range of fracture opening rates is constrained, using the minimum average spacing and strain rate to calculate the minimum opening rate, and the maximum average spacing and strain rate to calculate the maximum opening rate. This corresponds to fracture opening rates between 1.0×10^{-2} and 5.1×10^{4} μm/m.y.

If cement precipitation is indeed limited by kinetics (Walderhaug, 1994), then quartz precipitation rates can be calculated using experimental rates and those Lander (2008) inferred from calibrated sandstone cement accumulation models. Using the Arrhenius equation (Equation 6-2), the precipitation rate parallel to the quartz c-axis, on a 1 mm^2 non-euhedral surface, is 1.7×10^{-4}

mm^3/m.y. at 60°C and $1.5x10^0$ mm^3/m.y. at 300°C. The latter figure represents the maximum upper-crustal quartz cement precipitation rate. The minimum precipitation rate can be estimated by reference to Lander et al.'s (2008) experimental results, which show that a-axis precipitation is roughly 17% that of the c-axis, and that precipitation upon euhedral surfaces slows down by a factor of 20 compared to non-euhedral surfaces. Therefore the minimum of the range of kinetics-limited quartz precipitation rates, i.e., upon euhedral surfaces, parallel to the a-axis, at 60°C, would be $1.5x10^{-6}$ mm^3/m.y.

If such cement volumes are close to equidimensional then the thickness of a cement accumulation, in μm, can be calculated by dividing by the area (1 mm^2). The resulting quartz precipitation rates are $1.5x10^{-3}$ μm/m.y. (minimum) and 1.5×10^3 μm/m.y. (maximum). These rates are comparable to those of fracture opening rates (Figure 9-1) at upper-crustal depths (1 to 7 km, for typical geothermal gradients). Thus a primary reason why power-law distributed fracture sizes are widely observed could be the unrelated but similar rates of fracture opening and cement precipitation within the upper crust.

To summarize, the observations of fracture-size distributions and fracture-cement textures presented herein suggest that fractures that grow amid precipitating cements feature a wide range of sizes and are often well-fit by power-law size distribution equations. Such size distributions can be replicated using rules that are abstract (i.e., rely on random-number generation to select

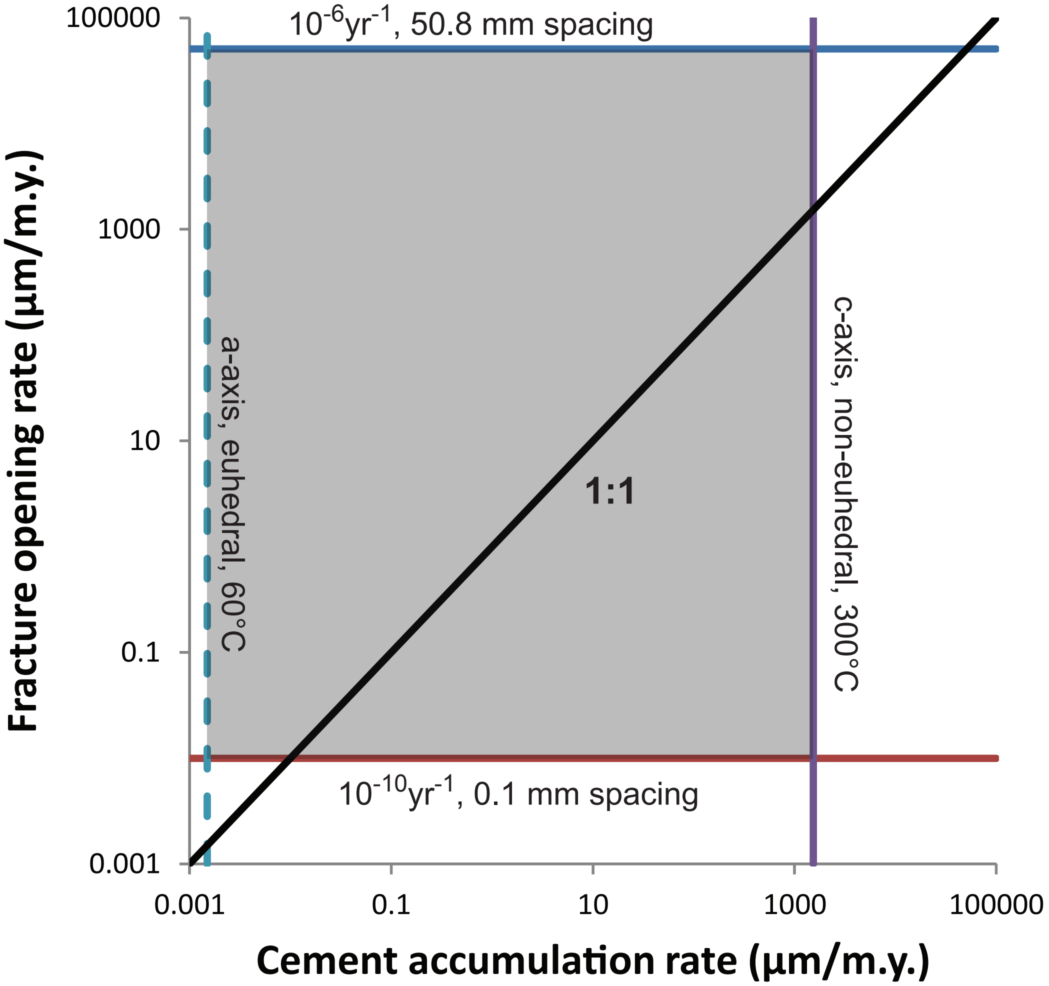

Figure 9-1. Ranges of expected fracture opening rates and quartz-cement accumulation rates expected in the upper crust. The shaded area represents the range of expected natural rates within the Earth's crust. Much of the 1:1 line resides within both of the ranges, indicating similar rates of these two seemingly independent variables. Thus the amount of energy within, and composition of, the crust may uniquely suit it to power-law size scaling of natural fractures.

fractures for growth) but nonetheless simulate likely effects of synkinematic cement precipitation (resistance to opening). Reconstructions of natural-fracture opening are broadly consistent with the opening sequences predicted by the simulation. Power-law size scaling of natural fractures does not require a wide range of strain increment sizes; rather, fracture scaling can be explained by the interaction of fracture opening and cementation.

Appendix A: Sample information and geologic settings

DATA SUMMARY TABLES

The following are tables summarizing fracture data collected for this study. The tables are followed by brief geologic descriptions of the sites from which these data were collected. Frequency and spacing data are given in Appendix B and C, respectively.

		chi2 values											
Sample Number	**Sample**	**Power law**	**Exponential**	**Normal**	**Log-normal**	***b***	***a***	**No. micro-fractures**	**Scanline length (mm)**	**Strain**	**No. macro-fractures**	**Scanline length (mm)**	**Total no. fractures**
1	Lochan Fada	**1.144**	65.553	*	23.843	0.830	4.2E-03	153	125.3	0.019292	61	2308.1	214
2	06JH105	**0.833**	33.417	17.41934347	17.419	0.781	5.5E-03	38	29.8	0.008759	123	3091.3	161
3	LMS-SL	**23.192**	301.205	1016465.468	57.170	1.152	5.1E-03	101	27.1	0.072641	52	6523.1	153
4	PVSCN NE	**3.519**	35.424	28.1169189	21.732	0.926	2.9E-03	104	47.9	0.015525	47	7198.0	151
5	K2-3A	**0.024**	0.071	0.639509	0.151	1.102	3.0E-04	11	37.1	0.001374			11
6	K2-5B	**0.046**	0.326	2.161231583	0.703	0.354	2.3E-02	11	16.3	0.035727			11
7	SFE2-8254.6	0.340	**0.086**	0.230873955	0.092	1.890	2.0E-06	24	74.8	0.000958			24
8	SFE2-8274.9	0.009	**0.007**	0.013783275	0.019	0.848	2.0E-04	4	90.9	0.000152			4
9	SFE2-9511.4	0.036	0.027	0.243545344	**0.023**	0.738	1.1E-03	12	94.4	0.000927			12
10	SFE2-9547.1	**0.010**	0.030	0.096239871	0.062	0.274	8.5E-03	6	89.7	0.006006			6
11	SFE2-9870.0	0.152	**0.042**	0.34760285	0.059	1.213	6.0E-05	18	82.7	0.00054			18
12	SFE2-9936.9	0.001	**0.000**	0.010495749	0.009	1.195	3.0E-05	3	88.8	0.000107			3
13	Well 1-8881.6	**0.005**	0.024	0.091525478	0.040	0.406	7.4E-03	7	79.0	0.003917			7
14	Well 1-9476.0	**0.017**	0.100	0.359589804	0.137	0.335	1.1E-02	8	61.1	0.009456			8
15	Well 1-9502.2	0.062	0.068	0.751135858	**0.041**	0.696	4.2E-03	18	86.0	0.004659			18
16	Well 1-9526.9	**0.239**	0.890	741.8968778	0.317	0.823	2.1E-03	27	83.5	0.003812			27
17	Well 1-10888.6	**0.015**	0.063	0.180786197	0.083	0.461	6.5E-03	10	91.7	0.004804			10
18	Well 1-10940.3	**0.242**	2.787	102226.3073	18.222	0.769	3.5E-03	37	85.6	0.010235			37
19	Well 1-10979.1	**0.022**	0.041	0.248782049	0.048	0.318	1.9E-02	10	74.5	0.01718			10
20	Well 1-11011.8	**0.004**	0.011	0.048457395	0.029	0.561	1.7E-03	5	93.7	0.000668			5
21	Well 1-12302.7	**0.039**	0.287	3.181684041	0.508	0.455	7.9E-03	14	92.9	0.013236			14
22	Well 2-12186.6	**0.042**	0.142	0.317100103	0.190	0.399	1.2E-02	12	78.4	0.011901			12
23	Well 6-9876.0	0.004	**0.004**	0.016324941	0.017	0.607	2.3E-03	3	90.4	0.000758			3
24	Well 6-9893.5	**	**	**	**	**		0	87.3	0			0
25	Well 9-9631.5	**0.036**	0.148	1.236744158	0.123	0.644	3.1E-03	12	88.0	0.002974			12
26	Well 9-9639.2	0.332	0.609	780.8925971	**0.109**	0.817	3.7E-03	36	89.2	0.006832			36
27	Well 7-9663.8	**0.029**	0.266	3.123432534	0.422	0.579	3.6E-03	14	92.6	0.003259			14
28	Well 7-9683.6	0.002	**0.000**	0.009712431	0.011	0.290	9.5E-03	3	90.6	0.004903			3
29	LD2806	0.058	**0.018**	0.113630672	0.058	1.764	1.0E-06	14	108.1	0.000209			14
30	LD3561	0.014	**0.003**	0.038447633	0.021	1.429	2.0E-05	10	97.6	0.000374			10
31	LD4414	**0.005**	0.007	0.043684484	0.028	1.588	3.0E-06	7	92.7	0.00019			7
32	LD6043	**0.042**	0.100	0.329448568	0.174	1.242	7.0E-05	20	98.1	0.000697			20
33	MWX4538	0.005	**0.001**	0.115726286	0.082	1.991	2.0E-06	6	22.4	0.000737			6
34	MWX4629	0.471	**0.159**	0.742599873	0.161	1.252	8.0E-05	14	38.3	0.000724			14
35	MWX4931	**	**	**	**	**		0	20.1	0			0
36	MWX5098	**0.047**	0.625	21.88516147	0.242	0.745	4.8E-03	18	38.8	0.006068			18
37	19G-10298	**0.172**	2.847	18.64398342	3.507	0.738	8.0E-04	174	2067.3	0.003434			174
38	19G-7348	**0.130**	0.287	1.046115698	0.135	0.454	1.9E-02	32	111.8	0.020852			32
39	GV2-6957C	0.290	**0.032**	0.178071364	0.057	0.782	2.1E-03	12	43.2	0.001645			12
40	SHCT	**0.018**	0.139	0.228183499	0.206	0.743	3.0E-04	16	554.0	0.002769	26	33053.5	42
41	GR1-3SH total	**0.012**	0.204	0.099397593	0.071	0.873	8.0E-05	20	1016.7	0.000105	10	52151.3	30
42	Tranquitas 1	**1.441**	16.723	83662.30091	4.576	0.647	1.1E-02	173	229.5	0.025069			173
42a	Tranquitas 1 filtered	**0.638**	8.428	949.5758745	2.818	0.597	1.2E-02	131	229.5	0.023863			131
43ew	RC2010 E-W strike	**0.018**	0.407	0.428016624	0.268	0.524	3.1E-03	14	194.7	0.018051	25	2972.2	39
43ne	RC2010 NE strike	**0.013**	0.219	3.209752776	0.122	0.888	8.0E-04	26	194.7	0.001494			26
43	RC2010-6 all	**0.080**	4.214	2.758382854	1.497	0.733	3.3E-03	46	194.7	0.021066	25	2972.2	71
44	10JH10	**0.654**	23.121	217533.3623	9.279	0.874	2.0E-03	101	222.0	0.009142	114	14235.3	215
45	Well C-3483L	**0.555**	28.096	446211337.3	5.341	0.635	2.0E-02	157	121.6	0.035972			157
46	Well C-3483U	**1.805**	45.646	8.22235E+11	10.335	0.728	2.4E-02	160	67.5	0.053792			160
47	Well C-3484	**0.067**	3.804	6315956208	1.789	0.643	5.0E-03	65	204.6	0.012788			65
48	Well C-3499	**0.190**	3.563	9381.749456	0.715	0.776	3.2E-03	77	182.8	0.006715			77
49	Well C-3556	0.027	**0.016**	0.038559546	0.042	1.216	5.0E-05	11	108.7	0.000316			11
50	Well M-3237.5	0.070423	**0.012**	0.128974935	0.029	1.142	1.0E-04	12	94.2	0.000597			12
51	Well M-2724.0	0.026	**0.007**	0.024862578	0.023	1.053	2.0E-04	8	81.6	0.00047			8
52	Well M-2992.1	0.215	**0.058**	1.2788972	0.077	1.592	3.0E-05	19	89.6	0.001278			19
53a	08JH07 set A	**1.079**	37.310	54.22450117	13.746	0.846	5.5E-03	134	112.1	0.035903	42	3594.3	176
53	08JH07 all	**16.213**	268.136	2492.191532	86.850	0.974	5.5E-03	342	112.1	0.046578	67	3594.3	409
54a	A-28 set A	**4.595**	45.040	*	115.185	0.895	5.0E-03	150	97.1	0.02255			150
54	A-28 all	**40.088**	337.007	*	28863.286	1.120	3.4E-03	395	97.1	0.032029			395
55a	A-30 set A	**1.284**	29.228	12921861017	26.333	0.664	2.4E-02	97	61.4	0.099362			97
55	A-30 all	**2.089**	56.545	*	90.209	0.737	2.2E-02	131	61.4	0.104809			131
56	08JH09	**10.037**	294.359	*	56.142	0.824	1.6E-02	416	131.1	0.192968	24	1120.5	440
57	A-23	**330.612**	345.662	58779320049	785.524	1.746	9.0E-05	499	40.5	0.02987			499
58	08JH10	1.746	**0.057**	1.21717298	0.116	1.172	4.0E-04	64	93.7	0.003292			64
58a	08JH10 azrange	0.587	**0.032**	0.566381016	0.056	1.229	2.0E-04	38	93.7	0.002057			38
59	08JH11	0.224	0.061	1.148255777	**0.055**	1.127	1.0E-04	17	85.3	0.000536			17
59a	08JH11 azrange	**0.005**	0.007	0.030890913	0.028	0.703	5.0E-04	4	85.3	0.000241			4

Table A-1. Scanline sample statistics.

Sample number	Sample name	Location	Formation	Sample type	Notes				
1	Lochan Fada	NW Highlands	Eriboll	Outcrop	UK Nat'l Grid Ref NH	4232	69410	Reported in Gomez and Laubach 2006	
2	06JH105	NW Highlands	Eriboll	Outcrop	UK Nat'l Grid Ref NH	6100	71378		
3	LMS-SL	NW Highlands	Eriboll	Outcrop	UK Nat'l Grid Ref NG	99500	65450	Reported in Diaz-Tushman 2007	
4	PVSCN NE	NW Highlands	Eriboll	Outcrop	UK Nat'l Grid Ref NH	7768	74406	Reported in Diaz-Tushman 2007	
5	K2-3A	NW Highlands	Eriboll	Outcrop	UK Nat'l Grid Ref NH	7768	74406	Reported in Pinzon 2007	
6	K2-5B	NW Highlands	Eriboll	Outcrop	UK Nat'l Grid Ref NH	7768	74406	Reported in Pinzon 2007	
7	SFE2-8254.6	East Texas	Travis Peak	Vertical core	Staged field experiment #2 well				
8	SFE2-8274.9	East Texas	Travis Peak	Vertical core	Staged field experiment #2 well				
9	SFE2-9511.4	East Texas	Travis Peak	Vertical core	Staged field experiment #2 well				
10	SFE2-9547.1	East Texas	Travis Peak	Vertical core	Staged field experiment #2 well				
11	SFE2-9870.0	East Texas	Travis Peak	Vertical core	Staged field experiment #2 well				
12	SFE2-9936.9	East Texas	Travis Peak	Vertical core	Staged field experiment #2 well				
13	Well 1-8881.6	Piceance Basin	Williams Fork	Vertical core	North Piceance Basin				
14	Well 1-9476.0	Piceance Basin	Williams Fork	Vertical core	North Piceance Basin				
15	Well 1-9502.2	Piceance Basin	Williams Fork	Vertical core	North Piceance Basin				
16	Well 1-9526.9	Piceance Basin	Williams Fork	Vertical core	North Piceance Basin				
17	Well 1-10888.6	Piceance Basin	Williams Fork	Vertical core	North Piceance Basin				
18	Well 1-10940.3	Piceance Basin	Williams Fork	Vertical core	North Piceance Basin				
19	Well 1-10979.1	Piceance Basin	Williams Fork	Vertical core	North Piceance Basin				
20	Well 1-11011.8	Piceance Basin	Williams Fork	Vertical core	North Piceance Basin				
21	Well 1-12302.7	Piceance Basin	Williams Fork	Vertical core	North Piceance Basin				
22	Well 2-12186.6	Piceance Basin	Williams Fork	Vertical core	North Piceance Basin				
23	Well 6-9876.0	Piceance Basin	Williams Fork	Vertical core	North Piceance Basin				
24	Well 6-9893.5	Piceance Basin	Williams Fork	Vertical core	North Piceance Basin				
25	Well 9-9631.5	Piceance Basin	Williams Fork	Vertical core	North Piceance Basin				
26	Well 9-9639.2	Piceance Basin	Williams Fork	Vertical core	North Piceance Basin				
27	Well 7-9663.8	Piceance Basin	Williams Fork	Vertical core	North Piceance Basin				
28	Well 7-9683.6	Piceance Basin	Williams Fork	Vertical core	North Piceance Basin				
29	LD2806	Piceance Basin	Williams Fork	Vertical core	Mamm Creek Field				South Piceance Basin
30	LD3561	Piceance Basin	Williams Fork	Vertical core	Mamm Creek Field				South Piceance Basin
31	LD4414	Piceance Basin	Williams Fork	Vertical core	Mamm Creek Field				South Piceance Basin
32	LD6043	Piceance Basin	Williams Fork	Vertical core	Mamm Creek Field				South Piceance Basin
33	MWX4538	Piceance Basin	Williams Fork	Vertical core	Multiwell Experiment site, Rulison Field				South Piceance Basin
34	MWX4629	Piceance Basin	Williams Fork	Vertical core	Multiwell Experiment site, Rulison Field				South Piceance Basin
35	MWX4931	Piceance Basin	Williams Fork	Vertical core	Multiwell Experiment site, Rulison Field				South Piceance Basin
36	MWX5098	Piceance Basin	Williams Fork	Vertical core	Multiwell Experiment site, Rulison Field				South Piceance Basin
37	19G-10298	Piceance Basin	Williams Fork	Deviated core	North Piceance Basin				
38	19G-7348	Piceance Basin	Williams Fork	Deviated core	North Piceance Basin				
39	GV2-6957C	Piceance Basin	Williams Fork	Vertical core	Grand Valley Field				South Piceance Basin
40	SHCT	Piceance Basin	Cozzette	Deviated core	Slant Hole Completion Test well, Rulison Field				South Piceance Basin
41	GR1-3SH total	Piceance Basin	Cozzette	Deviated core	Grand Valley Field				South Piceance Basin
42	Tranquitas 1	SMO	El Alamar	Outcrop				Reported in Gomez 2007	
43	RC2010-6 all	SMO	La Boca	Outcrop					
44	10JH10	SMO	El Alamar	Outcrop					
45	Well C-3483L	Canadian Rockies	Nikinassin	Vertical core					
46	Well C-3483U	Canadian Rockies	Nikinassin	Vertical core					
47	Well C-3484	Canadian Rockies	Nikinassin	Vertical core					
48	Well C-3499	Canadian Rockies	Nikinassin	Vertical core					
49	Well C-3556	Canadian Rockies	Nikinassin	Vertical core					
50	Well M-3237.5	Canadian Rockies	Nikinassin	Vertical core					
51	Well M-2724.0	Canadian Rockies	Nikinassin	Vertical core					
52	Well M-2992.1	Canadian Rockies	Nikinassin	Vertical core					
53	08JH07 all	Andes	Meson	Outcrop					
54	A-28 all	Andes	Meson	Outcrop					
55	A-30 all	Andes	Meson	Outcrop					
56	08JH09	Andes	Meson	Outcrop					
57	A-23	Andes	Meson	Outcrop					
58	08JH10	Andes	Meson	Outcrop					
59	08JH11	Andes	Meson	Outcrop					

Table A-2. Sample information and collection notes.

GEOLOGIC SETTINGS

Sandstones

This section comprises short summaries of the geologic settings of each dataset studied and short descriptions of the datasets themselves. Datasets are presented in the increasing order of the magnitude of the maximum fracture strain measured at each locality (Table 3-3).

Piceance Basin—Cretaceous Mesaverde Group

The Piceance Basin sediments consist of marginal marine and non-marine siliciclastics deposited in or near the Cretaceous seaway that covered much of present-day North America (Quigley, 1965; Johnson and Keighin, 1981). The sequence features minor transgressions but is broadly regressive, from marine to paludal upsection. Samples studied for fracture analysis derive from the Mesaverde group; mostly from the Williams Fork Formation and the Iles Formation. The sequence's burial history, constrained by Nuccio and Condon (1996) and Nuccio and Roberts (2003) using vitrinite reflectance and heat-flow modeling, indicates that maximum burial was attained near 35 Ma and exhumation began near 10 Ma. At maximum burial the Cozzette sandstone reached a temperature of approximately 170°C. Analysis of fluid inclusion assemblages within synkinematic fracture cements indicates that fractures were opening throughout this extended period of maximum burial. Despite its intramontane setting, the Piceance basin is relatively undeformed by tectonic activity; the maximum fracture strain recorded by microfractures among Piceance basin samples is 0.021 and the average is 0.0047 (Table A-1).

Because of natural gas accumulations, the Piceance basin has been extensively drilled, and all analyzed samples come from recovered core (Table 3-2). The relatively low tectonic deformation present in the area means that in most sample locations bedding is close to horizontal and fractures dip steeply. This arrangement makes deviated (from vertical) core a valuable tool for subsurface fracture quantification. Deviated core enabled the sampling of multiple macrofractures within single layers in three samples. These include the MF31-19G slant core, from which I sampled the Williams Fork Formation, and the Slant Hole Completion Test (SHCT) core and the GR 1-3 Slant Hole core (Figure A-1), from which I sampled the underlying Cozzette Sandstone of the Iles Formation.

East Texas Basin—Cretaceous Travis Peak Formation

Fracture samples are derived from vertical core drilled through the Cretaceous Travis Peak Formation, a Lower Cretaceous fluvial-deltaic accumulation (Dutton et al., 1991) on the western flank of the Sabine Arch (Laubach and Jackson, 1990). Geologic controls on macrofracture distribution in the core were summarized by Laubach et al. (1995). In that study, fracture abundance was calculated by normalizing the cumulative fracture height by the core height (Figure A-2). The authors report that channel sands are highly fractured relative to floodplain and lacustrine sediments; layer thickness poorly

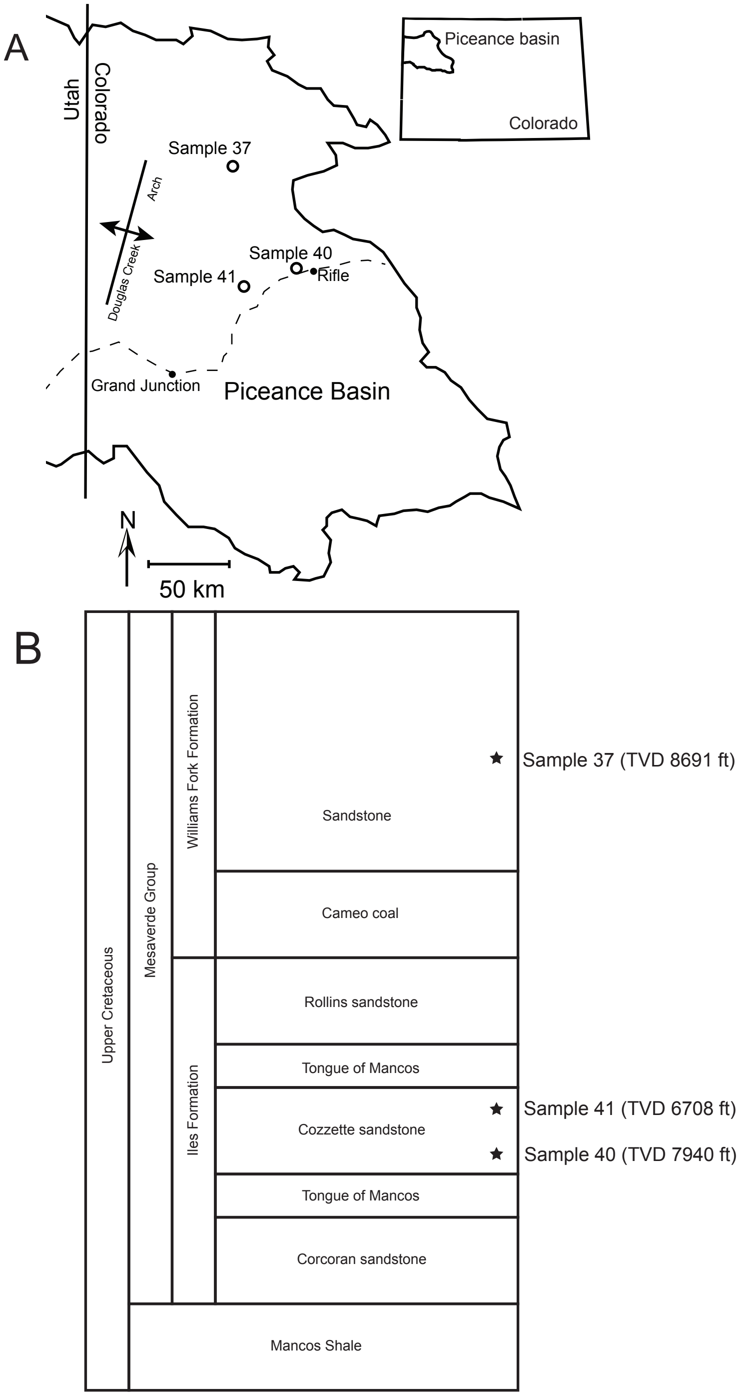

Figure A-1. (A) Map of the Piceance basin. (B) Upper Cretaceous stratigraphy. SHCT (Sample 40) and GR 1-3 (Sample 41) cores were drilled roughly parallel to bedding. (C) Diagram of MF31-19G (Sample 37) core, drilled at 45 degress to bedding.

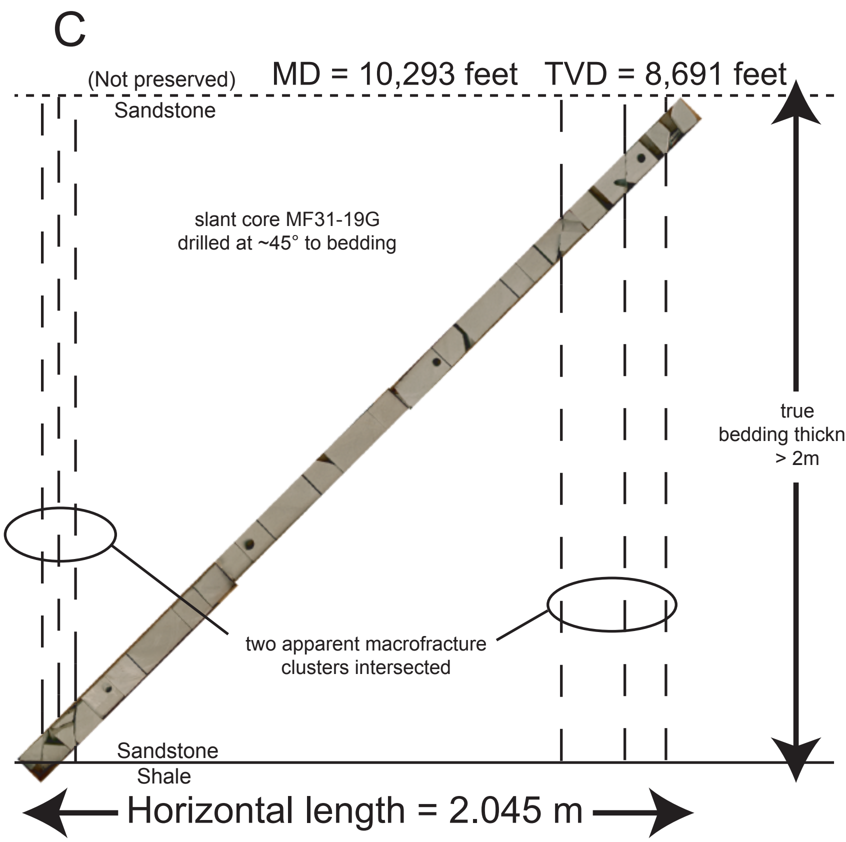

Figure A-1, continued.

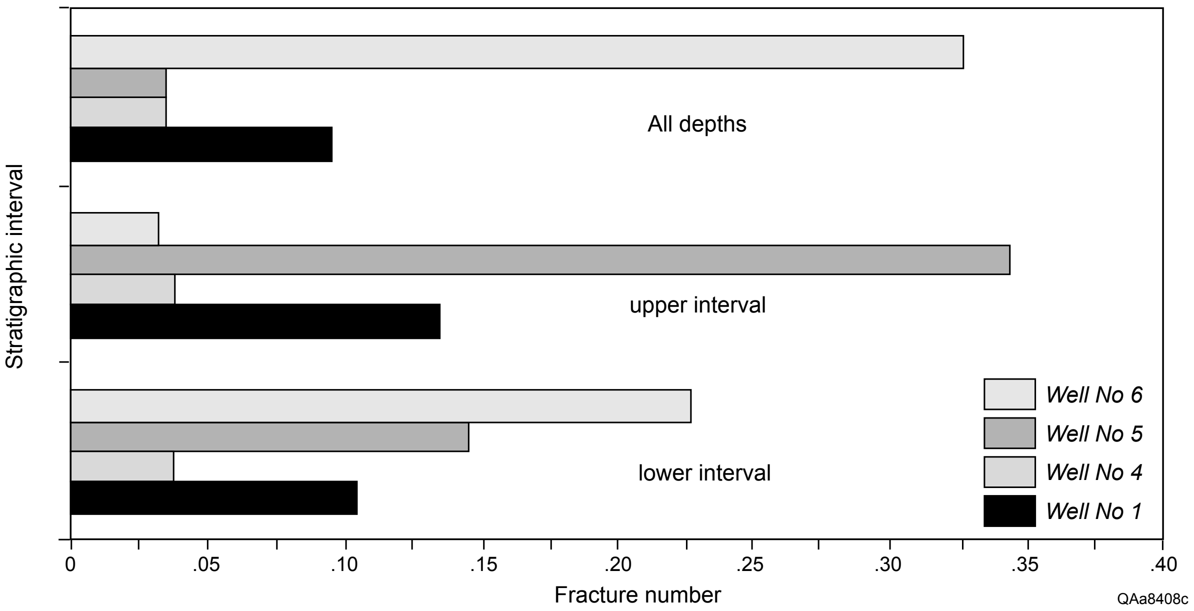

Figure A-2. Fracture abundance versus stratigraphic position for SFE wells (Travis Peak Fm., East Texas Basin), from Laubach et al. (1995a). Fracture abundance was calculated by dividing the cumulative fracture height by the core height.

correlates with fracture abundance in the core. Fluid inclusions in synkinematic quartz cement have homogenization temperatures (a proxy for precipitation temperature) between 134 and 151 °C (Becker et al., 2010), corresponding to fracture propagation initiation near maximum burial depth and persisting for ~48 m.y. (Becker et al., 2010).

Central Andes—Cambrian Mesón Group

Fractures were measured in the Mesón Group at Huasamayo Canyon, approximately 5 km southeast of Tilcara, Argentina, and Perchel Canyon, 10 km to the north (Figure A-3). The lowest rocks exposed there are of the Puncoviscana Formation (latest Precambrian), a mostly turbiditic sequence that underwent low-grade metamorphism and exhumation before deposition of overlying sediments (Turner, 1960; Aceñolaza et al., 1999). Unconformably overlying these are hundreds of meters of pink and red, well sorted, medium- to fine-grained sandstone of the Cambrian Mesón Group (Turner, 1970; Kumpa and Sanchez, 1988; Such et al., 2007). The sandstones are quartzarenites and are thoroughly indurated with quartz cement. Beds are typically several centimeters to a few decimeters thick; crossbedding is common but does not generally affect fracture orientation. The sandstone’s mature mineralogy, crossbedding, and local Skolithos burrows indicate deposition in a high wave-energy, marginal marine setting (Turner, 1970). Conformably overlying the Mesón Group in the study area is the Ordovician Santa Victoria Group (Figure A-3). Bedding in the study area

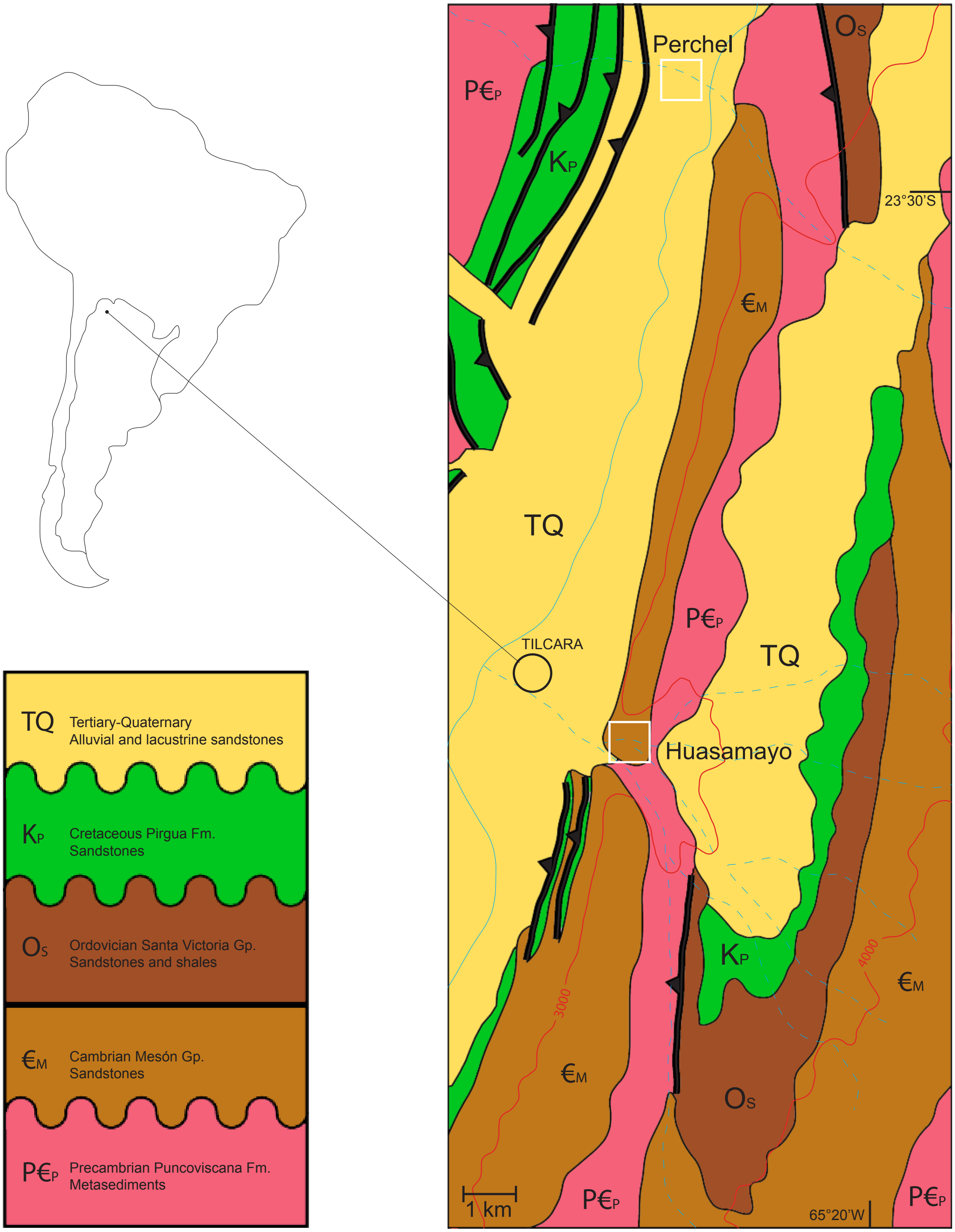

Figure A-3. Map showing locations of Perchel Canyon and Huasamayo Canyon, NW Argentina, modified from Gonzalez et al., 2004. Exposure of Meson Group at Perchel Canyon is too small for map scale.

strikes NNE and dips moderately (25 to 30°) to the west, consistent with regional Andean folding, which was likely most active from the Eocene to the Miocene in the Eastern Cordillera of Argentina (Horton, 2005; Carrera and Muñoz, 2008; DeCelles et al., 2011; Siks and Horton, 2011). The absence of a major unconformity between the Cambrian and Ordovician sequences suggests that these rocks were not strongly affected by Ordovician orogenesis (Mon and Hongn, 1991; Mon and Salfity, 1995). Regional rifting occurred during the Cretaceous, along with deposition of the Pirgua Formation (Kley et al., 1997; Kley et al., 2005; Deeken et al., 2006). As well, Cretaceous deformation does not appear to have left an outcrop-scale structural imprint on the study area.

Canadian Rockies—Jurassic Nikanassin Formation

Fractures were sampled from the Canadian Rockies from core drilled through the Nikanassin Formation (Jurassic) in the Western Canada Basin. The Nikanassin Formation is a syn-orogenic sequence that was deposited in a foreland basin to the east of the uplifting Columbian Orogeny in the Late Jurassic (Poulton et al., 1990). The samples are dominantly sub-litharenites, with abundant chert fragments and detrital dolomite.

All cores studied were drilled vertically. One core (Core C, Figure A-4) was drilled through a sequence of tight folds that overlie nearly horizontal beds. Bedding in core M is flat-lying and mesoscopically structureless. Bedding planes within the folds of core C are commonly smooth with faint striae, particularly in

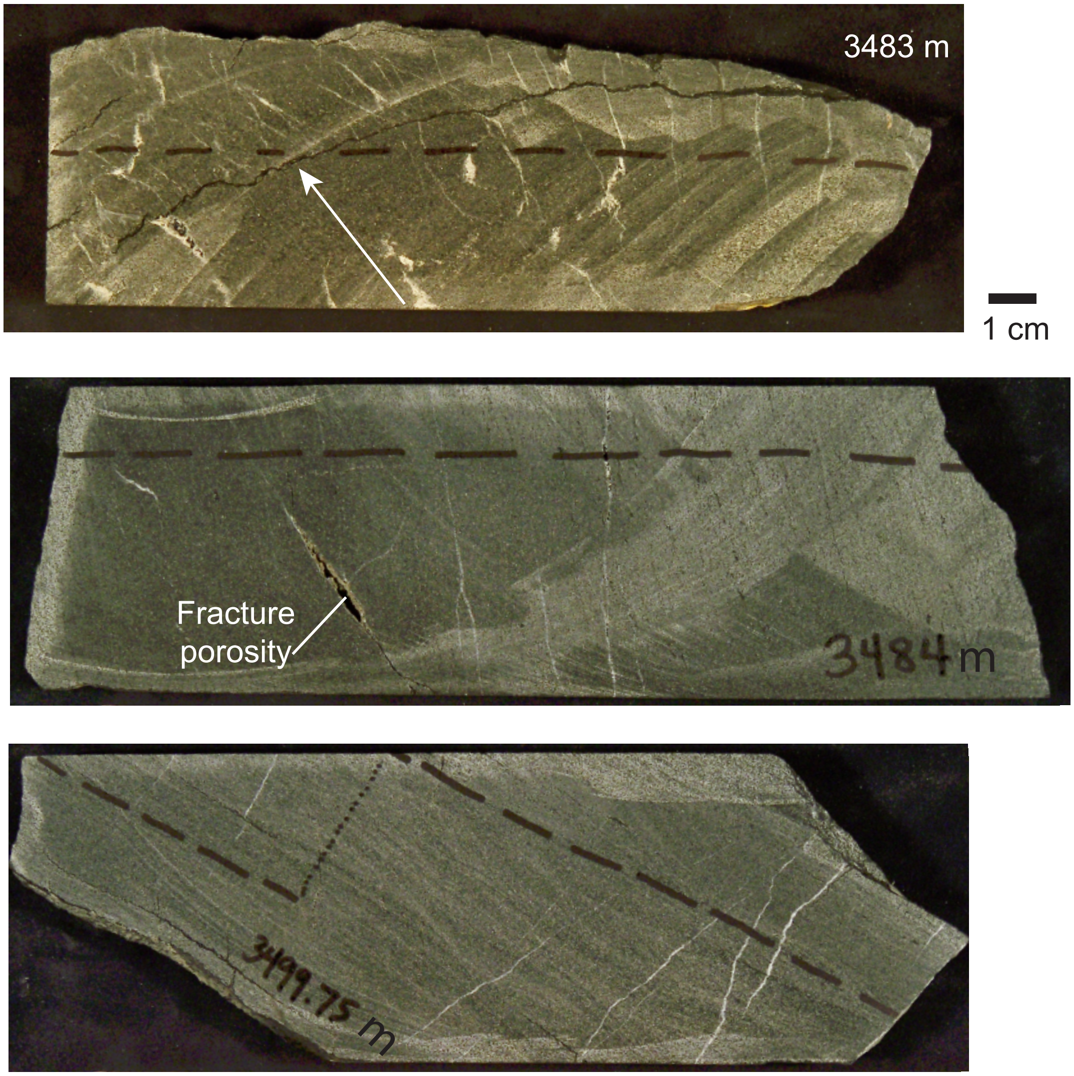

Figure A-4. Three segments of core from Well C, in which bedding is folded and therefore at low angle to the core axis, allowing for long bedding-parallel scanlines from vertical core. Dashed lines represent locations of planes from which thin sections were cut. At depth 3483 m, fractures abut against a bedding plane; this scanline is therefore separated into “Upper” and “Lower” (layer) subsets. From a fourth depth in this core (3556 m), and from three depths in a different vertical core, typical core-width scanlines were drawn across thin sections from horizontal beds.

horizons rich in organic matter. Quartz cement is present in all fractures observed. Carbonate cement is less abundant but locally important; late-stage carbonate cement is present in the zone of highest fracture intensity (3488-3496 m). In other intervals above depth 3507 m macroscopic fractures include abundant porosity (up to 50% of entire fracture volume, measured from cross-sectional area) as they are partially occluded by bridging quartz cement and carbonate cements are rare/absent.

Fractures in the Nikanassin Formation dataset show a tendency to develop perpendicular to bedding but exceptions are abundant. Fractures commonly show multiple orientations in the same interval; crosscutting and abutting relationships indicate simultaneous propagation of fractures with different orientations.

Increased fracture intensity correlates with bedding-parallel slip planes and intervals with tightly folded beds. However, fractures show a consistent (high) abundance between depths 3496 and 3507 m despite a gradual change in bed dip. Throughout this interval the fractures with preserved porosity show consistent moderate (40-60°) dips; sealed fractures in the same interval display a wide range of orientations.

In the absence of core orientation or image log data, my measurements of fracture strikes and dips were made relative to arbitrary core reference marks on the core, apparent scribe lines, and bedding dip. Orientations of representative macrofractures in core and in thin section were measured using SEM-CL.

No macroscopic fractures are present in samples derived from Core M.

Mexican Sierra Madre Oriental—Triassic-Jurassic Huizachal Group

Samples studied from northeast Mexico (Figure A-5) derive from the Triassic-Jurassic Huizachal Group, a fluvial succession deposited at the margin of Pangea (Mixon et al., 1959; Michalzik, 1991). Barboza-Gudiño et al. (2010) established the El Alamar Formation at the base of the Huizachal Group, distinct from the overlying Jurassic redbed succession. These outcrops were previously interpreted to be part of the La Boca Formation (Laubach and Ward, 2006). The Huizachal Group is overlain by Jurassic evaporites and Cretaceous limestones, dolostones, and shales, which comprise the passive margin paleodepositional environments of the Gulf of Mexico (Goldhammer and Johnson, 1991; Ocampo-Diaz et al., 2008). The sandstones studied, where exposed near Galeana, Nuevo Leon, consists of feldspathic litharenites; grain size is medium in the lower unit (El Alamar Formation) and coarse in the upper unit (La Boca Formation—Ward, 2006; Barboza-Gudiño et al., 2010).

The overlying evaporites (Minas Viejas Formation) represent a detachment layer, separating km-scale, Laramide-age folds of the Sierra Madre Oriental (SMO) above from complexly deformed, but more gently folded, strata below (Marrett and Aranda, 2001; Zhou et al., 2006; Latta and Anastasio, 2007).

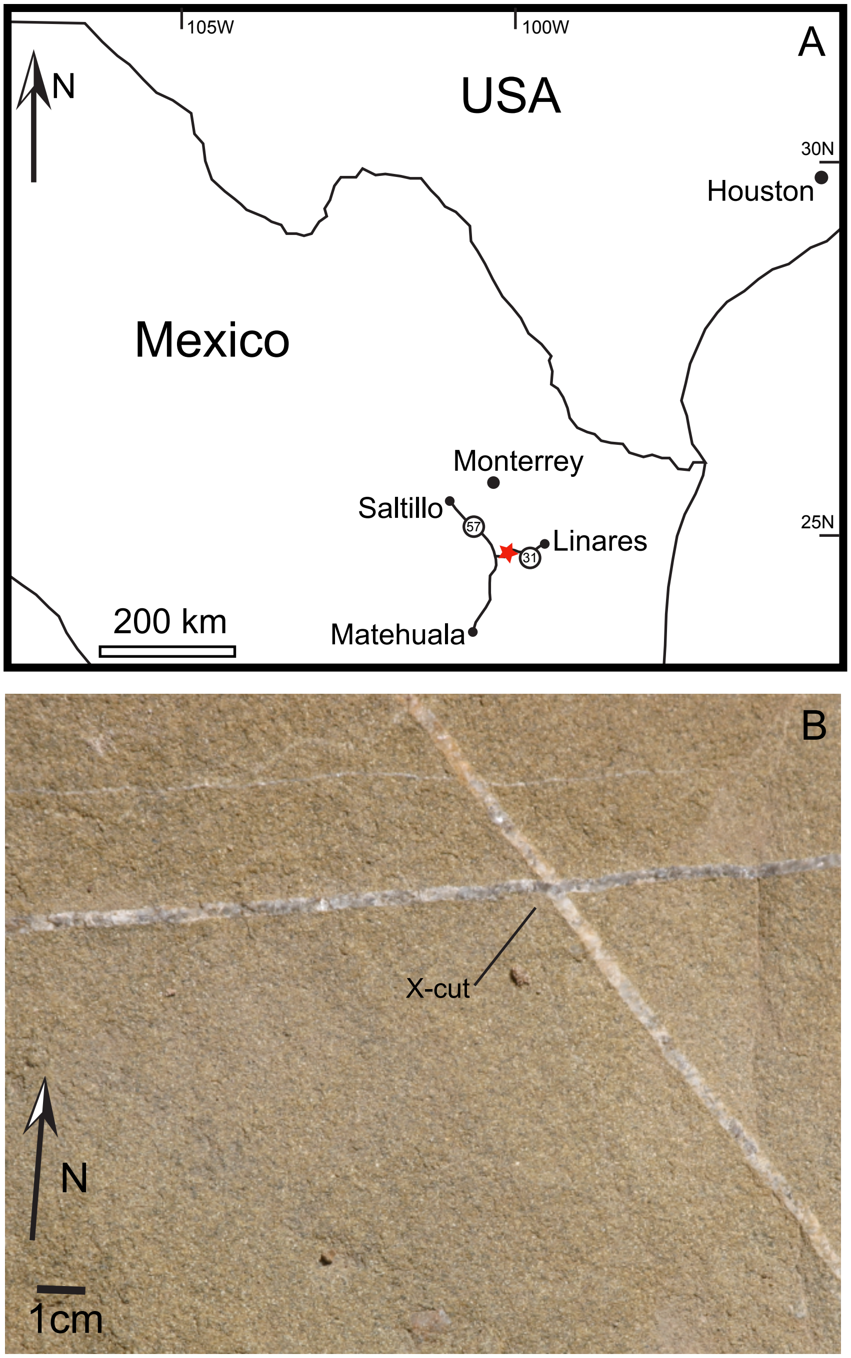

Figure A-5. (A) Location of field area. (B) Plan-view outcrop photograph of El Alamar Formation, showing relative timing of E-W striking (younger) and NW-striking (older) fracture sets.

Laubach and Ward (2006) identified four fracture sets in the El Alamar Formation sandstone and showed that fracture cements and size-scaling match patterns found in core. This study focuses on NW-SE and E-W striking fractures, which are the orientations of the two most abundant fracture sets. By tying new fluid-inclusion measurements to high resolution micro-imaging it was possible to thoroughly document how individual fractures and fracture populations grew through time (Chapter 6). Crosscutting relationships indicate the NW-SE striking set predates the E-W striking set (Figure A-5). Fractures in the La Boca Sandstone strike E-W and NE-SW; the relative timing is unclear. All fractures deep steeply, near vertical. The study area features numerous but sparse igneous sills and dikes in the La Boca sandstone strata; similar intrusions in equivalent strata elsewhere formed during the Lower Jurassic (Barboza-Gudiño et al., 2008).

Scottish Highlands—Cambrian Eriboll Formation

The Cambrian Eriboll Formation of the Ardvreck Group crops out west of and within the Moine Thrust Belt (MTB), from Loch Eriboll at the northern coast to near Loch Carron in the south (Figure A-6). The Eriboll Formation comprises the 75- to 125-m-thick Basal Quartzite Member and the overlying 75- to 100-m-thick Pipe Rock Member. This study focuses on fractures from the latter in this study. This sedimentary sequence records marine transgression that continued into the Ordovician (Wright, 1985; McKerrow et al., 1992; Park et al., 2002).

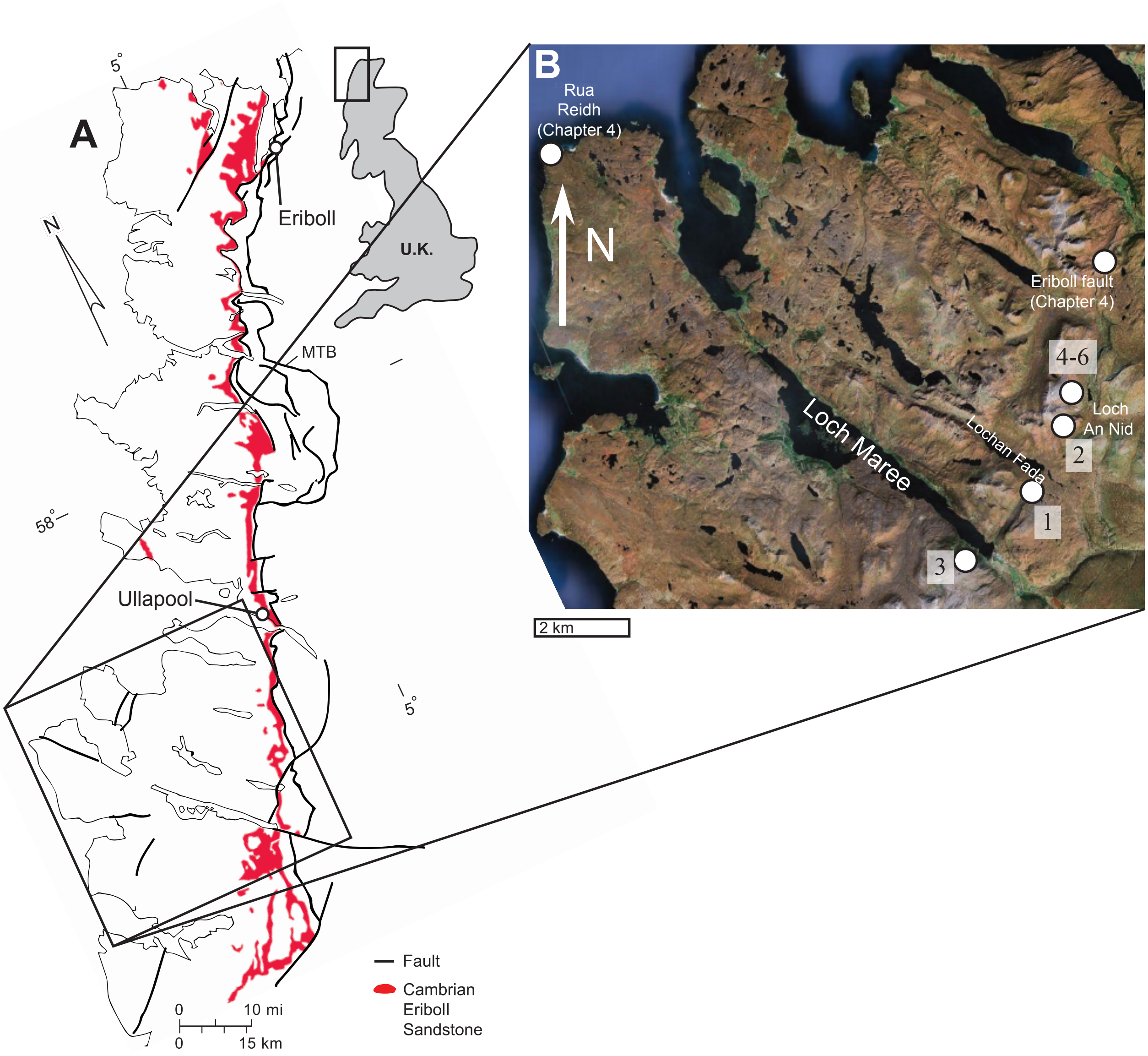

Figure A-6. (A) Outcrop belt of Cambrian Eriboll Sandstone, simplified from Peach et al., 1907. (B) Locations of fractures analyzed in this study; satellite image from Google Maps. Numbers (1-6) correspond to sample numbers in Table 3-3.

Cambro-Ordovician rocks that dip gently (10–15º) SE beneath the adjacent thrust belt are unconformable on Archaean Lewisian gneisses and Proterozoic Torridonian sandstone. The ESE-dipping MTB marks Silurian and Early Devonian WNW-directed shortening, juxtaposing Neoproterozoic sedimentary rocks to the east over the Cambro-Ordovician sequence to the west (Strachan et al., 2002; Cawood et al., 2004; Strachan et al., 2010). The Eriboll Formation is cut by the lowest thrust faults of the MTB, which are primarily associated with brittle deformation and repeated imbricate sequences (Coward, 1984; Holdsworth et al., 2007). Higher in the MTB the thrust faults are associated with mylonitization and ductile deformation (Coward, 1980; Holdsworth et al., 2007). The Eriboll Formation is also cut by later faults whose motion accommodated extension, tilting, and wrenching in the Palaeozoic and Mesozoic (Peach et al., 1907; Laubach and Marshak, 1987; Roberts and Holdsworth, 1999; Wilson et al., 2010; Ellis et al., 2012). Faults that can be ascribed to MTB emplacement or movement of later faults are not apparent in outcrops we studied; the only structures present are opening-mode fractures (though one study location is within one km of the Loch Maree Fault—Figure A-6). The late uplift history of NW Scotland is complex (Holford et al., 2010) and given the low strains that can drive opening-mode fracture growth (Olson et al., 2009) this history cannot be dismissed as irrelevant to fracture pattern development. After exhumation the MTB foreland rocks were affected by

Pleistocene glaciation (Hall, 1991; Ballantyne et al., 1998). Eriboll sandstones are indurated, quartz-cemented quartz arenites. Samples I tested have negligible porosity and a grain size of about 100 μm.

Carbonate rocks

Scaling data from carbonate rocks were compared to sandstone fracture datasets in Chapter 4. Below is a brief summary of each carbonate rock geologic setting.

Lower Ordovician Ellenburger Group

Fractures from the Ellenburger Group are from a core sample from the Goldrus Unit No. 3 well, Barnhart field, a West Texas oil reservoir, at a depth of 2767 m (9079 ft) (Gale, 2004; Gale and Gomez, 2007), which was analyzed using CL. The Ellenburger Group at this location comprises shallow-water dolostones and limestones (Holtz and Kerans, 1992). The fractures studied postdate brecciation associated with Paleozoic near-surface paleokarst (Gale and Gomez, 2007), which has disrupted bedding so that no clear relationship between fractures and stratigraphy is discernible. The fractures studied are subvertical, mostly parallel, and thoroughly cemented with synkinematic dolomite and postkinematic calcite. These fractures are likely regional fractures formed at depth in an intraplate setting.

Pennsylvanian Marble Falls Formation

Fracture data were collected within the Marble Falls Limestone where exposed at Pedernales Falls State Park, Texas (Marrett et al., 1999). Fractures are systematically oriented and mostly filled with authigenic cement. Fractures are exposed in gently dipping strata of the Upper Member of the Marble Falls Limestone (Gomez, 2007). Upper Marble Falls facies comprise mainly phylloidal algal mounds, skeletal grainstones, siliceous (spiculitic) limestones and shales (Erlich and Coleman, 2005). The maximum thickness measured in outcrop is 82 m with an estimated additional 10 m of section eroded (Erlich and Coleman, 2005).

Lower Cretaceous Cupido Formation

Fractures from the Cupido Dolostone are from outcrop exposures in NE Mexico (Gomez, 2007). The Cupido Formation is a 500- to 800-m-thick, Upper Hauterivian to Lower Aptian, shallow-water carbonate sequence overlain by the La Pena Shale (Imlay, 1937; Goldhammer et al., 1991). Opening-mode fractures in the Cupido Formation are typically strata bound; fracture abundance varies significantly from bed to bed (Ortega et al., 2006; Ortega et al., 2010). The fractures we examined are from an 80-cm-thick dolostone bed exposed in the forelimb of the San Blas Anticline, an upright isoclinal fold above an evaporite décollement within the Monterrey Salient 20 km SW of Monterrey, Mexico (Padilla y Sanchez, 1985; Higuera-Díaz et al., 2005). Fractures contain synkinematic dolomite and postkinematic calcite. The fractures in this outcrop are likely regional fractures that formed at depth prior to folding in a platform setting.

Upper Cretaceous Austin Chalk

Fractures from the Austin Chalk Formation occur in outcrop near Waxahachie, Texas, USA. Fractures were measured within a flat-lying chalk bed near the top of the formation; the chalk is bound above and below by marl layers (Gale, 2002). The overlying marl layer arrested the propagation of some, but not all, fractures (Stowell, 2001). The down-section extent of the fractures is uncertain owing to poor exposure. Although the fractures in this outcrop are not associated with folds or faults, regionally the fractures are associated with meter- to decimeter-displacement normal faults (Laubach et al., 1995b). Narrow fractures are calcite filled but wider fractures are calcite lined and bridged and contain residual fracture porosity. Similar fractures occur in horizontal core from the Austin Chalk play in Pearsall Field (Gale, 2002), and in a dilatant jog of a fault in the Austin Chalk outcrop belt near San Antonio (Lee and Wiltschko, 2000), and on this basis the cement in our outcrop example is likely synkinematic.

Appendix B: Fracture size-cumulative frequency plots

SCALING PLOTS

The following are plots of the size distributions for datasets listed in Appendix A. Trendlines best-fit to the data include power-law and exponential, represented by black lines (power-law); heavy dashed curves (exponential); normal distributions (light dashed curves); and log-normal distributions (dash-dot curves). The chi-squared fits are listed on page A-1; the lowest chi-squared value indicates the best fit.

The chi-squared calculation is as follows:

$$\chi^2 = \sum \frac{(f_{obs} - f_{mod})^2}{|f_{mod}|}$$

where f_{obs} is the observed frequency and f_{mod} is the modeled frequency (the frequency from the best-fit equation). See Chapter 3 for discussion of statistical characterization of fracture size distributions.

Frequency is calculated by assigning a cumulative number to each fracture (1 to the largest, 2 to the second-largest, and so on) and dividing by the scanline length. For equation fitting, duplicate apertures are removed and only the greatest frequency value is kept. Fracture size lists are included in Appendix C.

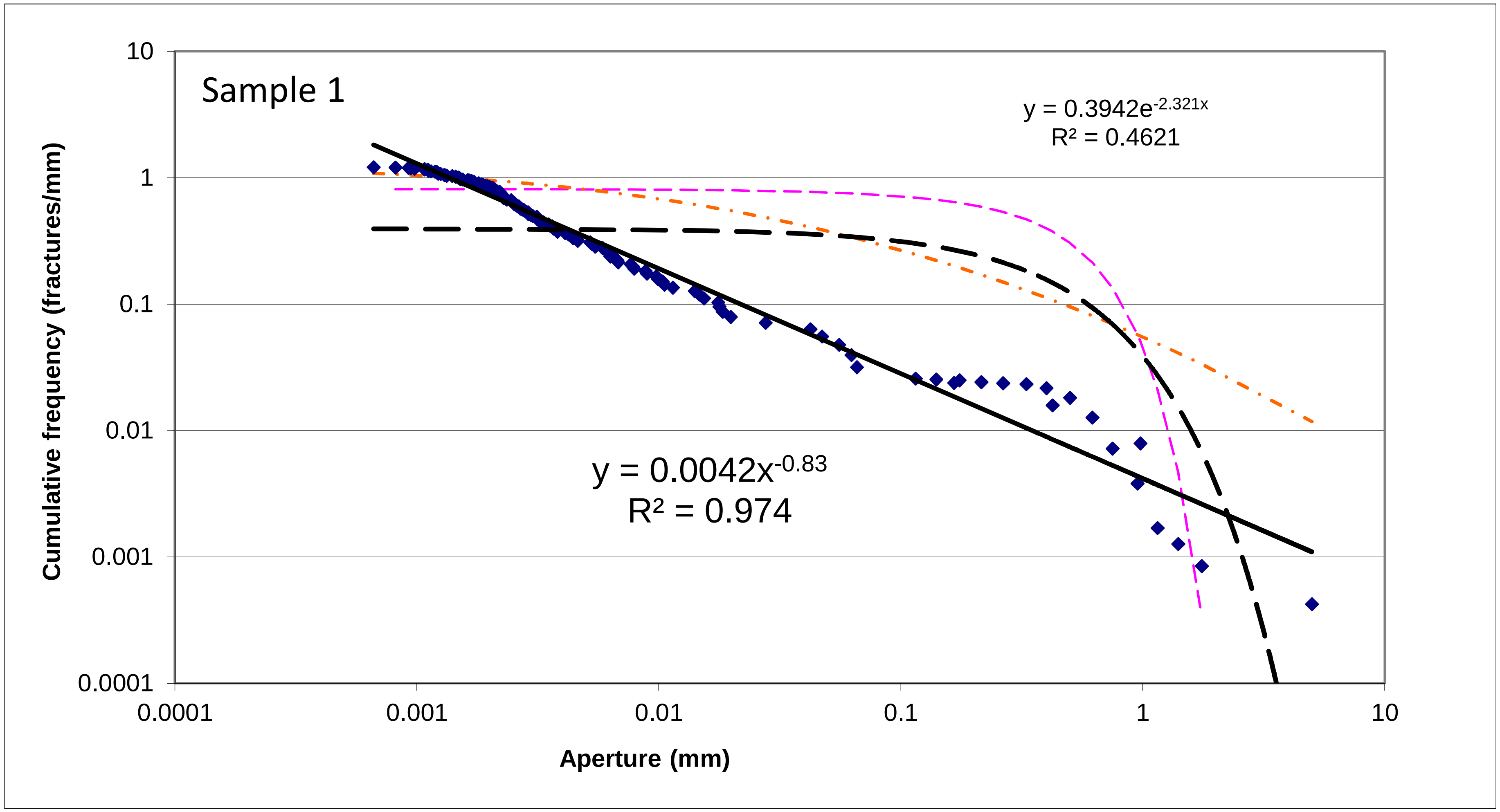
Sample 1
y = 0.3942e-2.321x
R² = 0.4621
y = 0.0042x-0.83
R² = 0.974
Cumulative frequency (fractures/mm)
10
1
0.1
0.01
0.001
0.0001
0.0001
0.001
0.01
0.1
1
10
Aperture (mm)

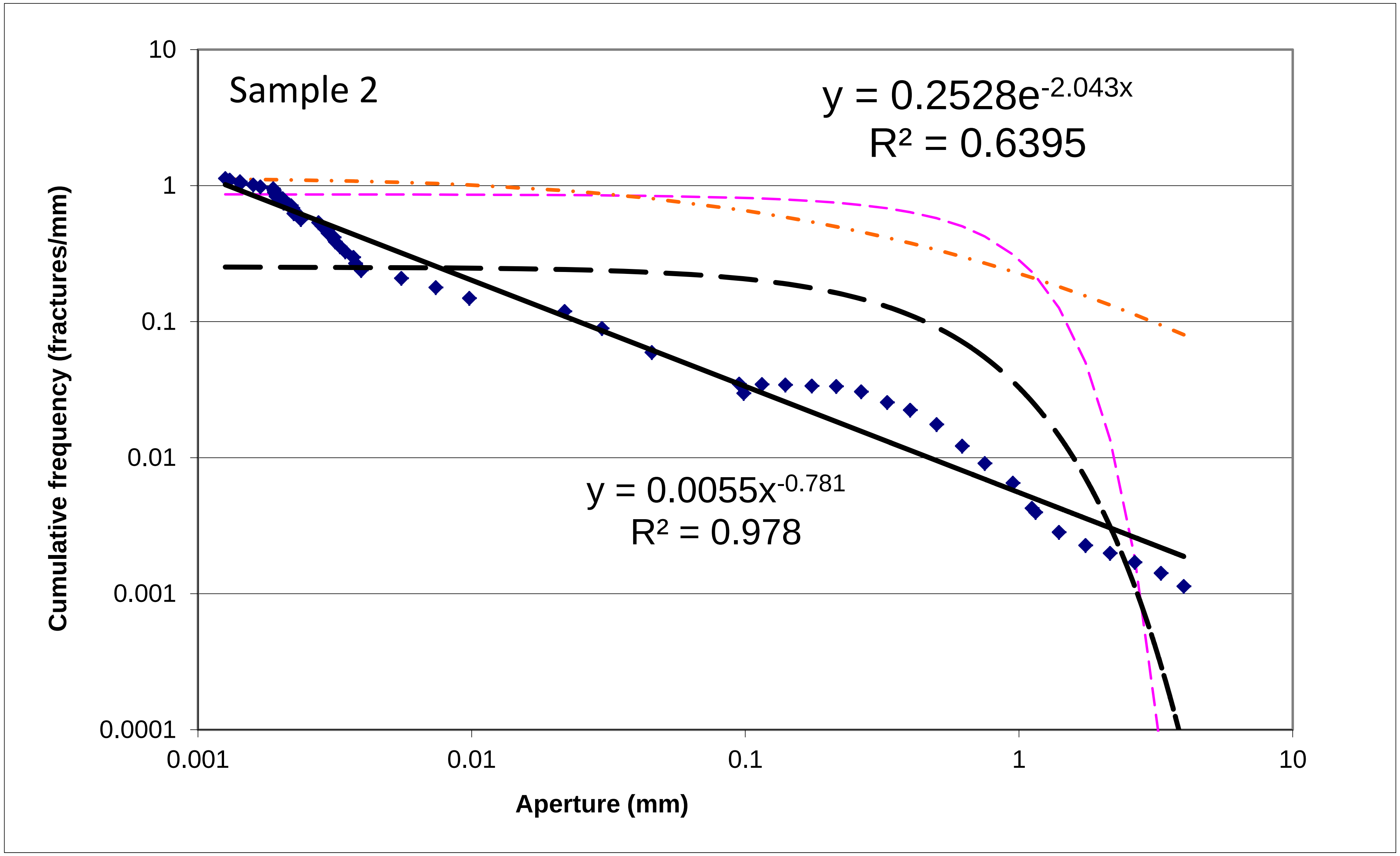
Sample 2
y = 0.2528e^-2.043x
R² = 0.6395
y = 0.0055x^-0.781
R² = 0.978
Cumulative frequency (fractures/mm)
10
1
0.1
0.01
0.001
0.0001
0.001
0.01
0.1
1
10
Aperture (mm)

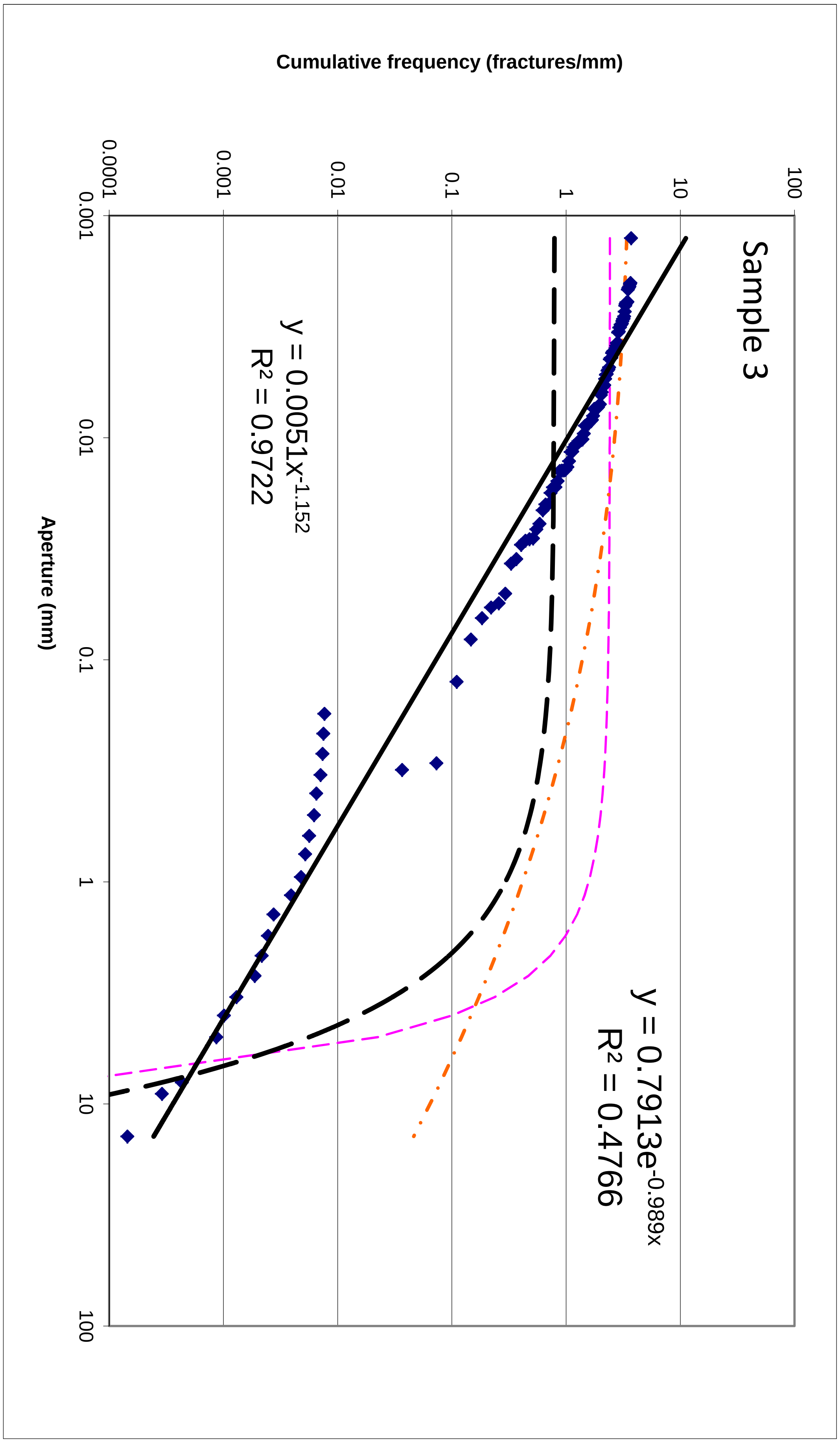
Sample 3
Cumulative frequency (fractures/mm)
Aperture (mm)
100
10
1
0.1
0.01
0.001
0.0001
0.001
0.01
0.1
1
10
100
y = 0.0051x^-1.152
R² = 0.9722
y = 0.7913e^-0.989x
R² = 0.4766

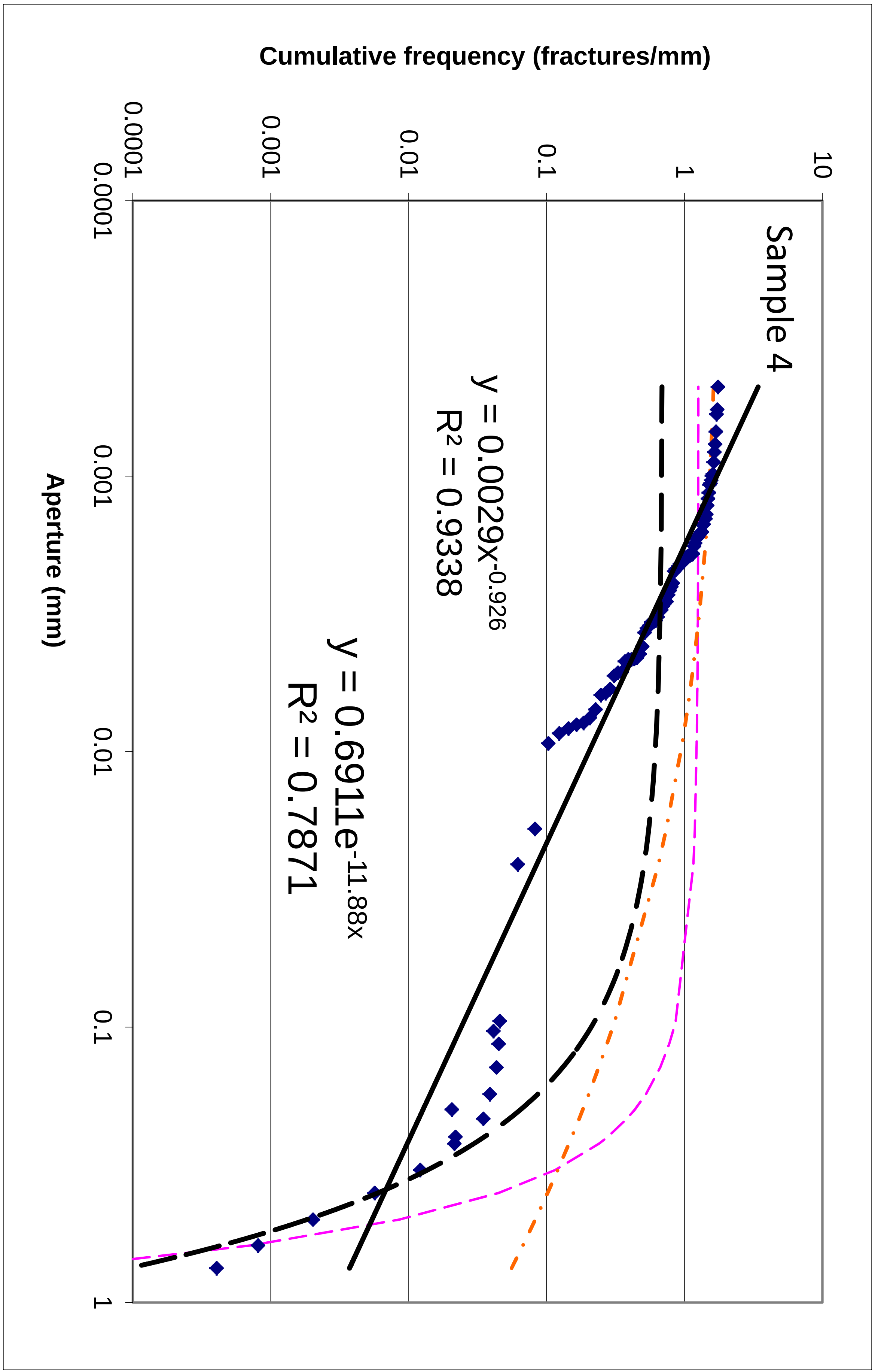
Sample 4
y = 0.0029x-0.926
R² = 0.9338
y = 0.6911e-11.88x
R² = 0.7871
Cumulative frequency (fractures/mm)
Aperture (mm)
0.0001
0.001
0.01
0.1
1
10
0.0001
0.001
0.01
0.1
1

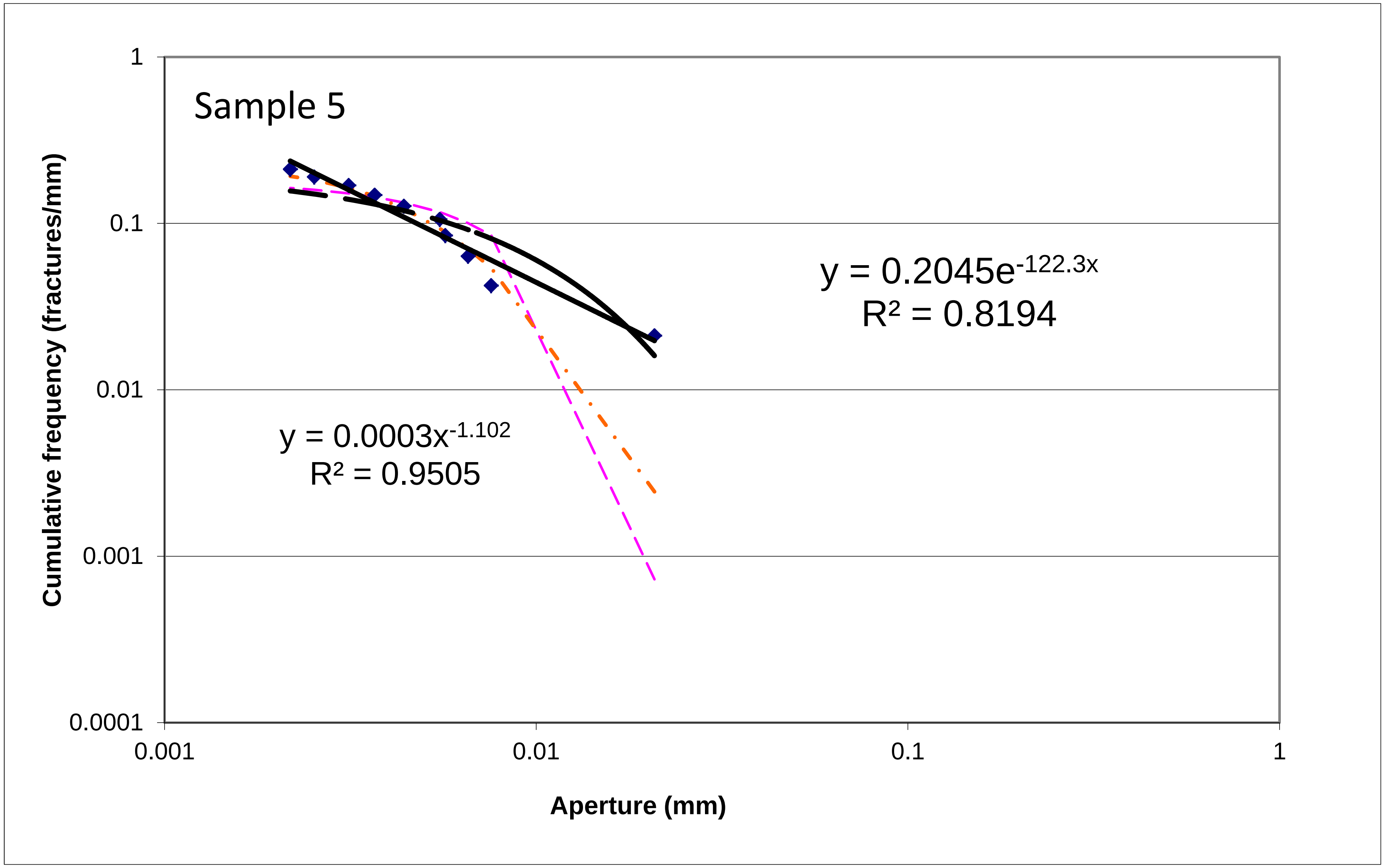
Sample 5
y = 0.2045e^-122.3x
R² = 0.8194
y = 0.0003x^-1.102
R² = 0.9505
Cumulative frequency (fractures/mm)
1
0.1
0.01
0.001
0.0001
0.001
0.01
0.1
1
Aperture (mm)

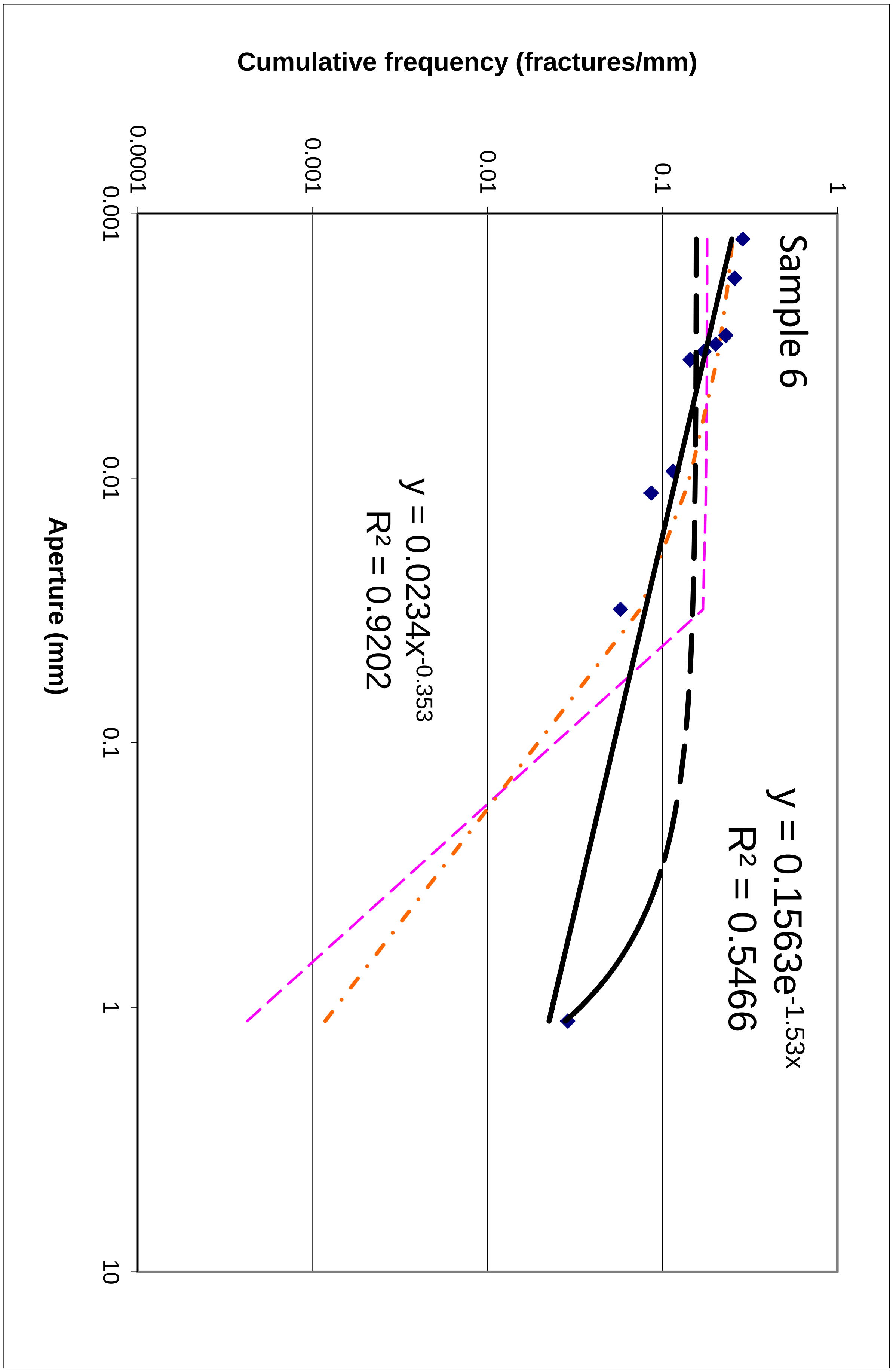
Sample 6
y = 0.1563e^-1.53x
R² = 0.5466
y = 0.0234x^-0.353
R² = 0.9202
Cumulative frequency (fractures/mm)
Aperture (mm)
0.0001
0.001
0.01
0.1
1
0.001
0.01
0.1
1
10

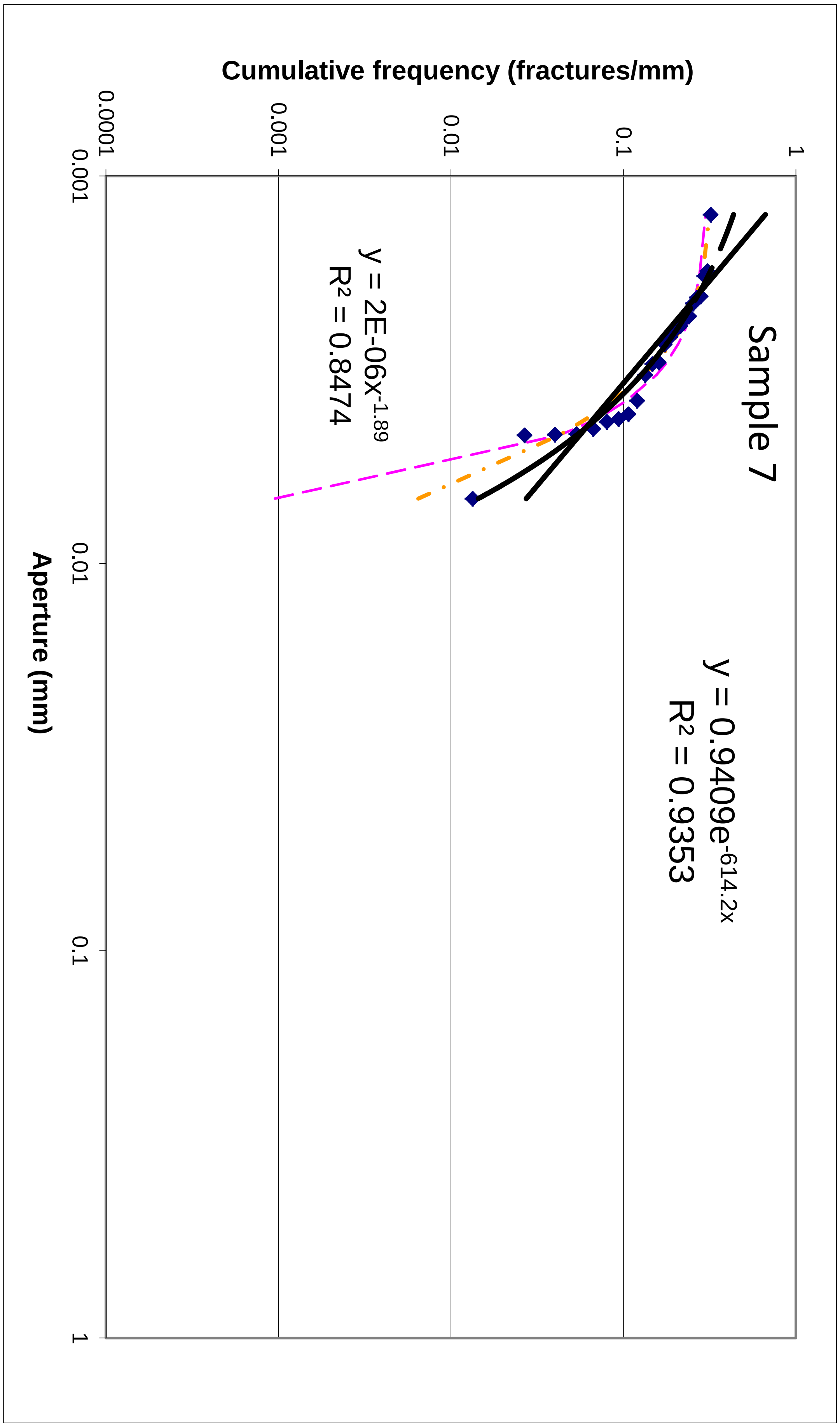
Sample 7
Cumulative frequency (fractures/mm)
1
0.1
0.01
0.001
0.0001
Aperture (mm)
0.001
0.01
0.1
1
y = 0.9409e^{-614.2x}
R² = 0.9353
y = 2E-06x^{-1.89}
R² = 0.8474

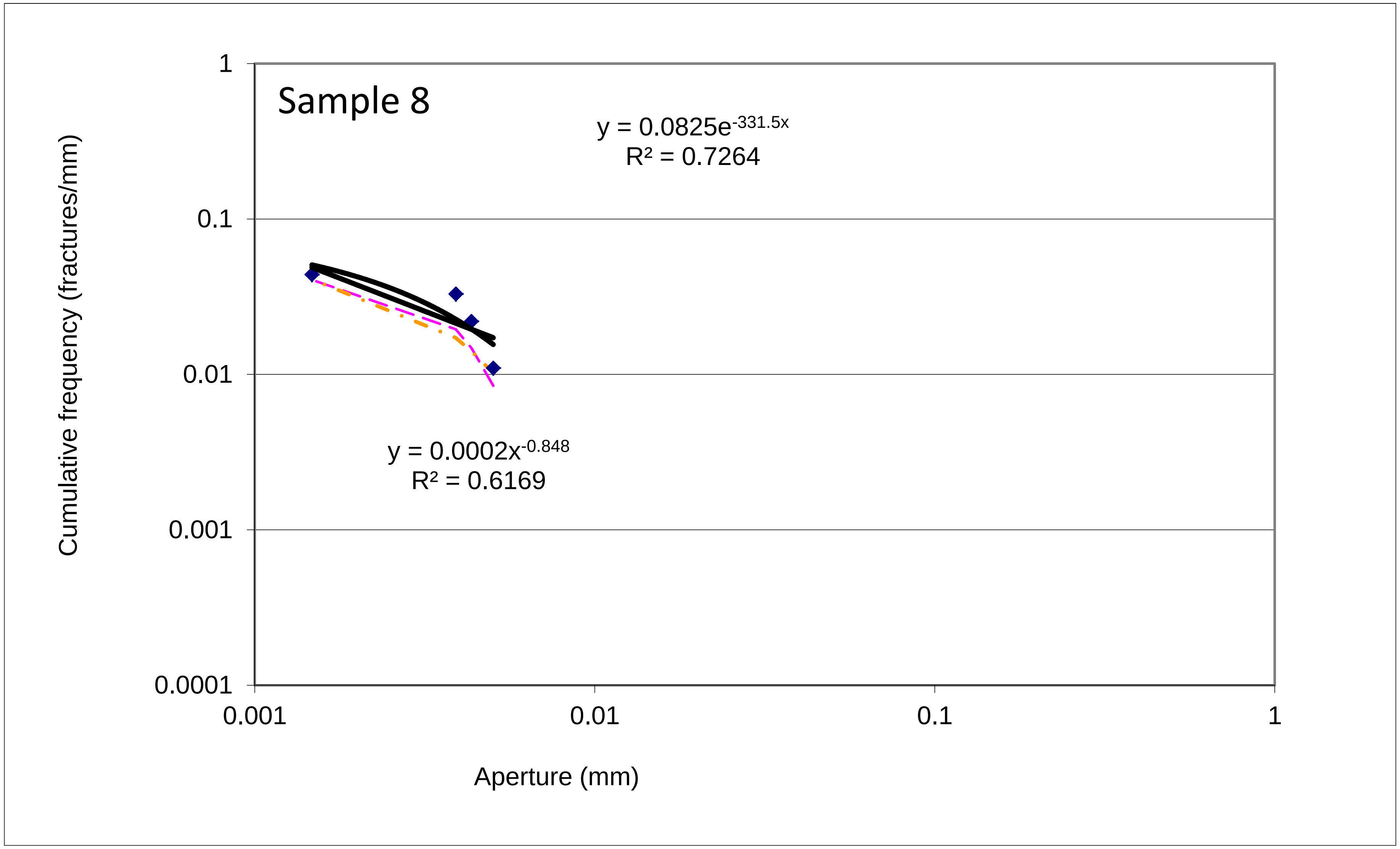
Sample 8
y = 0.0825e-331.5x
R² = 0.7264
y = 0.0002x-0.848
R² = 0.6169
Cumulative frequency (fractures/mm)
1
0.1
0.01
0.001
0.0001
0.001
0.01
0.1
1
Aperture (mm)

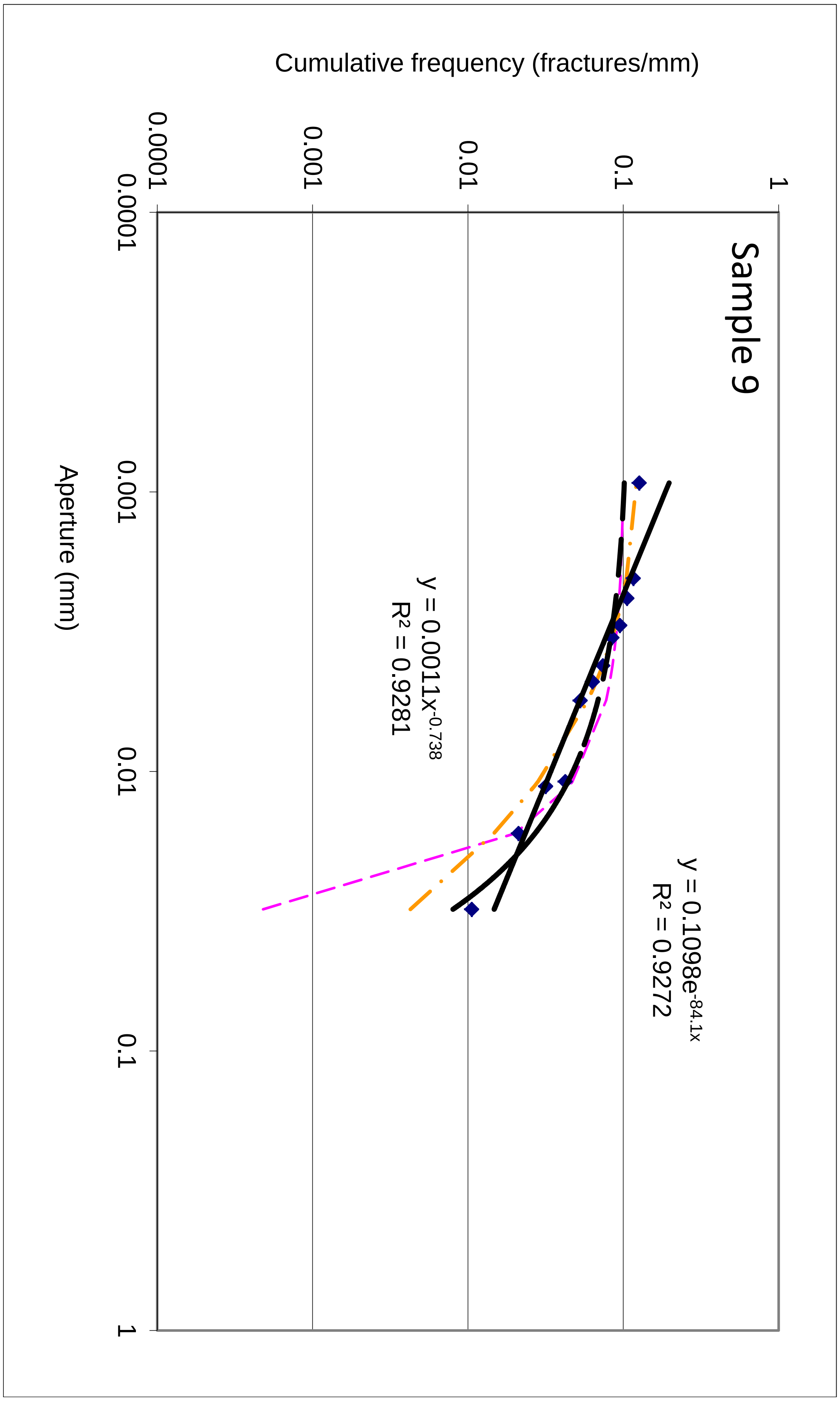
Sample 9
Cumulative frequency (fractures/mm)
1
0.1
0.01
0.001
0.0001
Aperture (mm)
0.0001
0.001
0.01
0.1
1
y = 0.1098e^-84.1x
R² = 0.9272
y = 0.0011x^-0.738
R² = 0.9281

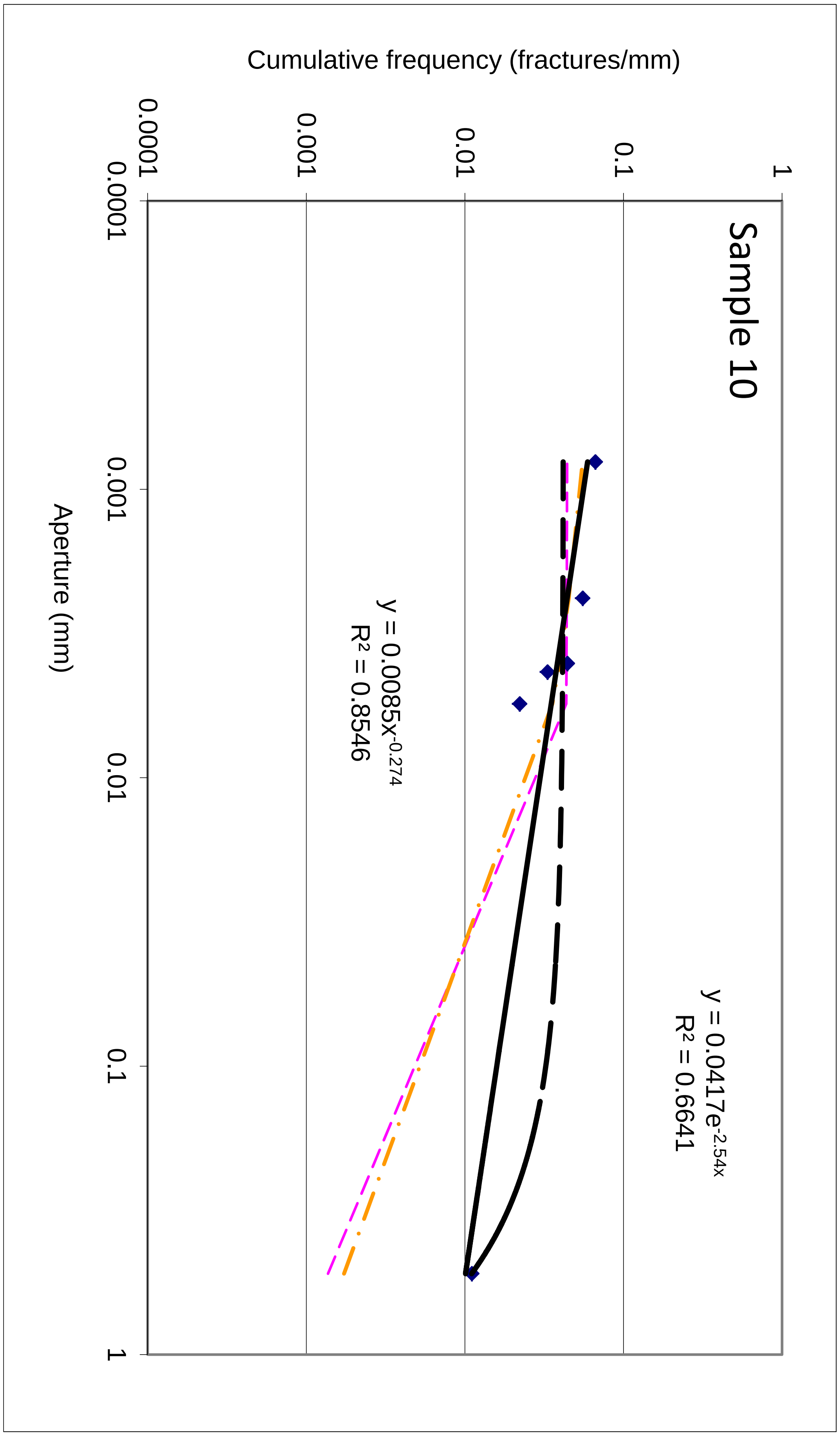
Sample 10
Cumulative frequency (fractures/mm)
1
0.1
0.01
0.001
0.0001
0.0001
0.001
0.01
0.1
1
Aperture (mm)
y = 0.0417e-2.54x
R² = 0.6641
y = 0.0085x-0.274
R² = 0.8546

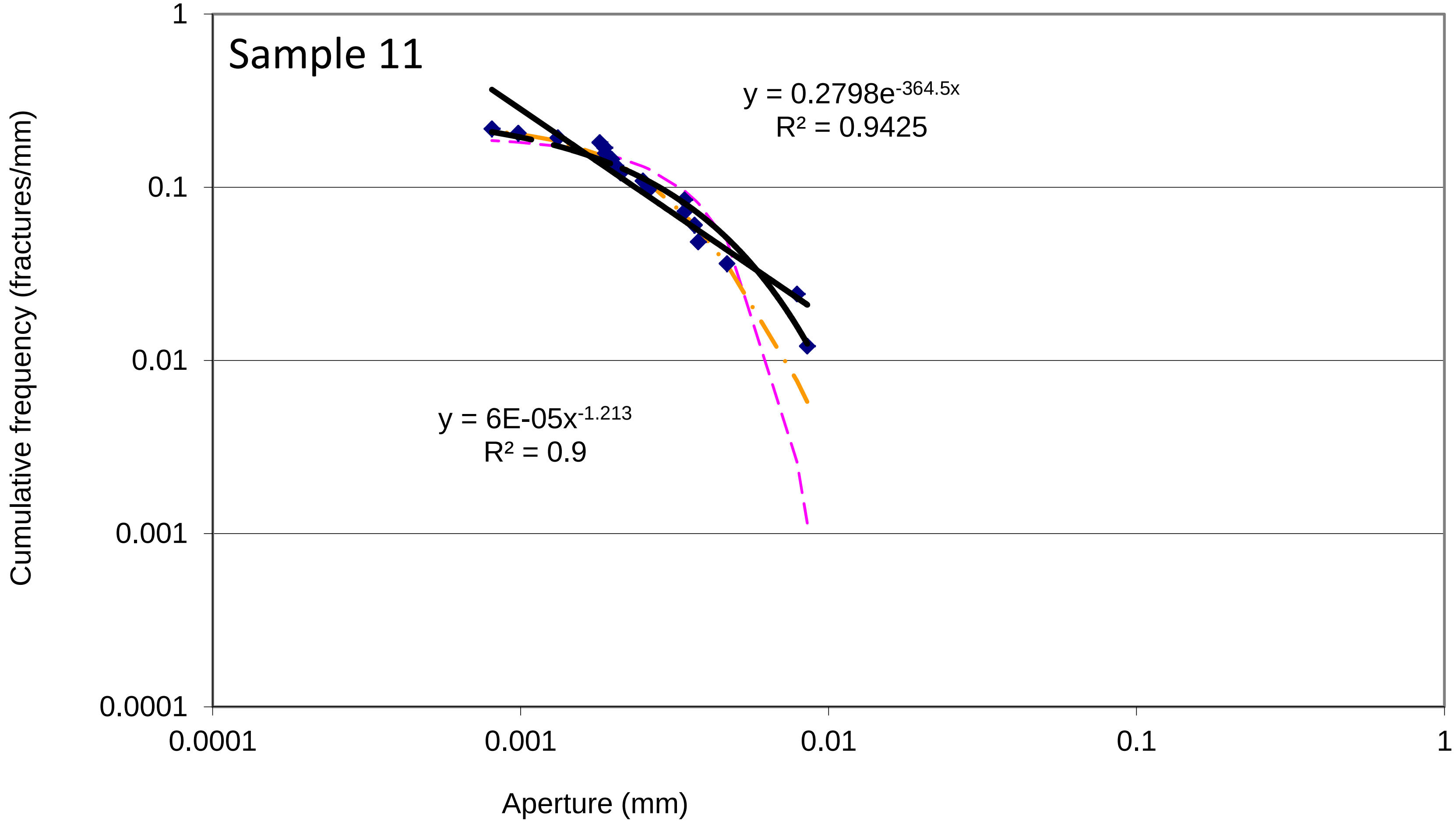Sample 11
y = 0.2798e^-364.5x
R² = 0.9425
y = 6E-05x^-1.213
R² = 0.9
Cumulative frequency (fractures/mm)
1
0.1
0.01
0.001
0.0001
0.0001
0.001
0.01
0.1
1
Aperture (mm)

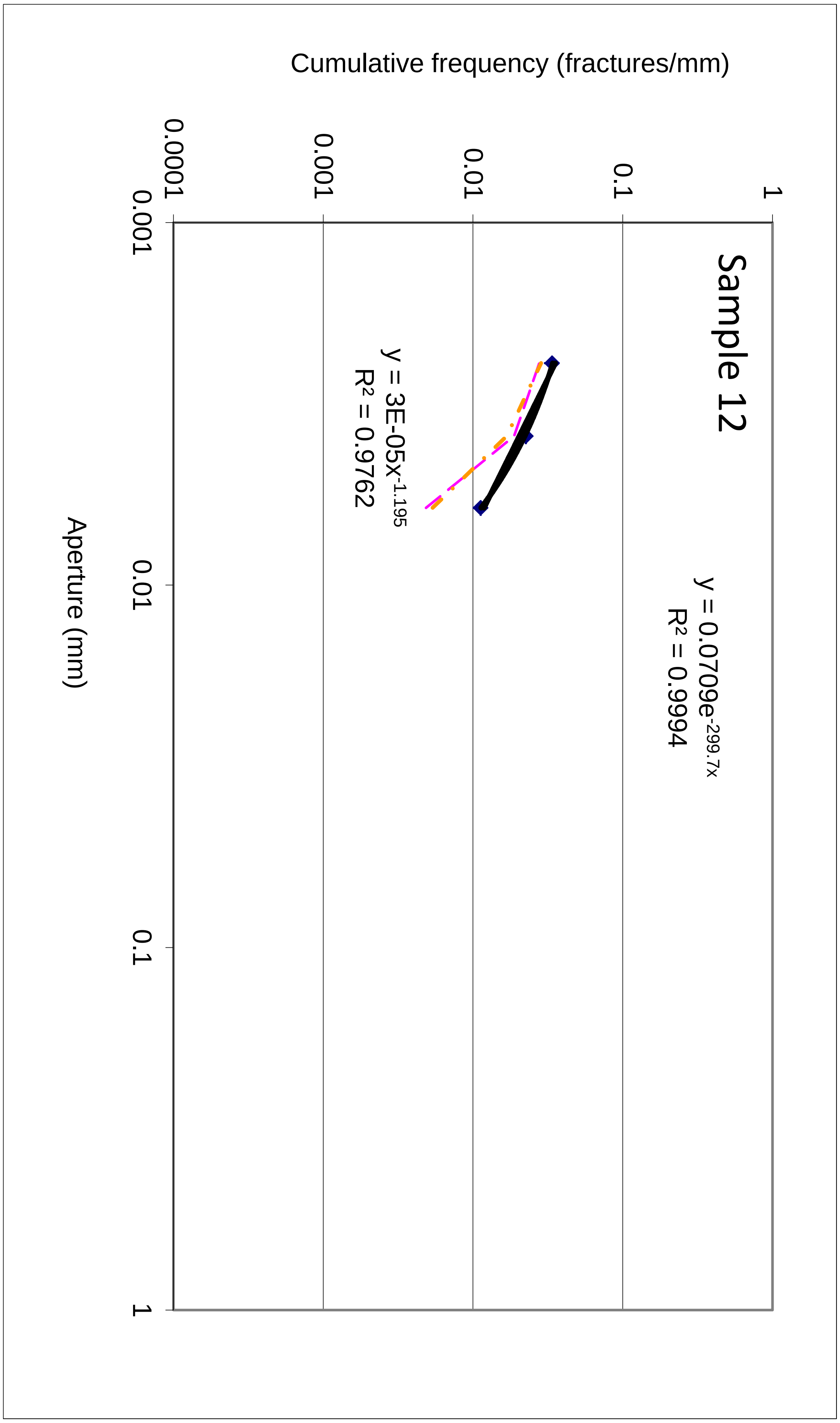
Sample 12
Cumulative frequency (fractures/mm)
1
0.1
0.01
0.001
0.0001
Aperture (mm)
0.001
0.01
0.1
1
y = 0.0709e^-299.7x
R² = 0.9994
y = 3E-05x^-1.195
R² = 0.9762

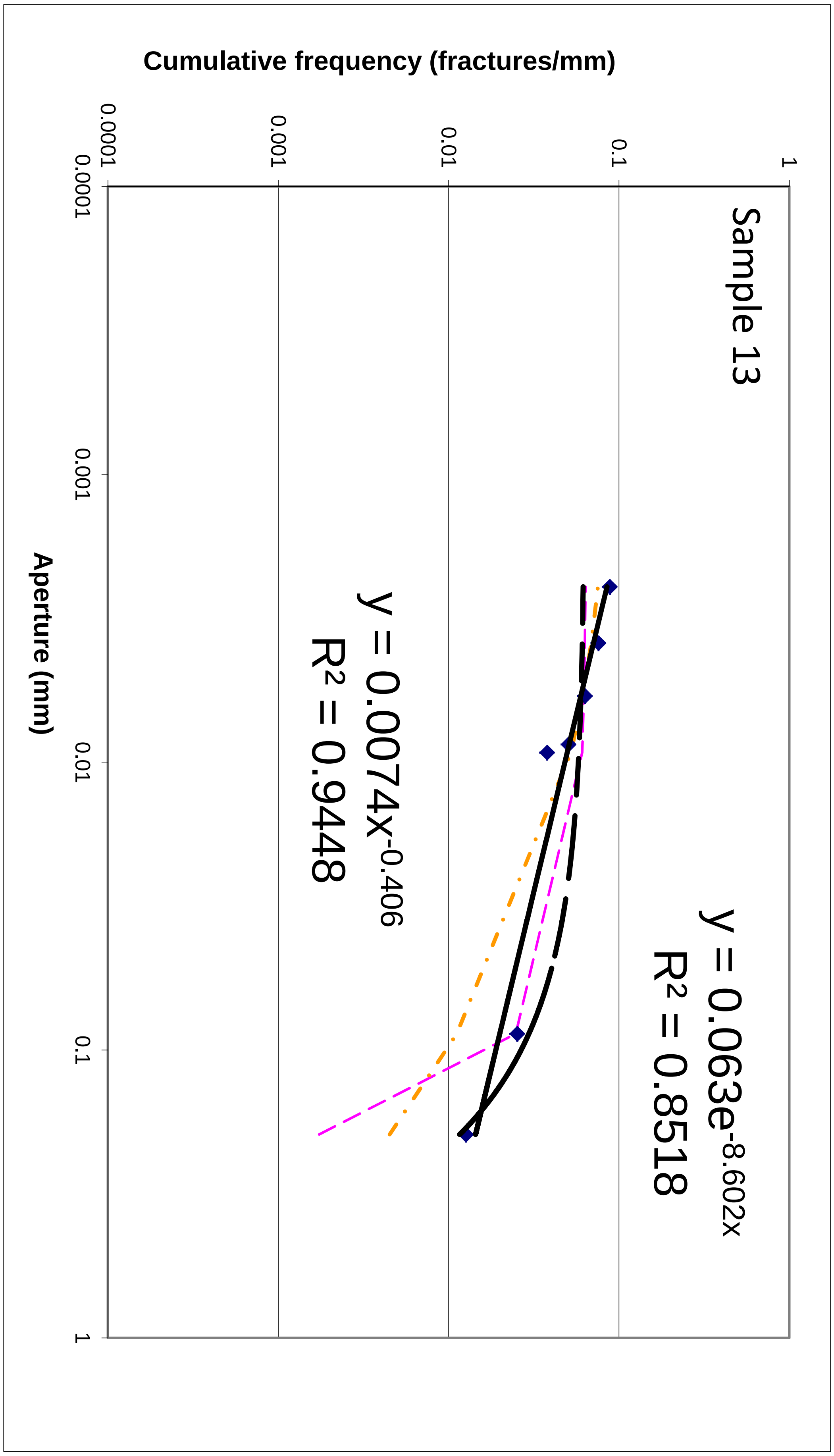
Sample 13
Cumulative frequency (fractures/mm)
1
0.1
0.01
0.001
0.0001
Aperture (mm)
0.0001
0.001
0.01
0.1
1
y = 0.063e^-8.602x
R² = 0.8518
y = 0.0074x^-0.406
R² = 0.9448

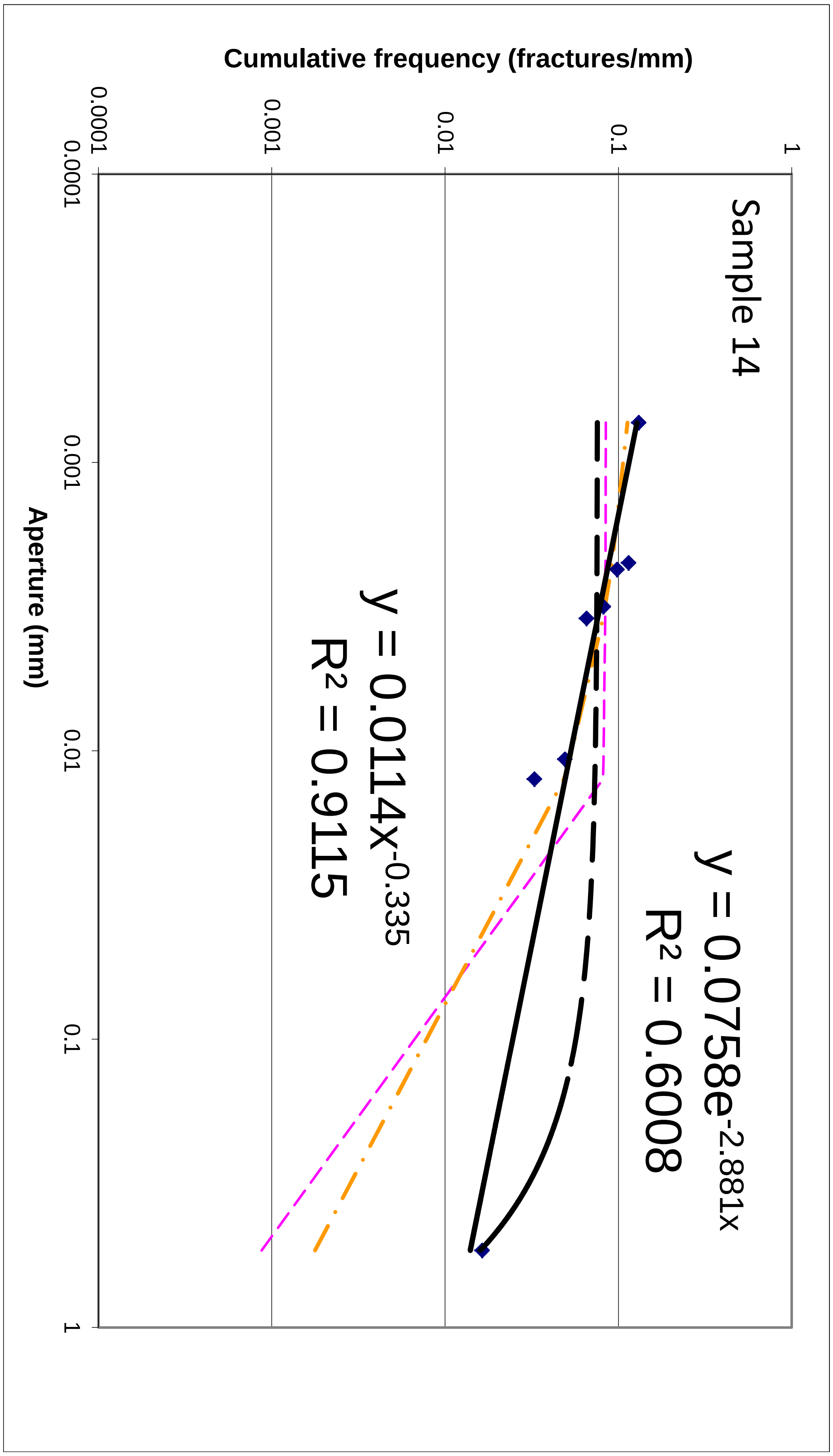
Sample 14
Cumulative frequency (fractures/mm)
1
0.1
0.01
0.001
0.0001
Aperture (mm)
0.0001
0.001
0.01
0.1
1
y = 0.0758e-2.881x
R² = 0.6008
y = 0.0114x-0.335
R² = 0.9115

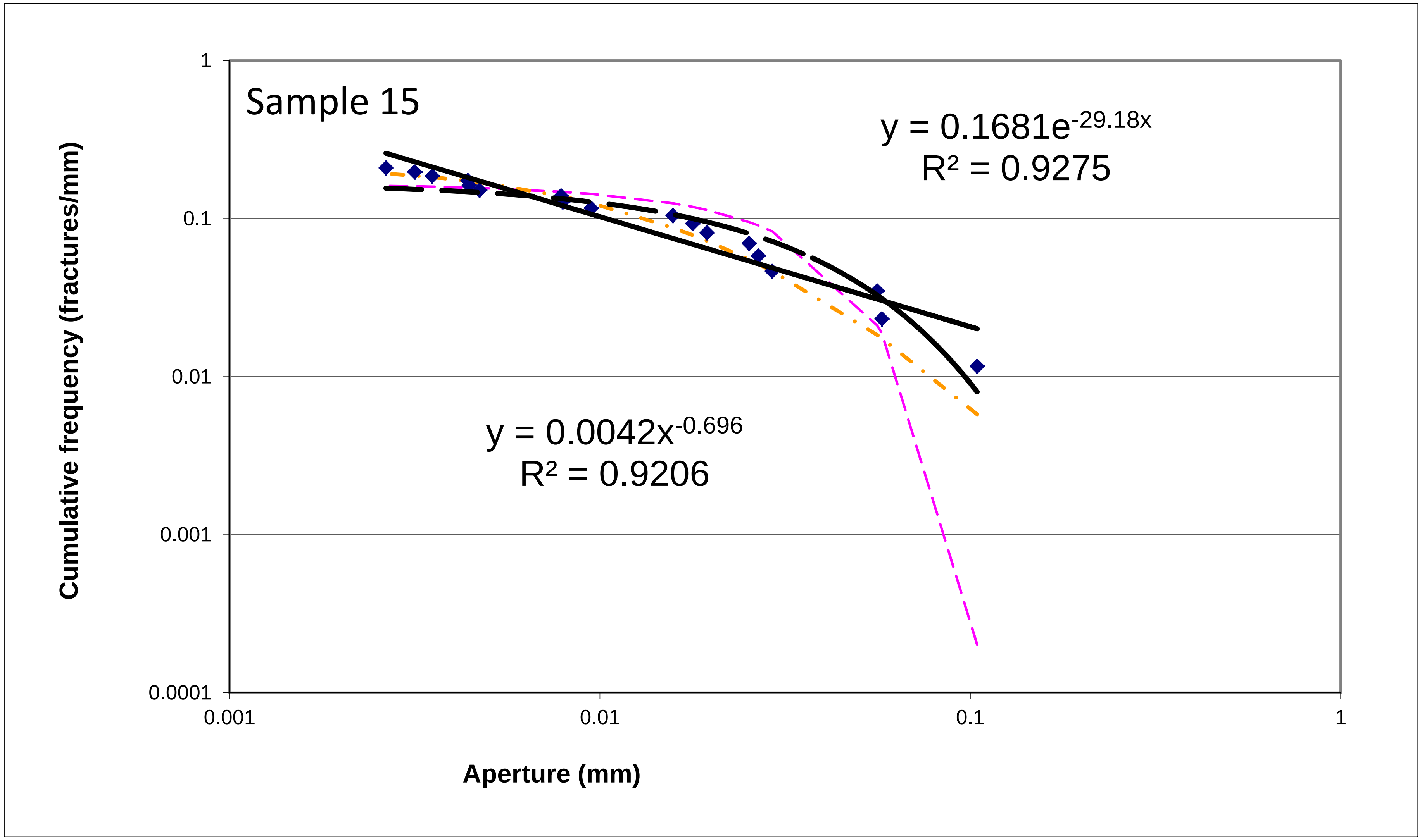
Sample 15
y = 0.1681e^-29.18x
R² = 0.9275
y = 0.0042x^-0.696
R² = 0.9206
Cumulative frequency (fractures/mm)
1
0.1
0.01
0.001
0.0001
0.001
0.01
0.1
1
Aperture (mm)

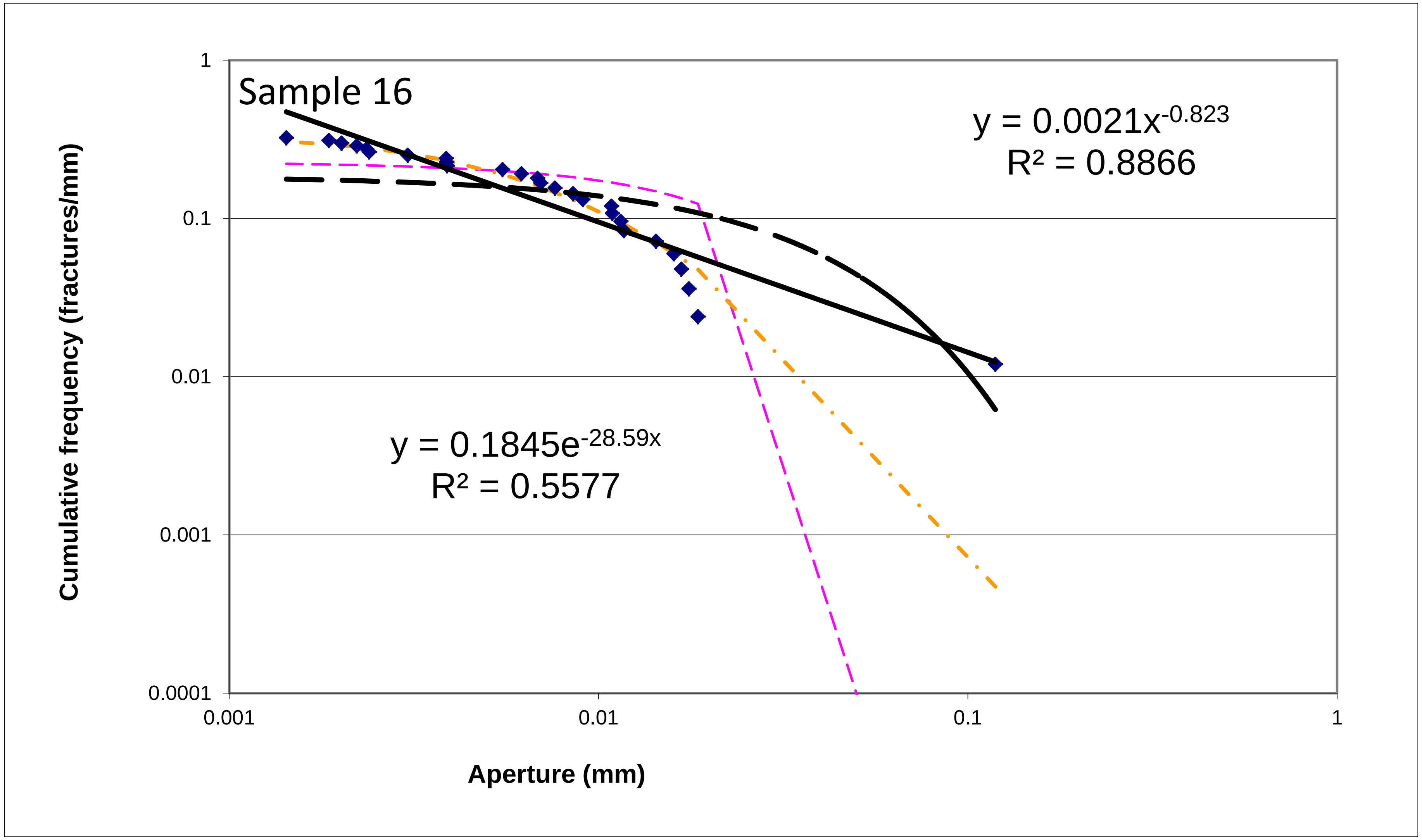
Sample 16
y = 0.0021x^-0.823
R² = 0.8866
y = 0.1845e^-28.59x
R² = 0.5577
Cumulative frequency (fractures/mm)
1
0.1
0.01
0.001
0.0001
0.001
0.01
0.1
1
Aperture (mm)

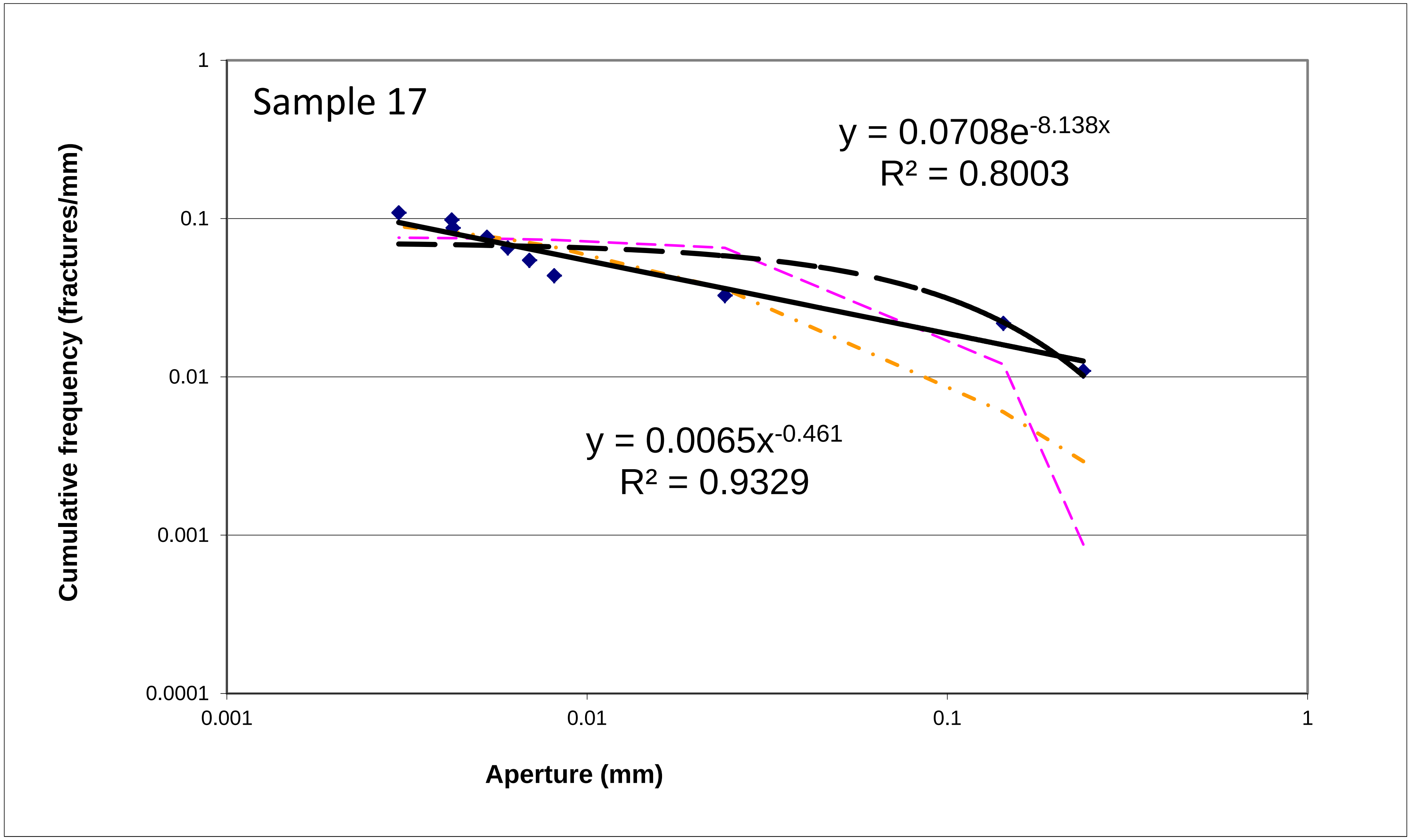
Sample 17
y = 0.0708e-8.138x
R² = 0.8003
y = 0.0065x-0.461
R² = 0.9329
Cumulative frequency (fractures/mm)
1
0.1
0.01
0.001
0.0001
0.001
0.01
0.1
1
Aperture (mm)

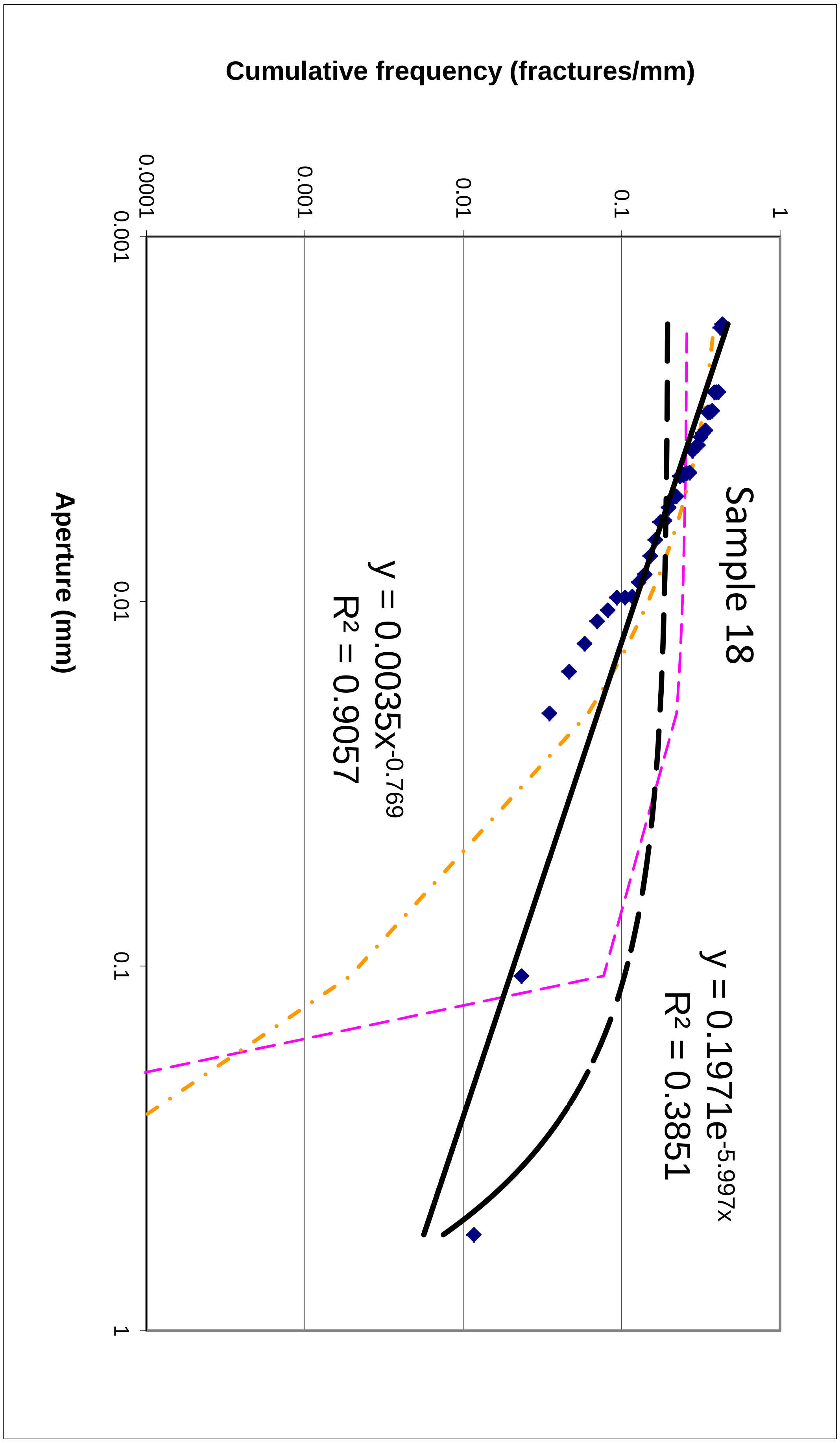
Cumulative frequency (fractures/mm)
1
0.1
0.01
0.001
0.0001
0.001
0.01
0.1
1
Aperture (mm)
Sample 18
y = 0.1971e-5.997x
R² = 0.3851
y = 0.0035x-0.769
R² = 0.9057

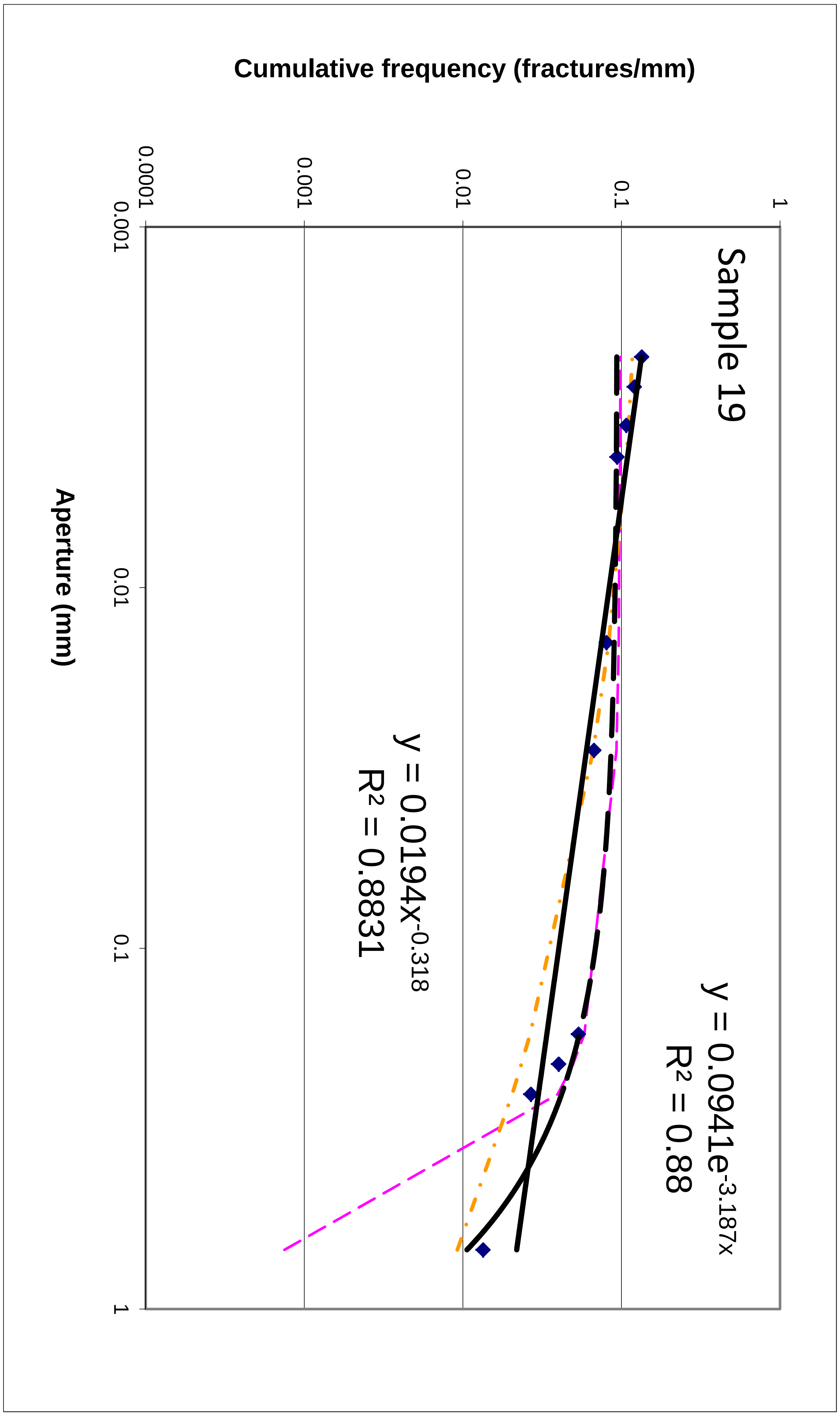
Cumulative frequency (fractures/mm)
Aperture (mm)
Sample 19
y = 0.0941e^-3.187x
R² = 0.88
y = 0.0194x^-0.318
R² = 0.8831
1
0.1
0.01
0.001
0.0001
0.001
0.01
0.1
1

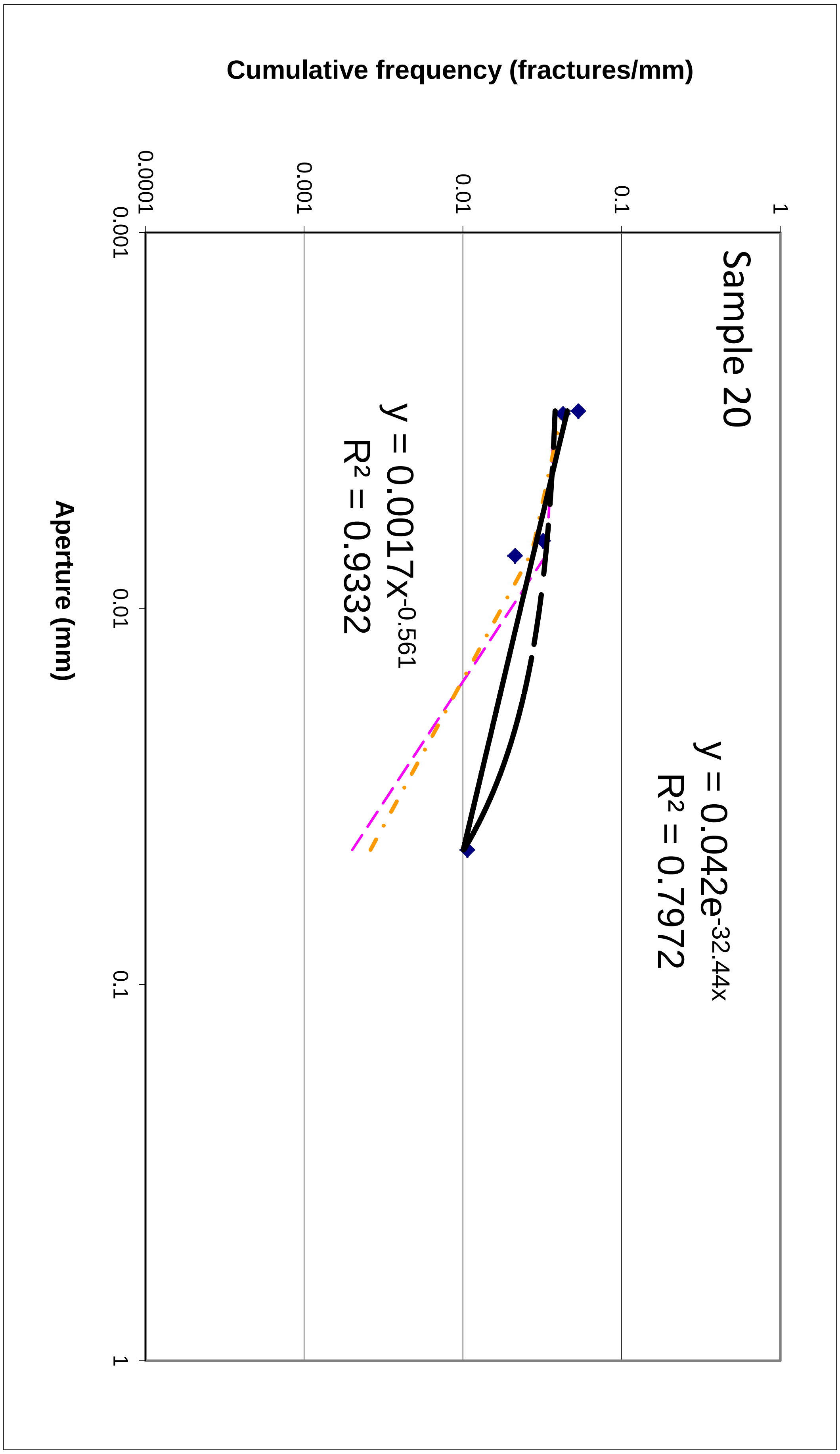
Sample 20
Cumulative frequency (fractures/mm)
Aperture (mm)
1
0.1
0.01
0.001
0.0001
0.001
0.01
0.1
1
y = 0.042e$^{-32.44x}$
R² = 0.7972
y = 0.0017x$^{-0.561}$
R² = 0.9332

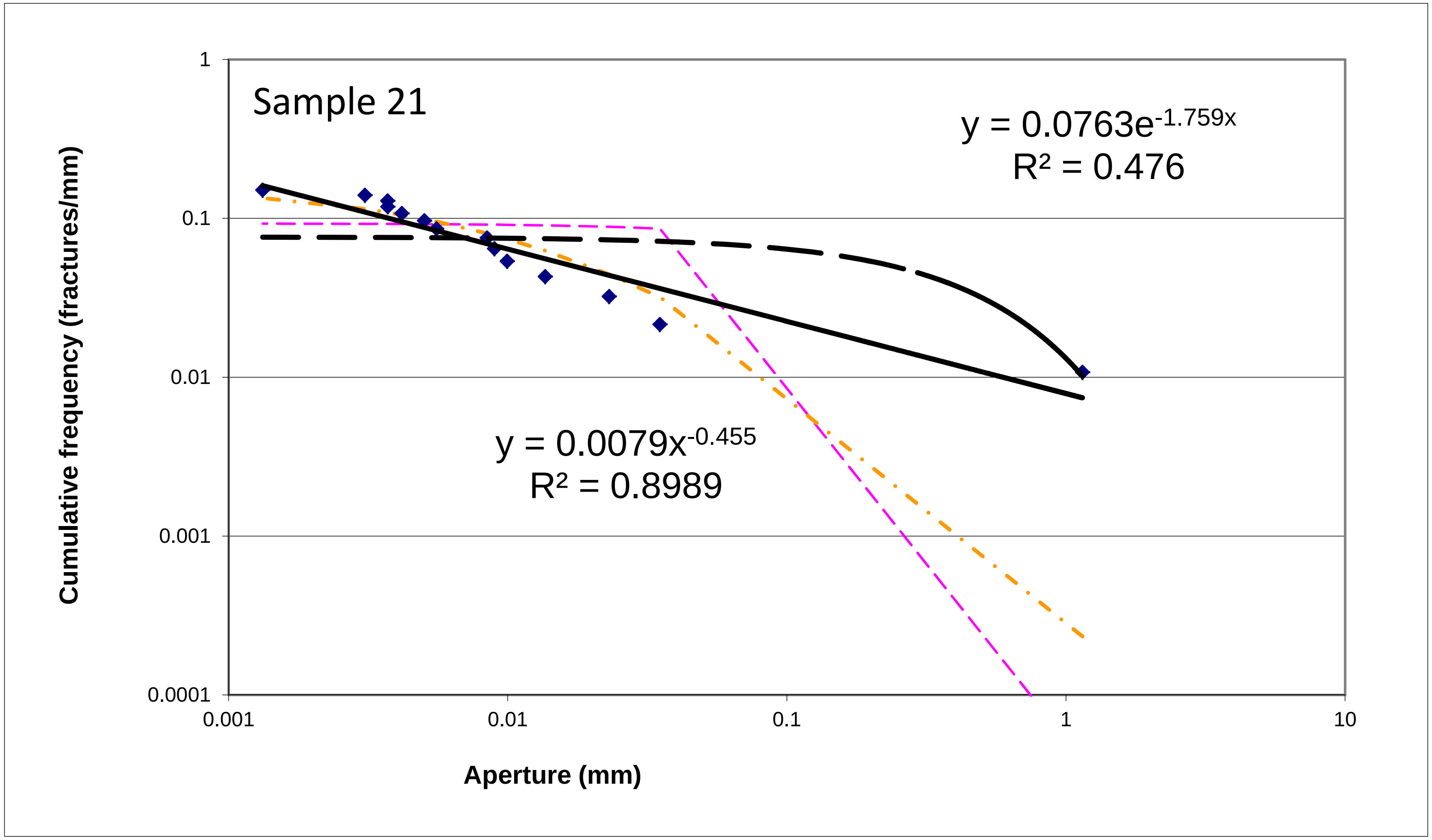
Sample 21
y = 0.0763e^-1.759x
R² = 0.476
y = 0.0079x^-0.455
R² = 0.8989
Cumulative frequency (fractures/mm)
1
0.1
0.01
0.001
0.0001
0.001
0.01
0.1
1
10
Aperture (mm)

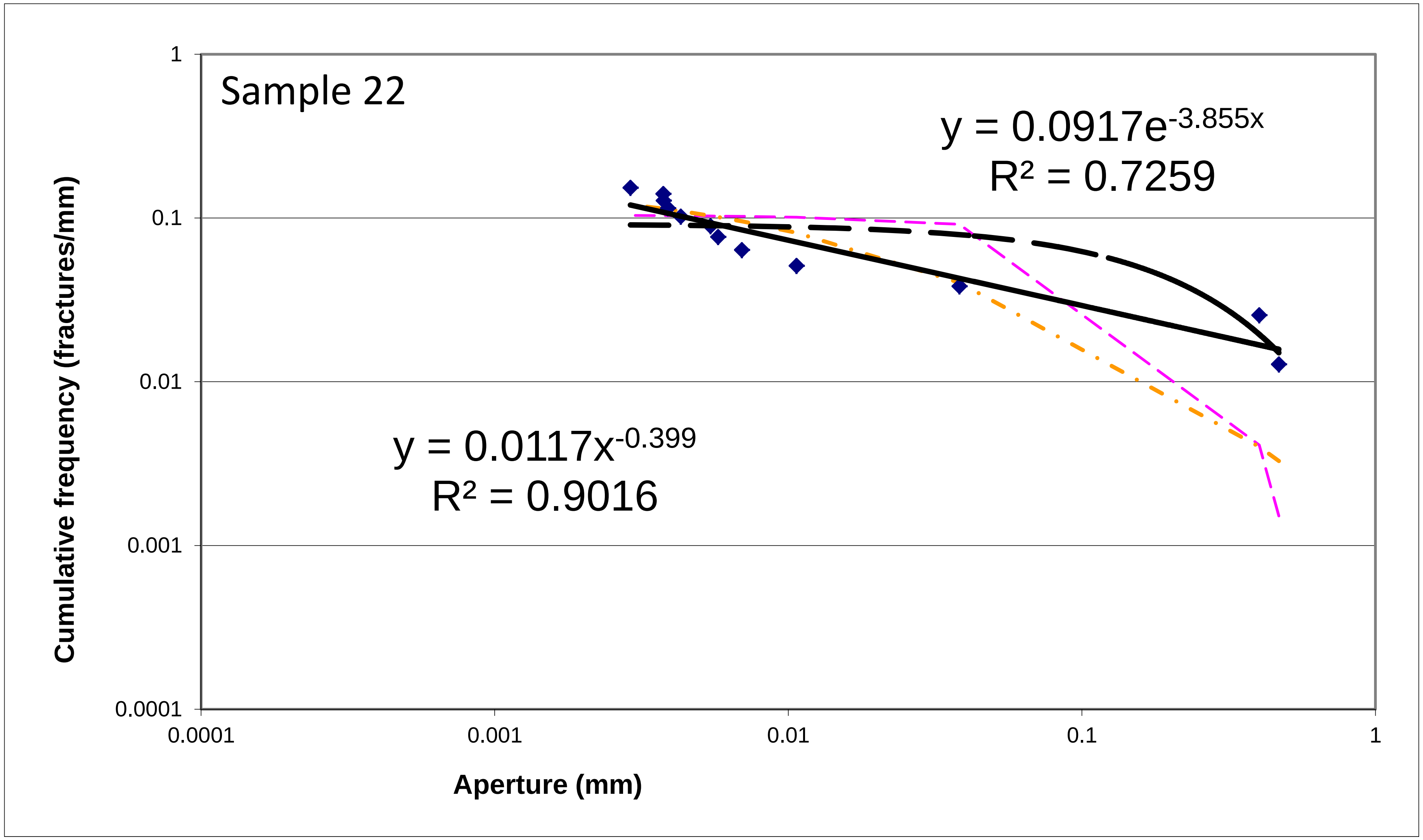
Sample 22
y = 0.0917e^-3.855x
R² = 0.7259
y = 0.0117x^-0.399
R² = 0.9016
Cumulative frequency (fractures/mm)
1
0.1
0.01
0.001
0.0001
0.0001
0.001
0.01
0.1
1
Aperture (mm)

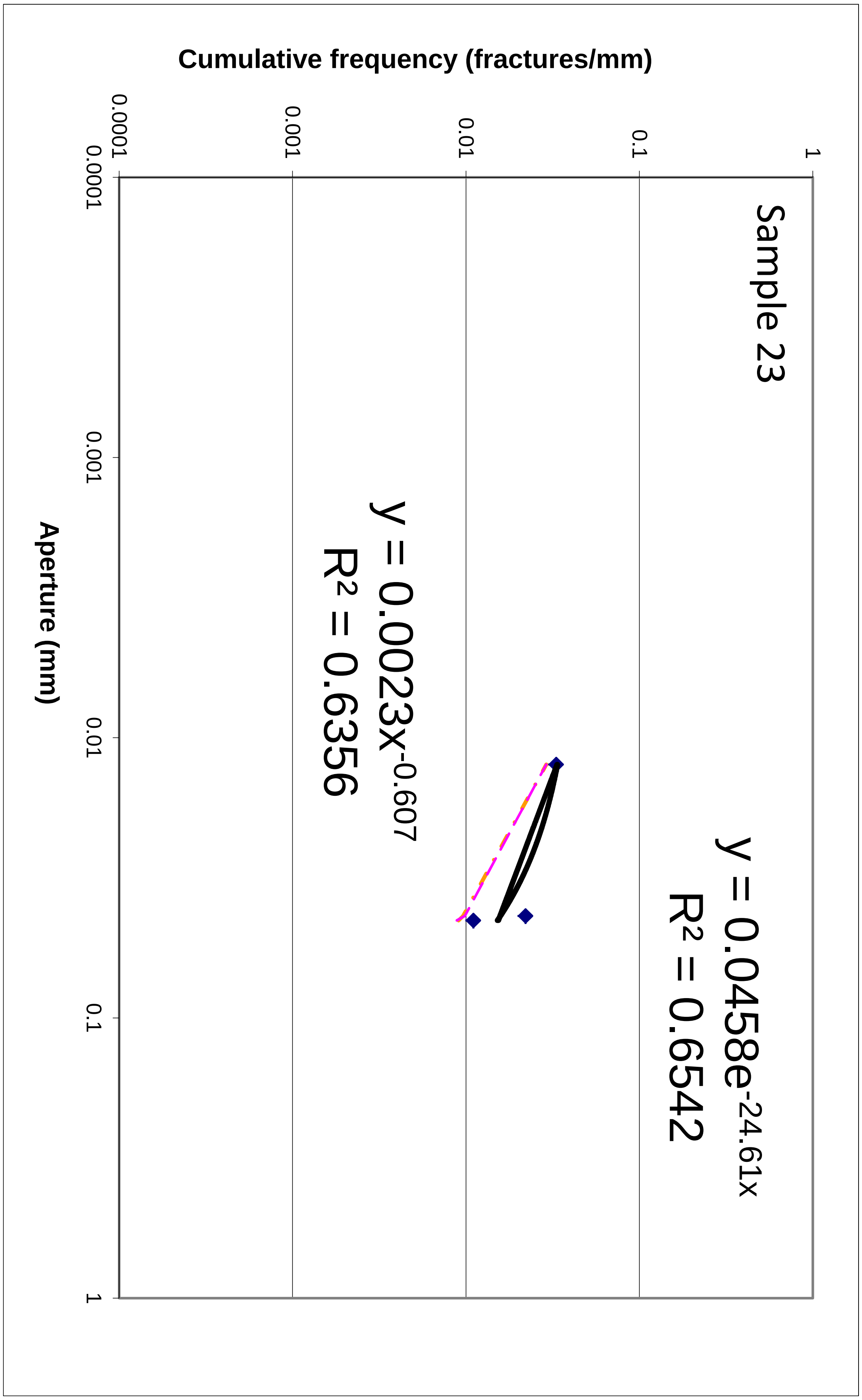
Sample 23
Cumulative frequency (fractures/mm)
Aperture (mm)
1
0.1
0.01
0.001
0.0001
0.0001
0.001
0.01
0.1
1
y = 0.0458e^-24.61x
R² = 0.6542
y = 0.0023x^-0.607
R² = 0.6356

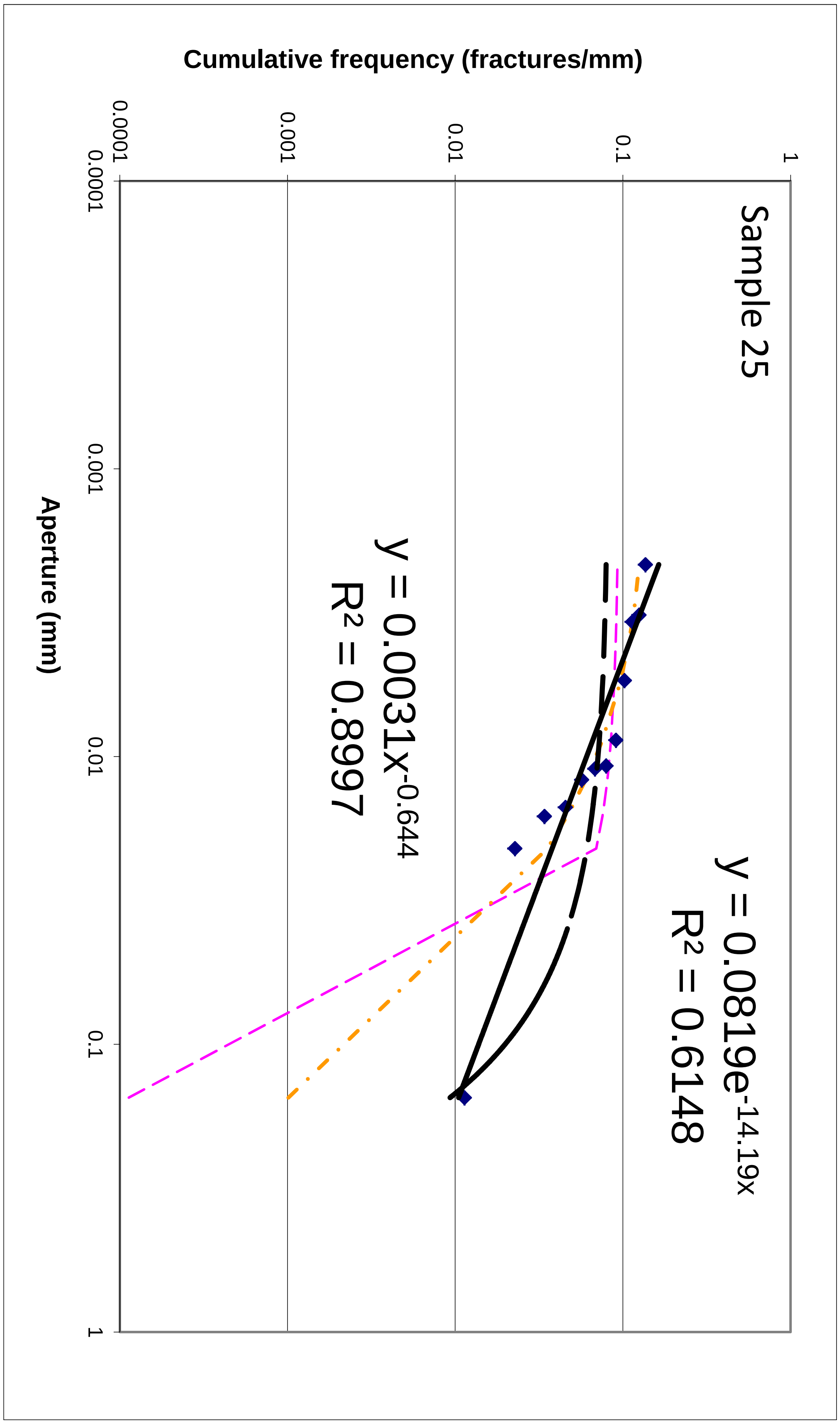
Sample 25
y = 0.0819e-14.19x
R² = 0.6148
y = 0.0031x-0.644
R² = 0.8997
Cumulative frequency (fractures/mm)
1
0.1
0.01
0.001
0.0001
Aperture (mm)
0.0001
0.001
0.01
0.1
1

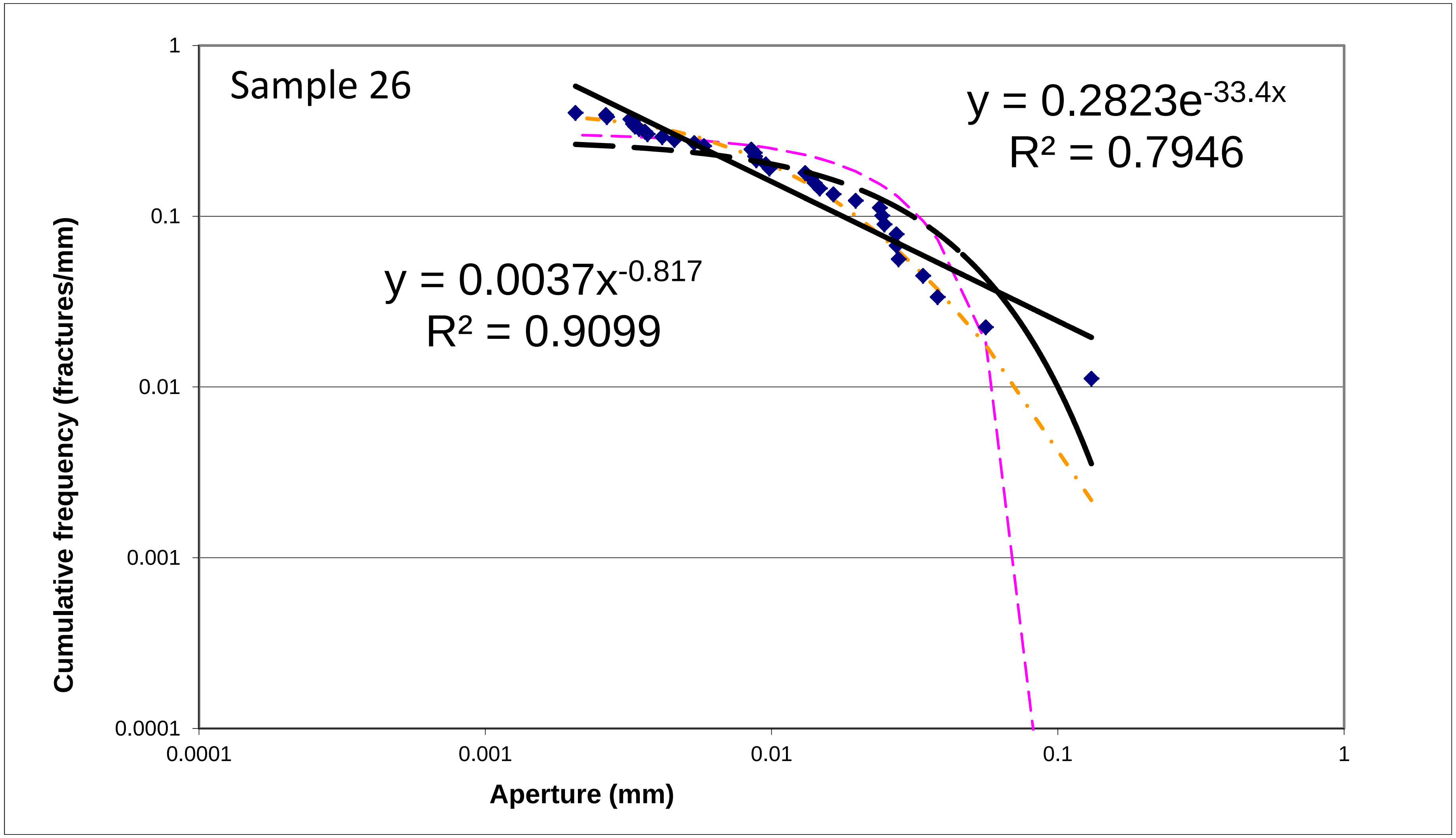
Sample 26
y = 0.2823e^-33.4x
R² = 0.7946
y = 0.0037x^-0.817
R² = 0.9099
Cumulative frequency (fractures/mm)
1
0.1
0.01
0.001
0.0001
0.0001
0.001
0.01
0.1
1
Aperture (mm)

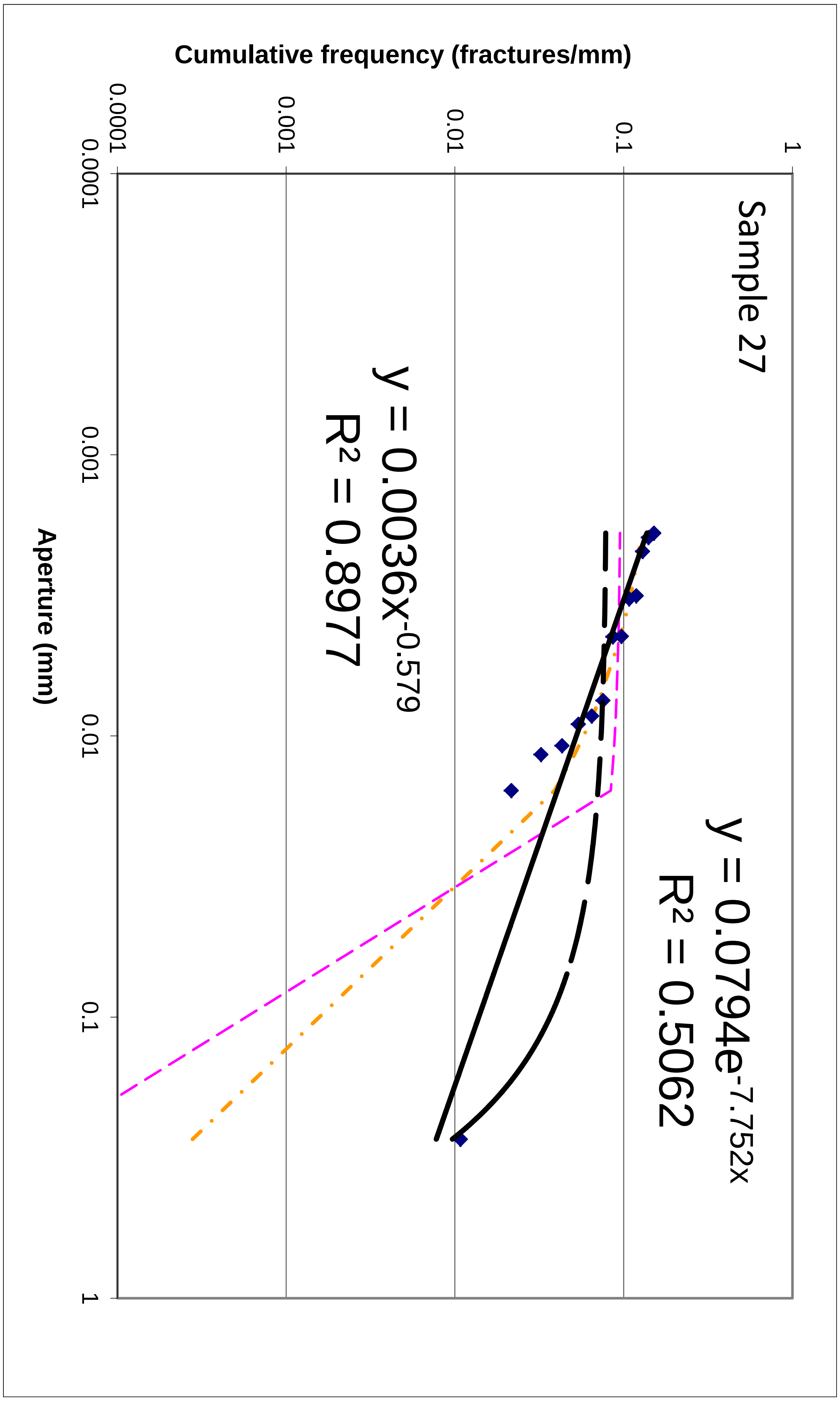
Sample 27
y = 0.0794e-7.752x
R² = 0.5062
y = 0.0036x-0.579
R² = 0.8977
Cumulative frequency (fractures/mm)
Aperture (mm)
1
0.1
0.01
0.001
0.0001
0.0001
0.001
0.01
0.1
1

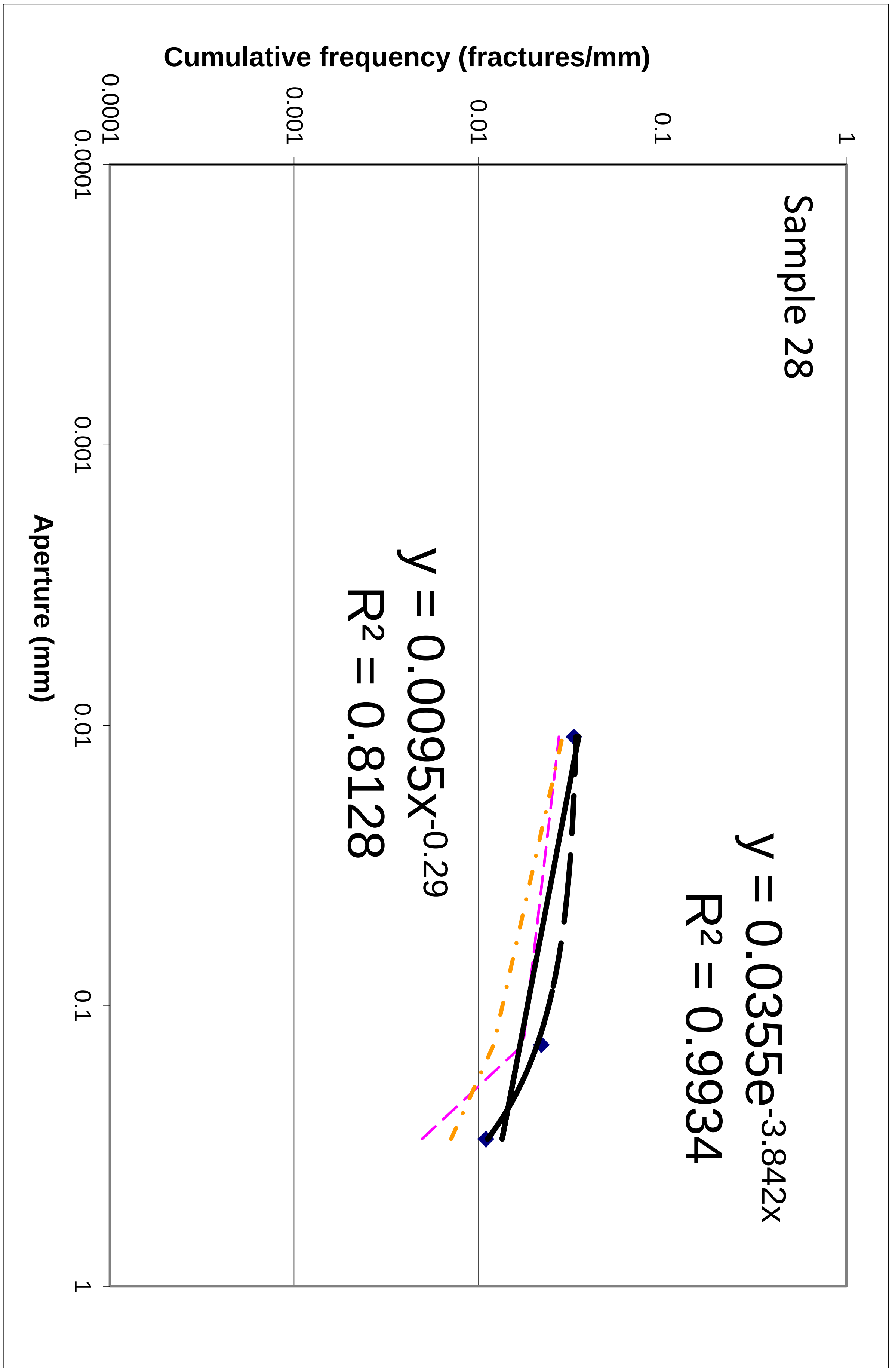
Sample 28
y = 0.0355e-3.842x
R² = 0.9934
y = 0.0095x-0.29
R² = 0.8128
Cumulative frequency (fractures/mm)
1
0.1
0.01
0.001
0.0001
Aperture (mm)
0.0001
0.001
0.01
0.1
1

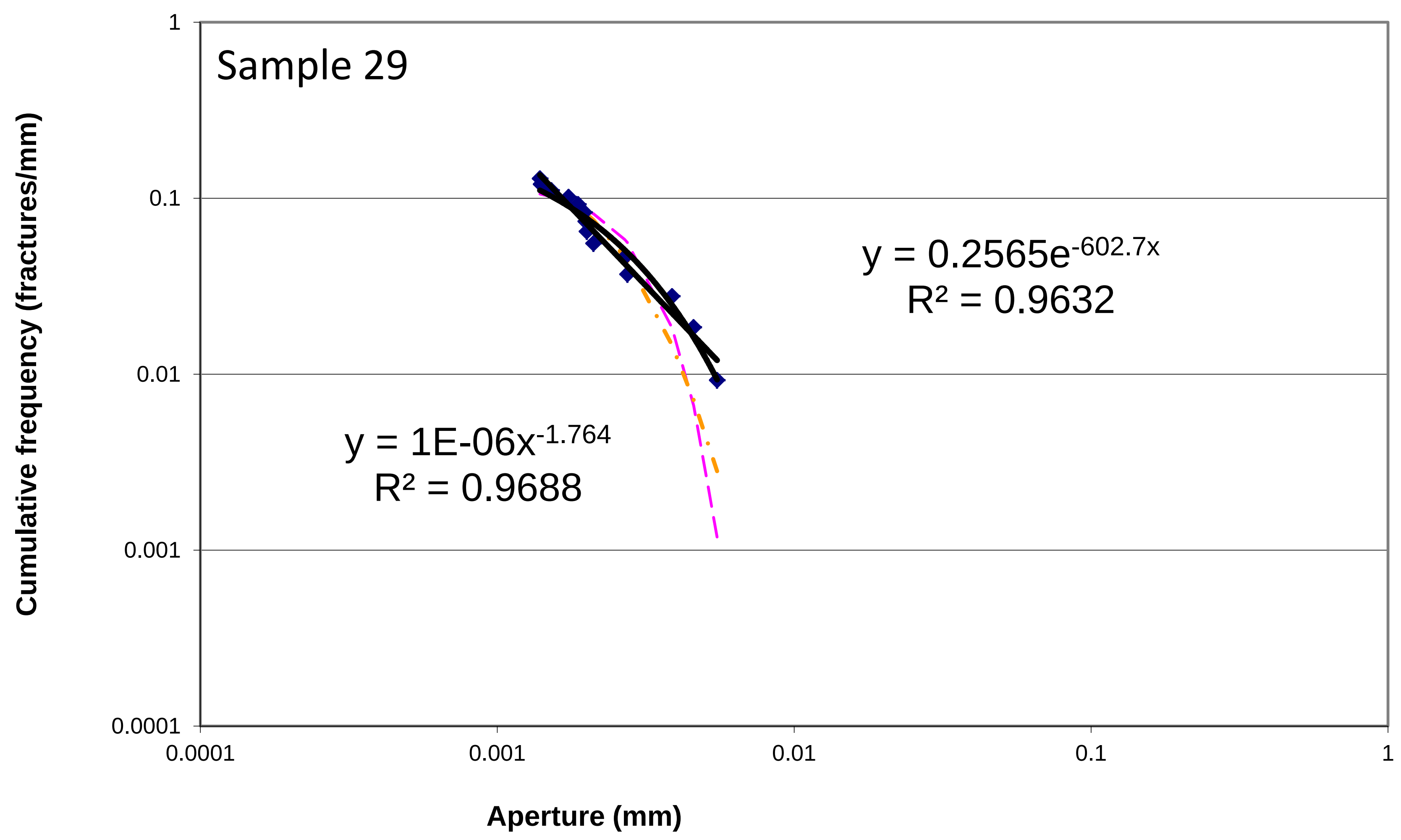
Sample 29
Cumulative frequency (fractures/mm)
1
0.1
0.01
0.001
0.0001
0.0001
0.001
0.01
0.1
1
Aperture (mm)
y = 0.2565e-602.7x
R² = 0.9632
y = 1E-06x-1.764
R² = 0.9688

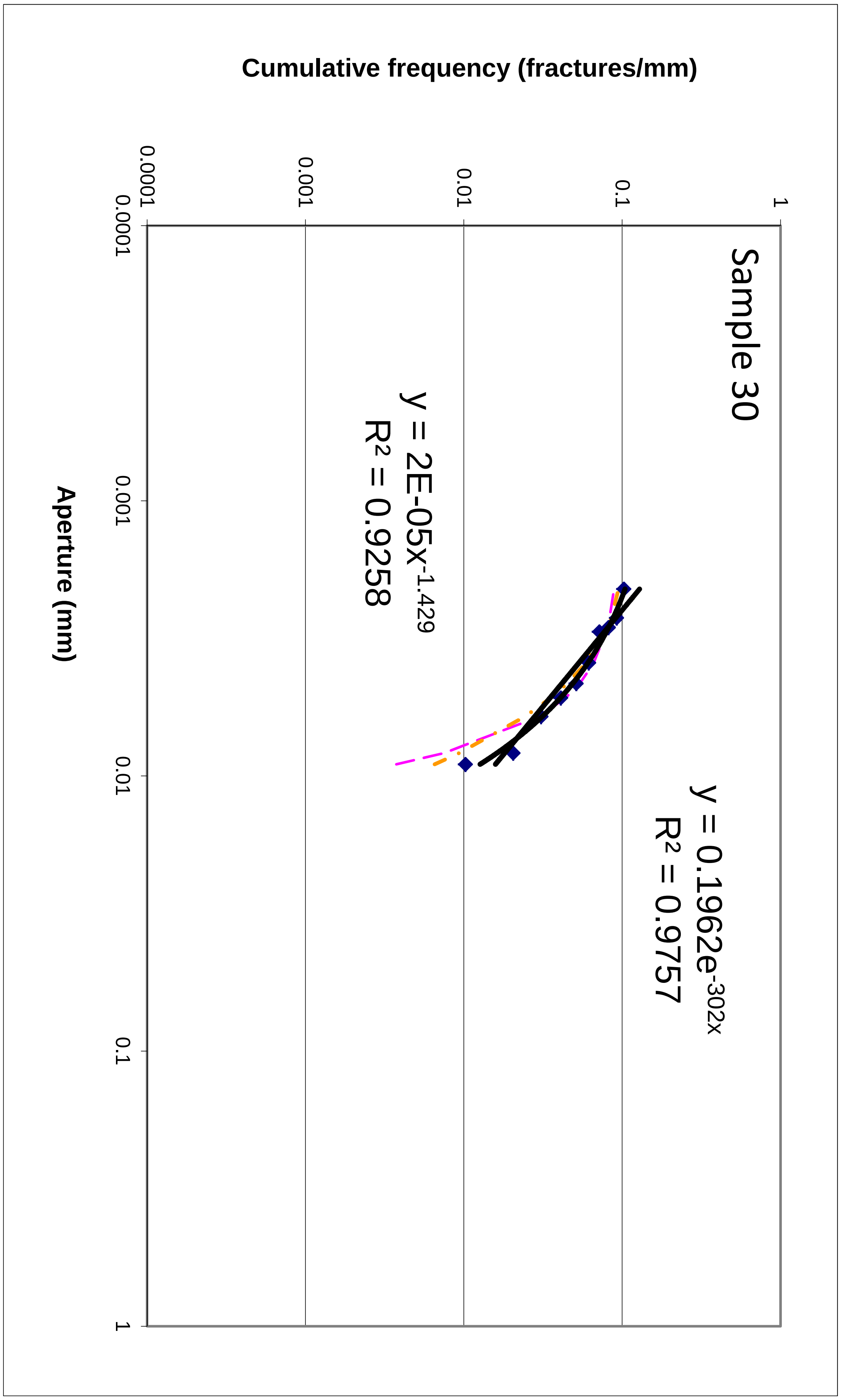
Sample 30
Cumulative frequency (fractures/mm)
1
0.1
0.01
0.001
0.0001
Aperture (mm)
0.0001
0.001
0.01
0.1
1
$y = 0.1962e^{-302x}$
$R^2 = 0.9757$
$y = 2E\text{-}05x^{-1.429}$
$R^2 = 0.9258$

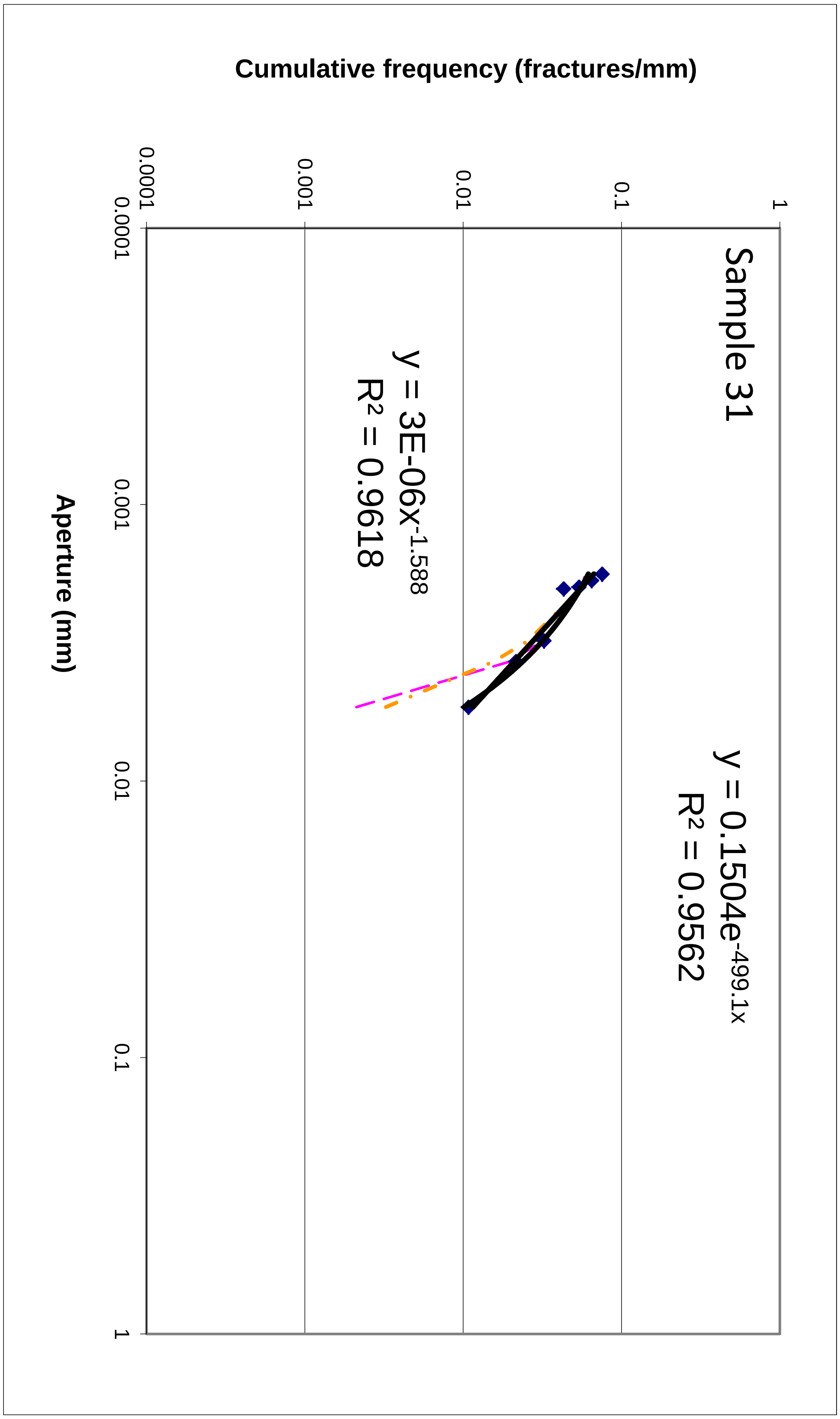
Sample 31
Cumulative frequency (fractures/mm)
Aperture (mm)
$y = 0.1504e^{-499.1x}$
$R^2 = 0.9562$
$y = 3E\text{-}06x^{-1.588}$
$R^2 = 0.9618$
1
0.1
0.01
0.001
0.0001
0.0001
0.001
0.01
0.1
1

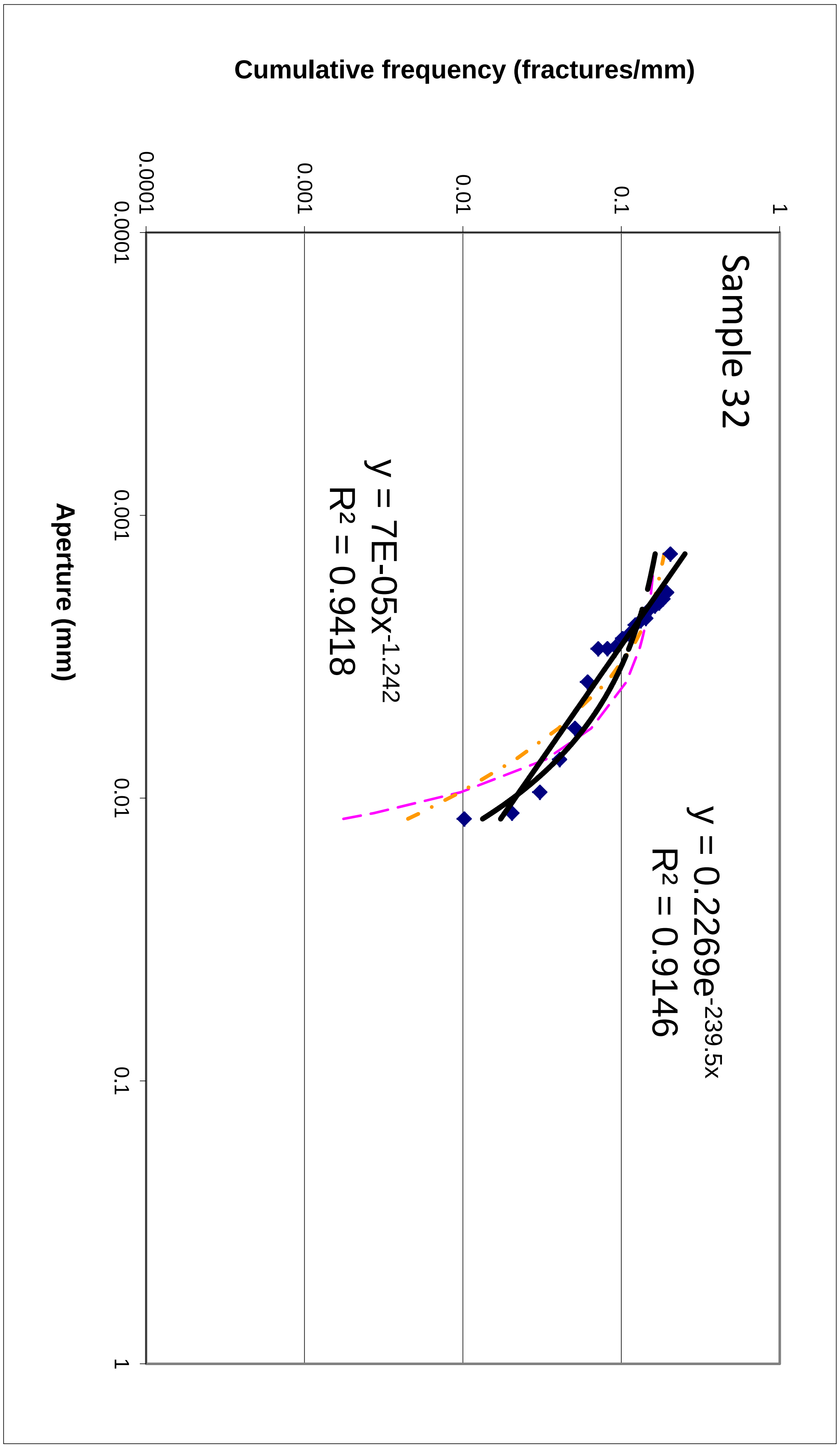
Sample 32
Cumulative frequency (fractures/mm)
1
0.1
0.01
0.001
0.0001
Aperture (mm)
0.0001
0.001
0.01
0.1
1
$y = 7E\text{-}05x^{-1.242}$
$R^2 = 0.9418$
$y = 0.2269e^{-239.5x}$
$R^2 = 0.9146$

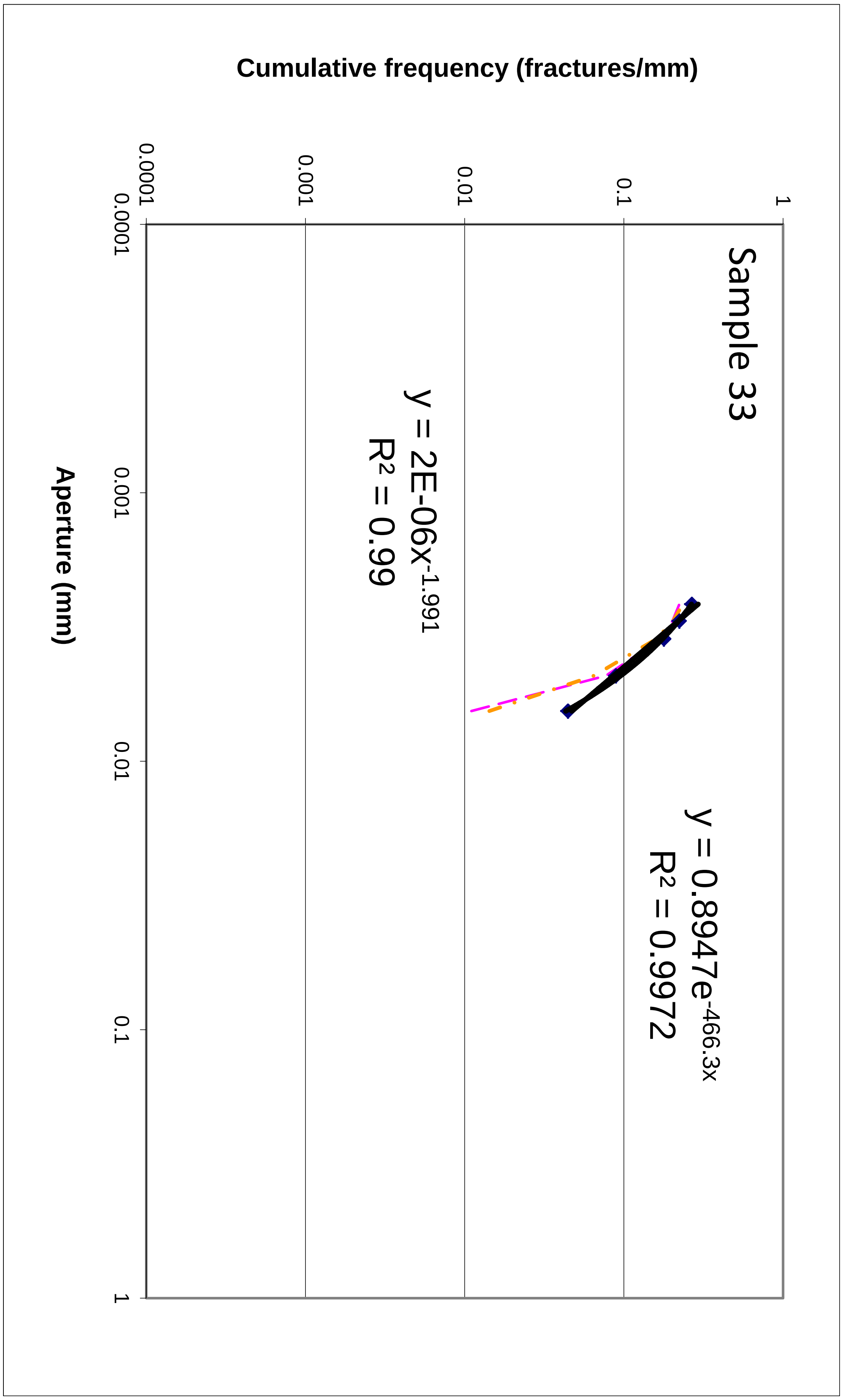

Sample 33
Cumulative frequency (fractures/mm)
1
0.1
0.01
0.001
0.0001
Aperture (mm)
0.0001
0.001
0.01
0.1
1
y = 0.8947e^-466.3x
R² = 0.9972
y = 2E-06x^-1.991
R² = 0.99

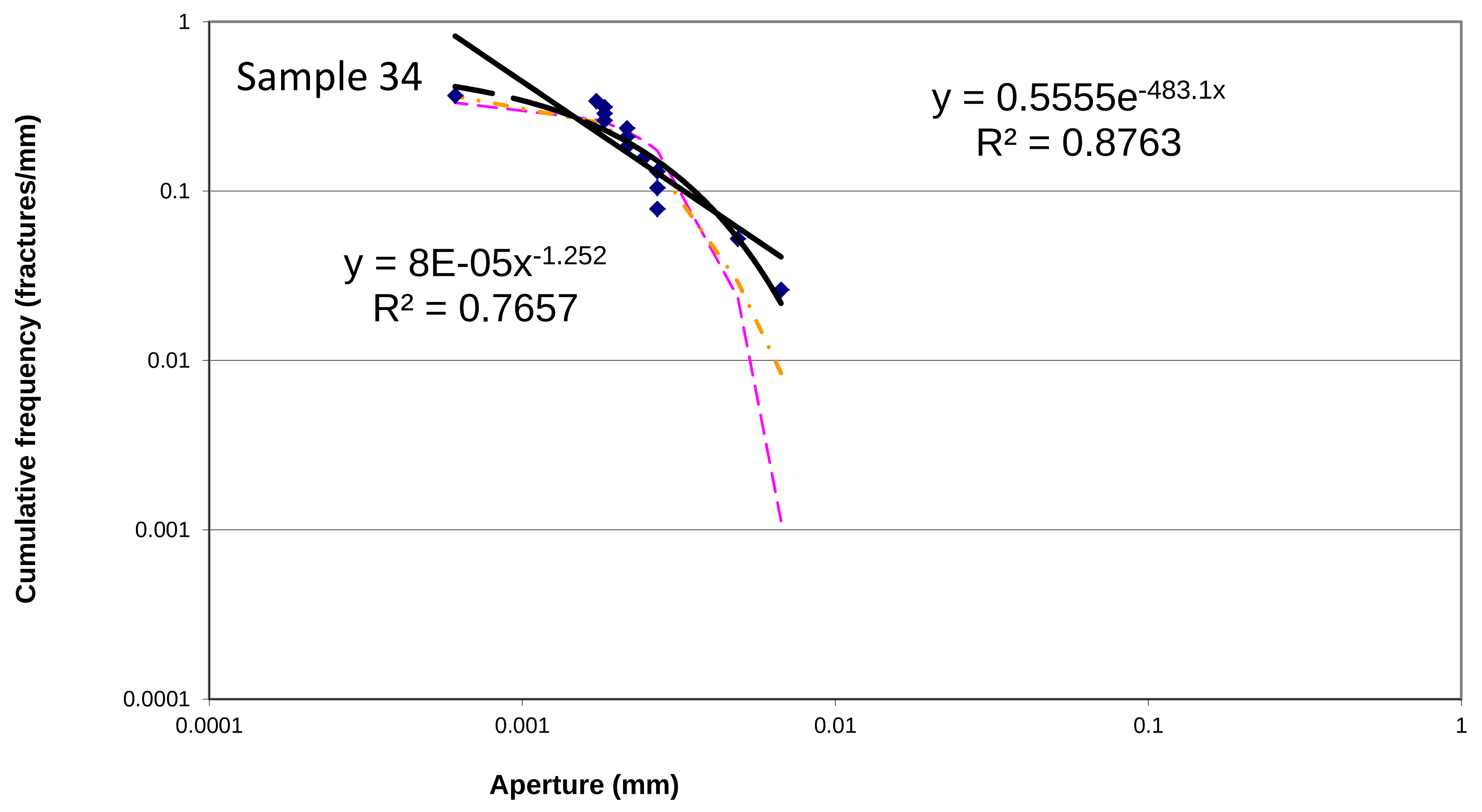
Sample 34
y = 0.5555e^-483.1x
R² = 0.8763
y = 8E-05x^-1.252
R² = 0.7657
Cumulative frequency (fractures/mm)
1
0.1
0.01
0.001
0.0001
Aperture (mm)
0.0001
0.001
0.01
0.1
1

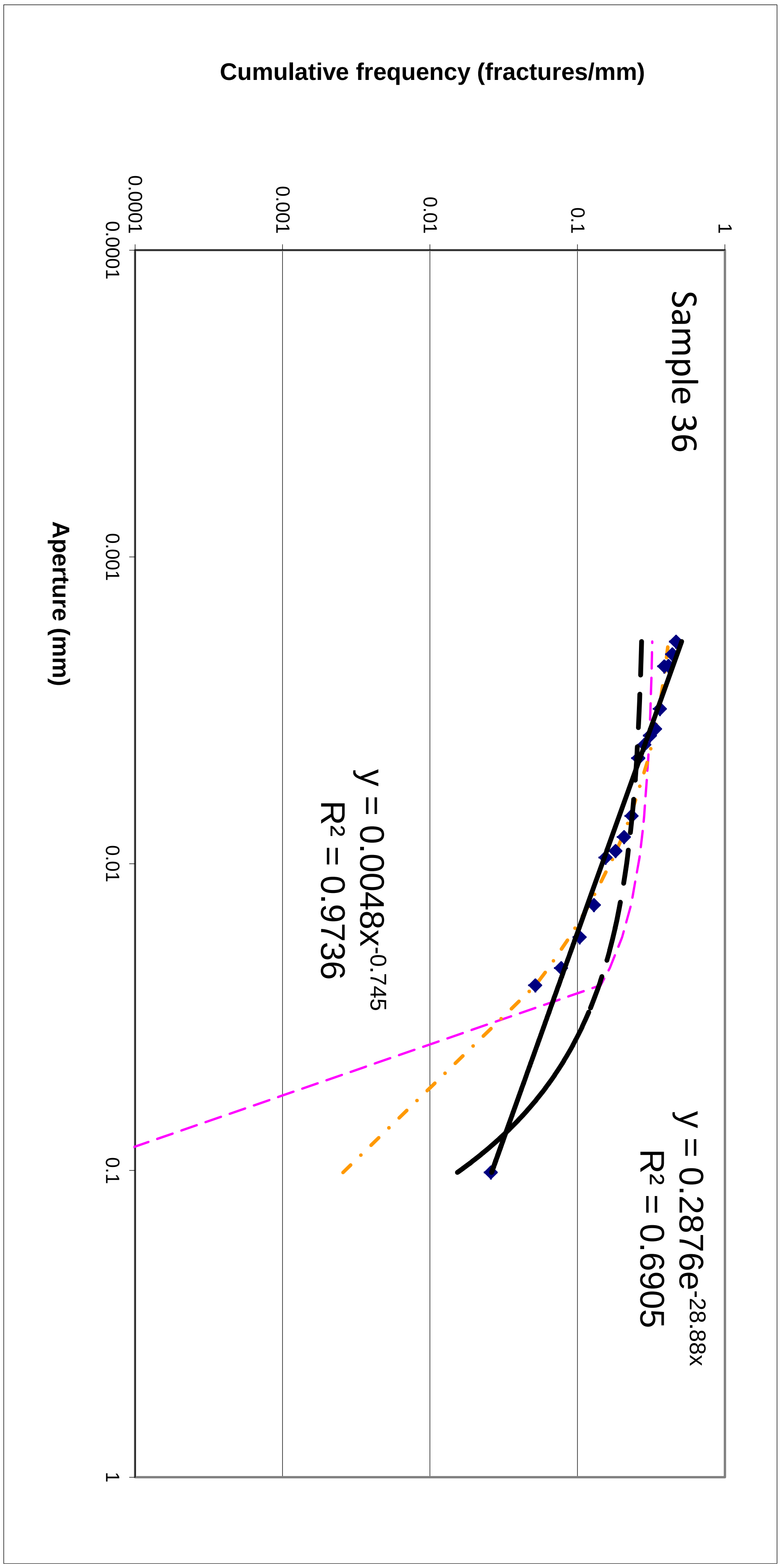
Sample 36
Cumulative frequency (fractures/mm)
1
0.1
0.01
0.001
0.0001
Aperture (mm)
0.0001
0.001
0.01
0.1
1
y = 0.2876e$^{-28.88x}$
R² = 0.6905
y = 0.0048x$^{-0.745}$
R² = 0.9736

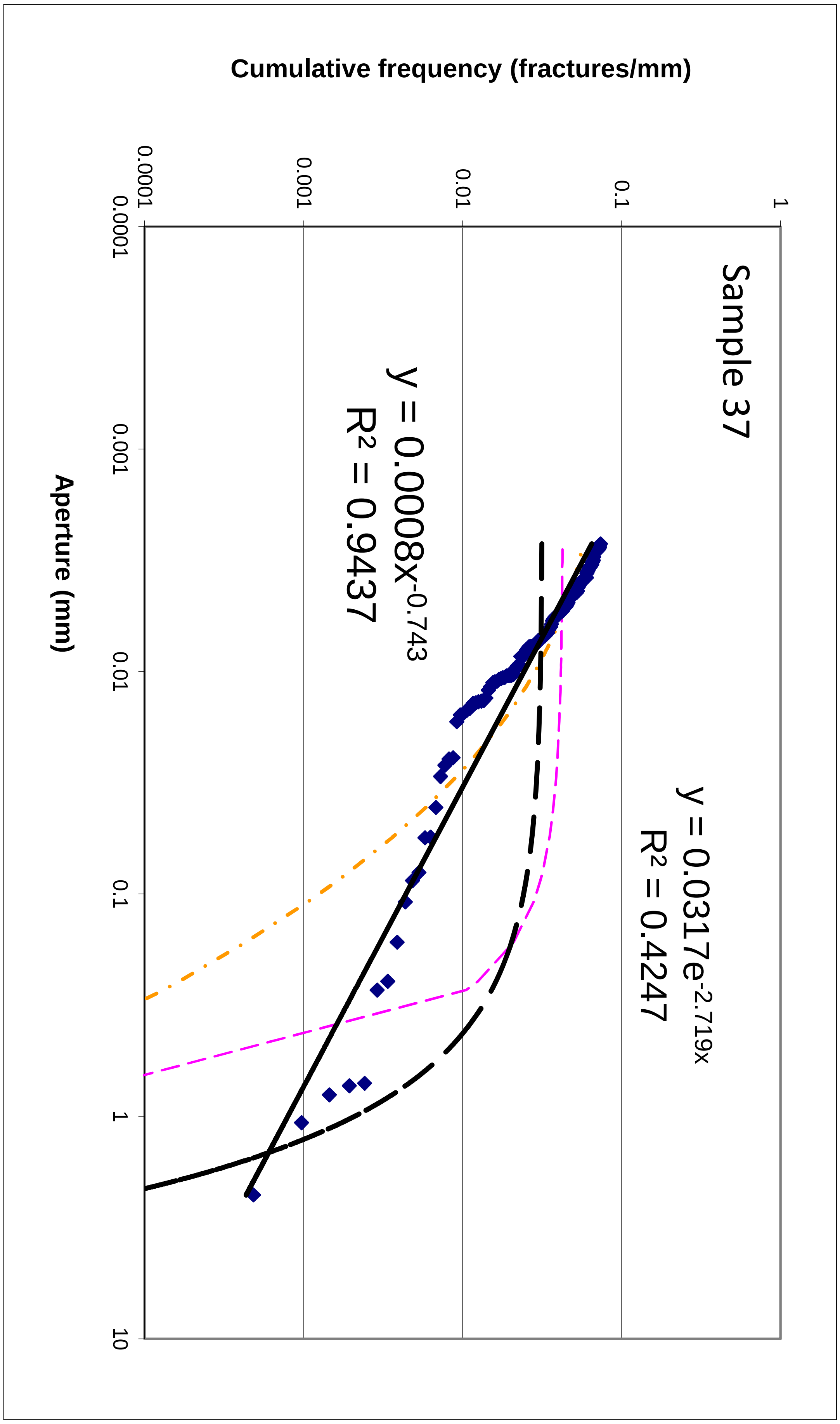
Sample 37
Cumulative frequency (fractures/mm)
Aperture (mm)
$y = 0.0317e^{-2.719x}$
$R^2 = 0.4247$
$y = 0.0008x^{-0.743}$
$R^2 = 0.9437$
1
0.1
0.01
0.001
0.0001
0.0001
0.001
0.01
0.1
1
10

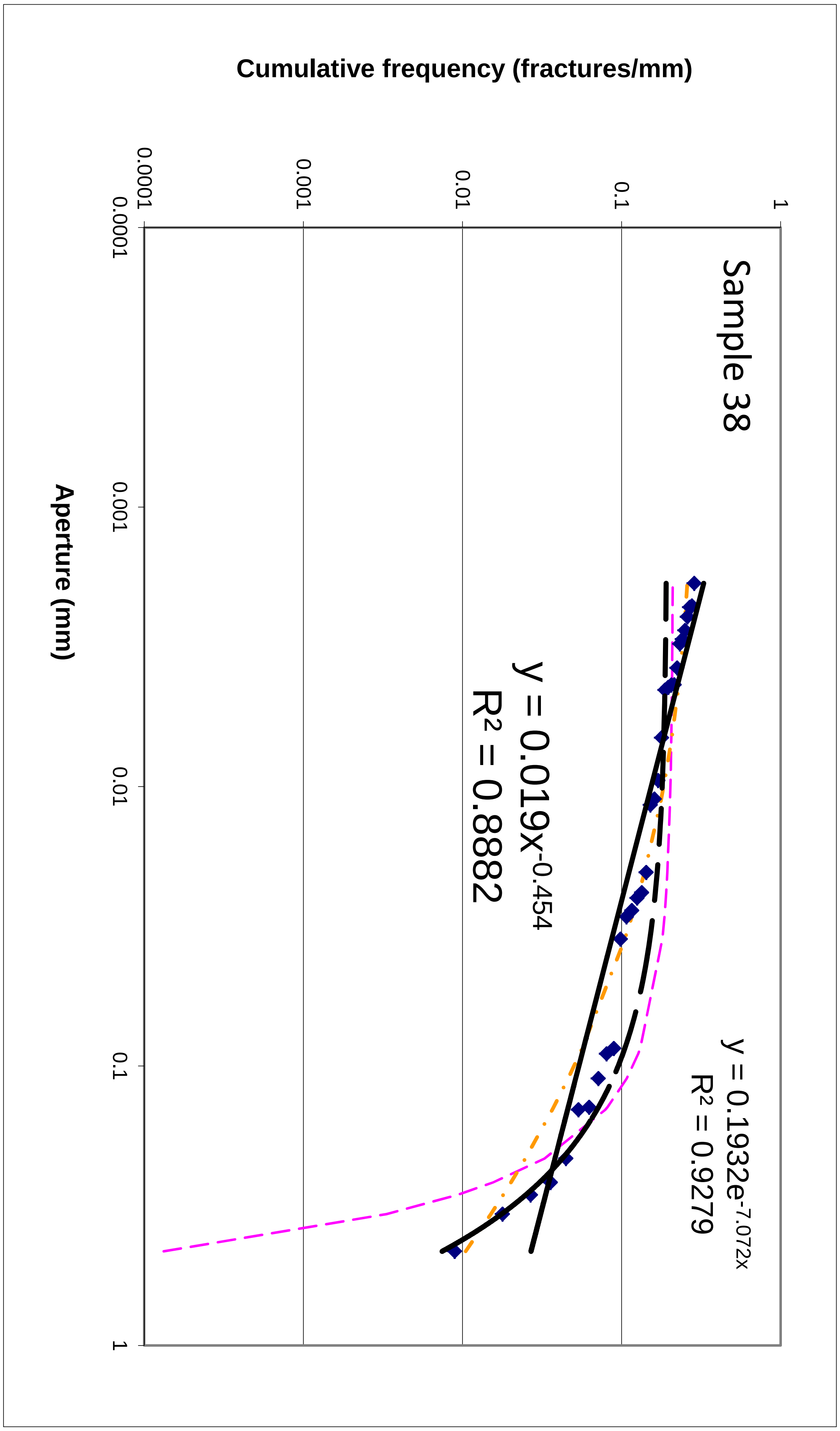
Sample 38
Cumulative frequency (fractures/mm)
Aperture (mm)
y = 0.1932e^-7.072x
R² = 0.9279
y = 0.019x^-0.454
R² = 0.8882
1
0.1
0.01
0.001
0.0001
0.0001
0.001
0.01
0.1
1

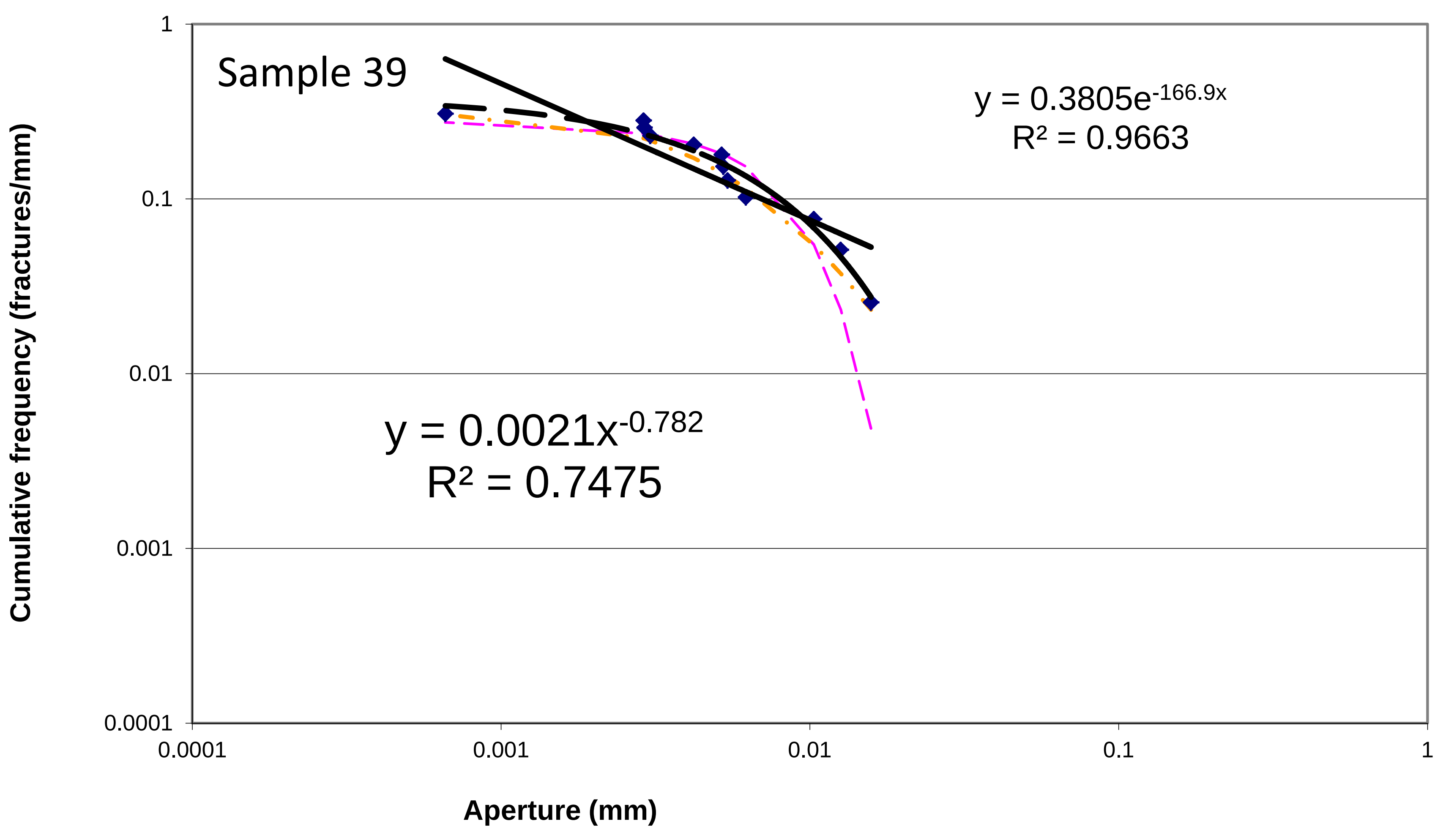
Sample 39
y = 0.3805e^-166.9x
R² = 0.9663
y = 0.0021x^-0.782
R² = 0.7475
Cumulative frequency (fractures/mm)
1
0.1
0.01
0.001
0.0001
0.0001
0.001
0.01
0.1
1
Aperture (mm)

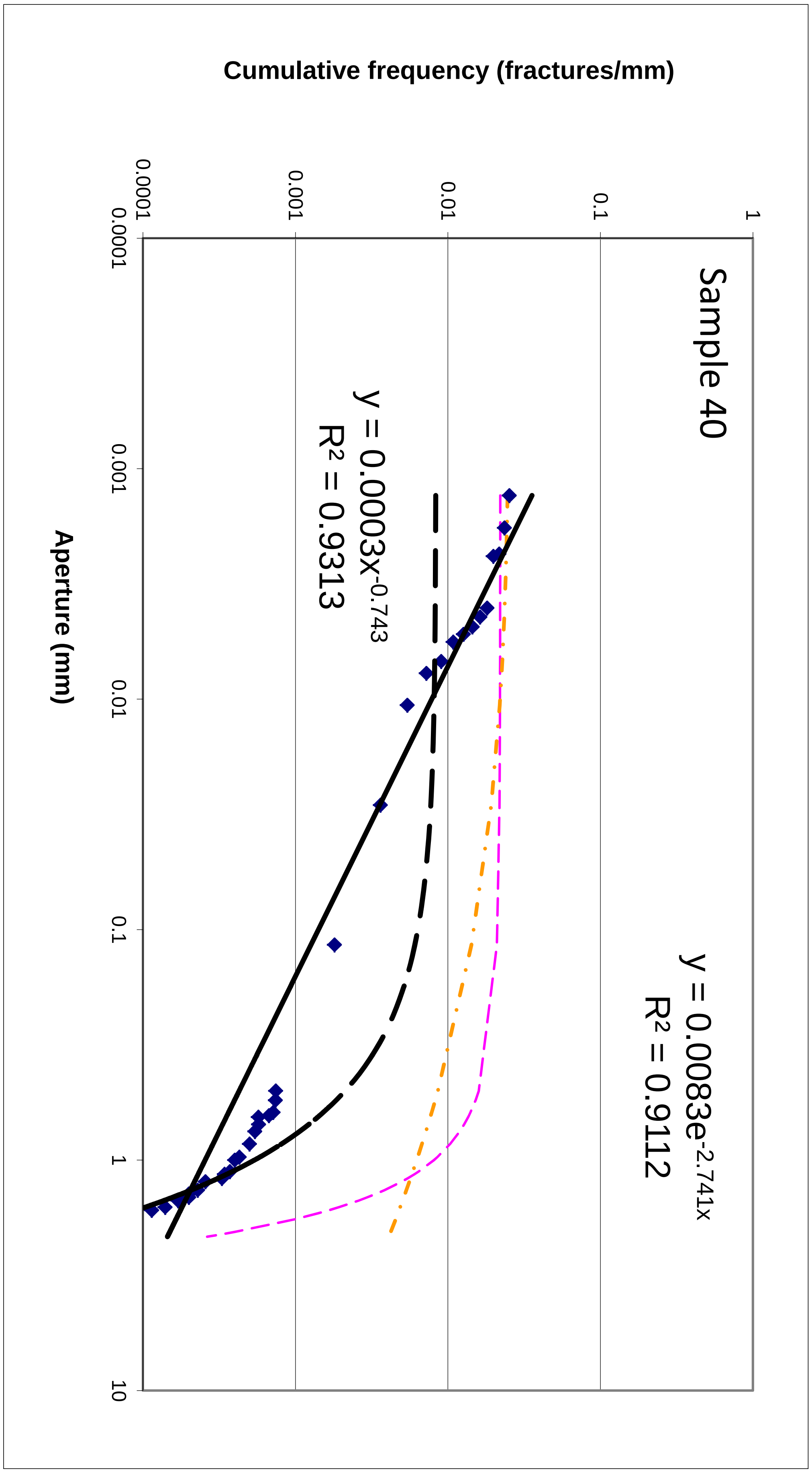
Sample 40
Cumulative frequency (fractures/mm)
Aperture (mm)
y = 0.0083e$^{-2.741x}$
R² = 0.9112
y = 0.0003x$^{-0.743}$
R² = 0.9313
0.0001
0.001
0.01
0.1
1
0.0001
0.001
0.01
0.1
1
10

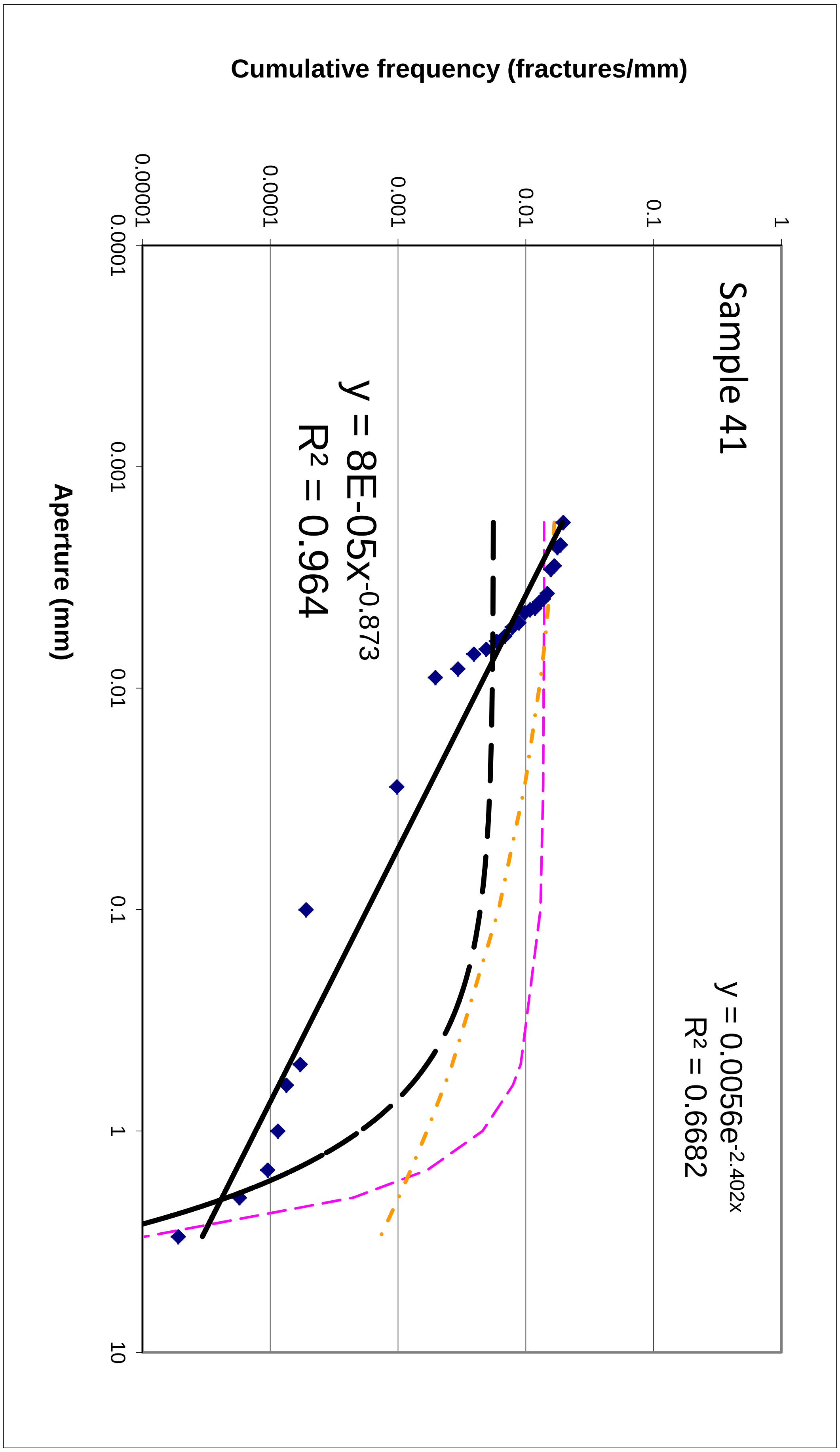
Sample 41
Cumulative frequency (fractures/mm)
1
0.1
0.01
0.001
0.0001
0.00001
Aperture (mm)
0.0001
0.001
0.01
0.1
1
10
$y = 0.0056e^{-2.402x}$
$R^2 = 0.6682$
$y = 8E-05x^{-0.873}$
$R^2 = 0.964$

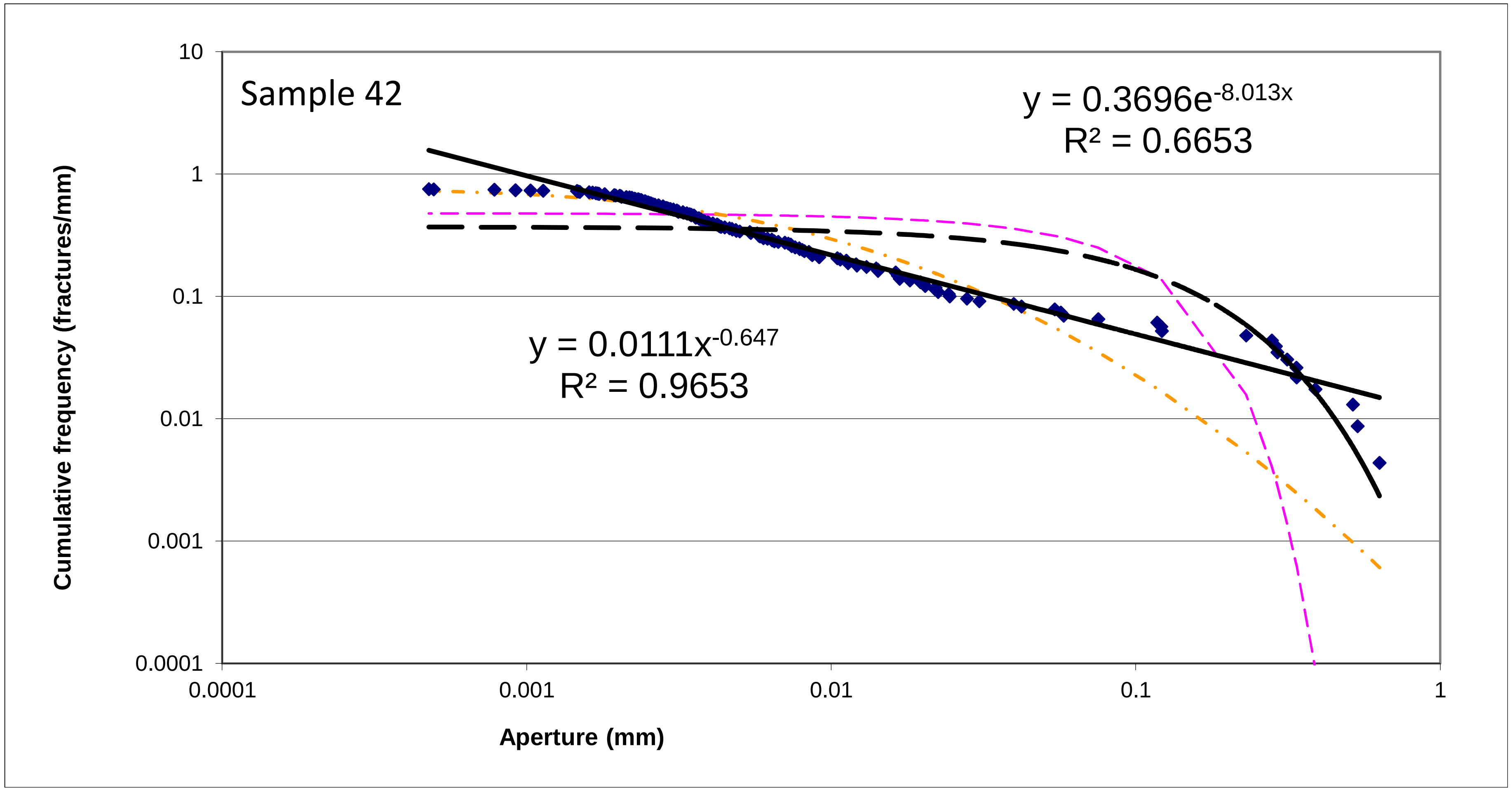Sample 42
y = 0.3696e^-8.013x
R² = 0.6653
y = 0.0111x^-0.647
R² = 0.9653
Cumulative frequency (fractures/mm)
10
1
0.1
0.01
0.001
0.0001
0.0001
0.001
0.01
0.1
1
Aperture (mm)

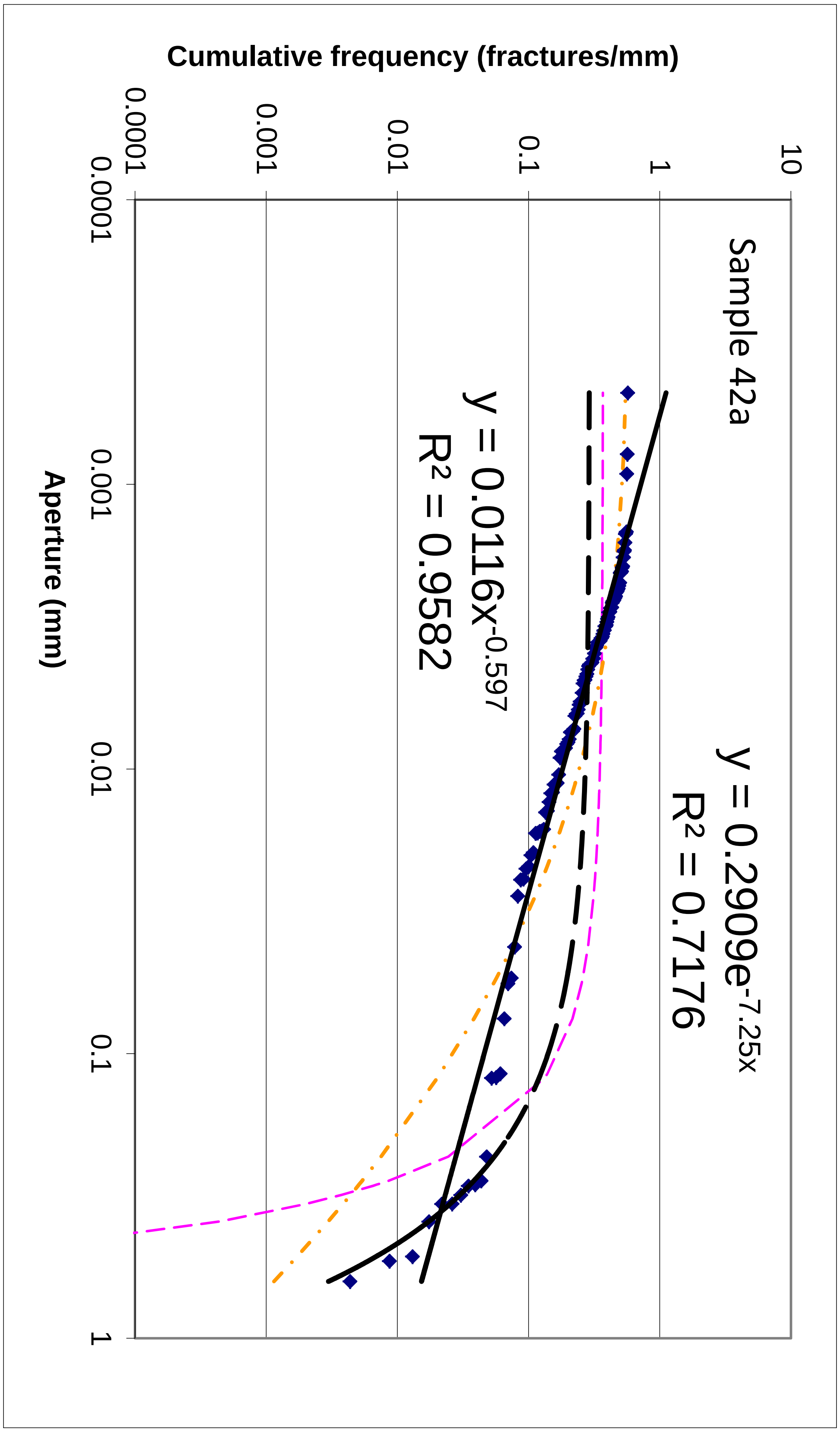
Sample 42a
y = 0.2909e^-7.25x
R² = 0.7176
y = 0.0116x^-0.597
R² = 0.9582
Cumulative frequency (fractures/mm)
10
1
0.1
0.01
0.001
0.0001
Aperture (mm)
0.0001
0.001
0.01
0.1
1

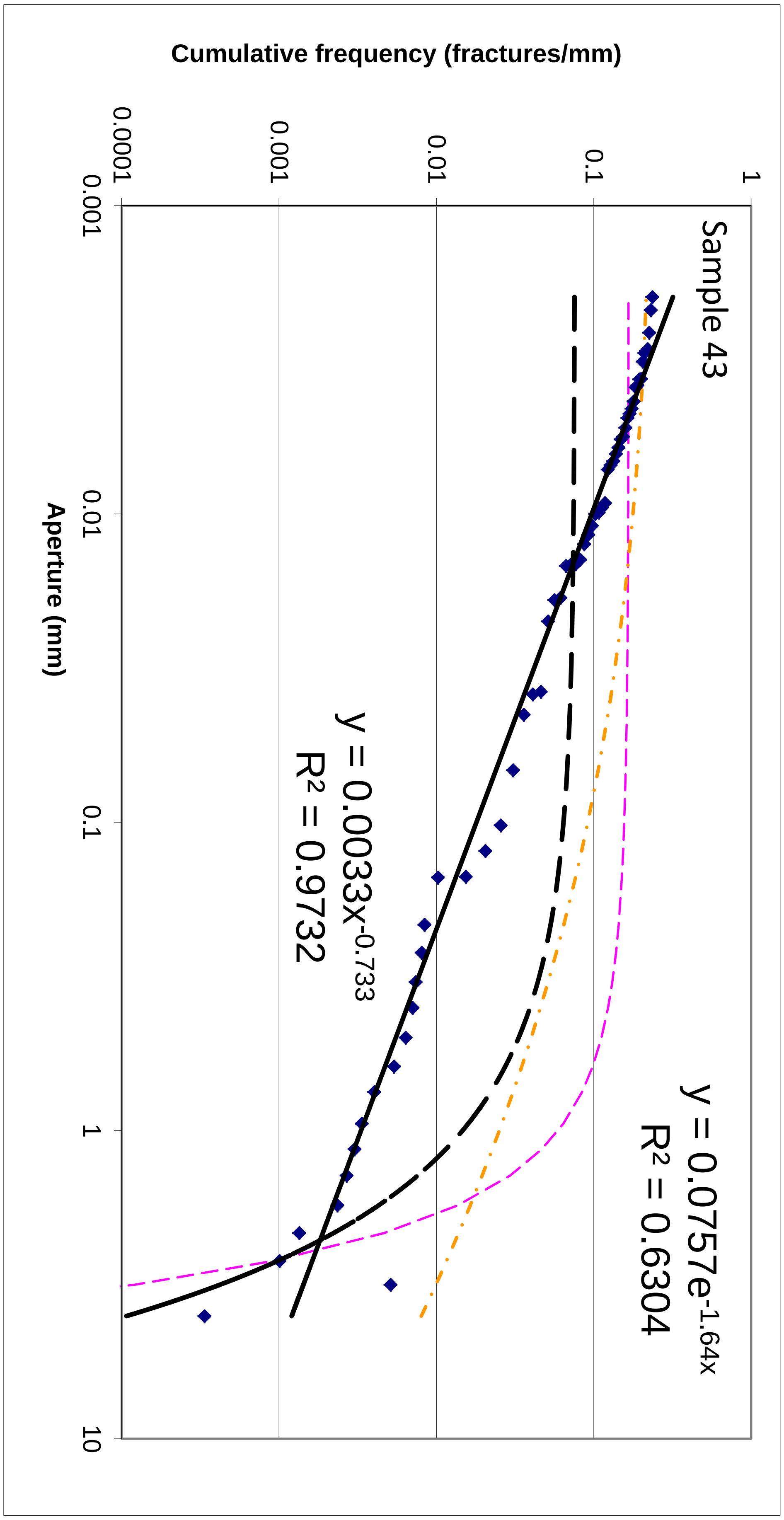
Sample 43
Cumulative frequency (fractures/mm)
Aperture (mm)
0.0001
0.001
0.01
0.1
1
0.001
0.01
0.1
1
10
y = 0.0033x$^{-0.733}$
R² = 0.9732
y = 0.0757e$^{-1.64x}$
R² = 0.6304

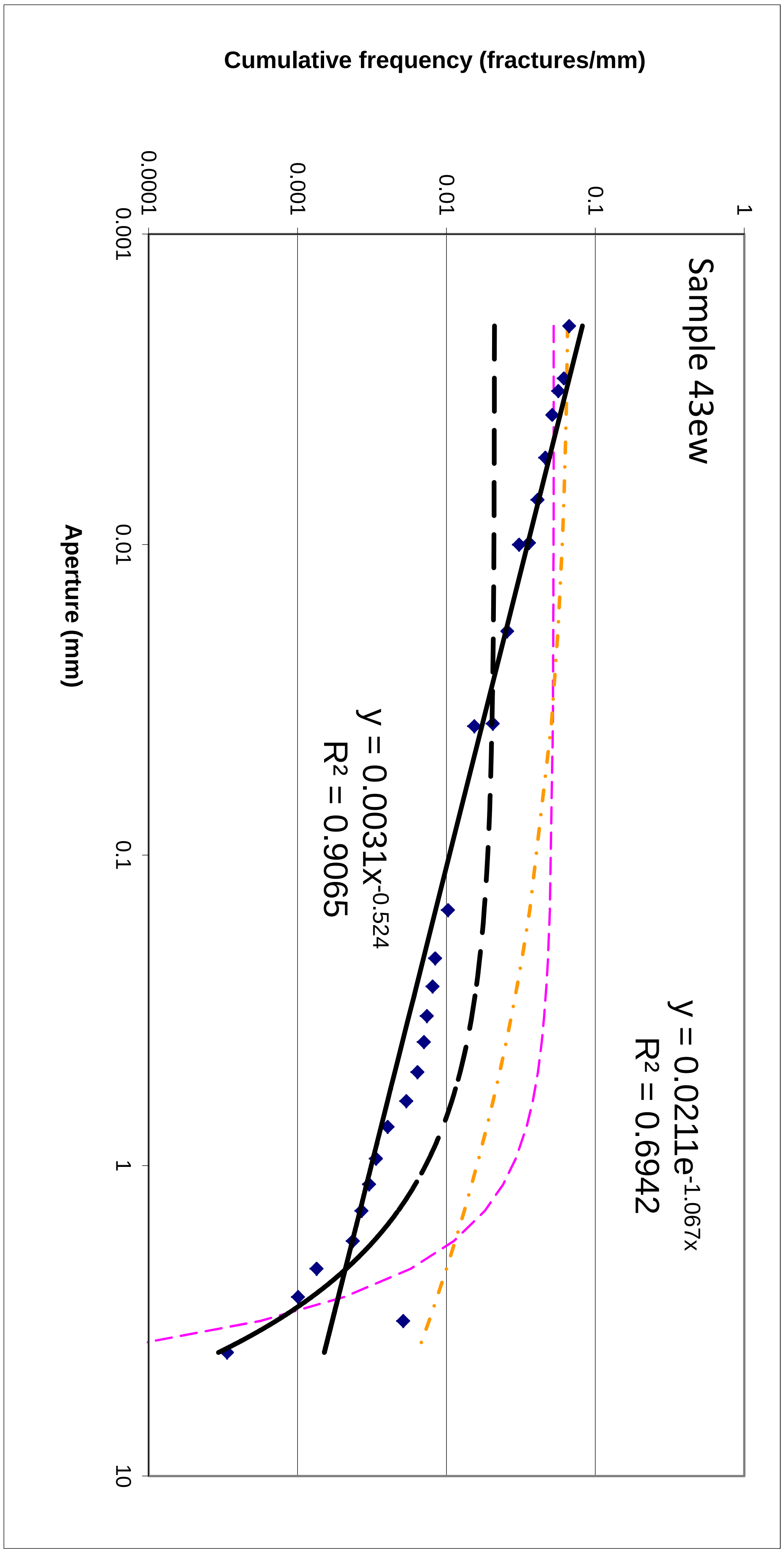
Sample 43ew
Cumulative frequency (fractures/mm)
1
0.1
0.01
0.001
0.0001
Aperture (mm)
0.001
0.01
0.1
1
10
y = 0.0211e$^{-1.067x}$
R² = 0.6942
y = 0.0031x$^{-0.524}$
R² = 0.9065

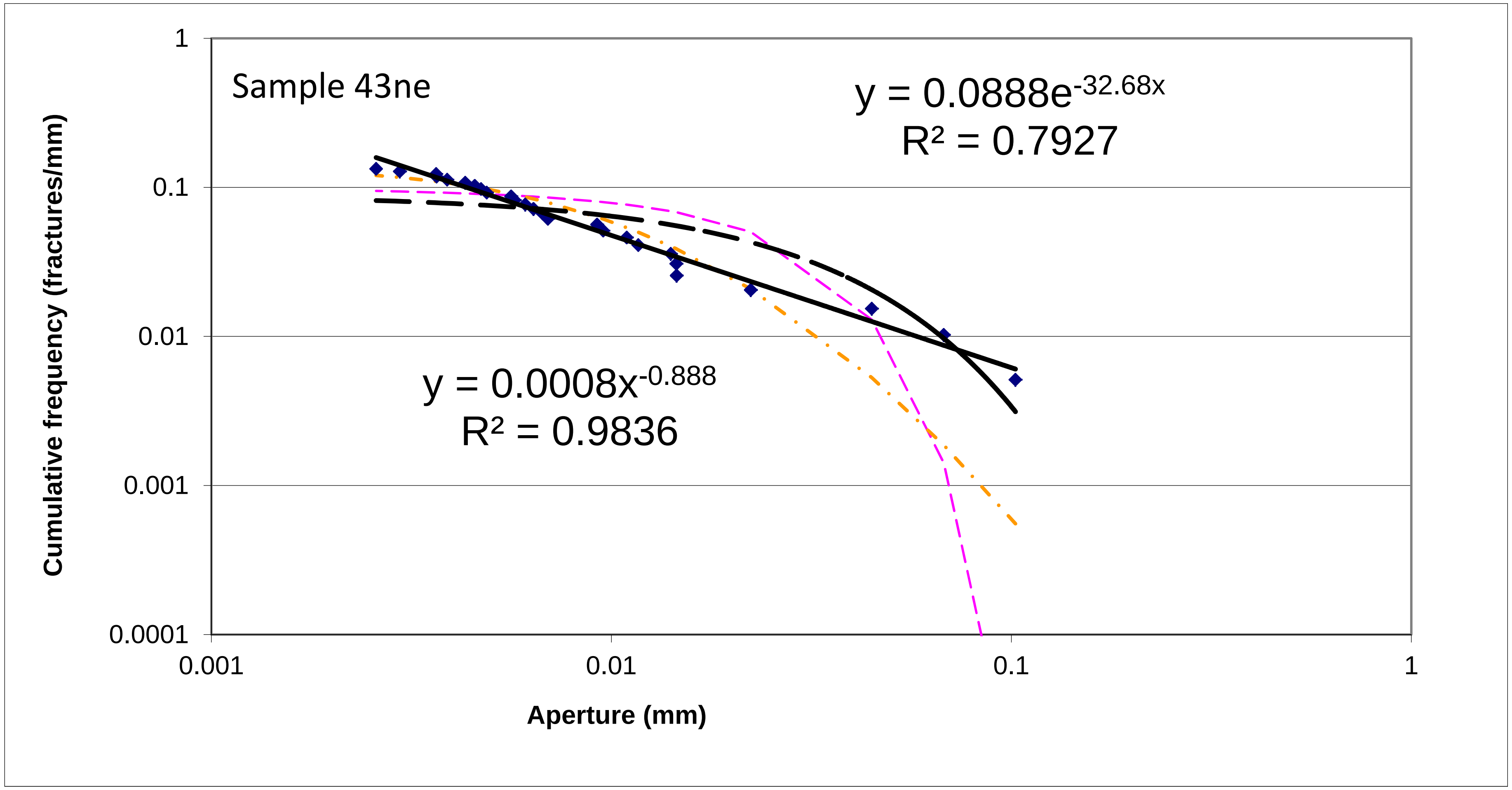Sample 43ne
y = 0.0888e^-32.68x
R² = 0.7927
y = 0.0008x^-0.888
R² = 0.9836
Cumulative frequency (fractures/mm)
1
0.1
0.01
0.001
0.0001
0.001
0.01
0.1
1
Aperture (mm)

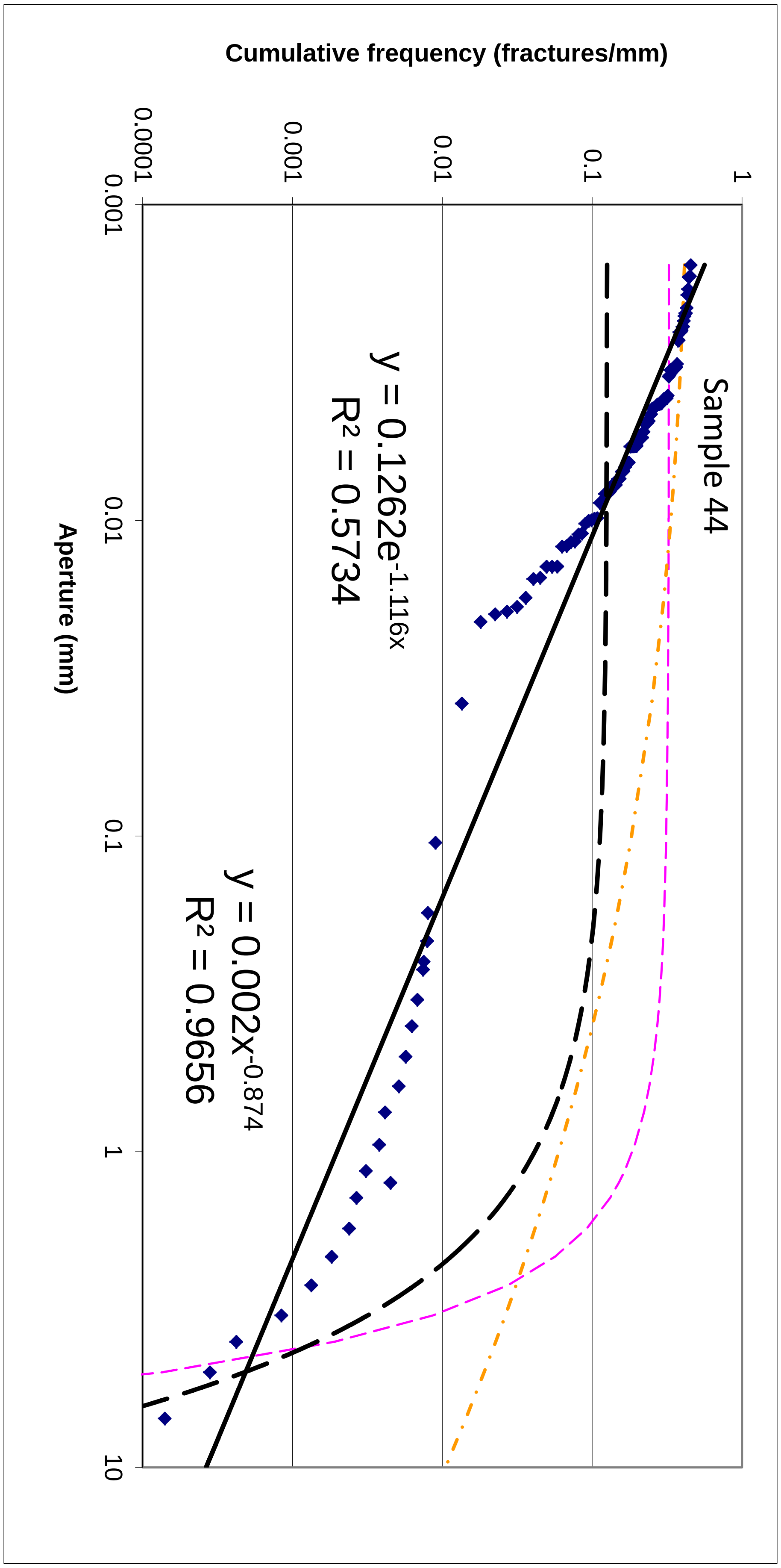
Sample 44
Cumulative frequency (fractures/mm)
1
0.1
0.01
0.001
0.0001
Aperture (mm)
0.001
0.01
0.1
1
10
y = 0.1262e^-1.116x
R² = 0.5734
y = 0.002x^-0.874
R² = 0.9656

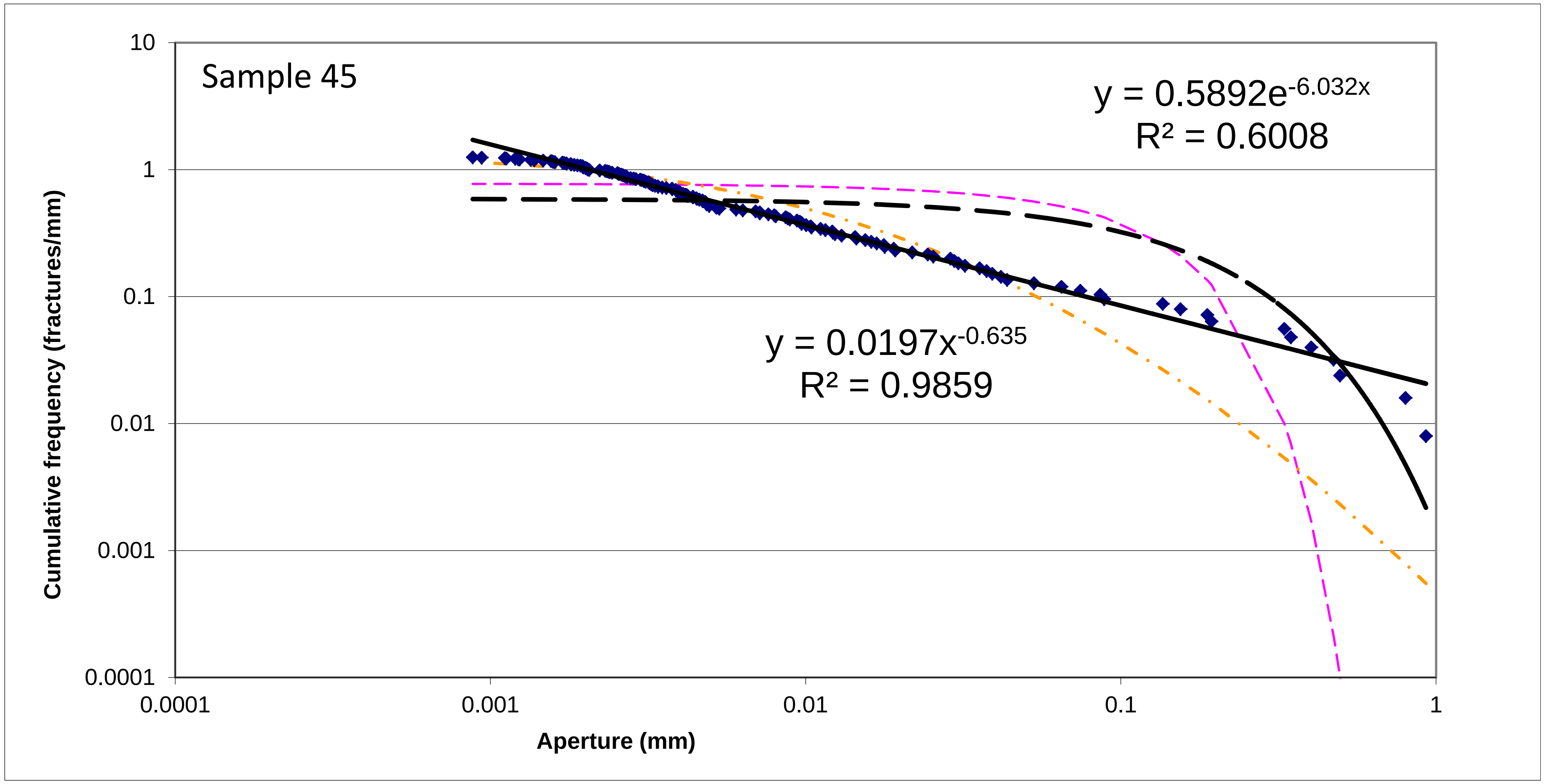
Sample 45
y = 0.5892e-6.032x
R² = 0.6008
y = 0.0197x-0.635
R² = 0.9859
Cumulative frequency (fractures/mm)
10
1
0.1
0.01
0.001
0.0001
0.0001
0.001
0.01
0.1
1
Aperture (mm)

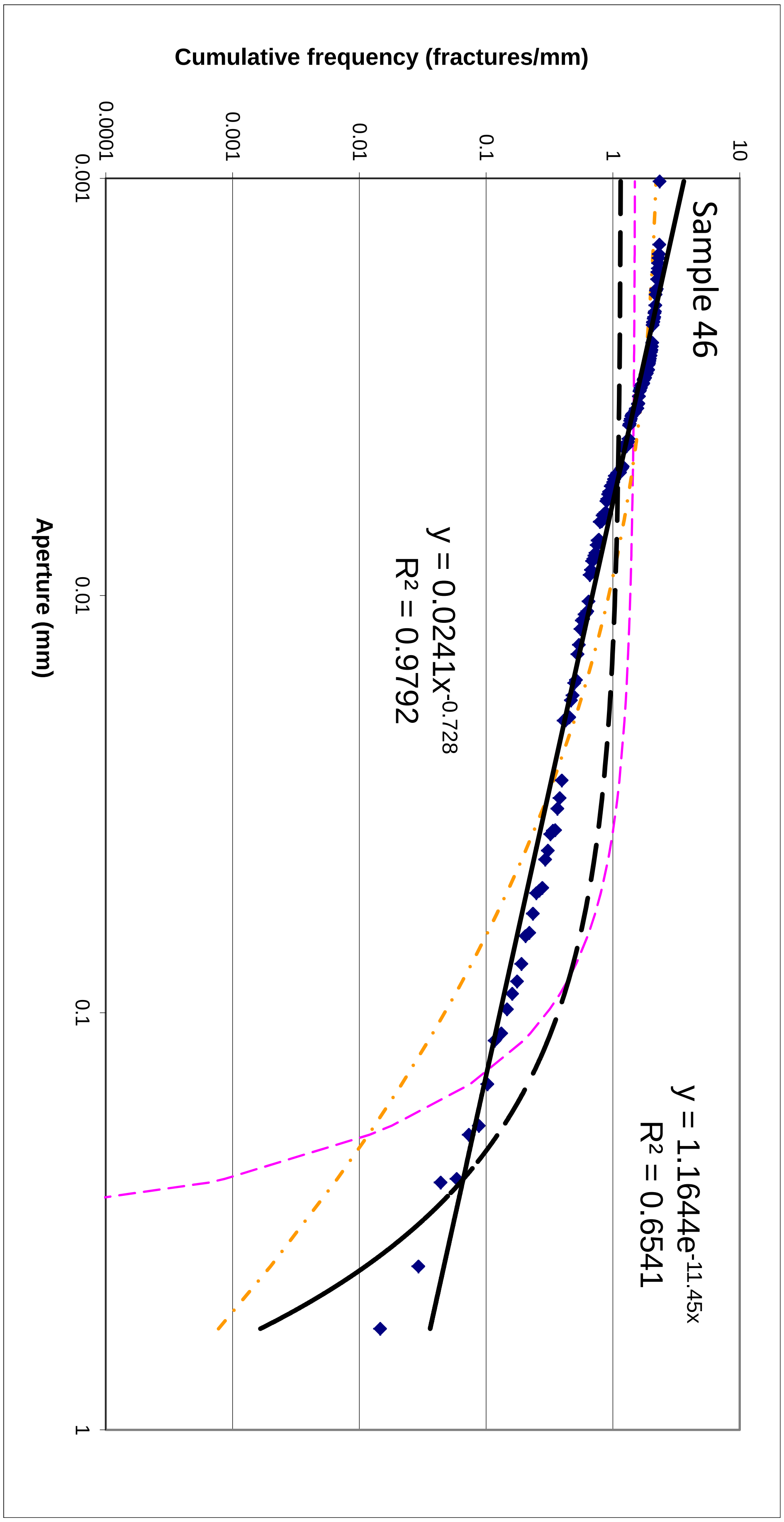
Sample 46
Cumulative frequency (fractures/mm)
10
1
0.1
0.01
0.001
0.0001
Aperture (mm)
0.001
0.01
0.1
1
y = 0.0241x^-0.728
R² = 0.9792
y = 1.1644e^-11.45x
R² = 0.6541

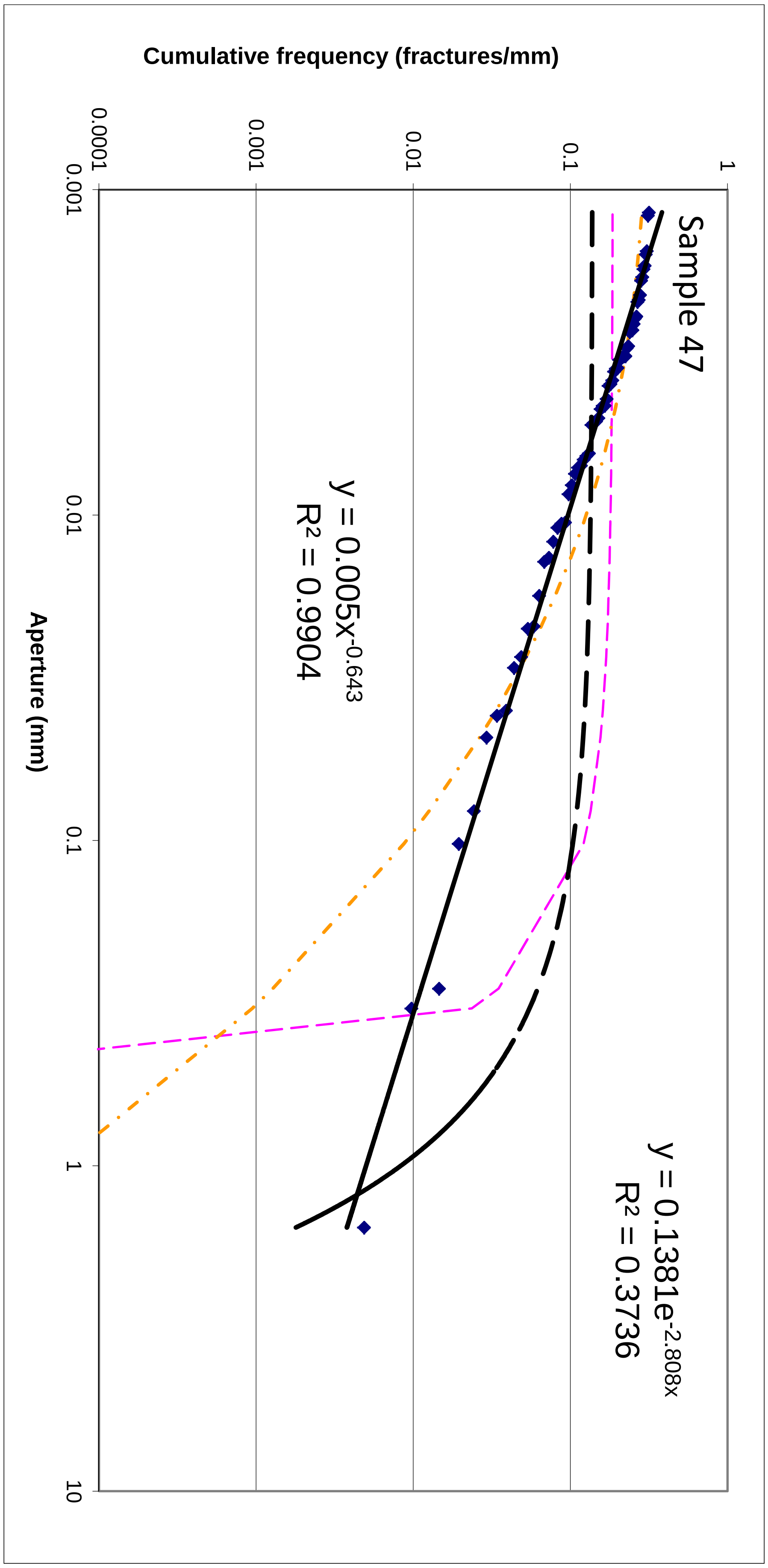
Sample 47
Cumulative frequency (fractures/mm)
1
0.1
0.01
0.001
0.0001
Aperture (mm)
0.001
0.01
0.1
1
10
$y = 0.005x^{-0.643}$
$R^2 = 0.9904$
$y = 0.1381e^{-2.808x}$
$R^2 = 0.3736$

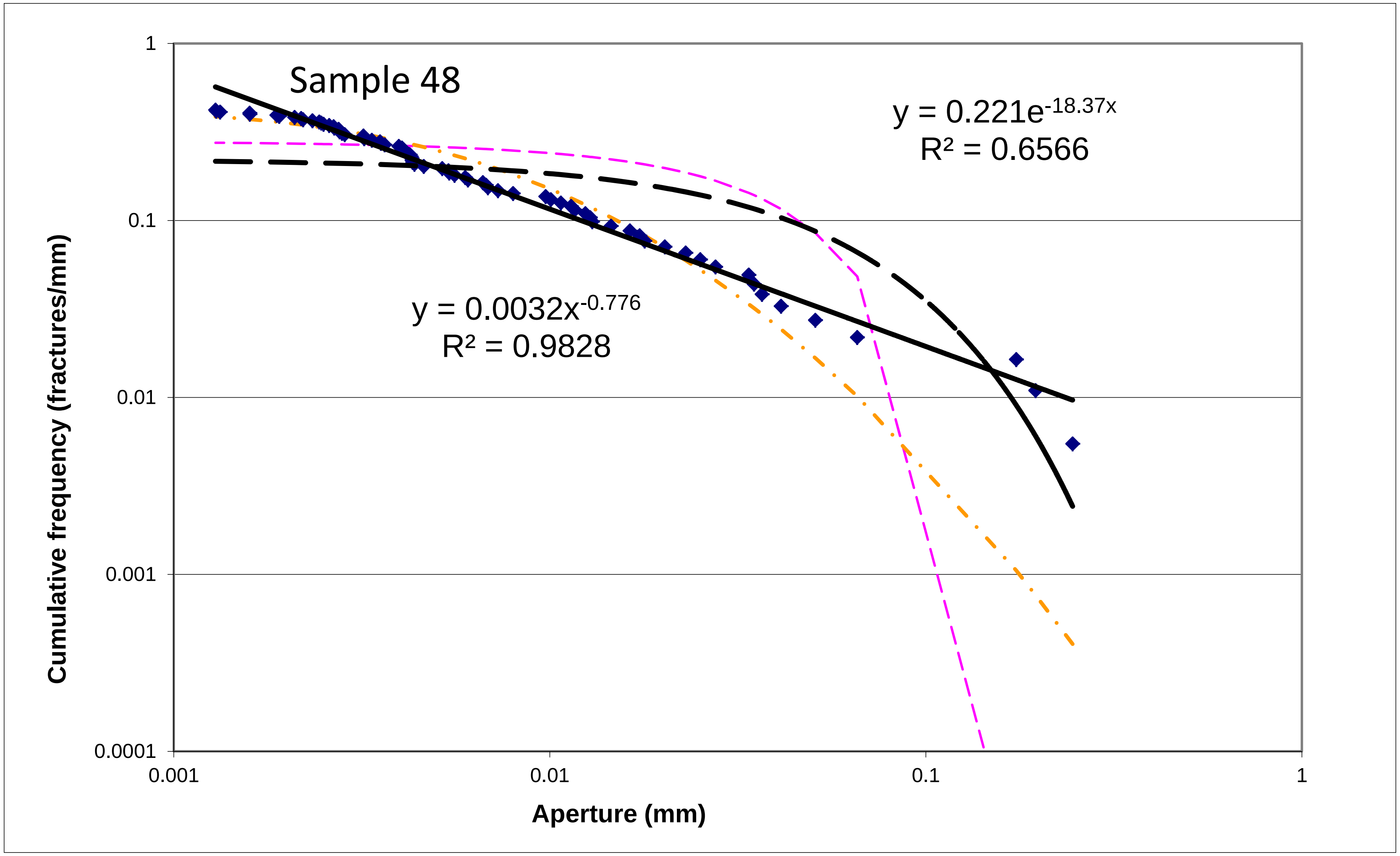
Sample 48
y = 0.221e$^{-18.37x}$
R² = 0.6566
y = 0.0032x$^{-0.776}$
R² = 0.9828
Cumulative frequency (fractures/mm)
1
0.1
0.01
0.001
0.0001
0.001
0.01
0.1
1
Aperture (mm)

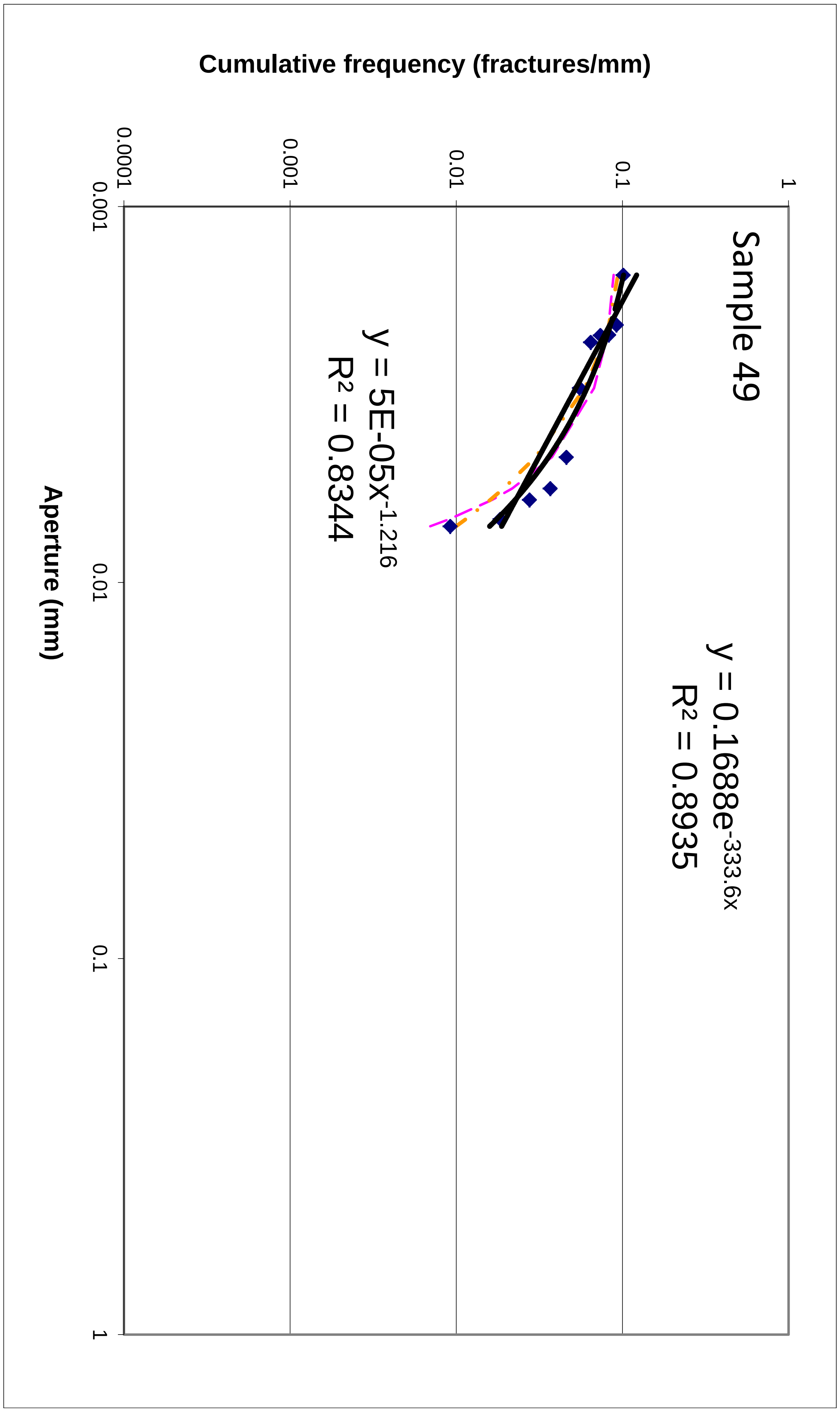
Sample 49
Cumulative frequency (fractures/mm)
1
0.1
0.01
0.001
0.0001
Aperture (mm)
0.001
0.01
0.1
1
y = 0.1688e^-333.6x
R² = 0.8935
y = 5E-05x^-1.216
R² = 0.8344

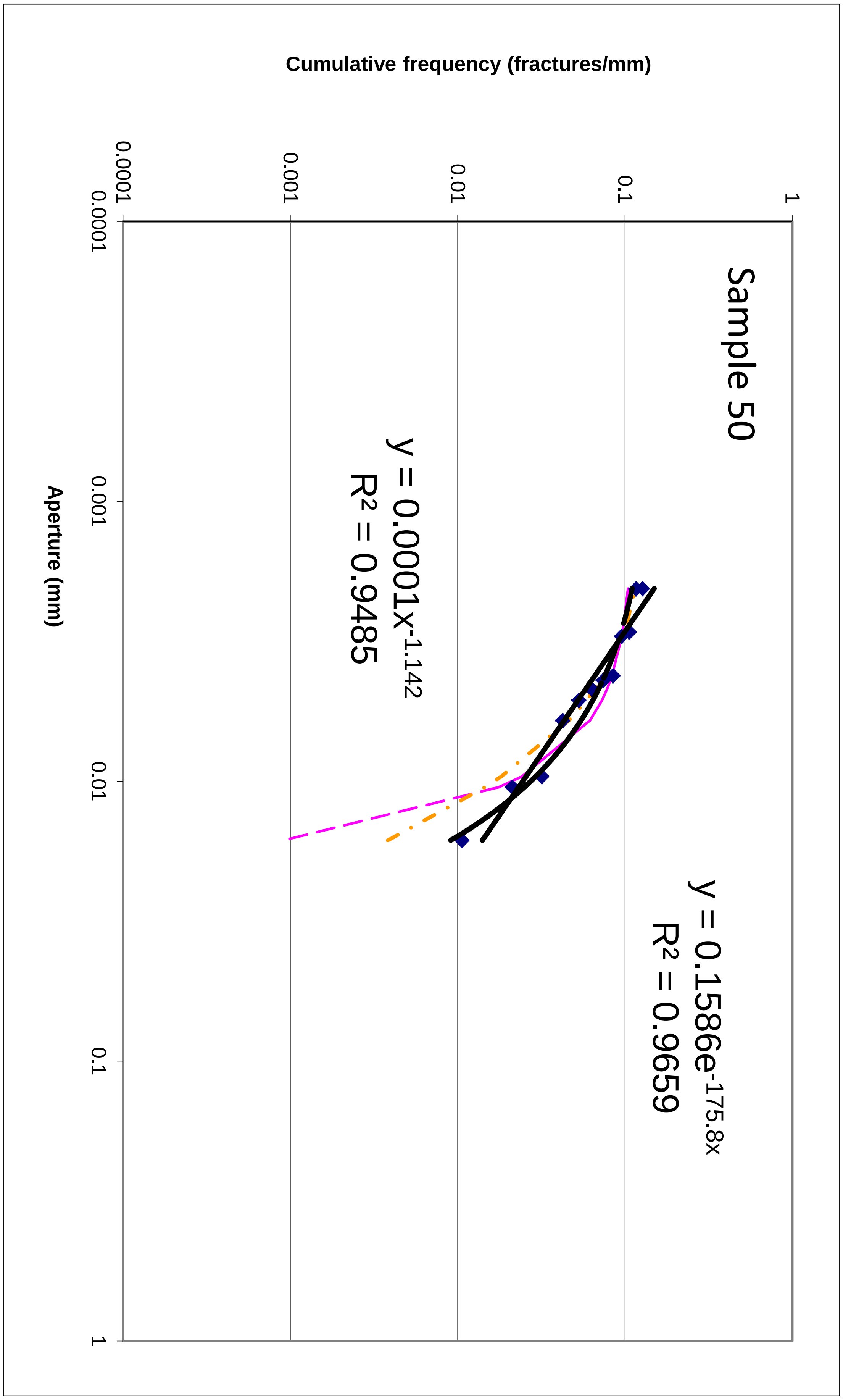
Sample 50
y = 0.1586e-175.8x
R² = 0.9659
y = 0.0001x-1.142
R² = 0.9485
Cumulative frequency (fractures/mm)
1
0.1
0.01
0.001
0.0001
Aperture (mm)
0.0001
0.001
0.01
0.1
1

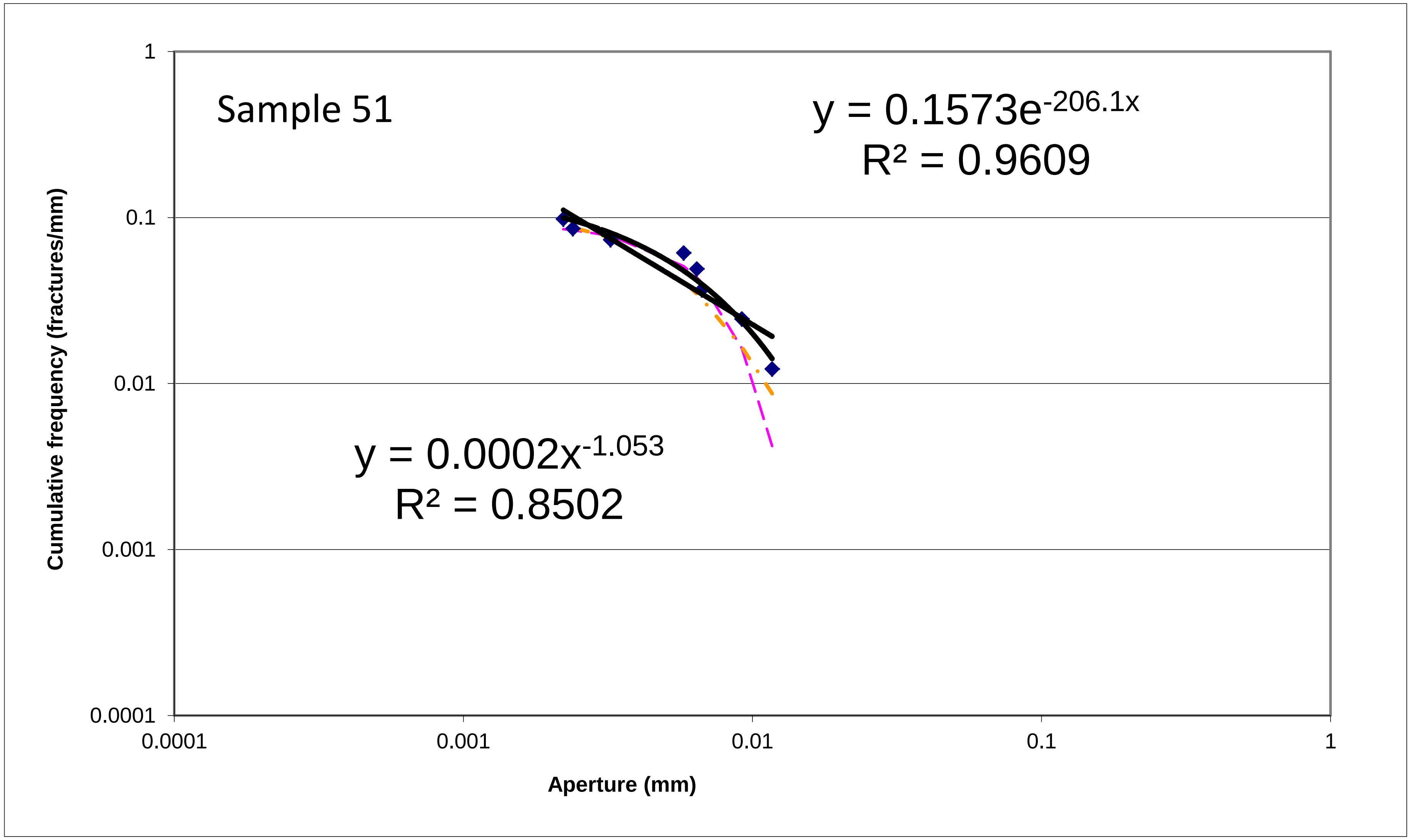
Sample 51
y = 0.1573e-206.1x
R² = 0.9609
y = 0.0002x-1.053
R² = 0.8502
Cumulative frequency (fractures/mm)
1
0.1
0.01
0.001
0.0001
0.0001
0.001
0.01
0.1
1
Aperture (mm)

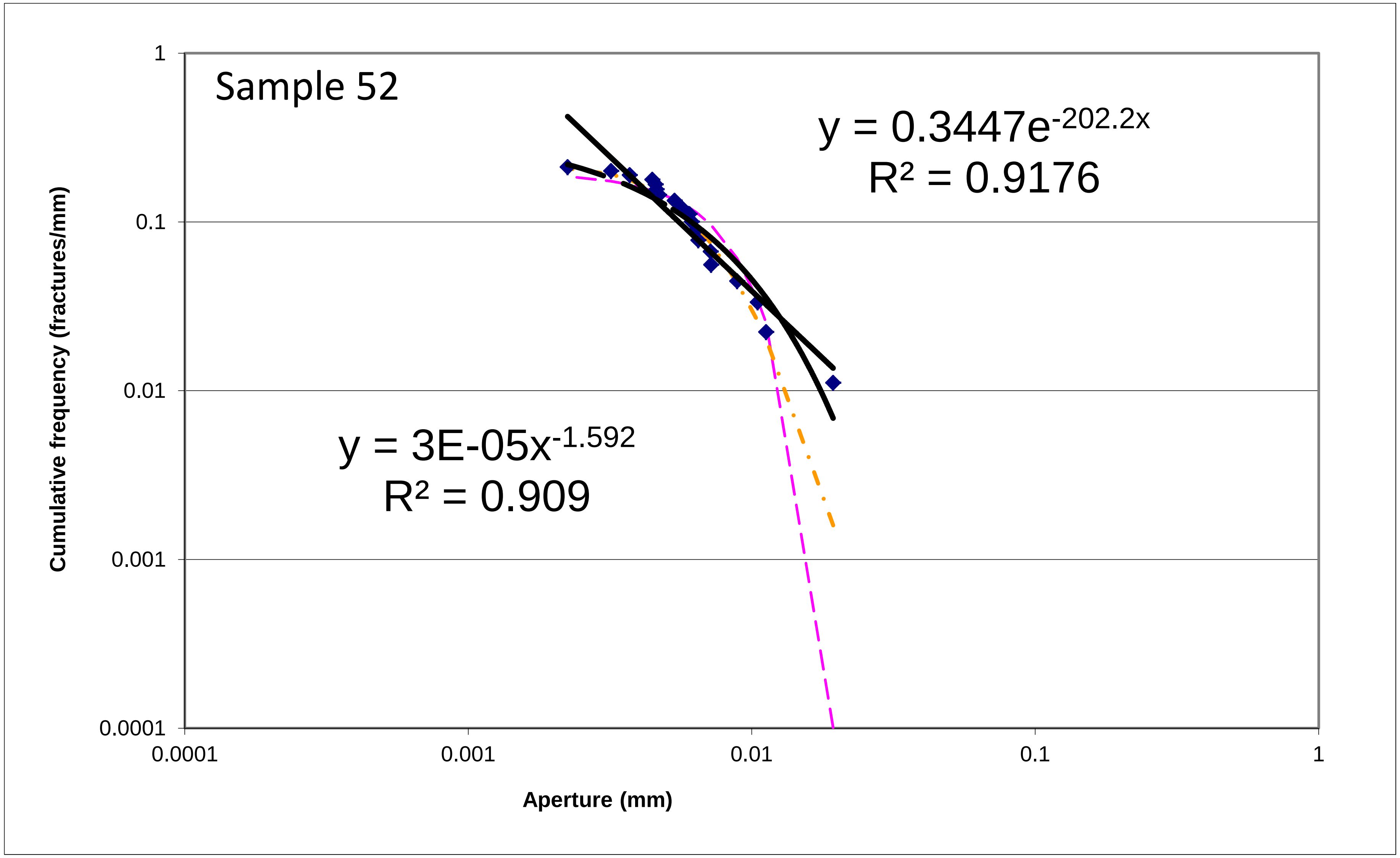
Sample 52
y = 0.3447e^-202.2x
R² = 0.9176
y = 3E-05x^-1.592
R² = 0.909
Cumulative frequency (fractures/mm)
1
0.1
0.01
0.001
0.0001
0.0001
0.001
0.01
0.1
1
Aperture (mm)

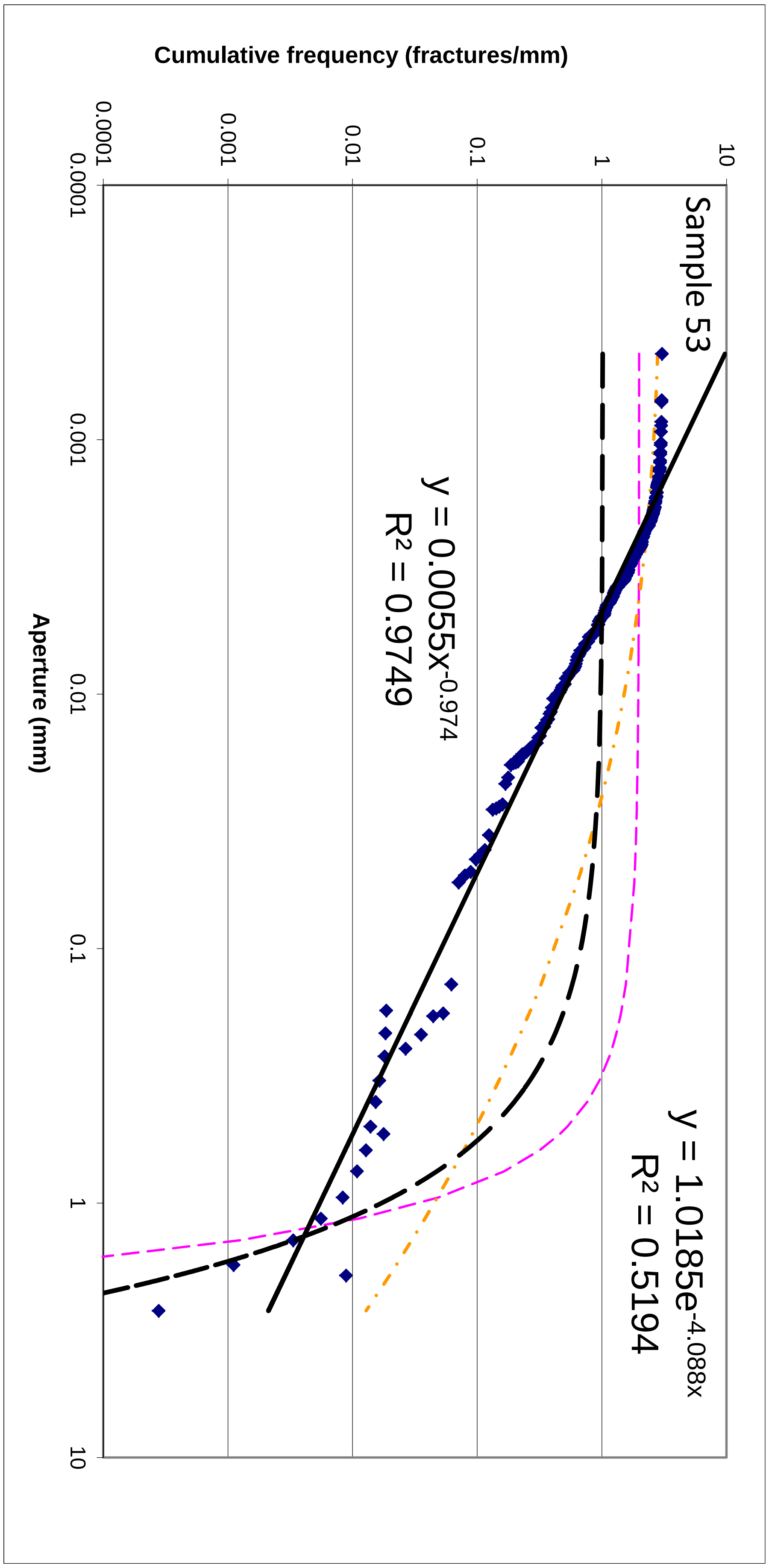
Sample 53
Cumulative frequency (fractures/mm)
Aperture (mm)
10
1
0.1
0.01
0.001
0.0001
0.0001
0.001
0.01
0.1
1
10
y = 0.0055x^-0.974
R² = 0.9749
y = 1.0185e^-4.088x
R² = 0.5194

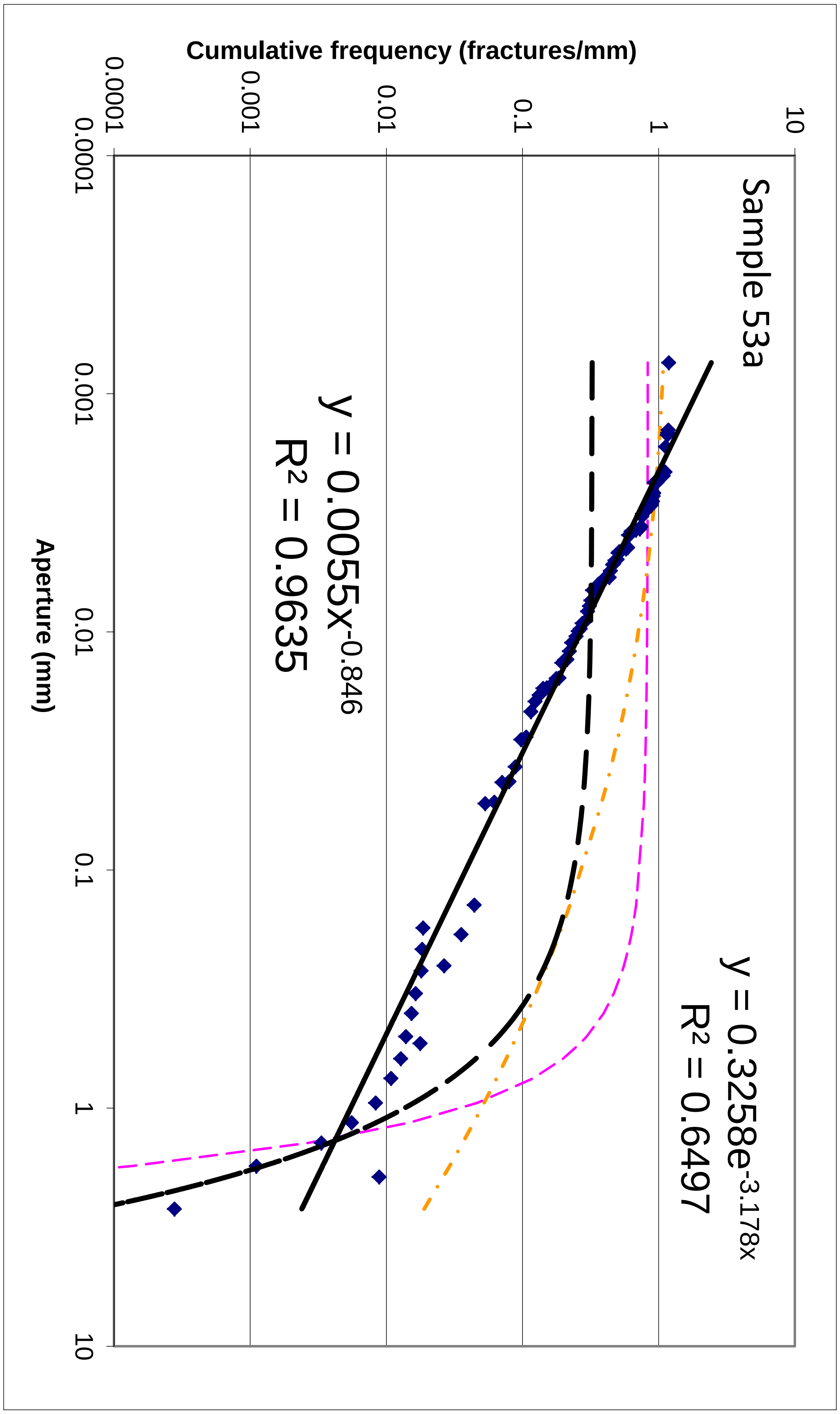
Sample 53a
Cumulative frequency (fractures/mm)
0.0001
0.001
0.01
0.1
1
10
Aperture (mm)
0.0001
0.001
0.01
0.1
1
10
$y = 0.0055x^{-0.846}$
$R^2 = 0.9635$
$y = 0.3258e^{-3.178x}$
$R^2 = 0.6497$

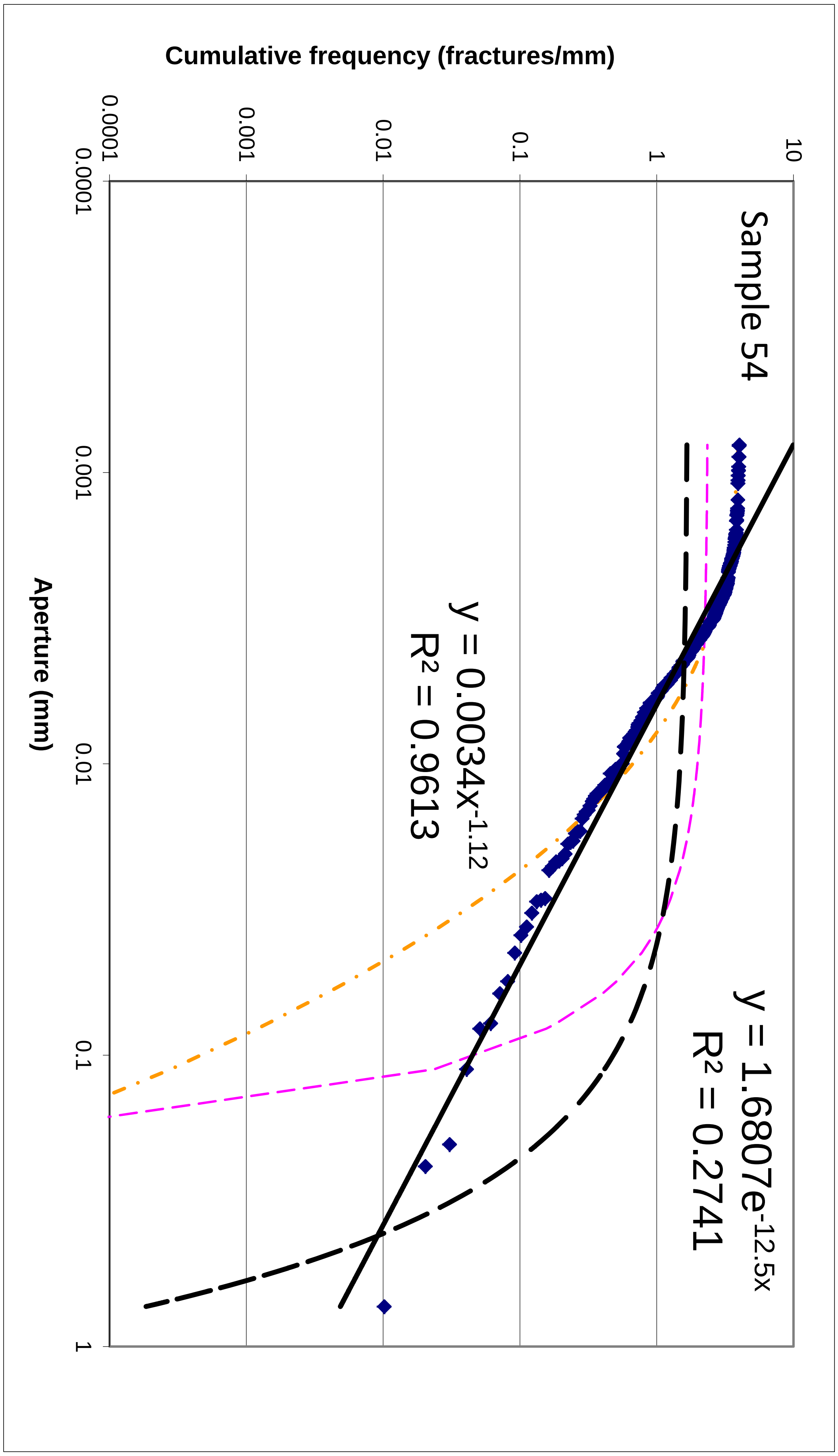
Sample 54
y = 1.6807e^-12.5x
R² = 0.2741
y = 0.0034x^-1.12
R² = 0.9613
Cumulative frequency (fractures/mm)
10
1
0.1
0.01
0.001
0.0001
Aperture (mm)
0.0001
0.001
0.01
0.1
1

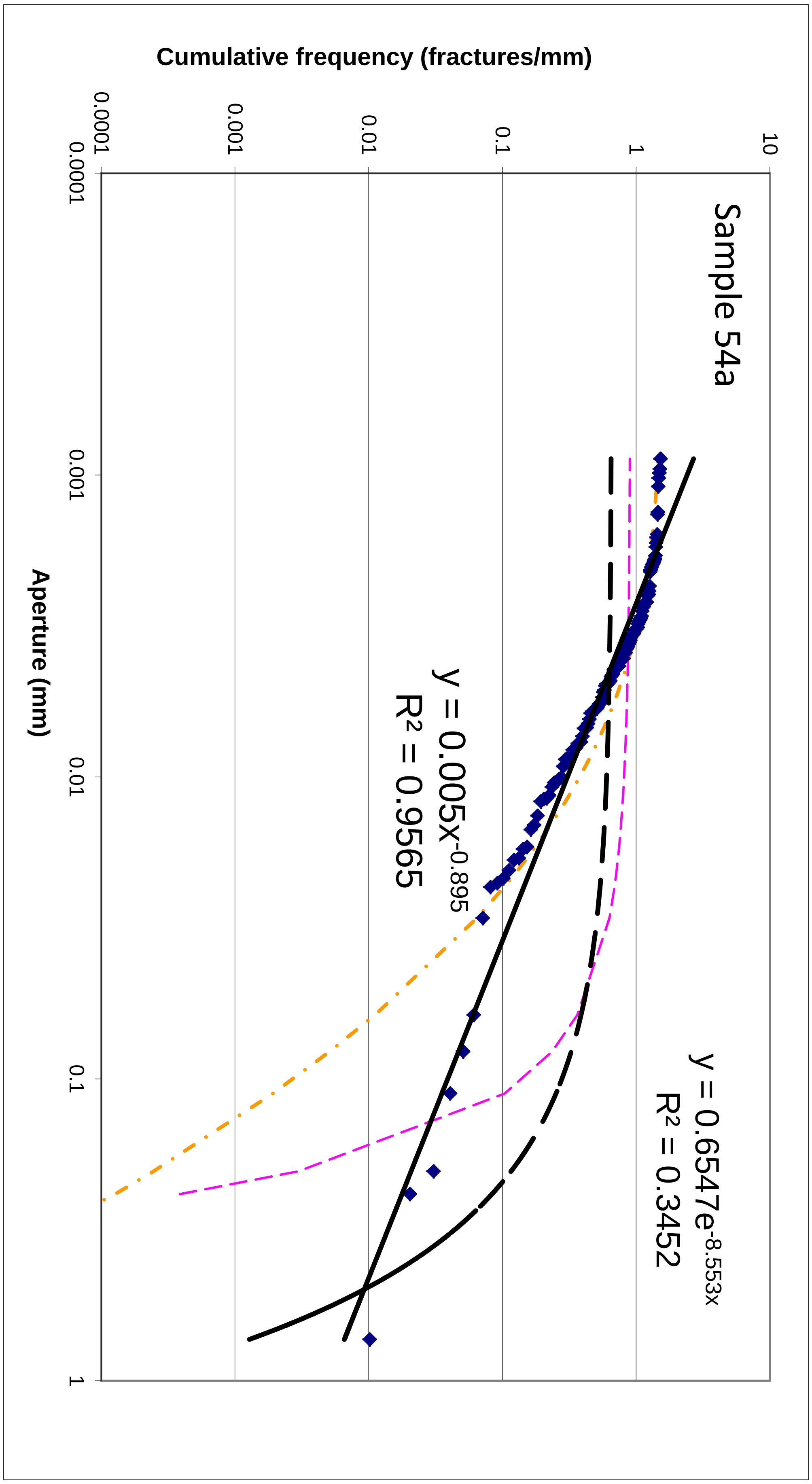
Sample 54a
Cumulative frequency (fractures/mm)
Aperture (mm)
0.0001
0.001
0.01
0.1
1
10
0.0001
0.001
0.01
0.1
1
$y = 0.005x^{-0.895}$
$R^2 = 0.9565$
$y = 0.6547e^{-8.553x}$
$R^2 = 0.3452$

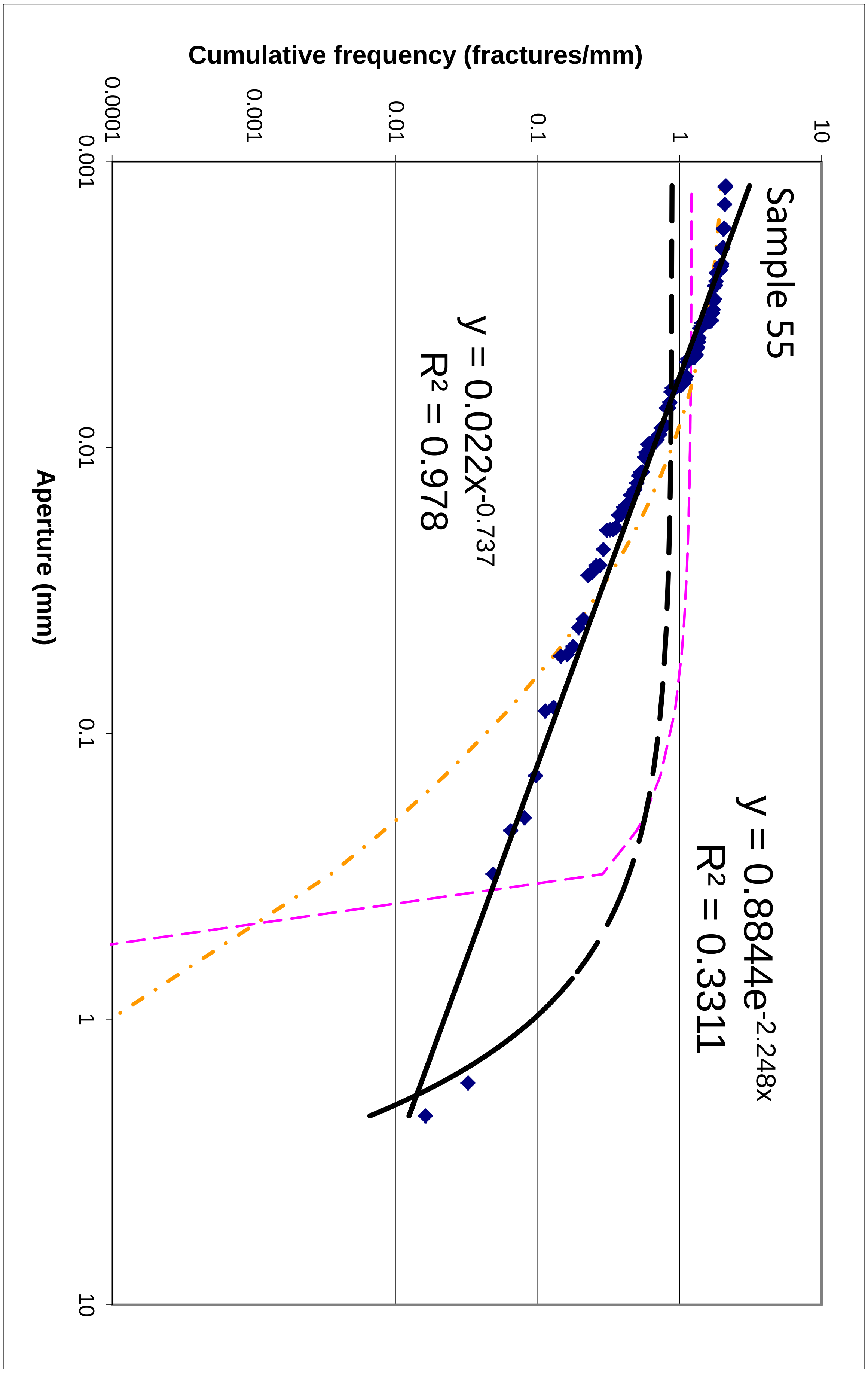

Sample 55
$y = 0.022x^{-0.737}$
$R^2 = 0.978$
$y = 0.8844e^{-2.248x}$
$R^2 = 0.3311$
Cumulative frequency (fractures/mm)
10
1
0.1
0.01
0.001
0.0001
Aperture (mm)
0.001
0.01
0.1
1
10

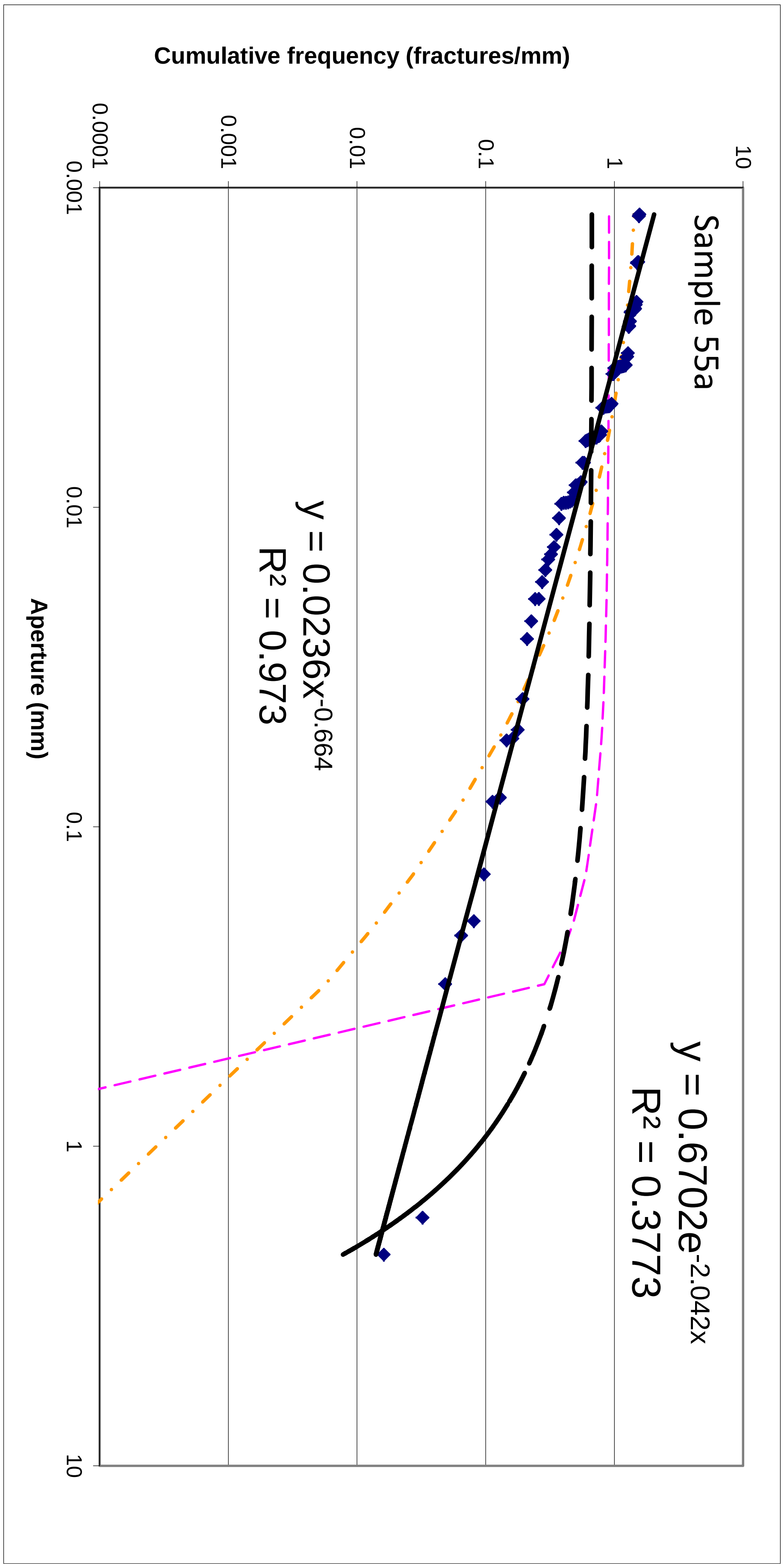
Sample 55a
Cumulative frequency (fractures/mm)
10
1
0.1
0.01
0.001
0.0001
Aperture (mm)
0.001
0.01
0.1
1
10
y = 0.0236x^-0.664
R² = 0.973
y = 0.6702e^-2.042x
R² = 0.3773

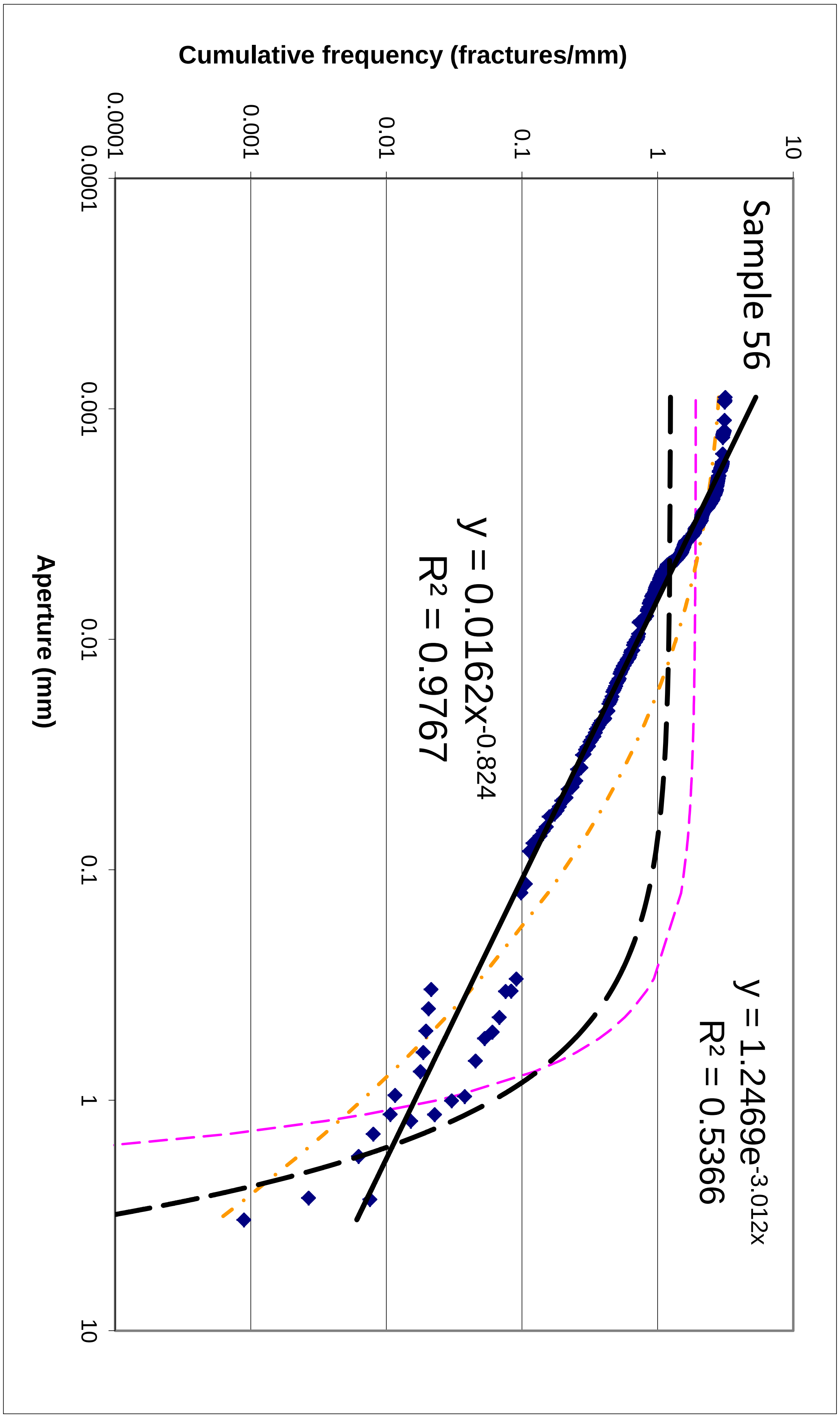
Sample 56
Cumulative frequency (fractures/mm)
10
1
0.1
0.01
0.001
0.0001
Aperture (mm)
0.0001
0.001
0.01
0.1
1
10
$y = 1.2469e^{-3.012x}$
$R^2 = 0.5366$
$y = 0.0162x^{-0.824}$
$R^2 = 0.9767$

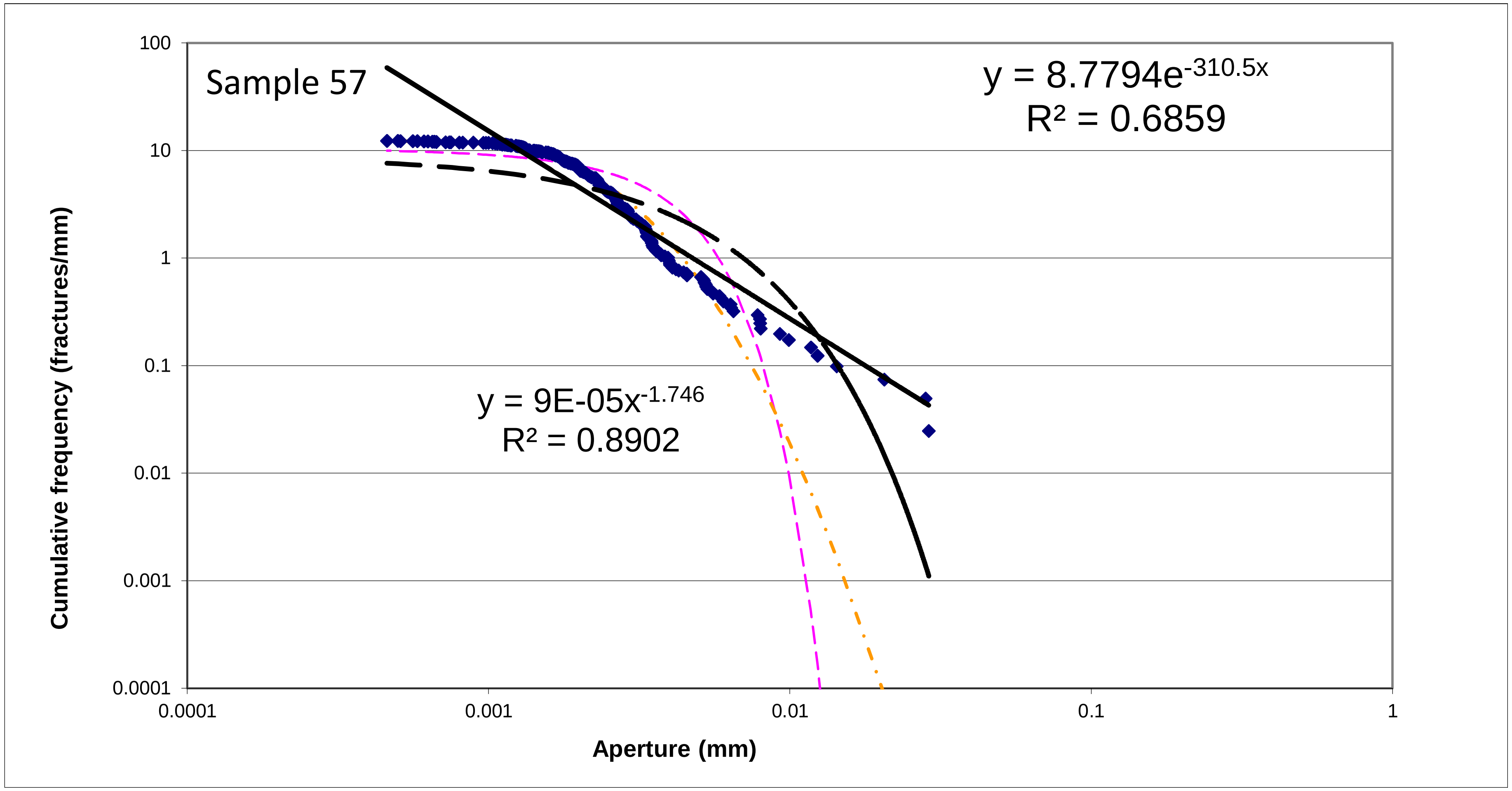
Sample 57
$y = 8.7794e^{-310.5x}$
$R^2 = 0.6859$
$y = 9E\text{-}05x^{-1.746}$
$R^2 = 0.8902$
Cumulative frequency (fractures/mm)
100
10
1
0.1
0.01
0.001
0.0001
0.0001
0.001
0.01
0.1
1
Aperture (mm)

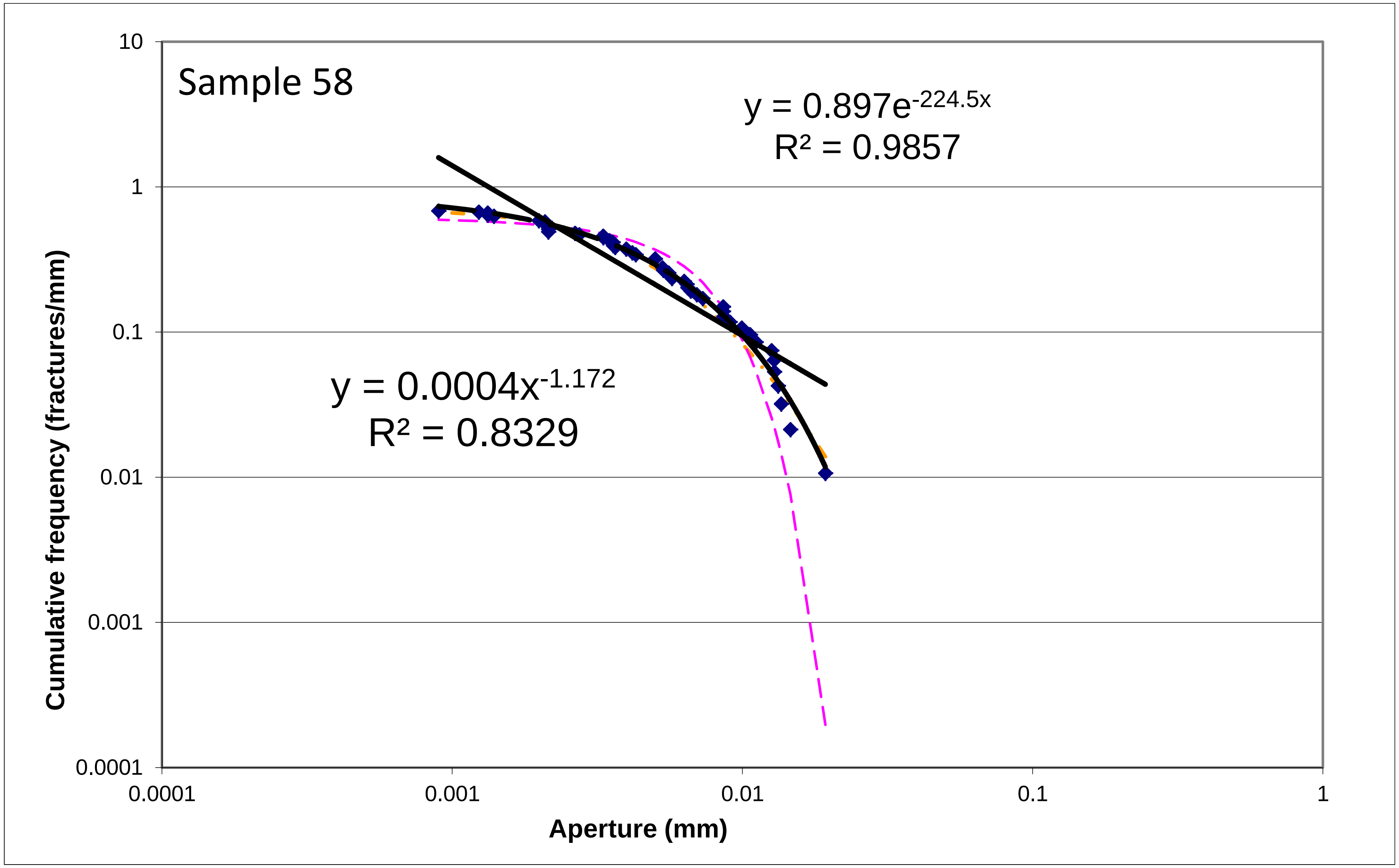
Sample 58
y = 0.897e^-224.5x
R² = 0.9857
y = 0.0004x^-1.172
R² = 0.8329
Cumulative frequency (fractures/mm)
10
1
0.1
0.01
0.001
0.0001
0.0001
0.001
0.01
0.1
1
Aperture (mm)

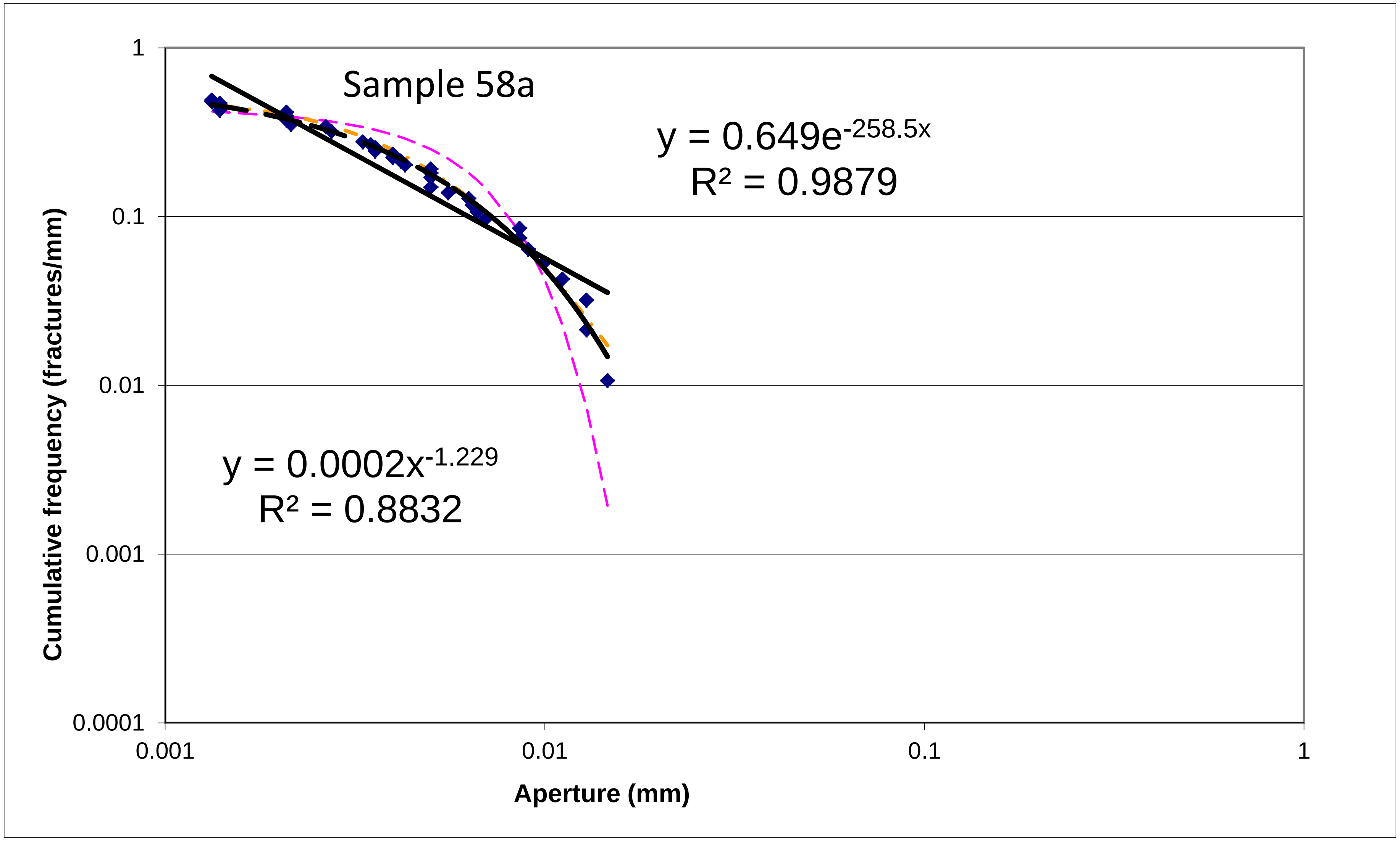
Sample 58a
y = 0.649e^-258.5x
R² = 0.9879
y = 0.0002x^-1.229
R² = 0.8832
Cumulative frequency (fractures/mm)
1
0.1
0.01
0.001
0.0001
0.001
0.01
0.1
1
Aperture (mm)

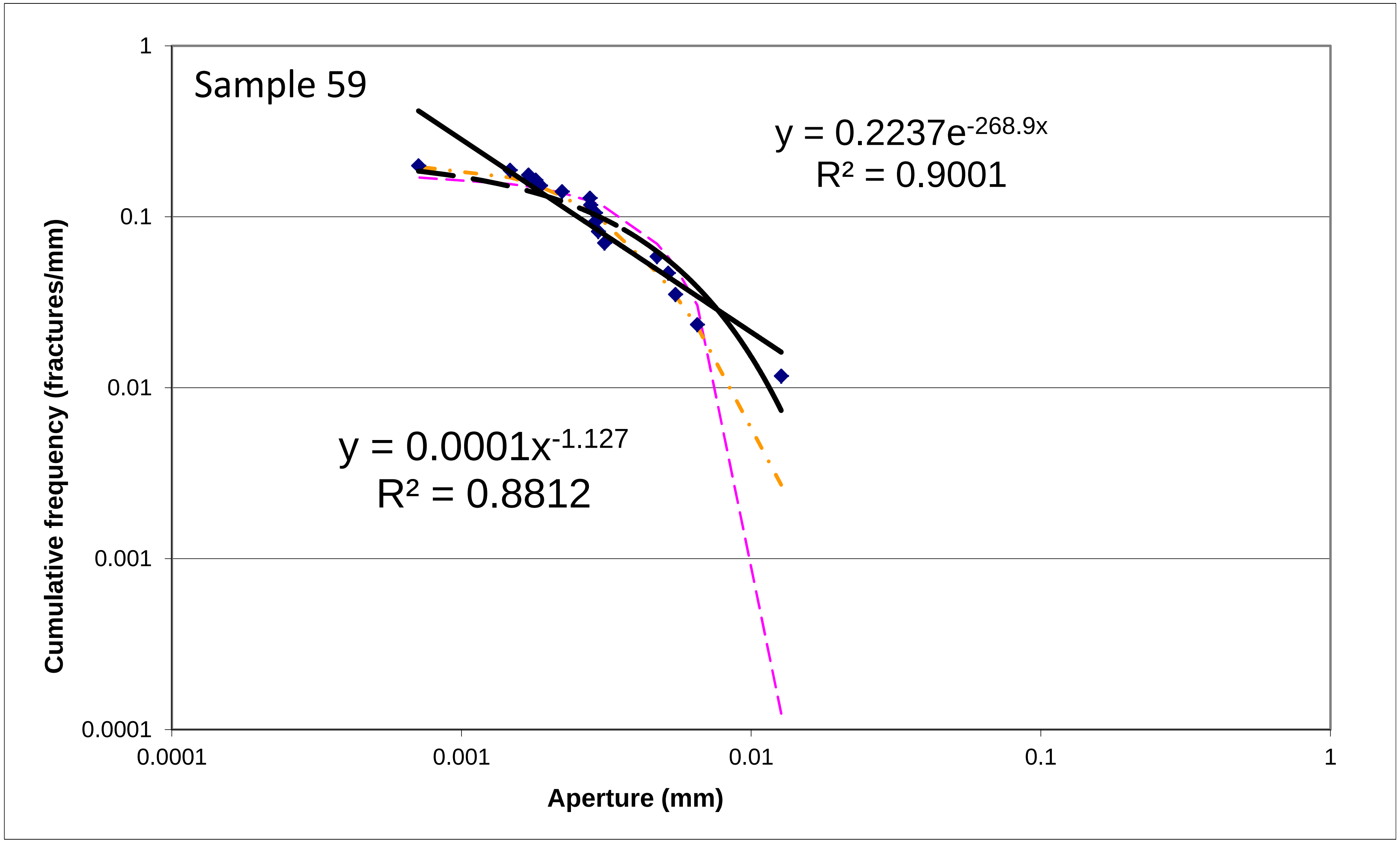
Sample 59
y = 0.2237e^-268.9x
R² = 0.9001
y = 0.0001x^-1.127
R² = 0.8812
Cumulative frequency (fractures/mm)
1
0.1
0.01
0.001
0.0001
0.0001
0.001
0.01
0.1
1
Aperture (mm)

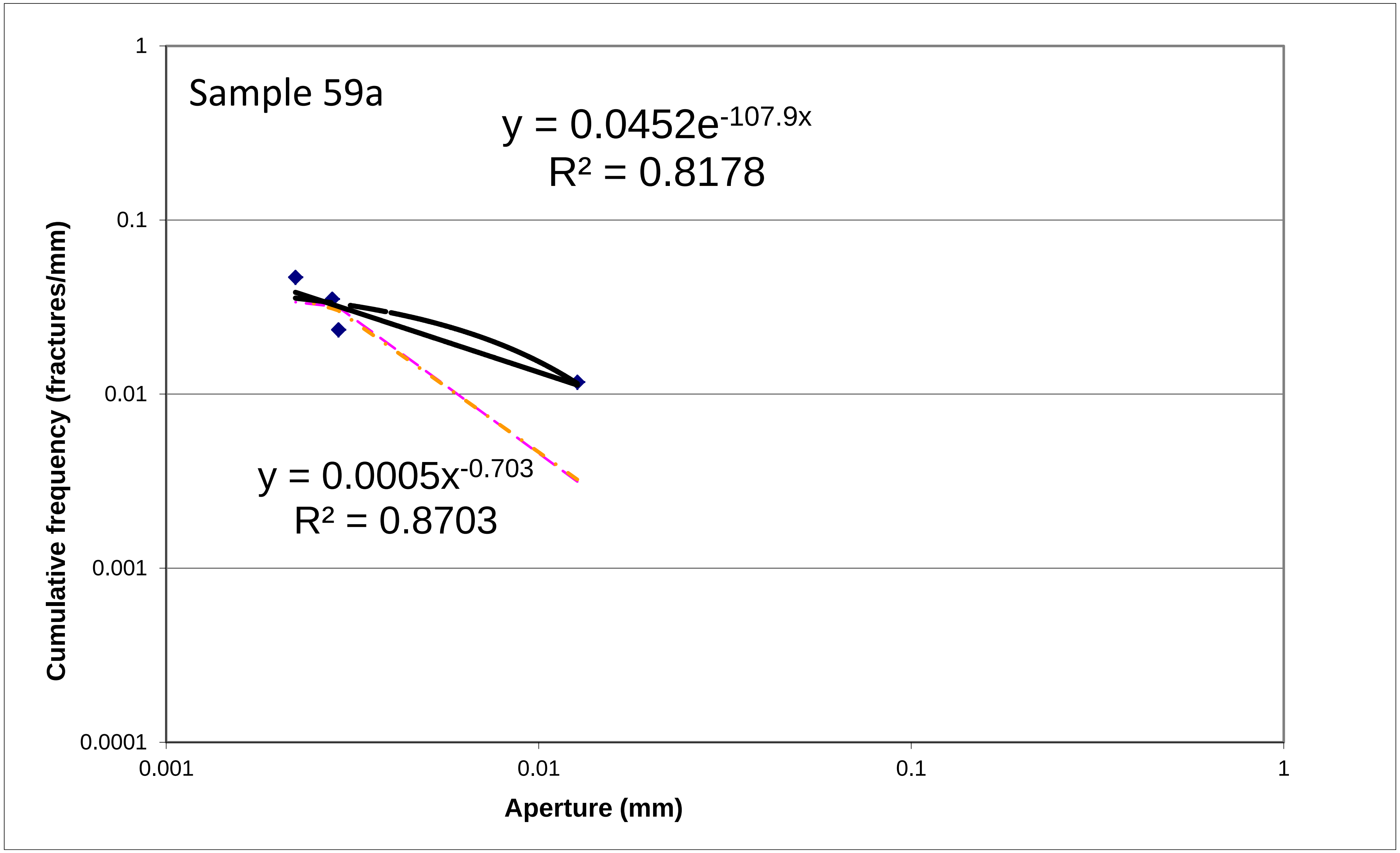
Sample 59a
y = 0.0452e^-107.9x
R² = 0.8178
y = 0.0005x^-0.703
R² = 0.8703
Cumulative frequency (fractures/mm)
1
0.1
0.01
0.001
0.0001
0.001
0.01
0.1
1
Aperture (mm)

Appendix C: Scanline data

SCANLINE DATA

The following pages include all data from scanlines (fractures and spacings).

Also included are the two measures of spatial heterogeneity for each fracture dataset discussed in Chapter 4. The coefficient of variation (Cv) is the standard deviation of fracture spacings divided by the mean fracture spacing. Random fracture arrangements will have a Cv near 1; regular spacing has Cv <1; clustered arrangements have a Cv >1.

The Kuiper test (Kuiper, 1960) result, V’, ranges from 0 to 1 and is calculated by comparing fracture cumulative aperture (third column) to a homogeneous strain line (fourth column). The homogeneous strain column is the total fracture strain times the fracture location and represents what the cumulative aperture would be if fracture strain were homogeneously distributed. The difference (fifth column) is a running total of the cumulative surplus or deficit in cumulative aperture, to that point in the scanline. V’ is the difference between the maximum surplus and maximum deficit in cumulative aperture, normalized to the total cumulative aperture. Therefore V’ = 0 represents homogeneous strain and V’ = 1 is maximum strain heterogeneity, which is possible if only one fracture is present.

Location (mm)	Aperture (mm)	Cum. Ap. (mm)	Hom. Strain	Difference	Spacing (mm)
Scotland		All Scotland samples azimuth-filtered according to hooker et al 2011			
Sample 1			V'		C
			0.408866074		1.530918437
xloc	ap	cumap	hom strain	difference	spacing
0		0	0	0	
3.385382436	0.004619566	0.004619566	0.064961217	0.060341651	7.439792087
10.82854021	0.002111806	0.006731372	0.207786023	0.201054651	0.667243417
11.49743324	0.001187433	0.007918805	0.220621237	0.212702431	4.458476191
15.95706006	0.001113813	0.009032619	0.306195848	0.29716323	2.045722257
18.00500888	0.003339314	0.012371933	0.345493402	0.333121469	0.002005767
18.01012991	0.00289122	0.015263153	0.345591668	0.330328515	0.2049741
18.21783098	0.002562707	0.01782586	0.34957719	0.33175133	0.587486258
18.80760248	0.002007778	0.019833638	0.360894161	0.341060523	0.338500247
19.14822174	0.002230249	0.022063887	0.367430214	0.345366328	0.652206795
19.80280408	0.002520848	0.024584735	0.379990824	0.355406089	0.009448949
19.8153421	0.003657298	0.028242033	0.380231412	0.35198938	0.663309657
20.4819214	0.002881973	0.031124006	0.393022228	0.361898222	0.474250372
20.95865389	0.002082269	0.033206276	0.402170123	0.368963848	0.287688275
21.25077445	0.006782303	0.039988579	0.407775548	0.367786969	0.168857987
21.42420055	0.002353924	0.042342503	0.411103376	0.368760873	0.08748044
21.51462415	0.003532385	0.045874888	0.412838491	0.366963603	0.176582941
21.69362324	0.001299924	0.047174812	0.416273258	0.369098445	1.059722928
22.75528858	0.002584883	0.049759695	0.436645276	0.38688558	0.249182147
23.01095337	0.010380408	0.060140103	0.441551161	0.381411057	1.418349022
24.43553264	0.002080084	0.062220188	0.468887039	0.406666851	0.654963586
25.30331989	0.423567251	0.485787438	0.485538782	-0.000248657	0.027343743
25.54361171	0.002328897	0.488116335	0.490149678	0.002033343	0.00924683
25.56783983	0.027633687	0.515750022	0.490614585	-0.025135437	2.663718759
28.2460976	0.001444343	0.517194365	0.542006973	0.024812608	0.459271692
28.71096477	0.009746596	0.526940961	0.550927187	0.023986226	0.169056828
28.88633984	0.002889899	0.52983086	0.554292414	0.024461553	0.188160846
29.0765168	0.001142324	0.530973184	0.557941669	0.026968485	1.879513676
30.95720575	0.001208234	0.532181419	0.594029717	0.061848299	0.528870672
31.48742194	0.001482791	0.533664209	0.604203897	0.070539688	0.060581617
31.5497957	0.002101507	0.535765716	0.605400771	0.069635054	0.013934263
31.56568335	0.001805255	0.537570971	0.605705635	0.068134663	0.134182355
31.70154066	0.00154467	0.539115641	0.608312565	0.069196924	2.847085493
34.55820015	0.017603318	0.556718958	0.663128256	0.106409298	0.047170496
34.64709478	0.065844953	0.622563912	0.664834032	0.04227012	0.554810996
35.23568837	0.001720236	0.624284148	0.6761284	0.051844252	3.263610846
38.50088171	0.001444755	0.625728903	0.738783341	0.113054437	0.162069632
38.66422881	0.001110171	0.626839074	0.741917765	0.115078691	0.001156822
38.66750772	0.003133999	0.629973073	0.741980683	0.11200761	0.010132105
38.68912437	0.019835104	0.649808177	0.74239548	0.092587303	0.00028951
38.70154185	0.004420832	0.654229008	0.742633756	0.088404747	0.086045344
38.79289107	0.006186913	0.660415921	0.744386632	0.083970711	0.895729574
39.77455886	0.165689527	0.826105448	0.763223598	-0.06288185	0.325034797
40.18473025	0.004583665	0.830689114	0.77109427	-0.059594844	0.443745778
40.6318691	0.002202478	0.832891592	0.7796743	-0.053217292	0.961481502
41.5951037	0.001303708	0.8341953	0.798157556	-0.036037743	0.485118118
42.08199972	0.002252105	0.836447405	0.807500477	-0.028946928	2.515627202
44.59988976	0.00227357	0.838720975	0.85581561	0.017094634	0.768283007
45.37063486	0.002650602	0.841371577	0.870605235	0.029233659	0.075898357
45.45674549	0.01777396	0.859145537	0.87225759	0.013112053	0.04209115
45.50886983	0.002292408	0.861437944	0.87325779	0.011819846	0.043748941
45.55475834	0.001986743	0.863424687	0.874138333	0.010713646	1.806283585
47.36259337	0.001116149	0.864540836	0.908828406	0.04428757	0.000561989

Location (mm)	Aperture (mm)	Cum. Ap. (mm)	Hom.Strain	Difference	Spacing (mm)
47.36426956	0.001112238	0.865653074	0.90886057	0.043207496	0.011254269
47.37718481	0.002209738	0.867862812	0.909108397	0.041245585	0.002308054
47.3827123	0.004229128	0.87209194	0.909214463	0.037122522	0.017159998
47.40268702	0.001400313	0.873492254	0.909597752	0.036105499	0.47344063
47.87766725	0.001678898	0.875171151	0.918712024	0.043540872	0.067785324
47.94727088	0.001957699	0.877128851	0.92004763	0.042918779	0.243915639
48.19279393	0.001257125	0.878385976	0.924758907	0.046372931	1.156300204
49.35467647	0.00990755	0.888293526	0.947053967	0.058760441	2.969260987
52.33015457	0.002526678	0.890820204	1.004149637	0.113329433	2.9719095
55.31035469	0.014054557	0.904874761	1.061335917	0.156461156	2.331757043
57.65305182	0.007825608	0.912700369	1.106289319	0.19358895	3.946242446
61.6054102	0.004406262	0.917106631	1.18213009	0.265023459	0.038247063
61.6466824	0.001644025	0.918750656	1.182922051	0.264171395	1.331581767
62.98002801	0.001883661	0.920634317	1.208507271	0.287872954	2.416424051
65.39780161	0.000815438	0.921449755	1.254901296	0.333451541	0.370084902
65.76892279	0.001257119	0.922706874	1.262022643	0.339315769	1.053737212
66.82512464	0.003672157	0.926379031	1.282289824	0.355910793	0.350030776
67.17914952	0.004316043	0.930695074	1.289083114	0.35838804	1.017806297
68.20013572	0.002043766	0.93273884	1.308674551	0.375935712	0.821199131
69.0226877	0.00066193	0.933400769	1.324458286	0.391057517	1.178667377
70.20249627	0.001620452	0.935021221	1.347097324	0.412076103	2.768925191
72.97284496	0.001226546	0.936247767	1.400256819	0.464009052	0.423245377
73.40007332	0.006739422	0.942987189	1.408454793	0.465467603	0.044564675
73.44960127	0.003187125	0.946174315	1.409405171	0.463230857	3.974395608
77.42716736	0.003153851	0.949328165	1.485729646	0.536401481	1.944090752
79.37349802	0.001325957	0.950654122	1.523077276	0.572423153	2.671901633
82.04667526	0.001225263	0.951879386	1.574372174	0.622492788	0.051664916
82.58724471	0.976583794	1.928463179	1.584745019	-0.34371816	0.411692011
83.48809528	0.001733329	1.930196508	1.602031205	-0.328165303	0.649176952
84.13862884	0.000979888	1.931176396	1.614514123	-0.316662273	2.763278004
86.90373146	0.002669355	1.933845751	1.667572954	-0.266272797	0.006131865
86.91276639	0.003136773	1.936982524	1.667746323	-0.269236201	0.31423477
87.22998573	0.002832359	1.939814883	1.673833362	-0.265981521	0.149457203
87.38172314	0.001728054	1.941542937	1.676745011	-0.264797926	0.004567
87.38839779	0.002487245	1.944030182	1.676873089	-0.267157092	0.018857808
87.4098311	0.002663768	1.946693949	1.677284367	-0.269409582	0.164161289
87.57795777	0.005266988	1.951960937	1.680510506	-0.271450431	0.690685233
88.30247344	0.062393893	2.014354831	1.694413048	-0.319941783	0.184120194
88.54141437	0.047247576	2.061602407	1.698998023	-0.362604384	0.19347396
88.75926241	0.001500592	2.063102999	1.703178252	-0.359924747	0.016172407
88.77781553	0.00326082	2.066363819	1.703534262	-0.362829556	0.006300892
88.78686265	0.002231652	2.068595471	1.703707865	-0.364887605	0.995287877
89.78517285	0.003812989	2.072408459	1.722864178	-0.349544281	0.652057458
90.44682807	0.015382531	2.087790991	1.735560507	-0.352230483	2.225638145
92.68172082	0.003126685	2.090917676	1.778445279	-0.312472396	0.545330649
93.23050719	0.003784756	2.094702432	1.788975797	-0.305726635	0.4186696
93.65233512	0.002531897	2.097234329	1.797070143	-0.300164186	0.272010238
93.92736197	0.003501321	2.10073565	1.802347561	-0.298388089	0.849713854
94.77929878	0.000944596	2.101680246	1.818695154	-0.282985093	0.478247369
95.26328678	0.010536659	2.112216905	1.827982272	-0.284234633	2.281695455
97.55356316	0.006625197	2.118842102	1.871929786	-0.246912316	0.173878593
97.73185372	0.002198744	2.121040846	1.875350957	-0.245689888	0.013669802
97.74932074	0.00539568	2.126436526	1.875686127	-0.250750399	3.456671973
101.2097273	0.002073537	2.128510062	1.942086963	-0.186423099	0.744800706
101.9612813	0.011432937	2.139942999	1.956508335	-0.183434664	0.196326621
102.1677333	0.008817892	2.148760891	1.960469889	-0.188291002	0.84199772

Location (mm)	Aperture (mm)	Cum. Ap. (mm)	Hom.Strain	Difference	Spacing (mm)
103.0179654	0.007650795	2.156411686	1.97678477	-0.179626916	0.615803275
103.6389892	0.002790351	2.159202037	1.988701434	-0.170500603	0.998300537
104.639534	0.001698154	2.160900191	2.007900626	-0.152999565	1.204298104
105.845826	0.002289585	2.163189775	2.031047847	-0.132141929	0.043325449
105.8914085	0.002224673	2.165414448	2.031922519	-0.133491929	2.401479947
108.2971538	0.006305894	2.171720342	2.078085734	-0.093634608	0.027558008
108.3289736	0.002217736	2.173938078	2.078696317	-0.095241762	0.554904004
108.8855248	0.001076662	2.17501474	2.089375832	-0.085638908	0.00226081
108.8914683	0.006288678	2.181303418	2.08948988	-0.091813538	0.004520354
108.8996703	0.001074747	2.182378165	2.089647267	-0.092730898	0.000376168
108.9013374	0.001507068	2.183885233	2.089679256	-0.094205977	0.732387472
109.6374918	0.006026641	2.189911874	2.103805129	-0.086106745	0.026378019
109.6683891	0.003012112	2.192923986	2.104398011	-0.088525975	0.006414842
109.6780026	0.003385052	2.196309038	2.10458248	-0.091726557	0.010924082
109.71174	0.042241553	2.238550591	2.105229858	-0.133320732	0.092934226
109.827112	0.002634018	2.241184608	2.107443702	-0.133740907	0.009040707
109.8414207	0.007902111	2.24908672	2.107718269	-0.141368451	0.169917562
110.0164099	0.002241077	2.251327796	2.11107609	-0.140251706	0.522822832
110.541829	0.002951387	2.254279184	2.121158219	-0.133120965	0.005213721
110.5494472	0.001857615	2.256136799	2.121304403	-0.134832396	0.140140134
110.6918806	0.002728932	2.258865731	2.12403752	-0.13482821	0.775175822
111.4693595	0.001877314	2.260743045	2.13895636	-0.121786684	0.049700402
111.5218819	0.003766545	2.264509589	2.139964198	-0.124545392	1.645233651
113.1708085	0.003619332	2.268128922	2.171605018	-0.096523903	0.236982223
113.4122018	0.005202925	2.273331846	2.176237052	-0.097094794	0.056136481
113.4718985	0.001917465	2.275249311	2.177382556	-0.097866755	2.413696494
115.8873015	0.001495535	2.276744846	2.223731092	-0.053013755	6.505523971
122.3941811	0.001215709	2.277960555	2.348589901	0.070629346	0.031735838
122.4277555	0.002461562	2.280422117	2.349234153	0.068812036	0.005852775
122.4360666	0.00245493	2.282877047	2.349393631	0.066516584	0.003389315
122.4412885	0.001210276	2.284087323	2.349493833	0.06540651	0.002464726
122.4457401	0.002763413	2.286850736	2.349579253	0.062728517	0.063165252
122.5132212	0.005868321	2.292719057	2.35087413	0.058155073	0.676335816
123.1937224	0.002462593	2.29518165	2.363932091	0.068750441	0.001847911
123.2041453	0.014687383	2.309869033	2.364132093	0.05426306	0.590945793
123.8051623	0.005455015	2.315324048	2.375664851	0.060340803	0.031428123
123.843781	0.008926023	2.324250071	2.376405894	0.052155823	0.046732964
123.8958775	0.001801102	2.326051173	2.377405561	0.051354388	0.001232363
123.9000557	0.004090543	2.330141716	2.377485735	0.047344019	0.000615548
123.9058482	0.006263458	2.336405174	2.377596886	0.041191713	0.004417834
123.9412002	0.055604865	2.392010039	2.378275247	-0.013734792	0.010528838
123.9886995	0.018335951	2.41034599	2.379186697	-0.031159293	0.896640393
124.8952653	0.001514896	2.411860886	2.396582551	-0.015278335	0.537372852
125.4338577	0.000924112	2.412784999	2.406917459	-0.005867539	0.039133704
125.4745228	0.002138756	2.414923755	2.407697772	-0.007225983	0.375504774
125.8510969		2.414923755	2.414923755	0	

Location (mm)	Aperture (mm)	Cum. Ap. (mm)	Hom.Strain	Difference	Spacing (mm)
Sample 1 macrofractures			V'		C
			0.23965425		1.175119663
xloc	ap	cumap	hom strain	difference	spacing
0	0.62	0.62	0	-0.62	
59.31	1.15	1.77	1.033379793	-0.736620207	1.75
61.885	0.5	2.27	1.078244958	-1.191755042	22.69
85.135	0.62	2.89	1.4833382	-1.4066618	52.8
138.445	0.4	3.29	2.412177802	-0.877822198	113.69
252.645	0.62	3.91	4.401926113	0.491926113	179.625
432.955	0.75	4.66	7.5435331	2.8835331	39.75
473.33	0.5	5.16	8.247001472	3.087001472	129.625
603.58	0.75	5.91	10.5163948	4.606394795	8.3
612.955	1.4	7.31	10.67973884	3.369738844	41.75
655.655	0.5	7.81	11.42371654	3.61371654	1.835
657.905	0.33	8.14	11.46291911	3.322919112	39.525
698.07	0.95	9.09	12.16272858	3.072728577	5.9425
704.545	0.115	9.205	12.27554487	3.070544867	59.93
764.6025	0.14	9.345	13.32194863	3.976948626	1.9125
766.6725	0.175	9.52	13.35801499	3.838014992	2.69
769.76	0.62	10.14	13.41180963	3.271809632	1.69
772.07	0.62	10.76	13.45205761	2.692057606	53.69
826.38	0.62	11.38	14.39832057	3.018320572	45.8
872.69	0.4	11.78	15.20519662	3.425196617	115.835
988.89	0.33	12.11	17.22979166	5.119791658	101.75
1091.055	0.5	12.61	19.00984977	6.399849769	29.8
1121.305	0.4	13.01	19.53690657	6.526906567	15.8
1137.505	0.4	13.41	19.81916508	6.409165084	13.8675
1151.705	0.265	13.675	20.06657687	6.391576871	33.5
1187.8375	5	18.675	20.69612662	2.021126616	49.75
1240.3375	0.5	19.175	21.61085329	2.435853291	59.75
1300.5875	0.5	19.675	22.66061105	2.985611047	17.625
1318.8375	0.75	20.425	22.97858746	2.553587463	19.8
1339.2125	0.4	20.825	23.33358853	2.50858853	5.625
1345.4125	0.75	21.575	23.44161339	1.866613394	3.8
1349.7875	0.4	21.975	23.51784062	1.542840617	41.75
1391.9875	0.5	22.475	24.25310663	1.778106631	87.835
1480.2375	0.33	22.805	25.79071861	2.985718614	3.8925
1484.4025	0.215	23.02	25.86328693	2.84328693	23.75
1508.51	0.5	23.52	26.28332071	2.763320708	19.525
1528.76	0.95	24.47	26.63614385	2.166143854	9.835
1539.235	0.33	24.8	26.8186536	2.018653605	3.69
1543.4	0.62	25.42	26.89122192	1.471221921	99.75
1643.71	0.5	25.92	28.63895969	2.718959689	2.9125
1646.96	0.175	26.095	28.69558563	2.600585626	25.69
1673.0475	0.62	26.715	29.15011767	2.435117667	19.75
1693.3575	0.5	27.215	29.50398621	2.288986215	3.69
1697.6075	0.62	27.835	29.57803552	1.743035517	37.8
1735.9175	0.4	28.235	30.24552464	2.01052464	17.525
1754.1175	0.95	29.185	30.56262989	1.377629887	7.69
1762.5925	0.62	29.805	30.71029291	0.905292908	19.8
1782.9025	0.4	30.205	31.06416146	0.859161456	17.125
1801.1025	1.75	31.955	31.3812667	-0.573733297	7.525
1809.9775	0.95	32.905	31.53589907	-1.36910093	6.75
1817.4525	0.5	33.405	31.66613873	-1.738861275	19.69
1837.7025	0.62	34.025	32.01896187	-2.006038129	9.625
1848.0125	0.75	34.775	32.19859677	-2.576403233	11.625

Location (mm)	Aperture (mm)	Cum. Ap. (mm)	Hom. Strain	Difference	Spacing (mm)
1860.3875	0.75	35.525	32.41421091	-3.110789088	211.625
2072.7625	0.75	36.275	36.11449811	-0.160501894	55.69
2129.1375	0.62	36.895	37.09674032	0.201740322	51.69
2181.4475	0.62	37.515	38.00815656	0.493156558	4.525
2186.7575	0.95	38.465	38.10067463	-0.364325373	39.625
2227.2325	0.75	39.215	38.80588534	-0.409114664	31.75
2259.6075	0.5	39.715	39.36996679	-0.345033214	45.75
2305.8575	0.5	40.215	40.17579743	-0.039202572	2
2308.1075		40.215	40.215	0	

Location (mm)	Aperture (mm)	Cum. Ap. (mm)	Hom.Strain	Difference	Spacing (mm)
Sample 2			V'		C
			0.475199231		1.804424346
xloc	ap	cumap	hom strain	difference	spacing
0		0	0	0	
0.0847	0.045560078	0.045560078	0.000773711	-0.044786367	0.018132523
0.13051367	0.009802217	0.055362294	0.001192206	-0.054170089	0.177758177
0.314353379	0.002360847	0.057723141	0.002871529	-0.054851612	0.166022129
0.496534455	0.029957046	0.087680187	0.004535702	-0.083144485	0.017123552
0.529587423	0.001901785	0.089581973	0.004837631	-0.084744341	0.188356551
0.719691101	0.001592468	0.091174441	0.006574175	-0.084600266	0.517873451
1.240012104	0.003302636	0.094477077	0.01132716	-0.083149917	0.15286539
1.395548103	0.002038582	0.096515659	0.012747938	-0.083767721	0.372939241
1.771233527	0.003453785	0.099969444	0.016179718	-0.083789726	0.419866456
2.193539537	0.001425321	0.101394765	0.020037364	-0.081357401	1.060646937
3.256018462	0.002238656	0.103633421	0.029742809	-0.073890612	0.014747794
3.27300533	0.00223949	0.105872911	0.029897979	-0.075974932	0.267655982
3.543270851	0.002979589	0.1088525	0.032366778	-0.076485722	5.818307416
9.364032085	0.001928047	0.110780547	0.085537787	-0.02524276	0.013157375
9.380920108	0.005533249	0.116313796	0.085692055	-0.030621741	2.658000804
12.04366057	0.003946061	0.120259857	0.110015436	-0.010244421	0.019504108
12.06655417	0.002832921	0.123092778	0.110224563	-0.012868215	1.171354397
13.24120534	0.003760621	0.126853399	0.120954669	-0.00589873	0.062787208
13.30772354	0.003701378	0.130554777	0.121562294	-0.008992483	0.061846331
13.3724529	0.002064677	0.132619454	0.122153579	-0.010465876	0.003647664
13.37797874	0.001691667	0.134311122	0.122204056	-0.012107066	0.621106682
14.00150138	0.003140251	0.137451373	0.127899759	-0.009551614	6.293049333
20.29730916	0.002376641	0.139828014	0.185410184	0.04558217	0.033477254
20.33293882	0.001928166	0.14175618	0.185735651	0.043979471	0.004923595
20.33985123	0.00204947	0.143805651	0.185798794	0.041993143	0.001908569
20.34389411	0.002219154	0.146024804	0.185835725	0.03981092	0.006340311
20.35283758	0.002987168	0.149011973	0.185917421	0.036905448	0.01301138
20.36872209	0.002759088	0.151771061	0.186062521	0.034291461	0.00809648
20.3891339	0.02187157	0.17364263	0.186248977	0.012606347	0.008264633
20.40928292	0.001897198	0.175539828	0.186433033	0.010893205	0.656671022
21.06848789	0.003170707	0.178710535	0.192454684	0.013744149	0.699908507
21.77092384	0.001884184	0.18059472	0.198871238	0.018276518	0.173679055
21.94688731	0.002684644	0.183279364	0.200478614	0.017199251	4.966429414
26.91742678	0.005535461	0.188814825	0.245883088	0.057068263	0.898104246
27.82067297	0.004748436	0.193563261	0.254133987	0.060570726	1.630694111
29.50305407	0.09862553	0.292188791	0.269502063	-0.022686728	0.30792587
29.86399052	0.007395626	0.299584417	0.272799115	-0.026785302	1.328685852
31.19948107	0.006213778	0.305798196	0.284998444	-0.020799752	2.273893111
33.47648107		0.305798196	0.305798196	0	

Location (mm)	Aperture (mm)	Cum. Ap. (mm)	Hom. Strain	Difference	Spacing (mm)
Sample 2 macrofractures			V'		C
			0.242689677		1.160390633
xloc	ap	cumap	hom strain	difference	spacing
0	0.4	0.4	0	-0.4	
6.2	0.215	0.615	0.166568811	-0.448431189	22.835
29.3075	0.33	0.945	0.787373454	-0.157626546	1.8675
31.4725	0.265	1.21	0.845538208	-0.364461792	26.8925
58.605	0.215	1.425	1.574478249	0.149478249	77.8675
136.7125	0.265	1.69	3.672909439	1.982909439	95.625
232.845	0.75	2.44	6.255599146	3.815599146	14.93
248.22	0.14	2.58	6.66866293	4.08866293	101.8
350.29	0.4	2.98	9.41086914	6.43086914	10.835
361.49	0.33	3.31	9.711767636	6.401767636	2.8925
364.655	0.215	3.525	9.796798328	6.271798328	15.8675
380.7625	0.265	3.79	10.22954141	6.439541411	20.75
401.895	0.5	4.29	10.79728583	6.507285829	3.8675
406.145	0.265	4.555	10.91146606	6.356466062	5.625
412.2775	0.75	5.305	11.07622142	5.771221422	2.8
415.6525	0.4	5.705	11.16689396	5.46189396	2.75
418.8525	0.5	6.205	11.25286496	5.047864959	3.93
423.1025	0.14	6.345	11.36704519	5.022045192	1.9425
425.1725	0.115	6.46	11.42265768	4.962657682	1.835
427.23	0.33	6.79	11.47793435	4.687934347	15.8675
443.395	0.265	7.055	11.91222222	4.857222222	7.75
451.5275	0.5	7.555	12.13070946	4.575709456	29.75
481.7775	0.5	8.055	12.94340406	4.888404057	49.8675
532.0275	0.265	8.32	14.2934174	5.973417401	48.835
581.16	0.33	8.65	15.61340806	6.96340806	21.525
603.325	0.95	9.6	16.20889156	6.608891558	4.525
608.8	0.95	10.55	16.35598256	5.805982564	14.69
624.275	0.62	11.17	16.77173294	5.601732942	11.75
636.585	0.5	11.67	17.10245263	5.432452629	47.69
684.835	0.62	12.29	18.3987341	6.108734098	22.8675
708.145	0.265	12.555	19.02497909	6.469979094	1.69
710.2775	0.62	13.175	19.08227071	5.907270705	7.69
718.5875	0.62	13.795	19.30552664	5.510526644	37.8925
756.8975	0.215	14.01	20.3347607	6.324760697	15.75
773.005	0.5	14.51	20.76750378	6.257503781	1.8
775.255	0.4	14.91	20.82795214	5.917952139	46.8675
822.455	0.265	15.175	22.09602438	6.921024375	19.75
842.5875	0.5	15.675	22.63690286	6.961902856	4.75
847.8375	0.5	16.175	22.77794903	6.602949026	160.75
1009.0875	0.5	16.675	27.1100814	10.4350814	6.835
1016.3375	0.33	17.005	27.30485944	10.29985944	7.625
1024.5025	0.75	17.755	27.52421982	9.76921982	13.525
1038.8775	0.95	18.705	27.91041767	9.205417667	11.835
1051.3525	0.33	19.035	28.24557023	9.210570234	7.8
1059.5175	0.4	19.435	28.46493061	9.029930611	23.75
1083.7175	0.5	19.935	29.11508629	9.180086291	55.8925
1139.9675	0.215	20.15	30.62629526	10.47629526	19.835
1160.075	0.33	20.48	31.16650209	10.68650209	27.69
1188.24	0.62	21.1	31.92318121	10.82318121	8.8675
1197.55	0.265	21.365	32.17330309	10.80830309	9.8675
1207.6825	0.265	21.63	32.4455222	10.8155222	0.9125
1208.815	0.175	21.805	32.47594787	10.67094787	14.8925
1223.9025	0.215	22.02	32.8812877	10.8612877	6.8

Location (mm)	Aperture (mm)	Cum. Ap. (mm)	Hom.Strain	Difference	Spacing (mm)
1231.01	0.4	22.42	33.07223735	10.65223735	7.835
1239.21	0.33	22.75	33.29253803	10.54253803	11.75
1251.375	0.5	23.25	33.61936216	10.36936216	20.8
1272.625	0.4	23.65	34.19026332	10.54026332	10.8925
1283.825	0.215	23.865	34.49116182	10.62616182	22.75
1306.9325	0.5	24.365	35.11196646	10.74696646	14.8675
1322.1825	0.265	24.63	35.521672	10.891672	14.8925
1337.315	0.215	24.845	35.9282208	11.0832208	25.835
1363.4225	0.33	25.175	36.62962325	11.45462325	36.69
1400.5875	0.62	25.795	37.62809581	11.83309581	180.8
1581.8975	0.4	26.195	42.49915888	16.30415888	17.75
1600.0975	0.5	26.695	42.98811894	16.29311894	2.8675
1603.3475	0.265	26.96	43.07543324	16.11543324	1.925
1606.48	2.15	29.11	43.15959078	14.04959078	2.525
1610.555	0.95	30.06	43.26906948	13.20906948	9.675
1622.03	2.65	32.71	43.57735611	10.86735611	18.8925
1642.355	0.215	32.925	44.12340628	11.19840628	9.625
1652.4625	0.75	33.675	44.39495374	10.71995374	9.525
1662.8375	0.95	34.625	44.67368784	10.04868784	2.8
1666.3125	0.4	35.025	44.76704697	9.742046971	12.525
1679.5125	0.95	35.975	45.12167734	9.146677342	87.8
1767.9875	0.4	36.375	47.49864114	11.12364114	14.8675
1783.1875	0.265	36.64	47.90700338	11.26700338	11.625
1795.32	0.75	37.39	48.23295436	10.84295436	11.8675
1807.695	0.265	37.655	48.56542034	10.91042034	3.69
1811.8275	0.62	38.275	48.67644382	10.40144382	6.8925
1819.1375	0.215	38.49	48.87283382	10.38283382	64.425
1884.245	1.15	39.64	50.62200783	10.98200783	8.625
1893.82	0.75	40.39	50.87924918	10.48924918	7.75
1902.195	0.5	40.89	51.1042514	10.2142514	47.69
1950.445	0.62	41.51	52.40053287	10.89053287	71.835
2022.755	0.33	41.84	54.34320879	12.50320879	29.75
2052.92	0.5	42.34	55.15361978	12.81361978	14.625
2068.17	0.75	43.09	55.56332533	12.47332533	25.8675
2094.545	0.265	43.355	56.27191442	12.91691442	29.8675
2124.6775	0.265	43.62	57.08145227	13.46145227	51
2177.81	4	47.62	58.50890668	10.88890668	19.525
2199.81	0.95	48.57	59.0999573	10.5299573	7.625
2208.285	0.75	49.32	59.32764612	10.00764612	31.425
2240.66	1.15	50.47	60.19743083	9.727430834	12.625
2254.235	0.75	51.22	60.56213593	9.342135931	33.8
2288.61	0.4	51.62	61.48565252	9.865652522	30.8675
2319.81	0.265	51.885	62.32386976	10.43886976	35.8
2355.9425	0.4	52.285	63.29460324	11.00960324	12.9525
2369.1425	0.095	52.38	63.64923361	11.26923361	10.8
2380.19	0.4	52.78	63.94603505	11.16603505	23.8675
2404.39	0.265	53.045	64.59619073	11.55119073	73.75
2478.5225	0.5	53.545	66.58782982	13.04282982	10.125
2489.7725	1.75	55.295	66.89007161	11.59507161	35.8
2526.6475	0.4	55.695	67.88075305	12.18575305	20.8
2547.8475	0.4	56.095	68.45031092	12.35531092	29
2579.0475	4	60.095	69.28852816	9.193528156	8.525
2590.0475	0.95	61.045	69.58405346	8.539053465	16.3
2607.5225	1.4	62.445	70.05353572	7.608535717	5.835
2614.2225	0.33	62.775	70.2335375	7.458537497	2.3
2617.3875	1.4	64.175	70.31856819	6.143568188	37.69

Location (mm)	Aperture (mm)	Cum. Ap. (mm)	Hom. Strain	Difference	Spacing (mm)
2656.0875	0.62	64.795	71.35827996	6.563279957	13
2671.3975	4	68.795	71.76959746	2.974597456	11.35
2686.3975	3.3	72.095	72.17258651	0.077586514	-1
2689.0475	4	76.095	72.24378125	-3.851218753	46.425
2738.0475	1.15	77.245	73.56021217	-3.68478783	37.75
2776.6225	0.5	77.745	74.5965657	-3.148434303	95.425
2872.8725	1.15	78.895	77.18241215	-1.712587848	67.8
2941.4475	0.4	79.295	79.0247438	-0.270256205	8.4425
2950.6475	1.115	80.41	79.27191042	-1.138089583	32.69
2984.205	0.62	81.03	80.1734641	-0.856535895	12.8
2997.515	0.4	81.43	80.53104973	-0.898950271	19.75
3017.715	0.5	81.93	81.07374166	-0.85625834	34.69
3052.965	0.62	82.55	82.02076595	-0.529234054	37.75
3091.275	0.5	83.05	83.05	0	

Location (mm)	Aperture (mm)	Cum. Ap. (mm)	Hom.Strain	Difference	Spacing (mm)
Sample 3			V'		C
			0.361216154		1.257776377
xloc	ap	cumap	hom strain	difference	spacing
0		0	0	0	
0.2209	0.008305871	0.008305871	0.015152893	0.006847022	0.145922482
0.375343661	0.008736487	0.017042358	0.025747137	0.008704779	0.910803212
1.304705041	0.028379848	0.045422205	0.089497765	0.04407556	1.800906467
3.12508291	0.010562956	0.055985162	0.21436871	0.158383548	0.052539436
3.215360784	0.064913921	0.120899083	0.220561426	0.099662343	0.116809688
3.368162363	0.007069861	0.127968944	0.231043029	0.103074084	0.438397946
3.813775965	0.00736145	0.135330394	0.261610414	0.12628002	0.189259445
4.009321859	0.005211449	0.140541843	0.275024113	0.134482269	0.689018106
4.710935046	0.019978712	0.160520555	0.323152088	0.162631533	0.319375713
5.044289791	0.007979354	0.168499909	0.346018946	0.177519037	0.31174924
5.362987518	0.00591762	0.174417529	0.367880388	0.193462859	0.337115926
5.705998953	0.005873398	0.180290927	0.391409658	0.211118731	0.026624856
5.737777801	0.004434586	0.184725513	0.393589565	0.208864052	0.997300452
6.740984268	0.007377444	0.192102958	0.462405684	0.270302726	0.092414012
6.842203966	0.010233928	0.202336885	0.469348967	0.267012082	0.264669318
7.118963897	0.013947299	0.216284184	0.488333638	0.272049454	0.113852495
7.248137233	0.016694383	0.232978567	0.497194433	0.264215866	0.453923792
7.739444714	0.058072994	0.291051561	0.530896243	0.239844682	0.092010086
7.875026941	0.029071288	0.320122849	0.540196665	0.220073816	0.59956272
8.502044771	0.025838931	0.34596178	0.583207684	0.237245905	0.211435989
8.730092663	0.007384876	0.353346656	0.598850896	0.24550424	0.105717994
8.849483274	0.019960358	0.373307013	0.607040634	0.233733621	0.112373893
8.975546783	0.007418875	0.380725888	0.615688108	0.23496222	0.370383182
9.361845741	0.024412678	0.405138566	0.642186736	0.237048169	0.076889365
9.454578742	0.007274592	0.412413158	0.648547864	0.236134706	0.034015047
9.499254265	0.014046361	0.426459519	0.651612434	0.225152915	0.473883595
9.997736554	0.035151027	0.461610546	0.685806408	0.224195862	0.263926545
10.28601606	0.013554893	0.475165439	0.705581277	0.230415838	0.755552655
11.05671042	0.016728525	0.491893964	0.758447957	0.266553993	0.00887105
11.10173709	0.055582713	0.547476677	0.761536614	0.214059937	0.882710719
12.01664433	0.008810317	0.556286994	0.824295743	0.268008749	0.136769756
12.1635888	0.011539122	0.567826116	0.834375571	0.266549455	0.060626122
12.23550222	0.011035478	0.578861594	0.839308556	0.260446962	0.091674359
12.47869281	0.291996981	0.870858575	0.855990498	-0.014868077	0.094160008
12.72072755	0.003752485	0.87461106	0.872593154	-0.002017906	0.000891024
12.72552953	0.004069424	0.878680484	0.872922551	-0.005757933	0.022679656
12.75166537	0.002842952	0.881523435	0.87471537	-0.006808066	0.077170002
12.83538153	0.010249351	0.891772787	0.880457977	-0.011314809	0.033071757
12.87480034	0.002444751	0.894217538	0.883161956	-0.011055581	0.002204113
12.87930365	0.002153645	0.896371183	0.883470866	-0.012900317	0.320331708
13.26351891	0.125613463	1.021984646	0.909826561	-0.112158086	0.294590725
13.62522898	0.008625232	1.030609879	0.934638485	-0.095971393	0.111029317
13.89715121	0.313160585	1.343770464	0.953291308	-0.390479156	0.030554038
14.09213106	0.015691038	1.359461502	0.966666178	-0.392795324	0.172292644
14.28744619	0.030353931	1.389815433	0.980064047	-0.409751385	0.371763217
14.67957718	0.010381632	1.400197064	1.006962731	-0.393234334	1.012332446
15.69810442	0.002007948	1.402205013	1.076829795	-0.325375217	1.220214235
16.92081504	0.002984827	1.405189839	1.160703058	-0.244486782	1.254795502
18.18021906	0.006232197	1.411422037	1.247093346	-0.164328691	0.35751835
18.54406444	0.006421863	1.4178439	1.272051744	-0.145792156	0.028301901
18.57978173	0.008408914	1.426252814	1.274501814	-0.151751001	0.113408866
18.69937316	0.003956217	1.430209031	1.282705327	-0.147503704	0.004994257

Location (mm)	Aperture (mm)	Cum. Ap. (mm)	Hom. Strain	Difference	Spacing (mm)
18.70769781	0.002704562	1.432913593	1.283276366	-0.149637227	0.21058294
18.92182022	0.00437439	1.437287983	1.297964343	-0.13932364	0.22577552
19.15123909	0.002912311	1.440200294	1.313701599	-0.126498696	0.087602956
19.2413488	0.0021012	1.442301495	1.319882779	-0.122418715	0.041409176
19.29082216	0.014027153	1.456328648	1.323276462	-0.133052186	0.00191856
19.30038602	0.001263464	1.457592113	1.323932506	-0.133659606	0.361652523
19.6652547	0.005168838	1.462760951	1.348961099	-0.113799852	0.014150944
19.6835395	0.003098881	1.465859832	1.350215366	-0.115644465	0.043282772
19.72941335	0.002083273	1.467943105	1.353362137	-0.114580969	0.522912305
20.25539564	0.004056693	1.471999798	1.389442506	-0.082557293	0.012927896
20.27921898	0.017734195	1.489733993	1.391076696	-0.098657298	0.337510915
20.631395	0.011596016	1.501330009	1.415234621	-0.086095388	0.55059631
21.19258182	0.009585001	1.51091501	1.453729886	-0.057185124	0.011660125
21.22746132	0.036853755	1.547768765	1.456122486	-0.091646279	0.970504672
22.21785586	0.00292598	1.550694745	1.524059755	-0.02663499	0.014566094
22.23511577	0.002461647	1.553156392	1.525243719	-0.027912673	0.260529079
22.50196259	0.010173828	1.56333022	1.543548388	-0.019781833	0.100711809
22.6113266	0.007130588	1.570460808	1.55105034	-0.019410468	0.219748345
22.84000023	0.010719968	1.581180776	1.566736474	-0.014444302	0.49965441
23.34693975	0.003850251	1.585031027	1.601510582	0.016479555	0.090606783
23.44070139	0.002459465	1.587490492	1.607942271	0.02045178	0.126150057
23.57249455	0.008826754	1.596317246	1.616982777	0.020665531	0.196846081
23.78080964	0.014111249	1.610428495	1.631272394	0.020843898	0.143161622
23.93343903	0.00482429	1.615252785	1.641742185	0.0264894	0.124087515
24.06284003	0.005802695	1.62105548	1.650618598	0.029563118	0.094472845
24.16268202	0.00493559	1.62599107	1.657467376	0.031476306	0.019143674
24.22476165	0.080936326	1.706927395	1.6617258	-0.045201595	0.23097509
24.49822146	0.004033106	1.710960501	1.680484095	-0.030476406	0.009571837
24.51135828	0.003096868	1.714057369	1.681385231	-0.032672138	0.253031622
24.76801695	0.004157233	1.718214602	1.698991032	-0.01922357	0.036816657
24.80909471	0.004364958	1.72257956	1.701808808	-0.020770751	0.176870086
25.0024406	0.028586655	1.751166215	1.715071595	-0.03609462	0.09532357
25.11358731	0.00305962	1.754225835	1.722695833	-0.031530001	0.048692638
25.17442221	0.021224919	1.775450754	1.726868875	-0.048581879	0.062425831
25.25383929	0.012757576	1.78820833	1.732316582	-0.055891748	0.065754986
25.35115729	0.050368448	1.838576778	1.738992224	-0.099584554	0.090315225
25.46767324	0.00203299	1.840609767	1.746984771	-0.093624996	0.000588087
25.47177441	0.004993187	1.845602954	1.747266096	-0.098336858	0.022892515
25.49987631	0.005425574	1.851028528	1.749193778	-0.10183475	0.260522431
25.76516513	0.004107208	1.855135736	1.767391575	-0.087744161	0.009571837
25.77785044	0.002119744	1.857255479	1.768261738	-0.088993741	0.067834973
25.8484233	0.003356031	1.860611511	1.773102766	-0.087508745	0.064089983
25.91578154	0.00318048	1.863791991	1.777723283	-0.086068708	0.389537788
26.30857102	0.003322897	1.867114889	1.804667136	-0.062447753	0.226391891
26.54084118	0.008433639	1.875548527	1.820599979	-0.054948549	0.055350881
26.60168215	0.002546541	1.878095068	1.824773436	-0.053321632	0.486500671
27.09070485	0.002497531	1.880592599	1.858318519	-0.02227408	0.10945739
27.20327417	0.003726324	1.884318923	1.866040343	-0.01827858	0.102795192
27.30953047	0.003195882	1.887514805	1.873329118	-0.014185687	0.205202059
27.51633047		1.887514805	1.887514805	0	

Location (mm)	Aperture (mm)	Cum. Ap. (mm)	Hom.Strain	Difference	Spacing (mm)
Sample 3 macrofractures			V'		C
			0.287050828		1.675557078
xloc	ap	cumap	hom strain	difference	spacing
0	0	0	0	0	
696.2	1.15	1.15	10.82767877	9.67767877	36.6
733.625	0.5	1.65	11.4097326	9.759732602	6.025
740.375	0.95	2.6	11.51471225	8.914712251	-0.45
742.9	5	7.6	11.55398242	3.953982416	138.8925
884.4	0.215	7.815	13.75466691	5.939666912	15.21
900.2925	1.15	8.965	14.00183566	5.036835664	4.65
905.7175	0.4	9.365	14.0862082	4.721208196	14.435
920.5175	0.33	9.695	14.3163858	4.621385797	15.345
937.3525	2.65	12.345	14.57821282	2.233212818	14.65
954.0275	1.4	13.745	14.83755143	1.092551433	74.125
1029.3275	0.95	14.695	16.00865774	1.313657741	134.9175
1164.8525	0.265	14.96	18.11641581	3.156415806	7.425
1172.72	0.62	15.58	18.23877542	2.658775419	6.905
1180.41	0.95	16.53	18.35837446	1.828374457	198.675
1379.935	0.75	17.28	21.46149512	4.181495121	7.085
1387.56	0.33	17.61	21.58008324	3.970083243	40.36
1428.395	0.62	18.23	22.21517124	3.985171239	8.805
1438.085	1.15	19.38	22.36587536	2.985875357	11.6
1450.51	0.5	19.88	22.55911567	2.679115674	28.335
1479.26	0.33	20.21	23.00625122	2.796251217	9.345
1490.095	2.65	22.86	23.17476299	0.314762994	172.7
1665.77	3.3	26.16	25.90695557	-0.253044435	1.5675
1669.12	0.265	26.425	25.95905658	-0.465943424	33.36
1702.9875	0.75	27.175	26.48578225	-0.689217755	22.175
1726.6125	2.15	29.325	26.85321102	-2.471788983	259.7625
1987.5375	0.175	29.5	30.91125767	1.411257675	11.575
1999.45	0.5	30	31.09652731	1.096527315	81.25
2081.2	0.5	30.5	32.36794751	1.867947509	218.925
2300.95	1.15	31.65	35.78561831	4.135618307	639.525
2942.375	2.65	34.3	45.76140667	11.46140667	6.65
2951.05	1.4	35.7	45.89632496	10.19632496	75.725
3028.35	1.75	37.45	47.09853634	9.648536344	18.75
3050.475	5	42.45	47.44263631	4.992636305	109
3168.975	14	56.45	49.28561237	-7.164387633	24.925
3201.975	2.15	58.6	49.79884621	-8.801153793	123.35
3328.9	5	63.6	51.77285242	-11.82714758	721
4056.4	8	71.6	63.08732571	-8.512674286	107.525
4168.4	0.95	72.55	64.82921026	-7.720789738	14.4
4184.925	3.3	75.85	65.086216	-10.763784	41.125
4228.275	1.15	77	65.76041863	-11.23958137	9.975
4239.7	1.75	78.75	65.93810641	-12.81189359	363.75
4608.825	9	87.75	71.67893796	-16.07106204	81.525
4695.325	0.95	88.7	73.02423272	-15.67576728	4.675
4700.85	0.75	89.45	73.11016051	-16.33983949	57.085
4758.475	0.33	89.78	74.00637566	-15.77362434	76.095
4835.31	1.15	90.93	75.20135512	-15.72864488	3.275
4839.735	1.15	92.08	75.27017511	-16.80982489	5.375
4846.16	0.95	93.03	75.37010018	-17.65989982	84.74
4931.685	0.62	93.65	76.70023122	-16.94976878	606.38
5540.375	4	97.65	86.16690716	-11.48309284	176.675
5720.375	2.65	100.3	88.96636447	-11.33363553	800.775
6523.05	1.15	101.45	101.45	0	

Location (mm)	Aperture (mm)	Cum. Ap. (mm)	Hom.Strain	Difference	Spacing (mm)
Sample 4			V'		C
			0.358127889		1.016389417
xloc	ap	cumap	hom strain	difference	spacing
0	0	0	0	0	
0.00761	0.001074312	0.001074312	0.000150543	-0.000923769	0.118625239
0.128119993	0.002695196	0.003769508	0.002534496	-0.001235011	0.208545134
0.338765487	0.001505524	0.005275032	0.006701528	0.001426496	0.281828116
0.621943923	0.001195114	0.006470146	0.012303422	0.005833276	0.033491851
0.656830246	0.00159383	0.008063976	0.012993551	0.004929575	0.013204135
0.671871902	0.00208121	0.010145187	0.013291108	0.003145921	0.421078768
1.094811253	0.001639956	0.011785143	0.021657781	0.009872639	1.281261549
2.377884785	0.00198401	0.013769153	0.047039805	0.033270653	0.119575155
2.499412212	0.001920534	0.015689686	0.049443886	0.0337542	0.312107627
2.813496641	0.002033068	0.017722754	0.055657169	0.037934414	0.097228888
2.912782637	0.00208115	0.019803904	0.057621265	0.037817361	0.687286433
3.602198359	0.002177427	0.021981331	0.071259428	0.049278097	0.363047368
3.968645456	0.00462203	0.026603362	0.07850856	0.051905198	0.369333184
4.341123542	0.001667774	0.028271135	0.085876998	0.057605863	0.234457043
4.577490377	0.002151809	0.030422944	0.090552855	0.060129911	0.096837035
4.67666316	0.002519686	0.032942631	0.092514712	0.059572081	0.098018868
4.776925345	0.00196695	0.03490958	0.094498119	0.059588538	0.5543736
5.332691091	0.000817342	0.035726922	0.105492391	0.069765469	1.808581746
7.142640351	0.001917686	0.037644608	0.141297179	0.103652571	0.00316075
7.147737419	0.00195495	0.039599558	0.14139801	0.101798453	0.265819301
7.415431729	0.001795069	0.041394627	0.146693594	0.105298967	0.558688565
7.975813708	0.00159176	0.042986387	0.157779186	0.114792799	0.11056429
8.088048711	0.001749664	0.04473605	0.159999442	0.115263391	1.310279078
9.405220647	0.012036052	0.056772102	0.186056007	0.129283905	0.026670648
9.438483121	0.001147601	0.057919703	0.186714013	0.128794309	0.68414616
10.12450218	0.002598192	0.060517895	0.200284982	0.139767087	0.04743972
10.17392815	0.00137432	0.061892215	0.201262737	0.139370522	0.167408604
10.34324644	0.002445045	0.06433726	0.204612226	0.140274967	0.141532008
10.48644596	0.000889985	0.065227245	0.207445029	0.142217784	0.392058364
10.88125109	0.00460354	0.069830785	0.215255145	0.14542436	0.342272371
11.22975489	0.007859328	0.077690113	0.222149319	0.144459206	0.009800953
11.34307678	0.199182533	0.276872646	0.224391076	-0.05248157	0.047439727
11.49060603	0.000996518	0.277869164	0.22730953	-0.050559634	0.757856222
12.25161154	0.005302061	0.283171224	0.242363897	-0.040807327	0.514069123
12.78114896	0.025634538	0.308805762	0.252839315	-0.055966447	0.141330884
12.93582834	0.001062446	0.309868208	0.255899214	-0.053968993	0.582350863
13.5193132	0.001205552	0.31107376	0.267441832	-0.043631928	0.047075642
13.56773848	0.001493732	0.312567491	0.268399791	-0.044167701	0.523418689
14.09287525	0.001942423	0.314509915	0.278788154	-0.035721761	1.139246953
15.23487094	0.003555054	0.318064969	0.301379347	-0.016685622	1.457970336
16.69581357	0.002389529	0.320454499	0.330280015	0.009825516	1.926220219
18.62470686	0.002956611	0.323411109	0.368437778	0.045026669	0.33860181
18.96502394	0.000473923	0.323885033	0.37517	0.051284968	0.131115914
19.09811976	0.003485897	0.327370929	0.377802929	0.050432	1.461754234
20.5619145	0.000595114	0.327966043	0.406760018	0.078793975	0.398551574
20.96542717	0.009327077	0.33729312	0.414742388	0.077449269	0.082814034
21.05433049	0.002851495	0.340144615	0.416501092	0.076356477	0.660599289
21.7168472	0.000983351	0.341127966	0.429607134	0.088479168	0.059282164
21.77700347	0.000764853	0.341892819	0.430797157	0.088904338	0.002655403
21.78239126	0.004699921	0.34659274	0.43090374	0.084311	0.150967855
21.93982327	0.0082284	0.35482114	0.434018092	0.079196953	0.201556281
22.14655362	0.002119729	0.356940869	0.438107674	0.081166806	0.006982143

Location (mm)	Aperture (mm)	Cum. Ap. (mm)	Hom. Strain	Difference	Spacing (mm)
22.15687414	0.004557023	0.361497892	0.438311837	0.076813945	0.248631713
22.40931408	0.003059433	0.364557326	0.443305656	0.07874833	0.243750315
22.65523282	0.001277425	0.365834751	0.448170471	0.08233572	0.017797909
22.6779572	0.008575516	0.374410267	0.448620009	0.074209743	0.816684123
23.50014343	0.002428701	0.376838968	0.464884666	0.088045698	0.367545801
23.86918991	0.000572639	0.377411607	0.472185219	0.094773612	0.225965342
24.09628428	0.001685431	0.379097038	0.476677647	0.097580609	0.110895441
24.20905211	0.002059345	0.381156383	0.478908443	0.09775206	0.472855646
24.68410661	0.002338355	0.383494738	0.488306069	0.104811331	0.003556743
24.68988986	0.002114656	0.385609394	0.488420474	0.102811081	0.317959492
25.0109814	0.004149455	0.389758849	0.494772373	0.105013524	0.042898681
25.05647199	0.001034356	0.390793205	0.495672278	0.104879072	1.027658558
26.08499196	0.000688465	0.39148167	0.516018671	0.124537001	0.149572282
26.23571861	0.001620272	0.393101942	0.519000377	0.125898435	0.014793324
26.25227781	0.001911487	0.395013429	0.519327954	0.124314525	1.378589603
27.6332714	0.002896473	0.397909902	0.546647053	0.148737151	0.362689225
27.99812257	0.001427415	0.399337317	0.553864614	0.154527297	0.138836035
28.14720485	0.019065095	0.418402412	0.55681379	0.138411379	1.200606354
29.35817394	0.001660378	0.42006279	0.58076943	0.16070664	0.984704042
30.34442599	0.001435629	0.421498418	0.60027967	0.178781252	1.601949145
31.9501558	0.006125707	0.427624125	0.632044547	0.204420422	0.398883709
32.35467885	0.005152965	0.43277709	0.640046905	0.207269815	1.800442275
34.15909089	0.002786573	0.435563663	0.675742155	0.240178492	0.822069031
34.98433685	0.003567284	0.439130948	0.69206734	0.252936393	0.410797377
35.39853853	0.003241319	0.442372266	0.700261163	0.257888897	0.918321398
36.31958792	0.002214663	0.444586929	0.718481551	0.273894622	0.213827925
36.53549451	0.001942667	0.446529596	0.72275266	0.276223064	0.319005425
36.85843289	0.005923254	0.45245285	0.729141093	0.276688243	0.281808668
37.1446855	0.002964616	0.455417466	0.734803801	0.279386335	0.406325784
37.55480488	0.004622586	0.460040053	0.742916867	0.282876814	0.261951947
37.82073841	0.003340576	0.463380628	0.748177619	0.28479699	0.178601409
38.00477861	0.007537	0.470917628	0.75181834	0.280900711	0.101708206
38.12027771	0.0200448	0.490962428	0.754103167	0.263140738	0.098945007
38.3048713	0.151252356	0.642214784	0.757754835	0.115540051	1.130666089
39.52035106	0.01837499	0.660589774	0.781799705	0.121209931	0.040197944
39.57744211	0.015411217	0.676000992	0.782929092	0.1069281	0.422203625
40.01046351	0.006224335	0.682225327	0.791495211	0.109269883	0.300652142
40.31607613	0.003696617	0.685921944	0.797540902	0.111618958	1.300350647
41.62226404	0.007977913	0.693899858	0.82338018	0.129480322	0.834479448
42.46242051	0.003376137	0.697275995	0.840000328	0.142724333	0.634229349
43.09987603	0.003076197	0.700352191	0.852610604	0.152258412	0.4475023
43.550608	0.003383137	0.703735329	0.861527076	0.157791747	0.817608345
44.37347388	0.007131936	0.710867265	0.877805178	0.166937913	0.130977622
44.55361844	0.091201942	0.802069207	0.881368835	0.079299628	0.353735087
44.95553722	0.005165454	0.807234662	0.889319675	0.082085013	0.036712721
45.046456	0.103246654	0.910481316	0.891118249	-0.019363067	1.020031746
46.12028525	0.004348364	0.91482968	0.91236096	-0.00246872	0.234168188
46.35849627	0.0037373	0.918566979	0.917073299	-0.00149368	0.268900983
46.63539218	0.012252543	0.930819523	0.922550911	-0.008268612	0.189352699
46.83549564	0.009248977	0.9400685	0.926509399	-0.013559101	0.288745705
47.13107416	0.004416649	0.944485149	0.932356594	-0.012128555	0.78735664
47.92415318	0.007028117	0.951513266	0.948045446	-0.003467821	0.171785941
48.09945318		0.951513266	0.951513266	0	

Location (mm)	Aperture (mm)	Cum. Ap. (mm)	Hom. Strain	Difference	Spacing (mm)
Sample 4 macrofractures			V'		C
			0.293697655		2.146605888
xloc	ap	cumap	hom strain	difference	spacing
0	0	0	0	0	
591.0875	0.62	0.62	1.067788144	0.447788144	68.6935
660.2225	0.263	0.883	1.192679185	0.309679185	129.005
789.734	0.75	1.633	1.426639206	-0.206360794	5.362
795.846	0.75	2.383	1.437680416	-0.945319584	147.1175
943.471	0.265	2.648	1.704362125	-0.943637875	99.1425
1042.8535	0.215	2.863	1.883894691	-0.979105309	1.665
1044.696	0.14	3.003	1.887223131	-1.115776869	23.6975
1068.551	0.175	3.178	1.930316728	-1.247683272	5.79
1074.4985	0.14	3.318	1.941060772	-1.376939228	7.6925
1082.3935	0.265	3.583	1.955322936	-1.627677064	45.7275
1128.386	0.265	3.848	2.038407499	-1.809592501	28.6775
1157.2535	0.115	3.963	2.090556079	-1.872443921	32.6875
1190.046	0.095	4.058	2.149795097	-1.908204903	5.815
1195.9785	0.14	4.198	2.160512043	-2.037487957	59.8575
1255.9535	0.095	4.293	2.268855722	-2.024144278	69.61
1325.861	0.5	4.793	2.395142269	-2.397857731	3.7725
1330.016	0.265	5.058	2.402648196	-2.655351804	9.4125
1339.6485	0.175	5.233	2.420049122	-2.812950878	24.665
1364.471	0.14	5.373	2.464890488	-2.908109512	11.7375
1376.366	0.175	5.548	2.486378576	-3.061621424	51.79
1428.3135	0.14	5.688	2.58022073	-3.10777927	0.6925
1429.2085	0.265	5.953	2.58183753	-3.37116247	229.7725
1659.201	0.175	6.128	2.997314536	-3.130685464	85.6025
1745.0235	0.265	6.393	3.152351224	-3.240648776	1210.515
2955.981	0.62	7.013	5.339922541	-1.673077459	66.6275
3023.026	0.215	7.228	5.461038038	-1.766961962	1251.2475
4274.5135	0.265	7.493	7.721826017	0.228826017	47.715
4322.431	0.14	7.633	7.808388054	0.175388054	3.6775
4326.236	0.115	7.748	7.815261713	0.067261713	5.8025
4332.1535	0.115	7.863	7.825951563	-0.037048437	0.7975
4333.096	0.175	8.038	7.827654171	-0.210345829	3.9675
4337.2835	0.265	8.303	7.835218809	-0.467781191	206.66
4544.241	0.33	8.633	8.209083532	-0.423916468	21.6275
4566.141	0.215	8.848	8.248645459	-0.599354541	103.5625
4669.9185	0.215	9.063	8.436117507	-0.626882493	7.585
4677.811	0.4	9.463	8.450375155	-1.012624845	3.6775
4681.796	0.215	9.678	8.457573981	-1.220426019	15.4675
4697.5035	0.265	9.943	8.485949276	-1.457050724	26.585
4724.421	0.4	10.343	8.534575219	-1.808424781	12.57
4737.356	0.33	10.673	8.557942047	-2.115057953	462.5125
5200.121	0.175	10.848	9.393918075	-1.454081925	308.295
5508.8785	0.75	11.598	9.951682531	-1.646317469	465.66
5975.0785	0.33	11.928	10.79386382	-1.13413618	2.085
5977.4935	0.33	12.258	10.79822647	-1.45977353	4.5375
5982.3285	0.265	12.523	10.8069608	-1.716039196	7.5625
5990.131	0.215	12.738	10.82105587	-1.91694413	1207.6025
7197.9735	0.265	13.003	13.003	0	

Location (mm)	Aperture (mm)	Cum. Ap. (mm)	Hom. Strain	Difference	Spacing (mm)
Sample 5			V'		C
			0.331839866		0.962469961
xloc	ap	cumap	hom strain	difference	spacing
0		0	0	0	
2.965	0.005835536	0.005835536	0.00428337	-0.001552166	1.751773581
4.723021632	0.006660567	0.012496104	0.006823086	-0.005673018	5.276420156
10.00401083	0.002477523	0.014973627	0.014452236	-0.000521391	0.258940596
10.26833835	0.00829631	0.023269937	0.014834095	-0.008435841	11.36857286
21.64331651	0.004514293	0.02778423	0.031266891	0.003482661	1.044309063
22.69139163	0.003017822	0.030802052	0.032780987	0.001978935	8.981792357
31.67605476	0.002723718	0.03352577	0.045760628	0.012234858	1.32387178
33.01202598	0.02147517	0.05500094	0.047690631	-0.007310309	5.604488515
38.62887208	0.00323999	0.05824093	0.055804975	-0.002435955	0.558621295
39.19227129	0.006315851	0.064556781	0.056618886	-0.007937895	0.892838328
40.09017346	0.003811826	0.068368607	0.057916035	-0.010452571	7.233489159
47.32556853		0.068368607	0.068368607	0	

Location (mm)	Aperture (mm)	Cum. Ap. (mm)	Hom.Strain	Difference	Spacing (mm)
Sample 6			V'		C
			0.917305274		1.550957296
xloc	ap	cumap	hom strain	difference	spacing
0		0	0	0	
4.94	0.003825274	0.003825274	0.175264278	0.171439004	0.114430748
5.072013732	0.031340695	0.035165969	0.179947941	0.144781971	0.490069332
6.148437443	1.141368063	1.176534032	0.218137946	-0.958396086	0.038475592
6.763291407	0.011388681	1.187922713	0.239952103	-0.94797061	0.056985133
6.830703043	0.009464326	1.197387039	0.242343773	-0.955043265	1.256071995
8.092950024	0.002885646	1.200272685	0.287126528	-0.913146157	3.413734303
11.50981573	0.003377163	1.203649848	0.408352136	-0.795297712	0.149252178
11.66166749	0.001822	1.205471848	0.413739623	-0.791732225	5.332987373
16.99796496	0.004798197	1.210270045	0.603063981	-0.607206064	4.194006632
21.19615188	0.003562368	1.213832413	0.75200977	-0.461822643	13.28524044
34.49210195	0.017856886	1.231689299	1.22373145	-0.00795785	0.215371557
34.71640195		1.231689299	1.231689299	0	

Location (mm)	Aperture (mm)	Cum.Ap. (mm)	Hom strain	Difference	Spacing (mm)
Sample 7			V'		C
			0.183870667		1.201822732
loc	ap	cumap	hom strain	difference	spacing
0	0	0	0	0	
0.266800	0.001258	0.001258	0.000274687	-0.000983313	1.515619976
1.785107	0.004117	0.005375	0.001837877	-0.003537123	0.209633098
1.998953	0.004308	0.009683	0.002058044	-0.007624956	6.141963151
8.145317	0.004493	0.014176	0.008386099	-0.005789901	0.151904793
8.300768	0.002599	0.016775	0.008546145	-0.008228855	0.675640019
8.978737	0.00206	0.018835	0.009244155	-0.009590845	0.835791319
9.816625	0.002134	0.020969	0.010106812	-0.010862188	6.191459287
16.010398	0.002493	0.023462	0.016483678	-0.006978322	0.13406902
16.147243	0.003059	0.026521	0.016624568	-0.009896432	7.502329481
23.654505	0.006805	0.033326	0.02435375	-0.00897225	3.455895759
27.115434	0.003262	0.036588	0.027916987	-0.008671013	0.131278484
27.249365	0.002043	0.038631	0.028054877	-0.010576123	6.311055651
33.562801	0.002717	0.041348	0.034554943	-0.006793057	0.13746419
33.703524	0.003801	0.045149	0.034699826	-0.010449174	5.859053738
39.566803	0.004651	0.0498	0.040736428	-0.009063572	0.028467918
39.598817	0.002441	0.052241	0.040769389	-0.011471611	1.314118802
40.915669	0.003025	0.055266	0.042125168	-0.013140832	3.310746621
44.230048	0.004239	0.059505	0.045537522	-0.013967478	11.16458734
55.397924	0.002339	0.061844	0.057035529	-0.004808471	0.109609167
55.509582	0.001758	0.063602	0.057150488	-0.006451512	0.388784061
55.901564	0.004638	0.06824	0.057554057	-0.010685943	12.32489774
68.229687	0.001812	0.070052	0.070246608	0.000194608	0.257371826
68.490298	0.004668	0.07472	0.070514924	-0.004205076	0.038759625
68.532543	0.002302	0.077022	0.070558418	-0.006463582	6.276849
74.810543		0.077022	0.077022	0	

Location (mm)	Aperture (mm)	Cum.Ap. (mm)	Hom strain	Difference	Spacing (mm)
Sample 8			V'		C
			0.467041206		1.081741418
loc	ap	cumap	hom strain	difference	spacing
0	0	0	0	0	
41.750000	0.003902	0.003902	0.006767278	0.002865278	22.77641164
64.530532	0.004338	0.00824	0.010459785	0.002219785	1.338947864
65.874163	0.005028	0.013268	0.010677575	-0.002590425	0.271789516
66.149203	0.001474	0.014742	0.010722156	-0.004019844	24.799263
90.949203		0.014742	0.014742	0	

Location (mm)	Aperture (mm)	Cum.Ap. (mm)	Hom strain	Difference	Spacing (mm)
Sample 9			V'		C
			0.34480365		1.782015299
loc	ap	cumap	hom strain	difference	spacing
0	0	0	0	0	
16.600000	0.010862	0.010862	0.016906168	0.006044168	8.606664909
25.213297	0.002403	0.013265	0.025678328	0.012413328	0.04688841
25.276953	0.031132	0.044397	0.025743158	-0.018653842	3.42197168
28.715510	0.002038	0.046435	0.029245135	-0.017189865	4.57596217
33.293993	0.003003	0.049438	0.033908063	-0.015529937	41.98596807
75.289793	0.016661	0.066099	0.076678428	0.010579428	2.294606818
77.595119	0.004777	0.070876	0.079026273	0.008150273	2.654063088
80.253662	0.004183	0.075059	0.08173385	0.00667485	8.60147232
88.858886	0.003322	0.078381	0.090497789	0.012116789	3.262691431
92.123703	0.000929	0.07931	0.093822821	0.014512821	0.293088483
92.420044	0.005575	0.084885	0.094124628	0.009239628	0.025528891
92.454013	0.011305	0.09619	0.094159223	-0.002030777	1.9883475
94.448013		0.09619	0.09619	0	

Location (mm)	Aperture (mm)	Cum.Ap. (mm)	Hom strain	Difference	Spacing (mm)
Sample 10			V'		C
			0.968452378		0.792566923
loc	ap	cumap	hom strain	difference	spacing
0	0	0	0	0	
0.004300	0.524164	0.524164	2.59513E-05	-0.524138049	33.93350304
34.202034	0.004298	0.528462	0.206415947	-0.322046053	12.61742656
46.822012	0.000804	0.529266	0.282579973	-0.246686027	12.89372479
59.717331	0.002386	0.531652	0.360405744	-0.171246256	2.941273195
62.661805	0.004014	0.535666	0.378176214	-0.157489786	4.049390109
66.715975	0.005546	0.541212	0.402643921	-0.138568079	22.957227
89.675975		0.541212	0.541212	0	

Location (mm)	Aperture (mm)	Cum.Ap. (mm)	Hom strain	Difference	Spacing (mm)
Sample 11			V'		C
			0.337530669		1.822394031
loc	ap	cumap	hom strain	difference	spacing
0	0	0	0	0	
7.108000	0.001977	0.001977	0.00475087	0.00277387	0.192797395
7.303086	0.002601	0.004578	0.004881263	0.000303263	0.077385669
7.383483	0.00342	0.007998	0.004934998	-0.003063002	3.280686321
10.667582	0.003406	0.011404	0.007130036	-0.004273964	9.673306892
20.344428	0.003672	0.015076	0.01359788	-0.00147812	0.657525707
21.004727	0.001875	0.016951	0.014039213	-0.002911787	0.0032201
21.010133	0.002496	0.019447	0.014042826	-0.005404174	0.019962938
21.032286	0.001885	0.021332	0.014057633	-0.007274367	0.044438724
21.07857125	0.001808	0.02314	0.014088569	-0.009051431	12.15817053
33.24159478	0.007898	0.031038	0.022218134	-0.008819866	0.0178401
33.26378688	0.000806	0.031844	0.022232967	-0.009611033	0.04517402
33.3100244	0.001321	0.033165	0.022263871	-0.010901129	0.010698536
33.32187494	0.000983	0.034148	0.022271792	-0.011876208	11.55401791
44.87744034	0.002112	0.03626	0.029995341	-0.006264659	0.994765731
45.87427957	0.002035	0.038295	0.030661612	-0.007633388	1.94330971
47.82287178	0.00853	0.046825	0.031964019	-0.014860981	4.108465977
51.93749026	0.003775	0.0506	0.034714162	-0.015885838	30.05677684
81.9984961	0.004683	0.055283	0.054806443	-0.000476557	0.7106585
82.7114961		0.055283	0.055283	0	

Location (mm)	Aperture (mm)	Cum.Ap. (mm)	Hom strain	Difference	Spacing (mm)
Sample 12			V'		C
			0.512191989		0.96218449
loc	ap	cumap	hom strain	difference	spacing
0	0	0	0	0	
15.577000	0.002443	0.002443	0.00218361	-0.00025939	0.036010648
15.617293	0.006121	0.008564	0.002189259	-0.006374741	46.87448101
62.496775	0.003882	0.012446	0.008760904	-0.003685096	26.286059
88.784775		0.012446	0.012446	0	

Location (mm)	Aperture (mm)	Cum. ap. (mm)	Hom. strain	Difference	Spacing (mm)
Sample 13			V'		C
			0.54968168		0.879059075
loc	ap	cumap	hom strain	difference	spacing
0	0	0	0	0	
11.640000	0.002461	0.002461	0.046307637	0.043846637	7.934499858
19.578674	0.005887	0.008348	0.077890216	0.069542216	0.013863934
19.600112	0.009261	0.017609	0.077975503	0.060366503	0.083955737
19.732590	0.087783	0.105392	0.078502542	-0.026889458	24.01656374
43.797385	0.008681	0.114073	0.174239984	0.060166984	8.194839188
52.094784	0.196439	0.310512	0.207249687	-0.103262313	12.53937512
64.734309	0.00386	0.314372	0.257533752	-0.056838248	14.28507
79.021309		0.314372	0.314372	0	

Location (mm)	Aperture (mm)	Cum. ap. (mm)	Hom. strain	Difference	Spacing (mm)
Sample 14			V'		C
			0.789330453		0.941793196
loc	ap	cumap	hom strain	difference	spacing
0	0	0	0	0	
5.887000	0.000728	0.000728	0.055415816	0.054687816	2.430333119
8.319278	0.003161	0.003889	0.078311459	0.074422459	17.16524145
25.487836	0.003472	0.007361	0.239923427	0.232562427	8.867577801
34.627210	0.540122	0.547483	0.325954667	-0.221528333	2.118680795
37.017127	0.00235	0.549833	0.348451557	-0.201381443	10.72321035
47.746861	0.010696	0.560529	0.449453244	-0.111075756	0.202844713
47.961318	0.012529	0.573058	0.451471984	-0.121586016	12.81878174
60.787478	0.002228	0.575286	0.572207866	-0.003078134	0.325886
61.114478		0.575286	0.575286	0	

Location (mm)	Aperture (mm)	Cum. ap. (mm)	Hom. strain	Difference	Spacing (mm)
Sample 15			V'		C
			0.35456826		1.202827445
loc	ap	cumap	hom strain	difference	spacing
0	0	0	0	0	
13.410000	0.017806	0.017806	0.062474097	0.044668097	6.810710229
20.242255	0.025284	0.04309	0.094303999	0.051213999	5.904433024
26.187373	0.056086	0.099176	0.122000933	0.022824933	0.941773039
27.158770	0.003161	0.102337	0.126526445	0.024189445	0.007906815
27.170624	0.004734	0.107071	0.126581672	0.019510672	0.488678934
27.690511	0.057682	0.164753	0.129003705	-0.035749295	0.045866307
27.769954	0.009472	0.174225	0.129373813	-0.044851187	11.13366046
38.910566	0.00443	0.178655	0.181275353	0.002620353	0.147075547
39.073247	0.026782	0.205437	0.182033248	-0.023403752	7.872640775
47.011465	0.104372	0.309809	0.219015574	-0.090793426	4.986432137
52.057950	0.015734	0.325543	0.242525985	-0.083017015	3.670175391
55.745715	0.019445	0.344988	0.259706431	-0.085281569	11.33397465
67.103996	0.029167	0.374155	0.312622041	-0.061532959	15.48451657
82.604859	0.003527	0.377682	0.38483699	0.00715499	0.043333333
82.652156	0.0044	0.382082	0.385057335	0.002975335	0.013263131
82.668941	0.002644	0.384726	0.385135533	0.000409533	0.013263536
82.687490	0.007927	0.392653	0.385221948	-0.007431052	0.143244089
82.838625	0.007855	0.400508	0.385926052	-0.014581948	3.1260725
85.968625		0.400508	0.400508	0	

Location (mm)	Aperture (mm)	Cum. ap. (mm)	Hom. strain	Difference	Spacing (mm)
Sample 16			V'		C
			0.568820804		1.699743775
loc	ap	cumap	hom strain	difference	spacing
0	0	0	0	0	
5.823000	0.008527	0.008527	0.022638864	0.014111864	0.363049707
6.191027	0.001427	0.009954	0.024069692	0.014115692	1.015518221
7.216552	0.018588	0.028542	0.028056767	-0.000485233	0.006482561
7.235813	0.006969	0.035511	0.02813165	-0.00737935	0.079222766
7.319528	0.002015	0.037526	0.02845712	-0.00906888	0.00648139
7.328124	0.002214	0.03974	0.028490539	-0.011249461	0.990239307
8.325215	0.011489	0.051229	0.032367064	-0.018861936	0.622167457
8.961123	0.015993	0.067222	0.034839371	-0.032382629	18.30651586
27.281490	0.011709	0.078931	0.106065938	0.027134938	0.222472404
27.518199	0.016763	0.095694	0.106986221	0.011292221	2.051928474
29.580031	0.003044	0.098738	0.115002284	0.016264284	7.297351053
36.882321	0.006834	0.105572	0.143392385	0.037820385	14.00372185
50.890390	0.001861	0.107433	0.19785345	0.09042045	9.76705164
60.661462	0.006179	0.113612	0.235841766	0.122229766	9.078578979
69.748552	0.010843	0.124455	0.271170874	0.146715874	0.073314512
69.832736	0.010896	0.135351	0.271498168	0.136147168	0.045418617
69.887411	0.007618	0.142969	0.271710738	0.128741738	0.0078131
69.900968	0.003869	0.146838	0.271763444	0.124925444	0.005189729
69.915246	0.014308	0.161146	0.271818955	0.110672955	0.015570083
69.940717	0.005494	0.16664	0.271917982	0.105277982	0.048015977
70.000263	0.017566	0.184206	0.272149487	0.087943487	0.005190441
70.016181	0.003889	0.188095	0.272211374	0.084116374	0.075270084
70.097930	0.009068	0.197163	0.272529199	0.075366199	2.061368207
72.223185	0.118707	0.31587	0.280791843	-0.035078157	0.21931289
72.503788	0.003873	0.319743	0.28188278	-0.03786022	3.159856648
75.666778	0.002393	0.322136	0.294179963	-0.027956037	0.455491654
76.124643	0.002353	0.324489	0.295960065	-0.028528935	7.3368235
83.462643		0.324489	0.324489	0	

Location (mm)	Aperture (mm)	Cum. ap. (mm)	Hom. strain	Difference	Spacing (mm)
Sample 17			V'		C
			0.614254761		1.279532634
loc	ap	cumap	hom strain	difference	spacing
0	0	0	0	0	
29.77	0.004241	0.004241	0.143877405	0.139636405	9.524561266
39.30073477	0.008106	0.012347	0.189939124	0.177592124	5.045159861
44.35258513	0.005275	0.017622	0.214354547	0.196732547	12.1613683
56.52865193	0.024122	0.041744	0.273201066	0.231457066	1.476211333
58.02038226	0.006916	0.04866	0.280410549	0.231750549	0.39336238
58.41930614	0.004207	0.052867	0.282338534	0.229471534	24.50149941
83.04209456	0.238371	0.291238	0.40133964	0.11010164	0.071701433
83.23448099	0.002999	0.294237	0.402269437	0.108032437	0.011446859
83.25043935	0.006024	0.300261	0.402346563	0.102085563	0.009236972
83.33420782	0.143039	0.4433	0.402751413	-0.040548587	8.3184805
91.72420782		0.4433	0.4433	0	

Location (mm)	Aperture (mm)	Cum. ap. (mm)	Hom. strain	Difference	Spacing (mm)
Sample 18			V'		C
			0.690550065		2.902402115
loc	ap	cumap	hom strain	difference	spacing
0	0	0	0	0	
3.186000	0.004491	0.004491	0.032444442	0.027953442	1.907121897
5.096881	0.003027	0.007518	0.051903784	0.044385784	0.012112986
5.112775	0.004535	0.012053	0.05206564	0.04001264	0.713179111
5.831972	0.007501	0.019554	0.059389541	0.039835541	0.645788314
6.484539	0.006056	0.02561	0.066034916	0.040424916	0.133247623
6.622678	0.003728	0.029338	0.067441653	0.038103653	0.138555965
6.765028	0.003859	0.033197	0.06889126	0.03569426	0.077233055
6.847578	0.006776	0.039973	0.069731909	0.029758909	0.035581418
6.888437	0.003778	0.043751	0.070147988	0.026396988	0.020455407
6.912282	0.003001	0.046752	0.070390811	0.023638811	0.305101716
7.220397	0.003026	0.049778	0.073528484	0.023750484	0.140060907
7.364970	0.005999	0.055777	0.075000739	0.019223739	1.242373326
8.616012	0.011338	0.067115	0.087740649	0.020625649	0.126434747
8.753396	0.010561	0.077676	0.089139693	0.011463693	0.389893921
9.155099	0.013057	0.090733	0.093230411	0.002497411	0.189273597
9.355748	0.009693	0.100426	0.095273704	-0.005152296	0.473934417
9.887748	0.106439	0.206865	0.100691299	-0.106173701	0.539044137
10.482588	0.005152	0.212017	0.106748813	-0.105268187	26.67194474
37.158443	0.002668	0.214685	0.378400797	0.163715797	0.356512025
37.521164	0.009751	0.224436	0.38209455	0.15765855	0.134249219
37.662062	0.003545	0.227981	0.383529368	0.155548368	0.094237976
37.765859	0.015574	0.243555	0.384586384	0.141031384	0.006222401
37.780736	0.001735	0.24529	0.384737882	0.139447882	0.002666253
37.785996	0.003452	0.248742	0.384791444	0.136049444	0.041782766
37.832106	0.005203	0.253945	0.385261005	0.131316005	0.001777355
38.109132	0.545295	0.79924	0.388082087	-0.411157913	0.224040359
38.607154	0.002667	0.801907	0.393153658	-0.408753342	0.113793726
38.732418	0.020274	0.822181	0.394429279	-0.427751721	0.264053595
39.008825	0.004433	0.826614	0.397244054	-0.429369946	0.008889593
39.024362	0.008862	0.835476	0.397402275	-0.438073725	0.761026868
39.790707	0.001775	0.837251	0.405206307	-0.432044693	0.204485055
39.998300	0.00444	0.841691	0.407320314	-0.434370686	12.07599749
52.081397	0.00976	0.851451	0.53036782	-0.32108318	0.692569761
52.780179	0.002663	0.854114	0.537483818	-0.316630182	2.835564941
55.619838	0.005526	0.85964	0.566401321	-0.293238679	0.51844862
56.142747	0.003394	0.863034	0.57172633	-0.29130767	1.577918911
57.726578	0.00843	0.871464	0.587855178	-0.283608822	27.845785
85.576578		0.871464	0.871464	0	

Location (mm)	Aperture (mm)	Cum. ap. (mm)	Hom. strain	Difference	Spacing (mm)
Sample 19			V'		C
			0.456955153		1.034195537
loc	ap	cumap	hom strain	difference	spacing
0	0	0	0	0	
10.964	0.01421	0.01421	0.202602825	0.188392825	0.157439957
11.25536196	0.253634	0.267844	0.207986877	-0.059857123	2.217348942
13.6136519	0.028248	0.296092	0.251565517	-0.044526483	0.009969015
13.63889191	0.002294	0.298386	0.252031925	-0.046354075	0.018279885
13.6600933	0.003549	0.301935	0.252423704	-0.049511296	9.332536774
23.08086107	0.172913	0.474848	0.426509271	-0.048338729	15.73886626
38.90835683	0.004346	0.479194	0.71898422	0.23979022	15.45133178
54.46655312	0.209383	0.688577	1.006482808	0.317905808	2.588695512
57.50246963	0.685059	1.373636	1.062583251	-0.311052749	4.163654739
62.01004187	0.002776	1.376412	1.145878295	-0.230533705	12.474112
74.48554187		1.376412	1.376412	0	

Location (mm)	Aperture (mm)	Cum. ap. (mm)	Hom. strain	Difference	Spacing (mm)
Sample 20			V'		C
			0.532533996		0.950342172
loc	ap	cumap	hom strain	difference	spacing
0	0	0	0	0	
1.558000	0.002982	0.002982	0.001059227	-0.001922773	38.44582343
40.008615	0.006602	0.009584	0.027200401	0.017616401	0.526213017
40.539647	0.003036	0.01262	0.02756143	0.01494143	18.49215897
59.055238	0.043827	0.056447	0.040149506	-0.016297494	33.11596292
92.196733	0.007237	0.063684	0.062681201	-0.001002799	1.4713815
93.671733		0.063684	0.063684	0	

Location (mm)	Aperture (mm)	Cum. ap. (mm)	Hom. strain	Difference	Spacing (mm)
Sample 21			V'		C
			0.893621032		1.241079605
loc	ap	cumap	hom strain	difference	spacing
0	0	0	0	0	
7.530000	0.004176	0.004176	0.103035876	0.098859876	20.73706105
28.271666	0.005033	0.009209	0.386852037	0.377643037	22.52530313
50.801343	0.003715	0.012924	0.695134245	0.682210245	12.82374606
63.628487	0.003082	0.016006	0.870652981	0.854646981	0.811311887
64.445560	0.008439	0.024445	0.881833296	0.857388296	2.584948601
67.035390	0.001325	0.02577	0.917270941	0.891500941	5.577160927
72.630760	0.035092	0.060862	0.993834526	0.932972526	0.102014661
73.323091	1.145541	1.206403	1.003307958	-0.203095042	2.756283707
76.657123	0.009955	1.216358	1.048928792	-0.167429208	7.690299386
84.355178	0.005558	1.221916	1.154264242	-0.067651758	1.996258163
86.361028	0.013624	1.23554	1.181711045	-0.053828955	0.481849755
86.854168	0.008958	1.244498	1.188458879	-0.056039121	1.670781518
88.531288	0.003719	1.248217	1.211407555	-0.036809445	0.674199852
89.218893	0.023091	1.271308	1.220816316	-0.050491684	3.6784545
92.908893		1.271308	1.271308	0	

Location (mm)	Aperture (mm)	Cum. ap. (mm)	Hom. strain	Difference	Spacing (mm)
Sample 22			V'		C
			0.883703602		1.30580076
loc	ap	cumap	hom strain	difference	spacing
0	0	0	0	0	
17.726000	0.005433	0.005433	0.216411321	0.210978321	3.51045939
21.241327	0.004303	0.009736	0.25932888	0.24959288	3.946449481
25.195261	0.010666	0.020402	0.307601252	0.287199252	0.46558328
25.867154	0.401952	0.422354	0.31580418	-0.10654982	0.01786738
26.087878	0.003761	0.426115	0.31849893	-0.10761607	0.24718526
26.340417	0.006947	0.433062	0.321582105	-0.111479895	0.860691708
27.206525	0.003887	0.436949	0.332156162	-0.104792838	1.041363252
28.251709	0.003753	0.440702	0.344916485	-0.095785515	0.304765215
28.792819	0.468937	0.909639	0.351522734	-0.558116266	10.09396946
39.122707	0.0029	0.912539	0.477637182	-0.434901818	21.84392214
60.970961	0.005763	0.918302	0.744375839	-0.173926161	7.947747712
68.940719	0.038258	0.95656	0.841676183	-0.114883817	9.390871
78.350719		0.95656	0.95656	0	

Location (mm)	Aperture (mm)	Cum. ap. (mm)	Hom. strain	Difference	Spacing (mm)
Sample 23			V'		C
			0.465249372		1.266121676
loc	ap	cumap	hom strain	difference	spacing
0	0	0	0	0	
48.960000	0.044877	0.044877	0.054466847	0.009589847	7.881048499
56.885104	0.043235	0.088112	0.063283339	-0.024828661	0.050759129
56.963711	0.01246	0.100572	0.063370787	-0.037201213	33.43377
90.403711		0.100572	0.100572	0	

Location (mm)	Aperture (mm)	Cum. ap. (mm)	Hom. strain	Difference	Spacing (mm)

Sample 24

(no fractures in 87.3mm scanline)

Location (mm)	Aperture (mm)	Cum. ap. (mm)	Hom. strain	Difference	Spacing (mm)
Sample 25			V'		C
			0.226997612		1.460928634
loc	ap	cumap	hom strain	difference	spacing
0	0	0	0	0	
6.274000	0.016123	0.016123	0.018681185	0.002558185	11.04188867
17.331454	0.015007	0.03113	0.051605371	0.020475371	0.100137848
17.444478	0.010766	0.041896	0.051941908	0.010045908	2.008203518
19.459141	0.002152	0.044048	0.057940678	0.013892678	0.276729699
19.738556	0.00322	0.047268	0.058772654	0.011504654	34.42277525
54.239565	0.153247	0.200515	0.161501334	-0.039013666	14.2548534
68.572744	0.003404	0.203919	0.204179175	0.000260175	7.099276192
75.676443	0.005441	0.20936	0.225330835	0.015970835	0.126197137
75.809743	0.008766	0.218126	0.225727745	0.007601745	0.021944035
75.841583	0.011025	0.229151	0.225822549	-0.003328451	4.411256367
80.264373	0.012043	0.241194	0.238991654	-0.002202346	0.540973617
80.821806	0.020875	0.262069	0.240651441	-0.021417559	7.1825625
88.014806		0.262069	0.262069	0	

Location (mm)	Aperture (mm)	Cum. ap. (mm)	Hom. strain	Difference	Spacing (mm)
Sample 26			V'		C
			0.4478215		2.701713079
loc	ap	cumap	hom strain	difference	spacing
0	0	0	0	0	
0.154000	0.024347	0.024347	0.001056173	-0.023290827	0.502470847
0.670249	0.003209	0.027556	0.004596744	-0.022959256	1.200843592
1.874330	0.003267	0.030823	0.012854654	-0.017968346	0.655603139
2.533290	0.003446	0.034269	0.017373974	-0.016895026	0.110368479
2.647020	0.003277	0.037546	0.018153964	-0.019392036	1.006342898
3.662073	0.014144	0.05169	0.025115469	-0.026574531	0.08304401
3.758744	0.013109	0.064799	0.025778461	-0.039020539	0.05682395
3.834057	0.02387	0.088669	0.02629498	-0.06237402	0.004370623
3.867279	0.033832	0.122501	0.026522823	-0.095978177	5.896027271
9.793878	0.027311	0.149812	0.067169005	-0.082642995	6.466401325
16.287589	0.027309	0.177121	0.111704596	-0.065416404	0.486235646
16.794348	0.013738	0.190859	0.115180084	-0.075678916	6.148392766
22.951276	0.003331	0.19419	0.15740592	-0.03678408	0.004158014
22.958419	0.00264	0.19683	0.157454912	-0.039375088	0.020791872
22.981861	0.00266	0.19949	0.157615683	-0.041874317	0.022861118
23.008737	0.005369	0.204859	0.157800003	-0.047058997	0.135791294
23.149288	0.004152	0.209011	0.158763944	-0.050247056	0.243167234
23.406923	0.024783	0.233794	0.160530871	-0.073263129	0.281272608
23.701620	0.002066	0.23586	0.162551982	-0.073308018	0.016625726
23.724053	0.009549	0.245409	0.162705835	-0.082703165	1.902373348
25.650220	0.038037	0.283446	0.175915993	-0.107530007	23.7186447
49.390785	0.005804	0.28925	0.338735071	0.049485071	0.218390093
49.625960	0.027765	0.317015	0.34034796	0.02333296	0.084599081
49.752461	0.056039	0.373054	0.341215538	-0.031838462	0.087567517
49.877881	0.019666	0.39272	0.342075702	-0.050644298	0.145594159
50.037733	0.00885	0.40157	0.34317201	-0.05839799	0.121989478
50.172373	0.016452	0.418022	0.34409541	-0.07392659	0.183951369
50.368803	0.008505	0.426527	0.345442578	-0.081084422	0.950291636
51.327723	0.008751	0.435278	0.352019103	-0.083258897	3.118428227
54.516015	0.130977	0.566255	0.373885254	-0.192369746	0.006886739
54.593303	0.009826	0.576081	0.374415318	-0.201665682	0.036394283
54.641976	0.01473	0.590811	0.374749125	-0.216061875	0.056077573
54.709781	0.008726	0.599537	0.375214154	-0.224322846	32.56479361
87.280782	0.003689	0.603226	0.598594697	-0.004631303	0.491003434
87.775437	0.003614	0.60684	0.601987171	-0.004852829	0.01568953
87.795225	0.004582	0.611422	0.602122879	-0.009299121	1.353609
89.151125		0.611422	0.611422	0	

Location (mm)	Aperture (mm)	Cum. ap. (mm)	Hom. strain	Difference	Spacing (mm)
Sample 27			V'		C
			0.7401777		1.075750524
loc	ap	cumap	hom strain	difference	spacing
0	0	0	0	0	
9.295000	0.011646	0.011646	0.035772703	0.024126703	5.11297665
14.418049	0.008498	0.020144	0.05548925	0.03534525	13.94892302
28.376638	0.010835	0.030979	0.109210227	0.078231227	1.292778545
29.677045	0.004421	0.0354	0.114214967	0.078814967	0.300637552
29.984435	0.009085	0.044485	0.115397989	0.070912989	1.454817154
31.444744	0.001898	0.046383	0.121018128	0.074635128	0.736579392
32.183900	0.003255	0.049638	0.123862841	0.074224841	1.506394004
33.692905	0.001968	0.051606	0.129670394	0.078064394	0.053165121
33.750793	0.007477	0.059083	0.12989318	0.07081018	12.76894541
46.525063	0.003173	0.062256	0.179056191	0.116800191	10.04745922
56.575212	0.002205	0.064461	0.217735155	0.153274155	1.957218676
58.669463	0.27186	0.336321	0.225795083	-0.110525917	19.89780822
78.705419	0.004437	0.340758	0.302905393	-0.037852607	2.919990367
81.635450	0.015643	0.356401	0.314181898	-0.042219102	10.9621785
92.605450		0.356401	0.356401	0	

Location (mm)	Aperture (mm)	Cum. ap. (mm)	Hom. strain	Difference	Spacing (mm)
Sample 28			V'		C
			0.419370242		0.596461931
loc	ap	cumap	hom strain	difference	spacing
0	0	0	0	0	
6.063000	0.01097	0.01097	0.029912327	0.018942327	40.88586131
47.103610	0.298528	0.309498	0.232389672	-0.077108328	9.129137048
56.450780	0.137538	0.447036	0.278504731	-0.168531269	34.091231
90.610780		0.447036	0.447036	0	

Location (mm)	Aperture (mm)	Cum. Ap. (mm)	Hom. strain	Difference	Spacing (mm)
Sample 29			V'		C
			0.404931706		1.610931375
loc	ap	cumap	hom strain	difference	spacing
0	0	0	0	0	
21.530000	0.001963	0.001963	0.007046949	0.005083949	0.065005592
21.596683	0.001392	0.003355	0.007068775	0.003713775	3.408846064
25.007570	0.002689	0.006044	0.008185187	0.002141187	0.150685127
25.160971	0.002743	0.008787	0.008235396	-0.000551604	25.51908196
50.682126	0.001404	0.010191	0.016588684	0.006397684	2.659479171
53.343177	0.00174	0.011931	0.017459668	0.005528668	0.253988445
53.600329	0.004587	0.016518	0.017543836	0.001025836	7.537323861
61.141002	0.00211	0.018628	0.020011961	0.001383961	0.071067055
61.213885	0.001522	0.02015	0.020035816	-0.000114184	3.711327543
64.926966	0.001986	0.022136	0.021251139	-0.000884861	0.011255973
64.940217	0.002003	0.024139	0.021255476	-0.002883524	1.373740453
66.317709	0.005501	0.02964	0.021706341	-0.007933659	31.13803306
97.459429	0.001872	0.031512	0.031899286	0.000387286	0.034143456
97.496448	0.00388	0.035392	0.031911403	-0.003480597	10.63206
108.130448		0.035392	0.035392	0	

Location (mm)	Aperture (mm)	Cum. Ap. (mm)	Hom. strain	Difference	Spacing (mm)
Sample 30			V'		C
			0.312235757		1.394237311
loc	ap	cumap	hom strain	difference	spacing
0	0	0	0	0	
1.126900	0.003878	0.003878	0.000551333	-0.003326667	10.19050449
11.323475	0.008263	0.012141	0.005539982	-0.006601018	1.447837392
12.776775	0.002663	0.014804	0.006251006	-0.008552994	0.118055358
12.898469	0.004614	0.019418	0.006310544	-0.013107456	41.09432081
53.997697	0.0052	0.024618	0.026418241	0.001800241	3.45963599
57.461376	0.002886	0.027504	0.028112837	0.000608837	3.645346481
61.112701	0.00907	0.036574	0.029899239	-0.006674761	2.991493195
64.109776	0.002094	0.038668	0.03136555	-0.00730245	7.460398572
71.572718	0.002993	0.041661	0.035016776	-0.006644224	0.09737896
71.674635	0.006084	0.047745	0.035066639	-0.012678361	25.910958
97.588635		0.047745	0.047745	0	

Location (mm)	Aperture (mm)	Cum. Ap. (mm)	Hom. strain	Difference	Spacing (mm)
Sample 31			V'		C
			0.383636371		0.864311718
loc	ap	cumap	hom strain	difference	spacing
0	0	0	0	0	
1.555000	0.005402	0.005402	0.000333321	-0.005068679	23.86496815
25.423678	0.002017	0.007419	0.005449669	-0.001969331	0.00512148
25.430748	0.001881	0.0093	0.005451185	-0.003848815	0.073897941
25.506478	0.001783	0.011083	0.005467418	-0.005615582	7.845696133
33.354911	0.00369	0.014773	0.007149762	-0.007623238	15.4362992
48.794610	0.00311	0.017883	0.010459324	-0.007423676	29.46459266
78.261752	0.001988	0.019871	0.016775727	-0.003095273	14.439006
92.701752		0.019871	0.019871	0	

Location (mm)	Aperture (mm)	Cum. Ap. (mm)	Hom. strain	Difference	Spacing (mm)
Sample 32			V'		C
			0.384559846		1.381087447
loc	ap	cumap	hom strain	difference	spacing
0	0	0	0	0	
6.114000	0.001369	0.001369	0.005131593	0.003762593	1.627099615
7.743100	0.002632	0.004001	0.006498927	0.002497927	0.172864651
7.918438	0.002314	0.006315	0.006646091	0.000331091	25.03075621
32.951810	0.002919	0.009234	0.027657062	0.018423062	6.072534965
39.027167	0.002724	0.011958	0.03275622	0.02079822	6.190295531
45.220765	0.003882	0.01584	0.037954622	0.022114622	5.139560257
50.363288	0.002042	0.017882	0.042270835	0.024388835	7.80746124
58.172990	0.002441	0.020323	0.048825663	0.028502663	0.300088885
58.475287	0.001974	0.022297	0.049079386	0.026782386	8.278181469
66.755936	0.002961	0.025258	0.056029487	0.030771487	0.571563283
67.334900	0.011841	0.037099	0.056515423	0.019416423	0.870663101
68.212421	0.001875	0.038974	0.057251942	0.018277942	2.501412436
70.715836	0.002129	0.041103	0.059353104	0.018250104	17.19032899
87.911994	0.00953	0.050633	0.073786157	0.023153157	0.647390741
88.566980	0.00566	0.056293	0.074335898	0.018042898	0.852295799
89.425755	0.007299	0.063592	0.075056684	0.011464684	1.813486382
91.244071	0.002359	0.065951	0.07658283	0.01063183	3.700214088
94.951115	0.011302	0.077253	0.079694221	0.002441221	2.051048225
97.009297	0.002965	0.080218	0.081421691	0.001203691	0.003959616
97.015784	0.00209	0.082308	0.081427135	-0.000880865	1.048455
98.065284		0.082308	0.082308	0	

Location (mm)	Aperture (mm)	Cum. Ap. (mm)	Hom. strain	Difference	Spacing (mm)
Sample 33			V'		C
			0.28850773		0.89612731
loc	ap	cumap	hom strain	difference	spacing
0	0	0	0	0	
4.591000	0.003049	0.003049	0.004906688	0.001857688	0.204123549
4.799916	0.006536	0.009585	0.005129969	-0.004455031	6.076680857
10.881607	0.003485	0.01307	0.011629852	-0.001440148	5.121197201
16.006943	0.004792	0.017862	0.017107618	-0.000754382	1.626896905
17.637979	0.003485	0.021347	0.018850807	-0.002496193	0.048362346
17.68939036	0.002614	0.023961	0.018905754	-0.005055246	4.728693
22.41939036		0.023961	0.023961	0	

Location (mm)	Aperture (mm)	Cum. Ap. (mm)	Hom. strain	Difference	Spacing (mm)
Sample 34			V'		C
			0.388382989		1.303192696
loc	ap	cumap	hom strain	difference	spacing
0	0	0	0	0	
6.099	0.001725	0.001725	0.005807234	0.004082234	11.28020722
17.38141972	0.0027	0.004425	0.016549922	0.012124922	0.03617668
17.4200264	0.00216	0.006585	0.016586682	0.010001682	3.199984284
20.62217069	0.00216	0.008745	0.019635641	0.010890641	0.003283478
20.62788416	0.0027	0.011445	0.019641082	0.008196082	1.239070073
21.86938374	0.002159	0.013604	0.02082319	0.00721919	0.203542026
22.07535526	0.0027	0.016304	0.021019308	0.004715308	3.072644948
25.15057071	0.002441	0.018745	0.023947411	0.005202411	3.981671741
29.13437795	0.00183	0.020575	0.027740639	0.007165639	0.107992071
29.24359002	0.00061	0.021185	0.027844627	0.006659627	4.288565651
33.53337567	0.00183	0.023015	0.031929197	0.008914197	1.345936471
34.88358264	0.006711	0.029726	0.033214812	0.003488812	0.920068321
35.80944647	0.00488	0.034606	0.034096384	-0.000509616	0.325807389
36.13860885	0.00183	0.036436	0.0344098	-0.0020262	2.127085
38.26660885		0.036436	0.036436	0	

Location (mm)	Aperture (mm)	Cum. Ap. (mm)	Hom. strain	Difference	Spacing (mm)

Sample 35

no fractures within 20.1 mm scanline

Location (mm)	Aperture (mm)	Cum. Ap. (mm)	Hom. strain	Difference	Spacing (mm)
Sample 36			V'		C
			0.471043695		1.380377229
loc	ap	cumap	hom strain	difference	spacing
0	0	0	0	0	
3.265	0.003126	0.003126	0.020257567	0.017131567	0.799010642
4.067392142	0.003637	0.006763	0.025235978	0.018472978	1.759557245
5.835585887	0.013636	0.020399	0.036206668	0.015807668	0.030912095
5.878088982	0.009546	0.029945	0.036470377	0.006525377	0.166364935
6.053317917	0.008182	0.038127	0.037557578	-0.000569422	0.655003883
6.716958299	0.009091	0.047218	0.041675109	-0.005542891	7.454158855
14.17679915	0.002273	0.049491	0.087959404	0.038468404	1.07682839
15.25680904	0.00409	0.053581	0.094660284	0.041079284	4.619830937
19.88059598	0.003822	0.057403	0.123348391	0.065945391	0.270615497
20.15415998	0.002075	0.059478	0.125045709	0.065567709	3.629006875
23.78533635	0.002264	0.061742	0.147575203	0.085833203	0.750900259
24.54085911	0.006981	0.068723	0.152262814	0.083539814	0.829068216
25.37436133	0.001887	0.07061	0.157434247	0.086824247	8.872221826
34.29826365	0.101474	0.172084	0.212802255	0.040718255	0.016231581
34.37391123	0.017358	0.189442	0.213271607	0.023829607	0.015490638
34.40902387	0.021886	0.211328	0.213489462	0.002161462	0.009057302
34.44147817	0.024908	0.236236	0.213690824	-0.022545176	0.063783409
34.51997958	0.004528	0.240764	0.214177883	-0.026586117	4.282736
38.80497958		0.240764	0.240764	0	

Location (mm)	Aperture (mm)	Cum. Ap. (mm)	Hom. strain	Difference	Spacing (mm)
Sample 37			V'		C
			0.641432255		1.63373718
loc	ap	cumap	hom strain	difference	spacing
0	0	0	0	0	
23.7026	0.004149	0.004149	0.088325423	0.084176423	14.83677367
38.54315217	0.003408	0.007557	0.143627291	0.136070291	6.19817341
44.74448558	0.002912	0.010469	0.166735954	0.156266954	4.533762455
49.28215153	0.004895	0.015364	0.183645123	0.168281123	66.73353087
117.1481299	2.26	2.275364	0.436541062	-1.838822938	0.005051811
118.3267177	0.087072	2.362436	0.440932954	-1.921503046	41.1015788
159.473262	0.002859	2.365295	0.594261532	-1.771033468	0.0120602
159.4879037	0.002304	2.367599	0.594316093	-1.773282907	15.53230782
175.0235365	0.004346	2.371945	0.652208111	-1.719736889	5.278192716
180.3058922	0.00398	2.375925	0.671892293	-1.704032707	33.75757671
214.0690475	0.007177	2.383102	0.797707393	-1.585394607	12.76983826
227.2424742	0.8	3.183102	0.846796881	-2.336305119	10.58888239
238.2366956	0.010678	3.19378	0.887765773	-2.306014227	28.53489476
266.7796464	0.005434	3.199214	0.99412829	-2.20508571	44.53939623
311.3273766	0.011234	3.210448	1.160131055	-2.050316945	0.778703387
312.246888	0.270382	3.48083	1.163557524	-2.317272476	25.56913608
337.9542756	0.006121	3.486951	1.259353593	-2.227597407	10.63443156
348.5950036	0.006472	3.493423	1.299005227	-2.194417773	0.01430124
348.6147469	0.004412	3.497835	1.299078798	-2.198756202	0.812336686
349.4307151	0.002851	3.500686	1.302119424	-2.198566576	11.45385471
360.8887858	0.005581	3.506267	1.344816805	-2.161450195	1.15177421
362.044416	0.002131	3.508398	1.349123148	-2.159274852	3.782357418
365.8296554	0.003633	3.512031	1.363228473	-2.148802527	5.090498162
370.9271806	0.010421	3.522452	1.382223902	-2.140228098	1.470225975
372.408677	0.01212	3.534572	1.387744554	-2.146827446	8.78866171
381.5583987	0.71	4.244572	1.421840098	-2.822731902	0.469646745
382.384702	0.003313	4.247885	1.424919237	-2.822965763	53.44755186
435.8361978	0.004575	4.25246	1.624101014	-2.628358986	15.67031397
451.5110988	0.004599	4.257059	1.682512001	-2.574546999	37.37718789
488.8912352	0.001298	4.258357	1.821805428	-2.436551572	0.030437081
488.9233433	0.002044	4.260401	1.821925075	-2.438475925	0.024212631
488.9499869	0.002818	4.263219	1.82202436	-2.44119464	0.017295105
488.9710065	0.004631	4.26785	1.822102688	-2.445747312	18.44806415
507.4233222	0.003872	4.271722	1.89086344	-2.38085856	0.9554258
508.3875815	0.013795	4.285517	1.894456658	-2.391060342	22.01082501
530.408769	0.00693	4.292447	1.976516462	-2.315930538	28.37697032
558.7950573	0.011706	4.304153	2.082295192	-2.221857808	35.80917102
594.6118448	0.003527	4.30768	2.215762952	-2.091917048	156.6337882
751.2494946	0.004196	4.311876	2.799457851	-1.512418149	4.255391258
755.5098113	0.005655	4.317531	2.815333506	-1.502197494	7.403379037
762.9173504	0.002665	4.320196	2.842936976	-1.477259024	4.788055139
767.7095755	0.005675	4.325871	2.860794735	-1.465076265	85.94784147
853.663454	0.006399	4.33227	3.181093466	-1.151176534	4.685086103
858.3556746	0.00787	4.34014	3.198578568	-1.141561432	29.4583702

Location (mm)	Aperture (mm)	Cum. Ap. (mm)	Hom. strain	Difference	Spacing (mm)
887.8222493	0.008539	4.348679	3.30838288	-1.04029612	7.519378165
895.3486359	0.005478	4.354157	3.336429225	-1.017727775	23.36825947
918.7219999	0.004731	4.358888	3.423527782	-0.935360218	2.739985192
921.4718096	0.014918	4.373806	3.433774679	-0.940031321	16.11014574
937.5911133	0.003398	4.377204	3.49384169	-0.88336231	3.089237476
940.6863248	0.00855	4.385754	3.505375693	-0.880378307	4.173045507
944.8648903	0.00249	4.388244	3.520946709	-0.867297291	3.345815885
948.2175052	0.011108	4.399352	3.533439901	-0.865912099	1.873278094
950.0988983	0.005122	4.404474	3.540450729	-0.864023271	0.176775717
950.2850725	0.013675	4.418149	3.541144489	-0.877004511	34.96988553
985.2664915	0.009392	4.427541	3.671499329	-0.756041671	18.16190254
1003.440787	0.015394	4.442935	3.739224066	-0.703710934	1.714399918
1005.165552	0.005336	4.448271	3.745651234	-0.702619766	0.073978276
1005.24605	0.007704	4.455975	3.745951203	-0.710023797	0.011555644
1005.263769	0.004623	4.460598	3.746017232	-0.714580768	0.00385119
1005.277262	0.01466	4.475258	3.746067511	-0.729190489	0.647227737
1005.933743	0.003847	4.479105	3.748513824	-0.730591176	3.125983524
1009.063556	0.003812	4.482917	3.760176767	-0.722740233	0.058557368
1009.125913	0.003787	4.486704	3.760409133	-0.726294867	0.08783286
1009.21641	0.001541	4.488245	3.760746361	-0.727498639	3.626054532
1012.847008	0.007545	4.49579	3.774275428	-0.721514572	1.538714914
1014.390879	0.002767	4.498557	3.780028512	-0.718528488	0.432268915
1014.825962	0.002863	4.50142	3.78164981	-0.71977019	5.376637501
1020.210983	0.013903	4.515323	3.801716563	-0.713606437	1.15563908
1021.380316	0.013485	4.528808	3.806073968	-0.722734032	2.539818205
1023.9278	0.001847	4.530655	3.815566919	-0.715088081	2.70915025
1026.63954	0.003333	4.533988	3.825671955	-0.708316045	7.003245278
1033.646137	0.00337	4.537358	3.851781353	-0.685576647	0.984466236
1034.635243	0.005908	4.543266	3.855467157	-0.687798843	16.85521101
1051.495459	0.004102	4.547368	3.918295105	-0.629072895	4.676109706
1056.177625	0.008011	4.555379	3.93574274	-0.61963626	2.128424919
1058.31229	0.004469	4.559848	3.94369736	-0.61615064	36.65400682
1094.972714	0.008366	4.568214	4.08030885	-0.48790515	14.18471741
1109.162368	0.001507	4.569721	4.133185209	-0.436535791	11.17814889
1120.342891	0.003242	4.572963	4.174848337	-0.398114663	0.004803561
1120.351708	0.004784	4.577747	4.174881191	-0.402865809	0.004736844
1120.36425	0.010827	4.588574	4.174927929	-0.413646071	0.018950084
1120.394136	0.011045	4.599619	4.175039297	-0.424579703	2.095862986
1122.499148	0.007252	4.606871	4.182883416	-0.423987584	0.04027781
1122.545861	0.005618	4.612489	4.183057487	-0.429431513	8.88092204
1131.43215	0.005116	4.617605	4.216171375	-0.401433625	10.97071504
1142.407954	0.005062	4.622667	4.257071637	-0.365595363	6.061420197
1148.473894	0.003979	4.626646	4.279675772	-0.346970228	0.872056839
1149.349467	0.003052	4.629698	4.282938507	-0.346759493	58.05040383
1207.402514	0.002236	4.631934	4.499267518	-0.132666482	14.12595897
1221.530637	0.002092	4.634026	4.551914588	-0.082111412	0.012207164
1221.544795	0.001808	4.635834	4.551967344	-0.083866656	0.229132224
1221.77623	0.002798	4.638632	4.552829764	-0.085802236	13.61636835
1235.396206	0.004417	4.643049	4.603583274	-0.039465726	6.736593087
1242.137579	0.005144	4.648193	4.628704344	-0.019488656	55.02110794

Location (mm)	Aperture (mm)	Cum. Ap. (mm)	Hom. strain	Difference	Spacing (mm)
1297.16909	0.015661	4.663854	4.833773892	0.169919892	63.44259232
1360.623386	0.007747	4.671601	5.070230128	0.398629128	0.951259926
1361.580736	0.004433	4.676034	5.073797599	0.397763599	8.281893561
1369.866271	0.002849	4.678883	5.104672834	0.425789834	0.071579383
1369.940162	0.001775	4.680658	5.104948183	0.424290183	0.042263602
1369.985021	0.003416	4.684074	5.105115346	0.421041346	0.042262231
1370.030111	0.00224	4.686314	5.10528337	0.41896937	3.39797003
1373.431423	0.004443	4.690757	5.117958026	0.427201026	6.062969026
1379.500488	0.007749	4.698506	5.140573803	0.442067803	16.81902047
1396.327163	0.007561	4.706067	5.203276766	0.497209766	14.48546155
1410.819746	0.006681	4.712748	5.257281959	0.544533959	8.304473644
1419.132941	0.010763	4.723511	5.28826027	0.56474927	56.50634366
1475.64611	0.002887	4.726398	5.498851072	0.772453072	18.96816358
1494.628932	0.026429	4.752827	5.569588703	0.816761703	0.13132401
1494.781888	0.016835	4.769662	5.570158678	0.800496678	0.256682808
1495.051865	0.009753	4.779415	5.571164721	0.791749721	26.20306431
1521.263312	0.007013	4.786428	5.668839118	0.882411118	1.657678689
1522.92785	0.006705	4.793133	5.675041855	0.881908855	6.159283492
1529.094167	0.007363	4.800496	5.698020035	0.897524035	0.494762476
1529.597448	0.009674	4.81017	5.699895463	0.889725463	2.404913501
1532.009693	0.00499	4.81516	5.70888446	0.89372446	0.433944987
1532.449681	0.007096	4.822256	5.710524032	0.888268032	46.76946438
1579.223673	0.001958	4.824214	5.884822741	1.060608741	52.2418349
1631.468763	0.004553	4.828767	6.079508967	1.250741967	22.59995734
1654.076161	0.010327	4.839094	6.163753225	1.324659225	8.041013184
1662.123683	0.002691	4.841785	6.19374153	1.35195653	9.021702356
1671.147907	0.002353	4.844138	6.22736942	1.38323142	0.091773832
1671.241529	0.001344	4.845482	6.227718295	1.382236295	21.34225168
1692.585416	0.001925	4.847407	6.307254202	1.459847202	22.77327324
1715.364317	0.009332	4.856739	6.392137554	1.535398554	0.133344323
1715.506541	0.008426	4.865165	6.392667535	1.527502535	13.02119514
1728.533056	0.002215	4.86738	6.441209573	1.573829573	13.23908786
1741.775227	0.003951	4.871331	6.490555229	1.619224229	0.01138181
1741.792211	0.007253	4.878584	6.490618517	1.612034517	0.113020179
1741.911108	0.004501	4.883085	6.491061576	1.607976576	1.918516767
1743.833457	0.003164	4.886249	6.498225023	1.611976023	1.650350041
1745.490607	0.010435	4.896684	6.504400229	1.607716229	4.594357701
1750.095412	0.01046	4.907144	6.521559586	1.614415586	44.71634991
1794.818973	0.003961	4.911105	6.688217564	1.777112564	4.855006306
1799.682764	0.01361	4.924715	6.706342009	1.781627009	17.95408862
1817.645437	0.003557	4.928272	6.773278152	1.845006152	2.883022524
1820.531661	0.002846	4.931118	6.784033384	1.852915384	4.218550559
1824.752928	0.002587	4.933705	6.799763523	1.866058523	26.64206232
1851.40147	0.010374	4.944079	6.899066715	1.954987715	0.011366634
1851.419248	0.002447	4.946526	6.89913296	1.95260696	12.37547988
1863.798718	0.005534	4.95206	6.945263847	1.993203847	6.527187995
1870.330276	0.003207	4.955267	6.969603061	2.014336061	38.84304711
1909.195369	0.040883	4.99615	7.11443003	2.11828003	0.09987251
1909.317132	0.002898	4.999048	7.114883768	2.115835768	0.040137445
1909.362587	0.007738	5.006786	7.115053154	2.108267154	4.625837503

Location (mm)	Aperture (mm)	Cum. Ap. (mm)	Hom. strain	Difference	Spacing (mm)
1914.020262	0.055936	5.062722	7.132409523	2.069687523	0.029384398
1914.082925	0.010623	5.073345	7.132643034	2.059298034	0.223217685
1914.365809	0.108709	5.182054	7.133697172	1.951643172	0.119447125
1914.540566	0.00191	5.183964	7.134348385	1.950384385	0.066568586
1914.611497	0.006816	5.19078	7.134612705	1.943832705	1.470488804
1916.113212	0.055635	5.246415	7.140208697	1.893793697	0.404646902
1916.910676	0.73	5.976415	7.14318037	1.16676537	0.378889464
1917.661143	0.013156	5.989571	7.145976914	1.156405914	17.78388121
1935.453306	0.003406	5.992977	7.212277668	1.219300668	24.62558325
1960.615691	1.070198	7.063175	7.306042838	0.242867838	20.53647653
1981.689179	0.003825	7.067	7.384571133	0.317571133	0.752454116
1982.455738	0.024385	7.091385	7.387427641	0.296042641	0.205144692
1982.675957	0.005763	7.097148	7.388248264	0.291100264	22.05525712
2004.735556	0.002922	7.10007	7.470451207	0.370381207	10.07955496
2014.940257	0.24737	7.34744	7.508478028	0.161038028	0.04292787
2015.119225	0.024709	7.372149	7.509144933	0.136995933	1.235116039
2016.44929	0.165189	7.537338	7.51410129	-0.02323671	6.546062947
2023.079937	0.00398	7.541318	7.53880975	-0.00250825	1.724132215
2024.809511	0.006904	7.548222	7.545254839	-0.002967161	0.004403894
2024.819286	0.003837	7.552059	7.545291263	-0.006767737	0.007154667
2024.843197	0.029676	7.581735	7.545380365	-0.036354635	0.042930196
2024.903667	0.005403	7.587138	7.5456057	-0.0415323	0.052836082
2024.963062	0.007715	7.594853	7.54582703	-0.04902597	0.091922254
2025.061523	0.005363	7.600216	7.546193936	-0.054022064	10.26446599
2035.368783	0.080224	7.68044	7.584602931	-0.095837069	0.004402074
2035.416203	0.005812	7.686252	7.584779638	-0.101472362	12.78616563
2048.207165	0.003782	7.690034	7.63244391	-0.05759009	0.254216534
2048.465876	0.005207	7.695241	7.633407972	-0.061833028	0.011460588
2048.480893	0.001905	7.697146	7.63346393	-0.06368207	7.388906955
2055.873908	0.006311	7.703457	7.661013278	-0.042443722	11.3868445
2067.263908		7.703457	7.703457	0	

Location (mm)	Aperture (mm)	Cum. Ap. (mm)	Hom. strain	Difference	Spacing (mm)
Sample 38			V'		C
			0.903985496		2.13862327
loc	ap	cumap	hom strain	difference	spacing
0	0	0	0	0	
11.046700	0.002762	0.002762	0.234673424	0.231911424	29.36873466
40.417753	0.001875	0.004637	0.858624977	0.853987977	0.112153323
40.531985	0.002283	0.00692	0.861051701	0.854131701	9.948727617
50.487392	0.011074	0.017994	1.072541942	1.054547942	0.186561773
50.724671	0.090361	0.108355	1.077582646	0.969227646	0.126378103
50.908751	0.025044	0.133399	1.081493209	0.948094209	0.595803509
51.647566	0.260978	0.394377	1.097188406	0.702811406	0.083526862
51.904821	0.086478	0.480855	1.102653466	0.621798466	0.077484133
52.095703	0.140318	0.621173	1.10670852	0.48553552	0.17378229
52.508956	0.338623	0.959796	1.115487563	0.155691563	0.862855716
53.685740	0.289235	1.249031	1.140486893	-0.108544107	0.036859317
53.873028	0.011622	1.260653	1.14446559	-0.11618741	0.965169052
54.845494	0.002971	1.263624	1.165124413	-0.098499587	0.70488733
55.659008	0.214282	1.477906	1.182406504	-0.295499496	0.139166699
55.917289	0.023947	1.501853	1.187893367	-0.313959633	0.503274124
56.434698	0.004322	1.506175	1.198885071	-0.307289929	0.708647112
57.200883	0.110755	1.61693	1.215161733	-0.401768267	0.21516202
57.486052	0.029259	1.646189	1.221219795	-0.424969205	0.064696392
57.579265	0.027773	1.673962	1.223199976	-0.450762024	1.109607605
58.720323	0.035129	1.709091	1.247440349	-0.461650651	0.018804681
58.766830	0.020275	1.729366	1.248428326	-0.480937674	0.010531978
58.790843	0.006687	1.736053	1.248938452	-0.487114548	0.00827413
58.804716	0.004512	1.740565	1.24923318	-0.49133182	0.024084805
58.835810	0.009506	1.750071	1.249893729	-0.500177271	0.02708132
58.939313	0.143336	1.893407	1.252092508	-0.641314492	0.173022316
59.414153	0.460301	2.353708	1.262179911	-1.091528089	1.243520242
60.890030	0.004411	2.358119	1.293533069	-1.064585931	2.052962966
62.946740	0.003084	2.361203	1.337225329	-1.023977671	0.086509886
63.036673	0.003762	2.364965	1.339135842	-1.025829158	15.23139686
78.271078	0.002255	2.36722	1.662771866	-0.704448134	4.650364991
82.923805	0.002468	2.369688	1.761613263	-0.608074737	14.47502178
97.402225	0.004328	2.374016	2.069189313	-0.304826687	14.346836
111.751225		2.374016	2.374016	0	

Location (mm)	Aperture (mm)	Cum. Ap. (mm)	Hom. strain	Difference	Spacing (mm)
Sample 39			V'		C
			0.586911199		1.026922152
loc	ap	cumap	hom strain	difference	spacing
0	0	0	0	0	
24.188000	0.005246	0.005246	0.041629696	0.036383696	1.191011284
25.383155	0.003041	0.008287	0.043686663	0.035399663	1.649044885
27.041604	0.015768	0.024055	0.046541002	0.022486002	0.272899304
27.324976	0.005178	0.029233	0.047028711	0.017795711	0.260477106
27.588373	0.00066	0.029893	0.047482039	0.017589039	1.911268789
29.502676	0.00541	0.035303	0.050776726	0.015473726	0.006414355
29.513898	0.004205	0.039508	0.05079604	0.01128804	0.011661782
29.530763	0.006201	0.045709	0.050825065	0.005116065	0.051312687
29.586632	0.002911	0.04862	0.05092122	0.00230122	4.932919452
34.527299	0.012585	0.061205	0.059424548	-0.001780452	2.77756398
37.316306	0.010301	0.071506	0.064224676	-0.007281324	3.833384747
41.156287	0.002892	0.074398	0.070833625	-0.003564375	2.069554
43.227287		0.074398	0.074398	0	

Location (mm)	Aperture (mm)	Cum. Ap. (mm)	Hom. strain	Difference	Spacing (mm)
Sample 40			V'		C
			0.754123312		0.80395552
loc	ap	cumap	hom strain	difference	spacing
0	0	0	0	0	
19.48	0.0056	0.0056	0.057145072	0.051545072	46.46939239
65.96659239	0.0288	0.0344	0.193514666	0.159114666	0.932422085
66.91726448	0.0077	0.0421	0.196303486	0.154203486	68.4367647
135.3604792	0.0052	0.0473	0.397083386	0.349783386	1.016949118
136.3834283	0.0068	0.0541	0.400084233	0.345984233	42.00153407
178.3936624	0.0106	0.0647	0.523322317	0.458622317	69.82461414
248.2817765	0.1164	0.1811	0.728340866	0.547240866	74.712121
323.053	0.001805	0.182905	0.947684139	0.764779139	25.17427375
348.2306042	0.004856	0.187761	1.021543278	0.833782278	28.35713633
376.5913661	0.002395	0.190156	1.104740289	0.914584289	0.021179136
376.6149132	0.002341	0.192497	1.104809365	0.912312365	32.79910637
409.4158436	0.001307	0.193804	1.201031723	1.007227723	60.40490968
469.8236068	0.0044	0.198204	1.378239423	1.180035423	54.81370329
524.7919596	0.304899	0.503103	1.539490475	1.036387475	11.60104949
537.1044845	1.118052	1.621155	1.575609578	-0.045545422	9.225451062
546.8909706	0.004018	1.625173	1.604318483	-0.020854517	7.107020394
554		1.625173	1.625173	0	

Location (mm)	Aperture (mm)	Cum. Ap. (mm)	Hom. strain	Difference	Spacing (mm)
Sample 40 macrofractures			V'		C
			0.227236916		1.176660327
loc	ap	cumap	hom strain	difference	spacing
0	0.75	0.75	0	-0.75	
591.95	0.62	1.37	0.503775879	-0.866224121	1562.15
2154.735	0.65	2.02	1.833775688	-0.186224312	5569.83
7725.59	1.4	3.42	6.574822018	3.154822018	106.52
7833.295	0.97	4.39	6.666483782	2.276483782	1803.4
9637.88	1.4	5.79	8.202266187	2.412266187	183.81
9823.215	1.65	7.44	8.359994547	0.919994547	89.225
9913.64	0.75	8.19	8.436950259	0.246950259	2184.915
12099.24	0.62	8.81	10.29699344	1.48699344	285.875
12385.675	0.5	9.31	10.54076241	1.230762414	291.79
12678.335	1.24	10.55	10.78982914	0.239829141	1428.625
14107.955	0.75	11.3	12.00649959	0.70649959	4260.895
18369.8	1.15	12.45	15.63351997	3.183519965	584.075
18954.95	1	13.45	16.13150874	2.681508741	25.6
18981.425	0.75	14.2	16.15404015	1.954040148	215.84
19198.2	1.12	15.32	16.33852535	1.018525351	146.115
19345.185	0.62	15.94	16.46361615	0.523616149	742.81
20089.005	1.4	17.34	17.09664018	-0.243359822	263.445
20354.175	2.05	19.39	17.32231169	-2.067688313	9.015
20364.79	1.15	20.54	17.33134553	-3.208654474	3079.7
23446.14	2.15	22.69	19.95371195	-2.736288049	4533.9
27981.69	1.15	23.84	23.8136675	-0.026332498	2438.8
30421.74	1.35	25.19	25.89025899	0.700258994	597.165
31019.89	0.62	25.81	26.39931135	0.58931135	444.865
31465.375	0.62	26.43	26.77843897	0.348438974	1586.96
33053.495	1.7	28.13	28.13	0	

Location (mm)	Aperture (mm)	Cum. Ap. (mm)	Hom. strain	Difference	Spacing (mm)
Sample 41			V'		C
			0.21540853		1.007577073
loc	ap	cumap	hom strain	difference	spacing
0	0	0	0	0	
43.764000	0.004347	0.004347	0.005082676	0.000735676	15.70633435
59.474549	0.004083	0.00843	0.006907273	-0.001522727	5.29178563
64.771710	0.006667	0.015097	0.007522476	-0.007574524	5.58648862
70.364432	0.0058	0.020897	0.008172005	-0.012724995	143.1647276
213.533926	0.003733	0.02463	0.024799467	0.000169467	38.06099921
251.600879	0.008175	0.032805	0.029220498	-0.003584502	102.2498374
353.856257	0.002905	0.03571	0.041096263	0.005386263	3.723179892
357.583956	0.006134	0.041844	0.041529192	-0.000314808	55.11916851
412.708720	0.005056	0.0469	0.047931288	0.001031288	36.02655905
448.740015	0.004416	0.051316	0.052115902	0.000799902	11.74748768
460.490867	0.002314	0.05363	0.053480626	-0.000149374	30.73806668
491.231490	0.002798	0.056428	0.057050789	0.000622789	24.86995908
516.105124	0.004551	0.060979	0.059939571	-0.001039429	16.68243533
532.792481	0.005293	0.066272	0.061877612	-0.004394388	0.595700239
533.394328	0.007001	0.073273	0.06194751	-0.01132549	5.635797565
539.034751	0.002249	0.075522	0.062602579	-0.012919421	164.4079025
703.445751	0.003946	0.079468	0.081696992	0.002228992	48.21214423
751.673807	0.027878	0.107346	0.087298117	-0.020047883	115.1870851
866.875723	0.001783	0.109129	0.100677471	-0.008451529	70.28612688
937.167213	0.008945	0.118074	0.108841005	-0.009232995	79.4955275
1016.667213		0.118074	0.118074	0	

Location (mm)	Aperture (mm)	Cum. Ap. (mm)	Hom. strain	Difference	Spacing (mm)
Sample 41 macrofractures			V'		C
			0.422716128		1.312449603
loc	ap	cumap	hom strain	difference	spacing
0	0	0	0	0	
3992.88	1	1	0.973886616	-0.026113384	14.43
4008.12	0.62	1.62	0.977603741	-0.642396259	14.68
4023.36	0.5	2.12	0.981320865	-1.138679135	5789.95
9814.56	2	4.12	2.393828171	-1.726171829	22858
32674.56	2	6.12	7.969514904	1.849514904	3138.39
35814	0.1	6.22	8.735242548	2.515242548	6705.3
42519.6	0.5	6.72	10.37077732	3.650777323	2741.45
45262.8	3	9.72	11.03985973	1.319859731	1216.95
46482	1.5	11.22	11.33722969	0.11722969	5667.78
52151.28	1.5	12.72	12.72	0	

Location	Aperture (mm)	Cum. Ap.(mm)	Hom. strain	Difference	Spacing (mm)
Sample 42			V'		C
			0.212855632		1.791150584
loc	ap	cumap	hom strain	difference	spacing
0	0	0	0	0	
3.727	0.005836	0.005836	0.094025665	0.088189665	16.17442485
20.04410535	0.279525	0.285361	0.505677576	0.220316576	0.066747487
20.25240033	0.003570	0.288931	0.510932492	0.222001492	0.020503697
20.27789003	0.006402	0.295333	0.511575553	0.216242553	3.625144892
23.90775042	0.003029	0.298362	0.603150556	0.304788556	1.260293738
25.33826566	0.337414	0.635776	0.639239943	0.003463943	0.420601858
25.93597452	0.016800	0.652576	0.654319087	0.001743087	3.972359634
29.92130015	0.009132	0.661708	0.754861854	0.093153854	0.99257574
30.91890089	0.000918	0.662626	0.780029569	0.117403569	1.701914601
32.62244599	0.002343	0.664969	0.82300702	0.15803802	4.252337424
36.87838492	0.004860	0.669829	0.930376884	0.260547884	0.0623286
36.94837502	0.010463	0.680292	0.932142612	0.251850612	0.014360162
36.99632068	0.056708	0.737	0.933352197	0.196352197	1.127049661
38.15882634	0.014204	0.751204	0.962680173	0.211476173	1.328927943
39.49594378	0.002175	0.753379	0.996413298	0.243034298	0.021479247
39.52564203	0.014263	0.767642	0.997162532	0.229520532	7.244577949
46.77922848	0.003754	0.771396	1.180157779	0.408761779	0.011071725
46.8043507	0.024347	0.795743	1.180791569	0.385048569	0.051569414
47.12614062	0.516094	1.311837	1.188909763	-0.12292724	0.017326876
47.40319099	0.003353	1.31519	1.195899258	-0.11929074	5.703923582
53.11077407	0.003966	1.319156	1.339891555	0.020735555	1.499161955
54.61320803	0.002578	1.321734	1.377795325	0.056061325	0.131264019
54.74910555	0.006689	1.328423	1.381223781	0.052800781	0.254451027
55.00847607	0.003150	1.331573	1.387767244	0.056194244	0.018490444
55.03458102	0.012079	1.343652	1.388425826	0.044773826	0.039527372
55.08386089	0.007426	1.351078	1.38966907	0.03859107	2.316475117
57.40506201	0.002026	1.353104	1.448228898	0.095124898	0.401785868
57.80990438	0.004087	1.357191	1.45844236	0.10125136	0.018113398
57.83108277	0.002043	1.359234	1.458976654	0.099742654	2.541276928
60.3773097	0.007857	1.367091	1.523213487	0.156122487	0.354239007
60.74648271	0.022011	1.389102	1.532527074	0.143425074	0.024971538
60.78373125	0.002543	1.391645	1.533466789	0.141821789	0.012992698
60.80637695	0.016763	1.408408	1.5340381	0.1256301	0.237726684
61.05950363	0.014037	1.422445	1.540424042	0.117979042	0.280275816
61.35779795	0.022000	1.444445	1.547949484	0.103504484	1.207755968
62.57868091	0.004254	1.448699	1.578750217	0.130051217	0.06900263
62.65807704	0.016533	1.465232	1.580753242	0.115521242	0.034259808
62.70140435	0.001602	1.466834	1.581846314	0.115012314	1.508702953
64.2262223	0.030628	1.497462	1.620314793	0.122852793	1.052504707
65.29478201	0.001482	1.498944	1.647272677	0.148328677	1.970668805
67.26999782	0.007612	1.506556	1.697103903	0.190547903	0.267261501

Location	Aperture (mm)	Cum. Ap.(mm)	Hom. strain	Difference	Spacing (mm)
67.54499982	0.007869	1.514425	1.704041721	0.189616721	0.885726048
68.43539387	0.001467	1.515892	1.726504799	0.210612799	0.635987538
69.0781954	0.012161	1.528053	1.742721553	0.214668553	0.10628943
69.34752833	0.313926	1.841979	1.749516349	-0.09246265	0.056969661
69.57128699	0.019652	1.861631	1.755161387	-0.10646961	5.303157959
74.88558795	0.002634	1.864265	1.889231868	0.024966868	0.025054429
74.92102238	0.018126	1.882391	1.890125816	0.007734816	0.015193705
74.94650709	0.002456	1.884847	1.89076875	0.00592175	0.044866807
74.99366339	0.002123	1.88697	1.891958421	0.004988421	6.831988458
81.82807335	0.002720	1.88969	2.064378582	0.174688582	1.962828361
83.79348271	0.002442	1.892132	2.113962408	0.221830408	0.099654584
83.8959143	0.003112	1.895244	2.116546577	0.221302577	0.201509587
84.15779088	0.117622	2.012866	2.123153263	0.110287263	0.031300433
84.24910182	0.002399	2.015265	2.125456878	0.110191878	0.06596553
84.33736185	0.042190	2.057455	2.127683523	0.070228523	1.303852369
85.66366472	0.002711	2.060166	2.161143815	0.100977815	0.17558505
85.84297076	0.004731	2.064897	2.165667392	0.100770392	2.355202565
88.20264833	0.004219	2.069116	2.225197913	0.156081913	0.014941811
88.22201714	0.004635	2.073751	2.225686554	0.151935554	0.175913791
88.40427143	0.008046	2.081797	2.23028451	0.14848751	0.103890546
88.52339548	0.022421	2.104218	2.2332898	0.1290718	0.009689234
88.54699521	0.005400	2.109618	2.23388518	0.12426718	0.04514418
88.59663539	0.003592	2.11321	2.235137515	0.121927515	1.728002609
90.3317845	0.010701	2.123911	2.278912279	0.155001279	2.093702498
92.4336905	0.005706	2.129617	2.331939676	0.202322676	2.536281185
94.97499868	0.004348	2.133965	2.396052419	0.262087419	0.476947597
95.45838528	0.008530	2.142495	2.408247414	0.265752414	0.006493746
95.53004753	0.121807	2.264302	2.410055326	0.145753326	0.2072564
95.80035643	0.004298	2.2686	2.416874745	0.148274745	1.013271357
96.93085128	0.230149	2.498749	2.445395145	-0.05335386	0.039675904
97.08645269	0.001702	2.500451	2.449320695	-0.05113031	0.129089755
97.21928944	0.005792	2.506243	2.452671933	-0.05357107	3.20023705
100.4251455	0.005446	2.511689	2.533550051	0.021861051	1.59513737
102.0247404	0.003469	2.515158	2.57390502	0.05874702	0.121707037
102.1517969	0.007230	2.522388	2.577110433	0.054722433	0.009476533
102.1667579	0.003739	2.526127	2.577487874	0.051360874	7.325758895
109.4958348	0.002897	2.529024	2.762387613	0.233363613	0.584077344
110.0848792	0.007037	2.536061	2.777248167	0.241187167	1.375268472
111.4648571	0.002382	2.538443	2.812062587	0.273619587	0.022301978
111.4939531	0.011206	2.549649	2.812796628	0.263147628	0.092184994
111.5925836	0.001685	2.551334	2.815284902	0.263950902	0.150542813
111.7540099	0.020082	2.571416	2.819357404	0.247941404	0.020962929
111.7858784	0.001729	2.573145	2.820161389	0.247016389	0.301385627
112.0890305	0.001804	2.574949	2.827809385	0.252860385	0.566355776
112.6575708	0.002565	2.577514	2.842152657	0.264638657	0.069962411
112.7299772	0.002323	2.579837	2.843979344	0.264142344	1.671892135
114.4044383	0.002815	2.582652	2.886223058	0.303571058	2.886968469
117.3127083	0.039788	2.62244	2.959593601	0.337153601	3.221790094
120.5565324	0.004280	2.62672	3.041429586	0.414709586	0.027636344
120.5875647	0.002512	2.629232	3.042212478	0.412980478	0.001947583

Location	Aperture (mm)	Cum. Ap.(mm)	Hom. strain	Difference	Spacing (mm)
120.5917483	0.001960	2.631192	3.042318022	0.411126022	0.00946435
120.6036011	0.002817	2.634009	3.042617049	0.408608049	1.14451891
121.7525001	0.005943	2.639952	3.071601751	0.431649751	0.061364639
121.8211262	0.008580	2.648532	3.073333068	0.424801068	3.011884395
124.8418391	0.009077	2.657609	3.149540349	0.491931349	4.458427517
129.3062056	0.002801	2.66041	3.262168476	0.601758476	4.458359938
133.7675995	0.003267	2.663677	3.374721609	0.711044609	6.458213522
140.2356896	0.016486	2.680163	3.537900161	0.857737161	0.01074698
140.423142	0.336925	3.017088	3.542629258	0.525541258	1.371045959
142.0003345	0.075368	3.092456	3.582419054	0.489963054	0.063650982
142.102782	0.002225	3.094681	3.585003624	0.490322624	0.624899825
142.7306358	0.003683	3.098364	3.600843273	0.502479273	0.374953367
143.1092122	0.003563	3.101927	3.61039409	0.50846709	0.048180395
143.1622641	0.006180	3.108107	3.611732496	0.503625496	0.022771339
143.2020944	0.027938	3.136045	3.612737346	0.476692346	0.02068109
143.239934	0.006379	3.142424	3.613691972	0.471267972	1.54142718
144.7874482	0.005795	3.148219	3.652733037	0.504514037	0.06927503
145.0039537	0.288666	3.436885	3.658195091	0.221310091	0.015712088
145.1676768	0.007356	3.444241	3.662325537	0.218084537	0.270252763
145.4440471	0.004879	3.44912	3.669297874	0.220177874	0.68370671
146.1383343	0.016282	3.465402	3.686813521	0.221411521	0.349568989
146.4973463	0.002604	3.468006	3.695870763	0.227864763	0.072823031
146.5732623	0.003582	3.471588	3.697785991	0.226197991	0.209467434
146.7852522	0.001463	3.473051	3.703134125	0.230083125	0.330701461
147.1170767	0.000783	3.473834	3.711505473	0.237671473	0.115732154
147.2343868	0.002373	3.476207	3.714465002	0.238258002	0.374435616
147.6156805	0.011343	3.48755	3.724084371	0.236534371	0.08529547
147.7088824	0.004470	3.49202	3.726435693	0.234415693	0.174011969
147.8866134	0.002968	3.494988	3.730919533	0.235931533	4.810638528
152.6989744	0.000477	3.495465	3.85232695	0.35686195	1.694916645
154.3952661	0.002273	3.497738	3.895121409	0.397383409	5.21227094
159.610232	0.003117	3.500855	4.026685841	0.525830841	0.214936176
159.8278337	0.002214	3.503069	4.032175549	0.529106549	0.149686658
159.9794493	0.001644	3.504713	4.036000546	0.531287546	0.573567499
160.5555523	0.003427	3.50814	4.050534613	0.542394613	0.558042443
161.3097793	0.388942	3.897082	4.069562434	0.172480434	11.7139952
173.2192155	0.001940	3.899022	4.370016593	0.470994593	0.020331549
173.2527695	0.024505	3.923527	4.370863103	0.447336103	0.029745569
173.2960186	0.002502	3.926029	4.371954201	0.445925201	1.091799139
174.3931482	0.008159	3.934188	4.399632855	0.465444855	0.01349533
174.4126866	0.003927	3.938115	4.400125773	0.462010773	0.049193797
174.4651964	0.002705	3.94082	4.401450503	0.460630503	5.228504633
179.8407485	0.291390	4.23221	4.537066242	0.304856242	0.176139766
180.1668043	0.008442	4.240652	4.545292057	0.304640057	0.198274868
180.3722956	0.005991	4.246643	4.550476243	0.303833243	0.058098243
180.4348244	0.002870	4.249513	4.552053734	0.302540734	1.487676204
181.9276186	0.007366	4.256879	4.58971431	0.33283531	0.135583575
182.0685692	0.003368	4.260247	4.593270245	0.333023245	0.07924781
182.151424	0.003846	4.264093	4.595360526	0.331267526	5.541581192
187.6960577	0.002259	4.266352	4.735241897	0.468889897	4.275047131

Location	Aperture (mm)	Cum. Ap.(mm)	Hom. strain	Difference	Spacing (mm)
191.9732568	0.002045	4.268397	4.843148119	0.574751119	0.026652357
192.0021666	0.002470	4.270867	4.843877464	0.573010464	1.273167912
193.2786176	0.004096	4.274963	4.876080079	0.601117079	0.012768429
193.2957955	0.004723	4.279686	4.876513448	0.596827448	1.269880112
194.6286561	0.121238	4.400924	4.91013918	0.50921518	0.007403166
194.7237813	0.054206	4.45513	4.912539021	0.457409021	0.00740505
194.7590363	0.001494	4.456624	4.913428444	0.456804444	0.014739756
194.7761511	0.003256	4.45988	4.913860219	0.453980219	0.007052817
194.7913589	0.013054	4.472934	4.914243886	0.441309886	0.0018561
194.802244	0.005004	4.477938	4.914518498	0.436580498	0.589192814
195.3956753	0.003473	4.481411	4.929489728	0.448078728	0.26051721
195.6681035	0.020349	4.50176	4.936362613	0.434602613	0.025758431
195.7330144	0.057956	4.559716	4.938000202	0.378284202	1.757793392
197.5213598	0.003148	4.562864	4.983117015	0.420253015	7.594517534
205.1203369	0.005771	4.568635	5.17482586	0.60619086	0.005740769
205.1307331	0.003540	4.572175	5.17508814	0.60291314	0.010414869
205.147254	0.008672	4.580847	5.175504932	0.594657932	0.1066556
205.2597656	0.003040	4.583887	5.178343402	0.594456402	1.125442018
206.6543136	0.535172	5.119059	5.2135254	0.0944664	3.416092297
210.3412469	0.006510	5.125569	5.306540252	0.180971252	0.401636616
210.7469985	0.001720	5.127289	5.316776652	0.189487652	2.34936345
213.413028	0.631612	5.758901	5.384035893	-0.37486511	0.138885802
213.8695553	0.003671	5.762572	5.395553275	-0.36701872	0.05522252
213.9280743	0.002922	5.765494	5.397029607	-0.36846439	3.44320181
217.3746086	0.003743	5.769237	5.483979615	-0.28525738	0.007135534
217.3855257	0.003820	5.773057	5.484255033	-0.28880197	0.014652759
217.4026029	0.001029	5.774086	5.484685862	-0.28940014	0.011271761
217.4149562	0.001134	5.77522	5.484997513	-0.29022249	9.35309269
226.7688634	0.000495	5.775715	5.720980164	-0.05473484	1.362316836
228.1324382	0.002021	5.777736	5.755380762	-0.02235524	0.247909996
228.3869832	0.011249	5.788985	5.761802485	-0.02718251	0.387483406
228.7809936	0.001805	5.79079	5.771742676	-0.01904732	0.7540975
229.5359936		5.79079	5.79079	0	

Location	Aperture (mm)	Cum. Ap.(mm)	Hom. strain	Difference	Spacing (mm)
Sample 42a			V'		C
	0-25,155-180		0.227171254		1.774302533
loc	ap	cumap	hom strain	difference	spacing
0	0	0	0	0	
20.04410535	0.279525	0.279525	0.475709657	0.196184657	0.066747487
20.25240033	0.003570	0.283095	0.480653152	0.197558152	0.020503697
20.27789003	0.006402	0.289497	0.481258103	0.191761103	4.888467629
25.33826566	0.337414	0.626911	0.601356731	-0.02555427	0.420601858
25.93597452	0.016800	0.643711	0.615542242	-0.02816876	3.972359634
29.92130015	0.009132	0.652843	0.710126553	0.057283553	0.99257574
30.91890089	0.000918	0.653761	0.733802756	0.080041756	1.701914601
32.62244599	0.002343	0.656104	0.774233238	0.118129238	4.252337424
36.87838492	0.004860	0.660964	0.875240054	0.214276054	0.0623286
36.94837502	0.010463	0.671427	0.876901139	0.205474139	0.014360162
36.99632068	0.056708	0.728135	0.87803904	0.14990404	1.127049661
38.15882634	0.014204	0.742339	0.905628955	0.163289955	8.611423139
46.77922848	0.003754	0.746093	1.110218209	0.364125209	0.011071725
46.8043507	0.024347	0.77044	1.110814438	0.340374438	0.051569414
47.12614062	0.516094	1.286534	1.118451525	-0.16808248	0.017326876
47.40319099	0.003353	1.289887	1.125026801	-0.1648602	7.207051537
54.61320803	0.002578	1.292465	1.296143181	0.003678181	0.392404045
55.00847607	0.003150	1.295615	1.305524134	0.009909134	0.018490444
55.03458102	0.012079	1.307694	1.306143687	-0.00155031	0.039527372
55.08386089	0.007426	1.31512	1.307313253	-0.00780675	2.316475117
57.40506201	0.002026	1.317146	1.362402656	0.045256656	0.401785868
57.80990438	0.004087	1.321233	1.372010838	0.050777838	0.018113398
57.83108277	0.002043	1.323276	1.372513468	0.049237468	2.541276928
60.3773097	0.007857	1.331133	1.432943441	0.101810441	0.354239007
60.74648271	0.022011	1.353144	1.441705077	0.088561077	0.024971538
60.78373125	0.002543	1.355687	1.442589102	0.086902102	0.012992698
60.80637695	0.016763	1.37245	1.443126556	0.070676556	0.237726684
61.05950363	0.014037	1.386487	1.449134048	0.062647048	1.510031784
62.57868091	0.004254	1.390741	1.485188903	0.094447903	0.06900263
62.65807704	0.016533	1.407274	1.487073223	0.079799223	0.034259808
62.70140435	0.001602	1.408876	1.488101516	0.079225516	2.59183566
65.29478201	0.001482	1.410358	1.549650524	0.139292524	3.139137354
68.43539387	0.001467	1.411825	1.62418712	0.21236212	0.635987538
69.0781954	0.012161	1.423986	1.639442822	0.215456822	0.10628943
69.34752833	0.313926	1.737912	1.64583494	-0.09207706	0.056969661
69.57128699	0.019652	1.757564	1.651145436	-0.10641856	12.24560036
81.82807335	0.002720	1.760284	1.942037523	0.181753523	2.269546532
84.15779088	0.117622	1.877906	1.997329047	0.119423047	0.031300433
84.24910182	0.002399	1.880305	1.999496143	0.119191143	0.06596553
84.33736185	0.042190	1.922495	2.001590831	0.079095831	1.303852369
85.66366472	0.002711	1.925206	2.033068169	0.107862169	0.17558505

Location	Aperture (mm)	Cum. Ap.(mm)	Hom. strain	Difference	Spacing (mm)
85.84297076	0.004731	1.929937	2.037323665	0.107386665	2.355202565
88.20264833	0.004219	1.934156	2.093326235	0.159170235	0.014941811
88.22201714	0.004635	1.938791	2.093785918	0.154994918	0.175913791
88.40427143	0.008046	1.946837	2.098111385	0.151274385	0.103890546
88.52339548	0.022421	1.969258	2.100938573	0.131680573	0.009689234
88.54699521	0.005400	1.974658	2.101498669	0.126840669	0.04514418
88.59663539	0.003592	1.97825	2.102676787	0.124426787	6.374393292
94.97499868	0.004348	1.982598	2.254055407	0.271457407	0.476947597
95.45838528	0.008530	1.991128	2.265527691	0.274399691	0.006493746
95.53004753	0.121807	2.112935	2.267228462	0.154293462	0.2072564
95.80035643	0.004298	2.117233	2.273643742	0.156410742	1.013271357
96.93085128	0.230149	2.347382	2.300473941	-0.04690806	0.039675904
97.08645269	0.001702	2.349084	2.304166851	-0.04491715	4.935702174
102.0247404	0.003469	2.352553	2.421367948	0.068814948	0.121707037
102.1517969	0.007230	2.359783	2.424383399	0.064600399	0.009476533
102.1667579	0.003739	2.363522	2.424738472	0.061216472	9.295038711
111.4648571	0.002382	2.365904	2.645411608	0.279507608	0.022301978
111.4939531	0.011206	2.37711	2.646102147	0.268992147	0.244412807
111.7540099	0.020082	2.397192	2.652274113	0.255082113	0.324077555
112.0890305	0.001804	2.398996	2.660225204	0.261229204	0.566355776
112.6575708	0.002565	2.401561	2.673718453	0.272157453	0.069962411
112.7299772	0.002323	2.403884	2.675436885	0.271552885	1.671892135
114.4044383	0.002815	2.406699	2.715177114	0.308478114	6.148546563
120.5565324	0.004280	2.410979	2.861185653	0.450206653	0.027636344
120.5875647	0.002512	2.413491	2.861922149	0.448431149	0.001947583
120.5917483	0.001960	2.415451	2.862021438	0.446570438	0.00946435
120.6036011	0.002817	2.418268	2.862302744	0.444034744	1.14451891
121.7525001	0.005943	2.424211	2.889569728	0.465358728	0.061364639
121.8211262	0.008580	2.432791	2.891198442	0.458407442	7.479388912
129.3062056	0.002801	2.435592	3.068842916	0.633250916	4.458359938
133.7675995	0.003267	2.438859	3.174725825	0.735866825	6.458213522
140.2356896	0.016486	2.455345	3.328233943	0.872888943	0.01074698
140.423142	0.336925	2.79227	3.33268278	0.54041278	1.371045959
142.0003345	0.075368	2.867638	3.370114517	0.502476517	0.063650982
142.102782	0.002225	2.869863	3.372545918	0.502682918	0.624899825
142.7306358	0.003683	2.873546	3.387446864	0.513900864	0.374953367
143.1092122	0.003563	2.877109	3.396431672	0.519322672	0.048180395
143.1622641	0.006180	2.883289	3.39769076	0.51440176	0.022771339
143.2020944	0.027938	2.911227	3.398636059	0.487409059	0.02068109
143.239934	0.006379	2.917606	3.399534112	0.481928112	1.54142718
144.7874482	0.005795	2.923401	3.43626149	0.51286049	0.06927503
145.0039537	0.288666	3.212067	3.441399847	0.229332847	0.015712088
145.1676768	0.007356	3.219423	3.445285511	0.225862511	0.270252763
145.4440471	0.004879	3.224302	3.451844646	0.227542646	0.68370671
146.1383343	0.016282	3.240584	3.468322265	0.227738265	0.349568989
146.4973463	0.002604	3.243188	3.476842749	0.233654749	0.072823031
146.5732623	0.003582	3.24677	3.478644475	0.231874475	0.541631895
147.1170767	0.000783	3.247553	3.491550901	0.243997901	0.115732154
147.2343868	0.002373	3.249926	3.49433504	0.24440904	0.374435616
147.6156805	0.011343	3.261269	3.503384336	0.242115336	0.08529547

Location	Aperture (mm)	Cum. Ap.(mm)	Hom. strain	Difference	Spacing (mm)
147.7088824	0.004470	3.265739	3.505596312	0.239857312	0.174011969
147.8866134	0.002968	3.268707	3.509814427	0.241107427	4.810638528
152.6989744	0.000477	3.269184	3.624026889	0.354842889	1.694916645
154.3952661	0.002273	3.271457	3.664285224	0.392828224	5.21227094
159.610232	0.003117	3.274574	3.788052767	0.513478767	0.214936176
159.8278337	0.002214	3.276788	3.793217139	0.516429139	0.724898157
160.5555523	0.003427	3.280215	3.810488191	0.530273191	0.558042443
161.3097793	0.388942	3.669157	3.828388368	0.159231368	11.7139952
173.2192155	0.001940	3.671097	4.111036744	0.439939744	0.020331549
173.2527695	0.024505	3.695602	4.111833087	0.416231087	0.029745569
173.2960186	0.002502	3.698104	4.112859523	0.414755523	1.091799139
174.3931482	0.008159	3.706263	4.13889786	0.43263486	0.01349533
174.4126866	0.003927	3.71019	4.139361566	0.429171566	0.049193797
174.4651964	0.002705	3.712895	4.140607788	0.427712788	5.228504633
179.8407485	0.291390	4.004285	4.268186546	0.263901546	0.176139766
180.1668043	0.008442	4.012727	4.275924875	0.263197875	1.752910315
181.9276186	0.007366	4.020093	4.317714536	0.297621536	10.04093271
191.9732568	0.002045	4.022138	4.556129124	0.533991124	0.026652357
192.0021666	0.002470	4.024608	4.556815246	0.532207246	1.273167912
193.2786176	0.004096	4.028704	4.58710944	0.55840544	1.287371541
194.6286561	0.121238	4.149942	4.6191501	0.4692081	0.007403166
194.7237813	0.054206	4.204148	4.62140772	0.41725972	0.00740505
194.7590363	0.001494	4.205642	4.622244433	0.416602433	0.014739756
194.7761511	0.003256	4.208898	4.62265062	0.41375262	0.007052817
194.7913589	0.013054	4.221952	4.623011549	0.401059549	0.0018561
194.802244	0.005004	4.226956	4.623269887	0.396313887	0.589192814
195.3956753	0.003473	4.230429	4.637353878	0.406924878	2.122374033
197.5213598	0.003148	4.233577	4.687803057	0.454226057	7.594517534
205.1203369	0.005771	4.239348	4.868150681	0.628802681	0.005740769
205.1307331	0.003540	4.242888	4.868397417	0.625509417	0.010414869
205.147254	0.008672	4.25156	4.868789509	0.617229509	0.1066556
205.2597656	0.003040	4.2546	4.871459763	0.616859763	1.125442018
206.6543136	0.535172	4.789772	4.904556773	0.114784773	3.416092297
210.3412469	0.006510	4.796282	4.992059295	0.195777295	0.401636616
210.7469985	0.001720	4.798002	5.001689057	0.203687057	2.34936345
213.413028	0.631612	5.429614	5.064962321	-0.36465168	0.197779322
213.9280743	0.002922	5.432536	5.07718599	-0.35535001	14.20189239
228.1324382	0.002021	5.434557	5.414300216	-0.02025678	0.247909996
228.3869832	0.011249	5.445806	5.42034137	-0.02546463	0.387483406
228.7809936	0.001805	5.447611	5.429692476	-0.01791852	0.7540975
229.5359936		5.447611	5.447611	0	

Location	Aperture (mm)	Cum. Ap.(mm)	Hom. strain	Difference	Spacing (mm)
Sample 43			V'		C
			0.773846873		1.261971822
loc	ap	cumap	hom strain	difference	spacing
0	0	0	0	0	
0.360500	0.007173	0.007173	0.007735785	0.000562785	2.078080572
2.443996	0.003657	0.01083	0.052444449	0.041614449	5.373385202
7.821487	0.004555	0.015385	0.167837277	0.152452277	0.022581144
7.849539	0.006387	0.021772	0.168439234	0.146667234	0.231740753
8.087944	0.006942	0.028714	0.17355505	0.14484105	2.445690804
10.612605	0.150998	0.179712	0.227730453	0.048018453	1.802753678
12.500206	0.018697	0.198409	0.268235519	0.069826519	0.075881534
12.586895	0.002918	0.201327	0.270095735	0.068768735	16.69748207
29.290838	0.010004	0.211331	0.628537091	0.417206091	0.601947888
29.899291	0.003005	0.214336	0.641593559	0.427257559	4.68590911
34.589326	0.005248	0.219584	0.74223463	0.52265063	3.941653563
38.555999	0.04479	0.264374	0.827353425	0.562979425	0.055636411
38.638637	0.009213	0.273587	0.829126709	0.555539709	4.975623631
43.624328	0.010923	0.28451	0.936112112	0.651602112	1.683732359
45.320888	0.014731	0.299241	0.97251771	0.67327671	5.571866498
50.901108	0.001977	0.301218	1.092260802	0.791042802	4.083376488
54.987630	0.004313	0.305531	1.179951373	0.874420373	0.136458048
55.133281	0.014073	0.319604	1.183076824	0.863472824	3.85663353
58.999758	0.005615	0.325219	1.266045585	0.940826585	7.204429807
66.214266	0.014541	0.33976	1.420858011	1.081098011	1.71198671
67.939360	0.011673	0.351433	1.457875913	1.106442913	0.039829377
67.986317	0.002582	0.354015	1.458883537	1.104868537	2.046171716
70.034869	0.00218	0.356195	1.50284238	1.14664738	22.97326102
93.060423	0.102406	0.458601	1.996935947	1.538334947	1.493095785
94.638611	0.067778	0.526379	2.03080147	1.50442247	8.120056527
102.802070	0.019026	0.545405	2.205976944	1.660571944	11.89168524
114.708039	0.009543	0.554948	2.461461049	1.906513049	0.076737599
114.792412	0.005726	0.560674	2.463271546	1.902597546	2.844096371
117.645634	0.012527	0.573201	2.524497394	1.951296394	15.07063164
132.741390	0.037721	0.610922	2.84842948	2.23750748	0.036556518
132.798720	0.003825	0.614747	2.849659685	2.234912685	2.341343605
135.146916	0.009881	0.624628	2.900048433	2.275420433	0.067804155
135.222102	0.004882	0.62951	2.901661803	2.272151803	8.340348886
143.568261	0.006738	0.636248	3.080757751	2.444509751	1.434961985
145.081761	0.150339	0.786587	3.113235182	2.326648182	0.771680302
147.511965	3.166708	3.953295	3.16538368	-0.78791132	14.37207367
163.469335	0.003885	3.95718	3.507804711	-0.44937529	0.206176414
163.684736	0.014563	3.971743	3.512426878	-0.45931612	4.070717049
167.764213	0.002958	3.974701	3.599966297	-0.3747347	3.235175704
171.002691	0.003647	3.978348	3.669459142	-0.30888886	0.054750671
171.070418	0.022304	4.000652	3.670912443	-0.32973956	0.05152043

Location	Aperture (mm)	Cum. Ap.(mm)	Hom. strain	Difference	Spacing (mm)
171.136136	0.006092	4.006744	3.672322661	-0.33442134	1.407209215
172.548754	0.004725	4.011469	3.702635301	-0.3088337	13.49243069
186.045148	0.003202	4.014671	3.992247509	-0.02242349	4.255957039
190.364674	0.123937	4.138608	4.084938016	-0.05366998	0.245806106
190.691686	0.038473	4.177081	4.091955179	-0.08512582	3.9477635
194.658686		4.177081	4.177081	0	

Location Aperture (mm) Cum. Ap.(mm) Hom. strain Difference Spacing (mm)

Sample 43 macrofractures			V'		C
			0.217180396		1.086986226
loc	ap	cumap	hom strain	difference	spacing
0	0	0	0	0	
17.325	2.65	2.65	0.160619604	-2.4893804	315
334.525	1.75	4.4	3.101372183	-1.29862782	102
437.65	0.5	4.9	4.057441255	-0.84255874	52
490.1	0.4	5.3	4.54370378	-0.75629622	77
568	1.4	6.7	5.265912562	-1.43408744	164
733.575	1.75	8.45	6.800953887	-1.64904611	160
894.76	0.62	9.07	8.295295642	-0.77470436	120
1015.27	0.4	9.47	9.412540576	-0.05745942	110
1126.345	1.75	11.22	10.44231388	-0.77768612	200
1328.545	2.65	13.87	12.31690459	-1.55309541	14
1344.0025	0.265	14.135	12.46021065	-1.67478935	280
1624.3	0.33	14.465	15.05884115	0.593841154	142
1766.94	0.95	15.415	16.38125272	0.966252717	15
1784.415	4	19.415	16.54326297	-2.87173703	140
1926.5475	0.265	19.68	17.86096951	-1.81903049	590
2516.99	0.62	20.3	23.33494588	3.034945881	44
2561.61	0.62	20.92	23.74861669	2.828616689	18
2580.495	1.15	22.07	23.92369901	1.85369901	60
2641.38	0.62	22.69	24.48816219	1.798162191	222
2864.065	0.75	23.44	26.55266877	3.112668773	22
2886.5475	0.215	23.655	26.76110342	3.10610342	12
2898.905	0.5	24.155	26.87566947	2.720669467	40
2939.405	0.5	24.655	27.25114387	2.596143866	30
2970.73	2.15	26.805	27.54155709	0.736557089	0
2972.18	0.75	27.555	27.555	0	

Location	Aperture (mm)	Cum. Ap.(mm)	Hom. strain	Difference	Spacing (mm)
Sample 43ew			V'		C
	0-20,170-180	EW strike	0.900368812		1.07008331
loc	ap	cumap	hom strain	difference	spacing
0	0	0	0	0	
0.360500	0.007173	0.007173	0.006424488	-0.00074851	12.22134969
12.586895	0.002918	0.010091	0.224311678	0.214220678	16.69748207
29.290838	0.010004	0.020095	0.521993468	0.501898468	5.290861998
34.589326	0.005248	0.025343	0.616418083	0.591075083	16.30816946
50.901108	0.001977	0.02732	0.907111151	0.879791151	51.89046001
102.802070	0.019026	0.046346	1.832040736	1.785694736	14.82778821
117.645634	0.012527	0.058873	2.096568632	2.037695632	15.07063164
132.741390	0.037721	0.096594	2.365590835	2.268996835	0.036556518
132.798720	0.003825	0.100419	2.366612507	2.266193507	2.341343605
135.146916	0.009881	0.1103	2.408459835	2.298159835	9.854735026
145.081761	0.150339	0.260639	2.585509196	2.324870196	0.771680302
147.511965	3.166708	3.427347	2.628817977	-0.79852902	36.94822785
186.045148	0.003202	3.430549	3.315519722	-0.11502928	4.625700145
190.691686	0.038473	3.469022	3.398325898	-0.0706961	3.9477635
194.6586855		3.469022	3.469022	0	

Location	Aperture (mm)	Cum. Ap.(mm)	Hom. strain	Difference	Spacing (mm)
Sample 43ew macrofractures			V'		C
	EW strike macros		0.217180396		1.086986226
loc	ap	cumap	hom strain	difference	spacing
0	0	0	0	0	
17.325	2.65	2.65	0.160619604	-2.4893804	315
334.525	1.75	4.4	3.101372183	-1.29862782	102
437.65	0.5	4.9	4.057441255	-0.84255874	52
490.1	0.4	5.3	4.54370378	-0.75629622	77
568	1.4	6.7	5.265912562	-1.43408744	164
733.575	1.75	8.45	6.800953887	-1.64904611	160
894.76	0.62	9.07	8.295295642	-0.77470436	120
1015.27	0.4	9.47	9.412540576	-0.05745942	110
1126.345	1.75	11.22	10.44231388	-0.77768612	200
1328.545	2.65	13.87	12.31690459	-1.55309541	14
1344.0025	0.265	14.135	12.46021065	-1.67478935	280
1624.3	0.33	14.465	15.05884115	0.593841154	142
1766.94	0.95	15.415	16.38125272	0.966252717	15
1784.415	4	19.415	16.54326297	-2.87173703	140
1926.5475	0.265	19.68	17.86096951	-1.81903049	590
2516.99	0.62	20.3	23.33494588	3.034945881	44
2561.61	0.62	20.92	23.74861669	2.828616689	18
2580.495	1.15	22.07	23.92369901	1.85369901	60
2641.38	0.62	22.69	24.48816219	1.798162191	222
2864.065	0.75	23.44	26.55266877	3.112668773	22
2886.5475	0.215	23.655	26.76110342	3.10610342	12
2898.905	0.5	24.155	26.87566947	2.720669467	40
2939.405	0.5	24.655	27.25114387	2.596143866	30
2970.73	2.15	26.805	27.54155709	0.736557089	0
2972.18	0.75	27.555	27.555	0	

Location	Aperture (mm)	Cum. Ap.(mm)	Hom. strain	Difference	Spacing (mm)
Sample 43ne			V'		C
	120-150	NE strike	0.350581153		1.269704504
loc	ap	cumap	hom strain	difference	spacing
0	0	0	0	0	
2.443996	0.003657	0.003657	0.004953199	0.001296199	5.373385202
7.821487	0.004555	0.008212	0.015851656	0.007639656	0.022581144
7.849539	0.006387	0.014599	0.015908509	0.001309509	0.231740753
8.087944	0.006942	0.021541	0.01639168	-0.00514932	30.44218865
38.555999	0.04479	0.066331	0.078140698	0.011809698	0.055636411
38.638637	0.009213	0.075544	0.078308179	0.002764179	4.975623631
43.624328	0.010923	0.086467	0.088412584	0.001945584	11.35568335
54.987630	0.004313	0.09078	0.111442368	0.020662368	0.136458048
55.133281	0.014073	0.104853	0.111737556	0.006884556	3.85663353
58.999758	0.005615	0.110468	0.119573671	0.009105671	7.204429807
66.214266	0.014541	0.125009	0.134195175	0.009186175	1.71198671
67.939360	0.011673	0.136682	0.137691389	0.001009389	0.039829377
67.986317	0.002582	0.139264	0.137786556	-0.00147744	25.02161273
93.060423	0.102406	0.24167	0.188603764	-0.05306624	1.493095785
94.638611	0.067778	0.309448	0.191802246	-0.11764575	20.03076777
114.708039	0.009543	0.318991	0.232476569	-0.08651443	0.076737599
114.792412	0.005726	0.324717	0.232647564	-0.09206944	20.42438629
135.222102	0.004882	0.329599	0.274052023	-0.05554698	8.340348886
143.568261	0.006738	0.336337	0.290967022	-0.04536998	19.89576296
163.469335	0.003885	0.340222	0.331300146	-0.00892185	0.206176414
163.684736	0.014563	0.354785	0.331736694	-0.02304831	4.070717049
167.764213	0.002958	0.357743	0.340004492	-0.01773851	3.235175704
171.002691	0.003647	0.36139	0.346567853	-0.01482215	0.054750671
171.070418	0.022304	0.383694	0.346705113	-0.03698889	0.05152043
171.136136	0.006092	0.389786	0.346838303	-0.0429477	1.407209215
172.548754	0.004725	0.394511	0.349701228	-0.04480977	22.10756934
194.6586855		0.394511	0.394511	0	

Location	Aperture (mm)	Cum. Ap.(mm)	Hom. strain	Difference	Spacing (mm)
Sample 44			V'		C
			0.605964163		1.65476457
loc	ap	cumap	hom strain	difference	spacing
0	0	0	0	0	
20.230000	0.01003	0.01003	0.185052096	0.175022096	22.27995705
42.517595	0.005245	0.015275	0.388925851	0.373650851	0.094362927
42.616177	0.003195	0.01847	0.38982763	0.37135763	3.855579225
46.478854	0.011	0.02947	0.425161116	0.395691116	0.472279085
46.957976	0.002686	0.032156	0.429543842	0.397387842	2.184524079
49.145579	0.003472	0.035628	0.449554743	0.413926743	0.124512481
49.273918	0.004181	0.039809	0.450728712	0.410919712	0.080715138
49.358855	0.004263	0.044072	0.451505667	0.407433667	0.675753187
50.038087	0.002693	0.046765	0.457718873	0.410953873	0.655944255
50.696640	0.002525	0.04929	0.463742929	0.414452929	0.025484337
50.724635	0.002497	0.051787	0.463999014	0.412212014	0.140943209
50.868095	0.002537	0.054324	0.465311304	0.410987304	0.113294922
50.987779	0.010241	0.064565	0.466406101	0.401841101	0.2572883
51.251154	0.001931	0.066496	0.468815294	0.402319294	0.07937855
51.332625	0.002254	0.06875	0.469560543	0.400810543	2.257625102
53.592645	0.002536	0.071286	0.490233873	0.418947873	1.597107222
55.191869	0.001697	0.072983	0.504862627	0.431879627	0.0033965
55.196956	0.001685	0.074668	0.504909164	0.430241164	4.447446572
59.646091	0.001691	0.076359	0.545607221	0.469248221	0.236045015
59.901987	0.038012	0.114371	0.547948011	0.433577011	0.056890301
59.980002	0.004238	0.118609	0.548661649	0.430052649	1.097280409
61.081579	0.004355	0.122964	0.558738224	0.435774224	8.880873814
69.966277	0.003293	0.126257	0.640010194	0.513753194	0.1359059
70.106295	0.004931	0.131188	0.641290995	0.510102995	1.036999936
71.149879	0.008236	0.139424	0.65083708	0.51141308	1.458716076
72.616404	0.007383	0.146807	0.66425199	0.51744499	0.087313206
72.709829	0.004841	0.151648	0.665106589	0.513458589	1.508960702
74.223268	0.004114	0.155762	0.678950628	0.523188628	0.026358668
74.253330	0.003293	0.159055	0.679225619	0.520170619	0.059303717
74.315496	0.002432	0.161487	0.679794279	0.518307279	2.09788736
76.416234	0.003269	0.164756	0.699010588	0.534254588	0.009060776
76.430631	0.007403	0.172159	0.699142281	0.526983281	5.307721759
81.743700	0.003293	0.175452	0.747743107	0.572291107	0.033769292
81.781166	0.0041	0.179552	0.748085822	0.568533822	3.491530984
85.281748	0.014001	0.193553	0.780107074	0.586554074	1.060884093
86.352086	0.004908	0.198461	0.7898979	0.5914369	3.241137775
89.597726	0.004097	0.202558	0.819587101	0.617029101	0.01070733
89.612950	0.004936	0.207494	0.819726359	0.612232359	0.009059135
89.676949	0.104944	0.312438	0.820311785	0.507873785	4.594422622
94.328761	0.009834	0.322272	0.862863812	0.540591812	0.387124783
94.722862	0.004119	0.326391	0.866468817	0.540077817	0.313819015

Location	Aperture (mm)	Cum. Ap.(mm)	Hom. strain	Difference	Spacing (mm)
95.048461	0.019441	0.345832	0.869447205	0.523615205	15.02746055
110.087772	0.00426	0.350092	1.007017943	0.656925943	0.008575884
110.100620	0.004284	0.354376	1.007135468	0.652759468	0.824407601
110.929314	0.004288	0.358664	1.014715868	0.656051868	1.768867428
112.701387	0.002123	0.360787	1.030925744	0.670138744	0.003484127
112.706858	0.001852	0.362639	1.030975796	0.668336796	0.051026753
112.760481	0.00334	0.365979	1.031466305	0.665487305	2.85053684
115.616072	0.006768	0.372747	1.057587564	0.684840564	0.103631694
115.724759	0.003342	0.376089	1.058581766	0.682492766	7.277907519
123.005440	0.002206	0.378295	1.125181141	0.746886141	2.63547156
125.644747	0.005465	0.38376	1.149323964	0.765563964	0.040115608
125.689806	0.004421	0.388181	1.149736134	0.761555134	5.380485891
131.699500	1.253995	1.642176	1.204709265	-0.43746673	0.457609023
132.788442	0.008671	1.650847	1.214670264	-0.43617674	0.005521653
132.799946	0.003294	1.654141	1.214775497	-0.4393655	0.210970164
133.013339	0.001552	1.655693	1.216727492	-0.43896551	0.023194793
133.047794	0.020969	1.676662	1.217042668	-0.45961933	0.015462555
133.076493	0.005503	1.682165	1.217305186	-0.46485981	0.669367805
133.751889	0.006553	1.688718	1.223483308	-0.46523469	6.00996426
139.767284	0.004308	1.693026	1.278508587	-0.41451741	3.278352148
143.049006	0.002433	1.695459	1.308527849	-0.38693115	6.477184298
149.530717	0.006621	1.70208	1.367818717	-0.33426128	0.022089737
149.564904	0.017573	1.719653	1.368131437	-0.35152156	0.022117238
149.599665	0.007715	1.727368	1.368449412	-0.35891859	0.018776342
149.623956	0.003313	1.730681	1.368671606	-0.36200939	5.169386463
154.801049	0.012101	1.742782	1.4160286	-0.3267534	5.219086197
160.028382	0.004392	1.747174	1.463845153	-0.28332885	0.119291055
160.159256	0.018774	1.765948	1.465042312	-0.30090569	0.00780867
160.184112	0.01532	1.781268	1.465269677	-0.31599832	3.658322139
163.852296	0.004405	1.785673	1.498824064	-0.28684894	1.320541125
165.180869	0.011658	1.797331	1.510977062	-0.28635394	2.243491301
167.437193	0.014008	1.811339	1.531616584	-0.27972242	2.239973122
169.686182	0.004023	1.815362	1.552189004	-0.263173	0.126193738
169.817305	0.005836	1.821198	1.553388442	-0.26780956	0.754849547
170.579162	0.008178	1.829376	1.560357456	-0.26901854	7.535532706
178.122851	0.008135	1.837511	1.629362671	-0.20814833	0.037405437
178.166645	0.004642	1.842153	1.629763272	-0.21238973	0.029209239
178.201085	0.00582	1.847973	1.630078311	-0.21789469	0.026875055
178.240785	0.019829	1.867802	1.630441459	-0.23736054	0.81442265
179.070977	0.01171	1.879512	1.638035567	-0.24147643	0.920753292
180.000497	0.005823	1.885335	1.646538265	-0.23879673	1.705989616
181.716401	0.014006	1.899341	1.662234343	-0.23710666	0.685903564
182.411611	0.004607	1.903948	1.668593714	-0.23535429	0.12736093
182.544770	0.006989	1.910937	1.669811773	-0.24112523	0.09231167
182.643481	0.00581	1.916747	1.670714725	-0.24603228	3.90155397
186.550847	0.005814	1.922561	1.706457002	-0.216104	0.037407601
186.594665	0.007008	1.929569	1.706857828	-0.22271117	1.385815224
187.991579	0.015188	1.944757	1.719635966	-0.22512103	10.39598438
198.396323	0.002333	1.94709	1.814812429	-0.13227757	0.109836226
198.509077	0.003501	1.950591	1.815843829	-0.13474717	2.850475689

Location	Aperture (mm)	Cum. Ap.(mm)	Hom. strain	Difference	Spacing (mm)
201.365177	0.007749	1.95834	1.841969752	-0.11637025	0.7795625
202.149718	0.002207	1.960547	1.849146265	-0.11140074	0.082178658
202.235771	0.005541	1.966088	1.849933424	-0.11615458	2.5862959
204.829238	0.008802	1.97489	1.873656932	-0.10123307	4.115430741
208.951828	0.005517	1.980407	1.911367954	-0.06903905	0.069965143
209.030572	0.012041	1.992448	1.912088259	-0.08035974	0.009993898
209.052127	0.01108	2.003528	1.912285426	-0.09124257	3.122667253
212.185269	0.00987	2.013398	1.940945561	-0.07245244	2.517455207
214.712649	0.009979	2.023377	1.964064538	-0.05931246	3.175965315
217.897486	0.007764	2.031141	1.993197545	-0.03794345	4.144118
222.045486		2.031141	2.031141	0	

Location	Aperture (mm)	Cum. Ap.(mm)	Hom. strain	Difference	Spacing (mm)
Sample 44 macrofractures			V'		C
			0.340419825		1.777752839
loc	ap	cumap	hom strain	difference	spacing
0	0	0	0	0	
0	7	7	0	-7	23
26.875	0.75	7.75	0.284641159	-7.46535884	85
113.9	3.3	11.05	1.206348949	-9.84365105	7
123.875	2.65	13.7	1.311997156	-12.3880028	12
137.575	0.75	14.45	1.457097951	-12.992902	28
170.95	10	24.45	1.810582553	-22.6394174	24
201.025	2.15	26.6	2.129115869	-24.4708841	102
304.41	0.62	27.22	3.224097309	-23.9959027	28
333.03	0.62	27.84	3.527220285	-24.3127797	4
338.99	3.3	31.14	3.590344426	-27.5496556	46
386.7725	0.265	31.405	4.096423168	-27.3085768	110
497.0375	0.265	31.67	5.264272745	-26.4057273	2
499.2775	0.215	31.885	5.287997254	-26.5970027	9
508.4925	0.215	32.1	5.385596074	-26.7144039	29
538.925	2.65	34.75	5.707915779	-29.0420842	251
791.415	0.33	35.08	8.382112847	-26.6978872	195
986.6875	0.215	35.295	10.45030227	-24.8446977	158
1145.105	0.62	35.915	12.12814937	-23.7868506	181
1327.74	2.65	38.565	14.06249125	-24.5025088	30
1359.265	0.4	38.965	14.39638195	-24.5686181	62
1421.715	0.5	39.465	15.05780857	-24.4071914	81
1504.615	3.3	42.765	15.93582725	-26.8291728	126
1632.39	0.25	43.015	17.28913047	-25.7258695	37
1670.39	1.75	44.765	17.69159983	-27.0734002	87
1758.84	1.15	45.915	18.62840022	-27.2865998	21
1780.725	0.62	46.535	18.8601908	-27.6748092	70
1852.685	3.3	49.835	19.62234067	-30.2126593	117
1972.66	2.65	52.485	20.89303176	-31.5919682	63
2037.86	1.75	54.235	21.58358445	-32.6514156	95
2135.385	3.3	57.535	22.61650088	-34.9184991	205
2342.1425	0.215	57.75	24.80633137	-32.9436686	112
2455.575	2.65	60.4	26.00772888	-34.3922711	3
2460.975	2.15	62.55	26.0649219	-36.4850781	9
2471.925	1.75	64.3	26.18089662	-38.1191034	2
2475.375	1.15	65.45	26.2174366	-39.2325634	74
2550.26	0.62	66.07	27.01056602	-39.059434	4
2555.445	1.75	67.82	27.06548191	-40.7545181	42
2600.82	5	72.82	27.5460621	-45.2739379	16
2619.52	0.4	73.22	27.74411939	-45.4758806	26
2646.195	0.95	74.17	28.02664229	-46.1433577	22
2669.245	1.15	75.32	28.27077173	-47.0492283	13

Location	Aperture (mm)	Cum. Ap.(mm)	Hom. strain	Difference	Spacing (mm)
2683.02	0.4	75.72	28.41666687	-47.3033331	34
2717.42	0.4	76.12	28.78100755	-47.3389924	8
2727.62	4	80.12	28.8890388	-51.2309612	14
2743.7525	0.265	80.385	29.05990293	-51.3250971	180
2924.195	0.62	81.005	30.97102339	-50.0339766	26
2950.67	0.33	81.335	31.25142803	-50.083572	641
3592.31	0.95	82.285	38.04722908	-44.2377709	41
3634.035	0.5	82.785	38.48915103	-44.295849	357
3991.4175	0.265	83.05	42.27429592	-40.7757041	52
4043.925	0.75	83.8	42.83041855	-40.9695815	86
4130.55	0.5	84.3	43.74788982	-40.5521102	7
4137.9325	0.265	84.565	43.82608008	-40.7389199	248
4386.375	0.62	85.185	46.45740887	-38.7275911	66
4452.995	0.62	85.805	47.1630012	-38.6419988	67
4520.47	0.33	86.135	47.8776491	-38.2573509	75
4595.7675	0.265	86.4	48.67514743	-37.7248526	58
4654.1	0.4	86.8	49.29296438	-37.5070356	21
4675.465	0.33	87.13	49.51924748	-37.6107525	32
4707.88	0.5	87.63	49.86256443	-37.7674356	23
4731.44	0.62	88.25	50.11209544	-38.1379046	50
4781.915	0.33	88.58	50.64669125	-37.9333088	157
4939.1875	0.215	88.795	52.31241131	-36.4825887	22
4961.605	0.62	89.415	52.54984176	-36.8651582	41
5003.0225	0.215	89.63	52.98850688	-36.6414931	116
5119.705	1.15	90.78	54.22432612	-36.5556739	12
5133.155	1.75	92.53	54.36677909	-38.1632209	183
5317.73	1.4	93.93	56.32166809	-37.6083319	73
5392.505	2.15	96.08	57.11363247	-38.9663675	16
5410.655	2.15	98.23	57.30586454	-40.9241355	84
5496.605	1.75	99.98	58.21618669	-41.7638133	9
5507.055	1.15	101.13	58.32686576	-42.8031342	148
5655.88	0.5	101.63	59.90311582	-41.7268842	6
5662.295	0.33	101.96	59.97105901	-41.988941	125
5787.66	0.4	102.36	61.2988372	-41.0611628	132
5920.025	0.33	102.69	62.70075448	-39.9892455	89
6010.065	1.75	104.44	63.65439504	-40.785605	100
6112.265	2.65	107.09	64.73682579	-42.3531742	121
6235.29	1.4	108.49	66.03982034	-42.4501797	68
6304.865	1.75	110.24	66.77670996	-43.46329	64
6371.065	2.65	112.89	67.47785395	-45.412146	94
6466.64	0.5	113.39	68.49011735	-44.8998827	218
6685.0225	0.265	113.655	70.80307169	-42.8519283	2
6687.405	0.5	114.155	70.82830546	-43.3266945	501
7189.03	0.75	114.905	76.14116579	-38.7638342	53
7243.105	1.4	116.305	76.71389028	-39.5911097	88
7332.88	2.15	118.455	77.66472414	-40.7902759	148
7482.53	1.15	119.605	79.24971203	-40.355288	74
7557.58	0.95	120.555	80.04458901	-40.510411	53
7611.1425	0.175	120.73	80.61188546	-40.1181145	29
7640.705	0.95	121.68	80.92499073	-40.7550093	17

Location	Aperture (mm)	Cum. Ap.(mm)	Hom. strain	Difference	Spacing (mm)
7658.43	0.5	122.18	81.11272151	-41.0672785	89
7747.845	0.33	122.51	82.0597425	-40.4502575	139
7887.21	0.4	122.91	83.53579888	-39.3742011	48
7935.885	0.95	123.86	84.05133035	-39.8086696	218
8154.735	0.75	124.61	86.36923613	-38.2407639	210
8365.2425	0.265	124.875	88.59878399	-36.276216	231
8596.5075	0.265	125.14	91.04818074	-34.0918193	109
8707.29	3.3	128.44	92.22151131	-36.2184887	146
8855.14	0.4	128.84	93.78743486	-35.0525651	510
9366.415	2.15	130.99	99.20250122	-31.7874988	12
9379.965	0.95	131.94	99.34601332	-32.5939867	283
9665.94	5	136.94	102.37486	-34.56514	187
9855.915	0.95	137.89	104.386942	-33.503058	201
10057.7	0.62	138.51	106.5241073	-31.9858927	5
10063.32	0.62	139.13	106.5836304	-32.5463696	128
10192.105	0.95	140.08	107.9476308	-32.1323692	809
11002.055	0.95	141.03	116.5260534	-24.5039466	18
11021.23	1.4	142.43	116.7291416	-25.7008584	117
11140.005	2.15	144.58	117.9871231	-26.5928769	75
11216.39	0.62	145.2	118.7961395	-26.4038605	998
12215.175	0.95	146.15	129.37457	-16.77543	175
12390.96	0.62	146.77	131.2363615	-15.5336385	1842
14235.27	4	150.77	150.77	0	

Location (mm)	Aperture (mm)	Cum. Ap (mm)	HomStrain	Difference	Spacing (mm)
Sample 45			V'		C
			0.309691789		1.869531408
loc	ap	cumap	hom strain	difference	spacing
0	0	0	0	0	
1.908000	0.007158	0.007158	0.092000918	0.084842918	0.035027418
1.967424	0.041636	0.048794	0.094866274	0.046072274	0.777530325
2.843124	0.154702	0.203496	0.137091191	-0.06640481	0.003447105
2.925808	0.003772	0.207268	0.141078096	-0.0661899	0.049629096
2.977762	0.000879	0.208147	0.143583269	-0.06456373	0.033093273
3.012512	0.002433	0.21058	0.145258827	-0.06532117	0.438396693
3.456911	0.009572	0.220152	0.166687094	-0.05346491	0.253663061
3.716956	0.003193	0.223345	0.179226104	-0.0441189	3.269361999
6.989553	0.003277	0.226622	0.337025855	0.110403855	0.002757189
6.995566	0.003234	0.229856	0.337315778	0.107459778	0.807174658
8.005418	0.40212	0.631976	0.386009321	-0.24596668	0.163364178
8.371157	0.00263	0.634606	0.403644719	-0.23096128	0.004135014
8.378711	0.004208	0.638814	0.404008962	-0.23480504	0.009673937
8.391677	0.002377	0.641191	0.404634185	-0.23655682	0.0158533
8.415898	0.014357	0.655548	0.405802052	-0.24974595	0.104085175
8.528786	0.003249	0.658797	0.411245351	-0.24755165	0.481132998
9.105622	0.188157	0.846954	0.439059524	-0.40789448	1.570229948
10.772405	0.00495	0.851904	0.519429338	-0.33247466	1.180085954
11.955985	0.002038	0.853942	0.576499801	-0.2774422	0.003446615
11.962006	0.00311	0.857052	0.576790106	-0.28026189	0.028261281
11.992788	0.001932	0.858984	0.578274381	-0.28070962	0.055147461
12.050350	0.002896	0.86188	0.581049909	-0.28083009	0.026202914
12.087519	0.019036	0.880916	0.582842139	-0.29807386	0.004824614
12.103946	0.004169	0.885085	0.58363423	-0.30145077	0.00068959
12.107877	0.002314	0.887399	0.583823781	-0.30357522	0.1399293
12.251575	0.005224	0.892623	0.590752699	-0.3018703	0.771323184
13.031620	0.012219	0.904842	0.628365292	-0.27647671	0.399108805
13.442057	0.010437	0.915279	0.648155943	-0.26712306	0.348098875
13.801447	0.012146	0.927425	0.665485211	-0.26193979	0.643805539
14.464034	0.025417	0.952842	0.697434171	-0.25540783	0.017246474
14.495344	0.00271	0.955552	0.698943892	-0.25660811	1.992079502
16.489340	0.001124	0.956676	0.795091432	-0.16158457	0.055147823
16.546986	0.003871	0.960547	0.797871004	-0.162676	0.097192757
16.663953	0.035677	0.996224	0.803510967	-0.19271303	0.244701685
16.935411	0.017836	1.01406	0.816600276	-0.19745972	0.287438096
17.232940	0.002347	1.016407	0.83094671	-0.18546029	1.222822099
18.458980	0.004088	1.020495	0.890064513	-0.13043049	1.288989958
19.771810	0.043592	1.064087	0.953367218	-0.11071978	0.004873808
19.800780	0.0046	1.068687	0.954764099	-0.1139229	0.042736989
19.847520	0.003407	1.072094	0.957017855	-0.11507614	0.037910633
19.889396	0.004523	1.076617	0.959037036	-0.11757996	0.85679918
20.749881	0.002848	1.079465	1.000528325	-0.07893667	0.113733708
20.867466	0.004855	1.08432	1.006198109	-0.07812189	0.043446955
20.916918	0.007156	1.091476	1.008582633	-0.08289337	0.075134402
20.999607	0.007952	1.099428	1.012569744	-0.08685826	0.376368237
21.381488	0.003075	1.102503	1.030983513	-0.07151949	0.005557472
21.389482	0.001798	1.104301	1.03136897	-0.07293203	0.020677973
21.413255	0.004392	1.108693	1.032515267	-0.07617773	0.042053041

Location (mm)	Aperture (mm)	Cum. Ap (mm)	HomStrain	Difference	Spacing (mm)
21.458485	0.001961	1.110654	1.034696168	-0.07595783	0.342915552
21.804851	0.00494	1.115594	1.051397424	-0.06419658	0.994816206
22.804798	0.005321	1.120915	1.099613364	-0.02130164	0.576013659
23.384161	0.001378	1.122293	1.127549392	0.005256392	0.067555276
23.457259	0.009708	1.132001	1.131074082	-0.00092692	0.130278479
23.593693	0.002603	1.134604	1.137652726	0.003048726	0.727750957
24.323647	0.001804	1.136408	1.172850042	0.036442042	0.036405465
24.361555	0.0012	1.137608	1.174677884	0.037069884	0.008037754
24.372603	0.004821	1.142429	1.175210614	0.032781614	0.002410328
24.378762	0.002677	1.145106	1.175507607	0.030401607	0.007108077
24.389097	0.003776	1.148882	1.176005925	0.027123925	0.00241011
24.395799	0.004808	1.15369	1.176329091	0.022639091	0.002410345
24.402619	0.004011	1.157701	1.176657934	0.018956934	0.003443399
24.409732	0.003329	1.16103	1.177000931	0.015970931	0.001891632
24.414293	0.002008	1.163038	1.177220814	0.014182814	0.004752617
24.420785	0.001471	1.164509	1.177533854	0.013024854	0.482745231
24.912665	0.0168	1.181309	1.20125161	0.01994261	0.560778624
25.497103	0.030518	1.211827	1.229432322	0.017605322	0.959527352
26.476279	0.00878	1.220607	1.276646747	0.056039747	0.002069062
26.486757	0.008038	1.228645	1.277151984	0.048506984	1.180582889
27.676379	0.010039	1.238684	1.334513755	0.095829755	0.227899286
27.924106	0.029617	1.268301	1.346458795	0.078157795	0.359346931
28.302583	0.008642	1.276943	1.364708365	0.087765365	0.232628424
28.541025	0.002987	1.27993	1.376205727	0.096275727	0.438779345
29.013714	0.064831	1.344761	1.398998055	0.054237055	0.216078023
29.269455	0.014495	1.359256	1.411329506	0.052073506	0.1148941
29.407611	0.03203	1.391286	1.417991212	0.026705212	0.077543401
29.508904	0.015469	1.406755	1.422875405	0.016120405	0.019857453
29.556052	0.039111	1.445866	1.425148785	-0.02071722	1.355912635
30.933221	0.003402	1.449268	1.491553829	0.042285829	0.330962541
31.267827	0.003886	1.453154	1.507688057	0.054534057	4.172439746
35.450293	0.016165	1.469319	1.709360301	0.240041301	0.052978327
35.520978	0.019248	1.488567	1.712768618	0.224201618	3.454215909
39.232678	0.495722	1.984289	1.891741306	-0.09254769	1.423537451
40.909654	0.011155	1.995444	1.972602588	-0.02284141	9.605150663
50.521400	0.002035	1.997479	2.436066645	0.438587645	1.3378398
51.874660	0.028805	2.026284	2.501318816	0.475034816	1.539370059
53.430241	0.003618	2.029902	2.576326641	0.546424641	0.01098891
53.448820	0.011561	2.041463	2.577222465	0.535759465	0.681889589
54.145336	0.017693	2.059156	2.610807457	0.551651457	0.166767248
54.721102	0.800304	2.85946	2.638570024	-0.22088998	0.337493734
55.501800	0.086105	2.945565	2.676214129	-0.26935087	2.499793786
58.046251	0.003208	2.948773	2.798903732	-0.14986927	0.215013362
58.264868	0.003999	2.952772	2.809445111	-0.14332689	0.646561371
58.914100	0.001343	2.954115	2.840750129	-0.11336487	0.014504777
58.930077	0.001601	2.955716	2.841520505	-0.1141955	0.028194208
58.960424	0.002705	2.958421	2.842983802	-0.1154372	0.00460893
58.967176	0.001581	2.960002	2.84330937	-0.11669263	0.011458756
58.980039	0.001227	2.961229	2.843929593	-0.11729941	0.003120517
58.984645	0.001744	2.962973	2.844151688	-0.11882131	0.016197944
59.002502	0.001575	2.964548	2.845012748	-0.11953525	0.001222153
59.005526	0.002029	2.966577	2.845158568	-0.12141843	0.007048502
59.015946	0.004713	2.97129	2.845660981	-0.12562902	0.001829667
59.020687	0.001111	2.972401	2.845889617	-0.12651138	0.001767057
59.025601	0.005182	2.977583	2.846126541	-0.13145646	0.004504459
59.033961	0.002529	2.980112	2.846529646	-0.13358235	0.002376017

Location (mm)	Aperture (mm)	Cum. Ap (mm)	HomStrain	Difference	Spacing (mm)
59.038954	0.002706	2.982818	2.846770426	-0.13604757	0.030294692
59.235753	0.330301	3.313119	2.856259742	-0.45685926	4.942537528
64.346600	0.006319	3.319438	3.102697195	-0.2167408	1.371826497
65.728087	0.013002	3.33244	3.16931044	-0.16312956	1.103102165
66.874872	0.074363	3.406803	3.224606688	-0.18219631	0.372654482
67.285554	0.001693	3.408496	3.244409186	-0.16408681	0.7993784
68.087061	0.002564	3.41106	3.283056655	-0.12800335	0.224726434
68.314266	0.002393	3.413453	3.294012138	-0.11944086	1.672251274
69.992168	0.008909	3.422362	3.374918086	-0.04744391	3.405249155
73.402730	0.001716	3.424078	3.539370288	0.115292288	0.012095745
73.416628	0.001889	3.425967	3.540040441	0.114073441	0.013565245
73.431607	0.000938	3.426905	3.540762693	0.113857693	1.080960982
74.686213	0.346352	3.773257	3.601257925	-0.17199908	0.085963163
74.946334	0.001964	3.775221	3.61380058	-0.16142042	0.046148972
74.994450	0.001969	3.77719	3.616120636	-0.16106936	2.130235328
77.126592	0.001845	3.779035	3.718929363	-0.06010564	0.011479944
77.139613	0.001238	3.780273	3.719557237	-0.06071576	0.002382635
77.143645	0.002059	3.782332	3.719751613	-0.06258039	1.565391129
78.713075	0.00602	3.788352	3.79542722	0.00707522	0.423790493
79.141631	0.00351	3.791862	3.816091527	0.024229527	0.584548576
79.964568	0.473268	4.26513	3.855772351	-0.40935765	0.005319923
80.208876	0.004708	4.269838	3.867552515	-0.40228548	0.027618149
80.249740	0.021783	4.291621	3.869522899	-0.4220981	1.327690624
82.052764	0.928885	5.220506	3.956462061	-1.26404394	0.049990112
82.572390	0.010385	5.230891	3.981517609	-1.24937339	0.035698295
82.614267	0.001974	5.232865	3.983536894	-1.24932811	1.585823913
84.203191	0.004225	5.23709	4.060152414	-1.17693759	2.493343675
86.699967	0.002641	5.239731	4.180543266	-1.05918773	0.755379389
87.457940	0.002546	5.242277	4.217091589	-1.02518541	0.003501831
87.463717	0.002004	5.244281	4.217370139	-1.02691086	0.051146101
87.520562	0.009394	5.253675	4.220111125	-1.03356387	0.003486916
87.529857	0.002222	5.255897	4.220559312	-1.03533769	0.006418554
87.539637	0.0045	5.260397	4.221030868	-1.03936613	6.434969748
93.978846	0.003979	5.264376	4.531519945	-0.73285606	6.406650227
100.388878	0.002784	5.26716	4.840602125	-0.42655787	4.762795807
105.156538	0.006946	5.274106	5.070491627	-0.20361437	0.023013209
105.185442	0.004834	5.27894	5.071885296	-0.2070547	1.961205868
107.149843	0.001557	5.280497	5.166605804	-0.1138912	0.629768044
107.877366	0.193952	5.474449	5.201685857	-0.27276314	0.295019167
108.273172	0.007623	5.482072	5.220771065	-0.26130093	0.207138933
108.552071	0.135897	5.617969	5.234219156	-0.38374984	3.099398496
111.738187	0.037537	5.655506	5.387848899	-0.2676571	0.046031876
111.809190	0.012406	5.667912	5.391272576	-0.27663942	0.021629849
111.881311	0.088577	5.756489	5.39475016	-0.36173884	0.092063922
112.044163	0.052999	5.809488	5.402602637	-0.40688536	0.354997347
112.437860	0.024399	5.833887	5.421586088	-0.41230091	0.166684642
112.618332	0.003176	5.837063	5.430288186	-0.40677481	3.220060633
115.842175	0.00439	5.841453	5.585737123	-0.25571588	0.546089898
116.391333	0.001745	5.843198	5.612216675	-0.23098133	1.800778098
118.197835	0.009703	5.852901	5.699323515	-0.15357749	1.929103035
120.133750	0.003921	5.856822	5.792670454	-0.06415155	0.265714122
120.402935	0.003021	5.859843	5.805650159	-0.05419284	0.010483705
120.416463	0.003068	5.862911	5.806302469	-0.05660853	1.172466
121.590463		5.862911	5.862911	0	

Location (mm)	Aperture (mm)	Cum. Ap (mm)	HomStrain	Difference	Spacing (mm)
Sample 46			V'		C
			0.299017389		1.850079615
loc	ap	cumap	hom strain	difference	spacing
0	0	0	0	0	
0.642000	0.001844	0.001844	0.037439927	0.035595927	0.186449872
0.830379	0.002015	0.003859	0.048425768	0.044566768	0.029957808
0.863299	0.003908	0.007767	0.050345544	0.042578544	0.021666148
0.888528	0.003219	0.010986	0.051816878	0.040830878	0.453750835
1.344809	0.001841	0.012827	0.0784261	0.0655991	0.100051919
1.447021	0.002478	0.015305	0.084386829	0.069081829	0.079658578
1.528741	0.001645	0.01695	0.089152552	0.072202552	0.001274201
1.533028	0.004382	0.021332	0.0894026	0.0680706	0.014019416
1.550167	0.001857	0.023189	0.090402101	0.067213101	0.075836414
1.629481	0.005098	0.028287	0.095027502	0.066740502	0.957220772
2.591189	0.003877	0.032164	0.151112061	0.118948061	0.017843291
2.612797	0.003652	0.035816	0.152372177	0.116556177	0.003874786
2.620067	0.003138	0.038954	0.152796134	0.113842134	0.544887736
3.184775	0.036502	0.075456	0.185728558	0.110272558	0.63474444
3.841854	0.008168	0.083624	0.224047882	0.140423882	0.021029878
4.069763	0.40559	0.489214	0.23733899	-0.25187501	0.045882436
4.332314	0.027746	0.51696	0.252650313	-0.26430969	1.496367939
5.844103	0.003097	0.520057	0.340814309	-0.17924269	1.932284202
7.780796	0.00572	0.525777	0.453757662	-0.07201934	0.008284531
7.795099	0.006317	0.532094	0.454591781	-0.07750222	0.019754214
7.819789	0.003556	0.53565	0.456031685	-0.07961831	0.005734953
7.830237	0.005869	0.541519	0.456640956	-0.08487804	0.044608438
8.163857	0.572155	1.113674	0.476096914	-0.63757709	0.010196655
8.478433	0.036604	1.150278	0.494442254	-0.65583575	0.272127318
8.771582	0.005438	1.155716	0.511537972	-0.64417803	0.469681777
9.247173	0.006381	1.162097	0.539273335	-0.62282367	5.339901218
14.594049	0.007569	1.169666	0.851090552	-0.31857545	1.078298968
15.678868	0.00547	1.175136	0.914354607	-0.26078139	2.635205681
18.318205	0.002793	1.177929	1.06827453	-0.10965447	0.006372873
18.327707	0.003465	1.181394	1.068828657	-0.11256534	0.60798005
18.940240	0.005642	1.187036	1.10455017	-0.08248583	0.0356932
19.011499	0.065489	1.252525	1.108705809	-0.14381919	0.059905233
19.120360	0.032422	1.284947	1.115054311	-0.16989269	0.003876967
19.178616	0.076337	1.361284	1.11845169	-0.24283231	1.010111163
20.248359	0.042927	1.404211	1.18083659	-0.22337441	0.295068254
20.566404	0.003025	1.407236	1.199384181	-0.20785182	1.389937943
21.963403	0.011097	1.418333	1.280853866	-0.13747913	0.461399326
22.528430	0.19616	1.614493	1.313804957	-0.30068804	0.741810853
23.370995	0.005348	1.619841	1.362941353	-0.25689965	0.063729636
23.438957	0.003117	1.622958	1.366904745	-0.25605326	0.129371277
23.571507	0.00324	1.626198	1.374634735	-0.25156326	0.006372506
23.581056	0.003112	1.62931	1.375191582	-0.25411842	0.013382793
23.597364	0.002739	1.632049	1.376142643	-0.25590636	0.795981384
24.396303	0.003176	1.635225	1.422734875	-0.21249012	0.439095934
24.930284	0.186595	1.82182	1.453875414	-0.36794459	0.661521498
25.687008	0.00381	1.82563	1.498005774	-0.32762423	0.010195116
25.701214	0.004211	1.829841	1.498834212	-0.33100679	0.015930087
25.720009	0.001519	1.83136	1.499930297	-0.3314297	0.011489042

Location (mm)	Aperture (mm)	Cum. Ap (mm)	Hom. Strain	Difference	Spacing (mm)
25.733207	0.001899	1.833259	1.500699976	-0.33255902	0.017206016
25.752956	0.003186	1.836445	1.501851662	-0.33459334	0.142752056
25.899753	0.004905	1.84135	1.51041255	-0.33093745	0.005734734
25.912404	0.008927	1.850277	1.511150311	-0.33912669	0.05672079
25.975423	0.003669	1.853946	1.514825418	-0.33912058	1.049625557
27.034848	0.015931	1.869877	1.576608619	-0.29326838	0.0223042
27.070853	0.011471	1.881348	1.578708358	-0.30263964	0.005734236
27.086457	0.008268	1.889616	1.579618331	-0.30999767	0.003876828
27.103381	0.017827	1.907443	1.580605318	-0.32683768	1.071292066
28.185473	0.003771	1.911214	1.643710318	-0.26750368	1.202580011
29.391496	0.003115	1.914329	1.714042737	-0.20028626	0.017843784
29.413432	0.005071	1.9194	1.715322038	-0.20407796	0.404684868
29.878962	0.116619	2.036019	1.742470643	-0.29354836	0.301442386
30.241432	0.005435	2.041454	1.763609003	-0.277845	0.627098042
30.873438	0.004381	2.045835	1.800466106	-0.24536889	0.203295361
31.081416	0.004986	2.050821	1.812594943	-0.23822606	0.020402391
31.105184	0.001745	2.052566	1.81398103	-0.23858497	0.019755835
31.127953	0.00428	2.056846	1.815308826	-0.24153717	0.001273898
31.132418	0.002103	2.058949	1.815569237	-0.24337976	0.00892266
31.143477	0.002169	2.061118	1.816214152	-0.24490385	0.01721738
31.165109	0.006661	2.067779	1.817475702	-0.2503033	0.021028063
31.190799	0.002662	2.070441	1.818973856	-0.25146714	0.00446047
31.202282	0.011383	2.081824	1.819643516	-0.26218048	0.050343276
31.259702	0.002771	2.084595	1.822992131	-0.26160287	0.122947139
31.385852	0.003635	2.08823	1.83034891	-0.25788109	0.355087253
31.748271	0.011029	2.099259	1.851484346	-0.24777465	0.351396392
32.106306	0.002247	2.101506	1.872364068	-0.22914193	0.011809848
32.123580	0.008682	2.110188	1.873371467	-0.23681653	0.248797053
32.378221	0.003005	2.113193	1.888221504	-0.2249715	0.143955567
32.530590	0.013822	2.127015	1.897107309	-0.22990769	0.021406271
32.684027	0.25024	2.377255	1.906055409	-0.47119959	0.053889486
32.865509	0.004945	2.3822	1.916639011	-0.46556099	0.041343434
32.910990	0.00333	2.38553	1.919291352	-0.46623865	0.593529086
33.508386	0.004405	2.389935	1.954130112	-0.43580489	0.039866658
33.554468	0.008025	2.39796	1.956817486	-0.44114251	0.847478718
34.408439	0.00496	2.40292	2.006619074	-0.39630093	0.033226048
34.493178	0.098066	2.500986	2.011560856	-0.48942514	0.565481784
35.109528	0.00367	2.504656	2.047504922	-0.45715108	1.05269648
36.170073	0.012026	2.516682	2.109353376	-0.40732862	0.886598506
37.091604	0.057839	2.574521	2.163094892	-0.41142611	0.915404189
38.037231	0.002607	2.577128	2.218241641	-0.35888636	0.578757403
38.627121	0.019659	2.596787	2.252642659	-0.34414434	0.022145306
38.674382	0.030572	2.627359	2.255398797	-0.3719602	4.069075413
42.761556	0.005624	2.632983	2.493753116	-0.13922988	2.1098328
44.874976	0.001552	2.634535	2.617002835	-0.01753216	0.007381857
44.883973	0.001678	2.636213	2.617527511	-0.01868549	1.423293478
46.309181	0.002151	2.638364	2.700642281	0.062278281	2.867984289
49.180452	0.004422	2.642786	2.868088025	0.225302025	0.059796169
49.245430	0.005941	2.648727	2.871877369	0.223150369	0.02214516
49.315577	0.090064	2.738791	2.875968215	0.137177215	0.024370511
49.386760	0.00356	2.742351	2.880119412	0.137768412	0.011072747
49.400716	0.002206	2.744557	2.880933278	0.136376278	0.070140359
49.480063	0.016209	2.760766	2.885560658	0.124794658	2.730678789
52.221479	0.005265	2.766031	3.045433565	0.279402565	0.00516757
52.230544	0.002529	2.76856	3.045962189	0.277402189	0.55292519
52.786173	0.00288	2.77144	3.078365203	0.306925203	0.003044264

Location (mm)	Aperture (mm)	Cum. Ap (mm)	HomStrain	Difference	Spacing (mm)
52.792395	0.003474	2.774914	3.078728012	0.303814012	0.022894759
52.859086	0.084119	2.859033	3.082617289	0.223584289	0.17274213
53.075397	0.003018	2.862051	3.095232015	0.233181015	0.057579961
53.136344	0.003716	2.865767	3.098786298	0.233019298	2.148959997
55.290375	0.006427	2.872194	3.224404338	0.352210338	0.155765631
55.453306	0.007903	2.880097	3.233906068	0.353809068	0.307841432
55.768771	0.007345	2.887442	3.252303268	0.364861268	0.514533468
56.289512	0.005069	2.892511	3.282671625	0.390160625	0.03912748
56.337736	0.013124	2.905635	3.285483934	0.379848934	1.095516195
57.449599	0.01957	2.925205	3.350325174	0.425120174	0.168311934
57.633151	0.01091	2.936115	3.36102949	0.42491449	1.045315345
58.716072	0.064302	3.000417	3.42418291	0.42376591	0.502726729
59.252387	0.002875	3.003292	3.45545955	0.45216755	1.014316784
60.270352	0.00442	3.007712	3.514824828	0.507112828	0.128445551
60.410961	0.019908	3.02762	3.523024845	0.495404845	0.016239841
60.437954	0.001598	3.029218	3.524599004	0.495381004	0.071599221
60.512887	0.005069	3.034287	3.528968904	0.494681904	0.12107778
60.637541	0.002085	3.036372	3.536238477	0.499866477	0.028787811
60.668661	0.002579	3.038951	3.538053311	0.499102311	0.019208078
60.690511	0.002705	3.041656	3.539327556	0.497671556	0.049478064
60.741850	0.001017	3.042673	3.542321529	0.499648529	0.005906986
60.749596	0.00266	3.045333	3.542773228	0.497440228	0.135837209
60.888283	0.00304	3.048373	3.550861139	0.502488139	0.093010245
60.984659	0.003691	3.052064	3.556481545	0.504417545	0.041343364
61.030430	0.005165	3.057229	3.559150823	0.501921823	0.019205971
61.053694	0.002951	3.06018	3.560507523	0.500327523	0.003691309
61.062174	0.006626	3.066806	3.561002045	0.494196045	0.008858767
61.076560	0.004428	3.071234	3.561840989	0.490606989	0.093018855
61.190461	0.037337	3.108571	3.568483448	0.459912448	0.137303784
61.366866	0.040865	3.149436	3.578770959	0.429334959	0.417845633
61.807679	0.00507	3.154506	3.604478142	0.449972142	0.015500939
61.835684	0.019939	3.174445	3.606111353	0.431666353	0.177917633
62.025038	0.002932	3.177377	3.617153981	0.439776981	0.024357039
62.051969	0.002216	3.179593	3.618724536	0.439131536	0.068663799
62.123185	0.00289	3.182483	3.622877732	0.440394732	0.027313001
62.153722	0.003558	3.186041	3.624658578	0.438617578	0.003688974
62.161014	0.003647	3.189688	3.6250838	0.4353958	0.012571379
62.180573	0.010329	3.200017	3.626224456	0.426207456	0.15576627
62.344821	0.006633	3.20665	3.63580297	0.42915297	0.0494618
62.399066	0.002935	3.209585	3.638966457	0.429381457	0.427430885
62.831655	0.00738	3.216965	3.664193992	0.447228992	0.00516557
62.841987	0.002953	3.219918	3.664796534	0.444878534	0.517496604
63.363543	0.005167	3.225085	3.695212486	0.470127486	0.056840193
63.431644	0.017353	3.242438	3.699183928	0.456745928	0.645944006
64.089445	0.006361	3.248799	3.737545332	0.488746332	0.441464717
64.535892	0.003604	3.252403	3.763581082	0.511178082	0.236964166
64.776812	0.004308	3.256711	3.777630978	0.520919978	0.020681834
64.873831	0.148367	3.405078	3.783288917	0.378210917	0.216297181
65.190158	0.051692	3.45677	3.801736343	0.344966343	0.685808747
65.903596	0.003566	3.460336	3.843342351	0.383006351	0.252475321
66.213893	0.112077	3.572413	3.86143813	0.28902513	0.007381908
66.302405	0.050185	3.622598	3.866599994	0.244001994	0.058317636
66.388396	0.00516	3.627758	3.871614736	0.243856736	0.006642569
66.398339	0.001441	3.629199	3.872194592	0.242995592	0.01183308
66.436351	0.050918	3.680117	3.874411397	0.194294397	0.889549545
67.479006	0.255292	3.935409	3.935216552	-0.00019245	
67.482306		3.935409	3.935409	0	

Location (mm)	Aperture (mm)	Cum. Ap (mm)	HomStrain	Difference	Spacing (mm)
Sample 47			V'		C
			0.57654075		1.370335813
loc	ap	cumap	hom strain	difference	spacing
0	0	0	0	0	
13.710000	0.003247	0.003247	0.19040139	0.18715439	5.815454407
19.528370	0.002585	0.005832	0.271205606	0.265373606	5.934340647
25.465056	0.002105	0.007937	0.353652959	0.345715959	10.02660185
35.498179	0.010937	0.018874	0.492990707	0.474116707	8.112716216
43.618138	0.003549	0.022423	0.605758871	0.583335871	0.064102121
43.686213	0.004397	0.02682	0.606704283	0.579884283	7.64133941
51.333485	0.007467	0.034287	0.712907864	0.678620864	1.491877362
52.829696	0.001201	0.035488	0.73368691	0.69819891	4.341161095
57.172335	0.001755	0.037243	0.793996503	0.756753503	0.004347036
57.178666	0.002212	0.039455	0.79408442	0.75462942	0.040567941
57.221583	0.002486	0.041941	0.794680441	0.752739441	0.022701652
57.246114	0.001174	0.043115	0.795021131	0.751906131	0.002938082
57.250411	0.001544	0.044659	0.795080808	0.750421808	0.007243258
57.259796	0.002739	0.047398	0.795211141	0.747813141	7.697670349
64.960762	0.003853	0.051251	0.902160426	0.850909426	6.347733683
71.312047	0.003248	0.054499	0.990365629	0.935866629	0.164839502
71.479366	0.001711	0.05621	0.992689318	0.936479318	1.54387431
73.028142	0.008093	0.064303	1.014198374	0.949895374	0.358500654
73.394211	0.007044	0.071347	1.01928226	0.94793526	4.340810399
77.739471	0.001856	0.073203	1.079628257	1.006425257	1.39478796
79.146174	0.021974	0.095177	1.099164231	1.003987231	0.16885982
79.339665	0.027287	0.122464	1.101851381	0.979387381	0.006365031
79.361207	0.003068	0.125532	1.102150559	0.976618559	0.283450114
80.419750	1.547118	1.67265	1.116851367	-0.55579863	1.651422183
82.850763	0.012063	1.684713	1.150612723	-0.53410028	0.100175715
82.963923	0.013906	1.698619	1.152184267	-0.54643473	0.210211908
83.183606	0.005035	1.703654	1.155235166	-0.54841883	0.046787359
83.235553	0.005284	1.708938	1.155956593	-0.55298141	3.574253862
86.813400	0.001903	1.710841	1.20564493	-0.50519607	1.747216455
88.564943	0.006751	1.717592	1.229969971	-0.48762203	0.198121802
88.775288	0.017695	1.735287	1.232891192	-0.50239581	5.263909832
94.049712	0.003332	1.738619	1.306141195	-0.43247781	0.029404245
94.082438	0.003312	1.741931	1.306595689	-0.43533531	2.935197128
97.021596	0.004611	1.746542	1.347414062	-0.39912794	1.909302776
98.936778	0.007147	1.753689	1.374011675	-0.37967733	0.215834398
99.176129	0.039886	1.793575	1.377335726	-0.41623927	0.92352097
100.121953	0.00472	1.798295	1.390471116	-0.40782388	2.619581922
102.748207	0.008625	1.80692	1.426943946	-0.37997605	0.468331409
103.227606	0.013509	1.820429	1.433601723	-0.38682728	0.088373718
103.325042	0.004616	1.825045	1.434954895	-0.39009011	1.350174178
104.698200	0.041352	1.866397	1.454025006	-0.41237199	0.099355698
104.820235	0.004007	1.870404	1.455719803	-0.4146842	0.047211652
104.871262	0.003622	1.874026	1.456428443	-0.41759756	6.513753689
111.388339	0.003026	1.877052	1.546936149	-0.33011585	1.882837662
113.278000	0.010621	1.887673	1.573179337	-0.31449366	3.759325827
117.206783	0.328292	2.215965	1.627741381	-0.58822362	0.004551162
117.378055	0.00515	2.221115	1.63011997	-0.59099503	2.87829329
120.299511	0.081176	2.302291	1.670692496	-0.6315985	20.69875008

Location (mm)	Aperture (mm)	Cum. Ap (mm)	HomStrain	Difference	Spacing (mm)
141.040200	0.002702	2.304993	1.958734511	-0.34625849	4.597019752
145.643841	0.01054	2.315533	2.022668836	-0.29286416	1.263016165
146.914731	0.005207	2.32074	2.040318666	-0.28042133	0.505606891
147.424919	0.003956	2.324696	2.047404047	-0.27729195	0.033483879
147.462016	0.00327	2.327966	2.04791924	-0.28004676	6.284942346
153.749949	0.002711	2.330677	2.135244634	-0.19543237	0.071656079
153.824187	0.002453	2.33313	2.136275636	-0.19685436	7.066459203
160.893638	0.00353	2.33666	2.234454574	-0.10220543	1.208101672
162.104594	0.00218	2.33884	2.251272067	-0.08756793	0.003347958
162.109823	0.001581	2.340421	2.251344679	-0.08907632	1.322615758
163.575831	0.285203	2.625624	2.271704264	-0.35391974	0.11585493
163.845458	0.022342	2.647966	2.275448789	-0.37251721	0.085049779
163.965791	0.048225	2.696191	2.277119951	-0.41907105	6.633844621
170.626980	0.006463	2.702654	2.369629037	-0.33302496	12.98420532
183.629157	0.02948	2.732134	2.550200338	-0.18193366	0.004391247
183.651581	0.006586	2.73872	2.55051176	-0.18820824	9.551265095
193.257341	0.102404	2.841124	2.683914392	-0.15720961	11.268798
204.577341		2.841124	2.841124	0	

Location (mm)	Aperture (mm)	Cum. Ap (mm)	HomStrain	Difference	Spacing (mm)
Sample 48			V'		C
			0.264233046		1.651780467
loc	ap	cumap	hom strain	difference	spacing
0	0	0	0	0	
0.396600	0.003209	0.003209	0.002874398	-0.0003346	4.653389107
5.053906	0.004625	0.007834	0.036628693	0.028794693	7.579983866
12.638789	0.005174	0.013008	0.091600899	0.078592899	1.432049484
14.075450	0.004048	0.017056	0.10201324	0.08495724	1.344914212
15.423436	0.002096	0.019152	0.111782906	0.092630906	0.034602536
15.460191	0.002208	0.02136	0.112049288	0.090689288	0.01794007
15.481297	0.004124	0.025484	0.112202257	0.086718257	4.588835044
20.079469	0.01455	0.040034	0.145527971	0.105493971	2.564027635
22.664570	0.027597	0.067631	0.164263752	0.096632752	0.701252838
23.386021	0.0128	0.080431	0.169492543	0.089061543	0.122655774
23.526568	0.022982	0.103413	0.17051117	0.06709817	3.048844764
26.588138	0.002468	0.105881	0.192700205	0.086819205	0.067814435
26.658965	0.003557	0.109438	0.193213531	0.083775531	0.051223256
26.714117	0.0043	0.113738	0.193613248	0.079875248	0.404008929
27.122317	0.004084	0.117822	0.196571726	0.078749726	1.686743582
28.813262	0.004318	0.12214	0.208827017	0.086687017	0.68176607
29.505357	0.01634	0.13848	0.213843046	0.075363046	2.105189006
31.620865	0.004298	0.142778	0.229175403	0.086397403	0.420598656
32.045597	0.003968	0.146746	0.232253688	0.085507688	0.018048877
32.067448	0.003637	0.150383	0.232412058	0.082029058	0.38886101
32.459081	0.001907	0.15229	0.235250458	0.082960458	0.013705391
32.474405	0.001329	0.153619	0.235361516	0.081742516	3.589943092
36.070364	0.010704	0.164323	0.261423595	0.097100595	8.990489768
45.069847	0.007283	0.171606	0.326648256	0.155042256	8.110441187
53.281862	0.195864	0.36747	0.386165659	0.018695659	0.224213608
53.609703	0.011391	0.378861	0.38854172	0.00968072	0.006572394
53.624109	0.004276	0.383137	0.388646128	0.005509128	0.05842637
53.686441	0.003536	0.386673	0.389097888	0.002424888	1.11231485
54.802122	0.003195	0.389868	0.397183894	0.007315894	5.201488608
60.005856	0.001297	0.391165	0.434898484	0.043733484	6.956634746
66.966458	0.006637	0.397802	0.485346146	0.087544146	3.474235025
70.566808	0.245592	0.643394	0.511440042	-0.13195396	0.049076102
70.741658	0.005957	0.649351	0.512707289	-0.13664371	1.621402441
72.366836	0.001593	0.650944	0.524485926	-0.12645807	0.891574661
73.261909	0.005405	0.656349	0.530973063	-0.12537594	0.001880184
73.291907	0.05083	0.707179	0.531190474	-0.17598853	0.182578503
73.504778	0.009755	0.716934	0.532733278	-0.18420072	10.36801341
83.878837	0.002337	0.719271	0.607920318	-0.11135068	0.027458537
83.913948	0.012967	0.732238	0.608174785	-0.12406322	0.043619619
83.966741	0.00538	0.737618	0.608557408	-0.12906059	0.01484834
83.985660	0.002762	0.74038	0.608694528	-0.13168547	0.032033228
84.019871	0.001592	0.741972	0.60894247	-0.13302953	0.006710521
84.036322	0.017889	0.759861	0.609061701	-0.1507993	0.012008414
84.067391	0.020233	0.780094	0.609286879	-0.17080712	2.185530735
86.268866	0.011655	0.791749	0.625242289	-0.16650671	0.075192747
86.354918	0.010063	0.801812	0.625865958	-0.17594604	16.02088136
102.383860	0.006059	0.807871	0.742037331	-0.06583367	18.28799753
120.676964	0.004153	0.812024	0.87461844	0.06259444	0.005581651

Location (mm)	Aperture (mm)	Cum. Ap (mm)	HomStrain	Difference	Spacing (mm)
120.685873	0.002503	0.814527	0.874683014	0.060156014	1.59412121
122.284632	0.006772	0.821299	0.886270178	0.064971178	4.538107037
126.830120	0.00799	0.829289	0.91921406	0.08992506	0.058490366
126.905178	0.025145	0.854434	0.91975805	0.06532405	5.019555678
132.024285	0.173958	1.028392	0.956859294	-0.07153271	0.107991303
132.221438	0.004366	1.032758	0.958288183	-0.07446982	0.003187792
132.227455	0.001291	1.034049	0.958331787	-0.07571721	0.073378435
132.318384	0.033812	1.067861	0.95899081	-0.10887019	0.009418524
132.365309	0.041199	1.10906	0.959330897	-0.1497291	0.811649837
133.215031	0.034946	1.144006	0.965489345	-0.17851665	0.006671971
133.240857	0.003363	1.147369	0.965676525	-0.18169247	1.263197751
134.507110	0.002746	1.150115	0.974853816	-0.17526118	0.002242185
134.519390	0.017331	1.167446	0.974942821	-0.19250318	0.029878041
134.559358	0.002848	1.170294	0.97523249	-0.19506151	0.465645119
135.027721	0.002589	1.172883	0.978627003	-0.194256	7.781276049
142.811894	0.003205	1.176088	1.03504358	-0.14104442	1.823219631
144.638090	0.002747	1.178835	1.048279117	-0.13055588	0.527757143
145.168160	0.001879	1.180714	1.052120854	-0.12859315	1.335758253
146.511079	0.012442	1.193156	1.061853792	-0.13130221	0.044567812
146.563203	0.002671	1.195827	1.062231569	-0.13359543	16.75744709
163.323205	0.002439	1.198266	1.183701371	-0.01456463	5.332224062
168.659440	0.005583	1.203849	1.222376272	0.018527272	4.98021272
173.643536	0.002182	1.206031	1.258499003	0.052468003	3.557493538
177.234981	0.065721	1.271752	1.284528363	0.012776363	0.009953887
177.296129	0.036668	1.30842	1.284971542	-0.02344846	0.036135301
177.352724	0.004251	1.312671	1.285381718	-0.02728928	0.300264602
177.656515	0.002801	1.315472	1.287583471	-0.02788853	0.047863965
177.709202	0.006847	1.322319	1.287965333	-0.03435367	0.048545019
177.762502	0.002662	1.324981	1.288351626	-0.03662937	5.052669
182.816502		1.324981	1.324981	0	

Location (mm)	Aperture (mm)	Cum. Ap (mm)	HomStrain	Difference	Spacing (mm)
Sample 49			V'		C
			0.297612783		1.203060707
loc	ap	cumap	hom strain	difference	spacing
0	0	0	0	0	
0.635400	0.002295	0.002295	0.000254161	-0.00204084	0.042220087
0.679865	0.002194	0.004489	0.000271946	-0.00421705	1.406882128
2.089363	0.003039	0.007528	0.000835747	-0.00669225	16.64733374
18.741759	0.007086	0.014614	0.007496721	-0.00711728	6.113816047
24.861439	0.004641	0.019255	0.009944599	-0.0093104	5.995085523
30.861859	0.006027	0.025282	0.012344772	-0.01293723	33.98968082
64.855586	0.002066	0.027348	0.025942295	-0.0014057	1.189014593
66.046734	0.002201	0.029549	0.026418755	-0.00313024	12.37515538
78.426379	0.006779	0.036328	0.031370625	-0.00495737	0.411286627
78.841816	0.001521	0.037849	0.0315368	-0.0063122	1.719358521
80.564745	0.005621	0.04347	0.032225974	-0.01124403	28.1071895
108.674745		0.04347	0.04347	0	

Location (mm) Aperture (mm) Cum.Ap. (mm) Hom. strain Difference Spacing (mm)

Sample 50

V'
0.488842285

C
1.06140711

loc	ap	cumap	hom strain	difference	spacing
0	0	0	0	0	
6.019800	0.003035	0.003035	0.00453073	0.00149573	24.78788386
30.811381	0.00436	0.007395	0.023189814	0.015794814	10.9233268
41.739239	0.004701	0.012096	0.031414534	0.019318534	1.81118915
43.557585	0.009614	0.02171	0.032783091	0.011073091	0.10094169
43.665433	0.004197	0.025907	0.032864261	0.006957261	3.289720161
46.958278	0.002053	0.02796	0.035342581	0.007382581	0.060421204
47.020750	0.002049	0.030009	0.0353896	0.0053806	6.82111705
53.844356	0.002929	0.032938	0.040525305	0.007587305	0.665332042
54.519285	0.016265	0.049203	0.041033282	-0.008169718	3.606040319
58.136492	0.006069	0.055272	0.043755729	-0.011516271	8.862582856
67.007364	0.010508	0.06578	0.050432284	-0.015347716	8.156746498
75.171932	0.005135	0.070915	0.056577247	-0.014337753	19.0474325
94.221932		0.070915	0.070915	0	

Location (mm)	Aperture (mm)	Cum.Ap. (mm)	Hom. strain	Difference	Spacing (mm)
Sample 51			V'		C
			0.477041374		1.389430278
loc	ap	cumap	hom strain	difference	spacing
0	0	0	0	0	
1.129800	0.011697	0.011697	0.00065917	-0.01103783	14.65083525
15.789374	0.00578	0.017477	0.009212146	-0.008264854	3.18724113
18.982845	0.006681	0.024158	0.011075343	-0.013082657	1.749567618
20.737368	0.003228	0.027386	0.012099001	-0.015286999	1.027013734
21.767103	0.002216	0.029602	0.01269979	-0.01690221	3.176839384
24.946246	0.00239	0.031992	0.014554627	-0.017437373	6.712360903
31.664396	0.009188	0.04118	0.018474262	-0.022705738	42.89780003
74.569998	0.006417	0.047597	0.043507089	-0.004089911	7.0067915
81.579998		0.047597	0.047597	0	

Location (mm)	Aperture (mm)	Cum.Ap. (mm)	Hom. strain	Difference	Spacing (mm)
Sample 52			V'		C
			0.379815266		1.302855115
loc	ap	cumap	hom strain	difference	spacing
0	0	0	0	0	
2.533000	0.002242	0.002242	0.003612696	0.001370696	8.18945925
10.725870	0.00458	0.006822	0.015297792	0.008475792	2.168692179
12.899159	0.004614	0.011436	0.01839745	0.00696145	5.95486676
18.859509	0.006351	0.017787	0.026898409	0.009111409	0.066268596
18.930548	0.003191	0.020978	0.02699973	0.00602173	1.257540313
20.191540	0.003711	0.024689	0.028798221	0.004109221	2.064024818
22.260659	0.006479	0.031168	0.031749307	0.000581307	7.625809962
29.894951	0.010485	0.041653	0.04263773	0.00098473	5.491786742
35.401665	0.019369	0.061022	0.05049169	-0.01053031	0.547027669
35.963999	0.011243	0.072265	0.05129372	-0.02097128	2.369434217
38.343493	0.008876	0.081141	0.054687477	-0.026453523	0.081946619
38.433470	0.007185	0.088326	0.054815807	-0.033510193	0.151604171
38.591738	0.006143	0.094469	0.055041538	-0.039427462	14.42965255
53.026692	0.00446	0.098929	0.075629418	-0.023299582	3.237093857
56.269594	0.007157	0.106086	0.080254613	-0.025831387	3.16179114
59.437979	0.006031	0.112117	0.084773528	-0.027343472	0.04885032
59.492200	0.00471	0.116827	0.084850861	-0.031976139	24.1632952
83.660523	0.005345	0.122172	0.119320976	-0.002851024	2.716680779
86.382688	0.005624	0.127796	0.123203469	-0.004592531	3.217188
89.602688		0.127796	0.127796	0	

Location	Aperture (mm)	Cum. Ap (mm)	Hom. strain	difference	Spacing (mm)
Sample 53			V'		C
			0.356124392		1.595122148
loc	ap	cumap	hom strain	difference	spacing
0	0	0	0	0	
0.105000	0.054982	0.054982	0.005050995	-0.049931005	-0.010333755
0.123248	0.002181	0.057163	0.005928798	-0.051234202	0.09548798
0.227643	0.015633	0.072796	0.010950688	-0.061845312	0.693812208
0.930658	0.002773	0.075569	0.044769034	-0.030799966	0.258127195
1.191879	0.003414	0.078983	0.057334981	-0.021648019	0.205167442
1.399677	0.001848	0.080831	0.067331066	-0.013499934	0.19620575
1.598522	0.003431	0.084262	0.07689646	-0.00736554	0.476711564
2.078172	0.002445	0.086707	0.099969865	0.013262865	0.043273957
2.124202	0.003068	0.089775	0.102184147	0.012409147	0.155181461
2.284937	0.008038	0.097813	0.109916233	0.012103233	0.298415975
2.588108	0.001473	0.099286	0.12450021	0.02521421	0.155917315
2.747000	0.004475	0.103761	0.132143631	0.028382631	0.099226434
2.852574	0.008221	0.111982	0.137222259	0.025240259	0.024617176
2.883434	0.004265	0.116247	0.138706779	0.022459779	0.018664019
2.909276	0.01009	0.126337	0.139949878	0.013612878	0.025363351
2.940407	0.001445	0.127782	0.141447419	0.013665419	0.05670007
2.998638	0.001617	0.129399	0.144248608	0.014849608	0.012029168
3.020958	0.018965	0.148364	0.145322313	-0.003041687	0.044019352
3.079264	0.009609	0.157973	0.148127124	-0.009845876	0.202918624
3.288352	0.002729	0.160702	0.158185224	-0.002516776	0.040289686
3.331386	0.002761	0.163463	0.160255395	-0.003207605	0.010444297
3.345050	0.003678	0.167141	0.160912688	-0.006228312	0.008206111
3.357892	0.005593	0.172734	0.16153043	-0.01120357	0.170843884
3.532197	0.00133	0.174064	0.169915341	-0.004148659	0.320047976
3.856374	0.006928	0.180992	0.185509782	0.004517782	0.22530616
4.086436	0.002583	0.183575	0.196576833	0.013001833	0.877336233
4.966118	0.002109	0.185684	0.238893695	0.053209695	0.041781265
5.013280	0.008653	0.194337	0.241162423	0.046825423	0.080569227
5.103342	0.010332	0.204669	0.245494816	0.040825816	0.152196816
5.265682	0.009955	0.214624	0.253304151	0.038680151	0.5878814
5.859663	0.002243	0.216867	0.281877408	0.065010408	0.00749683
5.872412	0.008262	0.225129	0.282490711	0.057361711	0.401371587
6.279801	0.003773	0.228902	0.302088047	0.073186047	0.111162323
6.395786	0.005872	0.234774	0.307667464	0.072893464	0.134284539
6.535546	0.005078	0.239852	0.314390557	0.074538557	0.011959214
6.551136	0.002185	0.242037	0.315140543	0.073103543	0.001491531
6.555351	0.003262	0.245299	0.315343306	0.070044306	0.064905511
6.642361	0.040946	0.286245	0.319528874	0.033283874	0.079824031
6.744839	0.004363	0.290608	0.324458574	0.033850574	0.011935768
6.760074	0.002234	0.292842	0.325191415	0.032349415	0.005968112
6.890804	0.24729	0.540132	0.331480149	-0.208651851	0.065663592
7.087410	0.014596	0.554728	0.340937853	-0.213790147	0.027601525
7.130293	0.015966	0.570694	0.343000705	-0.227693295	0.088784052
7.231294	0.008468	0.579162	0.347859332	-0.231302668	0.039544758
7.276865	0.003585	0.582747	0.350051524	-0.232695476	1.034000067
8.315840	0.006364	0.589111	0.400031099	-0.189079901	0.12085813
8.441395	0.003031	0.592142	0.406070917	-0.186071083	0.351385366
8.796529	0.004466	0.596608	0.42315453	-0.17345347	0.094751608

Location	Aperture (mm)	Cum. Ap (mm)	Hom. strain	difference	Spacing (mm)
8.894257	0.001487	0.598095	0.427855713	-0.170239287	0.096980665
8.992721	0.001479	0.599574	0.432592279	-0.166981721	0.019409739
9.014354	0.002968	0.602542	0.43363294	-0.16890906	0.035807716
9.052764	0.002235	0.604777	0.435480604	-0.169296396	0.906436576
9.961768	0.0029	0.607677	0.479207986	-0.128469014	0.071618542
10.035669	0.001665	0.609342	0.482762974	-0.126579026	0.817645894
10.867698	0.027102	0.636444	0.522787511	-0.113656489	0.008206295
10.891315	0.00372	0.640164	0.523923614	-0.116240386	0.055207708
10.956412	0.016058	0.656222	0.527055073	-0.129166927	0.025363756
10.991706	0.003803	0.660025	0.528752893	-0.131272107	0.083552541
11.087789	0.021257	0.681282	0.533374916	-0.147907084	0.096243303
11.195657	0.001993	0.683275	0.53856389	-0.14471111	0.312589018
11.512226	0.005967	0.689242	0.553792352	-0.135449648	0.487909297
12.007829	0.009421	0.698663	0.577633207	-0.121029793	0.272299133
12.285857	0.002035	0.700698	0.591007623	-0.109690377	0.077585849
12.365113	0.001306	0.702004	0.594820227	-0.107183773	0.037306645
12.404298	0.00245	0.704454	0.596705194	-0.107748806	0.074602843
12.493952	0.027653	0.732107	0.60101799	-0.13108901	0.493877034
13.003465	0.003619	0.735726	0.625527969	-0.110198031	0.365559658
13.372899	0.004129	0.739855	0.64329947	-0.09655553	0.572954113
13.949278	0.002722	0.742577	0.671026047	-0.071550953	0.035815929
13.986920	0.000929	0.743506	0.672836777	-0.070669223	0.005967933
13.993955	0.001206	0.744712	0.673175214	-0.071536786	0.020887111
14.016198	0.001506	0.746218	0.674245213	-0.071972787	0.330491682
14.348282	0.001678	0.747896	0.690220004	-0.057675996	0.027601594
14.384851	0.016257	0.764153	0.691979149	-0.072173851	0.05744499
14.452909	0.00497	0.769123	0.695253084	-0.073869916	1.343612996
15.801899	0.005784	0.774907	0.760145862	-0.014761138	0.032086688
15.840944	0.008131	0.783038	0.762024072	-0.021013928	0.431955411
16.277714	0.001499	0.784537	0.783034788	-0.001502212	0.815416384
17.105141	0.022523	0.80706	0.822837946	0.015777946	0.654260135
17.771993	0.00266	0.80972	0.854916654	0.045196654	0.058931944
17.833794	0.003078	0.812798	0.85788957	0.04509157	0.469252596
18.307481	0.005791	0.818589	0.880676153	0.062087153	0.256635713
18.568506	0.002987	0.821576	0.893232672	0.071656672	0.385708735
18.956883	0.00235	0.823926	0.911915448	0.087989448	0.190977858
19.151908	0.005745	0.829671	0.921297087	0.091626087	0.049240138
19.204955	0.001868	0.831539	0.923848881	0.092309881	0.052970511
19.261004	0.004289	0.835828	0.926545102	0.090717102	0.488654044
19.756421	0.009237	0.845065	0.950376998	0.105311998	0.161139964
19.922922	0.001485	0.84655	0.958386479	0.111836479	0.226798218
20.151555	0.002184	0.848734	0.969384791	0.120650791	0.18203275
20.336694	0.004028	0.852762	0.978290838	0.125528838	0.138760508
20.546555	0.138173	0.990935	0.988386142	-0.002548858	0.006714234
20.623804	0.002897	0.993832	0.992102194	-0.001729806	0.024629384
20.651731	0.003699	0.997531	0.993445633	-0.004085367	0.002236836
20.658794	0.005954	1.003485	0.993785413	-0.009699587	0.578175381
21.241297	0.0027	1.006185	1.021806523	0.015621523	0.020900475
21.264241	0.001387	1.007572	1.022910237	0.015338237	0.026855016
21.294135	0.004691	1.012263	1.02434828	0.01208528	0.194724339
21.505413	0.028416	1.040679	1.03451174	-0.00616726	0.240225935
21.760417	0.00114	1.041819	1.046778631	0.004959631	0.334966803
22.097623	0.003339	1.045158	1.062999844	0.017841844	0.036560815
22.140763	0.00982	1.054978	1.065075097	0.010097097	0.079077481

Location	Aperture (mm)	Cum. Ap (mm)	Hom. strain	difference	Spacing (mm)
22.226242	0.002982	1.05796	1.069187015	0.011227015	0.02462809
22.256700	0.008678	1.066638	1.070652193	0.004014193	0.183525329
22.453105	0.017081	1.083719	1.080100191	-0.003618809	0.02761145
22.491318	0.004123	1.087842	1.081938438	-0.005903562	0.167254211
22.669238	0.017208	1.10505	1.090497215	-0.014552785	0.138604903
22.817776	0.002659	1.107709	1.097642612	-0.010066388	0.140178044
22.960848	0.003128	1.110837	1.104525028	-0.006311972	0.126075918
23.089800	0.002624	1.113461	1.110728223	-0.002732777	0.004763416
23.097038	0.002326	1.115787	1.111076425	-0.004710575	0.05247072
23.152501	0.003658	1.119445	1.113744444	-0.005700556	0.017245497
23.173386	0.003621	1.123066	1.11474911	-0.00831689	0.075179293
23.251498	0.002244	1.12531	1.118506656	-0.006803344	1.080686951
24.334386	0.002158	1.127468	1.170598672	0.043130672	0.00391472
24.340789	0.00282	1.130288	1.170906721	0.040618721	0.010179426
24.355655	0.006553	1.136841	1.171621842	0.034780842	0.005481374
24.365732	0.002637	1.139478	1.172106563	0.032628563	0.31794118
24.686855	0.003727	1.143205	1.187554102	0.044349102	0.276432651
24.967743	0.005184	1.148389	1.201066146	0.052677146	0.047773217
25.019439	0.002662	1.151051	1.203552978	0.052501978	0.552872501
25.575435	0.003584	1.154635	1.230298983	0.075663983	0.137045597
25.721676	0.014808	1.169443	1.237333893	0.067890893	0.034455611
25.764706	0.00234	1.171783	1.23940382	0.06762082	0.108075774
25.875243	0.002582	1.174365	1.24472116	0.07035616	0.955387605
26.832760	0.001677	1.176042	1.290782247	0.114740247	0.176196893
27.012297	0.005003	1.181045	1.299418818	0.118373818	0.029766293
27.045716	0.002304	1.183349	1.301026468	0.117677468	0.576363822
27.624324	0.002184	1.185533	1.328860232	0.143327232	0.010179679
27.637089	0.002986	1.188519	1.329474273	0.140955273	0.047774252
27.687079	0.001445	1.189964	1.331879016	0.141915016	0.727495118
28.415724	0.000855	1.190819	1.366930281	0.176111281	0.893512966
29.311855	0.004382	1.195201	1.41003843	0.21483743	0.015681022
29.330874	0.002293	1.197494	1.41095331	0.21345931	0.281913999
29.615057	0.002246	1.19974	1.424623877	0.224883877	0.197346673
29.814588	0.002122	1.201862	1.434222243	0.232360243	0.075974619
29.894305	0.005362	1.207224	1.438056988	0.230832988	0.005537211
29.903663	0.00228	1.209504	1.438507162	0.229003162	0.729062184
30.635822	0.003914	1.213418	1.47372747	0.26030947	0.137045367
30.777339	0.005029	1.218447	1.480535099	0.262088099	0.156744075
30.938164	0.003133	1.22158	1.488271543	0.266691543	0.012268179
30.952354	0.00071	1.22229	1.488954134	0.266664134	0.20780705
31.161455	0.001878	1.224168	1.49901288	0.27484488	0.006134255
31.169373	0.00169	1.225858	1.499393786	0.273535786	0.812806959
31.984750	0.003451	1.229309	1.538617285	0.309308285	0.19144327
32.179482	0.003126	1.232435	1.547984802	0.315549802	0.095284044
32.280893	0.009128	1.241563	1.552863151	0.311300151	0.009200852
32.295796	0.002277	1.24384	1.553580072	0.309740072	0.87622712
33.174089	0.001853	1.245693	1.595830064	0.350137064	0.343688705
33.522062	0.006717	1.25241	1.61256924	0.36015924	0.170991377
33.698428	0.004032	1.256442	1.62105327	0.36461127	0.052145774
33.774878	0.044577	1.301019	1.624730889	0.323711889	0.080514589
33.879146	0.002928	1.303947	1.629746627	0.325799627	0.00996836
33.891273	0.00139	1.305337	1.630330011	0.324993011	0.446281689
34.339616	0.002733	1.30807	1.651897432	0.343827432	1.581904559
35.924452	0.003129	1.311199	1.728135494	0.416936494	0.078980554

Location	Aperture (mm)	Cum. Ap (mm)	Hom. strain	difference	Spacing (mm)
36.006410	0.002827	1.314026	1.732078087	0.418052087	0.14799322
36.158112	0.004591	1.318617	1.739375679	0.420758679	0.095848775
36.263014	0.013515	1.332132	1.744421949	0.412289949	0.531381538
36.802360	0.002413	1.334545	1.770367012	0.435822012	0.166394803
36.970851	0.001779	1.336324	1.778472214	0.442148214	1.19564707
38.169103	0.003431	1.339755	1.836113788	0.496358788	0.85865587
39.030530	0.002112	1.341867	1.877552505	0.535685505	0.032652443
39.065605	0.002733	1.3446	1.879239775	0.534639775	0.319936134
39.387636	0.001456	1.346056	1.894730967	0.548674967	0.270319554
39.659790	0.002213	1.348269	1.90782286	0.55955386	0.231782754
39.896360	0.007363	1.355632	1.919203029	0.563571029	0.8027512
40.704670	0.003753	1.359385	1.958086512	0.598701512	0.339865755
41.047623	0.002423	1.361808	1.974584205	0.612776205	0.079662941
41.130495	0.003995	1.365803	1.978570736	0.612767736	0.395023179
41.530864	0.006696	1.372499	1.997830357	0.625331357	0.041137864
41.576679	0.002659	1.375158	2.000034292	0.624876292	0.815962269
42.397511	0.00708	1.382238	2.03952017	0.65728217	1.296915539
43.703170	0.010407	1.392645	2.102328525	0.709683525	0.047665742
43.765225	0.018371	1.411016	2.105313651	0.694297651	0.013057453
43.788729	0.002523	1.413539	2.106444326	0.692905326	0.612445786
44.404897	0.00492	1.418459	2.136084877	0.717625877	0.363025297
44.772004	0.003245	1.421704	2.153744493	0.732040493	1.702835354
46.484881	0.016838	1.438542	2.236141945	0.797599945	0.502104338
46.997619	0.004428	1.44297	2.260807029	0.817837029	0.105118964
47.111448	0.012992	1.455962	2.266282738	0.810320738	0.363031811
47.483170	0.004389	1.460351	2.284164334	0.823813334	0.007211025
47.493550	0.001949	1.4623	2.284663662	0.822363662	0.008486699
47.504838	0.003653	1.465953	2.285206654	0.819253654	0.012404584
47.520897	0.003656	1.469609	2.285979171	0.816370171	0.012473491
47.536498	0.002599	1.472208	2.286729653	0.814521653	1.734382972
49.272694	0.001027	1.473235	2.370248864	0.897013864	0.023609273
49.299037	0.004442	1.477677	2.371516124	0.893839124	0.294405464
49.597760	0.004193	1.48187	2.385886107	0.904016107	0.250131364
49.853329	0.006681	1.488551	2.39818015	0.90962915	0.00590262
49.864415	0.003686	1.492237	2.398713445	0.906476445	0.534206963
50.401770	0.002611	1.494848	2.424562776	0.929714776	0.758516022
51.163746	0.004308	1.499156	2.461217391	0.962061391	0.004427506
51.171861	0.003067	1.502223	2.461607761	0.959384761	1.798896414
52.979066	0.013551	1.515774	2.548542862	1.032768862	0.029511967
53.018313	0.005918	1.521692	2.550430802	1.028738802	0.142406528
53.164649	0.001942	1.523634	2.557470279	1.033836279	0.096657788
53.263696	0.002836	1.52647	2.562234896	1.035764896	1.396775448
54.663565	0.003351	1.529821	2.629575192	1.099754192	0.432378931
55.101567	0.007895	1.537716	2.65064515	1.11292915	0.019920529
55.128754	0.006638	1.544354	2.651952974	1.107598974	0.068621783
55.201792	0.002195	1.546549	2.65546646	1.10891746	0.061244529
55.353938	0.179607	1.726156	2.662785377	0.936629377	0.358601042
55.803699	0.002713	1.728869	2.684421004	0.955552004	0.017708271
55.823523	0.001518	1.730387	2.685374621	0.954987621	0.004427896
55.830797	0.004175	1.734562	2.685724554	0.951162554	0.355648529
56.189962	0.002858	1.73742	2.703002085	0.965582085	0.137974697
56.596809	0.534886	2.272306	2.722573329	0.450267329	0.114372467
56.981420	0.005592	2.277898	2.741074954	0.463176954	0.110675316
57.097471	0.005159	2.283057	2.746657545	0.463600545	0.007377818

Location	Aperture (mm)	Cum. Ap (mm)	Hom. strain	difference	Spacing (mm)
57.128817	0.042777	2.325834	2.748165427	0.422331427	0.139454945
57.291501	0.003681	2.329515	2.755991292	0.426476292	0.028036895
57.322844	0.002932	2.332447	2.757499057	0.425052057	0.124700531
57.449359	0.000697	2.333144	2.763585026	0.430441026	0.004427845
57.455184	0.002096	2.33524	2.763865205	0.428625205	0.512073581
57.969224	0.001837	2.337077	2.788592956	0.451515956	2.93520298
60.906434	0.002177	2.339254	2.929886604	0.590632604	0.098140843
61.008554	0.005783	2.345037	2.934799098	0.589762098	0.025086044
61.038338	0.003613	2.34865	2.936231851	0.587581851	1.002753753
62.046396	0.006995	2.355645	2.984724181	0.629079181	0.540109342
62.591881	0.003755	2.3594	3.01096455	0.65156455	1.773810582
64.368570	0.002003	2.361403	3.096431695	0.735028695	0.422080947
64.792782	0.002258	2.363661	3.116838265	0.753177265	0.024345339
64.820129	0.003746	2.367407	3.118153801	0.750746801	0.439099341
65.265183	0.008163	2.37557	3.139562989	0.763992989	0.061981703
65.333168	0.003845	2.379415	3.142833422	0.763418422	0.503958475
65.840818	0.003537	2.382952	3.167253755	0.784301755	0.64120149
66.485241	0.002907	2.385859	3.198253563	0.812394563	0.117316933
66.605482	0.00294	2.388799	3.204037695	0.815238695	0.172664246
66.780664	0.002095	2.390894	3.212464763	0.821570763	0.235383266
67.023367	0.012545	2.403439	3.224139934	0.820700934	0.312130265
67.343982	0.004424	2.407863	3.239563016	0.831700016	1.300840375
68.648842	0.003616	2.411479	3.302332952	0.890853952	1.603368239
70.259665	0.011294	2.422773	3.379821144	0.957048144	1.899987538
72.165738	0.000877	2.42365	3.471512244	1.047862244	0.002149285
72.194078	0.051504	2.475154	3.472875521	0.997721521	1.100719459
73.323693	0.006287	2.481441	3.527215326	1.045774326	0.081902732
73.411592	0.005706	2.487147	3.531443693	1.044296693	0.006641845
73.424003	0.005831	2.492978	3.53204069	1.03906269	0.242753983
73.673241	0.007138	2.500116	3.544030236	1.043914236	0.129865854
73.807654	0.001956	2.502072	3.550496128	1.048424128	0.592269259
74.404059	0.006316	2.508388	3.579186032	1.070798032	0.006900751
74.415229	0.002223	2.510611	3.579723374	1.069112374	0.008121877
74.426398	0.003871	2.514482	3.58026065	1.06577865	0.023125691
74.452592	0.002265	2.516747	3.58152069	1.06477369	0.625489638
75.085523	0.012618	2.529365	3.611967662	1.082602662	0.028747723
75.122411	0.003663	2.533028	3.613742159	1.080714159	0.055611889
75.180729	0.001749	2.534777	3.616547524	1.081770524	0.054356808
75.237638	0.003355	2.538132	3.619285106	1.081153106	0.265568117
75.506460	0.003153	2.541285	3.632216718	1.090931718	0.011263931
75.520360	0.002118	2.543403	3.632885346	1.089482346	0.017493826
75.540236	0.002647	2.54605	3.633841491	1.087791491	0.038743425
75.585502	0.010399	2.556449	3.636019019	1.079570019	0.00812216
75.602192	0.006736	2.563185	3.636821871	1.073636871	0.008124225
75.619561	0.011753	2.574938	3.637657388	1.062719388	0.336182453
75.962144	0.001048	2.575986	3.654137243	1.078151243	0.04124155
76.004714	0.001609	2.577595	3.656185063	1.078590063	0.009373879
76.015662	0.001539	2.579134	3.656711708	1.077577708	0.005623654
76.031326	0.018542	2.597676	3.657465228	1.059789228	0.026242191
76.069938	0.006198	2.603874	3.659322656	1.055448656	0.084358582
76.157954	0.001116	2.60499	3.66355662	1.05856662	0.129973637
76.313435	0.0499	2.65489	3.67103602	1.01614602	0.146225914
76.485229	0.001235	2.656125	3.679300093	1.023175093	0.089355469
76.576992	0.00358	2.659705	3.683714325	1.024009325	0.008122266

Location	Aperture (mm)	Cum. Ap (mm)	Hom. strain	difference	Spacing (mm)
76.587546	0.001285	2.66099	3.684222059	1.023232059	0.012496345
76.601556	0.001741	2.662731	3.684895974	1.022164974	0.152463579
76.755846	0.001912	2.664643	3.692318054	1.027675054	0.141219841
76.901823	0.007603	2.672246	3.699340253	1.027094253	0.960422396
77.866899	0.001704	2.67395	3.745764953	1.071814953	1.026028168
78.894666	0.001774	2.675724	3.7952054	1.1194814	0.268692172
79.167539	0.006587	2.682311	3.808331862	1.126020862	0.038743089
79.210908	0.002666	2.684977	3.810418143	1.125441143	0.034387047
79.249419	0.005581	2.690558	3.812270682	1.121712682	0.18620903
79.440186	0.003534	2.694092	3.821447452	1.127355452	0.262443839
79.705377	0.001962	2.696054	3.834204429	1.138150429	0.228700052
79.938177	0.006237	2.702291	3.845403185	1.143112185	0.675480021
80.618286	0.003021	2.705312	3.878119636	1.172807636	0.128007862
80.750083	0.004558	2.70987	3.88445971	1.17458971	0.001737958
81.716276	1.924352	4.634222	3.930938147	-0.703283853	0.125156299
82.81139158	0.015566	4.649788	3.983618356	-0.666169644	1.250065797
84.07120038	0.00392	4.653708	4.044221098	-0.609486902	1.595182517
85.77721639	0.217747	4.871455	4.126288512	-0.745166488	0.384802916
86.27379031	0.005795	4.87725	4.150176058	-0.727073942	0.90424157
87.18495188	0.008045	4.885295	4.194007225	-0.691287775	0.031185518
87.2220759	0.003832	4.889127	4.195793066	-0.693333934	0.843310952
88.06941835	0.004231	4.893358	4.236554233	-0.656803767	2.030997066
90.10370592	0.00235	4.895708	4.334413055	-0.561294945	0.906379098
91.01380501	0.00509	4.900798	4.378193113	-0.522604887	0.065189516
91.08319353	0.003308	4.904106	4.381531027	-0.522574973	1.167867537
92.25537557	0.005321	4.909427	4.43791851	-0.47150849	0.070151964
92.32919503	0.002014	4.911441	4.441469574	-0.469971426	0.078653928
92.41056896	0.003426	4.914867	4.445384044	-0.469482956	0.707943918
93.12126488	0.002078	4.916945	4.479571868	-0.437373132	0.207633211
93.34784459	0.035815	4.95276	4.49047142	-0.46228858	0.451414171
93.82595076	0.017569	4.970329	4.513470581	-0.456858419	0.68668942
94.52388418	0.004919	4.975248	4.547044469	-0.428203531	0.010629709
94.53840339	0.00286	4.978108	4.547742911	-0.430365089	0.034011835
94.57982122	0.011952	4.99006	4.549735304	-0.440324696	0.010629691
94.59887991	0.004906	4.994966	4.550652117	-0.444313883	0.012774183
94.6150891	0.001964	4.99693	4.551431855	-0.445498145	0.072984651
94.69025825	0.002405	4.999335	4.555047846	-0.444287154	0.014190556
94.7977433	0.184184	5.183519	4.560218384	-0.623300616	0.2827559
95.1741392	0.003096	5.186615	4.578324801	-0.608290199	1.465495945
96.64578865	0.009211	5.195826	4.649118078	-0.546707922	0.017728159
96.67200981	0.007775	5.203601	4.650379439	-0.553221561	0.241653776
96.91896008	0.002818	5.206419	4.662258912	-0.544160088	0.096369771
97.01783985	0.002202	5.208621	4.667015495	-0.541605505	0.05598241
97.07562926	0.001412	5.210033	4.669795438	-0.540237562	0.07298802
97.15176178	0.004877	5.21491	4.673457771	-0.541452229	0.561960525
97.72111231	0.009903	5.224813	4.700846216	-0.523966784	0.082915118
97.81137993	0.004802	5.229615	4.705188514	-0.524426486	0.008504336
97.82321226	0.001854	5.231469	4.705757705	-0.525711295	0.085748983
97.91094174	0.002107	5.233576	4.709977906	-0.523598094	0.200560853
98.1127871	0.000462	5.234038	4.719687619	-0.514350381	0.060941208
98.17469081	0.001463	5.235501	4.72266548	-0.51283552	0.561251484
98.73914679	0.004946	5.240447	4.749818474	-0.490628526	0.053869318
98.79778411	0.00459	5.245037	4.752639205	-0.492397795	0.004250452
98.80535556	0.002052	5.247089	4.753003428	-0.494085572	0.003541278

Location	Aperture (mm)	Cum. Ap (mm)	Hom. strain	difference	Spacing (mm)
98.81087334	0.001901	5.24899	4.753268859	-0.495721141	0.06660939
98.87963973	0.002413	5.251403	4.756576846	-0.494826154	1.465503938
100.3473697	0.002039	5.253442	4.827181576	-0.426260424	0.42589535
100.7752765	0.001984	5.255426	4.847765913	-0.407660087	0.004961686
100.7825937	0.002727	5.258153	4.848117904	-0.410035096	1.273447633
102.0656758	0.016542	5.274695	4.909840204	-0.364854796	0.596687897
102.6723122	0.003355	5.27805	4.939022275	-0.339027725	4.971209407
107.6480781	0.005758	5.283808	5.178380073	-0.105427927	0.060234186
107.7205248	0.018667	5.302475	5.181865101	-0.120609899	0.211176045
107.9420289	0.001989	5.304464	5.192520489	-0.111943511	0.002127027
107.9494169	0.008533	5.312997	5.192875888	-0.120121112	0.007086037
107.9621494	0.00276	5.315757	5.193488384	-0.122268616	0.134647644
108.0992801	0.002206	5.317963	5.200085014	-0.117877986	1.758870259
109.8621118	0.005717	5.32368	5.284885533	-0.038794467	0.004310926
109.8712648	0.003967	5.327647	5.285325831	-0.042321169	0.090709989
109.9653403	0.002764	5.330411	5.289851306	-0.040559694	0.44645328
110.4141135	0.001876	5.332287	5.311439417	-0.020847583	0.323871597
110.7420506	0.006255	5.338542	5.327214737	-0.011327263	0.002836308
110.7490594	0.00209	5.340632	5.327551894	-0.013080106	0.242351371
110.9942098	0.003508	5.34414	5.339344782	-0.004795218	0.013463841
111.0234742	0.028093	5.372233	5.340752535	-0.031480465	0.002125282
111.0410459	0.0028	5.375033	5.341597821	-0.033435179	0.00292136
111.0520768	0.013419	5.388452	5.342128457	-0.046323543	0.00566804
111.0655733	0.002238	5.39069	5.342777704	-0.047912296	0.994881
112.0615733		5.39069	5.39069	0	

Location	Aperture (mm)	Cum. Ap (mm)	Hom. strain	difference	Spacing (mm)
Sample 53 macrofractures			V'		C
			0.141431684		1.147095638
loc	ap	cumap	hom strain	difference	spacing
0	0	0	0	0	
52.016	0.4	0.4	0.813160859	0.413160859	216.408
269.499	1.75	2.15	4.213050566	2.063050566	15.24
285.7465	0.265	2.415	4.467046087	2.052046087	51.816
338.17	0.95	3.365	5.286577352	1.921577352	70.104
409.224	0.95	4.315	6.397357336	2.082357336	12.192
422.766	1.75	6.065	6.60905805	0.54405805	15.24
439.356	0.95	7.015	6.86840784	-0.14659216	27.432
467.3955	0.265	7.28	7.306746503	0.026746503	24.384
492.222	0.62	7.9	7.694856662	-0.205143338	12.192
505.099	0.75	8.65	7.896161499	-0.753838501	42.672
548.621	0.95	9.6	8.576536516	-1.023463484	18.288
568.084	1.4	11	8.880799623	-2.119200377	18.288
587.547	0.95	11.95	9.185062731	-2.764937269	21.336
610.058	1.4	13.35	9.536974913	-3.813025087	21.336
632.569	0.95	14.3	9.888887096	-4.411112904	3.048
636.2245	0.265	14.565	9.946033157	-4.618966843	3.048
639.57	0.33	14.895	9.998333019	-4.896666981	18.288
658.1555	0.265	15.16	10.28887826	-4.871121742	3.048
661.4685	0.265	15.425	10.34067005	-5.084329948	24.384
686.1175	0.265	15.69	10.72600537	-4.963994629	15.24
702.065	1.15	16.84	10.97531102	-5.864688977	155.448
858.788	1.4	18.24	13.42534581	-4.814654194	33.528
893.391	0.75	18.99	13.966291	-5.023709001	15.24
909.206	0.4	19.39	14.21352529	-5.176474708	73.152
982.723	0.33	19.72	15.36280911	-4.357190894	70.104
1053.692	1.4	21.12	16.47226029	-4.647739707	115.824
1170.416	0.4	21.52	18.29699476	-3.223005239	9.144
1179.925	0.33	21.85	18.44564799	-3.404352005	131.064
1311.404	0.5	22.35	20.50104588	-1.848954118	6.096
1318	0.5	22.85	20.60416048	-2.245839518	6.096
1324.721	0.75	23.6	20.70922919	-2.890770806	24.384
1350.055	1.15	24.75	21.10527305	-3.64472695	12.192
1363.522	1.4	26.15	21.3158013	-4.834198703	82.296
1447.093	1.15	27.3	22.62225827	-4.677741726	18.288
1466.206	0.5	27.8	22.92104987	-4.878950134	225.552
1692.208	0.4	28.2	26.45411624	-1.745883762	6.096
1698.814	0.62	28.82	26.55738717	-2.262612834	9.144
1708.3755	0.215	29.035	26.70686113	-2.328138873	6.096
1714.6665	0.175	29.21	26.80520769	-2.404792307	6.096
1721.015	0.33	29.54	26.90445315	-2.63554685	85.344
1806.899	0.75	30.29	28.24706902	-2.042930978	237.744
2045.493	0.95	31.24	31.97698485	0.736984854	30.48
2077.148	1.4	32.64	32.47184426	-0.168155738	109.728
2187.826	0.5	33.14	34.20206222	1.062062224	18.288
2206.939	1.15	34.29	34.50085382	0.210853817	30.48
2238.304	0.62	34.91	34.99117968	0.081179684	73.152
2312.341	1.15	36.06	36.14859261	0.088592605	30.48
2343.871	0.95	37.01	36.6414979	-0.368502099	21.336

Location	Aperture (mm)	Cum. Ap (mm)	Hom. strain	difference	Spacing (mm)
2367.007	2.65	39.66	37.00318065	-2.656819355	21.336
2390.043	0.75	40.41	37.3633001	-3.0466999	146.304
2537.422	1.4	41.81	39.66726108	-2.142738923	51.816
2590.413	0.95	42.76	40.49566401	-2.264335989	30.48
2622.068	1.4	44.16	40.99052342	-3.16947658	51.816
2675.459	1.75	45.91	41.82517951	-4.084820486	152.4
2829.209	0.95	46.86	44.22873769	-2.631262311	54.864
2884.923	0.75	47.61	45.09970901	-2.510290993	30.48
2916.088	0.62	48.23	45.58690829	-2.643091705	33.528
2950.126	0.4	48.63	46.1190209	-2.5109791	39.624
2990.325	0.75	49.38	46.7474478	-2.632552205	15.24
3006.315	0.75	50.13	46.99741785	-3.132582155	60.96
3068.225	1.15	51.28	47.9652506	-3.314749396	36.576
3105.686	0.62	51.9	48.55087462	-3.349125378	76.2
3182.771	1.15	53.05	49.75593662	-3.294063382	246.888
3430.544	0.62	53.67	53.62934683	-0.040653174	146.304
3577.468	0.62	54.29	55.92619483	1.636194834	6.096
3584.249	0.75	55.04	56.03220152	0.992201521	9.144
3594.343	1.15	56.19	56.19	0	

Location	Aperture (mm)	Cum. Ap (mm)	Hom. strain	difference	Spacing (mm)
Sample 54			V'		C
			0.256265576		1.624630893
loc	ap	cumap	hom strain	difference	spacing
0	0	0	0	0	
0.1014	0.005156	0.005156	0.003816016	-0.001339984	0.222742974
0.332099474	0.010757	0.015913	0.012497999	-0.003415001	0.181999467
0.520687441	0.00242	0.018333	0.019595186	0.001262186	0.191722031
0.715079471	0.00292	0.021253	0.026910799	0.005657799	0.341222664
1.059228136	0.002932	0.024185	0.039862249	0.015677249	0.059584368
1.131103004	0.021649	0.045834	0.042567137	-0.003266863	0.047672446
1.19219995	0.0052	0.051034	0.044866417	-0.006167583	0.019497069
1.216760519	0.004927	0.055961	0.045790712	-0.010170288	0.021664549
1.250299568	0.018822	0.074783	0.047052897	-0.027730103	0.192814873
1.45431994	0.003589	0.078372	0.054730857	-0.023641143	0.022771892
1.480200832	0.002629	0.081001	0.05570484	-0.02529616	0.097489798
1.58151363	0.005017	0.086018	0.059517575	-0.026500425	0.132162028
1.717801159	0.003234	0.089252	0.064646524	-0.024605476	0.015165264
1.736477423	0.003788	0.09304	0.065349374	-0.027690626	0.102905393
1.842901316	0.003249	0.096289	0.069354456	-0.026934544	0.060667701
1.914387017	0.018387	0.114676	0.072044699	-0.042631301	0.566542738
2.491722255	0.003198	0.117874	0.093771728	-0.024102272	0.046588902
2.541647658	0.003475	0.121349	0.095650586	-0.025698414	0.168986679
2.716560336	0.008377	0.129726	0.102233127	-0.027492873	0.411635355
3.171248192	0.077728	0.207454	0.119344531	-0.088109469	0.599047999
3.811627691	0.004935	0.212389	0.143444124	-0.068944876	0.412718706
4.228652397	0.003677	0.216066	0.159138139	-0.056927861	0.00649864
4.238214537	0.00245	0.218516	0.159497994	-0.059018006	0.017330778
4.262124315	0.010708	0.229224	0.160397798	-0.068826202	0.076903605
4.345372419	0.001981	0.231205	0.163530699	-0.067674301	0.067165887
4.424297307	0.021537	0.252742	0.166500902	-0.086241098	0.021664643
4.45862595	0.003791	0.256533	0.167792802	-0.088740198	0.212324495
4.700744445	0.055797	0.31233	0.17690452	-0.13542548	0.343403141
5.076378586	0.008665	0.320995	0.191040872	-0.129954128	0.089908036
5.176526122	0.011814	0.332809	0.194809754	-0.137999246	0.132162501
5.316022623	0.002854	0.335663	0.200059468	-0.135603532	0.262145912
5.581220035	0.003249	0.338912	0.210039721	-0.128872279	0.339055071
5.923913605	0.004028	0.34294	0.222936411	-0.120003589	0.021689504
5.948639609	0.002045	0.344985	0.223866932	-0.121118068	0.003249255
5.954323865	0.002825	0.34781	0.224080849	-0.123729151	0.068247307
6.024969172	0.001971	0.349781	0.226739465	-0.123041535	0.045492798
6.07411647	0.005338	0.355119	0.22858904	-0.12652996	0.067164205
6.145795675	0.003692	0.358811	0.231286565	-0.127524435	0.302232088
6.451822264	0.003897	0.362708	0.242803355	-0.119904645	0.249146964
6.704136227	0.002437	0.365145	0.252298762	-0.112846238	0.106171246
6.812921473	0.002791	0.367936	0.256392709	-0.111543291	0.045492687
6.86142016	0.003221	0.371157	0.258217875	-0.112939125	0.015163807
6.880831468	0.005274	0.376431	0.258948386	-0.117482614	0.010832321
6.896476289	0.004351	0.380782	0.259537153	-0.121244847	0.170070202
7.070598491	0.003753	0.384535	0.266089945	-0.118445055	0.015165689
7.18880368	0.202326	0.586861	0.270538397	-0.316322603	0.561113071
7.852377751	0.002596	0.589457	0.295510878	-0.293946122	0.094259538
7.950982789	0.006095	0.595552	0.299221711	-0.296330289	0.066108841

Location	Aperture (mm)	Cum. Ap (mm)	Hom. strain	difference	Spacing (mm)
8.03069863	0.021119	0.616671	0.302221681	-0.314449319	0.148409714
8.191600344	0.003865	0.620536	0.308276943	-0.312259057	0.109398139
8.304958983	0.004056	0.624592	0.312543003	-0.312048997	0.064998112
8.373585095	0.0032	0.627792	0.31512563	-0.31266637	0.005415035
8.38158713	0.001974	0.629766	0.315426773	-0.314339227	0.122415399
8.509243028	0.008507	0.638273	0.320230885	-0.318042115	0.009808388
8.528290917	0.009972	0.648245	0.32094772	-0.32729728	0.162477245
8.710411662	0.029315	0.67756	0.327801524	-0.349758476	0.046574559
8.773466721	0.003646	0.681206	0.330174494	-0.351031506	0.036844054
8.813691275	0.003115	0.684321	0.331688277	-0.352632723	0.010830267
8.840925542	0.029693	0.714014	0.332713192	-0.381300808	0.009748505
8.883632548	0.036224	0.750238	0.334320398	-0.415917602	0.006499165
8.910992713	0.005498	0.755736	0.335350051	-0.420385949	0.007582831
8.924272044	0.005895	0.761631	0.335849796	-0.425781204	0.08992755
9.018682094	0.00307	0.764701	0.339402758	-0.425298242	0.151645269
9.173567863	0.003411	0.768112	0.34523162	-0.42288038	0.347736214
9.526464577	0.00691	0.775022	0.358512288	-0.416509712	0.007580978
9.540589555	0.006178	0.7812	0.359043857	-0.422156143	0.001083718
9.545679273	0.001834	0.783034	0.3592354	-0.4237986	0.259978379
9.806976652	0.000804	0.783838	0.369068882	-0.414769118	0.010830594
9.820422246	0.004426	0.788264	0.369574884	-0.418689116	0.250230656
10.0742889	0.002846	0.79111	0.379128724	-0.411981276	0.178734203
10.25851061	0.008129	0.799239	0.386061595	-0.413177405	0.155990063
10.41961117	0.002092	0.801331	0.39212434	-0.40920666	0.03900871
10.46065088	0.00197	0.803301	0.3936688	-0.4096322	0.092094164
10.55476204	0.002064	0.805365	0.397210513	-0.408154487	0.008666122
10.56778266	0.006645	0.81201	0.397700522	-0.414309478	0.111394334
10.684494	0.003989	0.815999	0.402092755	-0.413906245	0.017777251
10.70531975	0.002108	0.818107	0.402876496	-0.415230504	0.007381261
10.71455851	0.001607	0.819714	0.403224182	-0.416489818	0.196273591
10.9140266	0.004782	0.824496	0.410730824	-0.413765176	0.106479097
11.0253552	0.004917	0.829413	0.414920486	-0.414492514	0.045931108
11.07807531	0.008661	0.838074	0.416904518	-0.421169482	0.029227752
11.11407606	0.004885	0.842959	0.418259345	-0.424699655	0.041768147
11.16115121	0.005729	0.848688	0.420030938	-0.428657062	0.067859738
11.23591944	0.008088	0.856776	0.422844713	-0.433931287	0.06997089
11.31151983	0.003171	0.859947	0.425689805	-0.434257195	0.372698835
11.68720467	0.002801	0.862748	0.439828065	-0.422919935	0.565826673
12.25613484	0.003406	0.866154	0.461238784	-0.404915216	0.011482718
12.27101656	0.003392	0.869546	0.461798832	-0.407747168	0.10230382
12.37622388	0.002415	0.871961	0.465758131	-0.406202869	0.101260682
12.48263356	0.007883	0.879844	0.469762678	-0.410081322	0.021920768
12.52007983	0.023168	0.903012	0.471171905	-0.431840095	0.009394854
12.54244518	0.002773	0.905785	0.472013587	-0.433771413	0.084559729
12.63067691	0.004571	0.910356	0.475334038	-0.435021962	0.006263817
12.64182223	0.005192	0.915548	0.475753473	-0.439794527	0.195229187
12.84102042	0.002746	0.918294	0.483249958	-0.435044042	0.461434416
13.30684283	0.00603	0.924324	0.500780392	-0.423543608	0.473088164
13.7848975	0.003903	0.928227	0.518771166	-0.409455834	0.129074401
13.9212829	0.010719	0.938946	0.523903799	-0.415042201	0.040712303
13.9697827	0.004856	0.943802	0.525729006	-0.418072994	0.236979235
14.21531444	0.012249	0.956051	0.534969175	-0.421081825	0.087692145
14.31061908	0.002976	0.959027	0.538555803	-0.420471197	0.314233136
14.62828122	0.003882	0.962909	0.550510478	-0.412398522	0.057421732

Location	Aperture (mm)	Cum. Ap (mm)	Hom. strain	difference	Spacing (mm)
14.69004745	0.004807	0.967716	0.552834945	-0.414881055	0.065772241
14.75974169	0.003037	0.970753	0.555457769	-0.415295231	0.006263977
14.77019167	0.005335	0.976088	0.555851036	-0.420236964	0.040712122
14.81485579	0.002569	0.978657	0.557531894	-0.421125106	0.066816727
14.88527852	0.004643	0.9833	0.560182134	-0.423117866	0.180617093
15.07008711	0.00374	0.98704	0.567137091	-0.419902909	0.014613943
15.08898955	0.004837	0.991877	0.567848452	-0.424028548	0.040710076
15.13321163	0.002187	0.994064	0.569512675	-0.424551325	0.073072538
15.20925517	0.003755	0.997819	0.572374444	-0.425444556	0.354954274
15.56713094	0.002088	0.999907	0.58584249	-0.41406451	0.441601627
16.01141457	0.003276	1.003183	0.602562348	-0.400620652	0.014614096
16.02965066	0.003968	1.007151	0.603248632	-0.403902368	0.007381302
16.03990446	0.001777	1.008928	0.603634517	-0.405293483	0.096058786
16.14205825	0.010413	1.019341	0.607478901	-0.411862099	0.176427859
16.32547711	0.003569	1.02291	0.614381558	-0.408528442	0.455170887
16.78939149	0.013918	1.036828	0.631840186	-0.404987814	0.366437535
17.16597203	0.006368	1.043196	0.646012154	-0.397183846	0.119004484
17.28936701	0.002413	1.045609	0.650655914	-0.394953086	0.055323915
17.34759943	0.003404	1.049013	0.652847392	-0.396165608	0.085604473
17.4368534	0.003895	1.052908	0.656206314	-0.396701686	0.021945482
17.46215738	0.002822	1.05573	0.657158586	-0.398571414	0.057413978
17.53546036	0.028956	1.084686	0.659917219	-0.424768781	0.245330315
17.79927168	0.008006	1.092692	0.669845309	-0.422846691	0.132588689
17.93669087	0.001655	1.094347	0.675016846	-0.419330154	0.018789532
17.9583244	0.004033	1.09838	0.675830987	-0.422549013	0.013568709
17.97485161	0.001884	1.100264	0.676452961	-0.423811039	0.043842752
18.02337436	0.007476	1.10774	0.678279032	-0.429460968	0.060552121
18.08997798	0.004627	1.112367	0.680785546	-0.431581454	0.100657996
18.19416947	0.00244	1.114807	0.684706616	-0.430100384	0.022418693
18.21896217	0.002308	1.117115	0.685639646	-0.431475354	0.447866522
18.67003719	0.004109	1.121224	0.702615088	-0.418608912	2.700747597
21.37455529	0.003432	1.124656	0.804395025	-0.320260975	0.168076993
21.54686128	0.005026	1.129682	0.810879468	-0.318802532	0.385223653
21.93637693	0.003558	1.13324	0.825538227	-0.307701773	0.711983124
22.65106306	0.001848	1.135088	0.852434223	-0.282653777	0.278731526
22.93214258	0.002848	1.137936	0.863012173	-0.274923827	0.019860098
22.95595868	0.005064	1.143	0.863908452	-0.279091548	0.010438045
22.97081573	0.003774	1.146774	0.864467571	-0.282306429	0.206712216
23.18143644	0.004043	1.150817	0.872393923	-0.278423077	0.052194892
23.23691133	0.002517	1.153334	0.874481627	-0.278852373	0.139882882
23.37954871	0.002992	1.156326	0.879849542	-0.276476458	0.267263472
23.64961369	0.002611	1.158937	0.890012978	-0.268924022	0.789236624
24.44203981	0.003768	1.162705	0.919834587	-0.242870413	1.00638504
25.46968235	0.038747	1.201452	0.958508165	-0.242943835	0.336153829
25.82729418	0.004169	1.205621	0.971966278	-0.233654722	0.826827194
26.65765187	0.002892	1.208513	1.003215377	-0.205297623	0.374786705
27.03571758	0.003666	1.212179	1.017443237	-0.194735763	0.020877741
27.06063732	0.004418	1.216597	1.018381049	-0.198215951	0.052193265
27.11738308	0.004687	1.221284	1.020516579	-0.200767421	0.269337534
27.39165112	0.005174	1.226458	1.03083819	-0.19561981	0.119020472
27.51633059	0.006144	1.232602	1.03553029	-0.19707171	0.161813784
27.68387837	0.005324	1.237926	1.041835666	-0.196090334	0.713058538
28.40141191	0.003626	1.241552	1.06883882	-0.17271318	0.070990357
28.47638427	0.004338	1.24589	1.071660277	-0.174229723	0.129443906

Location	Aperture (mm)	Cum. Ap (mm)	Hom. strain	difference	Spacing (mm)
28.60992817	0.003862	1.249752	1.076685975	-0.173066025	0.075158959
28.68968713	0.005338	1.25509	1.079687567	-0.175402433	0.550184878
29.24586151	0.006641	1.261731	1.100618244	-0.161112756	0.475019036
29.72652755	0.004653	1.266384	1.118707293	-0.147676707	0.116918935
29.85096698	0.010388	1.276772	1.123390359	-0.153381641	0.241155281
30.10012826	0.005624	1.282396	1.13276712	-0.14962888	0.634729705
30.74086197	0.006384	1.28878	1.156880043	-0.131899957	0.140928053
30.88659402	0.003224	1.292004	1.162364421	-0.129639579	0.703160896
31.59434992	0.005966	1.29797	1.18899961	-0.10897039	0.03810495
31.63796187	0.005048	1.303018	1.190640871	-0.112377129	0.205029436
31.8476623	0.004294	1.307312	1.198532591	-0.108779409	1.572895564
33.42491187	0.004414	1.311726	1.257889695	-0.053836305	0.14115189
33.57055276	0.004564	1.31629	1.263370642	-0.052919358	0.033625936
33.60928969	0.005658	1.321948	1.26482844	-0.05711956	0.107547882
33.72133058	0.003328	1.325276	1.269044908	-0.056231092	0.015683656
33.73975073	0.002145	1.327421	1.26973812	-0.05768288	0.059371474
33.80424771	0.008106	1.335527	1.272165354	-0.063361646	0.007920702
33.81793991	0.003437	1.338964	1.272680636	-0.066283364	0.314833459
34.13582687	0.00267	1.341634	1.284643771	-0.056990229	0.043689522
34.18227889	0.002855	1.344489	1.286391914	-0.058097086	0.287900641
34.47355153	0.003889	1.348378	1.297353464	-0.051024536	0.063862518
34.54154555	0.004374	1.352752	1.299912303	-0.052839697	0.029126436
34.57671348	0.007709	1.360461	1.301235789	-0.059225211	0.01120267
34.60028515	0.017029	1.37749	1.302122869	-0.075367131	0.118764623
34.72860978	0.002091	1.379581	1.306952148	-0.072628852	0.033607642
34.76489192	0.003258	1.382839	1.308317564	-0.074521436	0.010082572
34.77878049	0.004354	1.387193	1.308840237	-0.078352763	0.010082527
34.79264052	0.003201	1.390394	1.309361836	-0.081032164	0.058261859
34.85418038	0.003355	1.393749	1.311677783	-0.082071217	0.043687934
34.95540531	0.111719	1.505468	1.315487212	-0.189980788	0.061623325
35.07509414	0.004412	1.50988	1.319991497	-0.189888503	0.044808686
35.12482182	0.005426	1.515306	1.321862914	-0.193443086	0.022404481
35.1514163	0.002954	1.51826	1.322863752	-0.195396248	0.004480921
35.16409372	0.013439	1.531699	1.323340845	-0.208358155	0.062741906
35.23627913	0.005448	1.537147	1.32605742	-0.21108958	0.058251204
35.29779933	0.00109	1.538237	1.328372628	-0.209864372	0.100826537
35.40646187	0.014582	1.552819	1.332461958	-0.220357042	0.055171613
35.46941748	0.000986	1.553805	1.334831185	-0.218973815	0.00952291
35.4804784	0.00209	1.555895	1.335247444	-0.220647556	0.085646726
35.57083462	0.007329	1.563224	1.338647847	-0.224576153	0.016550003
35.59372262	0.005347	1.568571	1.339509198	-0.229061802	0.035873678
35.6353458	0.006152	1.574723	1.341075615	-0.233647385	0.009377449
35.64961075	0.003623	1.578346	1.341612452	-0.236733548	0.013792988
35.66728224	0.004134	1.58248	1.342277489	-0.240202511	0.116793411
35.78676365	0.001242	1.583722	1.346773968	-0.236948032	0.076325191
35.86515784	0.002896	1.586618	1.3497242	-0.2368938	0.009241586
35.88228243	0.01287	1.599488	1.350368655	-0.249119345	0.075400382
35.96986931	0.011503	1.610991	1.353664838	-0.257326162	0.083680331
36.06451914	0.010436	1.621427	1.357226824	-0.264200176	0.002758577
36.07333022	0.001669	1.623096	1.357558414	-0.265537586	0.252872873
36.32880709	0.003539	1.626635	1.367172851	-0.259462149	0.071728174
36.40547926	0.006349	1.632984	1.370058278	-0.262925722	0.019308895
36.43117916	0.006433	1.639417	1.37102545	-0.26839155	0.241785054
36.67662271	0.000884	1.640301	1.3802623	-0.2600387	0.291512308

Location	Aperture (mm)	Cum. Ap (mm)	Hom. strain	difference	Spacing (mm)
36.97213202	0.00711	1.647411	1.39138329	-0.25602771	0.143529785
37.11991831	0.001403	1.648814	1.396944976	-0.251869024	0.238032897
37.3595602	0.001815	1.650629	1.405963491	-0.244665509	0.104298552
37.46838426	0.007236	1.657865	1.410058899	-0.247806101	0.090050177
37.56258443	0.001064	1.658929	1.413603962	-0.245325038	0.418108324
37.98240326	0.002357	1.661286	1.42940313	-0.23188287	0.154224816
38.13947557	0.003338	1.664624	1.435314279	-0.229309721	0.091819935
38.23798101	0.010033	1.674657	1.439021364	-0.235635636	0.157789646
38.40180665	0.002039	1.676696	1.445186663	-0.231509337	0.225544288
38.62925594	0.001771	1.678467	1.45374633	-0.22472067	0.333407264
38.96550671	0.003916	1.682383	1.466400556	-0.215982444	0.082904445
39.05134065	0.001943	1.684326	1.46963077	-0.21469523	0.075774605
39.13091276	0.005652	1.689978	1.472625331	-0.217352669	0.629376663
39.76435692	0.002483	1.692461	1.496463924	-0.195997076	0.007130301
39.77379272	0.002128	1.694589	1.496819025	-0.197769975	0.106092957
39.88334768	0.004796	1.699385	1.500941939	-0.198443061	0.147976262
40.03601244	0.004581	1.703966	1.506687218	-0.197278782	0.12212538
40.16304782	0.005239	1.709205	1.511467978	-0.197737022	0.003566683
40.1709495	0.003431	1.712636	1.511765344	-0.200870656	0.184529413
40.35804041	0.001692	1.714328	1.518806193	-0.195521807	0.116787192
40.47687261	0.002398	1.716726	1.52327824	-0.19344776	0.354799675
40.83419078	0.002639	1.719365	1.536725302	-0.182639698	0.334297892
41.17074817	0.00188	1.721245	1.549391066	-0.171853934	0.303992926
41.4778581	0.004354	1.725599	1.560948626	-0.164650374	0.313797802
41.8024944	0.017323	1.742922	1.573165761	-0.169756239	0.900379647
42.71786055	0.01265	1.755572	1.607614009	-0.147957991	0.489413902
43.21455395	0.001909	1.757481	1.62630622	-0.13117478	0.114105504
43.33229245	0.005357	1.762838	1.630737108	-0.132100892	1.021135505
44.35692296	0.001633	1.764471	1.669297334	-0.095173666	0.210514795
44.57007125	0.003634	1.768105	1.677318808	-0.090786192	0.973549034
45.54679229	0.00271	1.770815	1.714076042	-0.056738958	0.015125894
45.56454068	0.002535	1.77335	1.714743973	-0.058606027	0.10481277
45.67407295	0.006904	1.780254	1.718866033	-0.061387967	0.218510007
45.90350196	0.014934	1.795188	1.727500204	-0.067687796	0.044410728
46.31984768	0.728936	2.524124	1.743168667	-0.780955333	0.005330047
46.70087673	0.022462	2.546586	1.757508047	-0.789077953	0.029312657
46.74228539	0.00173	2.548316	1.759066391	-0.789249609	0.013324481
46.75780387	0.002658	2.550974	1.759650403	-0.791323597	0.064839499
46.82560287	0.003261	2.554235	1.762201903	-0.792033097	0.008882934
46.8372823	0.002332	2.556567	1.762641438	-0.793925562	0.011580549
46.85134835	0.002639	2.559206	1.76317079	-0.79603521	0.056845076
46.95006243	0.081099	2.640305	1.766885727	-0.873419273	0.133244976
47.1260529	0.004392	2.644697	1.773508829	-0.871188171	0.059518738
47.19705664	0.018578	2.663275	1.776180934	-0.887094066	0.063069934
47.27449658	0.010162	2.673437	1.779095254	-0.894341746	0.139462626
47.4249527	0.011825	2.685262	1.784757414	-0.900504586	0.00621821
47.44726791	0.020369	2.705631	1.785597209	-0.920033791	0.031100484
47.4898714	0.002637	2.708268	1.787200519	-0.921067481	0.314443267
47.80636566	0.001465	2.709733	1.799111242	-0.910621758	0.162548065
47.97327373	0.007255	2.716988	1.805392543	-0.911595457	0.234505127
48.21310436	0.003396	2.720384	1.814418161	-0.905965839	0.714164257
48.93084161	0.00375	2.724134	1.841428981	-0.882705019	0.360635942
49.29487855	0.003052	2.727186	1.855128892	-0.872057108	1.33952242
50.63725697	0.00266	2.729846	1.90564702	-0.82419898	0.143006879

Location	Aperture (mm)	Cum. Ap (mm)	Hom. strain	difference	Spacing (mm)
50.78456485	0.005942	2.735788	1.911190702	-0.824597298	1.87692273
52.66580558	0.002694	2.738482	1.981987996	-0.756494004	0.030199401
52.69825598	0.001808	2.74029	1.983209212	-0.757080788	0.554285377
53.25517236	0.003454	2.743744	2.004167812	-0.739576188	0.950456026
54.20867839	0.002646	2.74639	2.04005139	-0.70633861	0.19808104
54.40977693	0.003389	2.749779	2.047619391	-0.702159609	1.350182213
55.76209514	0.000883	2.750662	2.098511586	-0.652150414	0.024869657
55.7891703	0.003528	2.75419	2.099530514	-0.654659486	0.29047088
56.08324868	0.003687	2.757877	2.110597653	-0.647279347	0.179430547
56.26609222	0.003139	2.761016	2.117478659	-0.643537341	1.987964402
58.25807463	0.004897	2.765913	2.192443528	-0.573469472	0.128796607
58.39090023	0.003161	2.769074	2.197442194	-0.571631806	0.437925934
58.83226267	0.003712	2.772786	2.214052118	-0.558733882	0.033752339
58.86868401	0.001626	2.774412	2.215422773	-0.558989227	0.310008415
59.18225192	0.005493	2.779905	2.227223368	-0.552681632	0.065734054
59.25204198	0.002619	2.782524	2.229849798	-0.552674202	0.051516791
59.30645677	0.003177	2.785701	2.231897606	-0.553803394	0.09681991
59.40559268	0.001455	2.787156	2.235628418	-0.551527582	0.228288237
59.63601091	0.002805	2.789961	2.244299816	-0.545661184	0.015988235
59.65964315	0.012483	2.802444	2.245189175	-0.557254825	0.049748441
59.71731809	0.00337	2.805814	2.247359673	-0.558454327	0.172324466
59.89268956	0.002724	2.808538	2.25395948	-0.55457852	0.268256014
60.16425757	0.0039	2.812438	2.26417948	-0.54825852	0.028436453
60.19589902	0.00251	2.814948	2.265370253	-0.549577747	0.015099421
60.21354244	0.002578	2.817526	2.266034233	-0.551491767	0.015099344
60.23714229	0.014423	2.831949	2.266922373	-0.565026627	0.007994737
60.25449603	0.004295	2.836244	2.267575451	-0.568668549	0.00266343
60.26234295	0.006072	2.842316	2.267870757	-0.574445243	0.03375238
60.30193383	0.005605	2.847921	2.269360692	-0.578560308	0.064847786
60.37166012	0.004152	2.852073	2.271984722	-0.580088278	0.079058251
60.45414537	0.002702	2.854775	2.275088915	-0.579686085	0.009771537
60.46689541	0.003255	2.85803	2.275568741	-0.582461259	0.020448834
60.49129574	0.004648	2.862678	2.276487006	-0.586190994	0.001776917
60.49927566	0.007758	2.870436	2.276787316	-0.593648684	0.00799477
60.51193543	0.001572	2.872008	2.277263745	-0.594744255	0.010657701
60.52940413	0.01205	2.884058	2.27792115	-0.60613685	0.007994832
60.54422846	0.001609	2.885667	2.278479038	-0.607187962	0.269154796
60.81668326	0.004991	2.890658	2.288732411	-0.601925589	0.123466506
60.94348377	0.001677	2.892335	2.293504333	-0.598830667	0.088825233
61.03752	0.008745	2.90108	2.297043226	-0.604036774	0.084385593
61.12912609	0.005696	2.906776	2.300490666	-0.606285334	0.017764566
61.15099466	0.002512	2.909288	2.301313652	-0.607974348	0.007106553
61.16060621	0.002498	2.911786	2.301675366	-0.610110634	0.168174929
61.33171164	0.003363	2.915149	2.308114628	-0.607034372	0.004828367
61.33922851	0.002014	2.917163	2.308397513	-0.608765487	0.173818833
61.51520134	0.002294	2.919457	2.315019951	-0.604437049	0.092438267
61.60926411	0.000955	2.920412	2.318559843	-0.601852157	0.159337015
61.77069712	0.003237	2.923649	2.3246351	-0.5990139	0.129676208
61.90300233	0.002021	2.92567	2.329614181	-0.596055819	0.203481457
62.10846279	0.001937	2.927607	2.337346336	-0.590260664	0.837352239
62.94814703	0.002727	2.930334	2.368946424	-0.561387576	0.091737384
63.04191141	0.001327	2.931661	2.372475087	-0.559185913	0.25797054
63.30164395	0.002197	2.933858	2.382249679	-0.551608321	0.193127278
63.49803623	0.004333	2.938191	2.389640569	-0.548550431	0.040696957

Location	Aperture (mm)	Cum. Ap (mm)	Hom. strain	difference	Spacing (mm)
63.54187419	0.001949	2.94014	2.391290336	-0.548849664	0.690438487
64.23473567	0.002897	2.943037	2.417364999	-0.525672001	0.016552089
64.25577126	0.00607	2.949107	2.418156637	-0.530950363	0.025526735
64.285709	0.002752	2.951859	2.419283293	-0.532575707	0.037939005
64.33091	0.011772	2.963631	2.420984356	-0.542646644	0.020702114
64.36289062	0.010785	2.974416	2.422187892	-0.552228108	0.048281036
64.41723915	0.00135	2.975766	2.424233207	-0.551532793	0.658727168
65.07917582	0.005069	2.980835	2.449144067	-0.531690933	0.007037689
65.09044951	0.003403	2.984238	2.449568333	-0.534669667	0.011787517
65.10541153	0.002946	2.987184	2.450131403	-0.537052597	0.030498369
65.1425584	0.010351	2.997535	2.451529363	-0.546005637	0.117407361
65.38544326	0.240604	3.238139	2.460669921	-0.777469079	0.356599955
65.86695771	0.009225	3.247364	2.478790898	-0.768573102	0.882774308
66.75532902	0.001969	3.249333	2.512223241	-0.737109759	0.228155192
66.98606371	0.00319	3.252523	2.520906549	-0.731616451	0.414151282
67.40477499	0.00593	3.258453	2.536664036	-0.721788964	0.069881435
67.47858593	0.001929	3.260382	2.539441785	-0.720940215	0.669021384
68.15189981	0.006656	3.267038	2.564780807	-0.702257193	0.203479845
68.36073516	0.004055	3.271093	2.57263997	-0.69845303	0.430627341
68.7968215	0.006863	3.277956	2.589051338	-0.688904662	0.17264254
68.97359404	0.001397	3.279353	2.595703872	-0.683649128	0.014387272
68.99050831	0.003657	3.28301	2.596340411	-0.686669589	0.080176759
69.07320257	0.001378	3.284388	2.599452469	-0.684935531	0.66285747
69.73879854	0.004099	3.288487	2.624501041	-0.663985959	0.025688433
69.76704797	0.001023	3.28951	2.625564161	-0.663945839	0.576535087
70.34512056	0.002052	3.291562	2.647318939	-0.644243061	0.080155331
70.42779839	0.002993	3.294555	2.650430378	-0.644124622	0.021580027
70.45241592	0.003082	3.297637	2.651356817	-0.646280183	0.333996495
70.79102941	0.006152	3.303789	2.66409996	-0.63968904	1.169508921
71.96463634	0.002044	3.305833	2.70826666	-0.59756634	0.282608879
72.25105021	0.005566	3.311399	2.719045359	-0.592353641	0.36689145
72.63697616	0.032503	3.343902	2.733569026	-0.610332974	0.151064239
72.8349849	0.061386	3.405288	2.741020748	-0.664267252	0.922861128
73.79624503	0.015412	3.4207	2.777196137	-0.643503863	0.217865738
74.02387127	0.004109	3.424809	2.785762463	-0.639046537	0.160328475
74.18837224	0.004236	3.429045	2.791953178	-0.637091822	0.013396107
74.20491435	0.002056	3.431101	2.792575712	-0.638525288	0.073991047
74.2815479	0.003229	3.43433	2.795459685	-0.638870315	0.132592713
74.41729311	0.003076	3.437406	2.800568225	-0.636837775	0.004110326
74.42429494	0.002707	3.440113	2.800831727	-0.639281273	0.089403221
74.51709916	0.004095	3.444208	2.804324256	-0.639883744	0.713215168
75.23481183	0.0049	3.449108	2.831334151	-0.617773849	0.056525672
75.294279	0.000983	3.450091	2.833572097	-0.616518903	0.031854573
75.32813507	0.00302	3.453111	2.834846213	-0.618264787	2.527072376
77.85814695	0.002859	3.45597	2.930058906	-0.525911094	0.361737966
78.22270791	0.002787	3.458757	2.943778537	-0.514978463	0.532338668
78.75751808	0.002156	3.460913	2.963905208	-0.497007792	0.634086661
79.39898624	0.012607	3.47352	2.988045771	-0.485474229	1.392509734
80.79965347	0.003708	3.477228	3.0407575	-0.4364705	0.811867205
81.61542918	0.004109	3.481337	3.07145783	-0.40987917	0.721435016
82.3455092	0.013181	3.494518	3.09893315	-0.39558485	0.364854357
82.71851255	0.003117	3.497635	3.112970497	-0.384664503	0.770750837
83.49150089	0.001358	3.498993	3.142060598	-0.356932402	0.560097683
84.05416107	0.003767	3.50276	3.163235356	-0.339524644	0.005136788

Location	Aperture (mm)	Cum. Ap (mm)	Hom. strain	difference	Spacing (mm)
84.06212736	0.001892	3.504652	3.163535154	-0.341116846	0.028770665
84.09224853	0.000809	3.505461	3.164668713	-0.340792287	0.69883229
84.79371032	0.00445	3.509911	3.191067034	-0.318843966	1.026648833
85.82516565	0.005163	3.515074	3.229884101	-0.285189899	0.202453751
86.0312659	0.00213	3.517204	3.237640333	-0.279563667	0.386412644
86.42049904	0.003511	3.520715	3.25228846	-0.26842654	0.361751751
86.78612929	0.004246	3.524961	3.266048333	-0.258912667	0.709091726
87.49829702	0.001906	3.526867	3.292849553	-0.234017447	2.31331665
89.81664167	0.00815	3.535017	3.38009651	-0.15492049	0.092486978
89.91674615	0.007085	3.542102	3.383863772	-0.158238228	0.012331067
89.94115021	0.017061	3.559163	3.384782178	-0.174380822	0.417233247
90.36921196	0.004596	3.563759	3.400891553	-0.162867447	0.19834407
90.57307103	0.006434	3.570193	3.408563442	-0.161629558	0.092485354
90.67169438	0.005842	3.576035	3.412274965	-0.163760035	0.011349585
90.68776097	0.003592	3.579627	3.412879603	-0.166747397	0.029798289
90.74160626	0.044502	3.624129	3.414905979	-0.209223021	0.038032894
90.80425965	0.004739	3.628868	3.417263833	-0.211604167	0.4100416
91.21858125	0.003821	3.632689	3.432856121	-0.199832879	0.200397858
91.42471611	0.007653	3.640342	3.440613656	-0.199728344	2.102629527
93.53287464	0.003405	3.643747	3.519950616	-0.123796384	0.392576531
93.92942117	0.004535	3.648282	3.53487397	-0.11340803	2.966924682
96.90079185	0.004357	3.652639	3.646696451	-0.005942549	0.011303178
96.91563753	0.002728	3.655367	3.647255142	-0.008111858	0.214186
97.13118753					

Location	Aperture (mm)	Cum. Ap (mm)	Hom. strain	difference	Spacing (mm)
Sample 53a			V'		C
		0-20, 340-360	0.478150793		1.868564765
loc	ap	cumap	hom strain	difference	spacing
0	0	0	0	0	
0.123248	0.002181	0.002181	0.00434791	0.00216691	0.09548798
0.227643	0.015633	0.017814	0.008030735	-0.009783265	1.887209115
2.124202	0.003068	0.020882	0.07493719	0.05405519	0.619025752
2.747000	0.004475	0.025357	0.096908108	0.071551108	0.13206461
2.883434	0.004265	0.029622	0.101721221	0.072099221	0.05411737
2.940407	0.001445	0.031067	0.103731081	0.072664081	0.402082197
3.345050	0.003678	0.034745	0.118006021	0.083261021	1.662064628
5.013280	0.008653	0.043398	0.176857513	0.133459513	0.080569227
5.103342	0.010332	0.05373	0.180034693	0.126304693	0.152196816
5.265682	0.009955	0.063685	0.185761703	0.122076703	0.5878814
5.859663	0.002243	0.065928	0.206716026	0.140788026	0.417130417
6.279801	0.003773	0.069701	0.221537586	0.151836586	0.111162323
6.395786	0.005872	0.075573	0.225629275	0.150056275	0.134284539
6.535546	0.005078	0.080651	0.230559685	0.149908685	0.011959214
6.551136	0.002185	0.082836	0.231109691	0.148273691	0.069659042
6.642361	0.040946	0.123782	0.234327892	0.110545892	0.079824031
6.744839	0.004363	0.128145	0.237943109	0.109798109	0.011935768
6.760074	0.002234	0.130379	0.238480541	0.108101541	0.005968112
6.890804	0.24729	0.377669	0.243092412	-0.134576588	0.212611168
7.231294	0.008468	0.386137	0.255104157	-0.131032843	0.039544758
7.276865	0.003585	0.389722	0.25671181	-0.13301019	1.515638563
8.796529	0.004466	0.394188	0.310322218	-0.083865782	0.094751608
8.894257	0.001487	0.395675	0.313769851	-0.081905149	0.096980665
8.992721	0.001479	0.397154	0.317243433	-0.079910567	0.019409739
9.014354	0.002968	0.400122	0.318006606	-0.082115394	0.035807716
9.052764	0.002235	0.402357	0.319361599	-0.082995401	0.906436576
9.961768	0.0029	0.405257	0.351429265	-0.053827735	0.071618542
10.035669	0.001665	0.406922	0.354036331	-0.052885669	0.817645894
10.867698	0.027102	0.434024	0.383388499	-0.050635501	0.008206295
10.891315	0.00372	0.437744	0.384221665	-0.053522335	0.055207708
10.956412	0.016058	0.453802	0.386518134	-0.067283866	0.025363756
10.991706	0.003803	0.457605	0.387763238	-0.069841762	0.083552541
11.087789	0.021257	0.478862	0.391152819	-0.087709181	0.410825321
11.512226	0.005967	0.484829	0.406126035	-0.078702965	0.487909297
12.007829	0.009421	0.49425	0.42360983	-0.07064017	3.78646751
15.801899	0.005784	0.500034	0.55745628	0.05742228	0.032086688
15.840944	0.008131	0.508165	0.558833673	0.050668673	2.459576471
18.307481	0.005791	0.513956	0.645847694	0.131891694	0.948482954
19.261004	0.004289	0.518245	0.679485888	0.161240888	0.659031008
19.922922	0.001485	0.51973	0.7028369	0.1831069	0.226798218
20.151555	0.002184	0.521914	0.71090256	0.18898856	0.324821258
20.546555	0.138173	0.660087	0.724837284	0.064750284	0.006714234
20.623804	0.002897	0.662984	0.727562467	0.064578467	0.024629384
20.651731	0.003699	0.666683	0.728547683	0.061864683	1.7909835
22.453105	0.017081	0.683764	0.792096181	0.108332181	0.198988661
22.669238	0.017208	0.700972	0.799720884	0.098748884	0.281441946
22.960848	0.003128	0.7041	0.810008242	0.105908242	0.133463334
23.097038	0.002326	0.706426	0.814812738	0.108386738	1.58679016

Location	Aperture (mm)	Cum. Ap (mm)	Hom. strain	difference	Spacing (mm)
24.686855	0.003727	0.710153	0.870897975	0.160744975	1.074817578
25.764706	0.00234	0.712493	0.908922192	0.196429192	1.869720066
27.637089	0.002986	0.715479	0.974975751	0.259496751	1.691145359
29.330874	0.002293	0.717772	1.034728758	0.316956758	0.281913999
29.615057	0.002246	0.720018	1.044754127	0.324736127	0.275443292
29.894305	0.005362	0.72538	1.054605358	0.329225358	0.005537211
29.903663	0.00228	0.72766	1.054935495	0.327275495	0.729062184
30.635822	0.003914	0.731574	1.080764462	0.349190462	1.540140156
32.179482	0.003126	0.7347	1.135221399	0.400521399	0.113612896
32.295796	0.002277	0.736977	1.139324715	0.402347715	1.580746565
33.879146	0.002928	0.739905	1.19518179	0.45527679	2.275207382
36.158112	0.004591	0.744496	1.275578733	0.531082733	3.226499633
39.387636	0.001456	0.745952	1.389509211	0.643557211	4.309603057
43.703170	0.010407	0.756359	1.541751784	0.785392784	0.047665742
43.765225	0.018371	0.77473	1.543940939	0.769210939	0.013057453
43.788729	0.002523	0.777253	1.544770125	0.767517125	0.612445786
44.404897	0.00492	0.782173	1.566507152	0.784334152	0.363025297
44.772004	0.003245	0.785418	1.579457908	0.794039908	1.702835354
46.484881	0.016838	0.802256	1.639884439	0.837628439	0.502104338
46.997619	0.004428	0.806684	1.657972685	0.851288685	0.105118964
47.111448	0.012992	0.819676	1.661988321	0.842312321	0.363031811
47.483170	0.004389	0.824065	1.675101867	0.851036867	0.0498338
47.536498	0.002599	0.826664	1.676983155	0.850319155	2.057866709
49.597760	0.004193	0.830857	1.749699972	0.918842972	0.250131364
49.853329	0.006681	0.837538	1.758715863	0.921177863	0.00590262
49.864415	0.003686	0.841224	1.759106956	0.917882956	5.259177096
55.128754	0.006638	0.847862	1.944821269	1.096959269	0.068621783
55.201792	0.002195	0.850057	1.947397899	1.097340899	0.985643267
56.189962	0.002858	0.852915	1.982258356	1.129343356	0.137974697
56.596809	0.534886	1.387801	1.996611014	0.608810014	0.114372467
56.981420	0.005592	1.393393	2.010179261	0.616786261	0.110675316
57.097471	0.005159	1.398552	2.014273279	0.615721279	0.007377818
57.128817	0.042777	1.441329	2.01537909	0.57405009	0.139454945
57.291501	0.003681	1.44501	2.021118222	0.576108222	0.028036895
57.322844	0.002932	1.447942	2.022223948	0.574281948	0.124700531
57.449359	0.000697	1.448639	2.026687121	0.578048121	0.004427845
57.455184	0.002096	1.450735	2.026892591	0.576157591	3.449113561
60.906434	0.002177	1.452912	2.148645107	0.695733107	0.098140843
61.008554	0.005783	1.458695	2.152247706	0.693552706	0.025086044
61.038338	0.003613	1.462308	2.153298421	0.690990421	1.002753753
62.046396	0.006995	1.469303	2.188860483	0.719557483	0.540109342
62.591881	0.003755	1.473058	2.208103972	0.735045972	3.245291385
65.840818	0.003537	1.476595	2.322719342	0.846124342	0.64120149
66.485241	0.002907	1.479502	2.345453186	0.865951186	0.117316933
66.605482	0.00294	1.482442	2.349695004	0.867253004	0.172664246
66.780664	0.002095	1.484537	2.355875031	0.871338031	0.560058532
67.343982	0.004424	1.488961	2.375747653	0.886786653	1.300840375
68.648842	0.003616	1.492577	2.421780259	0.929203259	3.517676062
72.194078	0.051504	1.544081	2.546848395	1.002767395	1.100719459
73.323693	0.006287	1.550368	2.586698728	1.036330728	0.081902732
73.411592	0.005706	1.556074	2.58979962	1.03372562	0.006641845
73.424003	0.005831	1.561905	2.59023743	1.02833243	1.652296052
75.085523	0.012618	1.574523	2.648852223	1.074329223	0.028747723
75.122411	0.003663	1.578186	2.650153558	1.071967558	0.380640814

Location	Aperture (mm)	Cum. Ap (mm)	Hom. strain	difference	Spacing (mm)
75.506460	0.003153	1.581339	2.663701956	1.082362956	0.780448512
76.313435	0.0499	1.631239	2.692170261	1.060931261	3.596673205
79.938177	0.006237	1.637476	2.820043181	1.182567181	0.675480021
80.618286	0.003021	1.640497	2.844035933	1.203538933	0.128007862
80.750083	0.004558	1.645055	2.848685454	1.203630454	0.001737958
81.716276	1.924352	3.569407	2.882770618	-0.686636382	0.125156299
82.81139158	0.015566	3.584973	2.921403879	-0.663569121	9.509013451
92.32919503	0.002014	3.586987	3.257171065	-0.329815935	0.078653928
92.41056896	0.003426	3.590413	3.260041758	-0.330371242	0.707943918
93.12126488	0.002078	3.592491	3.285113548	-0.307377452	0.207633211
93.34784459	0.035815	3.628306	3.293106782	-0.335199218	0.451414171
93.82595076	0.017569	3.645875	3.309973317	-0.335901683	0.68668942
94.52388418	0.004919	3.650794	3.334594874	-0.316199126	0.010629709
94.53840339	0.00286	3.653654	3.33510708	-0.31854692	0.034011835
94.57982122	0.011952	3.665606	3.33656821	-0.32903779	0.010629691
94.59887991	0.004906	3.670512	3.337240559	-0.333271441	0.10431839
94.7977433	0.184184	3.854696	3.344256022	-0.510439978	1.751347844
96.64578865	0.009211	3.863907	3.409451	-0.454456	0.017728159
96.67200981	0.007775	3.871682	3.410376024	-0.461305976	0.241653776
96.91896008	0.002818	3.8745	3.419087887	-0.455412113	0.096369771
97.01783985	0.002202	3.876702	3.422576148	-0.454125852	0.05598241
97.07562926	0.001412	3.878114	3.424614832	-0.453499168	0.07298802
97.15176178	0.004877	3.882991	3.42730062	-0.45569038	0.561960525
97.72111231	0.009903	3.892894	3.447386055	-0.445507945	10.21497056
107.9420289	0.001989	3.894883	3.807957526	-0.086925474	2.795899759
110.7420506	0.006255	3.901138	3.906736139	0.005598139	0.002836308
110.7490594	0.00209	3.903228	3.906983395	0.003755395	0.242351371
110.9942098	0.003508	3.906736	3.915631761	0.008895761	0.013463841
111.0234742	0.028093	3.934829	3.916664143	-0.018164857	0.002125282
111.0410459	0.0028	3.937629	3.917284036	-0.020344964	0.00292136
111.0520768	0.013419	3.951048	3.917673181	-0.033374819	0.00566804
111.0655733	0.002238	3.953286	3.918149309	-0.035136691	0.994881
112.0615733		3.953286	3.953286	0	

Location	Aperture (mm)	Cum. Ap (mm)	Hom. strain	difference	Spacing (mm)
Sample 53a macrofractures			V'		C
			0.259208688		1.298702936
loc	ap	cumap	hom strain	difference	spacing
0	0	0	0	0	
285.7465	0.265	0.265	2.745893786	2.480893786	51.816
338.17	0.95	1.215	3.249659757	2.034659757	83.246
422.766	1.75	2.965	4.062588807	1.097588807	15.24
439.356	0.95	3.915	4.222011155	0.307011155	27.432
467.3955	0.265	4.18	4.491457986	0.311457986	24.384
492.222	0.62	4.8	4.730029349	-0.069970651	55.614
548.621	0.95	5.75	5.271998065	-0.478001935	18.288
568.084	1.4	7.15	5.459028635	-1.690971365	18.288
587.547	0.95	8.1	5.646059205	-2.453940795	21.336
610.058	1.4	9.5	5.862379667	-3.637620333	21.336
632.569	0.95	10.45	6.07870013	-4.37129987	3.048
636.2245	0.265	10.715	6.113827821	-4.601172179	21.666
658.1555	0.265	10.98	6.324574747	-4.655425253	27.697
686.1175	0.265	11.245	6.593276838	-4.651723162	15.24
702.065	1.15	12.395	6.746525053	-5.648474947	190.376
893.391	0.75	13.145	8.585080817	-4.559919183	15.24
909.206	0.4	13.545	8.737055768	-4.807944232	73.152
982.723	0.33	13.875	9.443520671	-4.431479329	70.104
1053.692	1.4	15.275	10.12550045	-5.149499546	256.762
1311.404	0.5	15.775	12.60199546	-3.173004542	6.096
1318	0.5	16.275	12.66538002	-3.609619985	6.096
1324.721	0.75	17.025	12.72996577	-4.295034234	24.384
1350.055	1.15	18.175	12.97341397	-5.201586027	12.192
1363.522	1.4	19.575	13.10282571	-6.472174287	334.282
1698.814	0.62	20.195	16.3248292	-3.8701708	9.144
1708.3755	0.215	20.41	16.41671086	-3.993289138	98.041
1806.899	0.75	21.16	17.36347685	-3.796523153	237.744
2045.493	0.95	22.11	19.65625657	-2.453743427	30.48
2077.148	1.4	23.51	19.96044671	-3.549553287	128.516
2206.939	1.15	24.66	21.20767914	-3.452320861	30.48
2238.304	0.62	25.28	21.50908251	-3.770917489	104.782
2343.871	0.95	26.23	22.52353332	-3.706466676	45.322
2390.043	0.75	26.98	22.96722523	-4.012774774	494.13
2884.923	0.75	27.73	27.72279674	-0.007203255	30.48
2916.088	0.62	28.35	28.02227821	-0.327721792	73.552
2990.325	0.75	29.1	28.73566198	-0.364338017	76.95
3068.225	1.15	30.25	29.48424552	-0.765754479	113.396
3182.771	1.15	31.4	30.58498044	-0.815019563	246.888
3430.544	0.62	32.02	32.96596618	0.945966175	146.304
3577.468	0.62	32.64	34.37783893	1.737838932	6.096
3584.249	0.75	33.39	34.44300126	1.053001255	9.144
3594.343	1.15	34.54	34.54	0	

Location	Aperture (mm)	Cum. Ap (mm)	Hom. strain	difference	Spacing (mm)
Sample 54			V'		C
	set A	0 to 30	0.401775599		1.790828497
loc	ap	cumap	hom strain	difference	spacing
0	0	0	0	0	
0.1014	0.005156	0.005156	0.002342036	-0.002813964	0.415499441
0.520687441	0.00242	0.007576	0.012026318	0.004450318	0.535864695
1.059228136	0.002932	0.010508	0.024464992	0.013956992	0.059584368
1.131103004	0.021649	0.032157	0.026125086	-0.006031914	0.072369515
1.216760519	0.004927	0.037084	0.028103517	-0.008980483	0.021664549
1.250299568	0.018822	0.055906	0.028878169	-0.027027831	3.084671352
4.345372419	0.001981	0.057887	0.100365065	0.042478065	0.725683167
5.076378586	0.008665	0.066552	0.117249114	0.050697114	0.872200279
5.954323865	0.002825	0.069377	0.137527016	0.068150016	1.112985627
7.070598491	0.003753	0.07313	0.163309611	0.090179611	0.015165689
7.18880368	0.202326	0.275456	0.166039796	-0.109416204	1.012964303
8.304958983	0.004056	0.279512	0.191819634	-0.087692366	0.064998112
8.373585095	0.0032	0.282712	0.193404692	-0.089307308	0.005415035
8.38158713	0.001974	0.284686	0.193589515	-0.091096485	0.122415399
8.509243028	0.008507	0.293193	0.196537983	-0.096655017	0.182257634
8.710411662	0.029315	0.322508	0.201184375	-0.121323625	0.087064613
8.813691275	0.003115	0.325623	0.203569824	-0.122053176	0.356613588
9.173567863	0.003411	0.329034	0.211881893	-0.117152107	0.347736214
9.526464577	0.00691	0.335944	0.220032749	-0.115911251	0.724526528
10.25851061	0.008129	0.344073	0.236940815	-0.107132185	0.155990063
10.41961117	0.002092	0.346165	0.240661755	-0.105503245	0.133072874
10.55476204	0.002064	0.348229	0.243783335	-0.104445665	0.517950764
11.07807531	0.008661	0.35689	0.255870301	-0.101019699	0.075880899
11.16115121	0.005729	0.362619	0.257789105	-0.104829895	0.067859738
11.23591944	0.008088	0.370707	0.259516027	-0.111190973	1.268532385
12.52007983	0.023168	0.393875	0.289176279	-0.104698721	0.772164004
13.30684283	0.00603	0.399905	0.307348144	-0.092556856	0.657496869
13.9697827	0.004856	0.404761	0.322660066	-0.082100934	0.33692038
14.31061908	0.002976	0.407737	0.330532363	-0.077204637	0.314233136
14.62828122	0.003882	0.411619	0.337869406	-0.073749594	0.057421732
14.69004745	0.004807	0.416426	0.33929602	-0.07712998	0.065772241
14.75974169	0.003037	0.419463	0.340905748	-0.078557252	3.034008486
17.79927168	0.008006	0.427469	0.411109771	-0.016359229	4.84686438
22.65106306	0.001848	0.429317	0.523171594	0.093854594	5.747611855
28.40141191	0.003626	0.432943	0.6559874	0.2230444	3.442290391
31.8476623	0.004294	0.437237	0.735585444	0.298348444	1.718461455
33.57055276	0.004564	0.441801	0.775379044	0.333578044	0.033625936
33.60928969	0.005658	0.447459	0.776273751	0.328814751	0.107547882
33.72133058	0.003328	0.450787	0.778861559	0.328074559	0.748612454
34.47355153	0.003889	0.454676	0.796235606	0.341559606	0.063862518
34.54154555	0.004374	0.45905	0.797806064	0.338756064	0.029126436
34.57671348	0.007709	0.466759	0.798618338	0.331859338	0.01120267
34.60028515	0.017029	0.483788	0.799162773	0.315374773	0.154463265
34.76489192	0.003258	0.487046	0.802964695	0.315918695	0.010082572
34.77878049	0.004354	0.4914	0.803285479	0.311885479	0.010082527
34.79264052	0.003201	0.494601	0.803605604	0.309004604	0.105304793
34.95540531	0.111719	0.60632	0.807364983	0.201044983	0.061623325
35.07509414	0.004412	0.610732	0.810129435	0.199397435	0.080074087

Location	Aperture (mm)	Cum. Ap (mm)	Hom. strain	difference	Spacing (mm)
35.16409372	0.013439	0.624171	0.812185059	0.188014059	0.062741906
35.23627913	0.005448	0.629619	0.813852325	0.184233325	0.058251204
35.29779933	0.00109	0.630709	0.815273257	0.184564257	0.17058015
35.46941748	0.000986	0.631695	0.819237122	0.187542122	0.097259637
35.57083462	0.007329	0.639024	0.821579553	0.182555553	0.07330013
35.64961075	0.003623	0.642647	0.823399045	0.180752045	0.013792988
35.66728224	0.004134	0.646781	0.823807204	0.177026204	0.294768571
35.96986931	0.011503	0.658284	0.830796057	0.172512057	0.083680331
36.06451914	0.010436	0.66872	0.832982184	0.164262184	0.35822552
36.43117916	0.006433	0.675153	0.841450931	0.166297931	0.241785054
36.67662271	0.000884	0.676037	0.84711994	0.17108294	1.555899795
38.23798101	0.010033	0.68607	0.883182632	0.197112632	1.520117911
39.76435692	0.002483	0.688553	0.918437336	0.229884336	0.394829899
40.16304782	0.005239	0.693792	0.9276459	0.2338539	0.667203962
40.83419078	0.002639	0.696431	0.943147288	0.246716288	0.95832262
41.8024944	0.017323	0.713754	0.965512197	0.251758197	3.85946505
45.67407295	0.006904	0.720658	1.054934045	0.334276045	0.218510007
45.90350196	0.014934	0.735592	1.060233167	0.324641167	0.044410728
46.31984768	0.728936	1.464528	1.069849504	-0.394678496	0.005330047
46.70087673	0.022462	1.48699	1.078650131	-0.408339869	0.029312657
46.74228539	0.00173	1.48872	1.079606547	-0.409113453	0.013324481
46.75780387	0.002658	1.491378	1.079964978	-0.411413022	0.064839499
46.82560287	0.003261	1.494639	1.081530931	-0.413108069	0.008882934
46.8372823	0.002332	1.496971	1.081800691	-0.415170309	0.011580549
46.85134835	0.002639	1.49961	1.082125574	-0.417484426	0.056845076
46.95006243	0.081099	1.580709	1.084405573	-0.496303427	0.133244976
47.1260529	0.004392	1.585101	1.088470425	-0.496630575	0.059518738
47.19705664	0.018578	1.603679	1.090110399	-0.513568601	0.063069934
47.27449658	0.010162	1.613841	1.091899029	-0.521941971	0.139462626
47.4249527	0.011825	1.625666	1.095374114	-0.530291886	0.00621821
47.44726791	0.020369	1.646035	1.095889528	-0.550145472	0.031100484
47.4898714	0.002637	1.648672	1.096873541	-0.551798459	3.144737077
50.63725697	0.00266	1.651332	1.169568704	-0.481763296	0.143006879
50.78456485	0.005942	1.657274	1.172971074	-0.484302926	2.465909507
53.25517236	0.003454	1.660728	1.230034695	-0.430693305	0.950456026
54.20867839	0.002646	1.663374	1.252057823	-0.411316177	0.19808104
54.40977693	0.003389	1.666763	1.256702596	-0.410060404	1.350182213
55.76209514	0.000883	1.667646	1.287937089	-0.379708911	0.024869657
55.7891703	0.003528	1.671174	1.288562444	-0.382611556	2.464691829
58.25807463	0.004897	1.676071	1.345586727	-0.330484273	1.455109964
59.71731809	0.00337	1.679441	1.379290872	-0.300150128	0.44330448
60.16425757	0.0039	1.683341	1.389613833	-0.293727167	0.028436453
60.19589902	0.00251	1.685851	1.390344656	-0.295506344	0.032776766
60.23714229	0.014423	1.700274	1.391297252	-0.308976748	0.007994737
60.25449603	0.004295	1.704569	1.391698071	-0.312870929	0.00266343
60.26234295	0.006072	1.710641	1.391879311	-0.318761689	0.223592789
60.49129574	0.004648	1.715289	1.397167434	-0.318121566	0.001776917
60.49927566	0.007758	1.723047	1.397351746	-0.325695254	0.00799477
60.51193543	0.001572	1.724619	1.397644149	-0.326974851	0.010657701
60.52940413	0.01205	1.736669	1.398047623	-0.338621377	0.007994832
60.54422846	0.001609	1.738278	1.398390021	-0.339887979	0.269154796
60.81668326	0.004991	1.743269	1.404682909	-0.338586091	0.123466506
60.94348377	0.001677	1.744946	1.40761162	-0.33733438	0.088825233
61.03752	0.008745	1.753691	1.409783575	-0.343907425	0.084385593

Location	Aperture (mm)	Cum. Ap (mm)	Hom. strain	difference	Spacing (mm)
61.12912609	0.005696	1.759387	1.411899401	-0.347487599	0.017764566
61.15099466	0.002512	1.761899	1.412404499	-0.349494501	0.007106553
61.16060621	0.002498	1.764397	1.412626498	-0.351770502	0.168174929
61.33171164	0.003363	1.76776	1.41657852	-0.35118148	0.004828367
61.33922851	0.002014	1.769774	1.416752137	-0.353021863	0.2685511
61.60926411	0.000955	1.770729	1.422989149	-0.347739851	0.159337015
61.77069712	0.003237	1.773966	1.426717767	-0.347248233	0.129676208
61.90300233	0.002021	1.775987	1.42977362	-0.34621338	1.042770696
62.94814703	0.002727	1.778714	1.453913327	-0.324800673	0.091737384
63.04191141	0.001327	1.780041	1.456079003	-0.323961997	0.453294818
63.49803623	0.004333	1.784374	1.466614118	-0.317759882	0.040696957
63.54187419	0.001949	1.786323	1.467626643	-0.318696357	0.709887577
64.25577126	0.00607	1.792393	1.484115523	-0.308277477	0.025526735
64.285709	0.002752	1.795145	1.484806995	-0.310338005	0.037939005
64.33091	0.011772	1.806917	1.485851003	-0.321065997	0.020702114
64.36289062	0.010785	1.817702	1.486589659	-0.331112341	0.048281036
64.41723915	0.00135	1.819052	1.487844947	-0.331207053	0.719468743
65.1425584	0.010351	1.829403	1.504597646	-0.324805354	0.117407361
65.38544326	0.240604	2.070007	1.510207557	-0.559799443	0.356599955
65.86695771	0.009225	2.079232	1.521329096	-0.557902904	0.882774308
66.75532902	0.001969	2.081201	1.541847808	-0.539353192	0.645496474
67.40477499	0.00593	2.087131	1.556848061	-0.530282939	0.069881435
67.47858593	0.001929	2.08906	1.558552873	-0.530507127	0.669021384
68.15189981	0.006656	2.095716	1.574104403	-0.521611597	0.203479845
68.36073516	0.004055	2.099771	1.578927873	-0.520843127	0.430627341
68.7968215	0.006863	2.106634	1.589000159	-0.517633841	0.936496042
69.73879854	0.004099	2.110733	1.610757002	-0.499975998	0.025688433
69.76704797	0.001023	2.111756	1.611409479	-0.500346521	0.658742418
70.42779839	0.002993	2.114749	1.626670832	-0.488078168	0.358658522
70.79102941	0.006152	2.120901	1.635060378	-0.485840622	2.010186489
72.8349849	0.061386	2.182287	1.682269618	-0.500017382	1.156138866
74.02387127	0.004109	2.186396	1.709729325	-0.476666675	0.177960582
74.20491435	0.002056	2.188452	1.713910877	-0.474541123	0.073991047
74.2815479	0.003229	2.191681	1.715680882	-0.476000118	0.132592713
74.41729311	0.003076	2.194757	1.71881619	-0.47594081	0.096220547
74.51709916	0.004095	2.198852	1.72112141	-0.47773059	0.713215168
75.23481183	0.0049	2.203752	1.737698419	-0.466053581	0.056525672
75.294279	0.000983	2.204735	1.739071932	-0.465663068	0.031854573
75.32813507	0.00302	2.207755	1.739853906	-0.467901094	5.468154404
80.79965347	0.003708	2.211463	1.866229564	-0.345233436	3.250770098
84.05416107	0.003767	2.21523	1.941398925	-0.273831075	0.005136788
84.06212736	0.001892	2.217122	1.941582922	-0.275539078	3.434270659
87.49829702	0.001906	2.219028	2.020948132	-0.198079868	2.867663941
90.36921196	0.004596	2.223624	2.087257653	-0.136366347	0.297263424
90.67169438	0.005842	2.229466	2.094244089	-0.135221911	0.011349585
90.68776097	0.003592	2.233058	2.094615179	-0.138442821	0.731332641
91.42471611	0.007653	2.240711	2.111636632	-0.129074368	5.485730919
96.91563753	0.002728	2.243439	2.238460442	-0.004978558	0.214186
97.13118753		2.243439	2.243439	0	

Location	Aperture (mm)	Cum. Ap (mm)	Hom. strain	difference	Spacing (mm)
Sample 55			V'		C
			0.494027427		1.376327236
loc	ap	cumap	hom strain	difference	spacing
0	0	0	0	0	
0.003500	0.310855	0.310855	0.000341033	-0.310513967	0.498237986
0.659620	0.00491	0.315765	0.064272053	-0.251492947	2.075645566
2.740135	0.004827	0.320592	0.266993032	-0.053598968	0.547566068
3.303763	0.027298	0.34789	0.321911831	-0.025978169	1.587828909
4.911905	0.013328	0.361218	0.478605846	0.117387846	0.391473641
5.313087	0.006089	0.367307	0.517696202	0.150389202	0.287801232
5.606322	0.004779	0.372086	0.546268435	0.174182435	0.165862278
5.778049	0.00695	0.379036	0.563001136	0.183965136	0.231707297
6.015655	0.004848	0.383884	0.586153002	0.202269002	0.487818142
6.511098	0.010401	0.394285	0.634427906	0.240142906	0.075616067
6.593728	0.003627	0.397912	0.642479208	0.244567208	0.241462646
6.838163	0.002317	0.400229	0.666296414	0.266067414	0.014633618
6.855492	0.003075	0.403304	0.667984976	0.264680976	0.024419994
6.883331	0.003763	0.407067	0.670697549	0.263630549	1.076842259
7.965080	0.00605	0.413117	0.776100906	0.362983906	0.081712063
8.051035	0.002436	0.415553	0.78447619	0.36892319	0.053655036
8.107703	0.003589	0.419142	0.789997757	0.370855757	0.04026045
8.151113	0.002711	0.421853	0.794227581	0.372374581	0.048793672
8.228097	0.053669	0.475522	0.801728711	0.326206711	0.007315893
8.371830	0.219166	0.694688	0.815733794	0.121045794	0.015852621
8.503363	0.012194	0.706882	0.82855006	0.12166806	0.137802897
8.672117	0.049709	0.756591	0.844993139	0.088402139	0.185360977
8.883643	0.00262	0.759211	0.865603743	0.106392743	0.363413622
9.249585	0.002437	0.761648	0.901260385	0.139612385	0.397570376
9.651409	0.00607	0.767718	0.940413271	0.172695271	0.143900085
9.801365	0.006043	0.773761	0.95502473	0.18126373	0.019548248
9.824796	0.001721	0.775482	0.957307724	0.181825724	0.01589967
9.843470	0.003829	0.779311	0.959127346	0.179816346	0.018454481
9.865202	0.002725	0.782036	0.961244816	0.179208816	0.287812832
10.159257	0.009759	0.791795	0.989896909	0.198101909	0.097563374
10.263524	0.003649	0.795444	1.000056506	0.204612506	0.001218903
10.270739	0.008344	0.803788	1.00075956	0.19697156	0.326832433
10.606007	0.008526	0.812314	1.033427324	0.221113324	0.026828983
10.638317	0.002437	0.814751	1.036575591	0.221824591	0.217076277
10.859051	0.004878	0.819629	1.058083432	0.238454432	0.12195103
10.992063	0.017244	0.836873	1.071043849	0.234170849	0.242696817
11.264734	0.042705	0.879578	1.097612377	0.218034377	0.429273544
11.724887	0.019054	0.898632	1.142448736	0.243816736	0.064643055
11.801950	0.005785	0.904417	1.149957551	0.245540551	0.06708067
11.884877	0.025907	0.930324	1.158037754	0.227713754	0.175618809
12.080788	0.014678	0.945002	1.177126946	0.232124946	0.245121747
12.335068	0.003638	0.94864	1.201903438	0.253263438	0.010975206
12.350094	0.004465	0.953105	1.203367609	0.250262609	0.224391844
12.579686	0.005934	0.959039	1.225738513	0.266699513	0.102440846
12.687914	0.005641	0.96468	1.236284059	0.271604059	0.00975599
12.703682	0.006382	0.971062	1.237820411	0.266758411	0.490242765
13.200750	0.007269	0.978331	1.286253712	0.307922712	0.078055237
13.283452	0.002024	0.980355	1.294311998	0.313956998	0.257330303

Location	Aperture (mm)	Cum. Ap (mm)	Hom. strain	difference	Spacing (mm)
13.543617	0.003647	0.984002	1.319662015	0.335660015	0.507314835
14.057023	0.008535	0.992537	1.369687215	0.377150215	0.648787724
14.711279	0.0024	0.994937	1.433436488	0.438499488	0.046338969
14.759424	0.001213	0.99615	1.438127683	0.441977683	0.286613289
15.051441	0.009595	1.005745	1.466581242	0.460836242	2.150025859
17.206970	0.001411	1.007156	1.676611507	0.669455507	0.023168638
17.232669	0.003649	1.010805	1.679115529	0.668310529	0.580502632
17.822017	0.014042	1.024847	1.736540389	0.711693389	0.031706739
17.861940	0.002391	1.027238	1.740430427	0.713192427	0.474404727
18.339053	0.003026	1.030264	1.786919351	0.756655351	0.174385307
18.585339	0.140775	1.171039	1.810916929	0.639877929	0.098097649
19.844535	2.181422	3.352461	1.933610392	-1.418850608	0.021135802
20.970395	0.028026	3.380487	2.043311838	-1.337175162	0.013095473
21.002003	0.008998	3.389485	2.046391605	-1.343093395	0.024482482
21.034087	0.006205	3.39569	2.049517801	-1.346172199	0.014246262
21.056842	0.010813	3.406503	2.051735027	-1.354767973	0.009109709
21.073048	0.003379	3.409882	2.053314077	-1.356567923	0.014804828
21.099224	0.019365	3.429247	2.055864693	-1.373382307	1.912626722
23.023180	0.003293	3.43254	2.243330951	-1.189209049	1.349476717
24.394226	0.039845	3.472385	2.376922804	-1.095462196	0.089965411
24.505811	0.003395	3.47578	2.387795455	-1.087984545	0.116154168
24.624801	0.002277	3.478057	2.399389611	-1.078667389	2.760815504
27.392832	0.012153	3.49021	2.669100766	-0.821109234	0.081216213
27.481955	0.003661	3.493871	2.677784747	-0.816086253	0.370375802
27.867077	0.025831	3.519702	2.715310217	-0.804391783	0.290404617
28.171011	0.001228	3.52093	2.744924928	-0.776005072	1.184975728
29.365172	0.017142	3.538072	2.861281474	-0.676790526	0.013534921
29.390339	0.006123	3.544195	2.863733735	-0.680461265	0.03198991
29.426619	0.002456	3.546651	2.867268726	-0.679382274	0.032015392
29.461697	0.003671	3.550322	2.87068674	-0.67963526	0.731489256
31.030896	1.671747	5.222069	3.023586166	-2.198482834	0.068958533
31.962205	0.052954	5.275023	3.114330988	-2.160692012	0.366593161
32.360039	0.009528	5.284551	3.153095124	-2.131455876	1.419148944
33.787022	0.00614	5.290691	3.292137385	-1.998553615	1.918821899
35.710719	0.00361	5.294301	3.479578423	-1.814722577	1.759113912
37.473447	0.003618	5.297919	3.651334978	-1.646584022	0.333916591
37.814008	0.009672	5.307591	3.684518593	-1.623072407	0.572253225
38.400830	0.019465	5.327056	3.741697286	-1.585358714	0.258902886
38.677417	0.015903	5.342959	3.768647339	-1.574311661	0.879558169
39.566087	0.002321	5.34528	3.855237518	-1.490042482	0.016936921
39.625925	0.083482	5.428762	3.86106805	-1.56769395	0.399239895
40.068971	0.004129	5.432891	3.904237475	-1.528653525	0.696879074
40.776021	0.016214	5.449105	3.973131018	-1.475973982	0.740426478
41.527462	0.005814	5.454919	4.04634982	-1.40856918	0.076216743
41.611286	0.0094	5.464319	4.054517432	-1.409801568	2.474124731
44.091910	0.003599	5.467918	4.296224316	-1.171693684	1.30058543
45.396809	0.005029	5.472947	4.423371012	-1.049575988	0.206884212
45.617579	0.022741	5.495688	4.444882306	-1.050805694	0.066549153
45.736044	0.081091	5.576779	4.456425305	-1.120353695	2.353142124
48.130729	0.001996	5.578775	4.689758509	-0.889016491	1.451798482
49.586524	0.005996	5.584771	4.831608106	-0.753162894	0.310932231
49.906719	0.012529	5.5973	4.862807217	-0.734492783	0.810603809
50.727821	0.008468	5.605768	4.942813724	-0.662954276	1.457859526
52.192286	0.004744	5.610512	5.08550821	-0.52500379	1.307844503

Location	Aperture (mm)	Cum. Ap (mm)	Hom. strain	difference	Spacing (mm)
53.507027	0.009049	5.619561	5.213613848	-0.405947152	0.044777859
53.558589	0.004518	5.624079	5.21863788	-0.40544112	0.411338494
53.975270	0.006167	5.630246	5.259238412	-0.371007588	0.043552386
54.031581	0.01935	5.649596	5.264725229	-0.384870771	0.324240436
54.367910	0.004828	5.654424	5.297496472	-0.356927528	0.133079483
54.511267	0.015727	5.670151	5.311464879	-0.358686121	0.085902251
54.607163	0.004261	5.674412	5.320808811	-0.353603189	0.729541322
55.340650	0.00363	5.678042	5.392278247	-0.285763753	1.173552531
56.519008	0.005981	5.684023	5.507095011	-0.176927989	0.070167595
56.593376	0.002419	5.686442	5.514341235	-0.172100765	0.032686452
56.629691	0.004839	5.691281	5.517879738	-0.173401262	0.030243472
56.667192	0.009676	5.700957	5.521533754	-0.179423246	0.048389688
56.727704	0.014568	5.715525	5.527429888	-0.188095112	0.025404398
56.762206	0.003628	5.719153	5.53079173	-0.18836127	0.064129008
56.830061	0.003824	5.722977	5.537403381	-0.185573619	0.846896196
57.683694	0.00965	5.732627	5.620579631	-0.112047369	0.457319785
58.147639	0.0036	5.736227	5.665785449	-0.070441551	0.159694211
58.311576	0.004886	5.741113	5.681759151	-0.059353849	0.83236535
59.147239	0.001708	5.742821	5.763184359	0.020363359	0.072586443
59.224307	0.007255	5.750076	5.770693699	0.020617699	0.110096871
59.341659	0.007256	5.757332	5.782128271	0.024796271	0.026642963
59.374953	0.006045	5.763377	5.785372317	0.021995317	0.327868301
59.804511	0.197336	5.960713	5.827227636	-0.133485364	0.499673649
60.404058	0.00241	5.963123	5.885646219	-0.077476781	0.464577265
60.870695	0.00171	5.964833	5.931114387	-0.033718613	0.016980014
60.890345	0.00363	5.968463	5.933029044	-0.035433956	0.284319006
61.178884	0.00481	5.973273	5.961143686	-0.012129314	0.027824977
61.210923	0.003617	5.97689	5.964265449	-0.012624551	0.060499446
61.275650	0.004839	5.981729	5.970572357	-0.011156643	0.1120805
61.390150		5.981729	5.981729	0	

Location	Aperture (mm)	Cum. Ap (mm)	Hom. strain	difference	Spacing (mm)
Sample 55a			V'		C
		0-20,340-360	0.524069826		1.466264812
loc	ap	cumap	hom strain	difference	spacing
0	0	0	0	0	
0.003500	0.310855	0.310855	0.000320471	-0.310534529	2.578793552
2.740135	0.004827	0.315682	0.250895283	-0.064786717	2.162692977
4.911905	0.013328	0.32901	0.449749374	0.120739374	0.391473641
5.313087	0.006089	0.335099	0.486482865	0.151383865	0.287801232
5.606322	0.004779	0.339878	0.513332399	0.173454399	0.404519575
6.015655	0.004848	0.344726	0.550812215	0.206086215	0.573835209
6.593728	0.003627	0.348353	0.603742358	0.255389358	1.366513517
7.965080	0.00605	0.354403	0.729307634	0.374904634	0.081712063
8.051035	0.002436	0.356839	0.737177949	0.380338949	0.053655036
8.107703	0.003589	0.360428	0.742366605	0.381938605	0.04026045
8.151113	0.002711	0.363139	0.746341402	0.383202402	0.048793672
8.228097	0.053669	0.416808	0.753390267	0.336582267	0.007315893
8.371830	0.219166	0.635974	0.766550946	0.130576946	0.015852621
8.503363	0.012194	0.648168	0.778594484	0.130426484	0.137802897
8.672117	0.049709	0.697877	0.794046164	0.096169164	0.185360977
8.883643	0.00262	0.700497	0.813414097	0.112917097	0.363413622
9.249585	0.002437	0.702934	0.846920902	0.143986902	0.397570376
9.651409	0.00607	0.709004	0.883713151	0.174709151	0.143900085
9.801365	0.006043	0.715047	0.897443645	0.182396645	0.019548248
9.824796	0.001721	0.716768	0.899588992	0.182820992	0.01589967
9.843470	0.003829	0.720597	0.901298903	0.180701903	0.018454481
9.865202	0.002725	0.723322	0.903288705	0.179966705	0.287812832
10.159257	0.009759	0.733081	0.930213285	0.197132285	0.097563374
10.263524	0.003649	0.73673	0.939760331	0.203030331	0.001218903
10.270739	0.008344	0.745074	0.940420996	0.195346996	0.326832433
10.606007	0.008526	0.7536	0.97111913	0.21751913	0.026828983
10.638317	0.002437	0.756037	0.974077579	0.218040579	0.217076277
10.859051	0.004878	0.760915	0.994288653	0.233373653	0.937567445
11.801950	0.005785	0.7667	1.080623427	0.313923427	0.528406226
12.335068	0.003638	0.770338	1.129437352	0.359099352	0.23983205
12.579686	0.005934	0.776272	1.151835345	0.375563345	0.95914114
13.543617	0.003647	0.779919	1.240095939	0.460176939	0.507314835
14.057023	0.008535	0.788454	1.287104981	0.498650981	0.648787724
14.711279	0.0024	0.790854	1.347010634	0.556156634	0.046338969
14.759424	0.001213	0.792067	1.351418984	0.559351984	0.286613289
15.051441	0.009595	0.801662	1.378156999	0.576494999	2.758757129
17.822017	0.014042	0.815704	1.631839562	0.816135562	0.031706739
17.861940	0.002391	0.818095	1.635495058	0.817400058	0.651816034
18.585339	0.140775	0.95887	1.701731735	0.742861735	0.098097649
19.844535	2.181422	3.140292	1.817027669	-1.323264331	0.062257275
21.002003	0.008998	3.14929	1.92300899	-1.22628101	0.024482482
21.034087	0.006205	3.155495	1.925946699	-1.229548301	0.014246262
21.056842	0.010813	3.166308	1.928030242	-1.238277758	0.009109709
21.073048	0.003379	3.169687	1.929514088	-1.240172912	0.014804828
21.099224	0.019365	3.189052	1.93191092	-1.25714108	1.912626722
23.023180	0.003293	3.192345	2.108074318	-1.084270682	1.349476717
24.394226	0.039845	3.23219	2.233611549	-0.998578451	0.089965411
24.505811	0.003395	3.235585	2.243828657	-0.991756343	0.116154168

Location	Aperture (mm)	Cum. Ap (mm)	Hom. strain	difference	Spacing (mm)
24.624801	0.002277	3.237862	2.254723769	-0.983138231	2.854184717
27.481955	0.003661	3.241523	2.516333692	-0.725189308	0.370375802
27.867077	0.025831	3.267354	2.551596648	-0.715757352	0.290404617
28.171011	0.001228	3.268582	2.579425805	-0.689156195	1.184975728
29.365172	0.017142	3.285724	2.688766893	-0.596957107	0.013534921
29.390339	0.006123	3.291847	2.691071301	-0.600775699	0.03198991
29.426619	0.002456	3.294303	2.694393157	-0.599909843	0.032015392
29.461697	0.003671	3.297974	2.69760509	-0.60036891	0.731489256
31.030896	1.671747	4.969721	2.841285786	-2.128435214	0.068958533
31.962205	0.052954	5.022675	2.926559352	-2.096115648	0.366593161
32.360039	0.009528	5.032203	2.962986291	-2.069216709	1.419148944
33.787022	0.00614	5.038343	3.093645309	-1.944697691	1.918821899
35.710719	0.00361	5.041953	3.269785008	-1.772167992	1.759113912
37.473447	0.003618	5.045571	3.431185884	-1.614385116	0.333916591
37.814008	0.009672	5.055243	3.462368768	-1.592874232	1.74608228
39.566087	0.002321	5.057564	3.622794576	-1.434769424	0.016936921
39.625925	0.083482	5.141046	3.628273569	-1.512772431	4.422443922
44.091910	0.003599	5.144645	4.037193059	-1.107451941	1.512498642
45.617579	0.022741	5.167386	4.176888048	-0.990497952	0.066549153
45.736044	0.081091	5.248477	4.187735087	-1.060741913	3.806936606
49.586524	0.005996	5.254473	4.540297079	-0.714175921	1.13406504
50.727821	0.008468	5.262941	4.644797802	-0.618143198	1.457859526
52.192286	0.004744	5.267685	4.778888842	-0.488796158	1.777527855
53.975270	0.006167	5.273852	4.94214437	-0.33170763	0.043552386
54.031581	0.01935	5.293202	4.947300371	-0.345901629	0.324240436
54.367910	0.004828	5.29803	4.978095745	-0.319934255	0.133079483
54.511267	0.015727	5.313757	4.991221958	-0.322535042	0.819704572
55.340650	0.00363	5.317387	5.067162864	-0.250224136	1.173552531
56.519008	0.005981	5.323368	5.175057008	-0.148310992	0.070167595
56.593376	0.002419	5.325787	5.181866337	-0.143920663	0.032686452
56.629691	0.004839	5.330626	5.185191494	-0.145434506	0.030243472
56.667192	0.009676	5.340302	5.1886252	-0.1516768	0.048389688
56.727704	0.014568	5.35487	5.194165839	-0.160704161	0.025404398
56.762206	0.003628	5.358498	5.197324986	-0.161173014	0.064129008
56.830061	0.003824	5.362322	5.203538003	-0.158783997	0.846896196
57.683694	0.00965	5.371972	5.281699326	-0.090272674	0.457319785
58.147639	0.0036	5.375572	5.32417956	-0.05139244	0.159694211
58.311576	0.004886	5.380458	5.339190164	-0.041267836	0.83236535
59.147239	0.001708	5.382166	5.41570602	0.03354002	0.072586443
59.224307	0.007255	5.389421	5.422762602	0.033341602	0.110096871
59.341659	0.007256	5.396677	5.433507751	0.036830751	0.026642963
59.374953	0.006045	5.402722	5.436556205	0.033834205	0.327868301
59.804511	0.197336	5.600058	5.475887951	-0.124170049	0.499673649
60.404058	0.00241	5.602468	5.530784316	-0.071683684	0.464577265
60.870695	0.00171	5.604178	5.573511082	-0.030666918	0.016980014
60.890345	0.00363	5.607808	5.575310299	-0.032497701	0.284319006
61.178884	0.00481	5.612618	5.601729832	-0.010888168	0.027824977
61.210923	0.003617	5.616235	5.604663375	-0.011571625	0.060499446
61.275650	0.004839	5.621074	5.610590022	-0.010483978	0.1120805
61.39015023		5.621074	5.621074	0	

Location	Aperture (mm)	Cum. Ap (mm)	Hom. strain	difference	Spacing (mm)
Sample 56			V'		C
			0.394766871		1.979017081
loc	ap	cumap	hom strain	difference	spacing
0	0	0	0	0	
0.73	0.002342901	0.002342901	0.076836146	0.074493245	1.445550747
2.210528569	0.067612744	0.069955645	0.232669172	0.162713527	0.373537117
2.618990815	0.002237513	0.072193158	0.275661864	0.203468705	1.456208235
4.078610997	0.004586382	0.076779541	0.429294178	0.352514637	1.768076692
5.849889253	0.001816743	0.078596284	0.615730061	0.537133776	1.127725885
6.979688416	0.002329813	0.080926097	0.734647065	0.653720968	0.302396445
7.285104264	0.003708994	0.084635091	0.766793609	0.682158518	0.196842064
7.48520893	0.00281621	0.087451301	0.787855624	0.700404323	0.149412776
7.638015324	0.003971027	0.091422328	0.80393926	0.712516932	0.029645232
7.67154104	0.00378994	0.095212268	0.807468009	0.712255741	1.802473037
9.478279183	0.004740272	0.09995254	0.997636223	0.897683682	0.0095603
9.492046211	0.003673183	0.103625724	0.999085271	0.895459547	0.011858093
9.530372354	0.049262918	0.152888641	1.003119289	0.850230648	0.021377373
9.582226801	0.011691229	0.164579871	1.008577228	0.843997358	0.01541357
9.605261745	0.003551519	0.168131389	1.011001771	0.842870382	0.030831042
9.639647134	0.003557175	0.171688564	1.014621005	0.842932441	0.029645232
9.673336278	0.00453065	0.176219214	1.018166956	0.841947742	0.023745813
9.700373824	0.002052815	0.178272029	1.021012793	0.842740763	0.017787139
9.721286919	0.004199096	0.182471125	1.023214	0.840742875	0.675931192
10.40501522	0.011395128	0.193866253	1.095179819	0.901313566	0.024930213
10.4369251	0.0025642	0.196430454	1.098538493	0.90210804	0.20039592
10.63973724	0.002268247	0.198698701	1.119885484	0.921186783	0.020193605
10.66343383	0.004737711	0.203436412	1.122379668	0.918943256	0.01073796
10.67833118	0.003581077	0.20701749	1.123947689	0.916930199	0.004743237
10.686004	0.00227809	0.209295579	1.124755292	0.915459712	1.596134748
12.28492504	0.003294492	0.212590071	1.293049717	1.080459645	0.027271663
12.31636694	0.005045969	0.217636041	1.296359133	1.078723092	0.010672284
12.33186027	0.004596142	0.222232183	1.297989884	1.075757701	2.519893947
14.85534899	0.002593402	0.224825585	1.563599676	1.33877409	0.360486026
15.21942985	0.004596259	0.229421845	1.601921004	1.37249916	0.075899108
15.30260387	0.009953571	0.239375416	1.610675485	1.37130007	0.184995602
15.49313646	0.001120403	0.240495818	1.630729992	1.390234174	0.005929046
15.50161743	0.003983434	0.244479252	1.631622656	1.387143404	0.015415521
15.52011417	0.00217901	0.246658262	1.63356953	1.386911269	0.004743237
15.55100394	0.050114063	0.296772324	1.636820833	1.340048509	0.91665822
16.49568274	0.005927096	0.30269942	1.736252995	1.433553575	0.056918846
16.55739651	0.003662743	0.306362163	1.742748677	1.436386514	0.559733556
17.12411828	0.010313681	0.316675844	1.802398974	1.485723129	0.311862298
17.44355872	0.004842604	0.321518449	1.836021676	1.514503227	1.619859593
19.06702323	0.002367227	0.323885675	2.006899423	1.683013748	0.246653884
19.32755402	0.025386592	0.349272268	2.034321591	1.685049323	0.345079091
19.68647387	0.002294921	0.351567188	2.072099697	1.720532509	0.142300106
19.83104692	0.002250971	0.353818159	2.087316733	1.733498573	0.01541357
19.84866798	0.002164015	0.355982174	2.089171438	1.733189263	0.017826623
19.8688113	0.002469375	0.358451549	2.091291623	1.732840073	1.158569063
21.28154942	0.50586875	0.864320299	2.239989366	1.375669067	0.983047547
22.52401635	0.012970001	0.8772903	2.370765215	1.493474915	1.475180289
24.00742165	0.003480019	0.880770319	2.526901031	1.646130712	1.170413177

Location	Aperture (mm)	Cum. Ap (mm)	Hom. strain	difference	Spacing (mm)
25.18987944	0.020609206	0.901379525	2.65136062	1.749981095	0.071156489
25.27350993	0.004338801	0.905718326	2.660163147	1.754444821	0.007114856
25.28484721	0.004106058	0.909824384	2.661356452	1.751532068	2.602906145
28.39212812	1.00464346	1.914467845	2.988413287	1.073945442	1.064884873
29.96330275	0.007936062	1.922403907	3.153787264	1.231383357	0.009486474
29.99478454	0.036054563	1.95845847	3.157100879	1.19864241	0.110303813
30.12429972	0.002368166	1.960826635	3.170732999	1.209906363	0.024900045
30.15387609	0.006984483	1.967811118	3.173846059	1.206034941	0.305951679
30.46563664	0.004633277	1.972444395	3.206660415	1.23421602	0.388951966
30.85808697	0.002363449	1.974807844	3.247967772	1.273159928	0.04980399
30.91085128	0.003557175	1.978365019	3.253521479	1.275156459	0.176697601
31.09169797	0.004741018	1.983106038	3.272556497	1.289450459	0.042689135
31.1385362	0.003557175	1.986663212	3.277486455	1.290823242	0.009486474
31.15215628	0.004710032	1.991373244	3.278920036	1.287546791	0.112654224
31.26893333	0.003535622	1.994908866	3.291211404	1.296302537	0.355752774
31.62876892	0.004630006	1.999538873	3.329085896	1.329547024	2.160303716
33.79256877	0.002362266	2.001901139	3.556836638	1.554935499	0.004743237
33.80142701	0.005867727	2.007768865	3.557769011	1.550000146	0.037945897
33.84349241	0.00237129	2.010140155	3.562196605	1.55205645	0.010672284
33.85653392	0.002367152	2.012507307	3.563569289	1.551061982	0.115025713
33.97448399	0.003481577	2.015988884	3.575984123	1.559995239	0.010672284
33.98866253	0.003530927	2.019519811	3.577476485	1.557956674	0.136384756
34.12847393	0.003322367	2.022842178	3.592192334	1.569350155	0.022654651
34.15397385	0.002368161	2.025210339	3.594876327	1.569665988	0.003557428
34.16106134	0.004691973	2.029902312	3.595622321	1.565720009	0.020158758
34.18587331	0.004614445	2.034516757	3.598233905	1.563717147	0.428021195
34.61793317	0.00346289	2.037979647	3.643710363	1.605730716	0.012720669
34.63509571	0.005420851	2.043400498	3.645516806	1.602116308	0.009062665
34.64777021	0.001802816	2.045203315	3.64685086	1.601647546	0.157701119
34.8082218	0.003698119	2.048901434	3.663739191	1.614837757	0.363459352
35.17978314	0.012505858	2.061407292	3.702847878	1.641440586	0.556508534
35.74341701	0.001744818	2.06315211	3.762173158	1.699021048	0.264666998
36.01165644	0.005400041	2.068552151	3.790406698	1.721854546	0.037169639
36.05330504	0.003557892	2.072110043	3.794790421	1.722680378	0.021769877
36.07848665	0.003265559	2.075375602	3.797440911	1.722065308	0.011816732
36.09291764	0.001962964	2.077338566	3.798959845	1.721621279	0.116011384
36.211225	0.002628981	2.079967547	3.811412285	1.731444738	0.067979801
36.28363363	0.006228692	2.086196239	3.819033656	1.732837416	0.00462184
36.29271856	0.002697477	2.088893717	3.819989889	1.731096173	0.059816002
36.3551454	0.002524205	2.091417922	3.826560626	1.735142705	0.048940502
36.40632435	0.001952692	2.093370614	3.831947467	1.738576853	0.023581261
36.43222393	0.002683936	2.09605455	3.834673526	1.738618976	0.088821456
36.52379902	0.002823347	2.098877897	3.844312263	1.745434366	0.006409338
36.53296013	0.002680179	2.101558076	3.845276514	1.743718439	0.023581261
36.55929284	0.002822729	2.104380805	3.848048164	1.743667359	0.058918065
36.62051141	0.001778274	2.106159079	3.854491724	1.748332645	0.02900083
36.65182865	0.002854558	2.109013637	3.85778802	1.748774384	0.962584195
37.61806245	0.004444638	2.113458275	3.959488953	1.846030678	0.059816002
37.68483109	0.009460653	2.122918928	3.966516687	1.843597758	0.039877837
37.73257696	0.006275414	2.129194342	3.971542178	1.842347836	0.24110559
37.97934718	0.005053832	2.134248174	3.997515975	1.863267801	0.068920676
38.05143566	0.001281776	2.135529951	4.005103648	1.869573697	0.025392851
38.07837565	0.001812501	2.137342452	4.007939216	1.870596764	0.072504336
38.15588176	0.008191059	2.145533512	4.016097122	1.870563611	0.05981751

Location	Aperture (mm)	Cum. Ap (mm)	Hom. strain	difference	Spacing (mm)
38.22080718	0.002024752	2.147558264	4.022930847	1.875372582	0.021750999
38.24583149	0.00452187	2.152080134	4.02556478	1.873484646	0.038065003
38.28802597	0.00373709	2.155817224	4.03000596	1.874188736	0.035345751
38.32705309	0.00362565	2.159442874	4.03411376	1.874670886	0.144115165
38.47421033	0.002458497	2.161901371	4.049602794	1.887701423	0.03086845
38.50767827	0.002740484	2.164641855	4.053125462	1.888483607	0.802156527
39.31386504	0.005319998	2.169961853	4.137980646	1.968018792	0.266478156
39.58708178	0.008157176	2.178119029	4.166738072	1.988619043	1.122129003
40.7139199	0.001261057	2.179380086	4.285343412	2.105963327	0.192155581
40.90897181	0.004531604	2.18391169	4.3058736	2.12196191	0.125083645
41.03858694	0.004531361	2.188443051	4.31951624	2.131073189	0.949632356
41.9913766	0.001783241	2.190226292	4.41980211	2.229575818	0.423965575
42.41689878	0.00132997	2.191556261	4.464590444	2.273034183	0.00666918
42.4262585	0.004051114	2.195607376	4.465575602	2.269968226	0.074038097
42.50465389	0.004663475	2.20027085	4.473827108	2.273556258	4.925772338
47.43379609	0.002076248	2.202347098	4.992643943	2.790296845	0.007306273
47.44430841	0.004335837	2.206682936	4.993750417	2.787067481	0.330834151
47.7786775	0.002734044	2.20941698	5.028944434	2.819527454	0.352583215
48.13441069	0.003565912	2.212982892	5.066387129	2.853404237	0.037169639
48.17470612	0.002685664	2.215668556	5.070628424	2.854959868	0.941739956
49.12001878	0.004459735	2.220128292	5.170127302	2.949999011	0.004532087
49.12842466	0.003287863	2.223416155	5.171012064	2.947595909	0.02267554
49.15367487	0.001861472	2.225277627	5.173669774	2.948392147	0.107865321
49.26916364	0.013385421	2.238663048	5.185825544	2.947162496	0.089743069
49.36764764	0.004096455	2.242759503	5.196191478	2.953431975	0.015406078
49.38732503	0.00444616	2.247205663	5.198262621	2.951056958	0.181282744
49.57197259	0.002283472	2.249489134	5.217697698	2.968208564	0.047136383
49.62145526	0.00240911	2.251898244	5.222905997	2.971007753	0.821188073
50.44885264	0.010009493	2.261907737	5.309993703	3.048085966	0.050753337
50.50641343	0.003605407	2.265513144	5.316052263	3.05053912	0.012720669
50.52623023	0.010586859	2.276100003	5.318138081	3.042038078	0.143223133
50.67654989	0.003606193	2.279706196	5.333959976	3.05425378	0.605467824
51.2877873	0.007932994	2.28763919	5.398295767	3.110656577	0.366176886
51.66920715	0.022552933	2.310192123	5.438442111	3.128249988	0.396999774
52.08904272	0.023118644	2.333310767	5.482631901	3.149321134	0.657135114
52.75930016	0.003126006	2.336436773	5.553179844	3.216743071	1.707635426
54.47019823	0.003399281	2.339836054	5.73326041	3.393424356	1.761127706
56.2338093	0.001567459	2.341403513	5.918889284	3.577485771	0.625418224
56.86088346	0.001744415	2.343147928	5.984891972	3.641744044	0.036263498
56.8993618	0.002685256	2.345833184	5.988942009	3.643108824	0.096072446
56.99803468	0.002515624	2.348348809	5.999327823	3.650979014	0.136864411
57.14566696	0.019020114	2.367368923	6.014866858	3.647497934	1.635125467
58.79347907	0.00635316	2.373722083	6.188307311	3.814585229	0.00997059
58.80800499	0.0027575	2.376479583	6.189836237	3.813356654	0.793094704
59.60428731	0.003617742	2.380097325	6.273648929	3.893551603	0.011025555
59.61776094	0.0012784	2.381375725	6.275067095	3.89369137	0.085197492
59.70570097	0.004206671	2.385582396	6.284323222	3.898740827	0.581447614
60.29078141	0.003058981	2.388641377	6.345905861	3.957264484	0.065260801
60.35893005	0.002716714	2.391358091	6.353078846	3.961720755	0.506666662
60.86785559	0.001801036	2.393159127	6.406645801	4.013486674	0.019958757
60.88999915	0.002568571	2.395727698	6.408976521	4.013248823	0.043503507
60.93664531	0.003716728	2.399444426	6.413886262	4.014441837	0.292778008
61.23243868	0.002313996	2.401758422	6.445019992	4.04326157	0.062076253
61.29613495	0.000926042	2.402684464	6.451724342	4.049039879	0.087228184

Location	Aperture (mm)	Cum. Ap (mm)	Hom. strain	difference	Spacing (mm)
61.38574163	0.003830953	2.406515417	6.461155893	4.054640476	0.197432071
61.5872444	0.004310451	2.410825868	6.482365066	4.071539199	0.504716612
62.10323892	0.01824536	2.429071228	6.536676066	4.107604839	0.547167477
62.660504	0.001949843	2.431021071	6.595330999	4.164309928	0.001306214
62.6637116	0.001852931	2.432874001	6.595668615	4.162794614	0.101857601
62.7671225	0.00125366	2.434127662	6.606553128	4.172425466	0.348675059
63.11775357	0.002658364	2.436786026	6.6434588	4.206672774	0.003970852
63.12499395	0.00388069	2.440666716	6.644220886	4.20355417	0.032650682
63.16087906	0.002588181	2.443254896	6.647997974	4.204743077	0.403521046
63.56757771	0.003767011	2.447021908	6.690805037	4.243783129	0.02546184
63.596237	0.002627904	2.449649811	6.693821571	4.24417176	0.914765934
64.52406681	0.023499848	2.473149659	6.791480293	4.318330633	0.517139039
65.05395648	0.002001409	2.475151069	6.847253827	4.372102758	0.212863236
65.26944068	0.003240525	2.478391593	6.869934615	4.391543022	0.603319653
65.88804086	0.027320513	2.505712106	6.935045373	4.429333266	0.81877535
66.72147959	0.002006253	2.507718359	7.022768962	4.515050603	0.022207777
66.74661982	0.003858663	2.511577022	7.025415097	4.513838075	0.110353278
66.85954306	0.001281251	2.512858273	7.037300832	4.524442559	0.091412579
66.98097519	0.058757853	2.571616126	7.05008217	4.478466044	0.065942775
67.08731888	0.022043987	2.593660112	7.061275375	4.467615263	0.232446898
67.33416725	0.00675895	2.600419062	7.087257398	4.486838336	0.432907952
67.77150756	0.002105764	2.602524826	7.13328965	4.530764825	0.027452253
67.80167586	0.003326327	2.605851152	7.136465014	4.530613862	0.039831815
67.88150397	0.076666259	2.682517411	7.144867321	4.46234991	0.091412579
68.01269208	0.002884811	2.685402222	7.158675525	4.473273304	0.119493548
68.13493322	0.002610376	2.688012598	7.171542016	4.483529418	0.01958761
68.15917867	0.006705302	2.6947179	7.174093971	4.479376071	0.071820473
68.23538006	0.002056538	2.696774438	7.182114548	4.48534011	0.003265535
68.24195632	0.004564918	2.701339356	7.182806732	4.481467376	0.457061004
68.70325621	0.003912854	2.70525221	7.23136085	4.52610864	0.011752193
68.71761187	0.001294067	2.706546277	7.232871854	4.526325577	0.077049699
68.79595898	0.00130075	2.707847027	7.241118278	4.533271251	0.007835417
68.80574489	0.002600244	2.710447271	7.242148295	4.531701023	0.015682573
68.82435883	0.0032625	2.713709772	7.244107505	4.530397734	0.050925546
68.90551277	0.057194274	2.770904046	7.252649362	4.481745316	0.037219763
68.97240624	0.00215315	2.773057196	7.259690234	4.486633039	0.003265535
68.97772618	0.001955657	2.775012853	7.260250185	4.485237331	0.198492653
69.17848127	0.002569207	2.77758206	7.28138066	4.5037986	1.027728651
70.20976666	0.004544285	2.782126345	7.389928599	4.607802254	0.09468715
70.30803209	0.002612273	2.784738617	7.400271526	4.615532908	0.12535855
70.43728826	0.005182961	2.789921578	7.413876383	4.623954805	0.299053391
70.74570368	0.013541098	2.803462676	7.446338646	4.64287597	0.920650551
71.67524971	0.004249858	2.807712533	7.544178008	4.736465475	0.011118284
71.69172881	0.006471779	2.814184312	7.545912516	4.731728204	1.29674388
72.99268296	0.001948768	2.816133081	7.682844438	4.866711358	0.080312918
73.07560122	0.003261917	2.819394998	7.691571999	4.872177002	0.214160364
73.29752607	0.012267054	2.831662052	7.714930698	4.883268646	0.129938266
73.43990998	0.012624224	2.844286276	7.729917315	4.885631039	0.016987741
73.47341906	0.020418456	2.864704731	7.733444313	4.868739582	0.103810601
73.58876658	0.002655382	2.867360113	7.745585216	4.878225102	0.250073545
73.84230055	0.004265473	2.871625586	7.772270933	4.900645346	0.052899129
73.89867586	0.002686879	2.874312466	7.778204715	4.90389225	0.357815691
74.25940028	0.003130594	2.87744306	7.816172763	4.938729703	0.193931176
74.45679305	0.003792585	2.881235645	7.836949337	4.955713692	0.14866963

Location	Aperture (mm)	Cum. Ap (mm)	Hom. strain	difference	Spacing (mm)
75.95458535	2.694452749	5.575688395	7.994599457	2.418911063	0.385842107
77.69055585	0.00580405	5.581492445	8.177319023	2.595826578	0.451632259
78.62605047	0.961920661	6.543413106	8.275784504	1.732371397	0.016443366
79.12598414	0.005059956	6.548473062	8.32840502	1.779931958	0.134108589
79.53213151	0.539017591	7.087490652	8.371154058	1.283663406	0.008320297
79.83424361	0.04856603	7.136056682	8.402952866	1.266896184	0.049970416
79.93744901	0.057903939	7.193960621	8.41381575	1.219855129	0.044910221
80.01688921	0.01115601	7.205116631	8.422177227	1.217060596	0.009488711
80.08947766	0.115043469	7.320160101	8.429817524	1.109657423	0.050602946
80.20984462	0.024484565	7.344644666	8.442486748	1.097842083	0.003225539
80.22945111	0.008277327	7.352921992	8.444550429	1.091628437	0.144849155
80.38535171	0.013825576	7.366747568	8.460959746	1.094212178	0.16446243
80.58329117	0.053128484	7.419876053	8.481793863	1.06191781	0.158139296
80.78123439	0.026479352	7.446355405	8.502628375	1.05627297	0.021515179
80.8178601	0.00374171	7.450097115	8.506483414	1.056386298	0.010119425
80.84438412	0.029067482	7.479164597	8.5092752	1.030110602	0.04617526
80.90635421	0.002522177	7.481686774	8.515797861	1.034111087	0.015812652
80.92466706	0.00247821	7.484164985	8.51772538	1.033560395	0.009507911
80.93604515	0.001262162	7.485427147	8.518922981	1.033495834	0.022777959
80.9607164	0.002524426	7.487951573	8.521519754	1.033568181	0.003847836
80.9674333	0.0032137	7.491165273	8.522226741	1.031061468	0.003223709
80.98616886	0.027809995	7.518975269	8.524198752	1.005223483	0.018352014
81.02095468	0.005057608	7.524032877	8.527860133	1.003827256	0.032256018
81.05857163	0.005664268	7.529697145	8.531819505	1.00212236	0.068951708
81.13193584	0.003160728	7.532857873	8.539541454	1.006683581	0.021504012
81.1575693	0.005098162	7.537956036	8.542239504	1.004283468	0.00569136
81.16833757	0.005055657	7.543011693	8.543372918	1.000361225	0.088555408
81.26068026	0.002518904	7.545530597	8.553092447	1.00756185	0.269461327
81.53551184	0.00822162	7.553752217	8.582019844	1.028267628	0.027837007
81.56871199	0.002504667	7.556256884	8.585514326	1.029257443	0.15118184
81.72240822	0.002524106	7.558780989	8.601691622	1.042910632	0.036049636
81.76129331	0.003146804	7.561927793	8.605784472	1.043856679	0.271368436
82.03643424	0.004398188	7.566325981	8.634744429	1.068418448	1.437134206
83.4833086	0.015082112	7.581408093	8.787035181	1.205627088	3.805352354
87.29712869	0.00185337	7.583261463	9.188458794	1.605197331	0.03226222
87.33150416	0.002373131	7.585634594	9.192076984	1.60644239	0.010752006
87.34661959	0.006353699	7.591988293	9.193667957	1.601679664	0.005693226
87.35896236	0.006945406	7.598933699	9.194967097	1.596033398	0.203040585
87.56793421	0.00491712	7.603850819	9.216962427	1.613111608	0.029732425
87.6357503	0.071250203	7.675101022	9.224100409	1.548999387	0.058191533
87.73255767	0.005981471	7.681082494	9.234289868	1.553207375	0.012017167
87.74997584	0.004820538	7.685903031	9.236123218	1.550220187	0.008221683
87.76181769	0.002419797	7.688322828	9.237369632	1.549046803	0.855822382
88.61978873	0.001877516	7.690200344	9.327675369	1.637475024	0.039850141
88.66120676	0.001258252	7.691458596	9.332034823	1.640576226	0.067686764
88.73108928	0.003133273	7.694591869	9.339390308	1.644798438	0.03858701
88.7727736	0.003061339	7.697653208	9.34377779	1.646124582	0.463646413
89.23949958	0.00309779	7.700750998	9.39290303	1.692152032	0.410515314
89.65339419	0.003660817	7.704411815	9.436467506	1.732055691	0.197347789
89.85319307	0.001241365	7.70565318	9.457497336	1.751844155	0.610401996
90.47018285	0.011934203	7.717587383	9.522438592	1.804851208	1.851442651
92.32919492	0.003204626	7.72079201	9.718108896	1.997316887	0.134723238
92.46705718	0.003073423	7.723865432	9.732619588	2.008754156	0.003795484
92.47412982	0.003480879	7.727346312	9.733364018	2.006017706	0.034790226

Location	Aperture (mm)	Cum. Ap (mm)	Hom. strain	difference	Spacing (mm)
92.51190918	0.002497385	7.729843697	9.737340484	2.007496787	0.074636008
92.58939402	0.003200286	7.733043983	9.745496151	2.012452168	3.241017893
95.83375047	0.00347683	7.736520812	10.08698087	2.350460059	1.218116586
97.07414443	0.041077916	7.777598729	10.21753853	2.439939802	1.081267947
98.39407881	0.436254954	8.213853682	10.35646822	2.142614534	4.034537721
102.6495621	0.00563617	8.219489853	10.80437909	2.584889233	0.450894998
103.1109019	0.015253392	8.234743244	10.8529374	2.618194157	0.731307486
104.4257391	1.151806097	9.386549341	10.99133059	1.604781246	0.160389
105.170473	0.016883691	9.403433032	11.06971755	1.666284517	0.007095232
105.1939913	0.015962393	9.419395425	11.07219296	1.65279754	0.044877584
105.255002	0.016303908	9.435699333	11.07861465	1.642915316	0.326394122
105.5916995	0.004302862	9.440002195	11.11405374	1.674051549	0.502496778
106.1173079	0.041920446	9.481922641	11.16937666	1.687454015	0.007849699
106.149317	0.006398302	9.488320942	11.17274577	1.684424828	0.035906734
106.1898677	0.002889672	9.491210614	11.17701394	1.685803322	0.038132255
106.2330652	0.007240705	9.498451319	11.18156068	1.683109364	0.090854575
106.3297923	0.004504379	9.502955698	11.1917417	1.688785997	0.025820822
106.364907	0.014083408	9.517039106	11.19543769	1.678398588	0.056076845
106.4296782	0.003305224	9.52034433	11.20225518	1.681910853	0.023553334
106.4564896	0.00321095	9.523555279	11.20507722	1.681521939	0.121135403
106.5833133	0.008165559	9.531720838	11.21842604	1.686705204	0.033648225
106.623169	0.004249514	9.535970352	11.22262106	1.686650708	0.508091906
107.1354014	0.004031355	9.540001707	11.27653607	1.736534365	0.136850122
107.2756934	0.002852483	9.54285419	11.29130251	1.74844832	0.10767549
107.3874202	0.005250065	9.548104256	11.30306231	1.754958054	0.071789257
107.4764907	0.02931256	9.577416815	11.31243743	1.735020617	0.201911014
107.6941939	0.002271686	9.579688502	11.33535177	1.755663273	0.010155013
107.7065539	0.002138351	9.581826852	11.33665273	1.754825877	0.029967077
107.7388401	0.002499953	9.584326805	11.34005102	1.755724211	0.201653083
107.9433781	0.003269755	9.587596561	11.36157966	1.773983095	0.021315688
107.9675639	0.00247061	9.590067171	11.36412534	1.774058169	0.059761177
108.0442992	0.031477581	9.621544751	11.37220211	1.750657359	0.035490563
108.1043902	0.017723333	9.639268085	11.37852699	1.739258906	0.008454285
108.2898717	0.33633099	9.975599074	11.39804984	1.422450764	0.214750122
108.6848489	0.024123187	9.999722262	11.43962316	1.439900901	0.057893243
108.7587572	0.007906984	10.00762925	11.44740238	1.439773138	0.033612217
108.7981029	0.003560012	10.01118926	11.45154372	1.440354459	0.004760838
108.806086	0.002884558	10.01407382	11.45238398	1.438310165	0.006536474
108.8252386	0.022347687	10.0364215	11.45439989	1.417978384	0.072824706
108.9242842	0.030093927	10.06651543	11.46482492	1.398309492	0.057887825
109.0297221	0.065006322	10.13152175	11.47592279	1.344401042	0.114854608
109.1991847	0.044209748	10.1757315	11.49375958	1.318028083	0.103638879
109.3271781	0.004499265	10.18023076	11.50723152	1.327000761	0.009383218
109.3429323	0.008242553	10.18847332	11.50888973	1.320416409	0.00373422
109.3528722	0.004168886	10.1926422	11.50993595	1.317293751	0.037346437
109.3935033	0.002400425	10.19504263	11.51421258	1.319169951	0.009336609
109.408909	0.009737753	10.20478038	11.51583411	1.311053724	0.052293779
109.4670009	0.001858467	10.20663885	11.52194857	1.315309719	0.006536474
109.476756	0.0045789	10.21121775	11.52297535	1.311757598	0.006534356
109.4869441	0.002728489	10.21394624	11.52404769	1.310101452	0.008402525
109.4979975	0.002573197	10.21651943	11.52521111	1.308691678	0.083100626
109.5833102	0.001850987	10.21837042	11.5341907	1.31582028	0.069096799
109.6546298	0.002594719	10.22096514	11.54169745	1.320732311	0.029892595
109.6874458	0.003251952	10.22421709	11.54515149	1.320934399	0.029875879

Location	Aperture (mm)	Cum. Ap (mm)	Hom. strain	difference	Spacing (mm)
109.7219995	0.006103706	10.2303208	11.54878844	1.318467644	0.00373422
109.7303759	0.00318071	10.23350151	11.5496701	1.316168595	0.003736338
109.7380636	0.004722069	10.23822358	11.55047927	1.312255697	0.007470558
109.749222	0.002653481	10.24087706	11.55165374	1.310776686	0.002800136
109.7548776	0.00305755	10.24393461	11.55224903	1.308314422	0.00373422
109.7615274	0.002773607	10.24670822	11.55294895	1.306240739	0.021495777
109.784855	0.000890089	10.24759831	11.5554043	1.307805999	0.015873083
109.8020216	0.001696876	10.24929518	11.55721117	1.30791599	0.00746844
109.8128598	0.005042674	10.25433785	11.55835195	1.304014092	0.031744048
109.8484681	0.002685743	10.2570236	11.56209989	1.305076296	0.037358117
109.9243036	0.074269006	10.3312926	11.57008196	1.238789354	0.045748962
110.0165045	0.018634915	10.34992752	11.57978657	1.229859046	0.02053927
110.0477134	0.002704329	10.35263185	11.58307146	1.230439609	0.010268576
110.0597934	0.000918645	10.35355049	11.58434294	1.230792451	0.116711355
110.1792487	0.004569077	10.35811957	11.5969162	1.238796632	0.010268576
110.1955621	0.007520748	10.36564032	11.59863328	1.23299296	0.023341523
110.2278349	0.010341749	10.37598207	11.60203015	1.226048082	0.008402525
110.2464478	0.010078962	10.38606103	11.60398925	1.217928218	0.006536474
110.2605306	0.005013615	10.39107464	11.60547153	1.214396884	0.225959908
110.5073325	0.036670452	10.4277451	11.63144867	1.203703569	0.881416477
111.408604	0.00303961	10.43078471	11.72631199	1.295527286	0.015870965
111.427545	0.003100422	10.43388513	11.72830563	1.294420497	0.016807168
111.4481162	0.004427729	10.43831286	11.73047085	1.292157994	0.006600782
111.4591355	0.004409176	10.44272203	11.73163068	1.288908648	0.188635203
111.6776277	0.055304905	10.49802694	11.75462808	1.256601142	0.321198527
112.3639562	0.674955053	11.17298199	11.82686758	0.653885592	0.731089575
113.4366602	0.008273736	11.18125573	11.93977503	0.758519307	0.703081267
114.1457318	0.003706929	11.18496266	12.01440836	0.829445705	0.228761975
114.3781782	0.003661862	11.18862452	12.0388745	0.850249985	0.058827208
114.4393026	0.000932636	11.18955715	12.04530816	0.855751003	0.023341523
114.4644678	0.0027148	11.19227195	12.04795693	0.85568497	0.030809964
114.4980243	0.002778191	11.19505015	12.05148891	0.856438764	0.580770473
115.083441	0.006514232	11.20156438	12.11310694	0.911542562	0.563954372
115.6531565	0.005008108	11.20657249	12.17307235	0.966499861	0.069090485
115.7269145	0.00432677	11.21089926	12.18083574	0.96993648	0.874873041
116.7717946	0.335687427	11.54658668	12.29081459	0.744227906	0.325855037
117.2710803	0.011173825	11.55776051	12.3433669	0.785606391	0.1157773
117.400741	0.016593055	11.57435356	12.35701434	0.782660776	0.010270694
117.4207764	0.002936298	11.57728986	12.35912316	0.781833301	0.113909193
117.5412835	0.010259591	11.58754945	12.37180714	0.784257688	0.091502692
117.679466	0.083100077	11.67064953	12.38635154	0.715702011	0.009336609
117.7380861	0.015466755	11.68611628	12.39252159	0.706405307	0.082163433
117.8382563	0.020546912	11.7066632	12.40306501	0.696401816	0.232486537
118.0838351	0.005637523	11.71230072	12.4289134	0.716612683	0.023360121
118.1155913	0.011154718	11.72345544	12.43225591	0.708800468	0.017739134
118.1430752	0.008334807	11.73179025	12.43514872	0.703358479	0.005602389
118.155179	0.004668014	11.73645826	12.43642271	0.69996445	0.052291661
118.2321761	0.044742764	11.78120102	12.44452703	0.66332601	0.06724827
118.9365519	1.229512394	13.01071342	12.51866611	-0.492047308	1.386556376
120.9395705	0.003412006	13.01412542	12.72949382	-0.284631605	0.391217094
121.3339835	0.002979813	13.01710524	12.77100776	-0.24609748	1.074702101
122.4120363	0.003721501	13.02082674	12.88447819	-0.136348544	0.01493688
122.4297622	0.001856549	13.02268329	12.88634393	-0.136339353	0.002800136
122.4553457	0.043710245	13.06639353	12.88903673	-0.177356803	0.014968173

Location	Aperture (mm)	Cum. Ap (mm)	Hom. strain	difference	Spacing (mm)
122.4955812	0.006824512	13.07321804	12.89327172	-0.179946323	0.120445459
122.6231335	0.007389087	13.08060713	12.90669723	-0.173909897	0.01120266
122.6384965	0.000931531	13.08153866	12.90831426	-0.173224399	0.025207574
122.6669938	0.005647937	13.0871866	12.91131375	-0.175872852	0.004668305
122.675417	0.001861809	13.08904841	12.91220033	-0.176848079	0.010270694
122.6870816	0.000926006	13.08997441	12.91342809	-0.176546327	1.205419085
123.8952125	0.004497737	13.09447215	13.0405899	-0.053882247	0.297848459
124.2016703	0.012721003	13.10719315	13.07284612	-0.034347033	0.03455681
124.2499918	0.014808364	13.12200152	13.0779322	-0.044069318	0.105506973
124.4257674	0.125728905	13.24773042	13.09643346	-0.151296963	0.033623018
124.5404555	0.036401074	13.2841315	13.10850494	-0.175626551	0.088702707
124.650107	0.005496656	13.28962815	13.12004632	-0.169581832	0.013104163
124.6678266	0.003734105	13.29336226	13.12191139	-0.171450866	0.027075743
124.712639	0.031739215	13.32510147	13.12662812	-0.198473352	0.005602389
124.735485	0.002747999	13.32784947	13.12903278	-0.198816695	0.070962684
124.8101556	0.004667888	13.33251736	13.13689223	-0.195625127	0.055093455
124.8704534	0.005740823	13.33825818	13.14323888	-0.195019304	0.097102688
124.9764801	0.0121072	13.35036538	13.15439872	-0.195966664	0.102704832
125.0861575	0.001838002	13.35220338	13.16594281	-0.186260568	0.002800136
125.0912687	0.002784106	13.35498749	13.16648079	-0.188506696	0.01962954
125.1136832	0.00278573	13.35777322	13.16884003	-0.188933193	0.025207574
125.1444853	0.008403397	13.36617662	13.17208211	-0.194094511	0.046690273
125.1967463	0.002738038	13.36891465	13.17758284	-0.191331819	0.052283318
125.2546241	0.008450894	13.37736555	13.18367476	-0.193690787	0.115775182
125.3806769	0.01210425	13.3894698	13.19694244	-0.192527355	0.010270694
125.4035324	0.013065407	13.40253521	13.1993481	-0.203187104	1.250239419
126.6611887	0.001768302	13.40430351	13.33172271	-0.072580802	0.097104806
126.7613373	0.00431948	13.40862299	13.34226386	-0.066359131	0.015870965
126.7802688	0.001801515	13.4104245	13.34425649	-0.066168015	0.155931296
126.9380333	0.001864783	13.41228928	13.36086198	-0.051427302	0.212882024
127.1532427	0.00279001	13.41507929	13.38351385	-0.031565445	0.187673452
127.3446442	0.004666075	13.41974537	13.40365981	-0.016085558	0.237165984
127.5855024	0.002718442	13.42246381	13.42901135	0.006547533	0.148463419
127.7367223	0.002794479	13.42525829	13.44492799	0.019669702	0.212882024
127.9528615	0.003719815	13.42897811	13.46767772	0.038699614	0.0224269
127.9788762	0.003455899	13.432434	13.4704159	0.037981898	0.535014083
128.5182309	0.005225228	13.43765923	13.52718567	0.08952644	0.665727252
129.1902785	0.00741546	13.44507469	13.59792204	0.152847347	0.599440451
129.8066046	0.026355879	13.47143057	13.66279344	0.19136287	0.13074252
129.9525336	0.0040171	13.47544767	13.6781532	0.202705526	0.01124347
129.9770476	0.022523906	13.49797158	13.68073342	0.182761838	0.007470558
129.9973393	0.003118386	13.50108996	13.68286922	0.181779256	0.027075743
130.1745379	0.297127473	13.79821744	13.70152027	-0.096697172	0.005677636
130.329643	0.001727302	13.79994474	13.71784584	-0.082098896	0.779136349
131.109643		13.79994474	13.79994474	0	

Location Aperture (mm) Cum. Ap (mm) Hom. strain difference Spacing (mm)

Sample 56 macrofractures

			V'		C
			0.375843983		1.487073404
loc	ap	cumap	hom strain	difference	spacing
0	0	0	0	0	
403.211	1.75	1.75	10.7594039	9.009403896	15.24
420.201	1.75	3.5	11.21277018	7.712770179	9.144
430.92	1.4	4.9	11.49879921	6.598799206	18.288
451.233	2.65	7.55	12.04083742	4.490837423	6.096
459.529	1.75	9.3	12.26221039	2.962210388	21.336
482.215	0.95	10.25	12.86757045	2.617570452	9.144
492.209	0.75	11	13.13425336	2.134253362	176.784
671.018	3.3	14.3	17.90564663	3.60564663	6.096
679.139	0.75	15.05	18.12234984	3.072349843	30.48
710.369	0.75	15.8	18.95570058	3.155700579	9.144
720.763	1.75	17.55	19.23305721	1.683057209	24.384
746.222	0.4	17.95	19.91241284	1.962412841	27.432
775.179	2.65	20.6	20.68511016	0.08511016	33.528
810.407	0.75	21.35	21.62514473	0.275144733	24.384
835.541	0.75	22.1	22.29582797	0.195827967	12.192
848.483	0.75	22.85	22.6411762	-0.208823802	9.144
858.252	0.5	23.35	22.90185514	-0.448144861	39.624
898.701	1.15	24.5	23.98120845	-0.518791549	9.144
908.585	0.33	24.83	24.24495609	-0.585043913	12.192
921.517	1.15	25.98	24.59003747	-1.389962526	12.192
934.659	0.75	26.73	24.94072256	-1.789277436	6.096
941.44	0.62	27.35	25.12166881	-2.228331187	158.496
1100.946	1.4	28.75	29.37797501	0.62797501	18.288
1120.509	1.15	29.9	29.9	0	

Sample 57			V'		C
			0.383236903		3.68685398
loc	ap	cumap	hom strain	difference	spacing
0	0	0	0	0	
1.264000	0.001331	0.001331	0.03924318	0.03791218	1.812569237
3.078229	0.001989	0.00332	0.095569227	0.092249227	0.063450351
3.143676	0.002003	0.005323	0.097601128	0.092278128	1.063887523
4.209797	0.002465	0.007788	0.13070081	0.12291281	4.453238407
8.664912	0.001288	0.009076	0.269017958	0.259941958	1.082590769
9.749183	0.002073	0.011149	0.302681132	0.291532132	0.051418122
9.803288	0.0033	0.014449	0.304360909	0.289911909	1.306970352
11.113222	0.002628	0.017077	0.345030204	0.327953204	0.007532365
11.122860	0.001583	0.01866	0.345329429	0.326669429	0.023725913
11.148292	0.001829	0.020489	0.346119009	0.325630009	0.043592406
11.194066	0.002535	0.023024	0.347540159	0.324516159	0.211392999
11.408107	0.002761	0.025785	0.354185451	0.328400451	0.023745669
11.434059	0.001651	0.027436	0.354991168	0.327555168	0.076154699
11.511587	0.001096	0.028532	0.357398172	0.328866172	0.038078573
11.550469	0.000511	0.029043	0.358605336	0.329562336	0.081668113
11.633477	0.002168	0.031211	0.361182459	0.329971459	0.015455457
11.651631	0.00323	0.034441	0.361746097	0.327305097	0.023728438
11.678011	0.002073	0.036514	0.36256511	0.32605111	0.006068467
11.685936	0.00164	0.038154	0.362811155	0.324657155	0.079466044
11.767323	0.002201	0.040355	0.365337948	0.324982948	0.184875784
11.954372	0.002145	0.0425	0.371145218	0.328645218	0.011597722
11.968323	0.002562	0.045062	0.371578359	0.326516359	0.039180695
12.009302	0.001034	0.046096	0.372850617	0.326754617	0.139615323
12.150509	0.002151	0.048247	0.377234671	0.328987671	0.034791108
12.186893	0.001033	0.04928	0.378364251	0.329084251	0.003356243
12.191619	0.001707	0.050987	0.378510986	0.327523986	0.191491512
12.384769	0.001611	0.052598	0.384507695	0.331909695	0.00717174
12.393298	0.001102	0.0537	0.384772469	0.331072469	0.009393028
12.404616	0.002748	0.056448	0.385123858	0.328675858	0.024296977
12.431374	0.002175	0.058623	0.385954624	0.327331624	0.026483192
12.460026	0.002163	0.060786	0.386844183	0.326058183	0.002757758
12.464662	0.001594	0.06238	0.386988124	0.324608124	0.008292526
12.474300	0.001096	0.063476	0.387287339	0.323811339	0.022623519
12.498103	0.001262	0.064738	0.388026331	0.323288331	0.018788423
12.518343	0.001643	0.066381	0.388654748	0.322273748	0.023745568
12.543705	0.001588	0.067969	0.389442128	0.321473128	0.094920896
12.640782	0.002725	0.070694	0.392456072	0.321762072	0.631333028
13.274290	0.001626	0.07232	0.412124497	0.339804497	0.038078279
13.313936	0.001509	0.073829	0.413355373	0.339526373	0.056290404
13.372741	0.00352	0.077349	0.415181078	0.337832078	0.007743953
13.382994	0.001498	0.078847	0.415499399	0.336652399	0.002758333
13.387292	0.001582	0.080429	0.415632849	0.335203849	0.022071207
13.417309	0.014309	0.094738	0.416564772	0.321826772	0.004413119
13.430072	0.00239	0.097128	0.416961011	0.319833011	0.007741248
13.439799	0.001582	0.09871	0.417263011	0.318553011	0.002758148
13.444417	0.002138	0.100848	0.41740639	0.31655839	0.00110479
13.447417	0.001653	0.102501	0.417499539	0.314998539	0.018788281
13.468382	0.0027	0.105201	0.418150429	0.312949429	1.313976225

Location	Aperture (mm)	Cum. Ap (mm)	Hom. strain	difference	Spacing (mm)
14.784860	0.002304	0.107505	0.459022891	0.351517891	0.103757468
14.890817	0.002094	0.109599	0.462312502	0.352713502	0.040282719
14.933694	0.003094	0.112693	0.463643688	0.350950688	0.007192345
14.944257	0.003649	0.116342	0.463971662	0.347629662	0.00994226
14.957033	0.002018	0.11836	0.464368308	0.346008308	0.155067751
15.114978	0.003736	0.122096	0.46927199	0.34717599	0.038630859
15.156267	0.001581	0.123677	0.470553894	0.346876894	0.029256818
15.187141	0.001652	0.125329	0.471512412	0.346183412	0.030895989
15.220541	0.003356	0.128685	0.472549375	0.343864375	0.014903185
15.237994	0.001745	0.13043	0.473091257	0.342661257	0.025950864
15.265851	0.002066	0.132496	0.473956108	0.341460108	0.183220564
15.452766	0.005323	0.137819	0.479759227	0.341940227	0.002275466
15.458535	0.001664	0.139483	0.479938335	0.340455335	0.249976734
15.710503	0.002319	0.141802	0.487761147	0.345959147	0.424748636
16.138200	0.003577	0.145379	0.501039767	0.355660767	0.014738738
16.156202	0.00295	0.148329	0.501598679	0.353269679	0.15993605
16.320363	0.0055	0.153829	0.506695358	0.352866358	0.077758287
16.401668	0.001593	0.155422	0.509219613	0.353797613	0.007368719
16.413023	0.006381	0.161803	0.509572172	0.347769172	1.419523478
17.836540	0.001606	0.163409	0.553767846	0.390358846	0.002201098
17.840684	0.002279	0.165688	0.553896492	0.388208492	0.005133414
17.849093	0.004273	0.169961	0.554157577	0.384196577	0.002932094
17.855619	0.002915	0.172876	0.554360192	0.381484192	0.014684294
17.872859	0.002196	0.175072	0.554895433	0.379823433	0.047684327
17.922678	0.002072	0.177144	0.556442133	0.379298133	1.574306505
19.499101	0.002162	0.179306	0.605385069	0.426079069	0.370467254
19.871742	0.002185	0.181491	0.616954379	0.435463379	0.010266359
19.883834	0.001466	0.182957	0.617329793	0.434372793	0.002406636
19.887841	0.001735	0.184692	0.617454202	0.432762202	0.135133761
20.024707	0.00173	0.186422	0.621703464	0.435281464	0.006955758
20.033668	0.002281	0.188703	0.621981682	0.433278682	0.023774569
20.059152	0.001137	0.18984	0.622772866	0.432932866	0.031904833
20.092190	0.00113	0.19097	0.623798601	0.432828601	0.161802999
20.255956	0.002795	0.193765	0.628882999	0.435117999	0.002897817
20.261901	0.0033	0.197065	0.629067582	0.432002582	0.037699285
20.302406	0.002312	0.199377	0.630325143	0.430948143	0.018586151
20.323066	0.001834	0.201211	0.630966543	0.429755543	0.002389636
20.327387	0.002029	0.20324	0.631100701	0.427860701	0.008116001
20.337668	0.002302	0.205542	0.631419909	0.425877909	0.012754181
20.352734	0.002321	0.207863	0.63188765	0.42402465	0.012173973
20.366924	0.001712	0.209575	0.632328219	0.422753219	0.161822585
20.530741	0.002277	0.211852	0.637414219	0.425562219	0.067847305
20.600886	0.002318	0.21417	0.639591992	0.425421992	0.002319828
20.604645	0.00056	0.21473	0.639708692	0.424978692	0.001834401
20.607591	0.001663	0.216393	0.639800153	0.423407153	0.020875633
20.629946	0.001295	0.217688	0.640494193	0.422806193	0.013346707
20.645386	0.002893	0.220581	0.640973578	0.420392578	0.0023181
20.649937	0.001573	0.222154	0.641114875	0.418960875	0.012188118
20.664384	0.002945	0.225099	0.641563412	0.416464412	0.031309174
20.697740	0.001148	0.226247	0.642598999	0.416351999	0.021481225
20.720984	0.002377	0.228624	0.643320643	0.414696643	0.023796306
20.746822	0.001706	0.23033	0.644122825	0.413792825	0.145563542
20.894397	0.002317	0.232647	0.648704561	0.416057561	0.013346842
20.910046	0.002287	0.234934	0.649190407	0.414256407	0.004637842

Location	Aperture (mm)	Cum. Ap (mm)	Hom. strain	difference	Spacing (mm)
20.916406	0.001159	0.236093	0.649387891	0.413294891	0.020901908
20.939627	0.003478	0.239571	0.650108811	0.410537811	0.144403541
21.086639	0.00174	0.241311	0.654673083	0.413362083	0.019718279
21.108096	0.001736	0.243047	0.655339232	0.412292232	0.056837763
21.168981	0.006359	0.249406	0.657229526	0.407823526	0.201241188
21.374850	0.002897	0.252303	0.663621109	0.411318109	0.005217809
21.382705	0.002378	0.254681	0.663864992	0.409183992	0.026691029
21.411780	0.002389	0.25707	0.664767663	0.407697663	0.008116152
21.422528	0.002875	0.259945	0.665101359	0.405156359	0.009872969
21.435876	0.004074	0.264019	0.665515756	0.401496756	0.008693271
21.447516	0.00182	0.265839	0.665877149	0.400038149	0.10321251
21.552548	0.001819	0.267658	0.669138059	0.401480059	0.221523371
21.776140	0.002318	0.269976	0.676079875	0.406103875	0.024374953
21.803141	0.002935	0.272911	0.676918185	0.404007185	0.004673792
21.810189	0.001814	0.274725	0.677137012	0.402412012	0.004099273
21.815769	0.001147	0.275872	0.677310246	0.401438246	0.009871113
21.827370	0.002313	0.278185	0.677670424	0.399485424	0.003478065
21.832921	0.001832	0.280017	0.677842751	0.397825751	0.00525022
21.840821	0.003468	0.283485	0.678088028	0.394603028	0.01800949
21.861755	0.002381	0.285866	0.678737961	0.392871961	0.019141031
21.882941	0.001709	0.287575	0.67939572	0.39182072	0.107881068
21.993127	0.0029	0.290475	0.682816632	0.392341632	0.01742831
22.013454	0.002898	0.293373	0.68344773	0.39007473	0.053923457
22.070275	0.002898	0.296271	0.685211856	0.388940856	0.014505479
22.087388	0.002317	0.298588	0.685743159	0.387155159	0.016231787
22.105975	0.002392	0.30098	0.686320204	0.385340204	0.019138317
22.128932	0.005246	0.306226	0.687032956	0.380806956	0.011013815
22.144015	0.002892	0.309118	0.687501229	0.378383229	0.019718347
22.166038	0.001717	0.310835	0.688184969	0.377349969	0.023194718
22.190953	0.001725	0.31256	0.688958523	0.376398523	0.06149083
22.254221	0.001828	0.314388	0.690922772	0.376534772	0.002389594
22.258104	0.00116	0.315548	0.691043345	0.375495345	0.00579795
22.265931	0.002898	0.318446	0.691286347	0.372840347	0.048146762
22.317004	0.002954	0.3214	0.692871994	0.371471994	0.002391645
22.321162	0.000578	0.321978	0.693001076	0.371023076	0.026690742
22.348720	0.001158	0.323136	0.693856687	0.370720687	0.034786483
22.385818	0.003465	0.326601	0.695008461	0.368407461	0.006980383
22.396270	0.003477	0.330078	0.695332943	0.365254943	0.013924038
22.412802	0.001739	0.331817	0.695846211	0.364029211	0.011014144
22.425550	0.001728	0.333545	0.696241984	0.362696984	0.006404851
22.433670	0.001704	0.335249	0.696494111	0.361245111	0.071326862
22.507016	0.002333	0.337582	0.698771251	0.361189251	0.034223548
22.543301	0.00179	0.339372	0.699897786	0.360525786	0.01103157
22.555744	0.001033	0.340405	0.700284104	0.359879104	0.003478328
22.560284	0.001091	0.341496	0.700425067	0.358929067	0.01276754
22.574749	0.002304	0.3438	0.70087416	0.35707416	0.034803257
22.611537	0.001666	0.345466	0.702016319	0.356550319	0.043493149
22.656153	0.000578	0.346044	0.703401477	0.357357477	0.017981497
22.674976	0.001105	0.347149	0.703985871	0.356836871	0.030745407
22.708002	0.003457	0.350606	0.705011236	0.354405236	0.001160165
22.711757	0.001733	0.352339	0.705127822	0.352788822	0.05568122
22.769459	0.002309	0.354648	0.706919293	0.352271293	0.030165892
22.802228	0.002896	0.357544	0.707936647	0.350392647	0.001157418
22.805699	0.001732	0.359276	0.708044424	0.348768424	0.0040578

Location	Aperture (mm)	Cum. Ap (mm)	Hom. strain	difference	Spacing (mm)
22.811489	0.001732	0.361008	0.708224178	0.347216178	0.002317884
22.815830	0.002314	0.363322	0.708358949	0.345036949	0.002957754
22.821119	0.002348	0.36567	0.708523148	0.342853148	0.003526074
22.826687	0.001737	0.367407	0.708696035	0.341289035	0.002317952
22.831034	0.00232	0.369727	0.708830978	0.339103978	0.004057736
22.837690	0.002877	0.372604	0.709037633	0.336433633	0.014503275
22.854783	0.002303	0.374907	0.709568325	0.334661325	0.004674553
22.862055	0.002892	0.377799	0.709794099	0.331995099	0.004058248
22.868415	0.001711	0.37951	0.709991549	0.330481549	0.03769944
22.907836	0.001733	0.381243	0.711215459	0.329972459	0.030165649
22.939735	0.001732	0.382975	0.712205795	0.329230795	0.004057926
22.945811	0.002304	0.385279	0.712394433	0.327115433	0.073079979
23.020912	0.001739	0.387018	0.714726096	0.327708096	0.015071787
23.037429	0.001152	0.38817	0.715238905	0.327068905	0.002955665
23.041822	0.001722	0.389892	0.715375283	0.325483283	0.002320051
23.046139	0.002272	0.392164	0.715509314	0.323345314	0.018160101
23.066489	0.002107	0.394271	0.716141104	0.321870104	0.0140194
23.082616	0.00211	0.396381	0.716641824	0.320260824	0.024033436
23.108760	0.00211	0.398491	0.717453495	0.318962495	0.002670974
23.113483	0.001995	0.400486	0.717600144	0.317114144	0.0394003
23.154854	0.001945	0.402431	0.71888456	0.31645356	0.009685104
23.166458	0.001894	0.404325	0.719244846	0.314919846	0.086489673
23.255309	0.002828	0.407153	0.722003377	0.314850377	0.022719644
23.280105	0.001324	0.408477	0.722773202	0.314296202	0.004353114
23.285922	0.001605	0.410082	0.722953821	0.312871821	0.019694359
23.308088	0.003337	0.413419	0.723641985	0.310222985	0.003404873
23.314829	0.003336	0.416755	0.723851283	0.307096283	0.00467264
23.322474	0.002609	0.419364	0.72408864	0.30472464	0.006676362
23.331305	0.001701	0.421065	0.724362826	0.303297826	0.010017632
23.343173	0.001999	0.423064	0.724731278	0.301667278	0.001669152
23.346175	0.000666	0.42373	0.72482447	0.30109447	0.0033381
23.350843	0.001994	0.425724	0.7249694	0.2992454	0.010019979
23.362521	0.001322	0.427046	0.725331964	0.298285964	0.003355186
23.370524	0.007973	0.435019	0.725580422	0.290561422	0.002691725
23.378201	0.001998	0.437017	0.725818775	0.288801775	0.004340185
23.384692	0.002304	0.439321	0.726020306	0.286699306	0.011021533
23.397711	0.001691	0.441012	0.726424505	0.285412505	0.013354437
23.412745	0.001668	0.44268	0.726891261	0.284211261	0.01435609
23.442045	0.02822	0.4709	0.727800936	0.256900936	0.004337714
23.460825	0.000664	0.471564	0.728383986	0.256819986	0.002691542
23.464902	0.002108	0.473672	0.728510581	0.254838581	0.0096849
23.476973	0.002663	0.476335	0.728885328	0.252550328	0.002031374
23.480837	0.001002	0.477337	0.729005289	0.251668289	0.027042987
23.509046	0.001331	0.478668	0.729881104	0.251213104	0.005350179
23.515541	0.000959	0.479627	0.730082759	0.250455759	0.032392057
23.549077	0.001329	0.480956	0.731123947	0.250167947	0.010036312
23.560109	0.000661	0.481617	0.731466434	0.249849434	0.004352537
23.565535	0.001486	0.483103	0.731634895	0.248531895	0.006008918
23.572952	0.00133	0.484433	0.731865167	0.247432167	0.004353208
23.578342	0.000744	0.485177	0.732032516	0.246855516	0.004061291
23.583460	0.00137	0.486547	0.732191422	0.245644422	0.052422177
23.636940	0.000746	0.487293	0.733851812	0.246558812	0.003003226
23.641475	0.002317	0.48961	0.733992601	0.244382601	0.00133668
23.644791	0.001642	0.491252	0.734095557	0.242843557	0.013035141

Location	Aperture (mm)	Cum. Ap (mm)	Hom. strain	difference	Spacing (mm)
23.659792	0.002289	0.493541	0.73456128	0.24102028	0.024373246
23.685959	0.001299	0.49484	0.735373689	0.240533689	0.031737921
23.719175	0.001657	0.496497	0.736404938	0.239907938	0.002360444
23.722888	0.001049	0.497546	0.736520229	0.238974229	0.000667481
23.724915	0.00167	0.499216	0.73658316	0.23736716	0.000999797
23.727418	0.001336	0.500552	0.736660864	0.236108864	0.002668542
23.731281	0.001053	0.501605	0.736780799	0.235175799	0.005017991
23.737560	0.001469	0.503074	0.736975742	0.233901742	0.052775111
23.792993	0.003847	0.506921	0.738696763	0.231775763	0.01336873
23.809778	0.002984	0.509905	0.73921786	0.22931286	0.006806044
23.819395	0.002638	0.512543	0.739516439	0.226973439	0.002670713
23.824710	0.002651	0.515194	0.73968146	0.22448746	0.002003782
23.828784	0.00149	0.516684	0.739807953	0.223123953	0.007343571
23.837874	0.002003	0.518687	0.740090171	0.221403171	0.021370806
23.860911	0.00133	0.520017	0.740805406	0.220788406	0.00867729
23.871923	0.003338	0.523355	0.741147271	0.217792271	0.009368597
23.884627	0.003334	0.526689	0.741541709	0.214852709	0.012017945
23.899646	0.002668	0.529357	0.742007999	0.212650999	0.01203431
23.914683	0.003337	0.532694	0.742474844	0.209780844	0.043413362
23.960754	0.001979	0.534673	0.743905214	0.209232214	0.082154327
24.045233	0.00267	0.537343	0.746528012	0.209185012	0.003404283
24.051674	0.003402	0.540745	0.746727963	0.205982963	0.043413071
24.098367	0.003158	0.543903	0.748177634	0.204274634	0.018037224
24.119357	0.002748	0.546651	0.748829314	0.202178314	0.021362792
24.143085	0.001983	0.548634	0.749566002	0.200932002	0.004007532
24.149079	0.00199	0.550624	0.749752097	0.199128097	0.018799042
24.170077	0.002407	0.553031	0.750404004	0.197373004	0.010033881
24.182981	0.003334	0.556365	0.750804644	0.194439644	0.00333772
24.189040	0.002108	0.558473	0.750992748	0.192519748	0.003404358
24.19416615	0.001336	0.559809	0.751151905	0.191342905	0.005381387
24.20187754	0.003324	0.563133	0.751391319	0.188258319	0.021373475
24.22690701	0.003988	0.567121	0.752168405	0.185047405	0.008678067
24.23823458	0.001311	0.568432	0.75252009	0.18408809	0.004060991
24.24400257	0.002103	0.570535	0.752699168	0.182164168	0.035405286
24.28183586	0.002753	0.573288	0.753873771	0.180585771	0.00533968
24.29252454	0.007945	0.581233	0.75420562	0.17297262	0.013366891
24.31386393	0.008	0.589233	0.754868141	0.165635141	0.012702921
24.33283585	0.004538	0.593771	0.755457158	0.161686158	0.149586405
24.48598625	0.00259	0.596361	0.760211991	0.163850991	0.010702137
24.50020389	0.004441	0.600802	0.760653404	0.159851404	0.094831074
24.59856546	0.00262	0.603422	0.763707218	0.160285218	0.068120788
24.67416725	0.012342	0.615764	0.766054413	0.150290413	0.101504682
24.78680443	0.009923	0.625687	0.769551439	0.143864439	0.001336647
24.79406058	0.001916	0.627603	0.769776719	0.142173719	0.080132174
24.87589475	0.001488	0.629091	0.77231741	0.14322641	0.005381471
24.88339622	0.002752	0.631843	0.772550307	0.140707307	0.047414669
24.93385539	0.003337	0.63518	0.774116904	0.138936904	0.025377027
24.96190092	0.002	0.63718	0.774987628	0.137807628	0.020037716
24.98460364	0.00333	0.64051	0.775692475	0.135182475	0.034071903
25.02134104	0.002001	0.642511	0.776833055	0.134322055	0.021372976
25.04662802	0.005827	0.648338	0.777618135	0.129280135	0.006675797
25.05755231	0.00267	0.651008	0.7779573	0.1269493	0.03607139
25.0979622	0.006007	0.657015	0.779211898	0.122196898	0.029380553
25.13168126	0.00267	0.659685	0.780258767	0.120573767	0.006006587

Location	Aperture (mm)	Cum. Ap (mm)	Hom. strain	difference	Spacing (mm)
25.14031134	0.002577	0.662262	0.780526704	0.118264704	0.01068107
25.15293741	0.001313	0.663575	0.780918704	0.117343704	0.016700975
25.17196989	0.00335	0.666925	0.781509601	0.114584601	0.005383415
25.1822758	0.006495	0.67342	0.781829567	0.108409567	0.008012762
25.19515907	0.003246	0.676666	0.782229552	0.105563552	0.008705283
25.20745935	0.003944	0.68061	0.782611436	0.102001436	0.006006671
25.21648552	0.002095	0.682705	0.78289167	0.10018667	0.008010726
25.22579525	0.000503	0.683208	0.783180707	0.099972707	0.021373348
25.24808659	0.001333	0.684541	0.783872783	0.099331783	0.066120085
25.31553968	0.001333	0.685874	0.785966987	0.100092987	0.009347008
25.32620969	0.001313	0.687187	0.786298256	0.099111256	0.016701506
25.34456619	0.001997	0.689184	0.786868168	0.097684168	0.016035117
25.36290981	0.00262	0.691804	0.787437679	0.095633679	0.13423825
25.49945656	0.001997	0.693801	0.791677021	0.097876021	0.002753008
25.50426257	0.002109	0.69591	0.791826232	0.095916232	0.014035622
25.52067519	0.002645	0.698555	0.792335792	0.093780792	0.006006923
25.52873311	0.001457	0.700012	0.792585965	0.092573965	0.018024596
25.54814321	0.001314	0.701326	0.793188586	0.091862586	0.005339441
25.55513865	0.001998	0.703324	0.793405773	0.090081773	0.010034166
25.56814331	0.003943	0.707267	0.793809526	0.086542526	0.010702148
25.58180946	0.001985	0.709252	0.794233817	0.084981817	0.010011903
25.59417287	0.002718	0.71197	0.794617661	0.082647661	0.04875073
25.6472521	0.005939	0.717909	0.796265602	0.078356602	0.042746674
25.69363527	0.001334	0.719243	0.797705652	0.078462652	0.00867784
25.70497961	0.003999	0.723242	0.798057858	0.074815858	0.002670929
25.71070454	0.002109	0.725351	0.798235599	0.072884599	0.002109881
25.71556842	0.003399	0.72875	0.798386607	0.069636607	0.020037138
25.73927806	0.003946	0.732696	0.799122716	0.066426716	0.030047805
25.77298086	0.003364	0.73606	0.800169081	0.064109081	0.017357716
25.79268008	0.001319	0.737379	0.800780679	0.063401679	0.00870343
25.80302951	0.001973	0.739352	0.801101995	0.061749995	0.069454646
25.87446966	0.001998	0.74135	0.803319985	0.061969985	0.018037348
25.895157	0.003302	0.744652	0.803962261	0.059310261	0.019372825
25.91749633	0.002631	0.747283	0.804655826	0.057372826	0.016036876
25.93615421	0.002611	0.749894	0.805235094	0.055341094	0.01468657
25.95312878	0.001965	0.751859	0.8057621	0.0539031	0.009368846
25.96444862	0.001937	0.753796	0.806113545	0.052317545	0.016701563
25.98310718	0.001977	0.755773	0.806692834	0.050919834	0.062781558
26.04915274	0.004551	0.760324	0.808743339	0.048419339	0.005341966
26.05775571	0.001971	0.762295	0.809010434	0.046715434	0.003338103
26.06306581	0.001973	0.764268	0.809175295	0.044907295	0.002668587
26.0693624	0.005283	0.769551	0.809370784	0.039819784	0.073457941
26.14744684	0.00397	0.773521	0.811795058	0.038274058	0.078797986
26.22914882	0.001838	0.775359	0.814331645	0.038972645	0.018034653
26.24944198	0.002679	0.778038	0.814961683	0.036923683	0.066770195
26.31854917	0.001995	0.780033	0.817107241	0.037074241	0.283846267
26.60404494	0.001304	0.781337	0.825970977	0.044633977	0.096164741
26.70288868	0.004054	0.785391	0.829039761	0.043648761	0.026710211
26.73293039	0.002609	0.788	0.82997246	0.04197246	0.044746592
26.77962148	0.00128	0.78928	0.83142207	0.04214207	0.004005175
26.78592816	0.003323	0.792603	0.831617872	0.039014872	0.038740981
26.82798714	0.003313	0.795916	0.83292367	0.03700767	0.00406033
26.83473097	0.002054	0.79797	0.833133044	0.035163044	0.036738595
26.87315056	0.001308	0.799278	0.83432585	0.03504785	1.745781117

Location	Aperture (mm)	Cum. Ap (mm)	Hom. strain	difference	Spacing (mm)
28.62018118	0.001191	0.800469	0.888565594	0.088096594	0.095498354
28.71676404	0.000978	0.801447	0.891564185	0.090117185	0.16764228
28.88554282	0.001295	0.802742	0.896804229	0.094062229	0.011348183
28.898431	0.001785	0.804527	0.897204366	0.092677366	0.021372827
28.92109683	0.000801	0.805328	0.897908068	0.092580068	0.042743782
28.96512561	0.001769	0.807097	0.899275022	0.092178022	0.008038209
28.97488282	0.001669	0.808766	0.899577952	0.090811952	0.004674933
28.98216675	0.003549	0.812315	0.899804095	0.087489095	0.021371025
29.00652578	0.002427	0.814742	0.900560365	0.085818365	0.062783863
29.07172464	0.002403	0.817145	0.902584583	0.085439583	0.002336587
29.07647223	0.002419	0.819564	0.90273198	0.08316798	0.001375521
29.08000475	0.001895	0.821459	0.902841654	0.081382654	0.00066728
29.08216703	0.001095	0.822554	0.902908785	0.080354785	0.000667057
29.08457408	0.002385	0.824939	0.902983517	0.078044517	0.002031523
29.08848011	0.001364	0.826303	0.903104786	0.076801786	0.007351047
29.09764865	0.002271	0.828574	0.903389441	0.074815441	0.002671118
29.10245577	0.002001	0.830575	0.903538686	0.072963686	0.006341583
29.11033235	0.001069	0.831644	0.903783229	0.072139229	0.002001413
29.11372777	0.001719	0.833363	0.903888646	0.070525646	0.003337669
29.11844244	0.001035	0.834398	0.904035022	0.069637022	0.004337585
29.12434702	0.002099	0.836497	0.90421834	0.06772134	0.001375315
29.12791684	0.00229	0.838787	0.904329172	0.065542172	0.004352742
29.13429058	0.001752	0.840539	0.904527056	0.063988056	0.002668594
29.13917067	0.002671	0.84321	0.904678567	0.061468567	0.00275334
29.14534951	0.00418	0.84739	0.904870401	0.057480401	0.033378658
29.18149667	0.001357	0.848747	0.905992655	0.057245655	0.004720169
29.18771934	0.001648	0.850395	0.906185849	0.055790849	0.022040482
29.21157332	0.001979	0.852374	0.906926439	0.054552439	0.002001462
29.21530729	0.001486	0.85386	0.907042367	0.053182367	0.002001427
29.21970121	0.003299	0.857159	0.907178784	0.050019784	0.022706998
29.24486421	0.001613	0.858772	0.907960016	0.049188016	0.016701578
29.26372629	0.002708	0.86148	0.908545623	0.047065623	0.009442168
29.27524246	0.00144	0.86292	0.908903163	0.045983163	0.002003439
29.2791264	0.002321	0.865241	0.909023747	0.043782747	0.002001059
29.28314745	0.001719	0.86696	0.909148588	0.042188588	0.005339462
29.29098092	0.003269	0.870229	0.909391793	0.039162793	0.003338305
29.29725922	0.002611	0.87284	0.909586714	0.036746714	0.012682909
29.31223363	0.001972	0.874812	0.910051622	0.035239622	0.003402087
29.31769072	0.002138	0.87695	0.910221047	0.033271047	0.004672579
29.3244638	0.002063	0.879013	0.910431329	0.031418329	0.008677853
29.33527015	0.002194	0.881207	0.910766832	0.029559832	0.004005334
29.34138448	0.002024	0.883231	0.910956663	0.027725663	0.01668825
29.35953073	0.000892	0.884123	0.911520046	0.027397046	0.025403271
29.385916	0.001072	0.885195	0.912339225	0.027144225	0.004005014
29.39068902	0.000464	0.885659	0.912487412	0.026828412	0.025376435
29.41744295	0.002291	0.88795	0.913318037	0.025368037	0.005381466
29.42471592	0.001492	0.889442	0.913543839	0.024101839	0.007373974
29.43407639	0.002481	0.891923	0.913834452	0.021911452	0.001334472
29.43776886	0.002235	0.894158	0.913949091	0.019791091	0.006676279
29.44618514	0.001245	0.895403	0.91421039	0.01880739	0.261119562
29.7107057	0.005557	0.90096	0.922422912	0.021462912	0.112182695
29.8315304	0.011727	0.912687	0.926174135	0.013487135	0.036722516
29.87480292	0.001373	0.91406	0.927517609	0.013457609	0.006709406
29.88312682	0.001856	0.915916	0.927776039	0.011860039	0.006675764

Location	Aperture (mm)	Cum. Ap (mm)	Hom. strain	difference	Spacing (mm)
29.89114009	0.000819	0.916735	0.928024826	0.011289826	0.099503638
29.99160772	0.001109	0.917844	0.931144026	0.013300026	0.073459992
30.06679772	0.002351	0.920195	0.933478437	0.013283437	0.075460923
30.14431614	0.001764	0.921959	0.935885137	0.013926137	0.052775433
30.19929457	0.002642	0.924601	0.937592043	0.012991043	0.195687958
30.39884003	0.005073	0.929674	0.943787294	0.014113294	0.005381067
30.4212201	0.028925	0.958599	0.944482124	-0.014116876	0.041391917
30.47875501	0.003361	0.96196	0.9462684	-0.0156916	0.020706266
30.50246228	0.002641	0.964601	0.947004436	-0.017596564	0.005383019
30.5104558	0.00258	0.967181	0.947252609	-0.019928391	0.038723299
30.5530391	0.00514	0.972321	0.948574685	-0.023746315	0.039409622
30.60529622	0.020555	0.992876	0.950197102	-0.042678898	0.004004826
30.62091405	0.002671	0.995547	0.950681986	-0.044865014	0.001334201
30.62458525	0.002003	0.99755	0.950795965	-0.046754035	0.150941528
30.77725378	0.001451	0.999001	0.955535838	-0.043465162	1.383824293
32.16251607	0.001425	1.000426	0.998543826	-0.001882174	0.072124116
32.23606319	0.001421	1.001847	1.00082723	-0.00101977	0.029403601
32.26738929	0.002424	1.004271	1.001799805	-0.002471195	0.068120637
32.33767392	0.001904	1.006175	1.00398192	-0.00219308	0.412727348
32.75236777	0.002029	1.008204	1.016856845	0.008652845	0.29318632
33.04786359	0.00259	1.010794	1.02603105	0.01523705	0.834815614
33.88427921	0.00061	1.011404	1.051999095	0.040595095	0.106842615
33.99265932	0.002465	1.013869	1.055363953	0.041494953	0.017368141
34.01276096	0.003002	1.016871	1.055988045	0.039117045	0.339936755
34.35544572	0.002494	1.019365	1.066627316	0.047262316	0.291186316
34.64920553	0.002653	1.022018	1.075747624	0.053729624	0.017367961
34.66885649	0.001913	1.023931	1.076357724	0.052426724	0.144935121
34.81508112	0.000666	1.024597	1.080897533	0.056300533	0.08547214
34.90248476	0.003197	1.027794	1.083611138	0.055817138	0.055442111
34.96342837	0.007806	1.0356	1.085503244	0.049903244	0.177651738
35.1469681	0.00397	1.03957	1.091201569	0.051631569	0.113517072
35.26377318	0.002606	1.042176	1.094827995	0.052651995	0.299901895
35.56564457	0.001333	1.043509	1.104200141	0.060691141	0.042061567
35.60942714	0.002109	1.045618	1.105559451	0.059941451	0.050753636
35.66189077	0.001311	1.046929	1.10718828	0.06025928	0.008677383
35.67227266	0.002098	1.049027	1.107510604	0.058483604	0.095498165
35.77013582	0.002632	1.051659	1.110548944	0.058889944	0.001334561
35.77407488	0.002577	1.054236	1.11067124	0.05643524	0.17965237
35.95565325	0.001275	1.055511	1.116308671	0.060797671	0.064117312
36.02172557	0.002635	1.058146	1.118360006	0.060214006	0.040076551
36.06442512	0.002611	1.060757	1.119685691	0.058928691	0.293853378
36.3599075	0.000647	1.061404	1.128859479	0.067455479	0.064786447
36.42616294	0.002291	1.063695	1.1309165	0.0672215	0.162284829
36.59422977	0.009273	1.072968	1.13613444	0.06316644	0.006675963
36.60814724	0.00521	1.078178	1.136566533	0.058388533	0.029403687
36.64274392	0.005176	1.083354	1.13764065	0.05428665	0.111534019
36.75807144	0.002411	1.085765	1.141221203	0.055456203	0.041410682
36.80203262	0.00269	1.088455	1.142586058	0.054131058	0.003338176
36.8076848	0.001938	1.090393	1.14276154	0.05236854	0.046747577
36.85639338	0.001984	1.092377	1.144273786	0.051896786	0.054775671
36.91337455	0.002427	1.094804	1.14604287	0.05123887	0.016034921
36.93149147	0.001737	1.096541	1.146605343	0.050064343	0.010014509
36.94321848	0.001688	1.098229	1.14696943	0.04874043	0.0420772
36.98787918	0.003479	1.101708	1.148356002	0.046648002	0.008010411

Location	Aperture (mm)	Cum. Ap (mm)	Hom. strain	difference	Spacing (mm)
36.99924109	0.003224	1.104932	1.148708753	0.043776753	0.134260231
37.13662282	0.003019	1.107951	1.152974019	0.045023019	0.055424765
37.19418258	0.001251	1.109202	1.154761067	0.045559067	0.022707168
37.21844425	0.001858	1.11106	1.155514314	0.044454314	0.004719723
37.22537797	0.00257	1.11363	1.155729585	0.042099585	0.005339111
37.23322309	0.002442	1.116072	1.15597315	0.03990115	0.003338084
37.23875967	0.001955	1.118027	1.156145044	0.038118044	0.010036438
37.25102711	0.002507	1.120534	1.156525909	0.035991909	0.002670432
37.25558854	0.001275	1.121809	1.156667526	0.034858526	0.122895446
37.38069149	0.00314	1.124949	1.160551575	0.035602575	0.24376982
37.62667481	0.001287	1.126236	1.168188575	0.041952575	0.017355249
37.64590405	0.002461	1.128697	1.168785582	0.040088582	0.002753125
37.65070568	0.001636	1.130333	1.168934657	0.038601657	0.009371095
37.66151028	0.001231	1.131564	1.169270105	0.037706105	0.066100953
37.73000523	0.003557	1.135121	1.171396656	0.036275656	0.022039599
37.75448983	0.001333	1.136454	1.172156825	0.035702825	0.009368547
37.76541837	0.001787	1.138241	1.172496121	0.034255121	0.010012329
37.7772247	0.001801	1.140042	1.17286267	0.03282067	0.010034284
37.78966399	0.003009	1.143051	1.17324887	0.03019787	0.004005265
37.79639675	0.002446	1.145497	1.173457901	0.027960901	0.018704248
37.818189	0.00373	1.149227	1.174134481	0.024907481	0.267812751
38.08922675	0.00272	1.151947	1.182549341	0.030602341	0.098168149
38.1899764	0.002443	1.15439	1.185677298	0.031287298	0.100170848
38.29278775	0.002838	1.157228	1.188869263	0.031641263	0.018034399
38.31356565	0.002649	1.159877	1.189514351	0.029637351	0.213055884
38.52883153	0.001771	1.161648	1.196197672	0.034549672	0.024040958
38.55457849	0.001641	1.163289	1.196997033	0.033708033	0.024707767
38.58165976	0.003106	1.166395	1.19783782	0.03144282	0.013369026
38.59840928	0.003655	1.17005	1.19835784	0.02830784	0.012034441
38.61407722	0.003612	1.173662	1.198844279	0.025182279	0.015353727
38.63219145	0.001909	1.175571	1.199406668	0.023835668	0.003404268
38.63755422	0.002008	1.177579	1.199573165	0.021994165	0.024737287
38.66392651	0.001262	1.178841	1.200391941	0.021550941	0.004005595
38.6688771	0.000628	1.179469	1.200545641	0.021076641	0.002003871
38.67187547	0.001361	1.18083	1.200638731	0.019808731	0.011348573
38.68457405	0.001339	1.182169	1.201032981	0.018863981	0.313226223
38.99940677	0.001874	1.184043	1.210807536	0.026764536	0.102171599
39.10311287	0.001195	1.185238	1.214027281	0.028789281	0.016034879
39.12005925	0.000628	1.185866	1.214553412	0.028687412	0.007343573
39.12830582	0.001178	1.187044	1.214809442	0.027765442	0.003335853
39.13345217	0.002443	1.189487	1.214969219	0.025482219	0.004719791
39.14027996	0.001773	1.19126	1.215181201	0.023921201	0.004672623
39.14671659	0.001755	1.193015	1.215381037	0.022366037	0.080818527
39.22932511	0.001825	1.19484	1.217945769	0.023105769	0.277153003
39.50809512	0.001409	1.196249	1.226600691	0.030351691	0.100215359
39.60992498	0.00182	1.198069	1.229762184	0.031693184	0.002003583
39.61403106	0.002385	1.200454	1.229889665	0.029435665	0.006008845
39.6228074	0.00315	1.203604	1.230162143	0.026558143	0.00406037
39.62998277	0.00308	1.206684	1.230384915	0.023700915	0.005339164
39.63840944	0.003095	1.209779	1.230646536	0.020867536	0.006709091
39.64812503	0.002918	1.212697	1.230948175	0.018251175	0.023364086
39.67353661	0.001177	1.213874	1.231737124	0.017863124	0.019359182
39.6941063	0.001244	1.215118	1.232375747	0.017257747	0.029378847
39.72510364	0.001993	1.217111	1.233338116	0.016227116	0.002001477

Location	Aperture (mm)	Cum. Ap (mm)	Hom. strain	difference	Spacing (mm)
39.72911512	0.002027	1.219138	1.233462659	0.014324659	0.015411841
39.74650496	0.001929	1.221067	1.234002559	0.012935559	0.004672511
39.75311597	0.001948	1.223015	1.234207809	0.011192809	0.076817902
39.83190737	0.001999	1.225014	1.236654032	0.011640032	0.019358973
39.85288035	0.001229	1.226243	1.237305176	0.011062176	0.073478943
39.92794129	0.001935	1.228178	1.23963558	0.01145758	0.006707154
39.93688844	0.002545	1.230723	1.23991336	0.00919036	0.042744252
39.9820037	0.002197	1.23292	1.241314045	0.008394045	0.080818378
40.06480007	0.001759	1.234679	1.243884609	0.009205609	0.064252265
40.13151434	0.003165	1.237844	1.245955875	0.008111875	0.053240518
40.18742386	0.002173	1.240017	1.247691688	0.007674688	0.109805898
40.29909226	0.001552	1.241569	1.251158637	0.009589637	0.00332422
40.30466298	0.002941	1.24451	1.25133159	0.00682159	0.084018383
40.39087386	0.001444	1.245954	1.254008163	0.008054163	0.01415847
40.40749933	0.00349	1.249444	1.254524331	0.005080331	0.01829257
40.4286724	0.002271	1.251715	1.255181688	0.003466688	0.024111241
40.45509164	0.002345	1.25406	1.256001921	0.001941921	0.011641585
40.46826623	0.000721	1.254781	1.25641095	0.00162995	0.048232461
40.51860619	0.003494	1.258275	1.257973846	-0.000301154	0.007953
40.52830619		1.258275	1.258275	0	

Location	Aperture (mm)	Cum. Ap (mm)	Hom. strain	difference	Spacing (mm)
Sample 58			V'		C
			0.31489862		1.534139494
loc	ap	cumap	hom strain	difference	spacing
0	0	0	0	0	
0.1504	0.007294	0.007294	0.000557169	-0.006736831	0.308027258
0.464063258	0.003978	0.011272	0.00171916	-0.00955284	0.115390782
0.58276854	0.002651	0.013923	0.002158914	-0.011764086	0.154508105
0.745240645	0.013277	0.0272	0.002760805	-0.024439195	0.750009578
1.503546724	0.003316	0.030516	0.005570012	-0.024945988	0.527194982
2.035051706	0.005304	0.03582	0.007539016	-0.028280984	0.080905237
2.120266943	0.003316	0.039136	0.007854703	-0.031281297	0.048420625
2.173018068	0.005345	0.044481	0.008050124	-0.036430876	0.037137443
2.218143511	0.010631	0.055112	0.008217295	-0.046894705	0.156495559
2.38061757	0.001326	0.056438	0.008819193	-0.047618807	0.851477492
3.239057062	0.012598	0.069036	0.011999353	-0.057036647	3.769967684
7.019633746	0.00862	0.077656	0.02600481	-0.05165119	0.629978307
7.654585053	0.001326	0.078982	0.028357039	-0.050624961	0.007984472
7.665221525	0.003978	0.08296	0.028396443	-0.054563557	7.858228537
15.52875456	0.006631	0.089591	0.057527546	-0.032063454	3.147935349
18.68099941	0.001988	0.091579	0.069205296	-0.022373704	0.046419165
18.72907608	0.001327	0.092906	0.0693834	-0.0235226	8.906652436
27.64003901	0.007294	0.1002	0.102394794	0.002194794	1.313689535
28.96234905	0.009947	0.110147	0.1072934	-0.0028536	0.339530003
29.30850955	0.003314	0.113461	0.10857578	-0.00488522	4.63731165
33.9485227	0.002089	0.11555	0.12576509	0.01021509	0.009045458
33.96035316	0.003481	0.119031	0.125808917	0.006777917	0.162855694
34.12599385	0.002089	0.12112	0.126422547	0.005302547	0.894325594
35.02345095	0.004174	0.125294	0.12974725	0.00445325	0.004176253
35.0304102	0.001392	0.126686	0.129773031	0.003087031	3.242508302
38.2809295	0.01463	0.141316	0.141814847	0.000498847	8.664103545
46.95687155	0.009047	0.150363	0.173955587	0.023592587	5.010970061
51.97340861	0.002087	0.15245	0.19253976	0.04008976	0.112746946
52.08789505	0.001392	0.153842	0.192963885	0.039121885	0.008350411
52.09763746	0.001392	0.155234	0.192999976	0.037765976	4.486214652
56.58559162	0.002087	0.157321	0.209625971	0.052304971	0.122488716
56.71260383	0.00696	0.164281	0.210096498	0.045815498	2.519405972
59.2382738	0.005568	0.169849	0.21945305	0.04960405	0.352851334
59.59495364	0.002089	0.171938	0.2207744	0.0488364	1.059956285
60.65875992	0.005611	0.177549	0.224715357	0.047166357	0.075162469
60.74229489	0.011134	0.188683	0.225024819	0.036341819	0.709887192
61.45844508	0.001392	0.190075	0.227677857	0.037602857	0.006960019
61.4692521	0.006302	0.196377	0.227717892	0.031340892	0.064026186
61.53747379	0.002089	0.198466	0.227970625	0.029504625	0.653735254
62.19868854	0.01287	0.211336	0.230420149	0.019084149	0.015730192
62.22407124	0.006435	0.217771	0.230514182	0.012743182	2.064464634
64.29357587	0.003645	0.221416	0.238180831	0.016764831	4.751036349
69.04893772	0.005006	0.226422	0.25579746	0.02937546	0.434773469
69.48728619	0.002144	0.228566	0.257421358	0.028855358	0.805903753
70.29604994	0.003576	0.232142	0.26041749	0.02827549	0.132296335
70.43442428	0.00858	0.240722	0.260930109	0.020208109	1.706183209
72.14813498	0.006475	0.247197	0.267278691	0.020081691	0.019317324
72.17354981	0.00572	0.252917	0.267372842	0.014455842	0.017876172

Location	Aperture (mm)	Cum. Ap (mm)	Hom. strain	difference	Spacing (mm)
72.19643148	0.004291	0.257208	0.267457609	0.010249609	0.843089691
73.04345467	0.003576	0.260784	0.270595476	0.009811476	0.2409805
73.29302517	0.013604	0.274388	0.27152003	-0.00286797	0.077226222
73.38670639	0.019306	0.293694	0.27186708	-0.02182692	0.512006595
73.91086899	0.005006	0.2987	0.273808884	-0.024891116	7.28601967
81.20153716	0.004291	0.302991	0.300817762	-0.002173238	1.197769126
82.40252379	0.002144	0.305135	0.305266916	0.000131916	2.21033369
84.61500248	0.002146	0.307281	0.313463225	0.006182225	0.027885412
84.64646389	0.005006	0.312287	0.313579776	0.001292776	0.332512522
84.98792441	0.01289	0.325177	0.314844745	-0.010332255	0.170189252
85.16706166	0.005006	0.330183	0.315508374	-0.014674626	4.035237135
89.2090928	0.008582	0.338765	0.33048241	-0.00828259	1.080586457
90.29576525	0.00359	0.342355	0.334508077	-0.007846923	0.01402682
90.31203607	0.000898	0.343253	0.334568354	-0.008684646	0.004487183
90.31758976	0.001235	0.344488	0.334588928	-0.009899072	3.312752808
93.63233006	0.00274	0.347228	0.346868656	-0.000359344	0.09563
93.72933006		0.347228	0.347228	0	

Location Aperture (mm) Cum. Ap (mm) Hom. strain difference Spacing (mm)

Sample 58a			V'		C
			0.252458475		1.27503742
loc	ap	cumap	hom strain	difference	spacing
0	0	0	0	0	
0.101989223	0.003978447	0.003978447	0.000211183	-0.003767264	0.115390461
0.220694505	0.002651196	0.006629642	0.000456979	-0.006172664	0.904517271
1.128195198	0.003315648	0.00994529	0.002336086	-0.007609204	0.850154709
1.98067053	0.001325598	0.011270888	0.004101256	-0.007169632	5.251424054
7.233420182	0.001325598	0.012596486	0.014977812	0.002381326	0.00798445
7.244056654	0.003978447	0.016574933	0.014999836	-0.001575097	7.858228166
15.10758969	0.006631295	0.023206228	0.031282385	0.008076157	13.41469562
28.53057443	0.009946943	0.033153171	0.059076559	0.025923388	4.97684171
33.51343409	0.002088952	0.035242123	0.069394269	0.034152145	0.00904549
33.52526455	0.003480984	0.038723107	0.069418765	0.030695658	1.057181201
34.58627339	0.004174285	0.042897392	0.071615733	0.028718341	0.004176095
34.59323264	0.001392032	0.044289424	0.071630143	0.02734072	3.242508174
37.84375194	0.014630225	0.058919648	0.0783608	0.019441151	8.664103282
46.51969399	0.0090473	0.067966948	0.096325555	0.028358607	5.01096984
51.53623105	0.002087142	0.070054091	0.106712999	0.036658909	0.112746859
51.65071749	0.001392032	0.071446122	0.10695006	0.035503937	0.008350379
51.6604599	0.001392032	0.072838154	0.106970233	0.034132079	4.486214565
56.14841406	0.002087142	0.074925296	0.116263172	0.041337875	0.122488566
56.27542627	0.006960158	0.081885454	0.116526168	0.034640714	2.51940583
58.80109624	0.005568126	0.08745358	0.121755922	0.034302342	1.487969505
60.29741703	0.011134442	0.098588023	0.124854265	0.026266242	0.709886955
61.01356722	0.001392032	0.099980054	0.126337154	0.0263571	0.006960158
61.02437424	0.006301692	0.106281746	0.126359532	0.020077786	0.064026364
61.09259593	0.002088952	0.108370698	0.126500794	0.018130096	0.653735029
61.75381068	0.012870497	0.121241195	0.127869932	0.006628737	0.015729819
61.77919338	0.006435248	0.127676443	0.12792249	0.000246047	6.815501133
68.60041493	0.005005587	0.132682031	0.142046787	0.009364756	1.240676973
69.84538266	0.003575926	0.136257957	0.144624667	0.00836671	0.132296502
69.98375699	0.00857974	0.144837697	0.144911191	7.34938E-05	2.58646656
72.57630139	0.003575926	0.148413623	0.150279418	0.001865794	0.830213695
73.41080584	0.005005587	0.153419211	0.152007377	-0.001411834	7.286019998
80.70147401	0.004290757	0.157709968	0.167103728	0.00939376	3.408102314
84.11279483	0.002146265	0.159856233	0.174167347	0.014311114	0.027885485
84.14425624	0.005005587	0.16486182	0.174232492	0.009370672	0.332512563
84.48571677	0.012890332	0.177752152	0.174939534	-0.002812618	0.170189292
84.66485402	0.005005587	0.18275774	0.175310463	-0.007447277	4.035237585
88.70688515	0.008581514	0.191339253	0.183680056	-0.007659198	4.41185408
93.12440023	0.002740479	0.194079733	0.192827141	-0.001252592	0.603559594
93.72933006		0.194079733	0.194079733	0	

Location Aperture (mm) Cum. Ap (mm) Hom. strain difference Spacing (mm)

Sample 59			V'		C
			0.33707962		1.01002289
loc	ap	cumap	hom strain	difference	spacing
0	0	0	0	0	
2.302	0.002776	0.002776	0.001669423	-0.001106577	0.288785894
2.594761394	0.005175	0.007951	0.001881735	-0.006069265	0.554855153
3.153651547	0.002895	0.010846	0.002287045	-0.008558955	0.003610189
3.159560736	0.001703	0.012549	0.002291331	-0.010257669	15.49430272
18.65507045	0.000711	0.01326	0.01352876	0.00026876	3.508211384
22.16453934	0.001804	0.015064	0.016073846	0.001009846	7.632849177
29.80065601	0.004731	0.019795	0.021611599	0.001816599	15.99758195
45.80216197	0.003117	0.022912	0.033215979	0.010303979	0.264299323
46.07127779	0.006516	0.029428	0.033411144	0.003983144	3.869005229
49.94989052	0.012699	0.042127	0.036223935	-0.005903065	4.395474203
54.35310922	0.00279	0.044917	0.039417173	-0.005499827	0.604207744
54.96145147	0.005479	0.050396	0.039858347	-0.010537653	5.101436899
60.06707787	0.0029	0.053296	0.043560975	-0.009735025	5.062566255
65.13203062	0.001873	0.055169	0.047234106	-0.007934894	4.836439364
69.97088898	0.002965	0.058134	0.050743273	-0.007390727	3.919888614
73.8933721	0.002224	0.060358	0.053587879	-0.006770121	9.905372822
83.80059292	0.001472	0.06183	0.06077265	-0.00105735	1.457264
85.25859292		0.06183	0.06183	0	

Location	Aperture (mm)	Cum. Ap (mm)	Hom. strain	difference	Spacing (mm)
Sample 59a			V'		C
			0.214578994		0.536985243
loc	ap	cumap	hom strain	difference	spacing
0	0	0	0	0	
47.64789052	0.012699	0.012699	0.011519847	-0.001179153	4.395474203
52.05110922	0.00279	0.015489	0.012584415	-0.002904585	5.711123643
57.76507787	0.0029	0.018389	0.013965883	-0.004423117	13.82373223
71.5913721	0.002224	0.020613	0.017308671	-0.003304329	13.66610882
85.25859292		0.020613	0.020613	0	

Appendix D: Fluid inclusion data and maps

FLUID INCLUSION DATA AND MAPS

The following pages include fluid inclusion data (T_h and freezing temperatures) tables and maps locating fluid inclusions within thin sections.

For SEM-CL maps of microfractures, data listed include the average temperature, the number of fluid inclusions analyzed, and the range of temperatures.

Macrofractures correspond to Figure 6-5; microfractures correspond to Figure 6-6. All comprise data from Sample 44 (Chapter 3).

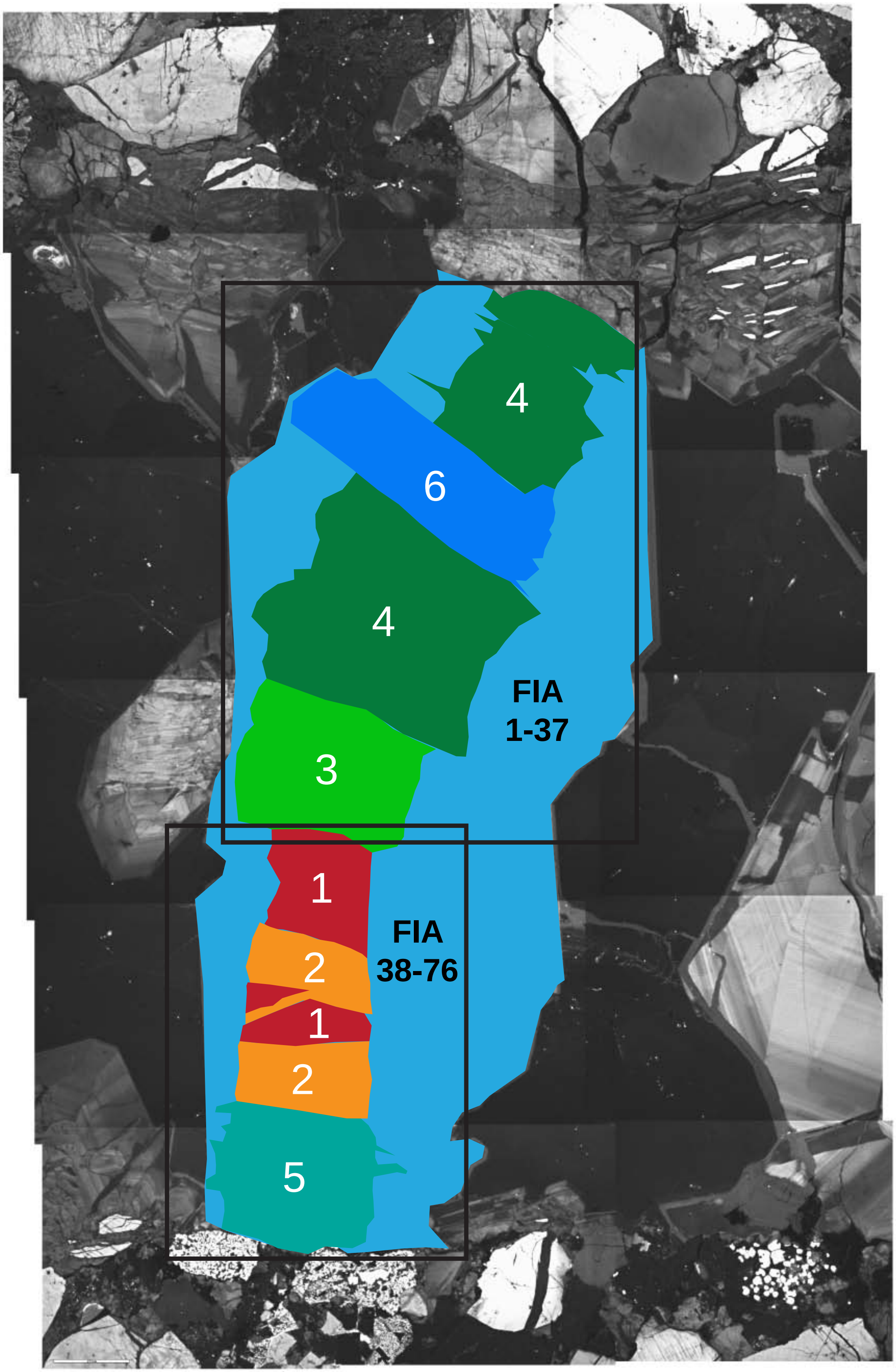

Macrofracture 1


1
2
3
4
5
6
7
8
9
10
11
11a
12
13
14
15
16
17
18
19
20
21
22
23
24
25
26
27
28
29
30
31
32
33
34
35
36
37

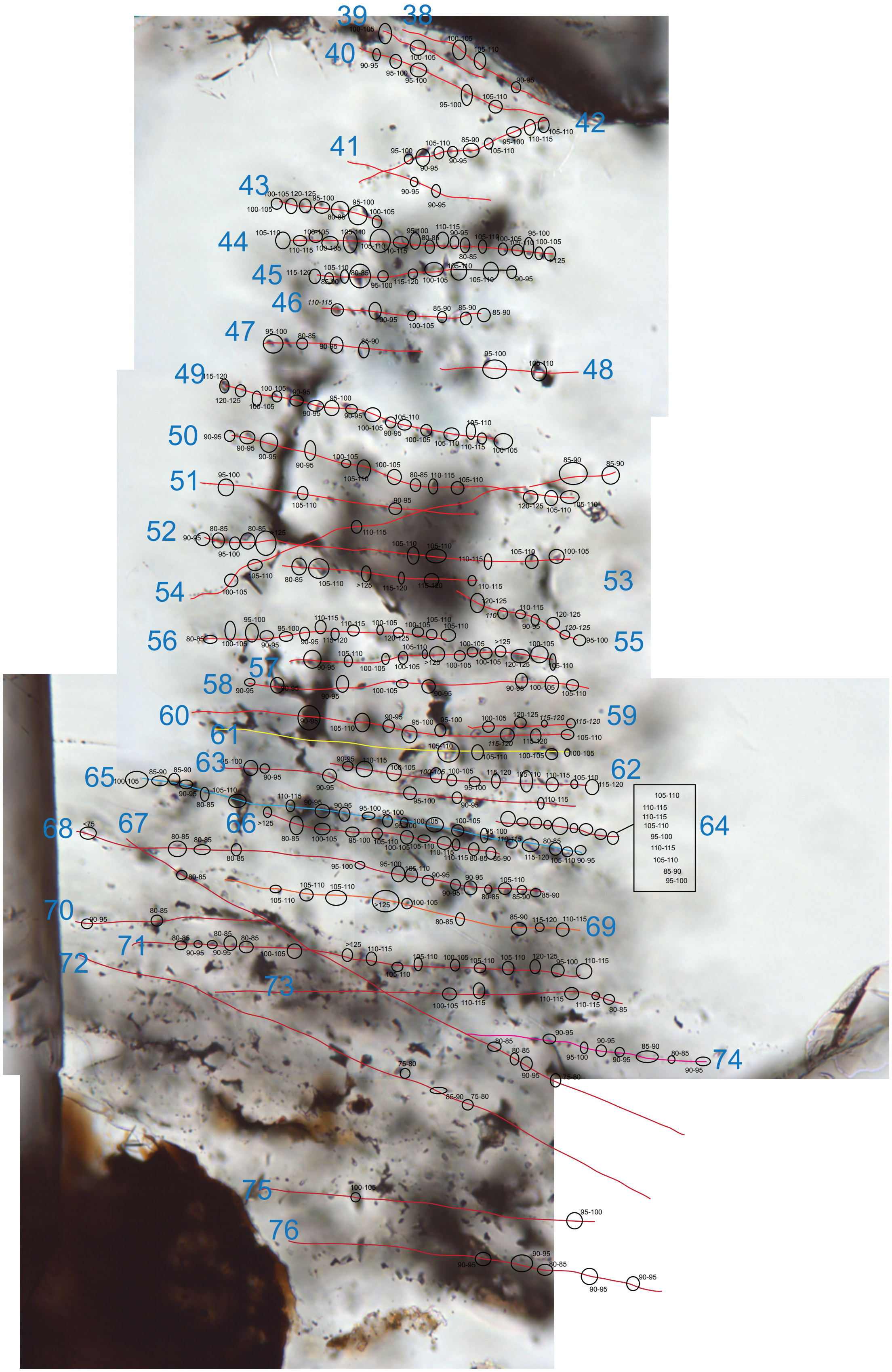

39
38
40
42
41
43
44
45
46
47
48
49
50
51
52
53
54
55
56
57
58
59
60
61
62
63
64
65
66
67
68
69
70
71
72
73
74
75
76
105-110
110-115
110-115
105-110
95-100
110-115
105-110
85-90
95-100

Macrofracture 1			10 degrees added/subtracted if outside measured range						freezing		
	top								min	max	average
FIA	1	2	3	4	5	6	7	8	8	8	8
Average	97.5	87.5	84.16667	90.27778	90.22727	92.5	91.5	106.6667			
Stdev	8.164966	0	5.773503	4.409586	3.437758	5.773503	4.1833	2.041241			
Min	87.5	87.5	77.5	87.5	82.5	87.5	87.5	102.5			
Max	107.5	87.5	87.5	97.5	92.5	102.5	97.5	107.5			
Range	20	0	10	10	10	15	10	5	0	0	0
FI Th (°C)											
	107.5	87.5	77.5	87.5	87.5	97.5	92.5	102.5	-25	-24	
	97.5	87.5	87.5	87.5	87.5	87.5	97.5	107.5	-25.6	-25.3	
	97.5		87.5	87.5	87.5	92.5	87.5	107.5			
	87.5			92.5	92.5	92.5	87.5	107.5			
				87.5	92.5	87.5	92.5	107.5			
				97.5	92.5	102.5		107.5	-25	-24.2	
				87.5	92.5	87.5					
				97.5	82.5						
				87.5	92.5						
					92.5						
					92.5						

			freezing								
			min	max	average						
9	10	11	11	11	11	11a	12	13	14	15	16
92.04545	95.625	90.14706				102.5	96.875	95.83333	104.375	90	92.5
5.754727	5.303301	5.33785				0	4.955156	9.309493	2.587746	11.90238	2.886751
82.5	92.5	82.5				102.5	92.5	87.5	102.5	82.5	87.5
107.5	107.5	102.5				102.5	107.5	107.5	107.5	107.5	97.5
25	15	20	0	0	0	0	15	20	5	25	10
92.5	92.5	87.5				102.5	107.5	87.5	102.5	82.5	92.5
92.5	97.5	92.5				102.5	92.5	92.5	102.5	107.5	97.5
97.5	92.5	87.5				102.5	92.5	87.5	102.5	82.5	92.5
92.5	92.5	97.5				102.5	92.5	92.5	102.5	87.5	87.5
92.5	92.5	92.5	-19.8	-18.8		102.5	97.5	107.5	102.5		92.5
92.5	92.5	82.5				102.5	97.5	107.5	107.5		92.5
102.5	107.5	87.5					97.5		107.5		92.5
92.5	97.5	97.5					97.5		107.5		
107.5		87.5	-22	-21							
92.5		87.5									
92.5		82.5									
92.5		92.5									
92.5		92.5									
92.5		102.5	-7	-6							
87.5		87.5									
92.5		87.5									
82.5		87.5									
87.5											
82.5											
82.5											
92.5											
92.5											

					freezing				freezing		
					min	max	average		min	max	average
17	18	19	20	21	21	21	21	22			
91.59091	91.07143	102.6471	85.83333	97.05				97.33696			
5.838742	7.480132	7.92821	5.773503	7.161483				6.46362			
82.5	87.5	87.5	82.5	82.5				87.5			
102.5	107.5	117.5	92.5	110				112.5			
20	20	30	10	27.5				25			
92.5	87.5	97.5	82.5	92.5				87.5			
82.5	87.5	102.5	92.5	102.5				105	-23	-22.9	
82.5	87.5	102.5	82.5	106	-18.6	-18.1		107.5			
87.5	87.5	92.5		87.5				92.5	-17.7	-17.2	
92.5	92.5	92.5		92.5				97.5			
92.5	107.5	107.5		92.5				97.5			
102.5	87.5	102.5		110				92.5	-16	-15	
92.5		97.5		92.5				97.5			
92.5		87.5		107.5				97.5			
92.5		97.5		107.5	-24	-23.5		97.5			
97.5		92.5		97.5				102.5	-20.6	-19.6	
		102.5		102.5				97.5	-17.5	-16.5	
		97.5		97.5	-23.8	-23		97.5			
		107.5		92.5				92.5			
		107.5		97.5				97.5	-23.4	-22.7	
		102.5		92.5				92.5	-24	-23	
		107.5		97.5				107.5			
		102.5		82.5				92.5			
		112.5		92.5				97.5			
		107.5		97.5				97.5			
		92.5						92.5			
		87.5						97.5			
		107.5						92.5			
		112.5						92.5			
		112.5						92.5			
		117.5						92.5			
		107.5						92.5			
		107.5						102.5			
		107.5						112.5			
		107.5						107.5			
		92.5						87.5			
		117.5						92.5			
		102.5						107.5			
		97.5						92.5			
								107.5			
								97.5			
								107.5			
								92.5			
								92.5			
								102.5			
								92.5			
								92.5			
								92.5			
								92.5			
								92.5			
								112.5			

	freezing										
	min	max	average								
23				24	25	26	27	28	29	30	31
94.77273				96.25	93.5	107.5	95.5	95.83333	96.91176	96.5	98.83333
7.537784				6.291529	9.617692	0	6.708204	2.886751	7.882408	6.146363	6.113996
82.5				87.5	82.5	107.5	92.5	92.5	82.5	92.5	92.5
107.5				102.5	107.5	107.5	107.5	97.5	107.5	112.5	107.5
25				15	25	0	15	5	25	20	15
92.5	-23.3	-22.6		87.5	97.5	107.5	92.5	97.5	87.5	97.5	92.5
92.5				97.5	107.5	107.5	92.5	92.5	82.5	97.5	92.5
107.5				97.5	87.5		92.5	97.5	87.5	92.5	92.5
97.5	-23.3	-22.3		102.5	82.5		92.5		87.5	92.5	97.5
97.5					92.5		107.5		92.5	97.5	92.5
102.5									97.5	92.5	92.5
87.5	-21.5	-21.1							97.5	112.5	102.5
87.5									97.5	97.5	107.5
102.5									107.5	92.5	97.5
92.5									107.5	92.5	102.5
82.5									107.5		102.5
									102.5		107.5
									102.5		92.5
									102.5		107.5
									102.5		102.5
									92.5		
									92.5		

						bottom					
32	33	34	35	36	37	38	39	40	41	42	43
102.5	96.94444	97.5	94.16667	105.7353	104.1667	100.8333	102.5	98.5	92.5	100.2778	101.0714
5	8.45741	10	2.886751	6.833094	5.920935	7.637626	0	5.477226	0	8.700255	11.80194
97.5	87.5	87.5	92.5	92.5	92.5	92.5	102.5	92.5	92.5	87.5	82.5
107.5	112.5	107.5	97.5	117.5	112.5	107.5	102.5	107.5	92.5	112.5	122.5
10	25	20	5	25	20	15	0	15	0	25	40
97.5	92.5	87.5	97.5	107.5	112.5	102.5	102.5	92.5	92.5	97.5	102.5
97.5	92.5	107.5	92.5	102.5	92.5	107.5	102.5	97.5	92.5	92.5	102.5
107.5	92.5	97.5	92.5	102.5	102.5	92.5		97.5		107.5	122.5
102.5	92.5			107.5	102.5			97.5		92.5	97.5
107.5	92.5			97.5	102.5			107.5		87.5	82.5
	107.5			112.5	102.5					107.5	97.5
	87.5			102.5	102.5					97.5	102.5
	102.5			97.5	102.5					112.5	
	112.5			102.5	107.5					107.5	
				107.5	107.5						
				92.5	102.5						
				112.5	102.5						
				107.5	107.5						
				107.5	107.5						
				117.5	97.5						
				117.5	102.5						
				102.5	112.5						
					102.5						
					107.5						
					107.5						
					92.5						
					112.5						
					92.5						
					107.5						
					92.5						
					112.5						
					107.5						
					107.5						
					107.5						
					107.5						

44	45	46	47	48	49	50	51	52	53	54	55
104.0278	102	95	90	102.5	103.4375	101.7308	99.16667	102.75	112.0833	99.5	111.4286
11.8551	11.89071	10.36822	6.454972	7.071068	8.984941	10.77152	7.637626	15.47624	17.20586	11.51086	12.4044
82.5	82.5	87.5	82.5	97.5	92.5	82.5	92.5	82.5	82.5	87.5	92.5
135	117.5	112.5	97.5	107.5	122.5	122.5	107.5	135	135	112.5	122.5
52.5	35	25	15	10	30	40	15	52.5	52.5	25	30
107.5	117.5	112.5	97.5	97.5	117.5	92.5	97.5	92.5	82.5	102.5	122.5
112.5	87.5	92.5	82.5	107.5	122.5	92.5	107.5	82.5	107.5	107.5	110
102.5	107.5	102.5	92.5		102.5	92.5	92.5	97.5	135	112.5	112.5
102.5	82.5	87.5	87.5		102.5	92.5		82.5	117.5	87.5	92.5
107.5	97.5	87.5			92.5	102.5		135	117.5	87.5	122.5
107.5	117.5	87.5			92.5	107.5		107.5	112.5		122.5
112.5	102.5				97.5	102.5		107.5			97.5
97.5	107.5				92.5	82.5		112.5			
82.5	107.5				102.5	112.5		107.5			
112.5	92.5				92.5	107.5		102.5			
92.5					107.5	122.5					
82.5					102.5	107.5					
107.5					107.5	107.5					
102.5					107.5						
107.5					112.5						
97.5					102.5						
102.5											
135											

56	57	58	59	60	61	62	63	64	65	66	67
103.5714	109.4231	96.875	115	103.75	105	106.5909	97.5	104.7222	98.5	102.7273	83.5
10.77365	13.11622	6.232117	8.660254	10.26436	2.886751	8.00568	7.745967	8.700255	9.814061	15.34823	5.477226
82.5	92.5	92.5	102.5	92.5	102.5	92.5	92.5	87.5	82.5	82.5	77.5
122.5	135	107.5	122.5	117.5	107.5	117.5	112.5	112.5	117.5	135	92.5
40	42.5	15	20	25	5	25	20	25	35	52.5	15
82.5	92.5	92.5	102.5	92.5	107.5	92.5	97.5	107.5	102.5	135	82.5
102.5	107.5	92.5	122.5	107.5	107.5	112.5	92.5	112.5	87.5	82.5	82.5
97.5	102.5	92.5	117.5	92.5	102.5	102.5	92.5	112.5	87.5	102.5	82.5
92.5	102.5	102.5	117.5	97.5	102.5	102.5	97.5	107.5	92.5	97.5	92.5
97.5	107.5	92.5		97.5		102.5	92.5	97.5	82.5	107.5	77.5
92.5	135	92.5		117.5		97.5	112.5	112.5	107.5	102.5	
112.5	102.5	102.5		117.5		117.5		107.5	112.5	107.5	
117.5	102.5	107.5		107.5		107.5		87.5	92.5	112.5	
112.5	102.5					112.5		97.5	92.5	112.5	
102.5	135					107.5			97.5	82.5	
122.5	122.5					117.5			97.5	87.5	
102.5	102.5								97.5		
107.5	107.5								102.5		
107.5									102.5		
									97.5		
									112.5		
									117.5		
									82.5		
									107.5		
									97.5		

									very top	
68	69	70	71	72	73	74	75	76	77	
89.82143	106.6667	87.5	102.9688	80.83333	104.5	91.07143	100	90.5	100.8333	
11.11411	15.51209	7.071068	14.55503	5.773503	13.0384	4.755949	3.535534	4.472136	6.831301	
65	82.5	82.5	82.5	77.5	82.5	82.5	97.5	82.5	92.5	
107.5	135	92.5	135	87.5	112.5	97.5	102.5	92.5	112.5	Average range
42.5	52.5	10	52.5	10	30	15	5	10	20	19.55357
65	107.5	92.5	82.5	77.5	102.5	92.5	102.5	92.5	102.5	
82.5	107.5	82.5	92.5	87.5	112.5	97.5	97.5	92.5	112.5	
82.5	107.5		92.5	77.5	112.5	92.5		82.5	97.5	
82.5	135		82.5		112.5	92.5		92.5	97.5	
97.5	102.5		82.5		82.5	87.5		92.5	92.5	
97.5	82.5		102.5			82.5			102.5	
107.5	87.5		135			92.5				
92.5	117.5		112.5							
92.5	112.5		107.5							
92.5			107.5							
82.5			102.5							
107.5			107.5							
87.5			107.5							
87.5			122.5							
			97.5							
			112.5							

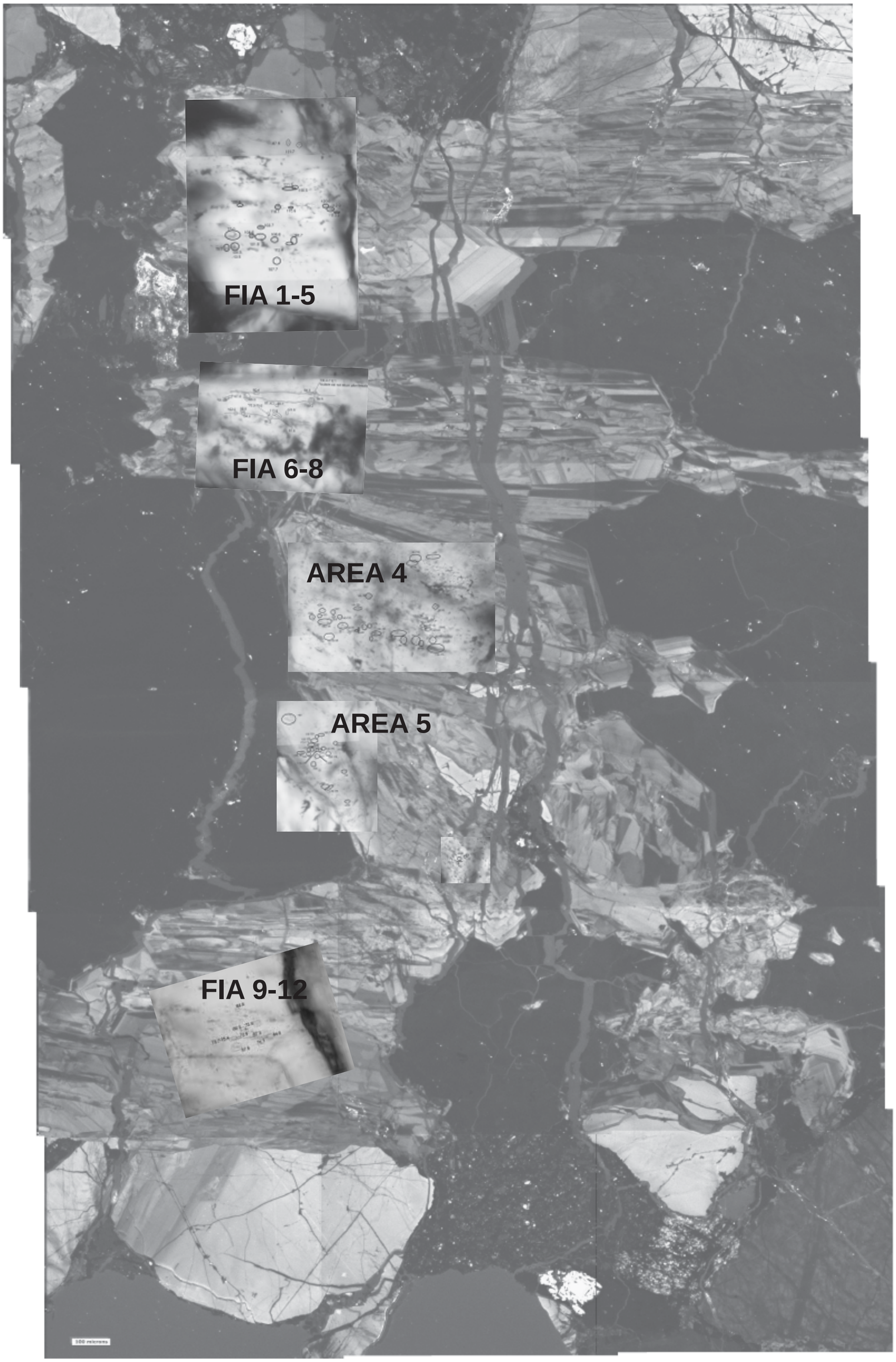

Macrofracture 2 (D1)

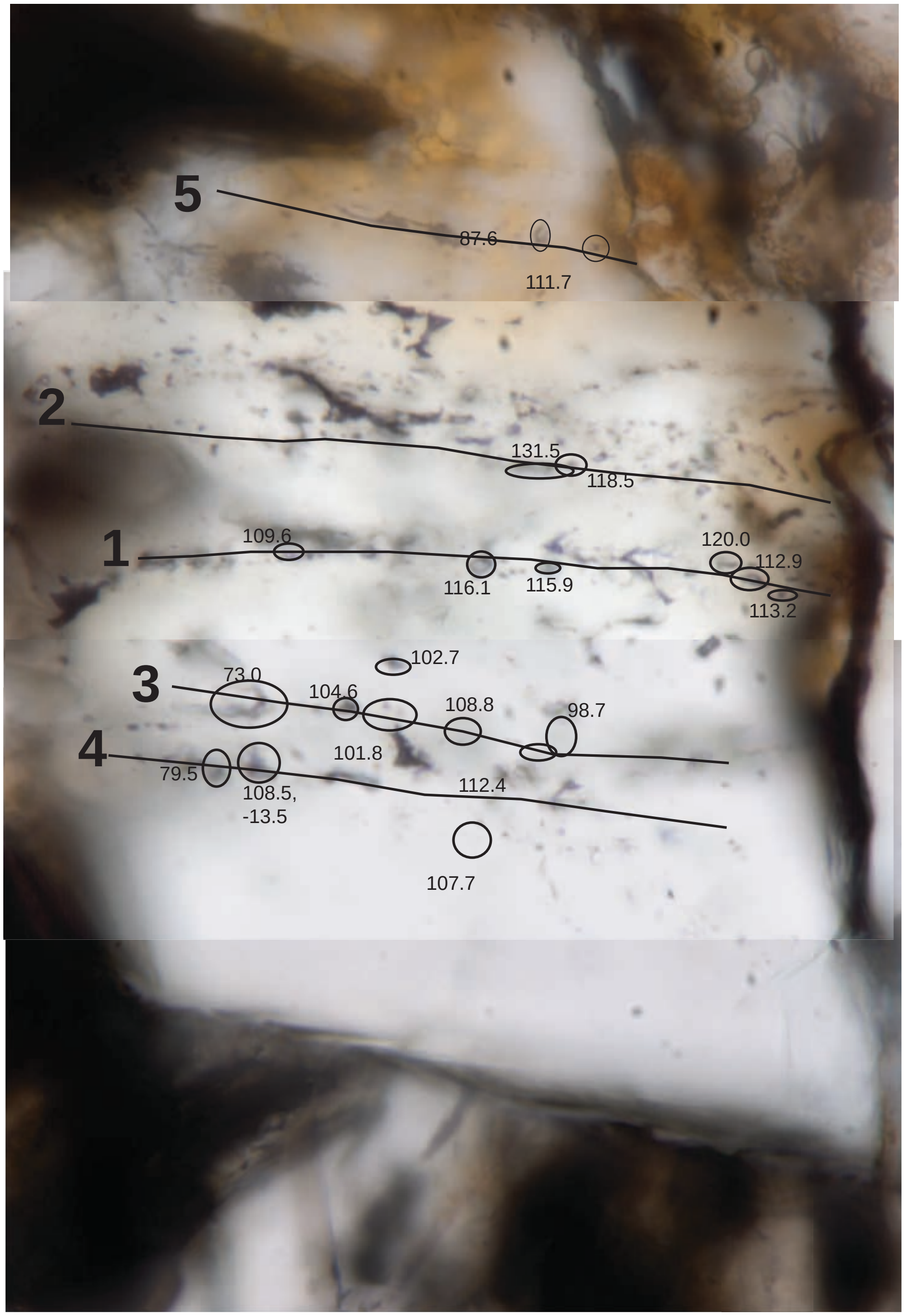
5
87.6
111.7
2
131.5
118.5
1
109.6
120.0
112.9
116.1
115.9
113.2
102.7
3
73.0
104.6
108.8
98.7
101.8
4
79.5
108.5,
-13.5
112.4
107.7

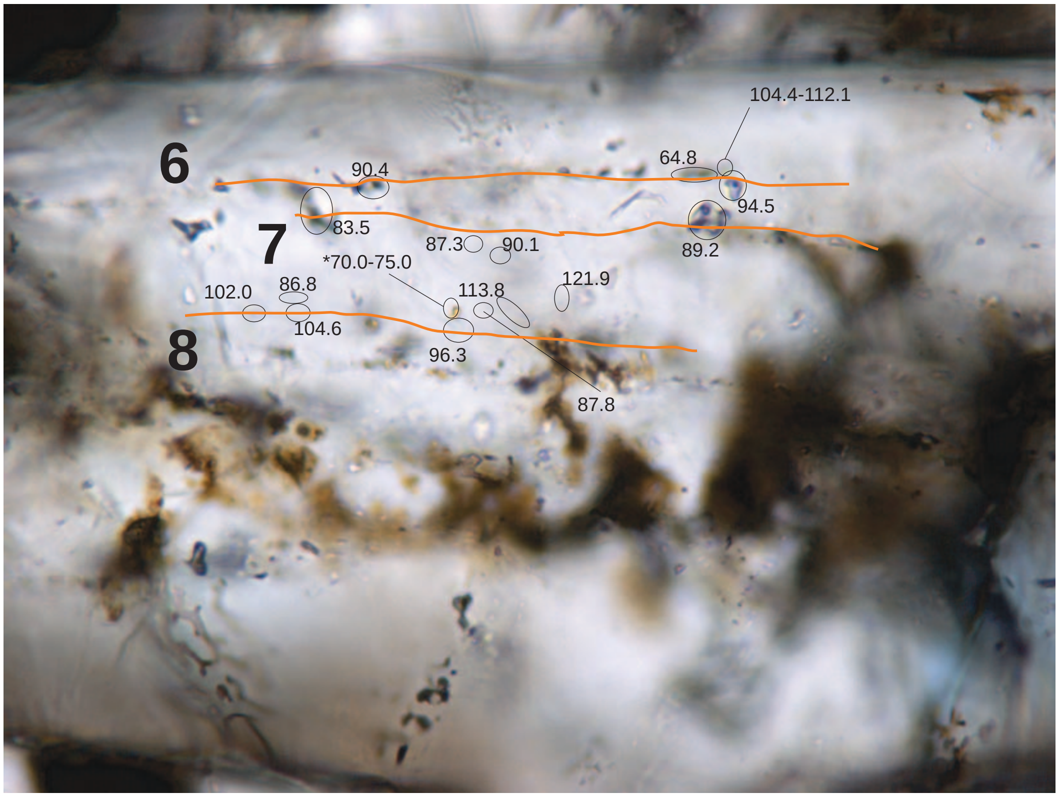
104.4-112.1
6
90.4
64.8
94.5
83.5
7
89.2
87.3
90.1
*70.0-75.0
121.9
102.0
86.8
113.8
104.6
8
96.3
87.8

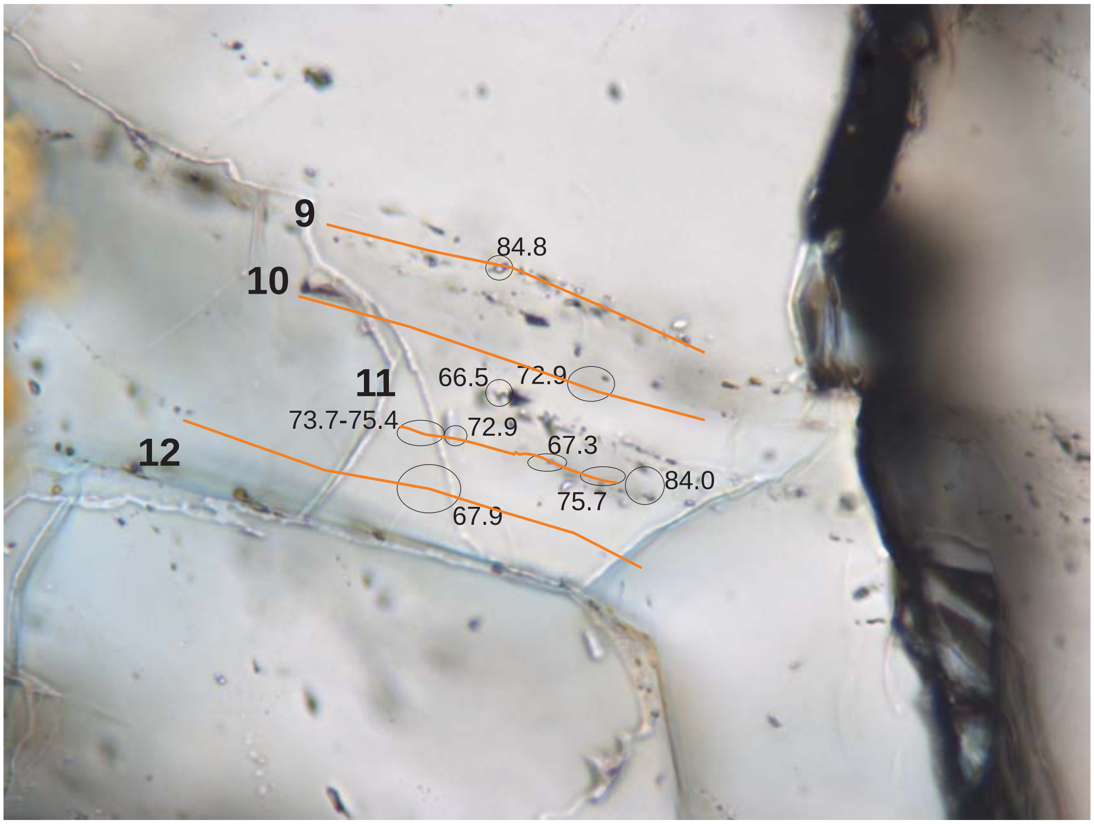
9
84.8
10
66.5
72.9
11
73.7-75.4
72.9
67.3
12
84.0
75.7
67.9

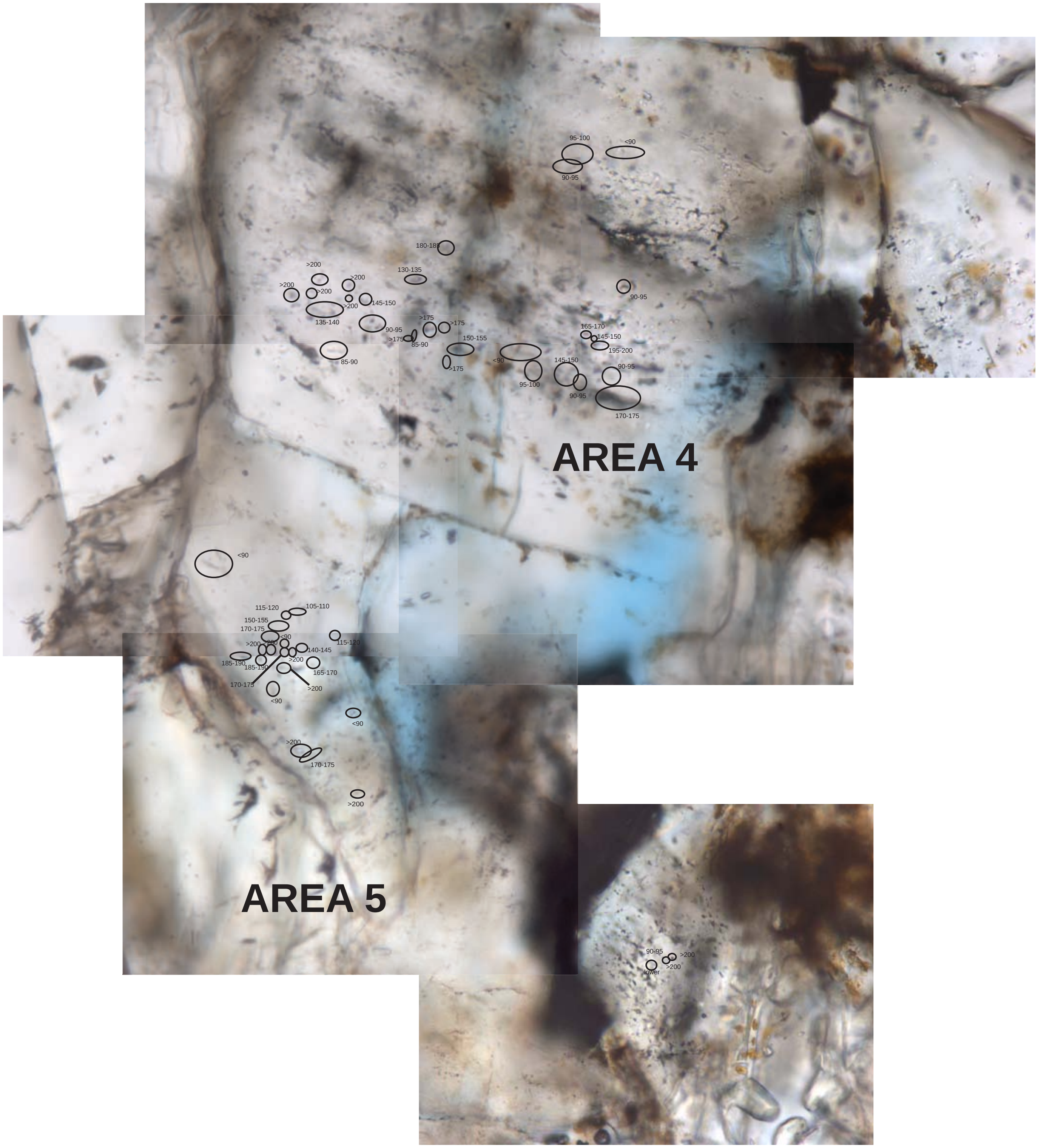
95-100
<90
90-95
180-185
130-135
>200
>200
>200
>200
>200
145-150
135-140
90-95
>175
>175
>175
85-90
85-90
150-155
>175
<90
95-100
90-95
165-170
145-150
195-200
145-150
90-95
90-95
170-175
AREA 4
<90
115-120
105-110
150-155
170-175
<90
>200
>200
115-120
140-145
185-190
185-190
>200
165-170
170-175
>200
<90
<90
>200
170-175
>200
AREA 5
90-95
>200
>200
lower

thin section	chip	fracture Xloc	aperture	avg temp	fracname
10JH10D	1		2650	#DIV/0!	D1
temp	lowrange	hirange	area	FIA	FIA avg
109.6			1	1	114.6167
112.9			1	1	
113.2			1	1	
116.1			1	1	
115.9			1	1	
120			1	1	
118.5			1	2	124.8
131.1			1	2	
73			1	3	97.275
104.6			1	3	
102.7			1	3	
108.8			1	3	
108.5			1	4	94
79.5			1	4	
111.7			1	5	99.65
87.6			1	5	
98.7			2		105.15
112.4			2		
101.8			2		
107.7			2		
94.5			3	6	77.24
90.4			3	6	
83.5			3	6	
53	51	55	3	6	
		47.6	3	6	
64.8			3	6	
89.2			3	7	88.86667
87.3			3	7	
90.1			3	7	
86.8			3	8	98.2125
102			3	8	
104.6			3	8	
72.5	70	75	3	8	
96.3			3	8	
87.8			3	8	
113.8			3	8	
121.9			3	8	
97.5	95	100	4		148.9167
92.5	90	95	4		51.4056
80	<90		4		
92.5	90	95	4		
182.5	180	185	4		
132.5	130	135	4		
167.5	165	170	4		
147.5	145	150	4		
197.5	195	200	4		
210	>200		4		
210	>200		4		
210	>200		4		

210	>200		4		
210	>200		4		
147.5	145	150	4		
137.5	135	140	4		
87.5	85	90	4		
92.5	90	95	4		
210	>200		4		
210	>200		4		
210	>200		4		
210	>200		4		
87.5	85	90	4		
152.5	150	155	4		
80	<90		4		
97.5	95	100	4		
147.5	145	150	4		
92.5	90	95	4		
92.5	90	95	4		
172.5	170	175	4		
80	<90		5		157.9167
107.5	105	110	5		50.57101
117.5	115	120	5		
152.5	150	155	5		
172.5	170	175	5		
80	<90		5		
117.5	115	120	5		
210	>200		5		
210	>200		5		
142.5	140	145	5		
210	>200		5		
172.5	170	175	5		
187.5	185	190	5		
187.5	185	190	5		
210	>200		5		
167.5	165	170	5		
80	<90		5		
80	<90		5		
210	>200		5		
172.5	170	175	5		
210	>200		5		
92.5	90	95	5		
210	>200		5		
210	>200		5		
84.8			6	9	84.8
72.9			6	10	72.9
66.5			6	11	73.49167
67.3			6	11	
75.7			6	11	
84			6	11	
74.55	73.7	75.4	6	11	
72.9			6	11	
67.9			6	12	67.9

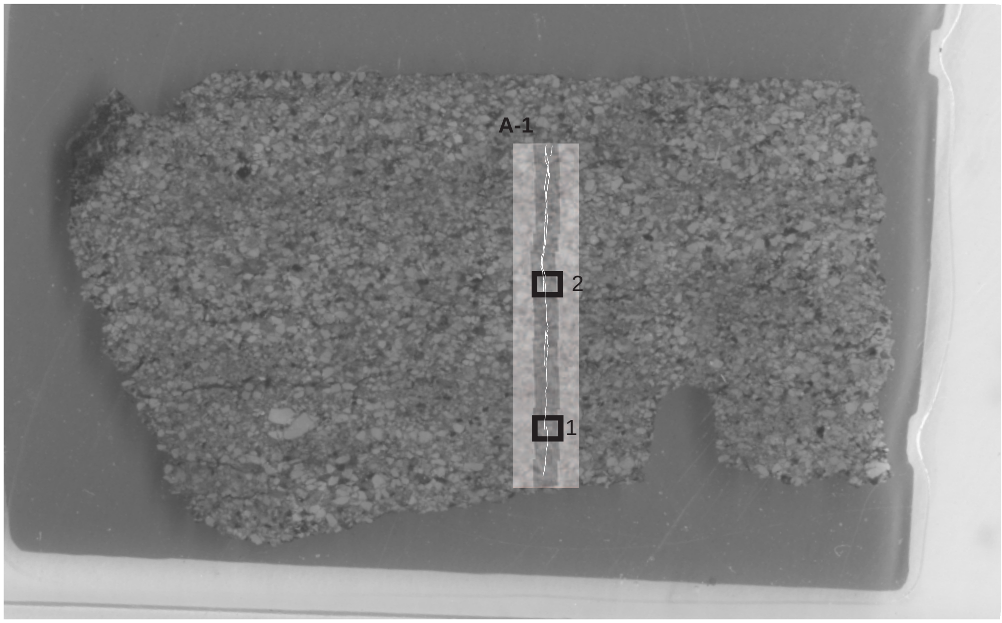

THIN SECTION A

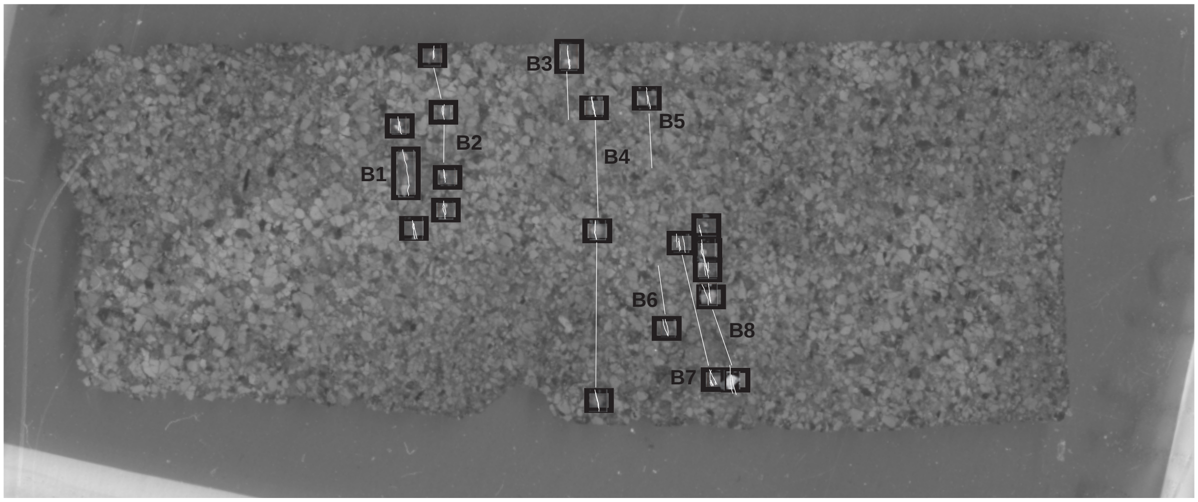

THIN SECTION B

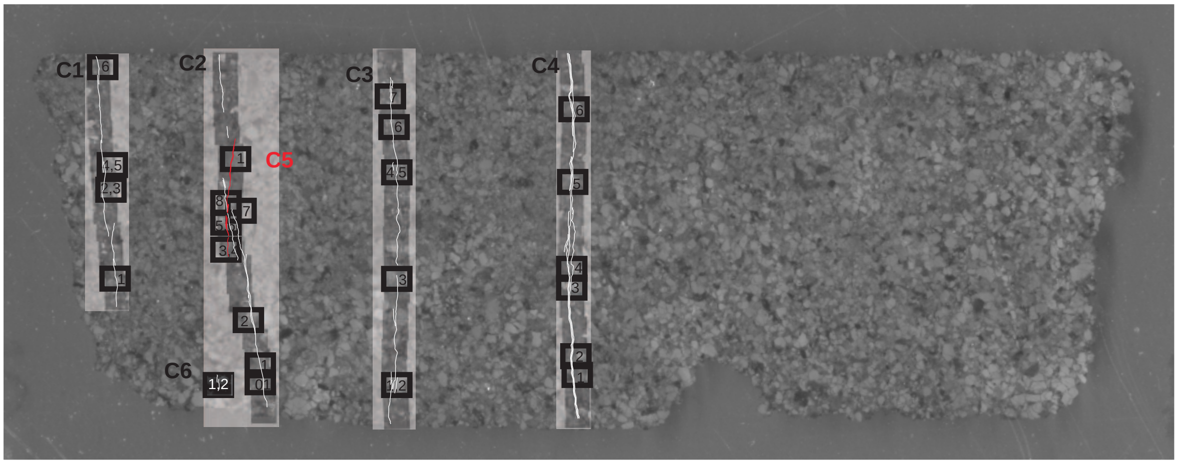

THIN SECTION C

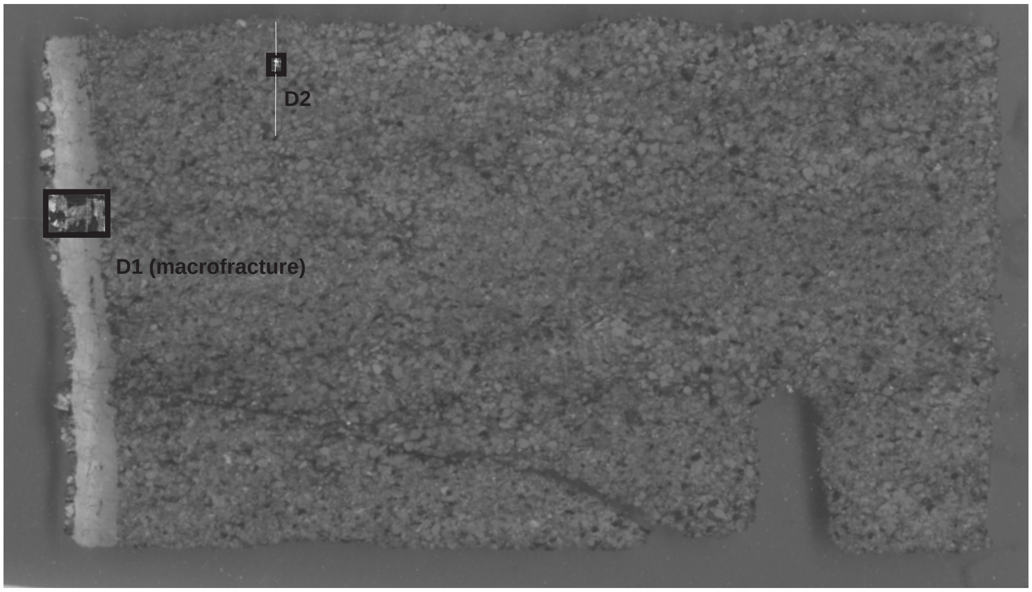

THIN SECTION D

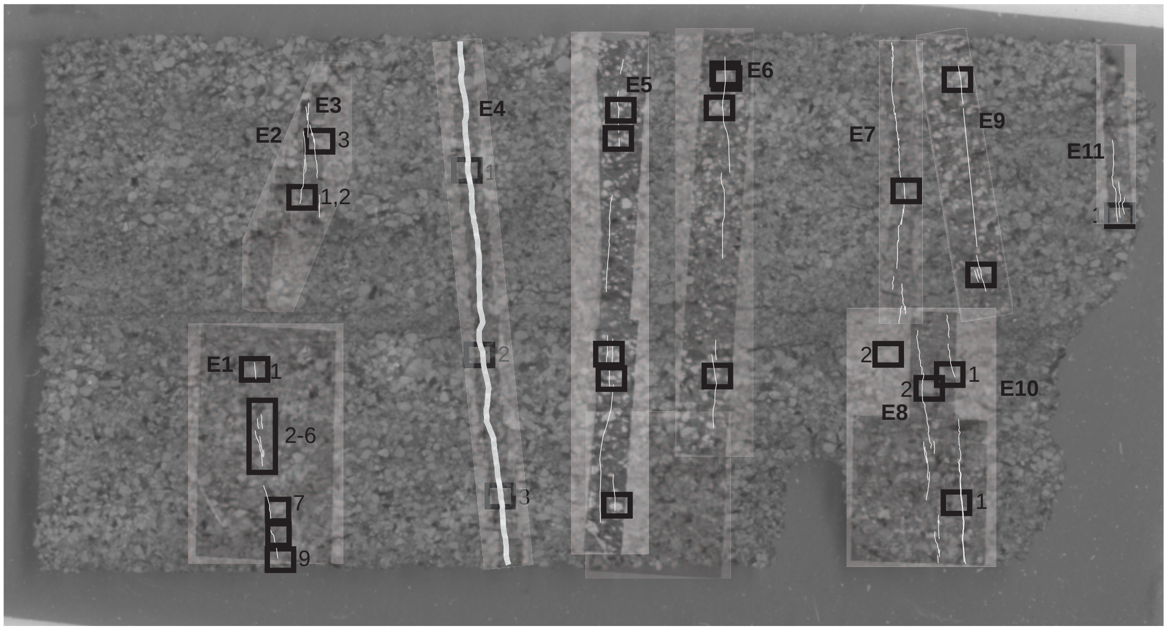

THIN SECTION E

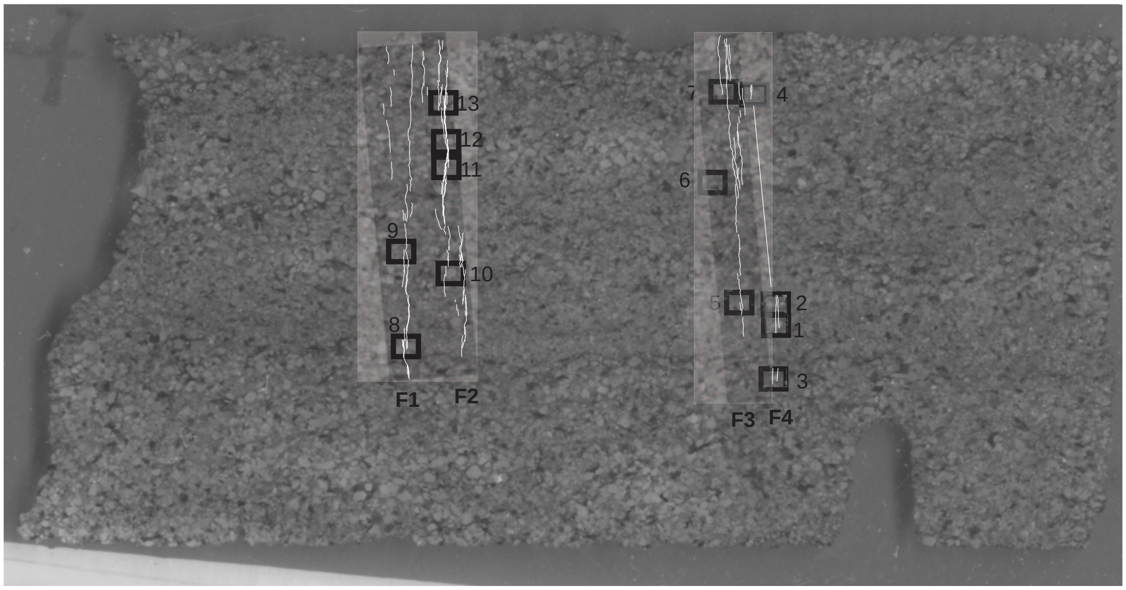

THIN SECTION F

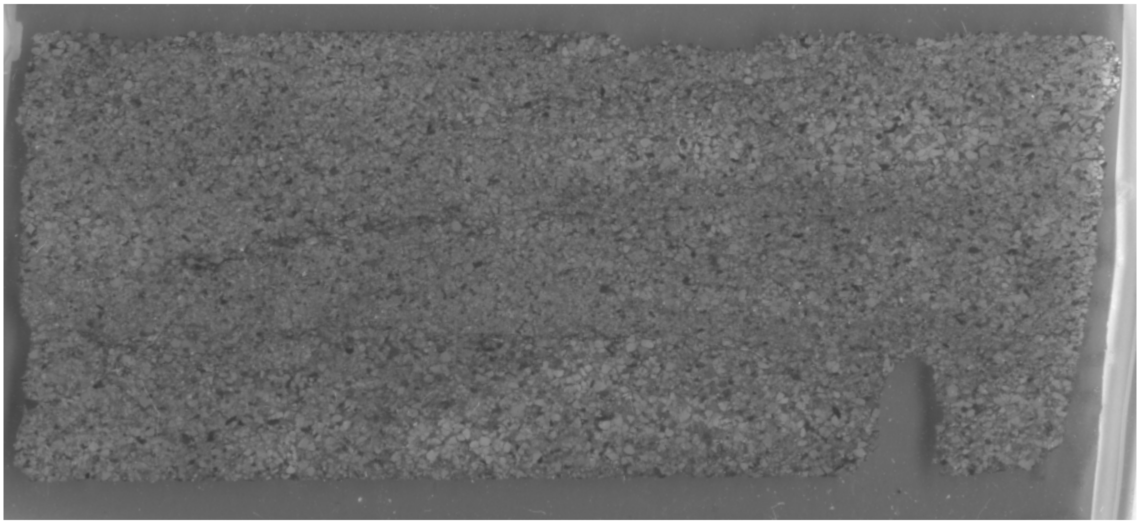

THIN SECTION G

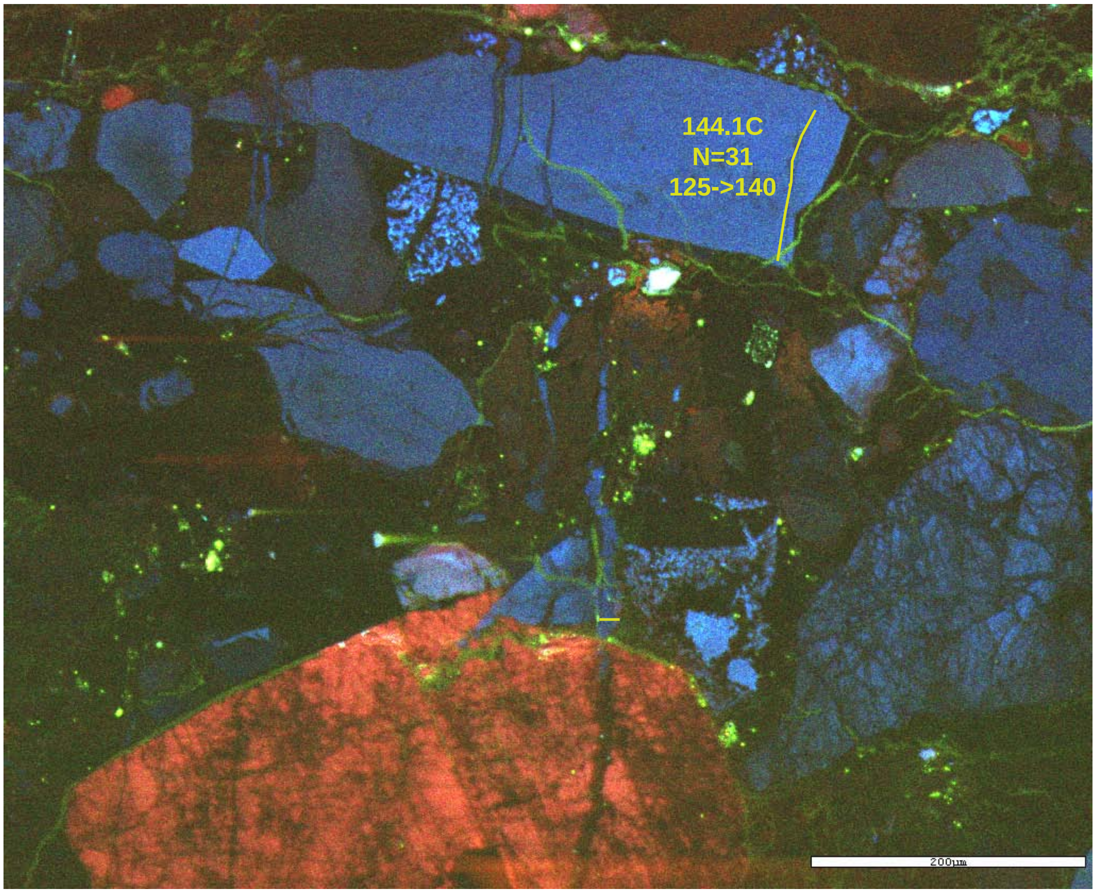

Microfracture A1, FIA 1

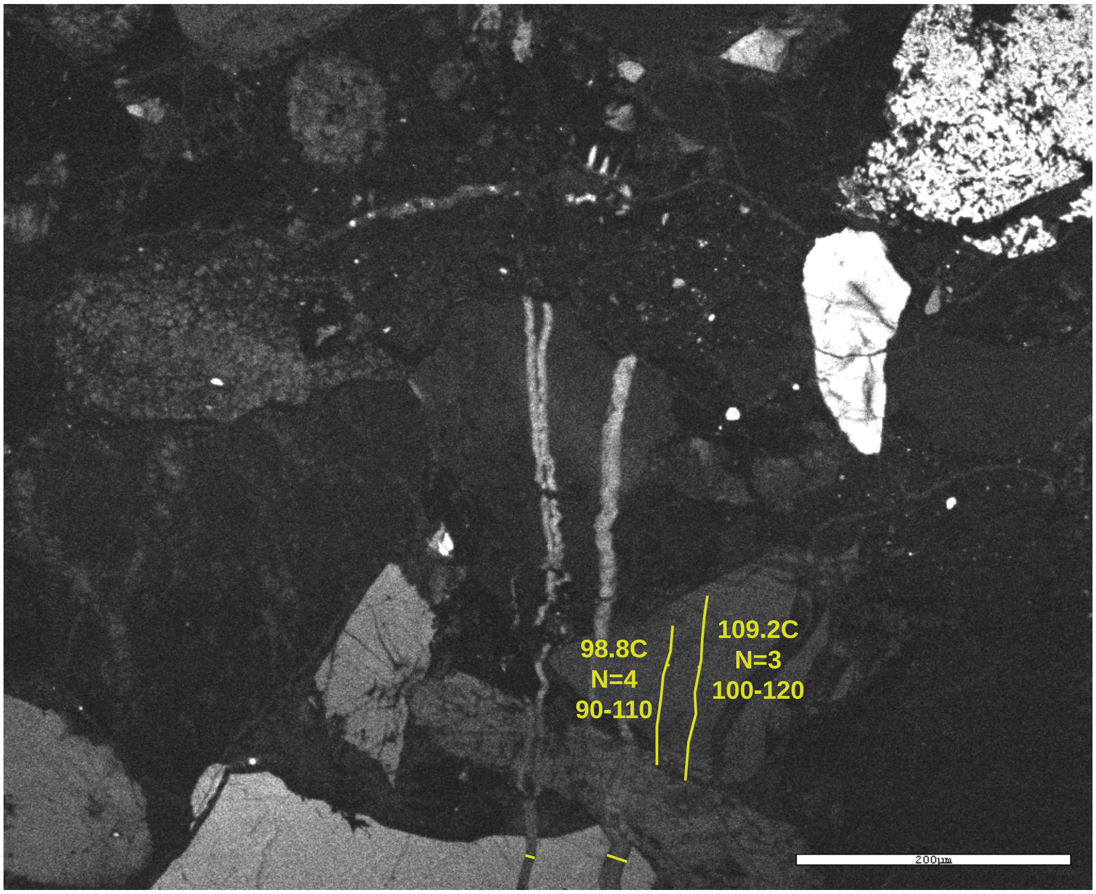

Microfracture A1, FIA 2 and 3

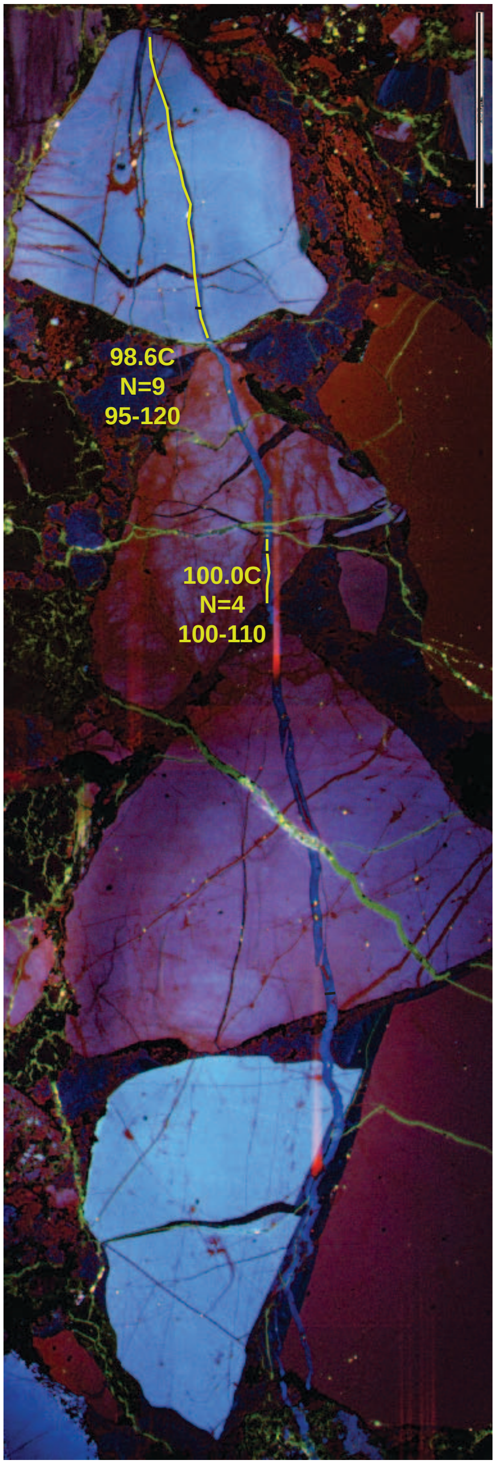

Microfracture B1, FIA 1-2

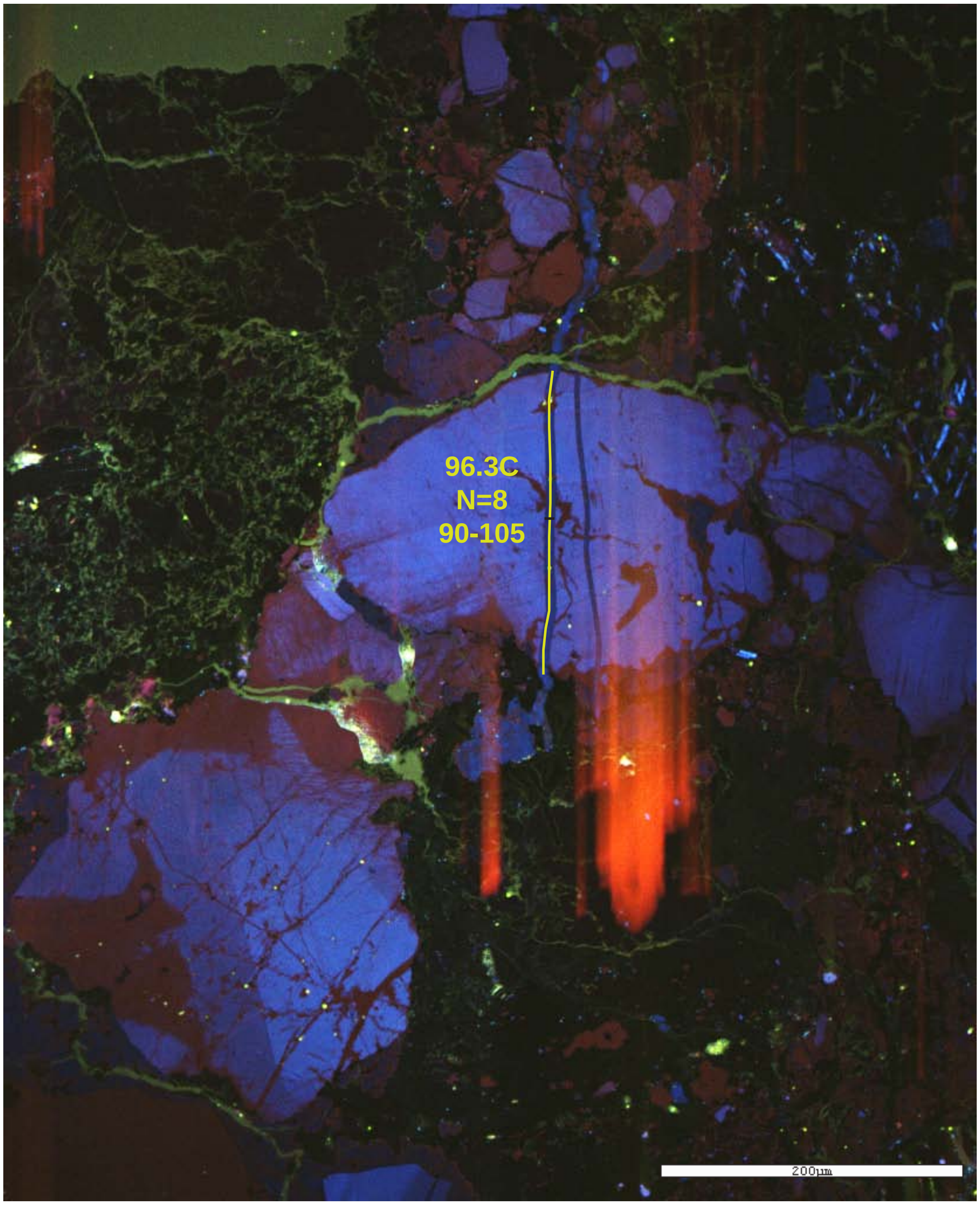

Microfracture B2, FIA 1

Microfracture B2, FIA 2

Microfracture B3, FIA 1

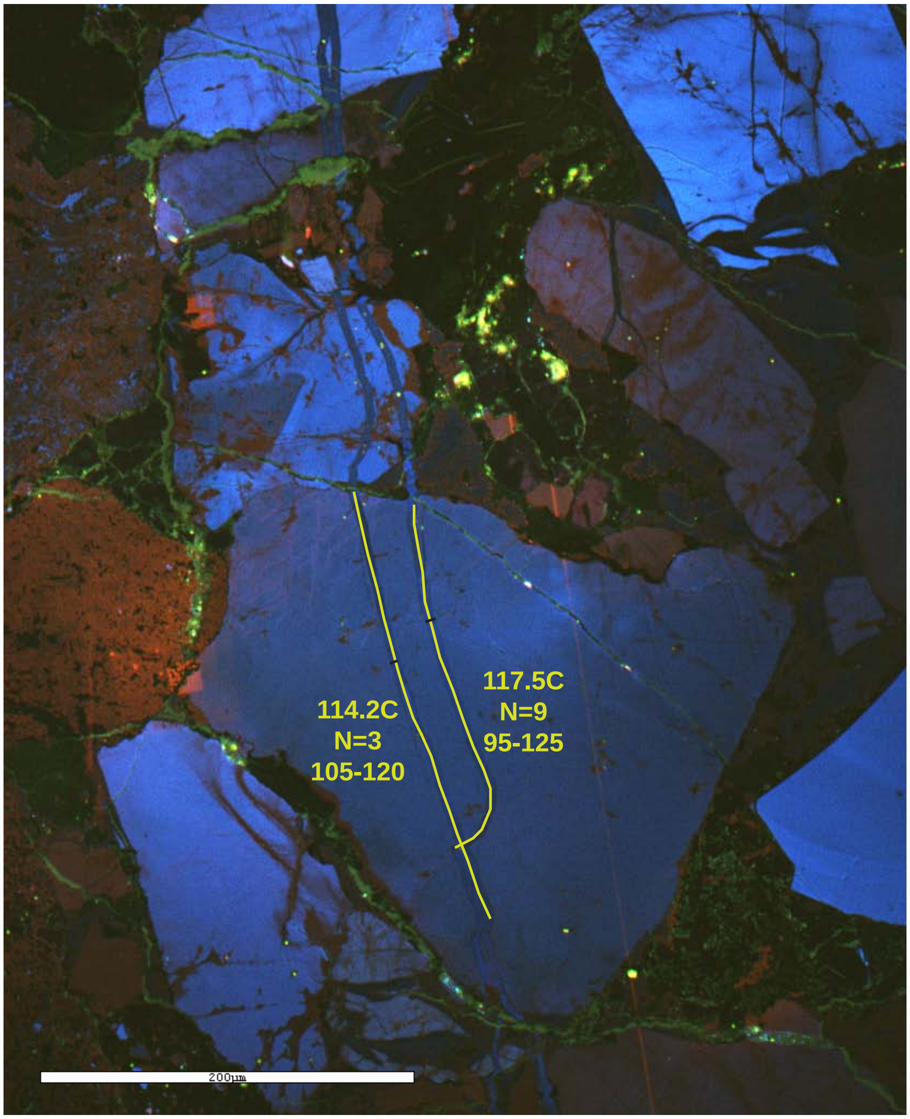

Microfracture B4, FIA 1-2

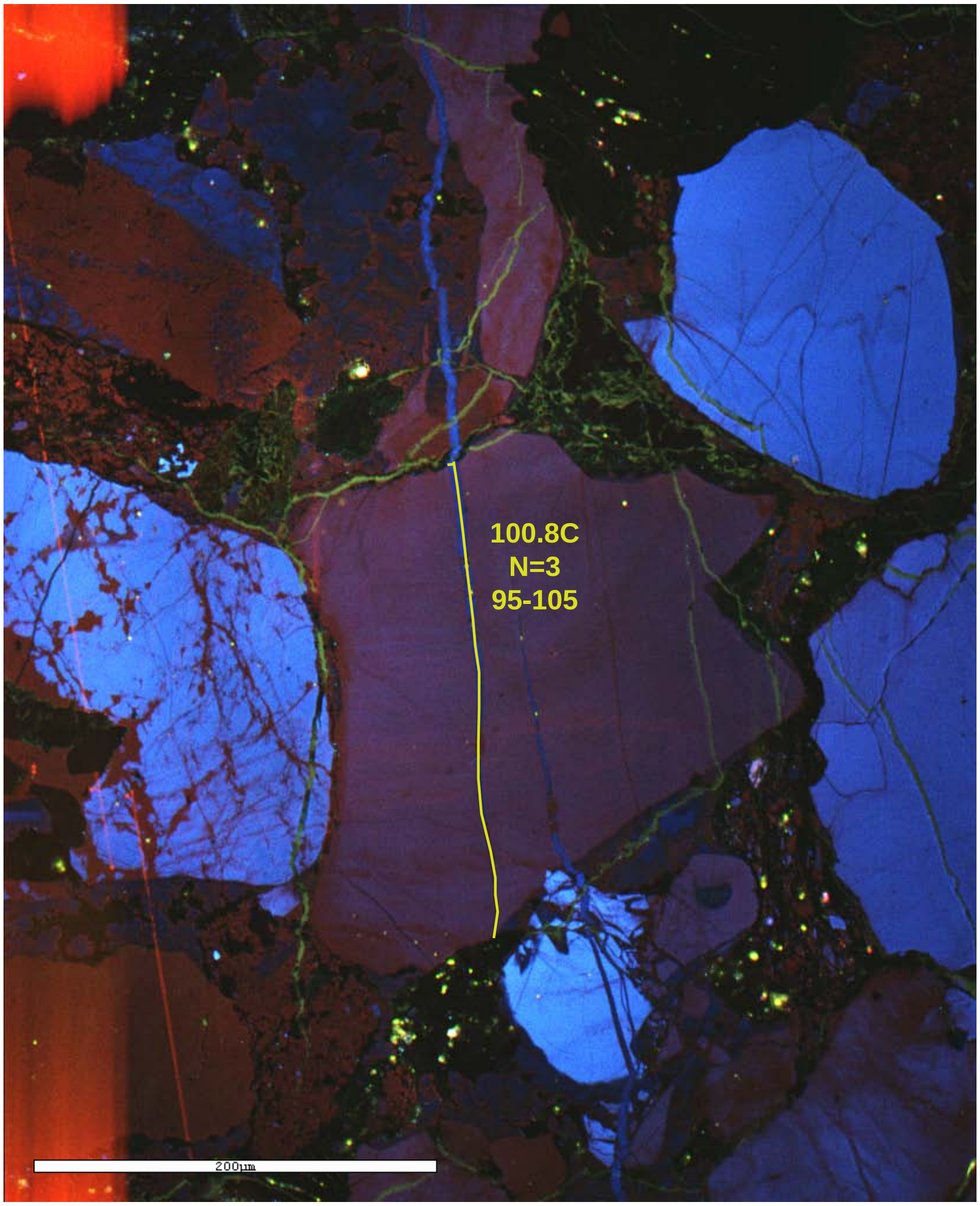

Microfracture B5, FIA 1

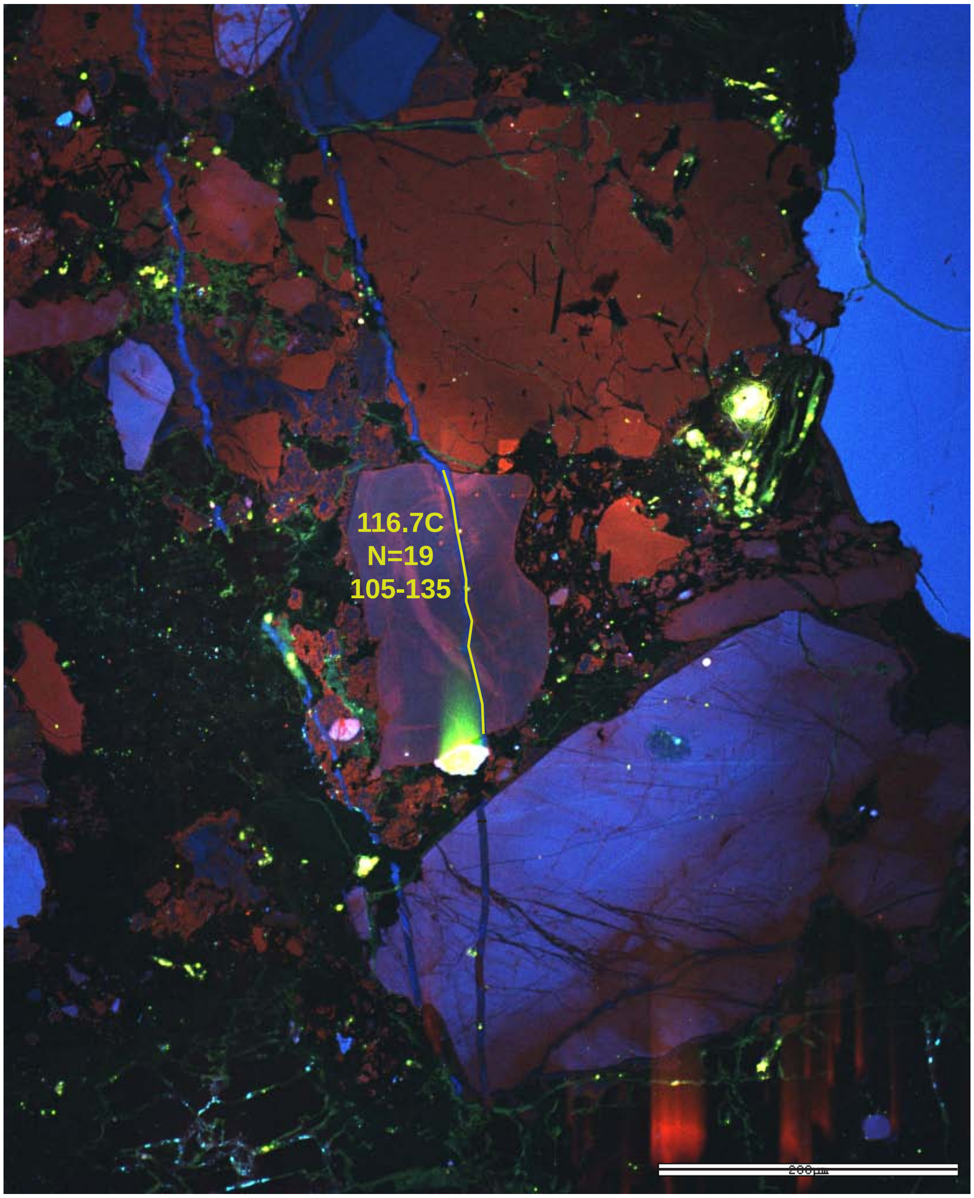

Microfracture B6, FIA 1

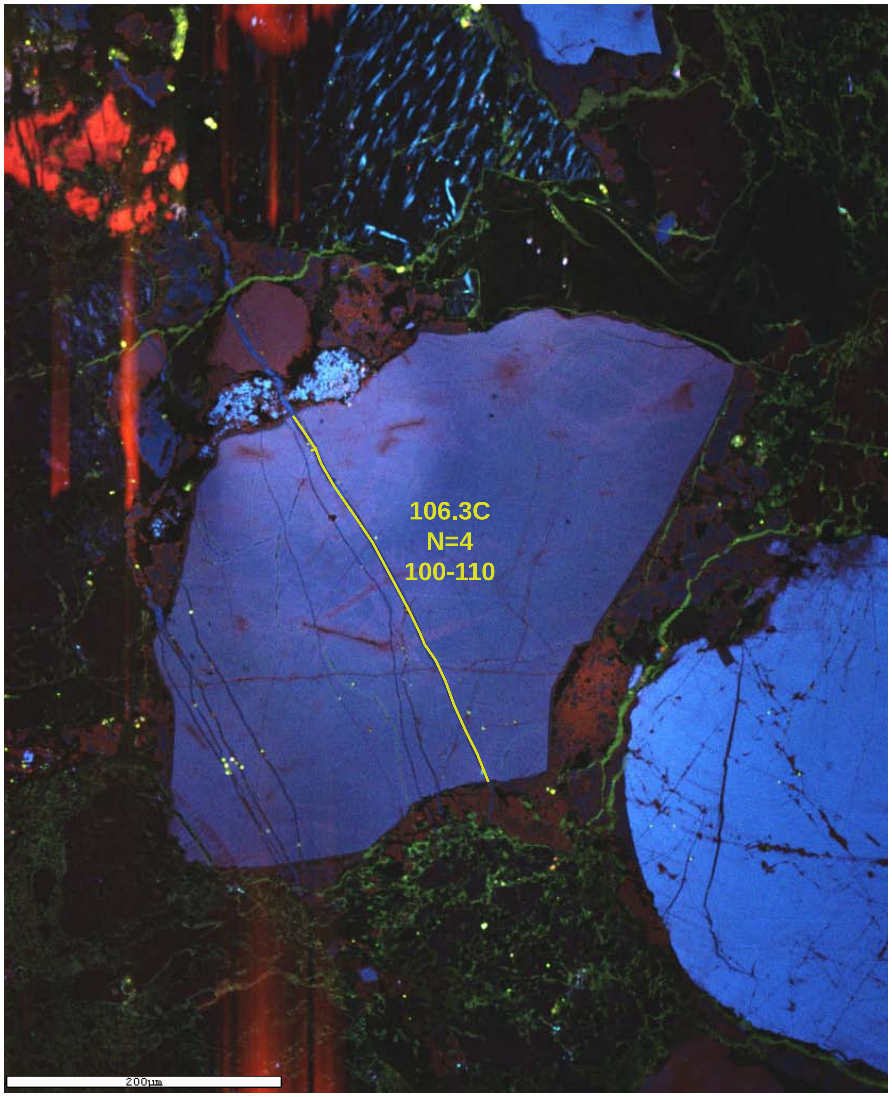

Microfracture B7, FIA 1

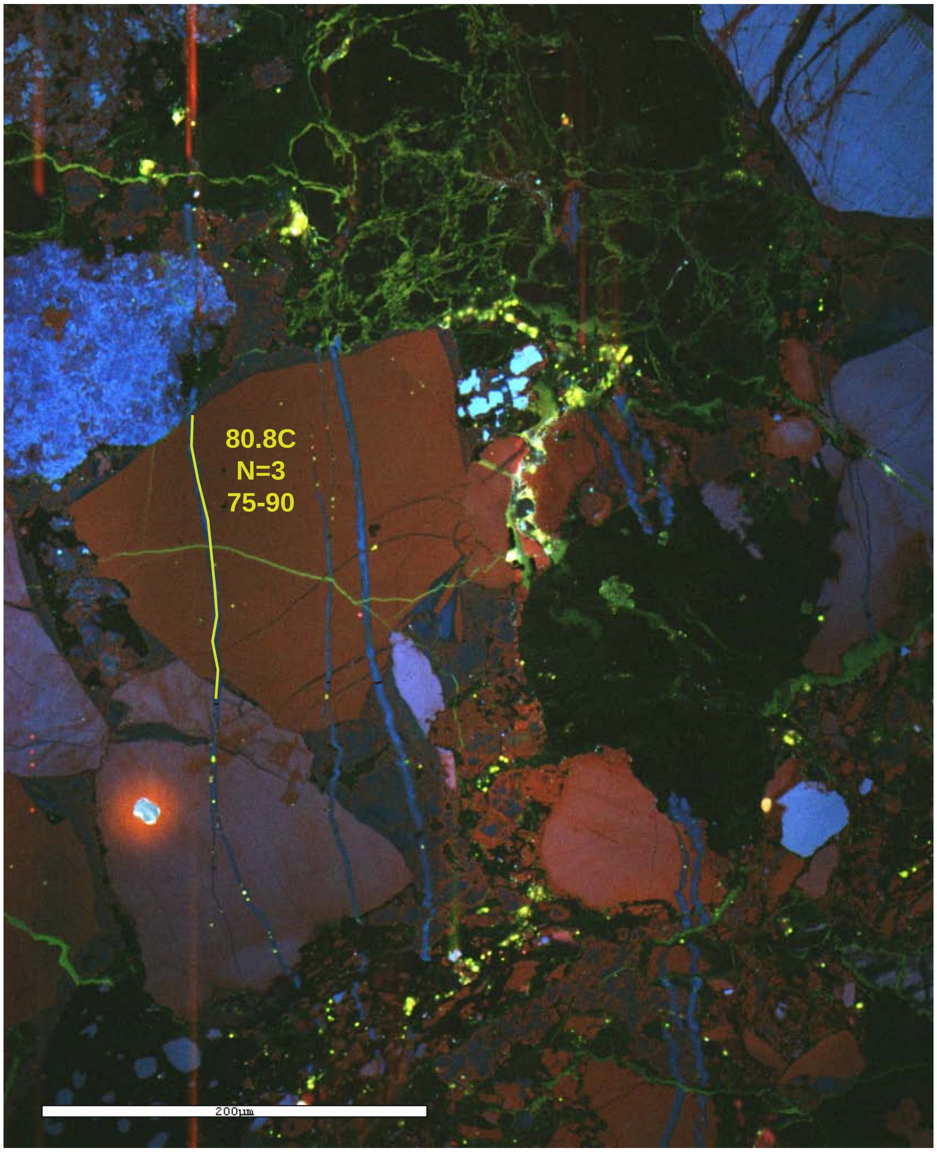

Microfracture B7, FIA 2

Microfracture B8, FIA 4

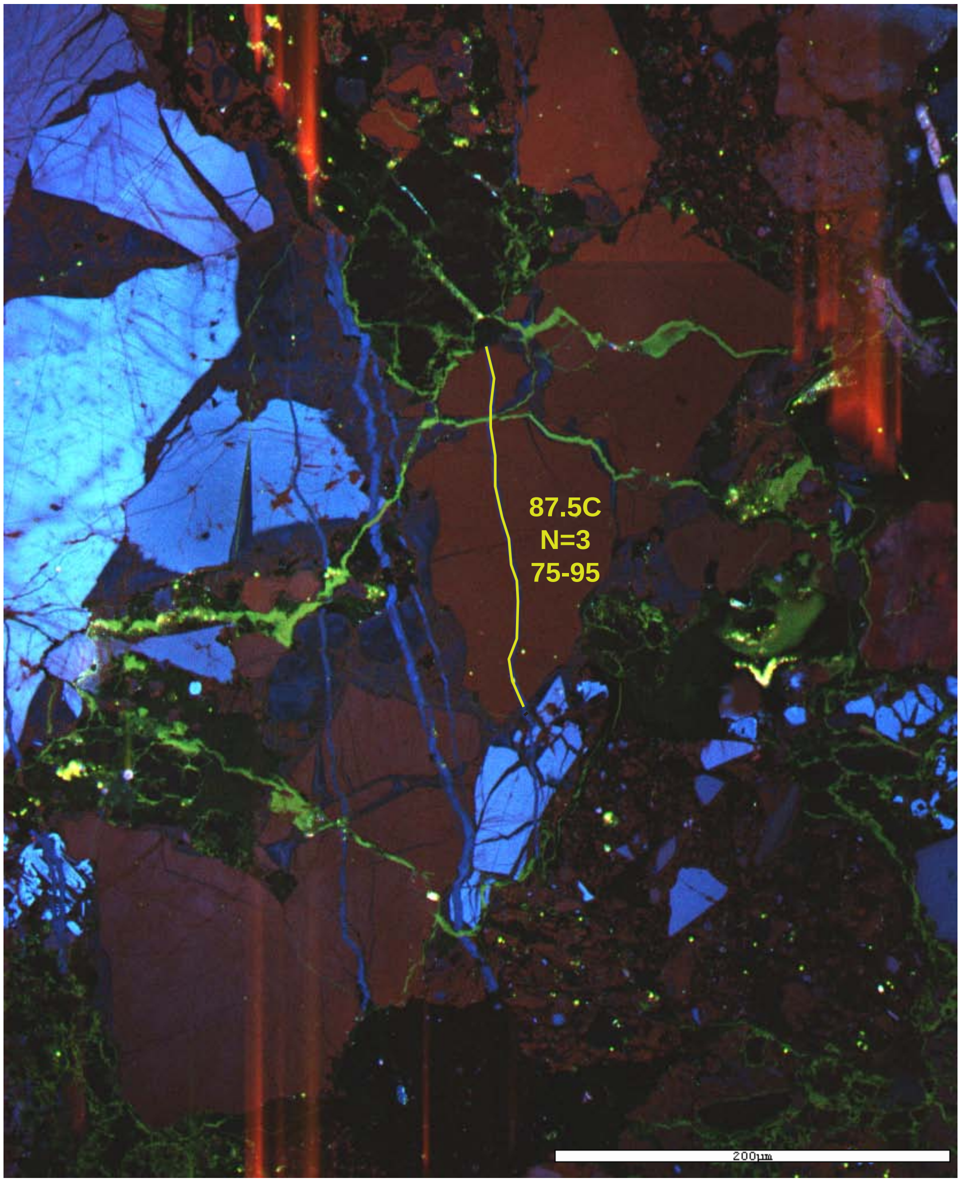

Microfracture B8, FIA 5

Microfracture B8, FIA 6

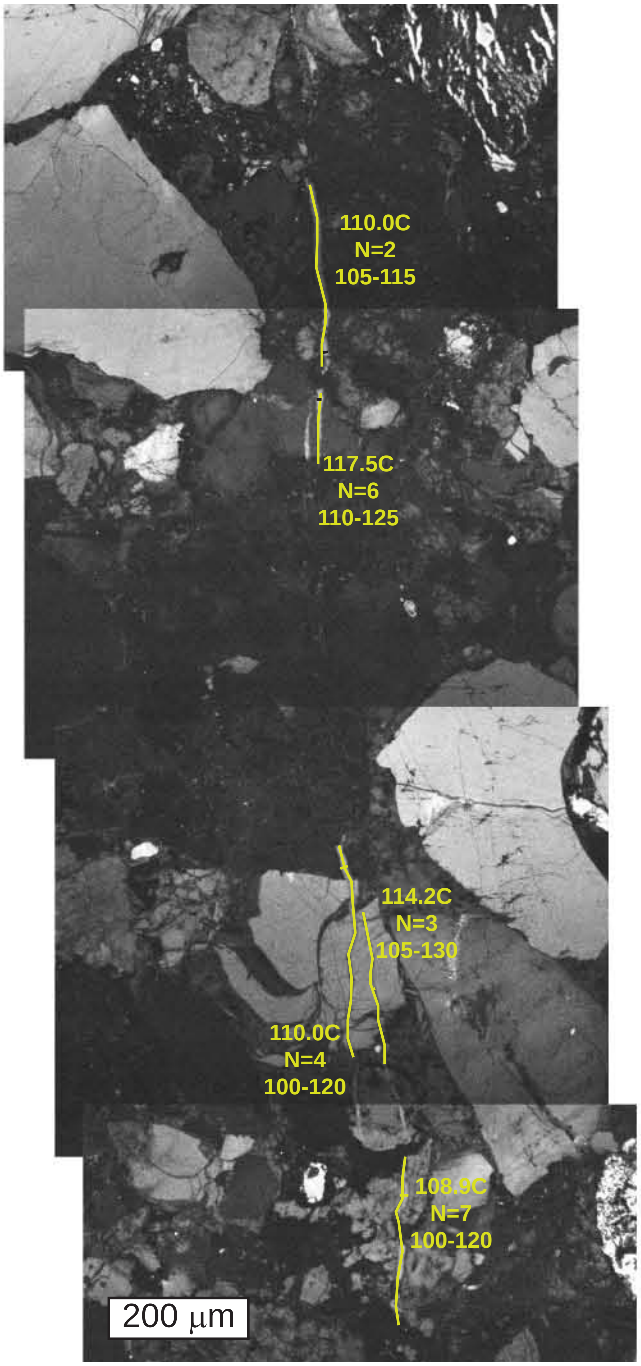

Microfracture C1

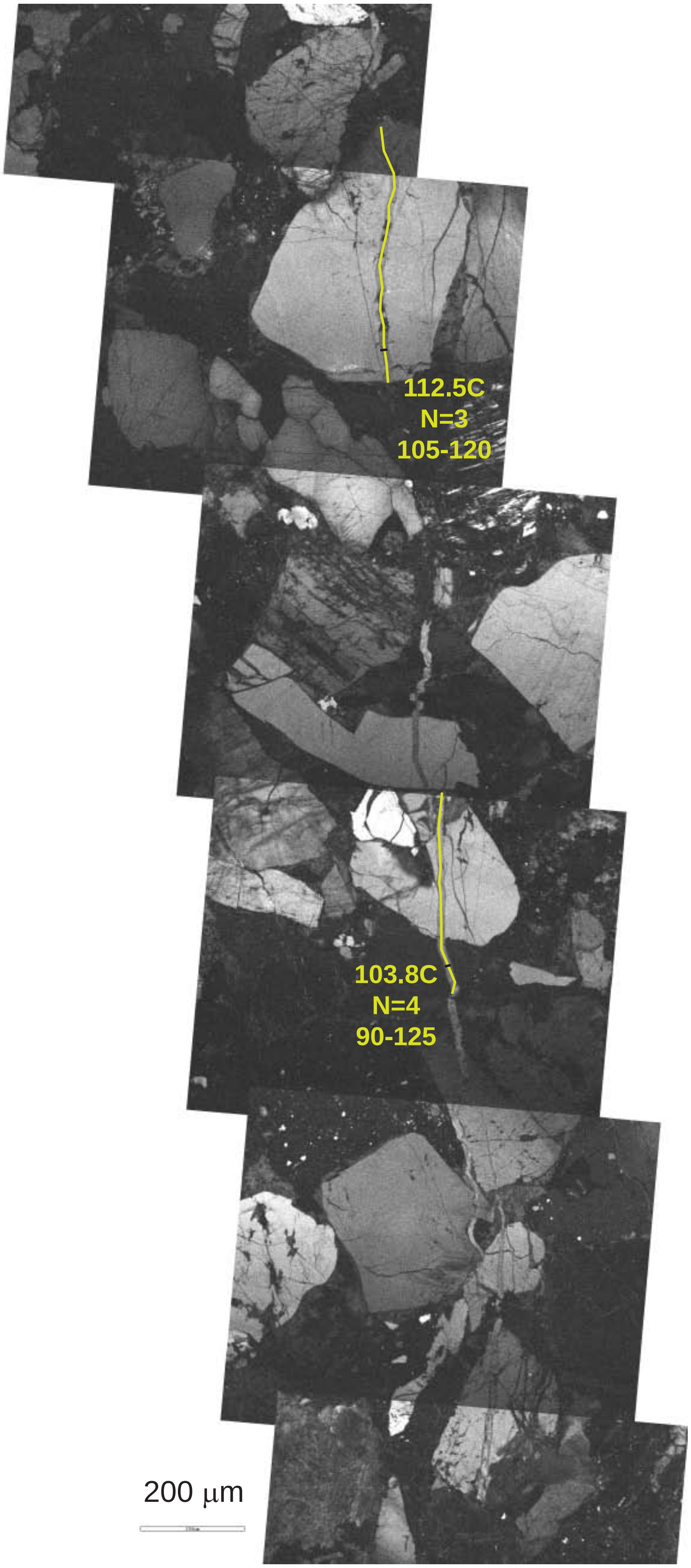

Microfracture C2, FIA 1-2

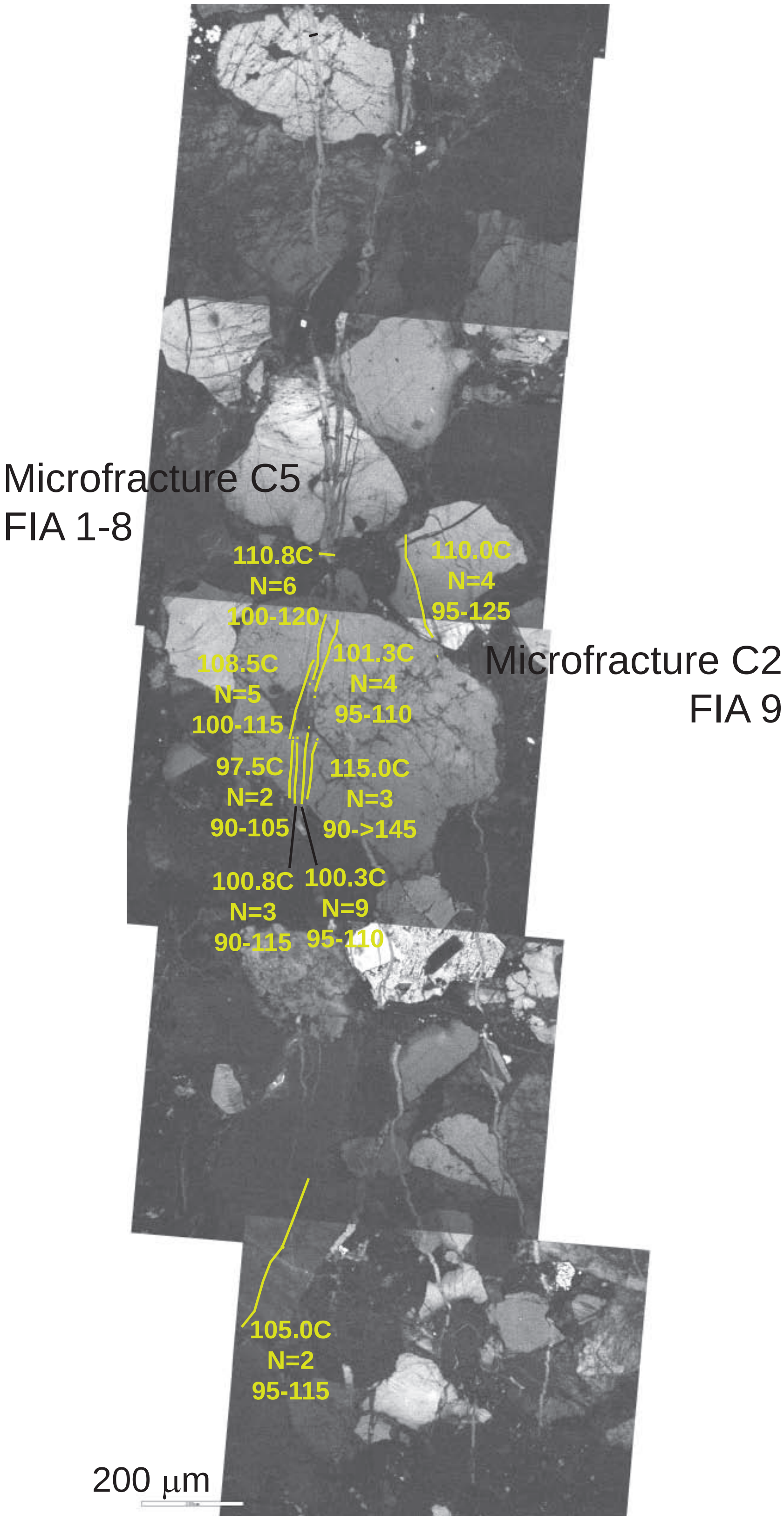
Microfracture C5
FIA 1-8
110.8C
N=6
100-120
110.0C
N=4
95-125
Microfracture C2
FIA 9
108.5C
N=5
100-115
101.3C
N=4
95-110
97.5C
N=2
90-105
115.0C
N=3
90->145
100.8C
N=3
90-115
100.3C
N=9
95-110
105.0C
N=2
95-115
200 µm

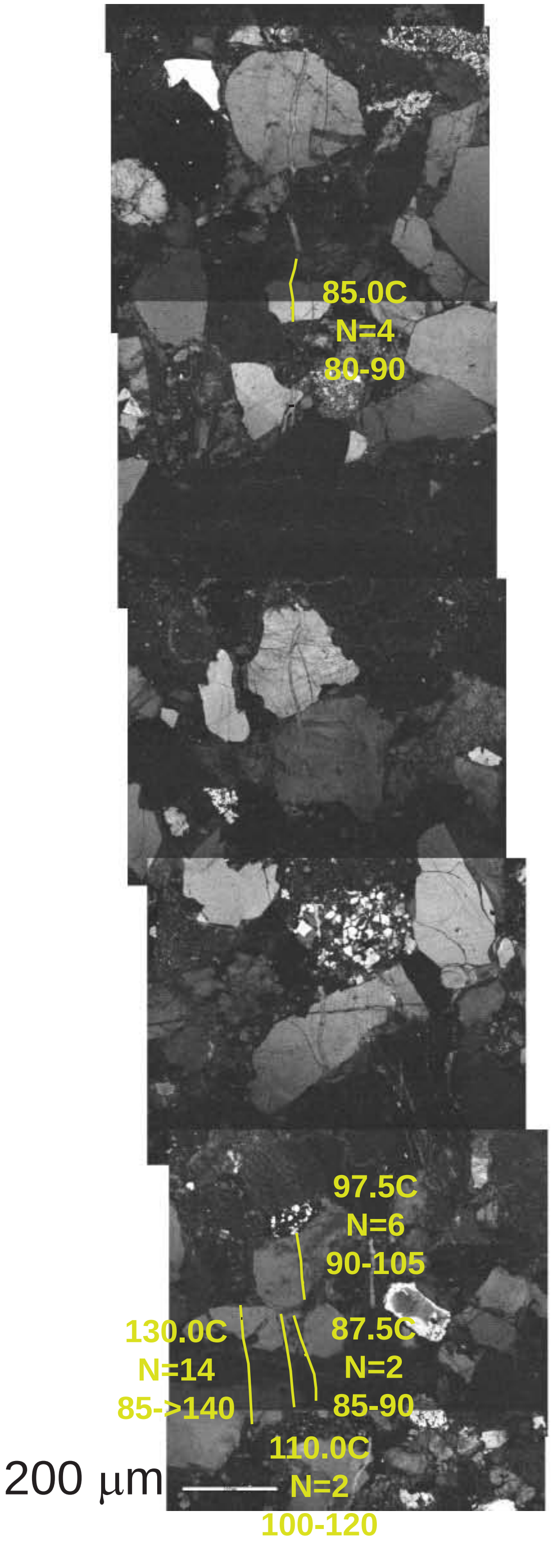

Microfracture C3

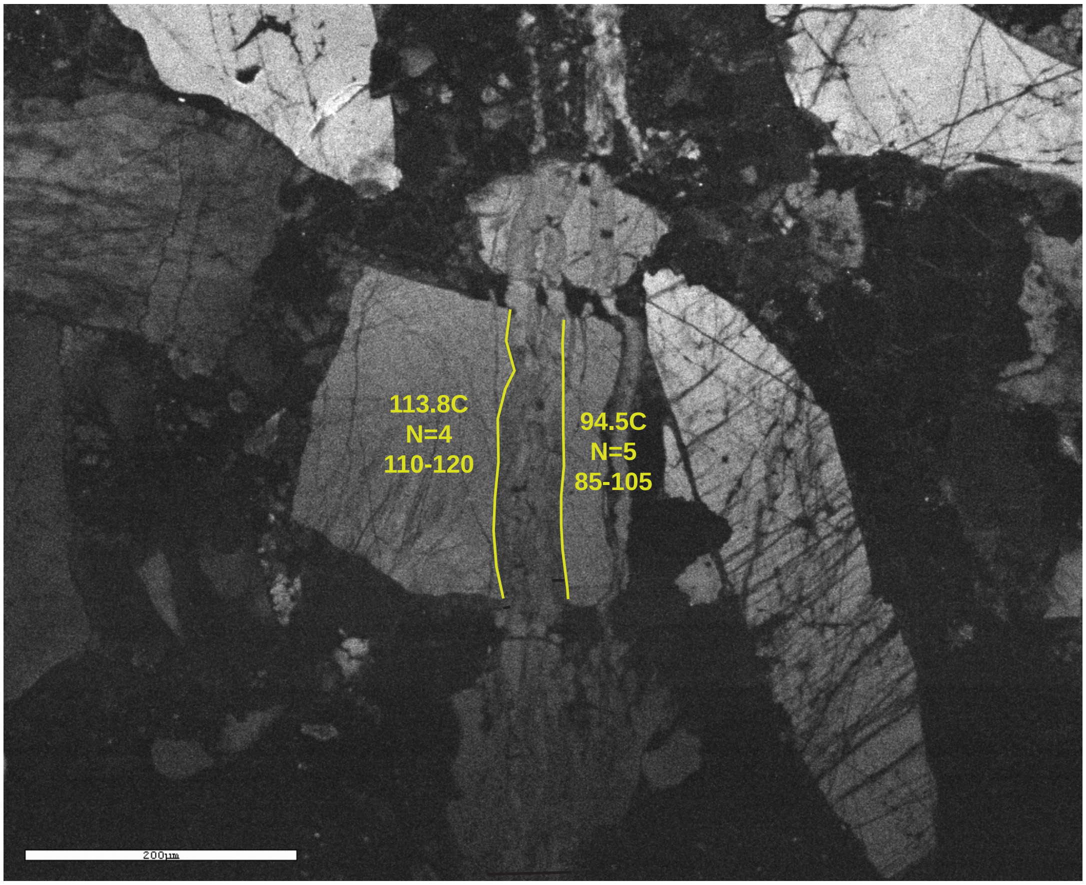

Microfracture C4, FIA 1-2

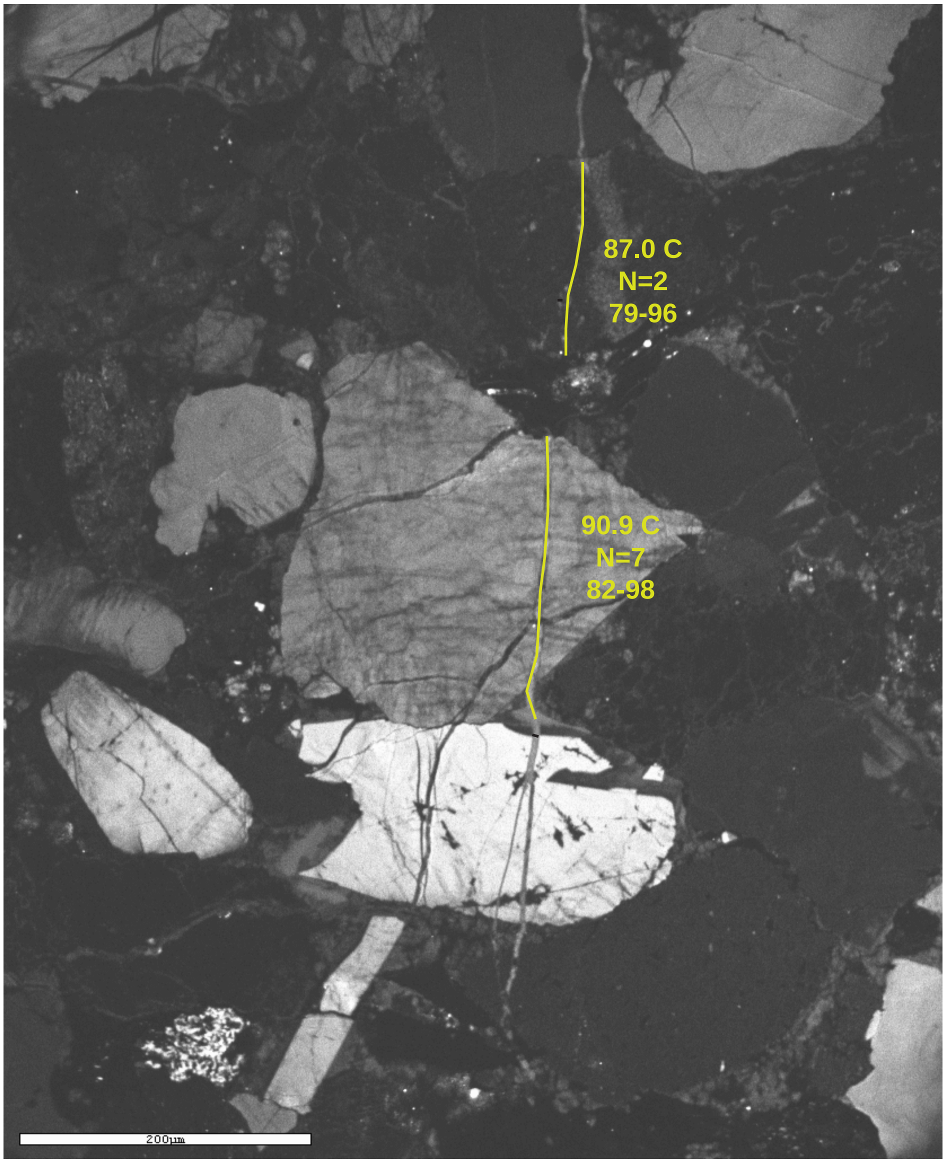

Microfracture D2, FIA 1-2

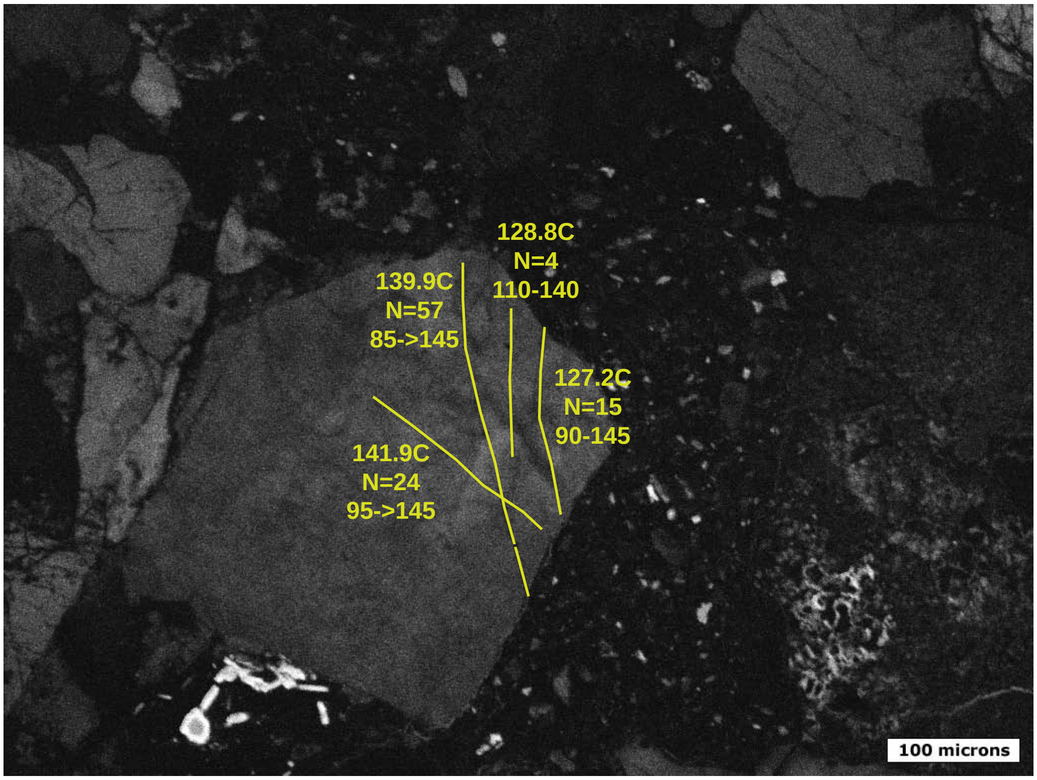

Microfracture E1, FIA 1-4

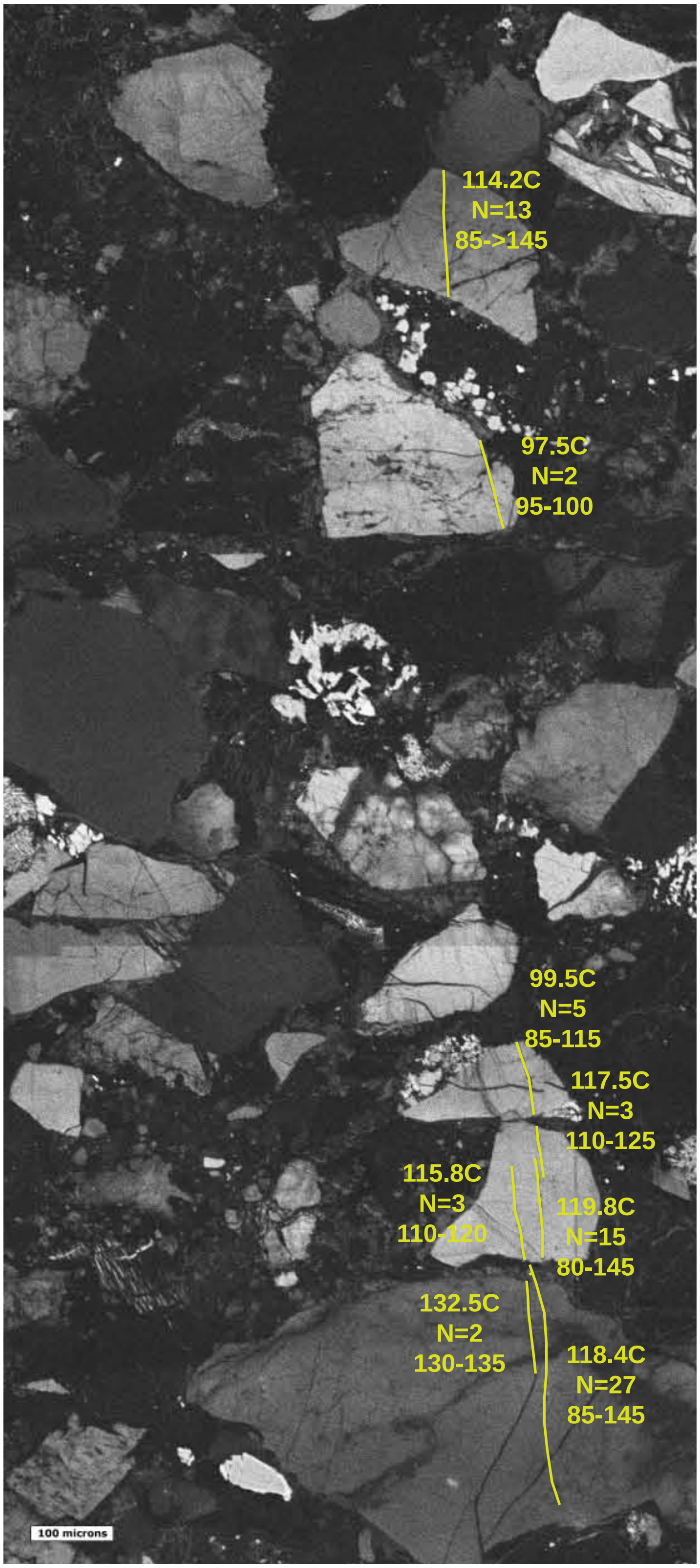

Microfracture E1, FIA 5-12

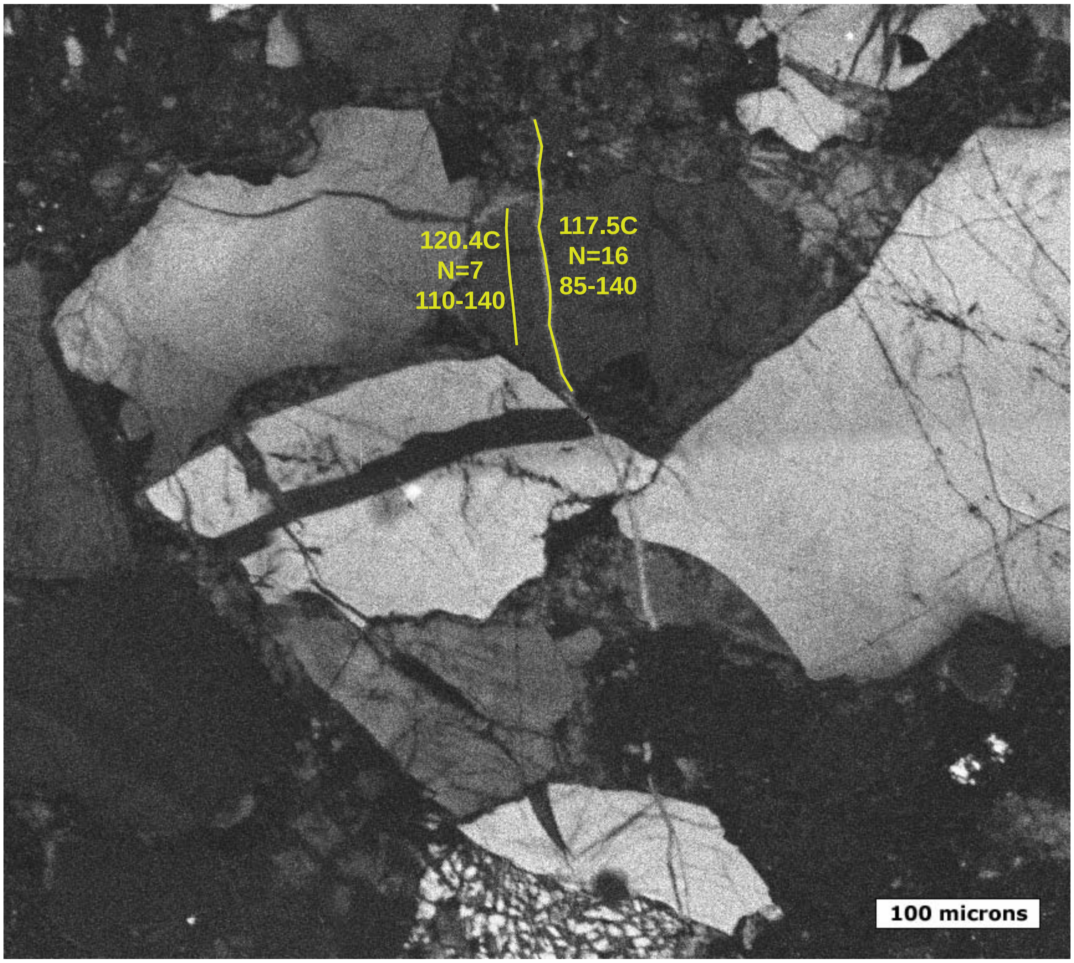

Microfracture E1, FIA 13-14

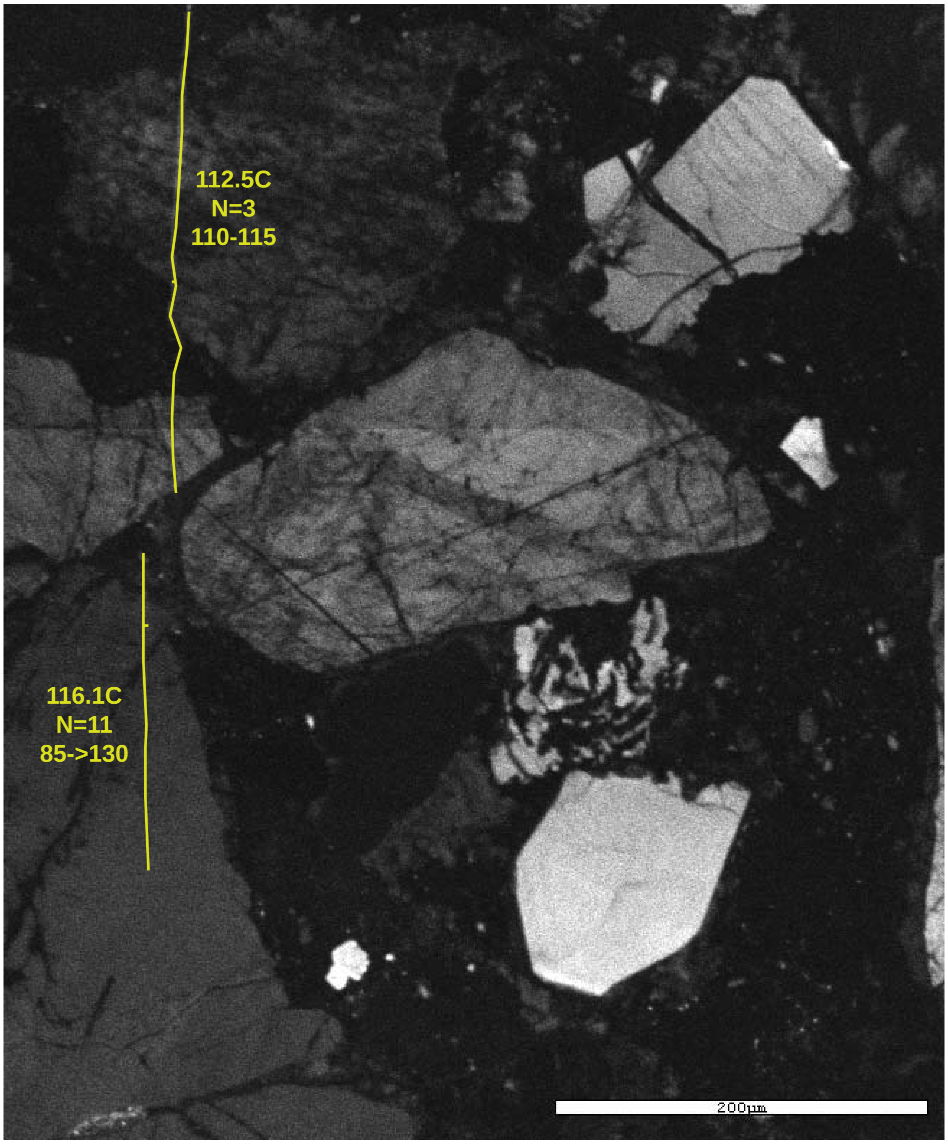

Microfracture E2, FIA 1-2

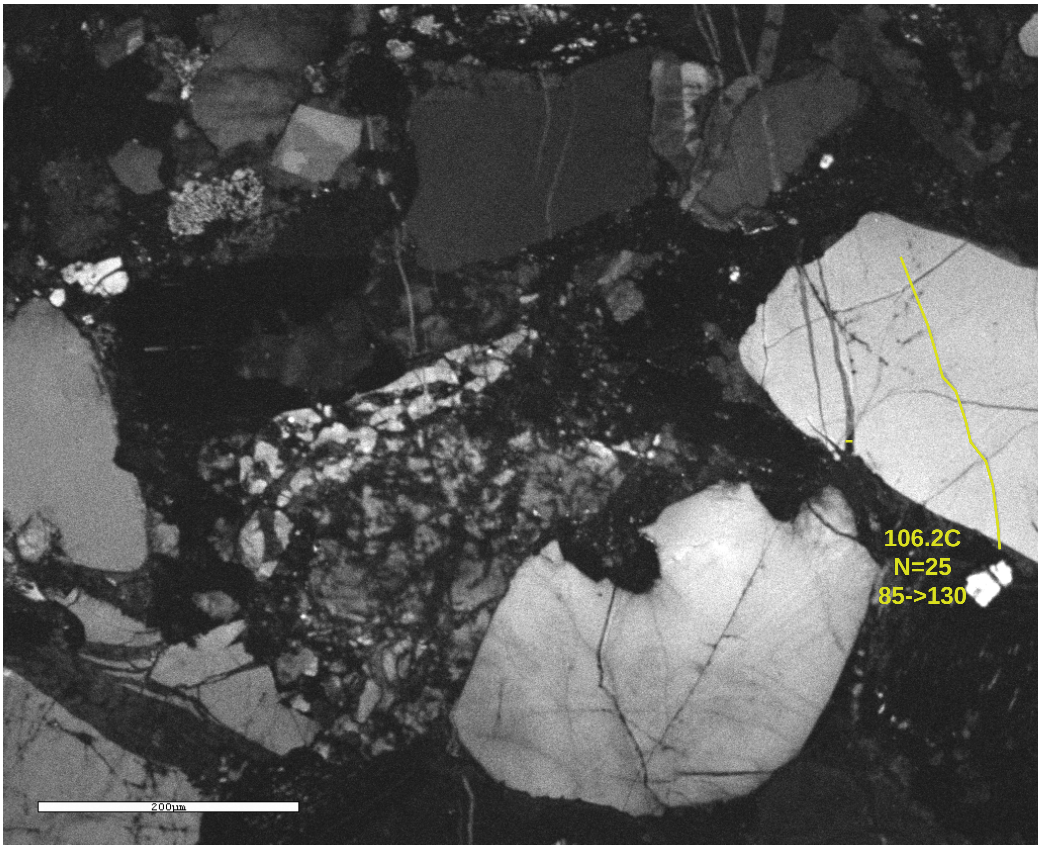

Microfracture E3

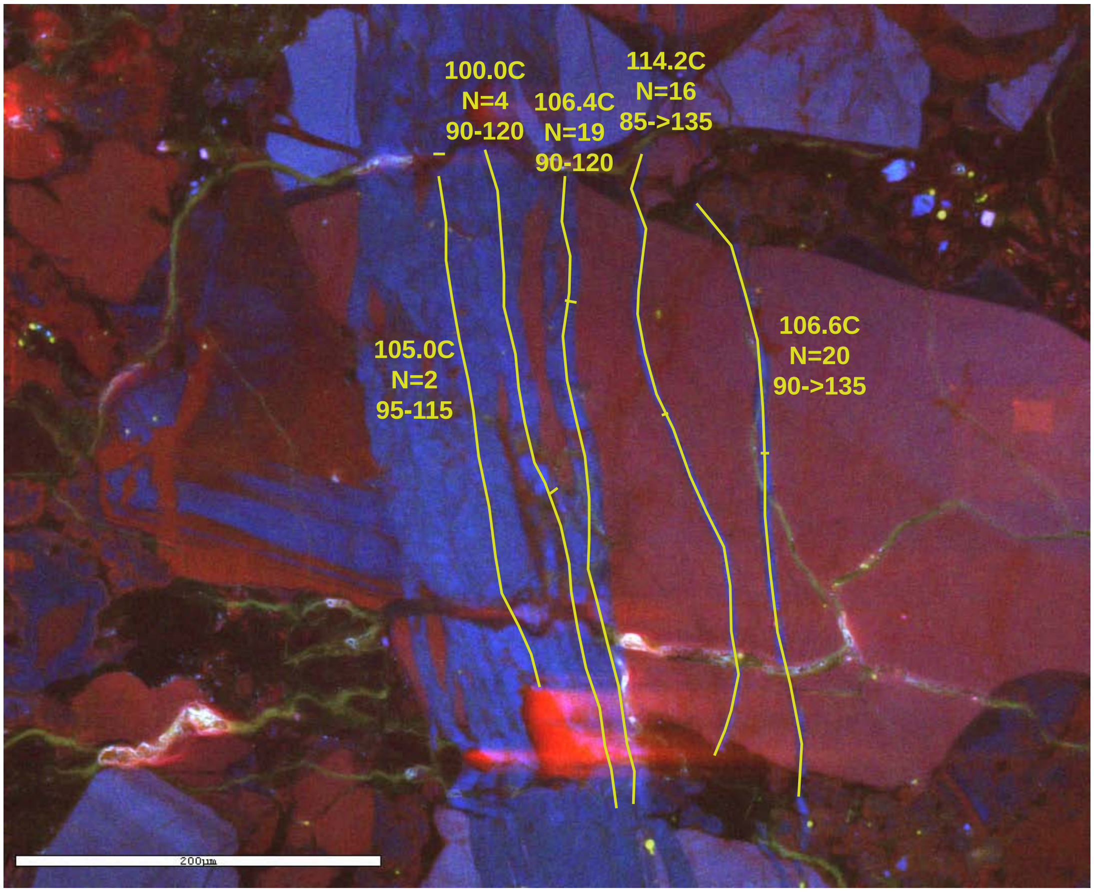

Microfracture E4, FIA 1-5

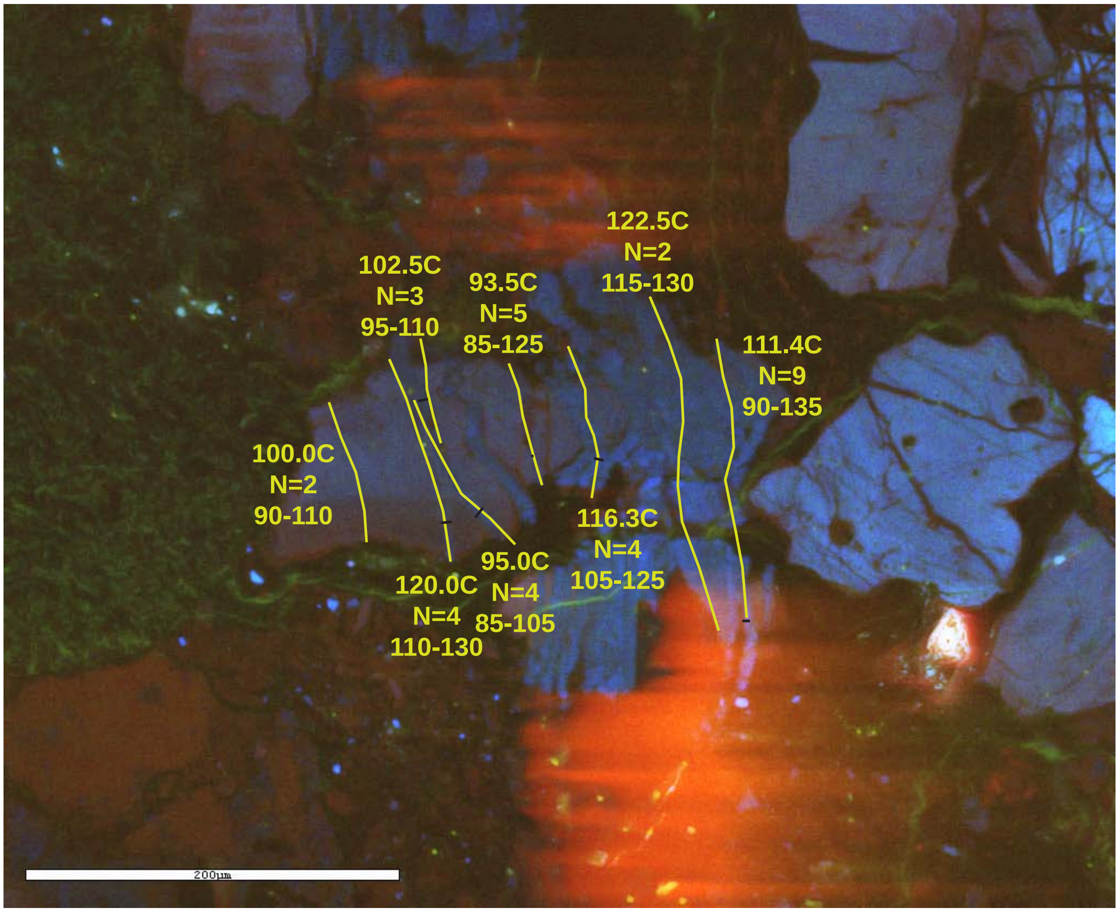

Microfracture E4, FIA 6-13

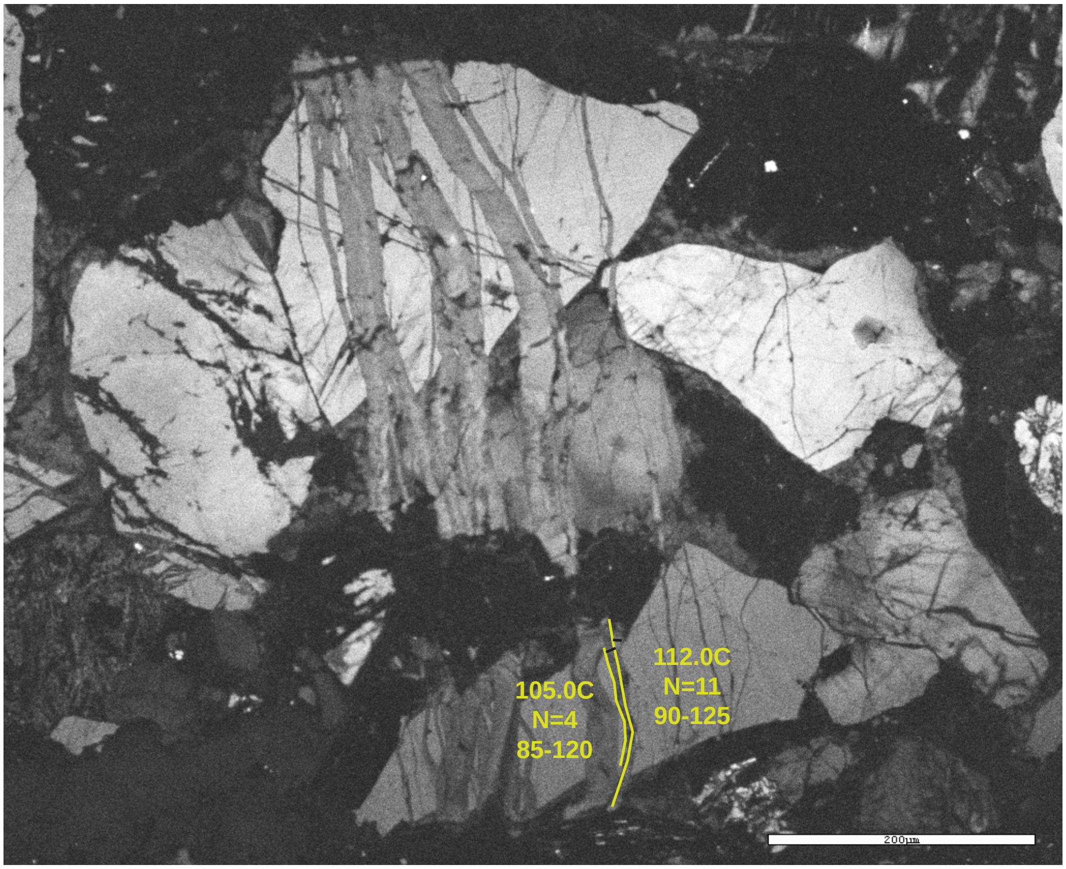

Microfracture E4, FIA 14-15

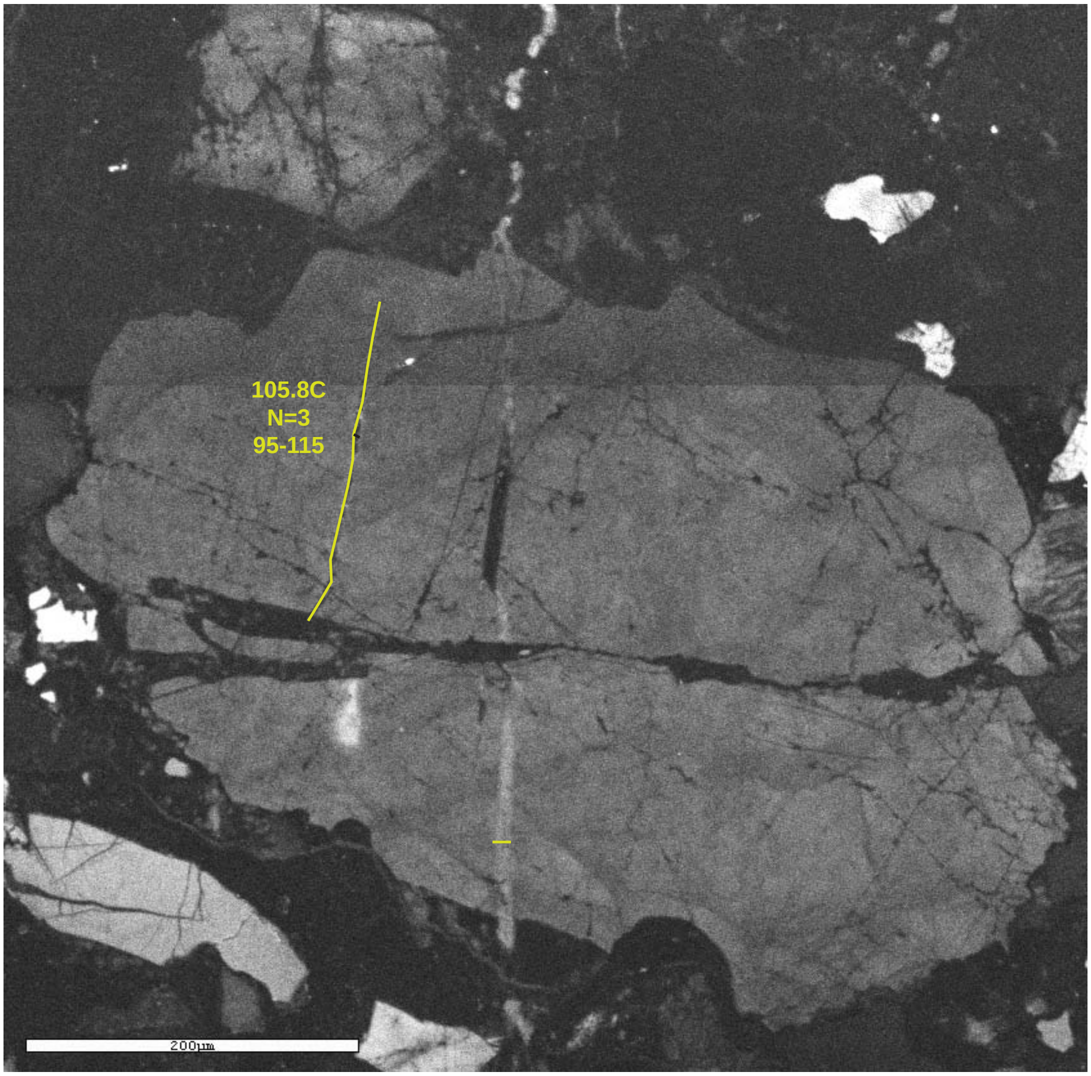

Microfracture E8

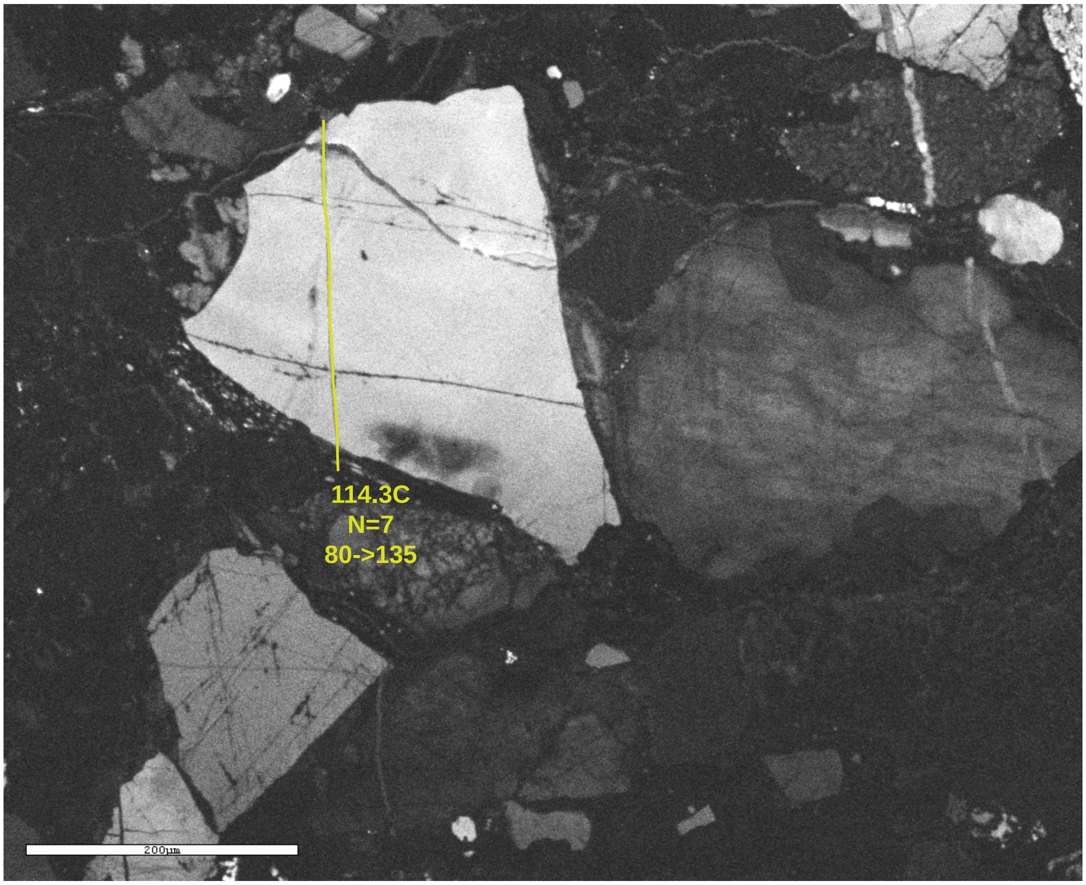

Microfracture E10, FIA 1

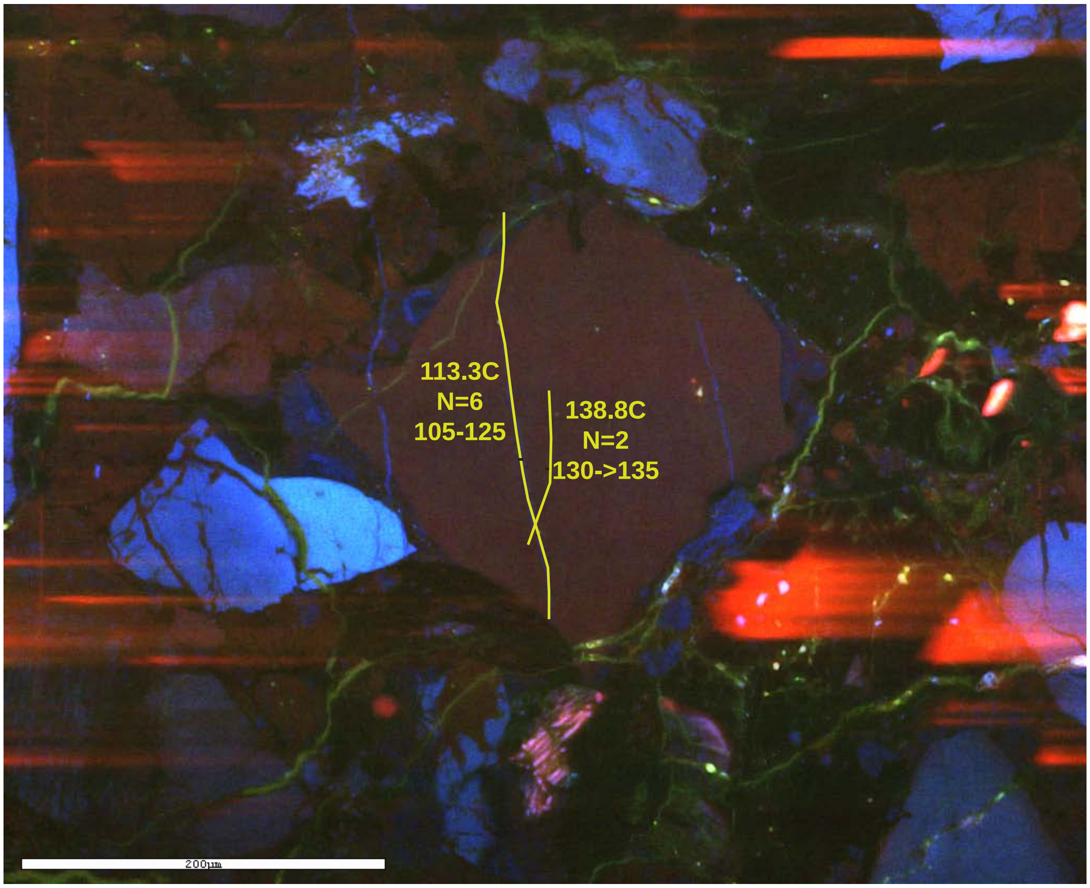

Microfracture E11

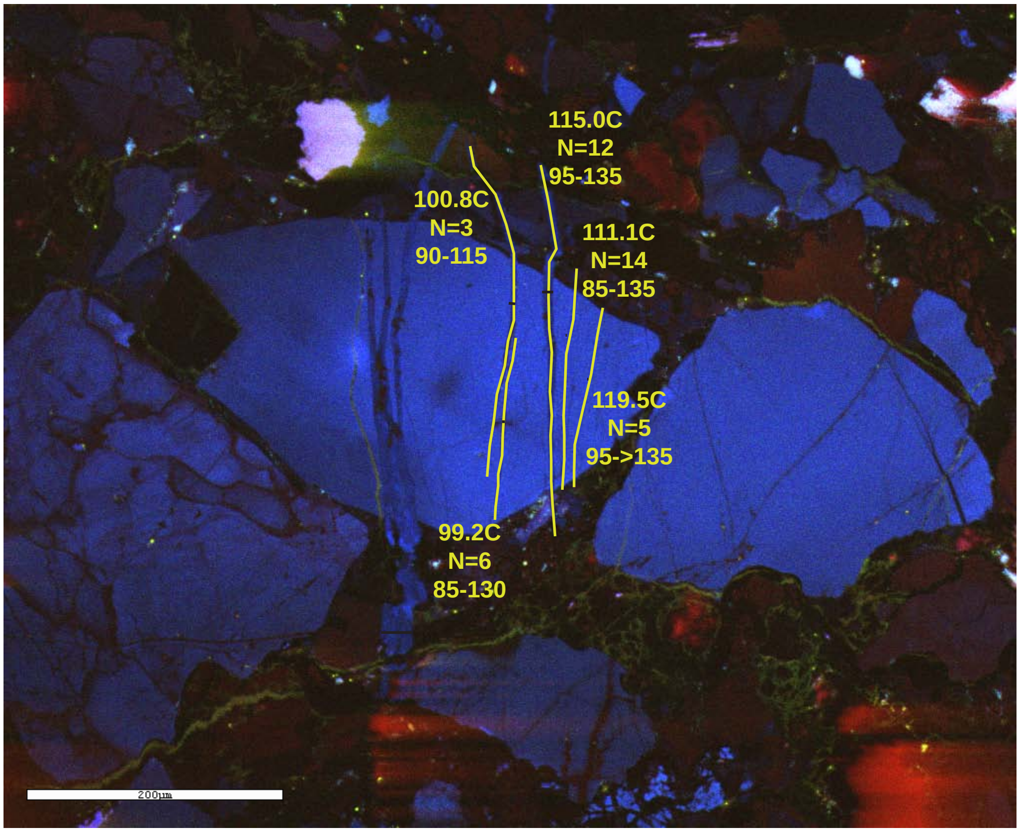

Microfracture F1, FIA 1-5

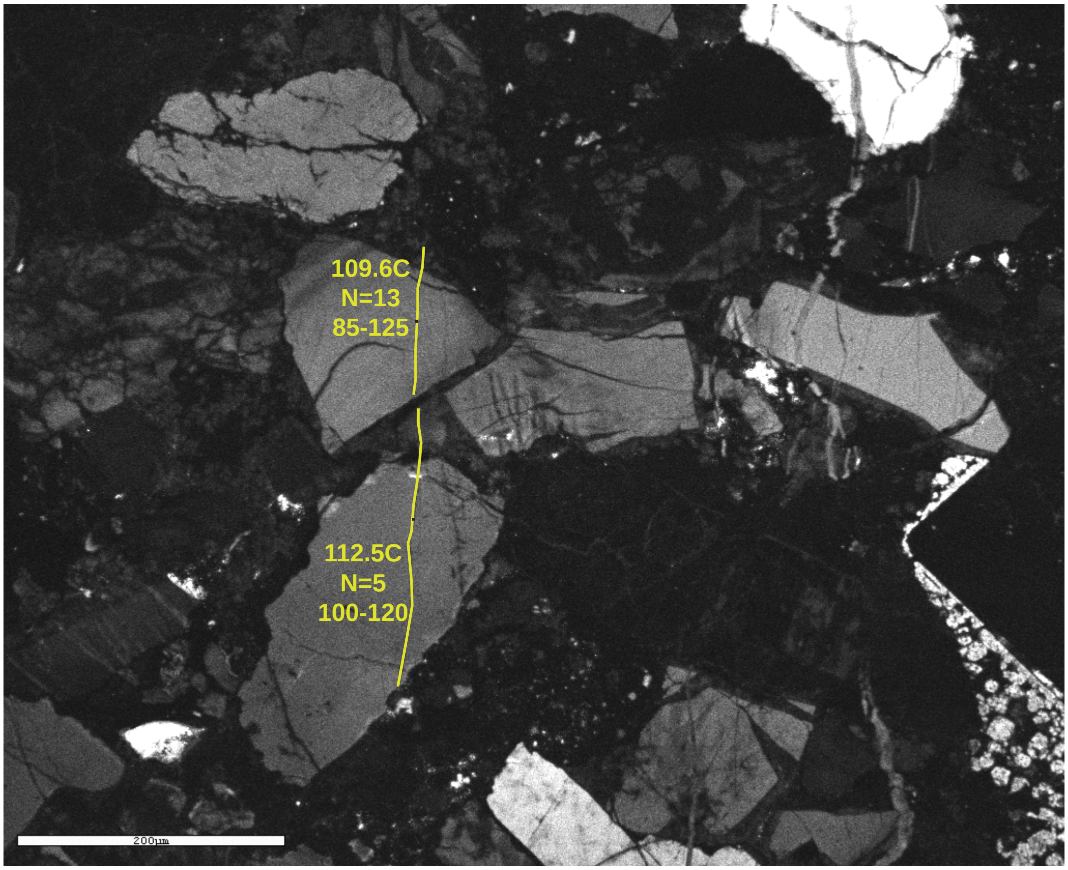

Microfracture F1, FIA 6-7

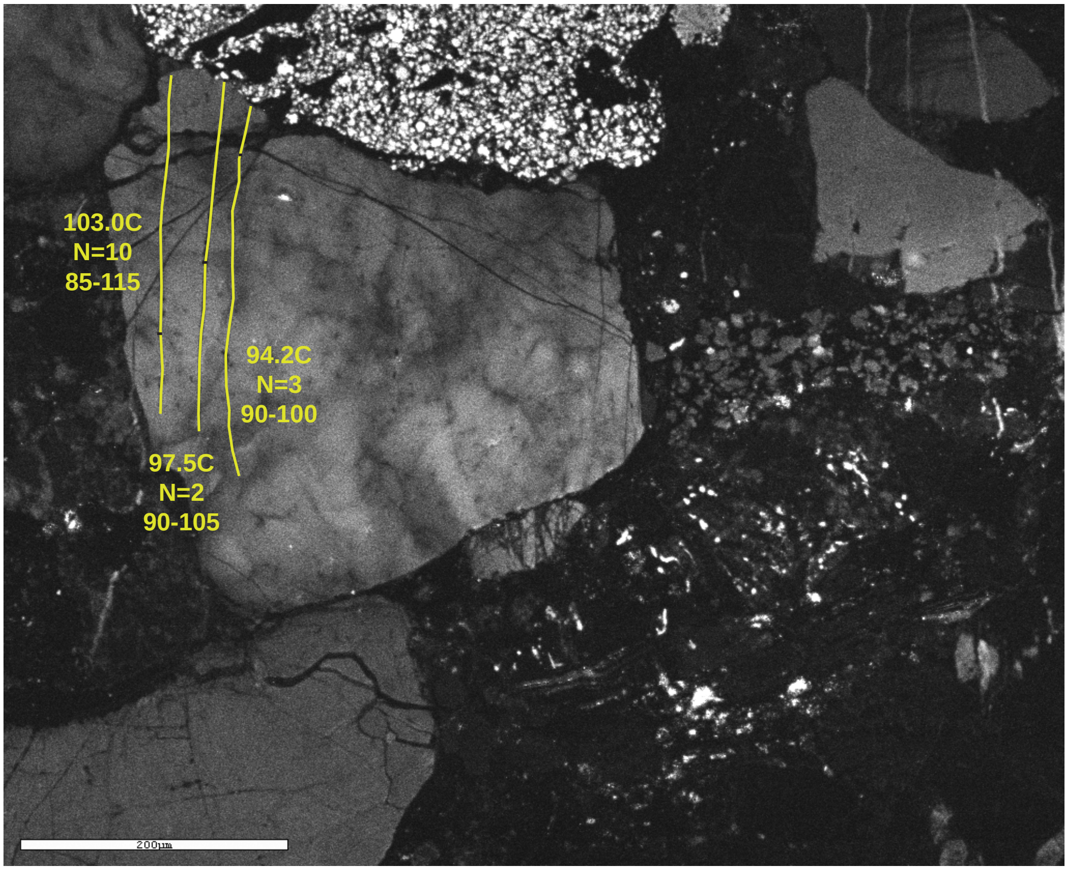

Microfracture F2, FIA 1-3

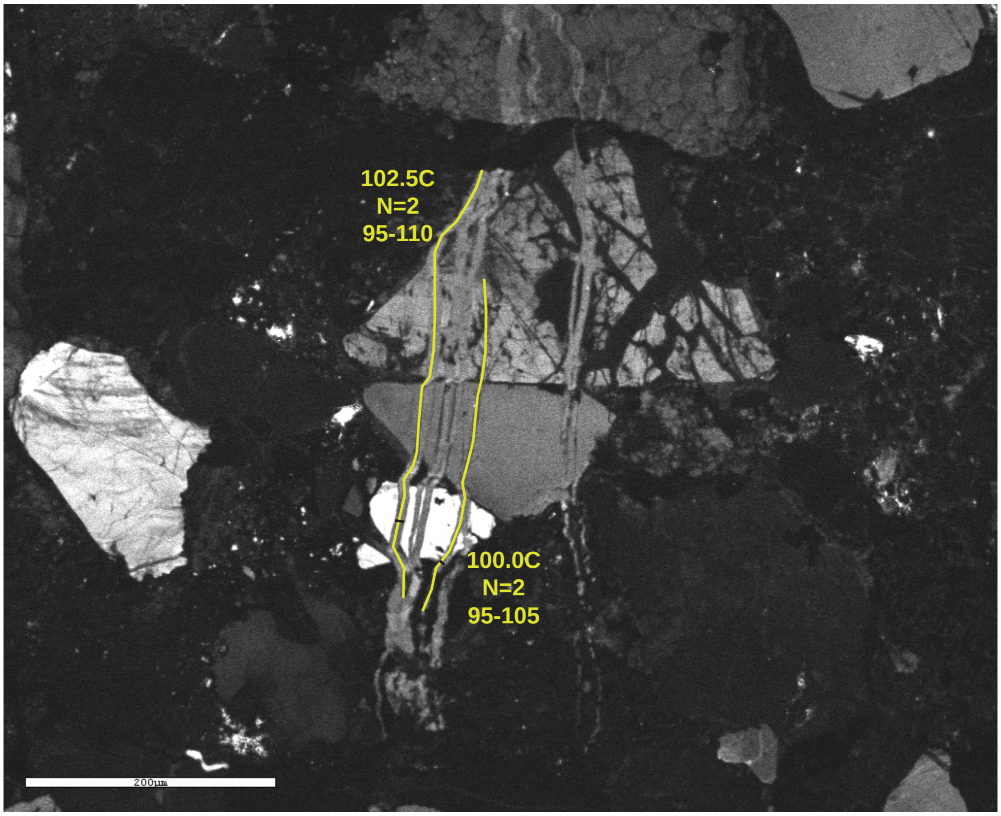

Microfracture F2, FIA 4-5

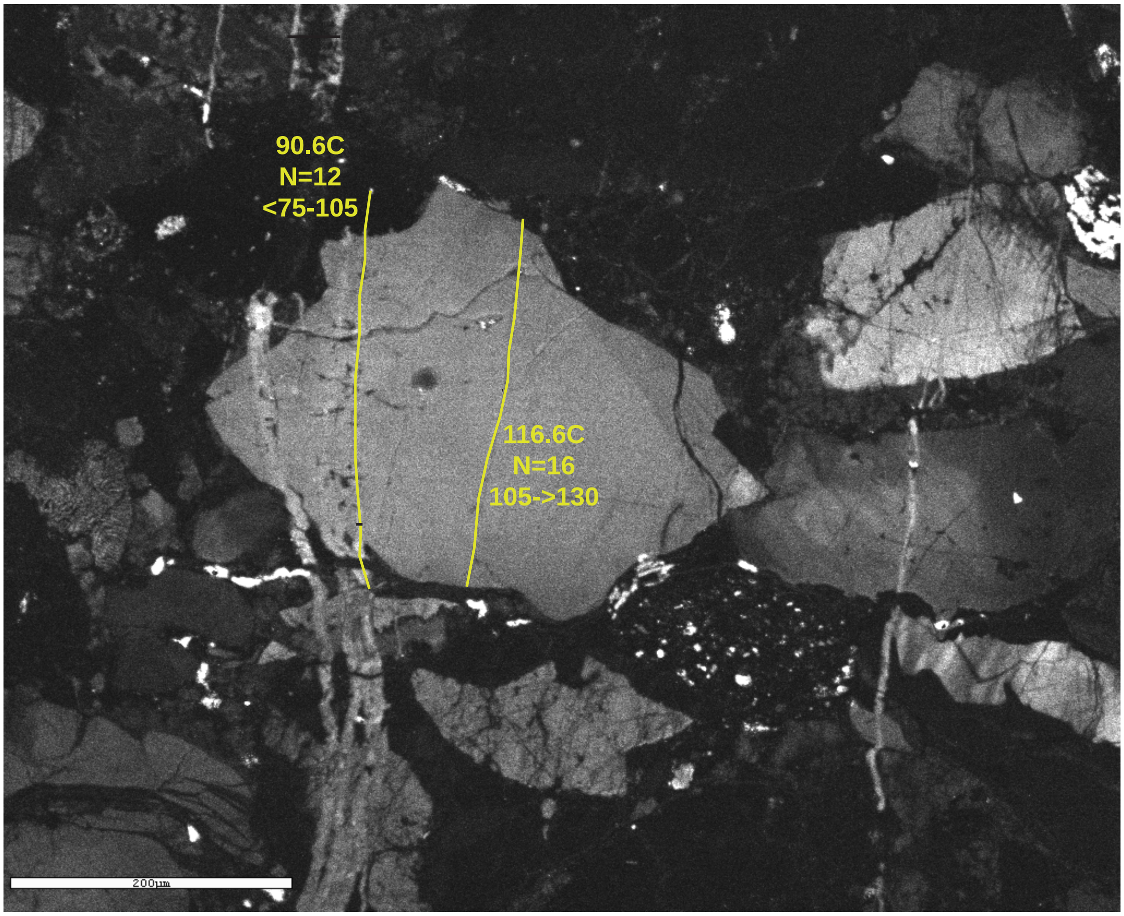

Microfracture F2, FIA 6-7

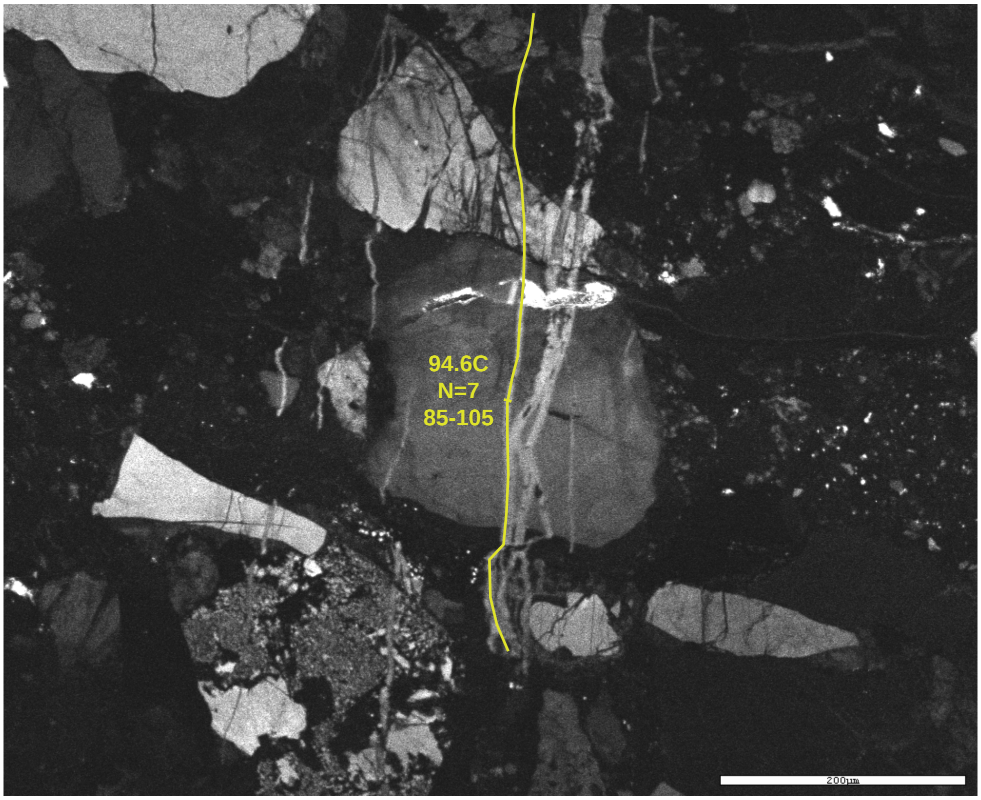

Microfracture F2, FIA 8

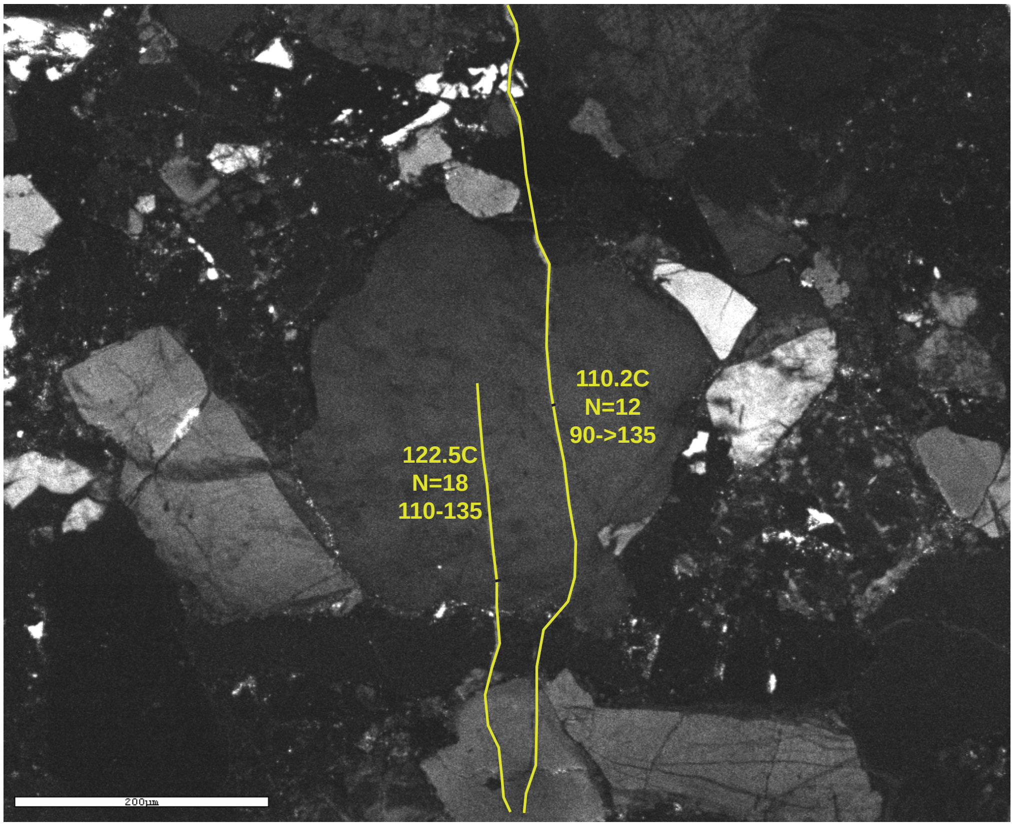

Microfracture F3, FIA 1-2

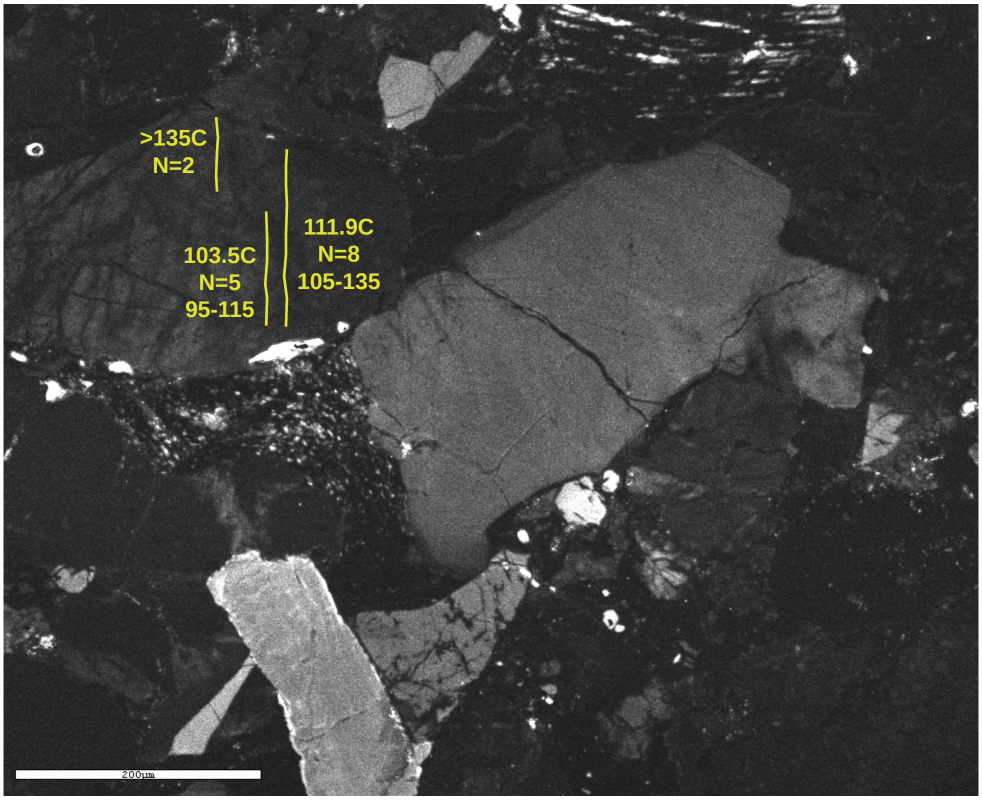

Microfracture F3, FIA 3-5

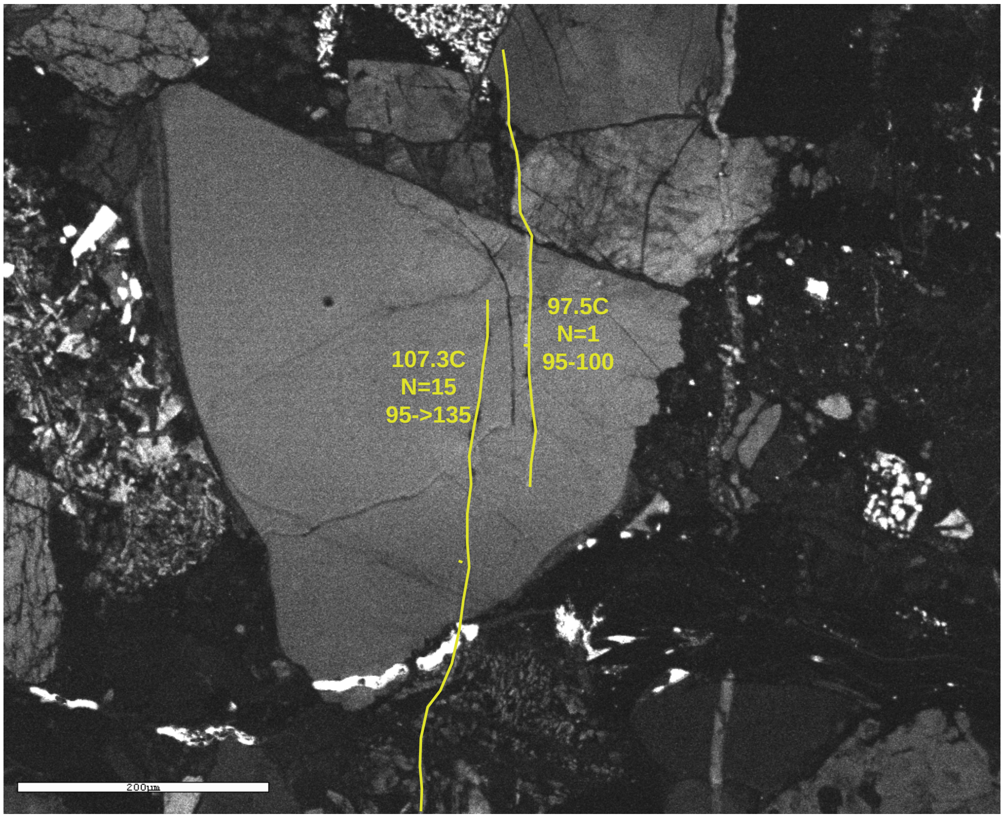

Microfracture F3, FIA 6

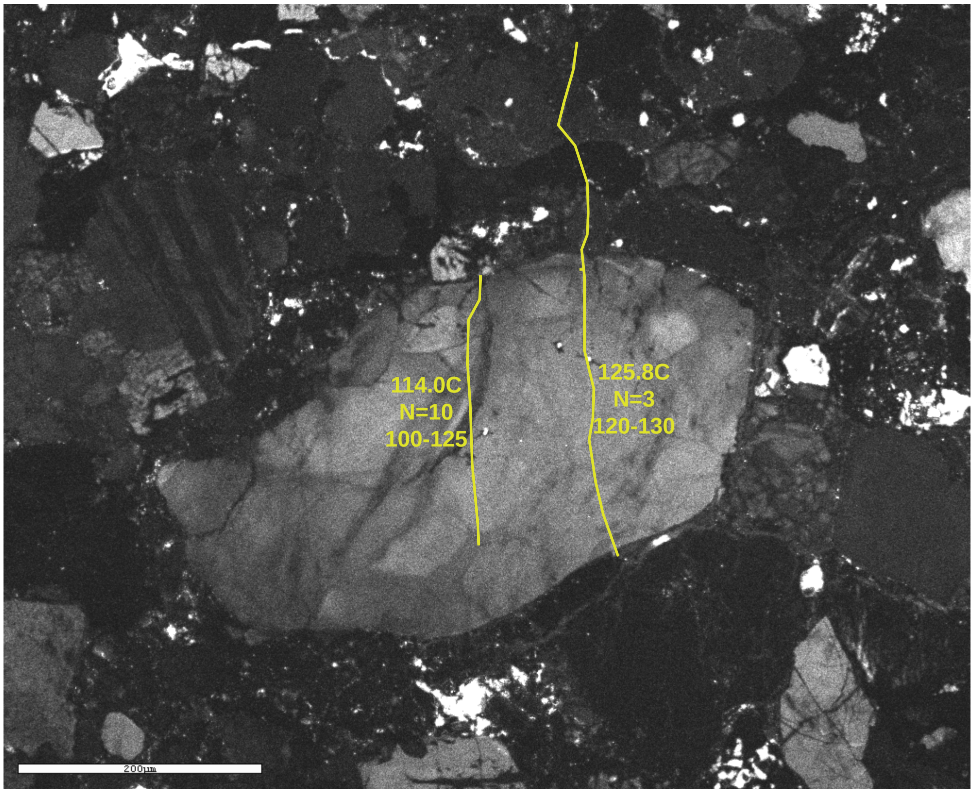

Microfracture F4, FIA 1-2

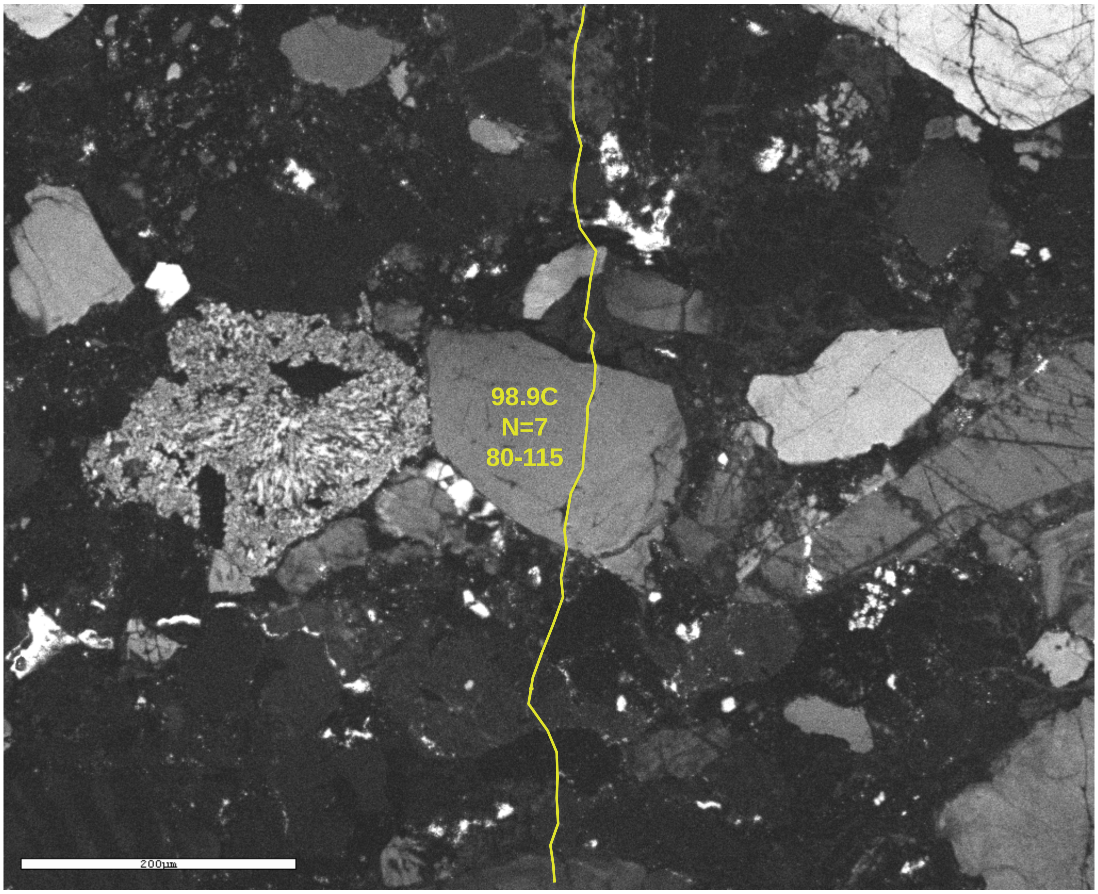

Microfracture F4, FIA 3

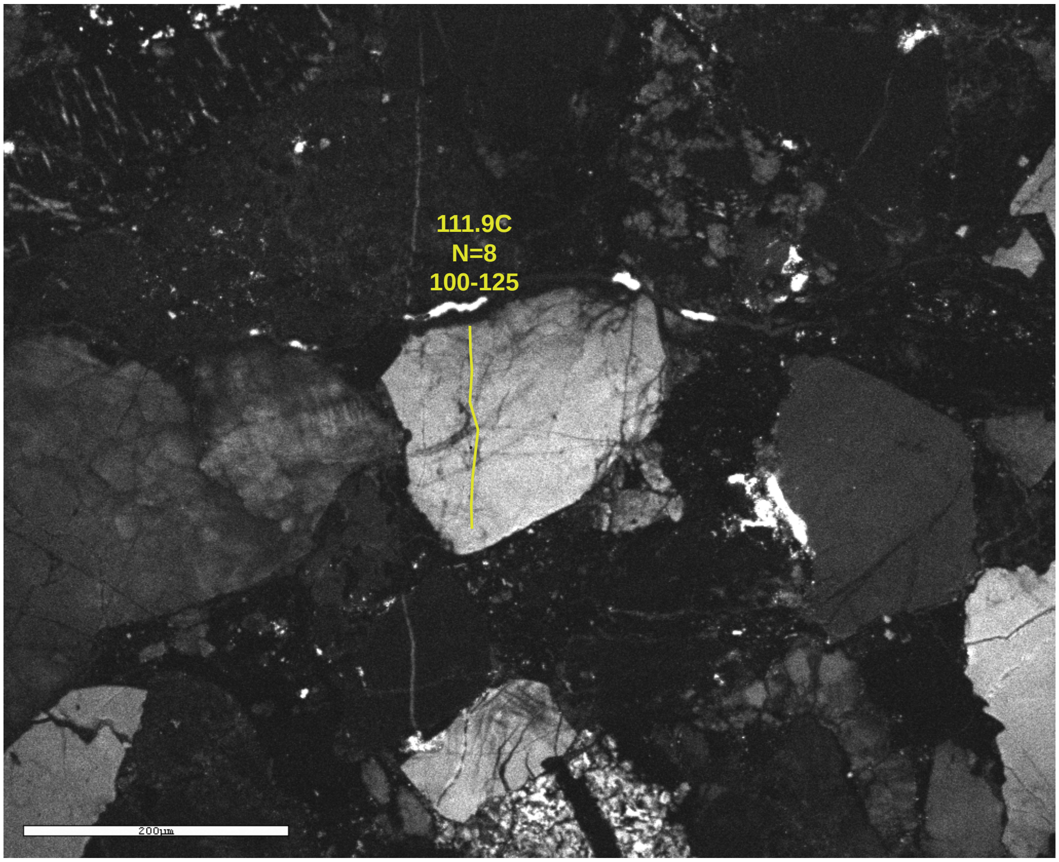

Microfracture F4, FIA 4

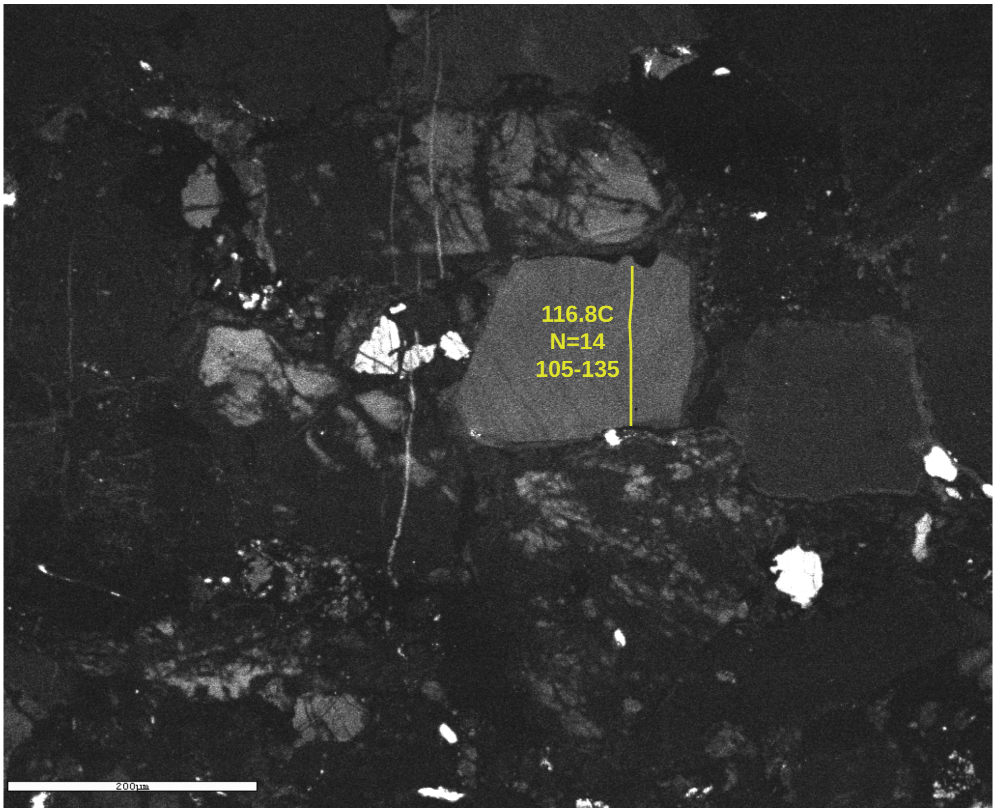

Microfracture F4, FIA 5

thin section	chip	fracture Xloc	aperture	avg temp	fracname
10jh10a	1		22.39	136.5789	A1
temp	lowrange	hirange	area	FIA	FIA avg
137.5	135		1	1	144.1129
137.5	135		1	1	
137.5	135		1	1	
150	140	x	1	1	
137.5	135		1	1	
137.5	135		1	1	
150	140	x	1	1	
132.5	130		1	1	
150	140	x	1	1	
127.5	125		1	1	
150	140	x	1	1	
137.5	135		1	1	
150	140	x	1	1	
137.5	135		1	1	
150	140	x	1	1	
137.5	135		1	1	
137.5	135		1	1	
150	140	x	1	1	
150	140	x	1	1	
150	140	x	1	1	
150	140	x	1	1	
150	140	x	1	1	
132.5	130		1	1	
150	140	x	1	1	
150	140	x	1	1	
150	140	x	1	1	
150	140	x	1	1	
137.5	135		1	1	
150	140	x	1	1	
150	140	x	1	1	
150	140	x	1	1	
107.5	105		2	2	98.75
107.5	105		2	2	
87.5	85		2	2	
92.5	90		2	2	
102.5	100		2	3	109.1667
117.5	115		2	3	
107.5	105		2	3	

thin section	chip	fracture Xloc	aperture	avg temp	fracname
10JH10B	2		11.02	100.1471	B1
temp	lowrange	hirange	area	FIA	FIA avg
97.5	95	100	2ab	1	98.61111
107.5	105	110	2ab	1	
97.5	95	100	2ab	1	
92.5	90	95	2ab	1	
92.5	90	95	2ab	1	
92.5	90	95	2ab	1	
112.5	110	115	2ab	1	
97.5	95	100	2ac	1	
97.5	95	100	2ac	1	
97.5	95	100	2ad	2	100
97.5	95	100	2ad	2	
102.5	100	105	2ad	2	
102.5	100	105	2ad	2	
107.5	105	110	2aa		
97.5	95	100	2ab		
107.5	105	110	2ae		
102.5	100	105	2af		

thin section	chip	fracture Xloc	aperture	avg temp	fracname
10JH10B	2		11.46	99.6	B2
temp	lowrange	hirange	area	FIA	FIA avg
102.5	100	105	2ba	1	96.25
97.5	95	100	2ba	1	
92.5	90	95	2ba	1	
97.5	95	100	2ba	1	
97.5	95	100	2ba	1	
92.5	90	95	2ba	1	
92.5	90	95	2ba	1	
97.5	95	100	2ba	1	
112.5	110	115	2ba		
112.5	110	115	2ba		
103.1			2ba		
106.7			2ba		
104.7			2ba		
92.5	90	95	2ba		
97.5	95	100	2bc		
92.5	90	95	2bd	2	98.5
92.5	90	95	2bd	2	
102.5	100	105	2bd	2	
102.5	100	105	2bd	2	
102.5	100	105	2bd	2	

thin section	chip	fracture Xloc	aperture	avg temp	fracname
10JH10B	4		7.16	117.5	B3

temp	lowrange	hirange	area	FIA	FIA avg
127.5	125	130	4dc	1	125
122.5	120	125	4dc	1	
102.5	100	105	4dd		
127.5	125	130	4de		
107.5	105	110	4de		

thin section	chip	fracture Xloc	aperture	avg temp	fracname
10JH10B	3 and 4		10.22	115.525	B4
temp	lowrange	hirange	area	FIA	FIA avg
122.5	120	125	4da-db	1	117.5
122.5	120	125	4da-db	1	
112.5	110	115	4da-db	1	
97.5	95	100	4da-db	1	
122.5	120	125	4da-db	1	
117.5	115	120	4da-db	1	
122.5	120	125	4da-db	1	
122.5	120	125	4da-db	1	
117.5	115	120	4da-db	1	
117.5	115	120	4da-db	2	114.1667
107.5	105	110	4da-db	2	
117.5	115	120	4da-db	2	
107.5	105	110	5aa	4	102.5
117.5	115	120	5aa	4	
92.5	90	95	5aa	4	
92.5	90	95	5aa	4	
97.5	95	100	6ab	3	100
102.5	100	105	6ab	3	
117.5	115	120	6ab		
140	130		6ab		
112.55	110.1	115	6ab		
112.55	110.1	115	6ab		
140	130		6ab		
140	130		6ab		

thin section	chip	fracture Xloc	aperture	avg temp	fracname
10JH10B	4		3.87	97.5	B5

temp	lowrange	hirange	area	FIA	FIA avg
97.5	95	100	4c	1	100.8333
102.5	100	105	4c	1	
102.5	100	105	4c	1	
87.5	85	90	4c		

thin section	chip	fracture Xloc	aperture	avg temp	fracname
10JH10B	3		12.43	118.0682	B6
temp	lowrange	hirange	area	FIA	FIA avg
122.5	120	125	3	1	116.7105
117.5	115	120	3	1	
117.5	115	120	3	1	
122.5	120	125	3	1	
122.5	120	125	3	1	
112.5	110	115	3	1	
112.5	110	115	3	1	
102.5	100	105	3	1	
117.5	115	120	3	1	
122.5	120	125	3	1	
117.5	115	120	3	1	
122.5	120	125	3	1	
107.5	105	110	3	1	
112.5	110	115	3	1	
102.5	100	105	3	1	
127.5	125	130	3	1	
122.5	120	125	3	1	
117.5	115	120	3	1	
117.5	115	120	3	1	
122.5	120	125	3		
117.5	115	120	3		
140	130		3		

thin section	chip	fracture Xloc	aperture	avg temp	fracname
10JH10B	3 and 4		7.5	94.5	B7
temp	lowrange	hirange	area	FIA	FIA avg
107.5	105	110	3b	1	106.25
107.5	105	110	3b	1	
102.5	100	105	3b	1	
107.5	105	110	3b	1	
87.5	85	90	3b		
97.5	95	100	3b		
77.5	75	80	4af	2	80.83333
87.5	85	90	4af	2	
77.5	75	80	4af	2	
92.5	90	95	4af		

thin section	chip	fracture Xloc	aperture	avg temp	fracname
10JH10B	3 and 4		10.5	107.1951	B8
temp	lowrange	hirange	area	FIA	FIA avg
107.5	105	110	3c	1	105.8333
107.5	105	110	3c	1	
102.5	100	105	3c	1	
62.5	60	65	3c	1	
112.5	110	115	3c	2	108.4091
107.5	105	110	3c	2	
122.5	120	125	3c	2	
107.5	105	110	3c	2	
112.5	110	115	3c	2	
107.5	105	110	3c	2	
112.5	110	115	3c	2	
107.5	105	110	3c	2	
102.5	100	105	3c	2	
102.5	100	105	3c	2	
97.5	95	100	3c	2	
112.5	110	115	3c	3	112.5
112.5	110	115	3c	3	
112.5	110	115	4ab	4	112.1053
112.5	110	115	4ab	4	
112.5	110	115	4ab	4	
107.5	105	110	4ab	4	
140	130		4ab	4	
117.5	115	120	4ab	4	
107.5	105	110	4ab	4	
107.5	105	110	4ab	4	
112.5	110	115	4ab	4	
117.5	115	120	4ab	4	
112.5	110	115	4ab	4	
117.5	115	120	4ab	4	
107.5	105	110	4ab	4	
107.5	105	110	4ab	4	
117.5	115	120	4ab	4	
102.5	100	105	4ab	4	
102.5	100	105	4ab	4	
107.5	105	110	4ab	4	
107.5	105	110	4ab	4	
77.5	75	80	4ac	5	87.5
92.5	90	95	4ac	5	
92.5	90	95	4ac	5	
102.5	100	105	4ad	6	102.5
102.5	100	105	4ad	6	

thin section	chip	fracture Xloc	aperture	avg temp	fracname
10jh10c	1		12.5	110.5769	C1

temp	lowrange	hirange	area	FIA	FIA avg
102.5	100		f1-01	1	100.8333
97.5	95		f1-01	1	
102.5	100		f1-01	1	
112.5	110		f1-02	2	108.9286
107.5	105		f1-02	2	
117.5	115		f1-02	2	
107.5	105		f1-02	2	
102.5	100		f1-02	2	
107.5	105		f1-02	2	
107.5	105		f1-02	2	
112.5	110		f1-03	3	110
117.5	115		f1-03	3	
102.5	100		f1-03	3	
107.5	105		f1-03	3	
107.5	105		f1-03	4	114.1667
127.5	125		f1-03	4	
107.5	105		f1-03	4	
122.5	120		f1-04	5	117.5
112.5	110		f1-04	5	
122.5	120		f1-04	5	
117.5	115		f1-04	5	
117.5	115		f1-04	5	
112.5	110		f1-04	5	
112.5	110		f1-05	6	110
107.5	105		f1-05	6	
102.5	100		f1-06		

thin section	chip	fracture Xloc	aperture	avg temp	fracname
10jh10c	1		17.02	107.8846	C2
temp	lowrange	hirange	area	FIA	FIA avg
97.5	95		f2-07	9	110
122.5	120		f2-07	9	
117.5	115		f2-07	9	
102.5	100		f2-07	9	
107.5	105		f2-04		
102.5	100		f2b-001		
102.5	100		f2b-01	1	103.75
97.5	95		f2b-01	1	
92.5	90		f2b-01	1	
122.5	120		f2b-01	1	
112.5	110		f2b-02	2	112.5
107.5	105		f2b-02	2	
117.5	115		f2b-02	2	

thin section	chip	fracture Xloc	aperture	avg temp	fracname
10jh10c	1		11.54	110.0714	C3
temp	lowrange	hirange	area	FIA	FIA avg
102.5	100		f3-01	1	104.1667
97.5	95		f3-01	1	
112.5	110		f3-01	1	
122.5	120		f3-04	2	130
122.5	120		f3-04	2	
150		>140	f3-04	2	
127.5	125		f3-04	2	
127.5	125		f3-04	2	
127.5	125		f3-04	2	
150		>140	f3-04	2	
137.5	135		f3-04	2	
137.5	135		f3-04	2	
137.5	135		f3-04	2	
150		>140	f3-04	2	
150		>140	f3-04	2	
92.5	90		f3-04	2	
87.5	85		f3-04	2	
87.5	85		f3-04	3	87.5
87.5	85		f3-04	3	
102.5	100		f3-04	4	110
117.5	115		f3-04	4	
97.5	95		f3-05	5	97.5
97.5	95		f3-05	5	
102.5	100		f3-05	5	
97.5	95		f3-05	5	
97.5	95		f3-05	5	
92.5	90		f3-05	5	
87.5	85		f3-07	6	85
87.5	85		f3-07	6	
82.5	80		f3-07	6	
82.5	80		f3-07	6	
97.5	95		f3-02		
122.5	120		f3-04		
92.5	90		f3-04		
87.5	85		f3-06		

thin section	chip	fracture Xloc	aperture	avg temp	fracname
10jh10c	2		61.91	102.4038	C4
temp	lowrange	hirange	area	FIA	FIA avg
117.5	115		f1-05	1	113.75
112.5	110		f1-05	1	
112.5	110		f1-05	1	
112.5	110		f1-05	1	
87.5	85		f1-05	2	94.5
102.5	100		f1-05	2	
97.5	95		f1-05	2	
87.5	85		f1-05	2	
97.5	95		f1-05	2	
92.5	90		f1-06	3	90.83333
92.5	90		f1-06	3	
87.5	85		f1-06	3	
97.5	95		f1-06a	4	105
112.5	110		f1-06a	4	
			f1-03		
87.5	85		f1-03		
97.5	95		f1-03		
92.5	90		f1-03		
92.5	90		f1-03		
102.5	100		f1-03		
140		>135	f1-04		
140		>135	f1-04		
140		>135	f1-04		
112.5	110		f1-05		
82.5	80		f1-05		
82.5	80		f1-05		
82.5	80		f1-06		

thin section	chip	fracture Xloc	aperture	avg temp	fracname
10jh10c	1		32.1	103.869	C5
temp	lowrange	hirange	area	FIA	FIA avg
97.5	95		f2c-01		
97.5	95		f2c-01		
97.5	95		f2-03	1	105
112.5	110		f2-03	1	
112.5	110		f2-05r	2	108.5
112.5	110		f2-05r	2	
107.5	105		f2-05r	2	
107.5	105		f2-05r	2	
102.5	100		f2-05r	2	
102.5	100		f2-05r	3	97.5
92.5	90		f2-05r	3	
107.5	105		f2-05r		
92.5	90		f2-05r	4	100.8333
112.5	110		f2-05r	4	
97.5	95		f2-05r	4	
102.5	100		f2-05r	5	100.2778
102.5	100		f2-05r	5	
102.5	100		f2-05r	5	
97.5	95		f2-05r	5	
97.5	95		f2-05r	5	
97.5	95		f2-05r	5	
97.5	95		f2-05r	5	
97.5	95		f2-05r	5	
107.5	105		f2-05r	5	
97.5	95		f2-05r	6	115
92.5	90		f2-05r	6	
155		>145	f2-05r	6	
102.5	100		f2-06	7	110.8333
107.5	105		f2-06	7	
107.5	105		f2-06	7	
112.5	110		f2-06	7	
117.5	115		f2-06	7	
117.5	115		f2-06	7	
102.5	100		f2-06	8	101.25
97.5	95		f2-06	8	
107.5	105		f2-06	8	
97.5	95		f2-06	8	
92.5	90		f2-03		
107.5	105		f2-05		
112.5	110		f2-05		
87.5	85		f2-08		
92.5	90		f2-08		

thin section	chip	fracture Xloc	aperture	avg temp	fracname
10jh10c	1			108.125	C6

temp	lowrange	hirange	area	FIA	FIA avg
107.5	105		f2-01	1	100
92.5	90		f2-01	1	
102.5	100		f2-01	2	114.1667
112.5	110		f2-01	2	
127.5	125		f2-01	2	
127.5	125		f2-02	3	107.5
102.5	100		f2-02	3	
92.5	90		f2-02	3	

thin section	chip	fracture Xloc	aperture	avg temp	fracname
10JH10D	1		4.39	90.935	D2
temp	lowrange	hirange	area	FIA	FIA avg
98.9	97.4	100.4	1		
79.3			2a	1	87.025
94.75	93.8	95.7	2a	1	
88.7	87.4	90	2b	2	90.91429
96.6	95.7	97.5	2b	2	
97.2			2b	2	
90.55	89	92.1	2b	2	
83.75	82.4	85.1	2b	2	
86.05	84.1	88	2b	2	
93.55	92.1	95	2b	2	

thin section	chip	fracture Xloc	aperture	avg temp	fracname
10jh10e	1a		3.61	125.5761	E1
temp	lowrange	hirange	area	FIA	FIA avg
137.5	135		f1-01	1	139.8684
137.5	135		f1-01	1	
142.5	140		f1-01	1	
137.5	135		f1-01	1	
137.5	135		f1-01	1	
112.5	110		f1-01	1	
142.5	140		f1-01	1	
137.5	135		f1-01	1	
137.5	135		f1-01	1	
87.5	85		f1-01	1	
132.5	130		f1-01	1	
142.5	140		f1-01	1	
142.5	140		f1-01	1	
137.5	135		f1-01	1	
155		>145	f1-01	1	
155		>145	f1-01	1	
155		>145	f1-01	1	
142.5	140		f1-01	1	
132.5	130		f1-01	1	
142.5	140		f1-01	1	
137.5	135		f1-01	1	
137.5	135		f1-01	1	
142.5	140		f1-01	1	
112.5	110		f1-01	1	
142.5	140		f1-01	1	
142.5	140		f1-01a	1	
142.5	140		f1-01a	1	
142.5	140		f1-01a	1	
142.5	140		f1-01a	1	
142.5	140		f1-01a	1	
155		>145	f1-01a	1	
142.5	140		f1-01a	1	
137.5	135		f1-01a	1	
137.5	135		f1-01a	1	
142.5	140		f1-01a	1	
142.5	140		f1-01a	1	
142.5	140		f1-01a	1	
142.5	140		f1-01a	1	
142.5	140		f1-01a	1	
142.5	140		f1-01a	1	
155		>145	f1-01a	1	
142.5	140		f1-01a	1	
137.5	135		f1-01a	1	
137.5	135		f1-01a	1	
142.5	140		f1-01a	1	
155		>145	f1-01a	1	
132.5	130		f1-01a	1	
142.5	140		f1-01a	1	
142.5	140		f1-01a	1	

142.5	140		f1-01a	1	
142.5	140		f1-01a	1	
142.5	140		f1-01a	1	
142.5	140		f1-01a	1	
142.5	140		f1-01a	1	
137.5	135		f1-01a	1	
137.5	135		f1-01a	1	
137.5	135		f1-01a	1	
127.5	125		f1-01	2	127.1667
92.5	90		f1-01	2	
137.5	135		f1-01	2	
127.5	125		f1-01	2	
117.5	115		f1-01	2	
142.5	140		f1-01	2	
137.5	135		f1-01	2	
127.5	125		f1-01	2	
142.5	140		f1-01	2	
142.5	140		f1-01	2	
137.5	135		f1-01	2	
127.5	125		f1-01	2	
127.5	125		f1-01	2	
97.5	95		f1-01	2	
122.5	120		f1-01a	2	
132.5	130		f1-01	3	128.75
132.5	130		f1-01	3	
137.5	135		f1-01	3	
112.5	110		f1-01	3	
137.5	135		f1-01	4	141.875
142.5	140		f1-01a	4	
155		>145	f1-01a	4	
155		>145	f1-01a	4	
155		>145	f1-01a	4	
155		>145	f1-01a	4	
155		>145	f1-01a	4	
142.5	140		f1-01a	4	
97.5	95		f1-01a	4	
155		>145	f1-01a	4	
137.5	135		f1-01a	4	
137.5	135		f1-01a	4	
137.5	135		f1-01a	4	
137.5	135		f1-01a	4	
142.5	140		f1-01a	4	
137.5	135		f1-01a	4	
137.5	135		f1-01a	4	
137.5	135		f1-01a	4	
142.5	140		f1-01a	4	
142.5	140		f1-01a	4	
142.5	140		f1-01a	4	

142.5	140		f1-01a	4	
142.5	140		f1-01a	4	
137.5	135		f1-01a	4	
142.5	140		f1-02	5	114.2308
97.5	95		f1-02	5	
102.5	100		f1-02	5	
117.5	115		f1-02	5	
127.5	125		f1-02	5	
87.5	85		f1-02	5	
155		>145	f1-02	5	
92.5	90		f1-02	5	
112.5	110		f1-02	5	
117.5	115		f1-02	5	
87.5	85		f1-02	5	
107.5	105		f1-02	5	
137.5	135		f1-02	5	
97.5	95		f1-03	6	97.5
97.5	95		f1-03	6	
87.5	85		f1-04	7	99.5
107.5	105		f1-04	7	
92.5	90		f1-04	7	
112.5	110		f1-04	7	
97.5	95		f1-04	7	
117.5	115		f1-05	8	117.5
112.5	110		f1-05	8	
122.5	120		f1-05	8	
117.5	115		f1-05	9	119.8333
112.5	110		f1-05	9	
122.5	120		f1-05	9	
117.5	115		f1-05	9	
117.5	115		f1-05	9	
112.5	110		f1-05	9	
132.5	130		f1-05	9	
127.5	125		f1-05	9	
117.5	115		f1-05	9	
137.5	135		f1-05	9	
117.5	115		f1-05	9	
117.5	115		f1-05	9	
82.5	80		f1-05	9	
122.5	120		f1-05	9	
142.5	140		f1-05	9	
117.5	115		f1-05	10	115.8333
112.5	110		f1-05	10	
117.5	115		f1-05	10	
112.5	110		f1-06	11	118.4259
107.5	105		f1-06	11	
137.5	135		f1-06	11	
137.5	135		f1-06a	11	
137.5	135		f1-06a	11	
117.5	115		f1-06a	11	
117.5	115		f1-06a	11	
117.5	115		f1-06a	11	

117.5	115	f1-06a	11	
142.5	140	f1-06a	11	
122.5	120	f1-06a	11	
112.5	110	f1-06a	11	
127.5	125	f1-06a	11	
107.5	105	f1-06a	11	
117.5	115	f1-06a	11	
97.5	95	f1-06a	11	
117.5	115	f1-06a	11	
122.5	120	f1-06a	11	
137.5	135	f1-06a	11	
137.5	135	f1-06a	11	
117.5	115	f1-06a	11	
92.5	90	f1-06a	11	
127.5	125	f1-06a	11	
107.5	105	f1-06a	11	
112.5	110	f1-06a	11	
107.5	105	f1-06a	11	
87.5	85	f1-06a	11	
132.5	130	f1-06	12	132.5
132.5	130	f1-06	12	
122.5	120	f1-07	13	117.5
112.5	110	f1-07	13	
117.5	115	f1-07	13	
137.5	135	f1-07	13	
107.5	105	f1-07	13	
122.5	120	f1-07	13	
132.5	130	f1-07	13	
117.5	115	f1-07	13	
117.5	115	f1-07	13	
137.5	135	f1-07	13	
112.5	110	f1-07	13	
112.5	110	f1-07	13	
87.5	85	f1-07	13	
112.5	110	f1-07	13	
117.5	115	f1-07	13	
112.5	110	f1-07	13	
112.5	110	f1-07	14	120.3571
117.5	115	f1-07	14	
117.5	115	f1-07	14	
122.5	120	f1-07	14	
117.5	115	f1-07	14	
117.5	115	f1-07	14	
137.5	135	f1-07	14	
102.5	100	f1-09	15	104.0789
117.5	115	f1-09	15	
97.5	95	f1-09	15	
87.5	85	f1-09	15	

107.5	105	f1-09	15
102.5	100	f1-09	15
92.5	90	f1-09	15
82.5	80	f1-09	15
97.5	95	f1-09	15
117.5	115	f1-09	15
97.5	95	f1-09	15
137.5	135	f1-09	15
107.5	105	f1-09	15
107.5	105	f1-09	15
97.5	95	f1-09	15
102.5	100	f1-09	15
87.5	85	f1-09	15
117.5	115	f1-09	15
117.5	115	f1-09	15
127.5	125	f1-01	2 or 3
117.5	115	f1-01	
142.5	140	f1-01a	
87.5	85	f1-04	
142.5	140	f1-06a	
122.5	120	f1-06a	
142.5	140	f1-06a	
117.5	115	f1-06a	
117.5	115	f1-07	
142.5	140	f1-07	
132.5	130	f1-07	
122.5	120	f1-07	
137.5	135	f1-07	
132.5	130	f1-07	
137.5	135	f1-07	
117.5	115	f1-08	
102.5	100	f1-08	
102.5	100	f1-09	

thin section	chip	fracture Xloc	aperture	avg temp	fracname
10jh10e	1b		2.66	113.125	E2
temp	lowrange	hirange	area	FIA	FIA avg
112.5	110		f2-01	1	112.5
112.5	110		f2-01	1	
112.5	110		f2-01	1	
87.5	85		f2-02	2	116.1364
112.5	110		f2-02	2	
140		>130	f2-02	2	
102.5	100		f2-02	2	
102.5	100		f2-02	2	
117.5	115		f2-02	2	
122.5	120		f2-02	2	
122.5	120		f2-02	2	
140		>130	f2-02	2	
107.5	105		f2-02	2	
122.5	120		f2-02	2	
102.5	100		f2-01		
92.5	90		f2-01		

thin section	chip	fracture Xloc	aperture	avg temp	fracname
10jh10e	1b		6.14	106.2	E3
temp	lowrange	hirange	area	FIA	FIA avg
107.5	105		f2-03	3	106.2
87.5	85		f2-03	3	
117.5	115		f2-03	3	
107.5	105		f2-03	3	
97.5	95		f2-03	3	
112.5	110		f2-03	3	
122.5	120		f2-03	3	
97.5	95		f2-03	3	
97.5	95		f2-03	3	
102.5	100		f2-03	3	
97.5	95		f2-03	3	
102.5	100		f2-03	3	
102.5	100		f2-03	3	
107.5	105		f2-03	3	
140		>130	f2-03	3	
122.5	120		f2-03	3	
107.5	105		f2-03	3	
127.5	125		f2-03	3	
117.5	115		f2-03	3	
87.5	85		f2-03	3	
87.5	85		f2-03	3	
97.5	95		f2-03	3	
107.5	105		f2-03	3	
92.5	90		f2-03	3	
107.5	105		f2-03	3	

thin section	chip	fracture Xloc	aperture	avg temp	fracname
10jh10e	1c		102.05	109.3217	E4
temp	lowrange	hirange	area	FIA	FIA avg
			f3-01		
127.5	125		f3-01	1	106.625
97.5	95		f3-01	1	
107.5	105		f3-01	1	
112.5	110		f3-01	1	
117.5	115		f3-01	1	
112.5	110		f3-01	1	
92.5	90		f3-01	1	
102.5	100		f3-01	1	
97.5	95		f3-01	1	
102.5	100		f3-01	1	
107.5	105		f3-01	1	
97.5	95		f3-01	1	
102.5	100		f3-01	1	
92.5	90		f3-01	1	
97.5	95		f3-01	1	
145		>135	f3-01	1	
97.5	95		f3-01	1	
102.5	100		f3-01	1	
112.5	110		f3-01	1	
107.5	105		f3-01	1	
117.5	115		f3-01	2	114.2188
145		>135	f3-01	2	
112.5	110		f3-01	2	
87.5	85		f3-01	2	
97.5	95		f3-01	2	
102.5	100		f3-01	2	
117.5	115		f3-01	2	
122.5	120		f3-01	2	
127.5	125		f3-01	2	
112.5	110		f3-01	2	
102.5	100		f3-01	2	
112.5	110		f3-01	2	
117.5	115		f3-01	2	
112.5	110		f3-01	2	
112.5	110		f3-01	2	
127.5	125		f3-01	2	
97.5	95		f3-01	3	106.4474
102.5	100		f3-01	3	
107.5	105		f3-01	3	
97.5	95		f3-01	3	
107.5	105		f3-01	3	
122.5	120		f3-01	3	
117.5	115		f3-01	3	
107.5	105		f3-01	3	
97.5	95		f3-01	3	
92.5	90		f3-01	3	
97.5	95		f3-01	3	
117.5	115		f3-01	3	

102.5	100	f3-01	3	
117.5	115	f3-01	3	
107.5	105	f3-01	3	
112.5	110	f3-01	3	
112.5	110	f3-01	3	
92.5	90	f3-01	3	
112.5	110	f3-01	3	
92.5	90	f3-01	4	100
92.5	90	f3-01	4	
97.5	95	f3-01	4	
117.5	115	f3-01	4	
112.5	110	f3-01	5	105
97.5	95	f3-01	5	
102.5	100	f3-02	6	111.3889
112.5	110	f3-02	6	
107.5	105	f3-02	6	
117.5	115	f3-02	6	
92.5	90	f3-02	6	
107.5	105	f3-02	6	
132.5	130	f3-02	6	
112.5	110	f3-02	6	
117.5	115	f3-02	6	
117.5	115	f3-02	7	122.5
127.5	125	f3-02	7	
107.5	105	f3-02	8	116.25
122.5	120	f3-02	8	
122.5	120	f3-02	8	
112.5	110	f3-02	8	
87.5	85	f3-02	9	93.5
87.5	85	f3-02	9	
87.5	85	f3-02	9	
82.5	80	f3-02	9	
122.5	120	f3-02	9	
102.5	100	f3-02	10	95
87.5	85	f3-02	10	
97.5	95	f3-02	10	
92.5	90	f3-02	10	
112.5	110	f3-02	11	120
122.5	120	f3-02	11	
117.5	115	f3-02	11	
127.5	125	f3-02	11	
97.5	95	f3-02	12	102.5
107.5	105	f3-02	12	
102.5	100	f3-02	12	
107.5	105	f3-02	13	100
92.5	90	f3-02	13	
112.5	110	f3-03	14	112.0455
107.5	105	f3-03	14	
122.5	120	f3-03	14	
122.5	120	f3-03	14	
102.5	100	f3-03	14	
117.5	115	f3-03	14	

102.5	100		f3-03	14	
92.5	90		f3-03	14	
122.5	120		f3-03	14	
122.5	120		f3-03	14	
107.5	105		f3-03	14	
107.5	105		f3-03	15	105
107.5	105		f3-03	15	
117.5	115		f3-03	15	
87.5	85		f3-03	15	
97.5	95		f3-01		
107.5	105		f3-01		
92.5	90		f3-01		
112.5	110		f3-01		
145		>135	f3-01		
132.5	130		f3-01		
117.5	115		f3-01		
97.5	95		f3-01		
92.5	90		f3-01		
145		>135	f3-02		
145		>135	f3-02		
127.5	125		f3-02		
145		>135	f3-02		
112.5	110		f3-02		
97.5	95		f3-03		
122.5	120		f3-03		
112.5	110		f3-03		
117.5	115		f3-03		
87.5	85		f3-03		
102.5	100		f3-03		

thin section	chip	fracture Xloc	aperture	avg temp	fracname
10jh10e	2a/b		15.72	113.8675	E5
temp	lowrange	hirange	area	FIA	FIA avg
102.5	100		FL-01		
122.5	120		FL-01	1	110
122.5	120		FL-01	1	
97.5	95		FL-01	1	
117.5	115		FL-01	1	
102.5	100		FL-01	1	
102.5	100		FL-01	1	
112.5	110		FL-01	1	
102.5	100		FL-01	1	
112.5	110		FL-01	2	116.0938
112.5	110		FL-01	2	
112.5	110		FL-01	2	
117.5	115		FL-01	2	
107.5	105		FL-01	2	
122.5	120		FL-01	2	
137.5	135		FL-01	2	
122.5	120		FL-01	2	
122.5	120		FL-01	2	
117.5	115		FL-01	2	
102.5	100		FL-01	2	
102.5	100		FL-01	2	
107.5	105		FL-01	2	
107.5	105		FL-01	2	
150		>140	FL-01	2	
102.5	100		FL-01	2	
107.5	105		FL-02	3	111.0714
102.5	100		FL-02	3	
112.5	110		FL-02	3	
117.5	115		FL-02	3	
107.5	105		FL-02	3	
117.5	115		FL-02	3	
112.5	110		FL-02	3	
132.5	130		FL-02	4	127.5
122.5	120		FL-02	4	
102.5	100		FL-02	5	112.8947
112.5	110		FL-02	5	
107.5	105		FL-02	5	
107.5	105		FL-02	5	
102.5	100		FL-02	5	
107.5	105		FL-02	5	
117.5	115		FL-02	5	
102.5	100		FL-02	5	
97.5	95		FL-02	5	
117.5	115		FL-02	5	
102.5	100		FL-02	5	
127.5	125		FL-02	5	
112.5	110		FL-02	5	
117.5	115		FL-02	5	
102.5	100		FL-02	5	

107.5	105		FL-02	5	
127.5	125		FL-02	5	
150		>140	FL-02	5	
122.5	120		FL-02	5	
122.5	120		FL-03	6	121.25
112.5	110		FL-03	6	
127.5	125		FL-03	6	
117.5	115		FL-03	6	
117.5	115		FL-03	6	
127.5	125		FL-03	6	
127.5	125		FL-03	6	
117.5	115		FL-03	6	
92.5	90		FL-03	7	100.8333
102.5	100		FL-03	7	
107.5	105		FL-03	7	
122.5	120		FL-03	8	107.5
92.5	90		FL-03	8	
127.5	125		FL-03	9	130.9615
145		>135	FL-03	9	
145		>135	FL-03	9	
145		>135	FL-03	9	
145		>135	FL-03	9	
145		>135	FL-03	9	
107.5	105		FL-03	9	
145		>135	FL-03	9	
145		>135	FL-03	9	
145		>135	FL-03	9	
112.5	110		FL-03	9	
102.5	100		FL-03	9	
92.5	90		FL-03	9	
107.5	105		FL-04	10	104.5
112.5	110		FL-04	10	
102.5	100		FL-04	10	
97.5	95		FL-04	10	
92.5	90		FL-04	10	
102.5	100		FL-04	10	
102.5	100		FL-04	10	
112.5	110		FL-04	10	
102.5	100		FL-04	10	
112.5	110		FL-04	10	
112.5	110		FL-04	11	118.2143
112.5	110		FL-04	11	
122.5	120		FL-04	11	
112.5	110		FL-04	11	
117.5	115		FL-04	11	
117.5	115		FL-04	11	
132.5	130		FL-04	11	
107.5	105		FL-05	12	106.25
102.5	100		FL-05	12	
97.5	95		FL-05	12	
82.5	80		FL-05	12	
97.5	95		FL-05	12	

107.5	105	FL-05	12
112.5	110	FL-05	12
122.5	120	FL-05	12
107.5	105	FL-05	12
112.5	110	FL-05	12
112.5	110	FL-05	12
112.5	110	FL-05	12
117.5	115	FL-01	
107.5	105	FL-01	
92.5	90	FL-01	
122.5	120	FL-02	
87.5	85	FL-02	
127.5	125	FL-02	
107.5	105	FL-02	
77.5	75	FL-02	
127.5	125	FL-02	

thin section	chip	fracture Xloc	aperture	avg temp	fracname
10jh10e	2a/b		3.49	106.5385	E6
temp	lowrange	hirange	area	FIA	FIA avg
102.5	100		f1-01	1	102.5
102.5	100		f1-01	1	
102.5	100		f1-01	1	
102.5	100		f1-01	1	
112.5	110		f1-02	2	107.5
102.5	100		f1-02	2	
107.5	105		f1-03	3	108.5714
87.5	85		f1-03	3	
97.5	95		f1-03	3	
102.5	100		f1-03	3	
102.5	100		f1-03	3	
145		>135	f1-03	3	
117.5	115		f1-03	3	

thin section	chip	fracture Xloc	aperture	avg temp	fracname
10jh10e	3		6.21	102.9348	E7
temp	lowrange	hirange	area	FIA	FIA avg
97.5	95		F1-01		
92.5	90		F1-01		
107.5	105		F1-01		
102.5	100		F1-01		
97.5	95		F1-01		
87.5	85		F1-02		
97.5	95		F1-02	1	104.8529
107.5	105		F1-02	1	
107.5	105		F1-02	1	
102.5	100		F1-02	1	
102.5	100		F1-02	1	
107.5	105		F1-02	1	
112.5	110		F1-02	1	
107.5	105		F1-02	1	
102.5	100		F1-02	1	
112.5	110		F1-02	1	
107.5	105		F1-02	1	
102.5	100		F1-02	1	
107.5	105		F1-02	1	
112.5	110		F1-02	1	
102.5	100		F1-02	1	
97.5	95		F1-02	1	
92.5	90		F1-02	1	

thin section	chip	fracture Xloc	aperture	avg temp	fracname
10jh10e	3		11.08	101.5	E8
temp	lowrange	hirange	area	FIA	FIA avg
112.5	110		F2-02	2	105.8333
107.5	105		F2-02	2	
97.5	95		F2-02	2	
102.5	100		F2-02		
87.5	85		F2-02		

thin section	chip	fracture Xloc	aperture	avg temp	fracname
10jh10e	3		8.79	96.25	E9

temp	lowrange	hirange	area	FIA	FIA avg
97.5	95		F4-01	1	92.5
92.5	90		F4-01	1	
97.5	95		F4-01	1	
87.5	85		F4-01	1	
87.5	85		F4-01	1	
102.5	100		F4-01		
102.5	100		F4-02	2	102.5
102.5	100		F4-02	2	

thin section	chip	fracture Xloc	aperture	avg temp	fracname
10jh10e	3		18.48	125.8333	E10
temp	lowrange	hirange	area	FIA	FIA avg
92.5	90		F2-01	1	114.2857
97.5	95		F2-01	1	
92.5	90		F2-01	1	
145	135	x	F2-01	1	
82.5	80		F2-01	1	
145	135	x	F2-01	1	
145	135	x	F2-01	1	
145	135	x	F3-01	2	126.8182
132.5	130		F3-01	2	
117.5	115		F3-01	2	
127.5	125		F3-01	2	
132.5	130		F3-01	2	
127.5	125		F3-01	2	
132.5	130		F3-01	2	
132.5	130		F3-01	2	
112.5	110		F3-01	2	
112.5	110		F3-01	2	
122.5	120		F3-01	2	
145	135	x	F3-01	3	132.1875
132.5	130		F3-01	3	
145	135	x	F3-01	3	
127.5	125		F3-01	3	
145	135	x	F3-01	3	
102.5	100		F3-01	3	
127.5	125		F3-01	3	
132.5	130		F3-01	3	
145	135	x	F3-01		

thin section	chip	fracture Xloc	aperture	avg temp	fracname
10jh10e	3		8.32	119.6875	E11
temp	lowrange	hirange	area	FIA	FIA avg
112.5	110		F5-01	1	113.3333
112.5	110		F5-01	1	
122.5	120		F5-01	1	
112.5	110		F5-01	1	
112.5	110		F5-01	1	
107.5	105		F5-01	1	
145	135	x	F5-01	2	138.75
132.5	130		F5-01	2	

thin section	chip	fracture Xloc	aperture	avg temp	fracname
10jh10f	3		23.99	110.9167	F1
temp	lowrange	hirange	area	FIA	FIA avg
92.5	90		8	1	100.8333
112.5	110		8	1	
97.5	95		8	1	
127.5	125		8		
127.5	125		8	2	99.16667
87.5	85		8	2	
92.5	90		8	2	
102.5	100		8	2	
87.5	85		8	2	
97.5	95		8	2	
97.5	95		8	3	115
107.5	105		8	3	
112.5	110		8	3	
122.5	120		8	3	
107.5	105		8	3	
132.5	130		8	3	
122.5	120		8	3	
117.5	115		8	3	
112.5	110		8	3	
112.5	110		8	3	
107.5	105		8	3	
127.5	125		8	3	
117.5	115		8	4	111.0714
112.5	110		8	4	
127.5	125		8	4	
97.5	95		8	4	
132.5	130		8	4	
107.5	105		8	4	
117.5	115		8	4	
117.5	115		8	4	
102.5	100		8	4	
87.5	85		8	4	
112.5	110		8	4	
112.5	110		8	4	
107.5	105		8	4	
102.5	100		8	4	
97.5	95		8	5	119.5
117.5	115		8	5	
137.5	135	x	8	5	
122.5	120		8	5	
122.5	120		8	5	
102.5	100		9	6	112.5
117.5	115		9	6	
112.5	110		9	6	
112.5	110		9	6	
117.5	115		9	6	
107.5	105		9a	7	109.6429
117.5	115		9a	7	
97.5	95		9a	7	

87.5	85	9a	7
117.5	115	9a	7
112.5	110	9a	7
107.5	105	9a	7
117.5	115	9a	7
122.5	120	9a	7
112.5	110	9a	7
107.5	105	9a	7
117.5	115	9a	7
107.5	105	9a	7
102.5	100	9a	

thin section	chip	fracture Xloc	aperture	avg temp	fracname
10jh10f	3 and 4		37.44	101.2712	F2
temp	lowrange	hirange	area	FIA	FIA avg
102.5	100		10	1	103
97.5	95		10	1	
107.5	105		10	1	
107.5	105		10	1	
97.5	95		10	1	
87.5	85		10a	1	
102.5	100		10a	1	
107.5	105		10a	1	
107.5	105		10a	1	
112.5	110		10a	1	
92.5	90		10	2	97.5
102.5	100		10a	2	
97.5	95		10	3	94.16667
92.5	90		10	3	
92.5	90		10a	3	
97.5	95		11	4	102.5
107.5	105		11	4	
102.5	100		11	5	100
97.5	95		11	5	
70	x	75	12	6	90.625
92.5	90		12	6	
87.5	85		12	6	
87.5	85		12	6	
102.5	100		12	6	
92.5	90		12	6	
92.5	90		12	6	
92.5	90		12	6	
92.5	90		12	6	
92.5	90		12	6	
92.5	90		12	6	
92.5	90		12	6	
87.5	85		12		
97.5	95		12		
92.5	90		12		
77.5	75		12		
107.5	105		12a	7	116.5625
107.5	105		12a	7	
127.5	125		12a	7	
117.5	115		12a	7	
107.5	105		12a	7	
117.5	115		12a	7	
117.5	115		12a	7	
122.5	120		12a	7	
122.5	120		12a	7	
107.5	105		12a	7	
107.5	105		12a	7	
122.5	120		12a	7	
122.5	120		12a	7	
112.5	110		12a	7	

132.5	130	x	12a		7	
112.5	110		12a		7	
102.5	100			13	8	94.64286
87.5	85			13	8	
92.5	90			13	8	
97.5	95			13	8	
92.5	90			13	8	
97.5	95			13	8	
92.5	90			13	8	
92.5	90			13		

thin section	chip	fracture Xloc	aperture	avg temp	fracname
10jh10f	1 and 2		8	114.7222	F3
temp	lowrange	hirange	area	FIA	FIA avg
122.5	120		5	1	122.5
127.5	125		5	1	
127.5	125		5	1	
117.5	115		5	1	
132.5	130		5	1	
102.5	100		5	1	
122.5	120		5	1	
117.5	115		5	1	
132.5	130		5	1	
122.5	120		5	1	
122.5	120		5	1	
122.5	120		5	1	
122.5	120		5	1	
122.5	120		5	1	
112.5	110		5	1	
127.5	125		5	1	
127.5	125		5	1	
122.5	120		5	1	
107.5	105		5	2	110.2083
112.5	110		5	2	
102.5	100		5	2	
102.5	100		5	2	
102.5	100		5	2	
112.5	110		5	2	
117.5	115		5	2	
92.5	90		5	2	
102.5	100		5	2	
145	135	x	5	2	
127.5	125		5	2	
97.5	95		5	2	
145	135	x	5		
145	135	x	5		
107.5	105		6	3	111.875
102.5	100		6	3	
102.5	100		6	3	
112.5	110		6	3	
102.5	100		6	3	
117.5	115		6	3	
117.5	115		6	3	
132.5	130		6	3	
97.5	95		6	4	103.5
102.5	100		6	4	
102.5	100		6	4	
102.5	100		6	4	
112.5	110		6	4	
145	135	x	6	5	145
145	135	x	6	5	
97.5	95		7		
97.5	95		7	6	107.3333

102.5	100		7	6
145	135	x	7	6
107.5	105		7	6
102.5	100		7	6
102.5	100		7	6
107.5	105		7	6
102.5	100		7	6
122.5	120		7	6
107.5	105		7	6
97.5	95		7	6
102.5	100		7	6
102.5	100		7	6
102.5	100		7	6
107.5	105		7	6

thin section	chip	fracture Xloc	aperture	avg temp	fracname
10jh10f	1 and 2		4.1	113.0814	F4
temp	lowrange	hirange	area	FIA	FIA avg
117.5	115		1	1	114
117.5	115		1	1	
117.5	115		1	1	
102.5	100		1	1	
122.5	120		1	1	
112.5	110		1	1	
112.5	110		1	1	
112.5	110		1	1	
112.5	110		1	1	
112.5	110		1	1	
122.5	120		1	2	125.8333
127.5	125		1	2	
127.5	125		1	2	
82.5	80		2	3	98.92857
102.5	100		2	3	
107.5	105		2	3	
97.5	95		2	3	
112.5	110		2	3	
82.5	80		2	3	
107.5	105		2	3	
122.5	120		2		
122.5	120		3	4	111.875
112.5	110		3	4	
112.5	110		3	4	
122.5	120		3	4	
107.5	105		3	4	
107.5	105		3	4	
107.5	105		3	4	
102.5	100		3	4	
117.5	115		4	5	116.7857
107.5	105		4	5	
132.5	130		4	5	
117.5	115		4	5	
107.5	105		4	5	
117.5	115		4	5	
107.5	105		4	5	
122.5	120		4	5	
122.5	120		4	5	
112.5	110		4	5	
117.5	115		4	5	
112.5	110		4	5	
122.5	120		4	5	
117.5	115		4	5	

References

Abramowitz, M. and Stegun, I.A., 1965. Handbook of Mathematical Functions: with Formulas, Graphs, and Mathematical Tables. New York: Dover, 1046 p.

Aceñolaza, F.G., Buatois, L.A., Mángano, M.G., Esteban, S.B., Tortello, M.F., and Aceñolaza, G.F., 1999. Cámbrico y Ordovícico del noroeste Argentino. Instituto de Geología y Recursos Minerales Anales 29: Geología Argentina, 169-187.

Albert, R. and Barabási, A.-L., 2002. Statistical mechanics of complex networks. Reviews of Modern Physics 74, 47-97.

Amaral, L.A.N., Scala, A., Barthélémy, M., and Stanley, H.E., 2000. Classes of small-world networks. Proceedings of the National Academy of Sciences 97, 11,149-11,152.

Anders, M.H. and Wiltschko, D.V., 1994. Microfracturing, paleostress and the growth of faults. Journal of Structural Geology 16 (6), 795-815.

Aviles, C.A., Scholz, C.H., and Boatwright, J., 1987. Fractal analysis applied to characteristic segments of the San Andreas Fault. Journal of Geophysical Research 92 (B1), 331-344.

Aydin, A., 2000. Fractures, faults, and hydrocarbon entrapment, migration and flow. Marine and Petroleum Geology 17, 797-814.

Baecher, G.B., and Lanney, N.A., 1978. Trace length biases in joint surveys, *in* 19th U.S. Symposium on Rock Mechanics: Reno, University of Nevada, 56-65.

Baecher, G.B., 1980. Progressively censored sampling of rock joint traces. Mathematical Geology 12 (1), 33-40.

Bahat, D., Rabinovitch, A., and Frid, V., 2008. Correlation of plume morphologies on joint surfaces with their fracture mechanic implications. Geological Magazine 145 (5), 733-744.

Bai, T., Pollard, D.D., and Gao, H., 2000. Explanation for fracture spacing in layered materials. Nature 403, 753-756.

Bak, P., Tang, C., and Wiesenfeld, K., 1987. Self-organized criticality: an explanation of 1/f noise. Physical Review Letters 59 (4), 381-384.

Ballantyne, C.K., McCarroll, D., Nesje, A., Dahl, S.O., and Stone, J.O., 1998. The last ice sheet in north-west Scotland: Reconstruction and implications. Quaternary Science Reviews 17, 1149-1184.

Barabási, A.-L. and Albert, R., 1999. Emergence of scaling in random networks. Science 286, 509-512.

Barboza-Gudiño, J.R., Orozco-Esquivel, M.T., Gómez-Anguiano, M., and Zavala-Monsiváis, A., 2008. The early Mesozoic volcanic arc of western North America in northeastern Mexico. Journal of South American Earth Sciences 25, 49-63.

Barboza-Gudiño, J.R., Zavala-Monsiváis, A., Venegas-Rodríguez, G., and Barajas-Nigoche, L.D., 2010. Late Triassic stratigraphy and facies from northeastern Mexico: Tectonic setting and provenance. Geosphere 6, 621-640.

Barton, C.A. and Zoback, M.D., 1992. Self-similar distribution of macroscopic fractures at depth in crystalline rock in the Cajon Pass scientific drill hole. Journal of Geophysical Research 97 (B4), 5181-5200.

Becker, S.P., Eichhubl, P., Laubach, S.E., Reed, R.M., Lander, R.H., and Bodnar, R.J., 2010. A 48 m. y. history of fracture opening, temperature, and fluid pressure: Cretaceous Travis Peak Formation, East Texas basin. GSA Bulletin 122, 1081-1093.

Bergbauer, S. and Pollard, D.D., 2004. A new conceptual fold-fracture model including prefolding joints, based on the Emigrant Gap anticline, Wyoming. GSA Bulletin 116 (3/4), 294-307.

Berkowitz, B. and Hadad, A., 1997. Fractal and multifractal measures of natural and synthetic fracture networks. Journal of Geophysical Research 102 (B6), 12,205-12,218.

Bernet, M. and Bassett, K., 2005. Provenance analysis by single-quartz-grain SEM-CL/optical microscopy. Journal of Sedimentary Research 75 (3), 492-500.

Bignall, G., Sekine, K., and Tsuchiya, N., 2004. Fluid-rock interaction processes in the Te Kopia geothermal field (New Zealand) revealed by SEM-CL imaging. Geothermics 33, 615-635.

Bodnar, R.J., 1993. Revised equation and table for determining the freezing-point depression of H_2O-NaCl solutions. Geochimica et Cosmochimica Acta 57, 683-684.

Bohnenstiehl, D.R. and Kleinrock, M.C., 1999. Faulting and fault scaling on the median valley floor of the trans-Atlantic geotraverse (TAG) segment, ~26°N on the Mid-Atlantic Ridge. Journal of Geophysical Research 104 (B12) 29,351-29,364.

Bonnet, E., Bour, O., Odling, N.E., Davy, P., Main, I., Cowie, P., and Berkowitz, B., 2001. Scaling of fracture systems in geological media. Reviews of Geophysics 39 (3), 347-383.

Borgos, H.G., Cowie, P.A., and Dawers, N.H., 2000. Practicalities of extrapolating one-dimensional fault and fracture size-frequency distributions to higher-dimensional samples. Journal of Geophysical Research 105 (B12), 28,377-28,391.

Brantley, S., Evans, B., Hickman, S.H., and Crerar, D.A., 1990. Healing of microcracks in quartz: Implications for fluid flow. Geology 18, 136-139.

Brenner, S.L. and Gudmundsson, A., 2004. Arrest and aperture variation of hydrofractures in layered reservoirs. *In* Cosgrove, J.W. and Engelder, T., *eds*., The initiation, propagation, and arrest of joints and other fractures. Geological Society, London, Special Publications 231, 117-128.

Burnett, W. and Fomel, S., 2011. Azimuthally anisotropic 3D velocity continuation. International Journal of Geophysics, doi:10.1155/2011/484653.

Caputo, R. and Hancock, P.L., 1999. Crack-jump mechanism and its implications for stress cyclicity during extension fracturing. Geodynamics 27, 45-60.

Carrera, N. and Muñoz, J.A., 2008. Thrusting evolution in the southern Cordillera Oriental (northern Argentine Andes): Constraints from growth strata. Tectonophysics 459, 107-122.

Cawood, P.A., Nemchin, A.A., Strachan, R.A., Kinny, P.D., and Loewy, S., 2004. Laurentian provenance and an intracratonic tectonic setting for the Moine Supergroup, Scotland, constrained by detrital zircons from the Loch Eli and Glen Urquhart successions. Journal of the Geological Society, London 161, 861-874.

Cladouhos, T.T. and Marrett, R., 1996. Are fault growth and linkage models consistent with power law distributions of fault lengths? Journal of Structural Geology 18, 281-293.

Clark, M.B., Brantley, S.L., and Fisher, D.M., 1995. Power-law vein-thickness distributions and positive feedback in vein growth. Geology 23 (11), 975-978.

Clauset, A., Shalizi, C.R., and Newman, M.E.J., 2009. Power-law distributions in empirical data. SIAM Review 51 (4), 661-703.

Clayton, R.N., O'Neil, J.R., and Mayeda, T.K., 1972. Oxygen isotope exchange between quartz and water. Journal of Geophysical Research 77 (17), 3057-3067.

Coward, M.P., 1980. The Caledonian thrust and shear zones of N.W. Scotland. Journal of Structural Geology 2, 11-17.

Coward, M.P., 1984. The strain and textural history of thin-skinned tectonic zones: examples from the Assynt region of the Moine thrust zone, NW Scotland. Journal of Structural Geology 6, 89-99.

Cowie, P.A., Vanneste, C., and Sornette, D., 1993. Statistical physics model for the spatiotemporal evolution of faults. Journal of Geophysical Research 98 (B12), 21,809-21,821.

Cross, G.E., 2012. Evaporite deformation in the Sierra Madre Oriental, northeastern Mexico: Décollement kinematics in an evaporite-detached thin-skinned fold belt. Ph.D. dissertation, The University of Texas at Austin, 547 p.

D'Lemos, R.S., Kearsley, A.T., Pembroke, J.W., Watt, G.R., and Wright, P., 1997. Complex quartz growth histories in granite revealed by scanning cathodoluminescence techniques. Geological Magazine 134 (4), 549-552.

Darabi, M.H. and Piper, J.D.A., 2004. Paleomagnetism of the (Late Mesoproterozoic) Stoer Group, northwest Scotland: implications for diagenesis, age and relationship to the Grenville Orogeny. Geological Magazine 141 (1), 15-39.

Davis, M., 2005. The Tectonics of Tranquitas: A field study of rift through passive margin development and Laramide deformation in Triassic and Jurassic strata of the Sierra Madre Oriental, NE Mexico. Master's thesis, The University of Texas at Austin, 106 p.

Davy, P., Le Groc, R., Darcel, C., Bour, O., de Dreuzy, J.R., and Munier, R., 2010. A likely universal model of fracture scaling and its consequence for crustal hydromechanics. Journal of Geophysical Research 115, B10411, doi:10.1029/2009JB007043.

DeCelles, P.G., Carrapa, B., Horton, B.K., and Gehrels, G.E., 2011. Cenozoic foreland basin systems in the central Andes of northwestern Argentina: Implications for Andean geodynamics and modes of deformation. Tectonics 30, TC6013, doi:10.1029/2011TC002948.

Deeken, A., Sobel, E.R., Coutand, I., Haschke, M., Riller, U., and Strecker, M.R., 2006. Development of the southern Eastern Cordillera, NW Argentina, constrained by apatite fission track thermochronology: From early Cretaceous extension to middle Miocene shortening. Tectonics 25, TC6003, doi:10.1029/2005TC001894.

Dershowitz, W.S. and Herda, H.H., 1992. Interpretation of fracture spacing and intensity. Proceedings of the 32nd U.S. Rock Mechanics Symposium, Santa Fe, New Mexico, 757-766.

Deschamps, A., Tivey, M., Embley, R.W., and Chadwick, W.W., 2007. Quantitative study of the deformation at Southern Explorer Ridge using high-resolution bathymetric data. Earth and Planetary Science Letters 259, 1-17.

Diaz-Tushman, K., 2007. Fracture tectonics, fracture porosity evolution and structural diagenesis, Cambrian Eriboll Sandstones, northwestern Scotland. Master's thesis, The University of Texas at Austin, 342 p.

Dutrow, B.L., Travis, B.J., Gable, C.W., and Henry, D.J., 2001. Coupled heat and silica transport associated with dike intrusion into sedimentary rock: Effects on isotherm location and permeability evolution. Geochimica et Cosmochimica Acta 65 (21), 3749-3767.

Dutton, S.P., Laubach, S.E., Tye, R.S., Baumgardner, R.W., Jr., and Herrington, K.L., 1991. Geologic characterization of low-permeability gas reservoirs, Travis Peak Formation, East Texas. The University of Texas at Austin, Bureau of Economic Geology Report of Investigations 204, 89 p.

Eichhubl, P. and Boles, J.R., 1998. Vein formation in relation to burial diagenesis in the Miocene Monterey Formation, Arroyo Burro Beach, Santa Barbara, California, *in* Eichhubl, P., *ed*., Diagenesis, deformation, and fluid flow in the Miocene Monterey Formation of coastal California. SEPM Pacific Section Special Publication 83, 15-36.

Eichhubl, P. and Boles, J.R., 2000. Rates of fluid flow in fault systems—evidence for episodic rapid fluid flow in the Miocene Monterey Formation, Coastal California. American Journal of Science 300, 571-600.

Eichhubl, P., Taylor, W.L., Pollard, D.D., and Aydin, A., 2004. Paleo-fluid flow and deformation in the Aztec Sandstone at the Valley of Fire, Nevada—Evidence for the coupling of hydrogeologic, diagenetic, and tectonic processes. GSA Bulletin 116 (9/10), 1120-1136.

Eichhubl, P., Laubach, S.E., Hooker, J.N., and Fall, A., 2009. 10^{-19} s^{-1} (abs.). Eos Transactions AGU 90 (52), Fall Meeting Supplement, Abstract T41E-02.

Ellis, M.A., Laubach, S.E., Eichhubl, P., Olson, J.E., and Hargrove, P., 2012. Fracture development and diagenesis of Torridon Group Applecross Formation, near An Teallach, NW Scotland: millennia of brittle deformation resilience? Journal of the Geological Society, London 169, 297-310.

Engelder, T., 1985. Loading paths to joint propagation during a tectonic cycle: an example from the Appalachian Plateau, U.S.A. Journal of Structural Geology 7 (3/4), 459-476.

English, J.M., 2012. Thermo-mechanical origin of regional fracture systems. AAPG Bulletin 96 (9), 1597-1625.

Erlich, R.N. and Coleman, J.L., 2005. Drowning of the Upper Marble Falls carbonate platform (Pennsylvanian), central Texas: A case of conflicting signals? Sedimentary Geology 175, 479-499.

Fagereng, A., 2011. Fractal vein distributions within a fault-fracture mesh in an exhumed accretionary mélange, Chrystalls Beach Complex, New Zealand. Journal of Structural Geology 33, 918-927.

Fall, A., Eichhubl, P., Cumella, S.P., Bodnar, R.J., Laubach,S.E., and Becker, S.P., 2012. Testing the basin-centered gas accumulation model using fluid inclusion observations: southern Piceance Basin, Colorado. AAPG Bulletin 96 (12).

Ferket, H., Guilhaumou, N., Roure, F., and Swennen, R., 2011. Insights from fluid inclusions, thermal and PVT modeling for paleo-burial and thermal reconstruction of the Córdoba petroleum system (NE Mexico). Marine and Petroleum Geology 28, 936-958.

Fischer, M.P., Higuera-Diaz, I.C., Evans, M.A., Perry, E.C., and Lefticariu, L., 2009. Fracture-controlled paleohydrology in a map-scale detachment fold: Insights from the analysis of fluid inclusions in calcite and quartz veins. Journal of Structural Geology 31, 1490-1510.

Fuller, C.M. and Sharp, J.M., 1992. Permeability and fracture patterns in extrusive volcanic rocks: Implications from the welded Santana Tuff, Trans-Pecos Texas. GSA Bulletin 104, 1485-1496.

Gale, J.F.W., 2002. Specifying lengths of horizontal wells in fractured reservoirs. SPE Reservoir Evaluation and Engineering 5, 266-272.

Gale, J.F.W., 2004. Self-organization of natural mode-I fracture apertures into power-law distributions. *In* 6th North America Rock Mechanics Symposium, Rock mechanics across borders and disciplines, June 5–9, Houston: ARMA/NARMS 04-488, CD-ROM [13 p].

Gale, J.F.W. and Gomez, L.A., 2007. Late opening-mode fractures in karst-brecciated dolostones of the Lower Ordovician Ellenburger Group, west Texas: Recognition, characterization, and implications for fluid flow. AAPG Bulletin 91, 1005-1023.

Gale, J.F.W. and Holder, J., 2008. Natural fractures in the Barnett Shale: Constraints on spatial organization and tensile strength with implications for hydraulic fracture treatment in shale-gas reservoirs. *In* 42nd US Rock Mechanics Symposium and 2nd U.S.–Canada Rock Mechanics Symposium: ARMA 08–96.

Gale, J.F.W. and Holder, J., 2010. Natural fractures in some US shales and their importance for gas production. Petroleum Geology Conference series 7, 1131-1140. doi: 10.1144/0071131.

Gale, J.F.W., Lander, R.H., Reed, R.M., and Laubach, S.E., 2010. Modeling fracture porosity evolution in dolostone. Journal of Structural Geology 32, 1201-1211.

Gillespie, P.A., Howard, C.B., Walsh, J.J., and Watterson, J., 1993. Measurement and characterisation of spatial distributions of fractures. Tectonophysics 226, 113-141.

Gillespie, P.A., Johnston, J.D., Loriga, M.A., McCaffrey, K.J.W., Walsh, J.J., and Watterson, J., 1999. Influence of layering on vein systematics in line samples. *In* McCaffrey, K. J. W., Longeran, L., and Wilkinson, J.J., *eds*., Fractures, Fluid Flow and Mineralization. Geological Society, London, Special Publications 155, 35-56.

Gillespie, P.A., Walsh, J.J., Watterson, J., Bonson, C.G., and Manzocchi, T., 2001. Scaling relationships of joint and vein arrays from The Burren, Co. Clare, Ireland. Journal of Structural Geology 23, 183-201.

Glazner, A.F. and Mills, R.D., 2012. Interpreting two-dimensional cuts through broken geologic objects: Fractal and non-fractal size distributions. Geosphere 8, 902-914.

Goldhammer, R.K., Lehmann, P.J., Todd, R.G., Wilson, J.L., Ward, W.C., Lawton, T.F., and Johnson, C.R., 1991. Sequence stratigraphy and cyclostratigraphy of the Mesozoic of the Sierra Madre Oriental, northeast Mexico. Houston: Gulf Coast Section, Society of Economic Paleontologists and Mineralogists Foundation, 85 p.

Goldhammer, R.K. and Johnson, C.A., 2001. Middle Jurassic-Upper Cretaceous paleogeographic evolution and sequence-stratigraphic framework of the northwest Gulf of Mexico rim. *In* C. Bartolini, R. T. Buffler, and A. Cantú-Chapa, *eds*., The western Gulf of Mexico Basin: Tectonics, sedimentary basins, and petroleum systems. AAPG Memoir 75, 45-81.

Goldstein, R.H. and Reynolds, T.J., 1994. Systematics of fluid inclusions in diagenetic minerals. SEPM Short Course Notes 31, 199 p.

Gomez, L.A., and Laubach, S.E., 2006. Rapid digital quantification of microfracture populations. Journal of Structural Geology 28, 408-420.

Gomez, L.A., 2007. Characterization of the spatial arrangement of opening-mode fractures. Ph.D. dissertation, The University of Texas at Austin, 844 p.

Gonzalez, M.A., Gonzalez, O.E., Pereya, F., Ramallo, E., and Tchilinguirian, P., 2004. Hoja geológica 2366-IV, Ciudad del Libertador General San Martín. Programa Nacional de Cartas Geológicas de la República Argentina 1:250.000, SEGEMAR, Buenos Aires, Boletín 274.

Götze, J., Plötze, M., and Habermann, D., 2001. Origin, spectral characteristics, and practical applications of the cathodoluminescence of quartz. Mineralogy and Petrology 71, 225-250.

Gray, G.G., Pottorf, R.J., Yurewicz, D.A., Mahon, K.I., Pevear, D.R., and Chuchla, R.J., 2001. Thermal and chronological record of syn- to post-Laramide burial and exhumation, Sierra Madre Oriental, Mexico. *In* C. Bartolini, Buffler, R. T., Cantú-Chapa, A., *eds.*, The western Gulf of Mexico Basin: Tectonics, sedimentary basins, and petroleum systems. AAPG Memoir 75, 159-181.

Green, P.F., Duddy, I.R., Gleadgow, A.J.W., Tingate, P.R., and Laslett, G.M., 1986. Thermal annealing of fission tracks in Apatite: 1. A qualitative description. Chemical Geology (Isotope Science Section) 59, 237-253.

Griffith, A.A., 1920. The phenomena of rupture and flow in solids. Philosophical Transactions of the Royal Society of London A221, 163-198.

Gross, M.R., and Engelder, T., 1995. Strain accommodated by brittle failure in adjacent units of the Monterey Formation, U.S.A.: scale effects and evidence for uniform displacement boundary conditions. Journal of Structural Geology 17 (9), 1303-1318.

Gudmundsson, A., 1987. Geometry, formation, and development of tectonic fractures on the Reykjanes Peninsula, southwest Iceland. Tectonophysics 139, 295-308.

Gudmundsson, A., 2011. Rock Fractures in Geological Processes. Cambridge: Cambridge University Press, 578 p.

Guerriero, V., Iannace, A., Mazzoli, S., Parente, M., Vitale, S., and Giorgioni, M., 2010. Quantifying uncertainties in multi-scale studies of fractured reservoir analogues: Implemented statistical analysis of scan line data from carbonate rocks. Journal of Structural Geology 32, 1271-1278.

Hall, A.M., 1991. Pre-Quaternary landscape evolution in the Scottish Highlands. Transactions of the Royal Society of Edinburgh. Earth Sciences 82, 1-26.

Hatton, C.G., Main, I.G., and Meredith, P.G., 1994. Non-universal scaling of fracture length and opening displacement. Nature 367, 160-162.

Haynes, F.M., 1984. Vein densities in drill core, Sierrita porphyry copper deposit, Pima County, Arizona. Economic Geology 79, 755-758.

Heffer, K.J. and Bevan, T.G., 1990. Scaling relationships in natural fractures: data, theory, and application. SPE 20981, 367-376.

Higuera-Diaz, I.C., Fischer, M.P., and Wilkerson, M.S., 2005. Geometry and kinematics of the Nuncios detachment fold complex: Implications for lithotectonics in northeastern Mexico. Tectonics 24, doi:10.1029/2003TC001615.

Hilgers, C. and Urai, J.L., 2002. Microstructural observations on natural syntectonic fibrous veins: implications for the growth process. Tectonophysics 32, 257-274.

Hobbs, D.W., 1967. The formation of tension joints in sedimentary rocks: an explanation. Geological Magazine 104, 550-556.

Holdsworth, R.E., Alsop, G.I., and Strachan, R.A., 2007. Tectonic stratigraphy and structural continuity of the northernmost Moine Thrust Zone and Moine Nappe, Scottish Caledonides. *In*: Ries, A.C., Butler, R.W.H., and Graham, R.D., *eds*., Deformation of the Continental Crust: The legacy of Mike Coward. Geological Society, London, Special Publications 272, 123-144.

Holford, S.P., Green P.F., Hillis, R.R., Underhill, J.R., Stoker, M.S., and Duddy, I.R., 2010. Multiple post-Caledonian exhumation episodes across NW Scotland revealed by apatite fission track analysis. Journal of the Geological Society, London 167, 675-694.

Holland, M. and Urai, J.L., 2010. Evolution of anastomosing crack-seal vein networks in limestones: Insight from an exhumed high-pressure cell, Jabal Shams, Oman Mountains. Journal of Structural Geology 32, 1279-1290.

Holtz, M.H. and Kerans, C., 1992. Characterization and classification of west Texas Ellenburger reservoirs. *In* Candelaria, M.P. and Reed, C.L., *eds*., Paleokarst, karst related diagenesis and reservoir development: Examples from Ordovician–Devonian age strata of west Texas and the midcontinent. Permian Basin SEPM Publication 92-33, 45-54.

Hooker, J.N., Marrett, R., and Laubach, S.E., 2002. Timing of faults and extension fractures in the Sierra Madre Oriental, northeastern Mexico. Gulf Coast Association of Geological Societies Transactions 52, 421-428.

Hooker, J.N. and Laubach, S.E., 2007. The geologic history of quartz grains, as revealed by color SEM-CL. Gulf Coast Association of Geological Societies Transactions 57, 375-386.

Hooker, J.N., Gale, J.F.W., Gomez, L.A., Laubach, S.E., Marrett, R., and Reed, R.M., 2009. Aperture-size scaling variations in a low-strain opening-mode fracture set, Cozzette Sandstone, Colorado. Journal of Structural Geology 31, 707-718.

Hooker, J.N. and Laubach, S. E., 2010. Using empirical trends in fracture size-frequency data to constrain subsurface fracture abundance. 44th U.S. Rock Mechanics Symposium and 5th U.S.–Canada Rock Mechanics Symposium, Salt Lake City, June 27-30: ARMA 10-325, 11 p.

Hooker, J.N., Laubach, S.E., Gomez, L.A., Marrett, R., Eichhubl, P., Diaz-Tushman, K., and Pinzon, E., 2011. Fracture size, frequency, and strain in the Cambrian Eriboll Formation sandstones, NW Scotland. Scottish Journal of Geology 47, 45-56.

Hooker, J.N., Gomez, L.A., Laubach, S.E., Gale, J.F.W., and Marrett, R., 2012. Effects of diagenesis (cement precipitation) during fracture opening on fracture aperture-size scaling in carbonate rocks. Geological Society, London, Special Publications 370, doi: 10.1144/SP370.9.

Horton, B.K., 2005. Revised deformation history of the central Andes: Inferences from Cenozoic foredeep and intermontane basins of the Eastern Cordillera, Bolivia. Tectonics 24, TC3011, doi:10.1029/2003TC001619.

Imlay, R.W., 1937. Geology of the middle part of Sierra de Parras, Coahuila, Mexico. Geological Society of America Bulletin 48, 587-630.

Iñigo, J.F., Laubach, S.E., and Hooker, J.N., 2012. Fracture abundance and patterns in the Subandean fold and thrust belt, Devonian Huamampampa Formation petroleum reservoirs and outcrops, Argentina and Bolivia. Marine and Petroleum Geology 35, 201-218.

Jensen, J.L., Lake, L.W., Corbett, P.W.M., and Goggin, D.J., 2000. Statistics for petroleum engineers and geoscientists. Amsterdam: Elsevier, 338 p.

Johnson, R.C. and Keighin, C.W., 1981. Cretaceous and Tertiary history and resources of the Piceance Creek basin, western Colorado. New Mexico Geological Society Guidebook, 32nd Field Conference, Western Slope Colorado.

Johnston, J.D. and McCaffrey, K.J.W., 1996. Fractal geometries of vein systems and the variation of scaling relationships with mechanism. Journal of Structural Geology 18, 349-358.

Kagan, Y.Y., 1997. Seismic moment-frequency relation for shallow earthquakes: Regional comparison. Journal of Geophysical Research 102 (B2), 2835-2852.

Kagan, Y.Y. and Jackson, D.D., 1991. Long-term earthquake clustering. Geophysical Journal International 104, 117-133.

Kawabe, I., 1978. Calculation of oxygen isotope fractionation in quartz-water system with special reference to the low temperature fractionation. Geochimica et Cosmochimica Acta 42 (6), 613-621.

Kaylor, A., 2011. A fluid inclusion and cathodoluminescence approach to reconstruct fracture growth in the Triassic-Jurassic La Boca Formation, northeastern Mexico. Master's thesis, The University of Texas at Austin, 202 p.

Ketcham, R.A., 2005. Forward and inverse modeling of low-temperature thermochronometry data. Reviews in Mineralogy and Geochemistry 58, 275-314.

Kinnaird, T.C., Prave, A.R., Kirkland, C.L., Horstwood, M., Parrish, R., and Batchelor, R.A., 2007. The late Mesoproterozoic-early Neoproterozoic tectonostratigraphic evolution of NW Scotland: the Torridonian revisited. Journal of the Geological Society, London 164, 541-551.

Kley, J., Müller, J., Tawacholi, S., Jacobshagen, V., and Manutsoglu, E., 1997. Pre-Andean and Andean-age deformation in the Eastern Cordillera of southern Bolivia. Journal of South American Earth Sciences 10, 1-19.

Kley, J., Rossello, E. A., Monaldi, C. R., and Habighorst, B., 2005. Seismic and field evidence for selective inversion of Cretaceous normal faults, Salta rift, northwest Argentina. Tectonophysics 399, 155-172.

Kreemer, C., Holt, W.E., and Haines, A.J., 2003. An integrated global model of present-day plate motions and plate boundary deformation. Geophysical Journal International 154, 8-34.

Kuiper, N.H., 1960. Tests concerning random points on a circle. Proceedings of the Koninklijke Nederlandse Akademie van Wetenschappen (A) 63, 38–47.

Kumpa, M. and Sanchez, M.C., 1988. Geology and sedimentology of the Cambrian Grupo Mesón (NW Argentina). *In* Bahlburg, H., Breitkreuz, C., and Giese, P., *eds*., Lecture notes in Earth Sciences 17: The South Central Andes: Contributions to Structure and Evolution of an Active Continental Margin. Berlin: Springer-Verlag, 261 p.

Ladeira, F.L. and Price, N.J., 1981. Relationship between fracture spacing and bed thickness. Journal of Structural Geology 3 (2), 179-183.

LaPointe, P.R. and Hudson, J.A., 1985. Characterization and interpretation of rock mass joint patterns. GSA Special Papers 199, 37 p.

Lander, R.H. and Walderhaug, O., 1999. Porosity prediction through simulation of sandstone compaction and quartz cementation. AAPG Bulletin 83, 433-449.

Lander, R.H., Larese, R.E., and Bonnell, L.M., 2008. Toward more accurate quartz cement models—The importance of euhedral vs. non-euhedral growth rates. AAPG Bulletin 92, 1537-1564.

Latta, D.K. and Anastasio, D.J., 2007. Multiple scales of mechanical stratification and decollement fold kinematics, Sierra Madre Oriental foreland, northeast Mexico. Journal of Structural Geology 29, 1241-1255.

Laubach, S.E., 1988. Subsurface fractures and their relationship to stress history in East Texas Basin sandstone. Tectonophysics 156, 37-49.

Laubach, S.E. and Marshak, S., 1987. Fault patterns generated during extensional deformation of crystalline basement, NW Scotland. *In* Coward, M.P., Dewey, J.F., and Hancock, P.L., *eds*., Continental extensional tectonics. Geological Society, London, Special Publications 28, 495-499.

Laubach, S.E., 1989. Paleostress directions from the preferred orientation of closed microfractures (fluid-inclusion planes) in sandstone, East Texas basin, U.S.A. Journal of Structural Geology 11, 603-611.

Laubach, S.E. and Jackson, M.L.W., 1990. Origin of arches in the northwestern Gulf of Mexico basin. Geology 18, 595-598.

Laubach, S.E., Hentz, T.F., Johns, M.K., Baek, H., and Clift, S.J., 1995a. Using diagenesis information to augment fracture analysis. Bureau of Economic Geology report for the Gas Research Institute, Contract No.5082-211-0708, 189 p.

Laubach, S.E., Mace, R.E., and Nance, H.S., 1995b. Fault and joint swarms in a normal fault zone. *In* Rossmanith, H.-P., *ed*., Mechanics of jointed and faulted rock. Rotterdam: Balkema, 305-309.

Laubach, S.E., 1997. A method to detect natural fracture strike in sandstones. AAPG Bulletin 81 (4), 604-623.

Laubach, S.E., 2003. Practical approaches to identifying sealed and open fractures: AAPG Bulletin 87 (4), 561–579.

Laubach, S.E., Lander, R.H., Bonnell, L.M., Olson, J.E., and Reed, R.M., 2004a. Opening histories of fractures in sandstones. *In* Cosgrove, J.W. and Engelder, T., *eds*., The initiation, propagation, and arrest of joints and other fractures. Geological Society, London, Special Publications 231, 1-9.

Laubach, S.E., Olson, J.E., and Gale, J.F.W., 2004b. Are open fractures necessarily aligned with maximum horizontal stress? Earth and Planetary Science Letters 222 (1), 191–195.

Laubach, S.E., Reed, R.M., Olson, J.E., Lander, R.H., and Bonnell, L.M., 2004c. Coevolution of crack-seal texture and fracture porosity in sedimentary rocks: cathodoluminescence observations of regional fractures. Journal of Structural Geology 26 (5), 967-982.

Laubach, S.E. and Ward, M.E., 2006. Diagenesis in porosity evolution of opening-mode fractures, Middle Triassic to Lower Jurassic La Boca Formation, NE Mexico. Tectonophysics 419 (1-4) 75-97.

Laubach, S.E. and Diaz-Tushman, K., 2009. Laurentian palaeostress trajectories and ephemeral fracture permeability, Cambrian Eriboll Group sandstones west of the Moine Thrust Zone, northwest Scotland. Journal of the Geological Society, London 166 (2), 345-360.

Lee, Y-.J. and Wiltschko, D.V., 2000. Fault controlled sequential vein dilation: competition between slip and precipitation rates in the Austin Chalk, Texas. Journal of Structural Geology 22, 1247-1260.

Longstaffe, F.J. and Ayalon, A., 1991. Mineralogical and O-isotope studies of diagenesis and porewater evolution in continental sandstones, Cretaceous Belly River Group, Alberta, Canada. Applied Geochemistry 6, 291-303.

Loriga, M.A., 1999. Scaling systematics of vein size: an example from the Guanajuato mining district (central Mexico). Geological Society, London, Special Publications 155, 57-67.

Mai, P.M. and Beroza, G.C., 2002. A spatial random field model to characterize complexity in earthquake slip. Journal of Geophysical Research 107 (B11), 2308, doi:10.1029/2001JB000588.

Makowitz, A. and Milliken, K.L., 2003. Quantification of brittle deformation in compaction, Frio and Mt. Simon sandstones. Journal of Sedimentary Research 73, 1007–1021.

Mandelbrot, B.B., 1982. The Fractal Geometry of Nature. San Francisco, W.H. Freeman, 460 p.

Marrett, R. and Allmendinger, R.W., 1992. Amount of extension on "small" faults: an example from the Viking graben. Geology 20, 47-50.

Marrett, R., 1996. Aggregate properties of fracture populations. Journal of Structural Geology 18, 169-178.

Marrett, R., Ortega, O.J., and Kelsey, C.M., 1999. Extent of power-law scaling for natural fractures in rock. Geology 27 (9), 799-802.

Marrett, R. and Aranda-García, M., 2001. Regional structure of the Sierra Madre Oriental fold-thrust belt, Mexico. *In* Marrett, R., *ed*., Genesis and controls of reservoir-scale carbonate deformation, Monterrey salient, Mexico. Bureau of Economic Geology Guidebook 28, 31-55.

Marrett, R., Laubach, S.E., and Olson, J.E., 2007. Anisotropy and beyond: Geologic perspectives on geophysical prospecting for natural fractures. The Leading Edge 26 (9), 1106-1111.

Matthews, A. and Beckinsale, R.D., 1979. Oxygen isotope equilibration systematics between quartz and water. American Mineralogist 64, 232-240.

McCaffrey, K.J.W. and Johnston, J.D., 1996. Fractal analysis of a mineralised vein deposit: Curraghinalt gold deposit, County Tyrone. Mineralum Deposita 31, 52-58.

McCaffrey, K.J.W. and Petford, N., 1997. Are granitic intrusions scale invariant? Journal of the Geological Society, London 154, 1-4.

McKerrow, W.S., Brasier, M.D., and Scotese, C. R., 1992. Early Cambrian continental reconstructions. Journal of the Geological Society, London 149, 599-606.

Michalzik, D., 1991. Facies sequence of Triassic-Jurassic red beds in the Sierra-Madre Oriental (NE Mexico) and its relation to the early opening of the Gulf-of-Mexico. Sedimentary Geology 71, 243-259.

Milliken, K.L., 1994. Cathodoluminescent textures and the origin of quartz silt in Oligocene mudrocks, South Texas. Journal of Sedimentary Research A64, 567–571.

Milnor, J., 1985. On the concept of attractor. Communications in Mathematical Physics 99, 177-195.

Mixon, R.B., Murray, G.E., and Diaz-Gonzales, T.E., 1959. Age and correlation of Huizachal Group (Mesozoic), State of Tamaulipas, Mexico. AAPG Bulletin 43 (4), 757–771.

Mon, R. and Hongn, F., 1991. The structure of the Precambrian and Lower Paleozoic basement of the Central Andes between 22° and 32°S. Lat. Geologische Rundschau 80, 745-758.

Mon, R. and Salfity, J.A., 1995. Tectonic evolution of the Andes of northern Argentina. *In* Tankard, A.J., Suarez Soruco, R., and Welsink, H.J., *eds*., Petroleum basins of South America. AAPG Memoir 62, 269-283.

Morad, S., Ketzer, J.M., and De Ros, L.F., 2000. Spatial and temporal distribution of diagenetic alterations in siliciclastic rocks: implications for mass transfer in sedimentary basins. Sedimentology 47, 95-120.

Morgan, F.L., 2011. Fracture aperture and spacing patterns in two folded quartz arenites: Cambrian Flathead Formation, Teton Range, Wyoming and Cambrian Eriboll Formation, Northwest Scotland. Bachelor's thesis, The University of Texas at Austin, 59 p.

Moros, J.G., 1999. Relationship between fracture aperture and length in sedimentary rocks. Master's thesis, The University of Texas at Austin, 120 p.

Morse, J.W., Arvidson, R.S., and Lüttge, A., 2007. Calcium carbonate formation and dissolution. Chemical Reviews 107, 342-381.

Mróz, K.P. and Mróz, Z., 2010. On crack path evolution rules. Engineering Fracture Mechanics 77, 1781-1807,

Müller, A., Wiedenbeck, M., van den Kerkhof, A.M., Kronz, A., and Simon, K., 2003. Trace elements in quartz—a combined electron microprobe, secondary ion mass spectrometry, laser-ablation ICP-MS, and cathodoluminescence study. European Journal of Mineralogy 15, 747-763.

Müller, A., van den Kerkhof, A.M., Behr, H.-J., Kronz, A., and Koch- Müller, M., 2010. The evolution of late-Hercynian granites and rhyolites documented by quartz—a review. Earth and Environmental Science Transactions of the Royal Society of Edinburgh 100, 185-204.

Murray, B.A., 2007. Two paradigms in landscape dynamics: self-similar processes and emergence. *In* Tsonis, A.A. and Elsner, J.B., *eds*., Nonlinear Dynamics in Geosciences. New York: Springer, 17-35.

Narr, W., 1996. Estimating average fracture spacing in subsurface rock. AAPG Bulletin 80, 1565-1586.

Nelson, R.A., 1985. Geologic Analysis of Naturally Fractured Reservoirs. Houston: Gulf Publishing, 320 p.

Nuccio, V.F. and Condon, S.M., 1996. Burial and thermal history in the Paradox basin, Utah and Colorado, and petroleum potential of the Middle Pennsylvanian Paradox Formation. U.S. Geological Survey Bulletin 2000-O.

Nuccio, V.F. and Roberts, L.N.R., 2003. Chapter 4: Thermal maturity and oil and gas generation history of petroleum systems in the Uinta-Piceance Province, Utah and Colorado, in Petroleum systems and geologic assessment of oil and gas in the Uinta-Piceance Province, Utah and Colorado. U.S. Geological Survey Digital Data Series DDS-69-B.

Nur, A., 1982. The origin of tensile fracture lineaments. Journal of Structural Geology 4 (1), 31-40.

Ocampo-Diaz, Y.Z.E., Jenchen, U., and Guerrero-Suastegui, M., 2008. Facies and depositional systems of the Galeana Sandstone Member (Taraises Formation, Lower Cretaceous, northeastern Mexico). Revista Mexicana De Ciencias Geologicas 25, 438-464.

Odling, N.E., 1997. Scaling and connectivity of joint systems in sandstones from western Norway. Journal of Structural Geology 19 (10), 1257-1271.

Odling, N.E., Gillespie, P., Bourgine, B., Castaing, C., Chiles, J-P., Christensen, N.P., Fillion, E., Genter, A., Olsen, C., Thrane, L., Trice, R., Aarseth, E., Walsh, J.J., and Watterson, J., 1999. Variations in fracture system geometry and their implications for fluid flow in fractured hydrocarbon reservoirs. Petroleum Geoscience 5, 373-384.

Olson, J.E., 1993. Joint pattern development: Effects of subcritical crack-growth and mechanical crack interaction. Journal of Geophysical Research 98, 12,251-12,265.

Olson, J.E., 2003. Sublinear scaling of fracture aperture versus length: An exception or the rule? Journal of Geophysical Research 108 (B9), 2413, doi:10.1029/2001JB000419.

Olson, J.E., 2007. Fracture aperture, length and pattern geometry development under biaxial loading: a numerical study with applications to natural, cross-jointed systems. Geological Society, London, Special Publications 289, 123-142.

Olson, J.E, Laubach, S.E., and Lander, R.H., 2009. Natural fracture characterization in tight gas sandstones: Integrating mechanics and diagenesis. AAPG Bulletin 93, 1535-1549.

Ortega, O.J. and Marrett, R., 2000. Prediction of macrofracture properties using microfracture information, Mesaverde Group sandstones, San Juan basin, New Mexico. Journal of Structural Geology 22 (5), 571-588.

Ortega, O.J., 2002. Fracture-size scaling and stratigraphic controls on fracture intensity. Ph.D. dissertation, The University of Texas at Austin, 427 p.

Ortega, O.J., Marrett, R., and Laubach, S.E., 2006. A scale-independent approach to fracture intensity and average spacing measurement. AAPG Bulletin 90 (2), 193-208.

Ortega, O.J., Gale, J.F.W., and Marrett, R., 2010. Quantifying diagenetic and stratigraphic controls on fracture intensity in platform carbonates. Journal of Structural Geology 32, 1943-1959.

Padilla y Sanchez, R.J., 1985. Las estructuras de la Curvatura de Monterrey, estados de Coahuila, Nuevo León, Zacatecas y San Luis Potosí. Universidad Nacional Autonomia de México Revista— Instituto de Geología 6, 1-20.

Park, R.G., Stewart, A.D., and Wright, D.T., 2002. The Hebridean terrane. *In*: Trewin, N.H., *ed*., The Geology of Scotland. London: The Geological Society, 45-81.

Parmentier, E.M. and Schedl, A., 1981. Thermal aureoles of igneous intrusions: some possible indications of hydrothermal convective cooling. Journal of Geology 89 (1), 1-22.

Peach, B.N., Horne, J., Gunn, W., Clough, C.T., Hinxman, L.W., and Teall, J.J., 1907. The Geological Structure of the Northwest Highlands of Scotland. Memoirs of the Geological Survey, U.K.

Peacock, D.C.P., 2004. Differences between veins and joints using the example of the Jurassic limestones of Somerset. *In* Cosgrove, J.W. and Engelder, T., *eds*., The initiation, propagation, and arrest of joints and other fractures. Geological Society, London, Special Publications 231, 209-221.

Persaud, M. and Pfiffner, O.A., 2004. Active deformation in the eastern Swiss Alps: post-glacial faults, seismicity and surface uplift. Tectonophysics 385, 59-84.

Philip, Z.G., Jennings, J.W., Jr., Olson, J.E., Laubach, S.E., and Holder, J., 2005. Modeling coupled fracture-matrix fluid flow in geomechanically simulated fracture networks. SPE Reservoir Evaluation & Engineering 8, 300-309.

Pickering, G., Bull, J.M., and Sanderson, D.J., 1995. Sampling power law distributions. Tectonophysics 248 (1-2), 1-20.

Pinzon, E.A., 2007. Fracture pattern prediction using geomechanical models incorporating diagenesis, with comparison to outcrop data (Cambrian Eriboll Group sandstones, Northwest Scotland) and core observations (Tertiary Mirador Formation sandstones, Llanos foothills Colombia). Master's thesis, The University of Texas at Austin, 158 p.

Pisarenko, V.F. and Sornette, D., 2004. Statistical detection and characterization of a deviation from the Gutenberg-Richter distribution above Magnitude 8. Pure and Applied Geophysics 161, 839-864.

Poblet, J. and Bulnes, M., 2007. Predicting strain using forward modelling of restored cross-sections: Application to rollover anticlines over listric normal faults. Journal of Structural Geology 29, 1960-1970.

Pollard, D.D. and Aydin, A., 1988. Progress in understanding jointing over the past century. GSA Bulletin 100, 1181-1204.

Poulton, T.P., Tittemore, J., and Dolby, G., 1990. Jurassic strata of northwestern (and west-central) Alberta and northeastern British Columbia. Bulletin of Canadian Petroleum Geology 38A, 159-175.

Quigley, M.D., 1965. Geologic history of Piceance Creek-Eagle basins. Bulletin of the American Association of Petroleum Geologists 49 (11), 1974-1996.

Ramsay, J.G., 1980. The crack-seal mechanism of rock deformation. Nature 284, 135–139.

Ramseyer, K. and Mullis, J., 1990. Factors influencing short-lived blue cathodoluminescence of α-quartz. American Mineralogist 75, 791-800.

Reed, R.M. and Milliken, K.L., 2003. How to overcome imaging problems associated with carbonate minerals on SEM-based cathodoluminescence systems. Journal of Sedimentary Research 73 (2), 328-332.

Renard, F., Andréani, M., Boullier, A.-M., and Labaume, P., 2005. Crack-seal patterns: records of uncorrelated stress release variations in crustal rocks. *In* Gapais, D., Brun, J.P., and Cobbold, P.R., *eds*., Deformation mechanisms, rheology and tectonics: from minerals to the lithosphere. Geological Society, London, Special Publications 243, 67-79.

Renshaw, C.E. and Park, J.C., 1997. Effect of mechanical interactions on the scaling of fracture length and aperture. Nature 386, 482-484.

Roberts, A.M. and Holdsworth, R.E., 1999. Linking onshore and offshore structures: Mesozoic extension in the Scottish Highlands. Journal of the Geological Society, London 156, 1061-1064.

Roedder, E., 1984. Fluid Inclusions. Mineralogical Society of America, Reviews in Mineralogy 12, 644 p.

Rubiolo, D., Seggiaro, R., Gallardo, E., Disalvo, A., Sanchez, M., Turel, A., Ramallo, E., Sandruss, A., and Godeas, M., 2001. Hoja Geológica 2366-II / 2166-IV, La Quiaca. Geología y Provincias de Jujuy y Salta. Instituto de Recursos Minerales, Servicio Geológico Minero Argentino Boletín 246, 87 p.

Rusk, B., and Reed, M., 2002. Scanning electron microscope-cathodoluminescence analysis of quartz reveals complex growth histories in veins from the Butte porphyry copper deposit, Montana. Geology 30 (8), 727-730.

Rusk, B.G., Reed, M.H., Dilles, J.H., and Kent, A.J.R., 2006. Intensity of quartz cathodoluminescence and trace-element content in quartz from the porphyry copper deposit at Butte, Montana. American Mineralogist 91, 1300-1312.

Sanderson, D.J., Roberts, S., and Gumiel, P., 1994. A fractal relationship between vein thickness and gold grade in drill core from La Codosera, Spain. Economic Geology 89, 168-173.

Seyedolali, A., Krinsley, D.H., Boggs, S., Jr., O'Hara, P.F., Dypvik, H., and Goles, G.G., 1997. Provenance interpretation of quartz by scanning electron microscope-cathodoluminescence fabric analysis. Geology 25 (9), 787-790.

Sharp, Z.D., 1990. A laser-based microanalytical method for *in situ* determination of oxygen isotope ratios of silicates and oxides. Geochimica et Cosmochimica Acta 54 (5), 1353-1357.

Sibson, R., 1977. Fault rocks and fault mechanisms. Journal of the Geological Society, London 133, 191-213.

Siks, B.C. and Horton, B.K., 2011. Growth and fragmentation of the Andean foreland basin during eastward advance of fold-thrust deformation, Puna Plateau and Eastern Cordillera, northern Argentina. Tectonics 30, TC6017, doi:10.1029/2011TC002944.

Sornette, D. and Sornette, A., 1999. General theory of the modified Gutenberg-Richter Law for large seismic moments. Bulletin of the Seismological Society of America 89 (4), 1121-1130.

Sprunt, E.S. and Nur, A., 1979. Microcracking and healing in granites: New evidence from cathodoluminescence. Science 205, 495-497.

Steele-MacInnis, M., Lecumberri-Sanchez, P., and Bodnar, R.J., 2012. HOKIEFLINCS_H2O-NACL: A Microsoft Excel spreadsheet for interpreting microthermometric data from fluid inclusions based on the PVTX properties of H_2O-NaCl. Computers and Geosciences doi:10.1016/j.cageo.2012.01.022.

Sterner, S.M. and Bodnar, R.J., 1984. Synthetic fluid inclusions in natural quartz I. Compositional types synthesized and applications to experimental geochemistry. Geochimica et Cosmochimica Acta 48, 2659-2668.

Stewart, A.D., 2002. The later Proterozoic Torridonian rocks of Scotland: their sedimentology, geochemistry and origin. Geological Society, London, Memoir 24, 130 p.

Stowell, J.F.W., 2001. Characterization of opening-mode fracture systems in the Austin Chalk. Gulf Coast Association of Geological Societies Transactions 51, 313-319.

Strachan, R.A., Smith, M., Harris, A.L., and Fettes, D.J., 2002. The northern Highland and Grampian terranes. *In*: Trewin, N.H., *ed*., The Geology of Scotland. London: The Geological Society, 81-148.

Strachan, R.A., Holdsworth, R.E., Krabbendam, M., and Alsop, G.I., 2010. The Moine Supergroup of NW Scotland: insights into the analysis of polyorogenic supracrustal sequences. *In*: Law, R., Butler, R.W.H., Strachan, R.A., and Krabbendam, M., *eds*., Continental tectonics and mountain building: the legacy of Peach and Horne. Geological Society Special Publications 335, 233-254.

Such, P., Buatois, L.A., and Mángano, M.G., 2007. Stratigraphy, depositional environments and ichnology of the Lower Paleozoic in the Azul Pampa area – Jujuy Province. Revista de la Asociación Geológica Argentina 62 (3), 331-344.

Supak, S., Bohnenstiehl, D.R., and Buck, W.R., 2006. Flexing is not stretching: An analogue study of flexure-induced fault populations. Earth and Planetary Science Letters 246, 125-137.

Trewin, N.H. and Rollin, K.E., 2002. Geological history and structure of Scotland. *In* Trewin, N.H., *ed*., The Geology of Scotland. London: The Geological Society, 577 p.

Turnbull, M.J.M., Whitehouse, M.J., and Moorbath, S., 1996. New isotopic age determinations for the Torridonian, NW Scotland. Journal of the Geological Society, London 153, 955-64.

Turner, J.C.M., 1958. Estratigrafia del cordón de Escaya y de la Sierra de Rinconado (Jujuy). Revista de la Asociación Geológica Argentina 18, 15-89.

Turner, J.C.M., 1960. Estratigrafía de la Sierra se Santa Victoria y adyacencias. Academia Nacional de Ciencias, Boletín 41 (2), 163-196.

Turner, J.C.M., 1970. The Andes of Northwestern Argentina. Geologische Rundschau 59, 1028-1063.

Urai, J.L., Williams, P.F., and van Roermund, H.L.M., 1991. Kinematics of crystal growth in syntectonic fibrous veins. Journal of Structural Geology 13 (7), 823-836.

Valley, J.W., Kitchen, N., Kohn, M.J., Niendorf, C.R., and Spicuzza, M.J., 1995. UWG-2, a garnet standard for oxygen isotope ratios: Strategies for high precision and accuracy with laser heating. Geochimica et Cosmochimica Acta 59 (24), 5223-5231.

van den Kerkhof, A.M., Kronz, A., Simon, K., Riganti, A., and Scherer, T., 2004a. Origin and evolution of Archean quartzites from the Nondweni greenstone belt (South Africa): inferences from a multidisciplinary study. South African Journal of Geology 107, 559-576.

van den Kerkhof, A.M., Kronz, A., Simon, K., and Scherer, T., 2004b. Fluid-controlled quartz recovery in granulite as revealed by cathodoluminescence and trace element analysis (Bamble sector, Norway). Contributions to Mineral Petrology 146, 637-652.

Vermilye, J.M. and Scholz, C.H., 1995. Relation between vein length and aperture. Journal of Structural Geology 17 (3), 423-434.

Vollbrecht, A., Rust, S., and Weber, K., 1991. Development of microcracks in granites during cooling and uplift: examples from the Variscan basement in NE Bavaria, Germany. Journal of Structural Geology 13 (7), 787-799.

Walderhaug, O., 1994. Precipitation rates for quartz cement in sandstones determined by fluid-inclusion microthermometry and temperature-history modeling. Journal of Sedimentary Research A64 (2), 324-333.

Ward, M.E., 2006. Opening history and porosity evolution of fractures in sandstone, Triassic to Jurassic La Boca Formation, northeast Mexico. Master's thesis, The University of Texas at Austin, 313 p.

Watt, G.R., Oliver, N.H.S., and Griffin, B.J., 2000. Evidence for reaction-induced microfracturing in granulite facies migmatites. Geology 28 (4), 327-330.

Wilson, T.J. and Paulsen, T.S., 1998. CRP-1 fracture arrays: constraints on the Neogene-Quaternary stress regime along the Transantarctic Mountains Front, Antarctica. Terra Antarctica 5 (3), 327-335.

Wilson, R.W., Holdsworth, R.E., Wild, L.E., McCaffrey, K.J.W., England, R.W., Imber, J., and Strachan, R.A., 2010. Basement-influenced rifting and basin development: a reappraisal of post-Caledonian faulting patterns from the North Coast Transfer Zone, Scotland. *In*: Law, R., Butler, R.W.H., Strachan, R.A., and Krabbendam, M., *eds*., Continental tectonics and mountain building: the legacy of Peach and Horne. Geological Society Special Publications 335, 795-826.

Wong, T.-F., Friedrich, J.T., and Gwanmesia., G.D., 1989. Crack aperture statistics and pore space fractal geometry of Westerly Granite and Rutland Quartzite:

implications for an elastic contact model of rock compressibility. Journal of Geophysical Research 94, 10,267-10,278.

Woodward, N.B., 2012. Evaluation, analysis and prediction of geologic structures. Journal of Structural Geology 41, 76-85.

Worden, R.H. and Morad, S., 2000. Quartz cementation in oilfield sandstones: a review of the key controversies. *In* Worden, R.H. and Morad, S., *eds*., Quartz cementation in sandstones. International Association of Sedimentologists, Special Publication 29, doi:10.1002/9781444304237.ch1.

Wright, S.C., 1985. The Study of the Depositional Environments and Diagenesis of the Durness Group of North-West Scotland. Ph.D. dissertation, The University of Oxford.

Xu, G., 2012. Fluid inclusion studies of microfractures in Eriboll Formation, NW Scotland: insights into timing of fracture opening. Master's thesis, The University of Texas at Austin, 210 p.

Young, G.M., 1999. Some aspects of the geochemistry, provenance and paleoclimatology of the Torridonian of NW Scotland. Journal of the Geological Society, London 156, 1097-1111.

Zhou, Y., Murphy, M.A., and Hamade, A., 2006. Structural development of the Peregrina-Huizachal anticlinorium, Mexico. Journal of Structural Geology 28, 494-507.

Zinkernagel, U., 1978. Cathodoluminescence of quartz and its application to sandstone petrology. Contributions to Sedimentology 8, 1-69.

Vita

John Noel Hooker was born in 1977 to Ann Manes and David Hooker. In 1995 he graduated from Central High School in Beaumont, Texas, and enrolled at The University of Texas at Austin. He earned a B.A. in 2000 and an M.S. in 2004, the latter supervised by Randy Marrett. In 2010 he married Jill Lieberman; their son, August, was born in 2012.

Permanent address: 515 Sacramento Drive, Austin, Texas 78704
This dissertation was typed by the author.